C55.612:979

PENNSYLVANIA STATE UNIVERSITY
MAY 03 1981
DOCUMENTS COLLECTION

Collected Reprints 1979

Atlantic Oceanographic and Meteorological Laboratories

December 1980

U.S. DEPARTMENT OF COMMERCE
National Oceanic and Atmospheric Administration

Digitized by the Internet Archive
in 2012 with funding from
LYRASIS Members and Sloan Foundation

http://archive.org/details/collectedreprint1979atla

Collected Reprints 1979

Atlantic Oceanographic and Meteorological Laboratories
Miami, Florida

December 1980

Boulder, Colorado

U.S. DEPARTMENT OF COMMERCE
Philip M. Klutznick, Secretary

National Oceanic and Atmospheric Administration
Richard A. Frank, Administrator

Environmental Research Laboratories
Joseph O. Fletcher, Acting Director

NOTICE

The Environmental Research Laboratories do not approve, recommend, or endorse any proprietary product or proprietary material mentioned in this publication. No reference shall be made to the Environmental Research Laboratories or to this publication furnished by the Environmental Research Laboratories in any advertising or sales promotion which would indicate or imply that the Environmental Research Laboratories approve, recommend, or endorse any proprietary product or proprietary material mentioned herein, or which has as its purpose an intent to cause directly or indirectly the advertised product to be used or purchased because of this Environmental Research Laboratories publication.

FOREWORD

The Atlantic Oceanographic and Meteorological Laboratories conduct research programs in the areas of physical, chemical, and geological oceanography, and sea-air interaction. Collected Reprints from these laboratories have been published for distribution to the libraries of scientific institutions here and abroad annually since the laboratories were established in 1965. The series provides a single reference source for articles published by AOML personnel in a broad spectrum of scientific and technical publications. Some back issues may be obtained upon request.

The volume, like the laboratories, is organized along functional, disciplinary, lines. Cross-disciplinary contributions resulting from collaboration among staff of the several parts of the organization appear according to the organizational affiliations of the senior author.

It is desired that those recipients with whom we do not already have an exchange arrangement will add the AOML Library to the distribution list for any relevant publications from their institution.

H. F. Bezdek, Director
Atlantic Oceanographic and
Meteorological Laboratories
4301 Rickenbacker Causeway
Miami, Florida 33149

CONTENTS

Page

Foreword iii

OFFICE OF THE DIRECTOR

1. Johnson, R. W., R. M. Glasgow, I. W. Duedall, and J. R. Proni

Monitoring the Temporal Dispersion of a Sewage Sludge Plume. Photogrammetric Engineering and Remote Sensing 45, No. 6, 763-768. 1

2. Proni, J. R., F. Ostapoff, and R. L. Sellers

Reply to Farmer and Smith's Letter to the Editor concerning the authors' "Acoustic Observations of . . . Internal Wave Groups . . ." Deep Sea Research 26A, 350. 7

PHYSICAL OCEANOGRAPHY LABORATORY

3. Behringer, D. W., L. Regier, and H. Stommel

Thermal Feedback on Wind-Stress as a Contributing Cause of the Gulf Stream. Journal of Marine Research 37, No. 4, 699-709. 8

4. Behringer, D. W.

On Computing the Absolute Geostrophic Velocity Spiral. Journal of Marine Research 37, No. 3, 459-470. 19

5. Chew, F.

Horizontal Divergence, Acceleration and Curvature Change, a Diagnostic Equation with Applications. Tellus 31, 548-557. 31

6. Hansen, D. V., and R. L. Molinari

Deep Currents in the Yucatan Strait. Journal of Geophysical Research 84, No. CI, 359-362. 41

7. Maul, G. A.

Interpreting ASTP Photographs of the Ocean and Locating the Area Photographed (Case Study of the Gulf of Mexico). Apollo-Soyuz Test Project: Summary Science Report, NASA SP-412, Vol. 2, 371-383. 45

8. McLafferty, S., M. Pryslak, and G. A. Maul

Determining Photograph Locations Over Oceans. Apollo-Soyuz Test Project: Summary Science Report, NASA SP-412, Vol. 2, 359-370. 58

9. Mayer, D. A., D. V. Hansen, and D. A. Ortman

Long-Term Current and Temperature Observations on the Middle Atlantic Shelf. Journal of Geophysical Research 84, No. C4, 1776-1792. 70

10. Molinari, R. L.

Thermal and Current Data from the Gulf of Mexico and South Atlantic Relative to Placement of OTEC Plants. Proceedings of the 6th OTEC Conference, Washington, D.C., 19-22 June 1979, G. L. Dugger, ed., Johns Hopkins University, 2, 13.3.1 to 13.3.9. (Only the abstract has been reprinted.) 87

11. Molinari, R. L.

Ocean Thermal and Current Velocity Data Requirements for Design of an OTEC Plant: An Update. Proceedings of the 6th OTEC Conference, Washington, D.C., 19-22 June 1979, G. L. Dugger, ed., John Hopkins University, 2, 13.2.1 to 13.2.10. (Only the abstract has been reprinted.) 88

12. Royer, T. C., D. V. Hansen, and D. J. Pashinski

Coastal Flow in the Northern Gulf of Alaska as Observed by Dynamic Topography and Satellite-Tracked Drogued Drift Buoys. Journal of Physical Oceanography 9, No. 4, 785-801. 89

OCEAN CHEMISTRY AND BIOLOGY LABORATORY

13. Atwood, D. K., P. N. Froelich, M. E. Q. Pilson, M. J. Barcelona, and J. L. Vilen

Deep Silicate Content as Evidence of Renewal Processes in the Venezuela Basin, Caribbean Sea. Deep-Sea Research 26A, 1179-1184. 106

14. Berberian, G. A., and M. Barcelona

Comparison of Manual and Automated Methods of Inorganic Micro-Nutrient Analyses. NOAA Tech. Memo. ERL AOML-40, 26 pp. (Only the abstract has been reprinted.) 112

15. Cummings, S. R., Jr., D. K. Atwood, and J. M. Parker

Inorganic Nutrients and Dissolved Oxygen Variation Determined From Historical Data at Three Proposed Ocean Thermal Energy Conversion (OTEC) Sites: Puerto Rico, St. Croix, and Northern Gulf of Mexico. NOAA Tech. Memo. ERL AOML-36, 67 pp. (Only the abstract has been reprinted.) 113

16. Harvey, G. R., A. D. Requejo, P. A. McGillivary, and J. M. Tokar

Observation of a Subsurface Oil-Rich Layer in the Open Ocean, Science 205, 999-1001. 114

17. Hatcher, G. H., and P. A. McGillivary

Sewage Contamination in the New York Bight. Coprostanol as an Indicator. Environmental Science & Technology 13, No. 10, 1225-1229. 117

18. Ortner, P. A., S. R. Cummings, R. P. Aftring, and H. E. Edgerton

Silhouette Photography of Oceanic Zooplankton. Nature 277, No. 5691, 50-51. 122

19. Requejo, A. G., R. H. West, P. G. Hatcher, and P. A. McGillivary

Polychlorinated Biphenyls and Chlorinated Pesticides in Soils of the Everglades National Park and Adjacent Agricultural Areas. Environmental Science & Technology 13, No. 8, 931-935. 124

MARINE GEOLOGY AND GEOPHYSICS LABORATORY

20. Bennett, R. H.

Slope Map of a Submarine Slide Seaward of the Baltimore Canyon Trough. Ocean Engineering Technical Bulletin 5, No. 2, 3. 129

21. Bennett, R. H., and J. R. Faris

Ambient and Dynamic Pore Pressures in Fine-Grained Submarine Sediments: Mississippi Delta. Applied Ocean Research 1, No. 3, 115-122. 130

22. Bennett, R. H., J. R. Faris, S. Sigmund, R. Perry, and A. F. Richards

NOAA Cooperative Seafloor Engineering Project. Ocean Engineering Technical Bulletin 5, No. 2, 3-4. 138

23. Bennett, R. H., W. R. Bryant, and G. H. Keller

Clay Fabric and Related Pore Geometry of Selected Submarine Sediment: Mississippi Delta. Scanning Electron Microscopy 1, 519-524 and p. 424. 139

24. Cronan, D. S., P. A. Rona, and S. Shearme

Metal Enrichments in Sediments from the TAG Hydrothermal Field. Marine Mining 2, No. 1-2, 79-89. 146

25. Freeland, G. L., D. J. P. Swift, and R. A. Young

Mud Deposits Near the New York Bight Dumpsites: Origin and Behavior. In: *Ocean Dumping and Marine Pollution: Geological Aspects of Waste Disposal*. H. D. Palmer and M. G. Gross, eds., Dowden, Hutchinson & Ross, Inc., Stroudsburg, Pa., 73-95. 157

26. Keller, G. H., D. N. Lambert, and R. H. Bennett

Geotechnical Properties of Continental Slope Deposits - Cape Hatteras to Hydrographer Canyon. Society of Economic Paleontologists and Mineralogists Special Publication No. 27, 131-151. 180

27. Lambert, D. N., and G. F. Merrill

Improvements in a Plastic-Barrel Sediment Corer. Applied Ocean Research *1*, 61-62. 201

28. Lesht, B. M.

Relationship Between Sediment Resuspension and the Statistical Frequency Distribution of Bottom Shear Stress. Marine Geology *32*, M19-M27. 203

29. McGregor, B. A.

Variations in Bottom Processes Along the U.S. Atlantic Continental Margin. American Association of Petroleum Geologists Memoir 29, Geological and Geophysical Investigations of Continental Margins, 139-149 (published previously in Seismic Profiles of the United States East Coast Continental Margin, NOAA Tech. Report ERL 398-AOML 28, 1978). 212

30. McGregor, B. A., and R. H. Bennett

Mass Movement of Sediment on the Continental Slope and Rise Seaward of the Baltimore Canyon Trough. Marine Geology *33*, 163-174. 223

31. McGregor, B. A.

Current Meter Observations on the U.S. Atlantic Continental Slope: Variations in Time and Space. Marine Geology *29*, 209-219. 235

32. McGregor, B. A., R. H. Bennett, and D. N. Lambert

Bottom Processes, Morphology, and Geotechnical Properties of the Continental Slope South of Baltimore Canyon. Applied Ocean Research *1*, No. 4, 177-187. 246

33. Nelsen, T. A.

Suspended Particulate Matter in the New York Bight Apex: Observations from April 1974 through January 1975. NOAA Tech. Memo. ERL MESA-42, 78 pp. (Only the table of contents has been reprinted.) 257

34. Rona, P. A.

Diving with ALVIN in Submarine Canyons. Museum (magazine of the Museum of Science, Miami, Fla.) 10, 5-8. 258

35. Rona, P. A.

Book review: Sea Floor Development: Moving into Deep Water. Sir Angus Paton et al., eds., The Royal Society, London, 1977. American Scientist 67, No. 4, 467. 262

36. Rona, P. A.

Letter to the Editor: Atlantic Hot Springs? Science 206, 1136. 263

37. Temple, D. G., R. B. Scott, and P. A. Rona

Geology of a Submarine Hydrothermal Field, Mid-Atlantic Ridge, 26°N Latitude. Journal of Geophysical Research 84, No. B13, 7453-7466. (Only the abstract has been reprinted.) 264

38. Swift, D. J. P., G. L. Freeland, and R. A. Young

Time and Space Distribution of Megaripples and Associated Bedforms, Middle Atlantic Bight, North American Atlantic Shelf. Sedimentology 26, 389-406. 265

SEA-AIR INTERACTION LABORATORY

39. Gonzalez, F. I., R. C. Beal, W. E. Brown, J. F. R. Gower, D. Lichy, D. B. Ross, C. L. Rufenach, and R. A. Shuchman

Seasat Synthetic Aperture Radar: Ocean Wave Detection Capabilities. Science 204, 1418-1421. 283

40. Lipes, R. G., R. L. Bernstein, V. J. Cardone, K. B. Katsaros, E. G. Njoku, A. L. Riley, D. B. Ross, C. T. Swift, and F. J. Wentz.

Seasat Scanning Multichannel Microwave Radiometer: Results of the Gulf of Alaska Workshop. Science 204, 1415-1417. 287.

41. Long, R. B.

Forecasting Hurricane Waves. Mariners Weather Log 23, No. 1, 1-10. 290

42. Long, R. B., and K. Hasselmann.

A Variational Technique for Extracting Directional Spectra from Multi-Component Wave Data. Journal of Physical Oceanography 9, No. 2, 373-381. 300

43. Ross, D.

Observing and Predicting Hurricane Wind and Wave Conditions. Papers submitted to the Joint IOC/WMO Seminar on Oceanographic Products and the IGOSS Data Processing and Services System, Moscow, 2-6 April 1979. Intergovernmental Oceanographic Commission [UNESCO] Workshop report No. 17-supplement, 408-420. 309

44. Thacker, W. C.

Irregular-Grid Finite-Difference Techniques for Storm Surge Calculations for Curving Coastlines. Marine Forecasting, J. C. J. Nihoul, ed., Elsevier Oceanography Series 25, Amsterdam, 261-283. 322

45. Thacker, W. C.

An Improved Triangulation Algorithm. Applied Mathematical Modelling 3, 471-472. 345

ADDENDUM

OFFICE OF THE DIRECTOR

46. Proni, J. R., F. C. Newman, E. R. Meyer, H. B. Stewart, Jr., D. J. Walter, R. Sellers, and C. A. Lauter, Jr.

On the Use of Acoustics in Applied Oceanographic and Coastal Engineering Problems with Emphasis on the Oceanic Transport of Particulate Materials. Thalassia Jugoslavica 13(3/4), 389-393 (plus six unnumbered pages of figures), 1977. 347

PHYSICAL OCEANOGRAPHY LABORATORY

47. Maul, G. A.

The 1972-1973 Cycle of the Gulf Loop Current Part II: Mass and Salt Balances of the Basin. CICAR-II Symposium on Progress in Marine Research in the Caribbean and Adjacent Regions, Caracas, 12-16 July 1976. FAO Fisheries Report No. 200 Supplement, Rome, 1977, 597-619. 358

48. Merrell, W. J., Jr., R. L. Molinari, J. M. Morrison, W. D. Nowlin, Jr., I. H. Brooks, and R. Yager

A Description of the Circulation Observed in the Eastern Gulf of Mexico during CICAR Survey Month II, May 1972. CICAR-II Symposium on Progress in Marine Research in the Caribbean and Adjacent Regions, Caracas, 12-16 July 1976. FAO Fisheries Report No. 200 Supplement, Rome, 1977, 51-61. 381

49. Mofjeld, H. O., and M. Wimbush

Tides in the Gulf of Mexico and Caribbean Sea. CICAR-II Symposium on Progress in Marine Research in the Caribbean and Adjacent Regions, Caracas, 12-16 July 1976. FAO Fisheries Report No. 200 Supplement, Rome, 1977, 79-102. 392

50. Molinari, R. L.

An Overview of the Cayman Sea-Gulf of Mexico Circulation Based on CICAR Survey Month and Other Data. CICAR-II Symposium on Progress in Marine Research in the Caribbean and Adjacent Regions, Caracas, 12-16 July 1976. FAO Fisheries Report No. 200 Supplement, Rome, 1977, 103-118. 416

OCEAN CHEMISTRY AND BIOLOGY LABORATORY

51. Atwood, D. K.

Chemical Oceanography: Summary of CICAR Results and Recommendations for the Future. CICAR-II Symposium on Progress in Marine Research in the Caribbean and Adjacent Regions, Caracas, 12-16 July 1976. FAO Fisheries Report No. 200 Supplement, Rome, 1977, 211-219. 432

52. Berberian, G. A., and R. B. Starr

The Circulation Between the Cayman Sea and the Gulf of Mexico as Deduced from Nutrient Distributions. CICAR-II Symposium on Progress in Marine Research in the Caribbean and Adjacent Regions, Caracas, 12-16 July 1976. FAO Fisheries Report No. 200 Supplement, Rome, 1977, 255-266. 441

MARINE GEOLOGY AND GEOPHYSICS LABORATORY

53. Freeland, G. L., and D. J. P. Swift

Surficial Sediments: MESA New York Bight Atlas Monograph 10. New York Sea Grant Institute, Albany, N.Y., 1978, 93 pp. (Only the abstract has been reprinted. 453

54. Swift, D. J. P., P. C. Sears, B. Bohlke, R. Hunt

Evolution of a Shoal Retreat Massif, North Carolina Shelf: Inferences From Areal Geology. Marine Geology 27 (1978) 19-42. (Figures 11, 13, 15, and 16 are reproduced as they were corrected in a later issue.) 454

SEA-AIR INTERACTION LABORATORY

55. Ostapoff, F., and S. Worthem

Air-Sea Interactions During Conditions of Squalls and Deep Convection. CICAR-II Symposium on Progress in Marine Research in the Caribbean and Adjacent Regions, Caracas, 12-16 July 1976. FAO Fisheries Report No. 200 Supplement, Rome, 1977, 479-486. 478

56. Worthem, S., and F. Ostapoff

The Response of the Tropical North Atlantic to Meteorological Forcing Functions. CICAR-II Symposium on Progress in Marine Research in the Caribbean and Adjacent Regions, Caracas, 12-16 July 1976. FAO Fisheries Report No. 200 Supplement, Rome, 1977, 505-530. 486

1. Photogrammetric Engineering and Remote Sensing 45, No. 6, 763-768.

DR. ROBERT W. JOHNSON
NASA Langley Research Center
Hampton, VA 23665
ROBERT M. GLASGOW
Vought Corporation
Hampton, VA 23665
DR. IVER W. DUEDALL
Marine Sciences Research Center
State University of New York
Stony Brook, NY 11794
DR. JOHN R. PRONI
NOAA Atlantic Oceanographic and Meteorological Laboratories
Miami, FL 33149

Monitoring the Temporal Dispersion of a Sewage Sludge Plume*

Remotely sensed monitoring and data analysis techniques may be used to study temporal dispersion characteristics of plumes resulting from dumping of sewage sludge.

(Abstract appears on following page)

INTRODUCTION

LARGE QUANTITIES of sewage sludge, dredge spoils, industrial waste, and cellar dirt are dumped (Pararas-Carayannis, 1973; Muller *et al.*, 1976) in the apex of the New York Bight (Figure 1). Little is known about the local dispersion of these wastes in coastal waters. Previous investigations of the dispersion of sewage sludge plumes include studies on the fate of sludge-derived ammonium in the water column (Duedall *et al.*, 1975), short term water column disturbances (Duedall *et al.*, 1977), surface distributions of suspended solids (Johnson *et al.*, 1977), and the distribution of suspended material in the water column as measured by an acoustical system (Proni *et al.*, 1976). The experiment described by Johnson *et al.* (1977), designated as STAX I (Sludge Tracking Acoustics Experiment), demonstrated the applicability of remote sensing techniques for identifying and synoptically mapping surface water distributions of suspended solids in plumes resulting from sewage sludge dumps.

It is the purpose of this investigation as part of the STAX II experiment, conducted on July 15, 1976, to apply the previously reported methodology (Johnson *et al.*, 1977) to study the temporal dispersion of a sewage sludge plume in the New York Bight apex. The work described here was conducted jointly by NASA, NOAA, and SUNY.

TEST SITE

The area selected by NOAA for this experiment was in the apex of the New York Bight (Figure 1). Within the apex, sewage sludge is dumped on a daily schedule in an Environmental Protection Agency (EPA) designated area about 18 km (9.7 nautical miles) south of Long Island.

EXPERIMENTAL METHOD

A sewage sludge dump and its plume were monitored by aircraft remote sensing and by the surface vessels *Black Coral* (NOAA) and *Onrust* (SUNY). Data from the aircraft platform were collected by a multispectral scanner and two mapping cameras. The sea-truth data were obtained by water sampling and acoustic profiling (from the *Black Coral*

---

* Presented at the ASP Annual Convention, Washington, DC, February 26-March 3, 1978.

PHOTOGRAMMETRIC ENGINEERING AND REMOTE SENSING,
Vol. 45, No. 6, June 1979, pp. 763-768.

ABSTRACT: *Sewage sludge from the Metropolitan New York City area is dumped in the apex of the New York Bight. Possible environmental effects due to this dumping are being studied. Results of a joint National Aeronautics and Space Administration (NASA), National Oceanic and Atmospheric Administration (NOAA), and State University of New York (SUNY) experiment on July 15, 1976, indicate remotely sensed monitoring and data analysis techniques may be used to study temporal dispersion characteristics of plumes resulting from dumping of sewage sludge. Remotely sensed data were collected by multispectral scanner and photography from a NASA aircraft platform. Multiple flights were made over the plume from a spot dump (rapid discharge from a stationary barge) at about 15 minute intervals for two hours after the dump, which was made at 10 A.M. (local time). Afternoon flights over the dump area indicated that the plume was well dispersed by about five hours after the dump. Concurrent sea-truth measurements were made from NOAA and SUNY ships in and around the dump plume. Concentrations of suspended solids in the plume were correlated with multispectral scanner radiance data to obtain a regression equation which was then used to map quantitative distributions of suspended solids in the plume. For the spot dump monitored, reflected radiances from the surface waters reached peak values about 45 minutes after the dump. After this time, spectral analysis indicated that the calibrated equation could be applied. The plume was dispersed within about five hours. Spectral characteristics of the experiment plume were similar to sewage sludge plumes that have been monitored in other experiments in the Atlantic Coastal Zone. These plumes are readily distinguished from acid wastes that are dumped in the same geographical area.*

only) in and around the sludge plume. In this paper, only the multispectral scanner data are considered, using the mapping camera data for visual location and identification of the surface features. Also, only sea-truth measurements of suspended solids at or near the surface are considered in the analysis. Prior investigations indicated that chlorophyll *a* analyses may produce ambiguous results (Johnson *et al.*, 1977). Results from acoustic investigations are presented in other reports (Proni *et al.*, in press).

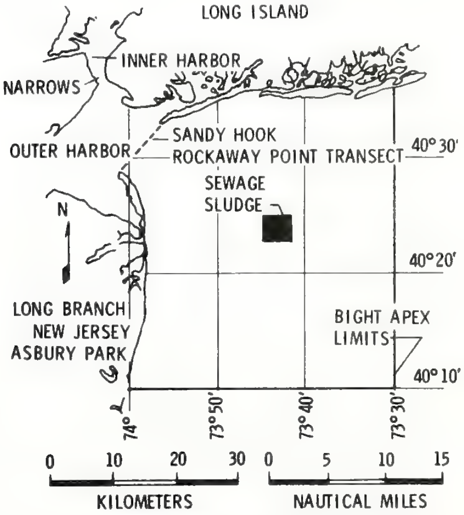

FIG. 1. Sewage sludge dump area in the New York Bight apex.

On July 15, 1976, 2,886 m^3 (102,000 ft^3) of sewage sludge was dumped from the *M/V North River* in the sewage sludge dump area. The material was dumped from the stationary barge from about 9:58 A.M. to 10:04 A.M. eastern daylight time (EDT). Based on analyses furnished by EPA, Region II, from samples obtained at the plant (Newtown Creek) during loading of the vessel, specific gravity at 20°C was 1.00 and percent solids was 3.54.

SEA-TRUTH MEASUREMENTS

The dumping vessel was identified as it approached the dumping area and observed closely as it performed its normal dump. Immediately after the dump was completed the barge moved out of the area to provide maximum operational flexibility for the scientific monitoring ships. The ***Black Coral*** made a number of transects in and around the plume to study its dispersion character-

TABLE 1. SEA-TRUTH MEASUREMENTS AND REMOTELY SENSED DATA

Sampling Time EDT	Location*	Suspended Solids mg/l	Remotely Sensed Radiances (mw/cm^2-sr-μm) M2S Band 1	2	3	4	5	6	7	8	9	10
11:05 a.m.	In Plume	4.00	6.280	**	4.475	**	2.281	**	1.578	1.307	0.599	0.205
11:45 a.m.	In Plume	6.93	7.133	5.971	5.501	4.001	2.967	2.541	1.992	1.384	0.789	0.323
1:25 p.m.	Water	1.01	No concurrent remote sensing data collections; in analysis radiance ratio is 1.00 for ocean water.									
1:45 p.m.	Water	1:33										

* Location procedure descibed in text.

** No usable data in these bands at sea truth location.

istics acoustically and to provide guidance to the *Onrust* for the water sampling. Surface and depth transect measurements were made by the *Onrust;* however, due to the dynamic nature of the plume and movement of the monitoring ships, only four measurements were suitable for the remote sensing data analysis. These measurements and times of the sampling are listed in Table 1 along with the corresponding remotely sensed radiance values, which will be discussed in a later section.

REMOTE SENSING MEASUREMENTS

Remote sensors that measure electromagnetic reflectance in the visible and near infrared (NIR) spectral range were flown over the test site. The NASA Johnson Space Center (JSC) NP-3A aircraft flew at a nominal altitude of 3.0 km (10,000 ft) and at a speed of 444 km/hour (240 knots). Two onboard remote sensor systems collected data for these analyses; an 11-band M2S multispectral scanner, which measured radiances in each of 10 bands in the visible and NIR spectral range and one thermal band; and two mapping cameras, which used aerial color and false color IR film. Spectral and spatial characteristics of the remote sensors are listed in Table 2. Only data in the visible and NIR spectral range are considered in the analysis.

TABLE 2. SPECTRAL AND SPATIAL CHARACTERISTICS OF REMOTE SENSORS (AT 3.0 KM ALTITUDE)

I MODULAR MULTISPECTRAL SCANNER (M2S)

BAND	BANDWIDTH
1	380-440 nm
2	440-490 nm
3	495-535 nm
4	540-580 nm
5	580-620 nm
6	620-660 nm
7	660-700 nm
8	700-740 nm
9	760-860 nm
10	970-1060 nm
THERMAL	8000-13,000 nm
SCAN WIDTH, m	8500
RESOLUTION, m	8

II ZEISS MAPPING CAMERAS

	SPECTRAL RANGE	FILM	RESOLUTION, m	FOOT PRINT, m
NO. 1	400-700 nm	COLOR	0.4	4550 x 4550
NO. 2	500-900 nm	COLOR IR	0.4	4550 x 4550

Digital data from the M2S scanner were recorded inflight on magnetic tape in a high density format. Inflight calibration was also provided for each line of data. Screening imagery from the scanner in conjunction with the mapping camera products were used to locate areas of interest in the scanner data. Digital data (measured in counts) in these areas were transferred to computer compatible tapes (CCT) with a typical format of 800 bits per inch. Inflight calibration based on a standard lamp provided information to convert instrument count data to average radiances in each band.

Remote sensing data collections were made over the plume and surface ships starting about 15 minutes after the dump, then at 15-minute intervals, for two hours and 15 minutes after the dump. A total of nine data collections were made during the morning period of the experiment. In the afternoon, two data collections were made over the dump area. The monitoring ships were used as targets in the afternoon since the plume was not visible. Times of the remote sensing data collections are listed in Table 3.

Example radiances in each of the M2S bands for the ocean water and in the sewage sludge plume at 10:12 A.M., 10:58 A.M., and 11:43 A.M. EDT (about 15, 60, and 105 minutes after the dump, respectively) are shown on Figures 2 and 3, respectively. Note the general increase in radiances due to higher sun angles as elapsed time after the dump increases.

PREPROCESSING OF REMOTELY SENSED DATA

Data preprocessing included locating the water sampling points in the imagery and

TABLE 3. TIMES OF REMOTE SENSING DATA COLLECTIONS OVER THE SEWAGE SLUDGE DUMP AREA

REMOTE SENSING DATA COLLECTION NUMBER	TIME, E.D.T.
MORNING	
1	1012
2	1028
3	1043
4	1058
5	1113
6	1126
7	1143
8	1158
9	1212
AFTERNOON	
10	1444
11	1542

determining radiance values in the M2S bands to be compared to the sea-truth measurements obtained from the *Onrust*. In the analysis, representative radiance values were determined by taking a 7 by 7 picture element (pixel) field centered at the best estimate of the sea-truth measurement. This pixel field was determined empirically as the minimum size that compensated for uncontrollable spectral and spatial errors. The average count in the 7 by 7 field was multiplied by a radiance conversion value obtained from calibration of the inflight system to known radiance sources. Evaluation of inflight calibration data indicates less than 2 percent, or negligible, instrument drift. Average radiances in individual band ranges have the units mw/cm^2-sr-μm or an average radiance per unit band width.

DATA ANALYSIS, RESULTS, AND DISCUSSION

In this experiment, the primary objective was to evaluate the temporal dispersion of the target sewage sludge plume. However, as the plume dispersed after the dump, sun angle increased from the horizon (with time). This increased sun angle produces higher reflected radiances from the background water as well as from the sewage sludge plume, as shown in Figures 2 and 3. A means of normalizing radiance changes due to sun angle and homogenous atmospheric changes used previously in spectral analyses of this plume and other ocean dumped materials (Johnson, 1977) was to determine ratios of plume radiances to ocean water radiances in each M2S band for each scene. After reviewing the remotely sensed data, it appeared that M2S Band 7 (700-740 nm) ratios are suitable for monitoring plume changes. Changes in the plume as indicated by the M2S Band 7 ratios for one hour and 45 minutes after the dump are shown in Figure 4. (Data for the last two remote sensing data collections were "noisy" and require additional analysis.) Interestingly, the spot dump reaches peak radiance ratio values about 45 minutes after the dump. This may be due to surfacing of floatable materials or organic liquids that are initially entrained with the heavier materials. However, as indicated by Duedall *et al.* (1977), the concentration of suspended solids in a spot dump plume appears to decrease with time after initial high values. Thus, it is suspected that a single radiance-suspended solids relationship is not applicable during the entire dispersion of a spot dump plume. However, it appears

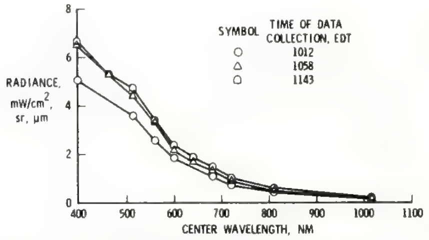

FIG. 2. Average radiances in M2S bands for ocean water, about 15, 60, and 105 minutes after sewage sludge dump.

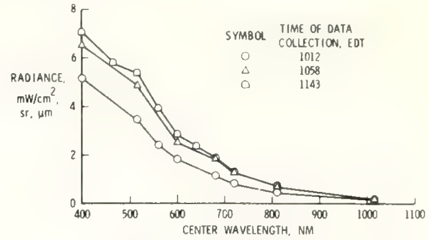

FIG. 3. Average radiances in M2S bands for sewage sludge plume, about 15, 60, and 105 minutes after dump.

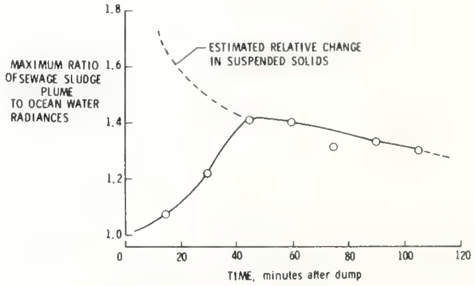

FIG. 4. M2S band 7 radiance ratio values (maximum plume to ocean water) after sewage sludge dump. Also shown is estimated relative change in suspended solids from Duedall *et al.* (1977).

that after about 45 minutes the radiance-ratio change is similar to that observed previously for suspended solids (Figure 4) and may be used to relate remotely sensed data to suspended solids.

Due to the limited number of observations in which sea-truth measurements were made concurrently with remotely sensed data (or sea-truth locations could be located reliably in the remotely sensed data), the regression analysis was limited to M2S Band 7 ratios as the independent variable. The dependent variable was suspended solids. Four observations and the corresponding ratio values were applicable; two of these were in ocean water (Table 1). The two usable suspended solids concentration measurements in the plume were made 65 and 105 minutes after the dump. The best fit linear regression equation was

$$\text{Suspended solids (mg/l)} = -21.05 + 22.22 \text{ RA7}$$

where RA7 is the ratio of plume to ocean water radiances in M2S Band 7, both for the same scene. The correlation coefficient (measure of relative change between variables) is 0.99, and the standard error of estimate (measure of scatter about the fitted regression line) is 0.42 mg/l. Note that total suspended solids concentrations are used and, thus, include ocean water material, as well as the plume. The comparison of remotely sensed data (radiance ratio) and measured suspended solids is shown in Figure 5. A linear equation appears to be adequate. Previous investigations have indicated a linear equation in this range of suspended solids (Johnson *et al.*, 1977).

QUANTITATIVE MAPPING

Quantitative distributions of suspended solids may be determined and mapped in each of the remotely sensed scenes where the plume is changing in a homogenous manner (e.g., overflights 3-9, from 45 minutes to two hours 15 minutes after the dump). For the water quality parameter, suspended solids concentrations were determined at each pixel by using the calibrated regression equation. This field of data is typically smoothed to remove local spectral and spatial noise features, and a contour map is developed by a computerized plotting routine. The smoothing routine used in this analysis is an averaging on a line-by-line and column-by-column basis in the data field, where the middle value is replaced by the mean of it and the two adjacent values. Edge values remain the same. In this analysis, each pixel in each line of data was used to generate the field of data for mapping. Two smoothing passes were made for the suspended solids concentrations.

Quantitative distributions of suspended solids in the sewage sludge plume for the data collection about 45 minutes after the dump are mapped in Figure 6. As indicated on the figure, both monitoring ships are around the plume. The scattered plume areas above and to the left of the main plume are due to residuals as the dumping barge moved out of the spot dump.

A further application of the computerized quantitative determinations is a histogram of the number of pixels for suspended solids concentration ranges. This information may be useful to measure the spread-concentration of the plume in the surface waters. The histogram for the scene 45 minutes after the dump is shown in Figure 7, where the number of pixels in remotely sensed suspended

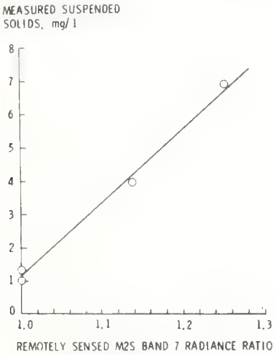

FIG. 5. Comparison of Measured Suspended Solids to Remotely sensed radiance ratios (plume at sea truth location to ocean water in the same scene).

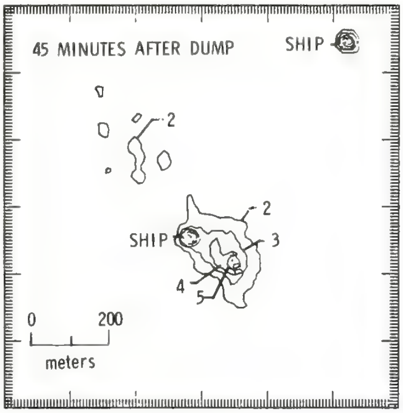

FIG. 6. Quantitative distribution of suspended solids concentrations, mg/l, in a "spot" sewage sludge dump in the New York Bight on July 15, 1976.

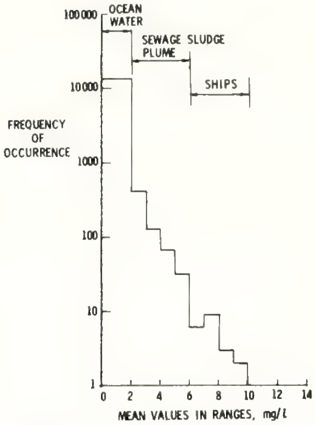

FIG. 7. Histogram of number of pixels in each suspended solids range (see Figure 6).

solids concentration ranges are indicated (the lowest range from 0-1.99 mg/l, mean value 1.0, includes background water). The histogram is based on suspended solids value ranges after the two smoothing operations and, thus, corresponds to the quantitative mapping shown in Figure 6. The total field is 120 by 120 pixels.

CONCLUDING REMARKS

Calibrated regression equations that relate remotely sensed data to sea-truth measurements may be used to provide maps of the synoptic distributions of suspended solids in plumes resulting from ocean dumping of sewage sludge. It appears that the spot dump of sewage sludge monitored in this experiment was about 45 minutes old before a uniform pattern of radiance to suspended solids change was established. After applying a normalizing technique to eliminate changing sun angle and homogenous atmospheric effects, a single regression equation was developed to study spatial and temporal dispersion patterns of the plume. It appears that developing the regression equation using ratios (to ocean water) may be an effective means to determine suspended solids distributions in remotely sensed scenes, even though in some cases sea-truth measurements have not been made concurrently with that particular remote sensing data collection. This approach may provide a means for more effective experiment design, data analysis, and interpretation.

Results of this experiment are encouraging for the use of remotely sensed data for studying pollution plumes and their spatial and temporal dispersion characteristics. Additional experiments should be performed in different environments and with different materials to define more accurately the role of remote sensing in monitoring and studying the effects of pollution in the coastal zones.

REFERENCES

Duedall, Iver W., Malcolm J. Bowman, and Harold B. O'Connors, Jr., 1975. Sewage Sludge and Ammonium Concentrations in the New York Bight Apex. *Estuarine and Coastal Mar. Sci.*, 3, p. 457.

Duedall, I. W., H. B. O'Conners, S. A. Oakley, and H. M. Stanford, 1977. Short-Term Water Column Perturbations Caused by Wastewater Sludge Dumping in the New York Bight Apex. *Journal Water Pollution Control Federation.*

Johnson, R. W., 1977. Multispectral Analysis of Ocean Dumped Materials. *Proceedings of the Eleventh International Symposium on Remote Sensing of Environment,* Ann Arbor, Michigan.

Johnson, R. W., I. W. Duedall, R. M. Glasgow, J. R. Proni, and T. A. Nelsen, 1977. Quantitative Mapping of Suspended Solids in Wastewater Sludge Plumes in the New York Bight Apex. *Journal Water Pollution Control Federation.*

Muller, J. A., J. S. Jeris, A. R. Anderson, and C. F. Hughes, 1976. *Contaminant Inputs to the New York Bight.* NOAA Tech. Memorandum ERL MESA-6, National Oceanic and Atmospheric Administration, Environmental Research Laboratories, Marine Ecosystems Analysis Program, New York Bight Project, Boulder, Colorado.

Pararas-Carayannis, G., 1973. *Ocean Dumping in the New York Bight: An Assessment of Environmental Studies.* Tech. Memorandum No. 39, Coastal Eng. Res. Center, U.S. Army Corps of Engineers, Fort Belvoir, Virginia.

Proni, John R., Fred C. Newman, Ronald L. Sellers, and Charles Parker, 1976. Acoustic Tracking of Ocean-Dumped Sewage Sludge. *Science,* vol. 193, pp. 1005-1007.

Proni, John R., Fred C. Newman, Robert A. Young, Donald Walter, Ronald Sellers, Phillip McGillivary, Iver W. Duedall, Harold Stanford, and Charles Parker, in press. Observations of the Intrusion into a Stratified Ocean of an Artificial Tracer and the Concomitant Generation of Internal Oscillations. *Journal of Geophysical Research* (In Press).

(Received November 21, 1978; accepted March 12, 1979)

2. Deep Sea Research 26A, 350.

Author's Reply

(*Received 7 August* 1978)

We wish to thank Farmer and Smith for their comments on our article, Proni, Ostapoff and Sellers (1978). We agree with their comments and calculations, particularly the point that acoustic reflectors need not reside at the depth of maximum vertical excursion. The acoustical system as developed in the summer of 1974, the time of the GATE, did not have sufficient sensitivity to detect any but the strongest reflectors below 50 or 60 m. Since 1974, the acoustic system has been improved steadily and reflectors have been detected at greater depths, thus opening the possibility of a more complete characterization of an internal wave profile.

National Oceanic Atmospheric Administration,
Atlantic Oceanographic and Meteorological Laboratories,
Miami, FL 33149, *U.S.A.*

John R. Proni
F. Ostapoff
R. L. Sellers

3. Journal of Marine Research 37, No. 4, 699-709.

Thermal feedback on wind-stress as a contributing cause of the Gulf Stream[1]

by David Behringer,[2] Lloyd Regier[3] and Henry Stommel[4]

ABSTRACT

A simple model is used to explore a feedback mechanism which may be significant in the formation of the Gulf Stream. The feedback operates through the drag coefficient which is a function of the sea-air temperature difference. The model is divided into interior and western boundary regions which are overlaid by an atmosphere with a constant meridional temperature gradient. The model predicts the interior sea-air temperature difference which determines, in sequence, the enhancement of the basic wind-stress distribution, the interior Sverdrup velocity, and the zonal velocity between the interior and the western boundary regions. All variables are functions of latitude only. Calculations for a two gyre ocean demonstrate the ability of the feedback mechanism to produce a "Gulf Stream" without higher order dynamics.

1. Introduction

The chart of Sverdrup transport (reproduced in Fig. 1) recently published by Leetmaa and Bunker (1978), based on recent recomputations of the wind-stress, shows a well developed Gulf Stream extending out from Cape Hatteras to about longitude 50W—much the same as the Gulf Stream which appears in the dynamic topography (Stommel, Niiler, and Anati, 1978). This is surprising because conventionally we have attributed the narrowness of the Gulf Stream to the operation of higher order dynamical processes, not to fine-structure in the mean wind-stress.

The new fine-structure depicted by Leetmaa and Bunker arises partly from their use of a variable drag coefficient in computing the wind-stress. Using averages of observations between 65W and 70W, they computed a wintertime drag coefficient which is nearly constant at about 1.6×10^{-3} between 21N and 27N but which increases sharply to about 2.2×10^{-3} in the warm core of the Gulf Stream at 37N. They found that using a variable drag coefficient in place of a constant coefficient made little difference in the wind-stress south of the Gulf Stream but caused a 20% to 25% increase in the stress over the Stream. This change occurs abruptly within

---

[1] Contribution No. 4251 from Woods Hole Oceanographic Institution.

[2] Atlantic Oceanographic and Meteorological Laboratories, Miami, Florida, 33149, U.S.A.

[3] Scripps Institution of Oceanography, La Jolla, California, 92093, U.S.A.

[4] Woods Hole Oceanographic Institution, Woods Hole, Massachusetts, 02543, U.S.A.

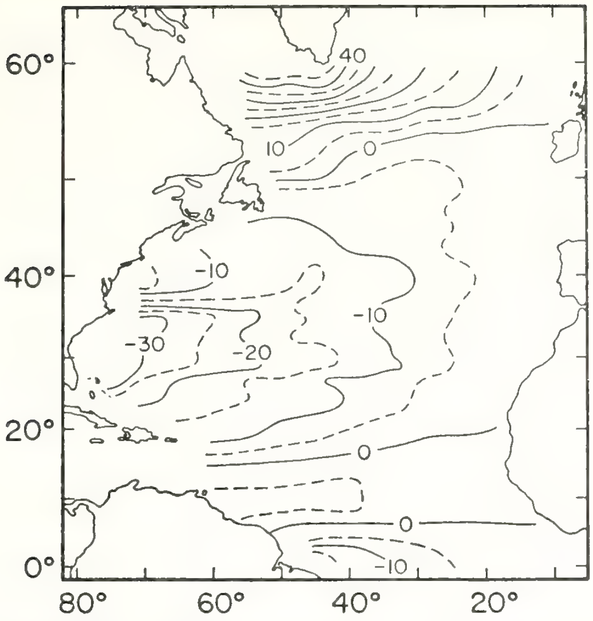

Figure 1. The field of Sverdrup transport computed by Leetmaa and Bunker (1978) showing the Gulf Stream-like current extending from Cape Hatteras to about 50W.

two degrees of latitude and hence the curl of the wind-stress is significantly enhanced near the Gulf Stream.

The drag coefficient is a function of the speed of the wind and the stability of the air (Bunker, 1976). Over the Gulf Stream both higher wind speeds and a greater temperature contrast between the cold air and the warm water contribute to a larger drag coefficient. Leetmaa and Bunker wondered whether the stronger winds somehow reflect the influence of the Stream. This may be so but there is no doubt that the anomalously high sea-air temperature difference is directly associated with the flow of the Gulf Stream and represents part of a feedback loop. A wind-stress pattern leads to a flow field configuration, which leads to a particular distribution of sea surface temperature; the sea surface temperature in conjunction with the air temperature leads, in turn, to a modification of the wind-stress pattern. It should be possible, using a simple model, to examine such a system to discover whether it leads naturally to the formation of an intense Gulf Stream in mid-latitudes.

2. The model

We consider a model which is one dimensional in the sense that the equations have been integrated over the vertical z-direction and over the zonal x-direction so that the variables are functions of the latitude, y, only. The model ocean has an active upper layer of uniform depth, H, which corresponds to an average thermocline depth and interior and western boundary regions of constant widths, W_i and W_b, respectively. The model allows for different meridional temperature distributions in the interior and western boundary by using a pair of coupled equations, one equation for each region.

We begin with an equation for the temperature, T, of an incompressible ocean,

$$\frac{\partial T}{\partial t} = -\left[\frac{\partial(uT)}{\partial x} + \frac{\partial(vT)}{\partial y} + \frac{\partial(wT)}{\partial z}\right] + A_h\left[\frac{\partial^2 T}{\partial x^2} + \frac{\partial^2 T}{\partial y^2}\right] + A_v\frac{\partial^2 T}{\partial z^2}. \qquad (1)$$

Heat flows across the surface into the ocean according to a simple Newtonian-type law and hence the surface boundary condition is

$$A_v\frac{\partial T}{\partial z} = -k'(T - T_a)$$

at $z=0$, where T_a is the air temperature. We choose the air temperature to be a linear function of latitude: $T_a(y)=T_0-By$, where T_0 is a representative equatorial air temperature and B is chosen to make T_a decrease toward the northern boundary of the ocean.

For simplicity, we assume that the heat is mixed instantaneously over the depth of the layer and that there is no heat loss through the bottom of the layer. Hence, the bottom boundary condition is

$$A_v\frac{\partial T}{\partial z} = 0$$

at $z=-H$. We also assume that the vertical velocity is zero at $z=0$ and $z=-H$.

Integrating equation (1) over the depth of the layer, we get

$$\frac{\partial T}{\partial t} = -k(T - T_a) - \left[\frac{\partial(\bar{u}T)}{\partial x} + \frac{\partial(\bar{v}T)}{\partial y}\right] + A_h\left[\frac{\partial^2 T}{\partial x^2} + \frac{\partial^2 T}{\partial y^2}\right] \qquad (2)$$

where $k=k'/H$ and the overbars represent vertical averages. The equation for continuity of mass, following the same assumptions, is

$$\frac{\partial \bar{u}}{\partial x} + \frac{\partial \bar{v}}{\partial y} = 0. \qquad (3)$$

Before integrating these equations in the x-direction we must specify the appropriate zonal boundary conditions. For the interior region, extending from $x=0$ to $x=W_i$, the boundary conditions are set to allow no flux of mass or heat through the wall: $\bar{u}=0$ and $\frac{\partial T}{\partial x} = 0$ at $x=W_i$. By integrating equation (3) from $x=0$ to $x=W_i$, we get the second boundary condition for $\bar{u}$:

$$\bar{u} = W_i\frac{\partial \bar{v}}{\partial y} \qquad \text{at } x=0.$$

Next, we use the condition,

$$A_h \frac{\partial T}{\partial x} = \frac{\mu}{W_b}[T_i - T_b] \qquad \text{at } x=0\,,$$

to represent the mixing of heat between the interior at the temperature, T_i, and the western boundary at the temperature, T_b. Finally, we need to specify T at $x=0$. In order to do so we distinguish between two regimes as functions of latitude. The distinction is necessary because, in general, the interior and western boundary temperatures are different and the direction of flow between the regions involves one or the other of these two temperatures. In regime I the water flows from the interior into the western boundary current and we set $T(x=0)=T_i$. In regime II the western boundary current flows into the interior and we set $T(x=0)=T_b$.

Using these boundary conditions, we can integrate equation (2) from $x=0$ to $x=W_i$ and obtain the model equations for the interior region. We write the equations in terms of the sea-air temperature difference, $\theta=T_i-T_a$, and take advantage of the fact that T_a is a linear function of y only.

Regime I $\left(\bar{u}(x=0)<0 \text{ or } \frac{\partial \bar{v}}{\partial y} < 0\right)$.

$$\frac{\partial \theta}{\partial t} = -k\theta - \bar{v}\frac{\partial(\theta + T_a)}{\partial y} + A\frac{\partial^2 \theta}{\partial y^2} - \frac{\mu}{W_i W_b}(\theta + T_a - T_b)\,. \tag{4}$$

Regime II $\left(\bar{u}(x=0)>0 \text{ or } \frac{\partial \bar{v}}{\partial y} > 0\right)$.

$$\frac{\partial \theta}{\partial t} = -k\theta - \bar{v}\frac{\partial(\theta + T_a)}{\partial y} + A\frac{\partial^2 \theta}{\partial y^2} - \left[\frac{\partial \bar{v}}{\partial y} + \frac{\mu}{W_i W_b}\right](\theta + T_a - T_b)\,. \tag{5}$$

In addition to equations (4) and (5) we use the following Sverdrup dynamical relationship:

$$\rho\, \beta\, \bar{v}\, H = -\frac{\partial \tau}{\partial y} \tag{6}$$

where the x-component of the wind-stress is given as

$$\tau = \tau_0(y)\,(1 + \epsilon\theta)\,. \tag{7}$$

In equation (7) the function $\tau_0(y)$ represents the stress in the absence of any effect of sea-air temperature difference, θ, and the expression $(1+\epsilon\theta)$ is introduced as a crude representation of the θ-dependence of the drag coefficient.

In order to close the system it is necessary to specify T_b. We obtain the equations for T_b by integrating equation (2) across the western boundary region from $x=0$ to $x=-W_b$. The boundary conditions are analogous to those in the interior region and we make use of the fact that the northward transport in the western boundary must balance the southward transport in the interior. There are two equations similar to the equations (4) and (5).

Regime I $\left(\dfrac{\partial \bar{v}}{\partial y} < 0\right)$.

$$\frac{\partial T_b}{\partial t} = -k(T_b - T_a) + \lambda \bar{v}\frac{\partial T_b}{\partial y} + A_b\frac{\partial^2 T_b}{\partial y^2} + \lambda\left[\frac{\partial \bar{v}}{\partial y} - \frac{\mu}{W_i W_b}\right](T_b - \theta - T_a)\,. \tag{8}$$

Regime II $\left(\dfrac{\partial \bar{v}}{\partial y} > 0\right)$.

$$\frac{\partial T_b}{\partial t} = -k(T_b - T_a) + \lambda \bar{v}\frac{\partial T_b}{\partial y} + A_b\frac{\partial^2 T_b}{\partial y^2} + \frac{\lambda\mu}{W_i W_b}(\theta + T_a - T_b)\,. \tag{9}$$

In equations (8) and (9) $\lambda = W_i/W_b$.

Equations (6), (7) and either of the combinations of (4) and (8) or (5) and (9), depending on the sign of $\dfrac{\partial \bar{v}}{\partial y}$, describe the system. Because $\bar{v}$ is a function of θ (through the thermally sensitive drag coefficient), the products of $\bar{v}$ and θ and their derivatives in equations (4) and (5) introduce an essential nonlinearity into the problem. The fact that there are two regimes, I and II, whose distribution in y at any time is determined by the instantaneous field of $\dfrac{\partial \bar{v}}{\partial y}$ also is strongly nonlinear.

In our calculations the basic value of $\tau_0(y)$ is taken as

$$\tau_0(y) = -\frac{\tau_0}{\rho}\cos\left[\frac{m\pi}{L}\,y\right]$$

where L is the meridional dimension of the basin. The form of the wind-stress can yield a two-gyre ocean ($m=2$) with both subpolar and subtropical gyres. The boundary conditions at the northern and southern ends of the ocean are $\bar{v}=0$ and $A\dfrac{\partial T_i}{\partial y} = 0 \left(\text{or } \dfrac{\partial \theta}{\partial y} = B\right)$.

Solutions have been obtained numerically by a simple time-step integration of equations (4), (5), (8) and (9), continuing until the time-rate of change of the θ-field becomes zero. We perform the time integration starting with $\theta=0$. A table for $\bar{v}$ is computed from equation (6) using the instantaneous value of $\tau(y)$ which at the first time step is simply $\tau_0(y)$. Once θ has been stepped forward, the new values of $\tau(y)$ are computed from equation (7) and the $\bar{v}$-table is recomputed from equation (6).

In the experimental results which follow, the final distributions of θ generally show that the gyre interiors gain heat from the air in the south and lose heat to the air farther north. In our discussion we treat this pattern of heat gain and loss in the

Table 1. Diffusivity coefficients for the experiments α_1 through α_6. The units are cm² sec⁻¹.

Exp.	α_1	α_2	α_3	α_4	α_5	α_6
A	0	1×10^7	4×10^7	1×10^7	1×10^7	1×10^7
A_b	$.85\times10^7$	1×10^7	4×10^7	1×10^7	1×10^7	1×10^7
μ	4×10^6	4×10^6	4×10^6	0	4×10^6	16×10^6

interior as essentially that of the basin as a whole. We can reasonably do this because, although the sea-air temperature difference in the western boundary can be greater than in the interior, the relative narrowness of the western boundary means that at any latitude the total heat exchange in the western boundary is only a few percent of the interior value.

3. The experiments

Since there are two sources of nonlinearity there are some interesting effects to be found even for the case of no feedback: $\epsilon=0$. Accordingly, we will first discuss this case. It yields some idea of the magnitude of the diffusivity required to transport properties from the southern to the northern gyre, which would otherwise be isolated.

The case $\epsilon=0$. In order to illustrate the nature of the sea-air temperature difference, θ, in a two gyre ocean a series of experiments were run using the diffusivity coefficients in Table 1. Otherwise, all of the experiments have the common parameters:

$\epsilon=0$, $k=8\times10^{-9}$ sec^{-1}, $H=1$ km, $L=6000$ km, $W_i=3000$ km,
$W_b=100$ km, $\tau_0=1$ dyne cm^{-2}, $T_0=17$°C, $B=2.83\times10^{-3}$ °C km^{-1},
and the y-grid dimension is 36 points.

The results are shown in Figure 2. Since the applied stress, τ, is a simple cosine function, the Sverdrup transport (velocity $\bar{v}$) is also trigonometric and, in the case $\epsilon=0$, it is wholly unaffected by the sea-air temperature difference.

In experiment α_1 there was no meridional diffusion in the interior and hence no heat transport between the two gyres except indirectly due to the small meridional diffusion in the western boundary current. A large temperature discontinuity (in θ) exists between grid points 18 and 19, at the boundary between the two noncommunicating gyres.

Curve α_1 shows large north-south asymmetry in each gyre. The amplitude of θ is greatest in the regimes II where the water from the western boundary currents enters the interior. Overall heat balance is nearly maintained separately in each gyre. Virtually all the heat that is absorbed from the air in each gyre is released again within the same gyre at a more northern latitude. The extent in latitude of the region of heat absorption in the subtropical gyre is greater than that in which it is given up again. The maximum meridional transport of heat by the combined gyre

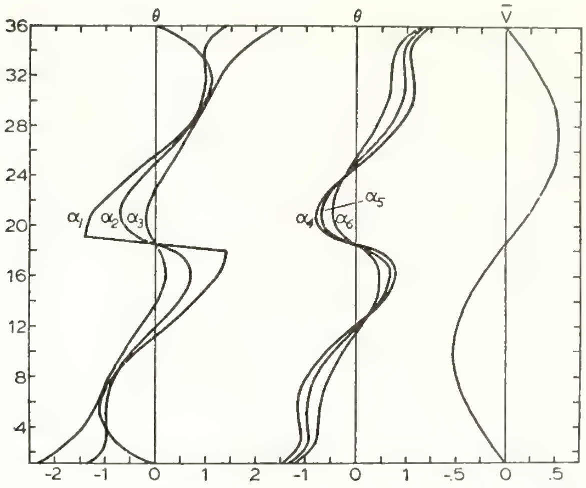

Figure 2. The sea-air temperature difference, θ, and the interior Sverdrup velocity, $\bar{v}$, for the experiments α_1 through α_6. The units are degrees Celsius and cm sec^{-1}, respectively. All experiments have $\epsilon=0$. The remaining parameters are given in the text.

and western boundary current system does not coincide with the maximum meridional mass transport of each gyre, but in both gyres occurs somewhat nearer to mid-latitude. In the interior there is no heat transport across the latitude bounding the two gyres.

The curves for experiments α_2 and α_3 show the sea-air temperature difference for two choices of the meridional diffusivity ($A=A_b = 1\times10^7, 4\times10^7$ cm^2 sec^{-1}). The temperature discontinuity is removed. For the larger value of A in experiment α_3 heat absorbed from the air at low latitudes is almost entirely transferred to high latitudes across the boundary between the gyres by the eddy diffusion.

Looking at the qualitative features of Bunker's (1976) heat balance charts one gets the impression that most of the heat absorbed in the subtropical gyre of the North Atlantic is released in the northern portion of the subtropical gyre and that only something less than half of it is transferred to the subpolar gyre. In this model it would require a diffusivity coefficient as in experiment α_1 to accomplish this.

The need for transfer between gyres is even more clear when one considers the oceanic fresh water balance. Because there is net evaporation over the subtropical gyre and net precipitation over the subpolar gyre, there would be no realistic steady state solution to our model in the absence of transport between the gyres. Eventually, the water would become so saline that its density would exceed that of the subpolar gyre.

The remaining curves in Figure 2 show the effect on the sea-air temperature difference of variations in the eddy diffusivity between the western boundary and the interior. The curve α_4 shows θ for an experiment in which there is no zonal

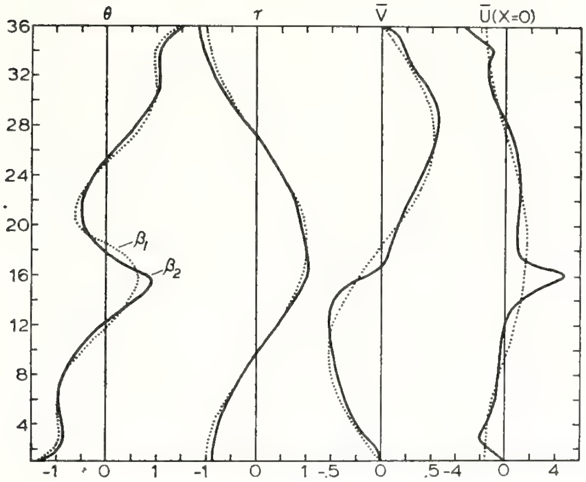

Figure 3. The sea-air temperature difference, θ, the wind-stress, τ, the Sverdrup velocity, $\bar{v}$, and the zonal velocity, $\bar{u}(x=0)$, for the experiments β_1 and β_2. The units are degrees Celsius, dynes cm^{-2}, cm sec^{-1}, and cm sec^{-1}, respectively. Experiment β_1 has $\epsilon=0$ and experiment β_2 has $\epsilon=0.125$. The remaining parameters are given in the text.

eddy diffusion; heat is transferred between the regions by advection alone. The curves α_5 and α_6 show that when diffusion is included ($\mu=4\times10^6$, 16×10^6 cm^{2}sec^{-1}) the amplitude of θ is reduced. In the subtropical gyre the diffusion has caused a warming of the southern interior and a cooling of the western boundary current which, in turn, has led to a less effective warming of the northern interior by the outflow of the western boundary current. This effect has its mirror image in the subpolar gyre.

The net effect of the diffusion between the western boundary and the interior is to partially short-circuit the oceanic flux of heat. Nevertheless, for reasonable values of μ this effect is less important in determining the nature of the solutions than the transfer of heat between the gyres.

The case $\epsilon\neq0$. With $\epsilon\neq0$ we have the possibility of feedback of the sea-air temperature difference upon the wind-stress, and the tendency for the development of a jet, or "Gulf Stream" at mid-latitudes. Figure 3 shows the results of two experiments with the two gyre system. The parameters are the same as in the previous case, except the diffusivity coefficients are $A=1\times10^7$ cm^2 sec^{-1}, $A_b=4\times10^7$ cm^2 sec^{-1} and $\mu=4\times10^6$ cm^2 sec^{-1}. The curve β_1 has zero ϵ and represents a control experiment. In curve β_2 some feedback is introduced ($\epsilon=0.125$) so that the stress is enhanced somewhat where θ is large. The maximum stress—which in the absence of feedback is between points 18 and 19—is displaced southward to between points 16 and 17 due to the high sea-air temperature difference there. This distorts the Sverdrup velocity, $\bar{v}$, as shown, so that it vanishes between points 16 and 17. There is also a northward shift of the point of maximum meridional velocity in each gyre: in the subtropical gyre from point 10 to point 12 and in the subpolar gyre from point 27 to point 28. The maximum velocity in the subpolar gyre is also increased by about 8%. In the subtropical gyre the displacement of the maximum $\bar{v}$ and of the vanishing $\bar{v}$ has a large effect upon $\frac{\partial \bar{v}}{\partial y}$ and, consequently, upon the eastward flowing current from the western boundary into the interior. As can be seen in Figure 3 the zonal current in the subtropical gyre has been halved in width and more than doubled in amplitude forming a jet in the region of the Leetmaa-Bunker Gulf Stream.

Zonal jets also form in the extreme north and south where the insulating boundary conditions $\left(\frac{\partial T_i}{\partial y} = 0\right)$ permit the buildup of large sea-air temperature differences. If the boundary conditions were changed to $\frac{\partial \theta}{\partial y} = 0$, then there would be a flux of heat across the boundaries from south to north which in the absence of advection would maintain the initial oceanic temperature distribution ($T_i = T_a$). At the southern boundary this could be considered to be a rough simulation of the cross-equatorial heat flux during the northern hemisphere winter. We reran the experiments shown in Figure 3 using these flux boundary conditions and, as expected, the sea-air temperature difference at meridional boundaries was reduced by nearly 70% and the zonal jets there were eliminated. However, in the vicinity of the "Gulf Stream", changes in all fields were no more than a few percent. The choice between the boundary conditions, $\frac{\partial T_i}{\partial y} = 0$ and $\frac{\partial \theta}{\partial y} = 0$, evidently has little effect on the formation of the model "Gulf Stream" at mid-latitudes.

If we attempt to compute results for larger ϵ, reversals in the sign of $\frac{\partial \bar{v}}{\partial y}$ begin to appear in the vicinity of the zonal jets and these introduce additional gyres which are resolved by only one or two grid points. Therefore, we doubled the number of grid points to 72 before running additional experiments for larger ϵ. The basic parameters for these experiments were the same as for the previous experiments, except that now $A_b = 8 \times 10^7$ cm^2 sec^{-1}. Experiments using the insulating condition $\left(\frac{\partial T_i}{\partial y} = 0\right)$ at the meridional boundaries developed a small third gyre south of the subtropical gyre and very strong zonal jets at the meridional boundaries. For example, an experiment with $\epsilon = 0.25$ formed a third gyre which had an eastward jet with a maximum speed of 8.7 cm sec^{-1} and a westward jet at the northern boundary with a maximum speed of 10.6 cm sec^{-1}. Both of these exceeded the

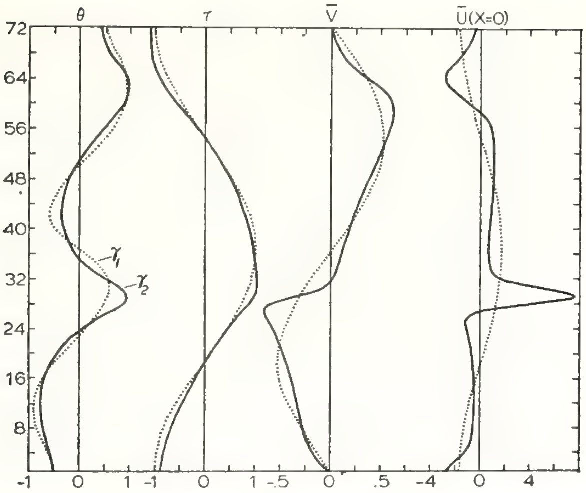

Figure 4. The same as in Figure 3, except for experiments γ_1 and γ_2. Experiment γ_1 has $\epsilon=0$ and experiment γ_2 has $\epsilon=0.25$.

maximum speed of 6.9 cm sec^{-1} in the model "Gulf Stream". Comparable experiments using the flux boundary $\left(\frac{\partial\theta}{\partial y}=0\right)$ again had essentially the same "Gulf Streams" but developed neither the third gyre nor the boundary jets. Figure 4 shows the results of two of these experiments. The curve γ_1 has $\epsilon=0$ and represents the control experiment. In experiment γ_2 enough feedback has been introduced ($\epsilon=0.25$) so that the wind-stress in the vicinity of point 29 has been enhanced by about 23%, comparable to the wintertime enhancement of the stress computed by Leetmaa and Bunker (1978) over the Gulf Stream. The results are much the same as in Figure 3—allowing for the difference in boundary conditions—except for the striking increase of about 30% in the maximum Sverdrup velocity in the subtropical gyre.

Further increases in ϵ eventually cause the calculations to become numerically unstable. We have not found an instance of a stable solution with more than three gyres. Neither have we found an instance of a stable but unsteady solution.

4. Conclusion and comments

Thermal feedback, through the drag coefficient, appears to be capable of producing a "Gulf Stream" without higher order dynamics. There may be other phenomena that can be produced by such a feedback: propagating waves, multiplication of gyres and generation of recirculations, and nonsteady (climate-related?) solutions. These can be explored by further, more sophisticated numerical experimentation.

Two dimensional ocean models deserve attention, and more thought is needed concerning distinctions between different kinds of layer depths: Ekman layers, mixed layers, and above-the-thermocline layers. The idea that sea-air temperature differences, through feedback upon the drag coefficient, can modify circulation patterns is not new; it has been used previously by Emery and Csanady (1973) to explain the direction of the circulation of lakes under uniform winds through heat transport by Ekman drift.

Acknowledgments. The authors would like to acknowledge their debt to Andrew Bunker's stress calculations as the source of some of these speculations, to Mrs. Mary Hunt for compiling the first version of the computer program, and to the National Science Foundation for the support that made the work possible. We are grateful for stimulating conversations with Drs. Pearn Niiler and Joseph Pedlosky.

REFERENCES

Bunker, Andrew F. 1976. Computations of surface energy flux and annual air-sea interaction cycles of the North Atlantic Ocean. Mon. Weather Rev., *104,* 1122–1140.

Emery, K. O. and G. Csanady. 1973. Surface circulation of lakes and nearly land-locked seas. Proc. Nat. Acad. Sci., *70,* 93–97.

Leetmaa, Ants and Andrew F. Bunker. 1978. Updated charts of mean annual wind-stress, convergences of the Ekman layers, and Sverdrup transports in the North Atlantic. J. Mar. Res., *36,* 311–322.

Stommel, Henry, Pearn Niiler, and David Anati. 1978. Dynamic topography and recirculation of the North Atlantic. J. Mar. Res., *36,* 449–468.

Received: *13 June, 1978;* revised: *15 August, 1979.*

4. Journal of Marine Research 37, No. 3, 459-470.

On computing the absolute geostrophic velocity spiral

by David W. Behringer[1]

ABSTRACT

Recently, Stommel and Schott (1977) have proposed a method for computing absolute geostrophic current spirals from observations of the density field alone. Some applications of the method have led to ambiguous results in which the computed spirals have depended on the depth range of the data used. It is shown that the method may be recast into a form which emphasizes its character as a synthesis of the dynamic method and the method of isopycnal analysis. In this form the computations require flow directions from the mapping of potential vorticity on isopycnal surfaces. These directions are a large source of error in the calculations and the likely cause of the aforementioned ambiguities. It is shown that the original method is badly biased in its response to the directional errors. Two variations on the method are presented which are less biased and which give different results than the original method. The discussion is illustrated by an example based on data centered at 28N and 27°30′W in the North Atlantic. Estimates of the errors associated with each method are presented.

1. Introduction

In the classical dynamical method, the vertical shear of the geostrophic velocity is determined from observations of the horizontal gradients in the field of density. The problem remains to determine an absolute reference velocity, and this problem is frequently solved by arbitrarily assuming a level of no motion. Recently, Stommel and Schott (1977) have proposed a quantitative solution which enables the determination of an absolute reference velocity from observations of the density field alone, the same data that are required by the dynamical calculation itself. Applications of their technique yield promising results, but in some instances the absolute velocity computed at a constant reference level depends on the depth range of data used in the calculation (Schott and Stommel, 1978). This ambiguity was not resolved.

The Stommel and Schott (1977) method can be recast in a form which emphasizes its character as a synthesis of the dynamical method and the method of isopycnal analysis. In this form the computation uses absolute flow directions deduced from the mapping of potential vorticity on isopycnal surfaces. If the direction changes with depth, then the directions at two depths and the geostrophic shear be-

---

[1] National Oceanic and Atmospheric Administration, Atlantic Oceanographic and Meteorological Laboratories, 15 Rickenbacker Causeway, Miami, Florida, 33149, U.S.A.

tween them are sufficient to determine a reference velocity. However, if the directions are subject to error, the reference velocity will depend on the pair of depths chosen. In order to reduce the influence of such errors on the reference velocity, Stommel and Schott employ an error minimization scheme which extends over a range of depths. However, the reformulation makes it clear that the minimization is biased by the parts of the depth range where the velocities are largest. Therefore, two simple variations on the original method were developed to give less biased results. When all three methods were applied to the same set of data, the two variations resulted in similar reference velocities which differed from the result of the original method.

In the following discussion, the three methods are briefly described and then applied to a sample set of data from the North Atlantic. The expected error associated with each method is also discussed.

2. Theory

For steady flow in an ideal and incompressible ocean, density, potential vorticity, and the Bernoulli function are materially conserved (Welander, 1971). Because intersections of material surfaces are streamlines, mapping isolines of potential vorticity or Bernoulli function on isopycnal surfaces is equivalent to mapping three-dimensional streamlines. If the dynamics are geostrophic, then the potential vorticity, $PV = f \dfrac{\partial \rho}{\partial z}$, can be determined from the field of density alone, and it becomes a useful parameter in isopycnal analysis (Behringer, 1972)[2]. The geostrophic Bernoulli function, $B = p + g\rho z$, is not immediately useful because its computation requires knowledge of a reference pressure. However, in principle streamlines deduced from isolines of the Bernoulli function on isopycnal surfaces (B/ρ-streamlines) must match identically those deduced from isolines of potential vorticity (PV/ρ-streamlines). This is true because any pair of material properties uniquely determines the flow field. The identity of the two sets of streamlines is a physical constraint on the computation of the reference velocity.

The isolines of potential vorticity on isopycnal surfaces can be represented by the vector,

$$\vec{t} = \vec{\nabla} PV \times \vec{\nabla} \rho \tag{1}$$

which is everywhere parallel to the field of streamlines. It follows from equation (1) that if ϕ is the angle between the horizontal projection of a streamline and the eastward direction, then

$$\tan \phi = -\frac{\partial(PV, \rho)}{\partial(x, z)} \Big/ \frac{\partial(PV, \rho)}{\partial(y, z)} \tag{2}$$

---

[2] The notation is standard. However, definitions of all symbols are given in the appendix.

where

$$\frac{\partial(a, b)}{\partial(x, z)} = \frac{\partial a}{\partial x}\frac{\partial b}{\partial z} - \frac{\partial a}{\partial z}\frac{\partial b}{\partial x}$$

is the Jacobian. An equation for the horizontal velocity components is obtained by setting the ratio of the northward to eastward components equal to tan ϕ:

$$v/u = \tan\phi. \qquad (3)$$

If the velocities are written as sums of the absolute reference velocities, u_0 and v_0, and the relative geostrophic velocities, u' and v', then equation (3) becomes

$$\frac{v_0 + v'}{u_0 + u'} - \tan\phi = 0. \qquad (4)$$

Because the relative geostrophic velocities are determined by the dynamical method, the reference velocities can be determined from any pair of equations (4), as long as ϕ changes with depth.

This analysis can be modified to account for the compressibility and unsteadiness of actual ocean flow if it is assumed that the mean flow is parallel to mean surfaces of constant potential density. The necessary changes are the replacement of *in situ* density by potential density in the calculation of the absolute directions (see appendix) and the treatment of all effects of time-dependent motion on the density observations as noise. Most observations will be contaminated by such noise and thus equation (4) will not be satisfied exactly. Therefore, rather than using only a pair of equations (4) to compute reference velocities, it is better to choose the velocities which minimize the error in the difference expressed by equation (4) over a range of depths. Three simple ways of doing this are as follows.

The first procedure is to choose u_0 and v_0 to minimize the expression,

$$S_1 = \sum \{(v_0 + v') - (u_0 + u')\tan\phi\}^2 \qquad (5)$$

summed over N discreet depths. This is equivalent to the Stommel and Schott (1977) method. The sum is easily minimized by any of several standard techniques; in the present study it was done by determining u_0 and v_0 as the coefficients for the linear regression of $(v' - u' \tan\phi)$ on $\tan\phi$. The flaw in choosing to minimize S_1 is that the procedure is biased in its response to error in tan ϕ. To understand the bias, suppose that the true reference velocity is somehow known *a priori,* then, assuming that the errors in tan ϕ are comparable throughout the depth range of the computation, disproportionately large contributions to S_1 will occur where the velocities, $(u_0 + u')$ and $(v_0 + v')$, are largest. Because S_1 will be minimized only when all contributions to S_1 are of similar magnitude, minimizing S_1 cannot recover the true reference velocity.

A second procedure minimizes the sum:

$$S_2 = \Sigma \left\{ \frac{v_0 + v'}{u_0 + u'} - \tan \phi \right\}^2 . \tag{6}$$

The hazard in minimizing S_2 is that an error in ϕ where the flow is nearly meridional ($\phi = \pm \pi/2$) will dominate the contributions to S_2 and badly bias the determination of the reference velocity. However, away from regions of purely meridional flow, the second procedure will give less biased results than the first.

The third and least biased procedure minimizes the sum:

$$S_3 = \Sigma \left\{ \tan^{-1} \left(\frac{v_0 + v'}{u_0 + u'} \right) - \phi \right\}^2 . \tag{7}$$

The problem here is that a subjective judgement must be made to determine the absolute direction (ϕ or $\phi + \pi$) when only $\tan \phi$ is computed from the data. The sums, S_2 and S_3, are more difficult to minimize than S_1, but it can be done readily enough on a computer using techniques of curvilinear regression. All regression techniques used in this study are discussed by Snedecor and Cochran (1967).

A judgment of the quality of a calculation can be made from an estimate of the 95% confidence limits on the reference velocity. This judgment can be further guided by comparisons of the flow directions, ϕ, defined by equation (2), and the directions, ϕ_g, determined by the computed absolute velocity components: $\tan \phi_g = v/u$. These comparisons may be based on the error sums, S_2 and S_3, which can be evaluated once the reference velocity has been determined. Two measures will be used: the reduction in variance of $\tan \phi$,

$$RV\,(\tan \phi) = 1 - \left\{ s^2_{\Delta\tan\phi} \Big/ s^2_{\tan\phi} \right\} , \tag{8}$$

and the reduction in variance of ϕ,

$$RV\,(\phi) = 1 - \left\{ s^2_{\Delta\phi} \Big/ s^2_{\phi} \right\} , \tag{9}$$

where $s^2_{\tan\phi}$ and s^2_{ϕ} are the sample variances of $\tan \phi$ and ϕ, respectively, and $s^2_{\Delta\tan\phi} = S_2/(N{-}2)$ and $s^2_{\Delta\phi} = S_3/(N{-}2)$ are the sample variances of ($\tan \phi - \tan \phi_g$) and ($\phi - \phi_g$), respectively. The values of these expressions will be less than +1 and will approach +1 as the differences between ϕ and ϕ_g become smaller. Values approaching +1 will also imply that the shorter scale variations in ϕ are small compared to the overall turning of the spiral, because, as experience suggests, ϕ_g is a much smoother function of depth than ϕ. The expressions (8) and (9) can be evaluated regardless of how the reference velocity has been determined, but they will be maximized when the reference velocity has been obtained by minimizing S_2 and S_3, respectively.

It was stated earlier that the B/ρ-streamlines should be identical with the PV/ρ-streamlines. The direction, ϕ_B, of a B/ρ-streamline is given by

$$\tan \phi_B = -\frac{\partial(B,\rho)}{\partial(x,z)} \bigg/ \frac{\partial(B,\rho)}{\partial(y,z)} \tag{10}$$

which reduces to

$$\tan \phi_B = -\frac{\partial p}{\partial x} \bigg/ \frac{\partial p}{\partial y} \, . \tag{11}$$

Because the pressure, p, cannot be established, ϕ_B cannot be determined independently. However, once the reference velocity has been computed, ϕ_B can be found diagnostically: $\phi_B = \phi_g = \tan^{-1} v/u$. In this way the expressions (8) and (9) also test whether a calculation is self-consistent with the constraint requiring the identity of the two kinds of streamlines. Obviously, tests of self-consistency are much more limited than what would be possible if ϕ_B could be determined independently.

3. Sample computations

To illustrate the three methods, data have been selected from hydrographic stations in the eastern North Atlantic. They are *Discovery* stations 3595 through 3599 along 24°15′N and 3636 through 3640 along 32N; sections and profiles of these temperature and salinity data can be found in Fuglister's (1960) atlas. The data are part of the data used by Schott and Stommel (1978) at their site B.

The temperature and salinity data at each station were first interpolated to standard depths. Then the five stations at each latitude were reduced to a pair of "least squares stations" based on linear regressions of temperature and salinity with longitude. The reduced stations are at the corners of a rectangle defined by the latitudes 24°15′N and 32N and the longitudes 24°30′W and 30°30′W. They are assumed to represent mean conditions with much of the noise due to measurement error and eddy motion removed.

The potential density used in the computations is referred to 1300 meters rather than to surface (see appendix). The directions of flow were then computed using a second order difference approximation to equation (2). The results are shown in Figure 1 as the angle measured with respect to the eastward direction. The smooth curve in Figure 1 is a third order polynomial fitted to the computed directions between 75 and 2000 meters.

The relative velocity hodograph, computed by the dynamic method from the reduced stations, is shown in Figure 2. The computed directions are also shown, represented by straight lines on the u, v-plane and intersecting the hodograph at the appropriate depths. The intersection of a pair of directional lines represents the origin for the hodograph which would be determined by solving the corresponding pair of equations (4) for the reference velocities. Ideally there would be a single intersection for all of the lines; in fact, there is a great amount of scatter.

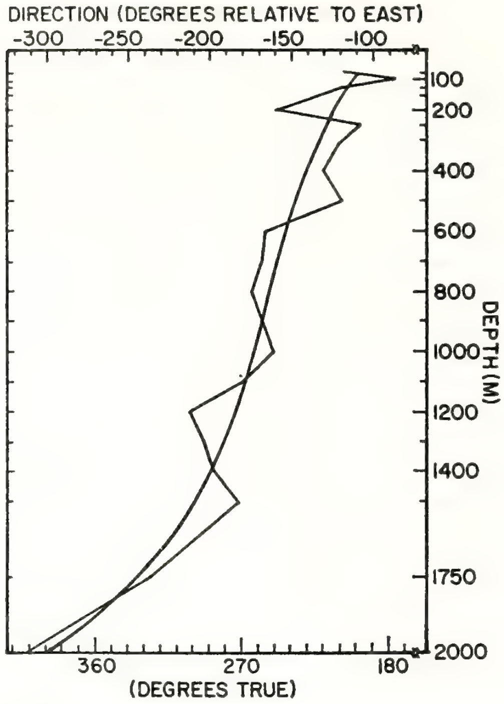

Figure 1. Absolute flow directions. The broken line connects the raw directions computed from equation (2). The smooth curve is a third order polynomial fitted to the raw directions for the depths between 75 and 2000 meters.

It is apparent in Figure 2 that the directional lines fall into distinct groups which are associated with particular depth ranges. Some groups have a strong focus at a single intersection (e.g., 1200-1500 meters) while others have little or no focus (e.g., 600-1000 meters). Table 1 lists the reference velocities at 1500 meters as they are computed by the three different procedures for several of these groups. Two points are clear; first, as expected, the three procedures give similar reference velocities only for groups with well focused directions and, second, the reference velocities are

Table 1. Reference velocities (u_0, v_0) at 1500m in cm/sec.

Depth range (m)	Via procedure which minimizes sum: S_1	S_2	S_3
250- 400	(0.38, 0.69)	(0.34, 0.60)	(0.34, 0.62)
250- 500	(0.36, 0.59)	(0.23, 0.33)	(0.07, 0.09)
600-1000	(0.44, 0.45)	(8.25, 2.15)	—
800-1000	(0.65, 0.42)	(0.70, 0.43)	(0.71, 0.43)
1000-1200	(−0.04, 0.18)	(−0.04, 0.18)	(−0.04, 0.18)
1200-1500	(0.27, −0.03)	(0.29, −0.03)	(0.28, −0.03)

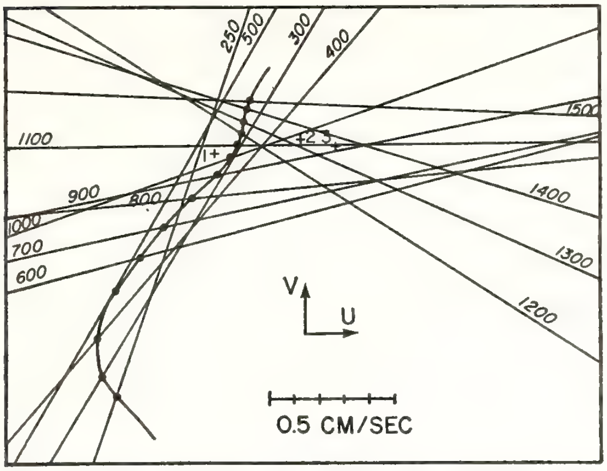

Figure 2. The relative velocity hodograph. The straight lines represent the raw flow directions computed from equation (2); they intersect the hodograph at the appropriate depths. The depth labels are in meters.

very different for different groups. The second point has been noted previously by Schott and Stommel (1978).

In the present example, the clustering of the directional lines does not appear to improve the overall focus of the intersections. On the contrary, the clustering seems to degrade the focus: most intersections within a group lie to the left of the hodograph, while most intersections between groups lie to the right (Fig. 2). Thus, if the underlying assumption of geostrophic flow confined to isopycnal surfaces is valid for the entire depth range, then it is unlikely that the clustering of the directional lines has any physical significance for the mean flow. It is more likely that it is the result of noise in the computation of the directions from equation (2), an equation which involves second order derivatives of density.

Because of the noisy flow directions, it is important to use a large depth range in the computations so that many standard levels are included and so that the overall change in ϕ is as large as possible. Table 2 lists the reference velocities at 1500 meters computed by the three methods for the depth range of 250 to 1500 meters.

Table 2. Reference velocities at 1500 m based on the depth range 250-1500 m. Units are cm/sec.

					Smoothed	
Procedure	u_0	v_0	$RV(\tan\phi)$*	$RV(\phi)$*	u_0	v_0
S_1	0.15±0.12	0.22±0.13	−5.50	−8.00	−0.32	0.19
S_2	−0.20±0.24	0.14±0.12	0.58	0.61	−0.34	0.18
S_3	−0.35±0.31	0.18±0.10	0.51	0.70	−0.37	0.18

* for this example, $S^2_{\tan\phi} = 1.0$ and $S^2_{\phi} = 32.6$.

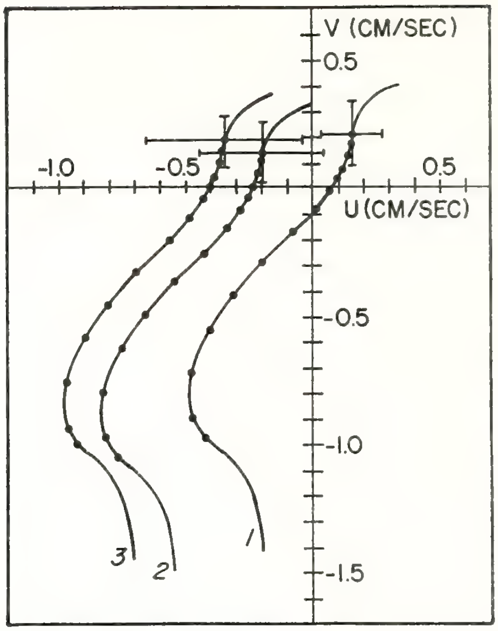

Figure 3. The absolute velocity hodographs computed by the three methods described in the text. The points mark the standard depths (250-1500 m) used in computations. The total range shown is 50 to 2500 meters. Error bars represent the 95% confidence limits.

The origins for the hodograph corresponding to these results are shown as numbered points in Figure 2, and the absolute hodographs are shown in Figure 3. The standard regression techniques used to compute the reference velocities also permit a formal estimate of the expected errors. Those shown represent the 95% confidence interval based on the deviation from regression and the *t*-distribution, assuming 12 degrees of freedom from the 14 standard levels in the calculation. Whether the assumption of 12 degrees of freedom is justified and, thus, whether the error estimates have meaning will be discussed later.

Table 2 shows that the east/west reference velocities at 1500 meters are barely, if at all, significantly different from zero. Also, the first method gives eastward velocity at 1500 meters which is significantly different from westward velocities given by other methods. This difference is the result of the bias of the first method toward matching the directions in the upper water column where the velocities are largest. The bias can be seen in Figure 2 if one imagines radial lines drawn from an origin at point 1 to intersections with the hodographs at various depths.

The differences between such radial lines and the directional lines would be relatively small at shallow depths but would increase sharply with increasing depth.

The reductions in variance of tan ϕ and ϕ listed in Table 2 show that the first method badly fails both tests. On the other hand, each of the other methods does well by either test, not only by the test it is best suited for.

The last column of Table 2 shows that for this particular example all three methods give similar results when smoothed directions are used. The smoothed directions are taken from the polynomial fit shown in Figure 1.

4. Discussion

A few conclusions can be drawn from this study with some certainty. First, the physical assumptions which form the basis for the computations require that PV/ρ- and B/ρ-streamlines must be identical. Although the B/ρ-streamlines cannot be determined independently of the computed velocity spiral, the second and third methods assure results which are more self-consistent with this constraint than the results of the first method.

Second, noise in the flow directions is the cause of the differences in the results of the three methods and the differences in the results when different depth ranges are used. In the present example, both kinds of differences were greatly reduced when a smoothed representation of the directions was used.

Third, the formal estimates of the errors in the reference velocities shown in Table 2 are large, but they should be larger. The computations were made under the assumption that the errors in the directions at each of the 14 standard depths were independent, thus allowing 12 degrees of freedom in the estimates of the velocity errors. This assumption is not justified, since much of the error in the data is likely to be due to the influence of eddy motion extending well into the main thermocline. A rough attempt to improve the error estimates can be made by reducing the number of standard levels used in the calculation to those thought to be independent. A subjective choice of five levels (500, 800, 1000, 1200 and 1500 meters) was made on the grounds that they were approximately evenly spaced and that the computed raw directions alternate back and forth across the mean trend of the directions (Fig. 1). Recomputing the reference velocities using the second method, the results were $u_0 = (-0.20 \pm 0.69)$ cm/sec and $v_0 = (0.17 \pm 0.31)$ cm/sec. A comparison of these numbers with the second line of Table 2 shows that the 95% confidence limits have more than doubled.

Beyond these essentially technical conclusions, any statements about the computations must be tempered by the large uncertainties in the results. However, some comparisons to other observations are encouraging. The second and third methods give a westward flow at 1200 meters, the depth at which one expects to find the westward outflow of the Mediterranean Sea. A troublesome aspect of the results of the first method and of the earlier Stommel and Schott (1977) results was the eastward velocity at this depth and location.

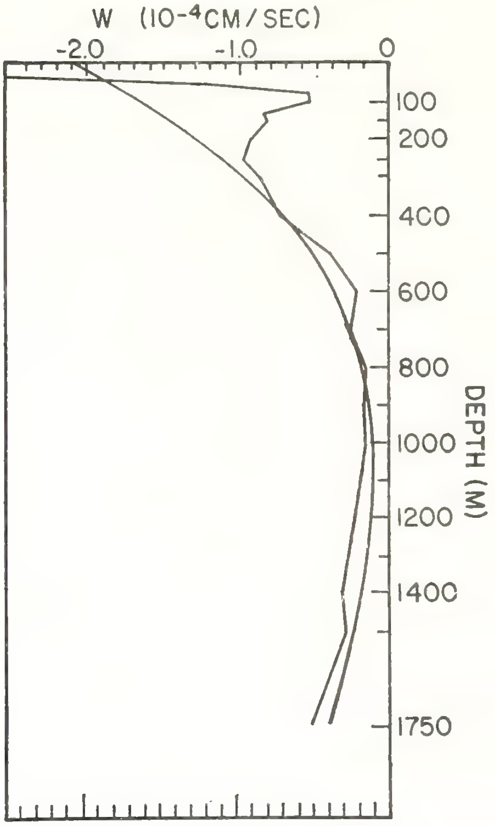

Figure 4. The vertical velocity in units of 10^{-4} cm/sec. See the text for an explanation of the two curves.

In addition, the comparison is good between the vertical velocity computed from the conservation law for potential density and from the equation:

$$w = w_0 + \int \beta/f \, v dz \,. \tag{12}$$

Figure 4 shows the two curves superposed. The smooth curve corresponds to equation (12); the integration constant is chosen so that the mean difference between the curves is zero for the 250-1500 meters depth range. Leetmaa (personal communication) has computed the vertical velocity at the surface due to Ekman pumping. For the area of the present study, his average value of -1.9×10^{-4} cm/sec compares very well with the value of -2×10^{-4} computed from equation (12).

Acknowledgments. I thank Dr. Ants Leetmaa for many useful discussions of this subject. Professor Henry Stommel and Dr. Fritz Schott generously made a copy of their 1978 paper available to me prior to its publication.

APPENDIX

The equations of motion for steady geostrophic, and hydrostatic flow are:

$$\rho f v = \frac{\partial p}{\partial x}, \tag{A.1}$$

$$-\rho f u = \frac{\partial p}{\partial y}, \tag{A.2}$$

$$-\rho g = \frac{\partial p}{\partial z}, \tag{A.3}$$

the continuity equation for compressible flow is:

$$\frac{\partial}{\partial x}\ (\rho u) + \frac{\partial}{\partial y}\ (\rho v) + \frac{\partial}{\partial z}\ (\rho w) = 0\ , \tag{A.4}$$

and the conservation equation for potential density is:

$$\vec{v} \bullet \vec{\nabla} \rho_\theta = R_\rho \tag{A.5}$$

where *x*, *y* and *z* are the eastward, northward and vertical (positive upward) coordinates, respectively, and *u*, *v*, and *w* are the corresponding components of the vector velocity, v; the pressure is *p*, the *in situ* density is ρ, and the potential density is ρ_θ. The residual, R_ρ, includes the effects of heating, and mixing, but here it is assumed that R_ρ is zero and that ρ_θ is materially conserved.

Cross-differentiating equations (A.1) and (A.2) and substituting from equations (A.3) through (A.5) leads to a conservation equation for potential vorticity:

$$\vec{v} \bullet \vec{\nabla} \left(f \ \frac{\partial p_\theta}{\partial z} \right) = R_{pv} \tag{A.6}$$

where

$$R_{pv} = g/\rho \left(\frac{\partial \rho}{\partial x} \frac{\partial p_\theta}{\partial y} - \frac{\partial \rho}{\partial y} \frac{\partial p_\theta}{\partial x} \right). \tag{A.7}$$

Next, let p_θ represent a pressure function which satisfies the equation

$$\frac{\partial p_\theta}{\partial z} = -g\rho_\theta \tag{A.8}$$

subject to the condition that $p_\theta = p$ at z_r, the reference level for p_θ. Using equation (A.8) in conjunction with the equations (A.1) through (A.5), allows the derivation of the Bernoulli equation:

$$\vec{v} \bullet \vec{\nabla}\ (p_\theta + g\rho_\theta z) = R_B \tag{A.9}$$

where

$$R_B = u \frac{\partial I}{\partial x} + v \frac{\partial I}{\partial y}$$

and

$$I = g \int_z^{z_r} (\rho - \rho_\theta)\, dz\ .$$

When considering the flow at depths greater than a few hundred meters, ρ_θ will be more nearly a material property if it is referred to a deep level rather than to the sea surface (Lynn and Reid, 1968). A deep reference level is also important to insure that R_{pv} and R_B are sufficiently small that potential vorticity, PV_θ, and the Bernoulli function, B_θ, are approximately

Table 3. Normalized values of R_{pv} and R_B and differences in computed flow directions for ρ_θ referred to 1300 m and to 0 m.

Depth (m)	R_{pv} for a reference level of: 1300 m	0 m	$\Delta\phi$	R_B for a reference level of: 1300 m	0 m
200	.01	0	2	−.02	.01
400	0	0	−1	−.04	.02
800	−.09	.09	10	−.07	.07
1000	−.06	.22	9	−.04	.04
1200	−.04	.51	17	0	.08
1500	.05	.84	17	0	.36

conserved. Table 3 lists R_{pv} and R_B at several depths when ρ_θ is referred to 1300 meters and to 0 meters. The numbers have been normalized. For example, R_{pv} was divided by the flow speed times the spatial rate of change of PV_θ parallel to the ρ_θ surface and normal to the flow direction. A value of ± 1 implies that the change in PV_θ is as great in the downstream direction as in the cross stream direction. The differences in the computed directions for the two reference levels are also shown. At 800 meters and below, the flow directions computed when ρ_θ is referred to 1300 m are systematically larger than when ρ_θ is referred to 0 meters.

REFERENCES

Behringer, D. W. 1972. Investigations of large scale oceanic circulation patterns using historical hydrographic data. Ph.D. dissertation University of California, San Diego.

Fuglister, F. C. 1960. Atlantic Ocean Atlas, Woods Hole, 209 pp.

Lynn, R. J., and J. L. Reid. 1968. Characteristics and circulation of deep and abyssal waters. Deep-Sea Res., *15,* 577–598.

Schott, F., and H. Stommel. 1978. Beta-spirals and absolute velocities in different oceans. Deep-Sea Res., *25,* 961–1010.

Snedecor, G. W., and W. G. Cochran. 1967. Statistical methods, 6th ed., Ames, Iowa, The Iowa State University Press, 593 pp.

Stommel, H. and F. Schott. 1977. The beta-spiral and the determination of the absolute velocity field from hydrographic station data. Deep-Sea Res., *24,* 325–329.

Welander, P. 1971. Some exact solutions to the equations describing an ideal-fluid thermocline. J. Mar. Res., *29,* 60–68.

Received: *24 May, 1978;* revised: *21 March 1979.*

Printed in U.S.A. for the Sears Foundation for Marine Research,
Yale University, New Haven, Connecticut, 06520, U.S.A.
Van Dyck Printing Company, North Haven, Connecticut, 06473, U.S.A.

5. Tellus 31, 548-557.

Horizontal divergence, acceleration and curvature change, a diagnostic equation with applications

By FRANK CHEW, *National Oceanographic and Atmospheric Administration, Atlantic Oceanic and Meterological Laboratories, 15 Rickenbacker Causeway, Virginia Key, Miami, Florida 33149, U.S.A.*

(Manuscript received February 8; in final form May 21, 1979)

ABSTRACT

The horizontal divergence of an accelerating flow is discussed in the contexts of meandering currents and the formation of eddy-rings. The purpose is to help discern areas of upwelling and other dynamical features. Two interrelated hypotheses, representing two meso-scale versions of the turning vorticity equation (Chew, 1975), are formulated with the help of the Florida Current data of Schmitz (1969). The first is a generalization of the pioneer work of Bjerknes (1937) on the relation between horizontal divergence and curvature vorticity change. Along a meandering flow in the northern hemisphere, and away from the equator, the hypothesis predicts horizontal convergence where there is a rapid increase in centripetal acceleration, and horizontal divergence where the increase is in centrifugal force. In particular, in a meandering surface flow with a succession of cyclonic and anticyclonic turns, the hypothesis predicts a series of alternating upwelling and downwelling tongues.

The second hypothesis illuminates a study by Fuglister (1972) of the role of vertical motion in the formation and evolution of eddy-rings. Eddies, as cut-off meanders, are initially irregular in shape. According to this hypothesis, an eddy evolving into a ring with circular symmetry is entering a stage of non-divergence and hence a stage of stability.

1. Introduction

Horizontal divergence in a surface flow is of general interest because it often brings nutrients to the euphotic zone, and is a key to the dynamics of the flow. The latter is better seen in meteorology where, e.g., horizontal divergence is a central consideration in weather analysis generally, and a building block in the theory of cyclones in particular. In this paper, the divergence intrinsic to an accelerating flow of inviscid fluid is considered. We seek to relate divergence explicitly to the process of acceleration, particularly that related to curvature change when a current turns.

Being a vector, horizontal acceleration has two components. In natural coordinates, they are the downstream acceleration and that related to curvature change, the centripetal acceleration or its equal and opposite the (apparent) centrifugal force. The relationship between these accelerations and the horizontal divergence is contained in the turning vorticity equation (Chew, 1974, 1975). But we will re-derive the relation more directly, calling it the divergence-acceleration equation.

The diagnostic potential of the divergence-acceleration equation is first illustrated using the observational results of Schmitz (1969). This serves two purposes: one, to show how hitherto overlooked information can be extracted from the observations, and two, to assess the relative magnitude of the different terms in the equation. On the basis of this assessment, and the prevalence of meandering flows we next pose two hypotheses. One, a quasi-steady hypothesis, relates the occurrence of divergence to downstream change in centripetal acceleration, or to curvature change since the sign of the centripetal acceleration depends on the sign of the curvature. This allows a ready determination of where divergence is likely to occur, as well as its order of magnitude, as will be illustrated in the Gulf Stream and a much weaker and smaller undulating frontal jet. The other hypothesis, emphasizing the time-dependent elements, relates divergence to curvature vorticity change in

0040-2826/79/060548-10$02.50/0 © 1979 Munksgaard, Copenhagen

eddy-rings. This views eddy-ring formation in the North Atlantic and off East Australia as sharing a common dynamics, where the evolution from a first asymmetric stage to a later one of symmetry corresponds to a transition from a first stage of appreciable divergence to a later one of non-divergence.

2. The divergence-acceleration equation

We consider a steady, adiabatic flow with horizontal velocity component $\mathbf{V}$ and vertical component $w\mathbf{k}$, where $\mathbf{k}$ is the vertical unit vector, positive upward. We adopt the Bousinesq approximation that the inertia of the fluid is unaffected by its horizontal density variation. And for notation convenience we write

$$d(\ )/dt = \mathbf{v}\cdot\nabla(\ ) + w\,\partial(\ )/\partial z \tag{1}$$

where ∇ is the horizontal del operator, and z the vertical coordinate. Then the equation of motion for the horizontal component of the flow is

$$d\mathbf{V}/dt = -\mathbf{k}\times f\mathbf{V} - (1/\rho_0)\,\nabla p \tag{2}$$

where f is the local planetary vorticity or the Coriolis parameter; p is pressure; and ρ_0 is the fluid density such that $\nabla\rho_0 = 0$.

A natural coordinate system uses the downstream and cross-stream directions of the local velocity as horizontal reference. Writing V for the magnitude of $\mathbf{V}$, we denote the downstream direction by the unit vector $\mathbf{s}$, defined by $\mathbf{s} = \mathbf{V}/V$; and the cross-stream direction by the unit vector $\mathbf{n}$, defined by $\mathbf{n} = \mathbf{s}\times\mathbf{k}$, positive to the right of $\mathbf{V}$. Then writing K for the horizontal curvature, we have

$$d\mathbf{V}/dt = \mathbf{s}\,dV/dt - \mathbf{n}KV^2 \tag{3}$$

where dV/dt is the magnitude of the downstream acceleration, and KV^2 the magnitude of the cross-stream or centripetal acceleration. Thus the vertical component of the curl of $d\mathbf{V}/dt$ is

$$\begin{aligned}\mathbf{k}\cdot\nabla\times d\mathbf{V}/dt &= \mathbf{k}\cdot\{\mathbf{s}(\partial/\partial s) + \mathbf{n}(\partial/\partial n)\}\\ &\quad\times\{\mathbf{s}\,dV/dt - \mathbf{n}KV^2\}\\ &= +(\partial/\partial s)\,KV^2 + (\partial/\partial n)\,dV/dt\\ &\quad + Kw\,\partial V/\partial z + KVD\end{aligned} \tag{4}$$

Where $D = \nabla\cdot\mathbf{V}$ is the horizontal divergence, and the last two terms a consequence of the changing orientations of the unit vectors $\mathbf{n}$ and $\mathbf{s}$ (Haltiner and Martin, 1957). Since the vertical component of the curl of the right-hand side of (2) is minus $fD + df/dt$, the divergence-acceleration equation is

$$\begin{aligned}(f+KV)\,D = &-(\partial/\partial s)\,KV^2 - (\partial/\partial n)\,dV/dt\\ &- Kw\,\partial V/\partial z - df/dt\end{aligned} \tag{5}$$

The first term on the right-hand side represents the downstream change in centripetal acceleration, the second the cross-stream change in downstream acceleration and has been called the banking term because in surface flows it is related to the lateral tilting of the sea surface, the third a vertical advection modulated by curvature and the fourth the so-called beta effect. Hence, in general, horizontal divergence is dependent on a centripetal effect, a banking effect, a curvature-vertical advection effect, and a beta effect. In contrast, in terms of the relative vorticity ζ, the divergence is given by

$$(f+\zeta)\,D = -d\zeta/dt - \mathbf{k}\cdot\nabla w\times(\partial/\partial z)\,\mathbf{V} - df/dt \tag{6}$$

(Haltiner and Martin, 1957).

3. The Schmitz observation and the evaluation of eq. (5)

Between May 24 and June 24, 1965, Schmitz measured the Florida Current along the two sections shown in Fig. 1, repeating them alternately for 12 transects along each section to achieve a representation of the mean flow. His observational results are reproduced in Table 1 for a one-moving-layer approximation. The variables u and v are respectively the eastward and northward velocity components averaged over the layer depth H, defined as the thickness of the surface layer with a vertically averaged sigma-t of 25.0. Plots of v and H are given in Fig. 2 where the abrupt shear zones at the extreme edges of the current are assumed to be frictional boundary layers. Of interest is the open region seaward of these boundary layers and sandwiched between the two sections. Regarding this open region Schmitz wrote that "In the anticyclonic (shear) zone, the flow pattern at the southern transect is wider, deeper, and slower than that at the narrower northern transect. However, the current is decelerating slightly in the cyclonic (shear) zone." Clearly, the Bernoulli acceleration is asymmetric, with the right flank accelerating but the left flank decelerating.

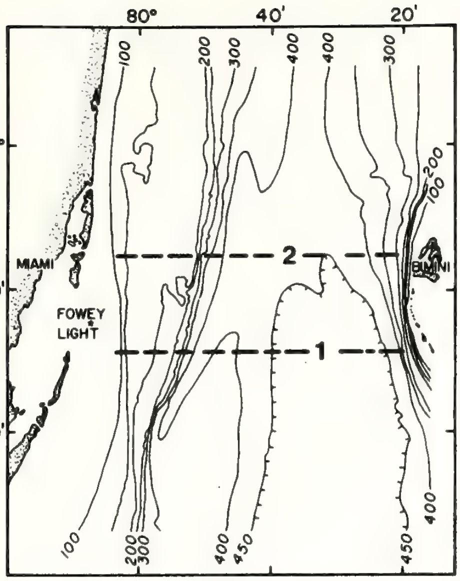

Fig. 1. The locations of sections and stations in the Schmitz observation. The north–south distance between the sections is 25 km (depth in fathoms).

There was no measurement of the flow curvature. But while Schmitz assumes the curvature effect to be negligible, we will estimate its importance by using his data to evaluate the other terms in (5), finding the curvature change effect as a residual. In this evaluation, due north (y) and east (x) are taken, respectively, as the down and cross-stream directions. The small departure is assumed insignificant.

To minimize estimation errors we consider averages for the region. The horizontal divergence $\langle D \rangle$ averaged over the region is obtained by using

$$\langle D \rangle = (B-A)^{-1} \int_A^B D\,dx = \{ \int_A^B (\partial v/\partial y)\,dx + (u_B - u_A) \} (B-A)^{-1} \quad (7)$$

where $\partial v/\partial y$ is approximated by the northward speed difference between the two sections divided by 25 km, and u_A and u_B by averaging the corresponding components at A where x = 10 km, and at B where x = 83 km. This yields

$$\langle D \rangle = 3.6 \times 10^{-6}/\text{s} \quad (8)$$

due principally to the northward acceleration of the flow since

$$(u_B - u_A)/(B-A) = (-1.5\text{–}6.0)\ (\text{cm/s})/(73\ \text{km}) = -1.0 \times 10^{-6}/\text{s}$$

Table 1. *The Schmitz data for a one-moving-layer approximation. Reproduced from Schmitz (1969)*

x coord. (km)	H Layer depth (m)	u E/W avg. current comp. (cm/s)	v N/S avg. current comp. (cm/s)	Transport. stream function (20×10^6 m^3/s)
6	20	0*	0*	0.00*
10	53	2	86	0.01
15	77	5	110	0.02
20	100	7	128	0.05
25	121	12	154	0.09
30	147	12	154	0.14
35	173	9	152	0.20
45	208	12	145	0.34
55	246	8	129	0.50
65	273	9	116	0.66
70	282	7	111	0.74
75	288	12	103	0.81
80	295	11	96	0.89
83	299	10	94	0.93
86	20	0*	0*	0.96
5	20	0*	0*	0.00*
10	77	10	94	0.01
15	92	12	119	0.03
20	126	21	139	0.07
25	146	22	145	0.12
30	173	20	146	0.18
35	200	19	139	0.24
45	233	17	130	0.39
55	265	13	118	0.54
65	286	4	96	0.69
75	305	−3	79	0.82
80	304	−10	67	0.87
83	310	−13	59	0.90
87	318	−19	46	0.94
90	20	0*	0*	0.95

* Indicates assumed value at boundary.

Hence for $f = 6.3 \times 10^{-5}$/s,

$$\langle fD \rangle = 2.27 \times 10^{-10}\ \text{s}^{-2} \quad (9)$$

In the one-moving-layer approximation of Schmitz, the steady-state downstream acceleration reduces to $dV/dt = \frac{1}{2}\partial V^2/\partial s$, and corresponds to the change of horizontal kinetic energy along a transport stream function. According to Table 1 the same stream function is located at x = 10 km at both sections, while the stream function 18×10^6 m^3/s is located at x = 83 km at the southern section but near 81 km at the northern section.

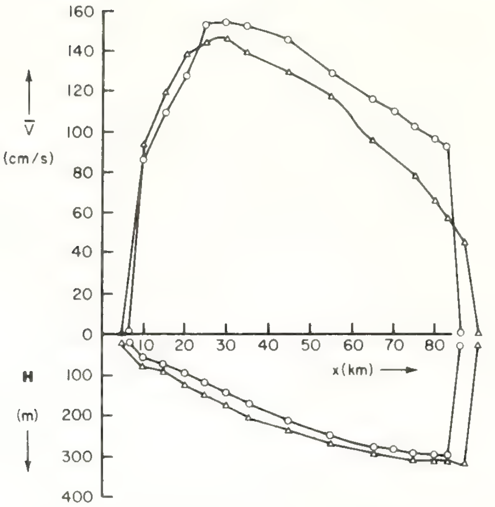

Fig. 2. Northward speed (v) and surface layer depth or thickness (H) vs. distance to the east (x). Triangles for the southern section and circles for the northern section as shown in Fig. 1. The narrow zones to the left of $x = 10$ km, and to the right of $x = 83$ and 87 km are assumed to be the frictional boundary layers. Reproduced from Schmitz (1969).

Hence along these stream functions, for A at $x = 10$ km,

$$(dV/dt)_A = \{\tfrac{1}{2}(\partial/\partial s)(u^2 + v^2)\}_A$$

$$= -3.1 \times 10^{-4} \text{ cm/s}^2$$

While for B near $x = 83$ km,

$$(dV/dt)_B = 1.1 \times 10^{-3} \text{ cm/s}^2$$

Thus we have

$$\langle(\partial/\partial n)\, dV/dt\rangle = \{(dV/dt)_B - (dV/dt)_A\}(B - A)^{-1}$$
$$= 1.1 \times 10^{-10} s^{-2} \tag{10}$$

While $\partial V/\partial z$ is identically zero in the one-moving-layer, it can be as large as 0.0075 s^{-1}, according to Niiler and Richardson (1973, Fig. 6). And if we use (8), at 100 m the vertical speed $w = 0.036$ cm/s. It follows that for $\langle K\rangle = 1/(150 \text{ km})$, the order of magnitude of the last two terms in (4) are

$$\left.\begin{aligned} \langle KVD\rangle &= \pm 0.3 \times 10^{-10} \text{ s}^{-2} \\ \langle Kw(\partial V/\partial z)\rangle &= \pm 0.2 \times 10^{-10} \text{ s}^{-2} \end{aligned}\right\} \tag{11}$$

The beta term is similarly small at

$$\langle df/dt\rangle = 0.3 \times 10^{-10} \text{ s}^{-2} \tag{12}$$

for $\langle v\rangle = 121$ cm/s in accordance with Table 1. Hence dropping these small terms we find

$$\langle(\partial/\partial s)\, KV^2\rangle = -3 \times 10^{-10} \text{ s}^{-2} \tag{13}$$

Schmitz gives typical errors of 5–10% of for the u component and 3–5% for the v component. A 15% error for (13) seems reasonable. So summarizing the evaluation we have

$$\left.\begin{aligned} \langle fD\rangle &= 2 \times 10^{-10} \text{ s}^{-2} \\ \langle(\partial/\partial s)\, KV^2\rangle &= -3 \times 10^{-10} \text{ s}^{-2} \\ \langle(\partial/\partial n) dV/dt\rangle &= 1 \times 10^{-10} \text{ s}^{-2} \\ \langle df/dt\rangle &= 0.3 \times 10^{-10} \text{ s}^{-2} \\ \langle KVD\rangle &= \pm 0.3 \times 10^{-10} \text{ s}^{-2} \\ \langle Kw\, \partial V/\partial z\rangle &= \pm 0.2 \times 10^{-10} \text{ s}^{-2} \end{aligned}\right\} \tag{14}$$

4. A curvature-dominated hypothesis

It is clear from (14) that the leading terms in (5) are the divergence and centripetal terms. So where

$$(\partial/\partial s)\, KV^2 > (\partial/\partial n)\, dV/dt \tag{15}$$

and

$$(\partial/\partial n)\, dV/dt > df/dt \tag{16}$$

we have approximately

$$\left.\begin{aligned} &(f + KV)\, D = -(\partial/\partial s)\, KV^2 \\ &\text{or} \\ &D = -(f + KV)^{-1}\, (\partial/\partial s)\, KV^2 \end{aligned}\right\} \tag{17}$$

That is, in a curvature-dominated meander where the flow is quasi-steady and $f > KV$, divergence occurs where the centrifugal force ($-KV^2$) increases downstream.

Where the amplitude of a meandering current is small, KV^2 varies from zero to a maximum in a distance approximately equal to a quarter wavelength ($L/4$). We denote this change in KV^2 by δKV^2, and the change in dV/dt across a current of width N by $\delta dV/dt$. Hence from (15) the wavelengths to which (17) is applicable is given by

$$L < 4N(\delta KV^2/\delta dV/dt) \tag{18}$$

barring such idealized regimes as gradient flow where dV/dt is zero but KV^2 may vary, accelerating rectilinear flow where KV^2 is zero but dV/dt may vary, and geostrophic flow where both KV^2 and dV/dt are zero. Where the magnitude of the acceleration ratio in (18) is of the order one, then for $N = 100$ km, the upper limit of applicable wavelengths is of the order

$$L = 0\ (400\ \text{km}) \tag{19}$$

Away from the equator where generally $f > KV$, mass distribution across a meandering flow reflects the approximate balance between the Coriolis and the cross-stream pressure gradient force. In the northern hemisphere and looking downstream this means that along the left flank, colder subsurface water is nearer the sea surface. Therefore, where divergence first succeeds in surfacing cold water, the upwelling will occur on the left side. The rate of upwelling, however, will be uneven in that region, since changes in centrifugal force are generally different for different parts of the flow. This is an important point in the following application of (17).

According to Taft (1971), upwelling north of the Somali Current off the Horn of Africa does not appear to be primarily wind-driven. Rather, it occurs north of where the current turns eastward abruptly. Since the north side is the left side and the abrupt turn corresponds to an abrupt increase in centrifugal force, this is in support of (17).

In the upwelling off Cochin, India, Banse (1968) also denies the winds a primary role. But while he suggest an adjustment process related to the strength of the current, the work of Duing (1970, Fig. 11) shows, interestingly, a meandering current turning anticyclonically off Cochin, again in support of (17).

The flow of the California Current around capes and points of land occurs over distances well within the limit of (19). In following the coastal contours the curvature of the current is positive where it rounds a cape and negative where it turns to resume its southward flow. Hence, according to (17) divergence is expected south of the cape, where the curvature changes from positive to negative, in agreement with the works of Arthur (1965) and Yoshida (1967, p. 63). Similarly, divergence may also be expected in the northbound Davidson Current if it rounds the capes with comparable speed. For the Davidson Current, however, any upwelling will be farther offshore, although it will still be to the south of a cape.

At the sea surface, the cold water from horizontal divergence is sometimes masked by insolation. Nevertheless, upper subsurface isotherms will rise in a divergence and fall in a convergence. Chew (1974) describes two such cases: one in the Loop Current in the Gulf of Mexico, and one in the meandering Florida Current north of Cuba. In both cases upper isotherms ascended as centrifugal force increased, and descended as the force decreased. Two other observed features are the fragments of warm water on the left side, and the change in horizontal temperature gradient. The fragments (Fig. 3) were at locations that could be interpreted as having been separated from the main flow by the upwelling that attends an increase in centrifugal force. More definite is the tendency for the horizontal temperature gradient to decrease with divergence and increase with convergence, a point to remember in the next example.

In his review of primary production in the sea, Yentsch (1974, p. 116) attributes increased productivity in western boundary currents to an imbalance between pressure gradient and Coriolis forces. An example of this imbalance in the Gulf Stream is the situation of February 26, 1975, shown in Fig. 4 from Legeckis (1978). On that day infrared image of sea surface temperature shows the stream to meander between Savannah and Cape Fear with a wavelength of about 250 km between anticyclonic turns. If the stream flow is assumed to be in the general direction parallel to the inshore boundary of the meander, then according to (17), convergence is indicated in the stream segment between Savannah and Long Bay, and divergence in the shorter segment between Long Bay and Cape Fear. Considering first the divergence segment, we estimate the curvatures at both the turns off Long Bay and Cape Fear at about 1/(55 km), positive at the cyclonic and negative at the anticyclonic turn 110 km downstream. Thus, for $V = 100$ cm/s, and f corresponding to 33° N, eq. (17) gives a divergence of the order of

$$D = 4.5 \times 10^{-6}\ \text{s}^{-1} \tag{20}$$

Because of the asymmetry of the meander, the convergence in the upstream segment is smaller at

$$D = -1.3 \times 10^{-6}\ \text{s}^{-1} \tag{21}$$

if we take $-1/(150$ km) for the curvature of the turn off Savannah, 250 km for the downstream distance to the next cyclonic turn, and V and f as before. Downstream of the turn off Cape Fear there is again convergence, according to (17).

This alternating pattern appears reflected in the surface temperature contrast across the inshore boundary. To see this, recall from the preceding example the observed tendency for decreasing horizontal temperature gradient with divergence, and increasing gradient with convergence, a tendency that parallels the meteorological one where divergence promotes frontolysis and convergence frontogenesis. In terms of Fig 4, a weaker temperature gradient means a softer contrast. Therefore, compared to the convergence segments immediately up and downstream, we expect a measure of softness across the inshore boundary of the short divergence segment. This seems to be the case. Moreover, in conjunction with the potential upwelling, there is in the frail appendage that extends south from the anticyclonic turn off Cape Fear, a potential counterpart of the warm water fragments in Fig. 3.

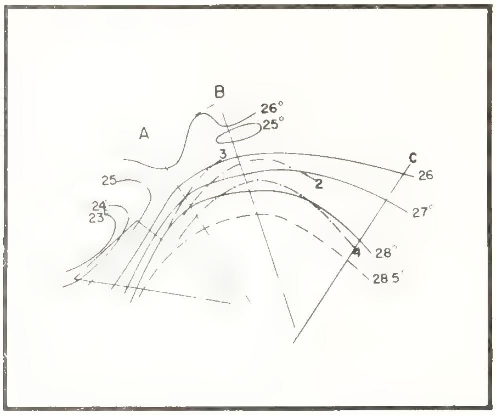

Fig. 3a. The 40 m temperature (°C) in the Loop Current in the Gulf of Mexico during a drogue tracking experiment in October, 1970. Water temperature tracked by drogues (dot-dashed curves labelled 2, 3, and 4) ranged from 26 to over 28 °C. The feature of interest lies to the left of the drogues where pools of cool water separated a warm (26 °C) water fragment of unknown dimensions near points marked *A* and *B*, about 85 km apart. Reproduced from Chew (1974).

A study by Woods, Wiley, and Briscoe (1977) of vertical motion in a meandering frontal jet both supports and provides evidence that (17) is applicable to flows of wavelengths of order as short as 10 km. They give values of $V = 10$ cm/s, $K = 1/(2$ km), and $L = 8$ km. In a sinusoidal flow this means an amplitude of $K(L/2\pi)^2 = 0.8$ km, and a downstream change in KV^2 of about

$$(\partial/\partial s)\, KV^2 = 2.0 \times 10^{-9}\ \mathrm{s}^{-2} \tag{22}$$

This compares to a beta term of $2 \times 10^{-12}\ \mathrm{s}^{-2}$, at most. But to estimate the banking term it is necessary to make some assumptions about the jet. First, for a liberal estimate, we take the components of the downstream acceleration to reinforce one another, so that $dV/dt = (\partial/\partial s)\, V^2 = 1.8 \times 10^{-4}$ cm/s, for a speed of 5 cm/s at one turn and 10 cm/s at the next turn. This immediately give $(\partial/\partial n)\, dV/dt = 1.2 \times 10^{-9}\ \mathrm{s}^{-2}$, for a jet width of 1.5 km. Hence both conditions (15) and (16) are met, and from (17) and (22) a divergence of the order of

$$D = 2 \times 10^{-5}\ \mathrm{s}^{-1} \tag{23}$$

is indicated. A central feature of their work is a

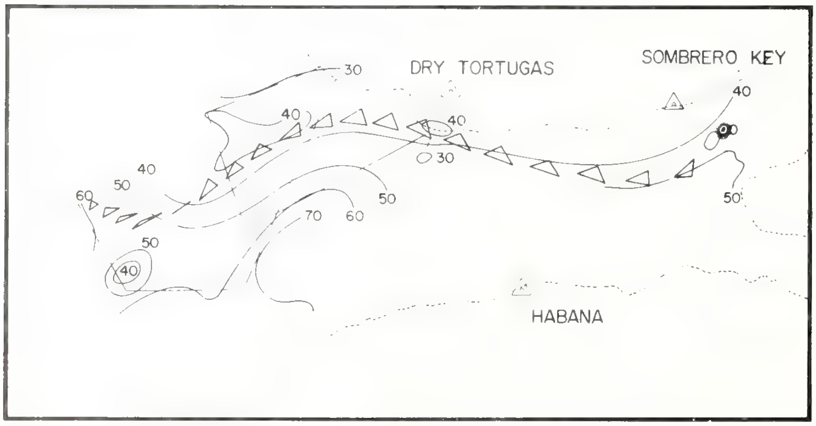

Fig. 3b. The depth (m) contour of the 28 °C surface in an upstream segment of the Florida Current during a drogue tracking experiment in August, 1971. The feature of interest is the closed 40 m contour in the left flank of the current as it approached the anticyclonic turn west of Dry Tortugas. Reproduced from Chew (1974).

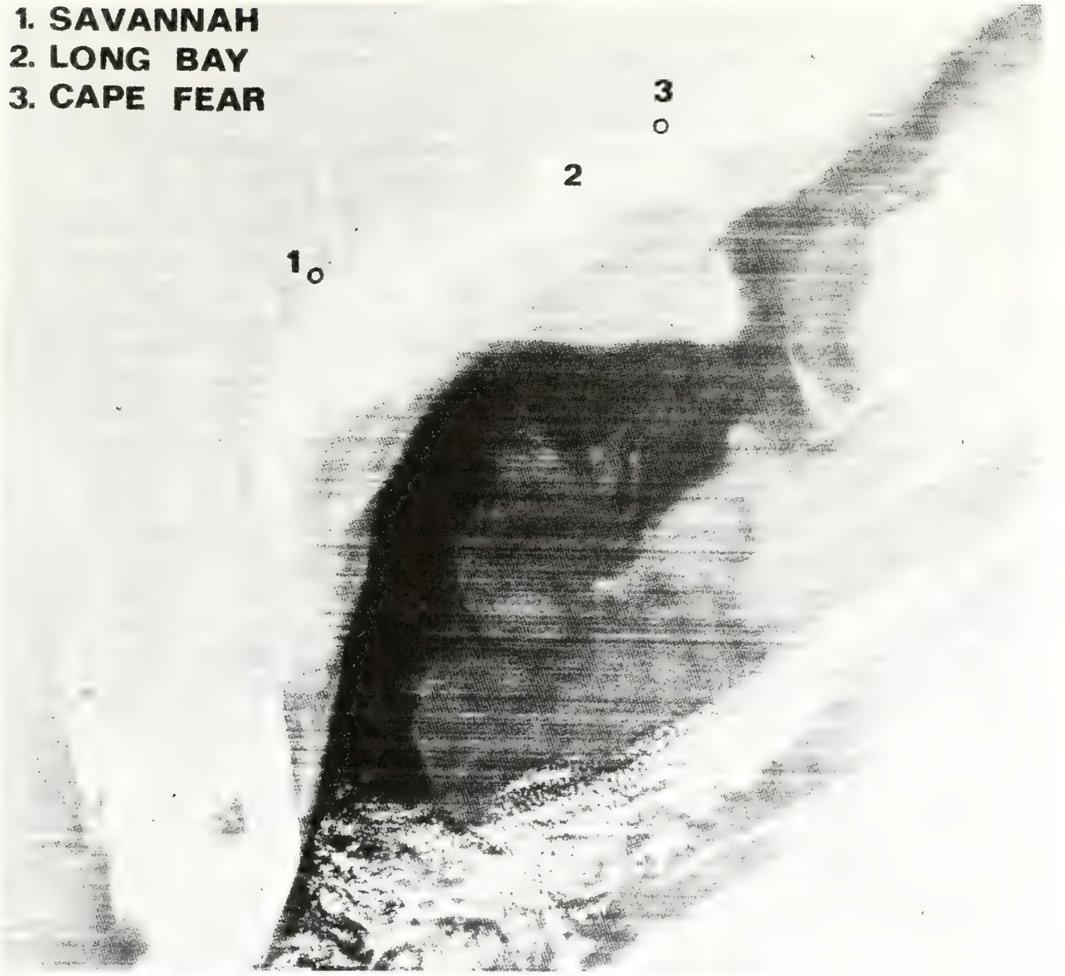

Fig. 4. Infrared image for February 26, 1975. Adopted from Legeckis (1978, Fig. 6).

series of alternating upwelling and downwelling tongues, upwellings that could mean upward nutrient flux. For meandering flows, (17) predicts just such a series. Moreover, depending on the sign of KV, the factor $(f + KV)$ in (17) may be greater or less than f. Thus where a flow is nearly sinusoidal, upwelling tongues tend to be more intense than downwelling ones. Hence, given the prevalence of meandering flow, the mechanism embodied in (17) appears to be a significant process in the general fertility of the sea.

5. An eddy-ring hypothesis

In the formation of eddy-rings from amplifying meandering flow, there is a large change in curvature vorticity in both time and space. Hence, for streamline curvature K_s, we suppose, in addition to (15) and (16) that

$$(D/Dt)\,K_s\,V > KV\,\partial V/\partial s \tag{24}$$

where $D/Dt = d/dt + \partial/\partial t$ is the individual derivative. Thus the turning vorticity equation (Chew, 1975, eq. 8) reduces to

$$(D/Dt)\,K_s\,V = -(f + K_s\,V)\,D \tag{25a}$$

Or for a layer of thickness h,

$$(D/Dt)\{(f_0 + K_s\,V)/h\} = 0 \tag{25b}$$

For the northern hemisphere and for $f > K_s V$, (25) simply states that a layer undergoing convergence (divergence) will gain cyclonic (anticyclonic) curvature vorticity. Three possible features may be inferred from (25). First, whatever the mechanism initiating vertical motion, with cyclonic curvature vorticity increasing with convergence, sufficient convergence will lead to cyclonic cutoffs, and sufficient divergence to anticyclonic cut-offs. This is in accord with the works of Saunders (1971), Fuglister (1972), and Newton (1978), and is consistent with the dynamics of the warm water fragments in Fig. 3 if they were or were becoming anticyclonic eddies. Second, where convergence and divergence are of equal magnitude, the factor $(f + K_s V)$ in (25) will favor cyclonic over anticyclonic cut-off. The implied greater population of cyclonic eddy-rings is consistent with the work of Lai and Richardson (1977) and Richardson, Cheney and Worthington (1978) who found three to four cyclonic rings for every anticyclonic eddy in the North Atlantic. But this disparity could also mean a bias toward greater subsidence in the North Atlantic. More important, however, is the longevity of cyclonic rings, bringing us to the last inference that rings are stable configurations. Cut-off eddies are initially irregular in shape. But as an eddy acquires circular symmetry on becoming a ring, $(D/Dt) K_s V$ approaches zero, as would $(\partial/\partial s) KV^2$ in (17) as the flow tends toward a steady state. It follows from (17) or (25) that there is no significant vertical motion in symmetric rings, and remains so as long as no other forces act.

To conclude this section we turn to an observation of eddy formation off East Australia where Nilsson, Andrews and Scully-Power (1977) found upper-layer convergence a cause in the closing off of an anticyclonic warm water eddy. They postulate a baroclinic triggering mechanism, but that aside, the dynamics is in accord with (25). For with $f < 0$ in the sourthern hemisphere, upper layer convergence is precisely what (25) prescribes as necessary to generate the negative curvature vorticity inherent in warm anticyclonic eddies. Moreover, with negative curvature vorticity now reinforcing a negative Coriolis parameter, for the same magnitude of convergence or divergence there is a greater likelihood for more numerous and more intense anticyclonic eddies than for cyclonic eddies. This is consistent with the works of Hamon (1965) and Boland and Hammon (1970).

6. Discussion and conclusion

Since the work of Wust (1924) most studies of the Florida Current off Miami have assumed negligible curvature effects. It was not realized that it is not always necessary for the current to have large curvature in order to have correspondingly large curvature effects. Chew (1979) shows examples of important curvature effects in flows with Rossby number, as a ratio of the centrifugal to the Coriolis force, of the order of 0.1 or less. In the light of (5) and (17), the Bernoulli acceleration arising from the channel constriction will, through the divergence effect, bias the curvature of all meander trains passing through. Assessing the full implication of this situation will require a combination of both the Lagrangian and Eulerian approach. And perhaps the absence of such a combination is one reason why progress has also been slow in the study of the upwelling and meandering of the Kuroshio, although Uda (1964) first posed the problem more than a decade ago.

Given the small terms in (14), the predominant divergence effect in (5) must be balanced by an equally large curvature change effect, as posed in (17). Although in (14) the observed field of divergence is tied to a channel constriction, precisely because the linkage between divergence and curvature change is strong even in a channel, we may expect the linkage to be no less in the open sea where flow curvature can be much larger.

Bjerknes (1937) and Bjerknes and Holmboe (1944) are the first to consider the curvature effects on divergence. They treat the longitudinal and transversal components of the horizontal divergence separately. For the longitudinal component they employ a model where the transport is confined to isobaric channels of constant depth, implying an assumption of zero downstream acceleration later made explicit by Palmen and Newton (1969, p. 143). The use of this assumption in (5) by setting the separate component terms in $dV/dt = V\,\partial V/\partial s + w\,\partial V/\partial z$ individually to zero immediately gives

$$\left.\begin{array}{l}(f + KV)\,D = -V^2\,\partial K/\partial s - df/dt \\ \text{or,} \\ \qquad fD = -V^2\,\partial K/\partial s - df/dt\end{array}\right\} \qquad (26)$$

on neglecting KV against f. The counterpart in Bjerknes and Holmboe (1944, eq. 5.4) is somewhat different, but may be put in the form,

$$fD = -V(\partial/\partial s)(KV + f) \tag{27}$$

Related, but also different is

$$fD = -(\partial/\partial s)\, KV^2 - df/dt \tag{28}$$

a starting point of numerical study of the so-called "free-inertial jet" (e.g. Godfrey and Robinson, 1971). But besides being inconsistent with the $dV/dt = 0$ assumption, there is no clear evidence that either (27) or (28) is superior to (26) in describing the relation between divergence and curvature change. Thus to the extent that $dV/dt = 0$ holds (26) is a generalization of the Bjerknes approach in that there is no restriction on the depth of isobaric channels and both the longitudinal and tranversal divergence components are included in D. But compared to (17) eq. (26) is unnecessarily restrictive and provides no obvious clue, such as, (18), to the range of its validity.

For meso-scale adiabatic flows we conclude that horizontal divergence and change of centripetal acceleration are closely linked and that in the northern hemisphere upwelling is strongly indicated where there is a rapid increase of centrifugal force in the surface flow.

7. Acknowledgement

It is my pleasure to acknowledge the hospitality of Mr Q. Q. Kao, Dr H. L. Mao, and Professors C. P. Ho, Z. H. Jing, and C. F. Diao in making possible my presentation of a version of this paper in a seminar at the Shangtung College of Oceanology in Tsingtao, China, May 30, 1978. Respectfully, I dedicate this contribution to the memory of Professor J. Bjerknes for his inspired teaching.

REFERENCES

Arthur, R. S. 1965. On the calculation of vertical motion in eastern boundary currents from determinations of horizontal motion. *J. Geophs. Res. 70*, 2799–2803.

Banse, K. 1968. Hydrography of the Arabian Sea shelf of India and Pakistan and effects on demersal fishes. *Deep-Sea Res. 15*, 45–79.

Bjerknes, J. 1937. Theorie der aussertropischen Zyklonenbildung. *Meteorol. Z. 54*, 462–466.

Bjerknes, J. and Holmboe, J. 1944. On the theory of cyclones. *J. Meterol. 1*, 1–22.

Boland, F. M. and Hamon, V. V. 1970. The East Australian Current, 1965–1968. *Deep-Sea Res. 17*, 777–794.

Chew, F. 1974. The turning process in meandering currents: A case study. *J. Phys. Oceanogr. 4*, 27–57.

Chew, F. 1975. The interaction between curvature and lateral shear vorticities in a mean and an instantaneous Florida Current, a comparison. *Tellus 27*, 606–618.

Chew, F. 1979. Difference in centrifugal force and the slope of the sea level off Miami. Accepted for publication in *Mar. Geodesy.*

Duing, W. 1970. *The monsoon regime of the currents in the Indian Ocean.* Honolulu: East-west Center Press.

Fuglister, F. C. 1972. Cyclonic rings formed by the Gulf Stream 1965–66. In *Studies in physical oceanography* (ed. A. L. Gordon). New York: Gordon and Breach.

Godfrey, J. S. and Robinson, A. R. 1971. The East Australian Current as a free inertial jet. *J. Mar. Res. 29*, 256–280.

Haltiner, G. J. and Martin, F. L. 1957. *Dynamical and physical meteorology.* New York: McGraw-Hill Book Co.

Hamon, B. V. 1965. The East Australian Current, 1960–1964. *Deep-Sea Res. 12*, 899–921.

Lai, D. Y. and Richardson, P. L. 1977. Distribution and movement of Gulf Stream rings. *J. Phys. Oceanogr. 7*, 670–683.

Legeckis, R. 1978. A survey of worldwide sea surface temperature fronts detected by environment satellites. *J. Geophys. Res. 83*, 4501–4522.

Newton, C. W. 1978. Fronts and wave disturbances in Gulf Stream and atmospheric jet stream. *J. Geophys. Res. 83*, 4697–4706.

Niiler, P. P. and Richardson, R. S. 1973. Seasonal variability of the Florida Current. *J. Mar. Res. 31*, 144–167.

Nilsson, C. S., Andrews, J. C. and Scully-Power, P. 1977. Observation of eddy formation off East Australia. *J. Phys. Oceanogr. 7*, 659–699.

Palmén, E. and Newton, C. W. 1969. *Atmospheric circulation systems.* New York: Academic Press.

Richardson, P. L., Cheney, R. E. and Worthington, L. V. 1978. A census of Gulf Stream rings, Spring 1975. *J. Geophys. Res. 83*, 6136–6144.

Saunders, P.M. 1971. Anticyclonic eddies formed from shoreward meanders of the Gulf Stream. *Deep Sea Res. 18*, 1207–1219.

Schmitz, W. J. 1969. On the dynamics of the Florida Current. *J. Mar. Res. 27*, 121–150.

Taft, B. 1971. Ocean circulation in monsoon areas. In *Fertility of the sea* (ed. J. D. Costlow). New York: Gordon and Breach.

Uda, M. 1964. On the nature of the Kuroshio, its origin and meanders. In *Studies on oceanography.* The Hidaka Jubilee Committee. Univ. of Tokyo.

Woods, J. D., Wiley, R. L. and Briscoe, M. G. 1977. Vertical circulation at fronts in the upper ocean. In *The voyage of discovery* (ed. M. Angel). New York: Pergamon Press.

Wust, G. 1924. *Florida and Antillenstrom.* Institut. f. Meereskunde, Berlin Univ. Reihe, Heft 12.

Yentsch, C. S. 1974. The influence of geostrophy on primary production. *Tetbys* *6*, 111–118.

Yoshida, K. 1967. Circulation in the eastern tropical oceans with special references to upwelling and undercurrents. *Japanese J. Geophys.* *4*, 1–75.

ГОРИЗОНТАЛЬНАЯ ДИВЕРГЕНЦИЯ, УСКОРЕНИЕ И ИЗМЕНЕНИЕ КРИВИЗНЫ; ДИАГНОСТИЧЕСКОЕ УРАВНЕНИЕ И ЕГО ПРИЛОЖЕНИЯ

Рассматривается горизонтадьная дивергенция потока с ускорением в связи с меандрирующими течениями и образованием вихрей-рингов. Цель работы-способствовать нахождению областей подьема вод и связанных с ним динамических явлений. Две гипотезы, представляющие две мезомасштабные версии уравнения вихря (Чу, 1975), формулируются с помощью данных Шмитца (1969) по Флоридскому течению. Первый подход является обобщением пионерской работы Бьеркнеса (1937) о связи между горизонтальной дивергенцией и изменением кривизны линий тока. Гипотеза предсказывает, что вдоль меандрирующего течения в северном полушарии и вдали от экватора имеет место горизонтальная конвергенция там, где есть быстрый рост центростремительного ускорения и имеет место горизонтальная дивергенция там, где растет центробежная сила. В частности, в меандрирующем поверхностном течении с последовательностью циклонических и антициклонических круговоротов гипотеза предсказывает последовательность языков подьема и опускания вод.

Вторая гипотеза представляет количественную теорию, основанную на исследовании Фуглистера (1972) роли вертикального движения в образовании и эволюции вихрей-рингов. Вихри, будучи отсеченными меандрами, вначале нерегулярны по форме. Согласно этой гипотезе вихрь, развивающийся в ринг с круговой симметрией, вступает в бездивергентную стадию и, следовательно, в стадию устойчивости.

6. Journal of Geophysical Research 84, No. CI, 359-362.

Deep Currents in the Yucatan Strait

DONALD V. HANSEN AND ROBERT L. MOLINARI

National Oceanic and Atmospheric Administration, Atlantic Oceanographic and Meteorological Laboratories, Miami, Florida

Current meter and hydrographic data were collected in the Yucatan Channel during a month in the autumn of 1970. Currents 15 m above the bottom are characterized by diurnal modulation and oscillations of 4- to 5-day periods. The observed tidal currents are in phase with their counterpart in the Straits of Florida but of insufficient amplitude for consistency with the amplitude of diurnal tide observed in the Gulf of Mexico. The average current observed over the month was 3.9 cm/s toward SSW. Geostrophic current circulation and dissolved oxygen observations indicate a generally southward flow below about 1000-m depth and at all depths in the eastern side of the channel during the latter part of the observation.

INTRODUCTION

The Yucatan Strait represents the primary inflow passage in the Gulf of Mexico. The sill depth of the Yucatan Strait is approximately 2000 m [*Uchupi,* 1973]. The Yucatan Strait is about 90 nautical miles wide, as measured from Cabo San Antonio, Cuba, to Isla Mujeres, Mexico (Figure 1).

The Yucatan Current flows north through the strait. Southerly flows have been observed or inferred below the Yucatan Current. *Schlitz* [1973] inferred southerly flow below 700 m from geostrophic data in the Yucatan Strait in April 1970. *Molinari and Yager* [1977] reported a similar flow in May 1972 in an analysis of geostrophic data referred to direct current measurements at the sea surface.

This report is based on current meter data recorded at a site near the greatest depth of the Yucatan Strait and data collected by the NOAA ship *Discoverer* in association with the mooring. The data were collected in October 1970.

CURRENT OBSERVATIONS

A Geodyne model A-102 current meter was deployed 15 m above the bottom at 1081 fm (1977 m) in the Yucatan Channel (Figure 1) in the vicinity of the greatest depth on the sill between the Gulf of Mexico and the Cayman Sea [*Uchupi,* 1973].

Slightly more than 30 days of usable current meter data were collected at 10-min intervals. These data are shown as vector component time series in Figure 2. The observed currents have characteristic speeds of the order of 10 cm/s, with a clear bias toward SSW. Also apparent are a dominant diurnal tidal current fluctuation primarily in the north component and, especially in the early part of the record, an irregular fluctuation of period about 4–5 days which is somewhat more clearly expressed in the east component than in the north component. A high resolution Fourier analysis of the data revealed significant fluctuation amplitudes only in association with the diurnal and 4–5 day periods, in addition to the low-frequency maximum usually found in records of a few months or less. The inertial period at the latitude of the current meter station is 32.45 hours. The 4- to 5-day current fluctuations are probably related to bottom pressure fluctuations of similar period which *Mofjeld and Wimbush* [1977] hypothesize may arise from incomplete inverse barometer compensation of easterly waves in the atmosphere. *Duing et al.* [1977] have observed a high level of current variability at a time scale of about 5 days in the Straits of Florida.

Tidal current constituents were determined from these data using standard National Ocean Survey procedures. The tidal currents are almost rectilinear in the direction 015°–195°, or generally parallel to the large scale topography (Figure 1). The amplitudes of the principal diurnal constituents, K_1 and O_1, are large relative to the semidaily constituents. This relationship is consistent with what is known about tides in the Gulf of Mexico as summarized by *Zetler and Hansen* [1970, 1972] and *Mofjeld and Wimbush* [1977].

The important diurnal constituents are nearly in phase with their counterparts in the Straits of Florida with respect to flow into the Gulf of Mexico. However, they are only about half as large as they should be to account for the observed amplitude of the K_1 barotropic tidal constituent in the Gulf of Mexico. These results on the tidal currents motivated the bottom pressure observations in the central Gulf reported by *Mofjeld and Wimbush* [1977]. The bottom pressure measurements indicate that the diurnal tidal constituents have little spatial structure over the Gulf of Mexico. We conclude therefore that the current measurements are representative of the barotropic tide and choose not to report the tidal constituents determined from them. The discrepancy may be due to the influence of the bottom frictional boundary layer, although results of *Weatherly* [1972] and *Wimbush and Munk* [1970] suggest that the effects on tidal currents at 15 m above the bottom should be small. Topographic excitation of baroclinic tides, as has been suggested by *Niiler* [1968], is another possible explanation.

Probably the most interesting aspect of the current measurements is the net movement past the mooring as shown by a progressive vector diagram (Figure 3). Following approximately a week of generally east-west oscillatory movement, flow to the SSW began, approximately parallel to the topography at speeds of up to nearly 10 cm/s. There is a period of very weak movement around days 19–23, followed by a resumption of tidally modulated flow to the south. The average flow over the full 30-day record is about 4 cm/s toward 210°T.

GEOSTROPHIC COMPUTATIONS AND OXYGEN DISTRIBUTIONS IN THE YUCATAN CURRENT

STD stations were occupied at the positions given in Figure 1. Stations 1–8 were taken from October 3 to 5, 1970, and stations 74–78 during October 26 and 27, 1970.

Vertical cross sections of geostrophic speed are given in Figure 4. The geostrophic speeds were computed relative to the deepest common data point between adjacent stations. Maximum speeds are similar in both sections over 1.5 m/s. However, the axis of the current was farther to the west during the second crossing. Both crossings indicate south flow below 1000 m, i.e., a second geostrophic level of no motion occurs at

This paper is not subject to U.S. copyright. Published in 1979 by the American Geophysical Union.

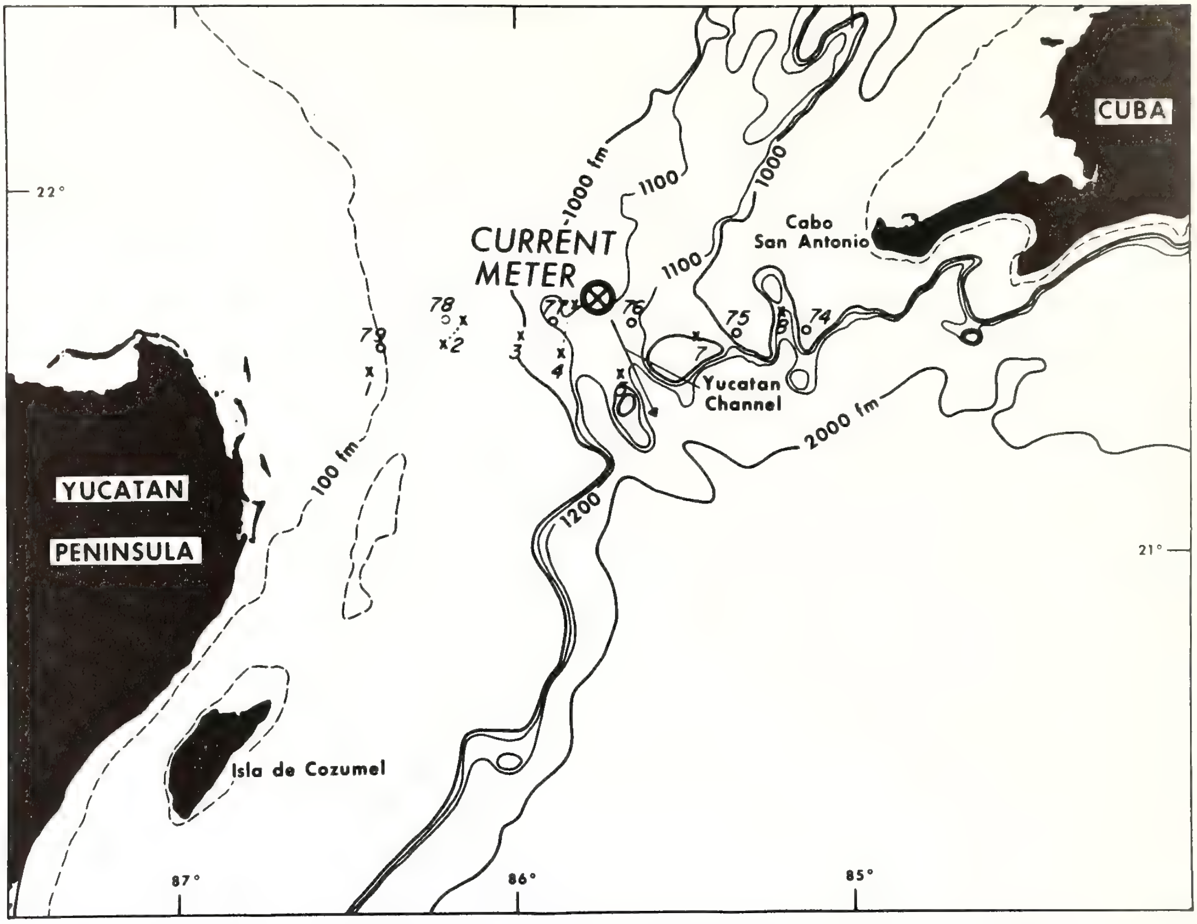

Fig. 1. Bathymetry of the Yucatan Strait in the vicinity of the current meter mooring. The position of the Yucatan Channel, the location of the sill in the Strait, is from *Uchupi* [1973]. The current meter data were collected at 21°42.0'N, 85°46.1'W. The positions of the STD stations are also given.

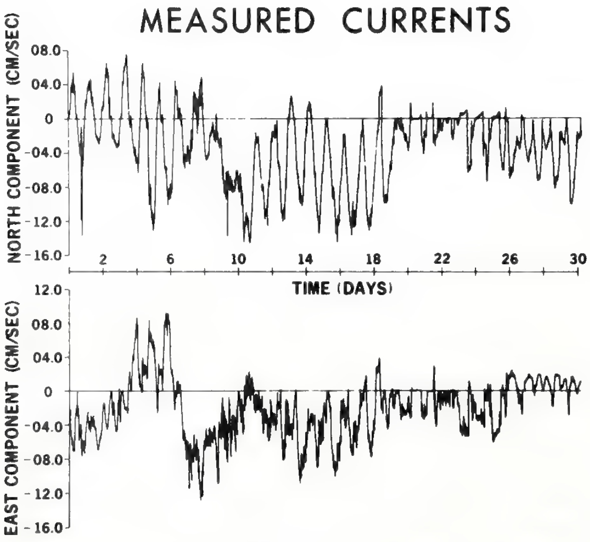

Fig. 2. Currents observed from 1450 UT October 3 to 1500 UT November 2, 1970, at 15 m above bottom at station shown in Figure 1.

about 1000-m depth. Although the speeds of these southerly flows are quite small, in the range of noise in the geostrophic computations, they are consistent with the current meter results. During the first crossing the average current meter speed was 0.05 m/s to the west (Figure 3), and during the second crossing the average speed was 3 cm/s to the southwest.

The total geostrophic transport through stations 1–8, computed relative to the deepest common data point between adjacent stations, is 25.8 × 10^6 m^3/s. *Niiler and Richardson* [1973] measured directly the transport through the Straits of Florida on October 2, 1970. Their value of 22.2 × 10^6 m^3/s is within 13% of the geostrophic transport at the Yucatan Straits. The transport through stations 74–79 some 3 weeks later is 27.1 × 10^6 m^3/s. The 5% increase in transport between the two crossings is probably not significant in view of the approximations in the geostrophic computations.

The net transport to the south during the first crossing is 1.7 × 10^6 m^3/s, and during the second crossing, 2.8 × 10^6 m^3/s. The upper layer countercurrent on the eastern side of the Yucatan Straits (Figure 4) contributes the increase of southerly transport during the second crossing; the deeper transports are similar.

Oxygen data reflect the current meter and geostrophic cur-

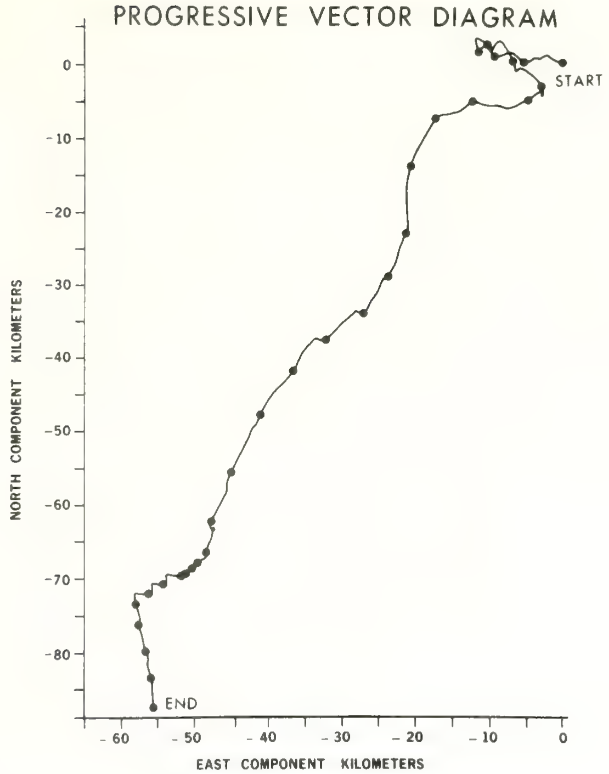

Fig. 3. Progressive vector diagram of currents observed in Yucatan Channel between October 3 and November 2, 1970. Dots denote 1-day intervals on the diagram.

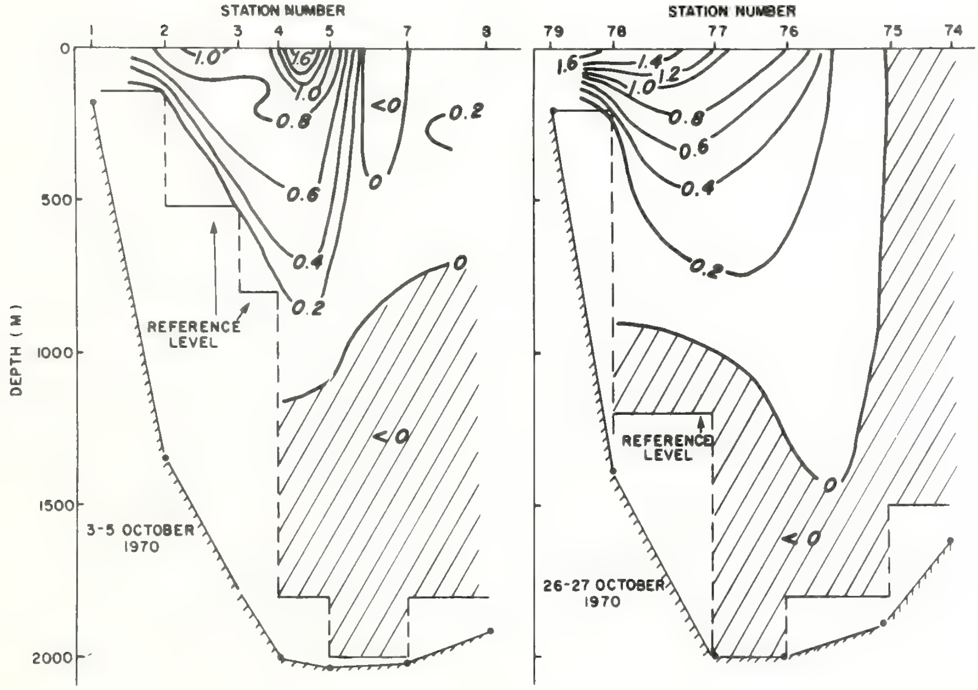

Fig. 4. Cross sections of geostrophic speed (m/s) computed relative to the variable reference level shown on the figure. The station positions are given in Figure 1.

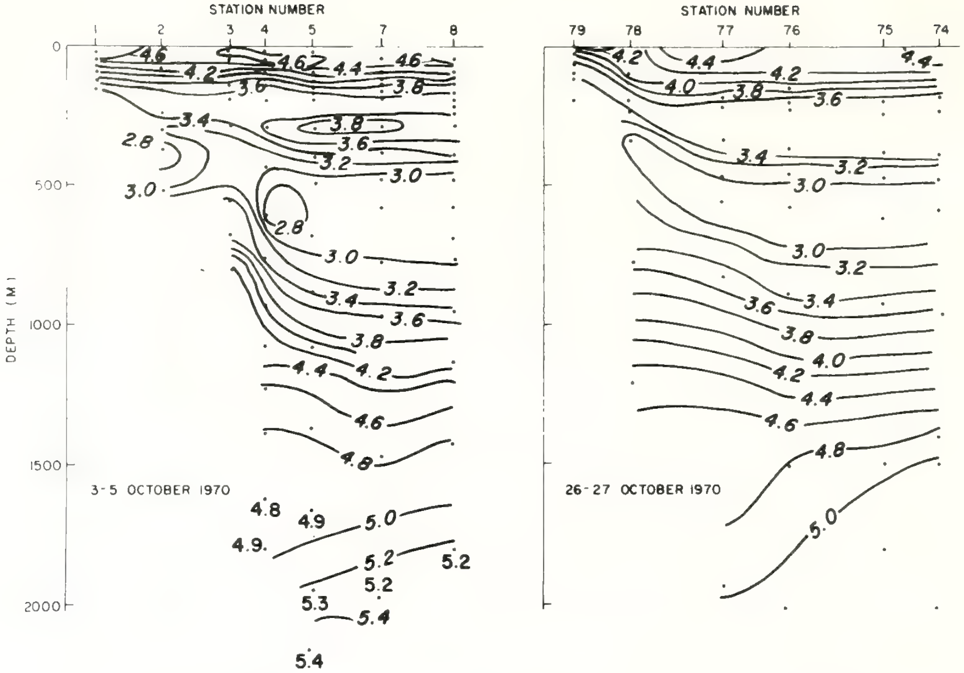

Fig. 5. Cross sections of oxygen distribution (ml/l) for station positions given in Figure 1.

rent calculations which indicate a deep southerly flow during the second crossing. *Nowlin et al.* [1969] describe oxygen data collected both north and south of the Yucatan Straits. Below 1500 m the average oxygen value for 11 samples in the Yucatan Basin was 5.6 ml/l, while in the Gulf basin the mean value for 55 samples was 5.0 ml/l. Vertical cross sections of oxygen concentrations observed in 1970 are shown in Figure 5. The average value of the seven samples taken below 1500 m during the first crossing is 5.1 (±0.2) ml/l, while during the second crossing the average for six samples is 4.9 (±0.1) ml/l. The samples below 1800 m during the second crossing contain considerably less oxygen than samples below 1800 m during the first crossing (Figure 5). The lower oxygen values of the second crossing reflect effects of southward flow past the current meter after approximately October 8, 1970 (Figure 3).

Acknowledgments. We wish to acknowledge gratefully the assistance of several people in conduct of the work described in this report. The current meter array used for collecting the current data was designed and prepared by Charles Kearse and Jack Falkenhof of the Engineering Development Laboratory, National Ocean Survey; the officers and crew of the NOAA ship *Discoverer* capably handled the deployment and recovery operations. J. Hazelworth worked up the STD data, and G. Berberian supervised collection and analysis of the oxygen data. Tidal current analyses were provided by Robert Dennis, Bernard Zetler assisted in their interpretation.

REFERENCES

Duing, W., C. N. K. Mooers, and T. N. Lee, Low frequency variability in the Florida Current and relations to atmospheric forcing from 1972–1974, *J. Mar. Res., 35,* 1977.

Mofjeld, H. O., and M. Wimbush, Bottom pressure observations in the Gulf of Mexico and Caribbean Sea, *Deep Sea Res., 24,* 987–1004, 1977.

Molinari, R. L., and R. E. Yager, Upper layer hydrographic conditions at the Yucatan Straits during May, 1972, *J. Mar. Res., 35,* 11–20, 1977.

Niiler, P. P., On the internal tidal motion in the Florida Straits, *Deep Sea Res., 15,* 113–123, 1968.

Niiler, P. P., and W. S. Richardson, Seasonal variability of the Florida Current, *J. Mar. Res., 31,* 144–167, 1973.

Nowlin, W. D., Jr., P. F. Paskausky, and H. McLellan, Recent dissolved oxygen measurements in the Gulf of Mexico deep waters, *J. Mar. Res., 27,* 39–44, 1969.

Schlitz, R. S., Net total transport and net transport by water mass categories for the Yucatan Channel based on data for April 1970, Ph.D. dissertation, 107 pp., Texas A&M University, College Station, 1973.

Uchupi, E., Eastern Yucatan continental margin and western Caribbean tectonics, *Amer. Ass. Petrol. Geol. Bull., 57,* 1075–1085, 1973.

Weatherly, G. L., A study of the bottom boundary layer of the Florida Current, *J. Phys. Oceanogr., 2,* 54–72, 1972.

Wimbush, M., and W. Munk, The benthic boundary layer, *The Sea,* vol. 4, pp. 731–758, John Wiley, New York, 1970.

Zetler, B. D., and D. V. Hansen, Tides in the Gulf of Mexico—A review and proposed program, *Bull. Mar. Sci., 20,* 57–69, 1970.

Zetler, B. D., and D. V. Hansen, Tides in the Gulf of Mexico, in *Contributions to the Physical Oceanography of the Gulf of Mexico, Texas A&M University Oceanographic Studies,* edited by L. R. A. Capurro and J. L. Reid, pp. 265–275, Gulf Publishing Company, Houston, Tex., 1972.

(Received May 1, 1978;
revised September 27, 1978;
accepted October 2, 1978.)

7. Apollo-Soyuz Test Project: Summary Science Report, NASA SP-412, Vol. 2, 371-383.

Interpreting ASTP Photographs of the Ocean and Locating the Area Photographed (Case Study of the Gulf of Mexico)

G. A. Maul[a]

ABSTRACT

Handheld-camera photographs, taken over the eastern Gulf of Mexico in July 1975, were evaluated for oceanic information. The areas photographed were located over the sea by comparing cloud formations in the photographs with the same formations in visible imagery acquired simultaneously by geostationary satellite. By using concurrently obtained ship data, patterns in the sunglint were interpreted as indicators of the cyclonic shear zone of the Gulf Loop Current. The study tested the hypothesis, based on Skylab experience, that frequently observed circular cloud features are indicators of mesoscale turbulence in ocean currents. It was found that the features could be consistently explained as being attributable entirely to atmospheric changes and that the features were not associated with cold-core ocean eddies.

INTRODUCTION

The importance of man's role as an ocean observer from space was recognized and discussed more than a decade ago (ref. 1). Astronauts have obtained photographs of ocean phenomena since the earliest space flights, and analyses of the Gemini and Apollo photographs have been made by Soules (ref. 2), Mairs (ref. 3), and others. During the Skylab 4 mission, the flightcrew was given special training in making visual observations and taking photographs of the Earth. The results of that effort and the variety of oceanic features observed and photographed are summarized in references 4 and 5.

During the Apollo-Soyuz Test Project (ASTP), the flightcrew received similar training, and the observational data have been cataloged by El-Baz (ref. 6). (No attempt is made here to review all the oceanographically interesting observations made during ASTP.) This report concerns some of the Skylab recommendations (refs. 4, 5, and 7) relative to the problem of locating the ocean area obtained in the handheld-camera photographs and the problem of interpreting data in the space photographs by comparison with shipboard observations that were acquired at approximately the same time.

The eastern Gulf of Mexico was chosen as a test site for the experiment. Near-simultaneous coverage from the Geostationary Operational Environmental Satellite (GOES) was available over the gulf; this was a key element in the technique to locate an ocean area in handheld-camera photographs. The eastern Gulf of Mexico is also a region of great oceanographic variability. Color boundaries are numerous; they result from the presence of Mississippi River sediments, the high productivity of marine organisms in regions such as the Campeche Bank, and the clear shallow areas such as the Florida Keys. A good potential signature in the visible part of the spectrum can be

---

[a] Atlantic Oceanographic and Meteorological Laboratories, National Oceanic and Atmospheric Administration.

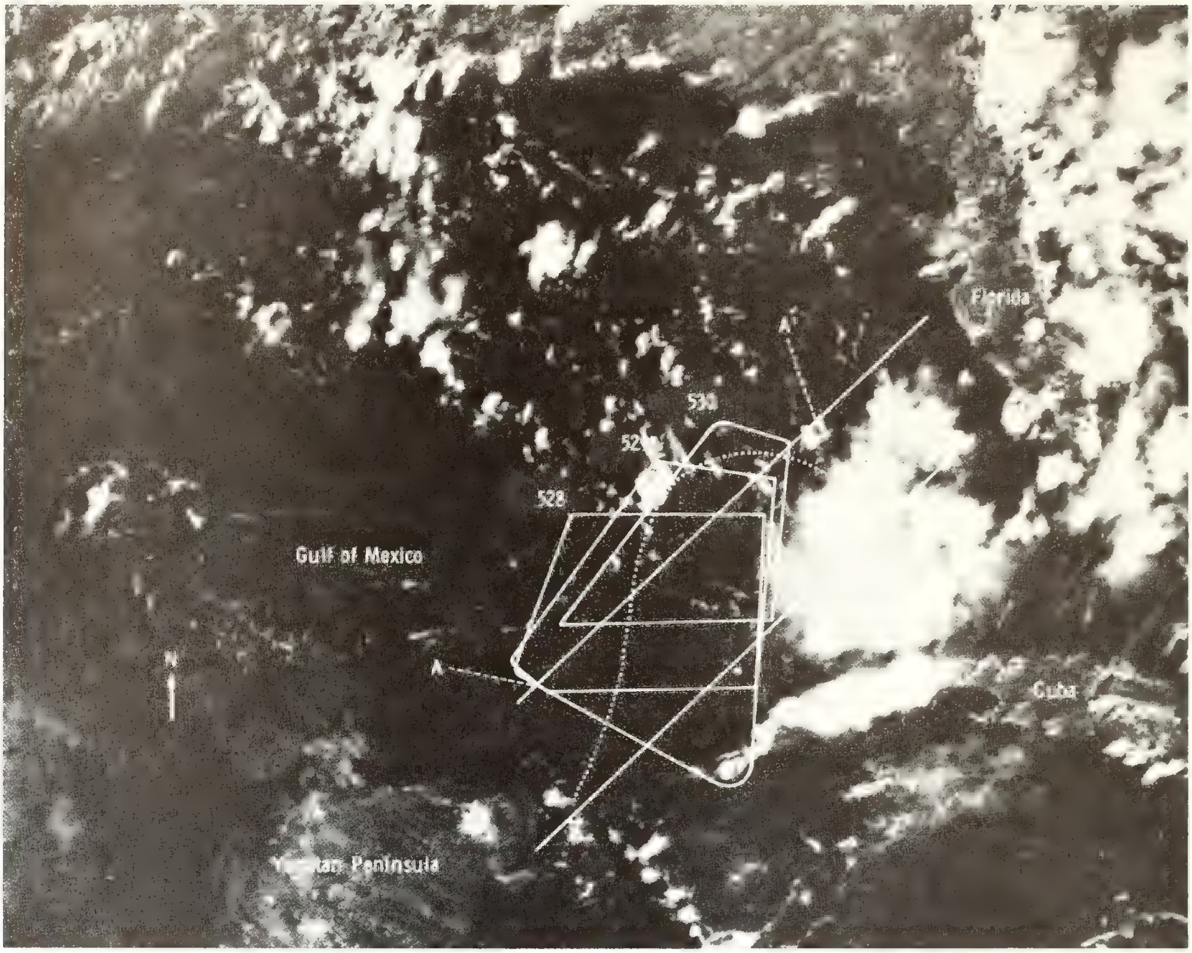

FIGURE 1.—The location of the test site in the eastern Gulf of Mexico is shown on this GOES 1-km-resolution visible-image taken at 19:00 UT on July 18, 1975. Northeast/southwest-trending lines are the surface tracks of the research vessel *Virginia Key*; the lines correspond to the suborbital tracks of the Apollo spacecraft. The three outlined areas represent the coverage of the handheld-camera photographs (frames AST-9-528 to AST-9-530) taken during the Apollo-Soyuz mission. (See also figs. 4(a) to 4(c).) The dotted line is the approximate locus of the cyclonic edge of the Gulf Loop Current as deduced from figure 2. The cross section in figure 3 is denoted by A-A'.

provided by current boundaries caused by the Gulf Loop Current and by the tidal currents through the Florida Keys. The National Oceanic and Atmospheric Administration (NOAA) research ship *Virginia Key* was assigned to this area for collecting oceanographic data "quasi-simultaneously" with the ASTP photographs taken from the Apollo spacecraft.

The test site is shown on the GOES image in figure 1. The two northeast/southwest-trending lines are the ship tracks, which are coincident with the groundtrack of the Apollo spacecraft. The

FIGURE 2.—Contours of the depth (in meters) of the 293-K (20° C) isothermal surface for June, July, and August of 1975, based on all data available from the National Oceanographic Data Center files. The dotted lines represent the outer limit of the Continental Shelf. Data in the region of the Gulf Loop Current were obtained between July 15 and 18 and are quasi-synoptic. The black sketch on the July map centered near latitude 25° N, longitude 86° W is the cloud feature imaged in figures 1 and 5(b), and photographed in figure 4(b). ⟶

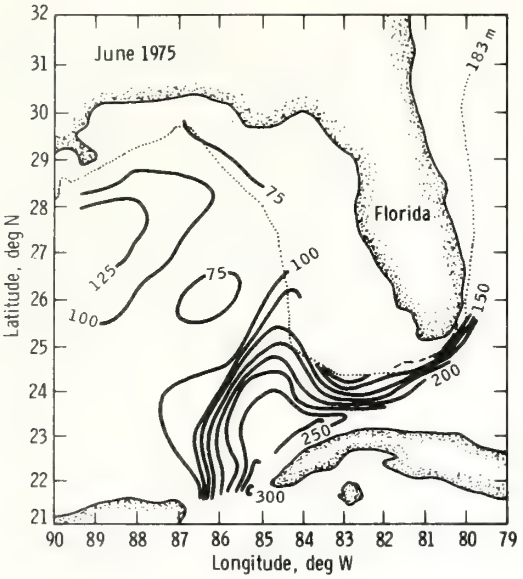
June 1975
Florida
183 m
75
125
100
75
100
150
200
250
300
32
31
30
29
28
27
26
25
24
23
22
21
Latitude, deg N
90 89 88 87 86 85 84 83 82 81 80 79
Longitude, deg W

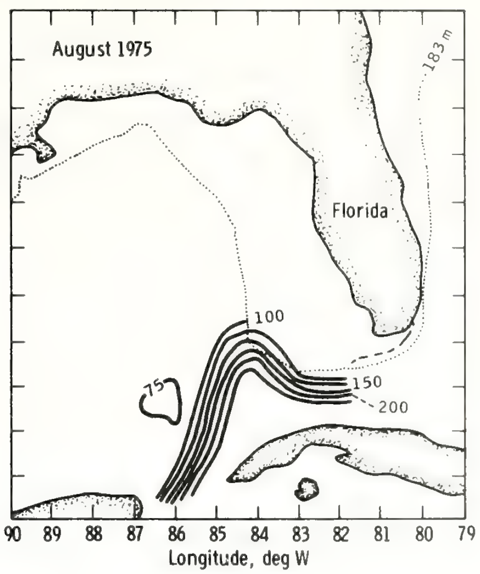
August 1975
Florida
183 m
100
75
150
200
90 89 88 87 86 85 84 83 82 81 80 79
Longitude, deg W

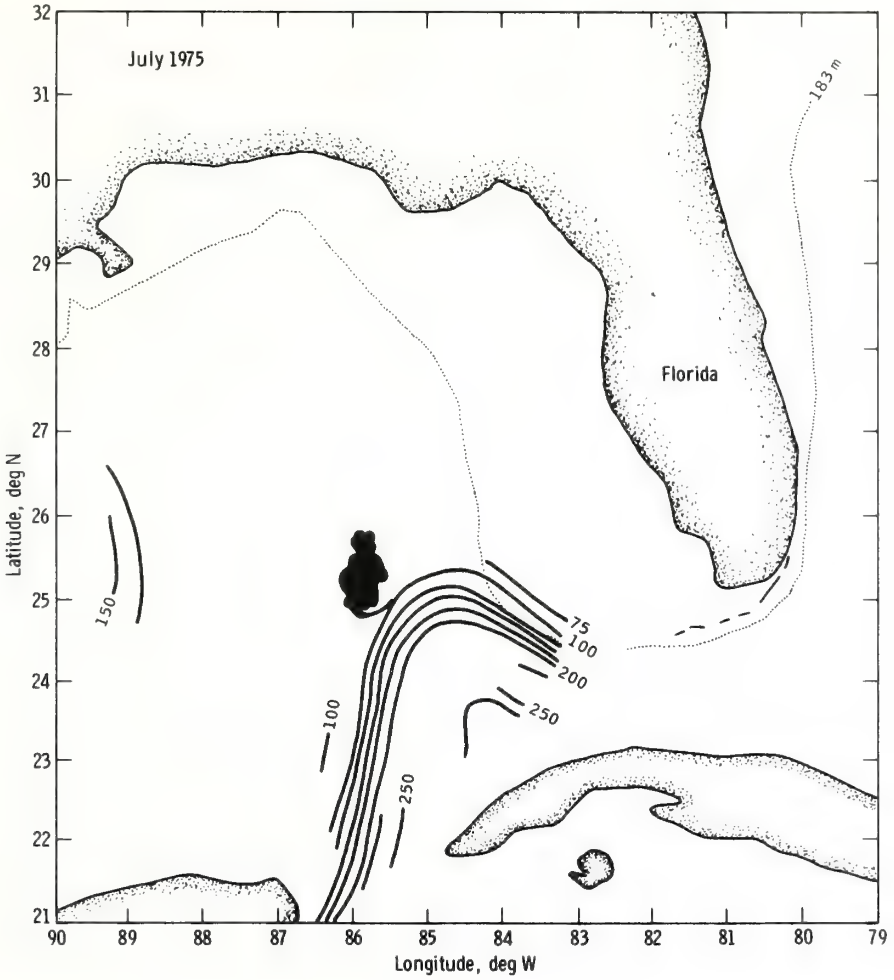
July 1975
Florida
183 m
150
75
100
200
250
100
250
32
31
30
29
28
27
26
25
24
23
22
21
Latitude, deg N
90 89 88 87 86 85 84 83 82 81 80 79
Longitude, deg W

southern line is revolution 15 (July 16, 1975), and the northern line is revolution 45 (July 18, 1975). Three handheld-camera photographs were taken by the spacecraft crew at approximately 18:43 UT on July 18; boundaries of the photographs are shown in figure 1. The dotted line is the locus of the 293-K (20° C) isotherm at a 100-m depth (fig. 2), which is approximately the left-hand edge of the Gulf Loop Current, facing downstream.

LOCATING AREAS IN THE PHOTOGRAPHS

Ocean photographs taken during ASTP can be divided into four groups: (1) vertical mapping photographs with exact data concerning latitude and longitude of the principal points, (2) mapping photographs with no data on the exact position of the principal point, (3) oblique photographs containing a coastline and/or islands, and (4) oblique photographs without any landmarks. In the second and third groups, routine photogrammetric techniques (ref. 8) can be used to locate the principal and corner points of most photographs. In the last group, clouds in the photographs were compared to clouds in near-simultaneous GOES visible imagery, and the clouds were used as reference points (fig. 1).

To properly interpret an oblique photograph, the nadir angle θ must be known. For a given camera altitude h, the arc length L on the Earth's surface from the nadir to the center point of the photograph is given by (ref. 8)

$$L = R \sin^{-1}[(K \sin \theta) - \theta]$$

where R is the mean radius of the Earth and K is defined as $(R + h)/R$. This is a transcendental equation in θ and can be solved quite readily. The solution requires finding the reference points on the photograph that lie on the principal line and measuring the distance from each reference point to the principal point. Then, by iteration, the angle θ is obtained and finally the latitude and longitude of the principal point.

With ocean photographs, several factors often make it difficult to find the principal line. First, the photograph is not annotated in a precise manner. Because the exact time of photoacquisition is often unknown, it is impossible to determine the nadir point; hence, the principal line is not defined. Second, locating clouds on a simultaneous GOES image has two pitfalls: (1) the best resolution of the visible imagery is 1 km, and (2) the geographical gridding of GOES imagery is not better than plus or minus several pixels. Not only are the scale and resolution of features on handheld-camera photographs not matched to the imagery, but the geographical positions of the features are poorly known. Third, GOES-type data are not available on a worldwide basis and special arrangements must be made in advance to ensure that 1-km-resolution images at 30-minute intervals are available. Other satellite data (available from NOAA, NASA, and the Department of Defense) were studied in this context, but they were found to have little value because of the time difference in observations (ref. 4).

The boundaries of the three photographs shown in figure 1 were located by comparing the major cloud features in the photographs with those in the 1-km-resolution GOES image. After careful comparison, an outline of each ASTP photograph was drawn over the GOES image. Then, by using dominant cloud features, the latitude and longitude of the principal point and of the corner points were interpolated across the photograph. It was not useful to calculate θ or to do any further quantification, because the exact time of photoacquisition was unknown.

EXAMPLE OF PHOTOINTERPRETATION

The ASTP mission provided an opportunity to supplement the visual observations from space by conducting a simultaneous research-ship cruise in the eastern Gulf of Mexico. The ship's southern trackline shown in figure 1 was quasi-synchronous with the Apollo spacecraft transit on July 16; the northern trackline was quasi-synchronous with transit on July 18. No photographs were taken on July 16; therefore, attention will be directed to the section from the Yucatan Peninsula to Florida observed on July 17 and 18, 1975. The temperature cross section as far as the west Florida platform is shown in figure 3.

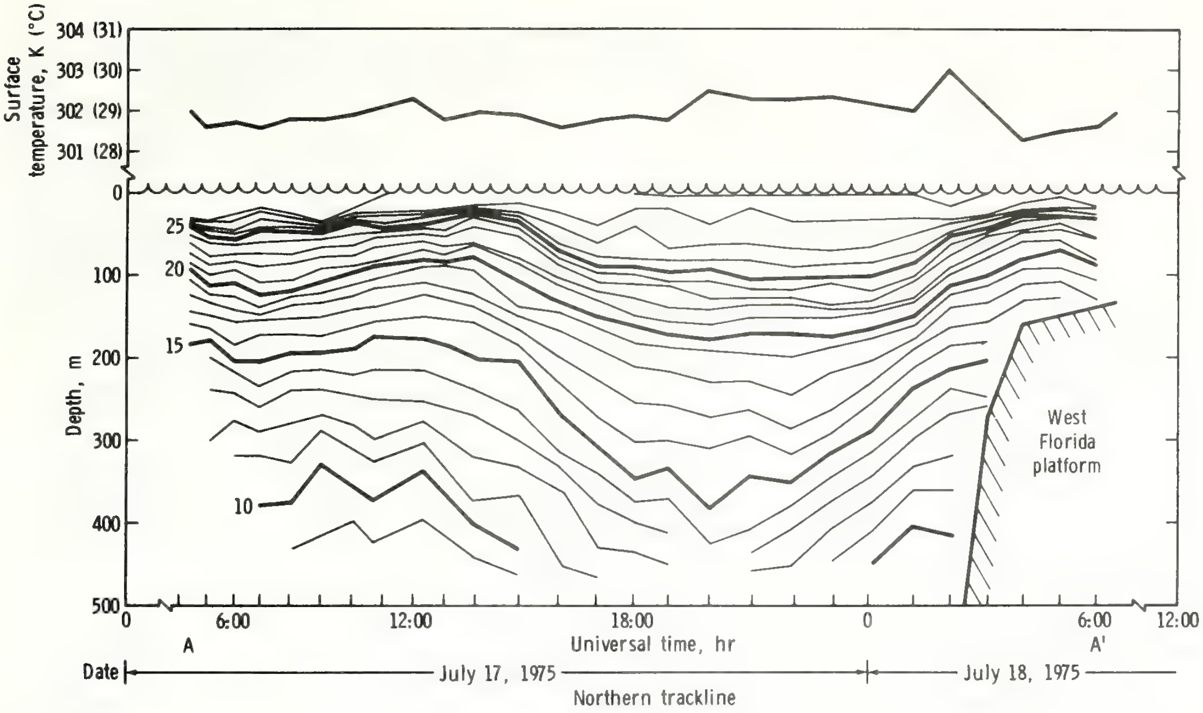

FIGURE 3.—Transect of water temperature and depth observed by the research vessel *Virginia Key* on July 17 and 18, 1975. This transect shows the part of the northern suborbital track sketched in figure 1 (A-A') between Campeche Bank and the Continental Shelf break of the west Florida platform. The sea-surface temperature profile was determined by means of a calibrated thermometer, which served as a control for the data. Eastern edge of the Gulf Loop Current occurs at approximately 14:00 UT, July 17, and the western edge at approximately 04:00 UT, July 18. (Isotherms are in Celsius (K = °C + 273.15).)

Temperature data were obtained from hourly (approximately 18-km spacing) expendable-bathythermograph (XBT) observations. In addition, hourly surface temperature and salinity observations were made, as well as continuous surface chlorophyll-*a* observations using Lorenzen's (ref. 9) method. The chlorophyll-*a* profile in the region covered in figure 3 was monotonic, thus suggesting that the edge of the Gulf Loop Current would not be indicated by a change in ocean color. Similarly, as expected for this time of the year, there is apparently no surface thermal indication of the current. From the many surveys into this area in the last 10 years (refs. 10 to 15 and others), the relation between the current and the thermal field is well known. The research vessel *Virginia Key* crossed into the Gulf Loop Current at approximately 14:00 UT on July 17 and left the current at approximately 04:00 UT on July 18 (fig. 3). In terms of the depth of the 293-K (20° C) isotherm, the cyclonic edge at the surface (left-hand side facing downstream) occurs just before the isotherm deepens to 100 m.

In figure 2, the areal distribution of the depth of the 293-K (20° C) isotherm, based on all available XBT and hydrographic station data for June, July, and August 1975, is plotted. The core of the Gulf Loop Current occurs in the thermal gradient region approximately bounded by the 125- and 200-m depths of the 293-K (20° C) isotherm. Also sketched on the July map is a significant cloud formation imaged in figure 1; this feature is discussed in later paragraphs. The position of the Gulf Loop Current changed very little during these 3 months. This suggests that the July shipboard data, spread over a 24-hour period, can be quasi-synoptically interpreted as satellite surface truth. Weather conditions over the eastern gulf were constant during the July data collection period; they were characterized by generally

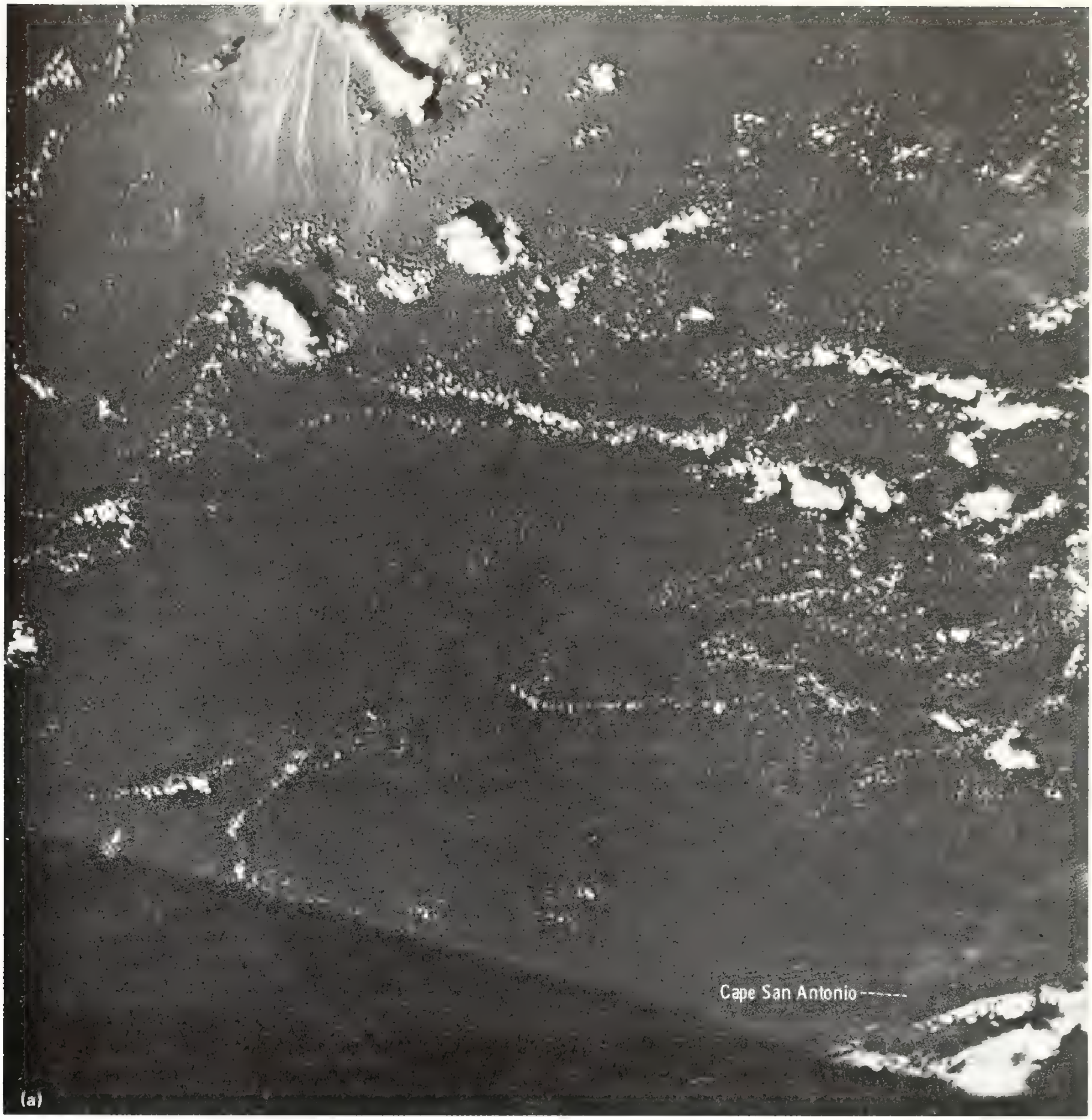

FIGURE 4.—Handheld-camera photographs over the eastern Gulf of Mexico taken by the Apollo crew at approximately 18:43 UT on July 18, 1975. Photographs were obtained with a 70-mm format camera using a 50-mm lens. The right-hand margin of each photograph is oriented approximately north-south, as shown in figure 1. The photographs were taken from the northeast, looking southwest. Clouds are easily differentiated from sea-surface features by comparing features in adjacent photographs or by their shadows. Approximate solar elevation is 77°, and approximate azimuth is 256° reckoned clockwise from north. (a) AST-9-528. (b) AST-9-529. (c) AST-9-530.

southeasterly winds at 2 to 3 m/sec interrupted by local thunderstorms.

The three ASTP photographs taken during this experiment are shown in figures 4(a) to 4(c). These are oblique 70-mm photographs taken with a 50-mm-focal-length lens. The black shadow in each photograph is the edge of a spacecraft window. Crew documentation and comments on

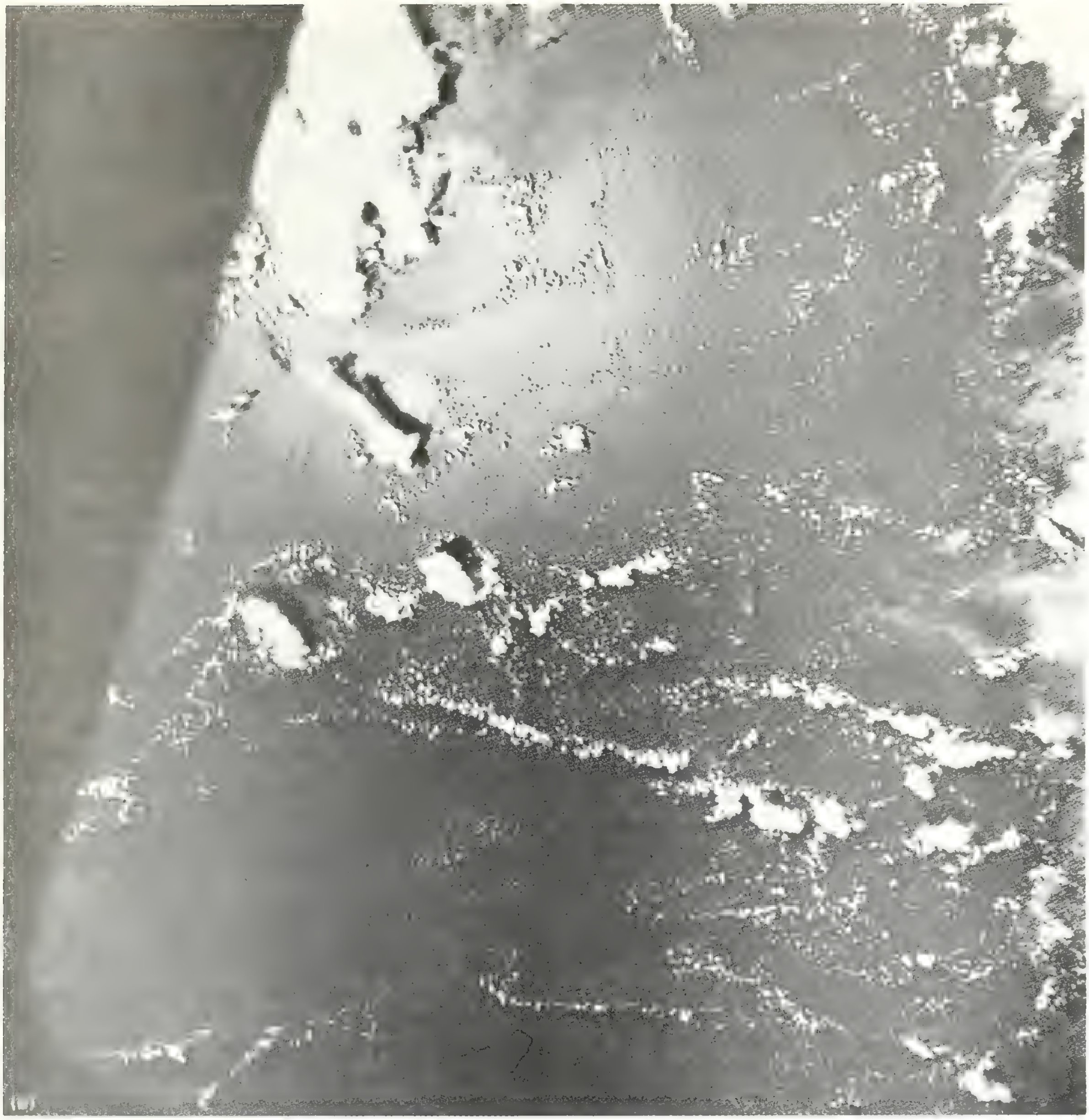

FIGURE 4.—Continued.

these photographs are minimal, and, except for knowing that they were taken over the gulf during revolution 45 (July 18), the only quantitative information was obtained by means of the location procedure discussed earlier. As can be seen by comparison with figure 1, the right-hand borders of figures 4(a) to 4(c) are oriented almost exactly north-south.

In figure 4(a), the western tip of Cuba can be seen in the lower right-hand corner and a series of streaks in the sunglint pattern appears near the upper left border. Water color patterns are quite evident near Cape San Antonio because of changes in bottom depth; but, in agreement with the ship data, there is no color evidence of the Gulf Loop Current. Because the streaks are to the

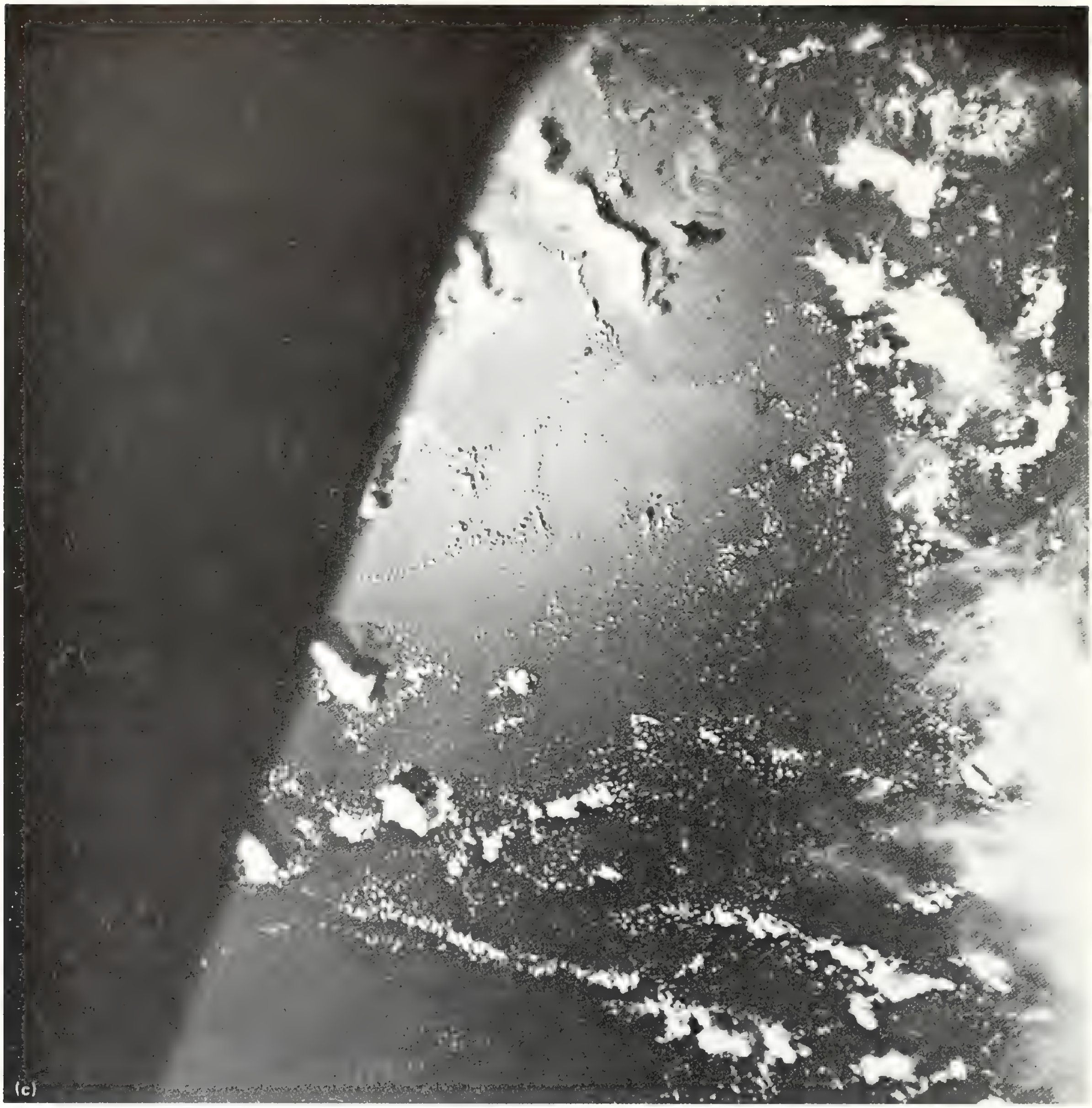

FIGURE 4.—Concluded.

west of the 293-K (20° C) isotherm at 100-m depth (fig. 1), it is likely that they are associated with the current's cyclonic edge. In figure 4(b), the streaks are again observable just to the right of the large cloud in the upper left corner of the photograph; this is the cloud sketched in figure 2. By comparing with figure 4(a), it is seen that the streaks in figure 4(b) are a continuation of those in figure 4(a) and can be followed through the sunglint into figure 4(c). The streaks show significant anticyclonic curvature in figures 4(b) and 4(c), in agreement with the ship data (fig. 2). Again, there is no color indication of the current in these last two photographs.

The interpretation of photographs showing slicks in sunglint has been reviewed by Soules (ref. 2). Because his photointerpretations were made without benefit of near-simultaneous shipboard observations, he was uncertain about the dynamic processes involved. Shipboard photographs (not shown) and logged observations indicate extensive areas of slicks in the time period 12:00 to 19:00 UT on July 17 (fig. 3); at 19:00 UT, the slicks were seen to be 20 to 30 m wide, separated by approximately 150 m. Judging from the wind conditions and following the discussion by McLeish (ref. 16), the slicks do not appear to be wind generated (particularly since they curve anticyclonically with the current). E. Mollo-Christensen and J. R. Proni[1] have proposed that horizontal shears (as inferred by the isotherms in fig. 3) can cause internal waves near the edge of the Gulf Stream; this would require a regularity in the slicks, which was not observed in figure 4. It appears then that an explanation for the slick pattern is the horizontal shear across the current. It has been observed elsewhere (ref. 17) that the horizontal velocity field can have a banded structure; i.e., bands of uniform current speed separated by a zone of very large shear. Such an explanation would be a horizontal analog of the vertical shear profile in the thermocline observed by Woods (ref. 18) and is consistent with other observations of layer quantization observed in the ocean (e.g., refs. 19 and 20).

The streaks in figure 4 show no indication of eddies embedded in the current such as those reported by Maul et al. (ref. 21) or by Maul (ref. 15). In the upper left corner of figure 4(b), however, is a cloud formation that is typical of what Stevenson (refs. 5 and 7) interpreted as a cold-core eddy embedded in the Yucatan Current. His interpretations were made from Skylab photographs, and there are several examples in figure 4. There is evidence to offer an alternative explanation for these data.

Scully-Power and Twitchell (ref. 22) gave a theoretical analysis of the conditions needed to form a cloud over a warm-core eddy. In contradistinction, a cold-core eddy should be characterized merely by a lack of cloud, much as observed in figure 4(b). Scully-Power and Twitchell found that for light wind conditions such as observed here, the height H of the convective condensation level (CCL) is given by

$$H = \tau/(\Gamma - \gamma) \tag{1}$$

where τ is the temperature excess (in degrees Celsius) of the warm waters relative to the surrounding waters, Γ is the dry adiabatic lapse rate (0.98° C/100 m), and γ is the observed lapse rate. Using the 12:00-UT Key West radiosonde data as input, the height of the CCL is 832 m and γ is 0.63° C/100 m. Solution of equation (1) requires $\tau = 2.9$ K (2.9° C), which is well beyond these or historical observations (ref. 23) of sea-surface temperature patterns in the Gulf of Mexico in July. In addition, careful examination of the streaks, especially in figures 4(b) and 4(c), shows that the streaks are continuous in their trend into and/or out of the circular feature. If the cloud feature was indeed an oceanic circulation feature, the streaks would show some indication of rotation. Also, the cloud feature in figure 4(b) is in the zone of maximum current shear, where streamline distortion due to the water's vorticity would be maximum. Third, the velocity of the feature, if it is as Stevenson (refs. 5 and 7) supposes, must be to the northeast at approximately 1 m/sec (i.e., with the current). Using the same image sequence technique employed by meteorologists to determine winds from cloud motion, the velocity of the main cloud feature was determined to be 5 m/sec to the west-southwest (i.e., against the current). Similar results were obtained with other cloud features (fig. 1); the analysis for the feature seen in figure 4 is given in figure 5, in which a sequence of GOES 1-km-resolution images is shown.

Gurka (ref. 24) offered an explanation of similar features that is consistent with the observations reported here. Gurka's analyses of GOES imagery and concurrent wind observations show that cloud features such as depicted in figure 4 are caused by strong wind zones accompanying thunderstorms. In a thunderstorm, circular bands of

---

[1] Personal communication, 1977.

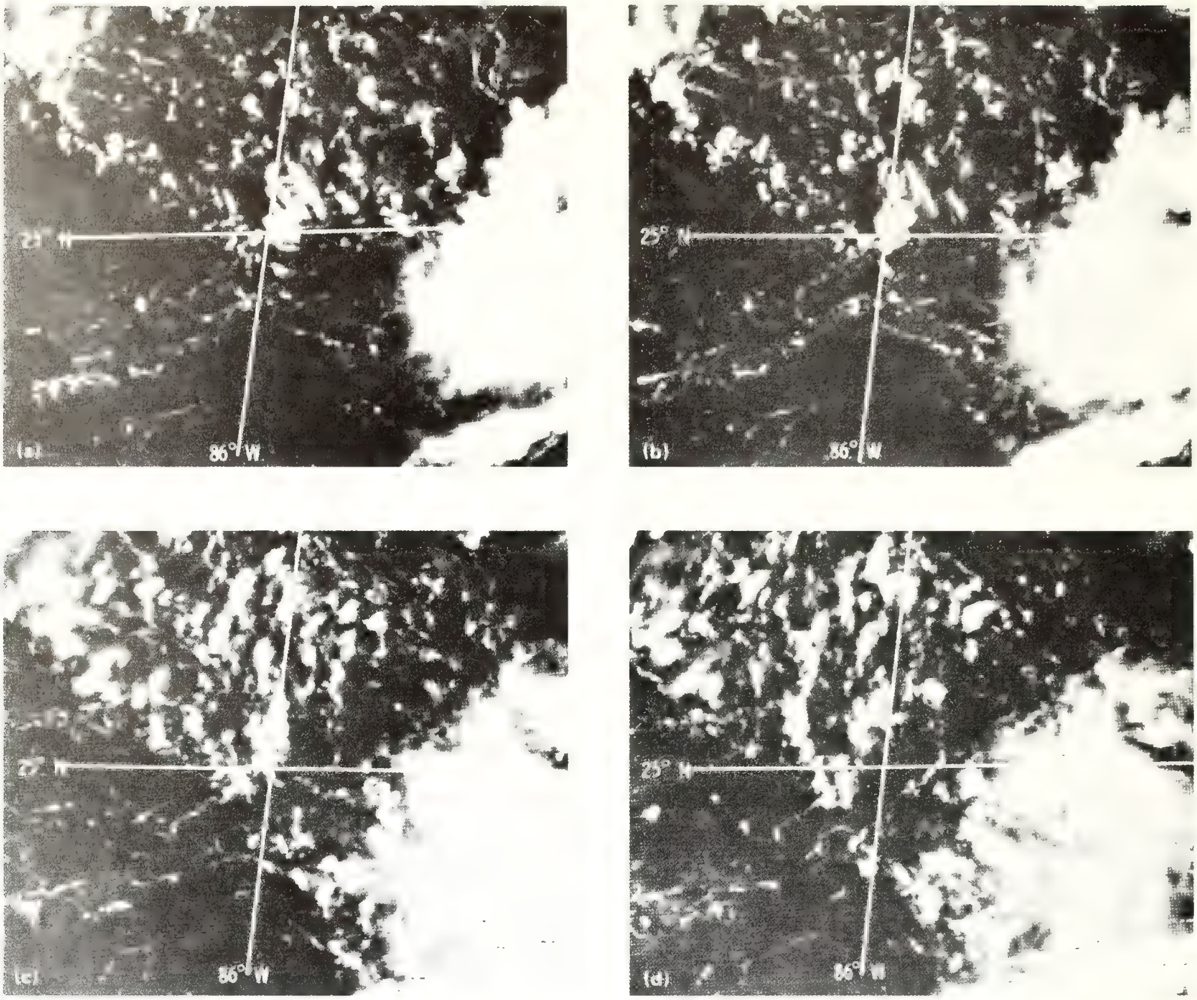

FIGURE 5.—Sequence of 1-km-resolution GOES visible images taken on July 18, 1975, centered at latitude 25° N, longitude 86° W. Evolution of the cloud feature noted in figures 1, 2, and 4(b) is seen to be toward the southwest. Dots in figures 5(c) and 5(d) are part of the electronic grid in the original images; the grid overlay was removed from figures 5(a) and 5(b) before final figure preparation. Data in figures 5(a), 5(c), and 5(d) were provided by the Environmental Data Service; figure 5(b) was specially imaged by the Miami Satellite Field Services Station, NOAA. (a) 18:00 UT. (b) 19:00 UT. (c) 20:00 UT. (d) 21:00 UT.

clouds (similar to those located southeast of the cumulonimbus in the upper left corner of fig. 4(b)) are caused by divergent winds that are orthogonal to the cloud ring. The clear area is an expression of dry air that has descended and diverged. Stevenson (refs. 5 and 7) noted that the color of the sea was often different in the center of the area; he ascribed this effect to cooler water. An alternate explanation based on the wind pattern is that the color change represents a change in reflectance, due to slopes caused by varying winds. Just such an abrupt change in sea state was seen from the research vessel *Virginia Key* during the morning of July 17. It was manifested as a marked change in ocean color from gray to blue after the passage of the wind front.

It is difficult to quantify the discussion in terms of wave-slope statistics (ref. 25) because the position of the spacecraft when the ASTP photographs were taken is not known. However, if the estimated photoacquisition time of 18:43 UT is nearly correct, the zenith angle Z and the azimuth angle A of the Sun relative to sunglint can be calculated from the solar declination d, the latitude of the sunglint ϕ, and the local meridian angle t.

$$Z = \cos^{-1}[\sin d \sin \phi + \cos d \cos \phi \cos t]$$

$$= 13^\circ$$

$$A = \sin^{-1}\left[\frac{\sin t \cos d}{\sin Z}\right]$$

$$= 256^\circ$$

Then, using Snell's law, the position of the spacecraft can be estimated by dead reckoning to be latitude 25.1° N, longitude 84.5° W; i.e., the photographs in figure 4 were taken from the northeast looking southwest. Using this perspective, the mean-square wave-slope σ^2 equation of Cox and Munk (ref. 25)

$$\sigma^2 = 0.003 + 5.12 \times 10^{-3} W$$

where W is the windspeed in meters per second, can be employed to discuss varying reflectances in the sunglint pattern.

Strong and Ruff (ref. 26) showed that the radiance distribution from sunglint could be adequately modeled by assuming that σ^2 is independent of the wind direction and by using a Gaussian probability distribution. Assuming a probability function of the form

$$\frac{\exp\left[-\dfrac{\left(\dfrac{\partial z}{\partial x}\right)^2}{\sigma^2}\right]}{\pi\sigma^2}$$

where $\partial z/\partial x$ is the root-mean-square wave slope, the probability of a wave slope occurring for windspeeds of 0, 2, 5, and 10 m/sec was calculated and is shown in figure 6 for the viewing geometry deduced earlier. Isopleths of wave slope required to reflect the Sun for $Z = 13^\circ$ describe an elliptical shape on the ocean surface. The diagram also shows how a sunglint pattern spreads over a larger area as a uniform windspeed increases. For the observer looking at the specular point ($\tan^{-1}(\partial z/\partial x) = 0^\circ$), the probability that a photon will be reflected decreases rapidly with increasing windspeed; i.e., the radiance decreases. This condition is analogous to the situation in figure 4(b) in the southwestern corner of the ring-cloud area, where a higher windspeed would be manifested by a lower radiance. The opposite case, in which the wind vector from the thunderstorm and the mean wind field tend to cancel and result in a higher radiance, can easily be envisioned. Thus, a complicated wind field can be inferred from the radiance pattern.

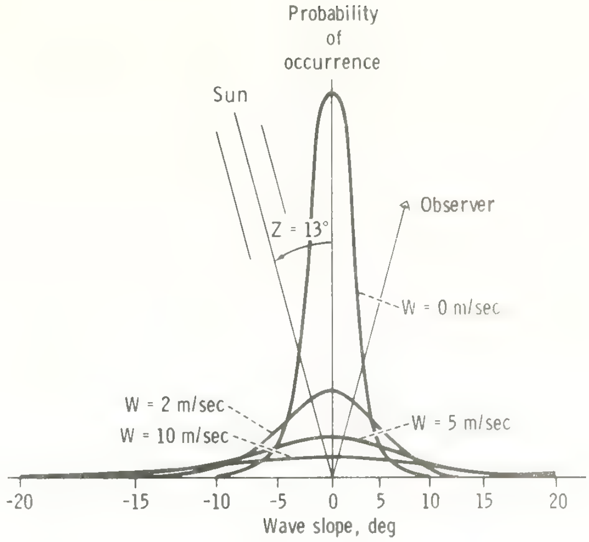

FIGURE 6.—Interpretation diagram for the sea-surface reflectance patterns seen in figure 4, neglecting the effects of upwelling diffuse radiance from beneath the sea and of atmospheric scattering. The probability that the Apollo observer would see specular return of the Sun is plotted for the range of windspeeds W and viewing geometry of figure 4. If an observer is looking at a point on the sea surface where a wave slope of +5° is required to reflect the Sun, the probability of reflection is much less for a 5-m/sec wind than for a 2-m/sec wind; this explains discontinuities in the reflectance pattern as spatial gustiness in the wind field.

DISCUSSION

The experiment described here was designed to evaluate the usefulness of ASTP handheld-camera photographs and visual observations over a specific study site. The Apollo spacecraft crossed the eastern Gulf of Mexico several times during the mission, and three space photographs were obtained over the Gulf Loop Current boundary at the same time that the research vessel *Virginia Key* observed oceanic conditions. The most serious difficulties in using the satellite data were the lack of accurate time annotation on the photographs and the absence of voice comments at the time of transit. (The former problem can be solved by using crystal-controlled light-emitting-diode day/time displays along the sprocket holes in all future space-qualified cameras. The latter problem can be adequately solved by use of voice-activated recorders coupled to the camera system whereby the observer can note the frame number and time from the camera in the visual observations log.) Results from this experiment suggest that, for this mission, the 70-mm format camera using the 50-mm lens was the best combination of photographic equipment for oceanic viewing.

Location of the photographs was accomplished by comparison with near-simultaneous, 1-km-resolution GOES imagery. To fully exploit this technique, all full-disk 1-km-resolution imagery must be archived from the routine 30-minute observing schedule; only hourly data were available for this study. In addition, for specific experiments, special observing schedules should be followed to provide synoptic observations. During the Space Shuttle missions, worldwide geostationary imagery will be available; special planning will be required to fully exploit those data for handheld-camera photographic purposes.

Photographing the sunglint pattern proved to be the most valuable contribution to observing the current boundary. The shipboard data show that during the summer, there may be no color boundary to the Gulf Loop Current and that surface reflection patterns will be the only remotely sensed indicators of its location. This suggests that for experiments with the coastal zone color scanner to be flown on Nimbus-G, the instrument should be tilted to observe sunglint under certain conditions. In view of the pattern in sea-surface reflectance associated with the current, microwave techniques would appear to be a valuable sensing tool. However, there are high-frequency sea-state (capillary) fluctuations associated with meteorological conditions that would make microwave analysis difficult without ancillary measurements.

Circular features in cloud fields have been interpreted by Stevenson (refs. 5 and 7) as being caused by cold-water eddies in the current. From an investigation into this interpretation, the following conclusions were reached: (1) the surface temperature differences required to support the hypothesis were not observed, (2) streaks on the water showed no evidence of eddy-induced vorticity, (3) the cloud feature observed moved at 5 m/sec against the current, and (4) the sea-surface reflectance patterns could be explained on the basis of fluctuations of the wind field associated with the typical ring-cloud formations around thunderstorms. Because these facts are consistent with concurrent shipboard observations of the surface and subsurface thermal fields and with the ship's weather log, it is concluded that Stevenson's observation of mesoscale turbulence in ocean currents can be better explained as being entirely meteorological in nature, driven perhaps by a relatively uniform, warm sea-surface temperature field.

ACKNOWLEDGMENTS

Gratitude is expressed to M. Pryslak, S. McLafferty, and M. McCaslin for their assistance in data acquisition and analysis. Ocean temperature data for June and August 1975 were provided by R. L. Molinari (NOAA); the 19:00-UT GOES image was specially recorded by the Miami Field Services Station of the NOAA National Environmental Satellite Service.

REFERENCES

1. Ewing, G. C., ed.: Oceanography From Space. Ref. 65-10, Woods Hole Oceanographic Institution (Woods Hole, Mass.), 1965.

2. Soules, Stanley D.: Sunglitter Viewed From Space. Deep-Sea Res., vol. 17, Feb. 1970, pp. 191-195.

3. Mairs, Robert L.: Oceanographic Interpretation of Apollo Photographs. Photogram. Eng. vol. 36, Oct. 1970, pp. 1045-1058.

4. Maul, George A.; and McCaslin, Michael: An Assessment of the Potential Contributions to Oceanography From Skylab Visual Observations and Handheld-Camera Photographs. Sec. 12 of Skylab Explores the Earth, NASA SP-380, 1977.

5. Stevenson, Robert E.; Carter, L. David; Vonder Haar, Stephen P.; and Stone, Richard O.: Visual Observations of the Ocean. Sec. 11 of Skylab Explores the Earth, NASA SP-380, 1977.

6. El-Baz, Farouk: Astronaut Observations From the Apollo-Soyuz Mission. In vol. I of Smithsonian Studies in Air and Space, Smithsonian Institution Press (Washington, D.C.), 1977.

7. Stevenson, Robert E.: Observations From Skylab of Mesoscale Turbulence in Ocean Currents. Nature, vol. 250, no. 5468, Aug. 23, 1974, pp. 638-640.

8. Thompson, Morris M.; Eller, Robert C.; Radlinski, William A.; and Speert, Julius L., eds.: Manual of Photogrammetry. Third ed. American Soc. Photogram. (Falls Church, Va.), 1966.

9. Lorenzen, C. J.: A Method for the Continuous Measurement of in vivo Chlorophyll Concentration. Deep-Sea Res., vol. 13, no. 2, 1966, pp. 223-227.

10. Cochrane, J. D.: The Yucatan Current. Annual Report, Project 286, Texas A. & M. Univ. Ref. 65-17T, 1965, pp. 20-27.

11. Nowlin, W. D., Jr.; and McLellan, H. J.: A Characterization of the Gulf of Mexico Waters in Winter. J. Marine Res., vol. 25, no. 1, 1967, pp. 29-59.

12. Leipper, Dale F.: A Sequence of Current Patterns in the Gulf of Mexico. J. Geophys. Res., vol. 75, no. 3, Jan. 20, 1970, pp. 637-657.

13. Molinari, Robert L.; and Yager, Robert E.: Upper Layer Hydrographic Conditions at the Yucatan Strait During May, 1972. J. Marine Res., vol. 35, no. 1, 1977, pp. 11-20.

14. Morrison, John M.; and Nowlin, Worth D.: Repeated Nutrient, Oxygen, and Density Sections Through the Loop Current. J. Marine Res., vol. 35, no. 1, 1977, pp. 105-128.

15. Maul, George A.: The Annual Cycle of the Gulf Loop Current, Part I: Observations During a One-Year Time Series. J. Marine Res., vol. 35, no. 1, 1977, pp. 29-47.

16. McLeish, W. L.: On the Mechanisms of Wind-Slick Generation. Deep-Sea Res., vol. 15, 1968, pp. 461-469.

17. Maul, George A.; and Hansen, Donald V.: An Observation of the Gulf Stream Front Structure by Ship, Aircraft, and Satellite. Remote Sens. Environ., vol. 2, 1972, pp. 109-116.

18. Woods, John D.: An Investigation of Some Physical Processes Associated With the Vertical Flow of Heat Through the Upper Ocean. Meteorol. Mag., vol. 97, no. 1148, Mar. 1968, pp. 65-72.

19. Stommel, Henry; and Fedorov, K. N.: Small-Scale Structure in Temperature and Salinity near Timor and Mindanao. Tellus, vol. 19, no. 2, 1967, pp. 306-325.

20. LaFond, E. C.; and LaFond, K. G.: Vertical and Horizontal Thermal Structures in the Sea. Rep. NEL 1395, U.S. Navy Electronics Laboratory (San Diego, Calif.), July 1968.

21. Maul, G. A.; Norris, D. R.; and Johnson, W. R.: Satellite Photography of Eddies in the Gulf Loop Current. Geophys. Res. Letters, vol. 1, Oct. 1974, pp. 256-258.

22. Scully-Power, P.; and Twitchell, P.: Satellite Observation of Cloud Patterns over East Australian Current Anticyclonic Eddies. Geophys. Res. Letters, vol. 2, Mar. 1975, pp. 117-119.

23. Robinson, Margaret K.: Atlas of Monthly Sea Surface and Subsurface Temperature and Depth of the Top of the Thermocline, Gulf of Mexico and Caribbean Sea. Ref. 73-8, Scripps Inst. Oceanography (La Jolla, Calif.), 1973.

24. Gurka, James J.: Satellite and Surface Observations of Strong Wind Zones Accompanying Thunderstorms. Mon. Weather Rev., vol. 104, no. 12, 1976, pp. 1484-1493.

25. Cox, C.; and Munk, W.: Measurements of the Roughness of the Sea Surface From Photographs of the Sun's Glitter. J. Opt. Soc. America, vol. 44, no. 11, 1954, pp. 838-850.

26. Strong, Alan E.; and Ruff, Irwin S.: Utilizing Satellite-Observed Solar Reflections From the Sea Surface as an Indicator of Surface Wind Speeds. Remote Sens. Environ., vol. 1, 1970, pp. 181-185.

8. Apollo-Soyuz Test Project: Summary Science Report, NASA SP-412, Vol. 2, 359-370.

Determining Photograph Locations Over Oceans

S. McLafferty,[a] M. Pryslak,[a] and G. A. Maul[b]

ABSTRACT

To increase the scientific usefulness of Apollo-Soyuz Test Project ocean photographs, more precise definitions of their geographic locations are needed. The methods used in this report to quantitatively define the photo-locations are based on photogrammetry, on a knowledge of the groundtracks of the spacecraft and the times during which the photographs were taken, and on a comparison with satellite imagery. Latitudes and longitudes with an estimated error of ±1 to ±3 seconds are calculated for the center points of photographs taken during mapping passes that lack photo-support data. A method is developed for determining the center points for photographs containing two or more recognizable features on landmasses. Because the method of locating cloud features of Apollo-Soyuz open-ocean photographs on satellite images was largely unsuccessful, a map is provided which shows the Apollo groundtracks that correspond to the times when the photographs were taken.

INTRODUCTION

The Apollo-Soyuz Test Project (ASTP) ocean photographs can be grouped into four categories: (1) vertical mapping photographs, which are taken with 60 percent stereo-overlap and for which the exact coordinates of the center point and the four corners are known; (2) vertical mapping photographs for which the exact coordinates of the center point and the four corners are not known; (3) handheld-camera photographs containing a coastline and/or island(s); and (4) open-ocean photographs.

In the case of mapping passes with no photo-support data, the location of at least one photograph could be determined by accurately identifying a coast or an island, and the positions of the remaining photographs could therefore be determined by using equations to calculate the latitude and longitude of the Apollo spacecraft groundtrack. In the case of handheld-camera photographs containing an identifiable landmass, 1:1 000 000-scale Operational Navigation Charts (ONC's), published by the Defense Mapping Agency, were used; the main difficulty in this case was the obliquity of many of the photographs. In the last case, clouds in the open-ocean photographs were compared with clouds on weather-satellite images. The main problems were the low resolution of the satellite images and the difficulty in obtaining satellite imagery taken at the same time as the ASTP photographs.

MAPPING PASSES WITH PHOTO-SUPPORT DATA

The 70-mm Hasselblad data camera was used to acquire mapping photography. It was equipped with a glass reseau plate and would accept both a 60-mm and a 100-mm lens. The camera was bracket-mounted in one of the spacecraft windows, and the spacecraft was oriented so that the perspective center of the camera lens would point at nadir. An intervalometer controlled the opening of the shutter. At the exact instant the photograph was taken, the time and the spacecraft position and orientation were recorded.

---

[a] National Air and Space Museum, Smithsonian Institution.

[b] Atlantic Oceanographic and Meteorological Laboratory, National Oceanic and Atmospheric Administration.

Through the use of a computer at the NASA Lyndon B. Johnson Space Center (JSC), the vectors for instrument pointing (one vector for the center of the photograph and one vector for each of the four corners) and spacecraft position were transformed into the geographic inertial coordinate system. This system is a Cartesian coordinate system, the origin of which is at the Earth's center, with the x-axis lying in the plane of the celestial equator of date through the Greenwich meridian, with the z-axis orthogonal to the celestial equator of date (the axis of rotation), and with the y-axis completing the right-handed system. The vectors were added together, and the resulting vector components were substituted in the following equations to obtain the latitude ϕ and the longitude λ:

$$\phi = \arctan \frac{z}{\sqrt{x^2 + x^2}}$$

for $-90^\circ \leq \phi \leq 90^\circ$, and

$$\lambda = \arctan \frac{y}{x}$$

for $0^\circ \leq \lambda < 360^\circ$. A detailed description of this method is given by Osburn et al. (ref. 1).

MAPPING PASSES WITHOUT PHOTO-SUPPORT DATA

Unfortunately, for several mapping passes, the photo-support data regarding time, spacecraft position, and orientation were not recorded. Thus, calculations for parameters essential in photogrammetry, such as the latitude and longitude of the center point and of the four corners of the photograph, could not be made. However, an approximation of the latitude and longitude could be made, although it was not as accurate as the photo-support data that were recorded.

The method used for the approximation was one that involved determining the subvehicle points for the times at which the photographs were taken. If the optical axis of the camera was at the vertical to the Earth (or nearly vertical), then the center point of the photograph would be on or very near the subvehicle point. If the center point of one photograph could be located by using "landmarks," then the center points of previous and subsequent mapping photographs could be determined because the interval at which they were taken was fixed by the intervalometer (a timing mechanism that automatically triggers the shutter at a predetermined interval).

Determination of Latitude

The latitude ϕ for a circular orbit is given by the following equation:[1]

$$\phi = \arcsin(\sin i \sin \sigma) \qquad (1)$$

where i = inclination of the orbit in degrees (51.77° for ASTP)

$$\sigma = \frac{360\left(t - t_o\right)}{\tau_n}$$

and where t represents time and τ_n represents the nodal period, or the interval between ascending nodes.

The value of σ from 0° to 360° represents a full cycle of latitude from ascending node to ascending node (the point at which the spacecraft crosses the Equator from the Southern to the Northern Hemisphere). For a circular orbit (i.e., the spacecraft altitude is constant), the value of σ is directly proportional to time. Thus, the $\Delta\sigma$ is constant for a given time interval.

---

[1] Personal communication from G. D. Griffith, JSC, 1974.

TABLE I.—Example of Three Latitudes and Corresponding Values of σ and $\Delta\sigma$

Day, 1975	UT, hr:min	Latitude, deg (a)	σ, rad	$\Delta\sigma$, rad
July 19	23:59	(a) 38.884 S	5.35733291	0.07100820
July 20	00:00	(b) 36.346 S	5.42834110	.07101589
July 20	00:01	(c) 33.682 S	5.49935700	Not applicable

[a] The letters "a, b, c" are designators used in the text.

The value of σ can be calculated—without knowing t, t_0, and τ_n—if a value of latitude is known.

$$\sigma = \arcsin \frac{\sin \phi}{\sin i} \tag{2}$$

The values of $\Delta\sigma$ for a given time interval were calculated from the σ's of two known values of latitude. For example, table I contains three latitudes (taken from the postmission computer printout of the latitude and longitude of the subvehicle point at 1-minute intervals) and the corresponding calculated values of σ and $\Delta\sigma$; the times correspond to the beginning of mapping pass 6 on spacecraft revolution 64.

If the $\Delta\sigma$ between "a" and "b" in table I is added to the σ of "b," the result (5.4993493 rad) should equal the σ of "c." The result differs slightly, but when it is substituted in equation (1), the value of the latitude is still 33.682° S. Therefore, once the $\Delta\sigma$ for a 1-minute interval was calculated, the $\Delta\sigma$ for any time interval could be determined. The interval between frames taken with the 60-mm lens was 10.02 seconds.

After the latitude of one photograph was determined, the σ for that latitude was calculated from equation (2). By subtracting or adding increments of $\Delta\sigma$ to the original σ, latitudes for frames before or after the known photograph were calculated by substituting the new σ into equation (1). For example, during mapping pass 6 on revolution 64, photographs AST-16-1121 to AST-16-1123 were taken over the Great Australian Bight. The center point of AST-16-1123, which was located on Flinders Island, was plotted on an ONC; and a latitude of 33.72° S was obtained from the map. From equation (2), σ was calculated and found to be 5.49836471 rad. A $\Delta\sigma$ of 0.01185965 rad was used to calculate the σ's for AST-16-1122 and AST-16-1121 (table II). The latitudes (together with longitudes, altitudes, footprint sizes, and times) for all ocean mapping passes without photo-support data are listed in table III.

TABLE II.—Calculated σ's and Corresponding Latitudes for Three ASTP Photographs With No Support Data

[Mapping pass 6, revolution 64]

Photograph no.	σ, rad	Latitude, deg
AST-16-1123	5.49836471	33.72 S
AST-16-1122	5.48650506	34.17 S
AST-16-1121	5.47464541	34.62 S

TABLE III.—Geophysical and Temporal Parameters for All ASTP Ocean Mapping Passes Without Photo-Support Data

Photograph no.	Latitude, deg	Longitude, deg	Altitude, km	Footprint size, km	Day, July 1975	UT, hr:min
Mapping pass 5, revolution 40						
AST-14-946	14.80 N	41.97 E	224	199	18	09:47
AST-14-947	15.32 N	42.38 E	224	199	18	09:47
AST-14-968	26.00 N	51.53 E	226	200	18	09:51
Mapping pass 6, revolution 64						
AST-16-1121	34.62 S	133.53 E	229	203	20	00:01
AST-16-1122	34.17 S	133.93 E	229	203	20	00:01
AST-16-1123	33.72 S	134.30 E	229	203	20	00:01
AST-16-1151	20.14 S	148.13 E	225	199	20	00:06
AST-16-1152	19.63 S	148.56 E	225	199	20	00:06
AST-16-1153	19.12 S	148.98 E	225	199	20	00:06
AST-16-1154	18.60 S	149.41 E	225	199	20	00:07
AST-16-1155	18.09 S	149.82 E	225	199	20	00:07
AST-16-1156	17.57 S	150.25 E	225	199	20	00:07
AST-16-1157	17.05 S	150.66 E	225	199	20	00:07
AST-16-1158	16.54 S	151.07 E	224	199	20	00:07
AST-16-1159	16.02 S	151.48 E	224	199	20	00:07
AST-16-1160	15.50 S	151.89 E	224	199	20	00:08
AST-16-1161	14.97 S	152.30 E	224	199	20	00:08
AST-16-1162	14.45 S	152.70 E	224	199	20	00:08
AST-16-1163	13.93 S	153.10 E	224	199	20	00:08
AST-16-1164	13.40 S	153.50 E	224	199	20	00:08
AST-16-1165	12.88 S	153.89 E	224	199	20	00:08
AST-16-1166	12.35 S	154.30 E	224	199	20	00:09
AST-16-1167	11.83 S	154.68 E	224	199	20	00:09
AST-16-1168	11.30 S	155.08 E	224	199	20	00:09
AST-16-1169	10.77 S	155.48 E	224	199	20	00:09
AST-16-1170	10.25 S	155.86 E	223	198	20	00:09
AST-16-1171	9.72 S	156.26 E	223	198	20	00:09
AST-16-1172	9.19 S	156.53 E	223	198	20	00:10
AST-16-1173	8.66 S	157.03 E	223	198	20	00:10
AST-16-1174	8.13 S	157.41 E	223	198	20	00:10
AST-16-1175	7.60 S	157.80 E	223	198	20	00:10
AST-16-1176	7.07 S	158.18 E	223	198	20	00:10
AST-16-1177	6.53 S	158.57 E	223	198	20	00:10
AST-16-1178	6.00 S	158.95 E	223	198	20	00:11
AST-16-1179	5.47 S	159.33 E	223	198	20	00:11

TABLE III.—*Concluded*

Photograph no.	*Latitude, deg*	*Longitude, deg*	*Altitude, km*	*Footprint size, km*	*Day, July 1975*	*UT, hr:min*
Mapping pass 6, revolution 64						
AST-16-1180	4.94 S	159.70 E	223	198	20	00:11
AST-16-1181	4.40 S	160.08 E	223	198	20	00:11
AST-16-1182	3.87 S	160.47 E	223	198	20	00:11
AST-16-1183	3.34 S	160.83 E	223	198	20	00:11
AST-16-1184	2.81 S	161.20 E	223	198	20	00:12
AST-16-1185	2.27 S	161.59 E	223	198	20	00:12
AST-16-1186	1.74 S	161.97 E	223	198	20	00:12
AST-16-1187	1.20 S	162.34 E	223	198	20	00:12
AST-16-1188	.67 S	162.72 E	223	198	20	00:12
AST-16-1189	.14 S	163.10 E	223	198	20	00:12
AST-16-1190	.40 N	163.48 E	223	198	20	00:13
AST-16-1191	.93 N	163.86 E	223	198	20	00:13
Mapping pass 7, revolution 71						
AST-16-1262	33.29 N	32.93 E	226	200	20	10:46
AST-16-1263	33.75 N	33.46 E	226	200	20	10:46
AST-16-1264	34.20 N	34.05 E	226	200	20	10:46
Mapping pass 9, revolution 72						
AST-17-1366	33.30 N	10.50 E	226	120	20	12:14
AST-17-1367	33.58 N	10.84 E	226	120	20	12:14
AST-17-1368	33.86 N	11.19 E	226	120	20	12:14
AST-17-1369	34.15 N	11.56 E	226	120	20	12:15
AST-17-1370	34.43 N	11.93 E	226	120	20	12:15
AST-17-1371	34.71 N	12.28 E	226	120	20	12:15
AST-17-1372	34.99 N	12.63 E	226	120	20	12:15
AST-17-1373	35.26 N	12.98 E	226	120	20	12:15
AST-17-1374	35.54 N	13.36 E	227	120	20	12:15
AST-17-1375	35.81 N	13.72 E	227	120	20	12:15
AST-17-1376	36.09 N	14.10 E	227	120	20	12:15
AST-17-1377	36.36 N	14.47 E	227	120	20	12:15
AST-17-1378	36.63 N	14.83 E	227	120	20	12:15
AST-17-1379	36.90 N	15.20 E	227	120	20	12:16

Determination of Longitude

Longitude λ for a circular orbit is given by the following equation:[2]

$$\lambda = \arctan(\cos i \sin \sigma) + \lambda_n - \left[\Omega_e\left(t - t_o\right)\right] - \left\{\frac{K_s}{R_o^{7/2}}\left[\cos i\left(t - t_o\right)\right]\right\} \tag{3}$$

where λ_n = longitude of the ascending node at t

Ω_e = rotation rate of the Earth (4.178074×10^{-3} deg sec^{-1})

K_s = super constant ($4.654992784 \times 10^{8}$ deg n.mi.$^{7/2}$ sec^{-1})

R_o = circular radius of Earth

The longitude was difficult to accurately calculate because exact values for the ascending node and for the time factor $t - t_o$ were not known. When approximations of the ascending node, the time factors, and the σ (calculated from a known value of latitude) were substituted into equation (3), the results were off by as much as 0.1° when compared to the corresponding known value of longitude.

Because of this problem, a "graphic" solution was used for determining the longitude. The groundtrack was plotted on ONC's, and the longitude was obtained from the intersection of the calculated latitude and the groundtrack.

Discussion of Error

Three sources of error affected the accuracy of the calculations of latitude and longitude. First, the assumption was made that the orbit was perfectly circular. The altitude during each ASTP orbit varied by approximately 15 km, giving the orbit an eccentricity of 0.065. For this reason, the $\Delta\sigma$ varies somewhat throughout the orbit. However, the $\Delta\sigma$ did not vary significantly from minute to minute, as indicated in the previous discussion on latitude. The values of $\Delta\sigma$ were taken from the part of the groundtrack corresponding to the time the photographs were taken.

The second source of error was concerned with how accurately the initial photograph was located. On mapping pass 5 (revolution 40), mapping data were obtained for three isolated pictures taken over Saudi Arabia. These three frames were used as the initial frames so that the accuracy of the center-point locations was excellent. For mapping pass 6 (revolution 64) and mapping pass 9 (revolution 72), the center points of the initial frames coincided with distinct landmarks that could be located on ONC's with an accuracy of ±1 second. On mapping pass 7 (revolution 71), the center point of the initial frame was located over the ocean so that the accuracy of location was approximately ±3 seconds.

The third source of error resulted from the spacecraft's platform not being perfectly stable, and this characteristic caused the optical axis of the camera to wobble. Thus, the center point of the photograph would not necessarily coincide with the subvehicle point.

On mapping passes with photo-support data, the result of this spacecraft-platform phenomenon was expressed as the tilt angle and the tilt azimuth (ref. 1). The tilt angle of one particular mapping pass varied by as much as 0.7°, and the tilt azimuth varied in all directions. During the plotting of the center points of photographs with landmarks, the center point varied from the groundtrack by as much as 4 seconds of longitude.

Corner Points

Although a somewhat complex problem to solve, it is possible to calculate the latitudes and longitudes of the corner points. These calculations were not performed, for the following reasons: (1) exact altitude data, which were needed to determine accurate footprint size, were not available; (2) the lack of spacecraft-platform stability, which caused discrepancies in the expected values of the center points, would cause even larger discrepancies in the values of the corner points; and (3) it could not be assumed that the nose of the spacecraft was pointed in the direction of the groundtrack. On mapping pass 5 (revolution 40), the nose of the spacecraft was skewed by approximately 48° from the direction of the groundtrack, thus resulting in a tilt azimuth of similar magnitude.

---

[2] Ibid.

Times, Altitudes, and Footprint Size

The times and altitudes were interpolated from the postmission computer printout of the groundtracks, which provided data at 1-minute intervals. The footprint size of the photograph can be calculated in one of two ways.

1. By using the flat-Earth approximation:

$$\text{Footprint size} = h\,\frac{f}{f_l}$$

where h = altitude above the Earth

f = format size (effectively 53.0 mm for the film in the Hasselblad cameras)

f_l = focal length of camera

2. By calculating the arc length A on the Earth (ref. 2, p. 1050):

$$A = R_o\theta$$

where R_o = circular radius of the Earth (6378 km)

$\theta = \arcsin\,[(R_o + h)/R_o]\sin\gamma - \gamma$

γ = half angle of lens

For a 60-mm lens, $\gamma = 23.82944942°$; for a 100-mm lens, $\gamma = 14.84222706°$.

The second method was used, and the results were rounded off to the nearest kilometer. (The result of the second method must be multiplied by 2 to obtain the full size of the footprint.) The results of the calculations for photographs taken on mapping passes with no photo-support data are given in table III.

PHOTOGRAPHS CONTAINING LANDMASSES

The remaining photographs were taken with a 70-mm Hasselblad reflex camera equipped to use both a 50-mm and a 250-mm lens. The camera was handheld, and the only data recorded were the approximate time when each photograph was taken, the lens size used, and some crewmember comments concerning the ocean scenes observed.

The ONC's were used to locate photographs that contained landmarks. In many instances, the scales of 180-mm-square prints of photographs taken with the 50-mm lens closely matched the 1:1 000 000-scale ONC's.

The first step in locating a handheld-camera ocean photograph was to obtain its approximate location from ASTP data provided by JSC.[3] A comparison was then made between the photograph and ONC's of the same area. When landmarks were recognized, an attempt was made to locate the center point and the corner points of the photograph. When landmarks fortuitously lay on one of these points, the latitude and longitude could be read directly from ONC's. But when landmarks were an appreciable distance from one of these points, the obliquity of the photograph had to be determined before the location of the center point could be interpolated.

Unfortunately, it is difficult to find the obliquity of a handheld-camera photograph. By using figure 22-1 in the "Manual of Photogrammetry" (ref. 2), it was found that

$$A = R\Big[\arcsin(k\sin\alpha) - \alpha\Big] \tag{4}$$

---

[3] The ASTP photographic data were documented by R. Underwood in a JSC publication entitled "ASTP Index to Onboard Photography," 1975.

where A = arc length on the Earth (km)

R = mean radius of the Earth (6367.475142 km)

h = altitude of camera (km)

$k = (R + h)/R$

α = nadir angle

Although α could not be solved explicitly in equation (4), it could be evaluated through an iterative method. The method involved finding two landmarks on the photograph that lay on the principal line (the line from the nadir point (NP) through the principal point (or center point) (PP)). (Refer to fig. 1 for a diagram of the terms used in this discussion.) Because the two landmarks were not always on opposite sides of the principal point, the distances between the landmarks and the principal point of the photograph were measured in the following manner. The distance d_c from landmark L_c to PP was measured positively in the direction away from PP toward NP. The distance d_f between landmark L_f and PP was measured positively in the direction away from NP toward PP.

The angles μ and γ (fig. 1) represent the angles formed by the optical axis (the line from the perspective center to the principal point) and the line from the perspective center to the landmark. The angles were calculated as follows.

$$\mu = \arctan \frac{d_c}{f_l} \qquad \gamma = \arctan \frac{d_f}{f_l}$$

where d_c = measured distance on the original photograph (70-mm film) between L_c and PP

d_f = measured distance on the original photograph (70-mm film) between L_f and PP

f_l = focal length of the camera lens

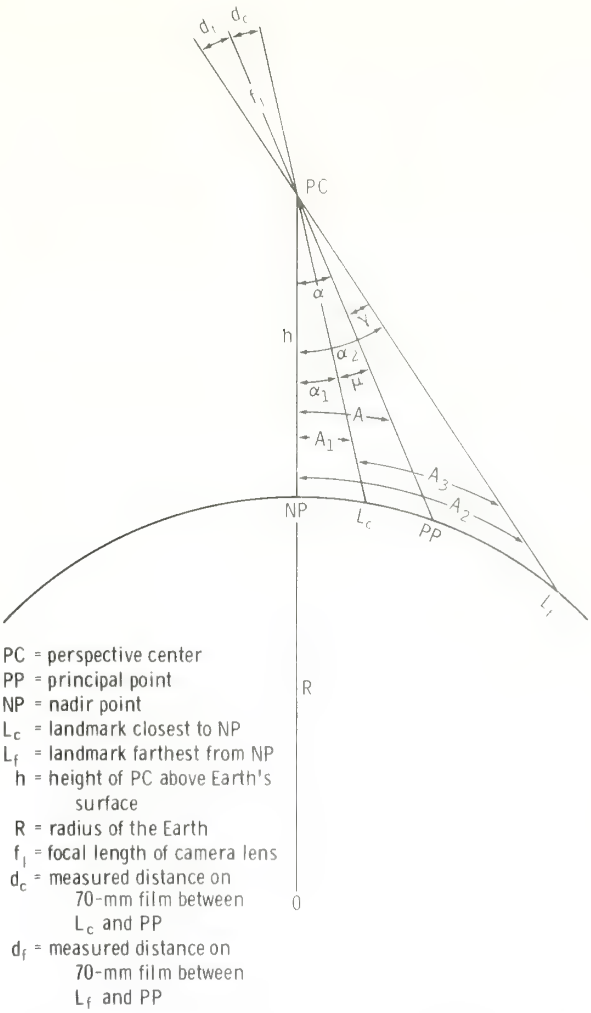

PC = perspective center
PP = principal point
NP = nadir point
L_c = landmark closest to NP
L_f = landmark farthest from NP
h = height of PC above Earth's surface
R = radius of the Earth
f_l = focal length of camera lens
d_c = measured distance on 70-mm film between L_c and PP
d_f = measured distance on 70-mm film between L_f and PP

FIGURE 1.—Diagram illustrating the relationships between various arc lengths and angles discussed in the section concerning photographs containing landmasses (modified from fig. 22-1 of ref. 2).

Next, an estimate was made of the value of α (the obliquity of the photograph), and the angles α_1 and α_2 (fig. 1) were calculated.

$$\alpha_1 = \alpha - \mu \tag{5}$$

$$\alpha_2 = \alpha + \gamma \tag{6}$$

The arc lengths A_1 and A_2 were calculated from the values of α_1 and α_2 as in equation (4):

$$A_1 = R\left[\arcsin\left(k \sin \alpha_1\right) - \alpha_1\right] \tag{7}$$

$$A_2 = R\left[\arcsin\left(k \sin \alpha_2\right) - \alpha_2\right] \tag{8}$$

$$A_3 = A_2 \quad A_1 \tag{9}$$

The value A_3 was an approximation of A', the arc length between landmarks L_c and L_f, which was measured between the landmarks on the ONC's. If the approximated value A_3 was larger than A', then the estimate of α was too large. If A_3 was smaller than A', then the estimate of α was too small. A new estimate for α was made, and the calculations from equations (5) to (9) were repeated until A_3 matched A'.

With the final value of α, the latitude and longitude of the principal point were determined through a dead reckoning method. The arc length A_1, between landmark L_c and the nadir point, was calculated from equations (5) and (7); and the arc length A, between the nadir point and the principal point, was calculated from equation (4). Arc length A_1 was subtracted from arc length A to give the arc length d between landmark L_c and the principal point. Latitude and longitude were calculated from the following equations, which are based on the model of the Earth as a Mercator projection.

$$\phi = \phi_0 + \frac{d \cos C}{60(1.852)}$$

$$\lambda = \lambda_0 + \frac{180}{\pi}\left(\tan C\right)\left(\ln \frac{\tan 45 + \frac{\phi_0}{2}}{\tan 45 + \frac{\phi}{2}}\right)$$

for $C \neq 90°$ or $C \neq 270°$, and

$$\lambda = \lambda_0 \quad \frac{d \sin C}{60\left(\cos \phi_0\right)(1.852)}$$

for $C = 90°$ or $C = 270°$, where

ϕ_0 = latitude of landmark L_c

λ_0 = longitude of landmark L_c

d = distance in kilometers from landmark L_c to the principal point

C = course or direction from landmark L_c to the principal point in degrees (north = 0°)

The method for determining the obliquity of the photograph and the latitude and longitude of the principal point presented several difficulties. The first difficulty was that two recognizable landmarks had to be located on the principal line or this method could not be used. The second difficulty involved finding the location of the principal line on the photograph because this line was not always symmetrical with the format of the photograph. In the case of high-oblique photographs, which contained the horizon, the location of the principal line was perpendicular to the horizon line and intersected the principal point. In the case of low-oblique photographs, an iterative method was used. Many lines were chosen through the principal point and through the various pairs of landmarks. Respective values of α were calculated by using the iterative method described earlier. The line with the maximum α was closest to the principal line.

The third difficulty was that the entire process required a great deal of time. It was estimated that the principal points for only one or two photographs could be determined per day. Unfortunately, although the time and funds were sufficient for developing this method, they were insufficient for the generation of data for specific photographs. It is hoped that this method will serve as a useful tool for persons interested in more specifically locating photographs that contain a coastline and/or islands.

PHOTOGRAPHS TAKEN OVER THE OPEN OCEAN

Photographs of the open ocean, of course, contained few or no landmarks from which to identify the geographical locations. However, the cloud pattern of a photograph acted as a temporary "fingerprint" of the Earth. Depending on weather conditions, this "fingerprint" might have remained for 15 minutes or longer in the atmosphere.

In an attempt to locate the area photographed over the open ocean, cloud patterns in the photographs were compared with the cloud patterns in satellite images. First, for each photograph, the revolution number and approximate time were obtained from the JSC photograph index.[4] This information, in conjunction with the groundtrack data, defined an area in which the photograph was taken. Then, a satellite image that was taken at approximately the same time and over the same area as the ASTP photograph was obtained. If the cloud patterns of the ASTP photograph could be matched with cloud patterns on the satellite image, then the location of the photograph was determined from the geographic coordinates on the satellite image.

For example, photographs AST-9-528, AST-9-529, and AST-9-530 were taken with a 50-mm lens over a highly cloud-covered area with a few points of exposed land. (A discussion of the ocean features seen in these photographs is given in the section entitled "Interpreting ASTP Photographs of the Ocean and Locating the Area Photographed (Case Study of the Gulf of Mexico).") The JSC photograph index listed the locations of the three photographs as Cuba, Cape San Antonio, and Yucatan Channel; Gulf of Mexico; and Gulf of Mexico, West of Florida, respectively. The photograph index listed the revolution number as 45 and the UT as between 199:18:41 and 199:18:55. During this time, the subvehicle point moved along the groundtrack from latitude 16.543° N and longitude 92.412° W to latitude 50.329° N and longitude 38.605° W. By limiting the area just to the Gulf of Mexico, the groundtrack was narrowed to a path between latitude 19.635° N, longitude 89.891° W at UT 199:18:42 and latitude 28.598° N, longitude 81.602° W at UT 199:18:45.

The Geostationary Operational Environmental Satellite 1 (GOES-1) images of the area were obtained from the National Oceanic and Atmospheric Administration (NOAA) National Environmental Satellite Service. The GOES-1 images were taken at 0.5-hour intervals; therefore, the appropriate images were chosen so that a time interval of 15 minutes or less existed between the acquisition of the satellite image and the acquisition of the ASTP photograph. The major cloud formations on the ASTP photographs were located on the GOES-1 images with little difficulty. After careful comparison between the ASTP photographs and the GOES-1 images, an outline of each photograph was drawn over the images. Using dominant landmarks on the GOES-1 images as a base, the latitude and the longitude of the principal point and the corner points of each ASTP photograph were interpolated across the GOES-1 images.

Unfortunately, the method of using satellite images only worked in the case of the three previously mentioned photographs over the Gulf of Mexico. Photographs taken with the 250-mm lens over the Gulf of Mexico were impossible to locate on the GOES-1 images because of the high resolution and large scale of the photographs as compared with the low resolution and small scale of the satellite images.

Data were obtained from the Defense Meteorological Satellite Program (DMSP) archive in Madison, Wisconsin, which contained two types of media: H channel (3.7-km (2 n. mi.) resolution) and V channel (0.6-km (0.33 n. mi.) resolution). The better data, the V channel, were found to be available only in coastal areas because the primary investigations using these data were usually land oriented. The H-channel data were found to be very difficult to use because of the large resolution and scale differences between the ASTP photographs and the satellite images. Because the orbital tracks of the DMSP satellite and the Apollo spacecraft crossed almost perpendicular to each other, comparison of the satellite data with the photographs was very difficult. Also, in most cases, the time interval between the acquisition of the DMSP data and the acquisition of the photographs was too large for the temporary pattern of clouds to be preserved.

---

[4] Ibid.

The last set of data was received from the Nimbus Data Utilization Center at the NASA Goddard Space Flight Center. These data were also unusable for locating ASTP photographs because of their extremely low resolution.

As a final tool to more specifically locate ocean photographs, the map in figure 2 shows the portions of groundtrack along which ocean photographs were taken. The user should refer to appendix B to obtain the revolution number for a specific photograph and then locate the appropriate groundtrack on the map.

From the altitude of the Apollo spacecraft, the horizon would appear on the Earth's surface approximately 1600 km from the subvehicle point. Thus, the photograph is located somewhere within a 3200-km-wide swath divided by and parallel with the groundtrack. Although the swath defined by the groundtrack encompasses a large area, the swath does exclude substantial areas over the ocean where the photograph was not taken.

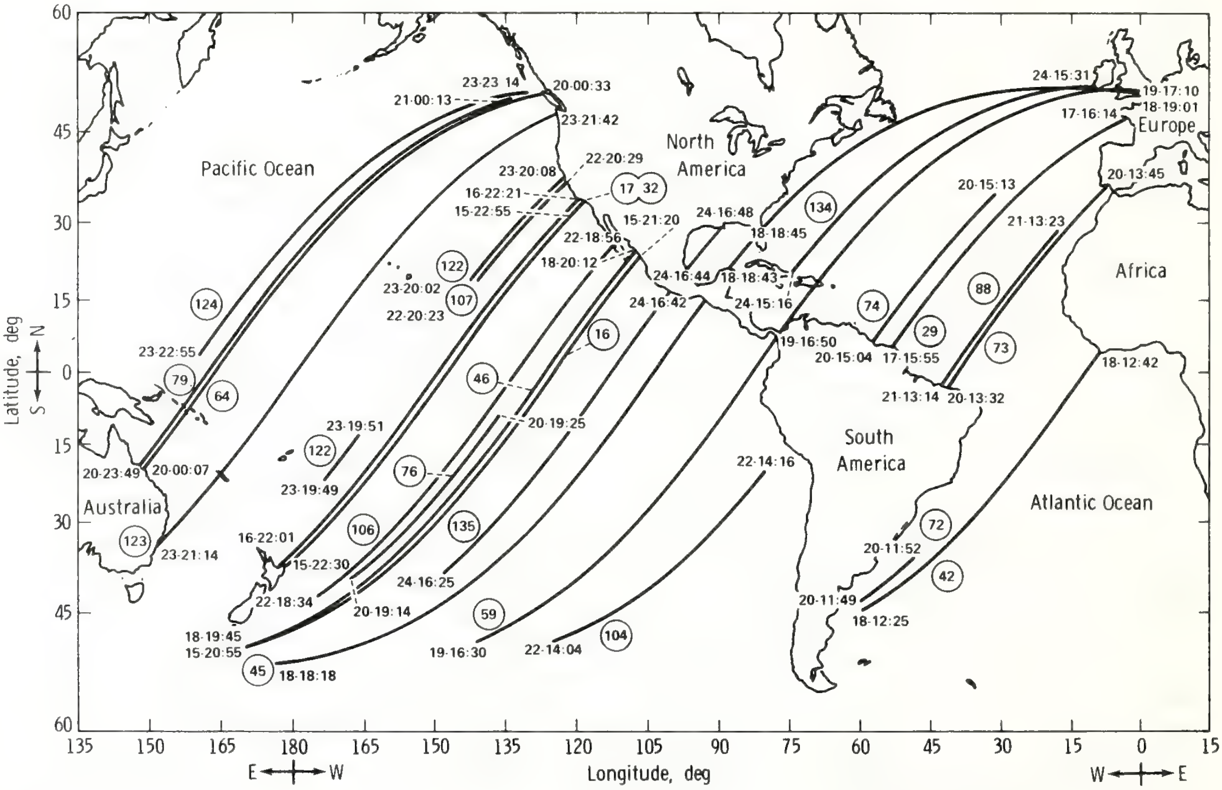

FIGURE 2.—Map of groundtracks along which ASTP photographs were taken; the user should obtain the time and/or revolution number for the particular photograph and find the corresponding groundtrack on the map. The two- and three-digit numbers are the revolution numbers. The six-digit numbers refer to the date in July (left of the dash) and the time (UT) in hours and minutes. The photograph will be somewhere within a 3200-km-wide swath divided by and parallel with the groundtrack.

SUMMARY AND SUGGESTIONS

The attempt to more specifically locate ASTP ocean photographs met with various degrees of success. Center points for mapping photographs with no photo-support data were estimated to ±1 to ±3 seconds of latitude and longitude. Footprint sizes were estimated to the nearest kilometer. Although a procedure for determining the principal point of handheld-camera oblique photographs containing a coastline and/or islands was developed, no data for specific photographs were generated. The use of satellite images in determining the location of the photographs taken over the open ocean met with very limited success because of the low resolution and the times of acquisition of the satellite imagery. Finally, a map was produced that shows the location of groundtracks during the times that photographs were taken over the ocean.

For future missions, the authors have two suggestions to greatly facilitate locating "ocean-looking" photographs.

1. Some type of timing device should be attached to the handheld camera to pinpoint the time of photoacquisition to seconds rather than minutes. Possibilities include attaching the handheld camera to a device similar to that used with the bracket-mounted camera of the ASTP mission, and placing a clock inside the camera as was done on the Earth terrain cameras of the Skylab missions.

2. Advance arrangements should be made for the acquisition of high-resolution satellite imagery over the same area and during the same time as photography planned for the mission.

REFERENCES

1. Osburn, R. K.; Barnett, Edward L.; Moore, Harry L.; and Ball, Jimmie R.: ASTP Experiment Support Data Processing. NASA CR-141915, 1975.

2. Thompson, Morris M.; Eller, Robert C.; Radlinski, William A.; and Speert, Julius L., eds.: Manual of Photogrammetry. Third ed., vol. II, American Soc. of Photogram. (Falls Church, Va.), 1966.

9. Journal of Geophysical Research 84, No. C4, 1776-1792.

Long-Term Current and Temperature Observations on the Middle Atlantic Shelf

DENNIS A. MAYER, DONALD V. HANSEN, AND DONALD A. ORTMAN

National Oceanic and Atmospheric Administration, Atlantic Oceanographic and Meteorological Laboratories, Miami, Florida 33149

Nearly 2200 days of current and temperature data were collected at a midshelf location in the Middle Atlantic Bight between June 1974 and March 1977. These data were examined for the average conditions and seasonal cycles of water circulation and temperature and some statistical properties of their variation at higher frequency. The average flow is found to be toward the south-southwest at about 5 cm/s near the surface, diminishing to about 1 cm/s near the bottom. The occurrence of energetic wind-driven transient current events which can exceed a 2-month duration makes it impossible to determine a clear seasonal pattern in the sequence of monthly mean flows. There is, however, a clear seasonal pattern in the distribution of higher-frequency fluctuations. Storm wind-induced transient currents of 3- to 10-day duration appear prominently in winter records. Inertial currents appear selectively in the summer, that is, in parts of the water column well insulated from the bottom by a strong thermocline. For low-frequency motions (periods from 3 to 10 days) in both summer and winter records the preferred directions of motion throughout the water column appear to be consistent with equilibrium (mean) Ekman veering arguments. The water column response was found also to be most sensitive to the component of wind stress parallel to the bathymetry. The temperature follows a well-known seasonal cycle of heating and stratification. During the unstratified seasons, very little high-frequency temperature variation is observed, but during summer, thermal oscillations due to daily heating and inertial and semidaily tidal frequencies (3/3, 4/3, and 6/3 cpd) and a 5/3-cpd oscillation appear prominently.

INTRODUCTION

General Background

The Middle Atlantic Bight 'extends from Nantucket Shoals on the east narrowing to Cape Hatteras to the south' [*Bumpus*, 1973]. Studies of this shelf region trace back to before the turn of the century, when *Libbey* [1891] noted the transition from shelf water, or coastal water, to slope water, each type having distinct temperature and salinity characteristics. Only since 1973, however, have extensive direct current meter measurements become available to describe this shelf circulation. Prior to 1973, circulation studies were largely confined to temperature and salinity measurements, drift bottles, and seabed drifters.

Studies by *Bigelow* [1933] and *Bigelow and Sears* [1935] describe the seasonal variability of the shelf water mass: unstratified conditions prevail from November through March, when freshwater runoff and spring warming build stratification that reaches a maximum in August. *Bumpus* [1973] reviewed the historical development of the concepts of shelf circulation and described the surface and bottom shelf circulation as inferred from drift bottle and seabed drifter data. These studies indicated a generally southwestward flow of surface waters at speeds of 20 cm/s or less and a bottom drift of the order of 1–2 cm/s, generally toward the southwest but with great regional variation of direction. The belief was expressed that the near-bottom flow is onshore over the inner one half to two thirds of the shelf and offshore farther seaward. *Csanady* [1976] showed how the mean circulation could be partitioned into four components. These were defined as the water motions associated with an offshore wind stress, with an alongshore wind stress, with a longshore pressure gradient, which is a consequence of bottom friction acting on the downshelf transport of shelf water and was first suggested by *Stommel and Leetmaa* [1972], and with a cross-shelf density gradient. The latter is maintained by the supply of low-salinity shelf water from the Gulf of Maine and Georges Bank and the freshwater runoff into the shelf water. Each of these circulation components has annual and seasonal cycles that vary greatly. In particular, the wind stress is nonstationary, with spatial scales that range from 1 to 2 shelf widths (100–200 km) to the length of the Middle Atlantic Bight (700–800 km). Much of the wind energy above the seasonal frequencies ranges from the band associated with the passage of energetic weather fronts in the winter (3–10 days) to the diurnal sea breeze in the summer. The spatial scales of these weather systems also add to the variability of the shelf water circulation. Two specific examples are the large-scale northeasters in the winter that exert a longshore wind stress on the shelf, producing large downshelf (southwestward) motions [*Beardsley and Butman*, 1974] and the small, rapidly moving weak hurricane (Belle) that passed through the bight in the summer of 1976. It produced high-frequency shelf water oscillations that are now being analyzed (D. A. Mayer and H. O. Mofjeld, unpublished manuscript, 1979).

The most comprehensive description of currents over the Middle Atlantic shelf from direct measurements is that of *Beardsley et al.* [1976]. They combined data sets collected at varying times over a large area of the bight and, although the most apparent forcing (surface winds) is generally stronger in winter, found some evidence of more vigorous average circulation in summer. This result was stated as being highly tentative because of the time-space structure of the available data. In the course of the Marine Ecosystems Analysis project, (Mesa) initiated in the New York Bight by the National Oceanic and Atmospheric Administration (NOAA) in late 1973, it has been possible to collect current meter data from a common midshelf site over many months. These data are used here to describe the relatively long term behavior of the currents at a typical midshelf location. The primary goal was to describe the seasonal variation of 'circulation,' or relatively slowly varying components of flow, but these same data lend themselves to

This paper is not subject to U.S. copyright. Published in 1979 by the American Geophysical Union.

Paper number 8C1313.

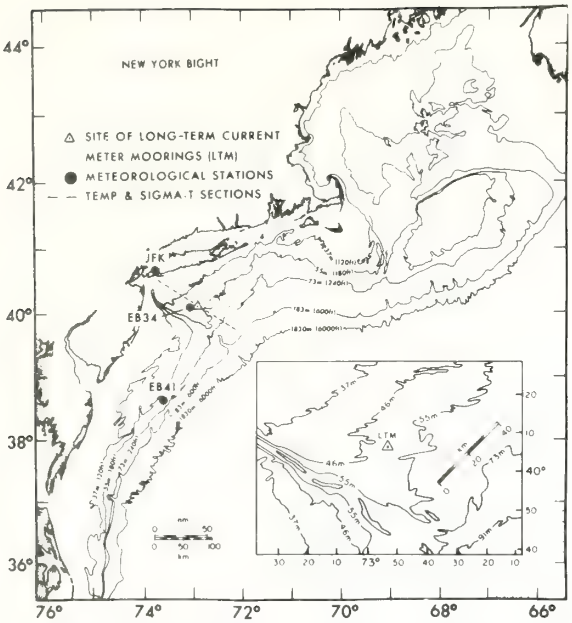

Fig. 1. Chart of study area showing location of the LTM site, the meteorological stations, and the cross-shelf hydrographic section.

analysis of the seasonal variation of higher-frequency fluctuations of currents and temperatures as well.

Physical Site and Bathymetry

Since September 1973, extensive sampling has been conducted in the New York Bight from Montauk Point to Cape May. Several moored current meter arrays were deployed inshore from the 100-m isobath. An attempt was made to maintain a single current meter mooring as consistently as possible at one location. This has resulted in more than 52,635 hours of current velocity and temperature data recorded at several depths on this site. Though there are many gaps in the records collected, the data analyzed here span a time from June 1974 through March 1977.

The long-term mooring (LTM) site shown in Figure 1 is in a midshelf region (nominal location 40°07′N, 72°54′W, in 47 m of water), approximately 24 km northeast of the Hudson Shelf Valley rim. All mooring installations were within 2 km of the nominal location except for a short record from the summer of 1974, which was in slightly deeper water 4.3 km east of the nominal location. From the best available charts (U.S. Department of Commerce bathymetric chart 0808N-54 (1967)) the bathymetry in the region can be characterized by large-scale (100 km) contours that run approximately parallel to 45° east of north and smaller features that fluctuate about the larger scales, approximately parallel to the shelf valley axis. Proximity to the Hudson Shelf Valley suggests that the location is less than ideal for the purpose of the present report. The mooring was installed here first to address questions associated with marine waste disposal, which made the most extensive records available at this site. We believe that its representativeness as an open shelf site is not seriously prejudiced by nearness to the shelf valley. This view is supported by a comparison between data at the LTM site and other current meter data obtained at a midshelf location directly upshelf (70 km) from the LTM site in 49 m of water (not shown on the chart). Data were obtained at the upshelf site for about 10 months during 1976 and at points quite close to the same depths as those from the LTM site (8 m and 28 m above the bottom). Upshelf current velocities for commensurate time periods were compared by computing 30-day means and cross spectra. The 30-day mean values at both locations agreed very well with each other. The coherence-squared values were excellent (greater than 0.75) for all frequencies where significant cross-spectral energy was present (from the 3- to 10-day band up to the semidaily tidal band). The coherence was particularly good for the velocities at 8 m above the bottom. Presentation of the specific analyses of longshore spatial coherence is the subject of another paper and is beyond the scope of this study.

Seasonal Characteristics of the Shelf Water Mass

From November through March the shelf waters are vertically unstratified. Temperature, salinity, and density all increase seaward during this season. Beginning in March with freshwater runoff and in April with vernal warming, stratification builds to a maximum in August. In October and November, autumnal winds and cooling break down the stratification, and the cycle is complete. Water column sampling cruises were conducted several times a year as a part of the Mesa field program. (See the water column chemistry cruise reports of *Hazelworth and Darnell* [1976], *Hazelworth et al.* [1977*a, b, c*], *Kolitz et al.* [1976*a, b*], and *Starr et al.* [1976, 1977].) Temperature T and density σ_t data for the shelf section in Figure 1 are in Figures 2*a*–2*d* for 1975 and in Figures 2*e*–2*h* for 1976. Beginning in February 1975 and ending in September 1976, these sections show how the stratification evolved during the 2 years when most of the current meter data were collected. The seasonally unstratified shelf water mass for both 1975 and 1976 is shown quite clearly in Figures 2*a* and 2*e*. Although Figure 2*a* shows February 1975 and Figure 2*e* shows April 1976, conditions appear to be quite similar except that the almost vertical isotherms have opposite slopes. This might be accounted for by the fact that the 1976 temperature contours are in April, when surface warming has begun. There is also a narrower region of dense water on the bottom in the vicinity of the LTM site in 1975 than there is in 1976. In February 1975 the density actually decreases before increasing again seaward of the LTM site. A significant and interesting aspect of the LTM site is that it is in the region of the midshelf minimum of bottom water temperature in summer, the so-called 'cold pool' or 'winter water' [*Ketchum and Corwin*, 1964]. The location of this water mass feature is evident in the temperature sections for the summer months of June and September for both years (Figures 2*b*, 2*c*, 2*g*, and 2*h*). A feature that distinguishes between the 2 years in the summer is that in 1975 the winter water appears to be colder and in a narrower band than the winter water in 1976, when it was warmer and extended across much of the shelf.

Temporal Variation of Wind Stress

Information on the surface winds associated with the current data is as important a part of the circumstantial background of the current data as are the bathymetry and hydrography. It has been shown by *Beardsley et al.* [1976] and numerous others that surface winds are one of the most important driving forces causing variations of flow over the continental shelf and conceivably have a profound effect even on the average flow. Annual and seasonal patterns of wind stress can be compared in progressive vector diagrams (PVD's) of stress and stick plots of stress (Figure 3) from 360 days of wind data which were obtained from Kennedy Airport (JFK) and 270 days (data unavailable from August 1976 to October 1976)

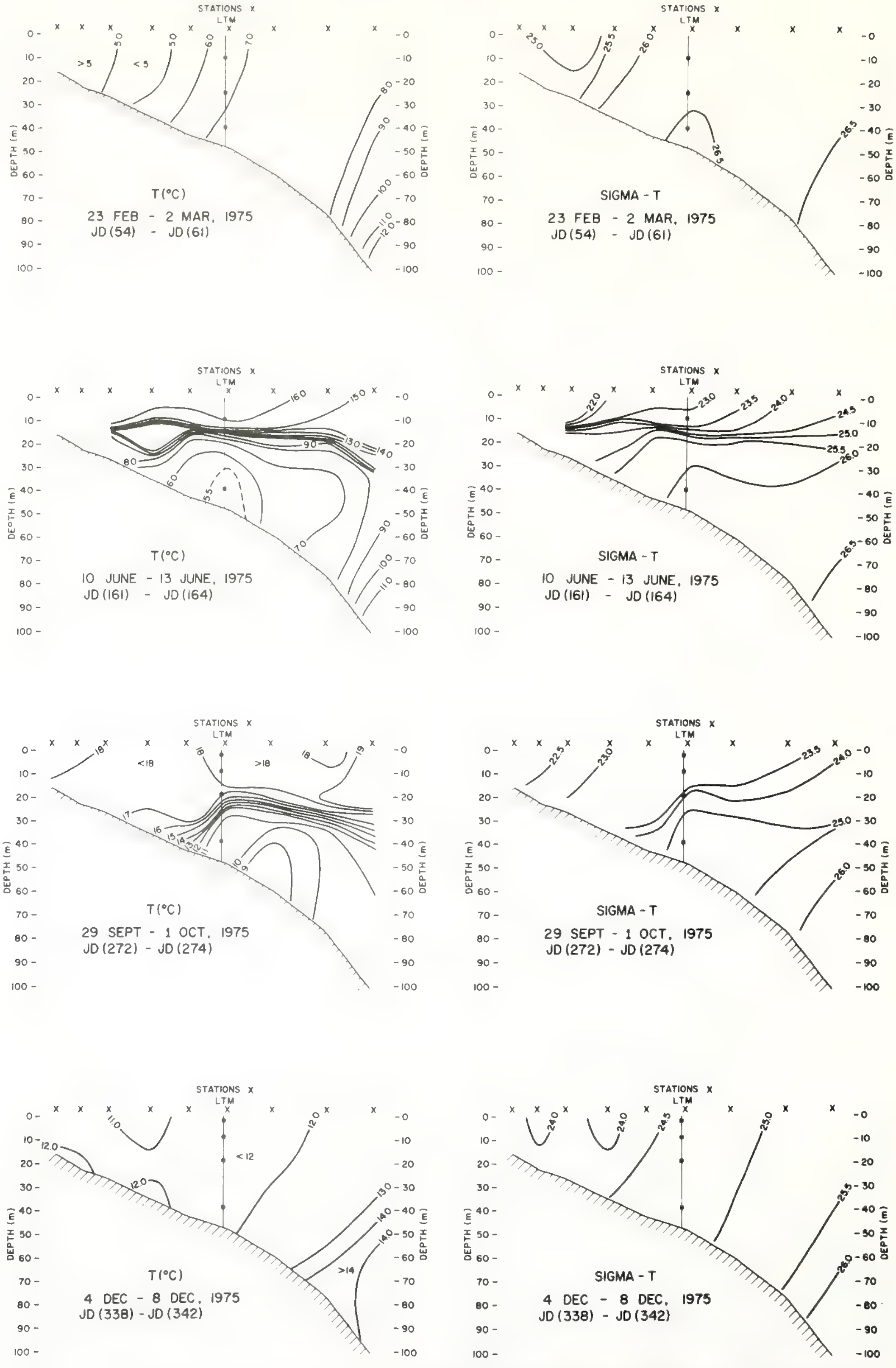

Figs. 2a–2d. *T* (degrees Celsius) and σ_t contours, eight panels from February through December 1975. Crosses denote station locations from which the data were contoured, and solid squares denote current meter locations. Julian days (JD) are also given below the dates on each panel.

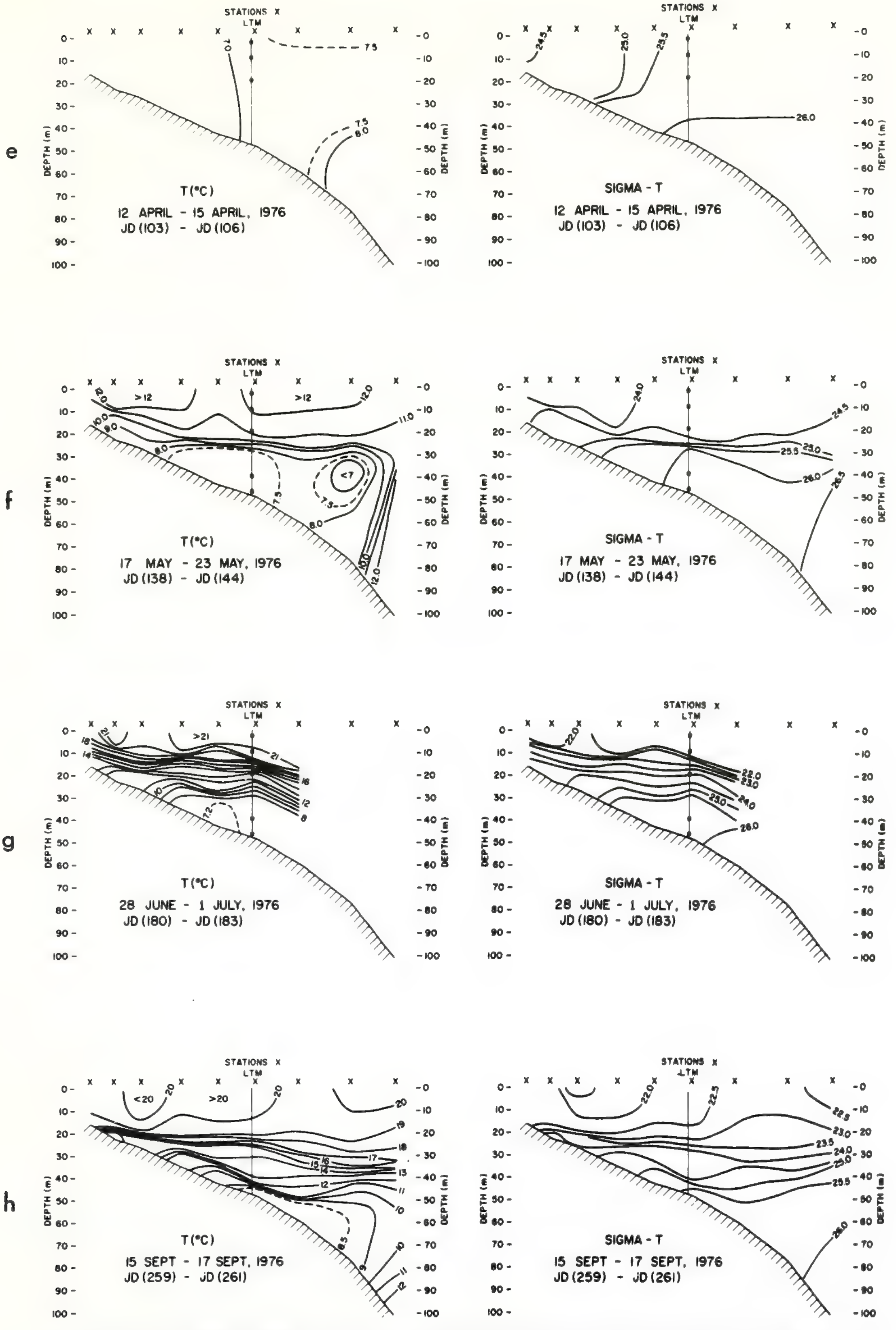

Figs. 2e–2h. T (degrees Celsius) and σ_t contours, eight panels from April through September 1976. Crosses denote station locations from which the data were contoured, and solid squares denote current meter locations. Julian days (JD) are also given below the dates on each panel.

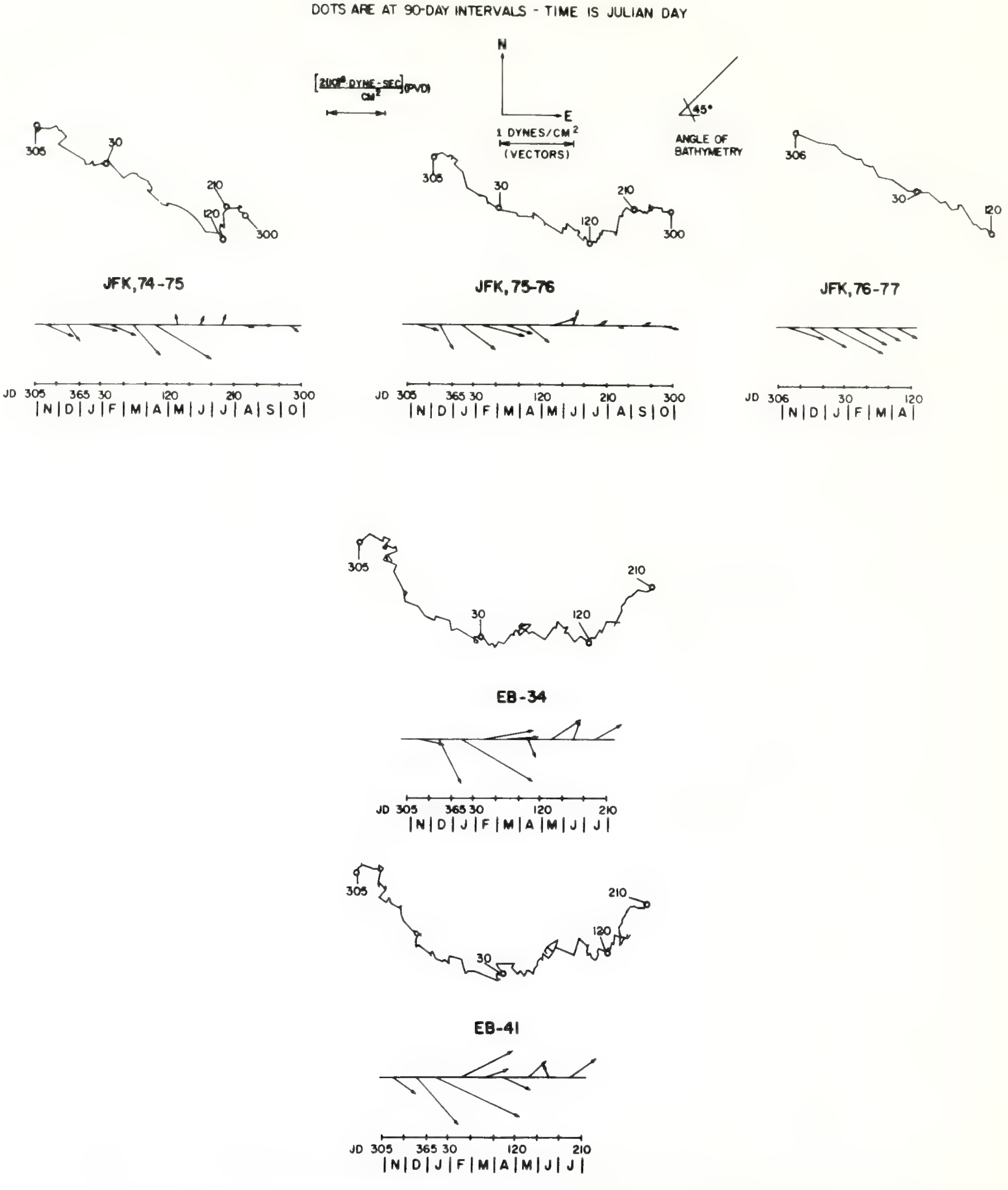

Fig. 3. Progressive vector diagrams and stick plots of wind stress. Stresses were computed according to *Wu* [1969].

from environmental buoys EB34 and EB41. Information pertaining to these stations is in Table 1. Upshelf and offshelf stress components were computed by rotating the coordinate system 45° clockwise so that the upshelf direction was aligned with the large-scale bathymetric contours. Energy spectra of these components were computed for three 90-day subsets of the data to demonstrate the importance of the higher-frequency (periods of 1 to several days) variations. These 90-day subsets correspond to the seasons from November to January (fall-winter), February to April (winter-spring), and May to July (spring-summer), respectively. Time series of wind stress were computed from

$$\tau_{N,(\mathrm{up})} = \rho_{\mathrm{air}} C_D |W| V \quad \mathrm{dyn/cm^2}$$
$$\tau_{E,(\mathrm{off})} = \rho_{\mathrm{AIR}} C_D |W| U \quad \mathrm{dyn/cm^2}$$

where U and V are east (offshelf) and north (upshelf) components of wind and $|W| = (U^2 + V^2)^{1/2}$. C_D was computed according to *Wu* [1969], that is

TABLE 1. Wind Station Information

Station	Position, deg	Sensor Distance Above Surface, m	Sampling Interval, h
JFK	40°39′N, 73°47′W	6	3
EB34	40°05′N, 72°58′W	5	1
EB41	38°42′N, 73°36′W	5	1

$$C_D = 5 \times 10^{-5} |W|^{1/2} \qquad |W| < 1500 \text{ cm/s}$$
$$C_D = 0.0026 \qquad |W| \geq 1500 \text{ cm/s}$$

where $|W|$ is in centimeters per second and $\rho_{AIR} = 1.2 \times 10^{-3}$ g/cm^3.

What is most apparent from the PVD's in Figure 3 is that maximum stress occurs in the winter and minimum stress occurs in the summer. In addition, the winter wind stress tends to be directed offshore, but in the summer it is directed more alongshore, toward the northeast. The stations over water also show a stress almost twice as great as that over land at JFK. *Saunders* [1977] reported that an offshore increase in stress was a dominant feature in the Middle Atlantic Bight and that it approximately doubled in going 200 km offshore. Although the EB buoys are only about 100 km from shore, stress values from Saunders' data are at least 50% greater at this distance in the winter and the spring. Data at EB34 were not available for the fall-winter season of 1976–1977, but data obtained from JFK during this season show a much higher stress directed more nearly upshelf than that during the previous 2 years. As will be shown, these stronger winds had a substantial influence on the circulation.

Wind stress spectra for each seasonal subset of 90 days were computed for upshelf and offshelf components (Figure 4).

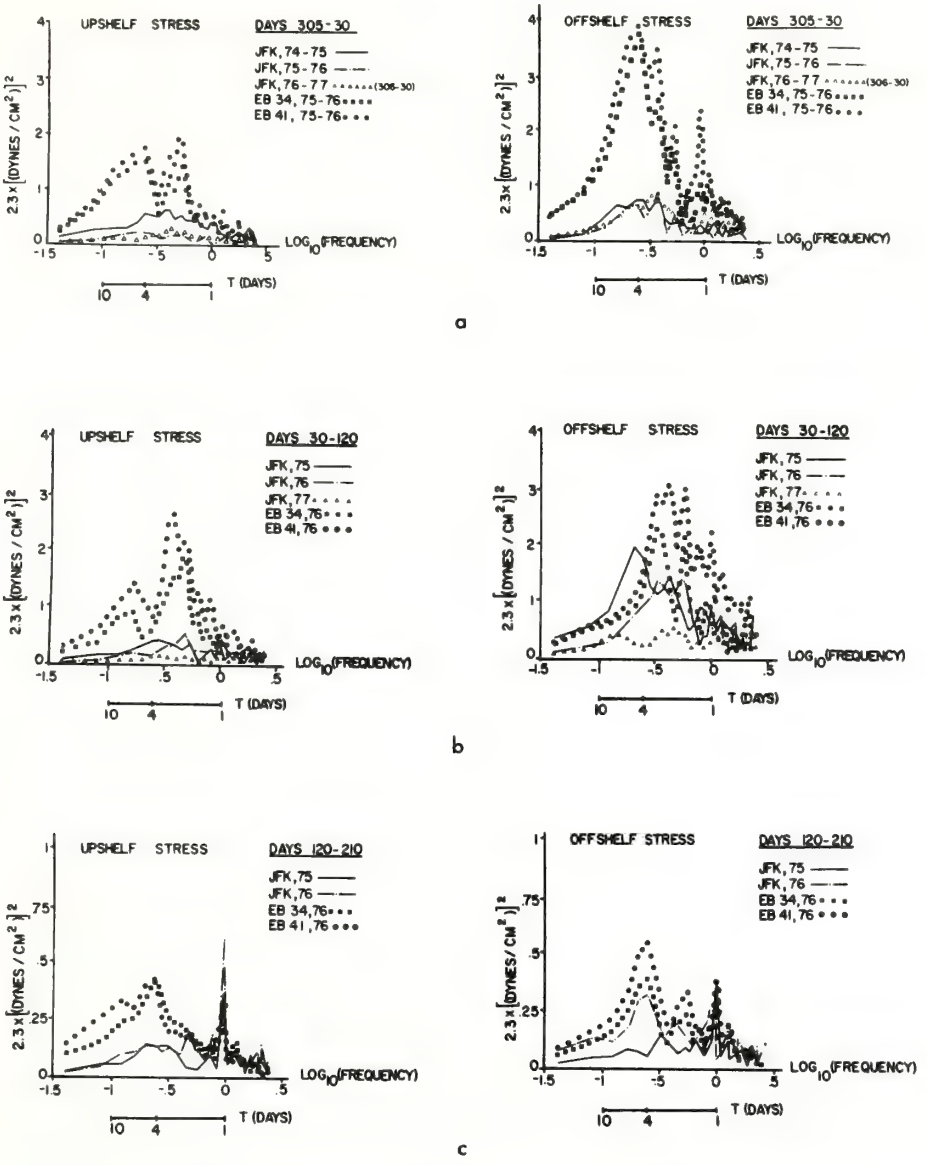

Fig. 4. (*a*) Wind stress spectra for the fall-winter season, November–January; (*b*) wind stress spectra for the winter-spring season, February–April; (*c*) wind stress spectra for the spring-summer season, May–July.

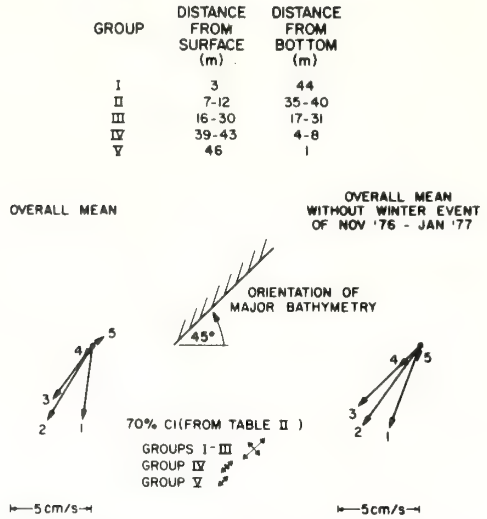

Fig. 5. (Left) Overall mean vectors from the five water column groups and (right) overall Mean vectors from the five water column groups without the winter event of 1976–1977.

Equal-area spectral plots are used for the wind data. Frequencies f are in $\log_{10}f$ units, amplitudes are $2.3(\tau)^2(f/\Delta f)$, and Δf is the resolution frequency. This transformation has the effect of spreading out the energy visually in the low frequencies, and most of the energy is low frequency except for the diurnal sea breeze in the summer. The low levels of energy in the summer are shown clearly in Figure 4*c*, as are the much higher energy levels for the stations over the water in all seasons. An interesting feature, and one that was not expected, is the high peak at the diurnal frequency for EB41 during the fall-winter season (Figure 4*a*). During this season in 1976 and 1977 the energy of the stress components at JFK was about the same as it was in the previous 2 years. As shown by the PVD, however, the mean stress was much greater. This is due to a period of strong and steady winds that increased the mean stress without effectively increasing the variance.

CURRENT METER MEASUREMENTS

Data Processing, Analysis, and Instrument Errors

More than 52,000 hours of current velocity and temperature data were collected at the LTM site. All of the current meter data obtained at this site from June 1974 through March 1977 were partitioned into five groups that consist of data from (group I) 3 m below the surface, (group II) 35–40 m above the bottom, (group III) 17–31 m above the bottom, (group IV) 4–8 m above the bottom, and (group V) 1 m above the bottom. The current meters were all Aanderaa RCM4's, and all except those in Group I were deployed on a taut wire subsurface mooring. The near-surface measurements, group I, were obtained with a spar buoy tethered to the subsurface float (B. J. Taylor, unpublished U.S. Department of Commerce Engineering Development Lab field use manual, 1975).

The spar buoy is essentially a wave follower and is decoupled from the subsurface float. Evidence that the spar buoy is effectively decoupled from the subsurface float is provided by L. Huff (manuscript in preparation, 1979), where data from two moorings, one with and one without the spar buoy, are not distinguishably different. The designers of the spar intended to minimize the effect of rectification of the rotor speed owing to the combined effects of mooring motion and wave orbital velocities. Some evidence that they were very successful is presented below. Further support is provided later for the discussions that follow, when velocity spectra are discussed.

Rotor rectification or pumping is achieved directly by surface gravity waves acting on those current meters near the surface and indirectly on those instruments below the influence of most of the surface gravity waves. The latter is accomplished by vibration and movement of the mooring cable induced by the motion of the subsurface float and was investigated by *Halpern and Pillsbury* [1976].

A comparison of the instrument errors of the RCM4 inherent in the taut wire spar buoy configuration with those of other current meter designs was investigated in an intercomparison experiment conducted in a shallow shelf region (30 m) off Long Island [*Beardsley et al.*, 1977]. Current direction measurements were generally excellent, but the speed errors discussed above were quite high for those instruments below the subsurface float and under the direct influence of surface gravity waves. This would affect the data obtained from groups II and III, with the errors as great as a factor of 2 throughout the speed range of the instrument [*Beardsley et al.*, 1977]. Hence the velocity data from these groups must be interpreted with caution. Data from groups IV and V, however, lie outside the region of direct influence by most of the surface gravity waves but are subjected to motion of the mooring cable nonetheless. *Halpern and Pillsbury* [1976] investigated this effect and found that the mean speeds of current meters at approximately the same depth as group IV could vary again by almost a factor of 2, depending on how close the subsurface float was to the

TABLE 2. Vector Velocity Data

Parameter	Group I	Group II	Group III	Group IV	Group V
			Overall Mean		
N	8,137	11,569	13,796	12,663	6,470
Speed, cm/s	4.5	5.4	3.9	0.9	0.8
Direction, deg	187	211	217	215	55
$u \pm \epsilon_u$, cm/s	-0.5 ± 0.5	-2.8 ± 0.5	-2.4 ± 0.5	-0.5 ± 0.2	0.6 ± 0.1
$v \pm \epsilon_v$, cm/s	-4.5 ± 1.0	-4.6 ± 1.0	-3.1 ± 1.0	-0.7 ± 0.5	0.4 ± 0.4
		Overall Mean Without Winter Event of November 1976–January 1977			
N	6,512	10,849	12,171	11,037	4,039
Speed, cm/s	5.2	5.9	4.7	1.6	0.7
Direction, deg	200	216	225	225	191
$u \pm \epsilon_u$, cm/s	-1.8 ± 0.5	-3.4 ± 0.5	-3.4 ± 0.5	-1.1 ± 0.2	-0.1 ± 0.1
$v \pm \epsilon_v$, cm/s	-4.9 ± 1.0	-4.8 ± 1.0	-3.3 ± 1.0	-1.1 ± 0.5	-0.7 ± 0.4

N is number of points. Parameters ϵ_v and ϵ_u define the 70% confidence limits for each component.

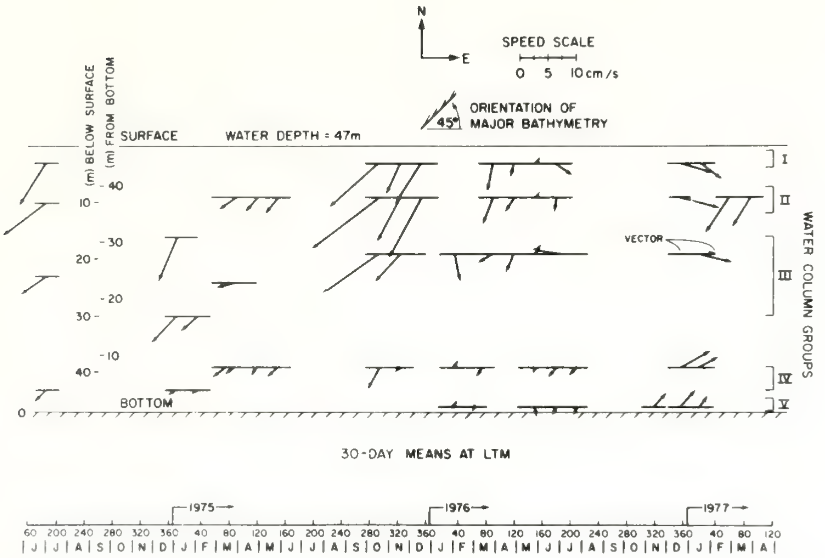

Fig. 6. Monthly mean vectors from June 1974 through March 1977. Horizontal lines indicate record lengths and are plotted at the proper depth. The five water column groups are also defined.

surface. They compared two moorings whose floats were 3 m and 18 m below the surface in about 50 m of water. The LTM subsurface float was usually about 8 m below the surface and had a net buoyancy close to 400 kg. We suggest that with such a stiff mooring and with the float at least 8 m below the surface the errors in the velocity data from groups IV and V are considerably less than those found by Halpern and Pillsbury.

Beardsley et al. [1977] found that the performance of the Aanderaa meters on the spar buoy was excellent in comparison to other current meters with superior sampling schemes for speeds above about 20 cm/s. Some rotor pumping was evident, however, for speeds below this level. At about 10 cm/s, rotor pumping accounted for about a 30% increase in speed. Cumulative frequency plots of speeds from most of the spar records show that between 34% and 43% of the hourly data exceed 20 cm/s except for one record in the late spring and early summer, where only 25% of the observations were greater than 20 cm/s. This is at a time of the year, however, when the problems of rotor pumping are nearing a minimum because of the low levels of wind stress energy. Thus the data obtained from group I, at this point, would seem to be closer to a description of what actually occurred than those from any of the other groups except perhaps for groups IV and V, in which measurements appear to be the least affected by mooring motion. Some additional evaluation will be presented in the discussion of velocity spectra.

Current meter sampling intervals were either 20 or 30 min. After careful editing, the raw data were smoothed with a 3-hour low-pass filter (6 dB down at 2.5 cph and 20 dB down at 2.0 cph), and then resampled hourly. Sufficient data are available to begin analyses of the monthly, seasonal, and annual variations. Standard spectral analysis cannot be used to resolve these low frequencies because no single current meter record is long enough. We have computed overall means for each group in the water column and 30-day averages of current velocity for annual, seasonal, and monthly comparisons. Owing to loss or failure of equipment we have no data at the site from mid-August through September in any of the years studied. Our ability to determine the annual mean and seasonal and monthly variations is therefore diminished, but the effort seems worthwhile nonetheless. Standard spectral analysis has been used to investigate current variation (periods of 3–10 days), normally associated with weather frontal systems, up to the daily, inertial, and semidaily tidal periods.

Overall Mean

Figure 5 (left) shows the resultant overall mean velocities for all current meter data at the site. Five sets of vectors correspond to the five current meter groups described previously. The most reliable estimates (in the sense of number of observations) for the mean velocities are those for groups II, III, and IV, where each estimate was computed from about 11,000 hours of observations. Groups I and V have a little more than 8,000 and 6,000 hours, respectively. The average velocity 1 m from the bottom shows the flow opposite to what is expected from previous work. In the winter of 1977 the water column velocities were dominated by a strong and steady upshelf (northeastward) flow for over 60 days, which biased the average of group V data because relatively few additional observations from this group were available. This event also distorted the mean current estimates of the other groups in that all components were directed more offshelf (seaward) than would have been the case otherwise. Without the event the overall means for groups III and IV are aligned with the large-scale bathymetry and are directed seaward for groups I and V (Figure 5 (right)). The sensitivity of the mean values to events such as occurred during the winter of 1977 demonstrates that even 250 days of current meter data are insufficient to define a stable mean flow. Table 2 contains the velocity data for each of the two sets of five vectors. The number of data points considered for each group is also given.

The uncertainty of the overall means can also be viewed in a more quantitative way. The standard error ϵ can be computed from $\epsilon = \sigma_{Lf}/(T/\tau_{cs})^{1/2}$ [*Bendat and Piersol,* 1966, p. 185], where σ_{Lf} is the low-frequency standard deviation, T is the length of the record in days, and τ_{cs} is the correlation time scale in days. The quantity T/τ_{cs} is the estimate of the number of independent observations in the time series $(v(t), u(t))$ if the time series is stationary and Gaussian. The probability statement can then be made that the velocity vector lies within the

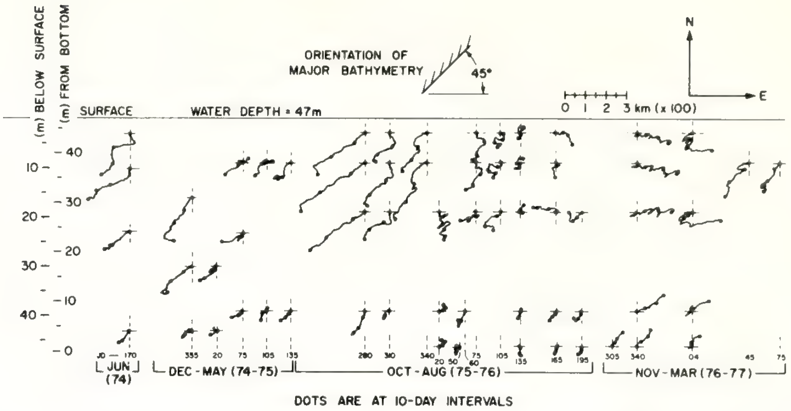

Fig. 7. Progressive vector diagrams (PVD's) corresponding to each of the monthly means. Crosshairs indicate the beginning of each PVD and are located at the correct depth for each record. The JD corresponding to the start of each PVD is indicated below each set of crosshairs.

limits $v \pm \epsilon_v$, $u \pm \epsilon_u$ about 70% of the time, where $\pm\epsilon$ is the confidence interval or error bars. These are also given in Table 2. The quantities σ_{Lf} and τ_{cs} were obtained by applying a 40-hour low-pass filter (6 dB down at 37 hours and 20 dB down at 30 hours) to the 3-hour low-passed data and computing the autocorrelation functions of the demeaned velocity components. Parameter τ_{cs} was estimated from the width of the autocorrelation peak and is about 3.5 days and 2.5 days for the upshelf and offshelf components, respectively. Table 2 summarizes the error bars for each of the velocity components. The error bars were determined with the number of points without the winter event and so are conservative estimates of the confidence intervals.

Annual, Seasonal, and Monthly Fluctuations

Annual, seasonal, and monthly variabilities were investigated by computing 30-day average current velocities for all data (Figure 6). What is most apparent here is that though the flow is mostly downshelf, events dominate the shelf water velocities, such that no well-defined seasonal cycle can be seen. There are three events, two in the winter and one in the summer, that demonstrate the different shelf water responses at different times of the year. For the two winter events, January 1976 and, more strongly, November 1976 through January 1977, there was upshelf flow in the bottom water, groups IV and V. In January 1976, data were not available from the upper part of the water column, but the middle water column data show an offshelf component of velocity and small upshelf velocities in the bottom water. From November 1976 through January 1977, however, much larger upshelf velocities in the bottom water are apparent. Data from groups I and III show large offshelf velocities for over 60 days. This event was probably caused by the large steady stress observed at JFK in the fall-winter season (Figure 3). The mean stress for the winter-spring season in 1977 was more like previous years, and the group II measurements from February to April 1977 show a return to strong downshelf flow. Data on summer currents are available for June and July 1974 and June and July 1976. For both years, downshelf flow in the bottom water was about 2 cm/s. For the upper and middle part of the water column, groups I–III, the velocities were quite different from year to year. In 1974, groups I–III show strong downshelf flows, but beginning in May 1976, there was a small reversal followed by a near-surface offshelf flow (group I), a veering shoreward

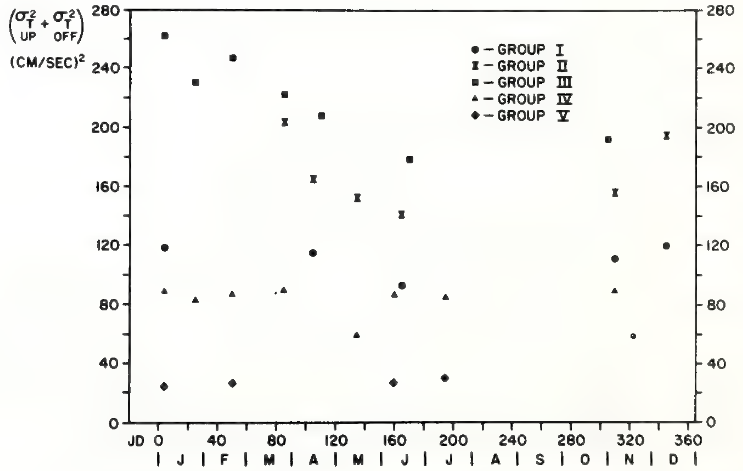

Fig. 8. Kinetic energy of the semidaily tides for both components of velocity as a function of time, computed from 30 60-day current meter records.

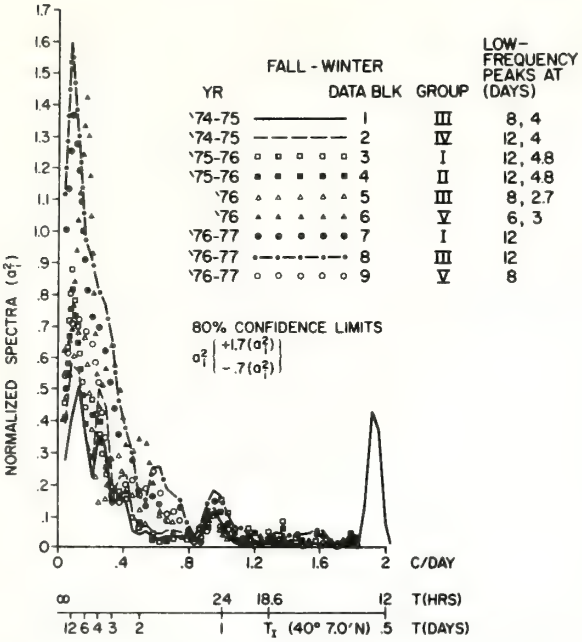

Fig. 9. Normalized spectra of the longshore velocity component in winter.

(group II), and a strong component of onshelf flow in the middle of the water column (group III). This event in 1976 was associated with the persistent upshelf wind stress during the spring-summer.

Representativeness of Monthly Means

The temporal structure of the currents composing the mean was investigated to determine how well monthly mean averages of current velocities represent low-frequency water motions. PVD's for each of the mean vectors in Figure 6 are shown in Figure 7. From these PVD's, qualitative comparison can be made as to the representativeness of the monthly means. Most of the mean vectors truly reflect the tendency of the slowly varying water motions. There are, however, a few exceptions. One of these is the mean vector beginning on January 4, 1977. Here the mean is greatly influenced by an event which occurred during the last 6 days of the 30-day record. One month is probably a minimum time scale for describing low-frequency water motions because energetic higher-frequency events still add some instability to the monthly means, particularly in the winter.

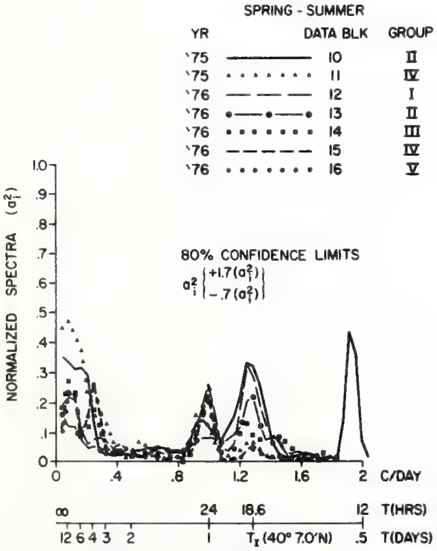

Fig. 10. Normalized spectra of the longshore velocity component in summer.

Spectral Analysis of Current Velocities

Current variations of higher frequency, beginning with the 3- to 10-day period associated with the passage of winter storms and including the daily and semidaily tidal bands, were analyzed with standard spectral analysis techniques. Spectral analyses were applied to 30 60-day subsets of current meter data from which nine records from the fall-winter and seven records from the spring-summer seasons were chosen to represent all the groups in the water column, from the surface to the bottom.

Surface wind waves, swell, and mooring motions cause the Aanderaa current meters, especially at the levels of groups II and III, to register excessively large current speeds under the weather conditions frequently encountered in winter. The result is that the current spectra are 'pumped up' over a broad band of frequencies, making comparison of spectra at different times and levels quantitatively meaningless. The energy level

TABLE 3. Upshelf Velocity Component

Block	Group	Start Times of 60-Day Subsets*	σ_T^2	σ_{49}^2	σ_T^2/σ_{49}^2
		Fall-Winter			
1	III	Dec. 21, 1974 JD 355	45.9	226.6	0.20
2	IV	Dec. 21, 1974 JD 355	15.2	90.0	0.17
3	I	Nov. 11, 1975 JD 315	23.5	157.3	0.15
4	II	Nov. 11, 1975 JD 315	44.8	278.9	0.16
5	III	Jan. 20, 1976 JD 20	57.7	359.5	0.16
6	V	Jan. 20, 1976 JD 20	6.2	64.7	0.10
7	I	Dec. 5, 1976 JD 340	20.3	221.3	0.09
8	III	Dec. 5, 1976 JD 340	42.8	569.3	0.08
9	V	Dec. 5, 1976 JD 340	7.2	54.4	0.13
		Spring-Summer			
10	II	April 15, 1975 JD 105	37.4	210.5	0.18
11	IV	April 15, 1975 JD 105	8.8	40.3	0.22
12	I	May 14, 1976 JD 135	22.2	107.4	0.21
13	II	May 14, 1976 JD 135	39.9	145.4	0.27
14	III	May 19, 1976 JD 140	42.3	168.6	0.25
15	IV	May 9, 1976 JD 130	13.8	48.6	0.28
16	V	May 9, 1976 JD 130	7.9	27.2	0.29

The average σ_T^2/σ_{49}^2 = 0.14 for winter and 0.24 for summer.
* Times are GMT.

of the strong semidaily tidal band varies by a factor of 2 over the seasons, being higher in winter, providing a quantitative measure of this effect. Ideally, one would wish to correct these spectra by means of an appropriate transfer function. The transfer functions are, of course, not known. Instead, we have attempted to transform the spectra to a common basis for more convenient semiquantitative discussion through normalizing each spectral estimate by the spectra associated with the semidaily tidal band. Spectral estimates were computed for a total of 49 frequencies, with a resolution frequency of 0.0417 cpd. The 49th frequency is 2.04 cpd. With a Tukey (cosine) lag window, 13.3 degrees of freedom were obtained. The semidaily tidal energy was spread over four frequencies from 1.8 to 2.0 cpd and was well within the noise level outside of these frequencies. These were summed and used to normalize the other estimates a_i^2, where

$$a_i^2 = (A_i^2/2)/(\sigma_T^2)$$

in which a_i is the normalized amplitude and A_i is the amplitude of each spectral component. The term σ_T^2 is defined as

$$\sigma_T^2 = \sum_{i=45}^{48} \frac{A_i^2}{2}$$

and is that part of the total variance accounted for by the semidaily band.

At this point in our discussion it is appropriate to complete our discussion of instrument errors now that σ_T^2 has been defined. The seasonal dependence of the semidaily tidal energy, which provides a semiquantitative measure of current meter rotor pumping, is best analyzed by plotting the total tidal energy in the semidiurnal band as a function of time. By total we mean the sum of σ_T^2 for both upshelf and offshelf velocity components. This was done for all 30 60-day records representing all five groups, plotted in Figure 8. It is quite clear that the energy from groups I, IV, and V is almost independent of the seasons. Energy from group I shows a small decrease of about 22% in the summer, with that from groups IV and V virtually independent of time. From groups II and III, however, the energy varies by about a factor of 2 during the year, with a clearly defined minimum in the summer. Thus credence is lent to our earlier arguments that measurements from groups I, IV, and V are of good quality.

Upshelf velocity spectra for 16 60-day records, nine in the fall-winter and seven in the spring-summer, are plotted in Figures 9 and 10, respectively. The normalizing quantity σ_T^2 for the upshelf velocity, the variance σ_{49}^2, and the ratio σ_T^2/σ_{49}^2 are tabulated for the 16 60-day records analyzed in Table 3. Hence σ_{49}^2 is defined as the sum of all the spectral lines $A_i^2/2$ for all 49 frequencies of the upshelf velocity spectra.

Because of the poor resolution in the low frequencies, those periods corresponding to the low-frequency peaks are given in Figure 9 for the fall-winter season. The intent here, however, is not to study the detailed low-frequency structure of the upshelf velocity but only those features in each frequency band that are seasonally dependent. Spectra were plotted only for the upshelf components because most of the low-frequency energy is along the shelf. Spectra for the offshelf components contain mostly semidaily tidal energy. Two features distinguish between the winter and summer spectral representations of upshelf current velocity. There is considerably more energy in the lower frequencies in the winter, and there is a pronounced band of energy around the inertial frequency in the summer. The former is attributable to the much greater storm energy supplied to the water column in the winter.

It should be pointed out that the variability in the low-frequency band from year to year seems to be real and is not an artifact of the normalization. Compare, for example, the spectra from data blocks 1 and 8, both from group III. The normalizing quantity σ_T^2 from Table 3 is about the same for each, so the large differences in their low-frequency energy appear to be real. Other examples are data blocks 6 and 9 from group V, where again σ_T^2 is about the same for each, giving further credence to the idea that the low-frequency differences in energy levels are real. To account for these differences, however, is another problem which should really be addressed only after careful studies of coherence between local winds and current velocities are completed. It is tempting, though, to compare qualitatively the wind stress spectra in Figure 4 with the upshelf velocity spectra in Figure 9. If local winds are responsible for the much greater energy in data block 8 in comparison to block 1, one might suspect that the longshore wind stress energy, for the same season in 1976–1977, Figure 4*a*, would be correspondingly larger than the energy in 1974–1975. That this is not the case is quite clear. The point here is that there seems to be a great deal of low-frequency variability in the upshelf current velocity that cannot be accounted for by local forcing.

In the summer, inertial energy is stratified such that in the bottom water (groups IV and V) the inertial band is almost in the noise level, whereas it is a maximum for groups I and II. Again, because of spectral smoothing, the inertial energy, like the semidaily tidal energy, is spread over four frequencies from 1.2 to over 1.3 cpd, or from the 29th to the 32nd spectral component, where the local inertial frequency is 1.28 cpd. There may also be another reason for the spreading of energy over frequencies below the local inertial frequency. There is evidence from recent studies (D. A. Mayer and H. O. Mofjeld, unpublished manuscript, 1979) that a considerable amount of subinertial motion can be generated by strong, rapidly moving wind systems. To be specific, hurricane Belle passed through the Middle Atlantic Bight in August 1976 and generated subinertial motions on the outer shelf (70 m of water) that dominated the currents for several days after the passage of the storm. The periods of the motions were analyzed and were found to be above the local inertial period by about 0.2 hours. Studies are presently directed toward interpreting these motions dynamically.

A possible explanation for the seasonal and depth distribution of inertial energy is that except in parts of the water column that are isolated from the bottom by a pycnocline of sufficient strength, such as occurs only in the upper waters during summer, inertial motion is frictionally dissipated too rapidly to register above the adjacent continuum.

Coherence and Phase Between Upshelf (v) and Offshelf (u) Velocity Components

Cross spectra between v and u were computed with the same resolution frequency, lag window, and degrees of freedom that were used in computing the normalized auto spectra of the upshelf velocity. The computations were performed on all 16 records in Table 3 and several other 60-day subsets as well.

Low-frequency motions can be analyzed by computing the ellipse suggested by the cross spectra of v and u. A velocity ellipse is defined on the hodograph for each frequency when the amplitudes for $v(A_v)$ and $u(A_u)$ and the relative phase ϕ between them are specified. The amplitudes of the velocity

TABLE 4. Low-Frequency Content

Group	Start Time of 60-Day Subset	Period, days	γ^2	Semimajor Axis, cm/s	Semiminor Axis, cm/s	Thickness Ratio	Angle of Major Axis Clockwise Positive From v (Upshelf)
I	Nov. 11, 1975	4.8	0.40	9.4	1.0	9.4	34
III	Jan. 20, 1976	6	0.78	15.5	0.5	31.0	26
IV	Jan. 20, 1976	3	0.61	7.4	3.2	2.3	3
V	Jan. 20, 1976	3	0.61	5.0	1.8	2.8	−25
V	Jan. 20, 1976	6	0.55	6.9	1.2	5.8	−20
I	May 14, 1976	4	0.63	5.9	0.4	14.8	59
IV	May 9, 1976	4	0.93	4.3	1.0	4.3	−20
V	May 9, 1976	4	0.92	3.2	0.7	4.6	−23

components were obtained from their auto spectra, and the phase was obtained directly from the cross-phase spectrum. Because of spectral smoothing, the energy at each frequency is spread over the adjacent spectral lines; hence estimates of the amplitudes A_v and A_u were obtained by adding three spectral lines together with the center line at the selected frequency. Eight 60-day records were diagnosed for their low-frequency content, five for the fall-winter and three for the spring-summer. The results are in Table 4, where the important features of each ellipse are summarized. These are the size of the semimajor and semiminor axes and the orientation of the major axis with respect to our bathymetrically oriented coordinate system. Only frequencies with identifiable cross-spectral peaks where the coherence squared (γ^2) values were at or above the 95% significance level (0.4) were diagnosed. The periods range from 3 to 6 days. The sense of rotation is clockwise for all but the record from November 1975, where the thickness ratio of the principal axes is 9.4/1, a ratio large enough so that a small uncertainty in the relative phase between v and u could produce rotation in either direction. There are two features that we wish to emphasize here: the orientation of the major axis and the thickness ratio.

The five records from the fall-winter show that in the top half of the water column (groups I–III), thickness ratios are quite large (thin ellipse) with the preferred directions of the major axis varying from 26° to 34° clockwise. This means that v and u are positively correlated with, at most, a small relative phase angle between them. Hence offshelf flow is positively correlated with upshelf flow, and conversely, which is consistent with Ekman veering in the upper part of the water column, resulting from a longshore wind stress.

In the bottom half of the water column, however, the thickness ratios are much smaller, and the preferred directions vary from 3° to −25°. For group IV the major axis is directed essentially upshelf, and for group V, for two frequencies, it varies from 20° to 25° anticlockwise. Thus near the bottom, v and u are negatively correlated such that $-u$ (onshore) leads v (upshelf) by, at most, 90° (one quarter of the period). Of course, the thinner the ellipse, the more rapidly the motions approach the preferred direction of the major axis. Thus motions near the bottom appear to be consistent with a bottom Ekman layer in that for upshelf motion, there is a shoreward component, and conversely.

The three records from the spring-summer show much the same structure except that coherence levels are generally higher, and for group IV, just as in group V, the same sort of onshelf veering of the major axis is manifest. In the summer both groups IV and V are below the bottom of the thermocline (Figures 2*f* and 2*g*), so we might suspect a veering toward shore of the major axis for group IV, although in the winter this is not the case.

Those important features of low-frequency motions in the band from 3 to 6 days have thus been shown to fall roughly into two categories, one where v and u are positively correlated in the upper part of the water column and one where v and u are negatively correlated in the lower part of the water column. These diagnosed motions are consistent with two of the four flow components identified by *Csanady* [1976] and supported

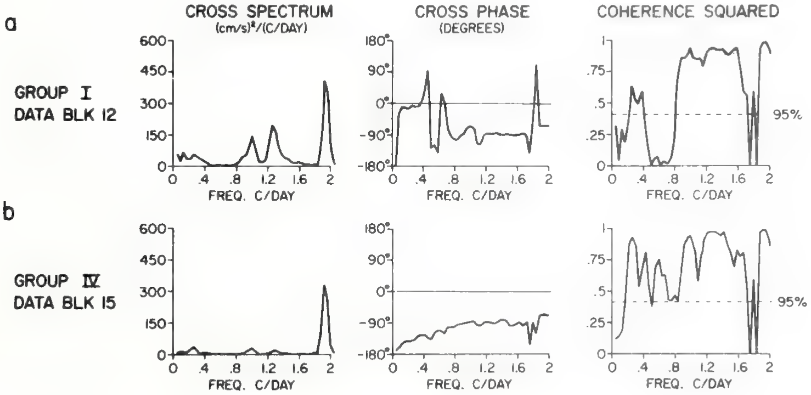

Fig. 11. Cross spectra between velocity components (v (upshelf) and u (offshelf)) for (*a*) group I and (*b*) group IV current meter data in the summer.

by the physical arguments of *Scott and Csanady* [1976], though they were concerned mostly with time-averaged velocities which were in agreement with classical steady state Ekman models. The two components are the longshore pressure gradient and the longshore wind stress, where the latter can explain the diagnosed low-frequency motions in the upper part of the water column but both can contribute to the Ekman veering in water near the bottom. It appears that the kinematics of the low-frequency motions are consistent with the simple Ekman models. The major difference is in the relative phase between v and u, where ϕ is something other than the 0° or 180° (no lag, hence steady state) required by the simple Ekman models.

Two 60-day records from the spring-summer were selected for Figure 11, in which cross spectrum, cross phase, and coherence squared are shown. The records are from block 12 in group I and block 15 in group IV and are the same records whose low-frequency analyses appear in Table 4 for the spring-summer. These records were chosen because coherence levels were generally lower in the winter in the low frequencies ($\simeq$ 0.2–0.4 cpd) and the energy in the inertial band (1.3–1.4 cpd) was not significant. The remaining frequency bands where both energy and coherence levels were high are the daily tides (0.9–1.1 cpd) and the semidaily tides (1.8–2.0 cpd). For the two selected 60-day records the cross-spectral energy levels are above the noise level and the coherence squared values are substantially above the 95% significance levels only in the above four frequency bands. For group I in the frequency range between 0.2 and 0.4 cpd the relative phase between v and u is quite close to zero, indicating that upshelf motion v is associated with offshelf flow u, and conversely. This is consistent with our earlier discussion of motion in the upper part of the water column. The cross phase of group IV, however, shows a linear relationship to the frequency up to the daily band. A linear phase dependence on frequency implies that v and u are related by a simple time shift, and in this case, negative u leads v. This is also consistent with the explanation of water motions near the bottom. The magnitude of the shift (τ) is proportional to the change of phase at maximum coherence with frequency. This lead is approximately $\tau(\text{hours}) = (24/360)(\partial\phi/\partial f)$, where f is the frequency in cycles per day and ϕ is the phase at maximum coherence. Use of the phase relationship in Figure 11*b* indicates a lead of about 5 hours for all of the low frequencies. It thus appears that at least for the water near the bottom a portion of the low-frequency response is independent of the forcing frequency. It is independent in the sense that regardless of frequency, upshelf flow lags onshelf flow by about 5 hours. An interpretation follows. An up (down) shelf motion in the bottom water is preceded by about 5 hours by an onshelf (offshelf) motion. This suggests that an offshore Ekman transport of near-surface water establishes a pressure gradient which drives an immediate onshore flow elsewhere in the water column until a quasi-geostrophic adjustment to the upshelf flow occurs about 5 hours later (about one quarter of the inertial period).

For the remaining frequency bands no important differences between groups I and IV are evident except that the inertial band in group IV is almost in the noise level. The daily tides and the inertial band have coherencies that are quite close to unity and relative phases of approximately −90°. A relative phase Φ in the range $-180° < \Phi < 0°$ implies that the velocity ellipses associated with each of these bands rotate in a clockwise sense, and the magnitude of 90° implies that a hodograph plot of each frequency would be close to circular, or the major or minor axis of each ellipse is aligned with our bathymetrically oriented coordinate system.

It turns out that the inertial motions are very nearly circular in the upper part of the water column. Cross spectra between v and u for data block 12 (Figure 11*a*) showed that the amplitudes of the velocity components are A_v = 6.6 cm/s and A_u = 7.2 cm/s for v and u, respectively, with a relative phase of −86°. The amplitude of each component was estimated by adding up the four spectral lines over which the inertial energy was spread. The variance of the inertial band for each component is 22.0 and 25.8 $(\text{cm/s})^2$ for v and u, respectively. The relative phase of −86° is very near −90°, and with the amplitudes about the same magnitude we know that the motions are almost circular.

The semidaily tidal band has coherencies very close to unity but, from Figure 11, the phase angles lie between −50° and −70°. This implies that the major or minor axes of the semidaily tidal ellipses are not aligned with the major bathymetry.

Tidal Analysis for the M_2 Constituent

Four 60-day subsets representing groups I and IV were analyzed for the M_2 tidal constituent. A modified Munk-Cartwright tidal response analysis that utilized one complex weight was used [*Munk and Cartwright,* 1966]. The reference series consisted of the tidal height at Sandy Hook, New Jersey, and was computed from 12 harmonic constants that were analyzed from 1 year of actual tidal height data. The results of each velocity ellipse analysis are summarized in Table 5 and plotted in Figure 12. Groups I and IV were selected, since these represent data of the best quality except perhaps in a region well within the bottom frictional boundary layer.

It is now possible, with good quality data, to set an upper bound on the amount of kinetic energy in the water column as represented by the M_2 tide, which by itself accounts for about 80% of the total kinetic energy of the semidaily tides. This was computed by dividing the variance of the M_2 signal by the variance of the prediction using 12 constituents. We suggest

TABLE 5. Characteristics of M_2 Tidal Constituent

Group	Start Time of 60-Day Subset	Semimajor Axis, cm/s	Semiminor Axis, cm/s	Thickness Ratio	Angle of Major Axis Clockwise Positive From v (Upshelf)	Absolute Phase,* deg	Total Variance $\frac{1}{2}(A_v^2 + A_u^2)$
I	May 14, 1976	11.3	5.0	2.26	71.6	5.9	75.9
I	Dec. 5, 1976	13.3	5.4	2.45	79.6	9.0	103.5
IV	May 9, 1976	11.1	4.2	2.65	78.2	39.8	70.1
IV	Dec. 5, 1976	11.9	3.7	3.25	79.6	8.2	77.5

*Absolute phase is the angle that the velocity vector (tagged by a zero in Figure 12) makes with the coordinate system at a time that coincides with the passage of the moon over the Greenwich Meridian.

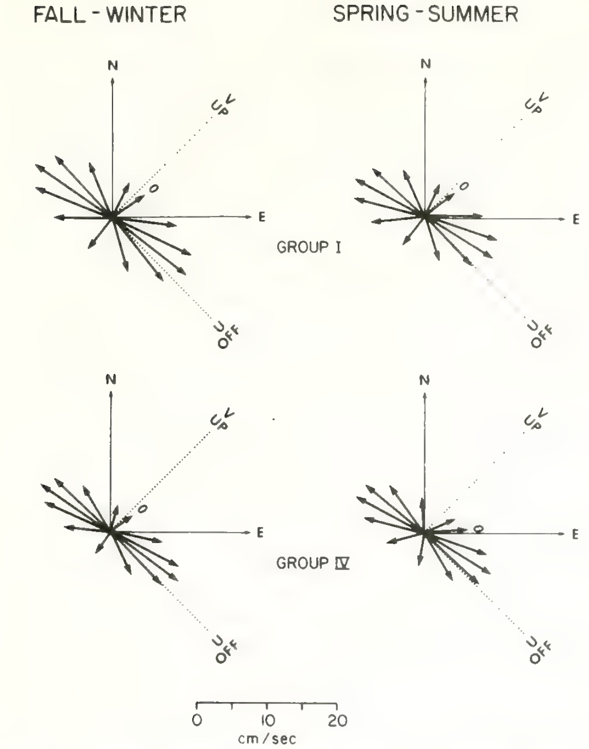

Fig. 12. M_2 tidal ellipses from groups I and IV for both fall-winter and spring-summer seasons.

that the kinetic energy of the M_2 constituent has an upper bound near 75 $(cm/s)^2$. The variance from Table 5 is a maximum in December for group I and is 32% above the lowest variance in group IV during the spring-summer season. This is roughly in agreement with the plots of total tidal variance computed from the velocity spectra and plotted in Figure 8 and again reflects the effects of surface gravity waves on the current meter measurements.

The other characteristics of the M_2 constituent of tidal current from groups I and IV is that the major axis is directed almost offshelf. The ellipses in group IV are somewhat thinner than those in group I and suggest that the frictional bottom boundary layer might have some influence on measurements obtained in the lowest 8 m of the water column. All the absolute phases are very close together except for group IV in May, where the starting angle leads group I by about 30°, or, in terms of time, about half an hour, since we are near the minor axis. This is consistent with the effects of friction [*Sverdrup et al.*, 1942, p. 577] on tidal ellipses as well as with the fact that for this same record the major axis is oriented 6° more clockwise than for group I, which is also consistent with the effects of friction. However, it must be pointed out that an error of as little as half an hour in the starting time of the current meter records could account for this difference in absolute phase. Thus it is uncertain whether the records from group IV in May are influenced more by friction than are those from group IV in December.

Cross Spectra Between Upshelf Wind Stress at EB34 and Velocity Components

To investigate further the different low-frequency responses associated with the upper and lower portions of the water column, cross spectra between upshelf wind stress τ_{up} and velocity components v (upshelf) and u (offshelf) were computed. Sixty-day subsets corresponding to data blocks 3, 6, 12, and 15 in Table 3 were used. These represent groups I and V for the fall-winter season in Figure 13 (left) and groups I and IV for the spring-summer season in Figure 13 (right). Although response to offshelf stress was also examined, only upshelf stress resulted in reasonably high coherence values coupled with distinct cross-spectral peaks.

For group I in the fall-winter the phase at maximum coherence between τ and v is essentially constant and near zero from 4 to 12 days. Parameter τ_{up} leads v by about 4 hours at 4.8 days. It is not shown in the figure, but near-zero phases were also obtained with the u component, although with coherence values somewhat lower. In the lower part of the water column, group V, the phases of u for the same range of low frequencies are quite close to −180°, which demonstrates again the onshore response to upshelf wind stress in water near the bottom. The response of the upshelf velocity, which is not shown for group V, behaves very much like that in group I, such that at 6 days the upshelf v lags τ_{up} by about 7 hours. The same sort of behavior is seen in Figure 13 (right) for the spring-summer season, with essentially zero phase for v in group I at 4 days and about a 4-hour lag for v in group IV, also at 4 days. Again, for the same group the onshore response is reflected in the phase of u which is near −180° at 4 days. Almost identical results were obtained for u in group V.

In summary, the principal difference between the seasons is that the onshore response to upshelf wind stress in the winter seems to be confined to water closer to the bottom than it is in the summer. Good coherence values for group IV in the winter for the u component were not obtained for any of the fall-winter records; hence only group V is shown in Figure 13 (left). This result is also reflected in the data of Table 4, where the major axis of group IV in the winter is aligned with the bathymetry. In the summer, however, both groups IV and V show almost identical onshelf flows associated with upshelf stress. The data in Table 4 for the summer also show this.

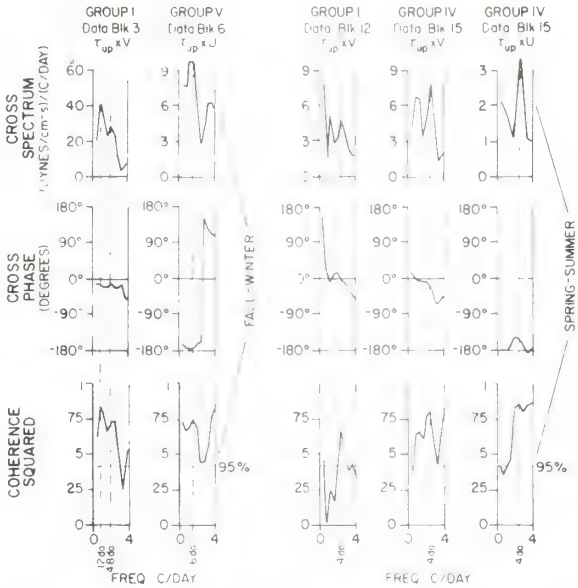

Fig. 13. (Left) Fall-winter and (right) spring-summer cross spectra between upshelf wind stress (τ_{up}) and velocity components (v (upshelf) and u (offshelf)) for groups I, IV, and V.

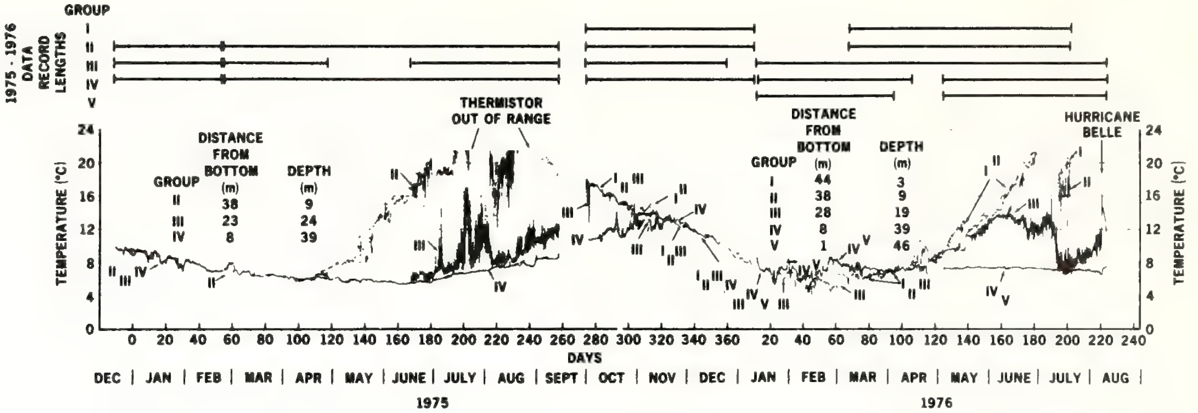

Fig. 14. Temperature composite at the LTM site showing the temperature fluctuations from November 1975 through August 1976.

3. TEMPERATURE DATA

Low-Frequency Fluctuations of Temperature

A composite of most of the temperature data collected at the LTM site is shown in Figure 14. The annual cycle, the establishment and breakdown of thermal stratification, is most apparent. Temperature data from November through March 1977 are available but are not shown in the figure for reasons of clarity. From November through January there is an almost constant rate of cooling of the water column. Toward the end of February, during both 1975 and 1976, there is an inversion of the usual vertical temperature gradient, and in 1977 the inversion occurred sporadically throughout January. This temperature inversion is stronger during 1976 and 1977 than during 1975. In the latter part of February 1976 the upper part of the water column was almost 4° colder than the bottom water, and for this same time of year in 1977 the upper water column reached its minimum temperature of about 2° or at least 4° colder than the two previous years (1975 and 1976). The water column presumably was stabilized against convective mixing during this time by low salinity occurring in the surface waters because of early spring river discharges. A similar circumstance of temperature inversion stabilized by salinity stratification has been reported for other parts of the New York Bight during this time by *Hazelworth and Cummings* [1979]. *Armstrong* [1979] documents the unusually early and large discharge from the Hudson River during 1976. It is interesting also that the minimum water column temperature in both 1976 and 1977 occurred in February, but in 1975 it occurred in June.

Another kind of event where stratification neared its maximum occurred in late July 1975 and during the first two weeks of July 1976. The temperature of the upper part of the water column decreased by 6° or more in only a few days, while the bottom water temperature remained unchanged. The bottom water (groups IV and V) is isothermal during all parts of the year for which data are available.

The effects of hurricane Belle, a rapidly moving and weak hurricane, appear near the end of the temperature records in August 1976. The temperature of the middle water column increased by about 6° after the passage of the storm, while the bottom water temperature changed but little. Probably, the upper part of the thermocline was mixed into the surface-mixed layer, increasing the midwater temperatures (group III) and decreasing the near-surface temperature (group I).

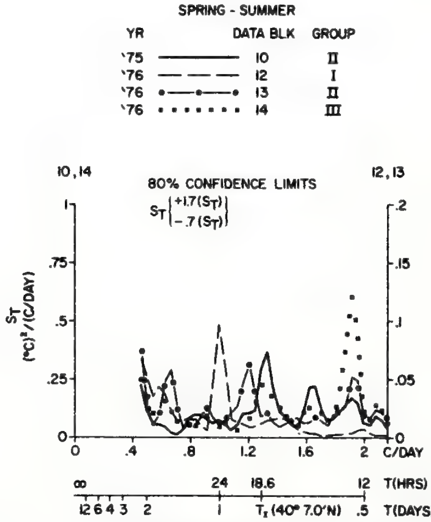

Fig. 15. Summer temperature spectra from groups I-III.

Spectral Analysis of Temperature Records

The higher-frequency temperature fluctuations were subjected to spectral analysis. The data were detrended to remove the high energy associated with the lower frequencies (periods greater than 3 days). Still, the first few spectral estimates were inconveniently large to plot. Of all the records analyzed, only those from the stratified periods contain features of significant interest (Figure 15). Two scales are used because the spectra were not normalized and the amount of energy, or variance, depends on the strength of stratification. The four records in Figure 15 are from groups I, II, and III, the upper part of the water column, and are from the records in which the current energy in the inertial band was a maximum (Figure 10). Near-surface temperature spectra for group I show a peak only at the diurnal frequency. This is probably due to diurnal heating and indicates a diurnal heating amplitude of 0.09°C at 3-m depth. Groups II and III show significant energy in the inertial and semidaily tidal bands (4/3 and 6/3 cpd). There is also an energy peak at 5/3 cpd, between the inertial and the tidal bands for the record from 1975.

DISCUSSION

The principal objectives undertaken in this report were to document, in some vertical detail, the long-term average currents and their seasonal pattern at a representative site in the Middle Atlantic Bight. Very near (3 m) the surface (group I) the long-term average flow has been determined to within perhaps 20% and is about 5 cm/s toward slightly west of south (190°-200°). Deeper in the water column the flow veers more to the west (210°-225°), but the indicated speeds of the order of 4-6 cm/s are overestimated owing to surface wave effects. At 8 m above the bottom (group IV) the instrumentation performs satisfactorily, but the weaker avearge flow is more difficult to determine with the ambient variability of the circulation. A reasonable estimate is 1-1.5 cm/s toward 220°. At 1 m above the bottom (group V) the mean flow is so weak (<1 cm/s) that it is not possible to make a reasonable estimate of either its speed or direction, and to substantially improve on the mean estimate for this group (V), at least 3 times as much data would be needed ($\approx$2 years). Thus the direction of the mean flow is slightly offshore near the surface and not distinguishably different from the orientation of the large-scale bathymetry elsewhere in the water column.

The attempt to distinguish a seasonal pattern in monthly means proved only partly successful. The data available are still inadequate to this purpose. There is superficial evidence of strongest flow to the southwest, especially in the upper part of the water column, during the late fall of 1975. Another period of notably strong flow toward the southwest occurred in midsummer of 1974. Comparable observations during the summer of 1976 showed much weaker flow and even reversal of the flow direction. It appears that the interannual variation of monthly mean currents is sufficiently large that several years of data are required to define the seasonal cycle of the circulation.

The 'cold pool' of bottom water over the middle-shelf region is not a pool in the sense of not partcipating in the shelf circulation but rather is water in motion, typically being displaced to the southwest at speeds of the order of 25-40 km/month in summer and in winter.

There is, however, a clear seasonal pattern in both the amplitude and nature of the current variations at higher than seasonal frequencies. Strong currents having a time scale of a few days are associated with the storms of winter. In the relatively calmer and stratified conditions of summer the energetic storm-driven events diminish, and free inertial oscillations become manifest with amplitudes comparable to those of the tidal currents. It is of interest that these inertial frequency current oscillations appear to be associated closely with density stratification. They are not observed at any level in the water column during unstratified winter season, and they are scarcely observed below the pycnocline in summer. The association of these motions with a pycnocline suggests that their momentum is too rapidly lost to bottom friction to register in the observations except in those special circumstances where a part of the water column is sufficiently insulated by a pycnocline against momentum transfer to the sea floor.

In contrast to the currents the water temperatures of the Middle Atlantic Bight have a clear annual pattern of warming and stratification. This has long been known, of course, and is included here primarily as context to the current meter results. Some transient features are of interest, however, We believe that the singular diurnal variation of temperature during the spring and summer at the sensor nearest the surface (group I) is a result of diurnal solar heating rather than tidal processes. An amplitude of $A(1 \text{ cpd}) = 0.09°$ is indicated for the diurnal temperature; that is, $(A^2/2)/\Delta f = 0.1$.

The appearance of temperature fluctuations of tidal and inertial frequencies in the thermally stratified part of the water column is expected, but we are unaware of any previous observation of energetic fluctuations of frequency intermediate to the inertial and semidaily frequencies. The unknown oscillation at a frequency near 5/3 cpd is found only in conjunction with a strong fluctuation at the local inertial frequency ($\sim$4/3 cpd) and the semidaily tidal frequency ($\sim$6/3 cpd). Generation by a resonant interaction of the inertial and tidal oscillations is suggested. We are confident that the variation is real and not an artifact of the analysis.

The circulation is heavily masked by events, some of which persist for as long as 3 months and appear to be primarily of atmospheric origin. Recent thoughts about the nature of wind-driven currents on continental shelves frequently are reflected in the data spanning these events. An example may be seen in the observations spanning November 1976 to January 1977. This period was one of strong winds from the west-northwest, with a substantial upshelf component. These upshelf winds caused offshore flow in the upper part of the water column, which presumably caused a drop of coastal sea level, providing a pressure gradient that drove a quasi-geostrophic upshelf flow of deeper water.

Although this was an unusually strong and persistent event, the tendency remains, for both stratified and unstratified shelf water, for the water column to be most sensitive to upshelf wind stress in the low frequencies (3-10 days) associated with energetic weather systems. Cross-spectral analyses between v (upshelf) and u (offshelf) and between upshelf wind stress τ_{up} and each of the velocity components have shown the distinctly different upper and lower water column responses.

During the summer of 1976 an extensive fish kill was caused by occurrences of very low dissolved oxygen in the water of the New York Bight, inshore and across the Hudson Shelf Valley from the LTM site. This event is the subject of an intensive study [*Swanson et al.*, 1979]. Critically low oxygen concentration occurred around day 180 (June 28) of 1976. It was preceded by a period of persistent southerly winds which produced a flow reversal (toward the northeast), observed in the set of monthly means shown in Figure 6. The reversal of flow occurred throughout most of the upper half of the water column during the period of strongest winds in June. This was followed by a period of offshelf flow near the surface and compensating flow in the thermocline. Little evidence of this reversal appeared in the currents near the bottom, at least for time scales of 30 days or more.

Acknowledgments. The authors express their appreciation for the support provided by Mesa operations in New York for management of the field program, i.e., deployment, maintenance, and retrieval of hardware and calibration of all instrumentation from 1973 through the 1977 field season. Our appreciation is also extended to the officers, crew, and scientific personnel on the following vessels: R/V *Venture* and the NOAA ship *Ferrel* in 1974, the *Advance II* and the NOAA ship *Researcher* in 1975, and the NOAA ship *Kelez* in 1975 and 1976. Thanks are extended to National Ocean Survey, NOAA, in particular, Bob Taylor in Rockville, Maryland, for the subsurface mooring designs and specifically the design of the very successful current measuring spar buoy system. NOS (Oceanographic Surveys Branch of the Oceanographic Division), Rockville, Maryland, provided support in converting the Aanderaa current meter tapes into a usable computer format. Appreciation is extended to Mike Minton for his assistance in providing spectral analyses of the current meter data and to several persons of the Atlantic Oceanographic and Meteorological Laboratories, NOAA, for collection and processing of the temperature and density data. Finally, we would like to thank Hal Mofjeld for his assistance in developing the tidal response analysis and for his analysis of Sandy Hook's tidal height data. The work was funded by the New York Bight Project of Mesa.

REFERENCES

Armstrong, R. S., Oxgyen depletion and associated benthic mortalities in the N. Y. Bight, 1976, Physical interpretation, chapter 6, professional paper, Nat. Oceanic and Atmos. Admin., Rockville, Md., in press, 1979.

Beardsley, R. C., and B. Butman, Circulation on the New England continental shelf: Response to strong winter storms, *Geophys. Res. Lett., 1,* 181–184, 1974.

Beardsley, R. C., W. C. Boicourt, and D. V. Hansen, Physical oceanography of the Middle Atlantic Bight, *Amer. Soc. Limnol. Spec. Symp., 2,* 20–34, 1976.

Beardsley, R. C., W. C. Boicourt, L. C. Huff, and J. Scott, A current meter intercomparison experiment conducted off Long Island in Feb.–March, 1976, *Tech. Rep. 77-62,* 123 pp., Woods Hole Oceanogr. Inst., Woods Hole, Mass., 1977.

Bendat, J. S., and A. G. Piersol, *Measurements and Analysis of Random Data,* 390 pp., John Wiley, New York, 1966.

Bigelow, H. B., Studies of the waters of the continental shelf, Cape Cod to Chesapeake Bay, 1, The cycle of temperature, *Pap. Phys. Oceanogr. Meteorol., 2*(4), 135 pp., 1933.

Bigelow, H. B., and M. Sears, Studies of the waters of the continental shelf, Cape Cod to Chesapeake Bay, 2, Salinity, *Pap. Phys. Oceanogr. Meteorol., 4*(1), 94 pp., 1935.

Bumpus, D. F., A description of the circulation on the continental shelf of the East Coast of the United States, *Progr. Oceanogr., 6,* 111–157, 1973.

Csanady, G. T., Mean circulation in shallow seas, *J. Geophys. Res., 81,* 5389–5399, 1976.

Halpern, D., and R. D. Pillsbury, Influence of surface waves on subsurface current measurements in shallow water, *Limnol. Oceanogr., 21,* 611–616, 1976.

Hazelworth, J., and S. Cummings, Oxygen depletion and associated benthic mortalities in the N. Y. Bight, 1976, Physical conditions compared with previous years, chapter 5, professional paper, Nat. Oceanic and Atmos. Admin., Rockville, Md., in press, 1979.

Hazelworth, J. B., and M. E. Darnell, MESA New York Bight project, Expanded water column characterization cruises (XWCC-2 and 3), NOAA ship *Researcher,* 22 February–5 March, 9–12 April, 1975 (microfiche), *NOAA Data Rep. ERL MESA-23,* 236 pp., Mar. Ecosyst. Anal. Program Office, Boulder, Colo., 1976.

Hazelworth, J. B., S. R. Cummings, S. M. Minton, and G. A. Berberian, MESA New York Bight project, Expanded water column characterization cruise (XWCC-11), NOAA ship *Researcher,* September 1976, *NOAA Data Rep. ERL MESA-29,* 189 pp., Mar. Ecosyst. Anal. Program Office, Boulder, Colo., 1977*a*.

Hazelworth, J. B., S. R. Cummings, R. B. Starr, and G. A. Berberian, MESA New York Bight project, Expanded water column characterization cruise (XWCC-8), NOAA ship *George B. Kelez,* April 1976, *NOAA Data Rep. ERL MESA-27,* 108 pp., Mar. Ecosyst. Anal. Program Office, Boulder, Colo., 1977*b*.

Hazelworth, J. B., R. B. Starr, S. R. Cummings, and G. A. Berberian, MESA New York Bight project, Expanded water column characterization cruise (XWCC-9), NOAA ship *George B. Kelez,* May 1976, *NOAA Data Rep. ERL MESA-31,* 184 pp., Mar. Ecosyst. Anal. Program Office, Boulder, Colo., 1977*c*.

Ketchum, B. H., and N. Corwin, The persistence of winter water on the continental shelf south of Long Island, New York, *Limnol. Oceanogr., 9,* 467–475, 1964.

Kolitz, B. L., J. B. Hazelworth, R. B. Starr, G. A. Berberian, and S. R. Cummings, MESA New York Bight project, Expanded water column characterization cruise (XWCC-7), NOAA ship *George B. Kelez,* December 1975 (microfiche), *NOAA Data Rep. ERL MESA-26,* 121 pp., Mar. Ecosyst. Anal. Program Office, Boulder, Colo., 1976*a*.

Kolitz, B. L., J. B. Hazelworth, R. B. Starr, and S. R. Cummings, MESA New York Bight project, Expanded water column characterization cruise (XWCC 4-5), NOAA ship *George B. Kelez,* May–June 1975 (microfiche), *NOAA Data Rep. ERL MESA-24,* 230 pp., Mar. Ecosyst. Anal. Program Office, Boulder, Colo., 1976*b*.

Libbey, W., Report upon a physical investigation of the waters off the southern coast of New England, made during the summer of 1889 by the U.S. fisheries schooner *Grampus, U.S. Fish Wildl. Serv. Fish. Bull., 9,* 391–394, 1891.

Munk, W. H., and D. E. Cartwright, Tidal spectroscopy and prediction, *Phil. Trans. Roy. Soc. London, Ser. A, 259,* 533–581, 1966.

Saunders, P. M., Wind stress on the ocean over the eastern continental shelf of North America, *J. Phys. Oceangr., 7,* 555–566, 1977.

Scott, J. T., and G. T. Csanady, Nearshore currents off Long Island, *J. Geophys. Res., 81,* 5401–5409, 1976.

Starr, R. B., J. B. Hazelworth, and G. A. Berberian, MESA New York Bight project, Expanded water column characterization cruise (XWCC-6), NOAA ship *George B. Kelez,* September–October 1975 (microfiche), *NOAA Data Rep. ERL MESA-25,* 132 pp., Mar. Ecosyst. Anal. Program Office, Boulder, Colo., 1976.

Starr, R. B., J. B. Hazelworth, S. R. Cummings, and G. A. Berberian, MESA New York Bight project, Expanded water column characterization cruise (XWCC-10), NOAA ship *George B. Kelez,* 28 June–1 July 1976, *NOAA Data Rep. ERL MESA-28,* 91 pp., Mar. Ecosyst. Anal. Program Office, Boulder, Colo., 1977.

Stommel, H., and A. Leetmaa, Circulation on the continental shelf, *Proc. Nat. Acad. Sci., U.S., 69,* 3380–3384, 1972.

Sverdrup, H. U., M. W. Johnson, and R. H. Fleming, *The Oceans,* 1087 pp., Prentice-Hall, Englewood Cliffs, N. J., 1942.

Swanson, R. L., C. J. Sinderman, and G. Han, Oxygen depletion and associated benthic mortalities in the N. Y. Bight, 1976, Oxygen depletion and the future: An evaluation, chapter 16, professional paper, Nat. Oceanic and Atmos. Admin., Rockville, Md., in press 1979.

Wu, J., Windstress and surface roughness at the air-sea interface, *J. Geophys. Res., 74*(2), 444–445, 1969.

(Received June 7, 1978;
revised November 28, 1978;
accepted December 1, 1978.)

10. Proceedings 6th OTEC Conference, G. L. Dugger, ed., Johns Hopkins University, 2, 13.3.1 to 13.3.9.

THERMAL AND CURRENT DATA FROM THE GULF OF MEXICO AND SOUTH ATLANTIC RELATIVE TO PLACEMENT OF OTEC PLANTS.

Robert L. Molinari*

Atlantic Oceanographic and Meteorological Laboratories
National Oceanic and Atmospheric Administration
15 Rickenbacker Causeway
Miami, Florida 33149

Abstract

Temperature and current data required for design of Ocean Thermal Energy Conversion (OTEC) plants have been collected at two proposed sites in the Gulf of Mexico, south of Mobile and west of Tampa, and in the tropical South Atlantic east of Brazil. The The Gulf sites are proposed as possible locations for moored plants and the South Atlantic site for grazing plants. The seawater temperature difference (ΔT) between 0 and 1000 m at the Mobile site for the July 1977 through October 1978 period ranged from an August maximum of 24.7°C to a February-March minimum of 10.5°C. The ΔT's at Tampa from March through October 1978 ranged from a low of 15°C to a high of 24°C. The July-August ΔT's of the South Atlantic site ranged from a low of about 21.4°C to a high of 22.5°C. Current speeds at Mobile at 90 m ranged from about 5 to over 30 cm/sec during all months; at 1000 m, from 2 to 15 cm/sec. The maximum speed observed at 90 m at Mobile was 60 cm/sec. Similar speeds were observed at Tampa. The highest surface speeds in the South Atlantic were about 50 cm/sec. From 3°S to 5°S, the surface flow was to the west, but the subsurface flow was to the east, as speeds as high as 30 cm/sec.

11. Proceedings 6th OTEC Conference, G. L. Dugger, ed., John Hopkins University, 2, 13.2.1 to 13.2.10.

OCEAN THERMAL AND CURRENT VELOCITY DATA REQUIREMENTS FOR DESIGN OF AN OTEC PLANT - AN UPDATE

Robert L. Molinari*

Atlantic Oceanographic and Meteorological Laboratories
National Oceanic and Atmospheric Administration
15 Rickenbacker Causeway
Miami, Florida 33149

Abstract

Oceanographic data are required in the OTEC plant design effort to evaluate the effect of plant operations on the environment and the effect of the environment on operations. The program designed to obtain current and thermal data at several proposed OTEC sites has been updated. The update is based on the results of workshops, reports, meetings with design engineers, journal articles and at sea experience. Data requirements for moored plant sites are somewhat different than those for grazing plants in that data are required over a larger area in the case of the grazing plant. Data requirements include upper layer temperature data to evaluate the resource available at the site. Sea surface data are not sufficient because the plant ingests water from a layer of finite thickness rather than just the plane of the sea surface. Current meter data are needed to evaluate the tendency for vortex shedding and the current loading on the cold water pipe. Surface drift is monitored at the grazing sites to determine propulsion requirements. Accuracy and required spatial and temporal resolution for these and other required measurements are given. In addition, the types of reports and formats used to present these data are also described.

12. Journal of Physical Oceanography 9, No. 4, 785-801.

Coastal Flow in the Northern Gulf of Alaska as Observed by Dynamic Topography and Satellite-Tracked Drogued Drift Buoys[1]

THOMAS C. ROYER

Institute of Marine Science, University of Alaska, Fairbanks 99701

DONALD V. HANSEN AND DAVID J. PASHINSKI[2]

Atlantic Oceanographic and Meterological Laboratories, NOAA, Miami, FL 33149

(Manuscript received 3 July 1978, in final form 20 December 1978)

ABSTRACT

Drifting buoys and dynamic topography over the continental shelf in the northern Gulf of Alaska are used to describe the coastal circulation and flow in the offshelf Alaska Current. One permanent anticyclonic eddy is detailed along with several shorter period features. In general, the buoys progressed shoreward and to the west from a release point near the continental shelf break. There was a tendency for the drifters to terminate their trajectories near or inside Prince William Sound.

Precipitation, runoff and wind stress suggest that the buoys' drogues are affected by entrainment. It is hypothesized that drifters move shoreward until their drogues encounter the offshore-moving, ageostrophic upper layer. Their position stabilizes between the onshore and offshore flow and their subsequent movement is parallel to this interface. Though drifters might not be monitoring surface flow, it can be inferred that the surface flow is offshore here.

The behavior of drogued, drifting buoys enables them to be especially valuable in measuring flow along frontal regions.

1. Introduction

As a part of a program to describe the physical oceanography of the continental shelf in the northeastern Gulf of Alaska, several satellite-tracked drifting buoys were released there in 1976. Hydrographic data were gathered at stations (Fig. 1) in connection with the deployments.

The flow over the continental shelf here is from east to west with the offshelf flow being dominated by the Alaska Current (Favorite, *et al.*, 1976; Dodimead *et al.*, 1963). Generally, the Alaska Current tends to follow the bathymetry along the shelf break (Royer and Muench, 1977). There is a seasonal change in wind speed and direction, from weak westerlies in summer to strong easterlies in winter which result in intense downwelling at the coast (Royer, 1975). There is also a very strong seasonal cycle in precipitation and runoff causing an influx of surface freshwater, especially at the coast (Royer, 1979). The precipitation is a maximum in fall and minimum in spring. Runoff generally follows this pattern but is augmented by summer snow melt. Numerous coastal rivers deliver this runoff to the ocean. An irregular topography characterizes the continental shelf here and there are numerous troughs and ridges and a few islands (Fig. 1). Water depths in excess of 200 m within 10 km of the shore are not unusual. The shelf width varies from 40 to 100 km. Mountains with heights in excess of 3 km are common on the nearby coast.

2. Hydrography

During September 1975 and May, June and July 1976, a total of nine drifting buoys was released in the northeastern Gulf of Alaska. The buoys were being tracked using the Random Access Measurement System of the Nimbus 6 satellite. Three of these buoys terminated transmission after a few days; the others operated for more than 70 days. A hydrographic survey of the area was carried out from 20–30 April 1976 with a second survey from 8–16 September 1976, after the buoys had transited the region. Conductivity-temperature-depth (CTD) profiles to within 10 m of the bottom or 1500 m were taken at each station in the grid. Salinity was determined from conductivity using the relationship developed by Bennett (1976). Temperature and salinity were averaged over 1 m intervals and corrected using discrete bottle samples gathered during some of the casts.

---

[1] Institute of Marine Science contribution No. 370.

[2] Present affiliation: Pacific Marine Environmental Laboratories, NOAA, Seattle, WA 98105.

0022-3670/79/040785-17$08.25

© 1979 American Meteorological Society

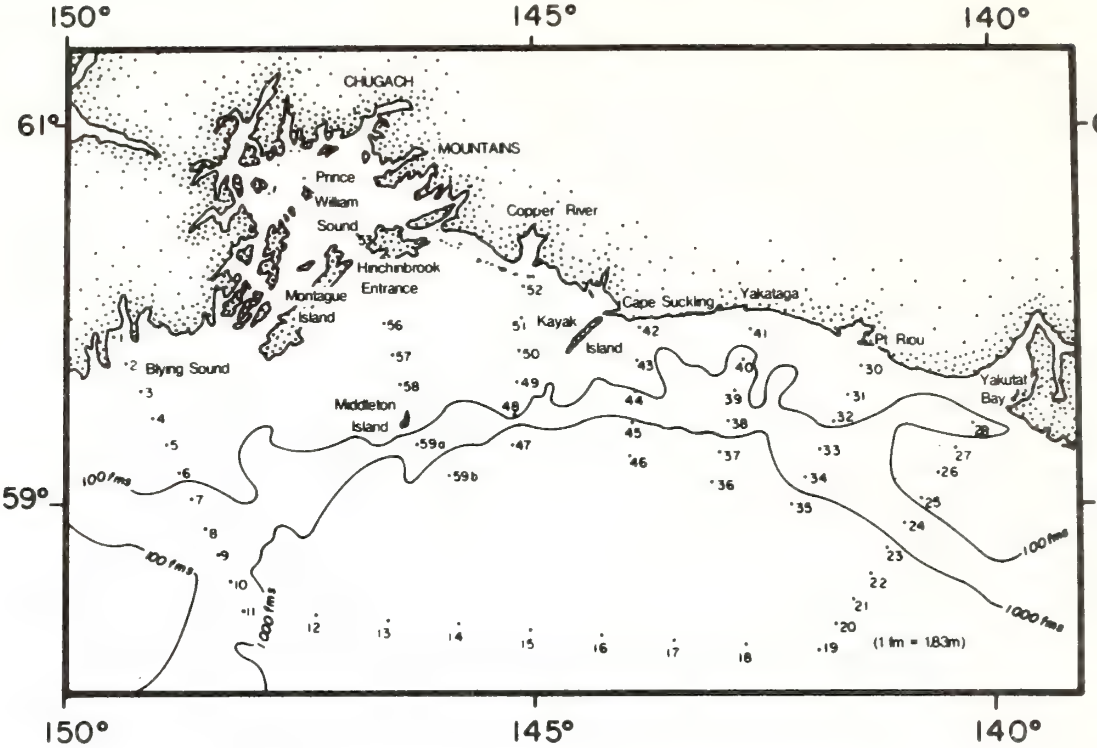

FIG. 1. Northern Gulf of Alaska with hydrographic station positions.

a. Conditions in April 1976

The 300–1000 db dynamic topography (Fig. 2) displays the deep cyclonic circulation in the Gulf of Alaska with its center at about 58.5°N, 146°W, but the data do not allow us to resolve whether the high centered at station 36 is a baroclinic meander or eddy. At shallower depths (100–1000 db), the

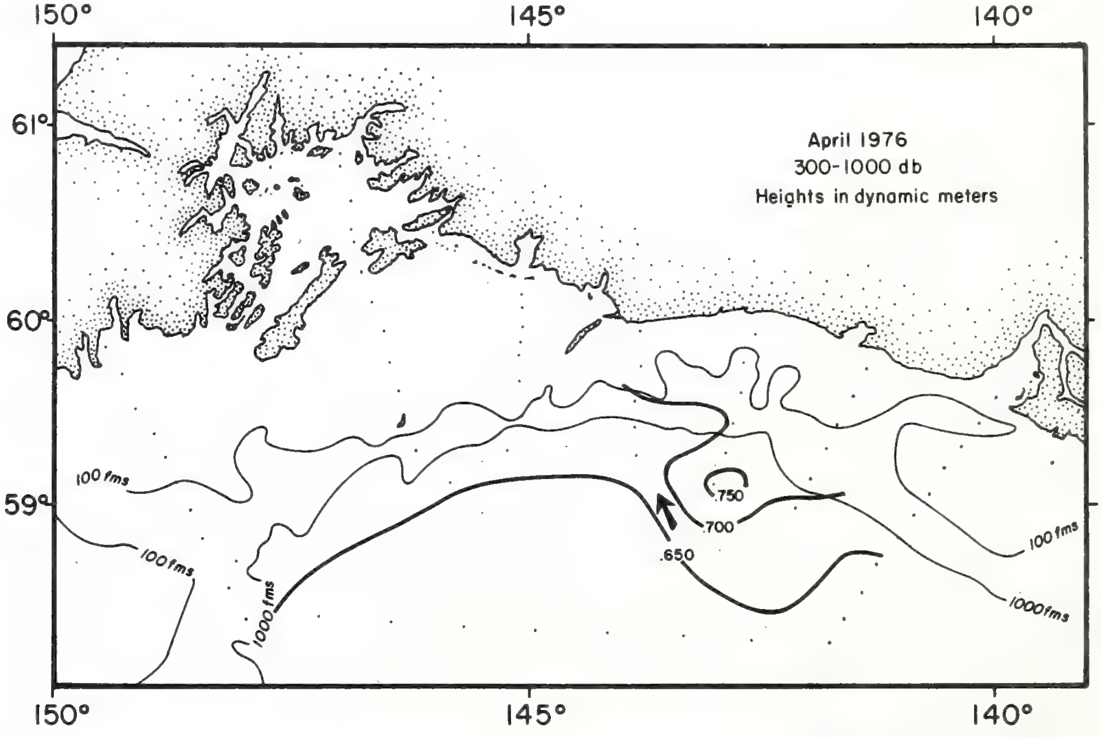

FIG. 2. Dynamic topography (300–1000 db) for April 1976.

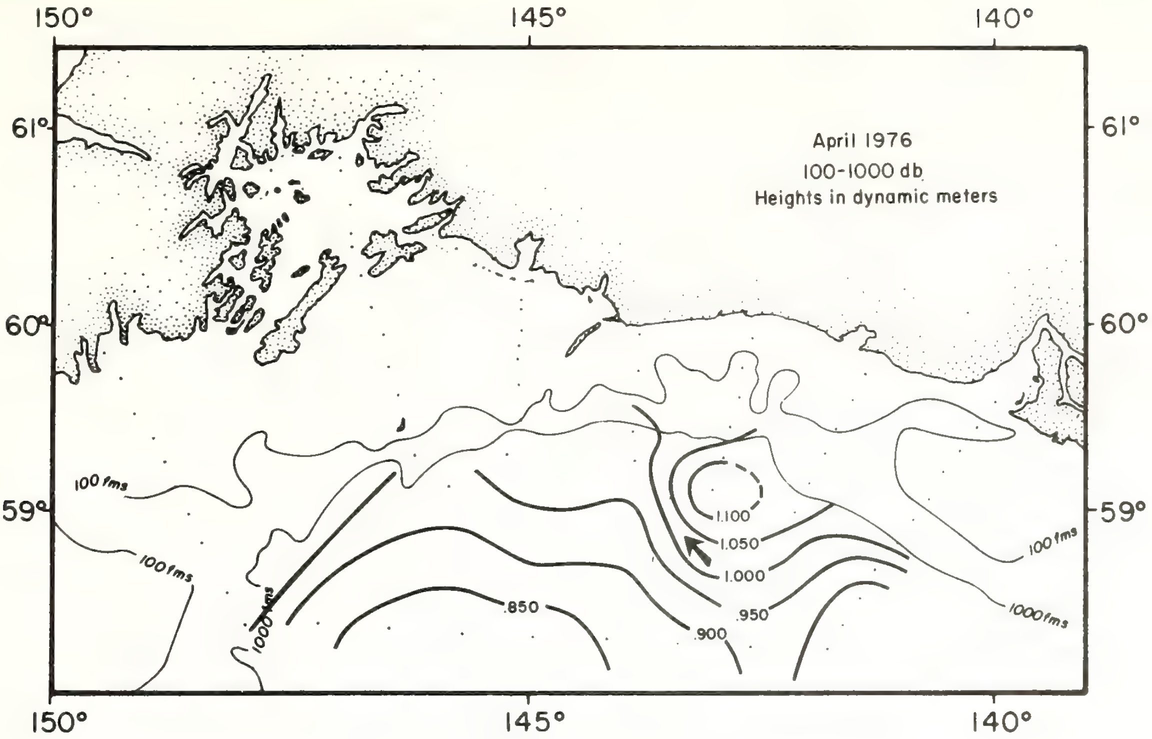

FIG. 3. As in Fig. 2 except for 100–1000 db.

anticyclonic feature is stronger, but in the same position (Fig. 3).

The 0–100 db dynamic topography (Fig. 4) shows this feature and a cyclonic eddy to the immediate northwest. A greater number of 0–100 db stations permits the resolution of that feature as an eddy. These data also reveal an anticyclonic eddy to the west of Kayak Island with surface baroclinic cur-

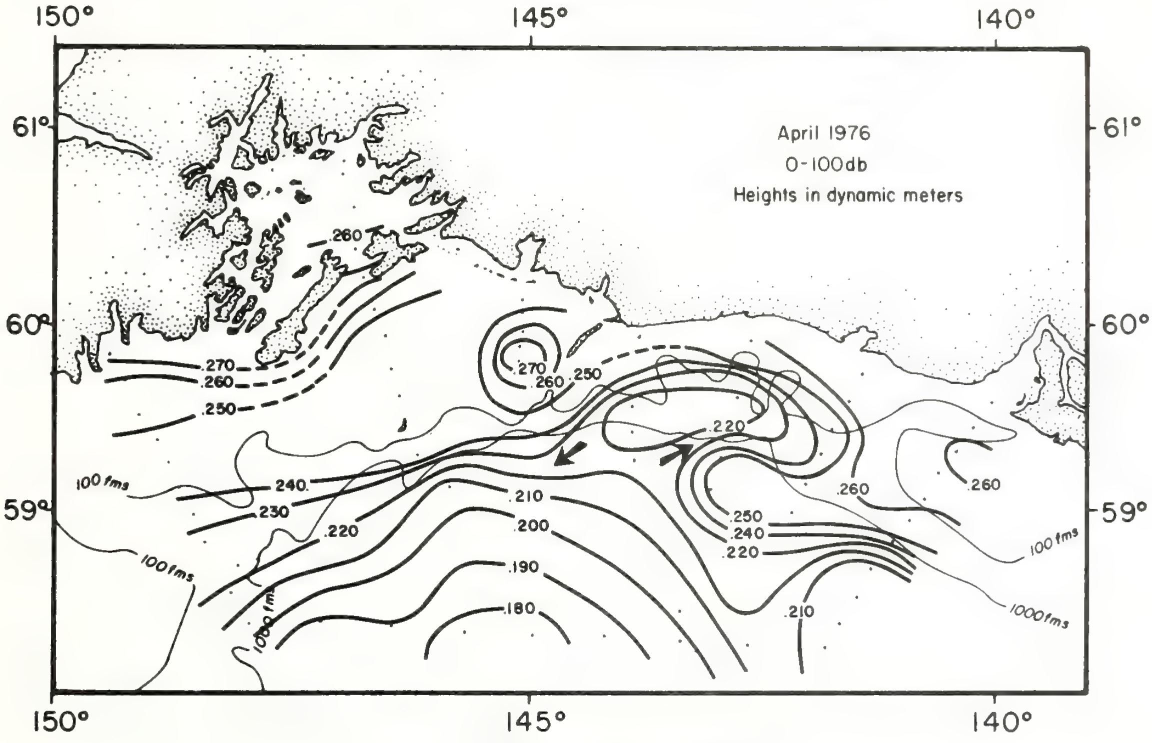

FIG. 4. As in Fig. 2 except for 0–100 db.

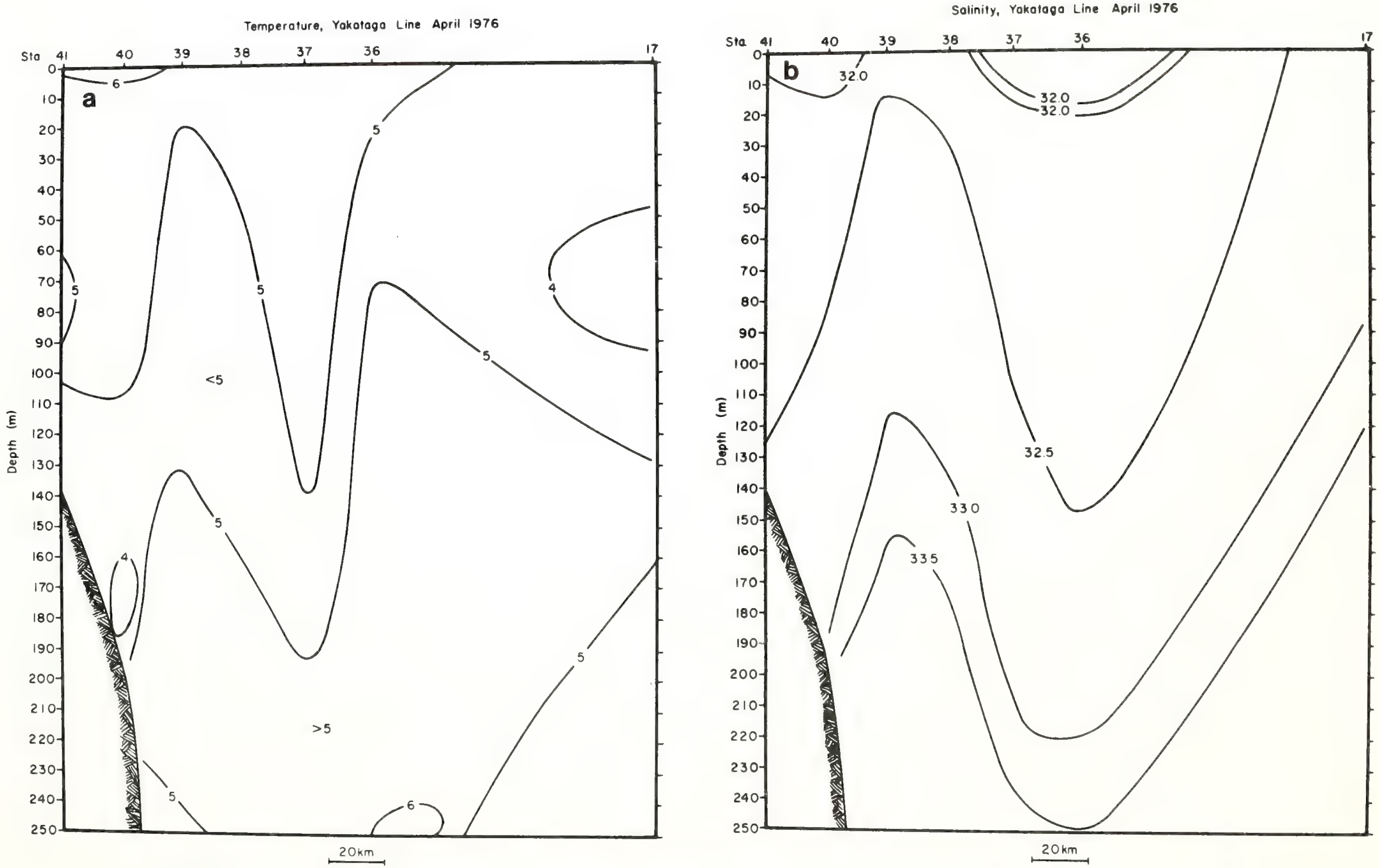

FIG. 5. Cross-sections of (a) temperature (°C), (b) salinity (‰) and (c) sigma-*t* for the Yakataga line in April 1976 and also for September 1976.

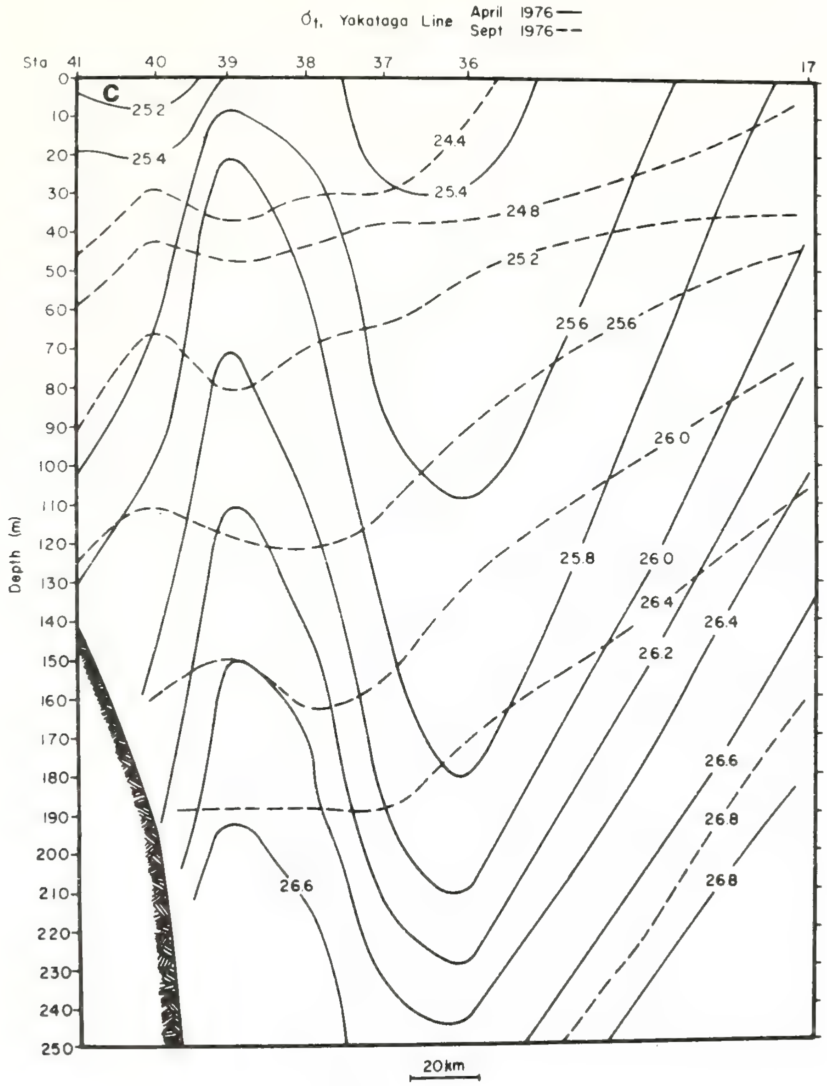

FIG. 5. (*Continued*)

rent speeds <10 cm s^{-1}, relative to 100 db. This particular eddy is a permanent feature here (Galt, 1976), which gives us confidence that its contours are closed though their symmetry is not necessarily as precise as it is shown in Fig. 4. Inshore of this eddy, water from the Copper River enters the system and is transported westward to Hinchinbrook Entrance. The brackish water here results in a horizontal pressure gradient that might cause ageostrophic, baroclinic flow of surface water into Prince William Sound at this time of year. Within the sound there is some evidence of a cyclonic circulation, in accord with the results of Muench and Schmidt (1975). On the shelf to the west, the 0–100 db dynamic topography indicates a narrow coastal jet moving westward through the western boundary and intensified flow at the shelf break.

Details of the vertical structure associated with cyclonic and anticyclonic features near Yakataga are shown in the cross sections of temperature, salinity and density (σ_t) (Figs. 5a–5c). The nonlinear nature of the equation of state of seawater with low water temperatures and high gradients of salinity make those gradients the primary determiner of density gradients in the Gulf of Alaska. For this reason, isopycnals and isohalines are usually parallel to one another but not necessarily to isotherms. The cyclonic eddy is seen in the cross section as a doming in the isopycnals while the anticyclonic feature is a depression. An interesting consequence of the temperature structure within this eddy is that it can be classified as both a warm and a cold eddy. At 100 m its center is cold, while at 150 m it is warm. An inversion in the vertical temperature structure produces this ambiguity. It could be classified as a high-density or high-salinity eddy which corresponds to cold eddies in the lower latitudes but it is probably best to refer to it simply as a cyclonic eddy. This eddy extends into the permanent halocline between 200 and 300 m. The eddy is on the shoreward side of the Alaska Current (between stations 36 and 17) and interacts with it to produce the adjacent upstream anticyclonic feature. It should be noted that within this cyclonic eddy, isotherms, isohalines and isopycnals are parallel to one another. This cyclonic eddy is similar in size as one observed in deeper water to the west in 1974 (Royer and Muench, 1977). It is evident that the large-scale cyclonic circulation in the Gulf of Alaska has smaller scale (~100 km diameter) eddies embedded in it. The baroclinic geostrophic currents at the surface in the cyclonic eddy are 17 cm s^{-1} relative to 100 db for the northern side and 13 cm s^{-1} (0–100 db) and 46 cm s^{-1} (0–1000 db) for the southern side.

b. Conditions in September 1976

Many similar features are found in the April and September dynamic topographies. The 300–1000 db dynamic topography in September (Fig. 6) has the same general cyclonic circulation, but the high has moved slightly westward to 59.3°N, 144°W and diminished by about 5 dynamic centimeters (dyn-cm), in comparison with April (Fig. 2). The 100–1000 db dynamic topography (Fig. 7) supports this weakening high and westward movement. The ridge on the southeastern boundary in April has been replaced by a trough.

The most significant changes in dynamic topography occurred in the upper 100 m. The cyclonic eddy at the shelf break off Yakataga has now disappeared (Fig. 8). The hint of an anticyclonic feature is due to the dynamic height at a single station (station 35) and is suspect. The surface flow in the anticyclonic eddy to the west of Kayak Island intensified from less than 10 cm s^{-1} in April to more than 35 cm s^{-1} relative to 100 db. Its maximum dynamic height increased by 17.5 dyn-cm. This increase is due to the decrease of salinity and increase of temperature. From April to September the cross-shelf gradient of the 0–100 db dynamic height doubled. The horizontal dynamic height gradient at Hinchinbrook Entrance increased from 17 to 46 dyn-cm,. Cyclonic flow within Prince William Sound also intensified.

From April to September, the slope of the isopycnals in the offshore waters ($\sigma_t = 26.8$) has not changed (Fig. 5c); the density surfaces have moved upward, though. At shallow depths ($\sigma_t < 26.8$) the horizontal density gradient has diminished. This change is due to the disappearance of the eddy structure found in the surface layer in April. Nearshore, the horizontal density gradients are nearly identical for the two cases but in September the densities have decreased significantly, with largest changes at the coast.

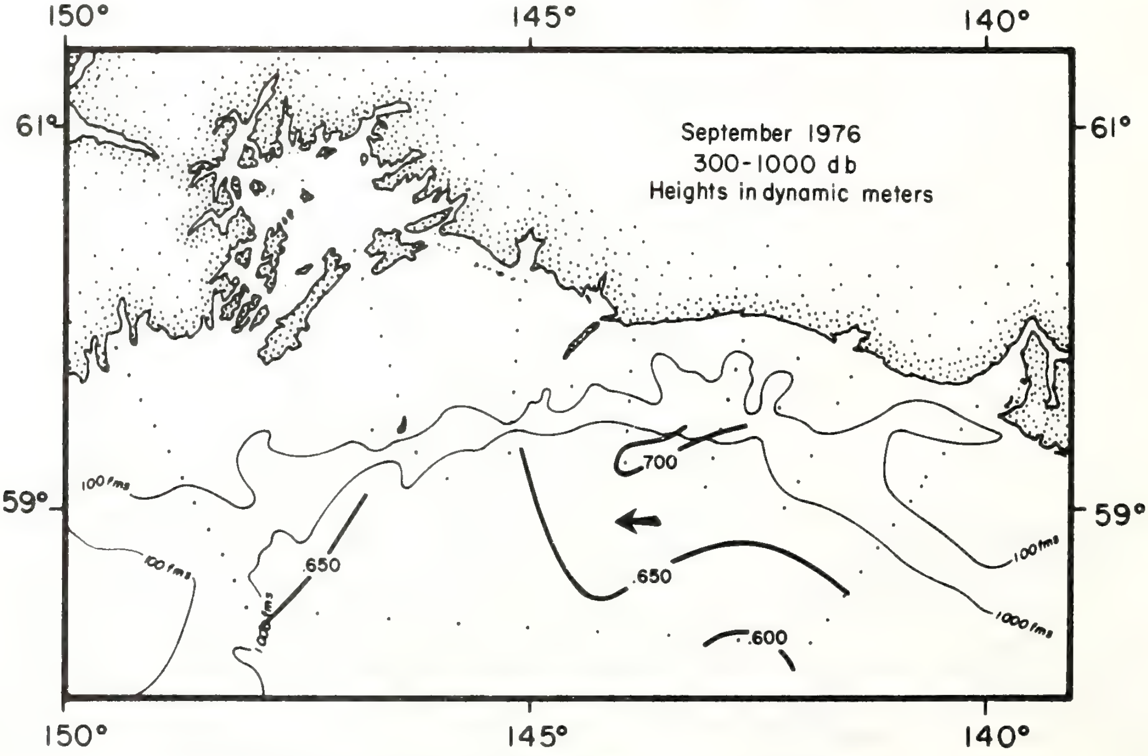

FIG. 6. Dynamic topography (300–1000 db) for September 1976.

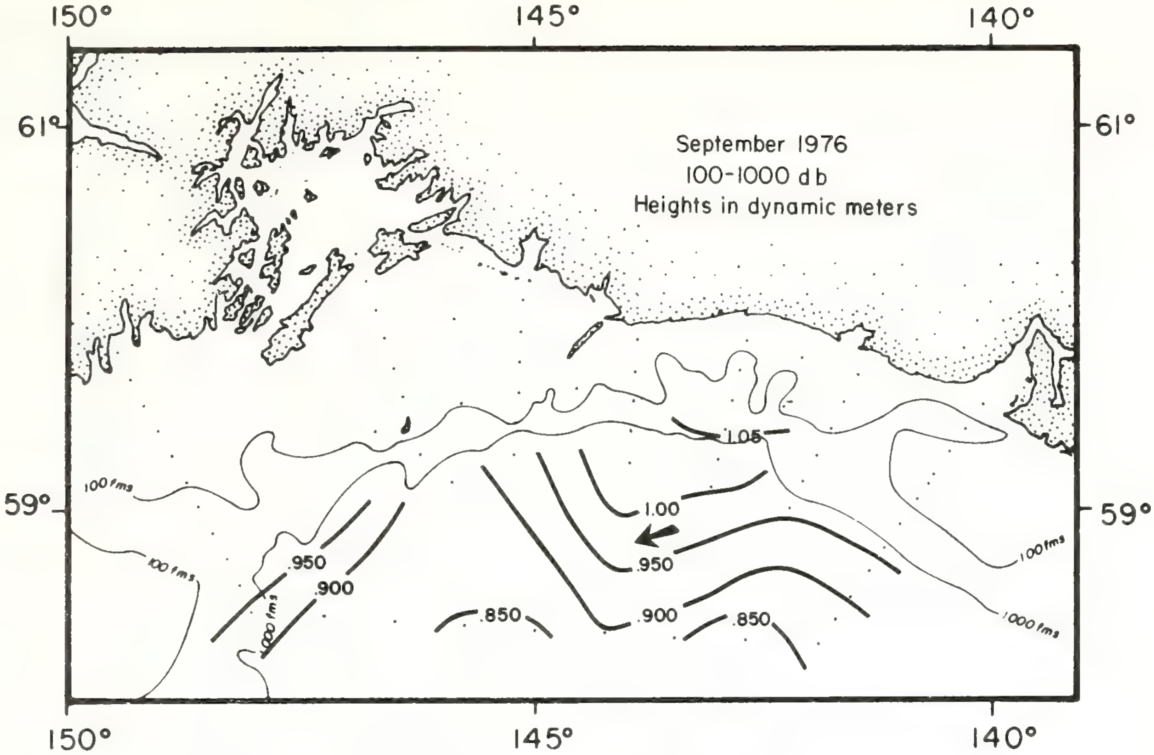

FIG. 7. As in Fig. 6 except for 100–1000 db.

Relative to the deeper pressure levels, there are still some eastward baroclinic currents. For stations 38–39, relative to 300 db there is a 3 cm s^{-1} eastward surface current, and stations 39–40 show a 3 cm s^{-1} eastward surface current relative to 190 db. Subsurface eastward baroclinic currents are also present in the Cape Suckling section. For stations 44–45, relative to 100 db there is a westward

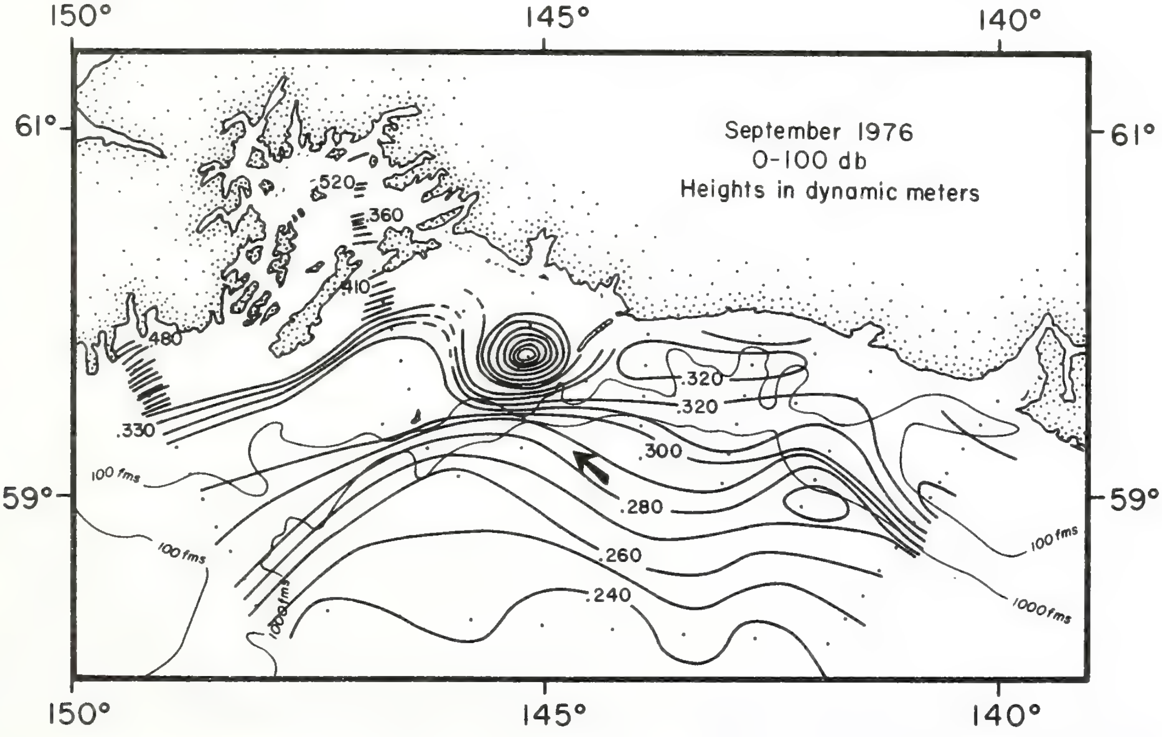

FIG. 8. As in Fig. 6 except for 0–100 db.

flow of 10 cm s^{-1}. However, for 100–1000 db there is an eastward flow of 10 cm s^{-1}. Stations 43–44 relative to the 100 db have eastward flow along with the 100–1000 db surfaces for stations 45–46. These eastward currents are associated with a subsurface perturbation which might be the remnants of the eddy in April. The nearshore current is westward at 20 cm s^{-1} for this section (Cape Suckling) relative to 85 db.

3. Drift buoy results

Nine drogued drift buoys were deployed in the region of the hydrographic surveys between September 1975 and September 1976. The buoys, designed and constructed at Nova University on contract to the NOAA Data Buoys Office, were fiberglass spars ~5 m long, attached to a 2 m × 10 m window-shade drogue by a 30 m long nylon tether. The designed center of drogue resistance was therefore near a depth of 35 m. Location of the buoys was determined by means of the Random Access Measurements System (RAMS) of the Nimbus 6 satellite (Levanon, 1975)., At the latitude of the northern Gulf of Alaska, the system provided up to five locations per day for each buoy, but at irregular times. The rms location error is ~4 km. Each satellite overpass provides data for an ambiguous pair of locations. Between sequential orbits it is usually, but not always, possible to identify the proper location. Hence, in addition to the location error arising from uncertainties in the satellite orbit, Doppler measurement, etc., individual errors of tens or even hundreds of kilometers occur in the data. These erroneous locations have been removed from the data by an objective routine that checks each location for displacement from preceding and succeeding locations, and rejects all locations that imply velocities in excess of an assignable criterion. For this Gulf of Alaska data set we used 150 cm s^{-1} as the criterion, which retained 70–80% of the original data. To facilitate automated computation of velocity time series and plotting of results, the position component data were smoothed and interpolated to 6 h intervals by piecewise least-square fit to a low-order, usually cubic, polynomial. Velocity series were additionally smoothed by a simple three-point triangular filter. The result of this procedure is a set of trajectories and associated velocity time series comparable to what would be done by a skilled subjective analyst, and in which features having a time scale of about 2 days are retained. Tidal flows and inertial currents where important are suppressed along with other rapid accelerations. The buoys were deployed on lines leading across the continental shelf south or southwest of Yakutat Bay in anticipation that they would be swept around the northern Gulf in the general cyclonic flow. The trajectories of these buoys indicate some agreement with flow patterns suggested by dynamic topography. There is a consistent cross-isobath shoreward movement not indicated in the dynamic topography. Half of the buoys grounded either within or at the entrance to Prince William Sound. So far as we are aware none of the buoys deployed in the region or other buoys that moved into the Gulf of Alaska from far to the south ever escaped from the Gulf of Alaska. Most have stranded on the coast while still transmitting; some that ceased transmission at sea were subsequently found ashore. This general pattern of accumulation in the northern Gulf of Alaska seems to support the results of modeling of surface movements by Dotson *et al.* (1977). Results of the individual deployments are as follows.

a. Drifter 0661 and 1745

Three drifters were deployed south of Yakutat Bay in September 1975. This was prior to the time of the hydrographic data described above and the buoys were relatively short-lived. The results, however, are consistent with subsequent observations and are presented here for completeness (Fig. 9a). One of these buoys (1745) moved slowly (~10 cm s^{-1}) toward the shore east of Yakutat Bay, while the other buoy (0661) became involved with a coastal current where speeds of up to 40 cm s^{-1} were encountered. Both terminated after less than two weeks, one for unknown reasons south of Yakutat Bay, the other by grounding on Cape Suckling. Part of a third buoy, deployed south of Yakutat Bay at the same time as 0661 and 1745, but which suffered an almost immediate transmission failure, was later found on Kayak Island.

b. Drifter 1133

Drifter 1133 was deployed southwest of Yakutat Bay on 16 May 1976 and grounded at Middleton Island four weeks later (Fig. 9b). This drifter began its trajectory with an anticyclonic movement similar to that implied in the 0–100 db dynamic topography observed in April. It then continued into the cyclonic turn, moving offshore, decreasing its speed until it apparently entered the Alaska Current 19–23 days after deployment. Individual speeds >65 cm s^{-1} were experienced in this current. Leaving the Alaska Current, it decelerated to speeds <25 cm s^{-1} as it passed onto the continental shelf. It then grounded on the west side of Middleton Island, and continued transmitting from a stationary position for several weeks. As will be seen, the path of this drifter differed from the general pattern shown by the others, although it was generally consistent with the dynamic topography observed in April.

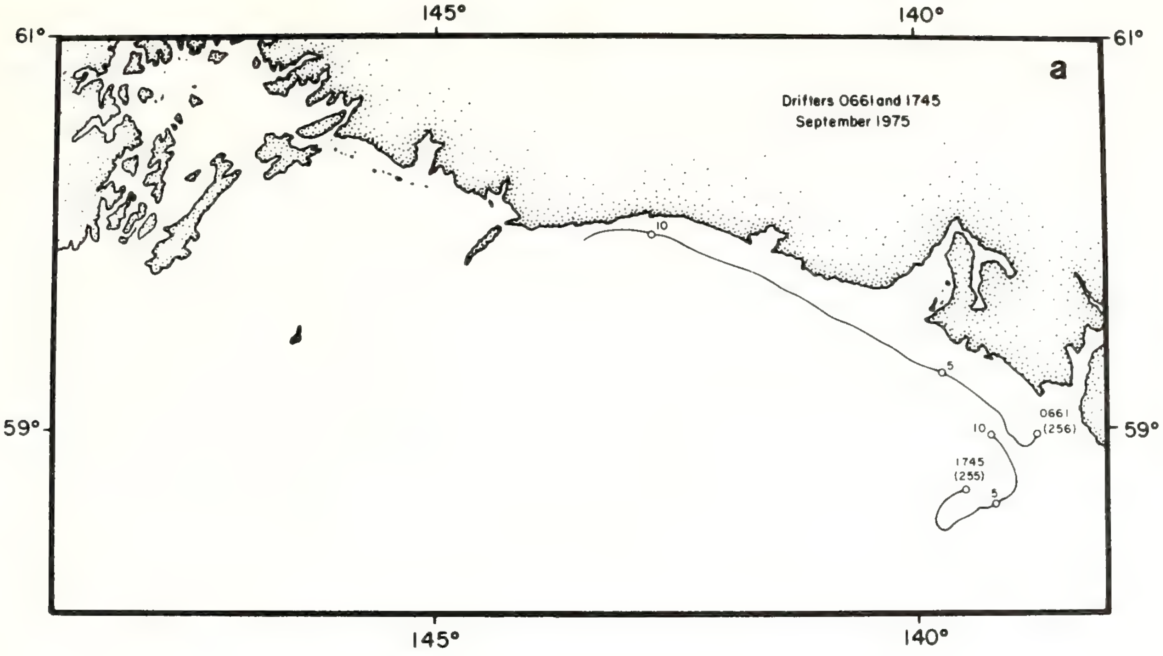

FIG. 9a. Drifter 0661 and 1745 trajectories, released September 1975.

Another buoy (1105) was deployed a few miles shoreward of 1133 at the same time. It exhibited an anticyclonic movement, generally at less than 15 cm s^{-1}, but is not shown because it ceased transmission after only six days.

c. Drifter 1174

Drifter 1174, released on 3 June 1976, was active for 69 days before terminating transmission near Hinchinbrook Entrance (Fig. 9c). Initially, it described the same anticyclonic feature as did 1133 and 1105. However, this drifter did not enter the cyclonic eddy, but rather continued northward until it entered the westward flowing coastal current 13 days after deployment. It experienced speeds of up to 45 cm s^{-1} in the coastal current, passing close along Kayak Island, to become involved with the anticyclonic eddy west of Kayak Island.

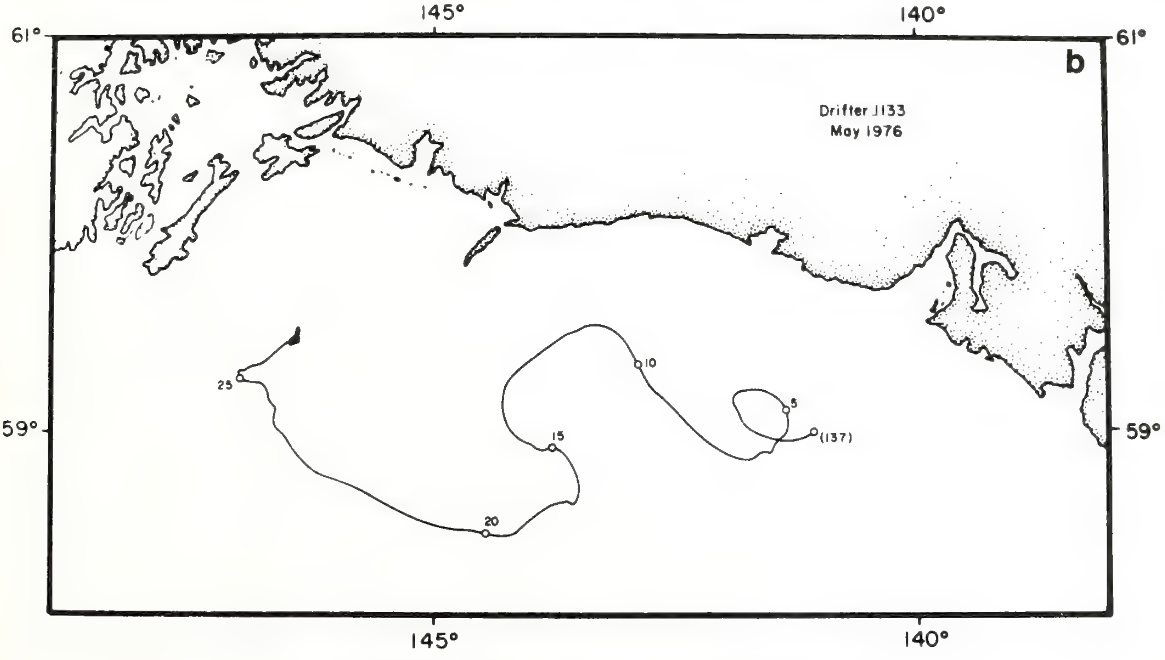

FIG. 9b. Drifter 1133 trajectory, released 20 May 1976.

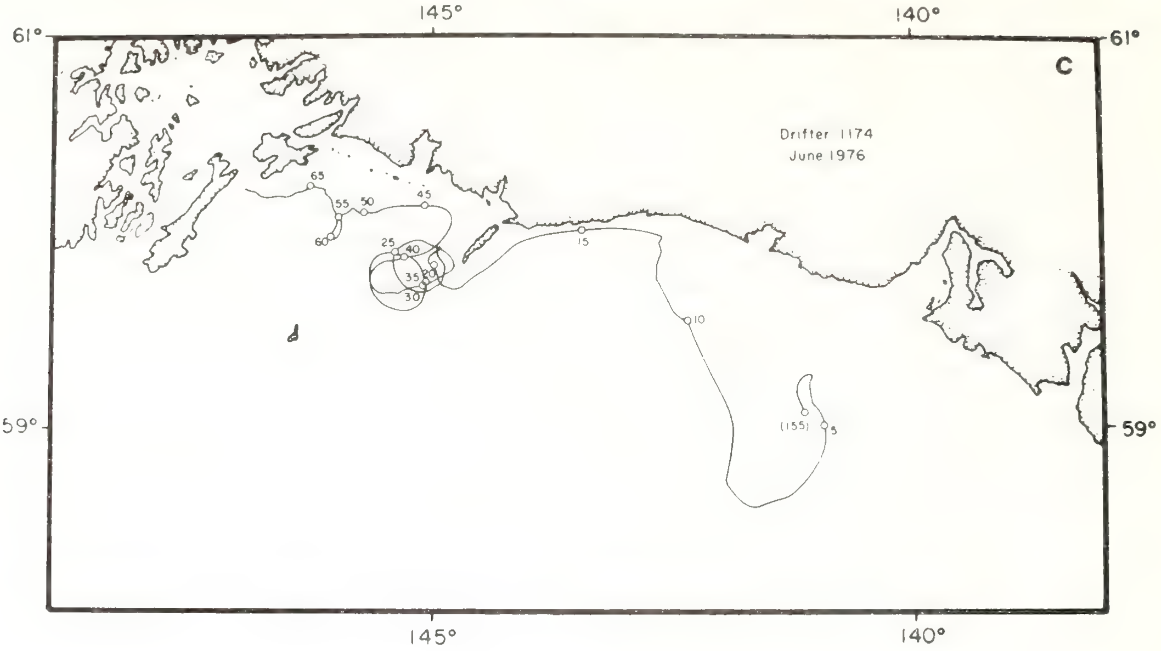

FIG. 9c. Drifter 1174 trajectory, released 6 June 1976.

It circuited this eddy three times in 27 days before resuming its westward movement in the coastal current. Typical current speeds in the eddy were ~20 cm s^{-1}. For the next two weeks it moved westward in the coastal current at speeds generally less than 10 cm s^{-1}, although it increased its speed to 20 cm s^{-1} shortly before terminating in the vicinity of Seal Rock in the approach to Hinchinbrook Entrance.

d. Drifter 1203

Drifter 1203 (Fig. 9d) was released on 22 July 1976 about 22 km southwest of where 1174 was released in early June. After about a week of very slow (<10 cm s^{-1}) movement in a small anticyclonic pattern, it made a slow cyclonic turn inshore and accelerated in the coastal current, much as had the buoys deployed in September 1975. It reached

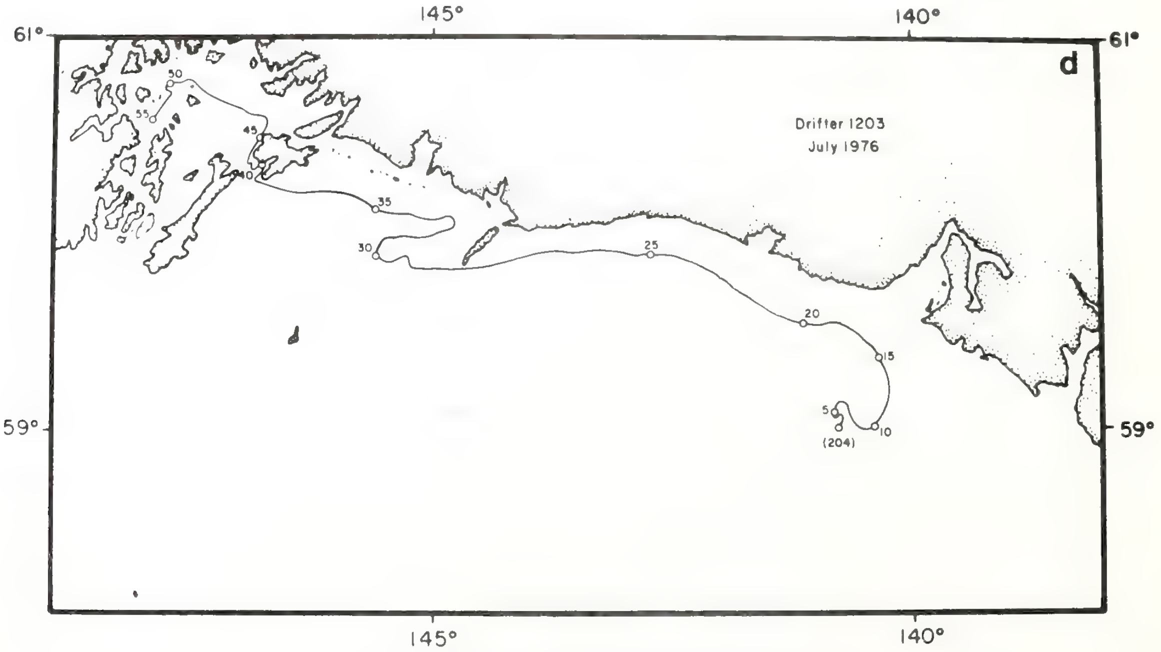

FIG. 9d. Drifter 1203 trajectory, released 26 July 1976.

speeds approaching 100 cm s^{-1} in passing close by Kayak Island. Like 1174, it came under the influence of the anticyclonic eddy west of Kayak Island, but after a partial circuit of the eddy moved westward with the coastal current, as had 1174, at speeds of up to 40 cm s^{-1}. It then passed through the Hinchinbrook Entrance into Prince William Sound where it drifted to the northwest and then the southwest, ultimately to anchor itself in Bainbridge Passage 55 days after deployment. Inside the sound, speeds of generally less than 10 cm s^{-1} were encountered. The buoy transmitted from its anchored position for several months, and ultimately was recovered by a fishing vessel. We were not able to obtain a definite report, but believe from the behavior of this buoy and buoys 1235 and 1142 that the subsurface drogue components were intact.

e. Drifter 1235

Drifter 1235, released about 22 km west-southwest of 1203 on the same day, moved quite rapidly (up to 40 cm s^{-1}) generally parallel to the continental shelf for about a week (Fig. 9e). It then slowed to less than 10 cm s^{-1} and made a sharp turn to the northeast, and then a turn to the west, becoming involved in the coastal current as was described for drifter 1203, but as much as 150 km ahead (west of 1203). Speeds of 45 cm s^{-1} were found in the coastal current, both east and west of Kayak Island. This drifter was influenced only slightly by the eddy west of Kayak Island, and hence approached and entered Prince William Sound through the Hinchinbrook Entrance ~10 days before 1203. Inside the sound its behavior was quite similar to that of 1203 except that speeds >20 cm s^{-1} were experienced shortly before the buoy anchored itself near Chicken Island in LaTouche Passage. [LaTouche Passage is west of LaTouche Island which is the island that is immediately westward of southern Montague Island (Fig. 1).] It continued transmission for several months and was subsequently recovered with its subsurface drogue components intact.

f. Drifter 1142

Drifter 1142 was deployed about 5 km east of 1235, or 15 km southwest of 1203, also on the same day. It closely duplicated the trajectory of 1235 for ~10 days (Fig. 9f), including slowing and entering the anticyclonic turn. In contrast to 1235 which entered the coastal current, 1142 continued an anticyclonic movement, completing two complete circuits suggestive of an anticyclonic eddy being advected in the larger scale westward flow. Speeds in the eddy were 15 cm s^{-1}. The buoy passed Kayak Island relatively farther offshore than any of the previous buoys except 1174 but, nonetheless, became involved in the eddy west of the island. Leaving the eddy, it experienced speeds of nearly 50 cm s^{-1} in the coastal current, and entered Prince William Sound about 5 days after 1203 or 15 days after 1235. Inside the sound it experienced movements sometimes slightly in excess of 20 cm s^{-1} moving north and west to anchor itself near the

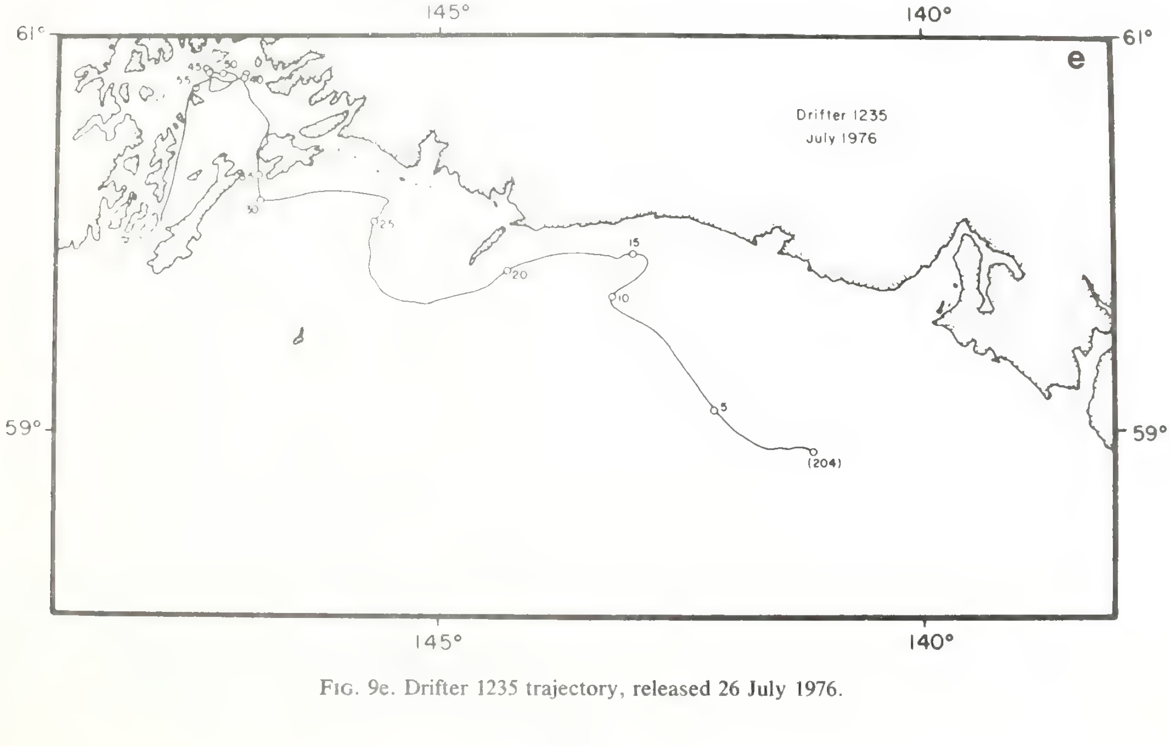

Fig. 9e. Drifter 1235 trajectory, released 26 July 1976.

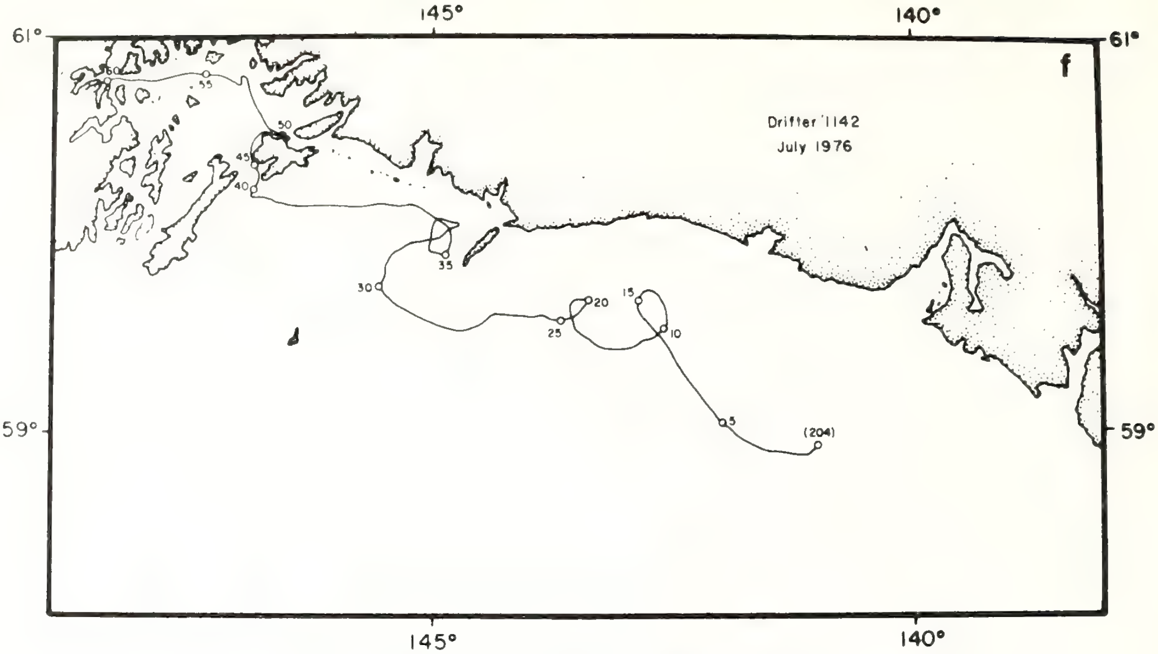

FIG. 9f. Drifter 1142 trajectory, released 26 July 1976.

head of Blackstone Bay some 60 days after deployment. It continued transmission from this location for the next several months, and was recovered with all components in excellent condition.

g. Other drifter observations

During the summer of 1977, two buoys, deployed in the vicinity of 45°N, 160°W as a part of the NORPAX program (A. D. Kirwan, personal communication), drifted far enough into the northern Gulf of Alaska to be of interest in the context of this paper. Both entered the coastal current east of Yakutat Bay. One grounded and was destroyed on Pt. Riou; the other followed the coastal current past Kayak Island, became briefly entrained in the eddy west of the island, and finally grounded near the south cape of Montague Island. Its behavior in the region of interest was quite similar to that shown above for drifter 1174.

4. Atmospheric forcing

Direct measurements of wind in the region are confined to sheltered coastal stations which do not represent marine conditions. A coastal upwelling index for 60°N, 146°W determined from 6 h sea level pressure observations on a 3° × 3° grid is used to estimate the wind effects. The indices were provided by A. Bakun, Fleet Numerical Weather Center, Monterey, and their computation is discussed elsewhere (Bakun, 1973). The index is a measure of the onshore–offshore component of the wind-driven Ekman transport. A positive index indicates an offshore transport, coastal divergence and upwelling. In the northern Gulf of Alaska strong coastal convergence and downwelling is predominant during October–April, and weak coastal divergence and upwelling normally occur during May–August. Throughout most of the drifter deployment period, weak upwelling persisted with occasional, brief periods of downwelling (Fig. 10). These downwelling periods became more frequent toward the end of the deployment. Because the wind-driven transport in the Northern Hemisphere is to the right of the wind, upwelling here is associated with eastward winds.

Some features in the drifter velocity data appear to reflect the major wind events shown in Fig. 10. The period of offshore and eastward movement of drifter 1133 during the first week of June coincides with the major positive index event of the summer. There are also some coincidences of rapid eastward movement with the times of large negative upwelling index. The relationship is inconsistent, however, suggesting that details of such a relationship as probably exists between wind and current are thoroughly obscured in a small number of Lagrangian measurements from a region in which the currents are as heterogeneous as in the northern Gulf of Alaska.

Another important atmospheric effect on the coastal circulation here is precipitation and runoff. Over the Gulf of Alaska, precipitation greatly exceeds evaporation on an annual basis. Precipitation also affects the nearshore dynamic height through runoff. It has been shown that the upper layer (<100 m) dynamic height at the coast responds to this annual cycle in precipitation and runoff (Royer, 1979). The monthly precipitation averaged over Alaska's south-coast increases dramatically during the drifter deployment from 6.8 cm in June to 17.2 cm in August and runoff is expected to increase as it goes through its annual cycle. For comparison, the upwelling index (wind stress) changes from 8 to −2 compared to an annual range of more than 150 m s^{-1} per 100 m of coastline.

5. Discussion

The trajectories of the drifting buoys were generally similar to paths suggested by the dynamic topography. This is somewhat surprising in view of the time span between observations. The anticyclonic feature and cyclonic eddy in April's hydrography were reproduced in drifter trajectories more than a month later. These features are either persistent or located where transient eddies are trapped. The former is suggested by the findings of Hayes (1979) which indicate that this anticyclonic feature was stationary. The anticyclonic eddy to the west of Kayak Island is a permanent feature. The coastal current, coastline and bathymetry are all important to its existence. The eddy had intensified in September but all of the drifters had passed through the area prior to the hydrographic cruise. The drifters deployed during 1976 were drawn strongly toward or into Prince William Sound. Limited evidence provided by the NORPAX buoys in 1977 suggests that such behavior is not unusual.

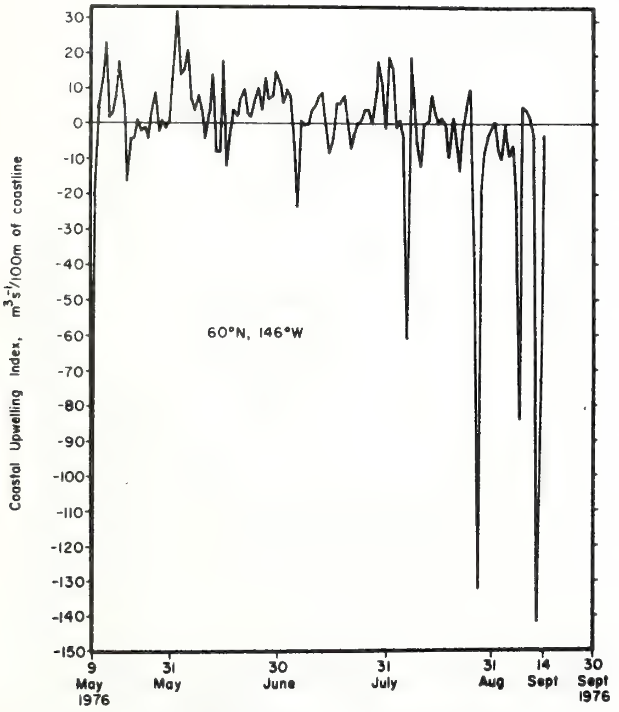

FIG. 10. Upwelling index at 60°N, 146°W, 9 May–14 September 1976.

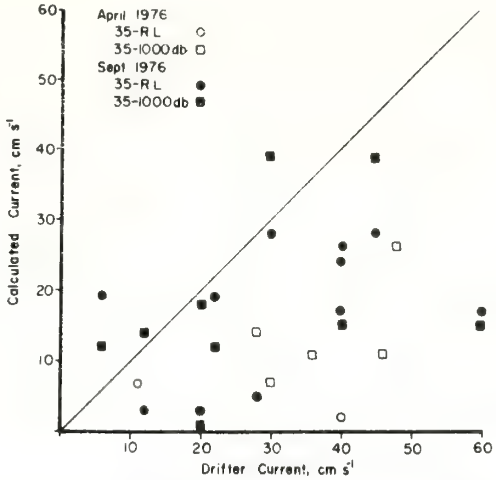

FIG. 11. Calculated baroclinic currents versus drifter currents for northern Gulf of Alaska, 1976 (line represents 1-1 correspondence).

Comparisons between the drifter and calculated baroclinic currents (Fig. 11) indicate that the drifter currents are consistently greater than calculated ones. For station pairs with a deepest common depth of less than 1000 m, the current for 35 db (approximate drogue position) relative to their deepest common depth was added to that current for their deepest common depth relative to 1000 db for the closest deep station pair. This assumes no horizontal current shear at their deepest common depth, which is not necessarily true. The scatter is large using either the shallow or deep reference levels (Rl), with the offset being 10–20 cm s^{-1}. This offset also applies to the eddy west of Kayak Island, where the eastward flow must also be increased by this same amount. The underestimate of the drifter currents should be caused by a barotropic current and/or the selection of an RL where the baroclinic current is not zero. Also, if the width of the current is less than the station spacing, the gradient of the dynamic topography will be underestimated. This leads to an underestimate of the current speed. Temporal changes in the density structure are also expected to produce significant differences in the geostrophic currents found month to month. In spite of these difficulties some qualitative comments about the drifters and dynamic topography can be made.

All drifters experienced a net northward displacement. The average northward velocity from the release point to Hinchinbrook entrance (Middleton Island in the case of 1133) for all the drifters deployed in 1976 is 3.9 cm s^{-1}. However, the drifters released in May–June had a mean northward speed of 2.2 cm s^{-1}, while those released in July had a mean northward speed of 5.0 cm s^{-1}. The longshore or westward mean speeds were 9.5 and 10.1 cm s^{-1} for the same periods. The difference between the longshore speeds would be greater if drifter 1133 were not included. Such an exclusion is reasonable because this drifter spent much of its time in or near the Alaska Current.

The upwelling index indicates offshore transport of upper layer waters during most of the 1976 drifter deployment, generally opposite to the shoreward movement of the drifters. Either the drifters were drogued beneath this upper layer flowing offshore, upwelling conditions did not occur, and/or other currents dominated the buoy motion. An Ekman depth of 50 m is estimated here for the homogeneous case. [This estimate uses an eddy viscosity A of 165 g cm^{-1} s^{-1}, where $D = \pi(2A/\rho f)^{-1/2}$ (Neumann and Pierson, 1966, p. 193), ρ is water density and f the Coriolis parameter. A similar Ekman depth is obtained using a relationship involving only wind speed $D = 7.6\ W/\sin\phi$ (Neumann and Pierson, 1966, p. 210), where W is the wind speed and ϕ the latitude—6 m s^{-1} is used for our case.] The stratified Ekman depth is less, possibly less than 35 m. If the drogue was positioned at a depth where the Ekman current was onshore for an eastward wind, its magnitude would be less than $V_0e^{-\pi}$ (Neumann and Pierson, 1966, p. 193), where V_0 is the surface value. V_0 would have to be 51 cm s^{-1} in June and 115 cm s^{-1} in August, requiring mean wind speeds of 35 and 79 m s^{-1}, respectively. Such winds did not occur. Furthermore, if the buoys were drogued below the Ekman layer, upwelling could be manifested as a shoreward movement. This effect would be greater in June than in August; however, drifters appear to move shoreward more rapidly in August.

If the drifters are drogued beneath the Ekman depth it is hypothesized they could respond to entrainment flow from both the offshore Ekman transport and the freshwater input along the coast. The freshwater input at the coastline will create a cross-shelf pressure gradient which is positive shoreward. An offshore ageostrophic flow associated with this pressure gradient would require, through entrainment, an onshore subsurface flow. Entrainment has previously been believed to be an important mechanism in the Gulf of Alaska because of the large amounts of freshwater involved (Tully and Barber, 1960). The entrainment process involves the upward movement of lower layer waters into the fresher overlying waters of the region. A continuous onshore flow in the layer immediately beneath the upper layer is required. The two layers are separated by the halocline (or pycnocline here). The drogue depth of 35 m could be beneath the upper, offshore flowing layer throughout the summer. Greater freshwater inflow would result in an increased onshore transport in the lower layer. The drogue position for June and August on the hydrographic sections for the Cape Suckling line (April and September) shows that the drogue is situated immediately beneath the layer between $S = 31.9$ and 31.7‰ (Fig. 12). From June to August, the precipitation rate more than doubled. Likewise, the northward (onshore) component of the drifter velocity nearly doubled, and the drogue positioned itself further offshore in August.

With entrainment, the drifter will continue to move shoreward until the "effective" drogue experiences no net onshore or offshore velocity components. Since the layer depth increases shoreward (Fig. 12), a deeper drogue should stabilize its position closer to the coast. If the upper layer increases its depth, the drogue should be farther offshore. These effects can be seen in the vicinity east of Kayak Island where drifters 1174, 1203 and 1235 begin moving parallel to the coast. Drifter 1174 proceeds shoreward until it is less than 5 km offshore. Its position apparently stabilizes there as it progresses westward parallel to the coast. Should the drogue move shoreward it will enter the offshore flowing upper layer. Moving offshore it will enter the lower layer, moving onshore again. In this manner it will stabilize on the interface between the two layers. Once the drifter enters this interface, it will remain until the interface is destroyed or the drogue strikes the bottom.

As the drifters progress westward, they follow this interface into the eddy west of Kayak Island. In the eddy the flow is probably dominated by more local effects like topography and river discharge. In the low freshwater input situation, the motion of drifter 1174 was dominated by the eddy dynamics for three weeks, while later in the season when freshwater input had increased, drifters 1142, 1203 and 1235 passed through the region of the eddy in only 2–5 days. The trajectories from this eddy to Hinchinbrook Entrance are quite similar in all cases. The position of the interface appears to move meridionally by up to 5 km over a period of several days in late August to early September. The longshore speeds off the Copper River changed from 10–20 cm s^{-1} in June to 40–50 cm s^{-1} in August–September.

The June drifter (1174) apparently grounded at Seal Rocks at Hinchinbrook Entrance. The interface between the layers at 35 m may have intersected the bottom at this location. Other possibilities include local winds forcing the buoy ashore. In August–September, all drifters entered Prince William Sound. The interface should be farther offshore at this time of year due to greater inflow of fresh water but Hinchinbrook Entrance is ~300 m deep. The flow might become ageostrophic here be-

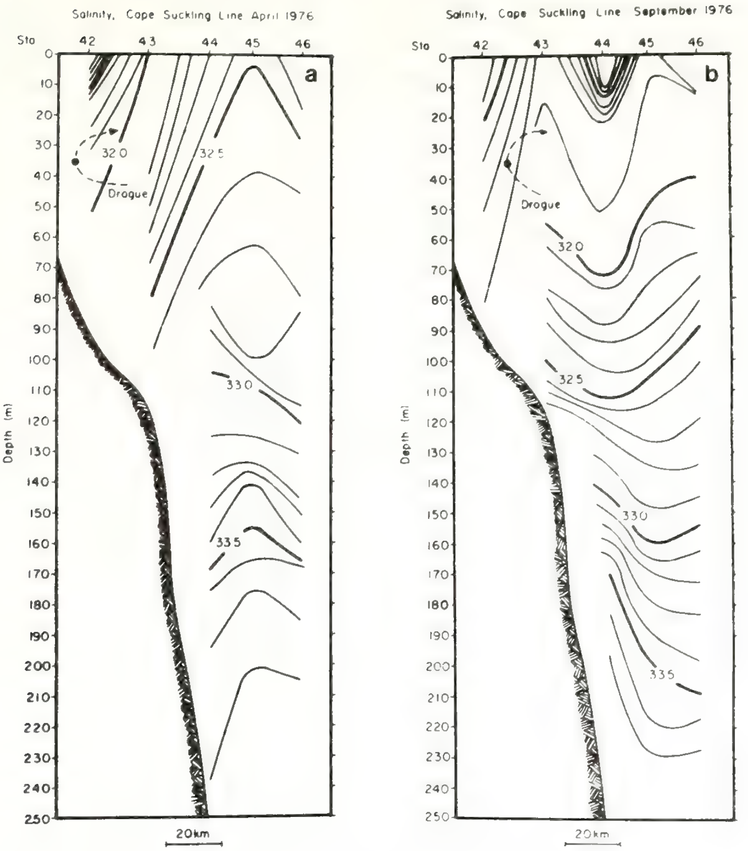

FIG. 12. Cross-section of salinity (‰) for (a) April 1976 and (b) September for the Cape Suckling line. Approximate position that drifter intersected the line is indicated.

cause of topographic effects. The dynamic height is greater at the outer entrance than inside Prince William Sound, allowing an ageostrophic baroclinic flow into the sound. Because of the consistent nature of this inflow at 35 m, it is unlikely that it is related to wind stress.

Within Prince William Sound, the drifters are carried in the cyclonic circulation. Two were grounded in shallow passages and so could not follow this circulation to Blying Sound. The final movement and ultimate position of the drifter that grounded near the head of Blackstone Bay (1142) may have been grounded by an estuarine circulation in this closed inlet, a more local entrainment phenomenon. Another possibility is that the major westward movement of this buoy across northern Prince William Sound occurred at the time of the strong east wind events in mid-September. Passages in that area are mostly in excess of 200–400 m, so a drogue at 35 m might easily be within the direct wind driven flow there.

Drifter 1133 never entered the coastal jet and hence had a much different path than the other drifters. This drifter became involved in the anticyclonic feature and cyclonic eddy offshore east of Kayak Island. It then continued a shoreward movement, passing onto the continental shelf west of Middleton Island. Its subsequent behavior suggests that it anchored for several weeks on the shoal area surrounding Middleton Island until broken loose and destroyed at the time of the moderate wind events around 3 August.

The entrainment hypothesis is upheld by current meter data from a station, located midway between Stations 32 and 39 (Fig. 1). The mean speeds and direction for four depths at two different time intervals (Table 1) indicate an onshore (or cross-bathymetric) flow. [The angle of 315° for the local bathymetry is given by Hayes and Schumacher (1976). However, the current data in that paper are not applicable here since they are only the alongshore components.] The highest onshore speeds (Table 1) are in the upper layer. This conforms with the entrainment hypothesis if the assumption is made that the outflowing freshwaters are at depth <20 m. The onshore flow ranges from $\sim 5-10$ cm s^{-1} and the estimated time of traverse across the shelf from 200 m to the coastal jet is 5–10 days. This time compares favorably with the drifter observations.

TABLE 1. Mean speed, direction and onshore component for current meter array at Station 62. (Compiled from Reynolds and Walter, 1975.)

	17 August–16 October 1974			17 October–16 December 1974		
Depth (m)	Speed (cm s^{-1})	Direction (°T)	Onshore component (cm s^{-1})	Speed (cm s^{-1})	Direction (°T)	Onshore component (cm s^{-1})
20	13.6	348	7.4	34.0	339	13.8
50	11.0*	338	4.3	—	—	—
100	10.6	332	3.1	22.6**	329	5.5
178	3.8	379	3.4	12.5	338	4.9

* To 4 October; **to 20 November.

6. Conclusions

The buoy and hydrographic data employed in this study support the hypothesis that entrainment of the deep layer, onshore-moving water into an off-shore-moving brackish upper layer occurs over the continental shelf in the Gulf of Alaska. In such a scheme, the buoys generally move shoreward in the lower layer until their drogues encounter the offshore-moving upper layer. Their position stabilized on the interface between the two layers where there is no on or offshore motion. The buoys then describe the longshore flow only. This positioning of the buoys indicates that their drogues are still intact. The buoys continue on this interface until they enter a region with locally different dynamics, the interface intersects the bottom or the drogues are lost.

Qualitative agreement between the drifter trajectories and dynamic topography is good in the longshore direction. Dynamic topography does not reproduce the cross-shelf flow which must be ageostrophic, and drifters reveal the cross-shelf flow only until they reach a position of drogue equilibrium between onshore and offshore flows. Cross-shelf flow must exist if entrainment occurs and because entrainment is consistent with the drifter trajectories, cross-shelf flow is assumed to be present.

The coastal system described here is similar to that discussed by Heaps (1972) for the Irish Sea. This system is driven by freshwater outflow and cross-shelf density gradients. Heaps obtains an onshore bottom flow and an along shore and slightly offshore flow at the surface. This surface flow is across density contours, similar to our proposed cross-shelf flow. Though the fresh-water outflow and cross-shelf density gradients are considerably greater for the Gulf of Alaska, a detailed comparison with the Irish Sea is limited because the shelf there is shallow (<50 m) and vertically well mixed.

The presence of persistent eddies and meanders in the Alaska Current is confirmed by this study. These 100 km diameter perturbations occur near the continental slope and have a life span of at least several months. Flows in the Alaska Current can be expected to be unsteady in this region.

A description of actual surface water or pollutant trajectories using the drifter data discussed here is very questionable. However, these results suggest that the surface water (<35 m) have an offshore movement near the coast, which will keep surface water offshore. Drogues nearer to the surface presumably would better represent the movement of near-surface waters in regions where important shear occurs in the upper few meters, but were not used in this study because of unsolved problems affecting drogue survival. It might be possible to map the horizontal slope of the interface through the use of several buoys drogued at different depths.

The stabilization of drogued, drifting buoys on an interface of current shear could be used to monitor convergences and divergences, in general. Buoys whose drogues are at depths to intersect this interface will remain on that interface and will move with the current normal to it. These drifters will be trapped on fronts and move parallel to them.

Acknowledgments. We would like to thank the officers and crew of the R/V *Moana Wave* and NOAA Ships *Surveyor* and *Discoverer* for their assistance in gathering the hydrographic data and deploying the drift buoys. A. Bakun generously provided the upwelling data and the NOAA Data Buoy Office provided assistance in the design and procurement of buoy hardware. Buoy data processing was done by Carol Cardwell. Special appreciation must be expressed to personnel of the Nimbus 6 Project (NASA) who provided the data collection service essential to conduct of the drifter buoy work. This study was supported under Contract 03-5-022-56 between the University of Alaska and NOAA, Department of Commerce, to which funds were provided by the Bureau of Land Management through an interagency agreement. This work was completed while one author (TCR) was on sabbatical leave from the University of Alaska and was a visiting faculty member of the Department of Oceanography, Texas A&M University. Appreciation is extended to both universities for making this arrangement possible.

REFERENCES

Bakun, A., 1973: Coastal upwelling indices. West coast of North America. NOAA Tech. Rep. NMFS SSRF-671, 103 pp.

Bennett, A. S., 1976: Conversion of *in situ* measurements of conductivity to salinity. *Deep Sea Res.* **23**, 157–165.

Dodimead, A. J., F. Favorite and T. Hirano, 1963: Review of oceanography of the subarctic Pacific region. *Salmon of the North Pacific Ocean, Bull. Int. N. Pac. Fish. Comm.*, **13**, 195 pp.

Dotson, A., L. Magaard, G. Niemeyer and K. Wyrtki, 1977: A simulation of the movements of fields of drifting buoys in the North Pacific Ocean, Hawaii Institute of Geophysics Ref. HIG-77-3, 59 pp.

Favorite, F., A. J. Dodimead and K. Nasu, 1976: Oceanography of the subarctic Pacific region, 1960–71. *Bull. Int. N. Pac. Fish. Comm.*, **33**, 187 pp.

Galt, J. A., 1976: Circulation studies on the Alaskan continental shelf off the Copper River delta. NOAA Tech. Rep., ERL, 46 pp.

Hayes, S. P., 1979: Variability of current and bottom pressure across the continental shelf in the northeast Gulf of Alaska. *J. Phys. Oceanogr.*, **9**, 88–103.

——, and J. D. Schumacher, 1976: Description of wind, current and bottom pressure variations on the continental shelf in the Northeast Gulf of Alaska from February to May 1975. *J. Geophys. Res.*, **81**, 6411–6419.

Heaps, N. S., 1972: Estimation of density currents in the Liverpool Bay area of the Irish Sea. *Geophys. J. Roy. Astron. Soc.*, **30**, 415–432.

Levanon, N., 1975: Special issue on data collection from multiple earth platforms. *IEEE Trans. Geosci. Elec.*, **13**, 1.

Muench, R. D., and G. M. Schmidt, 1975: Variations in the hydrographic structure of Prince William Sound. University of Alaska, Sea Grant Rep. R75-1, 135 pp.

Neumann, G., and W. J. Pierson, Jr., 1966: *Principles of Physical Oceanography*. Prentice-Hall, 545 pp.

Reynolds, R. M., and B. Walters, 1975: Current meter measurements in the Gulf of Alaska. 1. Tech. Memo. ERL PMEL-3, Seattle, 290 pp.

Royer, T. C., 1975: Seasonal variations of waters in the northern Gulf of Alaska. *Deep Sea Res.*, **22**, 403–416.

——, 1979: On the effect of precipitation and runoff on coastal circulation in the Gulf of Alaska. *J. Phys., Oceanogr.*, **9**, 555–563.

——, and R. D. Muench, 1977: On the ocean temperature distribution in the Gulf of Alaska, 1974–1975. *J. Phys. Oceanogr.*, **7**, 92–99.

Tully, J. P., and F. G. Barber, 1960: An estuarine analogy in the subarctic Pacific Ocean. *J. Fish. Res. Bd. Canada*, **17**, 91–112.

13. Deep-Sea Research 26A, 1179-1184.

Deep silicate content as evidence of renewal processes in the Venezuela Basin, Caribbean Sea

DONALD K. ATWOOD,* PHILIP N. FROELICH,† MICHAEL E. Q. PILSON,‡ M. J. BARCELONA,§ and JANICE L. VILEN

(*Received* 21 *February* 1978; *in revised form* 17 *April* 1979; *accepted* 30 *April* 1979)

Abstract—Average dissolved silicate concentrations in waters deeper than 1400 m of the Venezuela Basin (Eastern Caribbean Sea) increase from 27.7 μM in the north to greater than 29.0 μM in the south. Standard deviations of these values (a measure of temporal heterogeneity) decline from 1.8 in the north to 1.0 in the south. These gradients result from sporadic inflow of silicate-poor North Atlantic Deep Water over the Jungfern Sill at the north end of the basin. This inflow lowers the silicate concentrations and increases temporal variability in the north. Mixing of this inflow water southward across the basin causes the observed north-to-south gradients in mean silicate concentrations and in standard deviations about these means.

INTRODUCTION

OVER THE past two decades there has been considerable interest in renewal of deep water in the Caribbean Sea, particularly in the Venezuela Basin. Some investigators have presented evidence that the deep basin waters are practically stagnant and that any renewal occurring in the recent past was too small to be detected. For example, WORTHINGTON (1955, 1956, 1966, 1971), RICHARDS (1958), and STURGES (1965) noted that the deep basin has lower oxygen concentrations and higher silicate and phosphate concentrations than adjacent Atlantic water on equivalent sigma-*t* surfaces below sill depth. WORTHINGTON (1971) also noted that there is apparently no continuity in the lowest potential temperature surfaces from the Venezuela Basin into the Virgin Islands Basin and Atlantic.

Other investigators presented evidence that the deep basin waters were being renewed rather continually. SVERDRUP, JOHNSON and FLEMING (1942) and WÜST and GORDON (1964) observed that the oxygen concentrations in the basin increase slightly with depth, and that there is some meager evidence for the occurence of oxygen-rich upper North Atlantic Deep Water (NADW) in the basin.

It is now generally agreed that renewal does occur, primarily through the Anegada–Jungfern passage where the controlling sill depth is 1815 m at the Jungfern Sill (STALCUP and METCALF, 1973). Current meter and STD (salinity–temperature–depth) observations at and near the Jungfern Sill (STURGES, 1970, 1975; STALCUP, METCALF and JOHNSON, 1975) have shown that renewal takes place there by intermittent low-volume flows. STURGES (1975) estimated a mean net flow into the basin of about 50×10^3 m^3 s^{-1}

---

*NOAA/AOML/OCL, 15 Rickenbacker Causeway, Miami, FL 33149, U.S.A.
†Department of Oceanography, Florida State University, Tallahassee, FL 32306, U.S.A.
‡Graduate School of Oceanography, University of Rhode Island, Kingston, RI 02881, U.S.A.
§W. M. Kech Labs 138–78 California Institute of Technology Pasadena, CA 91125, U.S.A.
‖Route 4, Rochester, MN 55901, U.S.A.

and STALCUP *et al.*, (1975) estimated it as 56×10^3 m^3 s^{-1}. STURGES (1975) noted that, due to the physiography of the controlling sill, transport could be increased by a factor of four if the thickness of the inflowing layer were doubled. STURGES (1970) also calculated that an inflow of 80×10^3 m^3 s^{-1} is required to balance the heat flux through the basin floor. Similarly, an inflow of 117×10^3 m^3 s^{-1} is needed to balance the estimated oxygen consumption in the deep water. These results, indicating slight inflow over the Jungfern sill, are in good agreement with rotating tank model experiments by ICHIYE (1972), which predict a low volume inflow over the Jungfern Sill, in contrast to the intense inflow over the Windward Sill, which fills the whole bottom of the Cayman Trench.

RICHARDS (1958) and METCALF (1969) suggested using concentrations of dissolved silicate as a sensitive tool for studying the extent of renewal occurring in the deep water of the Venezuela Basin. Atlantic Water at sill depth has a silicate concentration of about 15 μM, whereas in the deep Venezuela Basin Water, the silicate concentration is about 28 μM or more. Thus an influx of NADW should cause a dilution of the deep silicate concentrations within the basin.

Both STURGES (1975) and STALCUP *et al.*, (1975) observed silicate-poor Atlantic Water in the basin on the lip of the sill. STALCUP *et al.* (1975) traced 3.8°θ and 16 to 19 μM-silicate-water downslope from the sill for 7.5 km to a depth of 2300 m. FROELICH (1973) and FROELICH and ATWOOD (1974; Fig. 1) demonstrated dilution of deep Caribbean water with silicate-poor NADW about 190 km west-southwest of the Jungfern sill (the University of Puerto Rico PESCA, Programa Estudios Caribe, serial hydrographic station: 17 36′N, 67 00′). Dissolved silicate concentrations below 4.1 θ were diluted by as much as 4 μM (14%). Observations extending over two years indicated that this dilution occurred sporadically, in agreement with the intermittent renewals observed by STURGES (1975) and STALCUP *et al.* (1975).

From 1971 to 1975, we collected more data at the UPR serial station and occupied nine hydrographic transects across the basin along 67°W (between Puerto Rico and Venezuela) during a three-year period. The extent of this data set allows a statistical treatment to estimate the extent of deep water renewal across the entire basin.

METHODS

The UPR/PESCA serial station is at 17°36′N and 67°00′W (Fig. 1). It was sampled to maximum depths of 2500 or 3000 m using Nansen or Niskin bottles from January 1971 to May 1976 by R/V *Crawford*. From January 1971 to May 1972 the station was occupied bi-weekly, but after that date it was occupied monthly or bi-monthly.

From June 1972 to June 1975, a transect of eight to nine hydrographic stations along 67 W between La Parguera, Puerto Rico, and La Guaira, Venezuela, (Fig. 1) was occupied in June and July, October and November, and February and March of each year (except for 1974 when the June–July transect was missed). These transects were occupied by R/V *Crawford* with the exception of the February and March 1974 transect, which was occupied by R/V *Knorr*.

Dissolved silicate was determined according to the method of STRICKLAND and PARSONS (1968) with the modifications of FANNING and PILSON (1973). The method and precautions taken were described by FROELICH (1973). The analytical results were reproducible to ±0.8 μM (95% confidence) at the 28-μM level.

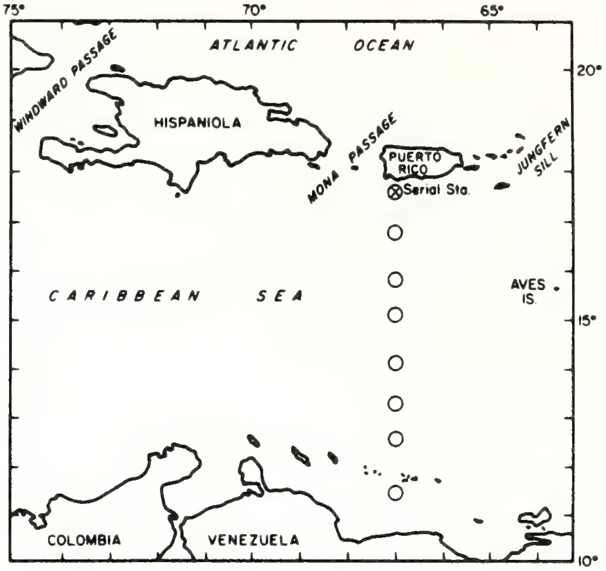

Fig. 1. Location of UPR PESCA serial station and approximate locations of stations along the PESCA 67 W hydrographic transect.

RESULTS

To demonstrate the effect of NADW inflow on mean silicate concentrations we grouped into depth intervals (Table 1) all data from the serial station and (separately) all data from stations occupied between 14 and 15 N (midway across the basin). The mean profile for the northern station is compared with that from the more southerly group of stations in Fig. 2.

There are two major differences in these profiles. First, the northern location has distinctly less dissolved silicate throughout the water column below 1500 m. Secondly, there is an apparent minimum in the profile from the serial station between 1600 and 2600

Table 1. Mean silicate values for 200-m intervals below 1000 *m at Pesca serial station* 17 36′*N*, 67 00′W (*53 stations*) *and for all PESCA Stations occupied in the middle of the Venezuela Basin* (*along* 67 00′ W *between* 14 N *and* 15 N)

Depth interval (M)	Serial station Number of observations	 Mean silicate (μM)	 SD	14 N to 15 N Number of observations	 Mean silicate (μM)	 SD
	N	x	σ	N	x	σ
1000–1199	49	26.0	1.3	19	26.6	1.0
1200–1399	37	26.9	1.5	14	27.2	0.9
1400–1599	43	27.4	1.6	15	27.4	1.4
1600–1799	47	27.3	1.3	15	28.3	1.0
1800–1999	36	26.9	1.3	13	28.1	1.4
2000–2199	39	27.1	1.6	14	28.6	1.0
2200–2399	35	27.3	1.8	6	29.1	1.4
2400–2599	30	27.2	2.1	11	29.2	1.2
2600–2799	18	28.0	2.0	9	28.7	1.4
2800–2999	10	28.0	1.9	7	28.7	1.7

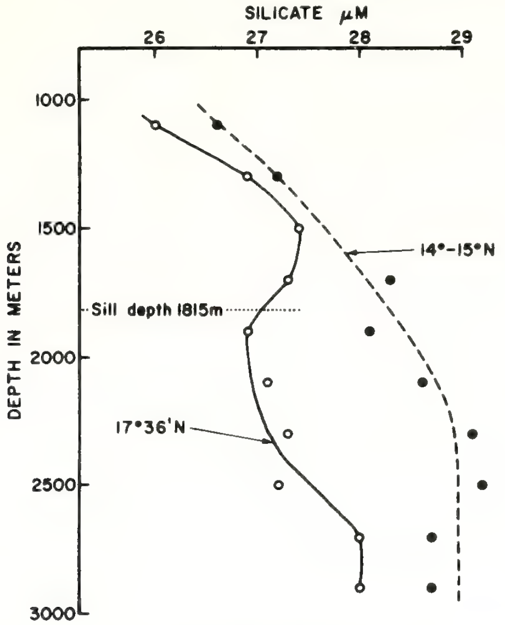

Fig. 2. Mean silicate values for 200-m intervals below 1000 m plotted vs depth for data from all 53 serial stations (17°36'N 67°00'W) (open circles and solid line) and for transect stations occupied between 14°N and 15°N along 67°00'W (solid circles and dashed line). The depth of the Jungfern Sill, as measured by Stalcup and Metcalf (1973), is shown at the left side of the figure.

m that is absent in the profile further south.

Sturges (1965) suggested that in sluggishly renewed basins, the degree of spatial heterogeneity of the deep water is related to rates of renewal and mixing. We have followed up his suggestion by testing data for north-south gradients in standard deviation, a measure of heterogeneity.

In the following analysis, we restricted ourselves to water below 1400 m, because the renewal water evidently does not extend shallower (Froelich and Atwood, 1974). We calculated the mean silicate values and standard deviations both between 1400 and 3000 m

Table 2. Mean silicate and standard deviation of that mean for 1° intervals of north latitude along 67°W across the Venezuela Basins. Values are given for two intervals, 1400 to 3000 m and 1400 m to deepest sample

	1400 to 3000 m			1400 m to deepest sample		
Latitude interval	N*	Mean silicate (µM)	SD	N*	Mean silicate (µM)	SD
17°–18°N	54	27.7	1.8	56	27.7	1.8
16°–17°N	66	27.8	1.5	91	27.9	1.5
15°–16°N	62	28.3	1.3	89	28.4	1.2
14°–15°N	90	28.4	1.3	134	28.6	1.3
13°–14°N	41	28.6	1.0	53	28.7	0.9
12°–13°N	55	29.2	1.0	69	29.2	1.0

*N = Number of observations.

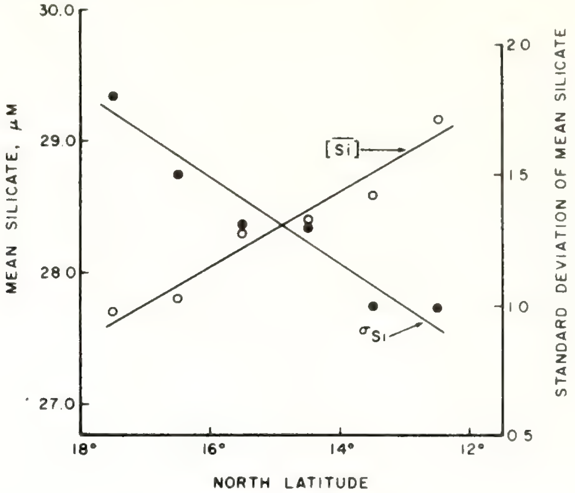

Fig. 3. Mean silicate values between 1400 and 3000 m (open circles) and standard deviation of those means (solid circles) plotted vs latitude for data from nine serial PESCA hydrographic transects across the Venezuela Basin along 67°N. Least squares fittings of the data plotted yield Si = −0.29 (latitude) + 32.6, $r = -0.97$ and $S_s = 0.16$ (latitude) = −1.0, $r = 0.96$. Plots including data below 3000 m yield essentially identical equations and correlation coefficients.

and between 1400 m and the bottom for 1° segments along the 67°W transect (Table 2). We included the 1400- to 3000-m analysis because the serial station and the data in the 17 to 18°N segment extend only to a maximum of 3000 m. Inclusion of the data from deeper than 3000 m makes little difference in the final results.

Mean silicate values increase from about 27.7 μM in the north to 29.0 μM in the south (Fig. 3). The standard deviations decrease from about 1.8 μM in the north to 1.0 μM in the south. The probability that the relationships of means and standard deviations versus latitude (Fig. 3) occurred by chance is less than 0.01 (N-6) in each case. We also tested the slope of the mean silicate versus latitude plot to see if it was significantly greater than zero using Fisher's (1950) extension of the Student's *t*-test. The *t* value obtained is 6.1 and the probability that the slope is zero is less than 0.01.

We also used the *t* test to determine whether or not there is a significant difference in mean silicate values for various latitude intervals along 67°W (Table 3). In each case, the means are decidedly different.

Thus, the evidence is strong that there is a real southward increase in mean silicate below 1400 m along 67°W. The increase is almost linear. Similarly, the standard deviations

Table 3. t-Test of significance of differences in mean silicate values for various latitude intervals along 67°00′W

Intervals compared	d.f.*	*t*-value	Probability†
17°-18°N vs 15°-16°N	114	2.0	0.05
17°-18°N vs 12°-13°N	107	5.4	0.01
15°-16°N vs 12°-13°N	115	4.3	0.01

* Degrees of freedom. † Probability that difference occurred by chance.

decrease from 1.8 in the north to about the level of analytical precision in the south. These lateral gradients are caused by intermittent injection of NADW into the deep basin in the north and by mixing of the resulting heterogeneous water mass southward across the basin.

Acknowledgements—The helpful suggestions of Mr WILLIAM G. METCALF and Mr MARVEL C. STALCUP of Woods Hole Oceanographic Institution, and of Dr C. PETER DUNCAN of the University of Puerto Rico are gratefully acknowledged. This research was supported by the Marine Sciences Department and the Comite de Investigaciones of the University of Puerto Rico in Mayaguez and National Science Foundation Grant No. DES75 22445

REFERENCES

FANNING K. A. and M. E. Q. PILSON (1973) On the spectrophotometric determination of dissolved silica in natural water. *Analytical Chemistry*, **45**, 136–140.

FISHER SIR RONALD (R.A.) (1950) *Contributions to mathematical statistics*, Wiley.

FROELICH P. N. (1973) Dissolved silicate in the Venezuela Basin of the Caribbean Sea. Masters Thesis, Department of Marine Science, University of Puerto Rico at Mayaguez, Puerto Rico, 62 pp.

FROELICH P.N. JR and D.K. ATWOOD (1974) New evidence for sporadic renewal of Venezuela Basin Water. *Deep Sea Research*, **21**, 969–975.

ICHIYE T. (1972) Experiments on circulation of the Gulf of Mexico and the Caribbean Sea with a rotating tank. Memorial de IV Congreso Nacional de Oceanografia. Mexico, D.F., 17–19 November 1969, pp. 37–57.

METCALF W. G. (1969) Dissolved silicate in the deep North Atlantic. *Deep-Sea Research, Supplement*, **16**, 139–145.

RICHARDS F.A. (1958) Dissolved silicate and related properties of some western North Atlantic and Caribbean waters. *Journal of Marine Research*, **17**, 449–465.

STALCUP M. C. and W. G. METCALF (1973) Bathymetry of the sills for the Venezuela and Virgin Islands basins *Deep-Sea Research*, **8**, 739–742.

STALCUP M. C., W. G. METCALF and R. G. JOHNSON (1975) Deep Caribbean inflow through the Anegada-Jungfern Passage. *Journal of Marine Research, Supplement*, **33**, 15–35.

STRICKLAND J. D. H. and E. PARSONS (1968) *A practical handbook of sea water analysis*, Fisheries Research Board of Canada 311 pp.

STURGES W. (1965) Water characteristics of the Caribbean Sea. *Journal of Marine Research*, **23**, 147–161.

STURGES W. (1970) Observations of deep water renewal in the Caribbean. *Journal of Geophysical Research*, **75**, 7602–7610.

STURGES W. (1975) Mixing of renewal water flowing into the Caribbean Sea. *Journal of Marine Research, Supplement*, **33**, 117–130

SVERDRUP H. U., M. W. JOHNSON and R. H. FLEMING (1942) *The oceans: their physics, chemistry and general biology*. Prentice-Hall, 1087 pp.

WORTHINGTON L. V. (1955) A new theory of Caribbean bottom water formation. *Deep-Sea Research*, **3**, 3301–3302.

WORTHINGTON L. V. (1956) The temperature increase in Caribbean deep water since 1933. *Deep-Sea Research*, **3**, 234–235.

WORTHINGTON L. V. (1966) Recent oceanographic measurements in the Caribbean Sea. *Deep-Sea Research*, **13**, 731–739.

WORTHINGTON L. V. (1971) Water circulation in the Caribbean Sea and its relationship to North Atlantic circulation. *Symposium on Investigations and Research in the Caribbean Sea and Adjacent regions*. UNESCO, 18 to 26 November 1968, Curaçao. pp. 181–191.

WUST G. and A. GORDON (1964) *Stratification and circulation in the Antillean-Caribbean basins*, Columbia University Press, 201 pp

14. NOAA Tech. Memo. ERL AOML-40, 26 pp.

COMPARISON OF MANUAL AND AUTOMATED METHODS OF INORGANIC MICRO-NUTRIENT ANALYSES

George A. Berberian
Michael Barcelona*

Abstract: This report covers the organization, execution and results of an experiment designed to intercompare manual wet-chemical analysis with AutoAnalyzer methods for the common micro-nutrients of interest to marine chemists and oceanographers. The results demonstrate that the sacrifice of sensitivity (shorter light paths, use of secondary absorption maxima) for economy and speed of sample throughout using AutoAnalyzer techniques is most serious for low levels of silicate, phosphate and nitrite/nitrate. However, at levels most often encountered in intermediate, eutrophic or deep waters, the loss of sensitivity is not so important. Both methods proved to yield similar accuracy in the analysis of synthetic standards at higher levels. The improved precision and convenience of the AutoAnalyzer techniques commends its use where appropriate.

---

*California Institute of Technology, Kerckhoff Marine Laboratory, Corona del Mar, CA 92625

15. NOAA Tech. Memo. ERL AOML-36, 67 pp.

NOAA Technical Memorandum ERL AOML-36

INORGANIC NUTRIENTS AND DISSOLVED OXYGEN VARIATION DETERMINED FROM HISTORICAL DATA AT THREE PROPOSED OCEAN THERMAL ENERGY CONVERSION (OTEC) SITES: PUERTO RICO, ST. CROIX, AND NORTHERN GULF OF MEXICO

Shailer R. Cummings Jr., Donald K. Atwood, Joan M. Parker,
Atlantic Oceanographic and Meteorological Laboratories, NOAA,
Miami, Florida 33149

Abstract

Inorganic nutrients and dissolved oxygen concentrations from the available historical data set at three proposed Ocean Thermal Energy Conversion (OTEC) sites were reviewed. These sites are Puerto Rico, St. Crox, and northern Gulf of Mexico. Dissolved oxygen and inorganic nutrients vary in a consistent manner with depth within a narrow range in the Puerto Rico and St. Croix study areas. Nutrient and dissolved oxygen variability is greater in the upper 800 m of the northern Gulf of Mexico than in the Carribbean. Short term local events influencing variability were identified only in the northern Gulf of Mexico areas where a large portion of the surface variability is due to the Mississippi River plane. Loop Current Eddies are a source of subsurface variability to depths between 700 m and 800 m in the northern Gulf of Mexico. These eddies decrease nutrient concentrations in the Gulf as they transport in lower nutrient Caribbean water. Dissolved oxygen concentrations increase as the loop Current Eddies traverse the Gulf of Mexico.

16. Science 205, 999-1001.

Observation of a Subsurface Oil-Rich Layer in the Open Ocean

George R. Harvey, Adolfo G. Requejo, Philip A. McGillivary, and John M. Tokar

Abstract. *A layer of water at a depth of 200 meters containing 3 to 12 milligrams per liter of oil was found during February and March 1978 over a distance of 800 nautical miles in the southwest North Atlantic and the eastern Caribbean. The geochemistry and carbon-14 activity of the oil shows it to be a weathered crude, probably from a submarine seep. Although the dimensions of the oily layer were not determined, conservative estimates indicate that more than 1 megaton could have been present.*

During February and March 1978, on a cruise investigating the chemistry of the subtropical underwater (*1*), we found an extended layer of unusually oil-rich water about 200 m below the surface of the southwestern North Atlantic Ocean and the eastern Caribbean Sea (Fig. 1). At stations 11 to 24, a transect of 800 nautical miles, hexane extracts of seawater obtained from depths of 150 to 250 m yielded 3 to 12 mg of weathered oil per liter (average of 6 mg per liter). Extracts of samples from both above and below the oily layer at stations 11 to 24 and from all depths at stations 26 to 38 had hydrocarbon concentrations (micrograms per liter) and distributions typical of the open ocean (*2*). Because the sampling at each station was centered about the subtropical underwater, the discovery of the oily layer was serendipitous.

Water was collected in a 90-liter polyvinyl chloride drop-top sampler and transferred into 20-liter glass bottles through steel tubing. Forty liters of each sample was batch-extracted with hexane within 1 hour of collection. The extracts were concentrated by means of a vacuum within 1 hour of collection, esterified with boron trifluoride-methanol reagent,

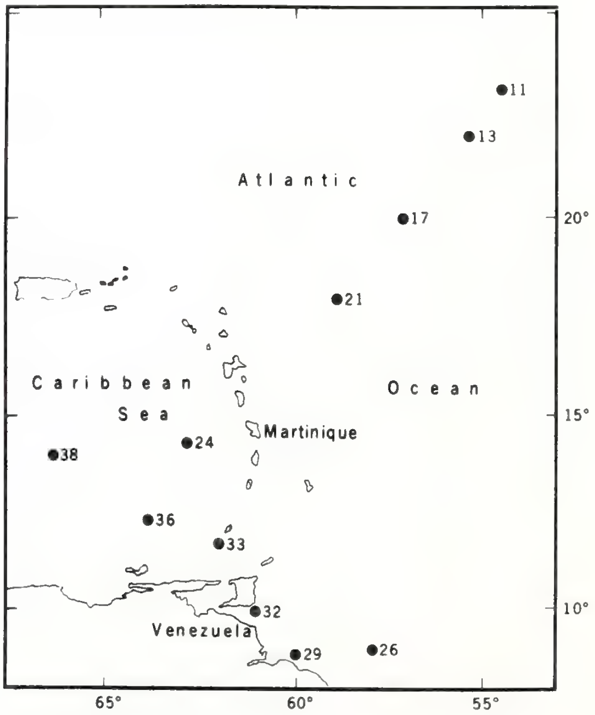

Fig. 1. Sampling stations of NOAA *Researcher* cruise R-78-1. The oily layer was found at stations 11 (12.6 mg, 200 m), 13 (5.8 mg, 200 m), 17 (9.6 mg, 270 m), 21 (3.2 mg, 145 m), and 24 (2.8 mg, 150 m and 5.7 mg, 200 m).

0036-8075/79/0907-0999$00.50/0 Copyright © 1979 AAAS

Table 1. Percentage of fatty acid distributions.

Station	Depth (m)	14:0[*]	15 br	15:0	16:1	16:0	17 br	17:0	18:1	18:0	20:1	20:0	22:0	24:0
11	56	10	1.7	3.0	6.5	33.6	2.9	1.5	13.6	15.4	0.5	0.8	0.8	0.8
11	200	0.2	0.0	0.0	0.0	32.1	0.4	0.0	33.2	13.6	1.0	5.0	0.8	2.9
17	130	6.2	2.0	3.0	9.6	26.8	1.9	2.3	4.3	10.3	0.6	0.6	0.1	0.2
17	270	0.0	0.0	0.0	0.0	28.1	0.3	0.0	31.1	12.7	0.9	6.1	0.3	5.1

[*] In this nomenclature, 14:0 is a 14-carbon straight-chain acid with no pi bonds, 16:1 has one pi bond, and br indicates branching as determined by the GC retention index and mass spectral analysis.

and fractionated (*3*). The paraffinic and aromatic hydrocarbons, fatty acid methyl esters, and silated sterol fractions were analyzed at sea by gas chromatography (GC) on 30 m by 0.25 mm wall-coated, open tubular glass capillary columns coated with either SE-30 silicone oil or Dexsil 300. During the cruise, all likely sources of extraneous contamination, such as the ship's fuel, lubricants and hydraulic fluid, the water sampler, and other associated hardware, were extracted, fractionated, and analyzed by GC. None of these extracts resembled those from the oily layer. Procedural blanks, run at regular intervals during the cruise, did not resemble the subsurface oil.

The fractionated oil consisted of 60 to 70 percent hydrocarbons, 5 to 10 percent fatty acids, and 4 to 8 percent sterols and fatty alcohols. The GC of the paraffin fraction showed a narrow-range (C_{16} to C_{26}) symmetrical, unresolved complex multiplet (*4*) centered at n-C_{20} with only traces of n-alkanes evident. Such symmetrical distributions are usually not observed in pelagic tars (*5*). The pristane to phytane ratio varies from 0.9 at station 24 to 1.2 at station 11. The C_{18} to phytane ratio of 0.3, the C_{22} to background ratio of 0.2, and the absence of alkanes above C_{25} indicate a biochemically weathered oil that has not undergone evaporative weathering (*6*). Comparison of these ratios with those from sunken tar weathering studies (*7*) indicates that the subsurface oil was weathered for 1 to 2 years when we found it. The infrared and mass spectra indicate only normal, saturated, cyclic and branched hydrocarbons in fraction 1 (*3*). Gravimetric and GC calculated weights agree within 10 percent. The aromatic fraction was analyzed by computer-assisted GC and mass spectrometry. In addition to abundant ions due to alkylated naphthalenes, anthracenes, and phenanthrenes, mass fragmentograms of mass to charge ratios of 184, 198, and 212 revealed the presence of dibenzothiophenes. Dibenzothiophenes are not biosynthesized and are known only in fossil fuels.

The nonhydrocarbon fractions in the extracted oil were distinct from those extracted from samples outside the oily layer and must have a different source. Table 1 shows the fatty acid distribution at two typical stations above and in the oily layers. The shallower samples had distributions similar to those observed by others in open-ocean waters (*8*). In contrast, the distribution of acids associated with the oil is biased toward the longer chain lengths, and $C_{18:1}$ accounts for one-third of the total acids.

The sterol distribution of open-ocean water has been studied by Gagosian (*9*). In the present study, analyses of water outside the oily layer agree with his work and indicate that cholesterol is the dominant sterol at a concentration of about 1 μg per liter. In contrast, the dominant sterol in the oil was β-sitosterol or clionasterol (*9*) at a concentration of more than 300 μg per liter; cholesterol was only a minor component at 5 μg per liter.

Because of its quantity, quality, and observed distribution, we believe this oil layer results from a natural seep. This is supported by the absence of natural ^{14}C activity in the sample from station 11, which thus has an apparent age of >22,000 years before present. The total amount of oil entering the sea from natural seeps is unknown. On the basis of limited data from known seeps and conservative extrapolations, Wilson *et al.* (*10*) estimated that between 0.2 × 10^6 and 6.0 × 10^6 tons of oil per year enter the oceans from seeps. Blumer (*11*) argued that such estimates were too high. The currently used estimate of 0.6 × 10^6 ton/year reported in a workshop of the National Academy of Sciences (*12*) is obviously a compromise figure.

The breadth and thickness of the oily layer reported here is not known, but integrating over a conservative estimate of its dimensions, that is, 800 nautical miles long, 1 nautical mile wide, and 100 m thick, results in a total of more than 1 megaton.

Accurate assessment of the quantity, frequency, and duration of subsurface oil seeps is beyond present resources or technology. Similar discharges of crude oil may occur elsewhere and would pass undetected except by chance. The quantity of the oil described here may have been greater than the total estimated oil entering the sea annually (*12*). An attempt was made, on another cruise in January 1979 to determine the width of the oily layer. Sampling was done between 10° and 21° north latitude on a course of 130°. This cruise crossed the 1978 track near Martinique. Gravimetric and GC analyses of detailed profiles from seven stations revealed no trace of the oil found 11 months before.

We believe the most likely source of the oily layer is a seep located on the Venezuelan shelf at a depth of about 200 m. This is an area where offshore seeps have been reported. Such oil could be carried north at depth, probably in a dispersed state, by the Guyana and Antilles currents until entrained by midwater easterly flows into the southern Sargasso Sea as discussed by Reid (*13*). In fact, observations of subsurface oil east of the Antilles represent independent evidence supporting physical indications of a mid-depth easterly return of water into the subtropical North Atlantic (*13*).

GEORGE R. HARVEY
ADOLFO G. REQUEJO
PHILIP A. MCGILLIVARY
JOHN M. TOKAR

NOAA/Atlantic Oceanographic and Meteorological Laboratories, Ocean Chemistry Laboratory, Miami, Florida 33149

References and Notes

1. L. V. Worthington, *On the North Atlantic Circulation* (Johns Hopkins Press, Baltimore, 1976), chap. 14.
2. R. A. Brown and H. L. Huffman, Jr., *Science* **191**, 847 (1976).
3. The fractionation is adapted from J. W. Farrington and B. W. Tripp, *Geochim. Cosmochim. Acta* **41**, 1627 (1977). A portion of the oil not exceeding 5 mg was chromatographed on 3 cm of alumina (5 percent deactivated with H_2O) over 3 cm of silica (5 percent deactivated with H_2O) in a disposable Pasteur pipette. Eight fractions (F) were eluted with 1.5 ml of each of the following: hexane, 10 percent benzene-hexane, 20 percent benzene-hexane, 50 percent benzene-hexane, benzene, 5 percent methanol-benzene, 10 percent methanol-benzene, and 20 percent methanol-benzene. Saturated hydrocarbons were in F-1, aromatics were in F-2 and F-3. Fatty acid methyl esters were in F-4 and F-5. Sterols were in F-7 and F-8.
4. J. W. Farrington and B. W. Tripp, in *Marine Chemistry in the Coastal Environment*, T. M. Church, Ed. (ACS Symposium Series No. 18, American Chemical Society, Washington, D.C., 1975), pp. 267–284.
5. J. N. Butler, B. F. Morris, J. Sass, "Pelagic tar from Bermuda and the Sargasso Sea," *Bermuda Biol. Stn. Res. Spec. Publ. No. 10* (1973), appendix 3.

6. M. Blumer, M. Ehrhardt, J. H. Jones, *Deep-Sea Res.* **20**, 239 (1973).
7. A. Zsolnay, *ibid.* **25**, 1245 (1978).
8. P. M. Williams, *J. Fish. Res. Board Can.* **22**, 1107 (1965).
9. R. B. Gagosian, *Geochim. Cosmochim. Acta* **39**, 1443 (1975).
10. R. D. Wilson, P. H. Monaghan, A. Osanik, L. C. Price, M. A. Rogers, *Science* **184**, 857 (1974).
11. M. Blumer, *ibid.* **176**, 1257 (1972).
12. *Petroleum in the Marine Environment* (National Academy of Sciences, Washington, D.C., 1975).
13. J. L. Reid, *J. Geophys. Res.* **83**, 5063 (1978).

14. We thank J. Farrington and N. Frew for the mass spectral analyses and M. Ehrhardt, J. Farrington, and W. Sackett for valuable discussions. The ^{14}C activity was run by E. Druffel, La Jolla Radiocarbon Laboratory (University of California, San Diego) through the courtesy of P. M. Williams under NSF grant No. EAR76-226-23. The officers and crew of the National Oceanic and Atmospheric Administration (NOAA) ship *Researcher* made the sampling both possible and enjoyable.

22 May 1979

17. Environmental Science & Technology 13, No. 10, 1225-1229.

Sewage Contamination in the New York Bight. Coprostanol as an Indicator

Patrick G. Hatcher*[1] **and Philip A. McGillivary**

National Oceanic and Atmospheric Administration, Atlantic Oceanographic and Meteorological Laboratories,
Ocean Chemistry Laboratory, 15 Rickenbacker Causeway, Miami, Fla. 33149

■ Sediments of the New York Bight are analyzed for coprostanol, a fecal steroid, to determine the degree of sewage contamination. Coprostanol, when reported as a percentage of total steroids (% coprostanol), can be quantitatively related to the amount of sewage-derived organic matter. Furthermore, coprostanol is quite persistent in anoxic silts of the Bight and, thus, can be used to delineate historical contamination in these silts. Based on the sediments analyzed, the New York Bight is shown to be highly contaminated with sewage (most likely ocean-dumped sewage sludge), especially in the topographically low areas near the dump site, where black silts have been known to accumulate.

With the ever-increasing need for our society to dispose of its fecal wastes in a way that will not endanger the environment, a means of delineating sewage contamination is of prime concern. Both chemical and biological indicators of sewage contamination have been considered to identify areas of contamination and potential health hazard. Fecal coliform counts have been used extensively to delineate such areas; however, chemical markers such as fecal steroids are now being considered as more suitable tracers of sewage contamination (*1–5*). These steroids are thought to be formed exclusively by enteric bacterial reduction of unsaturated sterols in higher animals (*6, 7*), and include primarily 5β-cholestan-3β-ol (coprostanol) and 24β-ethyl-5β-cholestan-3β-ol (24β-ethylcoprostanol).

Attempts have been made to detect fecal steroids in the marine environment adjacent to sewage discharges (*2, 8*). Smith et al. (*2*) failed to detect fecal steroids in both water and sediments of Galveston Bay, Tex.; however, Hatcher et al. (*8*) recently reported the presence of coprostanol and 24β-ethylcoprostanol in sewage contaminated sediments of the New York Bight and noted coprostanol's promise as a chemical marker for sewage contamination. Considering that 5×10^6 tons of sewage sludge is being barge dumped in the New York Bight per year, it was not surprising that fecal steroids were found in sediments near the dump site. More recently, Goodfellow et al. (*9*) reported the presence of fecal steroids in Clyde Estuary, Great Britain, supporting previous suggestions that they be used as tracers for sewage.

Sedimentation in the New York Bight is quite varied as a large range of sedimentary facies are observed (*10*). For the most part, fine- to medium-grained sands predominate. A topographic depression transects the Bight in a northwest to southeast direction (Figure 1). This feature is known as the Hudson Shelf Valley. In the inner portions of the Bight, the shelf valley broadens into a feature known as the Christiaensen Basin. Fine silts and muds accumulate in these topographic lows. In the Christiaensen Basin these silts are black and oily, presumably as a result of anthropogenic contamination (*10*). Sewage sludge, dredge spoils, acid wastes, and other anthropogenic materials are continuously being dumped in the area of the Christiaensen Basin. The continued dumping of wastes and the accumulation of black silts near bathing beaches of Long Island have generated a great deal of concern for the need to determine the source of these silts. More specifically, it is important that we be able to determine the degree to which they are contaminated by fecal materials. Thus, coprostanol provides an ideal tracer for such a need.

We have analyzed surficial sediments and a box core for fecal steroids in an effort to learn more about their spacial and temporal distribution in the various sedimentary facies of the New York Bight. Our aim is to identify the principal areas of sewage contamination and to estimate the relative amounts of anthropogenic components in the sedimentary organic matter.

Methods

Laboratory and Field Methods. Bottom sediment samples were collected from 1973 through 1977 (see Table I for dates of collection) in the New York Bight at the locations shown in Figure 1 using a Shipek grab sampler or Bouma box corer. The samples were immediately frozen and later freeze-dried. Weighed samples were solvent extracted (Soxhlet, 1:1 benzene/methanol) for 24 h and the extract was brought to a known volume. Two aliquots were taken, one of which was treated with an internal standard (cholesterol). Both aliquots were then saponified for 2 h at 100 °C with 0.5 N KOH in methanol, acidified with aqueous HCl, and extracted with CCl_4. The CCl_4 extracts were evaporated to dryness and esterified with 14% BCl_3 in methanol at 100 °C for 5 min. The solutions were then treated with H_2O and extracted with hexane. The hexane extracts were placed on a silica gel column (activated at 110 °C), and the column was successively eluted with hexane, benzene, and methanol. The methanol eluate was evaporated to dryness and silylated with *N,O*-bis(trimethylsilyl)acetamide.

The silylated solution was directly injected onto a Tracor 550 gas chromatograph equipped with a 2 m × 2 mm (i.d.) column packed with 1% Dexsil 300 on Supelcoport (80/100 mesh) or a 6 ft × 1/8 in. o.d. column packed with 3% OV-1 on Chromosorb W(HP). The columns were generally temperature programmed from 150 to 270 °C at 4 °C/min, with a

---

[1] Present address, U.S. Geological Survey, Office of Energy Resources, 956 National Center, Reston, Va. 22092.

Table I. Coprostanol, Total Steroid, and TOC Content of New York Bight Sediments

sample	date collected	physical description	TOC, % [a]	coprostanol, ppm	total steroids, ppm	(total steroids/TOC) × 10^4	coprostanol, % [b]
F2-3	9/73	clean sand	0.18	0.082	3.6	20	2.3
F2-5	9/73	clean sand	0.10				0.47
F2-7	9/73	black sand	1.3	4.3	39	30	11
F2-8	9/73	black sand	1.1				14
F2-12	9/73	sandy silt	0.65	1.5	18	28	6.5
F2-13	9/73	black silt	2.7	4.8	44	16	11
F2-15	9/73	clean sand	0.097				3.1
F2-19	9/73	clean sand	0.11	0.15	3.6	32	0.42
F2-21	9/73	clean sand	0.18				3.9
F4-21	11/73	clean sand					0.64
F2-25	9/73	clean sand	0.096	0.056	0.66	68	0.58
P-21	6/74	black silt	2.3	5.2	130	56	4.0
OP-4	6/74	black silt	1.6	2.8	90	56	3.1
MN-4	6/74	olive silt	2.6	1.1	65	25	1.7
LK-4	6/74	olive silt	0.34	0.10			
2B-96	8/73	black silt	3.1				9.1
K6-77-0	6/77	black silty sand	0.73				3.4
K6-77-12b	6/77	silty sand	0.31				>0.1
BX-6 (1-3)[c]	10/75	black silt	4.1				15
BX-6 (14-17)	10/75	black silt	4.1				14
BX-6 (21-24)	10/75	black silt	1.9				14
BX-6 (28-31)	10/75	black silty sand	0.89				11
BX-6 (36-39)	10/75	black silty sand	1.0				11

[a] Percent of dry sediment weight. [b] Percent of total steroids. [c] Centimeters depth in the core.

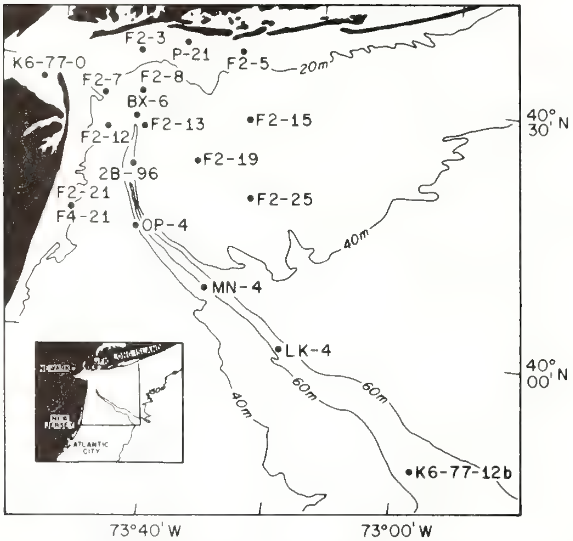

Figure 1. Index map of the New York Bight showing grab sample locations and location of the box core (BX 6)

4-min initial hold. The eluting gases were detected with a flame ionization detector, the response of which was recorded and integrated with a Hewlett-Packard 3380A reporting integrator. Concentrations of coprostanol were calculated with respect to the added internal standard, cholesterol, after corrections were made for the natural concentrations of cholesterol.

In the course of our analyses, our laboratory acquired glass capillary capabilities, and most samples analyzed on packed columns were rechromatographed on an 18 m × 0.2 mm WCOT glass capillary coated with SE-30. Additional samples were processed entirely on capillary columns. In this case, chromatograms were generated by a Hewlett-Packard 5840 gas chromatograph programming from 200 to 270 °C at 4 °C/min, with a 4-min initial hold. The capillary column yields much better resolution of the steroids. Both cholesterol and cholestanol are well resolved for quantification. The coprostanol content (parts per million) calculated from both packed and capillary columns agrees to within the analytical error of 20%. The total steroid content is calculated using only the capillary column, and the relative concentrations of individual steroids (percent of total steroids) are reported with a relative precision of ±10%.

Data Presentation. Steroids in New York Bight sediments are not nearly as varied as other near-shore sediments examined by Lee et al. (*11*). Coprostanol, cholesterol, cholestanol, brassicasterol, campesterol, 24β-ethylcoprostanol, stigmasterol, and sitosterol are the dominant steroids identified by gas chromatography/mass spectrometry. Aside from the fecal steroids, coprostanol and 24β-ethylcoprostanol, all others are common in uncontaminated coastal marine sediments (*11*, *12*).

Our immediate interests lie in the quantitative determination of fecal steroids in sediments to estimate the degree of sewage contamination. Coprostanol is better suited for quantitative determinations because 24β-ethylcoprostanol coelutes with campesterol on the gas chromatographic column. Since campesterol is fairly common in the New York Bight sediments, any quantitative estimate of the 24β-ethylcoprostanol content is impossible under the conditions used. The coprostanol peak is free of any coeluting compounds as determined by detailed mass spectrometry.

In general, the coprostanol content of sediments is related to the total organic carbon (TOC) content. The TOC of sandy sediments is probably related to the amounts of fine-grained particles trapped between the grains. Any comparison of coprostanol contents using dry mass as a normalizing parameter (e.g., reporting coprostanol as parts per million) is highly dependent on the grain-size distribution of sediments. In many contexts, it is more meaningful to normalize coprostanol content to total steroid content, as dependence on grain size would be eliminated. The resulting parameter, hereafter referred to as percent coprostanol, can then be used to determine what fraction of the steroids, or possibly the organic matter, is of fecal origin. Thus, the percent coprostanol for a sediment can be calculated by simply reporting the chromatographic peak area of coprostanol as a percentage of the sum of the areas for all steroids, after corrections are made for differences in chromatographic responses. Absolute concentrations need not be calculated.

In sewage sludge, coprostanol accounts for approximately 33% of the total steroids as determined by analysis of four sludges from various treatment plants in New York. Thus, the percent coprostanol content of a pure sludge-derived sediment is approximately 33%. If sewage sludge or sewage-derived particulate matter were to mix with nonsewage or natural materials containing steroids, the resultant mixture would have lower values of percent coprostanol. Theoretically, the lowest value obtainable would be 0%, as natural steroids do not contain coprostanol. Thus, a scale is established whereby the percent coprostanol content of a sediment would be indicative of the amount of sewage admixed with natural organic matter. This scale, however, may not be linear because the steroid concentration of sewage-derived organic matter may not be the same as that of natural organic matter. The steroid distribution resulting from the mixing of equal quantities of sewage and natural organic matter may be heavily influenced by that of either source. To determine the approximate steroid content of the two sources, the total steroid concentrations of both low and high coprostanol sediments are normalized to TOC (Table I). No significant relationship was observed between total steroids/TOC and percent coprostanol (Kendall τ test, $P > 0.05$). In fact, simple examination of these data indicates that, within an order of magnitude, the steroid content of the sedimentary organic matter is relatively constant regardless of the percent coprostanol or nature of the source materials. Notwithstanding other factors that may alter the coprostanol content of a sediment relative to total steroids, the percent coprostanol parameter can, therefore, be used in a quantitative sense to determine the amount of sewage-derived organic matter and the 0 to 33% scale appears to be at least close to linear.

Results

Coprostanol in Surficial Sediments. The coprostanol concentrations in New York Bight sediments along with bulk sediment data are presented in Table I. Concentrations of coprostanol range from 0.056 ppm for a clean sand to 5.2 ppm for a black silt near the Long Island coast. All the black silts (P-21, F2-7, F2-13, and OP-4) have relatively high coprostanol contents, an indication that sewage contamination is high in these sedimentary facies. Of special concern is sediment P-21, a black silt collected from a near-shore "mud patch" of Long Island. Its coprostanol content is approximately equal to that of sample F2-13 located near the sewage sludge dump site.

The distribution of percent coprostanol in New York Bight surficial sediments is presented in Figure 2. The highest values (10–15%) are located in the area of the Christiaensen Basin where black silts and muds, high in TOC, are accumulating. Thus, the fear that these black silts are of sewage origin is very real. Nearly half, or possibly more, of the organic matter is sewage derived. This is consistent with the reports on TOC (*13*), polychlorinated biphenyls (*14*), trace metals (*15*), and biological data (*16*), which all suggest that the black silts of the Christiaensen Basin are heavily contaminated with anthropogenic wastes.

The amount of sewage contamination in silts of the Bight diminishes quite rapidly as a function of distance from the center of the Christiaensen Basin. Within 10 nautical miles (nmi) of the BX6 sample, the percent coprostanol drops to less than 10%, indicating that less of the organic matter is sewage derived. Within 50 nmi, the percent coprostanol is below detection and the sample is free from sewage contamination. North of the Basin, at station P-21, the 4.0% coprostanol in this black silt indicates that sewage is a small contributor to the sediment organic matter. Northwardly flowing currents have been observed in the Christiaensen Basin (*17*), and it is possible that these currents assist in transporting the dumped sewage sludge toward the beaches, where it can accumulate in "mud patches" as observed by Harris (*18*). Sample P-21 was taken from one of these "mud patches" near Atlantic Beach, Long Island.

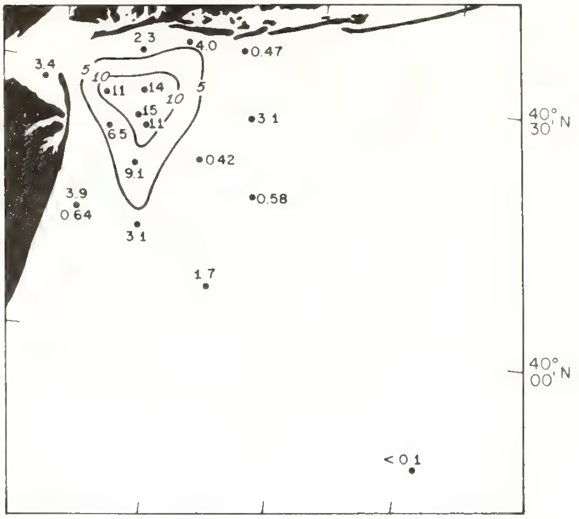

Figure 2. The percent coprostanol (percent of total steroids) distribution in surficial sediments of the New York Bight

Clean sands outside of the Christiaensen Basin are generally quite low in percent coprostanol (Table I) with values of less than 1%. However, several samples have values on the order of 2–3%, indicating some sewage contamination. There also appears to be a great deal of variability in the percent coprostanol content of sands. Two samples from the same location (F2-21 and F4-21) were collected within 2 months time of each other, and the percent coprostanol in one was 3.9 and in the other 0.42. Sands are mobile surfaces, and the organic matter trapped between or on sand grains may have numerous sources. If sewage is one of those sources, then it probably exists as fine-grained particles trapped in the sand. Sand in constant motion will not entrap significant amounts of fine-grained particles as it is constantly being overturned. The only organic matter present is most likely that attached to the larger grains. This material is likely to be nonsewage considering that sand grains are derived from other areas remote from the Bight. Samples low in percent coprostanol are probably characteristic of this type of sediment. However, if the sand is not in motion, fine-grained particles of the Bight can become entrapped between sand grains. Under these conditions, sewage can become a part of the sedimentary organic matter as is probably the case in samples F2-3, F2-21, and F2-15.

Coprostanol in the Core. In an attempt to determine the geochemical stability of coprostanol in the New York Bight sediments, we analyzed a box core taken in the Christiaensen Basin (see Figure 1 for location of box core BX6). The anoxic sediment is a black silt throughout its 39-cm length. Discrete horizons were subsampled and analyzed for coprostanol and total organic carbon (TOC). Furthermore, these same horizons were radiometrically dated by the ^{210}Pb method (*19*). Although the dating method suffers from some degree of uncertainty in nearshore sediments, the bottom of the core dates out at 26 ± 1 years B.P.

The percent coprostanol distribution and the percent TOC in this 26-year core are presented in Figure 3. At the surface, the percent coprostanol content is 15, one of the highest values observed to date for sediments in the Bight, an indication that

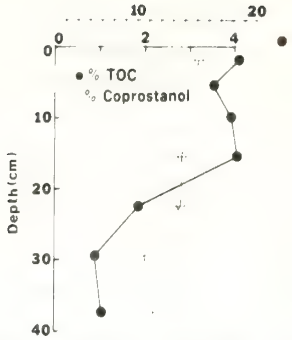

Figure 3. The percent coprostanol (O) and percent TOC (●) distributions in BX 6 core from the Christiaensen Basin. Percent coprostanol is reported as percent of total steroids

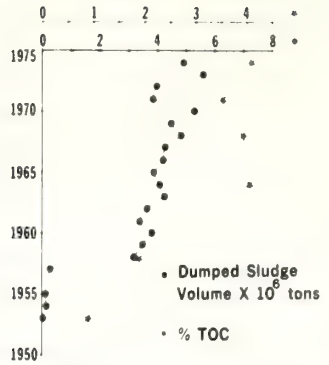

Figure 4. The volume of sewage sludge in 10^6 tons dumped in the New York Bight since 1953 (●) plotted with the TOC (★) of the corresponding time horizon as determined by the ^{210}Pb dates

sewage constitutes a large portion of the organic matter. With depth in the core, the percent coprostanol remains unchanged as the value of 11% recorded at the 36–39-cm horizon is, within analytical error, similar to the 15% at the surface. Therefore, for the 26-year time span of this core, the percent coprostanol has not changed greatly and has remained relatively high. This suggests that sewage contamination has dominated sedimentation in this area for at least 26 years.

Although the coprostanol data suggest a certain degree of constancy in the source nature of the organic matter throughout the core, the absolute amount of organic matter changes drastically as a function of depth as depicted by the TOC distribution. Above 20 cm, the TOC content is high with values of approximately 4%. Below 20 cm, the TOC drops to 2% or less. Assuming a reasonably steady sedimentation rate, the TOC content at each horizon should be related to the amount of organic matter that is supplied to the sediment at the time of deposition. Since the percent coprostanol suggests that the organic matter is largely sewage derived, the TOC distribution should record the history of sewage inputs to this area of the Bight. We managed to obtain volume estimates for the amount of sludge dumped in the Bight since 1953 (*20*) and plotted them along with TOC for the ^{210}Pb-dated horizons in the box core (Figure 4). The data suggest that the TOC content is directly related to the amount of sludge dumped, and therefore elevated levels of TOC in the Christiansen Basin are a direct result of sludge dumping operations. Prior to 1957, the volumes of dumped sludge were almost an order of magnitude less than in recent years. The TOC prifile reflects this, indicating that sewage contributed less to the sedimentary organic matter. In 1957, a large increase in the volume of dumped sludge occurred. At this time horizon in the core, an increase in TOC is also observed, suggesting that TOC and sludge volume are related. In 1971, a significant drop in the dumping volume is also reflected in the TOC, a further indication that the TOC in the Christiaensen Basin and the volume of dumped sludge are closely correlated.

Discussion

Coprostanol is an ideal tracer for sewage and, when reported as a percentage of total steroids (percent coprostanol), a quantitative estimate can be made of the amount of organic matter that is derived from sewage. However, several assumptions need to be made before any strict quantitative estimates are made based on percent coprostanol. First, we must assume that steroid contents of sewage sources and other nonanthropogenic sources are reasonably similar so that the percent coprostanol scale is linearly related to mixing or organic matter from the various sources. This linearity was shown earlier by noting that the total steroid/TOC ratio of all sediments was reasonably constant.

Second, factors other than simple mixing, which can possibly alter the percent coprostanol of a sediment, are differential solubilization and decomposition of coprostanol relative to other steroids. Although the solubility of cholesterol in distilled water has been examined (*3*), no definitive studies have been conducted to determine the solubility of coprostanol in seawater in the presence of particulate matter. Therefore, the solubility of coprostanol in New York Bight waters was investigated when samples of sewage sludge and of seawater-diluted sludge, collected in the plume of dumped sludge, were fractionated into dissolved and particulate phases (*21*). Greater than 95% of the steroids, including coprostanol, were present in the solid phase. Thus, differential solubility will have a small effect on the percent coprostanol since it has only a small effect on the absolute amount of coprostanol.

The other major factor that could affect the percent coprostanol content of a sediment is preferential decomposition, biological or chemical, of coprostanol relative to other steroids. Nishimura and Koyama (*22*) incubated cholesterol and cholestanol (the 5α isomer of coprostanol) in a lake sediment. Over a period of 450 days at 15 °C, the cholesterol and cholestanol added to sediments exhibited no significant changes. No aerobic/anaerobic control was imposed on these experiments, although the authors did note that their system was aerobic at the beginning and went anaerobic after 45 days. They observed minor decomposition of cholesterol while the system was aerobic. Under anaerobic conditions, essentially no decomposition was observed. Cholestanol was essentially preserved under aerobic and anaerobic conditions, at least for the duration of the experiment. If we accept the notion that cholesterol is typical of sterols and cholestanol of stanols, more specifically coprostanol, then little, if any, preferential alteration of coprostanol is expected to occur relative to other stanols and sterols in anoxic sediments similar to those examined by Nishimura and Koyama (*22*).

The silts and muds of the Christiaensen Basin are such sediments. The results obtained from our study of the core BX6 indicate that the coprostanol content relative to other steroids is relatively unaffected by decomposition as a function of time. Thus, for at least 26 years of sedimentation under anaerobic conditions, the percent coprostanol has not been altered significantly, as it provides a true historical measure of the degree of contamination.

In sandy sediments where the TOC content is usually less than 1% and aerobic conditions are present, the disposition of percent coprostanol as a quantitative indicator is unknown. Decomposition may play an important role in altering the relative concentrations of the various sterols and stanols.

Acknowledgments

We graciously acknowledge Lt. Larry E. Keister, Neryda Galceran, Lt. Richard H. West, Mike Macau, and Kevin O'Donnell for their laboratory assistance, as well as Dr. Donald K. Atwood, Dr. George R. Harvey, Dr. Peter Ortner, and Dr. John Farrington for their comments. Finally, we thank the officers and crew of the NOAA Ships Ferrel and G. B. Kelez and the R/V Venture for their sampling assistance.

Literature Cited

(1) Murtaugh, J. J., Bunch, R. L., *J. Water Pollut. Control Fed.*, **39**, 404–9 (1967).
(2) Smith, L., Kohler, D. P., Hempel, J. E., Van Lier, J. E., *Lipids*, **3**, 301–6 (1968).
(3) Kirchmer, C. J., Ph.D. Thesis, The University of Florida, Gainesville, Fla., 1971.
(4) Tabak, H. H., Bloomhuff, R. N., Bunch, R. L., in "Development in Industrial Microbiology", Vol. 13, American Institute of Biological Sciences Publication, Washington, D.C., 1972, pp 296–307.
(5) Dutka, B. J., Chau, A. S. Y., Coburn, J., *Water Res.*, **8**, 1047–55 (1974).
(6) Martin, W. J., Ravi Sabbiah, M. T., Kittke, B. A., Birk, C. C., Naylor, M. C., *Lipids*, **8**, 208–15 (1973).
(7) Eyssen, H., Parmentier, G., Compernolle, E., DePauw, G., Piessens-Denef, M., *Eur. J. Biochem.*, **36**, 411–21 (1973).
(8) Hatcher, P. G., Keister, L. E., McGillivary, P. A., *Bull. Environ. Contam. Toxicol.*, **17**, 491–8 (1977).
(9) Goodfellow, R. M., Cardoso, J., Eglinton, G., Dawson, J. P., Best, G. A., *Mar. Pollut. Bull.*, **8**, 272–6 (1977).
(10) Freeland, G. L., Swift, D. J. P., Stubblefield, W. L., Cok, A. E., *Am. Soc. Limnol. Oceanogr. Spec. Symp.*, **2**, 90–101 (1976).
(11) Lee, C., Gagosian, R. B., Farrington, J., *Geochim. Cosmochim. Acta*, **41**, 985–92 (1977).
(12) Huang, W. Y., Meinschein, W. G., *Geochim. Cosmochim. Acta*, **40**, 323–30 (1976).
(13) Hatcher, P. G., Keister, L. E., *Am. Soc. Limnol. Oceanogr. Spec. Symp.*, **2**, 240–8 (1976).
(14) West, R. H., Hatcher, P. G., Atwood, D. K., NOAA ERL-MESA Data Report, 1978, in press.
(15) Gross, M. G., *Geol. Soc. Am. Bull.*, **83**, 3163–76 (1972).
(16) Pearce, J. B., in "Marine Pollution and Sea Life", Ruivo, M., Ed., Fishing News (Books) Ltd., Surrey, England, 1972, pp 401–11.
(17) Charnell, R. L., Mayer, D. A., NOAA Technical Memo ERL MESA-3, 1975, 29 pp.
(18) Harris, W. H., *Am. Soc. Limnol. Oceanogr. Spec. Symp.*, **2**, 102–23 (1976).
(19) ^{210}Pb dates were obtained by L. Benninger, Yale University, (1977) under a NOAA, MESA Grant (04-4-022-35). The ages were determined after normalization to the organic matter as described by: Benninger, L. K., Ph.D. Thesis, Yale University, New Haven, Conn., 1976.
(20) Volumes prior to 1965 were supplied by Mr. Harold M. Stanford, NOAA, Marine Ecosystem Analysis Program; all others were obtained from Pararas-Carayannis, G., U.S. Army, Corps of Engineers Technical Memo, No. 39, 1973, 159 pp.
(21) Hatcher, P. G., Berberian, G. A., Cantillo, A., McGillivary, P. A., Hanson, P., West, R. H., in "Ocean Dumping of Industrial Wastes", Ketchum, B. H., Kester, D. R., and Park, P. K., Eds., Plenum Press, New York, in press.
(22) Nishimura, M., Koyama, T., *Geochim. Cosmochim. Acta*, **41**, 379–86 (1977).

Received for review June 19, 1978. Accepted June 6, 1979.

18. Nature 277, No. 5691, 50-51.

Silhouette photography of oceanic zooplankton

NO adequate method has been available to characterise a sample of zooplankton quickly and accurately. As Mullen noted[1], although relatively rapid, measures of standing crop such as displacement volume, dry weight, carbon content and electronic size spectra do not distinguish clearly between animals and plant or detrital material, much less between herbivores and carnivores. Direct microscopic enumeration has remained the only approach giving information detailed enough for many ecological studies. Unfortunately, this method is time-consuming, it cannot be undertaken routinely at sea, and it is feasible only after chemical agents have been added to 'fix' and then 'preserve' the sample. With time, plankton samples always deteriorate in preservatives, although the degree of this effect varies with species. We report here that a little-known photographic technique—high-speed silhouette photography[2,3]—can be used to analyse live zooplankton samples at sea.

The photographic system we used consisted of 8 × 10 inch Eastman fine-grain positive film 7302, an electronic flash with a xenon bulb (E.G. & G., Inc., FX6A) and a pulse duration of 3×10^{-6} s, and a plastic tray. Lamp-to-film distance was ~1.0 m. Immediately after collection, whole samples or aliquots of particularly dense samples were poured to a depth of about 1 cm into the plastic tray directly on top of the film. A glass plate was used to seal the top of the tray when seas were rough. One flash in a darkened room exposed the film. Samples were then preserved in the usual fashion (8% buffered formalin, pH ~8.2). Because of the shortness of the flash, action was stopped and results were unaffected by the motion of the ship or the subjects. Essentially any container and any powerful electronic flash could be used. The latter should be arranged to approximate a point-source as closely as possible. We housed the small-diameter xenon bulb in a non-reflective tube.

Fig. 1 Actual-size silhouette of a live zooplankton sample collected in the Sargasso Sea.

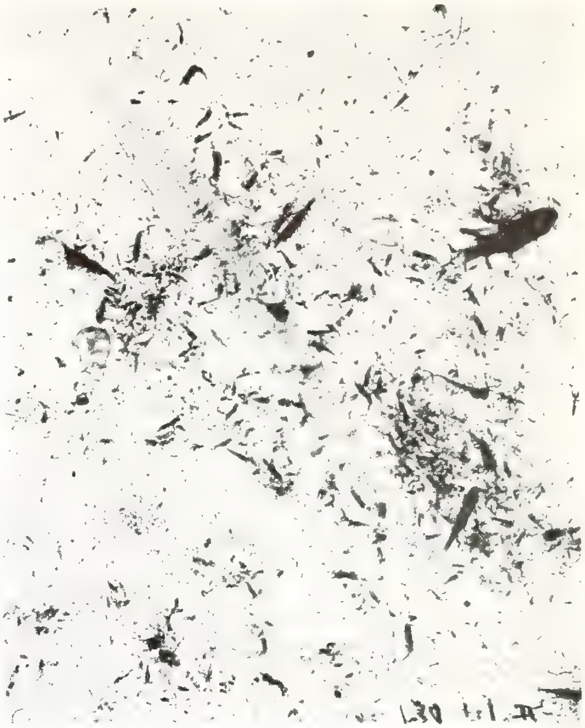

Figure 1 is the contact print of a negative produced as described above. The sample was collected between 0 and 89 m depth in the southern Sargasso Sea in February 1978 and represents 443 m^3 of seawater filtered through the 0.333-mm mesh of a MOCNESS net system[4]. The relatively large leaf-like animal is an eel larva at the leptocephalus stage.

Such negatives were generally examined at sea by placing them between two glass plates and counting random transects but, also, we have projected them on a viewing screen. To be enumerated in a negative, the density of organisms first would be considerably reduced by subsampling. Because the area of a

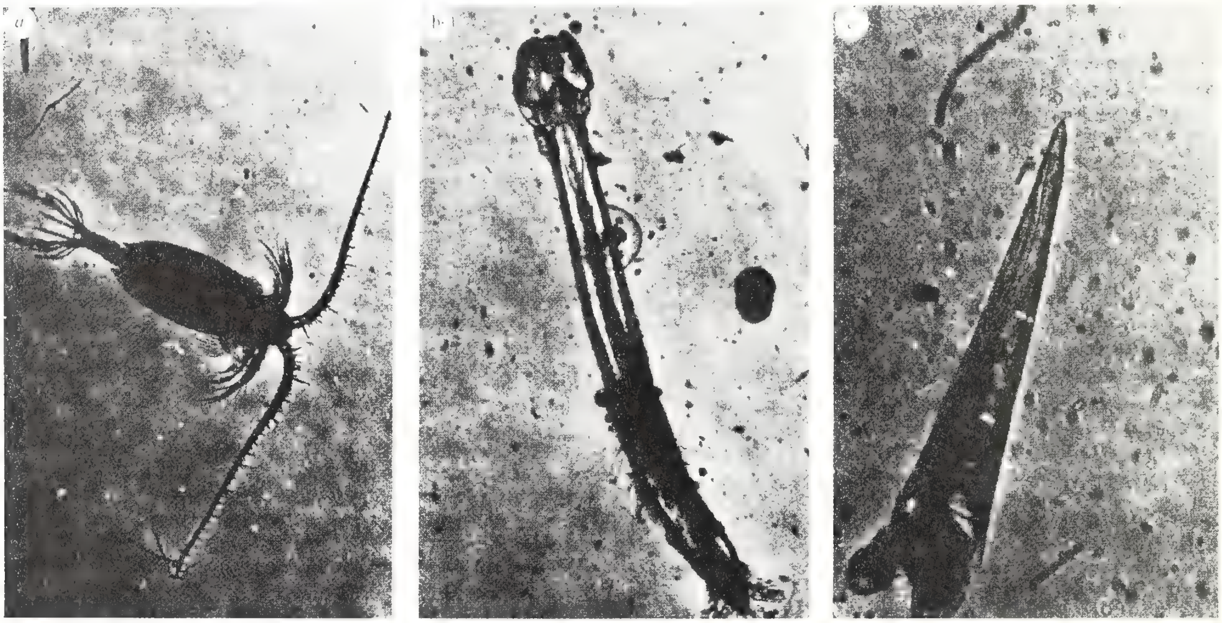

Fig. 2*a* Enlarged silhouette of a copepod, *Undinula vulgaris* female, ~2.5 mm. *b*, Enlarged silhouette of a chaetognath, *Pterosagitta draco* ~8 m. A fish egg lies just beyond the body trunk. *c*, Enlarged silhouette of a shelled pteropod, *Styliola subula*, ~2 mm.

negative corresponds to a known volume of ocean, it can be used to characterise quantitatively the plankton of a region if resolution were sufficient.

The resolution obtained by our optic-less imaging technique was more than adequate for this purpose. It was possible to make generic and, occasionally, specific identifications of specimens in many cases. Figure 2*a–c* shows enlargements of individual animals from actual-size negatives such as Fig. 1. The animals were alive when they were photographed. The copepod in Fig. 2*a* was moving rapidly and erratically. The chaetognath in Fig. 2*b* is easily identified even though the collarette is nearly gone, as frequently occurs in net collections. The pteropod mollusc in Fig. 2*c* has its wing-like flaps partly extended in their swimming position. The tissue of a preserved specimen typically would have contracted into an indistinguishable lump. A negative such as Fig. 1 could not have been obtained by conventional photographic or photomicrographic techniques, which do not give the breadth of the field of view and the depth of focus required to accommodate the entire sample, nor the high resolution we obtained despite ship and animal motion.

The rapidity, ease, and low cost of silhouette photography of plankton make it potentially useful to field workers with limited facilities. It can produce a permanent record of a live sample, which is unobtainable at present by any other means. Most important, the technique is non-destructive. Preservatives can be added after the image is recorded, and the sample can be sorted and examined on shore.

An *in situ* silhouette camera system designed to assess zooplankton patchiness has already been tested and a programme has been initiated to fully automate enumeration of our negatives by means of computer image-analysis techniques.

We thank Dr H. Michel for help in identifying species and Andrew Ramsey for technical advice.

PETER B. ORTNER
SHAILER R. CUMMINGS
R. PAUL AFTRING

National Oceanic and Atmospheric Administration,
Environmental Research Laboratories,
Atlantic Oceanographic and Meteorological Laboratories,
Ocean Chemistry Laboratory,
Miami, Florida 33149

HAROLD E. EDGERTON

Department of Electrical Engineering and Computer Science,
Massachusetts Institute of Technology,
Cambridge, Massachusetts 02139

Received 23 August; accepted 28 November 1978

1. Mullin, M. M. *Oceanogr. mar. Biol. A. Rev.* **7,** 293–314 (1969)
2. Edgerton, H. E. *J. of Microsc.* **110,** 79–81 (1977).
3. Burstyn, H. P. *Industrial Photography*, May 1977
4. Wiebe, P. H., Burt, K. H., Boyd, S. H. & Morton, A. W. *J. mar. Res.* **34,** 313–326 (1976)

Printed in Great Britain by Macmillan Production Ltd., Basingstoke, Hampshire

19. Environmental Science & Technology 13, No. 8, 931-935.

Polychlorinated Biphenyls and Chlorinated Pesticides in Soils of the Everglades National Park and Adjacent Agricultural Areas

Adolfo G. Requejo*[1], Richard H. West, Patrick G. Hatcher, and Philip A. McGillivary

National Oceanic and Atmospheric Administration, Atlantic Oceanographic & Meteorological Laboratories,
Ocean Chemistry Laboratory, Miami, Fla. 33149

■ Soil samples collected from the eastern Everglades National Park and adjacent farmlands were analyzed for certain chlorinated pesticides and polychlorinated biphenyls (PCBs). The results indicate that although concentrations of PCBs, 1,1,1-trichloro-2,2-bis(*p*-chlorophenyl)ethane (DDT), and chlordane are high at the agricultural sites, little contamination of parklands has occurred. Pesticide concentrations decrease by two orders of magnitude (to unit parts per billion levels) within 2 km of the agricultural sites sampled. Individual contributions of four Aroclors (1242, 1248, 1254, and 1260), calculated using pattern recognition techniques, suggest that plastic sheeting used in agricultural fields is a local source of PCBs. A comparison of the results to those from other environments reveals that PCB and DDT concentrations found within the Park (<1.0–33 and <1.0–22 ppb, respectively) are as low as any site in North America.

The Everglades National Park in South Florida is a unique, delicately balanced ecosystem. Within the last 30 years, lands adjacent to the southeastern boundary of the park have been extensively rock plowed and drained for farming. This agricultural activity has grown and currently accounts for a significant portion of the United States winter vegetable crop. The encroachment of man upon this wilderness has resulted in the introduction of industrial chemicals and pesticides, which threaten the environmental quality of pristine lands to the west. The National Park Service, in an effort to minimize contamination of parklands, obtained an indefinite moratorium on farming in an area known as "Hole-in-the Donut", located within the boundaries of the park. The moratorium was the result of a study which found elevated levels of 1,1,1-trichloro-2,2-bis(*p*-chlorophenyl)ethane (DDT), DDT metabolites, and dieldrin in soils and biota south of "Hole-in-the-Donut" (*1*). A monitoring program conducted by the U.S.G.S. has found increased levels of DDT and DDT metabolites in submerged soils collected from nearby Taylor Slough (*2*). Although domestic use of DDT was banned in 1972, the quantities used and the persistence of DDT degradation products continue to make these compounds environmentally hazardous. Other chlorinated pesticides, such as chlordane and toxaphene, are still applied to various crops. Chronic inputs of these pesticides to the park via irrigation runoff or careless application could have a disastrous effect on wildlife, especially the diverse avian population (*3–5*).

In addition to pesticides, industrial chemicals which may be affecting this region include polychlorinated biphenyls (PCBs), of which the toxicity and persistence have been widely researched (*6–10*). PCBs have been used as plasticizers in a variety of commercial plastics (*11*), and are suspected present in plastic sheeting used by farmers to aid seed germination (*1*). The sheeting (or mulching) also reduces the frequency of irrigation by preventing evaporation, and substantially improves crop yields. Following use, it is routinely burned and plowed into the soil, thereby releasing any PCBs present in the plastic matrix into the atmosphere. Once airborne, these compounds can be transported by wind into the adjacent parklands.

Because of the environmental and legal implications involved in determining whether the Everglades National Park is being contaminated by these anthropogenic pollutants, a study was undertaken to analyze soil samples from a southeastern section of the park, as well as samples of plastic sheeting obtained from local sources. The study area encompassed Taylor Slough, a major conduit of freshwater into the park, and adjacent agricultural lands. This paper presents the results of this study.

Experimental

Sampling. Samples were collected at sites along the southeastern boundary of the park as shown in Figure 1. The sampling grid was closely spaced in order to detect any horizontal gradients of agricultural chemicals in the area. Sites included both active (A1 and A2) and fallow (A3) agricultural lands, recently farmed lands (1, 3, 4, and 6), and locations in Taylor Slough and south and west of Context Road. All sampling was done in May 1976 in order to facilitate collection, as many of the locations sampled within the park are covered with water during the summer and early fall.

Surface soil samples were collected using a Teflon scoop to remove approximately the upper 2 cm of soil. Nonrepresentative surface debris (leaves, roots, etc.) was removed prior to collection. Samples were placed in cleaned glass jars and sealed with Teflon-lined caps. Upon return to the laboratory, all samples were immediately frozen. They were subsequently freeze-dried and stored frozen for later analysis.

Analysis. A weighed portion of the freeze-dried soil was extracted with hexane in a Soxhlet apparatus for 24 h. Saponification of random samples to determine extraction efficiency showed this procedure to be greater than 80% efficient for chlorinated hydrocarbons. However, this efficiency can vary with the chemical composition of the soil.

An aliquot of the hexane extract was concentrated to near dryness using a rotary evaporator and transferred onto a column of Florisil deactivated with 3% water. The column was

---

[1] Present address, University of Rhode Island, Graduate School of Oceanography, Kingston, R.I. 02881.

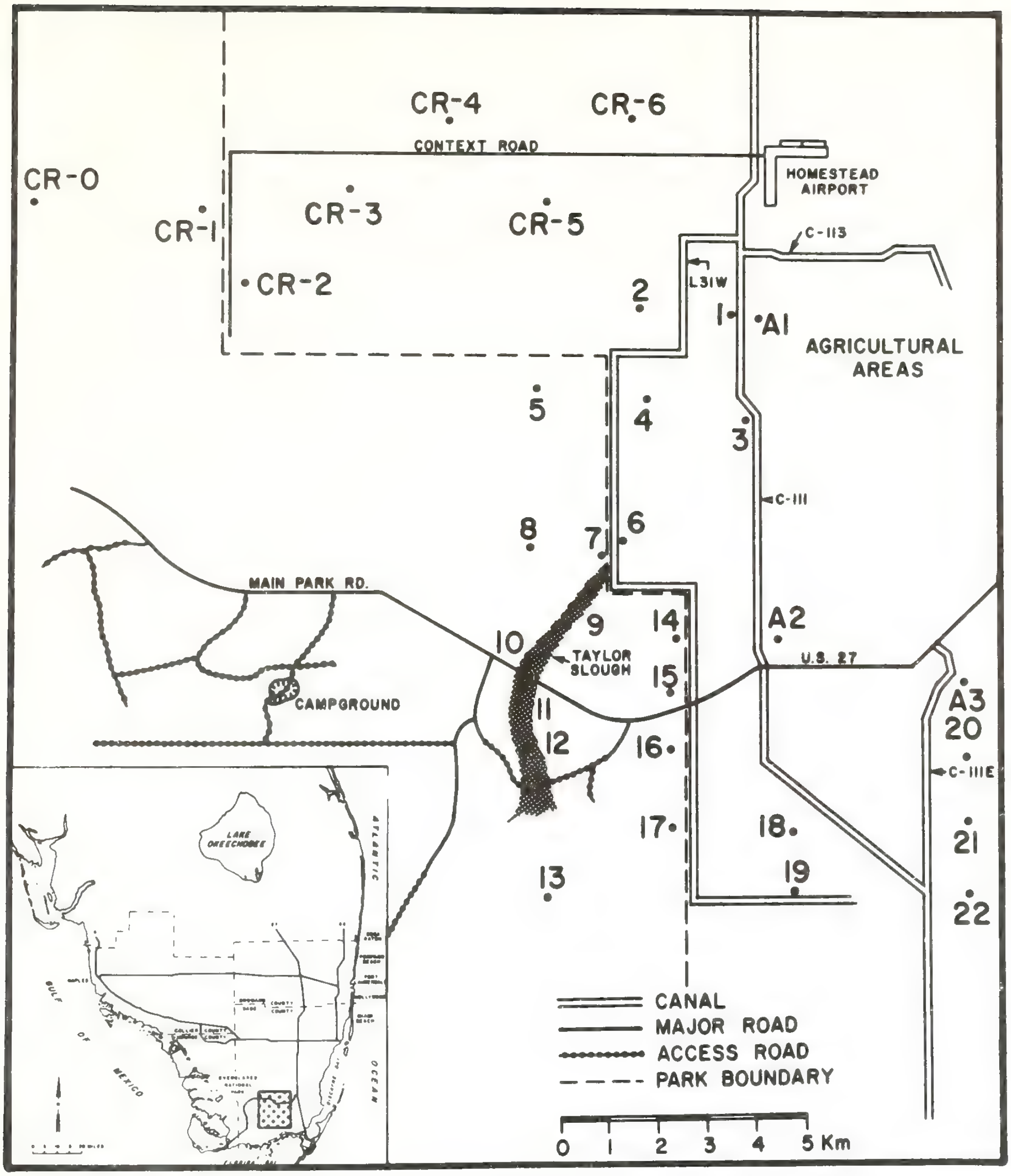

Figure 1. Location of sampling sites along the southeastern boundary of the Everglades National Park

eluted sequentially with hexane, 6% diethyl ether/hexane (v/v), and 50% diethyl ether/hexane (v/v). The 6 and 50% ether/hexane fractions were concentrated in preparation for analysis by gas chromatography. In order to separate PCBs from DDT and DDT metabolites, the hexane fraction was rechromatographed on 3% deactivated silicic acid (*12, 13*). The column was eluted with hexane followed by benzene. These fractions were similarly concentrated for gas chromatographic analysis. The separation scheme is detailed in Figure 2. Recovery of standard mixtures averaged 80–90%. No corrections for recovery were applied to the results. PCBs were extracted with hexane from plastic sheeting following treatment with boiling sulfuric acid. The hexane extract was analyzed using the procedure described above.

Chlorinated hydrocarbons were chromatographed and quantitated using a Tracor 550 gas chromatograph equipped with a ^{63}Ni electron-capture detector. Peak areas were measured by a Hewlett-Packard 3380A recording integrator. Three different column packings were used: glass columns (2 m × 2 mm i.d.) packed with 5% OV-210 on 100/120 mesh Supelcoport were used primarily for quantitation of pesticides while columns packed with 1.5% SP-2250/1.95% SP-2401 and 4% SE-30/6% QF-1, both on 100/120 mesh Supelcoport, were used for PCB analysis.

Pesticide concentrations were calculated using external standard techniques. Total DDT and total chlordane values were reported as the sum of DDTs (*p,p′*-DDT, *o,p′*-DDT), DDT metabolites (*p,p′*-DDE, *o,p′*-DDE, *p,p′*-DDD, *o,p′*-DDD), and the γ and α isomers of chlordane, respectively. Total pesticide concentrations less than 1.0 ppb were not reported.

PCB concentrations were also calculated using external

Table I. Chlorinated Hydrocarbon Concentrations in Soil Samples from the Everglades National Park and Adjacent Areas (ng/g Dry Weight)

Sites	Total Chlordane	Total DDT	Total PCB	% Aroclor 1242/1248	% Aroclor 1254/1260
Agricultural					
A1 (active)[a]	68	238	43	63	37
A2 (active)[a]	195	761	39	46	54
A3 (fallow)[a]	1.4	11	36	69	31
1 (winter only)[b]	<1.0	<1.0	23	91	9
3 (winter only)[b]	<1.0	<1.0	18	72	28
4 (winter only)[b]	<1.0	<1.0	11	91	9
6 (winter only)[b]	<1.0	<1.0	<0.1	--	--
Proximate					
West-southwest					
2	<1.0	<1.0	18	78	22
5[c]	<1.0	<1.0	24	92	8
8[c]	<1.0	<1.0	11	91	9
13[c]	1.4	1.7	1.7	76	24
14[c]	1.5	<1.0	12	92	8
15[c]	3.1	1.2	2.9	76	24
16[c]	<1.0	<1.0	5.0	84	16
17[c]	<1.0	<1.0	0.9	0	100
South					
18	1.3	<1.0	0.4	0	100
19	<1.0	<1.0	<0.1	--	--
20	4.8	2.4	12	0	100
21	<1.0	2.7	2.7	0	100
22	2.0	3.8	2.7	0	100
Taylor Slough					
7[c]	2.1	1.2	12	50	50
9[c]	1.6	22	<0.1	--	--
10[c]	2.8	6.7	2.1	0	100
11[c]	2.7	7.6	11	0	100
12[c]	1.1	1.7	11	18	82
Context Road					
CR-0[c]	<1.0	<1.0	33	54	46
CR-1[c]	1.6	<1.0	11	82	18
CR-2	<1.0	2.0	2.0	50	50
CR-3	<1.0	<1.0	5.0	92	8
CR-4	3.4	7.1	17	35	65
CR-5	<1.0	<1.0	5.7	50	50
CR-6	<1.0	<1.0	5.1	59	41

[a] Actively farmed since early 1900s. [b] Farming began approximately 1973. [c] Sites within the boundary of the park.

standards; however, individual contributions of four Aroclors (1242, 1248, 1254, and 1260), which accounted for the majority of domestic use from 1957 to 1971 (*14*), were calculated using a computerized pattern recognition program (*15*). Pattern matchings of PCBs isolated from soils are reported as percent Aroclor 1242/1248 and Aroclor 1254/1260. These percentages represent approximate pattern matchings and are not quantitative estimates of the PCB composition of each sample. The detection limit was 0.1 ppb. Since PCB pattern recognition programs had not been widely applied to environmental samples, it was difficult to assess whether this technique could be useful in determining sources and transport pathways of these compounds. West et al. (*16*) have used an identical program to characterize sources of sewage material in New York Bight sediments with limited success.

Results and Discussion

Pesticides. Chlordane, DDT, and DDT metabolites were the principal pesticides detected. Residues of other chlorinated and organophosphate pesticides examined in this study were present at only three sites (A1, A2, and 20). The results are summarized in Tables I and II. Agricultural sites Al and A2 were highest in total DDT and total chlordane. Detailed application histories of these fields were not available; however, the DDT metabolite *p,p′*-DDE accounted for a major portion of total DDT, indicating a lack of recent use. The detection of aldrin and dieldrin at site A2 indicates a recent application, as aldrin is quickly oxidized to dieldrin in soils (*17*). Low levels of total chlordane and total DDT at agricultural sites 1, 3, 4, and 6 can be explained by the fact that these are very recently farmed areas (ca. 1973) and, thus, have received little application of these compounds. In addition, these fields are cultivated only in the winter and left fallow the remainder of the year. This is in contrast to active agricultural sites A1 and A2, which are farmed most of the year. Lower levels of these compounds at the fallow agricultural site (A3) suggest it has been inactive for some time.

Nearly all sites proximate to the agricultural lands contained pesticide concentrations below the detection limits of the analysis (Tables I and II). Concentrations of total DDT drop from 761 ppb (site A2) to <1.0–1.2 ppb (sites 14 and 15, respectively) over a distance of slightly more than 2 km. The same is true of chlordane which falls from 190 to 1.5–3.1 ppb at the same sites. This drastic decrease in concentration suggests that little horizontal movement of pesticides has occurred. The highest concentrations of total DDT and total chlordane within the park are found in Taylor Slough. Elevated pesticide concentrations in the Slough would be indicative of a major pathway for these compounds into the park, i.e., transported by the sheetwater flow either adsorbed on particulate matter or in the dissolved phase. Although higher than in the surrounding areas, the extremely low levels de-

Table II. Occurrence of Other Pesticides in Soil Samples from the Everglades National Park and Adjacent Areas

pesticide	result
lindane	none detected at any site
heptachlor epoxide	none detected at any site
dieldrin	concentrations greater than 1.0 ppb detected at three sites: 20, 2.0 ppb; A1, 16 ppb; A2, 238 ppb
aldrin	detected at one site: A2, 11 ppb
endrin	none detected at any site
toxaphene	none detected at any site[a]
parathion/malathion	none detected at any site[b]

[a] Toxaphene is a complex mixture of chlorinated compounds and may be difficult to detect in the presence of other chlorinated pesticides. [b] Low levels of organophosphate pesticides cannot be adequately determined using an electron capture detector.

Table III. Individual Aroclor Distributions in Plastic Sheeting and the Sampling Grid (Percent of Total)

	Aroclor 1242	Aroclor 1248	Aroclor 1254	Aroclor 1260
plastic sheeting	34	30	17	19
sampling grid	31	29	18	22

tected indicate that these are not significant processes. It appears that agricultural activity adjacent to the park is responsible for only low-level contamination of parklands through Taylor Slough. Because of the importance of Taylor Slough to wildlife in the Everglades, however, pollutant levels in this area should be carefully monitored.

The low levels detected at these sites are surprising considering their proximity to active agricultural fields. Factors which could account for these low concentrations include the following:

(a) The application of fertilizers, pesticides, etc., is confined to the fields with little accidental application to surrounding areas.

(b) Canals C-111 and L31W that separate the agricultural lands from parklands are receiving most of the irrigation and rainwater runoff.

(c) Many soil samples contained relatively large amounts of organic matter. Humic substances, the major organic component of soils and sediments, have been shown to adsorb *p,p'*-DDT (*18*) and other hydrophobic organic compounds (*19, 20*). The amounts of chlorinated hydrocarbons bound in this manner, and, thus, not extractable by organic solvent, could be significant. However, the availability of humic bound chlorinated hydrocarbons to biological systems has not been documented.

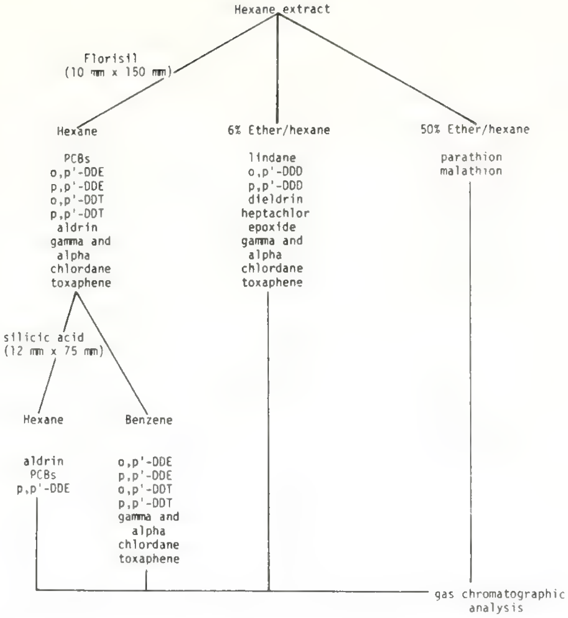

Figure 2. Separation scheme for chlorinated hydrocarbon analysis of soil samples

(d) The high rate of evaporation and intense heat in the dry season could account for loss of even moderately volatile or unstable components.

Further investigation is necessary to determine which of these factors, if any, is prevalent.

PCBs. Agricultural sites A1 and A2 are highest in total PCB, but concentrations are an order of magnitude less than the chlorinated pesticides (Table I). This is expected, as thousands of pounds of the pesticide DDT were used annually in South Florida (*21*), whereas plastic sheeting, the suspected source of PCBs, is a relatively new item in agriculture. Concentrations at these sites are only slightly greater than at other sites in the grid. PCBs apparently are not accumulated preferentially in farmland soils. A westerly decrease in concentration is also observed for PCBs, but is more gradual than that of the pesticides. In some areas, such as the transect through sites 3–4–5 and CR-5–CR-3–CR-1–CR-0, levels initially decrease and then increase away from the agricultural lands (Figure 1 and Table I). These increases may reflect alternate point sources of PCBs or physical differences in accumulative tendencies among the different soils. The widespread distribution of PCBs throughout the grid implies that

Table IV. PCB and DDT Concentrations in Various Soils and Marine Sediments throughout North America and the North Atlantic

environment[b]	total PCB, ng/g	total DDT, ng/g	source
(so) Monsanto production facility, Ill.	150–2.1 × 10^4		*25*
(so) agricultural lands, western Canada		760–4010	*26*
(se) New York Bight	0.5–1460	<0.1–120	*16*
(se) Mississippi Delta	0.2–35	0.2–9.3	*27*
(se) Irish Sea	<2–16	<0.2–1.8	*28*
(se) North Atlantic abyssal plain	0.2–2.8	0.5	*29*
(se) Firth of Clyde	10–2900		*30*
(se) Chesapeake Bay	11–1200	<1.0–273	*31*
(se) Santa Barbara Basin	103	178[a]	*10*
(so) Everglades National Park	<1.0–33	<1.0–22	this study

[a] As *p,p'*-DDE + *p,p'*-DDD. [b] se = marine sediment; so = soil.

dispersal of these compounds is not limited by physical boundaries such as canals or sloughs.

Two separate analyses of plastic sheeting for PCBs averaged 273 ppb. Although the sale of PCBs was voluntarily limited to closed systems after 1970, it is probable that materials containing PCBs were marketed and sold after this date. The levels detected in the sheeting, however, are indicative of contamination during the manufacture rather than deliberate formulation. In spite of these trace levels, the individual Aroclor distribution in plastic sheeting closely resembles the Aroclor distribution in the sampling grid; i.e., if PCBs isolated from all samples were combined, the pattern would be similar to that of plastic sheeting (Table III). These data suggest that plastic sheeting is the source material in this area. The individual Aroclor distribution in soil samples supports this assertion. A pattern similar to a mixture of Aroclor 1242 and 1248 is found almost exclusively west-southwest of the farmlands and, to a lesser degree, in the Context Road area, while Aroclors 1254 and 1260 predominate south of the farmlands and in Taylor Slough. In addition, the average PCB concentrations in the areas where Aroclor 1242/1248 predominate are nearly twice the concentrations where Aroclor 1254/1260 predominate (Table I). One explanation for these unequal distributions is the different volatilities of individual chlorobiphenyls. The major chlorobiphenyls in Aroclor 1242/1248, which have vapor pressures an order of magnitude greater than those of Aroclor 1254/1260 (*22, 23*), would be more easily volatilized during burning and, thus, more susceptible to aerial transport. The east-southeast winds which prevail during most of the year (*24*) would account for the observed distribution and the westerly concentration decrease. Differences in average PCB concentrations can be explained by the fact that PCBs in plastic sheeting consist of nearly twice as much Aroclor 1242/1248 as Aroclor 1254/1260 (Table III). The predominance of Aroclor 1254/1260 in Taylor Slough implies that transport of these chlorobiphenyls occurs by an alternate mechanism, probably adsorption on particulate matter, which is deposited and resuspended in the slough. Sampling of atmospheric particulates and volatiles, especially during the burning of plastic sheeting, should determine the validity of this atmospheric transport mechanism.

The data presented above suggest that volatile PCBs are being mobilized by the burning of plastic sheeting and transported by the prevailing winds. Thus, the levels detected in the park are probably the result of low level inputs occurring during the burning of contaminated sheeting. However, based on the magnitude of these levels, this input accounts for little contamination of parklands. A comparison of the data in this study to other areas (Table IV) shows that PCB and DDT levels found within the park are as low as at any site sampled in North America. Comparisons of this type can be misleading due to differing analytical techniques, but it is surprising to find lower levels of these compounds in the park, a region especially susceptible to direct inputs, than in coastal depositional environments which receive indirect inputs (via sedimenting particulate matter, sludge dumping, etc.). Although data presented herein indicate that the area is pristine with respect to chlorinated hydrocarbons, levels of other pollutants, such as phthalate esters and polycyclic aromatic hydrocarbons, as well as other insecticides and herbicides, should be determined in order to more accurately assess man's impact on this fragile environment.

Acknowledgments

The authors thank Mike Macau for assistance with the analyses and Adriana Cantillo and Philip Hanson for their assistance with the sampling. Special thanks go to George Harvey for his helpful suggestions and review of the manuscript. The cooperation of the National Park Service during the sampling period is greatly appreciated.

Literature Cited

(1) Hilsenbeck, C. E., "A Summary of Information About Synthetic Agricultural Chemicals With Reference to Their Presence in the Hole-in-the-Donut and Taylor Slough, Everglades National Park", Internal Report, Research Division, Everglades National Park, Homestead, Fla., 1976.

(2) Kolipinski, M. C., Higer, A. L., Yates, M. L., *Pestic. Monit. J.*, **5,** 281–8 (1971).

(3) Hickey, J. J., Anderson, D. W., *Science,* **162,** 271–3 (1968).

(4) Porter, R. D., Wiemeyer, S. N., *Science,* **165,** 199–200 (1969).

(5) Haegele, M. H., Tucker, R. K., *Bull. Environ. Contam. Toxicol.,* **11,** 98–102 (1974).

(6) Duke, T. W., Lowe, J. I., Wilson, A. J., *Bull. Environ. Contam. Toxicol.,* **5,** 171–80 (1970).

(7) Halter, M. T., Johnson, H. E., *J. Fish. Res. Board Can.,* **31,** 1543–7 (1974).

(8) Aulerich, R. J., Ringer, R. K., Iwamoto, S. J., *J. Reprod. Fertil., Suppl.,* **19,** 365–76 (1973).

(9) Tumasonis, C. F., Bush, B., Baker, F. D., *Arch. Environ. Contam. Toxicol.,* **1,** 312–24 (1973).

(10) Hom, W., Risebrough, R. W., Soutar, A., Young, D. R., *Science,* **184,** 1197–9 (1974).

(11) Peakell, D. B., Lincer, J. L., *BioScience,* **20,** 958–64 (1970).

(12) Armour, J. A., Burke, J. A., *J. Assoc. Off. Anal. Chem.,* **53,** 761–8 (1970).

(13) Masumoto, H. T., *J. Assoc. Off. Anal. Chem.,* **55,** 1092–7 (1972).

(14) Interdepartmental Task Force on PCBs, "PCBs and the Environment", NTIS, COM-72-10419, 1972.

(15) Zobel, M. G. R., *J. Assoc. Off. Anal. Chem.,* **57,** 791–5 (1974).

(16) West, R. H., Hatcher, P. G., Atwood, D. K., "Polychlorinated Biphenyls and DDTs in Sediments and Sewage Sludge of the New York Bight", NOAA-ERL Data Report, in press.

(17) Lichtenstein, E. P., Schulz, K. R., *J. Econ. Entomol.,* **52,** 118–24 (1959).

(18) Pierce, R. H., Olney, C. E., Felbeck, G. T., *Geochim. Cosmochim. Acta,* 1061–73 (1974).

(19) Ogner, G., Schnitzer, M., *Geochim. Cosmochim. Acta,* **34,** 921–8 (1970).

(20) Khan, S. U., Schnitzer, M., *Geochim. Cosmochim. Acta,* **36,** 745–54 (1972).

(21) Higer, A. L., Kolipinski, M. C., "Sources of Pesticides in Florida Waters", USGS Open File Report 70005, 1970.

(22) Mackay, D., Wolkoff, A. W., *Environ. Sci. Technol.,* **7,** 611–4 (1973).

(23) Spencer, W. F., Cliath, M. M., *J. Agric. Food Chem.,* **20,** 645–9 (1972).

(24) "Local Climatological Data, Miami, Florida", U.S. Department of Commerce, National Climatic Center, Asheville, N.C., 1976.

(25) Stratton, C. L., Sosebee, J. B., *Environ. Sci. Technol.,* **10,** 1229–33 (1976).

(26) Head, W. K., McKercher, R. B., *Can. J. Soil Sci.,* **51,** 423–30 (1971).

(27) Giam, C. S., Chan, H. S., Neff, G. S., Atlas, E. L., *Science,* **199,** 419–21 (1978).

(28) Dawson, R., Riley, J. P., *Estuarine Coastal Mar. Sci.,* **4,** 55–69 (1977).

(29) Harvey, G. R., Steinhauer, W. G., in "Environmental Biogeochemistry", J. O. Nriagu, Ed., Ann Arbor Science, Ann Arbor, Mich., 1976, pp 203–21.

(30) Halcrow, W., MacKay, O. W., Bogan, J., *Mar. Pollut. Bull.,* **5,** 134–6 (1974).

(31) Palmer, H. D., Tzou, K. T. S., Swain, A., "Transport of Chlorinated Hydrocarbons in Sediments of the Upper Chesapeake Bay", final report prepared for the Office of Water Resources Research, Westinghouse Ocean Research Laboratory, Annapolis, Md., 1976.

Received for review August 30, 1978. Accepted March 15, 1979. This study was supported by the National Park Service, Department of the Interior, under Contract No. 5297-1008-182.

20. Ocean Engineering Technical Bulletin 5, No. 2, 3.

SLOPE MAP OF A SUBMARINE SLIDE SEAWARD OF THE BALTIMORE CANYON TROUGH

An Application To Seafloor Engineering Investigations

While fulfilling the nation's demand for energy, increased engineering activities in offshore marine environments have dictated urgent requirements for detailed oceanographic data, particularly geotechnical information on seafloor characteristics and environmental hazards. To satisfy these needs, the Marine Geotechnical-Rational Use of the Sea Floor Program of NOAA's Atlantic Oceanographic and Meteorological Laboratories (AOML) is conducting numerous seafloor engineering, geological, and geophysical studies.

As a new application to geotechnical engineering and geological investigations, a precision bathymetric and slope map (clinometric map) has been constructed. The recently published map of a major submarine slide groups local areas with similar seafloor gradients or slopes. Four map categories (in color) define the major morphological features and declivities of a selected area of the continental slope seaward of Cape May, New Jersey. Moderately steep slopes are associated with the slide scar; nearly flat to gentle slopes characterize the slide block proper (<6 degrees); and very steep slopes are associated with an incised valley, and valley and ridge complex. Valley walls have gradients of greater than 26 degrees locally, but very small (<6 degrees) axial gradients. The map also provides a detailed perspective of the seafloor's morphological features.

The slope map can be used to evaluate engineering and geological information in an area. The map and slope categories are currently being used as part of a detailed seafloor stability investigation. Sediment cores collected in the study area have differences in mass physical properties which can be related to both the seafloor gradients and morphology. Preliminary analysis indicates reasonable correlation between predicted and measured values for maximum slopes at which sediments would be stable. Although a knowledge of seafloor gradient is important in stability analysis, the slope map provides an excellent data base for almost any activity that affects and is in contact with the seabed.

The slope map covers a small part of a much larger portion of the continental margin presently under investigation at AOML and Texas A&M University. The area is designated as Geotechnical Corridor I and is in proximity to the Baltimore Canyon Trough, an area of current offshore exploration. (See figure).

Numerous sediment cores, and bathymetric and seismic profiles have been collected. From these data, massive submarine slides and smaller scale seafloor instabilities have been identified in the Corridor. Based on the distribution of the geotechnical properties of the sediments and their relationships to seafloor gradient and morphology, future work is expected to include in situ measurements of sediment pore pressures with a NOAA deep-water probe (piezometer) in selected east coast continental margin areas. (See article entitled "NOAA Cooperative Seafloor Engineering Project.")

Integration of these different types of data and techniques is important for a comprehensive evaluation and understanding of sediment properties, soil behavior, and bottom characteristics relevant to seafloor stability assessment and general seabed activities.

CONTACT: R. H. Bennett,
NOAA/AOML, Miami, Florida

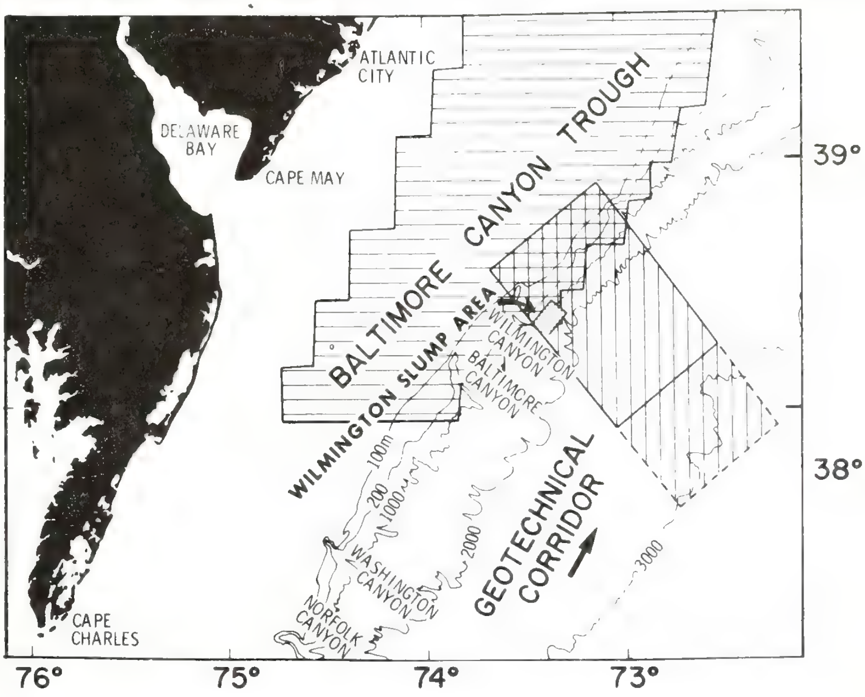

LOCATIONS OF GEOTECHNICAL CORRIDOR I AND WILMINGTON SLUMP AREA

21. Applied Ocean Research 1, No. 3, 115-122.

Ambient and dynamic pore pressures in fine-grained submarine sediments: Mississippi Delta

RICHARD H. BENNETT and J. RICHARD FARIS
Marine Geology and Geophysics Laboratory, Atlantic Oceanographic and Meteorological Laboratories, 15 Rickenbacker Causeway, Virginia Key, Miami, Florida 33149, USA

(Received 23 January 1979)

A multisensor piezometer probe has measured pore pressures in fine-grained submarine sediments of the Mississippi Delta over a period of approximately eight months. Data presented here cover the initial 2650 hours of the experiment. Dynamic and ambient pore pressures were recorded. Analogue data collected from the time of probe insertion include decay characteristics, steady-state (ambient) excess pore pressures, and the response of pore pressures to surface wave activity. The probe was installed in 43–44 ft of water near an offshore platform in the East Bay area of the Delta. Sensors were located at 21, 41 and 51 ft below the mudline. Ambient excess pore pressures were determined to be 0.7, 2.8 and 6.6 psi (lb/in^2) at the respective depths. The relatively high excess pressures and the measured laboratory wet unit weights of the soil result in a significantly low effective stress. Pressure fluctuations due to tidal and surface wave activity were observed to produce significant pore pressure response in these soils. Preliminary data obtained using high-air-entry and corundum stones indicate that considerably more research is necessary in order to fully understand the peculiarities observed in the data and to assess the role of dissolved and free gas on the pore pressures in submarine sediments.

INTRODUCTION

A shallow-water piezometer probe implanted in Mississippi Delta silty clay sediment has measured pore water and hydrostatic pressures for a period of approximately eight months (March to November 1977). Data reduction and preliminary analyses are completed for the initial 2650 hours of the experiment. The data discussed and presented herein include: (1) initial probe insertion pressures, (2) steady-state (ambient) excess pore pressures, (3) pore pressure decay characteristics, (4) dynamic response of 'hydrostatic' and pore pressures as a function of low amplitude, high frequency surface waves and low amplitude, low frequency tides. A brief discussion is given of the piezometer system and installation and the sediment (soil) geotechnical properties. A detailed engineering treatment of the piezometer data and the sediment properties will be presented elsewhere. Data presented here represent the most recent long-term piezometer measurements collected by the National Oceanic and Atmospheric Administration (NOAA) in a series of three such experiments (1975–1977) in the South Pass (East Bay) area of the Mississippi Delta. A modified piezometer was recently deployed in the Main Pass area, and preliminary data analysis is underway. Earlier test results of a prototype piezometer and the observed submarine sediment pore pressures have been discussed by Bennett *et al.*[1] and Bennett[2]. As part of a 1977 cooperative study, two additional piezometers from Texas A&M University/US Geological Survey and Lehigh University were implanted in the vicinity of the NOAA probe and have been discussed by Dunlap *et al.*[3].

Sediment pore pressure (u_w) is in equilibrium with the hydrostatic pressure (u_s) when the two are equal ($u_s = u_w$) and, in this case, no excess pore pressure (u_e) exists. For the case of equilibrium, a sedimentary deposit is considered to be normally consolidated with respect to the existing overburden stress. Under certain geological conditions, pore pressure disequilibrium may exist as discussed earlier by Bennett *et al.*[1]. Of importance here are conditions where positive excess pore pressure ($u_e = u_w - u_s$ when $u_w > u_s$) occurs due to natural or man-induced causes. In nature, excess pore pressure may occur in fine-grained sediments when sedimentation rates are high, permeabilities are low, and dewatering is inhibited during the consolidation process. Sediment shearing and deformation in normally consolidated and under-consolidated submarine sediments may also produce excess pressure, and the presence or generation of dissolved and undissolved gas is believed to have a significant influence on sediment pore pressure. All of these conditions can exist in the prodelta environment. In this investigation, additional excess pore pressure was generated due to the implacement of the piezometer probe producing effects similar to those observed by engineers during pile driving in certain soil types. Regardless of cause, the occurrence of excess pressure is significant because of its concomitant reduction in effective stress and strength in cohesive (non-cemented) sediments. Surficial submarine sediments characterized by excess pore pressures are considered to be more susceptible to instability and mass movement than normally consolidated sedimentary deposits in similar environmental conditions.

In situ measurement of pore pressure is necessary for making reliable estimates of vertical effective stress of sedimentary deposits that are underconsolidated and such measurements are also important in determining possible time-dependent changes in pore pressure during dynamic environmental conditions. When pore pressure distribution with depth is known, then reliable estimates of seafloor stability can be made based on effective stress methods. The importance of pore pressures on the

0141-1187/79/030115-09$02.00
© 1979 CML Publications

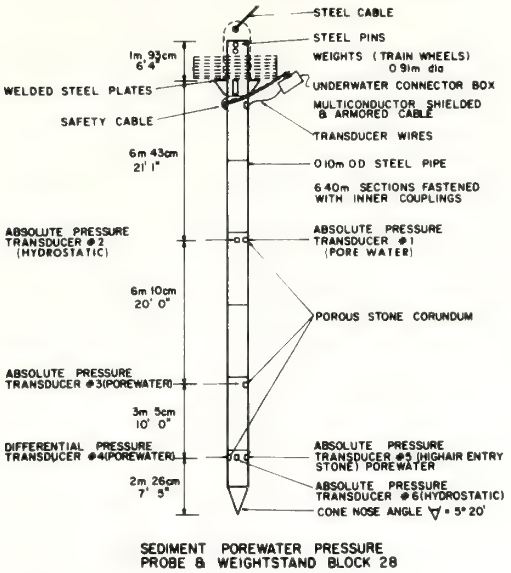
STEEL CABLE
STEEL PINS
WEIGHTS (TRAIN WHEELS) 0.91m dia
1m 93cm 6' 4"
WELDED STEEL PLATES
UNDERWATER CONNECTOR BOX
MULTICONDUCTOR SHIELDED & ARMORED CABLE
SAFETY CABLE
TRANSDUCER WIRES
6m 43cm 21' 1"
0.10m OD STEEL PIPE
6.40m SECTIONS FASTENED WITH INNER COUPLINGS
ABSOLUTE PRESSURE TRANSDUCER #2 (HYDROSTATIC)
ABSOLUTE PRESSURE TRANSDUCER #1 (PORE WATER)
6m 10cm 20' 0"
POROUS STONE CORUNDUM
ABSOLUTE PRESSURE TRANSDUCER #3(POREWATER)
3m 5cm 10' 0"
DIFFERENTIAL PRESSURE TRANSDUCER #4(POREWATER)
ABSOLUTE PRESSURE TRANSDUCER #5 (HIGHAIR ENTRY STONE) POREWATER
2m 26cm 7' 5"
ABSOLUTE PRESSURE TRANSDUCER #6(HYDROSTATIC)
CONE NOSE ANGLE ∀ = 5° 20'
SEDIMENT POREWATER PRESSURE PROBE & WEIGHTSTAND BLOCK 28

Figure 1. Shallow water piezometer

ultimate stability of a sedimentary deposit has been generally accepted for decades. Until recently, however, data on pore pressures in submarine sediments have been virtually unavailable with the exception of measurements by Richards *et al.*[4] and later by Bennett *et al.*[1] and Bennett[2]. In a discussion of the role of waves in causing submarine slides, Henkel[5] has stressed the need for *in situ* measurement of sea-floor bottom pressures, the need for detailed knowledge of shear strength distribution with subbottom depth, and an understanding of the energy transfer between waves and the soft submarine sediment. Studies of the interaction of hydrodynamic forces and bottom sediments were made by Suhayda *et al.*[6], and again during the 1977 Mississippi Delta cooperative study. In addition, laboratory and theoretical studies of these interactions have been presented by Schapery and Dunlap[7], and by Yamamoto *et al.*[8]. The combined influence of important geological and oceanographic factors on the ultimate instability of Mississippi Delta deposits has been discussed by Prior and Coleman[9] and Suhayda and Prior[10].

Geotechnical, geological, and environmental parameters are integrated in this study in order to provide fundamental information regarding the role of pore pressures during static and dynamic conditions and its relationship to seafloor stability, the effective stress and strength of submarine sediments, and the behaviour of fine-grained cohesive sediments in response to natural and man-induced loads. Other Mississippi Delta studies have investigated related geotechnical aspects, including the relationships among the clay fabric and geotechnical properties of naturally-consolidated prodelta sediment[11,33] and properties of anomalous 'crust' zones[12-15]. Excellent studies of the geology and geological aspects of seafloor stability of the Mississippi Delta have been carried out by Coleman and Wright[16-18]. Numerous contributions to the understanding of the geotechnical properties of the Delta sediments have been made since the advent of offshore drilling and the recovery of oil and gas[19].

INSTRUMENTATION

The current version of the NOAA second-generation piezometer is designed specifically for the study of shallow-water submarine sediments. The total system is composed of several subsystems: signal conducting cables; signal conditioners; voltage and frequency regulators; recorders; and probe with pressure sensing transducers. The probe shell enclosing the pressure transducers is a 4.0 in. (0.10 m) o.d. seamless steel pipe composed of several 10 ft (3.05 m) segments with O-ring sealed couplings. This allows for adjustment of the total probe length and for choice in sensor locations. The present probe has a total length of 65.3 ft (19.8 m) including a specially designed tip to control sediment disturbance during insertion. The probe tip has a cone angle of 5.3 degrees with the bottom transducers places approximately 22 pipe diameters above the point (Fig. 1). The tip is designed to simulate plane strain soil deformation during probe insertion. Design specifications for the tip were provided by Dr. Melvin Esrig, Woodward Clyde Consultants.

The piezometer contains six variable reluctance pressure transducers; three to measure absolute pore pressure, two to measure absolute hydrostatic pressure, and one to measure excess pore water pressure directly (differential above hydrostatic). A 5 kHz sine wave is supplied to each transducer by a carrier oscillator in the signal conditioner unit, producing an a.c. output from the wien bridge-type transducer circuitry which is amplitude-proportional to transducer unbalance. The a.c. signal is amplified, demodulated, and filtered by the conditioning unit, resulting in a 0–10 VDC output level corresponding to the 0-full-scale range of the transducer. This d.c. output of the signal conditioning units is connected to standard analogue recording equipment. Data presented in this paper were collected on three dual-pen, heat-sensitive strip chart recorders. Transducers installed in the current version of the probe have a maximum working range of 100 psia (689.5 kPa) for absolute measurements and 20 psi (137.9 kPa) for differential measurements. Rated linearity of the transducers is ±0.5 psi (3.5 kPa) and ±0.1 psi (0.7 kPa), respectively; however, during short time periods, they proved capable of sensing pressure variations much smaller than these values. Similar multiple-piezometer designs have been successfully employed in terrestrial sediments to measure ambient pressures, induced pressures and pore pressure dissipation[20].

Pore pressure is sensed through porous corundum or high-air-entry ceramic discs which are inset in the pipe and connected to the transducers by short tubing. The porosity of the corundum and high-air-entry stones are 45–50% and 35–38% respectively; approximate permeabilities (k) are $1–3 \times 10^{-2}$ cm/s and $1–3 \times 10^{-7}$ cm/s. Hydrostatic pressure is transmitted to sensors through the seawater-filled interior of the pipe, allowing for comparison of hydrostatic *versus* pore pressure measurements at desired locations. It should be noted that due to the dynamic effects of surface waves and tides in the marine environment, the use of the term 'hydrostatic' pressure may be misleading. For the purposes of this paper, hydrostatic pressure can be defined as the 'instantaneous' pressure measured in the free-water column.

This pressure is a function of the changes in total height of the water column due to surface activity and is, in reality, a very dynamic parameter. Thus, independent measurement of pore pressures and hydrostatic pressures enables the determination of wave effects on pore pressures. The differential transducer, having greater sensitivity than the absolute transducers provides detailed and direct information on excess pore pressures induced during probe insertion and pore pressure decay characteristics following installation. The entire piezometer system was calibrated at the laboratory prior to installation using a precision fused quartz Bourdon tube pressure gauge. Final field checks were carried out to verify transducer response immediately prior to probe insertion.

Installation of the system was accomplished from a surface work boat with diver assistance. The probe was fitted with a weight stand to provide the driving force necessary for full insertion in one smooth motion. Recording equipment and signal conditioners were placed in an air-conditioned house well above water level on a nearby offshore petroleum platform 1375 ft (420 m) from the piezometer (Fig. 2). Nearly 2000 ft (610 m) of armored cable with shielded triad conductors were used to transmit the signals to the platform. Prior to installation, the electronic system was operating in order to continuously monitor the pressures generated during lowering and insertion. Following insertion, divers inspected the exposed portion (~6 ft) of the probe insuring proper penetration and attitude following which the weight stand was returned to the boat. After ~60 min of recording, the electronic system was temporarily disconnected to remedy a surface connector problem which inhibited the response from one transducer, and ~130 min after insertion, data monitoring resumed.

Installation was completed in March 1977, and the systems were recovered in November of the same year. All transducers were recalibrated when returned to the laboratory and the 21 ft transducers, which showed excellent stability throughout the deployment, repeated to within ±0.3 psi (2 kPa) over their measuring range. The other four transducers showed shifts on the order of 1.0 psi (6.9 kPa) at pressures equivalent to ambient conditions in the field. Field abuse may have contributed to these shifts; excessive stress during probe recovery may have been placed on internal wires and connectors during disassembly and the effects of severe galvanic corrosion were evident on the oil-filled transducer housings. (The effects of dissimilar metals was considered prior to deployment; however, aluminium parts recovered from the prototype piezometer did not indicate the severity of the problem. Steps were taken to minimize use of dissimilar metals in the 1978 deployment.) The predeployment calibrations were employed to reduce all piezometer data in this paper and are believed to be most representative of the 110 days presented.

SOILS

The prodelta soils in the piezometer study area are predominantly silty clays having less than 1% sand. The clay fraction ranged from 60 to 80%. The Mississippi Delta submarine sediments are characterized generally by a dominance of smectite clay minerals with secondary contributions of illite in the fine-grained fraction. Kaolinite occasionally dominates the clay mineral assemblage locally in the surficial muds. A short 17 ft (5.2 m) piston core was recovered by Texas A&M University from the probe site for geotechnical properties measurements. Water contents were relatively high, 85–109% (dry weight; uncorrected for salt content), and greater than the liquid limit in the upper few metres. Average grain specific gravity values were 2.69–2.71. Wet unit weights ranged from 88.9 to 97.4 pcf (1.41–1.56 Mg m^{-3}). Low shear strengths are common in Mississippi Delta surficial submarine sediments, and results of miniature vane tests indicate strengths at the coring site average approximately 60 psf (2.9 kPa) within the upper 17 ft[21]. A soil boring approximately 6000 ft (1830 m) to the southwest of the probe site displayed the following geotechnical properties:

wet unit weight in pcf (Mg m^{-3})	89.2 (1.43)
water content (% dry weight)	90
liquid limit (%)	91
plastic limit (%)	32
liquidity index	1
plasticity index (%)	59

These averages for the upper 51.5 ft (15.7 m) are similar to the properties found for the short piston core recovered at the probe site, and remote field vane measurements indicate shear strength increasing to 190–240 psf (9.10–11.49 kPa) at 40–50 ft below mudline[22]. Methane gas is believed to be present in the sediments where the probe was implanted as cores recovered in the vicinity of the site showed gas bubble structures[21]. A detailed study of methane gas concentration in Mississippi Delta sediments was carried out by Whelan, *et al.*[34], which showed that methane probably exists not only in the dissolved phase but also in the bubble phase *in situ*.

DISCUSSION

Ambient and induced pressures

As a result of the low shear strengths, probe insertion was carried out in one motion without difficulty at 1130

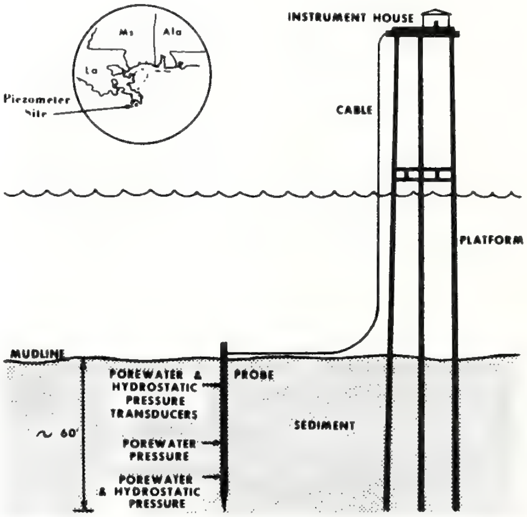

Figure 2. Typical installation of shallow water piezometer

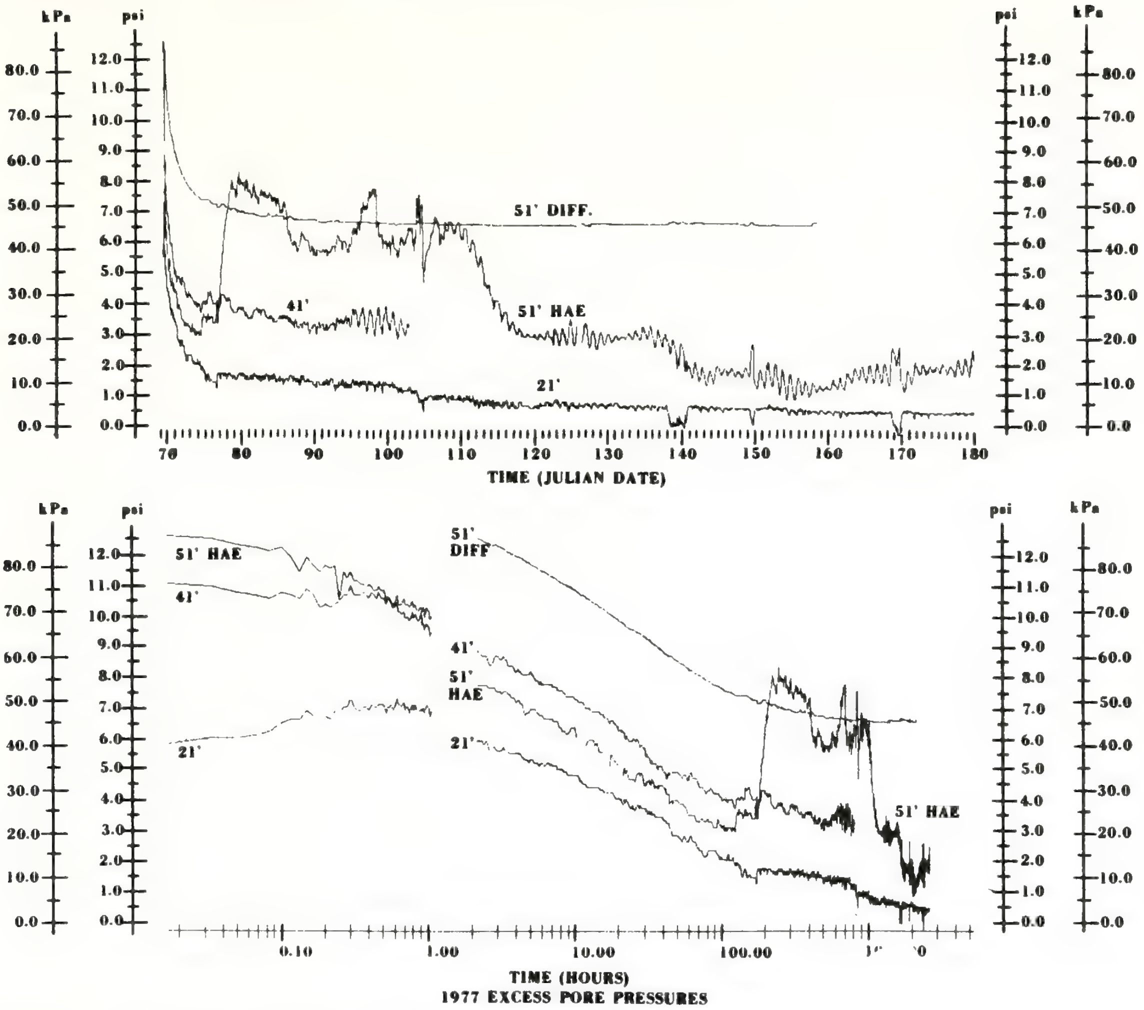

Figure 3. Mississippi Delta submarine sediments East Bay

hours on the morning of 10 March 1977 (Julian day 069). As expected, excess pore pressures resulted from the insertion, and their observed behaviour showed dramatic decays to ambient pressure during the subsequent 110 days (Fig. 3). With the exception of the differential transducer at 51 ft (15.5 m) below mudline (51′ DIFF), all excess pressures were computed based on hydrostatic observations at 21 ft (6.4 m) below mudline, corrected to the appropriate level based on the known separation between transducers and an assumed unit weight of sea water equal to 64 pcf (1.024 Mg/m^3). Since the differential transducer reference port was connected to hydrostatic pressure at 51 ft below mudline, its output is a direct reflection of excess pressure at that level. Measurements from the 21 ft hydrostatic transducer confirmed the estimated 43 ft (13.1 m) water depth at the site within 1 ft.

Excess pressures observed immediately following insertion ranged from 5.8 psi (40.0 kPa) at the 21 ft level through a corundum stone to 12.6 psi (86.9 kPa) through the high-air-entry stone at the 51 ft level (51′ HAE). Although the 51 ft differential transducer (corundum stone) was initially inoperative, its insertion excess pressure is estimated at 14.6 psi (100.7 kPa). This estimation is based on curve comparisons of excess pressure with the 41 ft (12.5 m) excess pressure sensor which was also measured through a corundum stone. The major portion of these large excess pressures results from sediment disturbance during piezometer insertion. Over a period of several weeks, measured pressures dissipated to levels that are considered to be representative of the ambient excess pressures existing at the site. Estimates of ambient pressure values are sensitive to the length of time that dissipation has been allowed to progress, so that ambient levels reported earlier[3] which were based on 25 days of data, are somewhat higher (in most cases) than those reported here. However, based on 110 days of observation, best estimates of the ambient excess pore pressures at the 21-, 41- and 51-ft levels are 0.7 psi (4.8 kPa), 2.8 psi (19.3 kPa), and 6.6 psi (45.5 kPa), respectively. The 51-ft ambient excess pore pressure, as measured through the 5-bar high-air-entry ceramic stone is estimated at 1.8 psi (12.4 kPa). The use of small pore size filter materials is

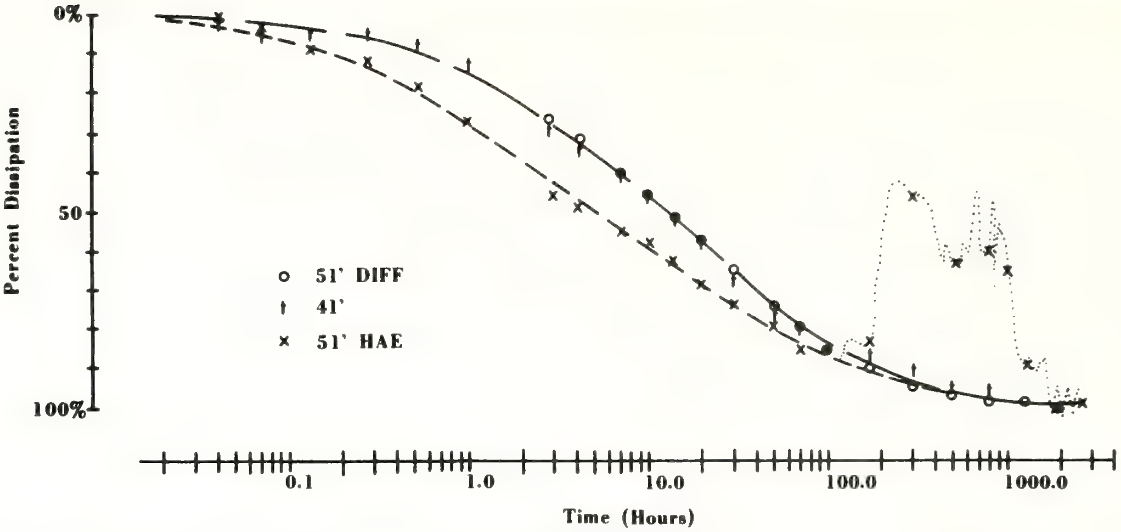

Figure 4. Dissipation of pore pressures induced by piezometer insertion.

generally accepted as a means of inhibiting, by capillary effects, direct communication with free pore gas so that pressures measured through corundum stones may contain a contribution from high pore gas pressure while those measured through stones with high-air-entry values should not[23]. Hence, if one accepts this reasoning, these observations imply a measured pore gas pressure in excess of the ambient pore water pressure by 4.8 psi (33.1 kPa) at 51 feet below mudline. Gas diffusion through high-air-entry ceramics can, in time, inhibit their effectiveness as a gas pressure filter[24] which may, in part, account for the observed fluctuations in the 51-foot HAE record as discussed later. Further research is necessary to understand the significance of the large differences observed between high-air-entry and corundum stones and the anomalous character of the high-air-entry pore pressure record.

One of the primary benefits of piezometric measurements in submarine sediments is a refined estimate of the *in situ* vertical effective stress. In the absence of pore pressure measurements, a linear hydrostatic fluid pressure distribution is often assumed for the calculation of geostatic stress. In this case, for saturated soils, vertical effective geostatic stress at depth z ($\bar{\sigma}_{vg}$) is calculated from:

$$\bar{\sigma}_{vg} = \sum_{x=0}^{x=z} \gamma_b \Delta x$$

where $\gamma_b = \gamma_t - \gamma_{sw}$ and γ_b = buoyant unit weight, γ_t = saturated unit weight, γ_{sw} = unit weight (density) of sea water. Based on the average wet unit weight of 89.2 pcf (1.43 Mg/m^3), estimates of the vertical geostatic effective stress at the 21-, 41-, and 51-ft levels are 3.68 psi (25.4 kPa), 7.18 psi (49.5 kPa), and 8.92 psi (61.5 kPa), respectively. In the case where excess pore pressures exist, effective vertical stress $\bar{\sigma}_v$ can be calculated from:

$$\bar{\sigma}_v = \bar{\sigma}_{vg} - u_e$$

where $u_e = u_w - u_s$ and u_e = excess pore water pressure at depth z, u_w = total pore water pressure at depth z, u_s = hydrostatic pressure at depth z. If the ambient levels of excess pore pressure (corundum stone) are used to revise these estimates, the *in situ* effective stress is reduced by 19% at 21 ft, 39% at 41 ft and 74% at 51 ft below mudline. Since pressures measured through corundum stones may reflect a contribution due to free pore gas, these values are probably an upper bound on reduction of effective stress estimates due to ambient excess pore pressures. However, applying the excess pore 'water' pressure as measured through the high-air-entry stone also significantly reduces the effective stress at 51 ft below mudline by 20% of the geostatic estimate, indicating that the sediments are significantly underconsolidated, as was found earlier by Shepard *et al.*[25] for sediments recovered from nearby borings and consolidated in the laboratory. Unfortunately, details concerning the distribution of dissolved and free gas occurring in the sediment and its effect on the pore water pressure are presently unknown and, therefore, a more precise determination of vertical effective stress cannot be made at this time. Considerably more research is needed to better define the role of gas and its effect on pore water pressure and effective stress.

Based on the above estimates of ambient pressure, the pore pressures induced by piezometer insertion become 8.2 psi (56.5 kPa) at 41 and 51 ft, and 10.8 psi (74.5 kPa) at 51 ft through the high-air-entry stone. (The anomalous increase in excess pressure during the first hour at 21 ft made selection of the true insertion pressure uncertain, and the 21-ft sensor was omitted from this comparison.) The above values were used to produce a normalized plot showing the time-related dissipation of induced pressures for the 41- and 51-ft transducers (Fig. 4). Applying the log-fitting method from consolidation theory[26], t_{100} is approximately 200 hours for all three sensors, with measured dissipation at that time on the order of 90%. This would indicate a 'set-up' (increase in bearing capacity and soil strength resulting from dissipation of induced excess pore pressure[26,27]) in 8–10 days for a 4 in. diameter displacement pile in this type of soil. It is interesting to note the differences in observed behaviour of the sensors at dissipation levels of less than 100%. For example, t_{50} for the 41 ft excess pressure is approximately 14 hours, while

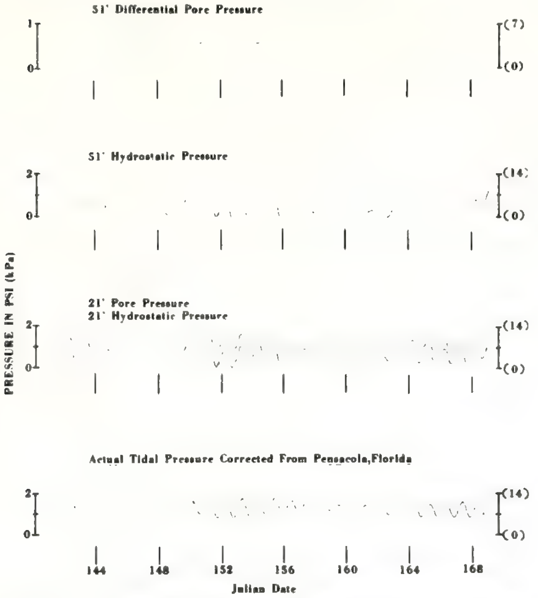

Figure 5. Pressure fluctuations induced by tides in 44 feet of water

the corresponding value for the 51 ft high-air-entry sensor is only 6 hours. The comparative method of estimating insertion pressure for the 51 ft differential transducer biases the dissipation curve (Fig. 4) and makes it uncertain whether this time effect is due to a change in soil characteristics with depth or to the different characteristics of the corundum and high-air-entry stones sensing the decay. Dramatic variations with depth of t_{50} values have been observed in peaty and silty clays using a 0.6 in. (1.5 cm) diameter piezometer sounding instrument[28]. Depth-related differences in decay characteristics also appear in the records from the NOAA Main Pass probe site (currently being analysed).

Estimates from Esrig *et al.*[29] based on a plane-strain, elastic-plastic model of soil behaviour during pile driving, indicate the maximum induced pore pressure (ΔU_{max}) at the pile–soil interface is approximately equal to six times the undrained shear strength (s_u) for lean inorganic clays of moderate to high sensitivities. Using this relationship, and the above pore pressures induced by piezometer insertion, approximations of undrained shear strength at 41 and 51 ft below mudline are 1.4–1.8 psi (9.7–12.4 kPa). These estimates are in good agreement with *in situ* strength measurements (1.3–1.7 psi; 9.1–11.5 kPa) at similar depths in a nearby boring[22]. In addition, laboratory strength tests (1.0–1.4 psi; 6.9–9.7 kPa) from several additional borings in adjacent areas (provided by F. P. Dunn, Shell Oil Company, personal communication) indicate reasonable agreement. Verification of these relationships using additional piezometer insertion data may prove valuable in providing *in situ* strength of submarine soils.

RESPONSE TO SURFACE ACTIVITY

Throughout the experiment, the piezometer system revealed significant response in measured hydrostatic and pore pressures resulting from water surface activity. A portion of the real-time piezometer record is compared with tidal activity derived from observed highs and lows at the National Ocean Survey tide station near Pensacola, Florida (Fig. 5). Tidal pressure fluctuations were computed (again, using 64 pcf for sea water) and corrected to Southwest Pass based on the *Table of Tidal Differences* as published by the National Ocean Survey[30]. A section of particular interest includes the tides of semidiurnal period on days 147 and 160 where tidal pressure fluctuations on the order of 0.2 psi (1.4 kPa) were measured by the hydrostatic and 21 ft pore pressure transducers. The cyclic response in the 21 ft pore pressure and the lack of response in the 51 ft differential (excess) pressure demonstrate that surface activity having a period of 12 hours or more can be felt as actual pressure fluctuations within the sediment pore fluid to depths of more than 50 ft below mudline, having little or no influence on the theoretical effective stress within the sediment.

To obtain preliminary assessment of pore pressure response to short-period surface activity, approximately one-half hour of data was recorded at increased chart speed during a routine maintenance visit on day 126 when surface wave heights were visually observed to be approximately 3 to 5 ft. Subsequent auto-correlation of the hydrostatic pressure records gave a period of 6.4 sec which corresponds to a calculated wavelength of 175 ft in 45 ft of water. The 30 min record was manually digitized on an electronic digitizing table and a smooth curve was generated from the resulting data points by cubic spline interpolation (using a method modified from Greville[31]). A representative portion of that record was selected for discussion (Fig. 6). Again, comparison of the cyclic response in the 21 ft pore and hydrostatic pressure transducers demonstrates that the wave pressure is felt within the sediment pore fluid at 21 ft below mudline with essentially the same magnitude as in the free water column. A large positive cross-correlation (+0.75) verifies the in-phase relationship between the pore and hydrostatic pressure records (Fig. 7). (The slight apparent phase shift is on the order of one second and is within the accuracy of time referencing between the individual strip chart records.) Similar wave pressure observations have been made by others at 13 ft below sea-bed in highly plastic marine clay, although the magnitude and period of the pressure fluctuations are not detailed[32]. The 51 ft excess pore pressure (Fig. 6) is in marked contrast with the 51 ft differential pore pressure record of tidal activity (Fig. 5). Significant activity and a large negative cross-correlation (−0.68) indicates that the excess pressure is dominated by the fluctuations of the hydrostatic (instantaneous) pressure on the reference port of the differential transducer, with limited contribution from the pore pressure port; implying essentially no short-term change in the total pore pressure at that depth.

An essentially straight-line response from the 51 ft high-air-entry sensor helps confirm that the pressure wave in the sediment pore fluid was severely attenuated at 51 ft below mudline. (However, as mentioned later, response of this sensor may be severely dampened after day 100.) Very slight cyclic activity is visually observed on the 41 ft pore pressure record, also confirming pressure wave attenuation with depth, but its magnitude approaches the resolution limits of the strip chart recorders and could not be adequately digitized with accuracy sufficient for further analysis at this time. This observed attenuation of wave induced pore pressure as a function of depth below

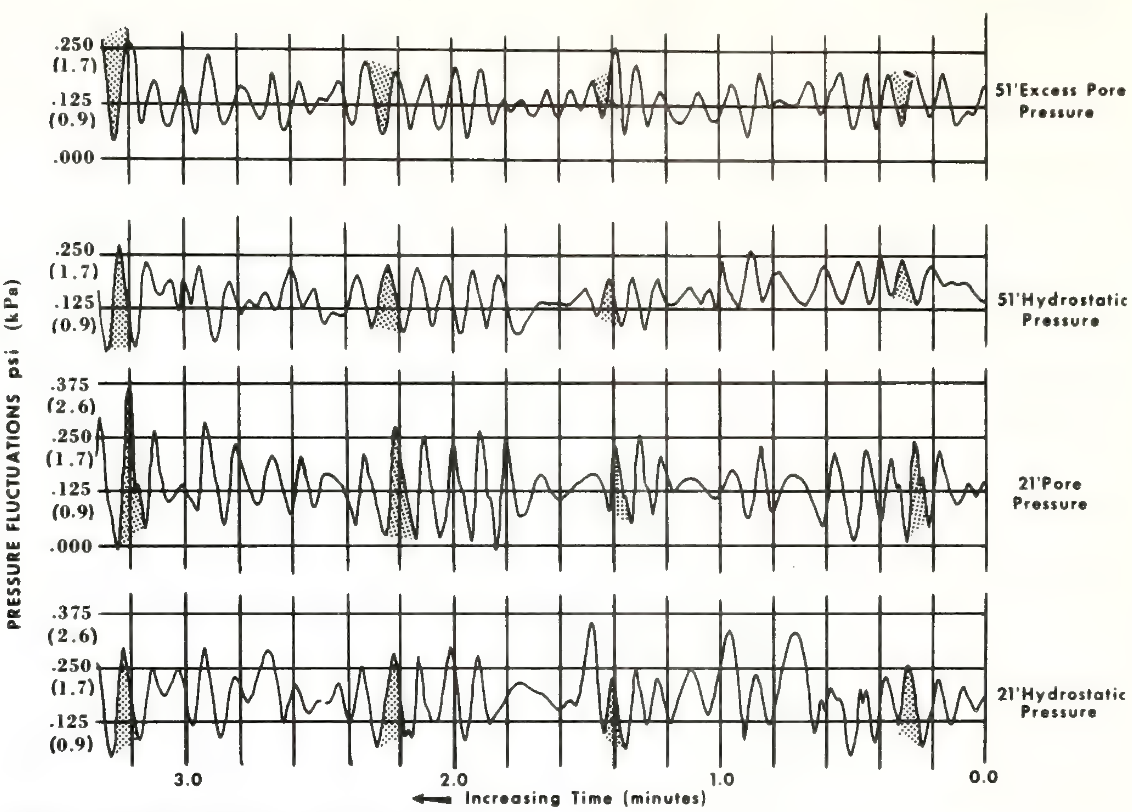

Figure 6. Piezometer response to surface wave activity

mudline is similar to the behaviour predicted by Yamamoto *et al.*[8]; however, further analysis and more detailed information of the wave loading function are needed before an exact comparison can be made.

ANOMALOUS BEHAVIOUR

During the course of the experiment, several apparent anomalies occurred in the data which deserve discussion. The initial loss of insertion pressure measurements by the differential transducer mentioned previously was the result of a short in a surface connector box which, once isolated, was easily rectified. At the same time, all other transducers were checked for similar electrical problems, and all appeared to function normally. A more persistent problem involved control of the environment in the platform instrument house. Occasional overloads of the 115 V power on the platform caused the circuit breaker for the instrument house air-conditioner to trip. This resulted in subsequent unstable temperature periods of up to several days until the problem was discovered and the circuit reset. The condition is known to have occurred on at least two occasions, perhaps more frequently, and is believed to be a factor responsible for the anomalies on days 76, 104, 138–140, 149, and 169 (Fig. 3). The thermal recorders are sensitive to changes in both temperature and humidity, and temperatures within the recorders reached levels sufficient to discolour the entire width of the recording paper (approximately 100 C). Another persistent problem involves the data obtained from the 51 ft hydrostatic transducer. Throughout the experiment, this sensor produced readings which were ~5–8 psi (34–55 kPa) below pressures that would be expected from the depth of water confirmed by the 21 ft hydrostatic transducer. Post-recovery inspection of the internal connecting wires revealed a small area where the insulation had abraded, exposing the conductors to salt water. The resulting parallel electrical path, bypassing the transducer, could account for the observed shift. Presumably, the defect occurred during shipping or assembly, resulting in unreliable absolute pressure readings from this transducer throughout the experiment; however, the sensor's response does not appear to be seriously affected in view of the excellent correlations with the 21 ft hydrostatic transducer during the period of surface wave observations.

The behaviour of the 51 ft pore pressure measured through the high-air-entry stone deserves special consideration. The large pressure increase near day 76 occurs during a period of known high temperature in the instrument house; however, the transducer's subsequent behaviour, indicates that other factors may have contributed to the anomalous performance. The fact that the high-air-entry pressure tends to fluctuate around the pressure level recorded by the 51 ft differential transducer (through a corundum stone) suggests that the transducer may have been measuring a combination gas water pressure; however, return of the measured pressures to lower values (following day 110) which appear reasonable, based on consideration of decay characteristics (Fig. 4), indicates that the behaviour does not result from a permanent change in the piezometer system. The sharp

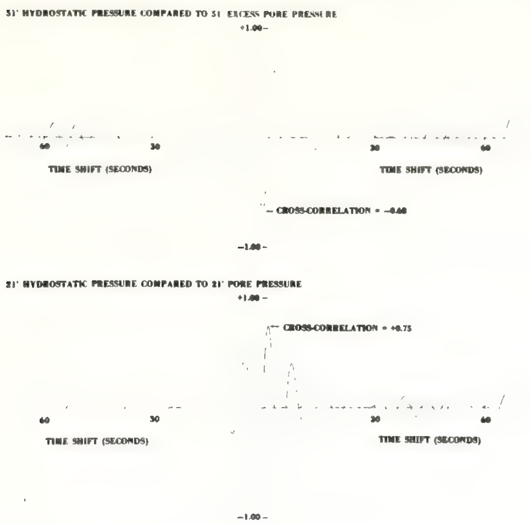

Figure 7. Cross-correlation of piezometer response to surface wave activity

spikes which appear in the vicinity of day 100 (Fig. 3) give some credence to a gas–water combination in the piezometer cavity since they result from severe dampening of response in the absolute pressure record of the 51 ft high-air-entry transducer. The fluctuations seen in the excess pore pressure plots result from differences in tidal pressure magnitudes as seen by the hydrostatic and pore pressure transducers. This would be the expected result of a gas water system, given the low permeability of the five-bar ceramic stone; however, the same type of activity occurs in the record of the 41 ft transducer near day 96. Given the high permeability of the corundum stones, such dramatic dampening would not normally be expected from the 41 ft transducer; however, in these fine-grained gassy sediments, it is possible that the *in situ* soil permeability is a limiting factor in controlling response of an unsaturated transducer system.

Despite the above uncertainties, piezometer performance during this deployment was reasonably good.

CONCLUSION

Pore pressures in fine-grained submarine sediments of the Mississippi Delta have been successfully measured using a multisensor piezometer probe and analogue data acquisition system for periods of 2650 hours. Probe insertion pressures, their decay characteristics, and ambient 'steady state' pore pressures were determined at 21, 41, and 51 ft below mudline. Total induced pressure due to probe insertion was 8.2 psi at 41 ft and 51 ft (pore pressures sensed through coarse corundum stones). Induced pressure at 51 ft sensed through a high-air-entry stone was 10.8 psi. Theoretical t_{100} values were very nearly 200 hours for each soil depth measured. However, the rate of dissipation of the excess pore pressure generated during probe insertion appears to vary significantly among the transducers. It is uncertain whether this behaviour is due to variation of *in situ* soil conditions or to measurement characteristics of the piezometer. Ambient excess pore pressures were observed to be 0.7, 2.8, and 6.6 psi at the 21-, 41-, and 51-ft levels, respectively. Considering these relatively high excess pressures and the average wet unit weight of the sediment, the estimated effective stress at the measured depths is significantly low as compared to a normally consolidated deposit.

Water surface activity by tides and short period low amplitude waves was observed to produce significant fluctuations in pore pressure. Although the precise physical characteristics of the 3–5 ft high short period waves ($\sim$6.4 sec) were unknown, correlations of hydrostatic *versus* pore pressure to depths of 21 ft showed strikingly good agreement. Pressure fluctuations, due to the short period waves having an effective calculated wavelength of 175 ft in 45 ft of water, were found to be highly dampened at 41 ft below mudline and virtually absent at 51 ft.

Pressure waves due to tidal activity were observed to produce cyclic pore pressure response at both 21 and 51 feet below mudline. The range of tidal activity is commonly on the order of 1.5 ft and these data indicate excellent sensitivity to relatively small pressure fluctuations. Data obtained during which short period low amplitude wave pressures were monitored also indicates that the piezometer system has relatively rapid response time capabilities. Throughout the experiment, the submarine sediment pore pressures were not 'static' but rather, ambient pressure varied in response to not only tidal activity, but also to surface waves.

Differences in measured pore pressures were observed through a corundum *versus* high-air-entry stone at 51 ft below mudline. Unexplained anomalies occurred in data obtained using the high-air-entry stone and more research and testing is necessary to fully explain these observed peculiarities. In addition, considerably more research seems warranted to provide a clear understanding of the role of pore gas pressure on pore pressure and effective stress analyses in submarine sediments.

ACKNOWLEDGEMENTS

Assistance by many colleagues during various phases of this project are appreciated, particularly the support of Messrs. D. N. Lambert and John Burns of AOML, and Drs. William Bryant and Wayne Dunlap of Texas A&M University. The help of Messrs. L. Shepard and W. Hottman of Texas A&M University is appreciated. Mr. E. Niper, Sandia Corporation, assisted in various phases of the field activities. Mr. T. Clarke and Ms. Frances Nastav of AOML are due special thanks for their assistance in various phases of the data reduction and computer applications. The authors appreciate the invitation by Dr. Louis Garrison of the U.S. Geological Survey to participate in their Mississippi Delta Project, and we appreciate the Survey's support in various phases of the field activities. Special thanks are due to Dr. Wilmot Hess, NOAA, ERL, for support in the development of the second generation shallow-water piezometer.

REFERENCES

1 Bennett, R. H., Bryant, W. R., Dunlap, W. A. and Keller, G. H. Initial results and progress of the Mississippi Delta sediment pore water pressure experiment, *Marine Geotechnol.* 1976, 1, (4), 327

2 Bennett, R. H. Pore water pressure measurements, Mississippi Delta submarine sediments, *Marine Geotechnol.* 1977, 2, 177

3 Dunlap, W. A., Bryant, W. R., Bennett, R. H. and Richards, A. F. Pore pressure measurements in underconsolidated sediments, *Offshore Technol. Conf. Proc.*, *Paper* 3168, 1978, 2, 1049

22. Ocean Engineering Technical Bulletin 5, No. 2, 3-4.

NOAA COOPERATIVE SEAFLOOR ENGINEERING PROJECT

The initial field phase of a cooperative NOAA-university-industry multidisciplinary seafloor engineering project was successfully completed during a September 1978 cruise aboard the NOAA Ship RESEARCHER. The project was designed to accomplish several high-priority marine geotechnical objectives relevant to NOAA's seafloor engineering program. The purpose of the investigations was to define the causes and mechanisms important in stability of the seafloor east of the Mississippi Delta (Main Pass Area), an area where potential sediment instability is critical to offshore engineering activities.

This project is being undertaken with the cooperation of NOAA's Atlantic Oceanographic and Meteorological Laboratories (AOML), Office of Ocean Engineering (OOE), and National Ocean Survey (NOS); the Marine Geotechnical Laboratory of Lehigh University; and the Mobil Oil Corporation.

An important first of the project is the intercalibration of NOAA-Lehigh University in situ and laboratory geotechnical instrumentation, including piezometers and vane shear devices. Other accomplishments of the project thus far include field measurements using the Lehigh "mini" piezometer at 12 sites; testing of the C-Floor 9 in situ geotechnical probe and subsystems; and the collection of shear strength data to depths of 11.5 feet below the mudline, which is believed to be the greatest penetration depth achieved for in situ strength measurements by an academic organization. NOS participants have conducted a detailed site-specific, geophysical survey of the seafloor and subbottom to characterize the geologic setting over the in situ probe and coring sites using sidescan and 3.5 kHz profiles. Five long sediment (piston) cores were recovered for laboratory geotechnical and intercalibration tests. The AOML 65-foot shallow-water piezometer was implanted near a Mobil Oil Corporation platform in approximately 144 feet of water, and a 14-channel analog magnetic tape data acquisition system was installed on the platform. Preliminary analyses of the data and laboratory testing of the sediment cores are currently in progress.

Initial evaluation of the pore pressure data has indicated significantly lower excess pressures (pore pressure greater than hydrostatic pressure) at the present probe site than was observed during earlier piezometer tests in the East Bay area of the Delta. These significant differences are presently interpreted as being the result of fundamental differences in the geological processes active (i.e., sedimentation rates, etc.) in these areas and of basic differences in the geotechnical properties of the seafloor soils (i.e., sediment grain size, permeabilities, etc.). However, many other factors are responsible for the ultimate behavior and fundamental properties of the two deposits.

During Phase II of the project, participants are continuing data analyses and efforts on the various technical aspects of the program, including data and equipment evaluation and intercalibrations of the ocean engineering instrumentation. This project is a precursor to a NOAA-planned future deep-water in situ seafloor testing program in areas of national economic importance.

CONTACTS: R. H. Bennett, AOML
J. R. Faris, AOML
S. Sigmund, OOE
R. Perry, NOS
A. F. Richards, Lehigh

23. Scanning Electron Microscopy 1, 519-524 and p. 424.

SCANNING ELECTRON MICROSCOPY/1979/I
SEM Inc., AMF O'Hare, IL 60666, USA

CLAY FABRIC AND RELATED PORE GEOMETRY OF SELECTED SUBMARINE SEDIMENT: MISSISSIPPI DELTA

R. H. Bennett, W. R. Bryant and G. H. Keller+*

NOAA, Atlantic Oceanographic and
Meteorological Laboratory
15 Rickenbacker Causeway
Miami, FL 33149

*Texas A&M Univ.--Dept. Oceanography
College Station, TX 77843

+Department of Oceanography,
Oregon State University,
Corvallis, OR 97331

Abstract

A study was made of the clay fabric of cored submarine sediment to subbottom depths of 150 m from the Mississippi Prodelta depositional environment. Analysis was carried out using techniques of transmission and scanning electron microscopy (TEM and SEM, respectively).

Clay fabric was related to porosity, and depth of burial. Relatively high porosity, naturally consolidated delta sediment was characterized by a fabric of randomly oriented domains and short linking chains with particles in edge-to-face and face-to-face contact. Lower, intermediate porosity sediment showed greater particle-to-particle packing, but a predominance of randomly-oriented domains with a few chains and a slight development of larger domains than observed in the high porosity sediment. The fabric of the low porosity, deeply-buried sediment consisted of highly oriented domains with thin, long voids.

KEY WORDS: Clay Fabric, Porosity, Submarine Sediment, Correlative Microscopy, Particle Shape, Pore Geometry

Introduction

Clay fabric and related pore geometry of cored submarine sediment from the Mississippi Delta were investigated. Samples were recovered from depths of 150 meters below the sediment-water interface. Analyses were carried out using transmission and scanning electron microscopy (TEM and SEM, respectively). Careful sample preparation and quality control were used.

Study Area

This study is restricted to selected areas of the Mississippi Prodelta (depth beyond which wave erosion is significant and at which predominantly silts and clays are deposited) depositional environment (Fig. 1). The birdfoot delta is the most modern depocenter of the Mississippi Delta complex. Sediments are prograding seaward depositing clays and silty clays. Cores (B-1, B-2) were recovered from water depths ranging from 67 m to 73 m with a lateral separation of approximately 610 m. Detailed analyses were restricted to cores B-1 and B-2. Three samples for SEM were recovered from two cores (3A and B-2) (Fig. 1). A detailed clay fabric and geotechnical study of these cores is given by Bohlke and Bennett (in press). The SEM micrographs are used for comparison with TEM results.

Samples were selected on the basis of sample quality and availability from 1.4 m to 151 m in core B-1. Supplemental samples were selected from core B-2, at depths ranging from 1.4 m to 27.6 m, for comparison with the fabric of core B-1.

Sediments

The clay mineral composition of recent sediment from the Mississippi Delta and adjacent offshore areas has been reported by Johns and Grim (1958). Montmorillonite was reported as the dominant clay mineral, with small amounts of illite and chlorite.

Fisk and McClelland (1959) discussed the clay-sized mineral assemblage carried by the Mississippi River. Montmorillonite was reported to dominate and kaolinite, illite, quartz, and feldspar were present in smaller quantities. Although quartz and feldspar are not clay minerals, they were reported as being present in the clay size fraction of the sediment transported by the river.

The lithology of the B cores investigated includes a massive, relatively hard, gray, old submarine clay which occurs at depths of approximately 85 m to at least 152 m below the mudline, and is overlain by 26 m of fine sand between 85 m and 59 m (Fig. 2). The sand forms the broad and extensive strand plain deposit of Pleistocene age. These sands form the base of the overlying fine-grained clays of the premodern and modern deposits of the Mississippi River (Coleman and Wright, 1974) which are on the order of 59 m thick.

Core B-1 was selected and studied in detail because of the long, continuous depth of sediment penetration compared to core B-2. The clay minerals composing the fine-grained sediment consisted primarily of smectite and illite, and secondarily in minor proportions, of kaolinite and/or chlorite. These platy materials constitute the "building blocks" of clay fabric.

General trends in the sediment mass physical properties are similar among the two cores with core depth. Porosities range from as high as 71% in the upper few meters of cored sediment to as low as 49% in the deeply buried Pleistocene clays. Porosity or void ratio (volume of the voids to the volume of the solids) is a good indicator of the dewatering which sediments undergo during natural consolidation as a function of increasing overburden stress with sediment depth. Porosity is related not only to water content but also to the grain specific gravity and wet bulk density (Bennett and Lambert, 1971), which in turn normally vary with increasing depth of burial. Thus the porosity of a deposit of relatively uniform grain specific gravity and grain size would reflect significant changes in bulk density and water content with increasing depth in response to sediment dewatering.

Based on the physical properties of Core B-1 discussed above, five general porosity zones can be delineated which reflect relative degrees of increasing natural consolidation and dewatering of the silty clay sediment (Fig. 3). These porosity zones form a framework for discussion and description of the clay fabric.

Subsampling Techniques

Selected sediment samples were carefully subsampled from the centers of core segments using a thin wire knife. The samples were trimmed into small blocks a few millimeters in size. The initial size of a subsample was generally less than 5 millimeters on a side, which was later trimmed to about 2 to 3 millimeters on a side. Subsamples were cut with two faces of the block lying generally parallel with the plane of bedding, such as normal to the core length. The remaining four faces of the blocks were then normal to the bedding plane. After careful trimming, the samples were ready for further processing.

Preparation of Samples for EM

The most critical steps in preparing clay samples for electron microscopy (EM) studies are the techniques employed in the dehydration of water-saturated specimens. Likewise, the techniques for embedding a sample with an appropriate medium, a necessary prerequisite to ultrathin sectioning (for TEM), must be accomplished with care. These factors were given paramount importance during this study. Careful techniques were employed in order to insure high quality comparable results by minimizing sample disturbance and maintaining the structural integrity, and particle-to-particle orientations, of the clay samples. Clay specimens for this study were critical point dried with liquid CO_2 and TEM samples were embedded with a low viscosity epoxy resin (SPURR) following the techniques described by Bennett et al, (1977). Fracture surfaces of SEM samples were electrostatically cleaned following techniques described by Hulbert and Bennett (1975).

Fabric of Shallow Versus Deep Core Samples

High-Porosity Clays

The relatively high-porosity sediment of the upper few meters of cores B-1 and B-2 is characterized by randomly arranged particles. The particles are for the most part domains and their presence can be verified not only by megascopic examination of the micrographs, but also by the graphic displays depicted by image enhancement (Bennett et al, 1977). Particles are composed of face-to-face clay platlets forming an essentially nearly perfect "stack." Micrographs 4, 5 and 6A depict the clay fabric which is characteristic of the upper few meters of high-porosity sediment of cores B-1 and B-2 (zone 1, Fig. 3). Numerous randomly arranged domains are apparent in edge-to-edge and edge-to-face contact producing a relatively high porosity sediment. The domains

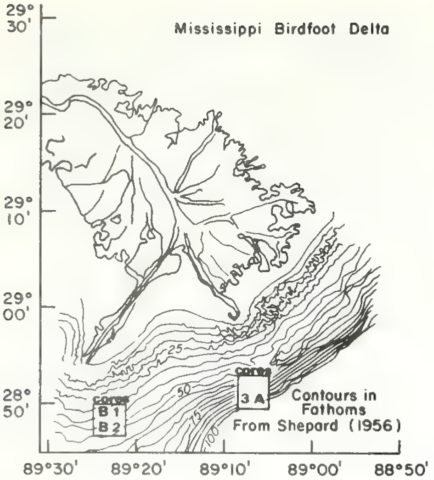

Figure 1. General study area.

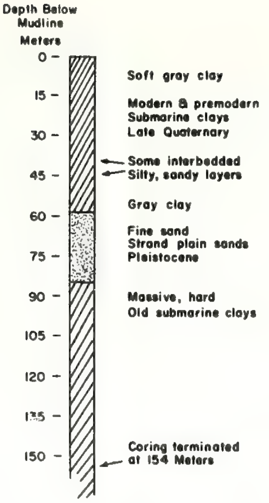
Depth Below Mudline Meters
0
15
30
45
60
75
90
105
120
135
150
Soft gray clay
Modern & premodern Submarine clays Late Quaternary
Some interbedded Silty, sandy layers
Gray clay
Fine sand Strand plain sands Pleistocene
Massive, hard Old submarine clays
Coring terminated at 154 Meters

Figure 2. Generalized core lithology.

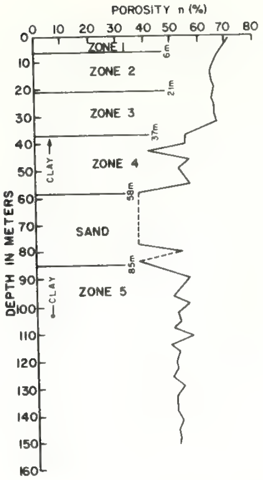

Figure 3. Porosity versus depth (clay porosity zones) core B-1.

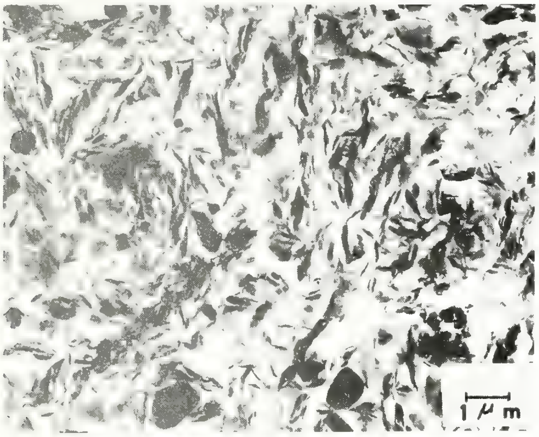

Figure 4. Clay fabric of randomly oriented domains. Core B-2 (1.4 m).

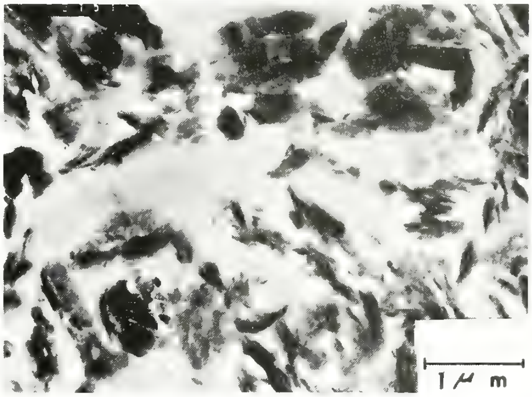

Figure 6A. Clay fabric of randomly oriented domains and large voids that vary over a range of sizes. Core B-2 (1.4 m).

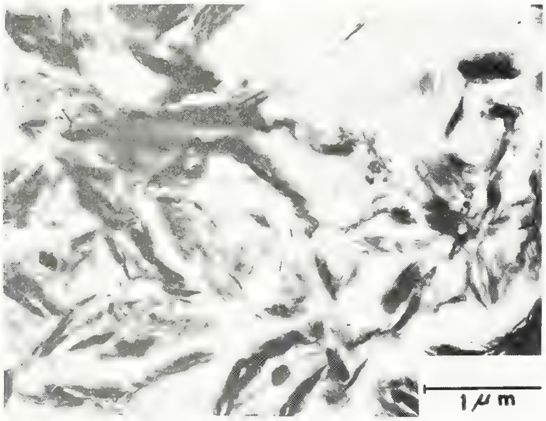

Figure 5. Clay fabric depicting well-defined, randomly-oriented domains and high porosity. Core B-2 (1.4 m).

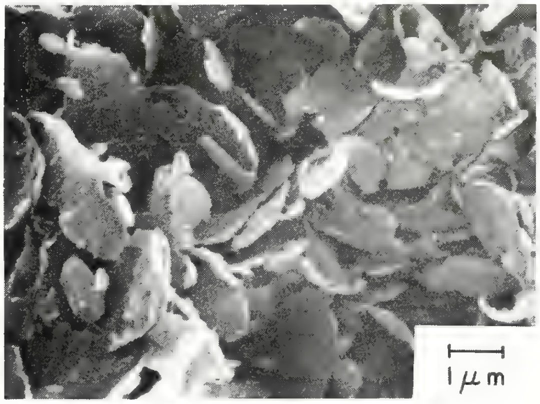

Figure 6B. SEM micrograph of sediment from core 3-A sampled at 0.3 m below mudline. Photo depicts randomly oriented particles with large voids. Fabric is similar to fabric depicted in TEM micrograph of Fig. 6A.

appear to vary over a considerable range of sizes. Large voids and particle contacts are apparent and a few short chains are present. An SEM micrograph (Fig. 6B) of surficial sediment (0.3 m below the mudline, core 3A) recovered from the East Bay area reveals fabric characteristics similar in appearance to the features observed in B-1 and B-2. The SEM provides a three-dimensional perspective of an irregular fracture surface of the sediment. Randomly arranged particles and large voids (high porosity) are apparent.

Clay samples from core B-2, 9.3 m below the mudline, reveal a slight increase in density and decrease in porosity within zone 2. Local areas show some apparent particle alignment (Fig. 7). Important to note is the fact that the decrease in porosity in zone 2 is due not only to the slight dewatering commensurate with the process of consolidation but also, possibly more important in this case, to the significant overall decrease in clay content and corresponding increase in silt-size particles within this interval (determined from laboratory grain size analyses). An SEM micrograph of sediment sampled from 12.5 m below mudline (core BH-3A, East Bay area) also reveals an open, random arrangement of particles. Large voids are characteristic and domains are the predominant apparent particle type (Fig. 8).

Clay samples from 27.7 m in porosity zone 3 are characterized by high porosities (Fig. 3). Despite the fact that zone 3 is deeper than zone 2, the porosities are high due to the significant increase in clay-size material in this zone and corresponding decrease in silt and sand size particles. The micrographs clearly depict the relatively high porous nature of these zone 3 sediments (Fig. 9). The clay particles, predominantly domains, are oriented randomly; however, the micrographs reveal a slight tendency of some of the particles toward common alignment, but it appears to be of a very minor degree. Of significance to note are some fairly large voids (depth of 27 m below the mudline) and the presence of some fairly large domains (Fig. 10). Numerous edge-to-face particle contacts are depicted. The fabric of zone 3, in general, appears to be quite similar to the overlying sediment clay fabric. The differences are the slight decrease in porosity with depth of burial and a slight increase in packing of the clay particles as compared with zone 1. Sediment from zones 1 through 3 have the highest porosities and void ratios as compared to the remainder of the cored material.

Low-Porosity Clays

The lowest porosity clays encountered in this study occurred at core depths in excess of 85 m (Fig. 3). Samples from zone 4 with porosities only slightly higher than zone 5 were not available for electron microscopy studies. However, the samples studied from zone 5 revealed significant clay fabric characteristics quite different from the overlying moderately high-porosity clays (zones 1-3).

Electron micrographs of the clay fabric sampled at a depth of 120.4 m below the mudline (core B-1) reveal a remarkable increase in overall density of particle packing, the presence of small, thin voids, low porosity, and strong particle-to-particle alignment (Fig. 11) as compared with the higher porosity clays. Very strong overall preferred particle orientation is observed; however, some particles in local areas are aligned at oblique angles to the general trend of the preferred particle orientation. Considerably long, continuous chains of particles are depicted which form the bulk of the preferred orientation. These chains undoubtedly developed in response to the process of natural consolidation and dewatering commensurate with increasing sedimentation and overburden stress. Some of the chains and particles are seen to bend and distort around relatively large electron-dense particles. Clearly, strong preferred orientation of the clay particles is apparent; however, numerous clay particles (domains) are aligned at high angles to the preferred orientation.

Micrographs depicting the clay fabric of the sediment sampled at a depth of 144.8 m reveals a quite similar fabric compared with the clays from 120.4 m (core B-1). The clay fabric is characterized by very strong preferred particle orientation of domains and rather continuous, long chains (Fig. 12). The clay particles are efficiently packed in close proximity, giving rise to the development of preferred particle orientation. As observed in the clay fabric from 120.4 m, not all of the particles are aligned parallel with one another and with the general trend of the preferred particle orientation of the sample. Likewise, these micrographs depict several areas where chains and particles wrap and bend around adjacent, larger particles and groups of particles. A few particles are oriented not only at oblique angles to the preferred particle orientation, but also some are observed to lie virtually normal to the preferred direction. Gillott (1969) also observed a strong, but not perfect, degree of preferred particle orientation of clay minerals in a well-developed fissile shale. Gipson (1965) observed a similar fabric relationship during the study of fissility in shale. Clearly strong preferred particle orien-

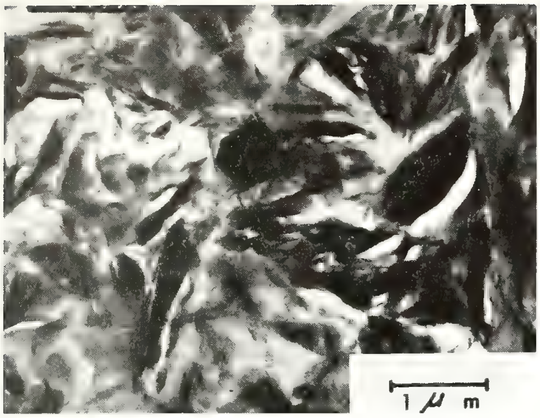

Figure 7. Clay fabric of randomly-oriented domains. Core B-2 (9.3 m).

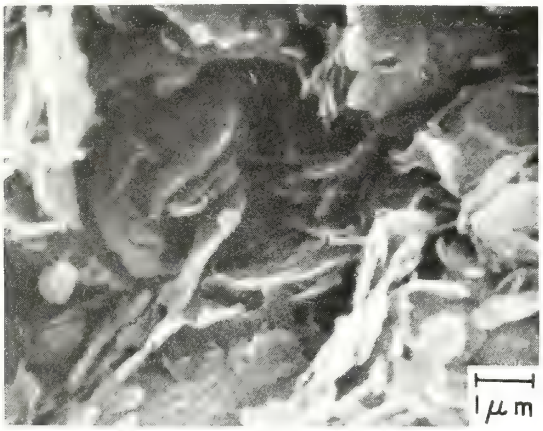

Figure 8. SEM micrograph of sediment from core BH-3A sampled at 12.5 m below mudline. Note open fabric characterized by large voids and randomly-oriented domains.

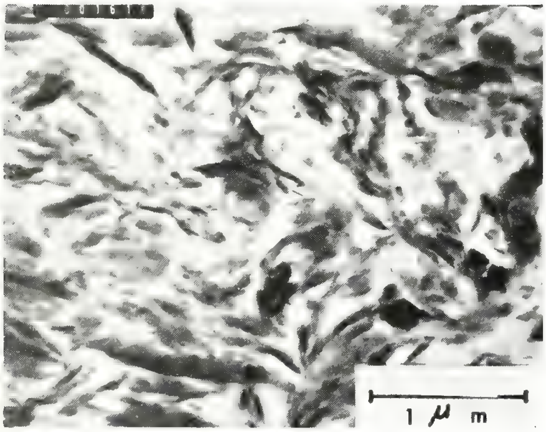

Figure 9. Clay fabric of well-defined domains. Core B-1 (27.7 m).

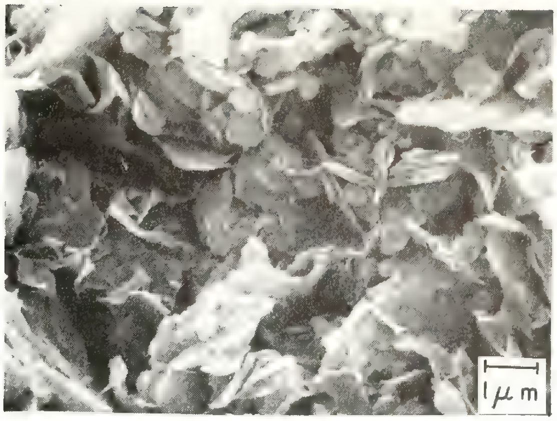

Figure 10. SEM micrograph of sediment from core B-2 sampled at 26.5 m below mudline. Randomly oriented domains and large voids are characteristic of the fabric. Edge-to-face particle contacts are apparent.

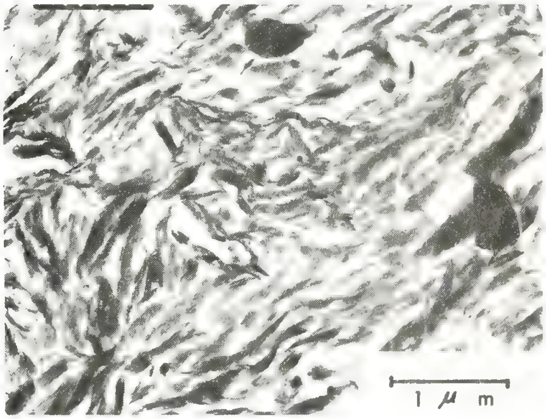

Figure 11. Clay fabric of highly oriented domains. Observe the obliquely oriented domains. Core B-1 (120.4 m).

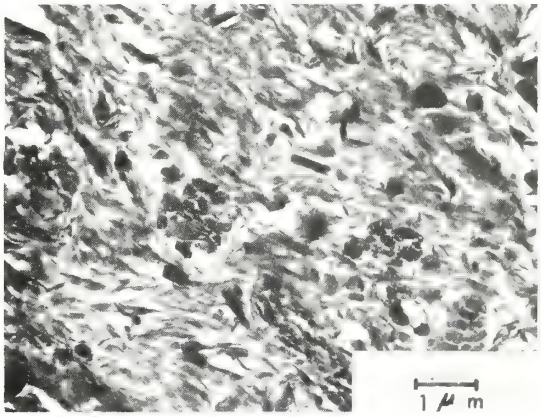

Figure 12. Clay fabric of highly orioriented domains. Core B-1 (144.8 m).

tation, but not perfect particle alignment is necessary to develop a relatively fissile sediment.

Void Geometry

The void geometry of the deeply buried clays is quite unlike the voids of the overlying high-porosity sediment. In general descriptive terms, the voids of the shallow, high-porosity clays are characterized by very irregular shape. Void geometry could be expressed by a length-to-width ratio which approaches a value of unity whereas the lower deeply buried clays would be characterized by a void geometry with a length to width ratio approaching infinity. The deeply buried submarine clays of porosity zone 5 are characterized by a preponderance of "thin," long, voids which are clearly produced by the particle-to-particle alignment and development of chains. Apparently a number of the obliquely trending particles and those lying normal to the overall general preferred orientation of the clay fabric are associated with a few of the larger irregularly-shaped voids of the deeply buried clays. Clearly, despite the strong degree of preferred clay particle orientation observed in these low-porosity clays, significant numbers of particles, usually in the form of domains, deviate from the preferred general direction. This influences the overall fabric characteristics and thus produces few irregularly-shaped voids and folding and bending of particles and chains. These characteristic features were not observed in the overlying high-porosity clays and they are interpreted here as being formed, and thus developed from the process of natural consolidation and imposed stress conditions given the fabric type and related geochemical conditions amenable to the development of strong preferred particle orientation at depths of burial within zone 5.

Conclusions

The significance of the clay fabric observed for the Mississippi Delta samples is the conclusion that domains do exist in these moderately high-porosity, only slightly consolidated, submarine sediments and that strong preferred particle orientation is achieved at depths of not greater than 120 m, and probably somewhat less. The strong preferred particle orientation is interpreted as being developed from the process of natural consolidation and imposed stress conditions. The overlying sand may have functioned as a relatively good drainage path for the underlying clays during consolidation and dewatering.

Acknowledgements

Discussions with Drs. Roland Pusch, W. D. Keller, Matthew H. Hulbert, and C. C. Mathewson are especially appreciated. Thanks are due Ms. Brenda Bohlke for providing the SEM micrographs.

References

Bennett, R. H., W. R. Bryant and G. H. Keller, 1977. Clay fabric and geotechnical properties of selected submarine sediment cores from the Mississippi Delta. U. S. Dept. Commerce, NOAA Prof. Paper 9, 86 pp.

Bennett, R. H. and D. N. Lambert, 1971. Rapid and reliable technique for determining unit weight and porosity of deep-sea sediments. Mar. Geol., 11:201-207.

Bohlke, B. M. and R. H. Bennett, 1979 (in press). Mississippi Prodelta crusts: A clay fabric and geotechnical analysis. Mar. Geotechnology.

Coleman, J. M. and L. D. Wright, 1974. Formative mechanisms in a modern depocenter. Stratigraphy and petroleum potential of northern Gulf of Mexico (Part II). New Orleans Geol. Soc. Seminar, Jan. 22-24, 1974, p. 90-139.

Fisk, H. N. and B. McClelland, 1959. Geology of continental shelf, Louisiana: Its influence on offshore foundation design. Bull. GSA, 70:1369-1394.

Gillott, J. E., 1969. Study of the fabric of fine-grained sediment with SEM. J. Sed. Petrol., 39:90-105.

Gipson, M. Jr., 1965. Applications of the electron microscope to the study of particle orientation and fissility in shale. ibid, 35: 408-414.

Hulbert, M. H. and R. H. Bennett, 1975. Electrostatic cleaning technique for fabric SEM samples. Clays and Clay Minerals, 23:331.

Johns, W. D. and R. E. Grim, 1958. Clay mineral composition of recent sediments from Mississippi Delta. J. Sed. Petrol., 28:186-199.

Shepard, F. P., 1956. Marginal sediments of the Mississippi Delta. Bull. Amer. Assoc. Petrol. Geol., 40:2537-2623.

Discussion with Reviewers

L. Dengler: Could swelling of clay minerals or adsorption of water affect your computations of water content, porosity, or void volume?

Authors: Mass physical properties of core samples are determined by laboratory techniques. The measurements thus obtained reflect the properties of the sediment at ambient laboratory pressure. When cores are recovered the in situ confining stresses are obviously changed and some sample swelling is expected to occur. If in situ estimates of porosity are desired, values can be determined using laboratory consolidation data and techniques described by E. L. Hamilton (1959).

Hamilton, E. L., 1959. Thickness and consolidation of deep-sea sediments. Bull. Geol. Soc. Amer., 70:1399-1424.

For additional discussion see page 424.

Additional discussion with reviewers of the paper "Clay Fabric and Related Pore Geometry of Selected Submarine Sediment..." by R.H. Bennett,et al, continued from page 524.

L. Dengler: Do you know if overburden pressure might effect such swelling or adsorption?

Authors: The reduction of in situ confining stresses, including lateral and vertical (overburden) effective stress, would result in sample swelling when a core is recovered.

L. Dengler: How was clay mineral orientation determined?

Authors: Both quantitative measurements and qualitative estimates were carried out on TEM micrographs using a defined reference line and measuring the angle of a given clay particle with respect to the reference line. Clay particle orientations were measured on micrographs of sections approximately 90° to one another.

L. Dengler: I infer that orientations and void dimensions were determined primarily from two-dimensional TEM photomicrographs. What feelings do you have for the three-dimensional structure or how might it be determined?

Authors: One would need to know what particular question(s) are being addressed with regard to the determination of three-dimensional clay structures. Each question may require different approaches to a particular problem. What can be said regarding the Mississippi Delta clays is that domains exist and constitute the "building blocks" of clay fabric. The domains can form edge-to-face, edge-to-edge, and face-to-face contacts. Face-to-face contacts can form sheets in a large "shingle-type" array, and edge-to-edge contacts can form chains both of which can be structured to form high-porosity sediments.

TEM micrographs provide a plane of reference for comparing void sizes (two dimensions) relative to particle sizes. SEM micrographs provide information of an irregular fracture surface of a clay specimen with virtually no common reference plane. SEM techniques provide a broader specimen areal coverage compared to TEM techniques.

W. D. Keller: Does a flat lying Paleozoic shale (not tectonically deformed) represent a statically deformed, by single vertical pressure, clay-mud deposit?

Authors: In general terms, yes, given the conditions that dewatering and densification occur in response to vertical effective stress.

W. D. Keller: Is a domain built of flocs, or vice versa?

Authors: A domain is an assemblage of face-to-face clay plates. Plates can be arranged in a "perfect stack" such as described by Sloan and Kell (1966) and by Sides and Barden (1971), or the platelets may have a slight offset to one another as described by Smalley and Cabrera (1969).

The domain is a basic particle and "building block" of clay fabric and soil structure. Thus domains can form flocs. We use the terminology of van Olphen (1963), that only edge-to-edge and edge-to-face types of particle association produce agglomerates termed "flocs." We use the term flocculation to imply a process by which two or more particles (domains or "single plates") agglomerate regardless of the particle orientations, one to another. The term "floc" denotes a fabric unit with relatively large intravoids which, conversely, is not produced by face-to-face particle association.

W. D. Keller: Isn't a "stack of plates" a face-to-face floc?

Authors: A "stack of plates" called a domain can be an original fabric unit of a rock or sediment, or it may be produced by processes of flocculation. A domain also can be produced by consolidation. The term "domain" is not used here to denote mode of origin.

References

Mathewson, C. C., K. A. Merkle, and T. R. McKee, 1973. Natural alteration of clay fabric with depth of burial (abstract). Clays and Clay Minerals Conf., Banff, Canada, Abstract No. 22, p. 15.

Sloane, R. L. and T. R. Kell, 1966. The fabric of mechanically compacted kaolin. 14th Nat'l Conf. on Clays and Clay Minerals, 14:289-296.

Sides, G. and L. Barden, 1971. The microstructure of dispersed and flocculated samples of kaolinite, illite, and montmorillonite. Canadian Geotech. Journal, 8:391-399.

Smalley, I. J. and Cabrera, J. G., 1969. Particle association in compacted kaolin. Nature, 22: 80-81.

van Olphen, H., 1963. An Introduction to Clay Colloid Chemistry. Interscience Publishers, John C. Wiley & Sons, 301 pp.

Metal Enrichments in Sediments from the TAG Hydrothermal Field

D. S. Cronan

Applied Geochemistry Research Group
Dept. of Geology, Imperial College
London SW7. U.K.

P. A. Rona

Marine Geology Division
Atlantic Oceanographic Labs, N.O.A.A.
Miami, U.S.A.

S. Shearme

Applied Geochemistry Research Group
Dept. of Geology, Imperial College
London SW7. U.K.

Abstract Metal distribution patterns in sediments from the TAG Hydrothermal Field on the Mid-Atlantic Ridge at 26°N indicate an overall enrichment of manganese relative to the North Atlantic average, and localized enrichments of Fe, Cu, and Zn in the vicinity of the supposed hydrothermal vents. These data indicate that metal dispersion haloes of the type occurring around the Atlantis II Deep in the Red Sea should not be sought as evidence for submarine hydrothermal activity on open ocean mid-ocean ridge segments, but that broad areas of manganese enrichment should be sought instead.

Marine Mining, Volume 2, Number 1–2
0149-0397/79/1030-0079/$02.00/0
Copyright © 1979 Crane, Russak & Company, Inc.

Introduction

Active hydrothermal systems are being found with increasing frequency on spreading centers at mid-ocean ridge crests and in other submarine volcanic areas, and more occurrences can be expected. In these systems, seawater enters hot, newly formed oceanic crust, becomes heated, reacts with crustal rocks, and then rises back to the sea floor as metal-rich hydrothermal solutions, precipitating some of their metals en-route and most of the remainder on discharge onto the sea floor.

The best developed and most intensively studied submarine hydrothermal system known is in the Atlantis II Deep of the Red Sea (Bischoff, 1969; Bignell *et al.,* 1976a; and others) in which Cu- and Zn-rich sulphides, iron oxides and silicates, and manganese oxides are selectively fractionated from each other on progressive mixing of a hydrothermal brine with seawater. Metal enrichments of the magnitude of those in the Red Sea have recently been found on the East Pacific Rise at 21°N and in the Gulf of California (Lonsdale, 1978; Francheteau *et al.,* 1979), and there is every reason to suppose that others occur.

In an attempt to develop geochemical exploration methods for submarine hydrothermal sulphide deposits, studies on the dispersion of metals around the Atlantis II Deep have been carried out by Bignell *et al.* (1976b). These workers found a dispersion halo of manganese enrichment in sediments up to 20 km in diameter around the deep, with a gradient of increasing manganese concentrations toward the deep. This was considered to result from the selective fractionation of manganese from iron, derived from the hydrothermal solutions within the deep as pH and Eh increased due to the brine mixing with seawater (Figure 1). The chemistry of this process has been described by Krauskopf (1957). Dispersion haloes of other metals were also found. Follow-up studies off the submarine volcano of Santorini in the eastern Mediterranean were made by Smith and Cronan in order to see if the manganese dispersion found around the Atlantis II Deep was unique, or whether it was an example of a more general phenomenon associated with

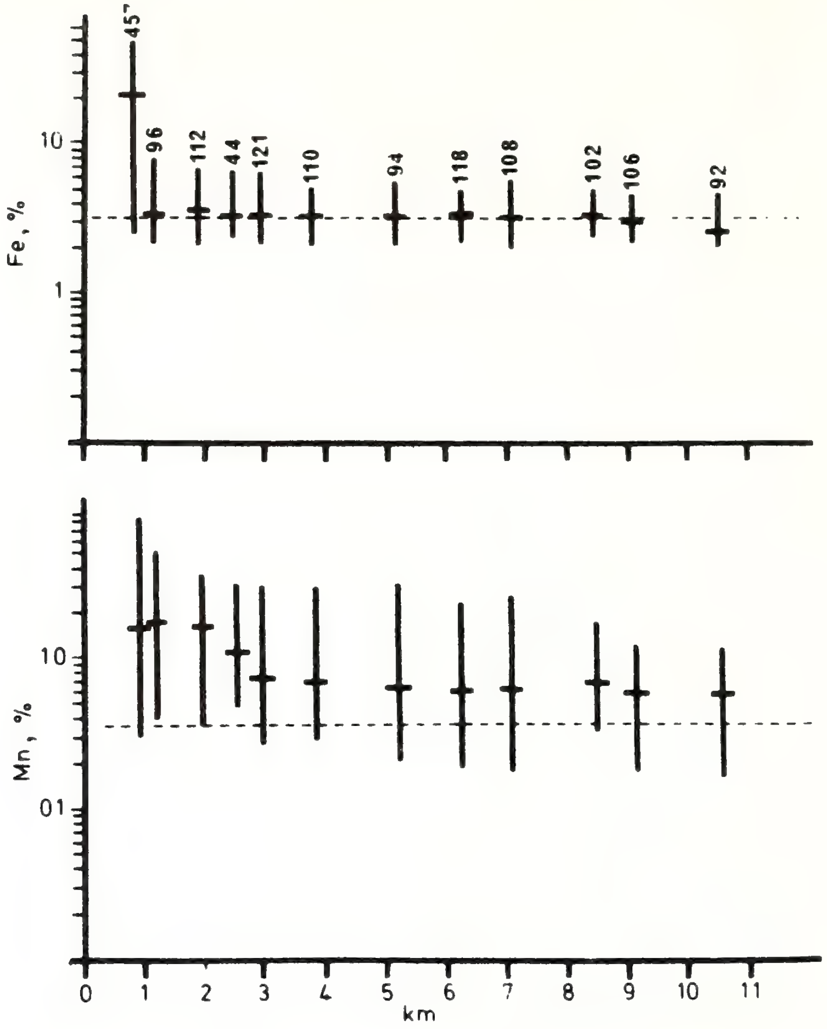

Figure 1. Selective dispersion of Mn from Fe around the Atlantis II Deep, Red Sea (after Bignell *et al.*, 1976b).

submarine hydrothermal activity, and thus would have an exploration potential. Fractionation of Mn from Fe was found in shallow-water embayments acting as hydrothermal discharge channels off Santorini (Smith and Cronan, 1975), demonstrating that the processes leading to the development of the dispersion halo around the Atlantis II Deep are not restricted to the Red Sea. It was to see if a similar dispersion halo of manganese, and possibly other elements too, might occur in sediments around a hydrothermal area on an elevated portion of the world Mid-Ocean Ridge System subjected to unrestricted circulation of bottom water, unlike the situation both in the Atlantis II Deep area and off Santorini, that a study of the geochemistry of sediments from the TAG hydrothermal field on the Mid-Atlantic Ridge crest at 26°N was undertaken.

Results

The TAG hydrothermal field (Figure 2) on the east wall of the rift valley of the Mid-Atlantic Ridge at 26°N contains a hydrothermal system which has been the subject of close study ever since the discovery there of hydrothermally deposited manganese oxide encrustations around a hydrothermal vent (Rona *et al.,* 1976) and a water temperature anomaly which indicated that the vent was still discharging. Near-bottom water temperature measurements made in 1977 revealed a second temperature anomaly indicative of a second active vent area about 2.5 km northeast of Vent 1 along the interval between the 2,800 and 3,000 m isobaths (Rona, 1979) (Figure 2). Bathymetric and bottom photographic transects suggest that the 2,900-m isobath is underlain by a fault zone (Rona *et al.,* 1976). The presence of the two active vent areas and the occurrence of patchy deposits of hydrothermal manganese oxide encrustations along the fault zone between them support the interpretation that segments of the fault zone are conduits for the discharge of hydrothermal solutions (Scott *et al.,* 1974).

The fault zone between the two vent areas is one of several such zones that trend sub-parallel to the axis of the rift valley and sepa-

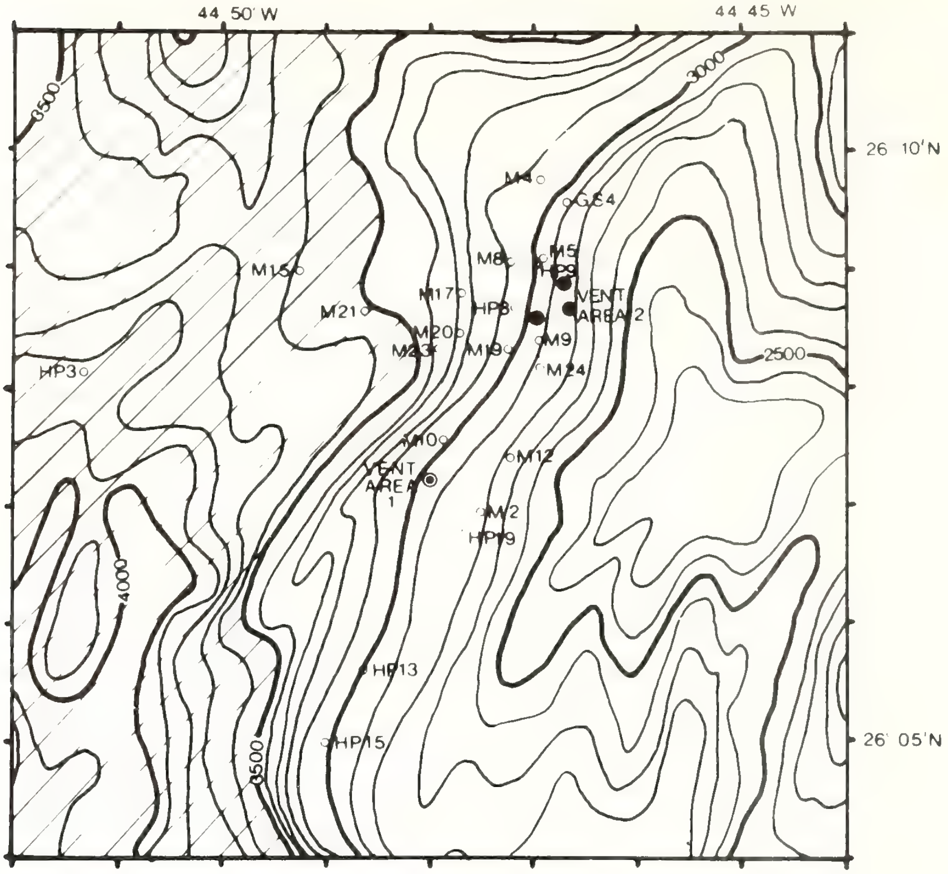

Figure 2. Bathymetry, location of vent areas, and sediment sample sites in the TAG area.

rate fault blocks that underlie its east wall (Rona *et al.,* 1976). The tops of the fault blocks form terraces, some hundreds of meters wide, that are veneered with predominantly carbonate sediments of the order of centimeters in thickness. In 1976 and 1977 the NOAA ship *Researcher* conducted a sampling program as part of the NOAA Metallogenesis Project to recover specimens of these sediments for the purpose mentioned previously. Core and grab stations are shown in Figure 2.

After being described, the sediment samples, all carbonate oozes, were totally digested in HF, HNO_3, and $HClO_4$ and analyzed for Mn, Fe, Ni, Co, Cu, Pb, Zn, Al, and Ca by Atomic Absorption Spectrophotometry. Following Bignell *et al.* (1976b) the data were plotted with increasing distance from both of the previously located vent areas. The distributions of Fe, Mn, Cu, and Zn in this regard are illustrated in Figures 3 and 4. Most of the elements determined show considerable variations throughout the TAG area, especially Fe, Cu, and Zn, which are markedly enriched in sediments from three sites, two of which are close to the fault zone between Vent Areas 1 and 2 and the other on the median valley floor. These sediments contain bands of dark red/brown material together with small streaks of hematite. However, none of the elements determined, including those not plotted in Figures 3 and 4, show any consistent trends in relation to the vent areas. Nevertheless, manganese is higher, on average, in the sediments from the TAG area as a whole than the North Atlantic sediment average (Table 1) which, coupled with a reported high accumulation rate of

Table 1
Comparison of metalliferous sediment compositions from different areas (recalculated carbonate free).

	$CaCO_3$ %	*Fe* %	*Mn* %	*Al* %	*Cu* *ppm*	*Zn* *ppm*	*Pb* *ppm*	*Co* *ppm*	*Ni* *ppm*	*Mg* %
1	80.37	7.76	0.66	5.76	1723	294	158	120	115	3.33
2	81.90	6.13	0.66	6.01	459	149	149	123	118	3.52
3		5.02	0.40	9.04	115		52	39	79	
4		5.88	0.28	10.60	79	161	122		107	2.61
5	81.04	7.96	0.41	5.79						

1. Average composition of TAG area sediments (this work).
2. Average composition of TAG area sediments excluding metal enriched samples M 19, 20 and 21.
3. Average Atlantic pelagic clay (Turekian and Wedephol, 1961).
4. Average of Atlantic DSDP basal sediments (Horowitz and Cronan, 1976).
5. Average composition of sediments from the Mid-Atlantic Ridge at 45°N (Cronan, 1972).

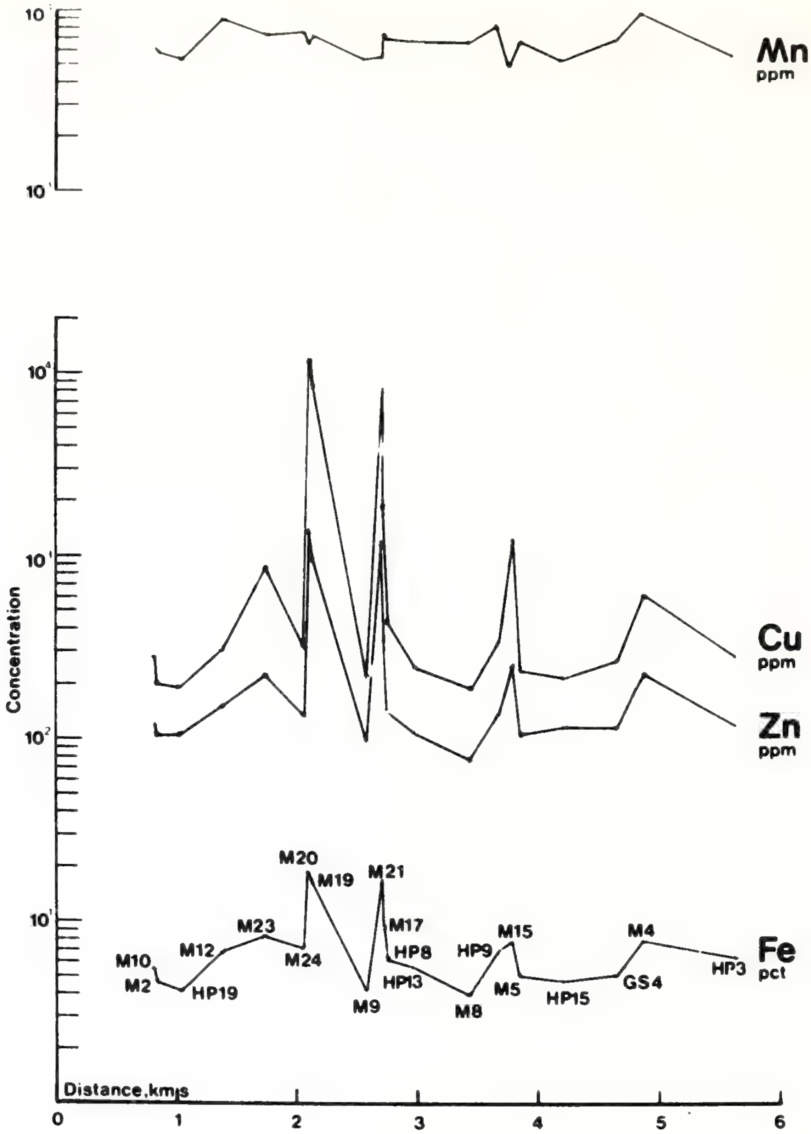

Figure 3. Distribution of Mn, Fe, Cu, and Zn in sediments in relation to Vent Area 1, recalculated CaCO$_3$ free.

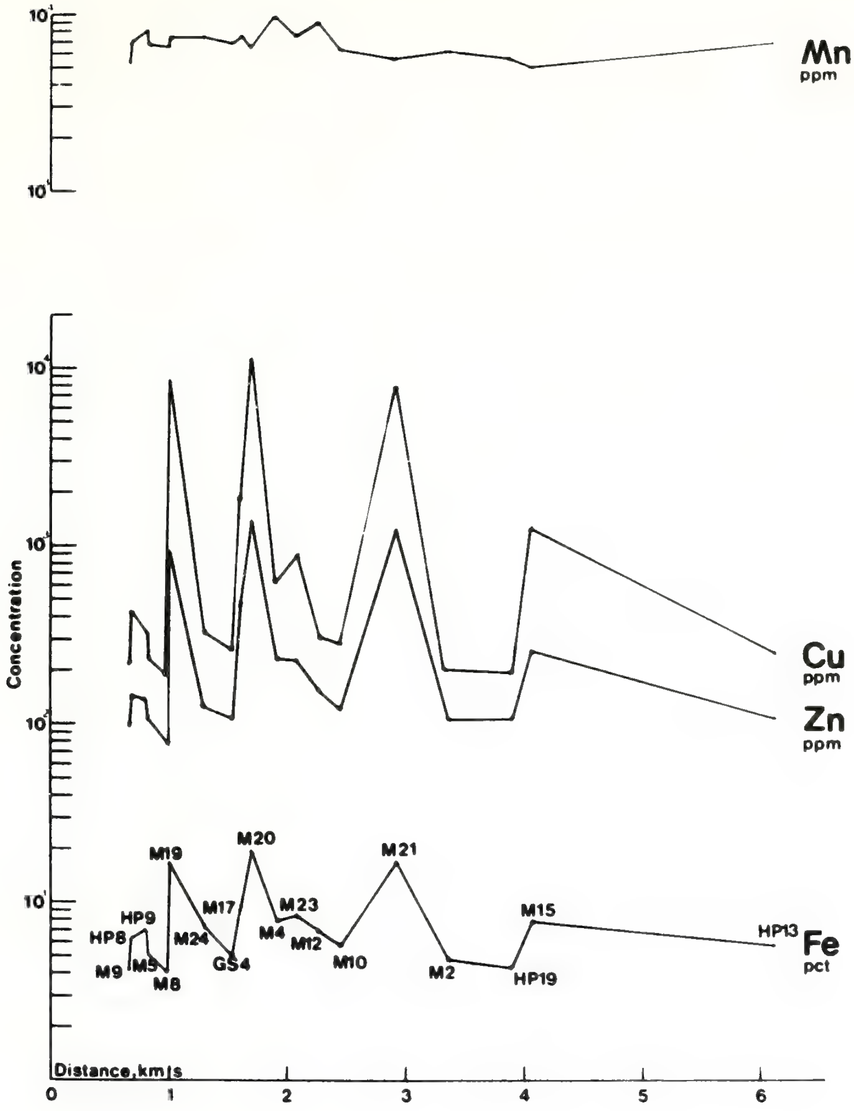

Figure 4. Distribution of Mn, Fe, Cu, and Zn in sediments in relation to Vent Area 2, recalculated $CaCO_3$ free.

manganese in the sediments (Scott *et al.,* 1978), suggests a hydrothermal supply of this element. A hydrothermal supply of Fe, Cu, and Zn is also possibly indicated at those sites where the elements are markedly enriched. They would be expected to precipitate before manganese in a submarine hydrothermal fractionation sequence (Krauskopf, 1957; Cronan, 1976; Bignell *et al.,* 1976b).

Discussion

Consideration of the likely behavior of a hydrothermal system on a portion of the world Mid-Ocean Ridge System subjected to unrestricted circulation of oxidizing bottom water, such as the TAG area, has led to the suggestion that much of the lateral differentiation of elements around a hydrothermal outlet as observed in and around the Atlantis II Deep would probably occur vertically within the upper part of the oceanic crust, and that the hydrothermal deposits on the sea floor in such areas would be the end products of the fractionation sequence (Cronan, 1976, 1978). This is because oxidizing seawater entering the fractures and fissures underlying the sea floor and mixing with the rising hydrothermal fluids would result in the selective precipitation of most of the metals that they contain. The reason why the precipitation of metals takes place principally on the sea floor in the Atlantis II Deep and off Santorini is because reducing conditions occur on or near the surface in both these areas, unlike in the TAG area. On this basis, therefore, one would expect that much of any hydrothermal precipitation of metals in the TAG area would take place below the sea floor and/or in the immediate vicinity of the hydrothermal vents, and that a wide manganese dispersion halo of the Atlantis II Deep type would not occur. From the present data, this is the situation that seems to prevail. Hydrothermal manganese is probably being flushed out of the vents, perhaps partly in a particulate form. It will become well mixed in the energetic bottom waters and precipitate out relatively uniformly throughout the TAG area to give higher manganese concentrations in the sediments, as noted, than the North Atlantic average. By contrast, Fe, Cu, and Zn which, as mentioned, would precipitate before manganese in a hydrothermal fractionation sequence, do show some enrichments close to the supposed hydrothermal discharge points in the fault zone between Vent Areas 1 and 2. It follows, therefore, that geochemical exploration for hydrothermal deposits on open ocean mid-ocean ridge segments should not be directed toward seeking dispersion haloes of manganese such as occurs around the Atlantis II Deep in the Red Sea. Rather, such exploration should be directed toward defining regions of uniformly elevated manganese values in which more localized enrichments of the elements of economic interest might occur.

Acknowledgments

We wish to thank the master and crew of the NOAA ship *Researcher* for the collection of the samples, and the Natural Environment Research Council for providing financial support which enabled them to be worked up. Sarah Shearme also thanks the Natural Environment Research Council for a research studentship under the supervision of D.S. Cronan.

References

Bignell, R., Cronan, D.S., and Tooms, J.S., 1976a, Red Sea Metalliferous brine precipitates. Geol. Assoc. Canada Special Paper No. 14, pp. 147–184.

Bignell, R.D., Cronan, D.S., and Tooms, J.S., 1976b, Metal dispersion in the Red Sea as an aid to marine geochemical exploration. Trans. Inst. Min. Met., Vol. 85, Sect. B, pp. 274–278.

Bischoff, J.L., 1969, Red Sea geothermal brine deposits; their mineralogy, chemistry and genesis. In: *Hot Brines and Recent Heavy Metal Deposits in the Red Sea,* Degens, E.T., and Ross, D.A., ed. New York: Springer Verlag, pp. 368–401.

Cronan, D.S., 1972, The Mid-Atlantic Ridge near 45°N, XVII, Al, As, Hg and Mn in ferriginous sediments from the median valley. Canadian Journal of Earth Sciences, Vol. 9, pp. 319–323.

Cronan, D.S., 1976, Implications of metal dispersion from submarine hydrothermal systems for mineral exploration on mid-ocean ridges and in island arcs. Nature (Lond.), Vol. 262, pp. 567–569.

Cronan, D.S., 1978, Recent advances in geochemical exploration for undersea mineral deposits. Trans. Inst. Min. Met. Vol. 87, Sect. A, pp. 143–146.

Francheteau, J., Needham, H.D., Choukroune, P., Juteau, T., Seguret, M., Ballard, R.D., Fox, P.J., Normark, W., Carranza, A., Cordoba, D., Guerrero, J., Rangin, C., Bougault, H., Cambon, P., and Hekinian, R., 1979, Massive deep-sea sulphide ore deposits discovered on the East Pacific Rise. Nature (Lond.), Vol. 277, pp. 523–528.

Horowitz, A. and Cronan, D.S., 1976, The geochemistry of basal sediments from the North Atlantic Ocean. Marine Geology, Vol. 20, pp. 205–228.

Krauskopf, K.B., 1957, Separation of manganese from iron in sedimentary processes. Geochim. Cosmochim. Acta, Vol. 12, pp. 61–84.

Lonsdale, P.F., 1978, S.I.O. Annual Report.

Rona, P.A., 1979, Near bottom water temperature anomalies: Mid-Atlantic Ridge crest at latitude 26°N. Geophys. Res. Letts., Vol. 5, pp. 993–996.

Rona, P.A., Harbison, R.N., Bassinger, B.G., Scott, R.B., and Nalwalk, A.J., 1976, Tectonic fabric and hydrothermal activity of mid-Atlantic Ridge crest (lat. 26°N). Geological Society of America Bulletin, Vol. 87, pp. 661–674.

Scott, R.B., Rona, P.A., McGregor, B.A., and Scott, M.R., 1974, The TAG hydrothermal field, Nature, Vol. 251, pp. 301–302.

Scott, M.R., Scott, R.B., Morse, J.W., Betzer, P.R., Butler, L.W., and Rona, P.A., 1978, Metal enriched sediments from the TAG hydrothermal field. Nature, Vol. 276, pp. 811–813.

Smith, P.A., and Cronan, D.S., 1975, Dispersion of metals associated with a submarine exhalative deposit. Proc. 3rd Oceanology International Conf. Brighton, UK. B.P.S. Exhibitions Ltd., pp. 111–114.

Turekian, K.K. and Wedephol, K.H., 1961, Distribution of elements in some major units of the earth's crust. Geological Society of America Bulletin, Vol. 72, pp. 175–192.

25. Ocean Dumping and Marine Pollution: Geological Aspects of Waste Disposal. H. D. Palmer and M. G. Gross, eds., Dowden, Hutchinson & Ross, Inc., Stroudsburg, Pa., 73-95.

Mud Deposits near the New York Bight Dumpsites: Origin and Behavior

George L. Freeland
Donald J. P. Swift
Robert A. Young

ABSTRACT

A detailed investigation of the floor of the New York Bight apex reveals that muddy sediment occurs in the Christiaensen Basin, in the fringing lagoons and marshes near the mouths of tidal inlets, and in ephemeral patches on the Long Island shoreface, where mud settles into the troughs of sandwave-like bedforms. The appearance and disappearance of these nearshore mud patches has led to an erroneous concept of a sewage-sludge "front" advancing toward the Long Island beaches from the sewage-sludge dumpsite. While Bight apex mud deposits do contain sewage sludge, this contamination is usually not apparent in gross physical properties or composition; sophisticated chemical techniques are required to detect the contamination. Fine-grained deposits near the New York Bight sewage-sludge dumpsite are primarily of natural origin and should, therefore, be called mud, not sludge. Fine-grained sediment at the dredge-spoil dumpsite is also mostly natural sediment, but it is anthropogenic in that it is dredged harbor and estuary sediment.

The impact of sewage-sludge dumping in the New York Bight apex depends to a large extent on the pathways and rates of the natural sediment transport system. The rate of sewage-sludge input is higher than the estimated rate of fine sediment input from land runoff. However, the input of suspended fine sediment into the Bight apex by coastwise shelf currents, though not precisely known, may be much higher than the input from either dumping or land runoff. The rate at which organic matter is cycled through the suspended-sediment system via biological production and consumption of organic suspended sediment is estimated to be almost an order of magnitude higher than the rate of suspended-sediment input from either land runoff or dumping. Such limited information as is available suggests that the rate of sewage-sludge dispersal is high relative to the rate of input. Our model leads us to infer that 1) sewage sludge is rapidly diluted in the Bight apex by natural sediment, and 2) the more stable sewage-sludge components are widely dispersed through the natural mud deposits of the New York Bight system.

INTRODUCTION

Intense public interest has been generated in recent years concerning the nature and distribution of mud deposits on the Long Island inner shelf (Figs. 1, 2). The interest stems from public concern over the high rate of sewage-sludge dumping at the dumpsite 25 km seaward of New York Harbor entrance (4×10^6 m^3, containing 5% solids, in 1973), and confusion concerning the difference between anthropogenic sewage-sludge deposits and naturally occurring ocean floor muds (Soucie, 1974). There has been a tendency, in public discussions, to refer to any fine-grained sea floor deposit as

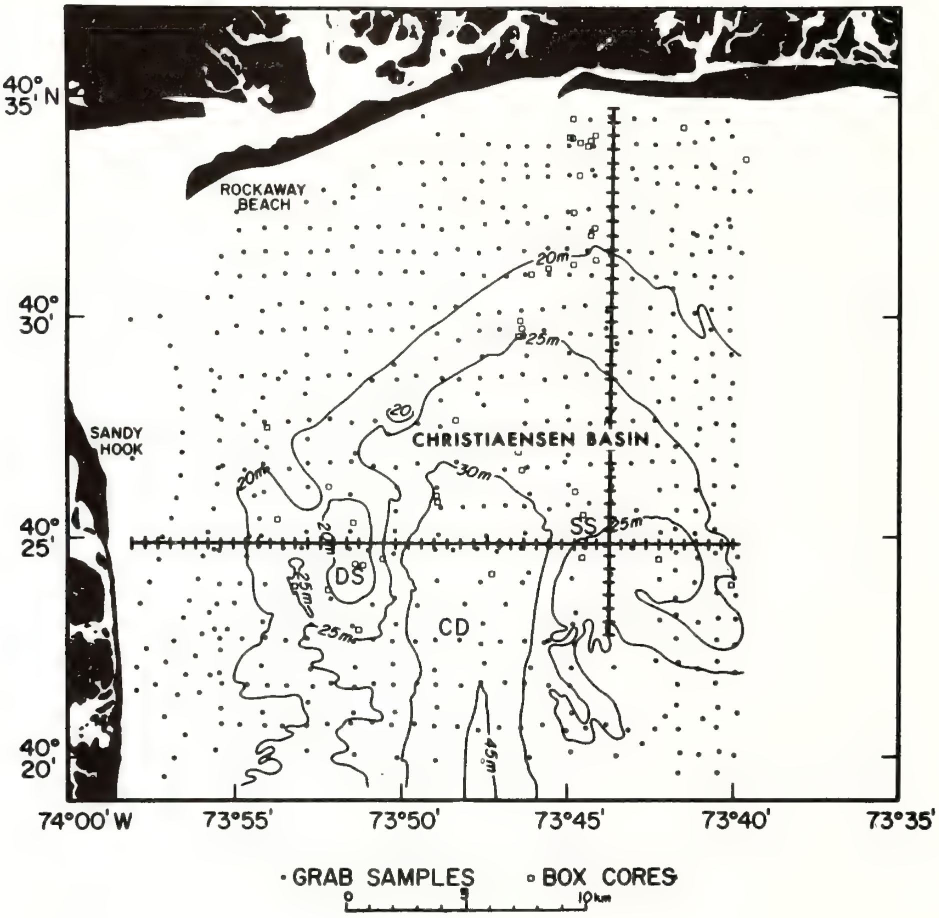

Figure 1
Bathymetry of the New York Bight apex mud grab-sample net on which map of bottom sediment distribution is based. CD is cellar-dirt dumpsite, DS is dredge-spoil dumpsite, SS is sewage-sludge dumpsite, HSV is the upper Hudson Shelf Valley, CV is Cholera Bank, and ticked lines are quarterly monitoring transects.

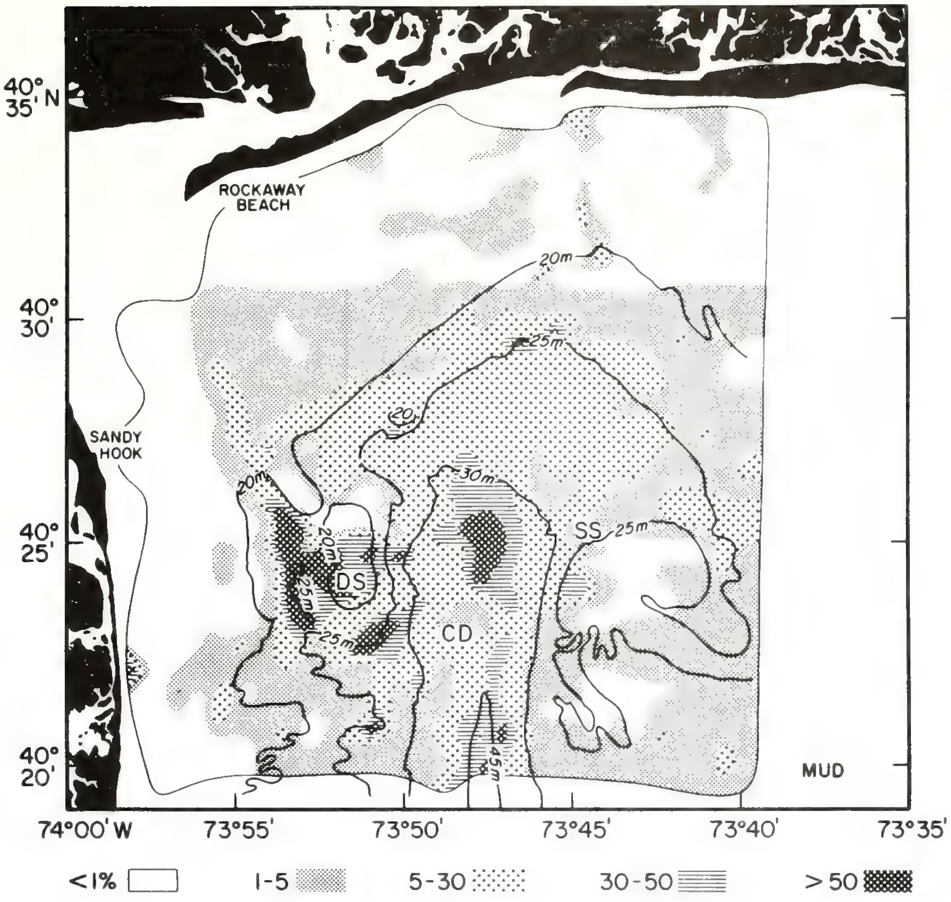

Figure 2
Map of percent mud (sediment finer than 62μ) on the floor of the New York Bight apex. From Freeland and others, in press.

"sewage sludge", and newspaper articles have referred to "sludge beds" and a sludge "front" creeping from the dumpsite toward the Long Island beaches (Pearson, 1974a, b, c). In addition to sewage-sludge particles, approximately 0.5×10^6 m^3/yr. of dumped dredge-spoil fine particles settle slowly to the bottom and are widely dispersed away from the dredge-spoil dumpsite proper (Freeland and Merrill, 1976). They also become mixed with natural and sewage-sludge muds.

Recent studies indicate that the mud deposits of the New York Bight apex (the inner shelf in the vicinity of New York Harbor mouth; Fig. 1) and upper Hudson Shelf Valley generally contain no more organic carbon than is found in continental shelf muds from other areas (Hatcher and Keister, 1975; Duedall, 1976). The muds of the New York Bight apex may well contain significant amounts of anthropogenic organic matter in addition to naturally occurring organic matter, but the detection of the differing chemical signatures of the "natural" organic component of shelf-floor mud versus that of sewage sludge requires sophisticated analytical techniques (see Segar and Cantillo, 1976; Harris, 1976; Hatcher and Keister, 1976; Hatcher and others, 1977; Schaeffer, 1977 for discussion of such methods). Gross (1972) and Mueller and others (1976) have pointed out that the input of anthropogenic sediment into the New York Bight apex exceeds the input of natural land-derived sediment, but this ignores the contribution of the alongcoast flux of natural sediment, which may be much greater than either the contribution from land or from sludge dumping. Drake (1977, p. 222), calculated that the resuspension of bottom sediment in the New York Bight apex during a two-day period of strong wind-driven currents was equivalent to between 10 and 20 days of sewage-sludge dumping. Dilution of sewage sludge with other sediment must be rapid during the stormy winter months, when strong wind-forcing of water flow occurs every seven to ten days.

The purpose of this paper is to assess the origin and behavior of fine particles in the apex in order to gain insight to the ultimate fate of fine dumped materials. We interpret data on fine-grained bottom deposits in the apex in light of existing models of fine sediment transport on the inner continental shelf.

DISTRIBUTION OF DEPOSITS

Mud deposits in the New York Bight apex occur primarily in the amphitheater-like basin at the head of the Hudson Shelf Valley referred to by Veatch and Smith (1939) as the Christiaensen Basin (Figs. 1, 2). The pattern is compatible with the thesis of McCave (1972, Fig. 94) that mud deposition on the continental shelf does not simply occur in quiet-water settling basins, but is controlled by near-bottom suspended-sediment concentration, as well as by the near-bottom hydraulic activity. In Figure 2, the 5% mud isopleth thus defines an area within which mean near-bottom hydraulic activity is offset by high prevailing near-bottom suspended-sediment concentration so that deposition may occur. In the winter, concentrations are commonly 1 to 3 mg/l 2 m above the sea floor (Drake, 1977)

Repeated occupation of two sampling and sidescan sonar transects indicates the extent of grain-size variation and the patchy distribution of bottom sediment types in the apex (Figs. 3, 4). Such changes in grain size suggest primarily small-scale spatial variations, with the major changes due to temporal variation. Some of the small-scale changes are, no doubt, due to the ship's maneuvering error over small sampling areas. The positions of grab samples are known to ± 3 m, but successive samples from a single station may be tens of meters apart. Furthermore, Figures 3 and 4 indicate that the Christiaensen Basin deposits are primarily muddy sands rather than sandy muds; over-50% mud occurs only near the dredge-spoil dumpsite and in a relatively small area in the central basin.

Of special concern are the temporal and spatial patterns of mud distribution on the Long Island south shore, where beaches are

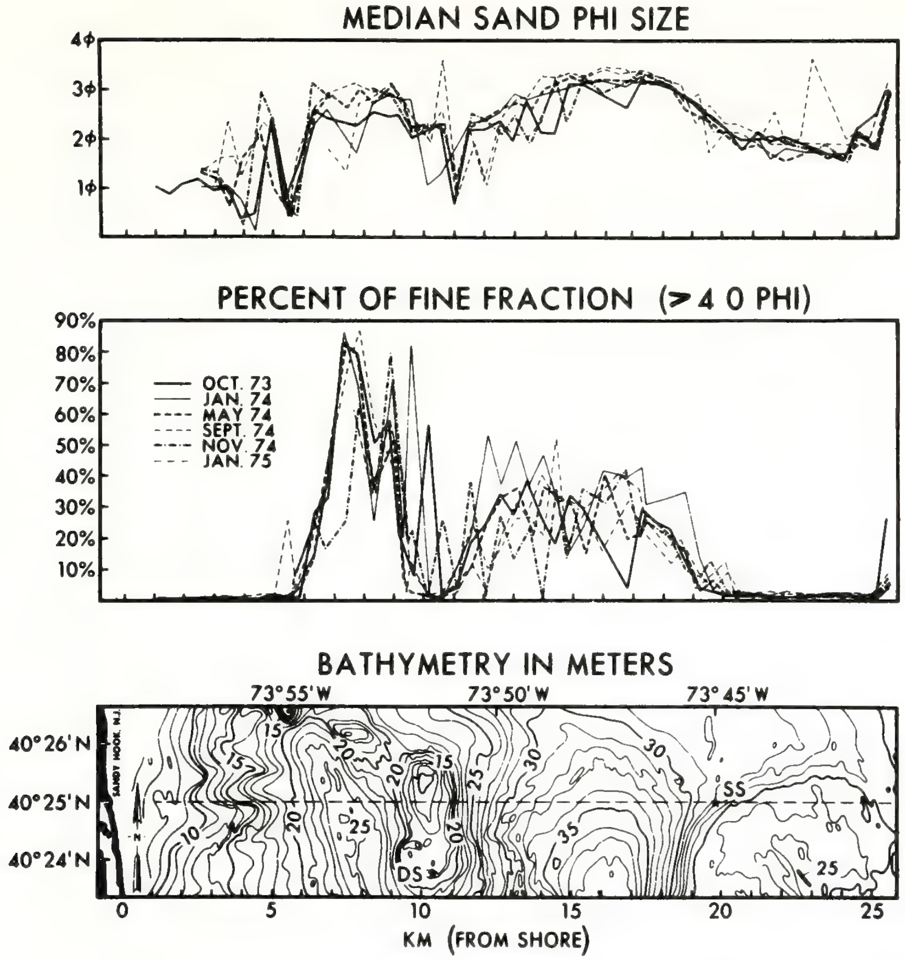

Figure 3
Median diameter of sand and percent mud on an east-west transect through the New York Bight apex for five consecutive reoccupations. From Stubblefield and others, 1977.

imputed to be threatened by the advance of "sludge beds" (Pearson, 1974a, b, c). The incomplete sample net shown on Figure 5 indicates that aureoles of greater than 5% mud in bottom sediment occur around the mouths of Fire Island Inlet and Jones Inlet; further sampling at the mouth of East Rockaway Inlet might show a similar aureole. Inside these inlets the lagoons of the western Long Island south shore are floored primarily by mud and fine muddy sand (Smith and Ali, 1973).

Highly localized mud deposits south of Atlantic Beach (Figs. 2, 5) have lead to reports of onshore movements of "sludge beds". Harris (1976) first called attention to the facts that these mud deposits tend to be found in the troughs of sandwave-like features,

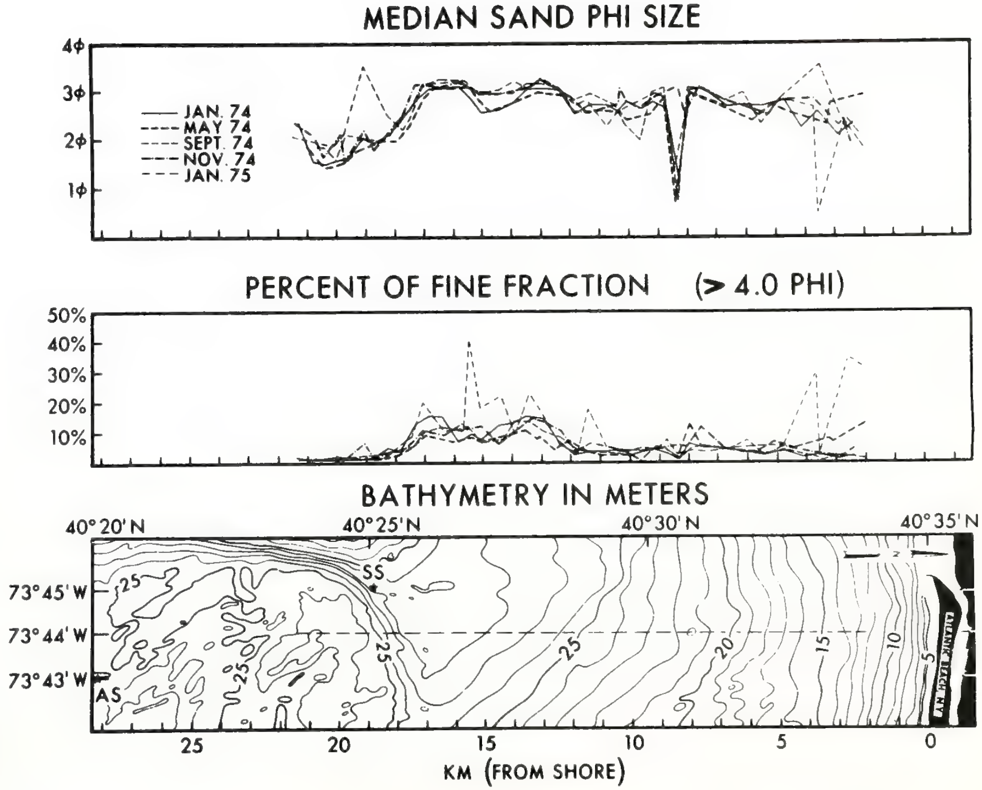

Figure 4 Median diameter of sand and percent mud on a north-south transect through the New York Bight apex for five consecutive reoccupations. From Stubblefield and others, 1977.

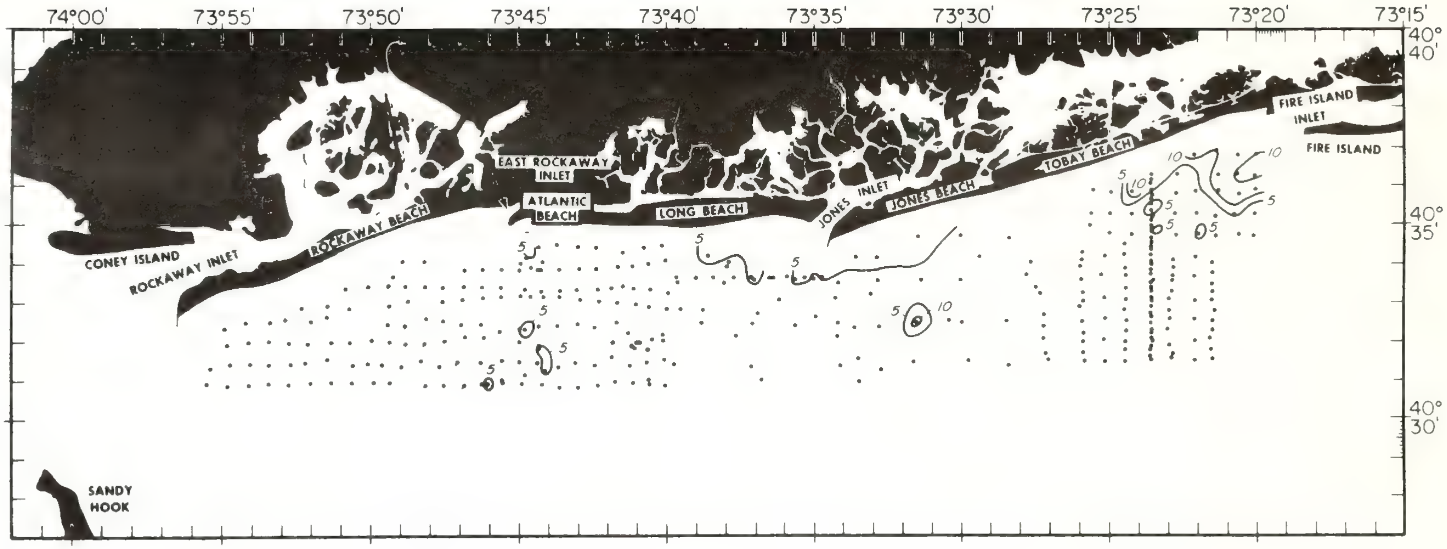

Figure 5
Percent mud on the western Long Island south shore. From Freeland and Swift, in press a)

and that their distribution changed markedly on a time scale of months. However, his results were hampered by inadequate precision in navigation positioning. Some of the same mud patches were encountered during the 1972-1974 grab sampling program of Freeland and others (in press), and in the 1974-1975 transects of Stubblefield and others (1977), especially their January 1975 survey (Fig. 4). However, the 0.5 km sample spacing was too wide for detailed resolution necessary to delineate the true extent of these deposits. Sidescan sonar records and grab samples taken in January 1975 did confirm that the mud patches are associated with the troughs of a sandwave-like pattern that slowly expanded during 1974 (Stubblefield and others, Fig. 14).

On the basis of fathometer records, Harris (1976) reported spacings of 3 to 10 m and heights of approximately 1 m for the sandwave-like bedforms of Atlantic Beach. The features observed on the transect of Stubblefield and others (1977, Fig. 14) had spacings of about 50 m. A detailed sidescan sonar study of the area off Atlantic Beach under calm conditions (Freeland and others, in press; Swift and Freeland, in press) indicates that the bedforms are primarily slight (less than 1 m) depressions, 2 to 200 m wide, floored by coarse, rippled, sand, gravel, and occasionally mud (Figs. 6, 7). The depressions are asymmetrical, with sharply defined northeast sides and gradational southwest sides (Fig. 7).

DISCUSSION

COASTAL TRANSPORT MODEL

The problem of the time and space distribution of coastal mud deposits must be reviewed in the light of existing models of coastal sedimentation. Several decades of studies, summarized by Postma (1967) and Drake (1976) indicate that estuaries and lagoons are generally more turbid than either the rivers that serve them or the adjacent shelf water mass. Hydrodynamic processes operating within these tidal water bodies (two-layer estuarine circulation; settling lag; scour lag, time-velocity asymmetry of the tidal cycle; see Postma, 1967) cause suspended-sediment particles to migrate into them from both rivers and the adjacent shelf. Particles which move into the estuary from both shelf and river sources are entrained and trapped in the turbidity maximum (Schubel, 1972; Schubel and Okubo, 1972). The sediment concentration increases until as much escapes as is added, and equilibrium is attained at a concentration that is many times that of the sources.

Outside the estuaries and lagoons, the zone of high suspended-sediment concentration decreases exponentially across the shelf. Near-bottom concentrations are high on the inner shelf as a consequence of more intense wave surge in the shallow water; near-surface values there are high because of the turbid plumes of brackish surface water that extend from inlets and estuary mouths during ebb tides and because of high primary biological productivity during spring and summer (Figs. 8, 9). Thus, there is a feedback loop on the inner shelf, especially in the nearshore turbid zone in the New York Bight apex analogous to the estuarine feedback loop causing the

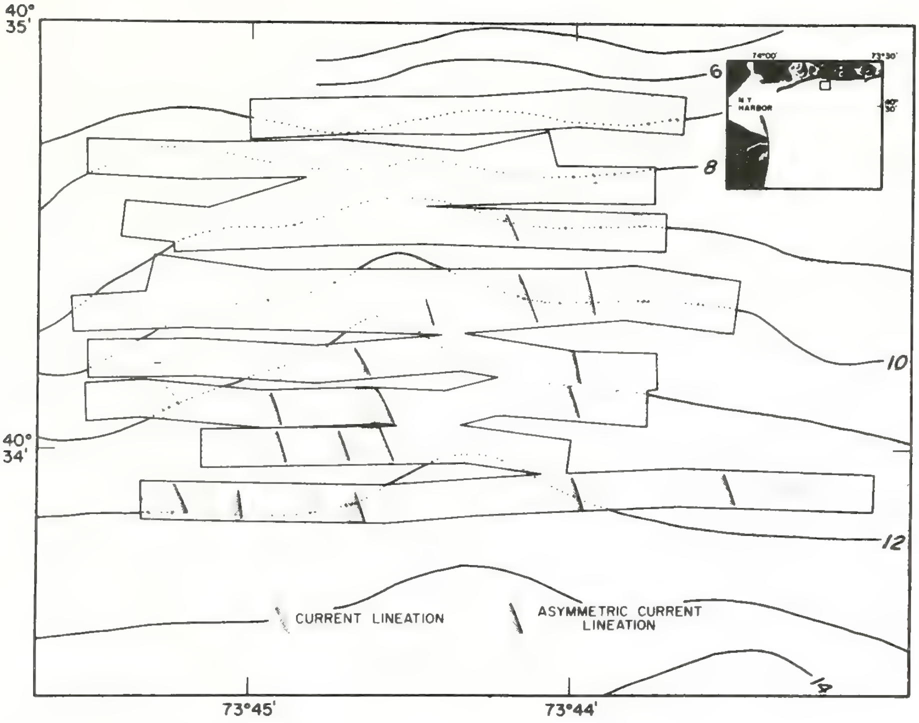

Figure 6
Array of sandwave-like bedforms at Atlantic Beach, Long Island. Asymmetric current lineations have sharply defined up-current sides and gradational down-current sides. Depths in meters. From Freeland and Swift, in press a.

estuarine turbidity maximum. Both the two-layer estuarine circulation system and the typical fairweather conditions of weak coastal upwelling (Lavelle and others, 1976; Baylor, 1973; Scott and Csanady, in press) serve as hydrodynamic traps to concentrate the suspended sediment thus introduced to the coastal water column. In the apex, another highly concentrated source is dredge-spoil and sewage-sludge dumping. While the bulk of the dredge spoils goes directly to the sea floor, most of the sewage sludge enters the inner-shelf and shelf-estuary feedback loops. An effective nearshore trapping mechanism is landward mass transport of more turbid bottom water, then seaward transport, by the wave-driven system of turbid rip-current

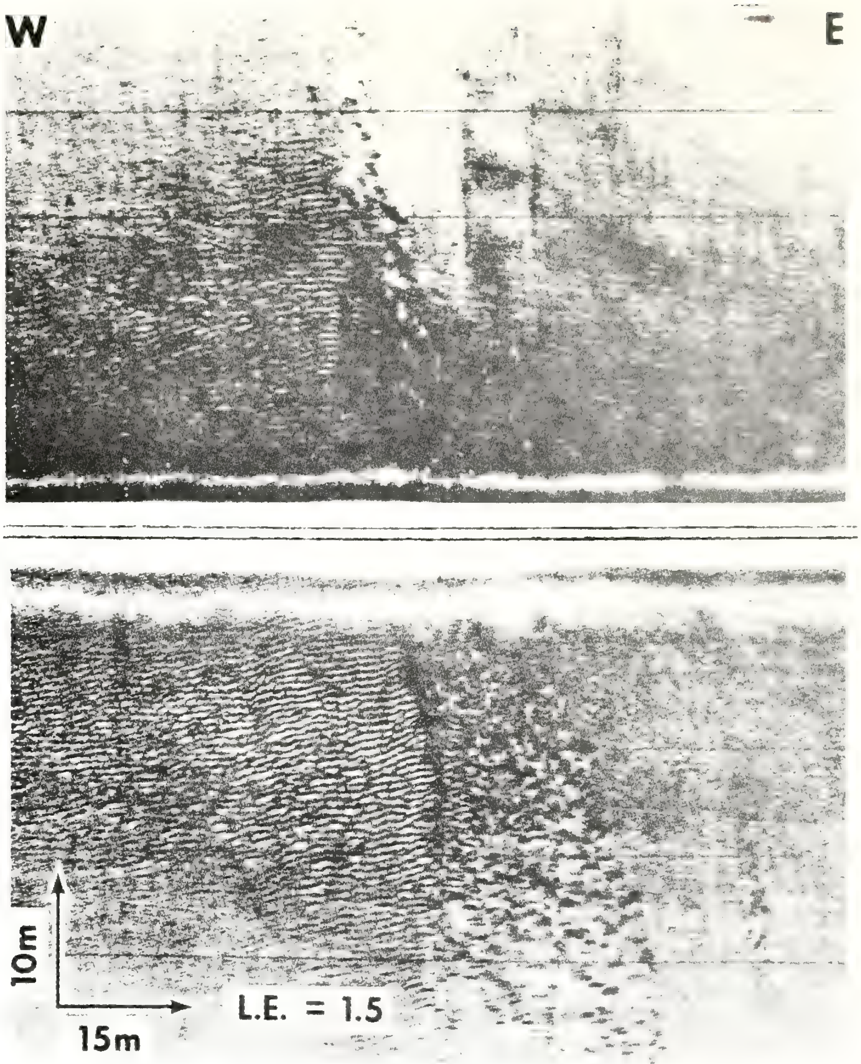

Figure 7
Sidescan sonar record of sandwave-like bedform at Atlantic Beach, Long Island. Fine sand to east, muddy gravel in center, coarse sand west, becoming finer toward west.

plumes (Fig. 10).

The suspended-sediment transport system in the New York Bight, then, may be viewed as consisting of two basic pathways (Fig. 11); 1) fluvial effluent, which joins 2) a coastwise transport path created by the net southerly drift of turbid inner-shelf water (Beardsley and others, 1976). In between are the feedback loops described above, and short to long term (days to centuries) storage

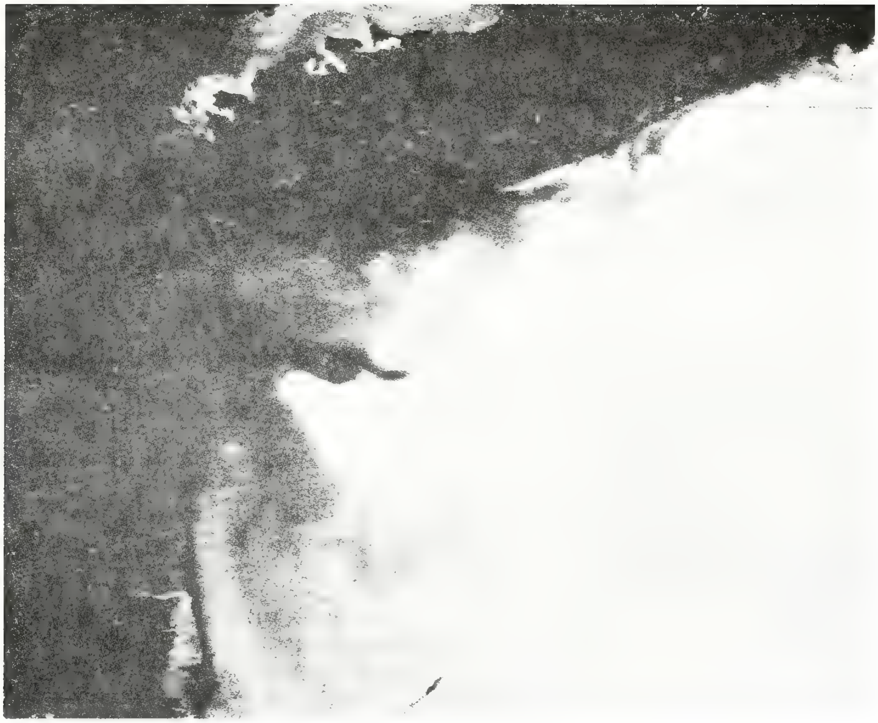

Figure 8
LANDSAT satellite image of the New York Bight apex revealing nearshore turbid water. Note Hudson-Rariton estuary plume, dark highly turbid water areas in the central apex, probably from acid-waste dumping, and nearshore Long Island and New Jersey turbid waters. Wind had been blowing an average of 15 to 22 mph from 240° to 300°T for the previous 58 hours. Scene 1258-15082, MSS Channel 5 (0.6 to 0.7 μm, orange-red), April 7, 1973, 1008 hrs EST. Courtesy of NASA and Dr. George Maul, AOML/PhOL.

on the estuary, lagoonal, or shelf floors, or on fringing salt marshes (Fig. 12). Sediment recycling on the estuarine feedback

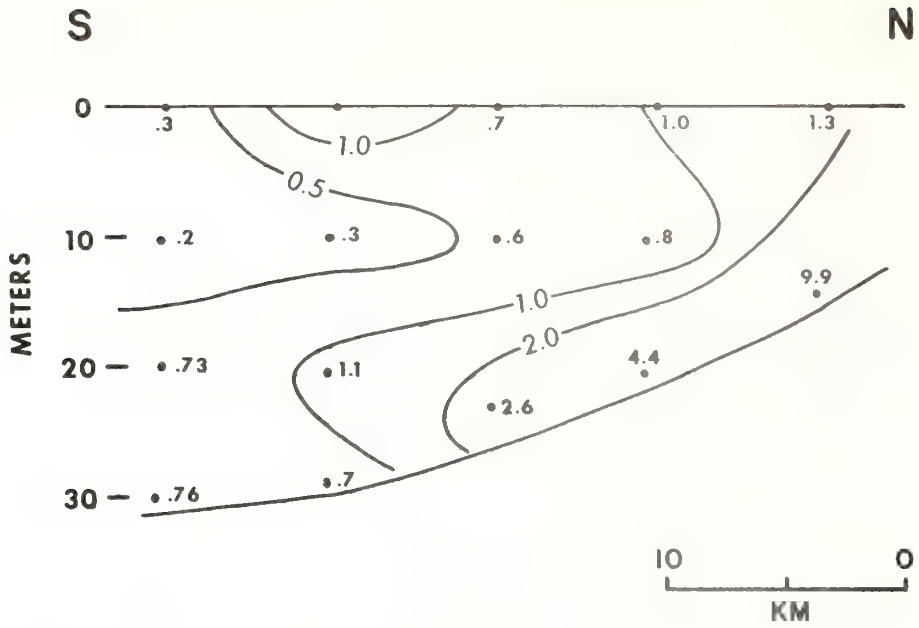

Figure 9
Vertical distribution of total suspended load on a north-south transect south of Atlantic Beach on September 16-20, 1973. From Swift and others, 1975; Drake, 1977.

loop is many times greater than is the throughput, as indicated by higher suspended-sediment concentrations in the Bight apex than in the adjacent coastal waters of New Jersey and Long Island (Drake, 1977; Manheim and others, 1970).

Application of this model to the mud distribution maps (Figs. 2-5) suggests that the Christiaensen Basin mud deposit is situated so as to constitute a reservoir in the cycle of suspended-sediment exchange between the Bight apex and the Hudson estuary. Suspended sediment can escape either downcoast to the south in the strong flows associated with the Hudson Shelf Valley (Gadd and others, in press) or north towards the long Island beaches when the circulation

Figure 10 (at right)
Schematic diagram of coastal circulation pattern believed to control nearshore suspended-sediment concentration. Above: wind and density-driven flow causes onshore bottom flow, upwelling, and offshore surface flow. Suspended sediment tends to settle out of this upper layer, so that sediment movement closes the "open loop" of fluid flux. In the very nearshore (below) this two-layer circulation is reinforced by landward mass transport of bottom water by waves, and seaward flowing rip currents on the surface. From Freeland and Swift, in press b.

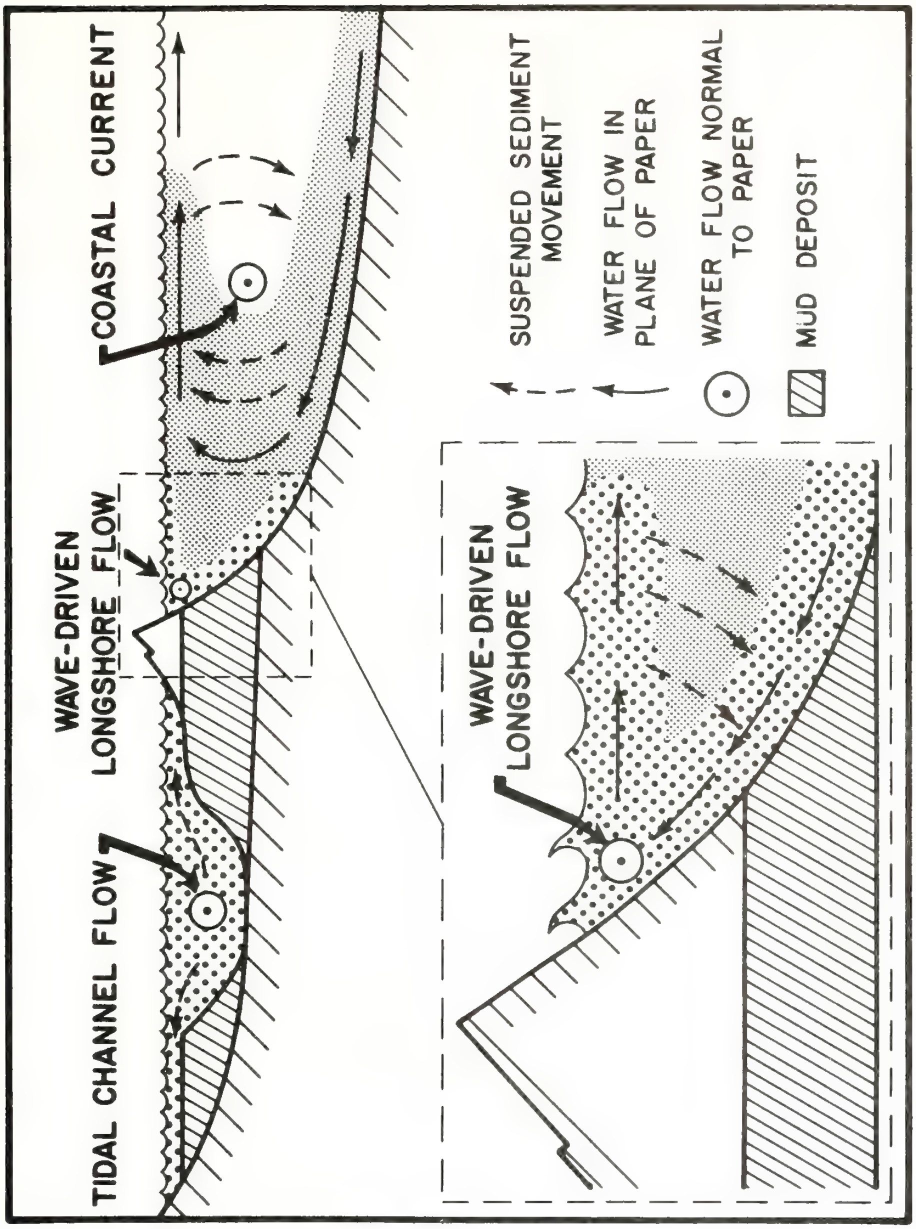
TIDAL CHANNEL FLOW
WAVE-DRIVEN LONGSHORE FLOW
COASTAL CURRENT
WAVE-DRIVEN LONGSHORE FLOW
SUSPENDED SEDIMENT MOVEMENT
WATER FLOW IN PLANE OF PAPER
WATER FLOW NORMAL TO PAPER
MUD DEPOSIT

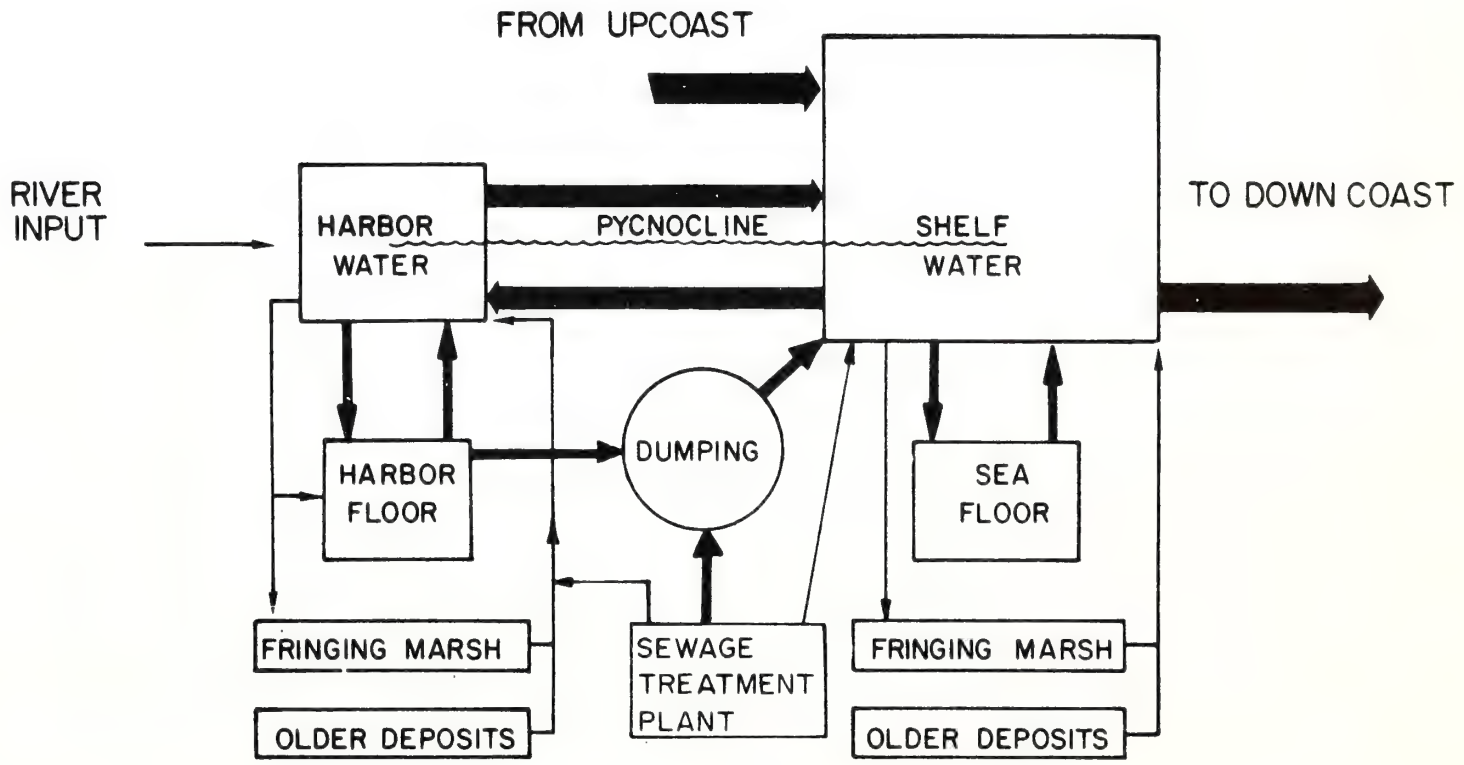

Figure 11
Schematic diagram of pathways and reservoirs controlling suspended-sediment budget of the New York Bight apex. From Freeland and Swift, in press b.

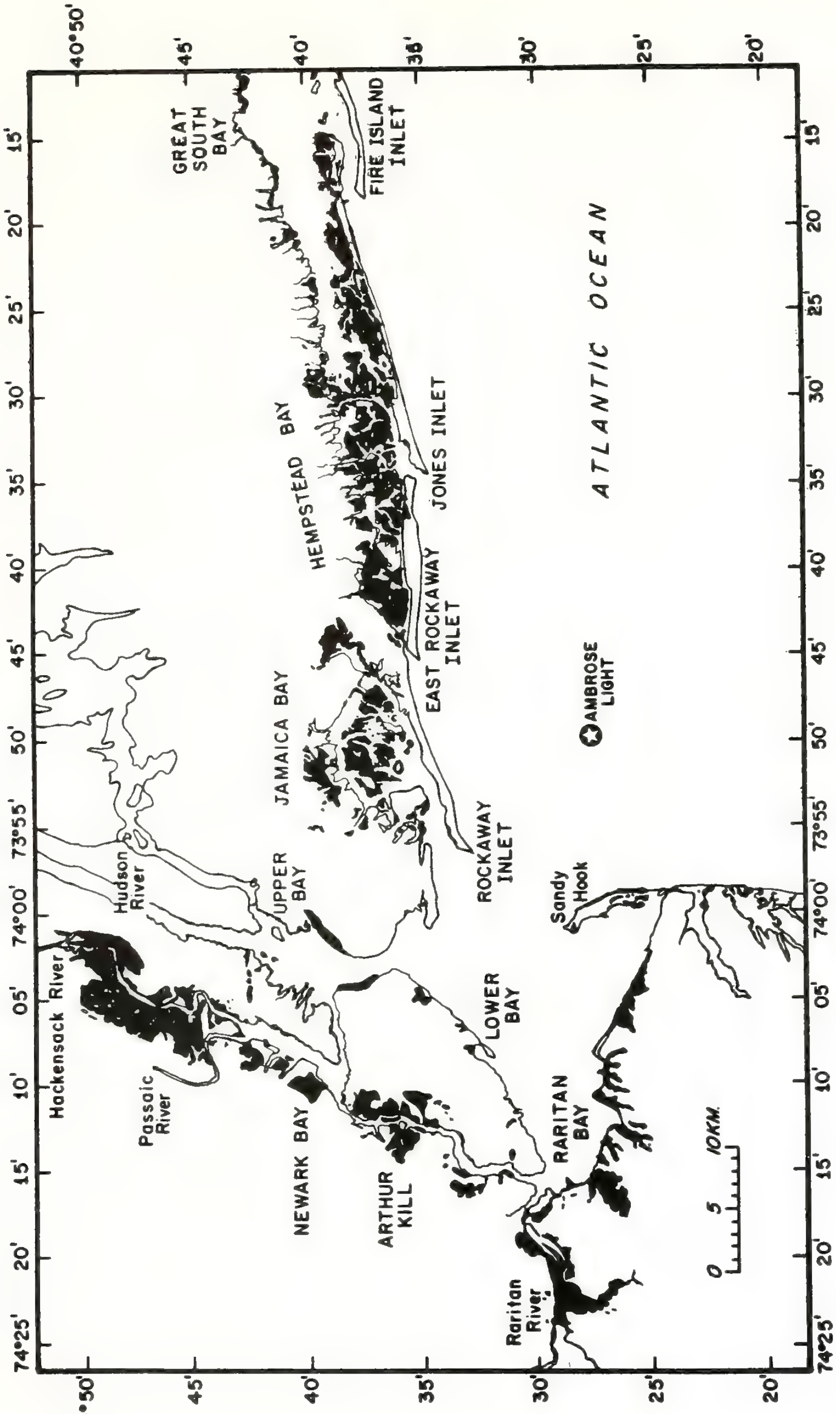

Figure 12
Wetlands of the New York Bight apex.

pattern known as the "Bight apex gyre" is in effect (Charnell and Mayer, 1975; Drake, 1977; Gadd and others, 1978). The fine-sediment transport budget approaches equilibrium in that nearly as much material escapes as is added to this system. Except in the immediate vicinity of the dredge-spoil dumpsite, the rate of accretion or erosion of the floor of the Christiaensen Basin is so low that during 37 years between bathymetric surveys, consistent trends cannot be distinguished from noise in the data (Fig. 13; Freeland and Merrill, 1976).

The entry of dumped waste into the fine-sediment transport system in the vicinity of the Christiaensen Basin mud deposit deserves special comment. Calculations indicate that of the sand, mud, and

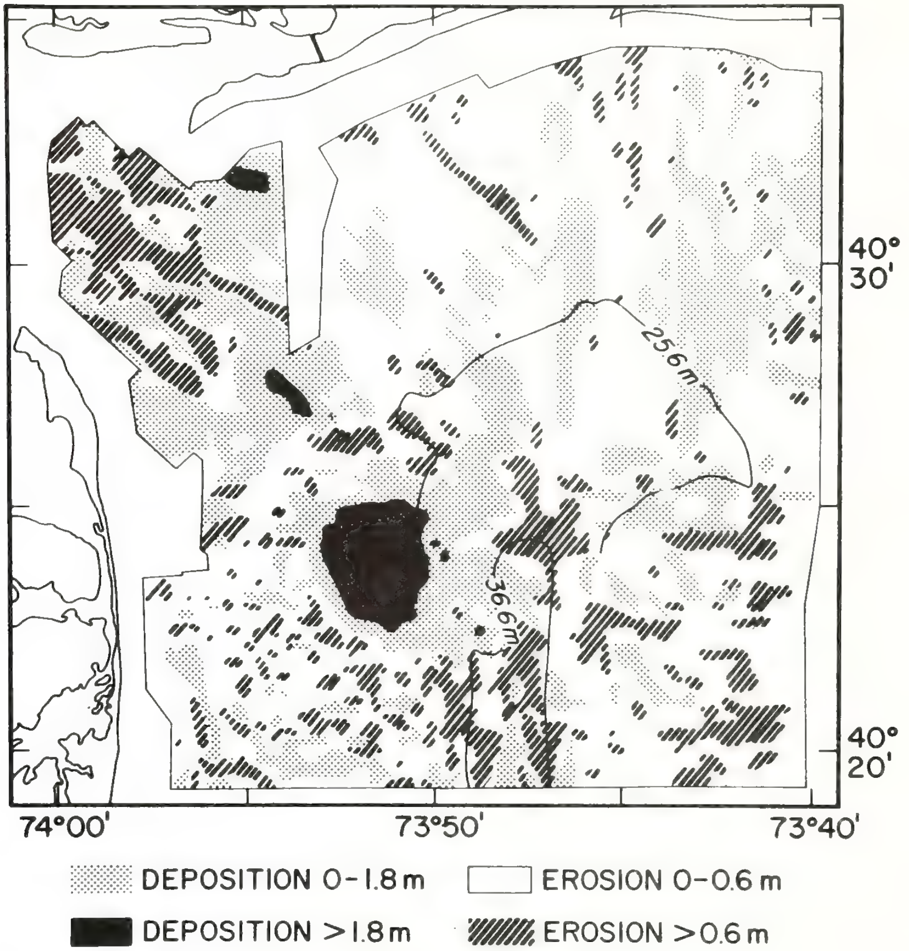

Figure 13
Net bathymetric change in the New York Bight apex between 1936 and 1973. From Freeland and Merrill, 1976.

gravel dumped at the dredge-spoil dumpsite since 1936, 87% has remained as a lag deposit, while the remainder has been dispersed (Freeland and Merrill, 1976). The nearly neutrally buoyant sewage sludge is considerably more mobile. The floor of the Christiaensen Basin beneath the sewage-sludge dumpsite proper is composed of sand containing negligible amounts of fine material (Fig. 2). Recent acoustical studies by Proni and others (in press) indicate that a large fraction of a sewage-sludge dump remains as a vertical column in the water, with high particulate concentrations, for several hours. Sludge particles are fed into the bottom nepheloid layer as a base surge of heavier particles during dumping. Less dense particles spread laterally at intermediate depths at the main thermocline and at secondary density discontinuities, and at the surface. Thus dispersion of sewage sludge through the transport pathways of the Bight apex begins even during the dumping process.

Our model for coastal fine-sediment transport suggests that the mud deposits of the western Long Island shoreface (Fig. 5) are controlled by the relationship between near-bottom hydraulic activity and near-bottom sediment concentration in turbid inner-shelf water. Major suspended-sediment inputs to this water mass are: 1) tidal exchange with inlets into Jamaica, Hempstead, and Great South Bays; 2) the Hudson River surface plume, driven eastward along the Long Island coast when blown by south and west winds; and 3) landward bottom drift from the Christiaensen Basin. The dominant flow component of this nearshore-water mass is constrained to an east-west direction by the proximity of land (Charnell and Mayer, 1975; Lavelle and others, 1976; Lavelle and others, in press; Gadd and others, 1978), but reverses its direction with a frequency of hours to days depending on tide and wind conditions. The sense of the weak two-layer flow (upwelling versus downwelling) also reverses on a similar time scale (Scott and Csanady, in press, especially Fig. 7). Thus, the exchange of sediment among the nearshore sediment sources, and between them and the shoreface mud deposits may be approximated as a stochastic process.

The shoreface mud patches seaward of Atlantic Beach (Fig. 5) that led to fears of a "creeping sludge front" have a complex distribution in time and space. In addition to being controlled by the model just described, they lie in the troughs of sandwave-like bedforms which are characteristic of the shoreface of the Middle Atlantic Bight and the Brazilian inner shelf (Swift and Freeland, in press; Figueiredo and Kowsmann, 1976). These bedforms appear to be flow-transverse features (therefore, "sandwave-like"), but their height (less than 1 m) is negligible with respect to spacing (greater then 200 m). Their orientation, with steeper flanks facing westward and slightly offshore, suggests that they are responses to the strong westward flows associated with winter "northeaster" storms (Beardsley and Butman, 1974; Lavelle and others, 1976, in press), which have a slight offshore component of bottom flow due to downwelling (Swift and others, 1975, Fig. 13; Magnell, 1976, p. 6-114 to 6-119, Figs. 6.5-1e, 6.5-5c). The shallow, gravelly troughs between sandwaves apparently become hydrodynamically sheltered zones during the quiescent summer months when net water movement is a slow eastward drift modulated by the surge of low amplitude swells. Mud deposited in troughs during the summer is buried or eroded (resuspended) during the winter season of repeated storms when the bedforms are reactivated.

FINE SEDIMENT BUDGET

The distribution of mud deposits in the New York Bight apex therefore appears to be controlled primarily by natural forces rather than by the activities of man except in the immediate area of the dredge-spoil dumpsite. There appears to be no compelling reason to believe that the distribution of muds is significantly different than when Henry Hudson's ships first visited the area, although the total area covered by mud may be somewhat greater. The 1845 chart of the apex (Survey of the Coast of the United States) shows "black mud", "mud", and "blue mud" mixed with "gray sand" in the Christiaensen Basin and the upper Hudson Shelf Valley at depths below 85 ft (26 m), a considerable area of "gray sand black specks" and "yellow sand black specks" on Cholera Bank at and around the present sewage-sludge dumpsite, and "mud", "muddy", "mud shells", and "black and white sand" to within 500 m of the shore off Rockaway, Long, and Jones Beaches.

Anthropogenic activities are more likely to change the composition of modern muds than their areal distribution. The degree of contamination of natural muds by dumped fine-grained wastes depends not only on the rate of dumped-waste input relative to the rate of natural mud input, but also on the rates of exchange of fine sediment along the pathways diagrammed in Figure 11 relative to the total fine sediment input. The exchange rates determine the extent to which dumped materials will be diluted with natural materials and dispersed. The concentration of suspended particulates and the level of hydraulic activity of the water masses determine the extent and duration of mud deposition and resuspension.

A few recent studies have provided preliminary numerical data on exchange rates and contamination. McLaughlin and others (1975), in their conceptual model of the New York Bight ecosystem, estimate sediment flux (both for fine and coarse sediment) into and out of the Bight (Table 1, this paper). An outstanding aspect of their budget is the importance of the biological subcycle. Biological assimilation (uptake) removes 14.3×10^6 tons/yr. of organic matter from the system, becoming unused dissolved matter. Schaeffer (1977) measured organic $^{13}C/^{12}C$ ratios in 14 Bight apex sediment samples, one mid-shelf Hudson Shelf Valley core, and two sewage treatment plant sludge samples. The results indicate that treatment plant organic matter (coming from both dumping of sludge and through outfalls) varies from 0% of the organic fraction in three samples off Rockaway Beach and Sea Bright, New Jersey, to 70-100% in the Christiaensen Basin near the sewage-sludge dumpsite. Total organic matter (based on the Wards Island treatment plant sample being 100% organic matter) reached a maximum of only 6.98% in a sample taken east of the dredge-spoil dumpsite and was less than 1% in all of the nearshore samples. Therefore, while contamination is occurring, the vast majority of all organic matter (including sludge) is being both biologically decomposed and physically dispersed. The figures presented in Table 1 also suggest that physical processes would tend to result in low ambient values of carbon due to dilution and dispersion.

An examination of the assumptions made by McLaughlin and others

Table 1
Estimates of fine sediment flux through New York Bight in 10^6 tons/yr. dry weight. From McLaughlin and others, 1975.

Pathway	Inflow	Outflow
Atmospheric input	0.1	
Dumped waste	2.1[a]	
Estuaries to shelf (includes river input)	0.5	
Shelf to estuaries		0.3
Biological production[b]	14.0	
Biological uptake[b]		14.3
Shelf advection		
From northeast	1.8	
To southwest		1.8
To shelf edge		1.0
Total	18.5	17.4
Net	1.1	
Total non-biological	4.5	3.1
Net non-biological	1.4	

[a] Does not include 4.0 x 10^6 tons/yr. of coarse dumped material (Mueller and others, 1976).

[b] Estimates for coarse sediment and fine sediment combined, marine organic materials only. See text.

(1975) suggests that their estimates for rates of exchange of fine sediment between the shelf and the estuary, and between the New York Bight and adjacent shelf compartments, may be too low. Even at these low estimates, the rate of transfer of fine sediment between the shelf and adjacent reservoirs results in a net inflow of only 1.1 x 10^6 tons/yr., or 6% of the total inflow. It may, therefore, be concluded that the system is a well-mixed one. Of all dumped fine materials which have not been destroyed by chemical or biological activity, about 50% will escape the Bight altogether, and the remaining will be uniformly dispersed through the natural mud deposits of the Bight apex--Hudson estuary system and its fringing bays, marshes, and secondary estuaries.

CONCLUSIONS

Although the input of fine-grained particles into the New York Bight apex is almost equally divided between anthropogenic and natural materials, relatively small amounts (by weight) of sewage sludge are causing the greatest environmental concern. Because of their low density, many of these organic particles do not settle rapidly to the bottom during a dumping operation, but are held in suspension in the water column to be dispersed and settle elsewhere. Most fine particles, including those from sewage-sludge, dredge-spoil, fluvial, estuarine, and shelf sources, settle temporarily in the low topography of the Christiaensen Basin and the Hudson Shelf Valley, or are carried by bottom currents into the estuaries which are semi-permanent sinks. Small patches of muddy sand also occur off the south shore of Long Island west of Fire Island Inlet.

Current knowledge of the behavior of these fine particles indicates that they settle out of the water column only during conditions of low bottom current speed and high concentration. This generally occurs in the Bight apex during the spring, summer, and early fall, from April to September. Because of shoal water depths throughout the apex, storms, particularly when winds are from the northeast, create bottom currents fast enough to erode muddy sediments even in the deeper low areas of the Christiaensen Basin and Hudson Shelf Valley along with more-easily-erodible sand. While sand particles redeposit rapidly during slowing bottom currents, fine particles stay in suspension considerably longer and are widely dispersed.

Water-mass studies in the nearshore shelf and estuary indicate that fine-grained matter is cycled between shelf and estuary, within the inner-shelf zone, and between deposits on shelf and estuary floors and the overlying water in time scales from diurnal to decades. Contaminated sediments that may be found during any one sampling are subject to transport at any time and cannot be considered as evidence of permanent accumulation.

ACKNOWLEDGMENTS

This work was done as part of NOAA's Marine Ecosystems Analysis (MESA) Project in the New York Bight. Thanks are due to the officers and crew of the NOAA Ship KELEZ, to students of Brooklyn College for aid in collection of samples, and to Messrs. John W. Kofoed and H. B. Stewart, Jr., for manuscript review.

REFERENCES

1. Baylor, E. R., 1973. Final Report of the Oceanographic and Biological Study for Southwest Sewer District No. 3, Suffolk County, New York. Report prepared for Bowe Walsh Associates by Marine Sciences Research Center, State University of New York at Stony Brook, V. 1, text, 695p.
2. Beardsley, R. C., and Butman, B., 1974. Circulation on the New England Continental Shelf: Response to Strong Winter Storms. Geophys. Res. Letters, 1:181-184.
3. Beardsley, R. C., Boicourt, W. C., and Hansen, D. V., 1976. Physical Oceanography of the Middle Atlantic Bight. p. 20-34, In: Gross, M. G., ed., Middle Atlantic Continental Shelf and the New York Bight. Special Symposia V. 2, American Society of Limnology and Oceanography, 440p.
4. Charnell, R. L., and Mayer, D. A., 1975. Water Movement Within the Apex of the New York Bight during Summer and Fall of 1973. NOAA Tech. Memo. ERL MESA-3, 29p.
5. Drake, D. E., 1976. Suspended Sediment Transport and Mud Deposition on Continental Shelves. p. 127-158, In: Stanley, D. J., and Swift, D. J. P., eds, *Marine Sediment Transport and Environmental Management*. New York, John Wiley and Sons, 602p.
6. Drake, D. E., 1977. Suspended particulate matter in the New York Bight Apex, Fall 1973. Jour. Sed. Petrol., 47:201-228.

7. Duedall, I. W., O'Connors, H. B., and Irwin, B., 1975. Sewage Sludge: Its fate in the New York Bight Apex. Jour. Water Pol. Control Fed.

8. Figueiredo, A. G., Jr., and Kowsmann, R. O., 1976. Interpretacao dos Registros de Sonar de Varredura Lateral Obtidos na Plataforma su riograndense Durante a Operasao GEOMAR VII. Rio de Janeiro, Brazil, Companhia de Pesquiesa de Recursos Minerais, 9p.

9. Freeland, G. L., and Merrill, G. F., 1976. Deposition and erosion in the Dredge Spoil and other New York Bight Dumping Areas. p. 936-946, In: Krenkel, P. A., Harrison, J., and Burdick, J.C., eds., *Dredging and its Environmental Effects.* New York, Amer. Soc. Civil. Eng., 1037p.

10. Freeland, G. L., Cok, A. L., and Swift, D. J. P., in press. Surficial Sediments of the New York Bight Apex. Boulder, Colorado, NOAA Tech. Report.

11. Freeland, G. L., and Swift, D. J. P., in press a. Surficial Sediments of the Long Island Inner Shelf. Boulder, Colorado, NOAA Tech. Memo.

12. Freeland, G. L., and Swift, D. J. P., in press b. Surficial Sediments. New York Bight Atlas Monograph 10, NY Sea Grant Institute, Albany, NY.

13. Gadd, P. E., Lavelle, J. W., and Swift, D. J. P., 1978. Calculations of Sand Transport on the New York Shelf Using Near Bottom Current Meter Observations. Jour.Sed.Petrol. 48:239-252.

14. Gross, J. G., 1972. Geologic Aspects of Waste Solids and Marine Waste Deposits, New York Metropolitan Region. Geol. Soc. Amer. Bull., 83:3163-3176.

15. Harris, W. H., 1976. Spatial and Temporal Variation in Sedimentary Grain Size Facies and Sediment Heavy Metal Ratios in the New York Bight Apex. p. 102-123, In: Gross, M. G., ed., Middle Atlantic Continental Shelf and the New York Bight. Soc. Limnol. Oceanogr. Spec. Symp. V. 2, 441p.

16. Hatcher, P. G., and Keister, L. E., 1976. Carbohydrates and Organic Carbon in New York Bight Sediments as Possible Indicators of Sewage Sludge Contamination. p. 240-248, In: Gross, M. G., ed., Middle Atlantic Continental Shelf and the New York Bight. Soc. Limnol. Oceanogr. Spec. Symp. V. 2, 441p.

17. Hatcher, P. G., Keister, L. E., and McGillivary, P. A., 1977. Steroids as Sewage Specific Indicators in New York Bight Sediments. Bull. Environ. Contam. Toxicol., 17:491-498.

18. Lavelle, J. W., Brashear, H. R., Case, F. N., Charnell, R. L., Gadd, P. E., Haff, K. W., Han, G. A., Kunselman, C. A., Mayer, D. A., Stubblefield, W. L., and Swift, D. J. P., 1976. Preliminary Results of Coincident Current Meter and Sediment Transport Observations for Wintertime Conditions, Long Island Inner Shelf. Geophys. Res. Letters, 3:97-100.

19. Lavelle, J. W., Swift, D. J. P., Gadd, P. E., Stubblefield, W. L., Case, F. N., Brashear, H. R., and Haff, K. W., in press. Fair Weather and Storm Transport on the Long Island Inner Shelf. Submitted to Jour. Geophys. Res.

20. McCave, I. N., 1972. Transport and Escape of Fine-Grained Sediment from Shelf Areas. Chapter 10, p. 225-248. In: Swift, D. J. P., Duane, D. B., and Pilkey, O. H., eds., *Shelf Sediment Transport: Process and Pattern.* Stroudsburg, PA, Dowden, Hutchinson, and Ross, 656p.

21. McLaughlin, D., Elder, J. A., Orlog, G. T., Kibler, D. F., and Buenson, D. E., 1975. A Conceptual Representation of the New York Bight Ecosystem. NOAA Tech. Memo. ERL MESA-4. National Oceanic and Atmospheric Administration, Boulder, Colorado, 359p.
22. Magnell, B., 1976. Summary of Oceanographic Observations in New Jersey Coastal Waters near 39°28'N Latitude and 74°15'W Longitude During the Period May 1974 through May 1975. EG&G Inc., Waltham, Massachusetts.
23. Manheim, F. T., Meade, R. H., and Bond, G. C., 1970. Suspended Matter in Surface Waters of the Atlantic Continental Margin from Cape Cod to the Florida Keys. Science, 167:371-376.
24. Mueller, J. A., Jeris, J. S., Anderson, A. R., Hughes, C. F., 1976. Contaminant Inputs to the New York Bight. NOAA Tech. Memo. ERL MESA-6, 347p.
25. Pearson, H., 1974a. Riding a Sludge Boat, Hearing of Alternatives. Newsday, August 1, 1974, Garden City, NY.
26. Pearson, H., 1974b. The Sludge Story: Muddy Waters. Newsday, August 1, 1974, Garden City, NY.
27. Pearson, H., 1974c. Buckley, Move Sludge Dump. Newsday, August 3, 1974, Garden City, NY.
28. Postma, H., 1967. Sediment Transport and Sedimentation in the Marine Environment. p. 158-180, In: Lauff, G. H., ed., *Estuaries.* Washington, Amer. Assoc. Advancem. Sci., 757p.
29. Proni, J. R., Newman, F. C., Young, R. A., Walter, D., Sellers, R., McGillivary, P., Duedall, I., Stanford, H., and Parker, C., in press. Observations of the Intrusion into a Stratified Ocean of an Artificial Tracer and the Concomitant Generation of Internal Oscillations. Jour. Geophys. Res.
30. Schaeffer, O. A., 1977. Anthropogenic Fluxes of Carbon into the Sediments of the New York Bight. Final Report, ERL-MESA Grant 0462244013, S.U.N.Y., Stony Brook, NY, 16p.
31. Schubel, J. R., 1972. Distribution and Transportation of Suspended Sediment in Upper Chesapeake Bay. p. 151-168, In: Nelson, B. W., ed., *Environmental Framework of Coastal Plain Estuaries.* Geol. Soc. Amer. Memoir 133, 617p.
32. Schubel, J. R., and Okubo, A., 1972. Comments on the Dispersal of Suspended Sediment Across Continental Shelves. p. 333-346, In: Swift, D. J. P., Duane, D. B., and Pilkey, O. H., eds., *Shelf Sediment Transport: Process and Pattern.* Dowden, Hutchinson, and Ross, Stroudsburg, PA, 656p.
33. Scott, J. T., and Csanady, G. T., in press. The COBOLT Experiment, First Current Meter Observations. Jour. Geophys. Res.
34. Segar, D. A., and Cantillo, A. Y., 1976. Trace Metals in the New York Bight. p. 171-198, In: Gross, M. G., ed., Middle Atlantic Continental Shelf and the New York Bight. Amer. Soc. Limnol. Oceanogr. Spec. Symp. V. 2, 441p.
35. Smith, R. N., and Ali, S. A., 1973. Sediment - Physical Aspects. p. 223-246, In: Baylor, E. R., ed., Final Report of the Oceanographic and Biological Study for the Southwest Sewer District #3, Suffolk County, New York. State University of New York, Stony Brook, NY, Marine Sciences Research Center, V. 1, 695p.
36. Soucie, G., 1974. Here Come de Sludge. Audubon, 76:108-113.

37. Stubblefield, W. L., Permenter, R. W., and Swift, D. J. P., 1977. Tiem and Space Variation in the Surficial Sediments of the New York Bight Apex. Estuarine and Coastal Mar. Sci., 5:597-607.
38. Swift, D., Cok, A., Drake, D., Freeland, G., Lavelle, J. W., McKinney, T., Nelson, T., Permenter, R., and Stubblefield, W., 1975. Geological Oceanography. p. 16-61, In: Charnell, R., ed., Assessment of Offshore Dumping: Technical Background. NOAA Tech. Memo. ERL MESA-1, 83p.
39. Swift, D. J. P., and Freeland, G. L., in press. Mesoscale Current Lineations on the Inner Shelf, Middle Atlantic Bight of North America. Estuarine and Coastal Marine Science.
40. Veatch, A. C., and Smith, P. A., 1939. Atlantic Submarine Valleys of the United States and the Congo Submarine Valley. Geol. Soc. Amer. Spec. Paper 7, 101p.

26. Society of Economic Paleontologists and Mineralogists Special Publication No. 27, 131-151.

GEOTECHNICAL PROPERTIES OF CONTINENTAL SLOPE DEPOSITS—CAPE HATTERAS TO HYDROGRAPHER CANYON

GEORGE H. KELLER
School of Oceanography
Oregon State University
Corvallis, OR 97331

DOUGLAS N. LAMBERT AND RICHARD H. BENNETT
NOAA, Atlantic Oceanographic and Meteorological Labs
Miami, FL 33149

ABSTRACT

The continental slope off the northeastern United States commonly displays gradients ranging from 3 to 10°, is heavily dissected by submarine canyons and valleys, and is an area of considerable slumping activity. A study of the geotechinal properties (sediment texture, shear strength, water content, wet bulk density, porosity, and Atterberg Limits) of 73 sediment cores from 21 transects across the continental slope from Cape Hatteras to Hydrographer Canyon provides insight into the general distribution and variation of these properties within the near-surface deposits of this province of the seafloor.

Although a general gradation in sediment texture from coarse to fine prevails in a down-slope direction all along the continental slope, fine-grained sediments (silty clay) appear to comprise the predominant sediment type along the slope particularly within the central portion of the Middle Atlantic Bight. This depositional pattern appears to account for the occurrence of generally higher water contents and porosities as well as the lower wet bulk densities found in the slope deposits of the Middle Atlantic Bight. Relatively coarse-grained sediments of low water content and porosity and high bulk density make up the slope deposits to the north of Block Canyon as well as in the general area of Cape Hatteras. Higher values of shear strength [7 to 14 kPa (1–2 psi)] are commonly found in the lower mid- to lower slope deposits except in the vicinity of submarine canyons where lower values [2 to 4 kPa (0.3–0.6 psi)] appear to be related to a combination of increased concentrations of organic matter and fine-grained sediments. Sediment sensitivities range from 1 to 12 with a mean of 3, giving the indication that these deposits may be "slightly quick" in places, but they are predominantly classed as "medium sensitive." Porosities vary from 44–82% with the higher values occurring along the lower slope. The mean value of 71% for these sediments is slightly higher than that reported for the hemipelagic sediments of the North Atlantic. An analysis of the plasticity characteristics of the mid and lower slope sediments indicates that they vary little from those of abyssal plain deposits which are classed as inorganic clays of low, medium, and high plasticity. An exception is found in the central part of the Middle Atlantic Bight where a large proportion of the sediments are classified as organic clays of medium to high plasticity and micaceous.

Distribution of the mean values of the various geotechnical properties in the near-surface (1–290 cm) deposits of the slope indicates that there is a general increase in water content, liquid limit, plastic limit, clay content, and porosity from off New England towards Cape Hatteras. Analyses of slope deposits, using the infinite slope analysis method, to determine the effects of overburden pressure on their stability revealed no indication of instability. Factors other than overburden, however, undoubtedly play a role in the slumping of slope deposits.

INTRODUCTION

The continental slope is the most consistent and significant topographic discontinuity in the ocean basins, yet it has escaped study to any degree approaching that devoted to continental shelves and abyssal plains. The submarine slope off the east coast of the United States has received probably more attention than any other continental slope in the world, with investigations dating back to the 1930's (Shepard, 1934; Stetson, 1938; Veatch and Smith, 1939). Studies of the slope have usually been part of broad regional investigations of the continental margin (Stetson, 1949; Drake et al, 1959; Uchupi and Emery, 1967; Knott and Hoskins, 1968; Pratt, 1968; Uchupi, 1968a, 1970; Emery et al, 1970, Emery and Uchupi, 1972; Milliman et al, 1972; McGregor 1978) or have dealt with stratigraphic, morphological or sedimentary features on a very local scale (Moore and Curray, 1963; Roberson, 1964; Krauss et al, 1966; Hoskins, 1967; Rona and Clay, 1967; Uchupi, 1967; Emery and Ross, 1968; Trumbull and Hathaway, 1968; Uchupi, 1968b; Oser, 1969; Kelling and Stanley, 1970; MacIlvaine, 1973). More recently, as part of a program to assess offshore petroleum resources, the U.S. Geological Survey has conducted a study of the continental margin's structural and stratigraphic characteristics off the eastern United States (Schlee et al, 1976).

Copyright © 1979, The Society of Economic Paleontologists and Mineralogists

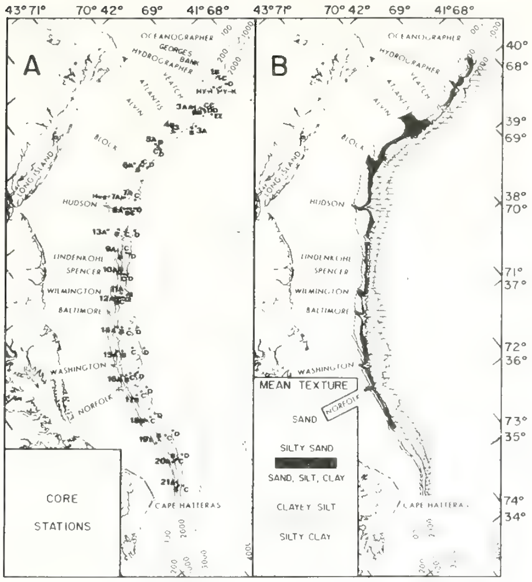

FIG. 1.—A) Core Stations; submarine canyons identified along inshore margin; isobaths in meters; B) Sediment texture distribution, mean composition for the respective cored intervals. Classification after Shepard (1954).

In 1974 the NOAA Atlantic Oceanographic and Meteorological Laboratories in cooperation with a number of university investigators initiated a geological study of the continental slope from Cape Hatteras to Hydrographer Canyon (Fig. 1A). The primary purpose of this effort was to improve the definition of the geological history, shallow structure, morphology, and sedimentary processes associated with the slope province. The basic field data collected during four crusies in the area consisted of five continuous seismic (air gun) reflection and narrow-beam echo sounder profiles paralleling the shelf break and approximately equally spaced along the slope from the shelf break to the lower slope-upper rise (McGregor et al, 1975; McGregor, 1978). In addition, 76 piston and 73 gravity cores were collected along 21 traverses; each one of which extended from the upper to the lower slope with two (traverses) continuing out onto the continental rise (Doyle et al, 1975) (Fig. 1A). The discussion presented here reports on the geotechnical properties of the slope deposits and the stability of these sediments in regard to both gravitational and bottom transport (currents) processes. In another section of this volume, Doyle, Pilkey, and Woo discuss the textural and mineralogical aspects of the piston cores collected during this study.

Location, Morphology, and Geological Setting

The continental slope between Cape Hatteras and Hydrographer Canyon is a classic example of a continental slope, bordered on the landward side by a relatively wide continental shelf and by a typical continental rise province seaward. The continental slope proper is a relatively steep incline, clearly delimited by the 120–140 and 2000 m isobaths (Fig. 1A). Considerable diversity in both bottom morphology and gradient is characteristic of the continental slope off the northeastern United States. The most pronounced morphological features on the slope are the submarine canyons which occur in great abundance. At least 190 canyons as well as numerous valleys entrench the slope from Labrador to Cape Hatteras (Oser, 1969; Emery and Uchupi, 1972; McGregor et al, 1975; McGregor and Bennett, 1977). The large number of canyons north of the Hudson Canyon undoubtedly owe their occurrence to the position of the former Wisconsin ice sheet and its associated drainage. To the south of Hudson Canyon the major canyons such as Wilmington, Baltimore, Washington, and Norfolk appear to have been linked to drainage through various estuarine systems carrying glacial meltwater from the north (Shideler and Swift, 1972; Milliman, 1973; Stout and McClennen, 1977; Twichell et al, 1977). Apparently the Pleistocene lowering of sea level resulted in the formation and/or re-excavation of a large number of the submarine canyons presently found along this margin of the Atlantic.

Morphologically, the continental slope from Georges Bank to Hudson Canyon consists of an upper and lower slope (Fig. 1A). Off Georges Bank the upper slope extends from the shelf break (120–140 m) to about 400 m with a gradient of 2°, and the lower slope extends to a depth of 2000 m with a declivity of about 7°. Between Georges Bank and the Hudson Canyon the upper slope extends to a depth of 1000 m with a gradient of 2°, and the lower slope to about 2200 m and has a declivity of 4°. From Hudson Canyon to Wilmington Canyon the continental slope narrows and increases in gradient to about 10°. The slope from Wilmington Canyon to lat. 36°30′N consists of a relatively steep (11°) upper slope between the depths of 120 to 1200 m and a much more gentle (1°) lower slope extending to a depth of 2200 m. Here the lower slope takes on an appearance similar to that of an area that has undergone extensive erosion due to currents and/or massive slumping. Between lat. 36°30′N and Cape Hatteras the continental slope displays a more uniform gradient than that to the north and is not cut by any submarine canyons, although numerous gullies are present (Fig. 1A). Off Cape Hatteras gullies and a number of canyons appear to form part of a dendritic drainage system which comprises the Hatteras Canyon system (Newton and Pilkey, 1969). From 36°30′N, with a gradient of about 3°, the slope steepens toward Cape Hatteras where it has a declivity of about 9°. Locally, along the eastern margin, gradients are often considerably more complex and variable, with slopes in some areas reaching angles of 20 to 25°.

The sedimentary framework of the overall continental slope appears to be one comprised of a thick Tertiary sequence which has buried Cretaceous strata as sediments were prograded seaward and deposited conformably to the present slope. Along much of the slope these Tertiary sediments have been since truncated as the slope has steepened due to erosion (Uchupi and Emery, 1967). Mass movements affecting Quarternary sediments reveal that slumping has been a continuing process along many parts of the slope (MacIlvaine, 1973; McGregor and Bennett, 1977).

Methods

In order to obtain the least disturbed samples as was practical, the gravity-type hydroplastic corer (Richards and Keller, 1961) was used to collect cores 8.2 cm in diameter and up to 3 m in length. The presence of open worm burrows in a number of the cores attests to the relatively low degree of sample disturbance.

All cores were x-radiographed aboard ship shortly after being collected and then stored vertically at a temperature of 4°C until the various geotechnical tests were performed.

Measurements of shear strength were made with a miniature laboratory vane-shear apparatus, a technique which is simple and particularly well suited to the testing of relatively low-strength submarine sediments. The tests were made on the center-most portion of the core (inner core) by inserting a small, four-bladed vane (2.50×1.25 cm) into the sample at right angles to the bedding and applying an increasing torque until shear occurred (Evans and Sherratt, 1948; Richards, 1961). In order to insure an undrained test condition, which is required for a valid vane-shear measurement, a vane rotation rate of 60°/min (1.7×10^{-2} rad/s) was used. Remolded shear strength was determined immediately after the natural strength measurement on the same material which had been thoroughly mixed with a spatula.

Considering the short core lengths (20–290 cm), relative to the scale of the study area, the respective values for each property along the entire length of each core were averaged. For example, if eight water content determinations were made on a core, the mean of these values along with the mean values of all the other cores, was used to define the areal distribution of this property as discussed in a later section.

AREAL VARIATIONS OF GEOTECHNICAL PROPERTIES

Sediment Texture

Complicated by the transport of sediments from the continental shelf, deposition of biogenic material, the presence of submarine canyons, the slumping of slope deposits themselves, and the effects of bottom currents, the sedimentation pattern along the continental slope off the northeastern United States is quite varied. Textural data from the cores collected during this program complemented by information from studies by Oser (1969, 1973), Hathaway (1971), and MacIlvaine (1973) serve as the basis for the sediment distribution pattern shown in Figure 1B. As seen from these data, clayey silts and silty clays are the predominant near-surface (0–3 m) sediment types found on the mid and lower portions of the continental slope, whereas sands and silts comprise the upper slope deposits. A marked change in sedimentation is noticed in the vicinity of Alvin Canyon (70°30′W) where to the east only the lowermost slope deposits are silty clays. Surface and near-surface deposits between Alvin and Hydrographer Canyons are considerably coarser-grained than those found elsewhere in the area north of the Hudson Canyon. The uppermost portions of the submarine canyons off New England commonly consist of reworked Pleistocene sand and gravels as the canyons erode farther into the shelf. Such headward erosion was observed in Veatch and Hudson Canyons from the submersible ALVIN by the senior author. The combination of strong bottom currents and a source of coarse-grained sediments on the adjacent shelf undoubtedly are prominent factors contributing to the greater concentration of coarse sediments along this segment of the continental slope. Current measurements and time-lapse camera observations in Hydrographer Canyon have recorded current velocities of up to 53 cm/sec and the actual migration of sand ripples seaward through the canyon down to depths of 710 m (Keller and Shepard, 1978). In contrast to these active canyons off New England, Hudson Canyon and those to the south are relatively inactive and presently are primarily depositional areas for fine-grained sediments.

In the vicinity of Cape Hatteras both the continental shelf and slope narrow considerably with the result that more of the coarse-grained shelf deposits appear to be spilling farther onto the slope. Relatively strong and complex currents in this area also undoubtedly contribute to the greater extension of coarse sediments down the slope. The extent of downslope transport of coarse-grained sediment along the entire study area is clearly seen from an analysis of the sand content of these deposits (Fig. 2A).

Shear Strength

Shear strength of a cohesive sediment is a function of the internal friction of the material, the cohesion, and the effective stress normal to the shear plane, which can be expressed as

$$\tau_f = c + \bar{\sigma} \tan \phi$$

where c is cohesion, $\bar{\sigma}$ is the effective stress, and ϕ the angle of internal friction. In theory, saturated, fine-grained sediments which are stressed without loss of pore water behave with

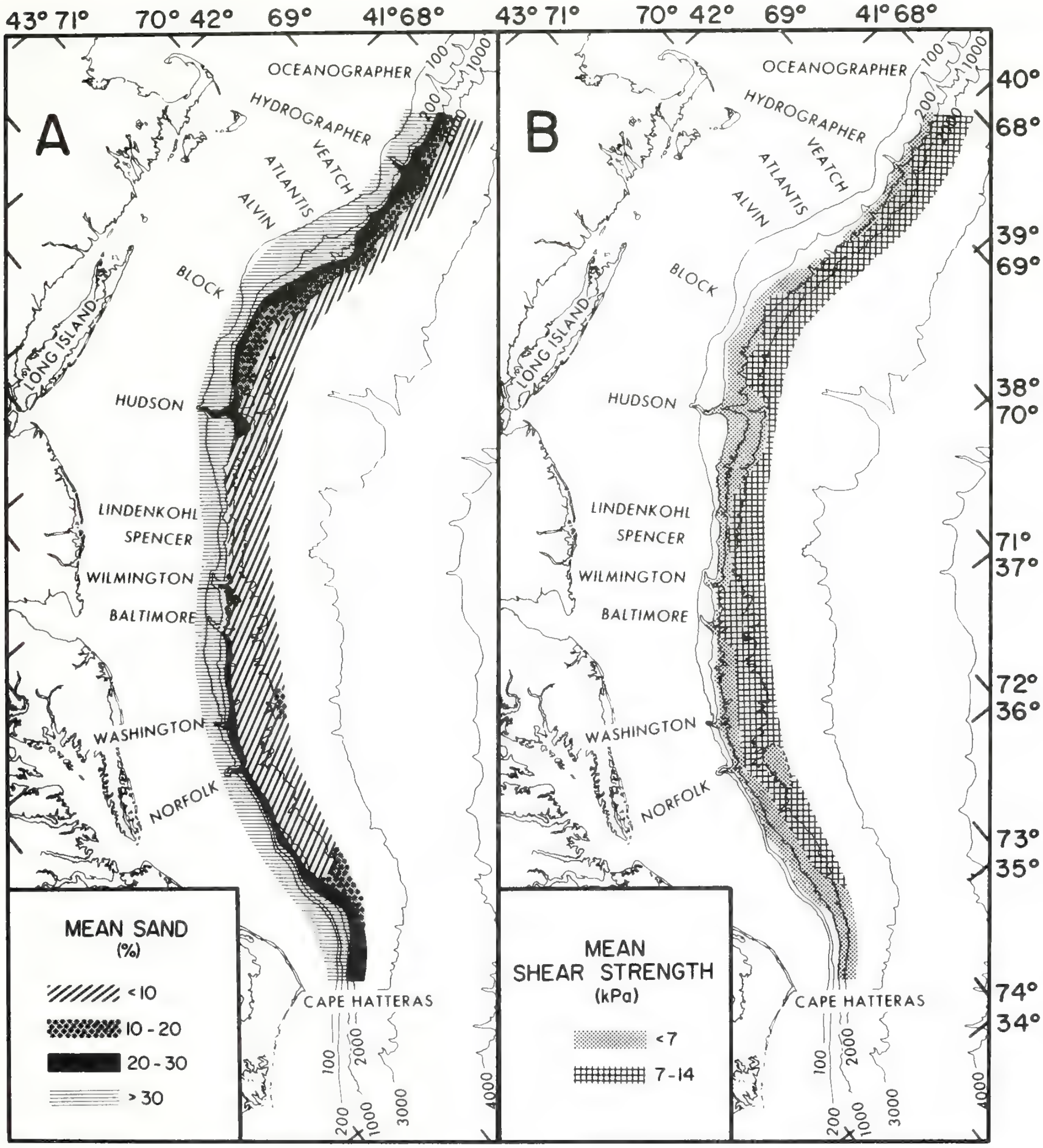

FIG. 2.—A) Sand distribution, mean concentrations for the respective cored intervals; B) Shear strength distribution, mean values for the respective cored intervals.

respect to an applied load as if they were cohesive materials without any internal friction ($\phi = 0$). In such a case, shear strength then is equal to cohesion ($\tau_f = c$). Care must be used, however, in assuming that shear strength and cohesion are synonymous since in reality some degree of internal friction does exist in these samples. Shear strength determinations were made on sub-samples comprised primarily of fine-grained cohesive sediments; intervals of high percentages of sand were not tested.

Mean shear strength values for the near-surface slope deposits range from 1.5 to 1.48 kPa (0.2–2.1 psi). An examination of these values for the continental slope as a whole reveals the presence of a generalized distribution pattern (Fig. 2B). Relatively low values [<7 kPa (1 psi)] comprise the upper and middle slope, and higher values [7–14 kPa (1–2 psi)] typify the lower slope as well as the upper rise. Overall, the near-surface slope deposits display a mean shear strength of 8.3 kPa (1.2 psi) (Table 1). Owing to the high concentrations (40% or more) of sand along the uppermost slope and at the shelf break, mean shear strength values based on vane shear tests are considered to be questionable and therefore have not been reported for this portion of the slope (Fig. 2B).

Lower shear strengths [2–4 kPa (0.3–0.6 psi)] are also generally found in association with a number of the submarine canyons. Indirectly, this may be an effect of the relatively high biological productivity commonly found in the canyons, which especially in the less active canyons results in higher concentrations of organic matter being incorporated into the fine-grained sediments. The combination of high organic carbon and fine-grained sediments may be a contributing factor to lower shear strengths particularly if any degree of remolding takes place (Pusch, 1973). An exception to the general shear strength distribution pattern is seen just south of the Hudson Canyon where relatively low values [<7 kPa (1 psi)] extend across the entire slope. An explanation for this occurrence is not readily apparent, but it is possible the very slight increase in sand content found in these sediments may be a contributing factor. The combination of textural components (sand, silt, clay) in the lower slope deposits in this area is somewhat similar to those of the lower upper slope sediments to the south, but is distinctly different from the mid and lower slope deposits farther south.

Off New England higher strength deposits [7–14 kPa (1–2 psi)] appear to blanket a considerable portion of the slope, in some areas extending from the mid slope on to the upper rise. The presence of strong bottom currents and the general setting of an erosional or nondepositional environment leads to the exposure of more cohesive sediment at the seafloor and the removal or nondeposition of soft, relatively low-shear strength material. A similar effect by currents on fine-grained sediments blanketing topographic highs has been found in other areas (Keller, 1970).

The lower and portions of the mid slope of the Middle Atlantic Bight are characterized by relatively high shear strengths. An explanation for this is not obvious from the available data, but a number of inferences may be made. The distribution pattern appears to correlate to some extent with the higher concentrations of clay-size material in the same area. In a number of areas the higher strengths are possibly due to the exposure of more cohesive sediments at the seafloor as a result of the extensive erosion that has affected the area in the past (Uchupi and Emery, 1967). Although adequate data are lacking, there is a good possibility that compositional characteristics such as unusual concentrations of various mineral assemblages may also contribute to the higher shear strengths displayed by these deposits. Any combination of these factors might possibly contribute to the higher shear strengths found along this portion of the slope.

Shear strengths are notably lower on the mid and lower slope in the vicinity of Cape Hatteras. This may be a reflection of the decrease in the

TABLE 1.—VARIATION OF GEOTECHNICAL PROPERTIES IN SLOPE DEPOSITS AND MEAN VALUES FOR THE ATLANTIC BASIN

	Maximum	Minimum	Mean	Altantic Mean[1]
Water Content (%)	165	33	88	86
Specific Gravity	2.84	2.60	2.72	2.73
Wet Bulk Density (Mg/m^3)	1.97	1.31	1.52	1.52
Porosity (%)	82	44	71	66
Shear Strength (kPa)	24.1	0.9	8.3	5.2
Sensitivity	12	1	3	4
Liquid Limit	124	23	79	65
Plastic Limit	56	16	36	77
Plasticity Index	74	3	42	34
Liquidity Index (%)	478	71	132	170

[1] from Keller and Bennett (1970)

proportions of fine-grained sediment in this area.

Sensitivity, the ratio of natural to remolded shear strength, is a measure of the strength lost as the result of disturbance or shock to the sediment. Sensitivities for the slope deposits off the northeastern United States vary from 1 to 12 thereby classifying them as insensitive to slightly quick (Rosenquist, 1953). Mean sensitivities for the cored intervals, however, range from 2 to 8 with values of 2–4 predominating for most of the slope deposits (Fig. 3A). Isolated areas of sediment with mean sensitivities of from 4 to 8 occur on the upper, middle, and lower slope, as well as on the upper rise. No clear pattern for the distribution of these more sensitive sediments can be defined from our data. Using the range of mean sensitivities reported here, slope deposits can be expected to lose from 50 to 87%

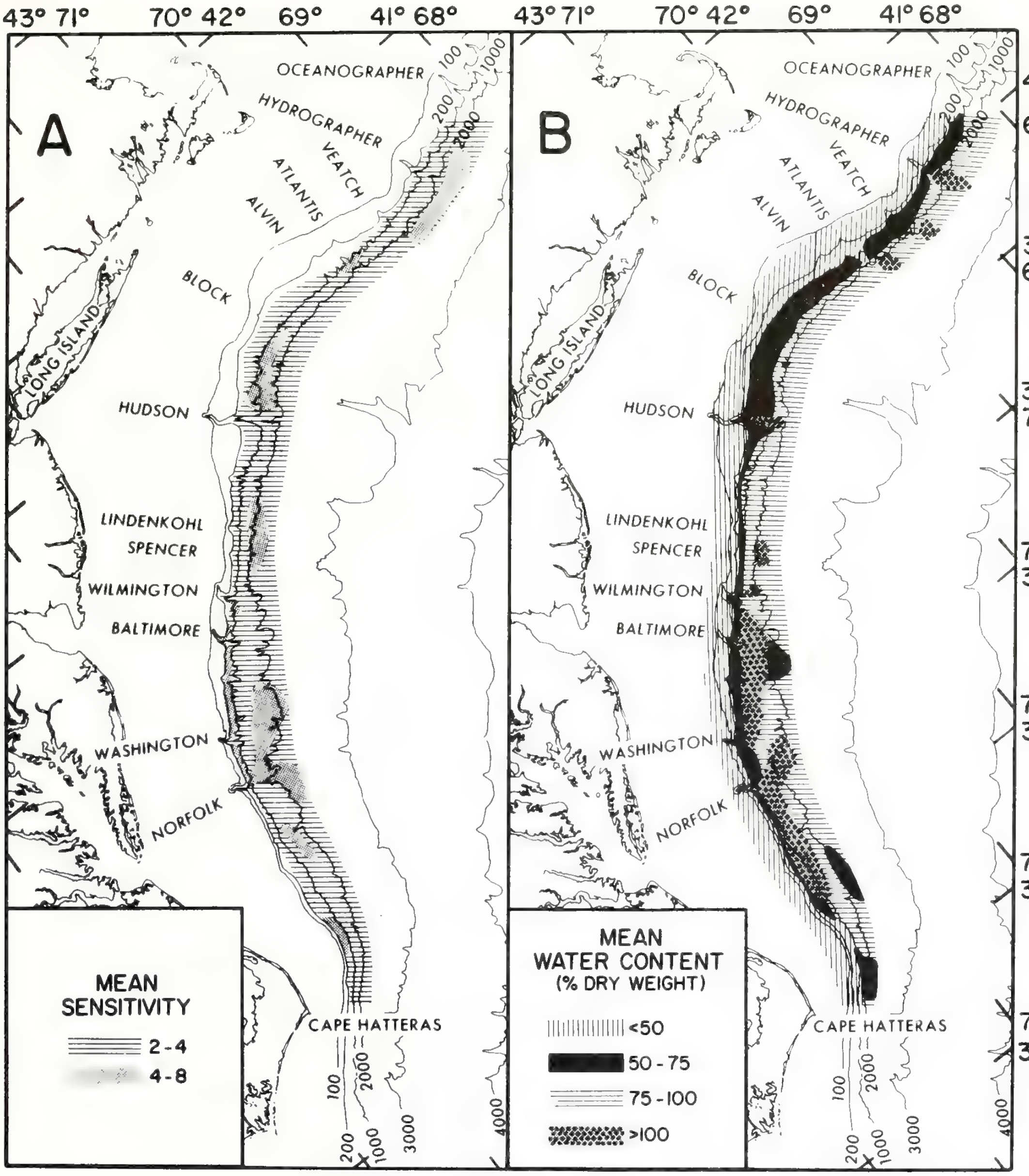

FIG. 3.—A) Sensitivity distribution, mean values for the respective cored intervals; B) Water content distribution, mean values for the respective cored intervals.

of their strength as a result of remolding (Richards, 1962). In comparison to the near-surface deposits of the Atlantic basin, which have a mean sensitivity of 4 (Keller and Bennett, 1970), the slope sediments display comparable characteristics.

Water Content

Water content as used here is the ratio, given as a percent, of the weight of water to the weight of oven-dried (110° C) solids in a given sediment mass. Correction for salt content has not been made in any of the data presented.

Mean water contents for the slope deposits range from 37 to 140% with an overall mean of 85%. The highest water contents are found in association with a number of submarine canyons and along the slope from Wilmington Canyon to about 36°N (Fig. 3B). Distribution of these relatively high values appears to be correlated with those areas in which sediments are fine-grained and contain relatively high concentrations of organic matter. It appears that the Hudson Canyon denotes a boundary between sediments possessing distinctly different water contents (Fig. 3B). To the north, water contents generally range from 45–75% except on the uppermost part of the slope where values of 37 to 45% are common. Water contents which are exceptional to the ranges noted above are associated with the lower portions of submarine canyons where values of 95 to 140% occur. South of Hudson Canyon, water contents are considerably higher for the most part, ranging from 75–130% over the mid and lower slope. This distribution pattern clearly reflects changes in sediment texture and the decree of induration in some cases, with the coarser-grained deposits north of Hudson Canyon having relatively lower water contents. This same area, to the north of Hudson Canyon, is also primarily one of erosion and non-deposition where exposed surface sediments are slightly indurated and possess lower water contents than would be found in recently deposited material. The coarser slope deposits off Cape Hatteras are also characterized by lower water contents. As might be expected, the lowest water contents along the entire slope occur in the vicinity of the shelf break and in the heads of submarine canyons where the sediments are the coarsest. In comparison to the adjacent rise and abyssal sediments, where water contents in the near-surface sediments range from 50–100% (Keller, 1968), slope deposits in the Middle Atlantic Bight display considerably higher water contents. An overall mean value of 85% for the slope deposits, however, corresponds remarkably well with the mean water content value (86%) reported for north Atlantic sediments as a whole (Keller and Bennett, 1970).

Wet Bulk Density

Wet bulk density, or wet unit weight, is the weight per unit volume of a sediment mass. The samples studied here are considered to be at 100% saturation and thus the term "saturated unit weight" applies to the values reported here.

Mean wet bulk densities for sediment cores collected along the continental slope range from 1.32 to 1.87 Mg/m^3 (82.4–116.7 pcf) with an overall mean of 1.52 Mg/m^3 (94.8 pcf) (Table 1). Relatively low bulk densities of 1.32 to 1.50 Mg/m^3 (82.4–93.6 pcf) predominate for the mid and lower slope deposits in the Middle Altantic Bight (Lindenkohl Canyon to 35°45′N) as well as along most of the adjacent upper continental rise (Fig. 4A). Lower density sediments are commonly found also in the outer portions of a number of the submarine canyons. This occurrence is particularly pronounced in Hudson Canyon where fine-grained, organic-rich sediments predominate (Keller, 1975).

A distinct contrast in wet bulk densities occurs in the vicinity of Lindenkohl Canyon where slope deposits to the north possess somewhat higher densities than those to the south. The general distribution pattern of bulk density values for slope deposits off the northeastern United States appears to correlate reasonably well with variations in sediment texture; the higher densities are commonly associated with coarser-grained deposits. This relationship is particularly evident in the vicinity of Atlantis Canyon where high densities are associated with relatively coarse deposits blanketing the entire slope. Mean bulk densities for the mid and lower slope deposits south of Lindenkohl Canyon as well as for the upper rise are generally lower than the 1.50 to 1.75 Mg/m^3 (93.6–109.2 pcf) values reported for the adjacent North Altantic (Keller and Bennett, 1970). These lower values from the Middle Atlantic Bight correlate with the increase in clay-size material and may possibly also reflect the slightly higher concentration of organic matter reported in these margin sediments (Emery and Uchupi, 1972).

Porosity

Porosity is the ratio, expressed as a percentage, of the volume of voids to the total volume of a given sediment mass and is calculated based on the measured water content, wet unit weight, and grain specific gravity. A detailed discussion of porosity determination as well as that of any of the other geotechnical properties discussed above can be found in most texts dealing with soil mechanics.

The overall porosity distribution pattern as shown in Figure 4B takes on much the same appearance as that displayed by bulk density (Fig.

4A). Mean porosity values for the slope as a whole range from 50 to 81%, but more commonly vary from 67 to 73%. The highest values (70 to 80%) predominate in the mid and lower slope deposits of the southern part of the study area as well as in the upper rise sediments. Porosities are considerably lower along the slope off New England where values commonly range from 62 to 65% and rarely exceed 67%. In the coarser, uppermost slope deposits of this area, porosities generally vary from 53 to 58%. It is clear from the distribution pattern that areas of coarser-grained or slightly indurated sediment are relfected by lower porosities.

Plasticity Characteristics

A means of classifying the plastic characteristics of cohesive sediments was worked out some three decades ago when Casagrande (1948) developed the plasticity chart. By means of this

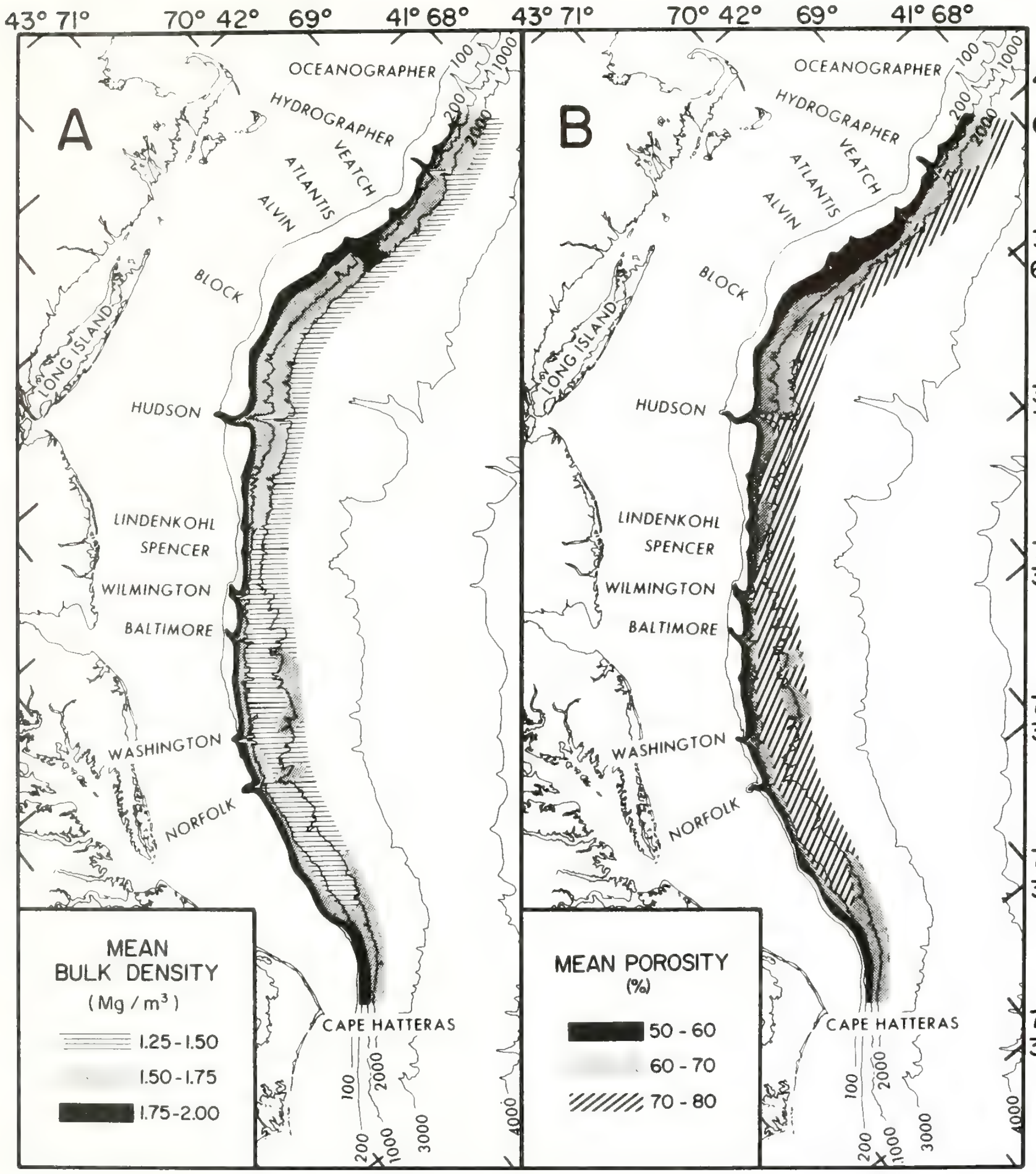

FIG. 4.—A) Bulk wet density distribution, mean values for the respective cored intervals; B) Porosity distribution, mean values for the respective cored intervals.

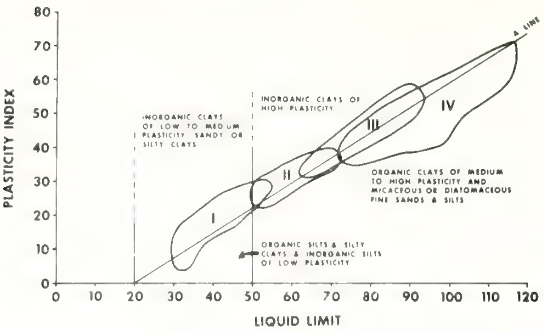

FIG. 5.—Plasticity chart.

chart, which relates plasticity index (range of water content between the liquid and plastic limit of the soil) to the liquid limit, cohesive sediments can be classed into eight categories (Terzaghi and Peck, 1948). An "A"-line is shown on the chart to represent an empirical boundary between inorganic clays, above the line, and organic clays along with inorganic silts below (Fig. 5).

Using Casagrande's classification, the continental slope deposits off the northeastern United States fall into four classes. The coarser-grained, upper-slope sediments are classed as inorganic clays of low to medium plasticity with sandy or silty clays and are designated as Group I (Fig. 5). This classification also applies to those sediments found in the heads of most submarine canyons. Sediments with these characteristics are found to extend down to mid-slope depths off New England (Fig. 6). Group II sediments which are inorganic clays of medium to high plasticity typify mid-slope deposits from Hudson Canyon to Cape Hatteras. In the Middle Atlantic Bight, south of Wilmington Canyon, the lower slope sediments are primarily classed as organic clays of medium to high plasticity containing micaceous sands and silts (Group IV). It is interesting to note that except for the outer portions of Hudson and Block Canyons, these highly plastic clays are limited essentially to this area of the continental slope. Lower slope deposits between Hudson and Wilmington Canyons and those of the upper rise along the entire northeastern margin of the United States are classed as inorganic clays of high plasticity (Group III) and are somewhat similar to the Group II material, but have higher liquid limits.

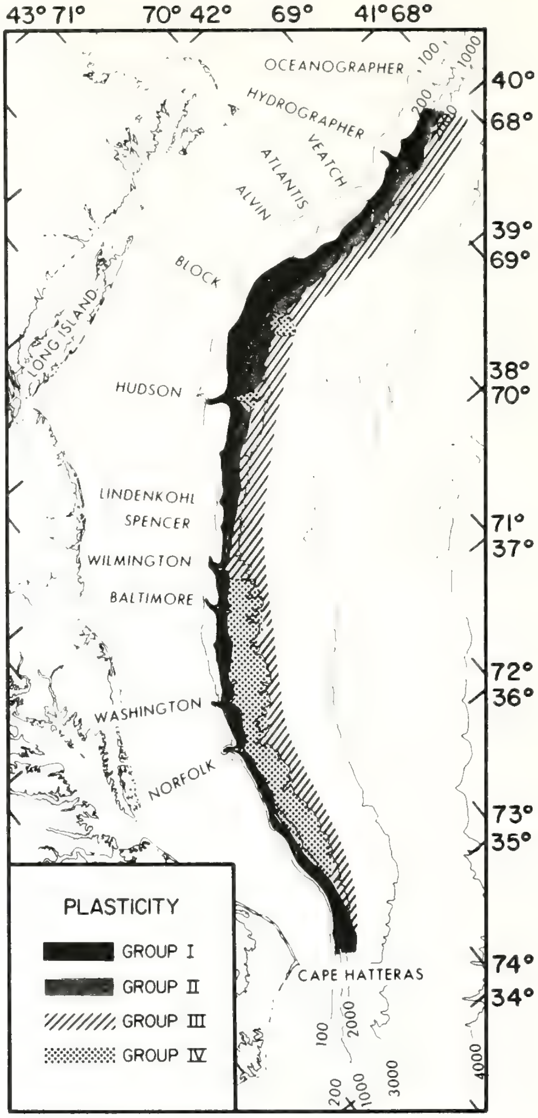

FIG. 6.—Distribution of plasticity characteristics. See Figure 5 for the basis of the four groups and the classification used.

In summary, it can be seen from Figures 5 and 6 that considerable variation in the plasticity characteristics exists among the slope deposits off the northeastern United States. There is, however, a clear indication that the degree of plasticity increases toward the lower slope. As might be expected, the sediments as a whole off new England and in the vicinity of Cape Hatteras display considerably lower plasticity indices than those blanketing the remainder of the slope off the northeastern United States. The highest plasticity indicies are primarily restricted to those sediments mantling the lower slope between Wilmington Canyon and 36°N. It is interesting to note that the occurrence of these high plasticity sediments coincides to a large degree with the area of anomalous bottom topography which is probably the result of a combination of extensive current erosion and slumping. Although the plasticity chart is a rather simple method of sediment classification, it provides a useful means of identifying similar and dissimilar depositional environments.

VERTICAL VARIATIONS OF GEOTECHNICAL PROPERTIES

The areal distribution of geotechnical properties has shown that considerable diversity exists among these properties along the continental slope off the northeastern United States. In order to better understand these variations on a local scale, it is appropriate to examine the vertical distribution and interrelationships of these properties from different areas of the slope. A series of vertical profiles of the geotechnical properties from four core transects is presented for this purpose (see Fig. 1A for core locations).

Georges Bank Transect

Continental slope deposits off New England exhibit large concentrations of sand extending across much of the slope, and only at its lower boundary are the near-surface sediments relatively free of sand (core 3EE) (Fig. 7). As might be anticipated in an environment influenced by oscillations of high energy, with erosion and deposition of coarse and fine sediments at varying intervals, the geotechnical properties vary considerably with depth. On the lowermost slope (core 3EE) the degree of these variations is markedly reduced. Progressing along the transect in a down-slope direction it is readily apparent that water contents and porosities increase as bulk densities decrease. It can also be seen that because of the more homogeneous nature of the sediments farther down on the slope, the geotechnical properties tend to vary with depth in a more uniform or defined manner. On the upper slope (cores 4B and 4C) the overall variation of any one property, except shear strength in core 4C, does not reveal any particular pattern of change with depth. This reflects the variations in the textural properties, particularly the sand content, which are somewhat variable throughout the sam-

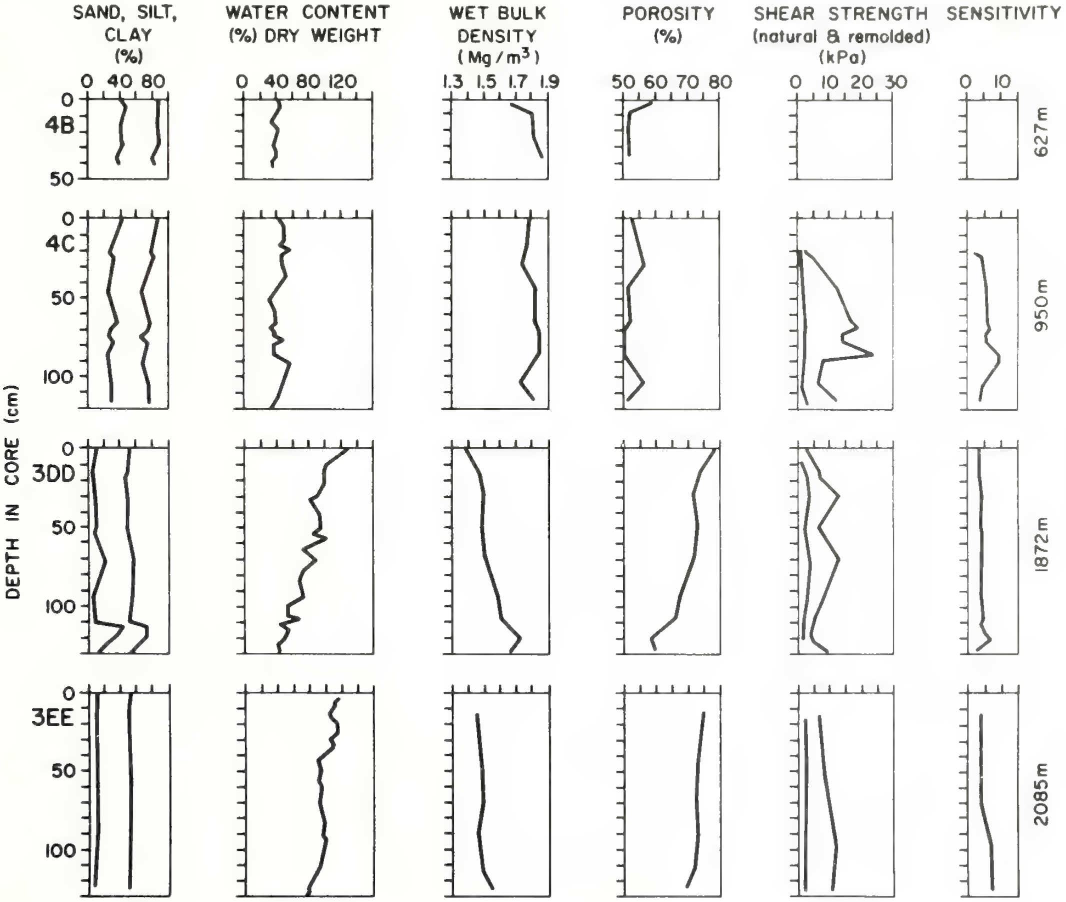

FIG. 7.—Vertical distribution of geotechnical properties, Georges Bank slope transect.

pled interval. Lower-slope sediments (cores 3DD & 3EE) display the more or less expected trends with depth of decreasing water contents and porosities and increasing bulk densities. Shear strengths vary only moderately along this core transect, except for the interval (45–85 cm) in core 4C of unusually high strength [25 kPa (3.6 psi)] which appears to reflect a zone of greater induration.

New Jersey Transect

As seen from the distribution of mean values of the geotechnical properties, slope sediments between Hudson and Wilmington Canyons appear to have somewhat distinct characteristics. Comparison of data profiles from the New Jersey slope reveals that the ranges of values for the various parameters vary relatively little from core to core (Fig. 8). Shear strength is an exception to this statement, in that the uppermost core (9B) in the transect is characterized by much lower shear strengths than are found in the deposits farther down on the slope.

At mid-slope (core 9B), variations in the geotechnical properties with depth are gradual and reflect the normal effects of burial. Further down slope (cores 9C & 9D), changes of these properties are also relatively uniform with depth, but with some minor variations being attributed to differences in sand and clay content. The marked

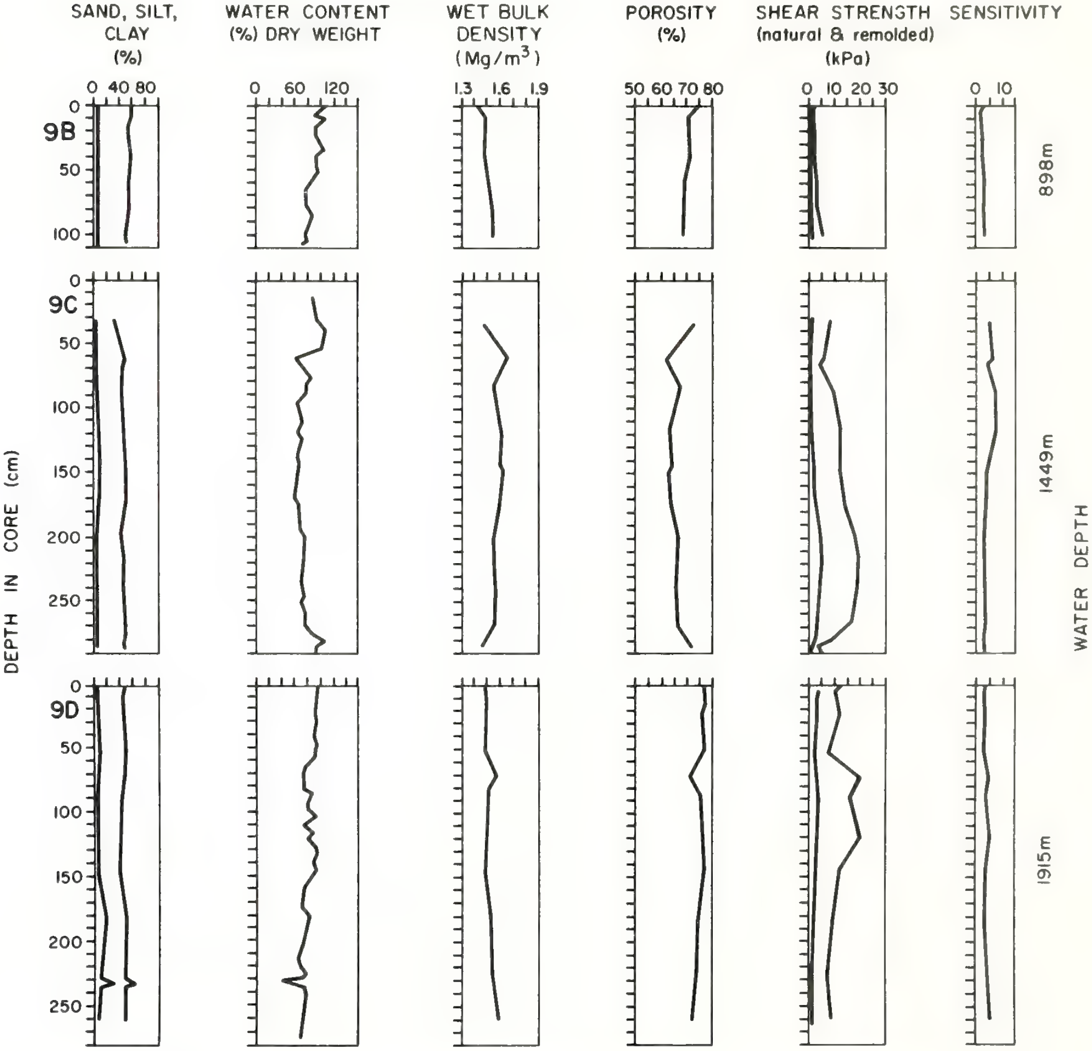

FIG. 8.—Vertical distribution of geotechnical properties, New Jersey slope transect.

changes such as higher water content and lower shear strength in the lower part of core 9C are attributed to burrowing activity.

Middle Atlantic Bight Transect

As noted earlier, the continental slope of the Middle Atlantic Bight, particularly from Wilmington Canyon south to about 36°N, displays sediment characteristics differing from those of other parts of the slope off the northeastern United States. Examination of profiles of geotechnical data from a series of cores across the slope off Virginia reveals pronounced variations from core to core (Fig. 9).

The uppermost slope sediments (core 15A) are characterized by high sand contents with relatively little change in water content (45–55%), wet bulk density [1.67–1.77 Mg/m^3 (104.2–110.4 pcf)], and porosity (55–60%) within the upper 50 cm. To a depth of 100 cm, the mid and lower-slope deposits (cores 15B & 15C) are almost free of sand and are relatively homogeneous. Although the rates of change of the geotechnical properties with depth are quite different for the two areas, the relatively uniform rate of change is attributed to the normal effects of overburden. The slightly anomalous values in core 15C at a depth of 70–77 cm are due to the presence of a worm burrow. On the lower most slope (core 15D) increased concentrations of sand result in lower water contents and porosities and higher wet bulk densities in the near-surface (20–30 cm) sediments. Below about 40 cm the geotechnical properties become quite uniform except for shear strength which decreases markedly through the remainder of the cored interval. This anomalous condition is attributed to a high degree of bioturbation found in the lower portion of this core.

Cape Hatteras Transect

The influence of the increased concentration of sand on the slope in the vicinity of Cape Hatteras in quite apparent from the profiles of geotechnical properties along a transect approxi-

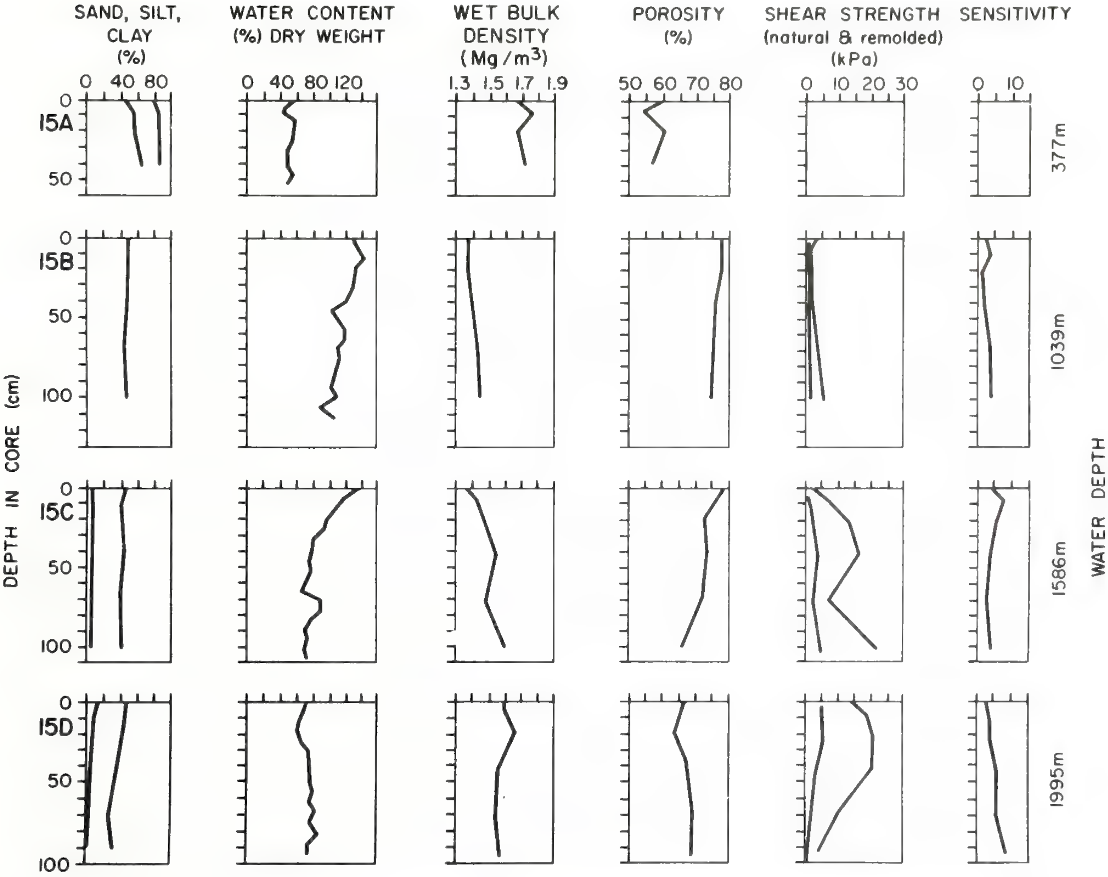

FIG. 9.—Vertical distribution of geotechnical properties, Middle Atlantic Bight slope transect.

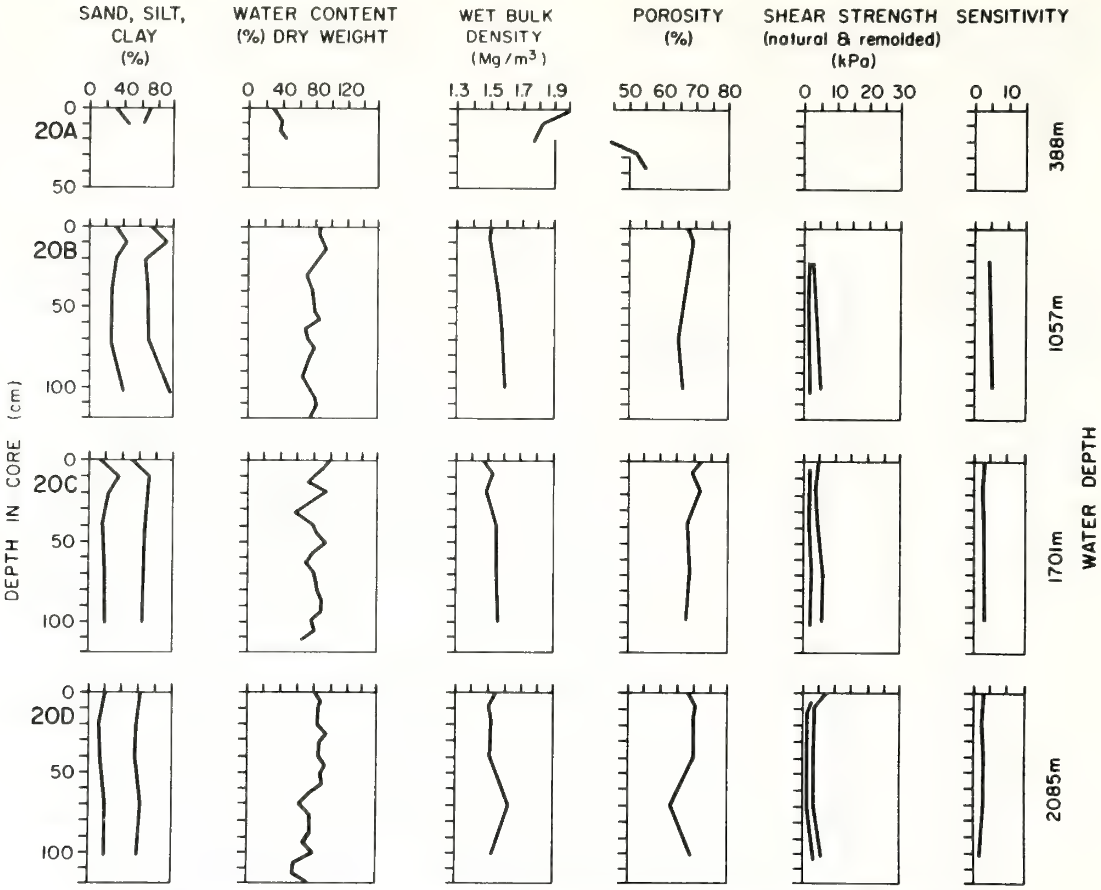

FIG. 10.—Vertical distribution of geotechnical properties, Cape Hatteras slope transect.

mately 65 km north of Cape Hatteras (Fig. 10). Sand is a major constituent to a depth of at least 100 cm even in the lowermost slope deposits of this area. A progressive change in the geotechnical properties in a downslope direction is clearly evident from the profiles shown in Figure 10. Water contents of 30 to 40% along with porosities as low as 44% are characteristic of the coarse-grained deposits on the uppermost slope (core 20A). Bulk densities of 1.97 Mg/m^3 (122.9 pcf) from the upper slope are the highest found along the entire northeastern slope. At mid-slope (Core 20B), sand contents are noticeably lower, whereas water contents and porosities have increased considerably, and bulk densities are reduced drastically from those found at the upper slope. Although there is a continued decrease in the coarse-grained fraction from mid-slope to the base of the slope, the other geotechnical properties remain rather uniform and do not vary markedly within the upper meter. Those vertical variations that do occur are attributed to minor changes in sand content along with the effect of overburden.

SEDIMENT STABILITY

General Setting

Seismic reflection and bathymetric surveys of the continental slope reveal that the margin off the northeastern United States has undergone extensive deposition, erosion due to currents, and mass movement of sediment. The incised nature of the slope with literally hundreds of submarine canyons, valleys, and gullies readily points to the history of intensive erosion. The lower stands of sea level during the Pleistocene probably accounted for most of the erosional features revealed by the present bathymetry. There is, however, evidence from off Georges Bank that in this area canyon erosion and infilling may have been an alternating process dating back to at least the Oligocene (Uchupi et al, 1977). Evidence such as turbidite sequences clearly indicates that a number of the major canyons have served as conduits for the transport of coarse-grained shelf deposits out onto the rise and abyssal plain (Horn et al, 1971; Cleary et al, 1977). Although erosion due to currents is still a prominent process in a few of the canyons, particularly in those off New England, indications are that the majority of the East Coast canyons are inactive at this time (Keller and Shepard, 1978).

Slumping is a process which continues strongly to alter the morphology of the continental slope between Cape Hatteras and Hydrographer Canyon. Slumping along with the extensive erosion mentioned above has been, and in some areas may continue to be, the primary processes contributing to the morphological characteristics of the slope today. The prominence of slumping along the entire continental slope off the northeastern United States is clearly documented by numerous reports of slump structures and scars (Moore and Curray, 1963; Uchupi, 1967, 1968b; Rona, 1969; Kelling and Stanley, 1970; Emery and Uchupi, 1972; MacIlvaine, 1973; Wilkniss, 1973; McGregor et al, 1977; Embley and Jacobi, 1977; McGregor and Bennett, 1977; Uchupi et al, 1977). On-site submersible observations of slump features along the slope just south of Baltimore Canyon (Malahoff et al, 1977) and in the vicinity of Norfolk Canyon (J. Musick, pers. comm., 1977) have more recently been made.

An examination of the bathymetry between Wilmington and Norfolk Canyons reveals a broad flattening of the mid and lower slope relative to the East Coast slope as a whole (Fig. 1A). This flattening at the foot of the slope takes on a morphological character similar to that ascribed to slumping off Nova Scotia by Stanley and Silverberg (1969) and may well reflect massive as well as small-scale slumping in this area. A seismic reflection profile across this portion of the slope shows jumbled subsurface reflectors in the vicinity of the lower slope which Schlee et al (1975) interpret to represent large-scale slumping. A similar conclusion was drawn by Embely and Jacobi (1977) based on their seismic reflection data from across the slope in an area just south of Baltimore Canyon. Another explanation for the broadening of the lower slope may be the extensive erosion believed to have been caused by turbidity currents along with slumping (Uchupi and Emery, 1967). Recent seismic reflection studies of this area tend to support the role turbidity or strong bottom currents may have played in reshaping the bottom topography (McGregor, 1978). The strong evidence for both current erosion and slumping suggests that this part of the slope probably has been affected significantly by both processes. The anomalous character of these deposits is also reflected in their geotechnical properties which differ considerably from those of other areas of the continental slope.

Slumping

A number of methods using strength data are available for making slope stability analyses. In the case of submarine deposits where sediment strength, slope gradients, and slumping mechanics are not sufficiently known, a relatively simple method such as the infinite slope stability analysis is appropriate. This method as described by Taylor (1948) and applied to submarine deposits by Moore (1961), Morelock (1969), Ross (1971), and Almagor and Wiseman (1977) assumes an infinite slope (meaning a constant slope of unlimited extent relative to the thickness of the sediment mass) and provides a means of using vane shear or other shear strength data to assess the stability characteristics of the near-surface slope deposits. Although these authors have discussed the method of analysis to varying degrees it is advisable to outline briefly the procedure used to arrive at the results presented here.

The forces acting on a saturated sedimentary slope of inclination i and sediment thickness Z along a shear plane, AB, are represented as in Figure 11A. The weight on plane AB is $\bar{\gamma}Zb \cos i$, where $\bar{\gamma}$ is the submerged sediment density and b the unit area. Vertical stress, P_v, is the effective weight of the overlying sediment divided by the unit area, b, or $P_v = \bar{\gamma}Z \cos i$. The diagram also

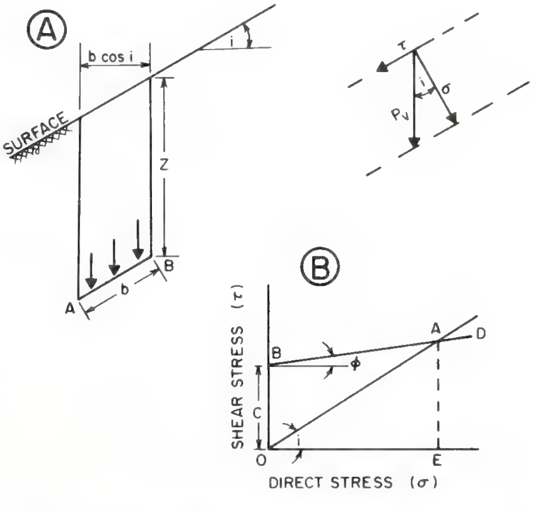

FIG. 11.—A) Schematic of elements of vertical pressure on a saturated sedimentary slope; B) illustration of the limited sediment accumulation that can occur on a slope when the gradient, i, is greater than the angle of internal friction, ϕ, of the sediment.

shows that the vertical stress has two components, shear stress τ directed downslope, and direct stress σ acting normal to the shear plane.

An illustration of these forces in relation to the strength envelope of a sediment is shown in Figure 11B. The vertical stress, P_v, for a given sediment is shown as *OA*; for the slope angle, *i*, to the direct stress, *OE* or σ, and has the corresponding shear stress, *AE* or τ. Also shown is the strength envelope, *BAD*, for the given sediment. It can be seen that a vertical stress of less than *OA* results in a shear stress lower than the shear strength of a given sediment. As long as the shear stress, τ, developed by the overburden pressure is less than the shear strength of the sediment, a stable condition is assumed to exist. If the vertical stress exceeds *OA*, the sediment mass may become unstable (Fig. 11B).

It is clear from Figure 11B that if vertical homogeneity of the sediment mass properties is assumed and the angle of internal friction ϕ of the sediment is greater than the slope *i*, the two lines will never intersect, and infinite sediment accumulation is theoretically possible.

Referring to Figure 11A, shear stress, τ, is determined using the equations

$$\tau = P_v \sin i$$

and

$$P_v = \bar{\gamma} Z \cos i,$$

therefore,

$$\tau = \bar{\gamma} Z \sin i \cos i.$$

Submerged density $\bar{\gamma}$, as used here, is equal to the wet bulk density minus the unit weight or density of sea water (1.028 Mg/m^3).

Using the method just described and by plotting the vane shear data as least-squares lines against burial depth, a comparison of shear strength and the shear stress generated by the overburden can be made. In all cases the data indicate that the sediments are presently stable. Of the 68 cores examined, only two indicated a potential for instability by extrapolation of existing data. Using an approximate slope of the seafloor at the respective core station as determined from small-scale bathymetric maps and the mean bulk density for the particular core, it can be seen from Figure 12 that extensions of the two lines in each case would result in their intersection. This analysis indicates that for cores 12C and 8D, given the respective slopes, at depths equal to 9 and 16 m failure might be expected to take place.

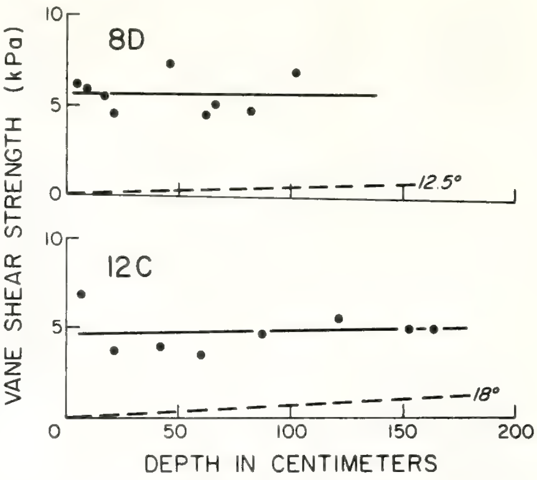

FIG. 12.—Least squares lines of vane shear strength versus depth for cores 8D and 12C. Dashed lines are the shear stresses due to overburden pressure with increasing sediment thickness on the respective slopes (12.5 and 18°) at sites 8D and 12C.

Comparing least-squares plots of shear strength data from a representative number of cores against shear stresses developed at slope gradients of 5, 10, 20, and 30° reveals that these deposits would be stable at relatively high slopes (Fig. 13). A bulk density of 1.52 Mg/m^3 (94.8 pcf) was used for these shear stress determinations. It can be seen from Figure 13 that at a mean gradient for the continental slope off northeastern United States of 7° (Emery and Uchupi, 1972), the near-surface sediments are stable insofar as overburden pressures are concerned using the infinite slope

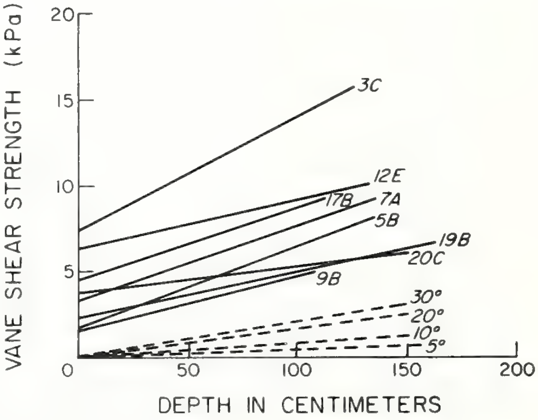

FIG. 13.—Least squares lines of vane shear strengths versus depth for a representative number of slope cores. Dashed lines are the shear stresses generated by overburden pressures with increasing sediment accumulation on slopes of 5 to 30°.

method of analysis. Even at gradients of up to 30°, a considerable thickness of sediments would have to be deposited before failure would occur.

Although the infinite slope analysis is a commonly used method for slope stability determinations, a word of caution is appropriate in light of at least three problems inherent in our analysis. First, it is assumed that the linear regressions determined from these short cores (1 to 2.9 m) are representative of the shear strength profiles which are extrapolated to depth; second, it is also assumed that the mass physical properties, specifically the wet unit weights used, are representative over the extrapolated depths; and finally, the actual slope gradient at the core sites are only approximately known. Additionally the infinite slope analysis method is limited in that it relates only to failure resulting from excess overburden on an inclined slope. It should be noted also that the shear strengths used in this study were undrained vane tests, thus, theoretically, the undrained strength is equal to the cohesion of the sediment if stressed without loss of pore water. Therefore, the stability analyses presented above should be considered as conservative estimates if the sediment were to fail under drained conditions.

With the above considerations in mind, it is interesting to note that two areas exhibiting possible incipient instability (cores 8D & 12C) are in submarine canyons where fine-grained, organic-rich sediments are being deposited. Evidence of slumping in Wilmington Canyon (core 12C) has been reported by Killing and Stanley (1970) and observed by the senior author in Hudson Canyon (core 9D) during submersible dives.

As pointed out earlier, slumping is a prominent process along portions of the continental slope, but solutions from our limited analyses indicate that slopes are generally stable. Mechanisms other than excess overburden such as the effect of internal waves on upper slope deposits or infrequent seismic shocks, which were not considered in the infinite slope analysis, are undoubtedly important factors contributing to the slumping process. Obviously, much longer cores are required and actual slopes at the respective core locations must be known for a rigorous analysis of slope stability.

Hydrodynamic Processes

Bottom currents play a significant role in the sedimentary processes along major portions of the continental slope off the northeastern United States. Although relatively few near-bottom (1 to 3 m above the bottom) current measurements have been made along the slope, there is sufficient evidence from bottom photographs to substantiate the fact that sediment transport occurs frequently along many portions of the slope. The few current observations that do exist indicate that velocities are generally higher along the slope off New England than off the Middle Atlantic Bight. Velocities as high as 70 cm/sec have been reported in Hydrographer Canyon (B. Heezen, pers. comm, 1973) and along the slope between Alvin and Block Canyons (Emery and Ross, 1968). Peak velocities reported from the area between Hudson Canyon and Cape Hatteras rarely exceed 20 to 30 cm/sec (Lyall et al, 1971; Rowe, 1971; Keller and Shepard, 1978; McGregor, 1979). It is obvious from bottom photographs, however, that the hydrodynamic processes resulting in the transport of bottom sediments are highly irregular even within a local area.

In order to relate current velocities to sediment transport it is appropriate to consider the threshold velocities (the velocity slightly less than that required to initiate motion for a certain sediment grain size) of the respective sediment types occurring on the continental slope. Since most of the current measurements referred to in the following discussion were made at or near a height of 300 cm above the bottom, the threshold velocity curve for $\bar{\mu}_{300}$ (current velocity 300 cm above the bottom) presented by Keller and Shepard (1978) is used as the basis for the threshold velocities mentioned herein. In using such a diagram, certain limitations must be kept in mind. Variations in conditions (fluid viscosity and grain shape and density) from those upon which the diagram is based will result in different threshold velocities. It must also be pointed out that the theory of threshold velocity and sediment transport is poorly developed for very fine-grained sediments. With this in mind, the threshold velocities presented here are considered to be approximations yet suitable for the overall discussion of sediment transport on the continental slope.

Although bottom currents off New England are relatively strong, their effect on the slope deposits varies markedly. In their study of East Coast canyons, Keller and Shepard (1978) recorded bottom currents of up to 53 cm/sec and the seaward migration of sand ripples along the axis of Hydrographer Canyon down to depths of 710 m. The study also found that threshold velocities of the canyon sediments were exceeded 26% of the time during a 11.5 day observation period. In the same general area, between Block and Alvin Canyons, Emery and Ross (1968) reported current velocities of 70 cm/sec, but found no expression of current activity in the microtopography of the sea floor. The reported median diameters (.009 to .017 mm) of the surface sediments in that area (Emery and Ross, 1968) should have threshold velocities of 18 to 20 cm/sec using the $\bar{\mu}_{300}$ curve, yet the 70 cm/sec velocities did not appear to be eroding or transporting these sediments. It is apparent that in dealing with very fine-grained sediments, grain-size in itself may not necessarily provide the basis for determing threshold velocity. Southard (1977), in studying fine-grained cohesive sediments, found that in addition to grain size such factors as water content, organic content, mineral composition, and amount of biogenic reworking may significantly influence the threshold velocity of a particular sediment.

The strong currents off New England are effective in transporting sand and silt-size material across the slope, but in those areas of fine-grained cohesive sediment little erosion appears to take place. At most, the currents tend to smooth out sharp irregularities in the microtopography and keep additional sediments from being deposited (McIlvaine, 1973). The resulting fine-grained sediments are found to have relatively high shear strengths and bulk densities and low water contents, all of which contribute to higher threshold velocities.

Although Keller and Shepard (1978) report currents in Hudson and Wilmington Canyons that exceed theoretical threshold velocities required to transport the bottom sediments, currents along the slope in the Middle Atlantic Bight do not at present appear to be a prominent factor in transporting bottom sediments. Bottom photographs and current measurements indicate that threshold velocities in the Bight are seldom exceeded except on the uppermost slope where coarser sediments commonly display streaming features and ripple marks.

Velocities of up to 30 cm/sec have been measured along the midslope between Baltimore and Washington Canyons (McGregor, 1979), but it is questionable as to whether they exceed the threshold velocity of the fine-grained (.008 mm median diameter) deposits found there. Bottom photographs from a mid-slope site with similar sediments, approximately 56 km to the southwest of McGregor's current meter station, showed no evidence of current activity.

In an examination of numerous bottom photographs from the slope and continental rise off Cape Hatteras, Rowe (1971) found evidence for a patchy distribution of current activity (sediment streamers, ripples) down to depths of 4400 m. Current measurements on the slope in the same area revealed near-bottom (3 to 25 m above the bottom) currents with velocities up to 20 cm/sec (Rowe, 1971). At the lower slope off Cape Hatteras, Barrett (1965) reported near-bottom velocities of 10 to 15 cm/sec based on geostrophic calculations. Although these velocities do not exceed the threshold velocities of the slope deposits, based on the grain-sizes (.008 to .025 mm) reported to Hathaway (1971), it is obvious from bottom photographs that currents are causing bottom sediments to be transported along this portion of the East Coast continental slope.

Hydrodynamic processes along the continental slope off the northeastern United States are influential in transporting bottom sediments along the uppermost slope and in those areas where coarse-grained sediments extend farther onto the slope. Although rather strong currents persist over certain parts of the slope, they appear to have little or no effect in eroding and transporting fine-grained cohesive sediments.

In contrast to the non-depositional and erosional environments of the slope off New England, the slope off the Middle Atlantic Bight, with its weaker currents and large sources of fine-grained sediment, is presently a zone of deposition for fine-grained material. A similar conclusion was reached by Doyle et al (1975) based on their study of mica distribution on the continental slope and by Keller and Shepard (1978) as a result of their investigation of sedimentary processes in the major East Coast canyons. It is, however, clear from an examination of the sedimentary structures in the cores collected during this study that considerable variation in the hydrodynamic processes has occurred over long periods of time. The presence of coarse-grained laminae, some of which display cross bedding, within thick sequences of fine-grained sediment attests to the drastic changes in the energy level of bottom currents from time-to-time.

SUMMARY

The continental slope off the northeastern United States is a province of the seafloor which has been the site of extensive deposition (marginal outbuilding) in the past. More recently (late Tertiary to present) it has become an area where erosion as well as large and small scale slumping are the predominant processes affecting the slope. As might be expected these deposits display considerable variability as is apparent from an examination of the areal and vertical distribution of their geotechnical properties (Table 1). Based on these properties, however, it appears that the near-surface slope deposits off the northeastern United States can be divided into distinct sedimentological provinces.

Factors, such as the existing strong bottom currents and previous glacial activity, combine to give the slope deposits off New England mass physical properties which strongly contrast with those of most other slope sediments off the northeast margin of the United States (Table 2). From just north of Hudson Canyon to Hydrographer Canyon, the slope is blanketed by coarse-grained sediments from the adjacent shelf and/or eroded from the uppermost slope, or is composed of fine-grained, relatively cohesive material which is exposed at the seafloor as a result of erosion. Textural characteristics appear to contribute strongly to the display of distinctly different geotechnical properties for this portion of the continental slope (Table 2). On the whole, the slope deposits off New England are characterized as having relatively low water contents, porosities and plasticity indices, and high wet bulk densities and shear strengths.

The area from the vicinity of Hudson Canyon to Lindenkohl Canyon is unique in that it is delineated by a certain degree of uniformity among the mass physical properties across the entire slope. Relatively low shear strengths along with intermediate values of water content and bulk density are typical from the upper to the lower slope. Normally, some degree of gradation in these properties would be expected across the slope. Gross textural characteristics are not distinctly different between this area and that to the south, but there appear to be subtle changes in the sand content of the lower slope sediments that result in their possessing geotechnical properties similar to those of the lower upper-slope deposits of the Middle Atlantic Bight.

As the result of extensive current erosion of a prograded margin coupled with large and small scale slumping, the mid and lower slope of the Middle Atlantic Bight is considerably wider and not as steep as found elsewhere. Bulk densities are notably low for the slope as a whole just as shear strengths and water contents are relatively high. Plasticity characteristics of the mid and lower-slope deposits are also significantly different from those found elsewhere along the entire slope. Plasticity indices of up to 70, the highest measured during this study, are unique to the slope deposits off the Middle Atlantic Bight. Relatively high concentrations of clay-size material plus the dynamic effects of currents and slumping appear to be major factors contributing to the observed distribution of geotechnical properties.

In the vicinity of Cape Hatteras, the effects of a narrowing shelf and slope plus the large concentration of sand on the adjacent shelf contribute to a distinct sedimentary environment. Varying concentrations of sand which has been transported down the slope appear to be the primary factor influencing the geotechnical properties of these slope deposits. As might be expected, bulk densities are relatively high, whereas water contents, porosities, and shear strengths are low.

Sediments in the major submarine canyons along the continental slope usually display mass physical properties considerably different from those of the adjacent slope. Axial deposits of canyons off New England commonly are relatively coarse-grained and thus possess geotechnical properties normally associated with coarse sediments. In the outermost part of these canyons, finer sediments prevail with usually higher water contents and porosities, and lower bulk densities. Those canyons from Hudson Canyon south generally are blanketed with fine-grained, organic-rich sediments and display higher water contents and porosities, but lower wet bulk densities and shear strengths than the nearby slope deposits.

Vertical variations of geotechnical properties in the near-surface (50 to 290 cm) slope deposits are relatively minor and are generally attributed to the normal effects of overburden. Variations of these properties from the normal gradation with depth are, however, observed at a number of sites which are influenced by irregularities in sand content or by what appear to be zones of increased induration.

It is readily apparent from reviewing the data that textural characteristics are a primary factor influencing the observed variations in the geotechnical properties (Table 2). Commonly, increases in water content and porosity along with decreases in bulk densities with distance downslope tend to correlate with increasing percentages of clay-size material and decreasing amounts of sand. Silt content varies remarkably little in rela-

TABLE 2.—COMPARISON OF MEAN VALUES OF GEOTECHNICAL PROPERTIES FOR CORED INTERVALS OF SLOPE SEDIMENTS

Region	Water Content (%)	Specific Gravity	Wet Bulk Density (Mg/m^3)	Porosity (%)	Shear Strength (kPa)	Sensitivity	Liquid Limit	Plastic Limit	Sand (%) >62µm	Silt (%) 2–62µm	Clay (%) <2µm
New England (cores 1–6)	78	2.71	1.57	66	7.8	3	62	30	18	44	38
Mid-Atlantic (cores 8–19)	91	2.72	1.50	70	7.4	3	78	36	9	43	48

tion to sand and clay content in the slope deposits as a whole, normally ranging from 37 to 45%.

A comparison of mean values of the various geotechnical properties for the slope with those of the adjacent Altantic basin indicates that there is considerable similarity between such properties as water content, wet bulk density, grain specific gravity, and sensitivity (Table 1). Mean values for porosity, shear strength, and plasticity index are, however, notably higher in the slope deposits.

An assessment of the effects of overburden pressure on the stability of the slope sediments, using the infinite slope analysis method, indicates that the areas sampled are stable. Analyses of cores from Hudson and Wilmington Canyons showed that unstable conditions might exist if additional sediment accumulations on the order of 9 and 16 m, respectively, should occur. Owing to the short lengths of core and thus the need to extrapolate geotechnical values to greater depths as well as being able only to approximate the slope of the sea floor at the core site results in severe limitations being placed on the stability analyses we were able to perform. Slumping is clearly a significant process along the northeastern margin of the United States and therefore factors other than overburden pressure, such as the impact of internal waves on the upper slope, undercutting by bottom currents, or infrequent seismic shocks, undoubtedly contribute to the slumping of the slope deposits.

Hydrodynamic processes acting on the continental slope off the northeast coast of the United States are effective in transporting bottom sediments in a number of areas. Of the areas considered in this study, bottom currents appear to be strongest along the New England slope. Here current velocities of up to 70 cm/sec have been recorded both on the slope and in a submarine canyon. Despite these strong currents, it is apparent that they are effective in transporting only relatively coarse-grained material. In areas of fine-grained sediment, these strong currents appear to do little more than serve to keep the area free of new sediments or at most to smooth out minor irregularities in the microtopography.

In contrast to the high energy conditions off New England, bottom currents along the slope of the Middle Altantic Bight are reported to have considerably lower velocities. Although a number of measurements have been made, velocities seldom have been found to exceed 30 cm/sec and more commonly are less than 15 cm/sec. Indications based primarily on bottom photographs are that transport of bottom sediments along this portion of continental slope does occur, but is rather limited. In contrast to the erosional and/or non-depositional environment of the New England slope, the slope off the Middle Atlantic Bight appears to be a depositional zone for fine-grained material.

ACKNOWLEDGMENTS

The authors acknowledge with great appreciation the outstanding efforts of George Lapiene during the field phase of this study. A successful field program was made possible by the fine support and cooperation received from the officers and crew of the NOAA ship RESEARCHER for which we are most grateful. To our colleagues, Bonnie McGregor, who reviewed the manuscript and assisted us at sea, as well as William Sawyer and Pamela Bates who carried out much of the laboratory work, we express our many thanks. This study was primarily funded by NOAA, with additional support to the senior author from NSF Grant OCE76-21869.

REFERENCES

Almagor, G., and Wiseman, G., 1977, Analysis of submarine slumping in the continental slope off the southern coast of Israel: Marine Geotechnology., v. 2, p. 349–388.

Barrett, J. R., Jr., 1965, Subsurface currents off Cape Hatteras: Deep-Sea Res., v. 12, p. 173–184.

Casagrande, A., 1948, Classification and identification of soils: Amer. Soc. Civil Engineers Trans., v. 113, p. 901–931.

Cleary, W. S., Pilkey, O. H., and Ayers, M. W., 1977, Morphology and sediments of three ocean basin entry points, Hatteras abyssal plain: Jour. Sed. Petrology, v. 47, p. 1157–1170.

Doyle, L. J., Pilkey, O. H., Hayward, G. L., and Arbogast, J. S., 1975, Sedimentation on the northeastern continental slope of the United States: proc. IX Congress International de Sedimentologie, Theme 6, p. 51–56.

———, ———, and Woo, C. C., Sedimentation on the eastern United States continental slope: This volume.

Drake, C. L., Ewing, M., and Sutton, G. H., 1959, Continental margins and geosynclines: the east coast of North America north of Cape Hatteras, *in* Physics and Chemistry of the Earth: London, Pergamon Press, v. 3, p. 110–198.

Embley, R. W., and Jacobi, R. D., 1977, Distribution and morphology of large submarine sediment slides and slumps on Atlantic continental margins: Marine Geotechnology, v. 2, p. 205–228.

Emery, K. O., and Ross, D. A., 1968, Topography and sediments of a small area of the continental slope south of Martha's Vineyard: Deep-Sea Res., v. 15, p. 415–422.

———, Uchupi, E., Phillips, J. D., Bowin, C. O., Bunce, E. T., and Knott, S. T., 1970, Continental rise off eastern North America: Am. Assoc. Petroleum Geologists Bull., v. 54, p. 44–108.

———, and Uchupi, E., 1972, Western north Atlantic ocean: topography, rocks, structure, water, life, and sediments: Am. Assoc. Petroleum Geologists Memoir 17, 532 p.

Evans, I. and Sherratt, G. G., 1948, A simple and convenient instrument for measuring the shear resistance of clay soils: Jour. Scientific Inst. and Phys, in Industry, v. 25, p. 411–414.

Hathaway, J. C., 1971, Data file, continental margin program, Atlantic coast of the United States, v. 2, Sample collection and analytical data: Woods Hole Oceanog. Inst. Ref. No. 71-15, 489 p.

Horn, D. R., Ewing, M., Horn, B. M., and Delach, M. N., 1971, Turbidities of the Hatteras and Sohm abyssal plains, western north Atlantic: Marine Geology, v. 11, p. 287–323.

Hoskins, H., 1967, Seismic reflection observations on the Atlantic shelf, slope, and rise southeast of New England: Jour. Geology, v. 75, p. 598–611.

Keller, G. H., 1968, Shear strength and other physical properties of sediments from some ocean basins, *in* Proc. Civil Eng. in the Oceans: Amer. Soc. Civil Eng., p. 391–417.

———, 1970, Mass properties of the sea floor in a selected depositional environment: Proc. Civil Eng. in the Oceans II, Amer. Soc. Civil Eng., p. 857–877.

———, 1975, Sedimentary processes in submarine canyons off northeastern United States: Proc. IX Congress International de Sedimentologie, Theme 6, p. 77–86.

———, and Bennett, R. H., 1970, Variations in the mass physical properties of selected submarine sediments: Marine Geology, v. 9, p. 215–223.

———, and Shepard, F. P., 1978, Currents and sedimentary processes in submarine canyons off the northeastern United States, *in* Stanley, D. J., and Kelling, G., eds., Sedimentation in submarine canyons, fans, and trenches: Stroudsburg, PA., Dowden, Hutchinson and Ross, Inc., p. 15–32.

Kelling, G., and Stanley, D. J., 1970, Morphology and structure of Wilmington and Baltimore submarine canyons, eastern United States: Jour. Geology, v. 78, p. 637–660.

Knott, S. T., and Hoskins, H., 1968, Evidence of Pleistocene events in the structure of the continental shelf off northeastern United States: Marine Geology, v. 6, p. 5–43.

Krauss, D. C., Chramiec, M. A., Walsh, G. M., and Wisotsky, S., 1966, Seismic profile showing Cenozoic development of the New England continental margin: Jour. Geophys. Res., v. 71, p. 4327–4332.

Lyall, A. K., Stanley, D. J., Giles, H. N., and Fisher, A., 1971, Suspended sediment and transport at the shelf-break and on the slope, Wilmington Canyon area eastern U.S.A.: Jour. Mar. Tech. Soc., v. 5, p. 15–27.

MacIlvaine, J., 1973, Sedimentary processes on the continental slope off New England: Woods Hole Oceanog. Inst. Ref. No. 73-58, 211 p.

Malahoff, A., Embley, R. W., Perry, R. B., and Fefe, C., 1977, Sedimentation processes on the continental shelf, slope and upper rise near Baltimore Canyon: Trans. Am. Geoph. Union, v. 58, p. 1160.

McGregor, B. A., 1979, Current meter observations on the U.S. Atlantic continental slope, variation in time and space: Marine Geology, v. 29, p. 209–219.

———, 1978, Seismic reflection profiles of the United States east coast continental margin: NOAA Tech. Rept. ERL 398-AOML28, 17 p.

———, Keller, G. H., and Bennett, R. H., 1975, Seismic profiles along the U.S. northeast coast continental margin: Trans. Am. Geoph. Union, v. 56, No. 6, p. 382.

———, and Bennett, R. H., 1977, Continental slope sediment instability northeast of Wilmington Canyon: Am. Assoc. Petroleum Geologists Bull., v. 61, p. 918–928.

———, Bennett, R. H., and Merrill, G. F., 1977, Continental slope south of Baltimore Canyon, U.S. East Coast: Proc. Geol. Soc. America, Ann. Mtg., p. 1089.

Milliman, J. D. 1973, Marine Geology, *in* Coastal and offshore environmental inventory. Cape Hatteras to Nantucket Shoals: Providence, RI, Univ. of Rhode Island, Marine pub. series No. 3, 91 p.

———, Pilkey, O. H., and Ross, D. A., 1972, Sediments of the continental margin off the eastern United States: Geol. Soc. America Bull., v. 83, p. 1315–1334.

Moore, D. G., 1961, Submarine slumps: Jour. Sed. Petrology, v. 31, p. 343–357.

———, and Curray, J. R., 1963, Sedimentary framework of continental terrace off Norfolk, Virginia, and Newport, Rhode Island: Am. Assoc. Petroleum Geologists Bull., v. 47, no. 12, p. 2051–2054.

Morelock, J., 1969, Shear strength and stability of continental slope deposits, western Gulf of Mexico: Jour. Geophys. Res., v. 74, p. 465–482.

Newton, J. G., and Pilkey, O. H., 1969, Topography of the continental margin off the Carolinas: Southeastern Geology, v. 10, No. 2, p. 87–92.

Oser, R. K., 1969, Bottom environmental oceanographic data report—Hudson Canyon area, 1967: Naval Oceanog. Office Informal Rept. No. 69-8, 43 p.

———, 1973, Seafloor bathymetry and sediment properties in deep water dump area *A*, *in* Wilkniss, P. I., Environmental condition report for deep water dump area *A*: Washington, D.C., Naval Research Lab., NRL Report 7553, p. 103–112.

Pratt, R. M., 1968, Atlantic continental shelf and slope of the United States—physiography and sediments of the deep-sea basin: U.S. Geol. Survey Professional Paper 529-B, 44 p.

Pusch, R., 1973, Influence of organic matter on the geotechnical properties of clays: Nat. Swedish Building Res. Document 11, 63 p.

Richards, A. F., 1961, Investigations of deep-sea sediment cores, I. Shear strength, bearing capacity, and consolidation: U.S. Navy Hydrographic Office, Tech. Rept. 63, 60 p.

———, 1962, Investigation of deep-sea sediment cores, II, Mass physical properties: U.S. Navy Hydrographic Office Tech. Rept. 106, 146 p.

———, and Keller, G. H., 1961, A plastic-barrel sediment corer: Deep-Sea Res., v. 8, p. 306–312.

Roberson, M. L., 1964, Continuous seismic profiler survey of Oceanographer, Gilbert and Lydonia Submarine Canyons, Georges Bank: Jour. Geophys. Res., v. 69, p. 4779–4789.

Rona, P. A., 1969, Middle Atlantic continental slope of United States: deposition and erosion: Am. Assoc. Petroleum Geologists Bull., v. 53, p. 1453–1465.

———, and Clay, C. S., 1967, Stratigraphy and structure along a continuous seismic reflection profile from Cape Hatteras, North Carolina to the Bermuda Rise: Jour. Geophys. Res., v. 72, p. 2107–2130.

Rosenquist, I., 1953, Consideration on the sensitivity of Norwegian quick-clays: Géotechnique, v. 3, p. 195–200.

Ross, D. A., 1971, Mass physical properties and slope stability of sediments of the northern Middle America Trench: Jour. Geophys. Res., v. 76, p. 704–712.

Rowe, G. T., 1971, Observations on bottom currents and epibenthic populations in Hatteras submarine canyon: Deep-Sea Res., v. 18, p. 569–581.

Schlee, J., Behrendt, J. C., Mattick, R. E., and Taylor, P. T., 1975, Structure of continental margin of Mid-Atlantic states (Baltimore Canyon Trough): U.S. Geol. Survey Open File Rept. 75-60, 59 p.

———, Behrendt, C., Grow, J. A., Robb, J. M., Mattick, R. E., Taylor, P. T., and Lawson, B. J., 1976, Regional geological framework off northeastern United States: Am. Assoc. Petroleum Geologists Bull., v. 60, p. 926–951.

Shepard, F. P., 1934, Canyons off the New England coast: Am. Jour. Sci., 5th Ser., v. 27, p. 24–36.

———, 1954, Nomenclautre based on sand-silt-clay ratios: Jour. Sed. Petrology, v. 24, p. 151–158.

Shideler, G., and Swift, D. J. P., 1972, Seismic reconnaissance of Post-Miocene deposits; middle Atlantic continental shelf-Cape Henry, Va. to Cape Hatteras, North Carolina: Marine Geology, v. 12, p. 165–185.

Southard, J. B., 1977, Erosion and transport of fine cohesive marine sediments: Trans. Am. Geoph. Union, v. 58, p. 1161.

Stanley, D. J., and Silverberg, N., 1969, Recent slumping on the continental slope off Sable Island Bank, southeast Canada: Earth and Planetary Sci. Letters, v. 6, p. 123–133.

Stetson, H. C., 1938, The sediments of the continental shelf off the eastern coast of the United States: Mass. Inst. Technology and Woods Hole Oceanographic Inst. Papers in Phys. Oceanog. and Meterol., v. 5, No. 4, p. 5–48.

———, 1949, The sediments and stratigraphy of the east coast continental margin—Georges Bank to Norfolk Canyon: Mass. Inst. Technology and Woods Hole Oceanog. Inst., Papers in Phys. Oceanog. and Meteorol., v. 11, No. 2, p. 1–60.

Stout, P. M., and McClennen, C. E., 1977, Buried valley segments on the continental shelf off Delaware Bay and New Jersey: Geol. Soc. America Northeast Reg. Mtg. (Abs.), March, p. 322.

Taylor, D. W., 1948, Fundamentals of soil mechanics: New York, Wiley, 700 p.

Terzaghi, K., and Peck, R. B., 1948, Soil mechanics in engineering practice: New York, Wiley, 566 p.

Trumbull, J. V. A., and Hathaway, J. C., 1968, Further exploration of Oceanographer Canyon: Woods Hole Oceanog. Inst. Ref. No. 68-32, 57 p.

Twichell, D., Knebel, H., and Folger, D. W., 1977, Delaware River evidence for its former extension to Wilmington submarine canyon: Science, v. 195, p. 483–485.

Uchupi, E., 1967, Slumping of the continental margin southeast of Long Island, New York: Deep-Sea Res., v. 14, p. 635–639.

———, 1968a, Atlantic continental shelf and slope of the United States physiography: U.S. Geol. Survey Professional Paper 529-C, 30 p.

———, 1968b, Seismic profiling survey of the east coast submarine canyons, Part 1, Wilmington, Baltimore, Washington, and Norfolk Canyons: Deep-Sea Res., v. 15, p. 613–616.

———, 1970, Atlantic continental shelf and slope of the United States—shallow structure: U.S. Geol. Survey Professional Paper 529-I, 44 p.

———, Emery, K. O., 1967, Structure of continental margin off Atlantic coast of United States: Am. Assoc. Petroleum Geologists Bull., v. 52, p. 1162–1193.

———, Ballard, P. D., and Ellis, J. P., 1977, Continental slope and upper rise off western Nova Scotia and Georges Bank: Am. Assoc. Petroleum Geologists Bull., v. 61, p. 1483–1492.

Veatch, A. C., and Smith, P. A., 1939, Atlantic submarine valleys of the United States and the Congo Submarine Valley: Geol. Soc. America Spec. Paper 7, 101 p.

Wilkniss, P. E., 1973, Environmental condition report for deep water dump area *A*: Washington, D.C., Navy Research Lab. Rept. 7753, 116 p.

27. Applied Ocean Research 1, No. 1, 61-62.

TECHNICAL NOTE

Improvements in a plastic-barrel sediment corer

DOUGLAS N. LAMBERT and **GEORGE F. MERRILL**
NOAA, Atlantic Oceanographic & Meteorological Laboratories, Marine Geology and Geophysics Laboratory, 15 Rickenbacker Causeway, Miami, Florida 33149, *USA*

The hydroplastic sediment corer (8.2 cm i.d.), originally developed by Richards and Keller[1], has been improved in durability, usefulness, and reduced in cost (Fig. 1). Expendable plastic core cutters and retainers have been produced which replace existing steel and spring copper components. A Teflon spray coating has replaced metal oxide rust-inhibiting paints on the interior surfaces of the weight stand and a hard rubber and plastic check-valve substituted for one made of aluminium. A plastic check-valve seat has also been added to the top of the weight stand. The improved corer is ideally suited for collecting samples for geochemical studies, such as trace metal analysis, where metal contamination is a problem.

The core barrel is standard 7.6 cm (3 in. iron pipe size) poly(vinyl chloride) (PVC) plastic pipe and is available at plumbing supply distributors in 6.2 m lengths at a nominal cost. The plastic core cutter is machined from a standard 7.6 cm PVC pipe coupling moulded of Geon 85796* which conforms to ASTM standard D1784, class 12454B for plastic pipe[2]. A 6.0 cm long piece of 7.6 cm schedule 40 PVC pipe is glued with PVC solvent cement into one end of the coupling and then machined in a lathe (Fig. 2). Total cost per cutter is approximately $5.00 including labour and materials. A comparable steel core cutter presently costs approximately $60.00.

The plastic core retainers (Fig. 2) were thermoformed (vacuum formed) out of high impact polystyrene sheet, 1.5 mm thick. Cost of the polystyrene retainers is under $2.00 per unit, while comparable spring copper and steel or stainless steel retainers are nearly $60.00 each. The plastic core retainers were designed to be expendable after each usage and can be left in the core during shipping and storage. Durability of the core cutters was an important consideration in the design and materials selection because, initially, the hydroplastic corer was to be used in the Mid-Atlantic Rift Valley where sediment cover commonly varies from a few millimetres to less than a metre and impact on a hard bottom was expected. Experience with metal cutters has shown that they are irreparably damaged after striking bedrock or large rock fragments. Impact tests were run by dropping the improved coring rig 4.0 m in air onto an asphalt surface. Very minimal (repairable) damage was done to the plastic core cutters and none to the core retainers, although the PVC core barrel shattered on impact. Impact tests, were also made in water at terminal velocity coring clayey silt sediment containing varying sizes of coral rock rubble. Numerous successful cores were recovered and no visible damage occurred to the core retainers or cutters.

With repeated usage of the high impact styrene core retainers, particularly in sandy sediment, some of the fingers were found to eventually break off. Since the core retainers are designed to be expendable, this is not a major consideration. Other types of plastic with higher impact and flexural strengths can be substituted for the high impact styrene to obtain longer useable life. Examples are: PVC, high density polyethylene (HDPE), and polypropylene[3,4].

During sea trials on the US east coast lower continental slope, up to 2.8 m (in a 3.0 m barrel) of silty clay sediment was successfully cored using approximately 180 kg of driving weight. The coring apparatus was free-spooled from a winch at approximately 100 m/min for 50 m prior to impact. Radiography was used to verify that no significant disturbance of the cored sediments took place during the coring operation.

During the cruise to the Mid-Atlantic Rift Valley in June 1977 the improved hydroplastic corer performed very satisfactorily. Although the corer hit bedrock on nearly every attempt, all of the PVC core cutters were reusable; some needed minor repair with a hand file to remove small burrs. The plastic core retainers performed better in retention of small amounts of sediment than previous attempts with metal core retainers.

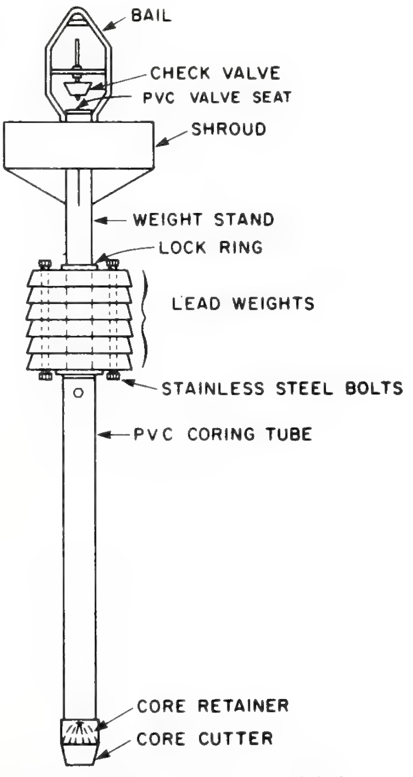

Figure 1. Hydroplastic corer (modified from Richards and Keller[1]*)*

---

* Geon is a registered trademark of B. F. Goodrich Co., Chemical Division, Cleveland, Ohio, USA

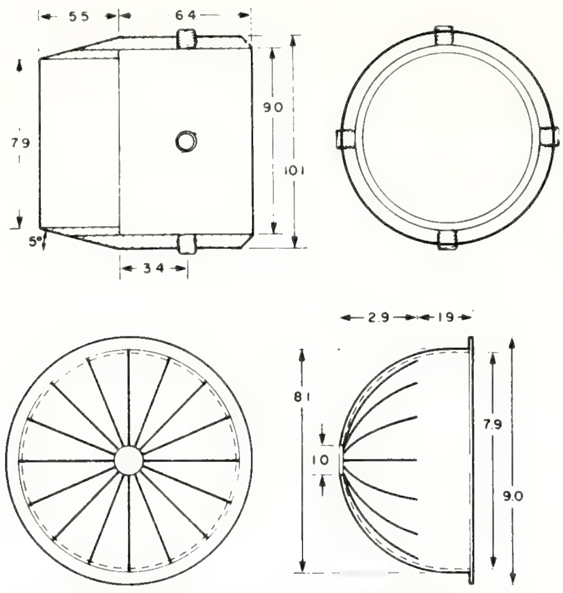

Figure 2. Details of the PVC core cutter and the thermoformed core retained (all dimensions in cm)

ACKNOWLEDGEMENTS

The authors acknowledge the support given by the officers and crew of the NOAA Ship *Researcher* in carrying out the coring operations and testing of this equipment. Dr P. A. Rona initially suggested the need for a modified corer to more effectively meet the research objectives of the Metallogenesis Program at AOML. The authors are grateful to Drs R. H. Bennett, G. H. Keller, B. A. McGregor, and Mr. J. W. Kofoed for their critical reviews of the manuscript. Mr. D. Holzer provided timely assistance in the machining of the component parts.

More detailed information and specifications can be obtained from the authors.

REFERENCES

1 Richards, A. F. and Keller, G. H. A plastic-barrel sediment corer, *Deep-Sea Res.* 1961, **8**, 306
2 *Annual Book of ASTM Standards*, Part 34, American Society for Testing Materials, Philadelphia, 1977, pp. 56 61
3 Glanville, A. B. *The Plastic Engineers Data Book*, Industrial Press, New York, 1974, 216 pp
4 *Modern Plastics Encyclopedia*, McGraw-Hill, New York, 1977, pp. 459 758

Letter Section

RELATIONSHIP BETWEEN SEDIMENT RESUSPENSION AND THE STATISTICAL FREQUENCY DISTRIBUTION OF BOTTOM SHEAR STRESS

BARRY M. LESHT*

Atlantic Oceanographic and Meteorological Laboratories, NOAA, Miami, Fla. 33149 (U.S.A.)

(Received February 19, 1979; revised and accepted April 19, 1979)

ABSTRACT

Lesht, B.M., 1979. Relationship between sediment resuspension and the statistical frequency distribution of bottom shear stress. Mar. Geol., 32: M19—M27.

Detailed observations of near-bottom turbidity and currents are used to examine the relationship between bottom shear stress and sediment resuspension. Turbidity is related to the statistical frequency distribution of bottom shear stress in a way that implies that a few high-stress events may be responsible for resuspension. Such short-period processes will usually be masked by conventional methods of data handling.

INTRODUCTION

Recently, several authors (Gordon and Witting, 1977; Lesht, 1977; Heathershaw and Simpson, 1978) have drawn attention to the fact that estimates of bottom shear stress made in a turbulent flow are subject to extreme sampling variation. This variability is thought to be the result of intermittent momentum flux in the bottom boundary layer. In an earlier paper, Gordon (1975) speculated that such intermittency would have a significant effect on the resuspension of non-cohesive sediment. The purpose of this note is to present some observations that support the notion of intermittent sediment resuspension and which also illustrate the difficulty inherent in attempting to predict sediment transport from observations of the mean shear stress alone.

EXPERIMENT LOCATION AND INSTRUMENTATION

This study was among several done to explore boundary-layer flow and associated sediment transport on the continental shelf in the New York Bight (Fig. 1). Four stations, with differing bottom types and water depths, were

---

*Present Address: Radiological and Environmental Research Division, Argonne National Laboratory, Argonne, Ill. 60439 (U.S.A.)

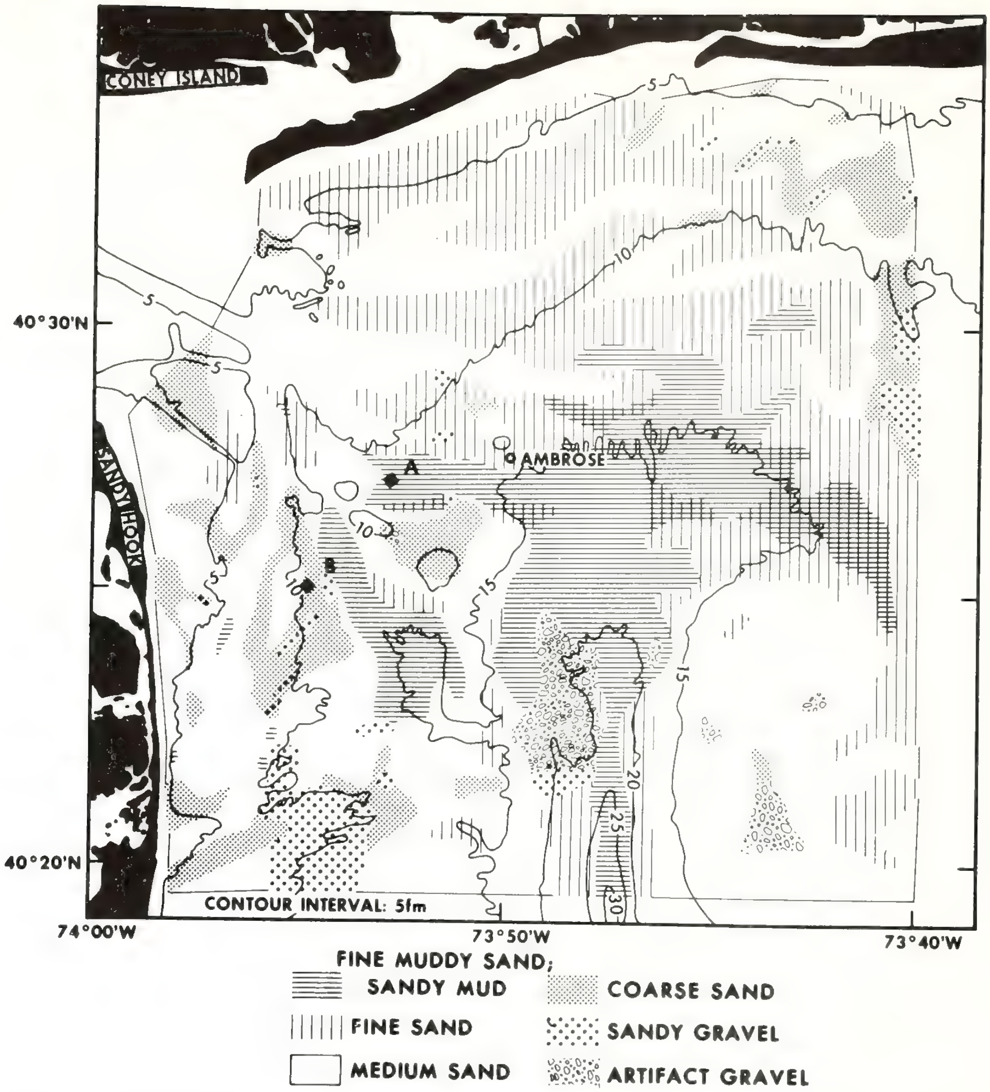

Fig. 1. Surficial sediment map of the New York Bight apex (from Freeland et al., 1976) showing experiment locations.

occupied at different times between May 1974 and October 1975. The data presented here were taken on two successive days in October 1975. Both experiments were done in 21 m of water. One, conducted at 40°25.1′N 73°54.8′W (site B), was over a bottom consisting of gravel and medium sand. The bottom at the second location (40°27.1′N 73°52.7′W), site A, is a sandy silt of the type thought to be associated with anthropogenic pollutants (Gross, 1972).

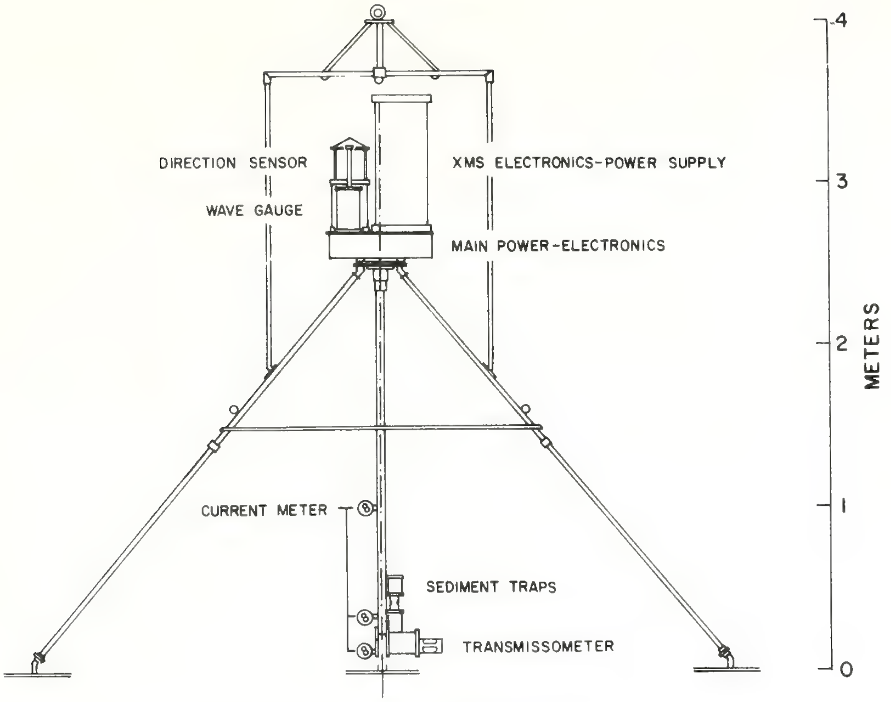

Fig. 2. Scale drawing of the instrumented tripod.

The instrumentation system (Fig. 2) is designed to make detailed measurements of near-bottom currents and turbidity in continental-shelf waters where such high-frequency processes as surface waves may have a significant effect on the bottom (Lesht et al., 1976). Three small, bidirectional, ducted impeller current meters are mounted on a central, freely rotating pipe held in a large steel tripod. These current meters, which are oriented into the mean flow by a large vane, are of a type which has proved to be useful in measuring wave orbital velocities (Shonting, 1967) and turbulent fluctuations at frequencies below 1 Hz (Gordon and Dohne, 1973). The meters are mounted at 18 cm, 40 cm and 100 cm above the bottom.

Near-bottom turbidity is monitored with a beam transmissometer (25 cm path length) positioned 15 cm above the bottom, and mounted opposite the current meters on the central rotating pipe. During this experiment, an array of electronically activated suspended sediment samplers was also mounted 15 cm above the bottom. These samplers were intended to provide an in-situ calibration for the transmissometer, but did not operate correctly. Therefore, turbidity is expressed here in normalized units of percent transmittance instead of absolute units of concentration.

Each of the sensors, except the transmissometer, was sampled every 1.64 sec. The sampling rate for the transmissometer was 3.28 sec. Sampling was continuous during each of the 12.5 hour deployments.

MEAN TURBIDITY AND SHEAR STRESS

The individual transmittance samples were averaged over successive seven minute (128 sample) intervals. Fig. 3 is a time-series representation of these averages. This figure shows data from the October 7 experiment, done at site B. Instrument problems resulted in the loss of six hours of data from the October 6 deployment, but the recovered data are similar to those illustrated here.

The near-bottom turbidity record shows semi-diurnal periodicity suggesting that bottom material is being resuspended and deposited in response to the daily tides. Local wind-driven currents and swell, two other processes known to be significant causes of sediment transport in this region (Lavelle et al., 1978), were weak during this set of observations. The transmissometer record also was checked for signs of an advecting nepheloid layer, using the technique suggested by Chriss and Pak (1977). Except for ad advection event at hour 11, corresponding to the onset of flood tide, the record is entirely due to local tidal resuspension.

Since sediment is resuspended when the bottom shear stress exceeds a critical value, some correlation between near-bottom turbidity and shear stress may be expected. This correlation would be reflected in the friction velocity, $u_* = \sqrt{\tau/\rho}$, where τ is bottom shear stress and ρ is fluid density. Fig. 4, a time-series plot of friction velocity, shows that the variability and uncertainty of the friction velocity estimates make correlation with the observed turbidity very difficult.

The friction velocity estimates plotted in Fig. 4 were computed by fitting

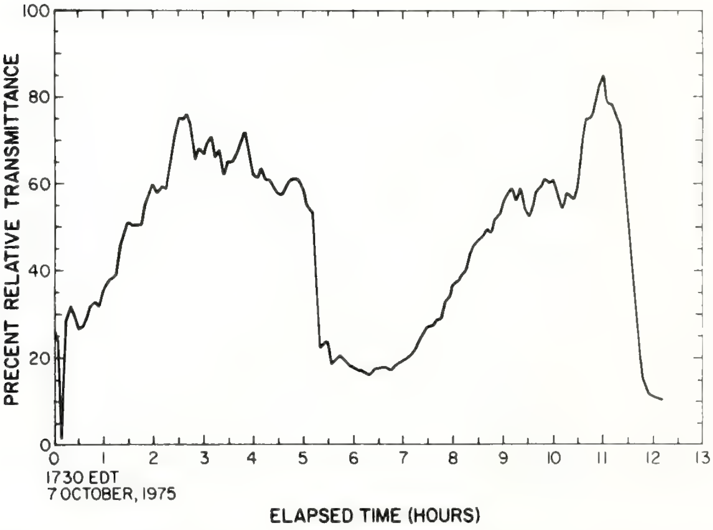

Fig. 3. Mean normalized transmittance as a function of time. Curve is drawn from sequential seven minute averages.

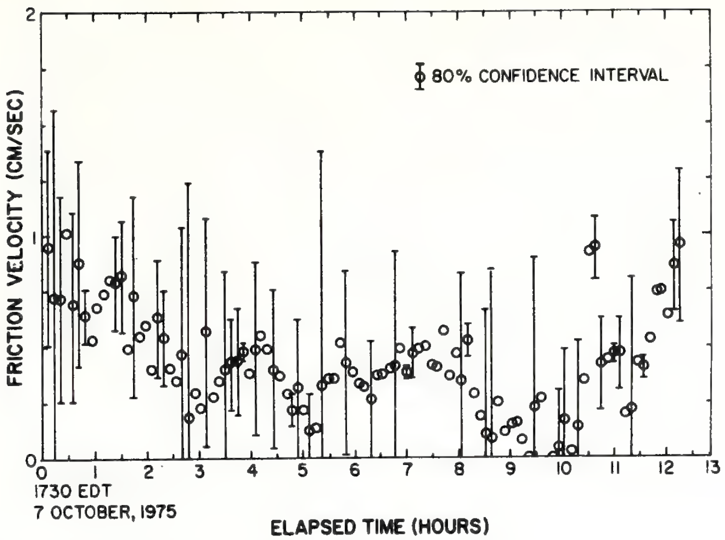

Fig. 4. Mean friction velocity as a function of time. Data points are best-fit values calculated using the Karman—Prandtl equation. Error bars are 80% confidence limits. Points without error bars are less reliable than those with error bars.

seven-minute (256 sample) averages of the horizontal speed at each of the three current meters to the Karman—Prandtl equation:

$$\bar{U} = (u_*/\kappa) \ln z - (u_*/\kappa) \ln z_0 \quad . \tag{1}$$

In this expression κ is the von Karman's constant, here taken equal to 0.4, and z_0 is the quantity known as roughness length, also calculated from eq. 1. The seven-minute period was chosen to be representative of averaging times found in boundary-layer studies done with more traditional current meters (i.e., Savonious rotor types). The problem of choosing an optimum averaging time is examined in a separate paper which is in preparation.

The quality of the friction velocity estimates was judged on the basis of the regression coefficient computed when fitting the data to eq. 1. The error bars plotted span the 80% confidence interval. Points without error bars are estimates in which the regression coefficient is less than 0.82, corresponding to less than 80% confidence in the correlation (Freund, 1971). The error bars in Fig. 4 are probably underestimates since they reflect only the statistical uncertainty of the correlation, and do not explicitly reflect the sampling error found by Heathershaw and Simpson (1978). Another possible measure of the general reliability of the stress estimates is the calculated value of z_0 the hydrodynamic roughness. The mean value of z_0 measured over the sandy silt is 0.005 cm. When measured over the gravel-sand, mean z_0 is 0.2 cm. These values are consistent with estimates made in previous studies (Sternberg, 1968).

Sediment transport predictions can be made either from established critical curves or from empirically determined threshold values (Wimbush and Lesht, 1979). The uncertainty associated with these stress estimates make predictions based on previously determined critical values questionable, and this record is too short to attempt to determine an internally consistent threshold friction velocity for resuspension. The advantage of an empirical threshold value is that it parameterizes the short-period processes absorbed by the original averaging technique. This, however, is accomplished at the expense of clarifying the details of the resuspension events. In the remainder of this note I discuss a treatment of these data which highlights the relationship between sediment resuspension and the short-period features of the current data which are normally hidden by the averaging process.

STATISTICAL APPROACH

Individual shear stress estimates based on short-period velocity averages (on the order of a few times the turbulent time scale of the flow) are subject to the same sampling variability as long-term averages. Gordon and Witting (1977) and Heathershaw and Simpson (1978), however, show that an ensemble of estimates, considered statistically, will contain significant information regarding the bottom shear stress lost in longer-period averaging. The problem is to relate the ensemble of short-period stress estimates to sediment resuspension. This is accomplished here by examining the cumulative frequency distribution of the short-period stress estimates as a function of the mean turbidity for each successive seven-minute interval.

The ensemble of short-period stress estimates was generated by treating the raw data with a 17-sample (29.77 second) moving average. This average length was found to result in a reasonable number of logarithmic profiles while still reflecting the higher frequency features of the flow. This technique yielded 25,600 values for each current meter. Some values at each end of the original record were discarded. The 25,600 resultant samples were divided into successive panels of 256 (7 minutes). Bottom shear stress estimates were made, using the profile method, for each of the samples. If fewer than half of the profiles within a panel were logarithmic (arbitrarily defined here as regression coefficient greater than 0.95) the panel was discarded. This occurred during times when the mean velocity was low.

The shear stress estimates calculated in the remaining panels were sorted into cumulative frequency distributions. In essence, these represent the probability distribution function of the shear stress observed within each 7 minute section of the record. Each distribution gives the expected number of times that a stress estimate would exceed a particular value. For example, all stress estimates would exceed 0.0 dynes/cm^2, but only a few might exceed 5.0 dynes/cm^2. Figs. 5 and 6 make use of these distributions to show how the probability of observing high stress values changes as a function of mean transmittance. To illustrate these, it was necessary to choose particular stress values and plot the percentage of estimates exceeding these few values. For example, in Fig. 5, one panel had 50% transmittance. During this seven-minute period

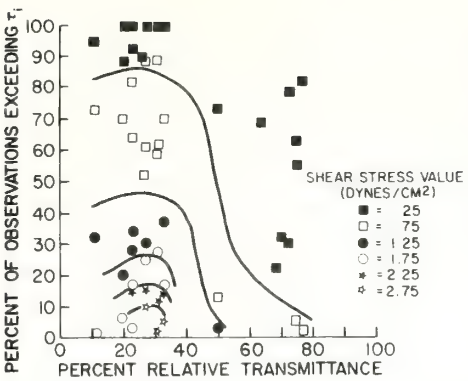

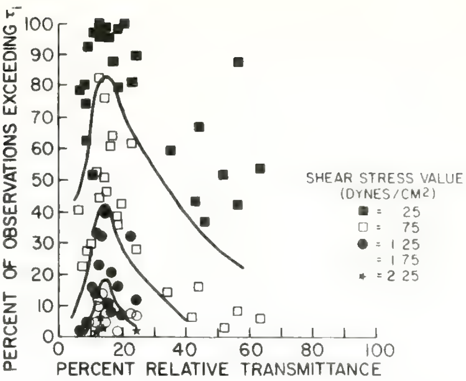

Fig. 5. Cumulative shear stress distribution as function of normalized transmittance. Data taken from the erosional sections of the October 6, 1975 experiment. Symbols represent percent of stress exceeding indicated stress value. Lines are drawn by eye to separate data fields.

Fig. 6. Cumulative shear stress distribution as function of normalized transmittance. Data taken from depositional sections of the October 6, 1975 experiment.

75% of the stress estimates exceeded 0.25 dynes/cm^2, 15% exceeded 0.75 dynes/cm^2.

Fig. 5 shows those sections of the record associated with erosion (decreasing transmittance), and Fig. 6 shows those sections associated with deposition (increasing transmittance). These data were taken from the October 6 deployment, thus there were fewer points in the erosional period than in the depositional. The boundary layer on October 7 was insufficiently developed to analyze by this method.

Figs. 5 and 6 may be compared to Fig. 7, a plot of the mean shear stress versus the mean transmittance for the same data. Although there is a tendency for high stress values to be correlated with low transmittance, the data are very scattered. The largest mean stress value is 1.33 dynes/cm^2, while the largest of the short-period estimates exceeds 2.75 dynes/cm^2.

Assuming that the average near-bottom transmittance will decrease as sediment is resuspended, Figs. 5 and 6 may be interpreted in the following way. Short-period fluctuations in the bottom shear stress may be expected in any turbulent flow (Gordon and Witting, 1977). As the flow accelerates the magnitude of these fluctuations will increase. It appears from these data that this increase is non-linear, being greater at higher mean stress values. The sediment responds to the short-period stress fluctuations causing the mean transmittance to decrease as more sediment is put into suspension.

These data also suggest that there may be differences between the stress distribution/transmittance relationship in depositional and erosional periods. This difference may be due either to increased intermittency during the

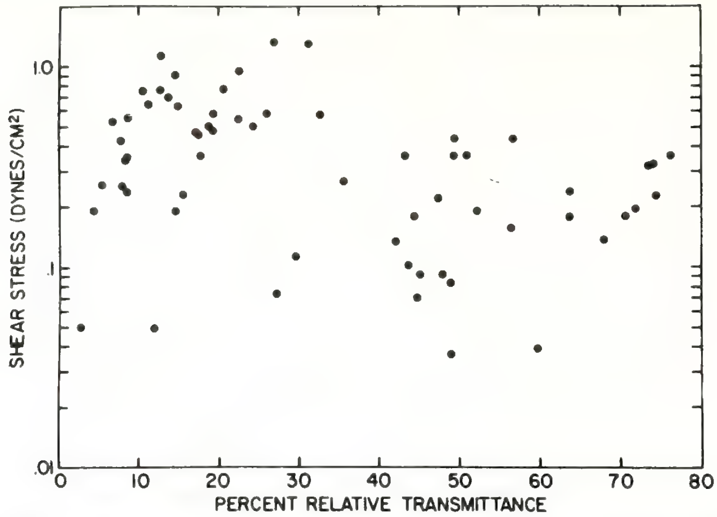

Fig. 7. Mean shear stress as a function of normalized transmittance, October 6, 1975

decelerating phase of the flow, or to a change in the turbulent structure caused by the high concentration of suspended sediment as demonstrated in the laboratory by Gust and Walger (1976).

CONCLUSIONS

Estimates of mean bottom shear stress made from long-term averages of near-bottom velocity observations are subject to sampling error as well as to statistical uncertainty. The statistical uncertainty makes it difficult to specify the stress within the limits necessary for prediction of sediment transport. The sampling error is due to the presence of short-period fluctuations in the shear stress which may be much greater in magnitude than the mean stress. Sediment resuspension is related to the statistical frequency distribution of short-period stress estimates in a way that implies that the sediment responds to a few instances of high stress. This is in accordance with Gordon's (1975) speculation that intermittent processes in the turbulent boundary layer may be responsible for the entrainment of non-cohesive sediments.

ACKNOWLEDGEMENTS

The research reported here was conducted at the University of Chicago. Primary support came from NOAA's Marine Ecosystems Analysis Program through contract COM/NOAA 03-3-022-111. This paper was written while the author was a National Research Council Resident Research Associate at the Atlantic Oceanographic and Meteorological Laboratories. The instrumentation described here was built in conjunction with R.V. White. W.C. Thacker made many suggestions for the improvement of the manuscript.

REFERENCES

Chriss, T.M. and Pak, H.J., 1977. Optical evidence of sediment resuspension — Oregon continental shelf. EOS, 58(6): 410.

Freeland, G.L., Swift, D.J.P., Stubblefield, W.L. and Cok, A.E., 1976. Surficial sediments of the NOAA-MESA study areas in the New York Bight. In: M.G. Gross (Editor), Middle Atlantic Continental Shelf and the New York Bight. Proc. of the Symp., New York. Am. Soc. Limnol. and Oceanogr., Allen Press, Lawrence, Kansas, 90: 101.

Freund, J.E., 1971. Mathematical Statistics. Prentice-Hall, Englewood Cliffs, N.J., 463 pp.

Gordon, C.M., 1975. Sediment entrainment and suspension in a turbulent tidal flow. Mar. Geol., 18: M57—M64.

Gordon, C.M. and Dohne, C.F., 1973. Some observations of turbulent flow in a tidal estuary. J. Geophys. Res., 78: 1971—1978.

Gordon, C.M. and Witting, J., 1977. Turbulent structure of the bottom boundary layer. In: J.J. Nihoul (Editor), Bottom Turbulence, Proc. 8th Int'l Liege Colloquium on Ocean Hydrodynamics. Elsevier, Amsterdam, pp. 59—81.

Gross, M.G., 1972. Geologic aspects of waste solids and marine waste deposits, New York metropolitan region. Geol. Soc. Am. Bull., 83: 3163—3176.

Gust, G. and Walger, E., 1976. The influence of suspended cohesive sediments on boundary-layer structure and erosive activity of turbulent seawater flow. Mar. Geol., 22: 189—206.

Heathershaw, A.D. and Simpson, J.H., 1978. The sampling variability of the Reynolds stress and its relation to boundary shear stress and drag coefficient measurements. Estuarine Coastal Mar. Sci., 6: 263—274.

Lavelle, J.W., Young, R.A., Swift, D.J.P. and Clarke, T.L., 1978. Near-bottom sediment concentration and fluid velocity measurements on the inner continental shelf. J. Geophys. Res., 83: 6052—6062.

Lesht, B.M., 1977. Frequency distribution of bottom shear stresses within a tidal cycle on the inner continental shelf. EOS, 58(6): 409.

Lesht, B.M., White, R.V. and Miller, R.L., 1976. A self-contained facility for analyzing near-bottom flow and associated sediment transport. NOAA Tech. Memo., ERL MESA-9, Boulder, Colo., 38 pp.

Shonting, D.H., 1967. Observations of particle motions in ocean waves. Tech. Memo. 377, Naval Underwater Systems Center, Newport, R.I., 620 pp.

Sternberg, R.W., 1968. Friction factors in tidal channels with differing bed roughness. Mar. Geol., 6: 243—260.

Wimbush, M. and Lesht, B.M., 1979. Current induced sediment movement in the deep Florida Straits: Critical parameters. J. Geophys. Res., in press.

Young, R.A. and Southard, J.D., 1978. Erosion of fine-grained marine sediments: seafloor and laboratory experiments. Geol. Soc. Am. Bull., 89: 663—672.

29. American Association of Petroleum Geologists Memoir 29, Geological and Geophysical Investigations of Continental Margins, 139-149 (published previously in Seismic Profiles of the United States East Coast Continental Margin, NOAA Tech. Report ERL 398-AOML 28, 1978).

Variations in Bottom Processes Along the U.S. Atlantic Continental Margin[1]

BONNIE A. MCGREGOR[2]

Abstract Seismic reflection data on strike lines along the slope and rise of the U.S. East Coast continental margin show variations in morphology and sedimentation pattern parallel to the margin. From these data, the regional versus localized extent of erosional or depositional features and events within each physiographic province of the margin can be determined. Two localized areas of extensive slope deposition were identified, one seaward of Albemarle Sound and the other seaward of the Delmarva Peninsula. A regional unconformity on the rise extends from Georges Bank to Wilmington Canyon and is believed to be Pliocene in age. The upper slope between Cape Hatteras and Hudson Canyon is dissected by many small valleys cut during the late Pleistocene, whereas northeast of Hudson Canyon the upper slope is only cut by major submarine canyons. The Florida-Hatteras slope and Blake Plateau have many unconformities with one in late Tertiary truncating an extensive sequence of foreset beds on the north end of the Blake Plateau.

INTRODUCTION

The sea floor adjacent to the continents is an important source of energy and mineral resources, in addition to being a potential area for waste disposal. The National Oceanic and Atmospheric Administration (NOAA) program RUSEF (Rational Use of the Sea Floor), through geological and geophysical research, is attempting to understand the environment of the continental margin and the dynamic bottom and near-bottom processes that affect the margin through time. Data have been collected over the past three years on the U.S. Atlantic continental margin (outer shelf, slope, and rise) using the NOAA ship *Researcher*. These data consist of single-channel seismic reflection profiles collected on strike lines parallel to the continental margin approximately 15 km apart, extending from Hydrographer Canyon on Georges Bank to Cape Canaveral, Florida (Fig. 1). Most seismic reflection data have been collected on lines perpendicular to the margin (e.g., Uchupi and Emery, 1967), with strike lines serving only as tie lines. The objective of using a suite of strike lines was to look at the variation in the sedimentation record as a continuum within each physiographic province of the margin (outer shelf, slope, and rise) as defined by Heezen et al (1959). From these data one can locate areas with different depositional histories for subsequent detailed study.

In order to assess recent sedimentation patterns, bottom sediment samples were collected coincidently with the seismic work. Transects of four evenly spaced 6-m piston cores with 1.5-m pilot cores were taken approximately 80 km apart along the margin, sampling the outer shelf, slope, and rise (Fig. 1). Sediment analyses of the 6-m piston cores are being done by Larry J. Doyle of the University of South Florida and Orrin H. Pilkey of Duke University. Preliminary results indicate that rapid deposition is occurring on the continental slope at a high sedimentation rate and/or by mass movement of sediment downslope (Doyle et al, 1975, 1976). The 1.5-m cores have been analyzed at AOML-NOAA to assess variations in slope stability and variations in the depositional environment (Keller et al, 1978).

Detailed studies are being carried out on three submarine canyons (labeled A, B, C, Fig. 1) to determine active processes and to assess the role of the canyons as conduits to the deep sea. These canyons were selected for their varying physiographic setting: Veatch Canyon (A) on Georges Bank is in a glaciated area, and Washington (B) and Norfolk (C) are in a nonglaciated area with a major river drainage system from the Chesapeake Bay region. High-resolution narrow-beam echo sounding surveys were run to determine maximum depths and to define the morphology; a suite of grab samples, hydroplastic cores, and seismic reflection profiles were also

---

[1] Manuscript received, April 18, 1977; accepted, December 22, 1977.

[2] Atlantic Oceanographic and Meteorological Laboratories, National Oceanic and Atmospheric Administration, Miami, Florida 33149. Present address: Department of Oceanography, Texas A&M University, College Station, Texas 77843.

The author would like to thank George H. Keller, Richard H. Bennett, Douglas Lambert, William Sawyer, George Merrill, and Evan Forde for assisting in the data collection. Appreciation is given to William L. Stubblefield and John W. Kofoed for critically reviewing the manuscript. Thanks are also given to the officers and crew of the NOAA ship *Researcher* for diligence and excellence in executing this study. Funds for this work were provided by the National Oceanic and Atmospheric Administration.

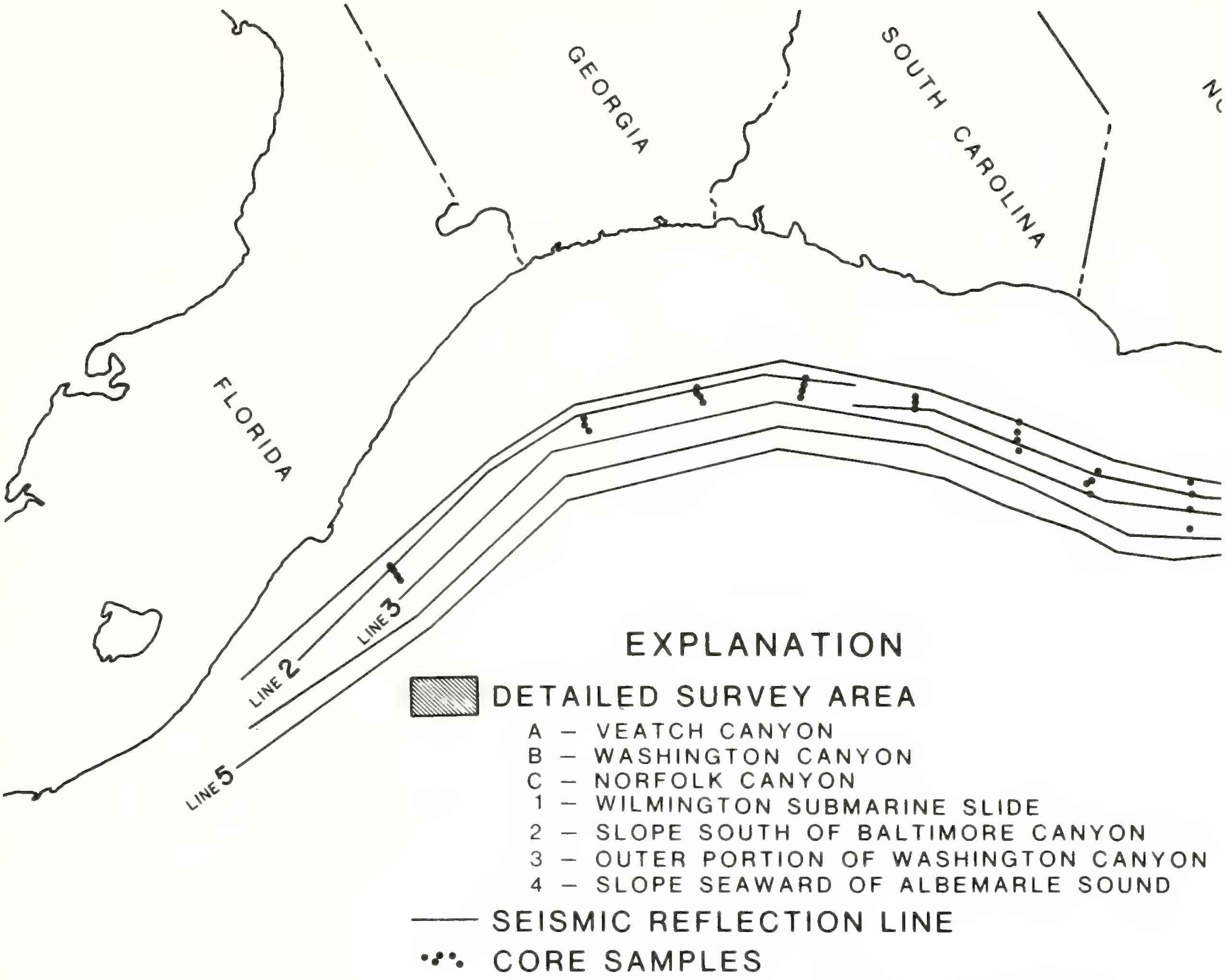
GEORGIA
SOUTH CAROLINA
FLORIDA
LINE 2
LINE 3
LINE 5
EXPLANATION
▨ DETAILED SURVEY AREA
A — VEATCH CANYON
B — WASHINGTON CANYON
C — NORFOLK CANYON
1 — WILMINGTON SUBMARINE SLIDE
2 — SLOPE SOUTH OF BALTIMORE CANYON
3 — OUTER PORTION OF WASHINGTON CANYON
4 — SLOPE SEAWARD OF ALBEMARLE SOUND
—— SEISMIC REFLECTION LINE
•:•. CORE SAMPLES

FIG. 1. Index map from Uchupi (1968)

taken in each canyon in order to understand their respective erosional and depositional histories and evaluate their present activity.

Four other portions of the margin have been studied in detail (Fig. 1): (1) a submarine slide on the slope north of Wilmington Canyon, (2) a portion of the slope where ridges of stratified sediment have undergone extensive erosion, (3) outer part of Washington Canyon to understand levee formation and to determine relative activity of two channels, and (4) the slope seaward of Albemarle Sound where several periods of deposition and erosion have occurred.

From the general seismic reflection data and the bottom samples, variations in the sedimentary history of the margin can be determined. Detailed studies may now focus on specific areas to understand the processes that have been and still remain active.

REGIONAL VARIATIONS IN SEDIMENTATION PATTERN

The morphology of the continental margin changes as one moves offshore from the outer shelf to the rise. The outer shelf is flat, except where cut by the heads of the major submarine canyons. The continental slope has irregular topography and is dissected by major submarine canyons as well as by numerous small valleys. The rise has irregular but subdued topography with many submarine canyons present. Noteworthy are the variations, not only among the margin provinces but also within each physiographic province.

Profile 2

Profile 2 (Fig. 2) is along the upper slope from Hydrographer Canyon on Georges Bank to Cape

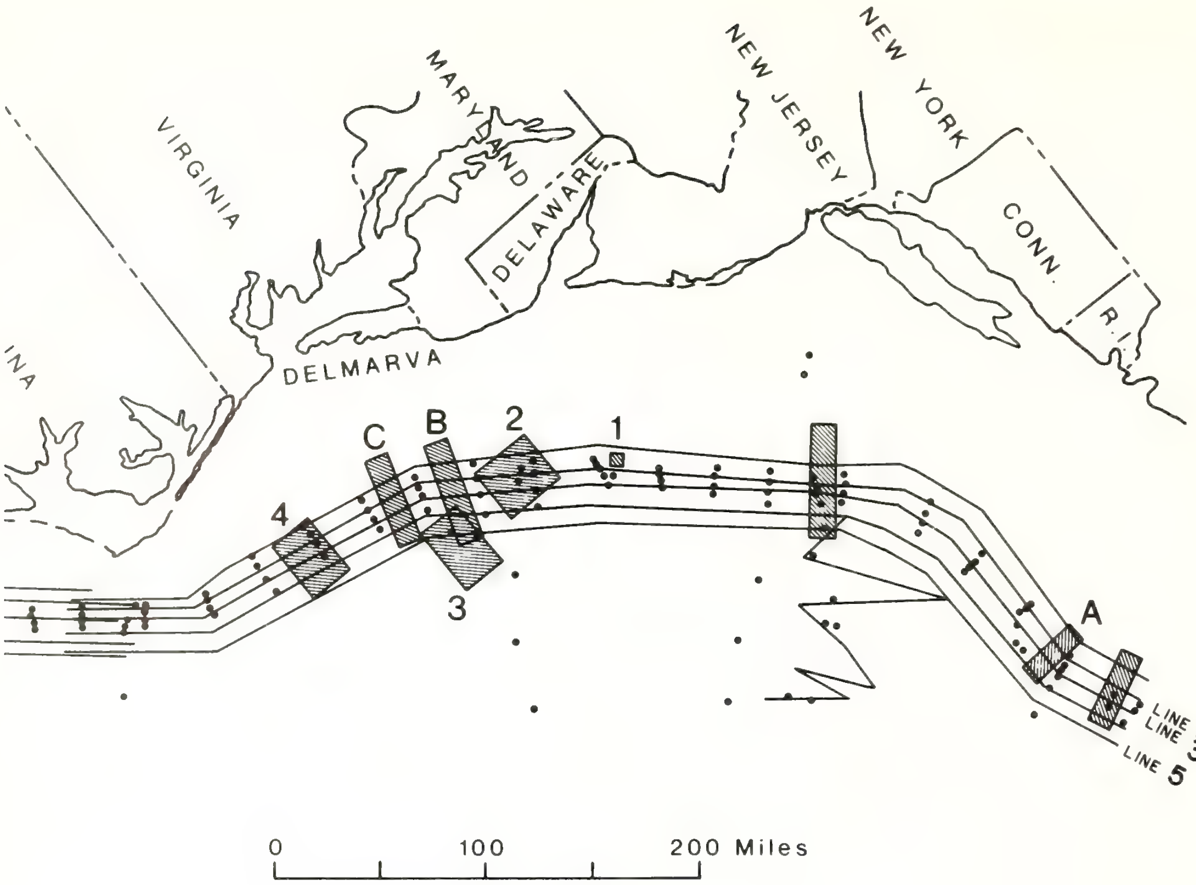

showing track lines and core locations.

Canaveral, Florida (Fig. 1). The total seismic record running north to south is shown in Figure 2 with the individual profiles reading from right to left, top to bottom. The profiles around Cape Hatteras (latitude 35°N) do not overlay exactly, due to ship's navigational problems in the Gulf Stream. In each profile the major canyons are labeled for reference. The numbers and x's refer to the location of the crossing profiles of Uchupi and Emery (1967).

In general, reflecting horizons can be traced over tens of kilometers, indicating that processes governing sedimentation were active over a wide area. A large wedge of sediment believed to be Tertiary, based on correlation with units of Hoskins (1967) and Garrison (1970), thickens toward Hudson Canyon (profiles 2a and 2b) and also slopes seaward with conformable reflectors on the slope (Uchupi and Emery, 1967). The sediment gives the slope a smooth appearance between Hudson and Veatch Canyons except for a few large canyons. Between Veatch and Hydrographer Canyons the slope is very dissected, and Uchupi and Emery (1967), on crossing profiles 55 and 56, show reflecting horizons cropping out on the slope, indicating extensive erosion. Upper Cretaceous material was cored 100 m below the sea floor at Caldrill Site 17 which is east of Veatch (Manheim and Hall, 1976). This region is seaward of Great South Channel, an erosional feature on the shelf that in the past probably was a drainage system around Georges Bank connecting with Hydrographer Canyon (Uchupi, 1968). The large, stratified block in the twin canyon west of crossing profile 62 appears to have been rotated or to have slid, because the reflectors within the block

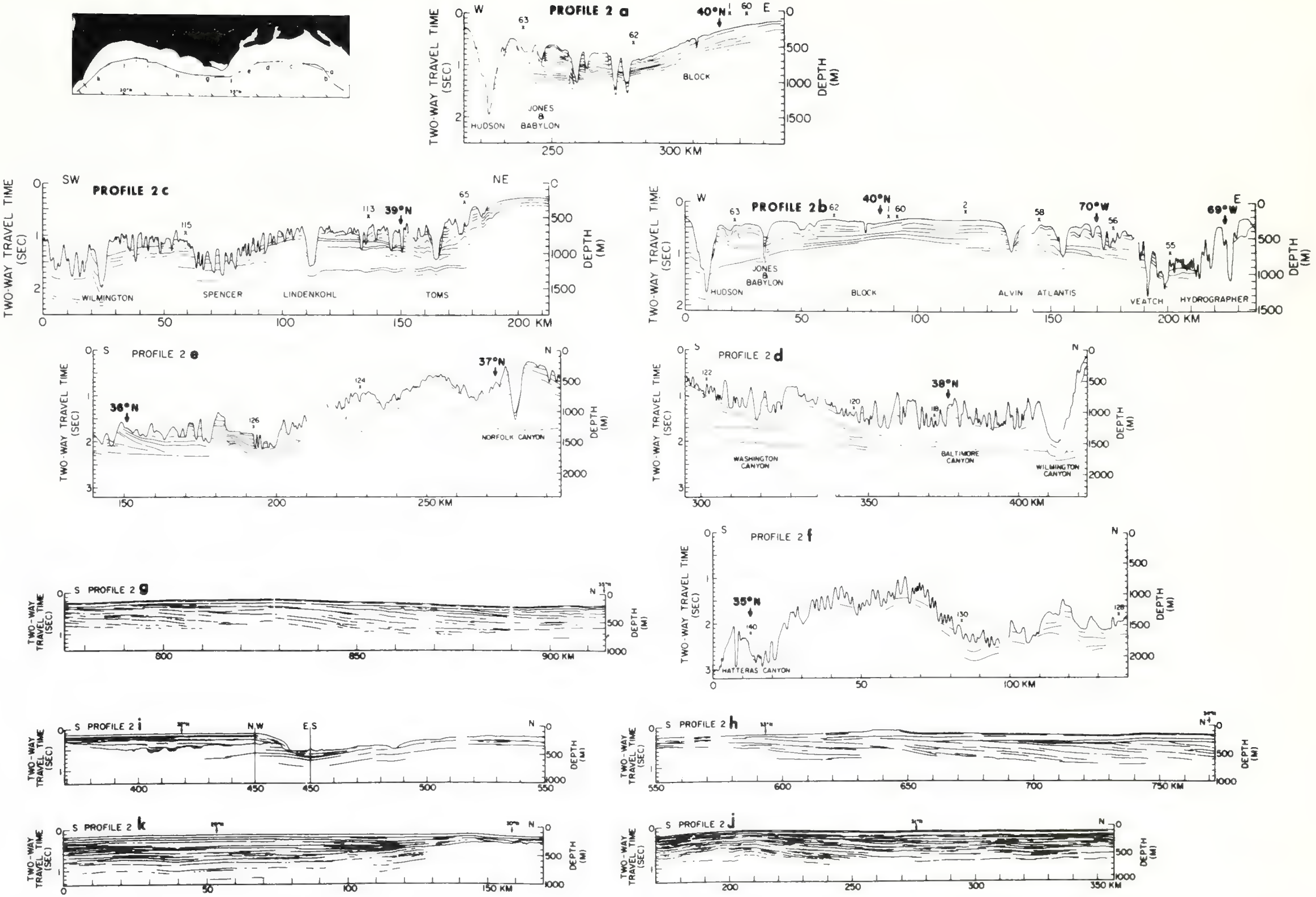

FIG. 2. Line drawing of original seismic reflection profile record for profile 2 (see Fig. 1 for location). Air guns with 160 × 10^{-6} m^3 (10 cu in.) and 1920 × 10^{-6} m^3 (120 cu in.) chambers were used as the sound source north of Cape Hatteras and a 640 × 10^{-6} m^3 (40 cu in.) chamber south of Cape Hatteras. A 50-element hydrophone was used to receive the returning signal which was filtered at 100 to 430 Hz. Vertical exaggeration = 30 × (assuming 1500 m/sec velocity). "X"s and numbers refer to crossing profiles of Uchupi and Emery (1967).

are not continuous with those of either wall as is the case with other canyons. Approximately 100 m of fill is present in each of the valleys flanking this rotated central block. Seismic penetration to reflecting horizons beneath the valleys was not achieved to demonstrate conclusively fault control in this area. Buried valleys are present northeast of Hudson Canyon and may be part of an old Hudson drainage system. Profile 2a shows that slumping has occurred in the walls of several canyons.

South of Hudson Canyon and north of Cape Hatteras (profile 2c-2f) the slope is dissected by many small valleys as well as by major canyons. Slumping is evident in many of the canyon walls. Just south of crossing profile 126 (profile 2e), which is seaward of Albemarle Sound, the sedimentation pattern has been different from that of the adjacent areas. Profile 126 (Uchupi and Emery, 1967) shows that the zone of stratified sediments is part of a wedge of sediments that tapers seaward, but landward it laps onto truncated strata of the continental slope. The stratified sediments represent renewed deposition after a major period of erosion on the slope. This deposition appears to have been confined to a narrow region by a physical barrier on the north which confined the multilayered sequence and since has been eroded. The small channel in the surface of this sequence suggests recent erosion. This region seaward of Albemarle Sound will be studied in detail (Fig. 1, area 4). Deposition in this area may be related to the Roanoke River or the James River, as shelf valleys and a shelf delta are present on the adjacent shelf (Swift, 1976). The reflecting horizons shown on profiles 2c-2e are believed to be Tertiary. In some cases the reflecting horizons appear to control the depth to which valleys are cut; for example, the four valleys southwest of Lindenkohl Canyon all stop at the horizon 200 m below the sea floor. The age of this horizon is believed to be Miocene, based on correlation with the profiles of Sheridan (1975).

South of Cape Hatteras on the Florida-Hatteras slope, a maximum of 800 m of sediment was penetrated seismically (profiles 2g-2k). Many buried unconformities are present with a major one north of 33°N (Fig. 2h). The unconformity truncates a 200 to 400-m-thick sequence of reflecting horizons that dip to the north; both this unconformity and the sequence of dipping horizons can be traced offshore on other profiles. On the short east-west segment at kilometer 450 (profile 2i), an erosional unconformity is present and the Florida-Hatteras slope can be seen to have prograded seaward about 25 km. The unconformity 300 m below the sea floor near 32°N (profile 2i) is Late Cretaceous based on drilled material from U.S.G.S. drill hole 6004 (Hathaway et al, 1976). Drill holes 2 and 5 in the vicinity of kilometer 180 (profile 2j) north of 30°N indicate that the deepest reflecting horizons are middle Eocene with less than 100 m of post-Miocene sediment (JOIDES, 1965). Bottom samples (Fig. 1) were primarily sand or sandy silt all along the slope. The location of the Gulf Stream appears to have controlled the erosional and depositional pattern on the Florida-Hatteras slope.

Profile 3.

Profile 3 (Fig. 3) is along the lower slope, which throughout much of the margin is well dissected. The portion of the slope between Block and Hudson Canyons is not shown. The irregular surface topography (profile 3a) from west of Veatch to Hydrographer Canyon is an eroded portion of the slope with the crossing profiles 56 and 55 (Uchupi and Emery, 1967) showing strata truncated by the slope. Hoskins (1967) believes this region has been eroded by current scour from meandering of the Gulf Stream. Some of the erosion may be related to the Great South Channel drainage system mentioned on profile 2. On profile 3b some of the valleys appear to have cut down to the same horizon as that in the vicinity of profile 113, suggesting a resistant stratum influencing the topography. DSDP Site 108 is located between Lindenkohl and Toms Canyons, and the ages of the reflecting horizons (Fig. 3, profile 3b) are determined on the basis of the drill information. The deepest reflector is believed to be the Eocene-Cretaceous boundary and the intermediate reflector Eocene, correlated with Horizon A (Hollister et al, 1972).

Three major canyons are present in the area of profile 3c (Fig. 3). The slope is not dissected by as many small valleys south of Wilmington Canyon as it is to the north. Norfolk and Washington Canyons appear to have associated levees with the levee on the south side of Washington Canyon being the largest. Baltimore Canyon is flanked on the south by a large ridge of stratified sediments, which is similar in appearance to the Nyckel Ridge described by Stanley and Kelling (1970). Because of the large volume of sediment composing the Nyckel Ridge and its internal structure Stanley and Kelling (1970) believe it is pre-Quaternary and not formed by overbank deposition. The slope between Washington and Baltimore Canyons has a different morphology and sedimentation pattern compared with the slope between Wilmington and Toms Canyon. Ridges of stratified sediments with many unconformities are present transverse to the slope. The ridges do not have the same spacing and frequency as the topography up-slope on profile 2 (Fig. 2). These ridges are similar in internal structure, although not as large as the ridge on the south side of Baltimore Canyon. From the volume and distribution of sediment, this region has been a major depositional site with subsequent modification by bottom currents and by slumping on the flanks of the ridges. This portion of the slope is between the major drainage systems of Chesapeake and Delaware Bays; the ancestral Delaware River drainage system can be traced across the shelf to the head of Wilmington Canyon (Twichell et al, 1977). However, the morphology of the slope south of Baltimore Canyon suggests a major drainage system existed in the area in the past and has since become buried on the shelf. The deposi-

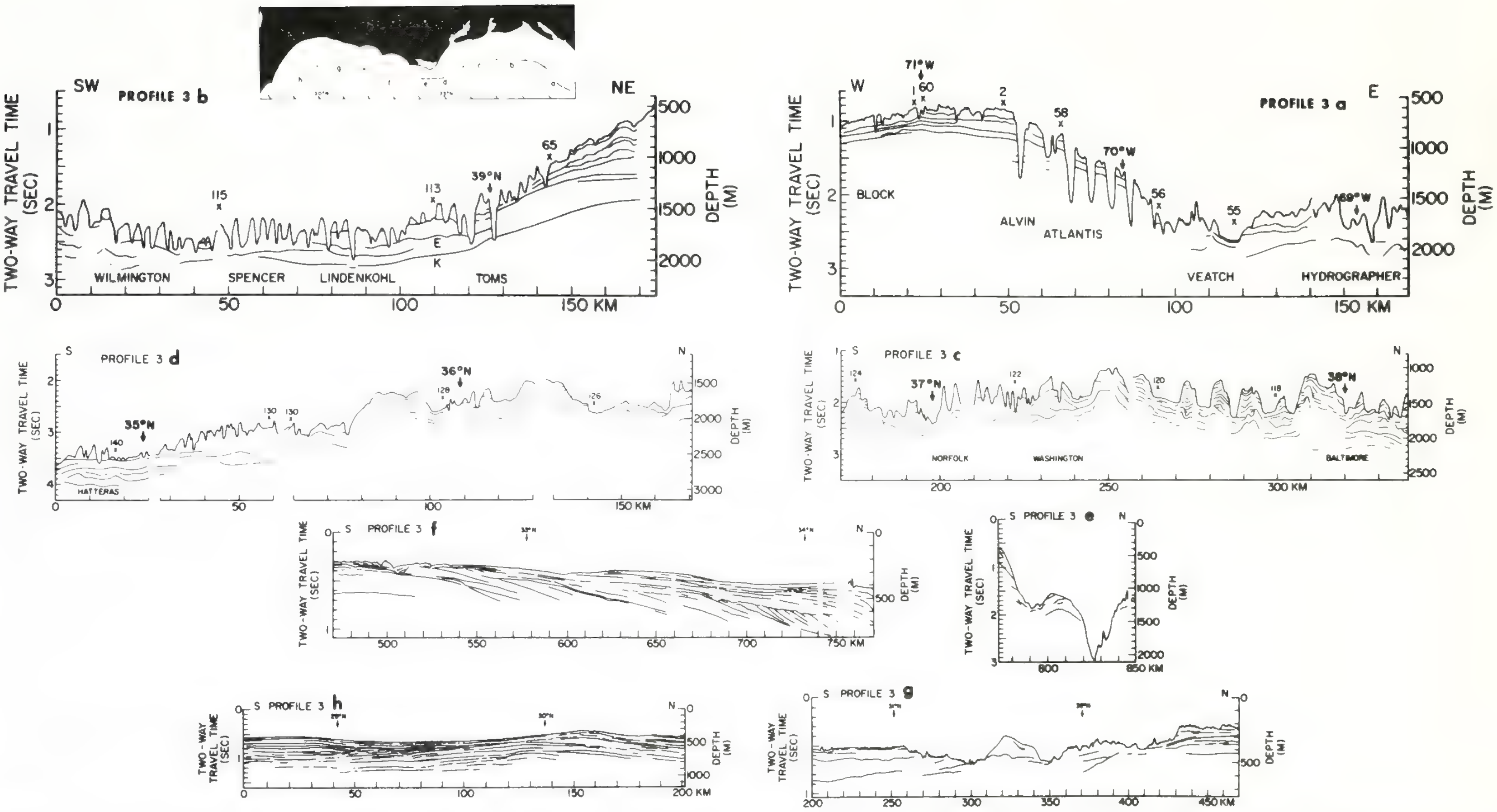

FIG. 3. Line drawing of original seismic reflection profile record for profile 3 (See Fig. 1 for location; shooting, recording and filtering specifications same as for Fig. 2). Vertical exaggeration = 20 to 30 × (assuming 1500 m/sec velocity). "X"s and numbers refer to crossing profiles of Uchupi and Emery (1967). Index map shows profile segment locations.

tional history of this area is being studied in detail (Fig. 1, area 2).

The stratified mass of sediments just south of crossing profile 126 (profile 3d, Fig. 3) is a continuation of the stratified sediments noted on profile 2. This area seaward of Albemarle Sound has been the site of slope deposition of a large volume of sediments. Hatteras Canyon and adjacent areas of the lower slope are different from previously discussed East Coast canyons, as Hatteras has no apparent shoaler wall on the south and both levees are very small. Pratt (1967) suggested that the origin of this canyon is due to slumping, as the slope is very steep. The absence of levees is perhaps due to the strong current regime in the vicinity of Cape Hatteras composed of the Gulf Stream and the Western Boundary Undercurrent, both of which transport large quantities of suspended matter (Betzer et al, 1974). These currents with opposite flow directions and fluctuations in their position should be responsible for the lack of preferential deposition as well as for erosion in the vicinity of Hatteras Canyon.

At the northern end of the Blake Plateau, reflecting horizons crop out. The buried unconformity noted on profiles 2h and 2g (Fig. 2) extending from south of 33°N to the edge of the plateau can be seen on profile 3f (Fig. 3). Beneath the unconformity, reflecting horizons dip to the north. The surface of the unconformity is irregular, indicating varying resistance of the truncated horizons. The age of this unconformity is believed to be late Miocene or Pliocene and will be discussed in the section on profile 5. Between 30°30′N and 32°45′N (profiles 3f-3h) the surface topography is very irregular, suggesting erosion and nondeposition attributable to the Gulf Stream. In contrast is the smooth surface topography south of 30°30′N (profile 3h) which indicates that deposition has dominated over erosion. Although unconformities are present in the sedimentary sequence (profile 3h), they are not as extensive as farther north on the Blake Plateau (profile 3f).

Profile 5.

Profile 5 was run along the continental rise where the topography is subdued (Figs. 4 and 5); only the major canyons have extensions at this depth. The sedimentary sequence has many reflecting horizons and unconformities. A very prominent reflecting horizon about 200 m below the surface can be traced from near Hydrographer Canyon to Wilmington Canyon, a distance of 440 km (profiles 5a and 5b). This implies a uniform environment on the rise for a time during the past. An age for this horizon can be estimated from the area south of Hudson Canyon. A buried trough 400 m deep is present between Hudson and Wilmington Canyons which is partially filled with acoustically transparent sediment, topped with a zone of stratified sediment, in turn truncated by an erosional unconformity. DSDP Site 106 is seaward of profile 5b in this area (Hollister et al, 1972). Correlation with lithology and seismic stratigraphy of the site suggests the bottom of the trough may be in material of Eocene age, with the acoustically transparent material which fills the bottom of the trough being Miocene clay. The stratified sediments would be Pliocene with the unconformity Pliocene, and the sediments burying the unconformity would be Pleistocene to Recent. Vail et al (1977) have identified several global unconformities in the late Tertiary; in the mid-Oligocene, late Miocene, and mid-Pliocene. Correlating these unconformities with the DSDP Site 106 data and with seismic reflection profile 5b between kilometer 70 and 120, erosion of the trough into Eocene material would have occurred during the mid-Oligocene: the late Miocene unconformity would represent the transition from the transparent material filling the trough to the overlying stratified sediments; and the erosional surface on the stratified sediments would correlate with the mid-Pliocene unconformity. The continuous reflecting horizon traced between Hydrographer and Wilmington Canyons would be, therefore, mid-Pliocene and represent the mid-Pliocene unconformity. If the age correlation is correct, the large volume of sediment in the levees around Hudson Canyon would be late Pliocene and Pleistocene in age, as the continuous horizon can be traced beneath them. This portion of Hudson Canyon has formed by both depositional and erosional processes, as described by Nelson and Kulm (1973).

A large levee is present on the south side of Baltimore Canyon (profile 5c) and a smaller levee on the south side of Wilmington Canyon (profile 5b). Reflecting horizons are truncated in the walls of all the canyons indicating that erosion has occurred at this depth on the rise. A 14-cm-thick graded sand layer was cored in Norfolk Canyon just seaward of profile 5, indicating transport of coarse sand this far seaward on the rise.

Just north of Hatteras Canyon a diapiric structure is present, with approximately 100 m of overlying sediment (profiles 5d and 5e). The level or horizon from which the structure originates cannot be identified on the basis of one crossing. It has no gravity or magnetic expression, indicating that it probably is composed of mud. More deeply buried diapirs have been identified in this area on CDP data by Grow Hatteras slope, one encounters the Blake Plateau (profile 5e). Near 34°N at 2,000 m depth on the edge of the Plateau, very friable middle Eocene material was cored (Florentine Maurrasse, personal communication, 1976). This cored sample is from the stratified sequence of horizons dipping to the north that extends from 32°30′N and crops out on the northern edge of the Blake Plateau. Erosional unconformities are present within this sequence and a major unconformity truncates the sequence. The surface of this unconformity is very irregular, with approximately 100 m of material eroded north of 33°N at kilometer 730 (profile 5e). Approximately 150 m of sediment blankets the unconformity. Because Eocene material was cored within a sequence of horizons that are truncated by the unconformity, the age of the unconformity is post-Eocene. Vail et al (1977) have identified three post-Eocene unconformities, as previously mentioned. As the Eocene horizon is buried

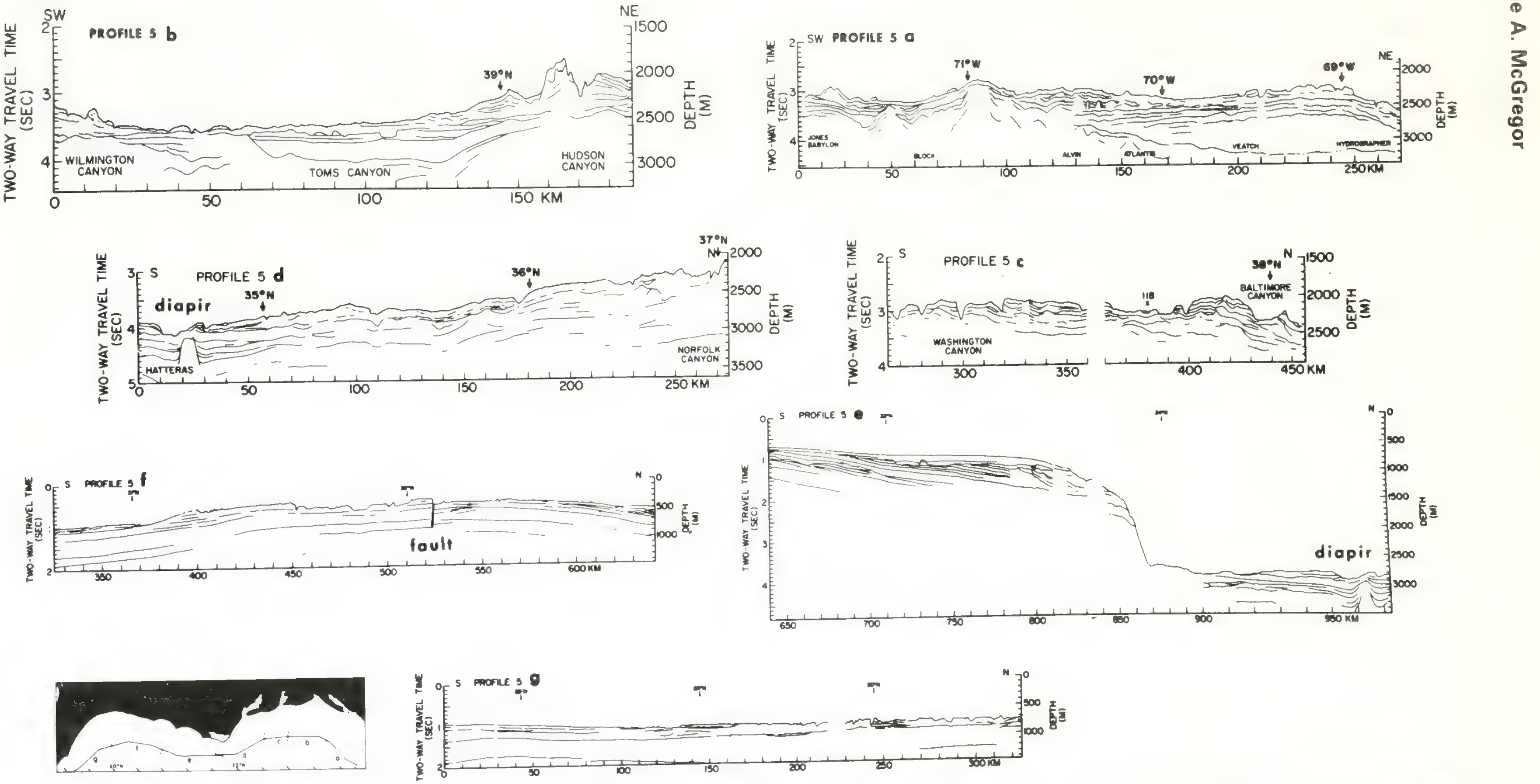

FIG. 4. Line drawing of original seismic reflection profile record for profile 5 (see Fig. 1 for location). Air guns with 160 × 10^{-6} m^3 (10 cu in.) and 1920 × 10^{-6} m^3 (120 cu in.) chambers were used as a sound source. A 50-element hydrophone was used to receive the returning signal which was filtered at 100 to 430 Hz. Vertical exaggeration = 20 to 30 × (assuming 1500 m/sec velocity). Index map shows profile segment locations.

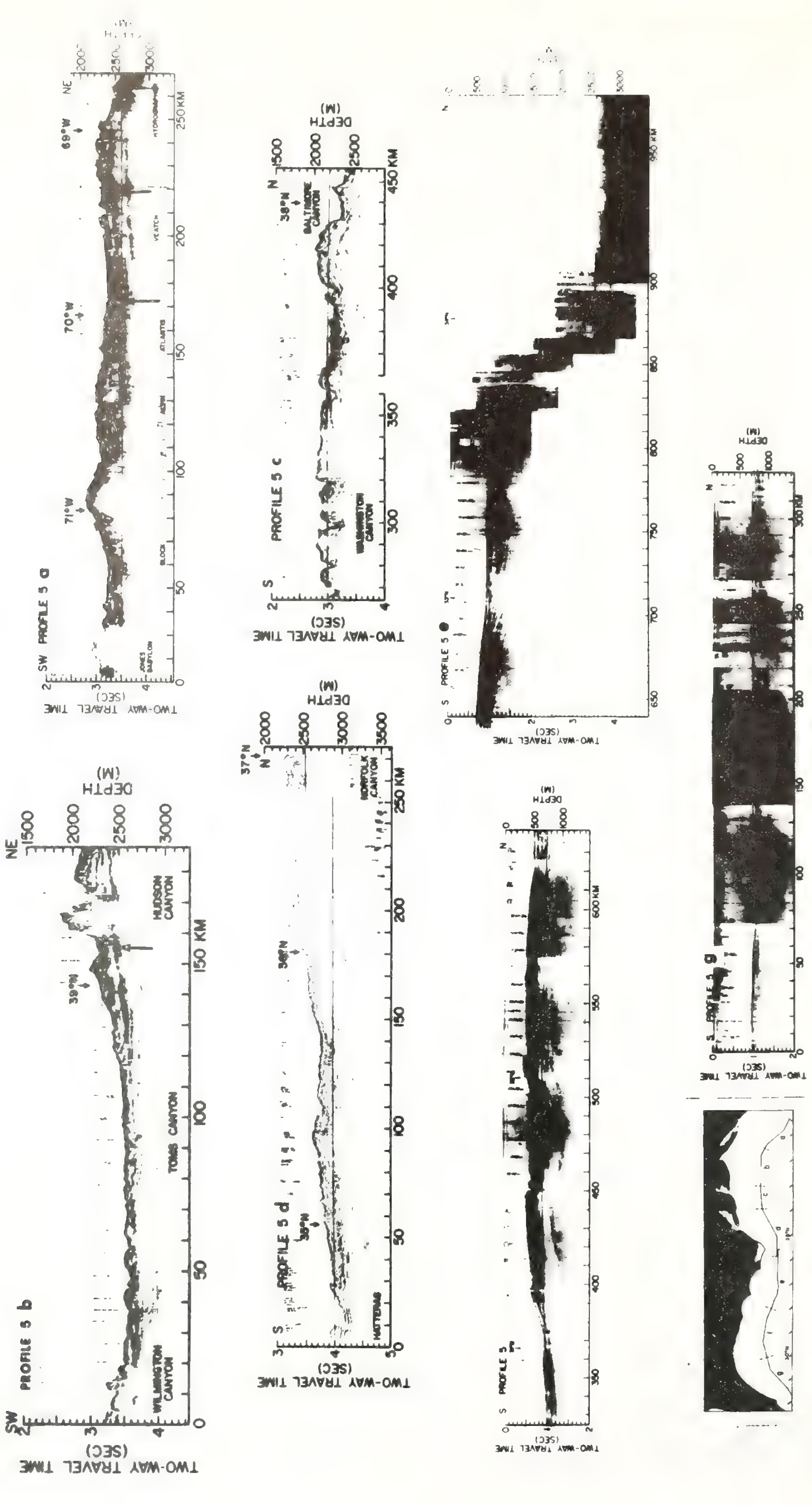

FIG. 5. Photograph of original seismic reflection profile record for profile 5. Index map shows profile segment locations. Arrow denotes continuous reflecting horizon.

by approximately 500 m of sediment and an unconformity near kilometer 800 is present within the sequence, the unconformity that truncates this sequence of dipping horizons and extends from 32°30′N off Cape Romain to the edge of the Blake Plateau off Cape Lookout is believed to be late Miocene or mid-Pliocene.

A fault is present in the area shown on profile 5f just north of 32°N at kilometer 522; it offsets buried horizons as well as the sea floor. Sheridan (1974) shows several faults in this general area based on magnetic anomaly patterns. The general surface of the Plateau is very irregular along much of the profile resulting from the activity of the Gulf Stream. Drill hole J-6 (JOIDES, 1965) which is just east of profile 5 near kilometer 280 penetrated lower Eocene material 100 m down. The continuous reflecting horizon about 100 m below the sea floor on profile 5g north of 30°N is, therefore, interpreted to be middle to lower Eocene. Very little deposition and/or a great deal of erosion has occurred in the area from middle Eocene to the present. Bottom currents, part of the Gulf Stream, have been and are very active in controlling the topography and the sedimentation pattern on this portion of the Blake Plateau.

DISCUSSION

Seismic reflection profiles parallel to the margin provide a different perspective from profiles oriented perpendicular to the margin. Variability within each province—slope and rise—is readily apparent, and as most morphologic features are perpendicular to the margin, they are better defined by track lines parallel to the margin.

The continental margin is cut by many large submarine canyons between Cape Hatteras and Cape Cod. Where seismic penetration beneath the canyons was achieved, there is no evidence of fault control for the canyons, even though alignment with some of the North Atlantic fracture zones suggests a correlation (Sheridan, 1974) and Kelling and Stanley (1970) believe a fault underlies the head of Wilmington Canyon. Extensive infilling of sediments in the canyons has not occurred except for the two valleys near crossing profile 62 (profile 2a, Fig. 2). The lack of infilling suggests the canyons are actively channelling material offshore. A graded sand bed found on the rise in Norfolk Canyon also supports the activity of this canyon.

The continental slope is dissected by many small valleys in addition to major submarine canyons (Figs. 2, 3). Small valleys are primarily located north of Veatch Canyon and south of Hudson Canyon to Hatteras Canyon. Profile 2b (Fig. 2) shows that much of the late Tertiary sediment has been removed between Veatch and Hydrographer Canyons. Uchupi and Emery (1967), on profiles perpendicular to the margin, show reflecting horizons truncated by the continental slope, indicating erosion such as on profile 55. On profiles parallel to the slope these eroded areas can be seen to be dissected by numerous small valleys that indicate the major process by which the erosion occurred. The age of this erosion is inferred to be Pleistocene, correlative with the valleys northeast of Wilmington Canyon shown on profile 2c of Figure 2 (McGregor and Bennett, 1977). The lack of infilling in the valleys also suggests that they are not very old, as the upper slope is a region of rapid deposition according to Doyle et al (1975, 1976), on the basis of the cores shown in Figure 1. Grow and Markl (1977) have found that the present shelf edge off New Jersey and Cape Hatteras was eroded 30 km landward of its Early Cretaceous location. This major erosion, they believe, occurred during the Tertiary. Several of the late Tertiary unconformities noted by Vail et al (1977) were possibly identified on the rise (profile 5, Figs. 4 and 5) and on the Blake Plateau (profiles 3 and 5, Figs. 3 and 4); however, the major erosion of the slope found by Grow and Markl (1977) was not identified.

Regions of major deposition are also present on the slope. Between Baltimore and Washington Canyons (profile 3c, Fig. 3) a large volume of sediment in the form of ridges is present on the slope. The age of some of this sedimentary sequence is believed to be older than Pleistocene, because of the thickness of sediment (over 600 m) and because of similarity to the Nyckel Ridge south of Wilmington Canyon, which is believed to be pre-Quaternary (Stanley and Kelling, 1970). Drainage from Delaware Bay was responsible in the late Tertiary and Pleistocene for a large volume of sediment deposited on the continental slope (McGregor et al, 1977). The slope seaward of Albemarle Sound (profiles 2e and 3d, Figs. 2 and 3) was another depocenter. Drainage from the Albemarle River or the James River, both shown by Swift (1976) to have been present on the adjacent shelf, may have been responsible for transporting the sediment and depositing it on the slope near the shelf edge. Since deposition, these sediments have undergone erosion. A detailed study of this area is presently underway using bottom samples and geophysical techniques. Deposition seaward of Albemarle took place on the upper slope, whereas between Baltimore and Washington Canyons deposition was primarily on the middle and lower slope.

The northern portion of the Blake Plateau, north of Cape Romain, can be seen to have built upward and to the northeast by a series of foreset beds (profiles 2h, 3f, 5e; Figs. 2–4). This depositional pattern lasted for most of the Tertiary on the basis of the middle Eocene age of material cored at 2,000 m on the northern edge of the Plateau (Florentine Maurrasse, personal communication, 1976). This Eocene horizon is within the dipping sequence of horizons, with older material beneath it, and it is truncated by a possible late Miocene or mid-Pliocene unconformity correlating with unconformities noted by Vail et al (1977). Many unconformities are present along the Blake Plateau, and even the surface topography is variable (profiles 3g and 3h, Fig. 3). Pratt and Heezen (1964) believe that the Gulf Stream is the controlling factor for determining the topography and locations of sediment deposition. The position of the Gulf Stream in the vicinity of 32°N has permitted the progradation of the Florida-Hatteras Slope 25 km seaward (profile 2i, Fig. 2), while on the adjacent Blake Plateau erosion is occurring (profiles 3g and 5f, Figs. 3 and 4), producing very irregular topography with less than 100 m of sediment overlying lower Eocene material.

SUMMARY

The physiographic provinces of the slope and rise are very different in morphology and erosional and depositional history. The slope has been well dissected as far south as Cape Hatteras. On the basis of the detailed study of the slope north of Wilmington Canyon, the general dissection of the upper slope by small valleys appears to have occurred in the Pleistocene. The rise is smoother in morphology with only the major canyons having extensions at this depth.

Within each physiographic province parallel to the margin, there are regional variations in the erosional and depositional history which show up on strike lines. The Florida-Hatteras slope and adjacent portions of the Blake Plateau have been and still are actively influenced by the Gulf Stream. The interaction of the Gulf Stream and the Western Boundary Undercurrent with the sea floor has exposed or inhibited deposition atop Eocene material in the north end of the Blake Plateau near Cape Hatteras. This same interaction has influenced deposition in the vicinity of Hatteras Canyon, as it has very small levees compared with those of other East Coast canyons. A graded sand layer with coarse to fine sand on the rise in Norfolk Canyon suggests that this canyon is serving as a conduit in transporting sediment to the rise. In addition to the vicinity of canyons, several other portions of the slope have been deposition sites for large volumes of sediment in the past; these areas are seaward of the Delmarva Peninsula and Albemarle Sound.

During the mid-Pliocene, the rise between Hydrographer and Wilmington Canyons appears to have been subjected to very uniform erosion followed by deposition. This unconformity can be traced beneath the levees of Hudson Canyon, suggesting that they are Pleistocene to Recent features.

On the basis of strike-line profiles, variations in morphology and sedimentation history along the continental margin can be readily assessed with identification of regional versus localized events and processes.

REFERENCES CITED

Betzer, P. R., P. L. Richardson, and H. B. Zimmerman, 1974, Bottom currents, nepheloid layers, and sedimentary features under the Gulf Stream near Cape Hatteras: Marine Geology, v. 16, p. 21–29.

Doyle, L. J., C. C. Woo, and O. H. Pilkey, 1976, Sediment flux through inter-canyon slope area: U.S. Atlantic continental margin (abstract): Geol. Soc. America, Abstracts with Programs, v. 8, p. 843.

——— et al, 1975, Sedimentation on the northeastern continental slope of the United States: Proc., IX Cong. Internat. de Sedimentologie (Nice), v. 6, p. 51–56.

Garrison, L. E., 1970, Development of continental shelf south of New England: AAPG Bull., v. 54, p. 109–124.

Grow, J. A., and R. G. Markl, 1977, IPOD-USGS multichannel seismic reflection profile from Cape Hatteras to the Mid-Atlantic Ridge: Geology, v. 5, p. 625–630.

Hathaway, J. C., et al, 1976, Preliminary summary of the 1976 Atlantic margin coring project of the U.S. Geological Survey: U.S. Geol. Survey Open File Report 76-844, 217 p.

Heezen, B. C., M. Tharp, and M. Ewing, 1959, The floors of the oceans, 1. The North Atlantic: Geol. Soc. America Spec. Paper 65, 122 p.

Hollister, C. D., et al, 1972, Site 108—continental slope, *in* Initial reports of the Deep Sea Drilling Project: Washington, D.C., U.S. Govt., v. 11, p. 357–363.

Hoskins, H., 1967, Seismic reflection observations on the Atlantic continental shelf, slope and rise southeast of New England: Jour. Geology, v. 75, p. 598–611.

JOIDES, 1965, Ocean drilling on the continental margin: Science, v. 150, p. 709–716.

Keller, G. H., D. N. Lambert, and R. H. Bennett, 1978, Geotechnical properties of continental slope deposits, Cape Hatteras to Hydrographer Canyon (abstract): AAPG Bull., v. 62, p. 529.

Kelling, G., and D. J. Stanley, 1970, Morphology and structure of Wilmington and Baltimore submarine canyons, eastern United States: Jour. Geology, v. 78, p. 637–660.

McGregor, B. A., and R. H. Bennett, 1977, Continental slope sediment instability northeast of Wilmington Canyon: AAPG Bull., v. 61, p. 918–928.

——— ——— and G. F. Merrill, 1977, Continental slope south of Baltimore Canyon, U.S. East Coast (abstract): Geol. Soc. America, Abstracts with Program, v. 9, p. 1089.

Manheim, F. T., and R. E. Hall, 1976, Deep evaporitic strata off New York and New Jersey—evidence from interstitial water chemistry of drill cores: Jour. of Research U.S. Geol. Survey, v. 4, p. 697–702.

Nelson, C. H., and L. D. Kulm, 1973, Submarine fans and deep-sea channels, *in* Turbidites and Deep-Water Sedimentation: Pacific Section S.E.P.M. Short Course, Anaheim, p. 39–78.

Pratt, R. M., 1967, The seaward extension of submarine canyons off the northeast coast of the United States: Deep-Sea Research, v. 14, p. 409–420.

——— and B. C. Heezen, 1964, Topography of the Blake Plateau: Deep-Sea Research, v. 11, p. 721–728.

Sheridan, R. E., 1974, Atlantic continental margin of North America, *in* C. A. Burke and C. L. Drake, *eds.*, Geology of Continental Margins: Berlin, Springer-Verlag, p. 391–407.

——— 1975, Dome structure, Atlantic continental shelf east of Delaware: Preliminary geophysical report: AAPG Bull., v. 59, p. 1203–1211.

Stanley, D. J., and G. Kelling, 1970, Interpretation of a levee-like ridge and associated features, Wilmington Submarine Canyon, eastern U.S.: Geol. Soc. America Bull., v. 81, p. 3747–3752.

Swift, D. J. P., 1976, Continental shelf sedimentation, *in* D. J. Stanley and D. J. P. Swift, eds., Marine Sediment Transport and Environmental Management: New York, John Wiley and Sons, Inc., p. 311–350.

Twichell, D. C., H. J. Knebel, and D. W. Folger, 1977, Delaware River: evidence for its former extension to Wilmington Submarine Canyon: Science, v. 195, p. 483–485.

Uchupi, E., 1968, Atlantic continental shelf and slope of the United States—physiography: U.S. Geol. Survey Prof. Paper 529, p. C1–C30.

——— and K. O. Emery, 1967, Structure of the continental margin off Atlantic coast of the United States: AAPG Bull., v. 51, p. 223–234.

Vail, P. R., R. M. Mitchum, Jr., and S. Thompson III, 1977, Seismic stratigraphy and global changes in sea level, *in* C. E. Payton, ed., Seismic stratigraphy—applications to hydrocarbon exploration: AAPG Memoir 26, p. 49–212.

30. Marine Geology 33, 163-174.

MASS MOVEMENT OF SEDIMENT ON THE CONTINENTAL SLOPE AND RISE SEAWARD OF THE BALTIMORE CANYON TROUGH

BONNIE A. McGREGOR* and RICHARD H. BENNETT

Department of Oceanography, Texas A&M University, College Station, Texas 77843 (U.S.A.)
Atlantic Oceanographic and Meterological Labs. — NOAA, Miami, Fla. 33149 (U.S.A.)

(Received October 13, 1978; revised and accepted March 30, 1979)

ABSTRACT

McGregor, B.A. and Bennett, R.H., 1979. Mass movement of sediment on the continental slope and rise seaward of the Baltimore Canyon Trough. Mar. Geol., 33: 163—174.

Sediment instability has produced large submarine slides on the continental slope and rise seaward of the coast of New Jersey and the Baltimore Canyon Trough. Sediment failure is confined to Quaternary material over a continuous mid-Pliocene unconformity. The thickness of Pleistocene sediment is greatest in proximity to Wilmington and Spencer Canyons, indicating that the canyons influence the amount of sediment on the lower slope and rise. Differences in thickness of sediment between both canyons suggest variations in the amount of sediment each transported. Sediment failure is ubiquitous in this area. Instability appears to be related to sediment thickness rather than to other trigger mechanisms. Rapid sediment accumulation and the probable low shear strength-under-consolidated condition of Pleistocene deposits on the mid-Pliocene unconformity are believed to be major factors controlling sediment instability in this area.

INTRODUCTION

A geotechnical corridor 60 × 140 km, seaward of the Baltimore Canyon Trough (Fig.1), was selected for geophysical and geotechnical study because of its proximity to a region of active petroleum exploration, and because it is representative of a margin seaward of a non-glaciated coast, characteristic of the sedimentary history and processes that have been active off such a coast.

Data collected with the NOAA ship "Researcher" include a 1 × 2.5 km grid of narrow-beam bathymetric, 3.5-kHz, and seismic reflection profiles. The seismic system consisted of a 40 in^3 air gun fired every 9 sec at 1500—2000 psi and a 50-element hydrophone. The seismic data were filtered at 50—125 Hz and recorded. Navigational control was based on Loran C and satellite systems.

The outer shelf, slope, and rise (Heezen et al., 1959) are included in the survey. Morphologic features on the margin include Wilmington, Spencer, and Lindenkohl Canyons as well as numerous valleys which dissect the slope (Fig.1). A submarine slide is present on the slope near profile A (McGregor

---

*Present address: Atlantic Oceanographic and Meteorological Labs.—NOAA, Miami, Fla. 33149 (U.S.A.)

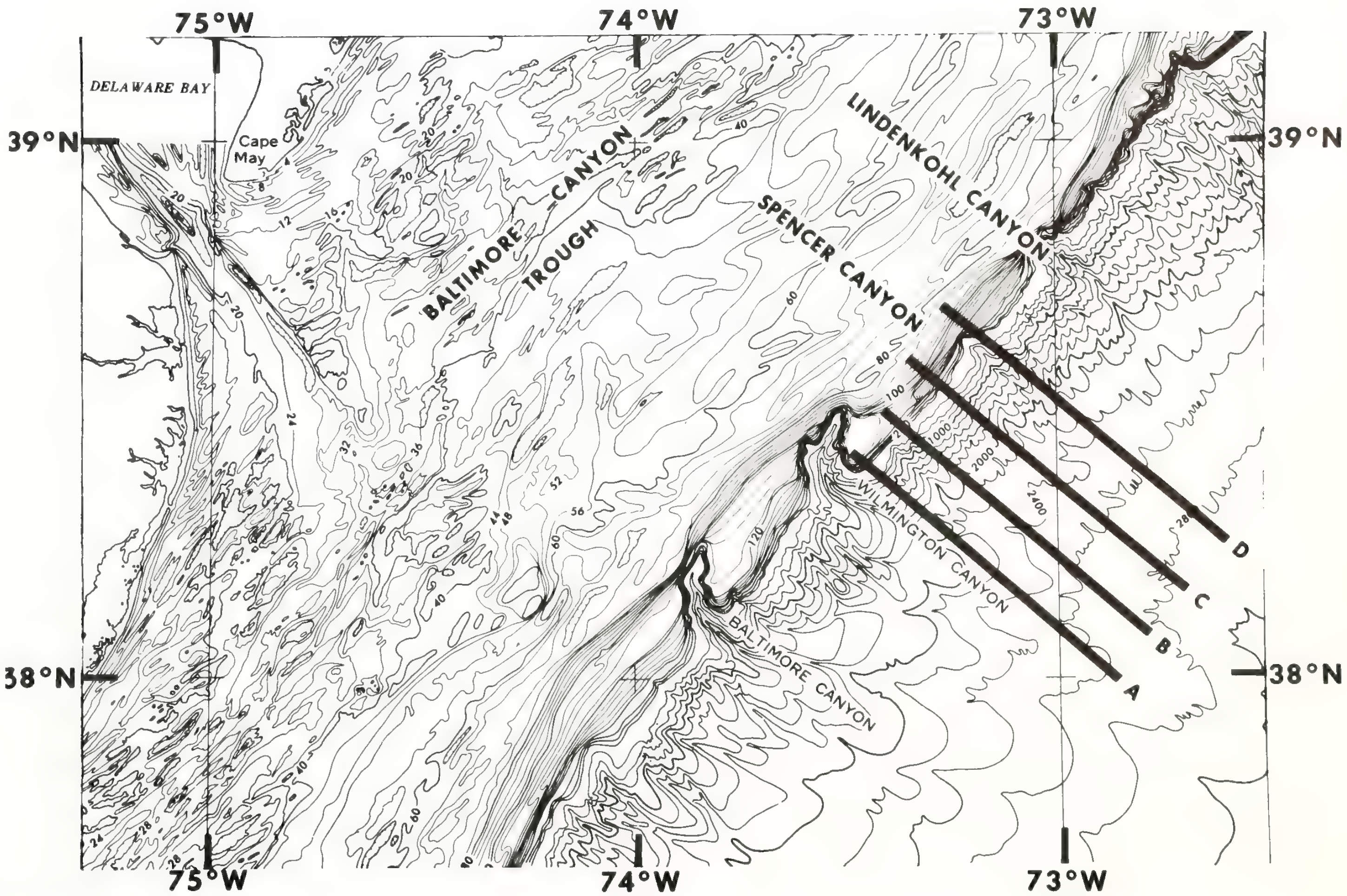

Fig.1. Index map from Uchupi (1970). Depths are in meters.

and Bennett, 1977; Bennett et al., 1977). Because sediment instability was initially identified on the slope, additional study was focused on a larger portion of the margin including the shelf, slope and rise.

SEISMIC REFLECTION PROFILES

Four profiles perpendicular to the margin, approximately 10 km apart have been selected for discussion from a total of 80 profiles in the area (Fig.1). Each profile (Figs.2—5) extends from 100 m to over 2600 m water depth with maximum sediment penetration of 600 m. Profile A (Fig.1) is adjacent to Wilmington Canyon and profile D is northeast of Spencer Canyon. A sand sheet covers the shelf in this area (Knebel and Spiker, 1977) and causes the poor sub-bottom return, or lack of acoustic penetration, on the shelf portion of the profiles (Figs.2—5). Reflecting horizons between kilometer 10—15 (Figs.2 and 3) and kilometer 15—20 (Figs.4—5) are truncated by the continental slope, indicating that the slope is erosional. Sediment up to 300 m thick covers this erosion surface and the truncated horizons (Fig.2, km 15—20). Reflecting horizons beneath the rise are continuous offshore, except for those above the continuous horizon on the rise accentuated by a heavier line and labeled Pl (e.g., Fig.2) which are more irregular and discontinuous than those below it. The sea-floor gradient varies with topography, however, in general the continental slope can be characterized as having an 8° slope and the rise a 1° slope.

No dated samples are available in this area, so the age of the reflecting horizons shown in Figs.2—5 must be inferred from dated Caldrill and DSDP cores which are located about 25 km northeast of this area, just south of Hudson Canyon (Hollister et al., 1972; Sheridan, 1975). Horizons, between 700 and 2000 m (Figs.2, 5) which are truncated by the slope, are believed to be Tertiary in age. By correlating these horizons with the profiles of Kelling and Stanley (1970) and Sheridan (1975), ages of Miocene (M) and Eocene (E) are assigned to the horizons observed in this study to be truncated by the slope and Cretaceous (K) for the non-truncated horizons continuous under the slope and rise (Figs.2—5). Grow and Sheridan (1976) suggest that the present shelf break is approximately 30 km landward of the position of the shelf break in the lower Cretaceous with draping of late Cretaceous horizons over this old shelf break. The inflection between the slope and rise of the inferred Cretaceous horizon (Figs.2—5) suggests the shelf break in the past in this area may have been 15 km seaward of its present location. The continuous heavy horizon labeled Pl, which occurs on the rise and truncates horizons on the slope (Figs.2—5), may be mid-Pliocene. This is the age of a global unconformity (Vail et al., 1977) which was identified on the rise and traced from Hydrographer Canyon on Georges Bank to Wilmington Canyon (McGregor, 1979). The material above this mid-Pliocene horizon is therefore inferred to be late Pliocene and Quaternary, and most is probably Pleistocene.

The surface of the lower slope and rise becomes more regular and smoother from profile A to C, with a slight increase in roughness on profile D. Surface roughness appears to be related to the inferred Pleistocene sediment thickness and, genetically, to the processes associated with sediment instability. Submarine canyons were apparently responsible for major transport of sediment to the lower slope and rise, since sediment thickness is greater near Wilmington and Spencer Canyons (profiles A and D) than on the inter-canyon portion of the slope (profiles B and C).

Mass movement of sediment has occurred and is an important process on this portion of the margin, contributing to the sediment distribution pattern on the slope and rise during the Quaternary. Profile A (Fig.2) crosses a submarine slide (McGregor and Bennett, 1977) on the slope between 950 and 1600 m water depth, and additionally a series of slides are present on the slope and rise. The topographic high on the upper rise is a large slide block. Furthermore, based on the contorted reflecting horizons, much of the material on the rise above the mid-Pliocene unconformity appears to consist of slide masses. A layer of acoustically transparent sediment occurs beneath and downslope from the large slide block at km 40. This non-stratified layer may have been (1) a homogeneous sediment layer that was deposited preslide, (2) a mudflow associated with the slide as in the Sunda Arc region (Moore et al., 1976), or (3) homogenization of stratified sediment at the base of the slide. Since this non-stratified layer is not present on profile C (Fig.4), the layer appears to be related to the slide. Reflecting horizons are faulted and rotated within the slide block (profile A, km 35—45). On profile A the sediment on the slope and rise failed as a series of slide blocks, which were possibly separated in time. The wedge of sediment which is buried at the base of the slope and upper rise (km 20) suggests that this mass failed first, sliding to the base of the slope; subsequently the large blocks on the rise slid over this wedge.

Profile B (Fig.3) northeast of Wilmington Canyon, shows a thinning of the sediment above the mid-Pliocene unconformity relative to profile A. A thin veneer of sediment is present on the slope. A slide block appears to be present at the base of the slope, and further seaward on the rise there is a slide mass with upturned beds in its toe. This block does not appear to have moved very far, but rather has primarily rotated.

Profile C (Figs.1 and 4) is located mid-way between Spencer and Wilmington Canyons. The post-reflector Pl sediments are usually not more than 100 m thick (sediment thicknesses based on assumed sound velocity of 1500 m/sec). Sediment failure has also occurred in this thinner sediment, even though no large blocks are observed, as on the preceeding two profiles. The sediments at the base of the slope and upper rise have failed as a series of units as shown by the irregular surface topography and rotated internal reflectors. Between km 60 and 70, a 30 m thick upper layer with hummocky surface topography suggests a slide deposit which may have originated at the 25 m high scarps on the upper rise. Truncation of reflecting horizons by these scarps indicates they are erosional. This hummocky topography with associated scarps is similar to the sediment slides described by Jacobi (1976) on the northwest margin of Africa.

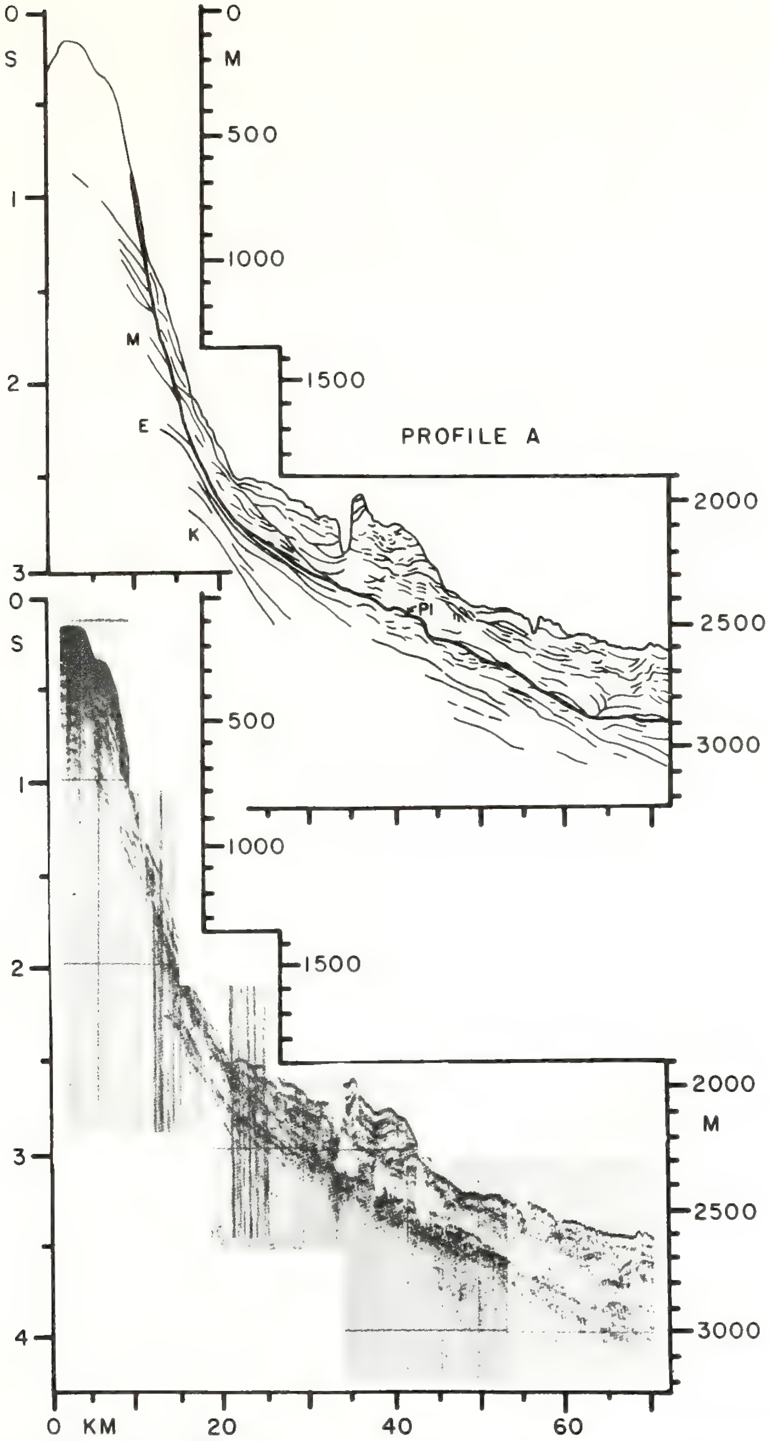

Fig.2. Profile A (see Fig.1 for location) line drawing and photograph of original record. Vertical axes are two-way travel time in seconds and depth in meters. Vertical exaggeration is approximately 30 × assuming 1500 m/sec sound velocity. *Pl* = Pliocene, *M* = Miocene, *E* = Eocene, *K* = Cretaceous.

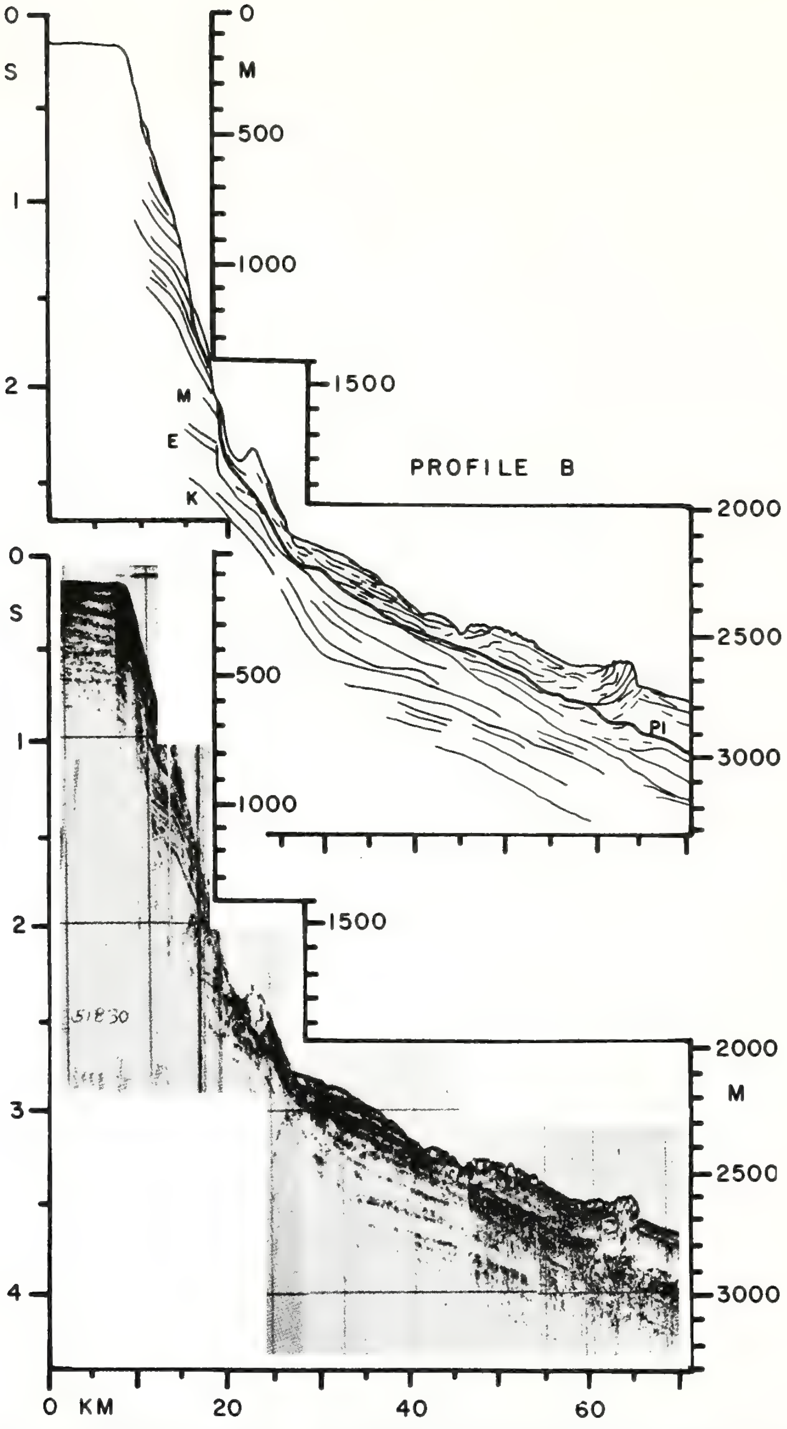

Fig.3. Profile B (see Fig.1 for location) line drawing and photograph of original record. Vertical axes are two-way travel time in seconds and depth in meters. Vertical exaggeration is approximately 30 × assuming 1500 m/sec sound velocity. *Pl* = Pliocene, *M* = Miocene, *E* = Eocene, *K* = Cretaceous.

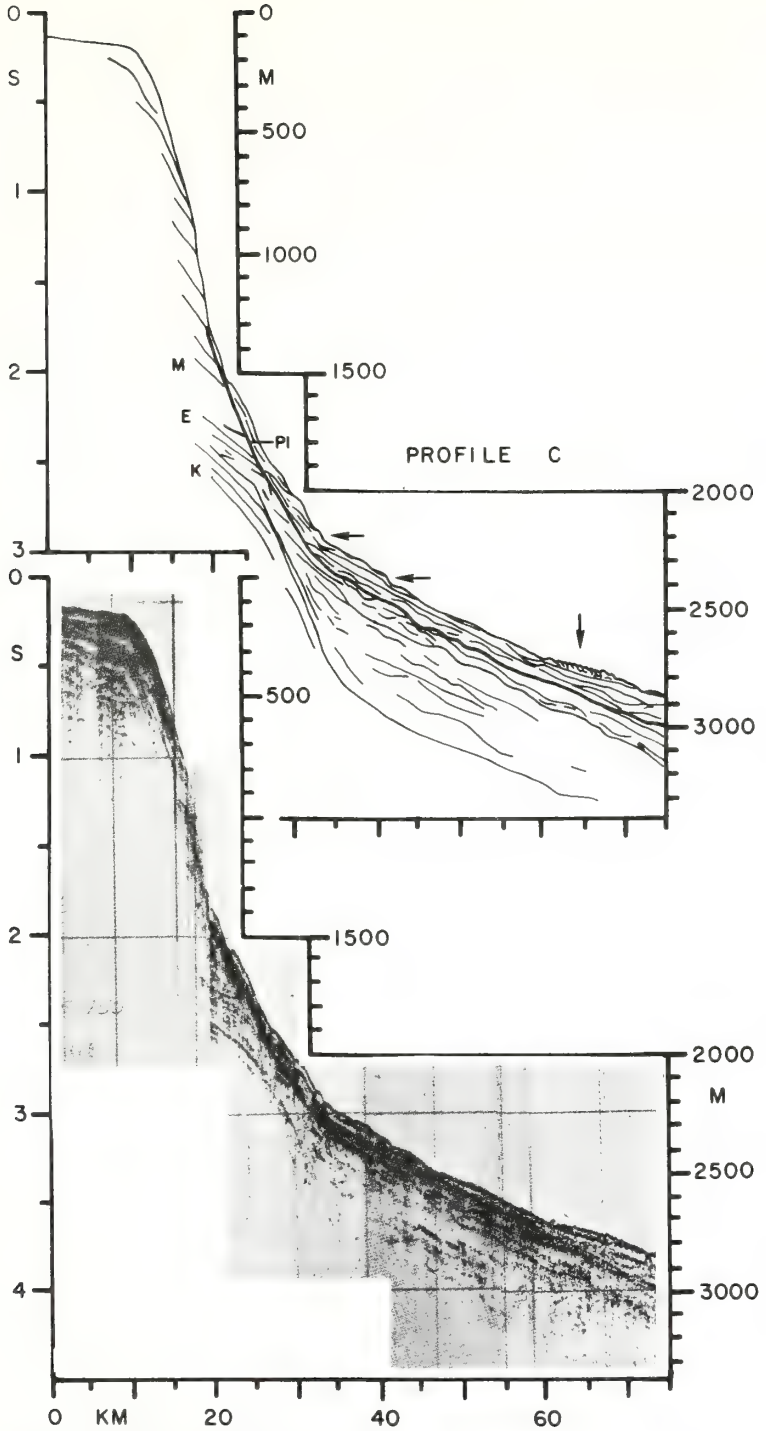

Fig.4. Profile C (see Fig.1 for location) line drawing and photograph of original record. Vertical axes are two-way travel time in seconds and depth in meters. Vertical exaggeration is approximately 30 × assuming 1500 m/sec sound velocity. *Pl* = Pliocene, *M* = Miocene, *E* = Eocene, *K* = Cretaceous. Arrows indicate hummocky topography and up slope scarps.

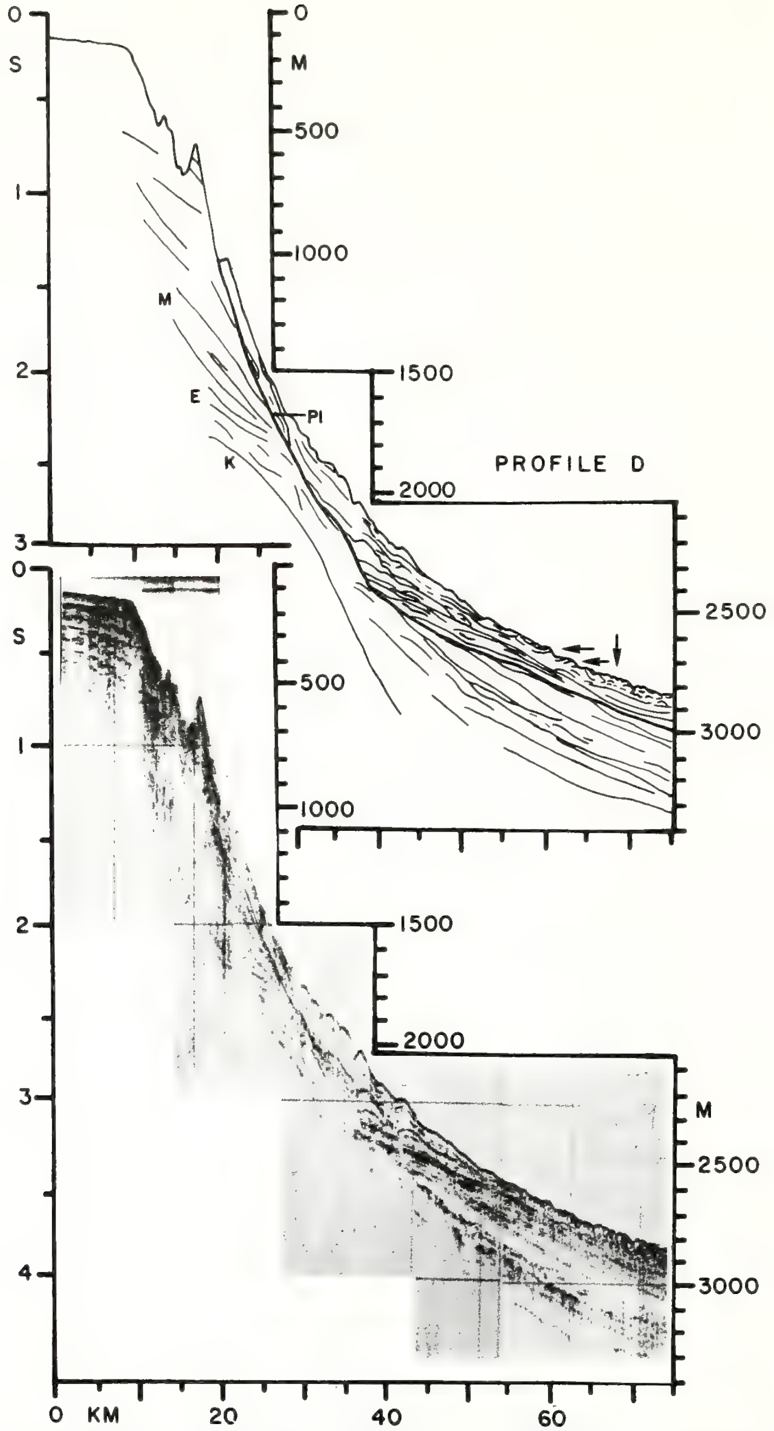

Fig.5. Profile D (see Fig.1 for location) line drawing and photograph of original record. Vertical axes are two-way travel time in seconds and depth in meters. Vertical exaggeration is approximately 30 X assuming 1500 m/sec sound velocity. *Pl* = Pliocene, *M* = Miocene, *E* = Eocene, *K* = Cretaceous. Arrows indicate hummocky topography and up slope scarps.

At Spencer Canyon (profile D, Figs.1 and 5), the post-reflector Pl sediment increases in thickness, especially in the region of the base of slope and upper rise. This suggests that the canyon was active during the Pleistocene in transporting sediment to the slope and rise. Since there is less Pleistocene sediment at Spencer Canyon than at Wilmington Canyon, Wilmington may have transported more sediment than Spencer. A layer of sediment 200 m thick is present on the mid-slope (between 1000 and 1700 m, Fig.5). Slumping has occurred at the base of the slope between 2000 and 2500 m, where buried horizons suggest that sediment failure has occurred in at least two phases. Seaward of km 60 on the rise the hummocky topography indicates a slide deposit. Scarps are present upslope from this hummocky topography. This slide deposit occurs at the same water depth as on profile C, approximately 2700 m; however, the deposit is 50 m thick as opposed to 30 m on profile C.

DISCUSSION

From these four profiles (Figs.2—5) it seems that sediment failure is common along this portion of the continental margin between Wilmington and Lindenkohl Canyons. The nature of the failures varies in character and has produced translated thick blocks, rotated blocks, and a thin hummocky layer. Features like these have been reported from other parts of the Atlantic continental margins. For example, from south of Georges Bank to Nova Scotia, there are large slide blocks on the slope and rise (Heezen and Drake, 1964; Uchupi, 1967; Emery et al., 1970; MacIlvaine, 1973). Rotational slides or slumps, in which there is little translation, occur on the African margin (Embley and Jacobi, 1977; Summerhayes et al., 1979). Slides with scarps about 150 m high and downslope debris flows are described by Embley and Jacobi (1977), two on the U.S. Atlantic margin seaward of Chesapeake and Delaware Bays. Northeast of Wilmington Canyon all three types of sediment failure occur next to each other. As the sea-floor gradient on all four profiles (Figs.2—5) is approximately the same, it seems unlikely that variations in gradient control the type of sediment failure in this area. A common feature of the different types of movement, however, is their occurrence in Quaternary age material. As discussed for each profile, the thickness of the Quaternary material varies on the slope and rise and in general decreases with increasing distance from Wilmington Canyon with a slight increase at Spencer Canyon. The types of sediment instability described appear to be in areas with different sediment thickness. The translated blocks are found where the sediment is thickest (approximately 300—400 m) (Fig.2), rotational blocks where sediment thickness is intermediate (approximately 200 m) (Fig.3), and thin slide masses with hummocky surface topography where the sediment is thin (approximately 100 m) (Figs.4—5).

Mechanisms which triggered the failure can only be surmised. The disgorging of sediment directly on to the upper continental slope during lower stands of sea level in the Pleistocene, as well as the increased sedimentation rate related to glacial erosion and runoff probably have been important factors on this portion of the margin. Rapid deposition of sediment on an unconformity (the mid-Pliocene unconformity) may also have contributed to sediment failure in the area. Increased energy input via surface and internal waves to the upper slope during lowered sea levels, or earthquake activity, are possible trigger mechanisms which cannot be assessed. Undercutting of sediments by bottom currents does not seem a likely mechanism because of the varied water depths where failure occurred, and the lack of recognizable channels. Undercutting to a depth sufficient to cause failure of the large blocks (profile A) should be evident on profile C, even if the channels are buried, since they should have been sufficiently deep to cut the unconformity.

Numerous sediment cores collected in the study area exhibit geotechnical properties worthy of comment, primarily the cores from the slide area on the slope near profile A (McGregor and Bennett, 1977). Because properties such as shear strength, consolidation-compressibilities, overburden stress, and the Atterberg limits (used to characterize and classify a deposit) are critically important in assessing the stability or instability of sedimentary deposits, these specific properties will be discussed. Expressed simply and in general terms, gravity-induced failure of a slope deposit is generated, under static conditions, by the overburden which imposes a shearing stress in the downslope direction. When shearing stress exceeds the shear strength of the sediment, then failure would occur.

Sediments along a core transect down the continental slope near profile A have liquid limits and plasticity indices which increase seaward (Bennett et al., 1977). Keller et al. (1978) found similar relationships in the Atterberg limits for very short cores recovered along transects normal to the slope between Hydrographer and Hatteras Canyons. Textural analyses of numerous slope cores indicate a general "fining" of the sediments downslope onto the continental rise, as shown also by Doyle et al. (1978). Seaward increase in the liquid limit and plasticity index, can be attributed primarily to the increase of fine-grained particles in the deeper water sediments. Compared to upper slope deposits, relatively higher sediment compressibilities are inferred from the Atterberg limits for the deeper water deposits. The Atterberg limits of many natural deposits plot along a relatively straight line approximating the slope of the A line on the plasticity chart (Casagrande, 1932, 1948). Generally, sediments of high compressibility are characterized by high liquid limits and plasticity indices. Also the natural water content of the surficial continental slope and rise sediments are considerably higher than the liquid limits. This seems to be common for the middle, lower slope, and rise sediments. Water contents greater than the liquid limits are characteristic of sediments having liquidity indices greater than 1, which defines the empirical boundary between the plastic and liquid state of a soil. The significance of this index parameter is readily apparent in the statement by Terzaghi and Peck (1967, p.32) that remolding of a soil having a natural water content higher than the liquid limit transforms the soil into a thick viscous slurry.

Based on the very low increases in shear strength with core depth, and the high liquidity indices, some of the slope and rise sediments are considered to be underconsolidated. Controlling factors probably include rapid rates of deposition during the Pleistocene and the "fining" of sediments seaward. Variable sediment thicknesses might be expected to accumulate even on similar gradients of the slope and rise at comparable water depths, but the ultimate amount of sediment deposition that would be stable on any given slope would depend upon the geotechnical properties (shear strength and down-slope shear stress) of the particular deposit before sediment failure would occur. Differences in wet bulk density (wet unit weight) and degree of sediment consolidation with depth might vary for each deposit. Thus deposits on various slopes would develop a shearing stress to different stratigraphic depths before the shearing resistance of the deposit was exceeded. Therefore, some deposits would fail as relatively thin slide masses, and others as large rotational and/or translational blocks. Obviously low shearing resistance of the surficial sediments is well exemplified by the very low shear strengths found for many of these deposits (Bennett et al., 1977; Keller et al., 1978). More geotechnical sampling and testing are needed before these hypotheses can be verified for this study area.

On this portion of the margin, sediments apparently failed during the Pleistocene on the lower slope and rise. The type of failure appears to depend on the original thickness and geotechnical properties (that developed prior to failure) of the sediment mass.

ACKNOWLEDGEMENTS

We would like to thank Colin P. Summerhayes, William R. Bryant and William L. Stubblefield for reviewing the manuscript. Data were collected with the assistance of the officers and crew of the NOAA ship "Researcher", as well as personnel from the Atlantic Oceanographic and Meteorological Labs., Texas A&M University, and Florida State University. This study is part of the RUSEF (Rational Use of the Sea Floor)/Marine Geotechnical Program of the Atlantic Oceanographic and Meteorological Laboratories. Funds for this study were provided by the National Oceanic and Atmospheric Administration.

REFERENCES

Bennett, R.H., Lambert, D.N. and Hulbert, M.H., 1977. Geotechnical properties of a submarine slide area on the U.S. continental slope northeast of Wilmington Canyon. Mar. Geotechnol., 2: 245—261.

Casagrande, A., 1932. Research on the Atterberg limits of soils. Public Roads, 13: 121—135.

Casagrande, A., 1948. Classification and identification of soils: Am. Soc. Civ. Eng. Trans., 113: 901—931.

Doyle, L.J., Pilkey, O.H. and Woo C.C., 1978. Sedimentation on eastern United States continental slope. AAPG—SEPM Annual Convention Abstracts, Oklahoma City, 62: p.510.

Embley, R.W. and Jacobi, R.D., 1977. Distribution and morphology of large submarine sediment slides and slumps on Atlantic continental margins. Mar. Geotechnol., 2: 205—228.

Emery, K.O., Uchupi, E., Phillips, J.D., Bowin, C.O., Bunce, E.T. and Knott, S.T., 1970. Continental rise off eastern North America. Bull. Am. Assoc. Pet. Geol., 54: 44—108.

Grow, J.A. and Sheridan, R.E., 1976. High velocity sedimentary horizons beneath the outer continental shelf off New Jersey. EOS, 57: 265 pp.

Heezen, B.C. and Drake, C.L., 1964. Grand Banks slump. Bull. Am. Assoc. Pet. Geol., 48: 221—225.

Heezen, B.C., Tharp, M. and Ewing, M., 1959. The floors of the oceans, 1. North Atlantic. Geol. Soc. Am. Spec. Pap., 65: 122 pp.

Hollister, D.C., Ewing, J.I., Habib, D., Hathaway, J.C., Lancelot, Y., Luterbacher, H., Paulus, F.J., Wilcoxon, C.W. and Worstell, P., 1972. Site 108 — continental slope. Initial Reports of the Deep Sea Drilling Project, XI, pp.357—363.

Jacobi, R.D., 1976. Sediment slides on the northwestern continental margin of Africa. Mar. Geol., 22: 157—173.

Keller, G.H., Lambert, D.N. and Bennett, R.H., 1978. Geotechnical properties of continental slope deposits — Cape Hatteras to Hydrographer Canyon. AAPG—SEPM Annual Convention Abstracts, Oklahoma City, 62: p.529.

Kelling, G. and Stanley, D.J., 1970. Morphology and structure of Wilmington and Baltimore submarine canyons, eastern United States. J. Geol., 78: 637—660.

Knebel, H.J. and Spiker, E., 1977. Thickness of age of surficial sand sheet, Baltimore Canyon Trough area. Bull. Am. Assoc. Pet. Geol., 61: 861—871.

MacIlvaine, J.C., 1973. Sedimentary processes on the continental slope off New England. Woods Hole Oceanographic Institution Tech. Rep. WHOI-73-58, pp.1—211.

McGregor, B.A., 1979. Variations in bottom processes along the U.S. Atlantic continental margin. Am. Assoc. Pet. Geol., Mem., 29: 139—149.

McGregor, B.A. and Bennett, R.H., 1977. Continental slope sediment instability northeast of Wilmington Canyon. Bull. Am. Assoc. Pet. Geol., 61: 918—928.

Moore, D.G., Curray, J.R. and Emmel, F.J., 1976. Large submarine slide (oliostrome) associated with Sunda Arc Subduction zone, northeast Indian Ocean. Mar. Geol., 21: 211—226.

Sheridan, R.E., 1975. Dome structure, Atlantic continental shelf east of Delaware: preliminary geophysical report. Bull. Am. Assoc. Pet. Geol., 59: 1203—1211.

Summerhayes, C.P., Bornhold, B.D. and Embley, R.W., 1979. Surficial slides and slumps on the continental slope and rise of South West Africa: A reconnaissance study. Mar. Geol., 31: 265—277.

Terzaghi, K. and Peck, R.B., 1967. Soil Mechanics in Engineering Practice. Wiley, New York, N.Y., 729 pp.

Uchupi, E., 1967. Slumping on the continental margin southeast of Long Island, New York. Deep-Sea Res., 14: 635—639.

Uchupi, E., 1970. Atlantic continental shelf and slope of the United States — shallow structure. U.S. Geol. Surv. Prof. Pap., 529-I, 1—44.

Vail, P.R., Mitchum, R.M., Jr. and Thompson, S., III, 1977. Global changes of sea level from seismic stratigraphy. Am. Assoc. Pet. Geol., Mem., 26: 83—97.

CURRENT METER OBSERVATIONS ON THE U.S. ATLANTIC CONTINENTAL SLOPE — VARIATION IN TIME AND SPACE

BONNIE A. McGREGOR*

Atlantic Oceanographic and Meteorological Laboratories, NOAA Miami, Fla. 33149 (U.S.A.)

(Received June 28, 1977; revised and accepted November 28, 1977)

ABSTRACT

McGregor, B.A., 1979. Current meter observations on the U.S. Atlantic continental slope — Variation in time and space. Mar. Geol., 29: 209—219.

Two current meters were deployed on the U.S. Atlantic continental slope in approximately 850 m of water for 83 days during the summer of 1976 to evaluate near-bottom fluid motions. Tidal oscillations up and down slope dominate records; however, occasional transport events to the southwest parallel to the margin were also present. Maximum velocities recorded were 30 cm/sec, which are believed to be sufficient to move the bottom sediments in the area. Bottom topography was found to influence the direction and magnitude of the bottom currents recorded. The passage of Hurricane Belle over the current meter site produced no measurable effect on the bottom currents.

INTRODUCTION

As part of the Atlantic Oceanographic and Meteorological Laboratories' RUSEF (Rational Use of the Sea Floor) program to study the bottom and near-bottom processes active on the continental margin, two Geodyne 102-C Savonius rotor current meters were taut-wire moored on the continental slope off the coast of Delaware and Maryland. The slope south of Baltimore Canyon (Fig.1) has an irregular morphology of ridges and valleys transverse to the slope. The current meters were deployed such that one meter was located on a ridge and the other was located in an adjacent valley with both meters at approximately the same water depth (Fig.2). Current meter 1 (CM1) was located on the ridge at 37°51.1′N 73°55.0′W at a water depth of 840 m, and current meter 2 (CM2) in a valley 6 km away at 37°54.0′N 73°54.6′W at a water depth of 877 m. Each meter was located 3 m above the bottom and recorded a speed and direction every 30 min averaged over 60 sec from June 20, to September 11, 1976. During this time, Hurricane Belle passed over the site on August 9, 1976. Surface weather observations for the time the meters were deployed were obtained from Chesapeake Lightship, Virginia, and Cape May Station, New Jersey. Tidal data were obtained for Wallops Islands Virginia.

---

* Present address: Department of Oceanography, Texas A & M University, College Station, Texas 77843 (U.S.A.).

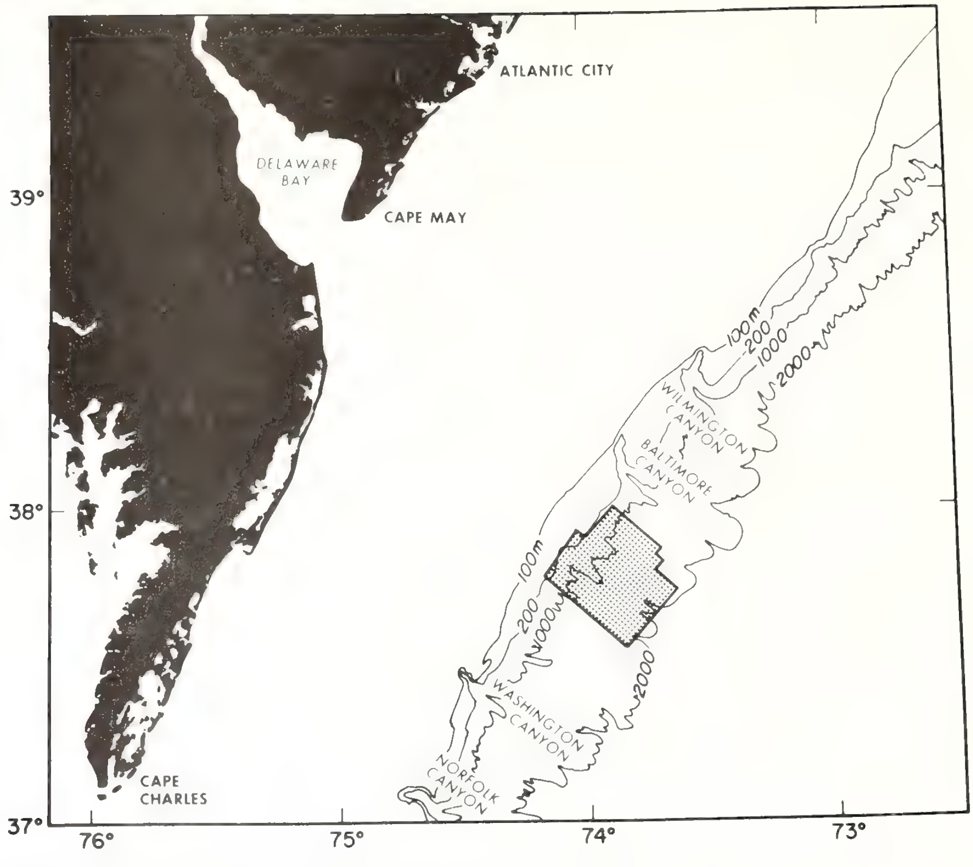

Fig.1. Contour map in meters of the slope south of Baltimore Canyon (Uchupi, 1970), showing general location of Fig.2.

CURRENT METER AND WEATHER DATA

Current meter observations were collected for an 83-day period during the summer of 1976. Velocity data in component form are shown for both meters in Figs.3 and 4 with 48 observations per day. Semi-diurnal tidal flow dominates the record but motion with an approximately 3-hour period can also be seen. The tidal amplitude at Wallops Island for the same time is also shown for correlation. Maximum velocity recorded during the 83-day period by CM1 was 30 cm/sec, the average velocity is considerably less between 3 and 4 cm/sec. CM1 also recorded flow in addition to the tidal flow. Current velocities at the CM2 site (Fig.4) are generally lower with a maximum velocity of approximately 20 cm/sec and an average velocity of about 2.5 cm/sec.

Averaging out the tidal oscillation for each current meter record shows the non-tidal flow. CM1 (Fig.5) shows several periods of flow with a maximum velocity of 10 cm/sec and a duration of two to six days. CM2 has only a slight flow coincident with the non-tidal events recorded on CM1 with a magnitude

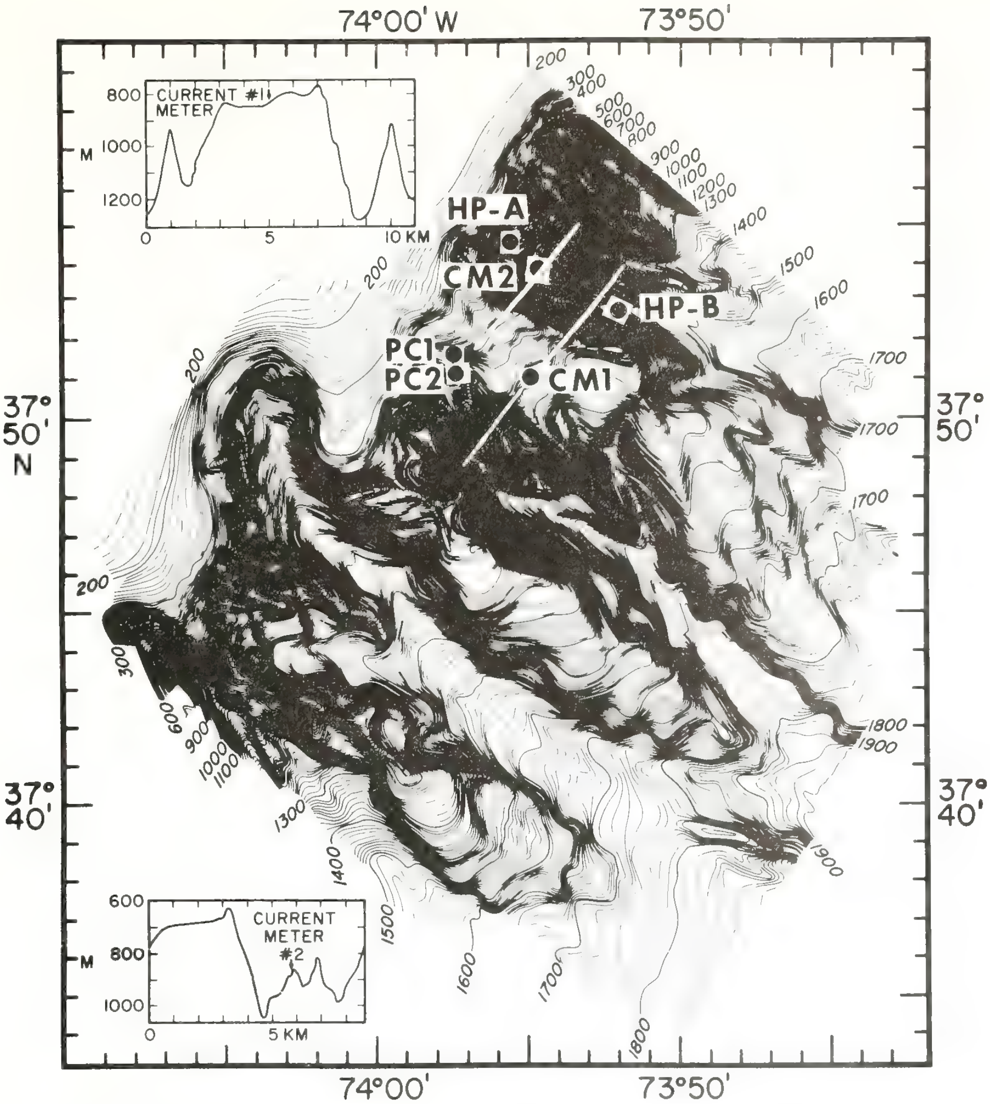

Fig.2. Bathymetry in corrected meters (Matthews, 1939). Contour interval is 10 m. Current meter and core locations are indicated. Bathymetric profiles show topographic setting for each current meter.

of 2 cm/sec. The passage of Hurricane Belle over the current meter site on August 9, 1976, did not seem to influence the currents at the slope sites.

Although the meters were only 6 km apart, the records are dissimilar in strength of currents as well as mean flow direction. This may be due to a difference in morphology at the respective sites. Site CM1 was located on a subdued slope on top of a ridge 5 km wide, transverse to the continental slope, while CM2 was located on a terrace on a small ridge in the adjacent

CURRENT METER #1

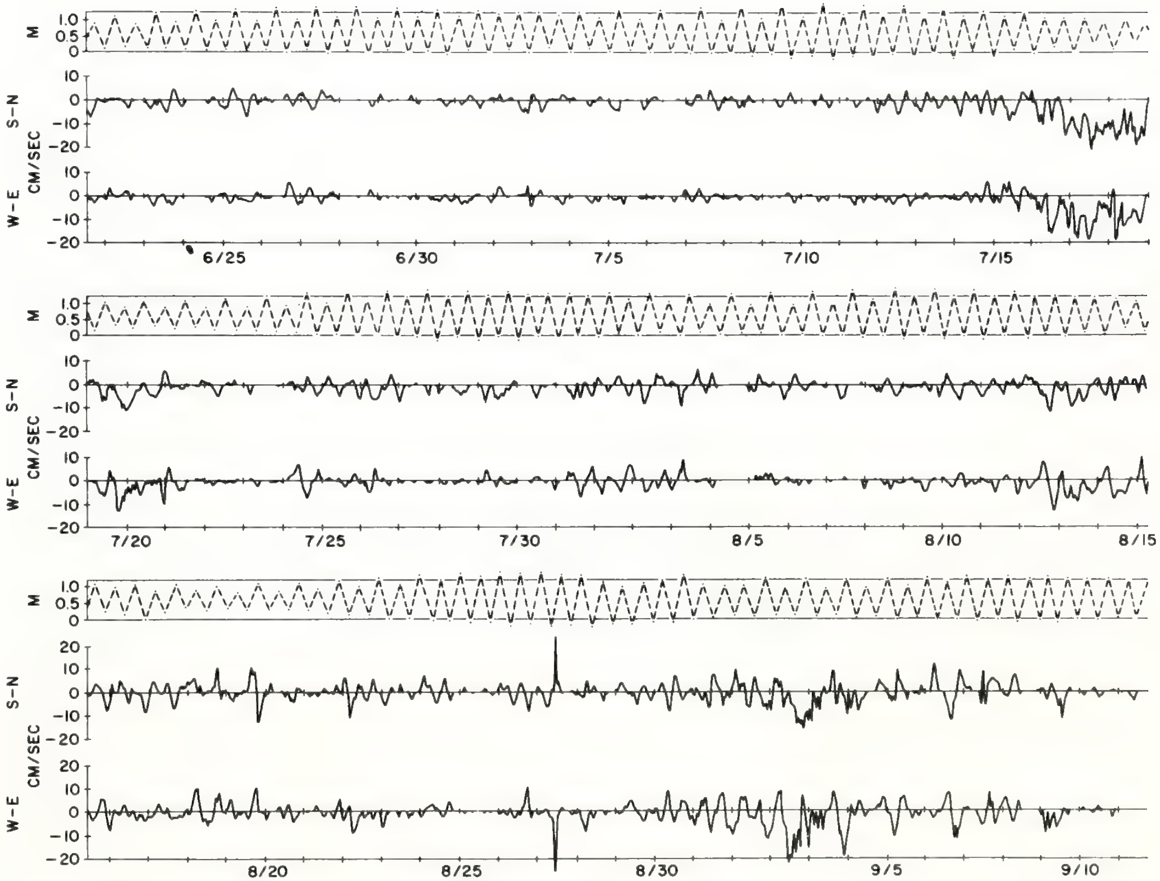

Fig.3. Current meter record of CM1. Tidal height for the same period is shown.

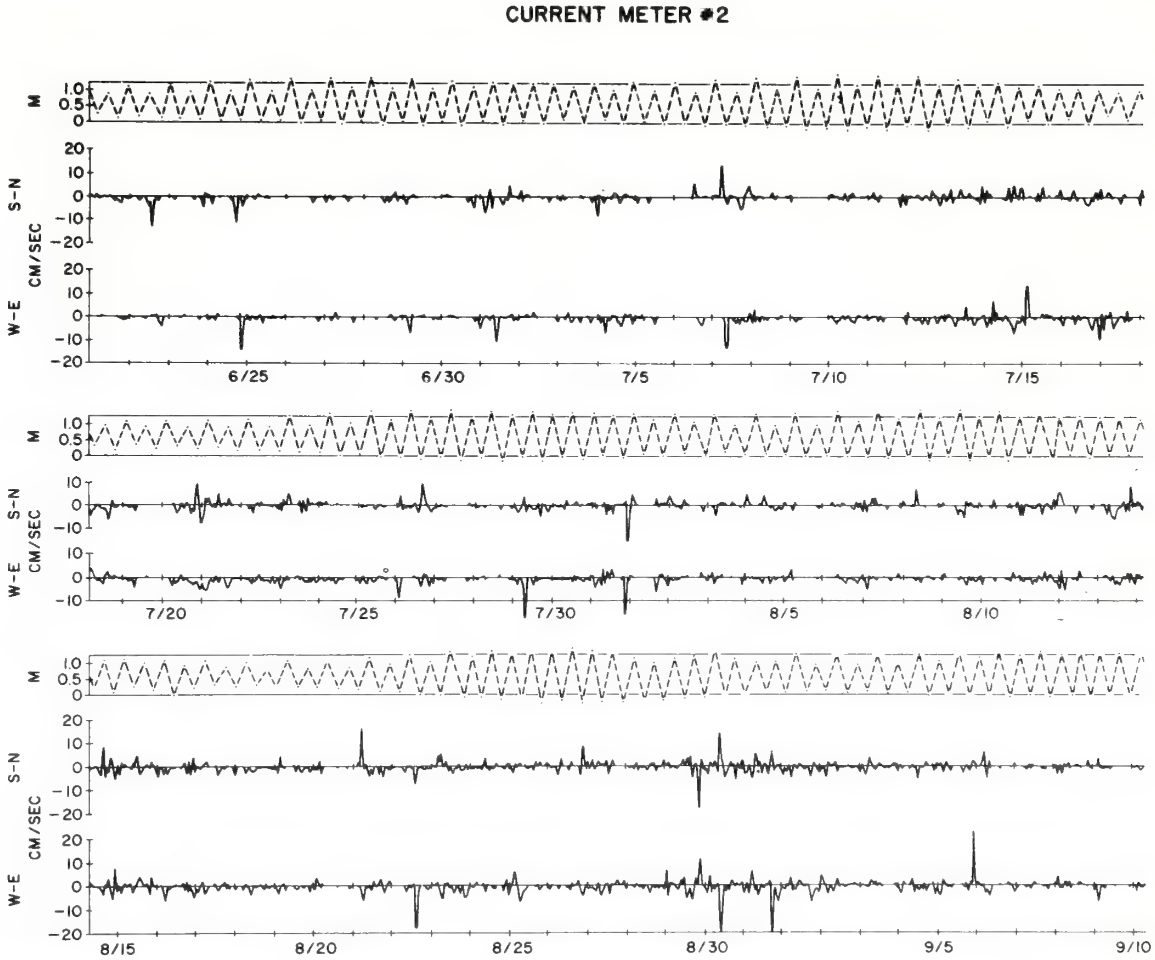

Fig.4. Current meter record of CM2. Tidal height for the same period is shown.

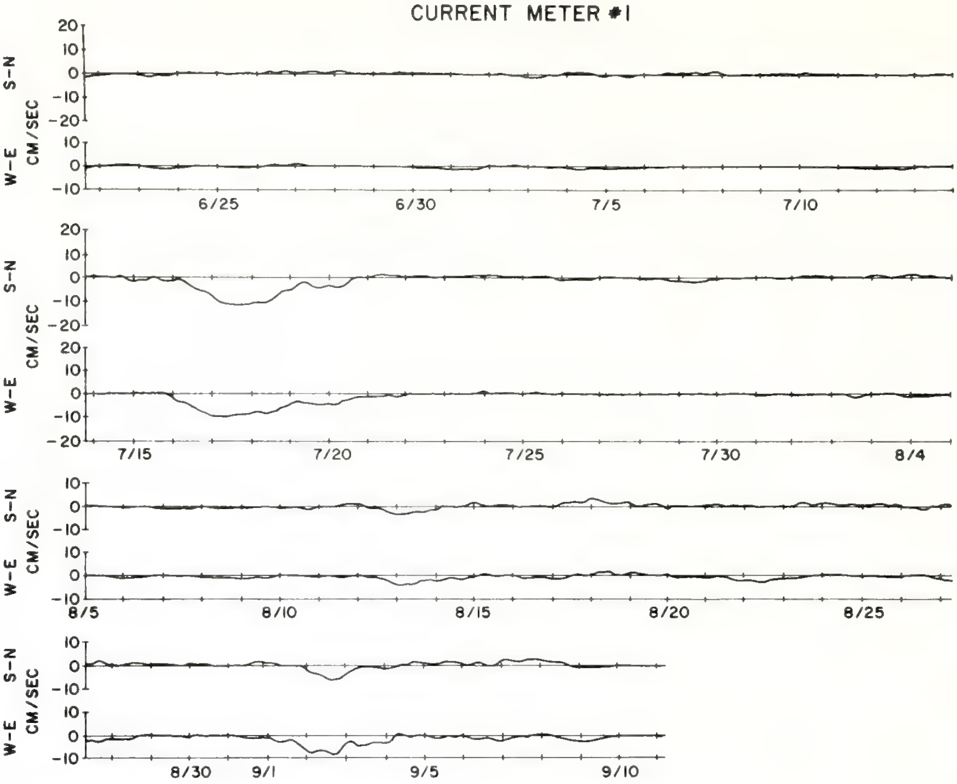

Fig.5. Current meter CM1 with the tidal flow averaged out.

valley (Fig.2). A steep slope bounds the terrace to the northeast. The valley also transverse to the continental slope is approximately 4 km wide. Keller et al. (1975) found that in a region of irregular topography, the topography can greatly influence both the velocity and direction of the currents. The presence of a steep slope northeast of CM2 may create a lee for the meter so that less of the southwest flow noted at CM1 influences this particular site.

Tidal oscillations dominate both current meter records, as indicated by the correlation of the meter and tide records (Figs.3 and 4). Tidal and internal wave effects have been found to dominate the flow in the submarine canyons off the northeast United States (Shepard, 1975, 1976; Keller and Shepard, 1978). Although up and down canyon flow occurs, in general the net transport is down canyon (Keller and Shepard, 1978). The progressive vector diagrams for each meter (Fig.6) show that on the open slope away from the confines of a submarine canyon net transport is along slope parallel to the continental margin. The line on each diagram represents the trend of the local topography. Besides the principal transport along the margin across the trend of the topography, a small amount of upslope transport is also visible on Fig. 6B.

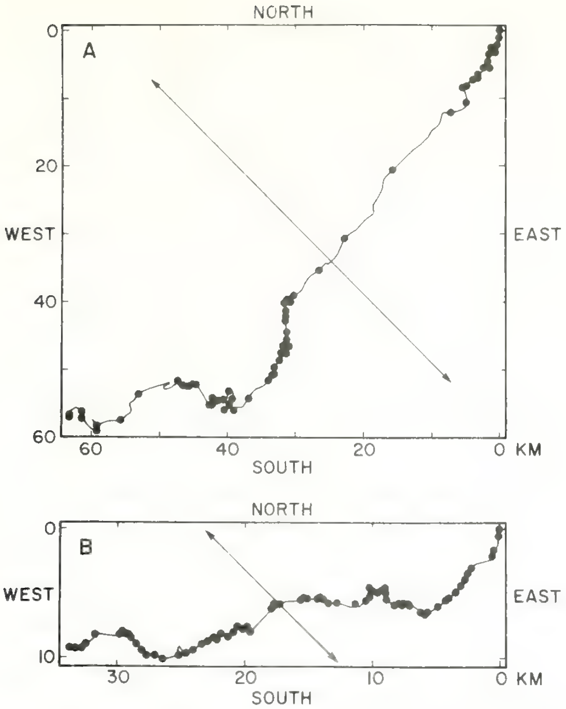

Fig. 6. Progressive vector diagrams: A = CM1; B = CM2. The dots represent days. The origin is in the upper right-hand corner. The line represents the trend of topography (ridge and valley) transverse to the slope.

Maximum current velocity measured was similar to that recorded at comparable water depths in nearby submarine canyons. Keller and Shepard (1978) reported maximum velocities of 44 and 22 cm/sec in Wilmington Canyon, 20 cm/sec in Washington Canyon, and 12 cm/sec on the slope adjacent to Washington Canyon. These measurements were for approximately two week periods during April, March, and September, respectively. This would indicate that the bottom currents on the slope in water depths between 600—900 m are similar in maximum strength to that found in submarine canyons; however, average values are greater in submarine canyons than on the slope. Bottom currents do not differ appreciably during the seasons of the year, but the short duration of the winter records may bias this apparent similarity, however.

The occurrence of the non-tidal southwesterly flow events parallel to the margin was suggested by cross-canyon flow reported by Keller and Shepard (1978), as well as their reported westerly flow in April on the shelf adjacent to Wilmington Canyon. They could find no unusual wind conditions to account for the flow. Butman et al. (1977) found on the middle Atlantic continental shelf that longshelf bottom current flow was coherent with the wind stress suggesting the currents are wind driven. Just to the north along the south coast of New England, Beardsley and Butman (1974) found that winter storms and their associated strong easterly winds set up flow along the shelf parallel to the coast.

In order to evaluate the role of atmospheric forces on the bottom currents at the slope stations, surface weather observations from Cape May to Chesapeake Lightship (36°54.3′N 75°42.8′W) were plotted and analyzed. The weather stations are both 160 km from the current meter locations. The barometric pressure was found to be high during the southwesterly transport events except for the 6-day event July 16—22, during which the pressure was both high and low. A correlation between bottom water flow parallel to the margin and barometric pressure does not appear to exist. The wind speed and direction varied between the two stations, but in general the winds were from a northerly direction before or during the times of bottom water flow along the margin. Periods of northerly winds with no apparent bottom water flow indicate that the winds alone cannot account for the southwesterly bottom water transport events. Although meteorological conditions greatly influence the shelf circulation, the slope circulation does not seem as directly related.

Although it may be fortuitous, the GOES (Geostationary Orbiting Earth's Satellite) photographs show a connected loop or a ring of the Gulf Stream in the vicinity of the meters when four of the five flow events occurred. The flow is not directly related to circulation in the ring, since the ring or loop were not directly over the site and also the direction is not compatible. The location of the meter relative to the ring would suggest flow to the northeast rather than the observed southwesterly flow.

Schmitz (1974) reported low-frequency (less than one c.p.d.) current flow parallel to the depth contours at a similar depth on the continental slope south of New England. Maximum velocity for this flow was 10—15 cm/sec, the same velocity as found on the slope south of Baltimore Canyon. Suggested mechanisms for the flow on the slope and rise include waves radiated by the Gulf Stream, atmospheric forcing, and flow associated with the passage of a Gulf Stream ring (Schmitz, 1974). The more likely mechanism Schmitz (1974) suggests is the horizontal trapping of a barotropic wave at the base of the slope-top of the rise with intensification over the slope.

On the basis of the data presented here, none of the possible mechanisms suggested by Schmitz can be selected as the single cause, nor can any be ruled out.

BOTTOM SEDIMENTS

The continental slope is a region of active sediment deposition (Doyle et al., 1975, 1976). Since the mechanism for transporting sediment onto the slope is not known, this bottom current study was undertaken to determine the effect of bottom currents. In order to assess the role of bottom currents in sediment transport and erosion, the type of bottom sediments present must be known. A series of hydroplastic and piston cores was taken in the vicinity of the current meters. Four cores were collected in water depths of 546, 705, 841, and

TABLE I

Physical properties of surface sediments

Core*	Water depth	Grain size in % by weight			Water content	Organic content
	(m)	>62 μm	62—3.9 μm	<3.9 μm	(weight %)	(% carbon)
HP-A	546	35	47	18	32	1.17
HP-B	1231	1.58	58	40.6	51	2.96
P-1	841	3.49	41.6	55.0	61	—
P-2	705	4.53	21.0	74.4	54	—

*HP = hydroplastic core; P = piston core.

1231 m (Fig.2 and Table I). The surface sediments were sandy-silt (HP-A), clayey-silt (HP-B), and silty-clay (P1 and P2) based on Link's (1966) textural classification. Core HP-A has a high surface sand content which is believed to have originated from shelf sands being transported over the shelf edge onto the slope. The surface fine sand layer, 9 cm thick, (mean grain size 0.14 mm) had apparent load structures extending into the silty-clay beneath. A similar sand layer with load structures was found on the slope northeast of Wilmington Canyon (McGregor and Bennett, 1977). Bottom currents, therefore, must be sufficient to erode and transport this shelf sand.

Young and Southard (1978) have conducted in-situ flume studies in Buzzard's Bay of fine-grained marine sediments to determine bottom current velocities capable of eroding them. They found that clayey-sandy silt (most particles <16 μm) could be eroded by a current with a velocity of 20 cm/sec or slightly less measured 100 cm above the bottom. The sediment properties shown in Table I are similar to those reported by Young and Southard (1978). The sediment they studied in Buzzard's Bay had water contents between 55 and 62 weight %, sand % by weight 6—14, silt % by weight 47—77, clay % by weight 9—46, and organic content 2—3%. Young and Southard (1978) found that the lower the organic content in the sediment, the lower the velocity necessary to erode them. Keller and Shepard (1978) have modified a threshold velocity curve of Miller et al. (1977) developed for velocities 100 cm above the bottom to a curve for velocities 300 cm off the bottom. The meters in this study recorded current velocities 300 cm above the bottom. Using Keller and Shepard's modified curve, some of the silt size cored sediments would have a threshold velocity of slightly less than 20 cm/sec.

The 20—30 cm/sec current velocities recorded during this study should be capable of eroding the sediment present on the slope and transporting the sand. The flow events in July and September had velocities sufficient to move the bottom sediments.

SUMMARY AND CONCLUSIONS

Current meter observations for 83 days during the summer of 1976 on the continental slope in 840 and 870 m of water show both tidal and sub-tidal flow. Bottom topography appears to be important in controlling the direction of flow recorded by the meters. Progressive vector diagrams show that on the slope south of Baltimore Canyon net transport is in general parallel to the margin to the southwest. Maximum velocities recorded three meters above the bottom were 30 cm/sec. Besides tidal oscillations, low frequency flow events were recorded with a maximum velocity of 10 cm/sec. The mechanisms responsible for these flow events can only be suggested. Neither atmospheric forces, surface winds,or barometric pressure, nor flow associated with a Gulf Stream loop or ring can be unequivocally correlated with each event, but they cannot be ruled out, since some correlation exists. The more likely mechanism according to Schmitz (1974) are internal waves radiated by the Gulf Stream that are trapped and intensified against the continental slope.

The passage of Hurricane Belle on August 9 over the current meter site showed no effect on the bottom currents. The storm's influence on the area lasted only one day, according to surface meteorological observations.

Physical properties, grain size, water content, and organic content, of the sediments in the vicinity of the current meters suggest, based on the findings of Young and Southard (1978), on sediments in Buzzard's Bay, that current velocities of approximately 20 cm/sec should be capable of moving the sediment. Two flow events occurred during the 83-day period with velocities of over 20 cm/sec. The surficial sand layer present on the upper slope is believed to represent spill-over of shelf sands onto the upper slope, a process discussed by Southard and Stanley (1976). Bottom currents as discussed here would aid in the transport of this material.

The cross-canyon flow occasionally found by Keller and Shepard (1978) within submarine canyons may be the result of major flow events parallel to the margin such as the events recorded during this study.

ACKNOWLEDGMENTS

I greatly appreciate the assistance of J. William Lavelle in providing computer programs and helpful discussions. Appreciation is expressed to John W. Kofoed for critically reviewing the manuscript. Frances Nastav and Sam Bush helped with the data reduction, and Fred Shields oversaw retrieval of the meters. I am grateful to George Keller and Robert Young for making available preprints of their papers. Also, thanks are extended to Donald Gaby and Stephen Baig of NOAA's Satellite Field Services Station for information on Hurricane Belle and for making available GOES satellite film loops and providing assistance in interpreting them. Surface weather observations were provided by Daniel Mitchell of the National Climatic Center and tidal data were provided by D.C. Simpson of the National Ocean Survey. Appreciation is expressed to the officers and crew of the NOAA Ship "Researcher" for their assistance in deploying and retrieving the current meters. Funds for this study were provided by the National Oceanic and Atmospheric Administration.

REFERENCES

Beardsley, R.C. and Butman, B., 1974. Circulation on the New England continental shelf: response to strong winter storms. Geophys. Res. Lett. 1:181-184.

Butman, B., Noble M,. and Folger, D.W., 1977. Observations of bottom current and bottom sediment movement on the mid-Atlantic continental shelf. EOS Trans. Am. Geophys. Union, 58: 408.

Doyle, L.J., Pilkey, O.H., Hayward, G.L. and Arbogast, J.S., 1975. Sedimentation on the northeastern continental slope of the U.S. IX Congress Internationale de Sedimentologie, Nice, 6: 51—56.

Doyle, L.J., Woo, C.C. and Pilkey, O.H., 1976. Sediment flux through inter-canyon slope area: U.S. Atlantic continental margin. Geol. Soc. Am. Ann. Meet. Abstr., 8: 843.

Keller, G.H. and Shepard, F.P., 1978. Currents and sedimentary processes in submarine canyons off the northeast United States. In: D.J. Stanley and G. Kelling (Editors), Sedimentation in Submarine Canyons, Fans and Trenches. Dowden, Hutchinson and Ross, Pa., pp.15—32.

Keller, G.H., Anderson, S.H. and Lavelle, J.W., 1975. Near-bottom currents in the Mid-Atlantic Ridge Rift Valley. Can. J. Earth Sci., 12: 703—710.

Link, A.G., 1966. Textural classification of sediments. Sedimentology, 7: 249—254.

Matthews, D.J., 1939. Tables of the velocity of sound in pure water and sea water for use in echo-sounding and sound ranging. Admiralty Hydrog. Dept. Pub. H.D. 282: 52p.

McGregor, B.A. and Bennett, R.H., 1977. Continental slope sediment instability northeast of Wilmington Canyon. Bull. Am. Assoc. Pet. Geol., 61: 918—928.

Miller, M.C., McCave, I.N. and Komar, P.D., 1977. Threshold of sediment motion under unidirectional currents. Sedimentology, 24: 507—527.

Schmitz Jr., W.J., 1974. Observation of low-frequency current fluctuations on the continental slope and rise near site D. J. Mar. Res., 32: 232—251.

Shepard, F.P., 1975. Progress of internal waves along submarine canyons. Mar. Geol., 19: 131—138.

Shepard, F.P., 1976. Tidal components of currents in submarine canyons. J. Geol. 84: 343—350.

Southard, J.B. and Stanley, D.J., 1976. Shelf break processes and sedimentation. In: D.J. Stanley and D.J.P. Swift (Editors), Marine Sediment Transport and Environmental Management. Wiley, New York, N.Y., pp. 351—377.

Uchupi, E., 1970. Atlantic continental shelf and slope of the United States-shallow structure. U.S. Geol. Surv. Prof. Pap., 529-I: 1—143.

Young, R.A. and Southard, J.B., 1978. Erosion of fine-grained marine sediments: sea-floor and laboratory experiments. Geol. Soc. Am. Bull., 89: 663—672.

32. Applied Ocean Research 1, No. 4, 177-187.

Bottom processes, morphology, and geotechnical properties of the continental slope south of Baltimore Canyon

BONNIE A. McGREGOR, RICHARD H. BENNETT and DOUGLAS N. LAMBERT
Atlantic Oceanographic and Meteorological Laboratories, National Oceanic and Atmospheric Administration, 15 Rickenbacker Causeway, Miami, Florida 33149, USA

(Received 26 December 1978; revised 18 July 1979)

The continental slope south of Baltimore Canyon seaward of the coasts of Delaware and Maryland has a different morphology and sedimentary structure than adjacent portions of the continental margin. Ridges of sediment 600 m thick and transverse to the slope contain many unconformities that can be traced from ridge to ridge. The age of the sediment is inferred to be late tertiary to recent with the morphology related to a major drainage system. Physical properties of a suite of sediment cores display a pattern that varies in relationship to the morphology and depositional environment. Sedimentary structures and low shear strengths indicate instability of surficial sediments present on the upper slope and can be correlated with regions where the seismic reflection profiles show slumping has occurred. A veneer of sand overlying the general silty clay of the area is present on the upper slope and on the ridges indicating sand spillover from the shelf with a recent change in deposition pattern.

INTRODUCTION

A portion of the continental margin was studied in detail seaward of the coasts of Delaware and Maryland (Delmarva Peninsula) (Fig. 1). A 40 × 50 km area of the continental slope south of Baltimore Canyon and seaward of the Baltimore Canyon Trough was surveyed with a grid of 1 km × 5 km spaced track lines (Fig. 2). Geophysical data collected simultaneously include narrow-beam echo sounding (NBES), 3.5 kHz, and seismic reflection profile data using a 40 in.^{3} air gun system, as well as bottom samples consisting of 3 piston cores, 19 hydroplastic cores, and one Shipek grab sample along with photographs of the seafloor (Fig. 2). These data were collected during 1975, 1976 and 1977 with the NOAA ship *Researcher*.

Navigational control was based on Loran C and satellite fixes. Water depths at track line crossings were used to refine the navigation to an accuracy of slightly less than 250 m.

Morphology of the slope and upper rise between Wilmington and Washington Canyons has a scalloped appearance in contrast to a serrated one such as north of Wilmington Canyon (Fig. 1). This suggests that the bottom processes controlling the depositional and erosional pattern for this area are different from the areas just north of Wilmington Canyon and south of Washington Canyon.

BATHYMETRY

A narrow-beam echo sounder was used to survey the bathymetry in a 1 km × 5 km grid pattern. The data are in corrected meters[1] with a 10 m contour interval (Fig. 3). The physiographic provinces[2] surveyed include the outer shelf, slope, and rise. Three ridges and four valleys are present trending downslope. The ridges extend a uniform distance from the shelf edge down the slope and have comparable heights. The southern two valleys are slightly shallower than the northern two. Only one of the valleys cuts back into the shelf edge and the northerly trend of its head is similar to the trend of the heads of Baltimore and Wilmington Canyons (Fig. 1). The ridges are approximately 6 km wide except on the upper slope where they are narrower due to the presence of many small valleys. The upper portion of the slope is dissected by many small valleys with only four main valleys remaining on the mid-slope. Offshore on the rise, two of the valleys merge and

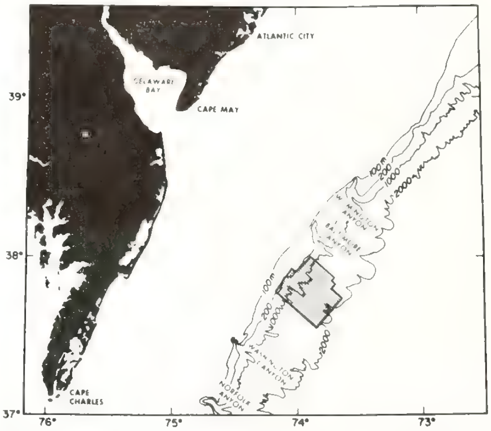

Figure 1. Index map showing location of the study area (after Uchupi[35]). Depth in metres.

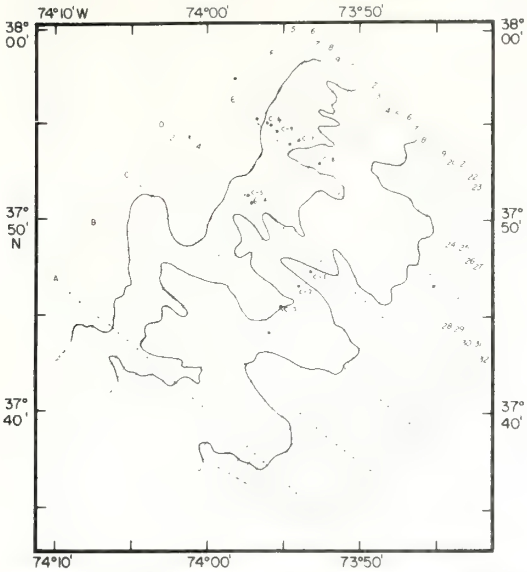

Figure 2. Survey grid showing trackline locations on the generalized bathymetry, 500, 1000 and 1500 m contours. ●, Bottom sample locations.

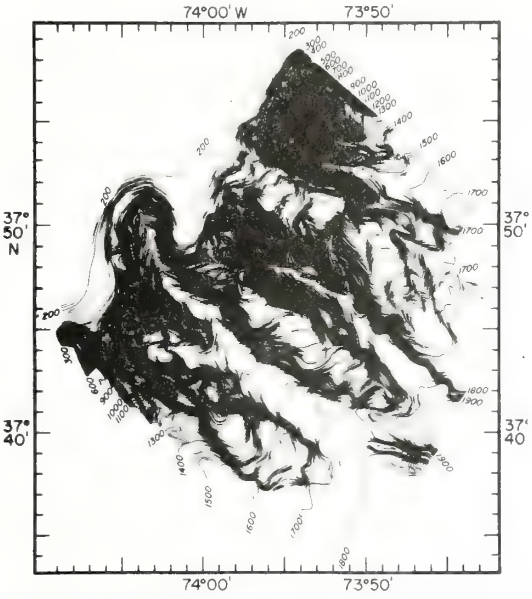

Figure 3. Bathymetric chart. Data in corrected metres[1] with a 10 m contour interval.

the intervening ridge terminates. A low linear ridge approximately 100 m high is present on the southeast side of this valley and appears to have no surface connection to the ridges on the slope. Decrease in seafloor gradients and inversion of contours in many areas, especially the northwest portion of the survey, suggests gravity movement of material downslope.

Profiles of bathymetry normal to the slope show that the ridges are convex up (profiles A and C, Fig. 4). The valleys shown on profiles B and D (Fig. 4) have a profile that is concave up. The profiles of the seafloor suggest the ridges represent accumulations of sediment deposited on the slope and that the valleys are erosional features.

The slope of the seafloor varies with the morphology as indicated by the contour spacing on Fig. 3. The upper portion of the slope, especially in the northwestern section (Fig. 3) and profile F (Fig. 4), has the steepest slope of about 9 to 10 . In general, the gentlest seafloor gradient, approximately 2 , was found in the axis of the four valleys, such as the seaward half of profile B (Fig. 4). The axis of the ridge crests was intermediate with a gradient of approximately 4 (profile C, Fig. 4).

Profiles 1–5 (Fig. 5) are parallel and close to the self edge. Two valleys are eroded into the shelf edge, exposing older, flat-lying horizons. On profiles 1 and 2, infilling of the valleys has occurred. Buried erosional features are present on the northeast of profile 5. On profiles 3 – 5 the valleys appear erosional with apparently slumped sediments at the base of the northeast wall on profiles 4 and 5. Terraces on the valley walls (profile 5) are associated with reflecting horizons. The continuous reflecting horizon labelled A (Fig. 5) is believed to be late tertiary in age, correlating with horizons found in Baltimore Canyon by Kelling and Stanley[3].

Further seaward, profile 10 traverses the upper slope (Fig. 6) and shows dissection by many small valleys. Farther offshore in the mid-slope area the valleys decrease in number (profile 18). The valleys are erosional features

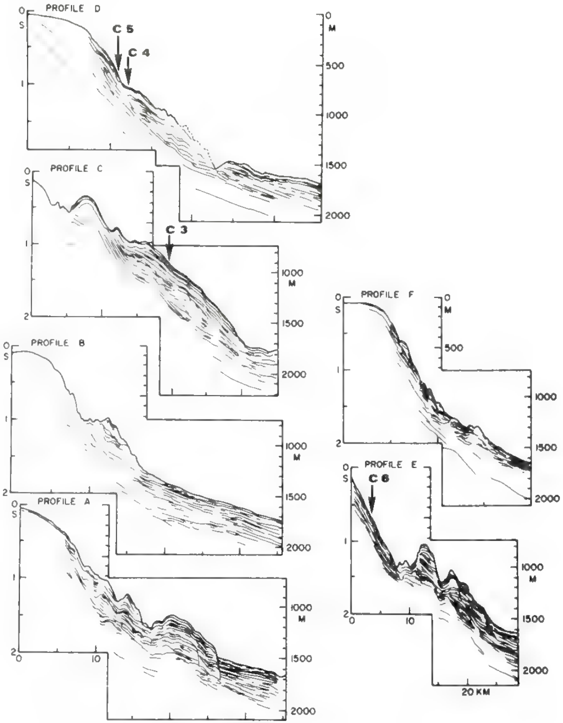

Figure 4. Seismic reflection profiles normal to the continental margin (see Fig. 2 for profile locations). Profiles are oriented NW to SE (left to right). Depth scales are two-way travel time in seconds and metres based on a sound velocity of 1500 m/s. Vertical exaggeration = 12 × and 18 ×.

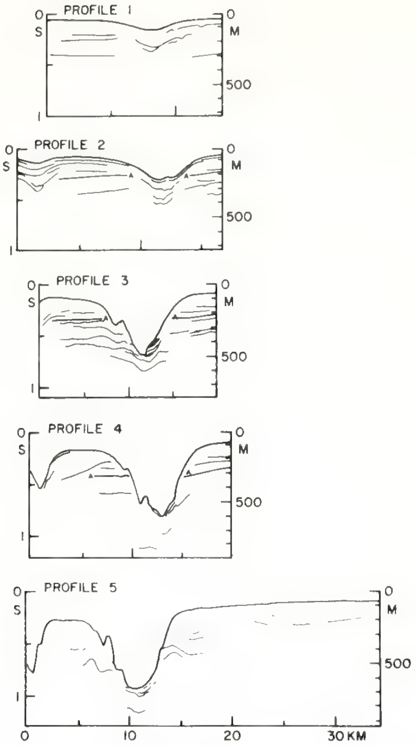

Figure 5. Seismic reflection profiles parallel to the shelf edge and oriented SW to NE. Depth scales are two-way travel time in seconds and metres based on a sound velocity of 1500 m/s. Vertical exaggeration = 14 ×.

as can be seen by the truncation of reflecting horizons in the walls of the valleys. The intervening ridges are composed of stratified sediments with many unconformities. The unconformities resembling erosion surfaces appear to be correlatable from ridge to ridge, but the depositional horizons are discontinuous over small distances, making them impossible to correlate. The ridges show both depositional and erosional phases, but more deposition than erosion has allowed the ridges to build up with time. Some of the valleys appear to have been in the same location for long periods based on the location of buried valleys (profile 12). Other valleys have migrated back and forth, based on the shape and location of the buried ridges (profile 16). In some cases more valleys existed in the past, as shown on profile 13 within the ridge between kilometers 20 and 30. The ridges and valleys are underlain by rather flat continuous reflecting horizons, between 1400 m (1.9 s) on profile 10 and 1900 m (2.3 s) on profile 18. The large volume of sediments composing the ridges has been piled on this rather flat surface.

On the lower slope and upper rise, the topography is much smoother (profiles 19–28, Fig. 7). A line spacing of 2 km exists between profiles 18 (Fig. 6) and 19 (Fig. 7) instead of the usual 1 km spacing. The valleys continue downslope to the rise, where they are broader than on the mid-slope portions. The ridges in profiles 19–25 are composed of stratified sediments with many erosional unconformities. On the rise profiles 26–28 the ridges have died out except for the two ridges flanking the main valley at kilometer 15. The ridge on the northeast side of the valley has continuous flat-lying reflecting horizons. Buried unconformities are present on the rise beneath this sequence of horizons (profile 27). Erosional surfaces appear to be correlatable from ridge to ridge (profiles 19–25).

Continuing farther offshore on the upper rise (profiles 29–32, Fig. 8), two ridges and the intervening valley are present. The ridge on the northeast is composed of continuous flat-lying horizons, and the ridge itself is an erosional feature with the reflecting horizons truncated in the flanks of the ridge. The northeast wall is very steep, giving no echo return, suggesting recent erosion. Reflecting horizons at a depth of approximately 2100 m (2.9 s) on profiles 31 and 32 are continuous for 20 km. They appear to be an erosion surface based on the truncation of internal reflecting horizons. A valley in this surface is narrower than the present seafloor valley and is displaced to the southwest. Except in the ridge on the northeast, the reflecting horizons are irregular, suggesting alternating periods of erosion and deposition.

Six profiles (A–F) as tie lines for the bathymetric and seismic reflection grid were run normal to the continental margin with 5 km line spacing (Fig. 4). Each profile shows a different surface morphology, depending on the ridges and valleys crossed. The sediments are thin on the upper slope and thicken on the mid and lower slope. Profiles A and C are, in general, along ridges, and show the large volume of sediment present on the slope which comprises the ridges. Numerous deposition and erosion cycles with progradation of the ridge seaward are shown in the ridge between kilometers 20 and 26 on profile A. Renewed deposition has occurred at the toe of the ridge on the rise (profile A). Small scarps at the toe of the ridge, kilometer 30 on profile C, suggest erosion is presently occurring. Profile B primarily shows the discontinuous, less irregular

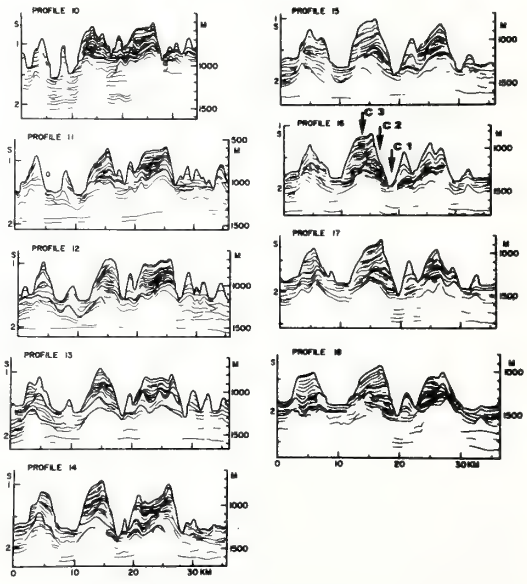

Figure 6. Seismic reflection profiles on the upper and mid-slope oriented SW to NE. Depth scales are two-way travel time in seconds and metres based on a sound velocity of 1500 m/s. Vertical exaggeration = 14 ×.

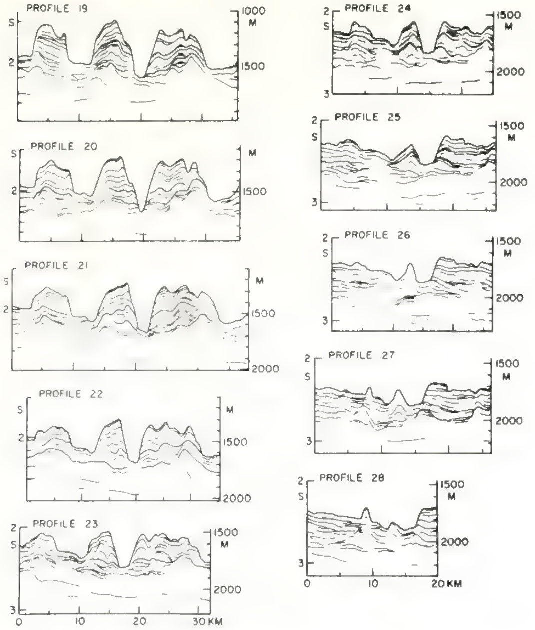

Figure 7. Seismic reflection profiles on the lower slope and upper rise oriented SW to NE. Depth scales are two-way travel time in seconds and metres based on a sound velocity of 1500 m/s. Vertical exaggeration = 18 ×.

reflecting horizons in a valley, kilometers 15–35. A diffuse bottom return is present on the mid-portion of profile D, suggesting a very irregular surface topography. The upper slope of profiles E and F has less sediment accumulation; this area is dissected by many small valleys (Fig. 3). Slumps are present on this portion of the upper slope (profiles E and F). A ridge is crossed on profile E showing periods of erosion and deposition with building of the ridge up and also seaward.

ORIGIN OF THE SLOPE MORPHOLOGY

The morphology on the slope and rise between Wilmington and Washington Canyons with its scalloped appearance (Fig. 1), is similar to the slope seaward of Sable Island Bank, Nova Scotia[4]. The distance between the 200 and 2000 m contours is also greater between Wilmington and Washington Canyons than to the north (Fig. 1). Comparing the distance between the 200 and 2000 m contours all along the Atlantic east coast margin from Cape Lookout, North Carolina, to Cape Sable Island, Nova Scotia, two areas have a broad contour spacing of approximately 50 km: (1) seaward of the Delmarva Peninsula; and (2) seaward of Nova Scotia[5]. The continental slope and upper rise in both these areas have been either built farther seaward or eroded less than adjacent regions.

Although the morphology is similar, the processes active in each area seem to have been different. Stanley and Silverberg[4] believe that the scalloped topography off Nova Scotia is due to mass-gravity processes throughout the tertiary, resulting in large slide blocks on the lower slope and rise. Slumping has occurred on the Delmarva slope, but the large ridges are not slump blocks. Large submarine slides on the slope and rise northeast of Wilmington Canyon had a well-defined slip surface and lacked continuity of reflecting horizons above the slip surface[6,7]. The correlation of reflecting horizons from ridge to ridge on profiles 10 and 24 (Figs. 6 and 7) and the buried undulating horizons beneath the ridges on profiles 10 and 22 (Figs. 6 and 7) indicate no slip surface is present, ruling out a slump block origin for the ridges.

Seismic reflection profiles on the African continental slope off Wadi Craa, Spanish Sahara[8] show buried ridges and valleys with similar internal structure to those studied here, and a broadening in the seaward extension of the 3000 m isobath. They believe that both the buried morphology and the contour spacing indicate a major drainage system. The submarine canyons on the US east coast suggest drainage systems have influenced this margin (Fig. 1). Baltimore and Wilmington Canyons are believed to be associated with the Delaware Bay drainage system[3] and the buried ancestral Delaware River valley has been traced across the shelf to Wilmington Canyon[9]. Washington and Norfolk Canyons to the south may be associated with a Chesapeake Bay system[10]. The location of this detailed study is between these two canyon pairs closer to the Delaware drainage system (Fig. 1). The volume of sediment on the slope profiles A and C (Fig. 4) would seem to favour proximity to an active drainage system which built the slope seaward.

The age of the reflecting horizons shown on Figs. 4–8 can only be inferred from dated drilled samples from

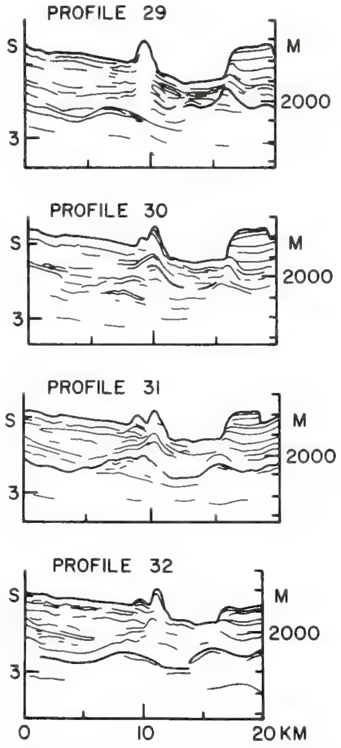

Figure 8. Seismic reflection profiles on the upper rise oriented SW to NE. Depth scales are two-way travel time in seconds and metres based on a 1500 m/s sound velocity. Vertical exaggeration = 16 ×.

Table 1 Statistics of the core geotechnical properties giving maximum, minimum and average values for each property

Core No.	Core length (cm)	Water depth (m)		%w_p Plastic limit	%w_l Liquid limit	%w_n Water† content	I_l Liquidity index	I_p Plasticity index	%S Sand	%Si Silt	%C Clay	Cohesion natural (kPa)	Cohesion remould (kPa)	Sensitivity S_t	Wet unit weight γ_t (Mg m^{-3})	%n Porosity	G_s grain specific gravity
1	226	1570	max	53	100	164	2.4	57	3	46	60	8.4	2.8	6.7	1.52	82	2.74
			min	35	80	73	1.3	33	1	38	52	3.4	1.0	2.3	1.42	66	2.62
			av	43	90	107	1.5	47	2	43	55	6.1	1.6	4.0	1.43	74	2.71
			max	51	98	148	1.6	62	4	66	52	10.8	3.2	3.9	1.53	80	2.78
2	127	1370	min	32	80	73	1.0	33	2	45	29	2.0	1.4	1.1	1.35	69	2.70
			av	38	87	90	1.2	48	3	52	45	6.8	2.4	2.6	1.48	72	2.73
			max	47	84	130	2.1	47	3	52	57	6.2	2.8	3.1	1.56	78	2.79
7	148	899	min	28	61	56	1.3	29	1	41	45	2.0	0.8	1.4	1.38	69	2.69
			av	36	73	94	1.7	37	2	48	50	3.8	1.9	2.2	1.46	73	2.73
			max	51	111	137	1.4	68	2	58	48	12.7	3.4	3.9	1.43	78	2.73
8	119	1229	min	41	99	110	1.2	51	1	51	41	2.8	1.0	2.2	1.37	75	2.69
			av	48	105	121	1.3	57	1	54	45	5.4	1.7	3.1	1.40	77	2.71
			max	31	63	110	2.2	33	48	55	73	9.2	4.0	7.6	1.73	72	2.84
3	267	1001	min	23	50	50	1.2	25	1	26	23	3.1	0.8	1.4	1.50	58	2.74
			av	28	56	79	1.8	27	7	31	62	5.5	1.7	4.0	1.57	68	2.79
			max	33	51	62	1.4	20	4	43	63	5.8	2.7	3.3	1.75	63	2.81
4*	200	841	min	27	46	30	1.1	15	3	34	53	1.9	1.6	1.1	1.65	58	2.77
			av	30	48	52	1.2	19	3	40	57	3.9	2.0	2.0	1.72	60	2.79
			max	32	51	54	1.2	21	10	46	74	26.3	5.5	5.6	1.94	60	2.82
5*	505	705	min	25	41	34	0.6	14	2	21	48	8.7	2.5	2.3	1.71	49	2.75
			av	29	46	46	1.0	17	5	39	56	15.0	3.8	4.0	1.78	56	2.78
			max	27	44	53	1.8	19	36	46	65	17.6	5.4	3.7	1.88	59	2.83
6	190	448	min	24	39	37	1.0	14	2	27	38	7.0	2.5	1.7	1.72	51	2.76
			av	25	42	46	1.3	16	6	37	57	10.8	4.1	2.7	1.79	56	2.79
			max	27	53	73	1.9	26	18	39	65	13.5	4.1	5.0	1.73	66	2.83
9	81	619	min	24	45	53	1.4	20	2	29	46	3.7	1.0	1.2	1.56	60	2.64
			av	25	48	61	1.7	23	7	34	59	9.6	3.8	2.6	1.64	64	2.78

* The topmost sand layers on these piston cores were not recovered, although it was recovered in the pilot core. Data on the sand layers in the pilot core are not included here

† Water contents uncorrected for salt

adjacent areas. DSDP site 108 is located on the continental slope in 1845 m of water, 130 km to the northeast, seaward of New Jersey. Horizons of eocene (horizon A) and eocene–cretaceous boundary age were identified[11]. Tracing these horizons south on a profile parallel to the margin[12], the flat horizon at depth on profiles 11–26 (Figs. 6 and 7) is believed to represent the cretaceous–eocene boundary. Kelling and Stanley[3] made the same age correlation for a buried flattish horizon in the vicinity of Baltimore and Wilmington Canyons. The horizon on profiles 2–4 (Fig. 5) at 0.3 to 0.4 s may be late tertiary in age, probably miocene[3,13]. The sediments comprising the ridges, therefore, are believed to be tertiary and quaternary in age, since they are deposited on a horizon believed to represent the eocene–cretaceous boundary. A pre-quaternary age for a major drainage system in the area is supported by the work of Laine[14]. He contoured the top of the pliocene sediments based on seismic reflection data on the lower rise, and found this pliocene surface to be a high, seaward of Hudson Canyon, and also seaward of the region between Norfolk–Washington and Baltimore–Wilmington Canyons. Those highs are believed to represent large volumes of pliocene sediments which have been transported seaward[14].

The Nyckel Ridge is a feature transverse to the slope flanking the south side of Wilmington Canyon. Pratt[15] interpreted the Nyckel Ridge to be a levee associated with Wilmington Canyon. The morphology and internal structure as described by Stanley and Kelling[16] are similar to the ridge features found on the slope south of Baltimore Canyon, and they identify the Nyckel Ridge as a structural feature of pre-quaternary age. Its continuity from shelf to slope, high relief, and consolidated rock outcrops rule out an overbank deposition origin[16]. Although many similarities exist between the Nyckel Ridge and the ridges of this study, a structural origin is not supported. The ridges south of Baltimore Canyon appear to have formed by a series of depositional and erosional events, based on the many unconformities in the ridges, as opposed to one major period of deposition followed by erosion and down-cutting of the valleys. This implies a major drainage system is buried beneath the shelf south of Baltimore Canyon. The data of Twichell *et al.*[9] in the vicinity of Wilmington Canyon did not show any branches off the ancestral Delaware River valley. The implied drainage system on the shelf to the south, however, may be older than the ancestral Delaware River valley found by Twichell *et al.*[9] and buried deeper than their seismic source penetrated. Profiles 1 and 2 (Fig. 5) show burial of the valleys on the shelf by approximately 200 m of sediment.

SEDIMENTS AND SELECTED GEOTECHNICAL PROPERTIES

Sixteen piston and hydroplastic cores were collected in locations considered representative of major morphological features and depositional environments; nine of these cores were analysed in detail (Table 1; Figs. 9 and 10). Sediment characteristics and geotechnical properties can be associated with the upper continental slope, ridge, valley, and valley walls within the study area. Sediment properties of two cores from a small submarine slide on the upper slope were investigated. The slide occurred in surficial sediment at water depths of approximately 700–800 m near the head of a major valley. The suite of samples are discussed, but profiles of the sediment and geotechnical data are shown of only a few representative cores which are plotted relative to the bathymetry (Figs. 2, 4 and 6).

Sediments

Sediments of the upper continental slope, to water depths of approximately 900 m, are characterized by as

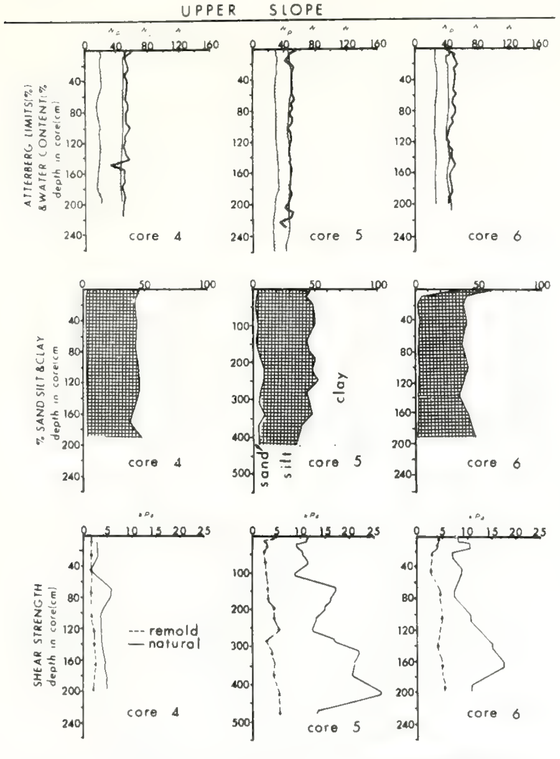

Figure 9. Profiles of the geotechnical properties of selected cores from the upper slope.

much as a few tens of centimeters of olive-gray (5Y4/2) silty sand and sandy silt overlying a dark grayish-brown (2.5Y4/2 to dark gray 5Y4/1) silty clay[17]. The topmost sand fractions are primarily quartz grains with lesser amounts of calcium carbonate foraminiferal tests, faecal pellets, mica, and heavy minerals in decreasing order of abundance. In the top-most sandy material, nearly all upper slope cores contained fine-grained, relatively stiff 'clay balls' which are probably the result of clay bed erosion on the continental shelf with subsequent deposition on the upper slope. The contact between the overlying sand and the silty clays is very sharp and highly undulatory. In several cores, 'sand balls' or clasts are present in the silty clays indicating the presence of load structures similar to those found on the upper slope north of Wilmington Canyon[18]. These apparent load structures represent unstable conditions and probably develop contemporaneously with slow creep of sediments down the continental slope[19].

The underlying silty clays are characterized by very abundant black pockets or 'splotches' (possibly hydrotrolite) approximately 1 to 2 mm in diameter throughout the cores. The sand fraction, normally less than a few percent of the sediment mass, is composed primarily of quartz, with lesser amounts of mica, pyrite, and heavy minerals. Calcium carbonate is conspicuously absent in this silty clay. Radiographs of the cores show that authigenic pyrite is common and occurs as burrow replacements and globular masses within 7 cm of the top of the core, although it is found more commonly deeper within the cores. The lack of foraminiferal tests in this silty clay sediment below the overlying sands is possibly a function of the present reducing environment which can cause a slightly acidic condition and dissolution of the tests[20]. The lack of foraminiferal tests in the silty clays may be due to a 'dilution' effect by abundant deposition of terrigenous muds that greatly reduces the relative percentage of the biogenic material. The overlying sands represent a significant change in depositional environment on the upper slope following the deposition of the silty clays. The radiographs also show that the silty clay was actively bioturbated in the past, but based on the absence of recent burrows, apparently is not being presently reworked in the current reducing conditions.

In contrast to the upper slope sediments, the cores taken in the valley and valley walls further down the continental slope are composed of relatively homogeneous olive-gray (5Y3/2) to dark olive-gray (5Y4/2) silty clays and clayey silts. These sediments are highly bioturbated by recent burrowers and contain numerous filled and unfilled burrows. The sand fraction from these cores, generally only a few percent of the total sediment mass, is primarily composed of planktonic foraminifera, with lesser amounts of benthic foraminifera, quartz, mica, and heavy minerals. No authigenic pyrite was found in any of these cores, nor any topmost silty sands as in the ridge and upper slope cores.

One core (C-3, Fig. 2) from a large ridge between two valleys contains a topmost sandy layer (48%) which is underlain by a dark grayish-brown (10YR4/2) silty clay. The sand fraction of the topmost sand is composed of approximately 60% foraminiferal tests, 30% quartz and 10% mica and faecal pellets. This sandy material is very similar to the sands overlying the finer-grained sediments on the upper slope, but here foraminiferal tests, rather than quartz, dominate. Radiographs reveal that the entire

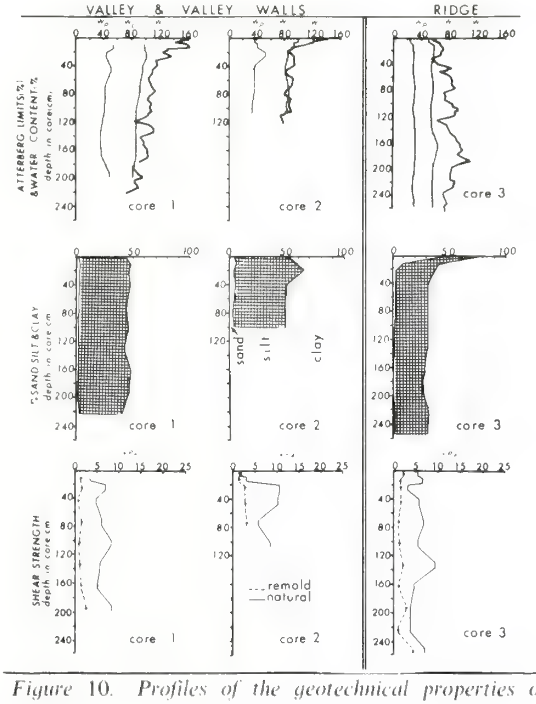

Figure 10. Profiles of the geotechnical properties of selected cores from the valley and valley walls and ridge.

sediment core is heavily reworked by burrowing organisms. Calcium carbonate tests dominate the sand fraction in the upper part of the silty clay core but decrease with depth and the sand fraction is dominated by quartz and mica below about 70 cm. Oxidized pyrite is present in the deeper part of the core, indicating possible erosion from the upper slope and redeposition on this ridge.

Geotechnical properties

Upper slope. The silty clay upper slope sediments display similar Atterberg limits and natural water contents. Plastic limits are very uniform and variability is low with core depth. Decrease in water content, w, with depth is very gentle and markedly different in depth profile from the valley and valley walls (cores 1 and 2), and the ridge (core 3) sediments (Figs. 9 and 10). Water contents are close to the liquid limit, but in general only slightly higher. The low variability of the Attberg limits for the upper slope sediment is probably due largely to the relatively uniform grain size and mineralogical composition with core depth (numerous Atterberg limits were tested on 7 cm subsections of the cores). Skempton[21] and Lambe and Whitman[22] have discussed relationships among Atterberg limits and related indices (plasticity index equals the liquid limit minus the plastic limit, $I_p = w_L - w_p$) particle size, and the percentage of clay minerals and species present in soils. Fine-grained sediments having similar grain size and mineralogical compositions, specifically similar clay minerals, would be expected to display common Atterberg limits. The upper slope sediments are characterized by relatively uniform grain-specific gravities, G_s averaging 2.78–2.79 and wet unit weights γ_t averaging 1.72–1.79 Mg/m^3, with the exception of a short core (9) which averages 1.64 Mg/m^3. This low wet unit weight average correlates with the average water content for core 9 which is somewhat higher than the averages for this suite of cores. The very uniform grain-specific gravities may indicate uniform mineralogical composition of the cored sediment.

Undrained shear strengths determined with a miniature vane shear apparatus (vane rotation rate 1.7×10^{-2} rad/s or 60°/min) reveal 'typical' increases with depth in the upper slope sediment cores in both the slide scar area (core 5) and a presently stable area (core 6) which apparently has not experienced mass movement. Shear strengths average 10–15 kPa (undisturbed or natural) and approximately 4 kPa (remoulded) in the upper 5 m of unslumped, relatively stable sediments (Fig. 9, cores 5 and 6). Sensitivities (S_t–ratio of the natural to remoulded shear strength) average about 3–4. Values of 4–8 are characteristic of sensitive clays indicating a strength loss of 75–87.5% through remoulding, whereas values of 2–4 are considered diagnostic of normal clays. Sensitivities of 4 are common for submarine sediments, particularly terrigenous deposits, whereas carbonates and 'red clays' usually have higher sensitivities[23]. Shear strengths of the slumped material (Fig. 9, core 4) downslope from the slide scar averaged slightly less than 4 kPa or approximately one-fourth to one-third of the average shear strength of the stable and slide scar area sediments. Shear strengths of the remoulded material averaged 2 kPa and sensitivity averages 2, or one-half the sensitivity of the upper slope unslumped sediment.

The sediment of cores 4, 5 and 6 is clearly of the same 'generic' type as reflected in the texture, composition and fundamental properties (compare Atterberg limits of cores 4, 5 and 6), despite the remarkable difference in shear strength profiles.

Valley and valley walls. The geotechnical properties characterizing the valley and valley wall silty clays and clayey silts differ markedly from the upper slope and ridge sediments. The percentage of silt in the valley and valley wall deposits averages 10–15% higher than in the upper slope sediments and is considerably higher than the ridge core C-3 (Figs. 6, 9 and 10). Even though the silt content is higher in contrast to the upper slope and ridge sediments, the natural water contents are considerably higher in comparison. Usually finer-grained deposits are associated with higher water contents in comparison to coarser sediments. Water contents average approximately 90–120% and may reflect greater quantities of finer silts than is present in the upper slope and ridge cores, although detailed grain size data are not available. Depositional environment and mode of deposition may be an influencing factor controlling the observed differences in water content between the various deposits in this study area. The highly bioturbated character of the valley and valley wall sediments undoubtedly contributes to the overall high water contents observed.

The water contents of the valley and valley wall sediments are strikingly different from the upper slope sediment, not only in overall magnitude but also in relationship to the liquid limit (Fig. 10, cores 1 and 2; Fig. 9, cores 4, 5 and 6). The liquid limit is the empirical boundary between the plastic and liquid (fluid-like) states, and remoulding of a sediment having a natural water content higher than the liquid limit transforms the material into a viscous slurry[24]. Natural water contents averaging approximately 90–120% are considerably higher than the liquid limits, which average 73–105%. Thus these valley and valley wall sediments exhibit a state much more susceptible to fluid-like behaviour if remoulded or shocked than sediments of the upper slope. In addition, liquid limits and plastic limits are considerably higher in the valley and valley wall sediments with a commensurate increase in plasticity index compared to the other sediments investigated. Although water contents decrease markedly but vary with core depth, the Atterberg limits are markedly uniform. On the average, liquid limits are higher by a factor of two or greater, and plastic limits are higher by a factor of slightly less than two as compared with the upper slope deposits. Likewise, in comparison, the range of water contents over which the valley and valley wall sediments remain plastic, as defined by the plasticity index, is considerable.

In harmony with the high water contents found for these sediments, shear strengths are low with core depth. Sensitivities range from 2 to 4 on average, and shear strengths are low for both natural and remoulded material. Average shear strength values for the valley and valley wall cores range from about 4 to 7 kPa, but commonly exhibit values averaging approximately 6 kPa and less. This is on the order of one-half the value for the shear strengths found for the upper slope undisturbed or unslumped deposits. The relatively low wet unit weights of 1.40–1.48 Mg/m^3 (range of average values for each core) and the grain-specific gravities averaging 2.71 to 2.73, are also noteworthy. Although the range of average grain-specific gravity values is small among the cores, the variability with core depth is considerable and much more variable than the upper slope deposits. The variable grain-specific gravities with core depth suggest changes in depositional patterns in the valley and valley walls and a more variable mineralogy compared with the upper slope surficial sediments.

Ridge. A single core, C-3, recovered from approximately 1000 m of water on a major ridge, displays characteristics intermediate with the properties of the cores sampled from the upper slope and the valley and valley walls. Sand content in the upper few centimeters reaches 48%. Below 20 cm it is less than 5% but averages 7% for the entire core. Silt and clay contents average 31 and 62%, respectively, reflecting the highest percentages of fines observed for the cores collected in this study area (Fig. 10, core 3). Despite the relatively high clay content relative to the other cores, however, water content averages only 79%, which is considerably lower than the valley and valley wall cores but higher than the upper slope cores. Likewise, the Atterberg limits are noteworthy, having liquid and plastic limits that are exceptionally uniform with core depth (Fig. 10, core C). Although the plastic limits are essentially comparable with the upper slope cores, the liquid limits are somewhat higher but considerably lower than the valley and valley wall sediments. Consequently, the plasticity index (av. $I_p = 27\%$) is intermediate with these other two groups of sediments.

Shear strengths are low, averaging 5.5 kPa over the entire length of the core with sensitivities averaging 4.0 despite the overall very low shear strength profile. The lack of 'normal' increase in shear strength and decrease in water content with core depth indicates a rather low degree of consolidation or underconsolidation over the cored interval for this ridge sediment (Fig. 10, core 3). Wet unit weights averaging 1.57 Mg/m^3 show an atypical, slight decrease in density with core depth, also suggesting a state of underconsolidation and a subtle increase in clay size material with depth. Grain-specific gravities average 2.79 but show a slight increase with core depth which, under conditions of relatively constant water content, would tend to slightly increase the wet unit weights with depth below the sediment-water interface[25]. In general, the mass physical properties of the ridge core are relatively uniform with core depth below the topmost sand layer, with the exception of water content, and examination of radiographs of the core revealed a rather homogeneous material but good core quality (undisturbed). The deposit is relatively homogeneous in texture within the cored interval. The one ridge core indicates that the ridge material appears to be underconsolidated relative to the upper slope and the valley and valley wall sediments. This relative degree of underconsolidation may be influenced by the somewhat higher overall clay content commensurate with low permeabilities, thus inhibiting the dewatering process with increasing depth of burial. As with the valley and valley wall sediments, bioturbation is undoubtedly a significant factor contributing to the relatively higher water contents with core depth compared with the upper slope cores. Bioturbation would be expected to inhibit dewatering and normal consolidation processes. Although speculative, the ridge sediments may be experiencing creep in a net downslope direction, thus inhibiting the development of strong interparticle bonds that contribute to shear strength development. The mass properties of the ridge core sediments are clearly atypical of the upper slope sediments and valley and valley wall deposits, but they more closely resemble the latter.

DISCUSSION

Significant differences are observed in the geotechnical properties of the cores from the upper slope, ridge, and valley and valley walls, although some similarities do occur. Textural differences in sand/silt/clay percentages are not remarkable, with the exception of the ridge core that is characterized by considerably more clay-sized material than observed in the other cores, and silt is more abundant in the valley and valley wall cores. The percentage of sand is low throughout all of the cores, although the presence of a topmost sandy layer, several centimeters thick, is common to virtually all the cores collected on the upper slope and on the ridge. The occurrence of the topmost sand is not obvious in cores 4 and 5 (Fig. 9) because it was washed out during coring. The pilot cores, however, recovered with cores 4 and 5 retained the topmost sand layer. The sandy material also was retained in the ridge core sample (Fig. 10, core 3). Quartz is dominant in the sand fraction of the topmost material of the slope cores whereas foraminiferal tests are the predominant sand-sized constituent of the topmost ridge sediment. These coarse sandy deposits represent a major change in depositional environment and energy levels on the upper continental slope following the deposition of the underlying silty clays and clayey silts. Since planktonic and lesser amounts of benthic foraminifera dominate the sand fraction (only a few percent) of the valley and valley wall sediments, it is inferred that only a small amount of shelf sand is reaching and thus being deposited in the valleys within this study area.

Statistics of the geotechnical properties giving maximum, minimum and average values for nine of the longest cores available are presented for comparison (Table 1). The Atterberg limits, indices, and water content relationships among the cores are noteworthy as follows: liquid and plastic limits are uniform with depth in the upper slope and the ridge cores compared with the valley and valley wall samples. This is exemplified in the profiles (Figs. 9 and 10) and in the maximum and minimum values and ranges (Table 1). Uniformity appears to be the rule in the upper slope and ridge sediments; however, the average liquid limit and plasticity index is significantly greater for the ridge core. Greater clay-sized material and an increase in organic material due to bioturbation are probably important factors affecting the liquid limits compared with upper slope cores. Mass property variability, high liquid limits and relatively high plasticity indices are common for the valley and valley wall sediments. Likewise, these sediments were found to be highly bioturbated.

The relationships among the Atterberg limits for the cores are clearly revealed in the plasticity chart of liquid limit *versus* plasticity index (Fig. 11). Following the classification of Skempton[21], the upper slope sediments are characterized by low plasticity. The ridge sediment is of intermediate plasticity whereas valley and valley wall deposits are clearly medium to high plasticity and show the greatest range or variability of the cores collected. Undoubtedly not only textural properties but also depositional environment, mineralogy, bioturbation, and perhaps relative age of the deposits contribute to the nature of the Atterberg limits are revealed by the plasticity

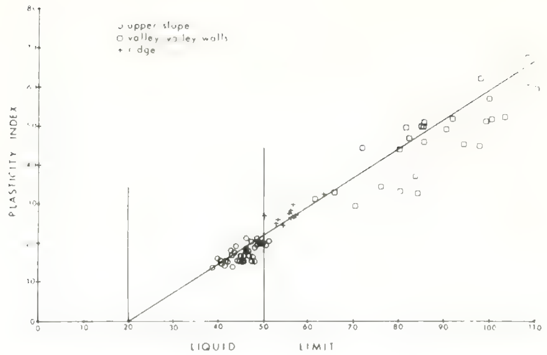

Figure 11. Plasticity chart showing the relationships among the Atterberg limits for the upper slope, valley and valley walls, and ridge cores.

chart. Applications and relationships of the Atterberg limits and plasticity chart were originally discussed by Casagrande[26,27]. In a local area of the continental slope northeast of Wilmington Canyon, Bennett *et al.*[18] found the upper slope sediment to be predominantly of low plasticity ($I_p = < 20\%$ and $W_L < 45\%$).

High water contents relative to the liquid limits are characteristic of the ridge sediment core and are common in the valley and valley wall deposits. The latter show a typical decrease in water content with core depth characteristic of 'normal' consolidation processes and dewatering (Fig. 10). Conversely, the ridge sediment, core 3 (Fig. 10) shows virtually no decrease in water content with depth and no increase in shear strength. Skempton[21] has shown that normally consolidated clays typically have decreasing liquidity indices and increasing shear strength with depth. This is not the case for the ridge sediment which has a relatively high liquidity index throughout the cored interval, strongly suggesting that the deposit (based solely on one available core) is underconsolidated. Although the valley and valley wall sediments also appear to be somewhat underconsolidated by virtue of the relatively high liquidity indices and low shear strength, the high water contents are a significant factor contributing to the overall low shear strength (Fig. 10, cores 1 and 2). It is interesting to note that the sediments associated with the slide (core 4) are exceptionally weak with little increase in shear strength with depth, as compared with the material cored in the scar (core 5). In addition, the average liquidity index is lower ($I_L < 1.0$) in core 5 compared with the upper slope cores (Table 1).

The geotechnical properties data were evaluated to assess the relative degrees of consolidation represented by the nine sediment cores using techniques described by Skempton[21] relating liquidity index and the logarithm of effective stress. Skempton showed a predictable relationship of a small range of liquidity index for a given stress level for normally consolidated sediments. Estimates of overburden stress were calculated for each core at depth intervals where Atterberg limits were determined. Calculations were made using buoyant unit weight ($\gamma_b = \gamma_t - \gamma_{sw}$) with γ_{sw} equal to 1.024 Mg/m^3 and γ_t equal to the sediment wet unit weights over specified core intervals. These data of liquidity index *versus* the logarithm of effective stress were plotted with Skempton's boundary lines[21] for normally consolidated sediment (Fig. 12). As a first approximation using the above criteria, the ridge sediment (core C-3) is obviously underconsolidated at stress levels greater than about 1 kPa. At lower stresses considerable scatter is observed among the data as would be expected. Physico-chemical forces and clay fabric play a significant role in maintaining an open microstructural framework at very low stress levels. An open framework or fabric has been observed in other submarine sediments having high porosities[19]. Noteworthy are the sediments from the slide scar, core C-5, that show the greatest degree of consolidation at lowest liquidity indices. As predicted, sediments from the slump block, core C-4, are less consolidated in comparison. With few exceptions the remainder of the data lie within the normally consolidated zone.

Sensitivities range from slightly greater than 1 to as high as 7.6, the highest value occurring in the ridge sediment core (Table 1). A plot of sensitivity *versus* liquidity index reveals a tendency for increasing sensitivity to be associated with increasing liquidity index. This relationship agrees with findings of Skempton[21] for various clays.

Based on the limited geotechnical data from the cores available in the study area, sedimentaion patterns favour fine-grained deposition of terrigenous silts and clays and foraminiferal tests in the valleys and valley walls. No significant recent sediment transport or erosion by currents seems likely on the valley and valley walls, based on the high water contents, high liquidity indices, low shear strengths, and lack of coarse-grained material. Valley axes do not appear to have steeply-dipping seaward gradients amenable to vast amounts of sediment transport and/or erosion. Very low axial gradients have been determined for other valleys that are likely inactive (in terms of sediment transport) on the continental slope northeast of Wilmington Canyon[28]. Doyle *et al.*[29] have suggested that canyons in the US Atlantic continental margin are presently inactive in terms of sediment flux to the deep sea. Based on bottom current measurements, bottom photographs, bottom samples, submersible observations, and time-lapse camera photographs, the canyons south of Hudson are presently inactive in the transport of large quantities of sediment seaward[30,31]. Their observations show that coarse-grained material is deposited in the canyon heads and fine-grained material in the middle and

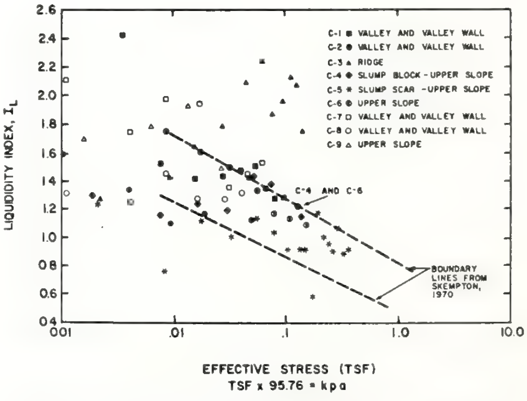

Figure 12. Liquidity index versus *effective stress for cores 1-9 plotted in relation to Skempton's boundary lines[21] for normally consolidated sediment*

outer parts of the canyons; however, massive transport of sediment off the shelf through the canyons is not presently a common process as was the case in the pleistocene[30]. In contrast, upper slope sedimentation patterns presumably favour recent deposition of coarse clastics over older silty clays and clayey silts, suggesting a significant recent change in depositional environment and energy levels on the upper slope and outer shelf. Stanley and Freeland[32] and Stanley[33] have suggested that the boundary between upper slope sands and muds, called the 'mudline', is an indicator reflecting a separation of energy zones. Threshold current velocities necessary to erode fine sediment apparently are not achieved below the depth where mud occurs. This seems reasonable in light of the observed sedimentological and geotechnical properties; however, in another context, deposition rather than erosion appears to be the dominant recent process in this study area of the continental slope-sandy muds on the upper slope and silty clays and clayey silts on the middle and lower slope. As mentioned earlier, slumping has been identified in the surficial sediments and may be a significant intermittent process in the transport and movement of sediment down the continental slope. Slumping in this area south of Baltimore Canyon is apparently restricted to the surficial sediments locally. The surficial sediment may be undergoing creep.

Sedimentological patterns, sediment types, and geotechnical properties appear to be related to depositional environment and morphology; however, these inferences are made from only a limited amount of available data. Obviously, additional sampling is necessary before broad generalizations regarding the processes and the distribution, variability and norms of the geotechnical properties can be more definitively established. Greater sediment sampling would invariably result in more variation in the sedimentological and mass physical properties data associated with similar depositional environments and morphological features; however, the above inferences seem reasonable based on the limited data.

CONCLUSIONS

The continental slope between Baltimore and Washington Canyons appears to have been primarily a site for deposition with occasional periods of erosion of sediments, in the geologic past. A drainage system possibly related to Delaware Bay is implied to be buried by 200 m of sediment beneath the shelf. The morphology of the slope consists of a series of ridges and valleys transverse to the slope. Many unconformities are present within the ridges and can be correlated between them. The age of the sediments composing the ridges is believed to be tertiary and quaternary, with many deposition and erosion events occurring on the slope during this time. During the pleistocene the upper slope in this area was dissected by many small valleys as was found elsewhere along adjacent portions of the margin[6,12].

The sediment cores from transects parallel and perpendicular to the slope show that sediment type and geotechnical properties can be correlated with morphology and depositional environment. Shear strength profiles and Atterberg limits indicate that the ridge sediment is significantly underconsolidated relative to the upper slope, valley and valley walls sediments. Silty clay is the general sediment type in the area with a thin veneer of sand up to 40 cm thick on the upper slope suggesting a recent change in depositional environment on the upper slope, resulting in sand spillover from the shelf, similar to that described by Stanley *et al.*[34] on the Scotian shelf. Variability in the distribution of this surficial sand and in the degree of bioturbation suggests the valleys with their low seafloor gradient presently are not active in the transport of sediment.

Sediment instability is present in the area as evidenced in the cored sediment geotechnical properties, as well as by slumping shown on the seismic reflection profiles. However, the overall morphology of the slope between Baltimore and Washington Canyons cannot be attributed to the process of sediment failure.

ACKNOWLEDGEMENTS

We would like to thank John Burns, Evan Forde, George Merrill, Alvyn Meyer, Richard Permenter, and George Lapiene for assisting in the data collection. Thanks also to William Sawyer, Frances Nastav and Sam Bush for assisting in the data reduction. Appreciation to the officers and crew of the NOAA ship *Researcher* for their cooperation and precision in executing the field work. The bathymetric contour map was prepared by George Merrill. The manuscript was critically reviewed by Mr. John W. Kofoed, Dr. Larry Doyle, Dr. Richard Faas, and Dr. Melvin Esrig. Funds for this study were provided by the National Oceanic and Atmospheric Administration (NOAA). Portions of this manuscript were prepared while B. McGregor was on the research staff of Texas A&M University.

REFERENCES

1 Matthews, D. J. *Tables of the velocity of sound in pure water and sea water for use in echo-sounding and sound ranging*, Admiralty Hydrographic Dept., London, 1939, 52 pp.

2 Heezen, B. C., Tharp, M. and Ewing, M. The floors of the oceans, I. The North Atlantic, *Geol. Soc. Am. Spec. Paper* 65 1959, pp. 1-122.

3 Kelling, G. and Stanley, D. J. Morphology and structure of Wilmington and Baltimore Submarine Canyons, eastern United States, *J. Geol.* 1970, **78**, 637

4 Stanley, D. J. and Silverberg, N. Recent slumping on the continental slope off Sable Island Bank, southeast Canada, *Earth Planet. Sci. Lett.* 1969, **6**, 123

5 Uchupi, E. Atlantic continental shelf and slope of the United States — physiography, *US Geol. Surv. Prof. Paper* 529C 1968, pp. 1-30

6 McGregor, B. A. and Bennett, R. H. Continental slope sediment instability northeast of Wilmington Canyon, *Am. Ass. Petrol. Geol. Bull.* 1977, **61**, 918

7 McGregor, B. A. and Bennett, R. H. Sediment failure on the U.S Atlantic continental slope, *EOS* 1978, **59**, 1114

8 Seibold, E. and Hinz, K. Continental slope construction and destruction, in *The Geology of Continental Margins*, (Ed. Burke, C. A. and C. L. Drake), Springer-Verlag, New York, 1974, pp. 179-196

9 Twichell, D. C., Knebel, H. J. and Folger, D. W. Delaware River: evidence for its former extension to Wilmington Submarine Canyon, *Science* 1977, **195**, 483

10 Swift, D. J. P. Continental shelf sediment, in (Eds. Stanley, D. J. and Swift, D. J. P.) *The New Concepts of Continental Margin Sedimentation*, II. Am. Geol. Inst. Short Course 1974, pp. 581–638

11 Hollister, C. D., Ewing, J. I., Habib, D., Hathaway, J. C., Lancelot, Y., Luterbacher, H., Paulus, F. J., Poag, C. W., Wilcoxon, J. A. and Worstell, P. *Initial reports of the Deep Sea Drilling Project*, XI, US Govt Printing Office, Washington DC, 1972, pp. 357–364

12 McGregor, B. A. Variations in bottom processes along the U.S. Atlantic continental margin, *Am. Ass. Petrol. Geol. Mem.* 1979, **29**, 139

13 Hathaway, J. C., Schlee, J. S., Poag, C. W., Valentine, P. C., Weed, E. G. A., Bothner, M. H., Kohout, F. A., Manheim, F. T., Schoen, R., Miller, R. E. and Schultz, D. M. Preliminary summary of the

1976 Atlantic margin coring project of the U S. Geological Survey. *U S Geol Surv. Open File Report* 76-844 1976. pp 63 92

14 Laine. E. P. Atlantic deep-sea sediments: the influence of contrasting pleistocene neogene patterns of terrigenous weathering. *Geol Soc Am A. Meet. Abstr* 1977. **9**. 1064

15 Pratt. R. M. The seaward extension of submarine canyons of the northeast coast of the United States. *Deep-Sea Res*. 1967. **14**. 409

16 Stanley. D. J. and Kelling. G. Interpretation of a levee-like ridge and associated features. Wilmington Submarine Canyon. eastern United States. *Geol. Soc. Am. Bull*. 1970. **81**. 3747

17 *Munsell Book of Color*. 1929 1960. Munsell Color Co.. Baltimore

18 Bennett. R. H . Lambert. D N and Hulbert. M H. Geotechnical properties of a submarine slide area on the U.S. continental slope northeast of Wilmington Canyon, *Marine Geotechnol*. 1977. **2**. 245

19 Bennett. R. H.. Bryant. W. R. and Keller. G. H. Clay fabric and geotechnical properties of selected submarine sediment cores from the Mississippi Delta. *NOAA Prof. Paper No*. 9 1977. US Dept. of Commerce. 86 pp.

20 Kukal. Z. *Geology of Recent Sediments*. Academia Publishing House, Czechoslovak Academy of Sciences, Prague, 1971, 490 pp.

21 Skempton, A. W. The consolidation of clays by gravitation compaction, *Q. J. Geol. Soc* 1970, **125**, 373

22 Lambe, T. W. and Whitman, R. V. *Soil Mechanics*, John Wiley, New York, 1969, 553 pp

23 Keller, G. H. and Bennett, R. H. Variations in the mass physical properties of selected submarine sediments. *Marine Geol*. 1970. **9**, 215

24 Terzaghi, K. and Peck, R. B. *Soil Mechanics in Engineering Practice*. John Wiley, New York, 1967, 729 pp.

25 Bennett, R. H. and Lambert, D. N. Rapid and reliable technique for determining unit weight and porosity of deep-sea sediments. *Marine Geol*. 1971. **11**. 201

26 Casagrande. A. Research on the Atterberg limits of soils. *Public Roads* 1932. **13**. 121

27 Casagrande. A. Classification and identification of soils. *Am. Soc. Civ. Eng Trans* 1948. **113**. 901

28 Bennett. R. H.. Lambert. D. N.. McGregor. B. A.. Forde. E. B. and Merrill, G. F., Slope map: A major submarine slide on the U S. Atlantic continental slope east of Cape May 4-5787 *USCOMM-NOAA-DC*. NOAA. Washington DC. 1978

29 Doyle. L. J.. Woo. C. C. and Pilkey. O. H. Sediment flux through intercanyon slope area: U.S. Atlantic continental margin. *Geol. Soc. Am. A. Meet. Abstr*. 1976. **8**. 843

30 Keller. G. H.. Lambert. D.. Rowe. G. and Staresinic. N. Bottom currents in Hudson Canyon. *Science* 1973. **180**. 181

31 Keller. G. H. and Shepard. F. P. Currents and sedimentary processes in submarine canyons off the northeast United States. in *Sedimentation in Submarine Canyons, Fans, and Trenches*. (Eds D. J. Stanley and G. Kelling) Dowden. Hutchinson and Ross. Stroudsburg. 1978. pp. 15 32

32 Stanley. D. J and Freeland. G L. The erosion-deposition boundary in the head of Hudson Submarine Canyon defined on the basis of submarine observations. *Marine Geol*. 1978. **26**. M37

33 Stanley. D. J. Erosion versus deposition on upper continental slope off mid-Atlantic states program, *Am. Ass. Petrol. Geol. Bull*. 1978. **62**. 564

34 Stanley. D. J.. Swift. D. J. P.. Silverberg. N.. James. N. P. and Sutton. R. G. Recent sand spill-over off Sable Island Bank. Scotian shelf. *Geol. Surv. Canada Paper* 1973. 71-23. 167-194

35 Upuchi. E. Atlantic continental shelf and slope of the United States — shallow structure, *U.S. Geol. Surv. Prof. Paper 529I* 1970. pp. 1 44

33. NOAA Tech. Memo. ERL MESA-42, 78 pp.

SUSPENDED PARTICULATE MATTER IN THE NEW YORK BIGHT APEX: OBSERVATIONS FROM APRIL 1974 THROUGH JANUARY 1975

CONTENTS

PAGE

1. INTRODUCTION 1

2. ANALYTICAL METHODS 5

3. RESULTS 8

   3.1 WCC-6: April 16-20, 1974 8
   3.2 WCC-7: May 6-9, 1974 13
   3.3 WCC-8: June 10-13, 1974 19
   3.4 WCC-9: July 16-19, 1974 24
   3.5 WCC-10: August 22-24, 1974 29
   3.6 WCC-11: September 29 - October 2, 1974 34
   3.7 WCC-12: November 4-7, 1974 39
   3.8 WCC-13: December 10-11, 1974 45
   3.9 WCC-14 (XWCC-1): January 15-19, 1975 50

4. PARTICLE SUITES OF LONG-TERM RESIDENCE 52

5. ACKNOWLEDGEMENTS 56

6. REFERENCES 57

7. APPENDICES

   7.1 Locations of 25-Station New York Bight Apex Grid
   7.2-7.10 Suspended Particulate Matter Concentration Data, WCC Cruises 6-14

34. Museum (magazine of the Museum of Science, Miami, Fla.) 10, 5-8.

Cans, Bottles Denizens of the Deep

Diving With ALVIN In Submarine Canyons

BY PETER A. RONA, Ph.D.

Three of us crouched in the seven-foot-diameter titanium sphere of the Deep Submergence Research Vehicle ALVIN as it gently bobbed on the surface of the Atlantic about 50 miles off Cape Hatteras, N.C. The pilot, Ralph Hollis from Woods Hole Oceanographic Institution, was busily checking the instrument panel in preparation for a dive, while my geologist colleague, Dr. Dan Stanley, and I organized our notebooks, tape recorders and cameras for observations of the ocean bottom. The "Cleared for dive" message came over the radio from the mother ship LULU several hundred yards away. Ralph adjusted the ballast system to make the submersible heavy, and we began a 1½-hour descent to the ocean bottom 12,000 feet beneath us.

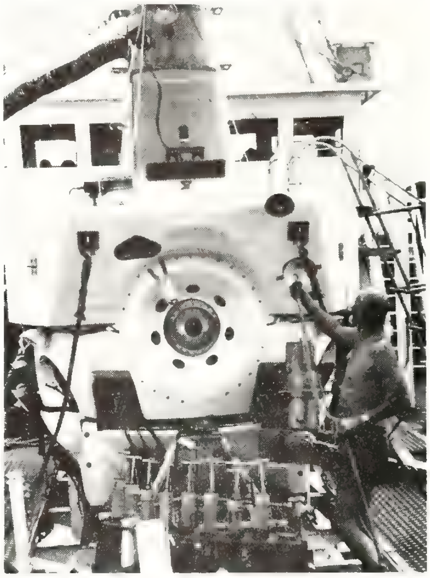

Photos by Peter A. Rona

The submersible ALVIN on the deck on its mother ship, the Research Vessel LULU.

The groundwork for this dive, one of a series of ten, was laid 12 years before when I first explored and mapped the vast submarine canyon system that extends from the continental shelf to the deep ocean basin off Cape Hatteras. At that time, I worked with oceanographic research vessels equipped with echo-sounders that used soundwaves to delineate the shape and depth of the ocean bottom.

Since that time, oceanographers

Dr. Rona, a vice president of the Museum, is a scientist serving with the National Oceanic and Atmospheric Administration's Atlantic Oceanographic and Meteorological Laboratories on Virginai Key.

April, 1979

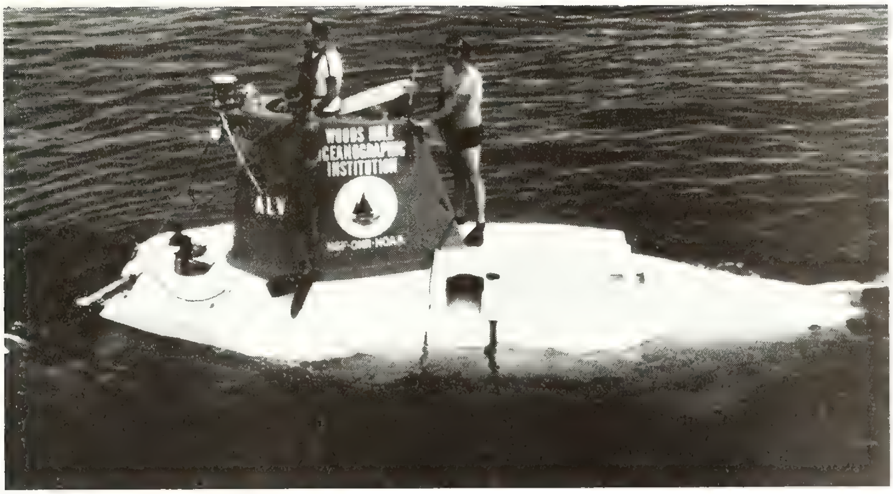

Photo by Peter A. Rona

Pilot and two swimmers prepare the submersible ALVIN to dive off Cape Hatteras.

at NOAA's Atlantic Oceanographic and Meteorological Laboratories in Miami have been investigating the fate of waste materials that are discharged and dumped on the continental shelf from cities along the Atlantic coast. The oceanographers found that some of the waste materials emanating from large northern coastal cities like New York were transported southward along with sediment eroded from beaches by longshore currents and appeared to pile up on the continental shelf off Cape Hatteras.

The remaining mystery with regard to the fate of the waste materials was where they went after they accumulated off Cape Hatteras. The objective of our dives was to determine by direct observation whether the waste materials and sediment were being funneled into the deep ocean basin through the submarine canyons off Cape Hatteras, or were continuing to move southward along the continental shelf.

Sediment Like Snow Blanket

An echo-sounder in the submersible told us that we were approaching the ocean bottom. The external lights were switched on and we watched through the viewing ports for the first sight of the bottom. Then we saw the shadow of the submersible gradually spreading on a background of nearly white sediment which mantled the ocean bottom like a fresh snowfall. Ralph trimmed the ballast until the submersible was hovering about six feet above the bottom, and turned on the stern propeller to push the submersible forward over the bottom. We were moving along a ledge on the north wall of Hatteras Canyon. We slowly descended some hundreds of feet down steep

Dr. Peter A. Rona inside the submersible ALVIN with camera to photograph the ocean bottom through the viewing ports.

cliffs into the axis of the canyon.

On previous dives, we had explored the upper reaches of this canyon where it originates at the continental shelf. There we had seen abundant life including small fish, crabs, worm burrows, neon-red shrimp and multi-hued anemones. We had also seen waste material in the form of food wrappers, tin cans and bottles lying on the canyon floor.

Here along the lower reaches of the canyon in the deep ocean basin, we saw similar kinds of living creatures but they were much less abundant. We were excited when we spotted a few food wrappers, tin cans and bottles indicating that such material was actually transported down the canyon; the food labels were faded showing they had been in the water for a long time.

PLENTY OF ENERGY

One day's released wind energy during a hurricane, if converted to electricity,would supply the electrical needs of the United States for more than six months.

Took Many Photos

We took many photographs as the submersible glided over the canyon floor. Periodically, we stopped to recover samples of the sand and silt on the ocean bottom and to measure the speed and direction of ocean currents flowing through the canyon. From analysis of these various observations back at the NOAA Laboratories in Miami, we would try to answer questions concerning the quantity and rate of flow of material through the canyon.

Engrossed in our observations, eight hours cramped in the small submersible passed quickly. Dwindling electrical and oxygen supplies told us that it was time to begin the 1½-hour ascent to the surface. As we floated upward through the dark depths, we had a sense of accomplishment that these dives were contributing to our understanding of the fate of man-made waste materials in the ocean.

We had learned that the vast submarine canyon system off Cape Hatteras was catching some of the waste materials from our coastal cities and funneling these

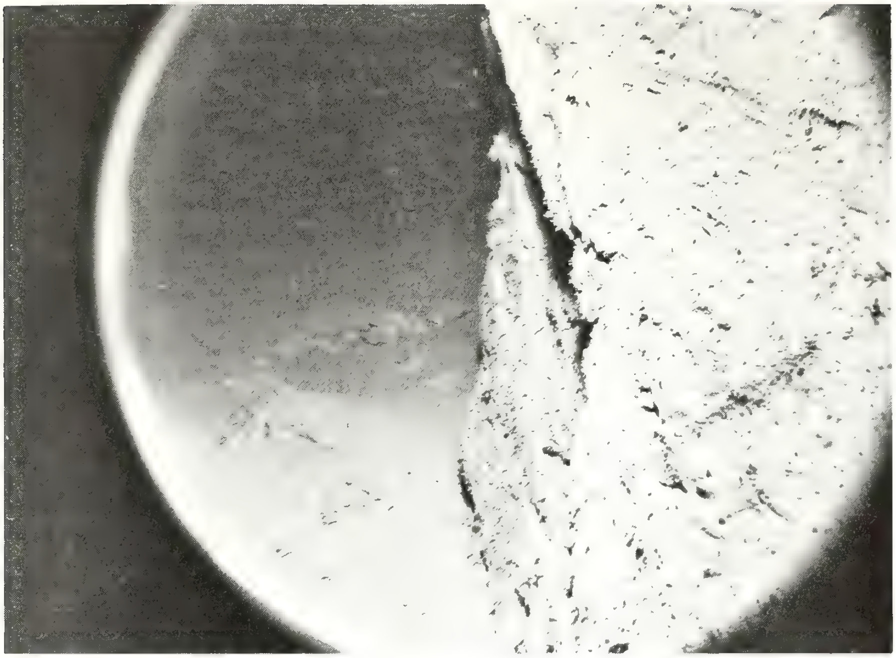

Photo By Peter A. Rona

Submarine canyon wall seen through one of the viewing ports of the submersible ALVIN.

materials from the continental shelf to the deep ocean basin. Without the submarine canyons off Cape Hatteras, this waste material may have continued to move southward to accumulate on the continental shelf adjacent to other inhabited areas. Our increasing knowledge of natural processes, such as transport of material through submarine canyons, can be applied to help man work with nature to resolve the pressing problem of waste disposal and to maintain a habitable environment.

35. American Scientist 67, No. 4, 467.

Sea Floor Development: Moving into Deep Water. Sir Angus Paton et al., eds. A Royal Society Discussion, 1977. 189 pp. London: The Royal Society. No price given.

Diminishing reserves of energy and mineral resources are forcing the search for new sources into deep water. The continental shelves already yield about 19% of the world's annual petroleum production and significant quantities of sand, gravel, tin, and titanium. The deep ocean basins do not yield any such resources at present, but an unknown potential exists for petroleum adjacent to continental margins and for various metals incorporated in nodules, sediments, encrustations, and massive ore bodies. In this book, which is the product of a symposium held by the Royal Society of London in 1977, specialists in marine science and engineering review the problems and prospects of extending exploitation of seafloor resources to the deep ocean basin.

The point of view of the 13 papers presented is national, addressing British interests and capabilities in deep-water activities. However, the subject is sufficiently universal to apply to the interests of other nations. Following the premise that science and engineering must progress concurrently to provide the basis of knowledge and technique to move into deeper water, the papers treat the morphology and currents of continental margins, subsea engineering, hydrocarbon potential, the geochemistry of ferromanganese deposits, environmental aspects, and ocean law. The level of treatment is that of introductory reviews with adequate references to guide further inquiry. Most of the material pertains to hydrocarbons and to manganese nodules as the resources closest to exploitation in deeper water.

The papers presented demonstrate how marine engineering is developing in a logical progression of mechanical innovations from shallow to deeper water, while a conceptual gap remains between our scientific knowledge of shallow and deep seafloor resources. Although our general knowledge of the seafloor has grown enormously since World War II, our special knowledge of the processes and localized conditions that concentrate energy and mineral resources of the deep seafloor remain limited. As a consequence, our ability even to locate, let alone assess, such resources is marginal.

The absence of an editorial overview of the diverse material may be justified by the difficulty of evaluating the feasibility of exploiting deep seafloor resources objectively at this early stage. The book provides a background for administrators, scientists, engineers, economists, and lawyers concerned with energy and mineral resources to formulate their own overviews of the problems and prospects of moving into deeper water.—*Peter A. Rona, Marine Geology and Geophysics, National Oceanic and Atmospheric Administration, Miami*

36. Science 206, 1136.

Atlantic Hot Springs?

Richard A. Kerr, in his article "How is new ocean crust formed?" (Research News, 14 Sept., p. 1115), repeatedly states incorrectly that no submarine hot springs have been found in the Atlantic. The TAG (Trans-Atlantic Geotraverse) Hydrothermal Field, a site of hot springs and hydrothermal metal deposits, was discovered on the mid-Atlantic ridge at latitude 26°N in 1972 and is well documented in the scientific literature (*1*). It is the first active submarine hydrothermal field found on any oceanic ridge.

PETER A. RONA
Atlantic Oceanographic and
Meteorological Laboratories,
National Oceanic and Atmospheric
Administration,
Miami, Florida 33149

References

1. M. R. Scott, R. B. Scott, P. A. Rona, L. W. Butler, A. J. Nalwalk, *Geophys. Res. Lett.* **1**, 355 (1974); R. B. Scott, P. A. Rona, B. A. McGregor, M. R. Scott, *Nature (London)* **251**, 301 (1974); P. A. Rona, B. A. McGregor, P. A. Betzer, G. W. Bolger, D. C. Krause, *Deep-Sea Res.* **22**, 611 (1975); B. A. McGregor and P. A. Rona, *J. Geophys. Res.* **80**, 3307 (1975); P. A. Rona, R. N. Harbison, B. G. Bassinger, R. B. Scott, A. J. Nalwalk, *Geol. Soc. Am. Bull.* **87**, 661 (1976); R. P. Lowell and P. A. Rona, *Earth Planet. Sci. Lett.* **32**, 18 (1976); P. A. Rona, *Geophys. Res. Lett.* **5**, 993 (1978).

37. Journal of Geophysical Research 84, No. B13, 7453-7466.

GEOLOGY OF A SUBMARINE HYDROTHERMAL FIELD, MID-ATLANTIC RIDGE, 26°N LATITUDE

Darcy G. Temple[1]

Department of Oceanography, Texas A&M University, College Station, Texas 77843

Robert B. Scott

Department of Geology, Texas A&M University, College Station, Texas 77843

Peter A. Rona

National Oceanic and Atmospheric Administration
Atlantic Oceanographic and Meteorological Laboratories, Miami, Florida 33149

Abstract. A comparison of structural and lithologic features observed from two stereophotographic traverses of the Trans-Atlantic Geotraverse (TAG) hydrothermal field, 26°N, Mid-Atlantic Ridge, with features of the French-American Mid-Ocean Undersea Study (Famous) hydrothermal site and the Mounds hydrothermal field of the Galapagos spreading center shows that all three areas have hydrothermal deposits with restricted and patchy lateral extent and are associated with closely spaced normal faults commonly of small displacement. No one lithology characterizes either the rocks or the sediments that underlie the hydrothermal deposits. Regions without hydrothermal manganese oxide deposits such as the rift valley at 37°N in the Famous area exhibit larger and fewer faults and lack the abundant permeable semiconsolidated breccia seen at 26°N. Thus structural factors which facilitate hydrothermal circulation by enhancing permeability appear critical to hydrothermal deposition. Structural features of the rift valley wall at 26°N include inward facing normal faulting, outward facing normal faulting, and outward tilting by rotation of fault blocks. These observations support a viscous drag mechanism of uplift of the rift valley walls.

38. Sedimentology 26, 389-406.

Time and space distribution of megaripples and associated bedforms, Middle Atlantic Bight, North American Atlantic Shelf

D. J. P. SWIFT, G. L. FREELAND *and* R. A. YOUNG

Atlantic Oceanographic and Meteorological Laboratories, NOAA
15 *Rickenbacker Causeway, Miami, Florida* 33149

ABSTRACT

Three genetically distinct size classes of lower regime transverse bedforms have long been known from laboratory studies, and from studies of the intertidal zone; ripples, megaripples, and sand waves. These features are also present on the subtidal shelf surface of the Middle Atlantic Bight, and their distribution in time and space allows us to draw inferences concerning the time and space pattern of sediment transport. Transverse bedforms in the Middle Atlantic Bight occur in response to tidal flows at estuary and inlet mouths and on tide-dominated banks; on the shelf surface, however, they are primarily responses to wind-driven flows. Ripples are the most widespread of the three classes. They are current-formed during peak storm flows, but are probably remade as oscillatory wave ripples as the flow wanes. Megaripples are found primarily on the inner shelf, also as responses to peak storm flows. Sand waves of several metres amplitude occur on the inner shelf in the vicinity of topographic highs; low amplitude sand waves (< 2 m), solitary or in trains, are widespread on the inner shelf. They survive through many seasons of storm flows. Megaripples are especially interesting as records of specific flow events. They are widespread on the inner shelf during the winter, occurring in fields up to several kilometres in diameter. On a portion of the Long Island inner shelf during December 1976, megaripple fields covered approximately 15% of the shelf surface. They tend to be erased during the succeeding summer months. Both megaripples (short-term response elements) and sand waves (long-term response elements) indicate that sand transport in the Middle Atlantic Bight is directed to the southeast, parallel with the regional trend of the isobaths.

INTRODUCTION

The fact that transverse bedforms fall into genetic populations when ordered by spacing, has been tacitly realized since the early studies of Cornish (1901a, b) in British estuaries, but has been systematically investigated only in recent decades. In 1963, Reineck distinguished between medium- and large-scale transverse bedforms (*Grossrippeln* and *Riesenrippeln*, p. 49), while in 1968a, Allen (pp. 66–71) showed that 'small-scale ripples' and 'large-scale ripples' (including both of Reineck's forms) comprise two distinct size populations. Allen cites Bagnold (1956) concerning the probable genetic differences between these ripple types. McCave (1971) noted a further distinction in a study of the Southern Bight of the North Sea between large-scale ripples which he calls 'megaripples' (term from van Straaten, 1950; 1953) and yet larger-scale 'sand waves' (term from Cornish, 1901; Bucher, 1919). His terms are equivalent to the *Grossrippeln* and *Riesenrippeln* of Reineck (1963). The nomenclature has become further confused as a consequence of the divergent traditions of flume workers and field workers; the former refer to the larger ripples (megaripples of field workers) as 'dunes'. Prior to the recognition of the difference between sand waves and megaripples, the term 'sand wave' had been used to describe both forms. The terms 'ripple', 'megaripple', and 'sand wave' will be adopted in this paper for small-, medium-, and large-scale transverse bedforms, respectively.

Generally speaking, ripple spacings are measured in centimetres, while megaripples spacings are measured in metres or tens of metres, and sand wave spacings are measured in many tens of metres or hundreds of metres. The 'spectral gaps' between these three classes are obvious in the field, and if more than one class is present, there is little problem in distinguishing among them. It is not possible, however, to erect a rigorous classification of transverse bedforms on the basis of spacing, since ranges overlap markedly (Jackson, 1975, Fig. 1, Table 2). The overlap occurs because the spacing of transverse bedforms varies with such flow parameters as flow depth (total or boundary flow; Yalin, 1977; Jackson, 1975, pp. 548–550) and grain size.

Jackson (1975) has reviewed earlier studies, and has presented a unifying model of bedform hierarchies, based on such flow parameters. He defines 'microforms' as responses to inner boundary layer flow, whose life spans are usually much shorter than that of the dynamic event that forms them. 'Mesoforms' are responses to outer boundary layer flow, and their life spans coincide with the duration of the dynamic event. The division between the inner and outer boundary layers varies with total boundary layer thickness, but is less than a few centimetres for most flows of geophysical scale. 'Macroforms' are time-averaged responses to the whole depth of flow, whose lifespans are much longer than the dynamic event. Jackson (1975) describes ripples as microforms whose spacings span a narrow interval from 5 to 2 m, and megaripples as mesoforms of 40 to 300 m spacing. Jackson refers to sand waves as mesoforms of larger scale, but in the marine environment their behaviour is more nearly that of his macroform class; their depth is a significant portion of total flow (McCave, 1971; see Stride, 1970 for an alternate viewpoint), and they appear to be time-averaged responses to a long sequence of flow events (Hunt, Swift & Palmer, 1977).

Very recent information on the distinction between sand waves and megaripples has been summarized by Middleton & Southard (1977, pp. 7.15–7.17; 7.36–7.38). Their stability diagrams indicate that for a given flow depth and grain size, sand waves occur at lower velocities than megaripples. Megaripples occur alone on finer sands (less than 2ϕ) but may occur on the backs of sand waves in coarser sands (Boothroyd & Hubbard, 1975; Dalrymple, Knight & Middleton, 1977). Sand waves are more regular, less sinuous, and have greater crestal continuity than megaripples.

Transverse bedforms were first described from the intertidal zones of estuaries (Cornish, 1901a; van Straaten, 1950, 1953), but were studied primarily in shallow, short laboratory flumes (studies summarized by Southard, 1971; Southard & Boguchwal, 1973) in which sand waves were not generally formed; hence the belated recognition of the distinction between megaripples and sand waves. With the advent of large-scale acoustic surveys of the continental shelves for marine charting purposes, the existence of subtidal sand wave fields became apparent (van Veen, 1935; Jordan, 1962; Jones, Kain & Stride, 1965; Dingle, 1965; Harvey, 1966; Uchupi, 1968; Nio, 1976; Bouma & Hampton, 1977). Vertical acoustical profiling methods were generally not adequate to resolve the smaller-scale megaripple patterns from irregularities in the acoustic record due to surface wave motion (for exceptions see McCave, 1971; Terwindt, 1971). Sidescan sonar records, however, are generally not subject to this limitation, because the transducer is towed near the bottom where it is less affected by surface wave motions, and because a plan view, as well as a profile, is presented. With such records (e.g. Langhorne, 1973) it is possible to assess the time and space distribution of megaripple patterns on the seafloor, and their relation to the larger-scale sand wave patterns.

In this paper we review earlier information, report new data concerning time and space scales of megaripples and related bedforms in the Middle Atlantic Bight of the North American Atlantic continental shelf, and draw from this information inferences concerning the pattern of sediment transport on the shelf surface.

CHARACTER AND DISTRIBUTION OF TRANSVERSE BEDFORMS, MIDDLE ATLANTIC BIGHT

Bedform provinces

The Middle Atlantic Bight is an arcuate, generally north–south trending shelf segment that extends from Cape Hatteras at 35° 00′ N to Cape Cod at 42° 00′ N, a distance of 777 km. The shelf ranges from 25 km wide at Cape Hatteras, where the shelf break occurs at 75 m, to 180 km at New York, where the lower shelf break (Nichols Shore) lies at 200 m. North of Cape Cod, a flat-topped bank (Georges Bank) separates the Gulf of Maine from the North Atlantic Ocean.

Figure 1 indicates localities in the Middle Atlantic Bight where ripples, sand waves, and megaripples have been reported. The pattern of sampling has been non-systematic, and is of low density; it indicates primarily where people have wished to take bottom pictures and collect side scan records, rather than the true distribution of bedforms. Nevertheless, it suffices to show that at least three genetic provinces of transverse bedforms exist. All three transverse bedform types (ripples, megaripples, and sand waves) are found together in regions dominated by strong tidal currents, such as the mouths of Chesapeake Bay (Ludwick, 1970a, b; 1972), Delaware Bay (Jordan, 1962), Long Island Sound (Bokuniewicz, Gordon & Kastens, 1977), and Nantucket Shoals-Georges Bank (Jordan, 1962; Uchupi, 1968; Sanders, Emery & Uchupi, 1969). Ripples, megaripples, and sand waves also occur together on the shelf edge at Cape Hatteras where the shelf is periodically swept by the north flank of the Gulf Stream (Hunt *et al*, 1977).

We are primarily concerned in this paper with a third province; the broad shelf surface away from tide-dominated estuary mouths and banks and landward of the shelf edge, where bedforms are primarily responses to wind-driven currents.

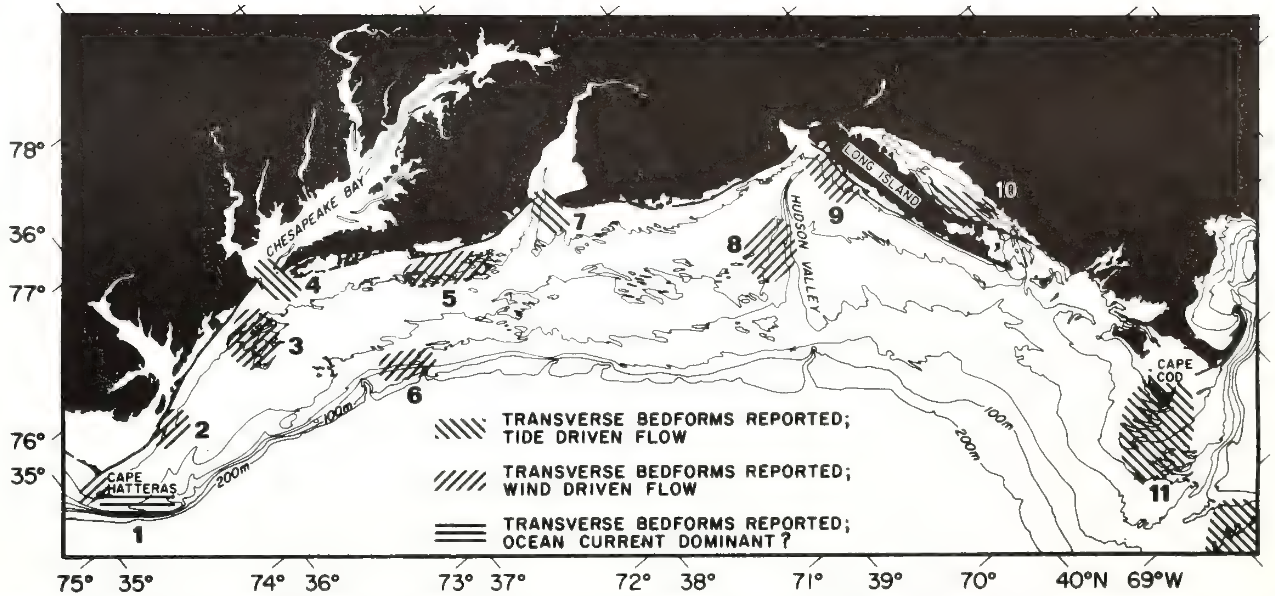
78°
36°
77°
76°
35°
75°
35°
74°
36°
73°
37°
72°
38°
71°
39°
70°
40°N
69°W
CHESAPEAKE BAY
CAPE HATTERAS
LONG ISLAND
HUDSON VALLEY
CAPE COD
100m
200m
1
2
3
4
5
6
7
8
9
10
11
TRANSVERSE BEDFORMS REPORTED; TIDE DRIVEN FLOW
TRANSVERSE BEDFORMS REPORTED; WIND DRIVEN FLOW
TRANSVERSE BEDFORMS REPORTED; OCEAN CURRENT DOMINANT?

Fig. 1 Localities in the Middle Atlantic Bight where transverse bedforms (ripples, megaripples, sand waves) have been reported and probable forcing agents. References: (1) Hunt *et al.*, 1977 (R, M, S). (2) Swift *et al.*, 1978 (R, M, S). (3) Swift *et al.*, 1977 (R, M, S). (4) Ludwick, 1970a, b; 1972 (R. M. S). (5) Swift & Freeland, 1978 (R, M, S). (6) Stanley & Kelling, 1968; Knebel & Folger, 1976 (R, S). (7) Jordan, 1962 (R?, M?, S). (8) Anonymous, 1976 (R, M). (9) Swift & Freeland, 1978, this paper (R, M, S). (10) Bokuniewicz *et al.*, 1976 (R?, M?, S). (11) Uchupi, 1968 (R?, M?, S). Queried occurrences are inferred, from discussion with authors.

Hydraulic climate

The interaction of winds with the Middle Atlantic Bight water mass to produce these currents has been described by Beardsley & Butman (1974), Beardsley, Boicourt & Hansen (1976), and Boicourt & Hacker (1976). Current speeds and directions are highly variable. Published results of near-bottom current meter observations (McClennen, 1973; Lavelle *et al.*, 1976; 1978; Gadd, Lavelle & Swift, 1978; Swift *et al.*, 1977) indicate that during winter months, flows sufficiently intense to exceed the threshold velocity may last for hours or days, and may occur several times a month (Fig. 2). Note that while a strong tidal signature is apparent in Fig. 2, and while peak tidal speeds approach the threshold of 18 cm/s^{-1} determined for the sediments of this area (Lavelle *et al.*, 1976), tidal currents are not efficient transporters of sediment. The storm flow of October 19–21 is efficient, however, because as indicated by the correspondance of panels A and B sufficient wave energy is present to resuspend the sediment, so that the storm flow can advect it. Such currents are usually nearly shore-parallel with an offshore component of near-bottom flow for southwest-trending flows, and an onshore component for northeast-trending flows. Many investigators (e.g. Beardsley & Butman, 1974; Boicourt & Hacker, 1976; Scott & Csanady, 1976; Lavelle *et al.*, 1976) have noted that southwest-trending flows tend to be more intense. Beardsley & Butman (1974) have described a scale-matching phenomenon, in which 'north-easter' storms move obliquely across the Middle Atlantic Bight so that for a period of time the trajectory of their winds parallels the isobath. Under such conditions, with northeast winds blowing down the arc of the Bight, there is strong geostrophic coupling of wind with water so that the water mass moves west and south with

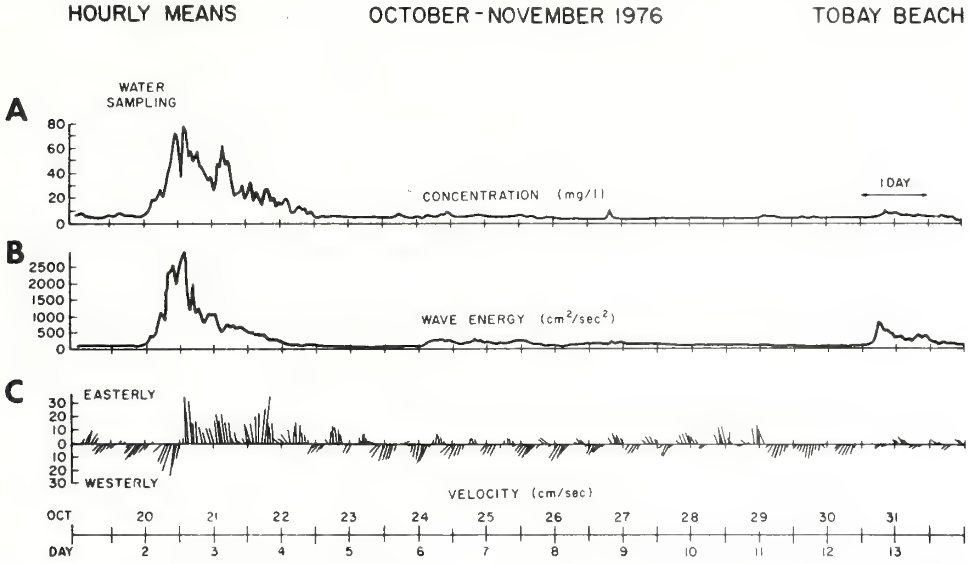

Fig. 2. (A) Burst mean sediment concentration for the period 1600 October 19 to 1600 November 1, 1976, at the 10 m isobath off Tobay Beach, Long Island, USA. Data was sampled once per second for an 8 min burst every hour. (B) Wave energy for the same period, calculated as burst mean of current speed measured by a Marsh McBirney electromagnetic current meter. (C) Burst mean current velocity for the same period presented as a successive vector diagram. Modified from Lavelle *et al.*, 1978

remarkable coherence, in 'slab-like' fashion. During a storm, near-bottom flow intensities tend to decrease from the shelf edge towards the shoreline, but may increase abruptly on the inner shelf as a consequence of jet-like coastal flows (Boicourt & Hacker, 1976; Csanady, 1976). Flows exceeding threshold are also more frequent in this nearshore region since the thinner water column responds more quickly, and is more likely to attain equilibrium with peak winds (Ludwick, 1978).

Ripples from wind-forced currents

Ripples, megaripples, and sand waves all occur on the portions of the Middle Atlantic Bight surface dominated by wind-forced currents, but they do not always occur together. Ripples are found everywhere on the Middle Atlantic Bight from the shoreline to the shelf edge (e.g. Swift *et al.*, 1977; Anonymous, 1976; Stanley, Fenner & Kelling, 1972). Their spacing varies from 1 to 150 cm, mainly as a function of grain size (Inman, 1957). During periods of peak flow, ripples may be primarily linguoid ripples formed in response to a unidirectional flow component (Fig. 2a) but by the time the seas are calm enough for observation by submersible or bottom photography, the ripples have usually changed to nearly symmetrical long-crested forms (forms with crests that can be traced for several metres across the direction of flow) and are now primarily responses to the surge generated on the bottom by the passage of surface waves (Fig. 3b). On the central and outer shelf, where surface wave trains are less frequently able to stir the bottom, ripples are commonly round-crested, indicating a long period of bioturbation since the last event (Fig. 3c). Over vast areas, crests are armoured and thus protected by sand dollars, who seek access to more rapidly flowing bottom water at the ripple crest.

Megaripples from wind-forced currents

Megaripples, in portions of the Middle Atlantic Bight dominated by a wind-forced flow component, occur together with sand waves (Figs 4–6) or alone (Fig. 7). They have been reported most frequently from the inner shelf (Swift *et al.*, 1977, 1978) and less frequently from the central shelf (Sanders, *et al.*, 1969; Anonymous, 1976, figs 28, 29, 31). Megaripples are invariably features of low crestal continuity, whose spacing-to-crest length ratios (span to chord ratios of Allen, 1968a) may be as low as 1 : 2. That is, their crests may extend normal to flow only twice as far as the downstream distance to the next megaripple. Megaripple crests frequently make small angles with the crests of sand waves with which they are associated (Fig. 4; Terwindt, 1971). Megaripple spacings lie between 1 and 40 m.

Megaripples form on the inner shelf during the storm months (November through March) in patches several kilometres in diameter. Side scan sonar records collected in December on the inner Long Island shelf (Fig. 8) reveal about 15% of the inner shelf surface so covered, suggesting that during a given winter, a given location on the floor of the inner Atlantic shelf has a 15% chance of being reworked by fluid motions to a depth of perhaps 30 cm.

Megaripple fields tend to be short lived, and are largely erased during the quiet summer months. The megaripple field of Fig. 7 occurs on a transect re-examined by side scan sonar at quarterly intervals (Stubblefield, Permenter & Swift, 1977). Megaripples were absent from this area in September, 1974, present in November, 1974, and absent again in January, 1975. A megaripple field off Virginia Beach, Virginia, was

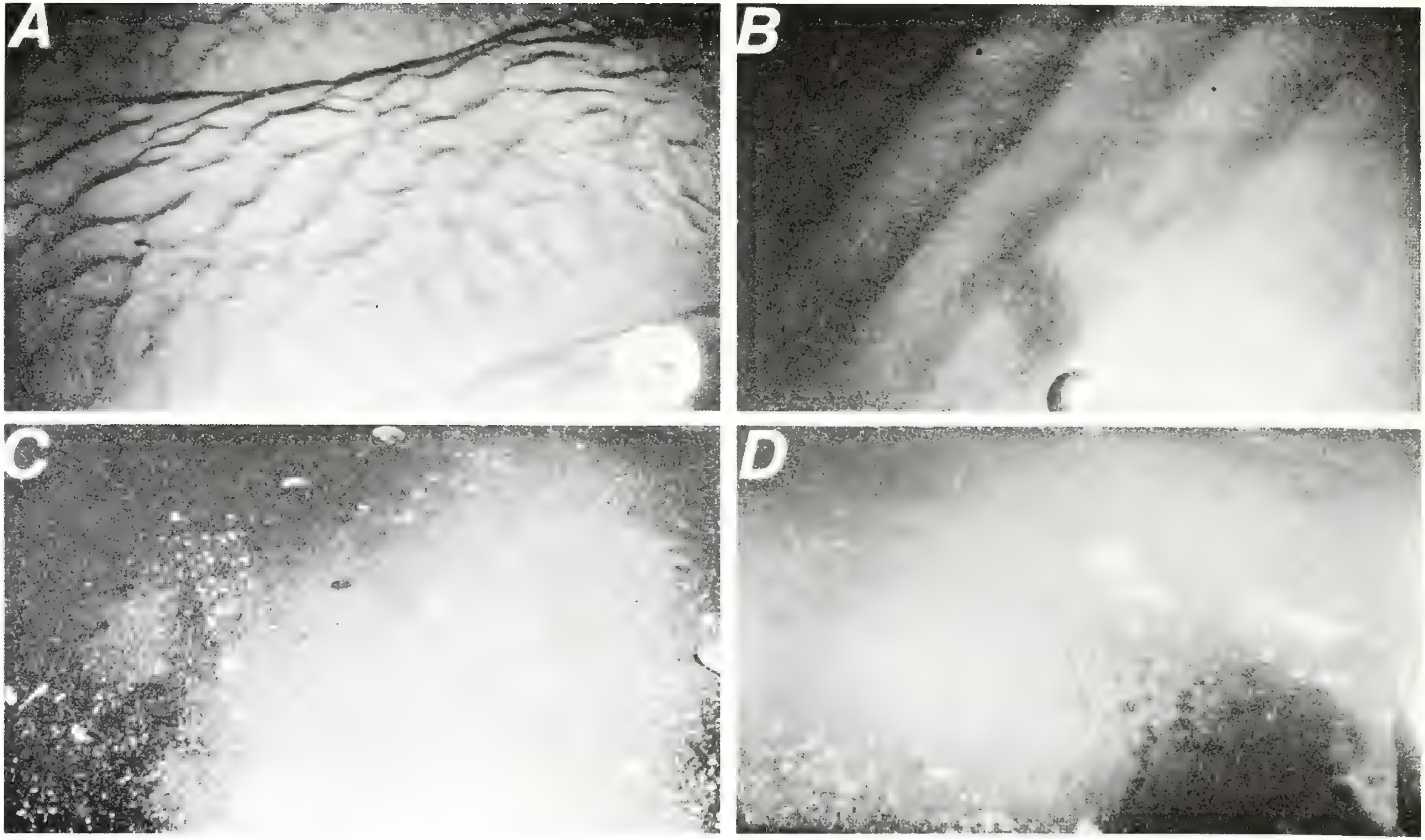

Fig. 3. (A) Megaripples with current ripples, near Cape Hatteras, depth 30 m (location 1, Fig. 1). (B) Wave ripples, Maryland inner shelf, depth 15 m (location 5, Fig. 1). (C) Degraded wave ripples, New Jersey central shelf, depth 34 m (location 8, Fig. 1). (D) Megaripple armoured with sand dollars, New Jersey central shelf, depth 48m (location 8, Fig. 1).

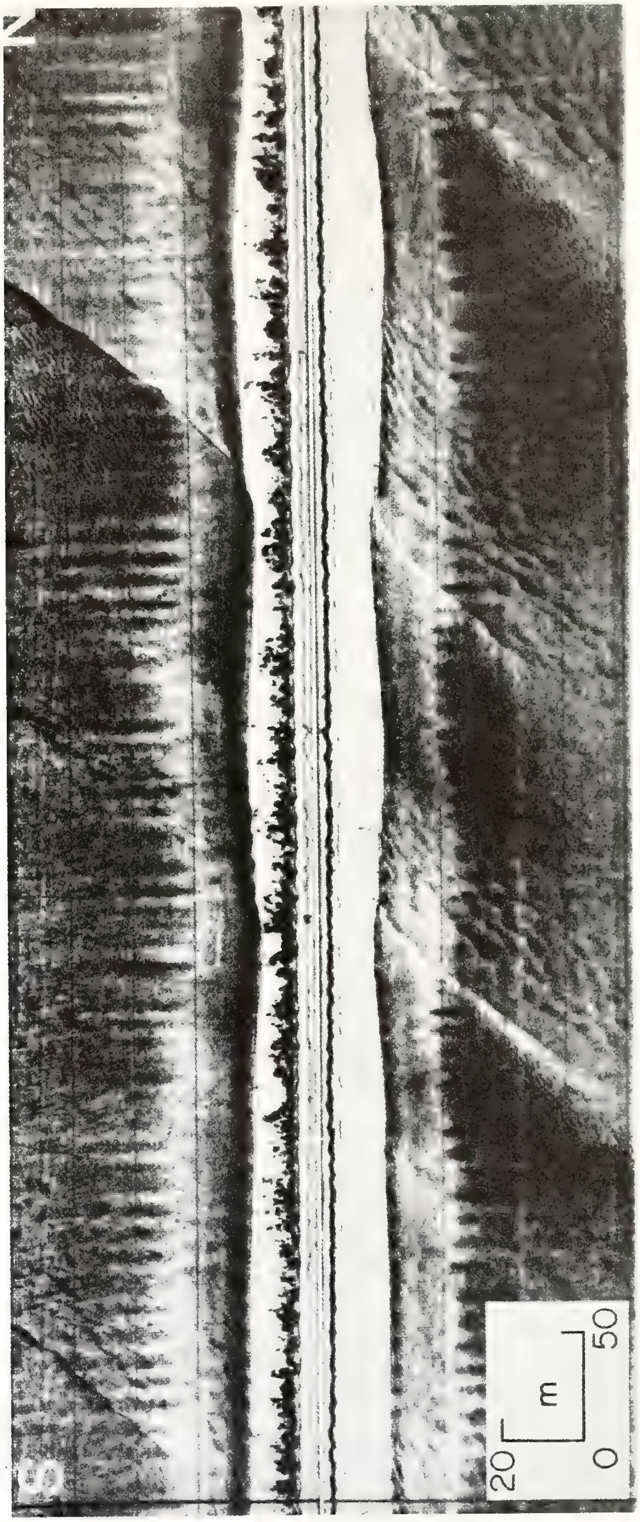

Fig. 4. Side scan sonar record of sand waves with megaripples, near Cape Hatteras (location 1, Fig. 1). Steep sides of sand waves face north. From Hunt *et al.*, 1977.

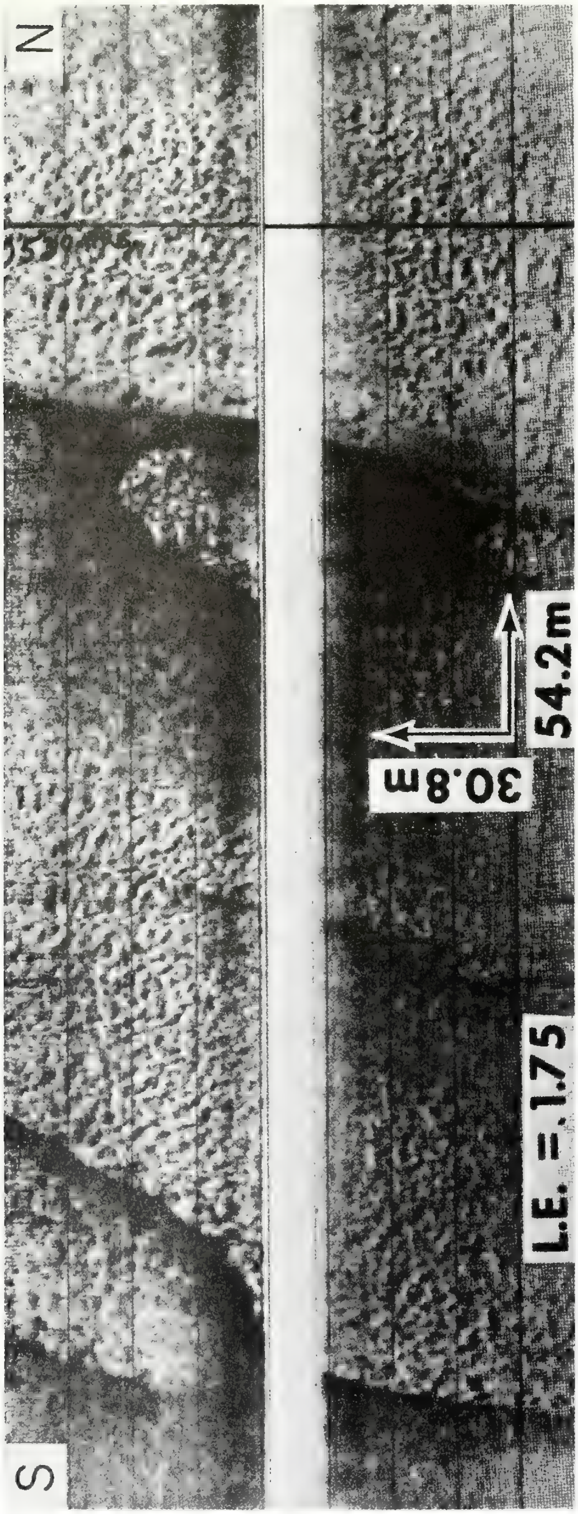

Fig. 5. Megaripples and low amplitude sand waves on the Long Island inner shelf. Dark zones are pebbly, shelly, coarse sand in sand wave troughs. Steep sides of sand waves face southwest. From area shown in Fig. 3.

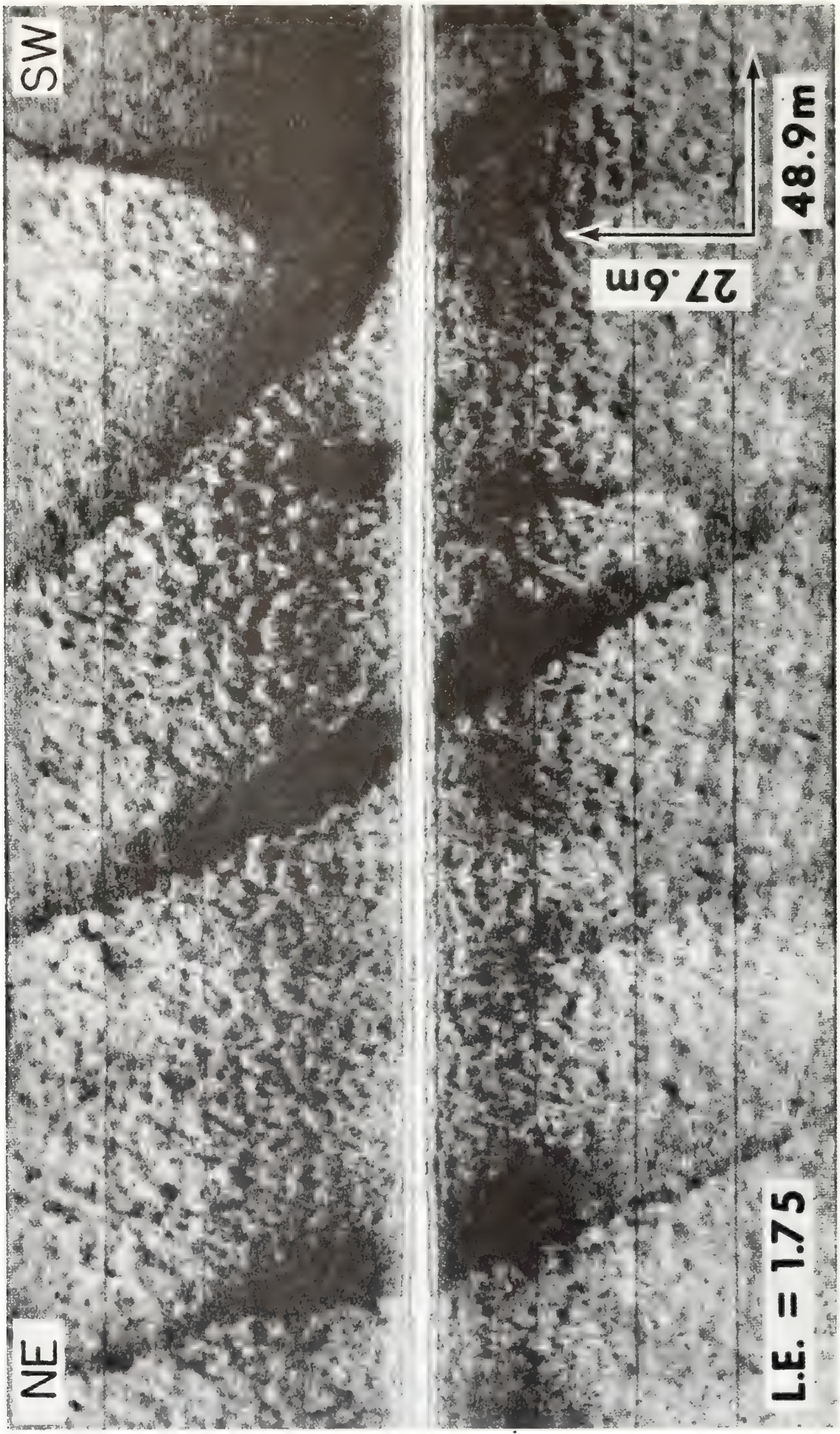

Fig. 6. Sand waves and megaripples on inner Long Island shelf. Steep sides of sand waves face southwest. From area shown in Fig. 3.

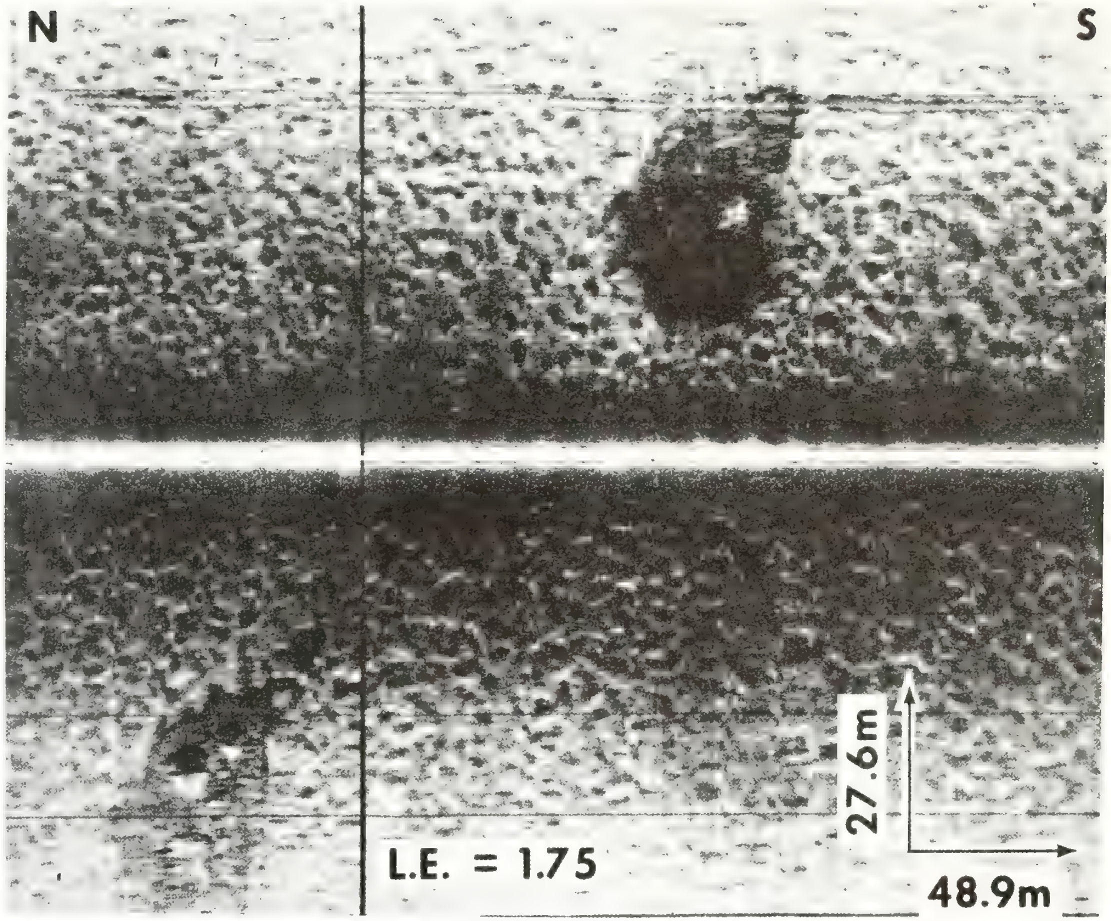

Fig. 7. Megaripples without sand waves on the Long Island inner shelf. Dark areas are dumped rubble. Steep sides of megaripples face west. From location 9, Fig. 1.

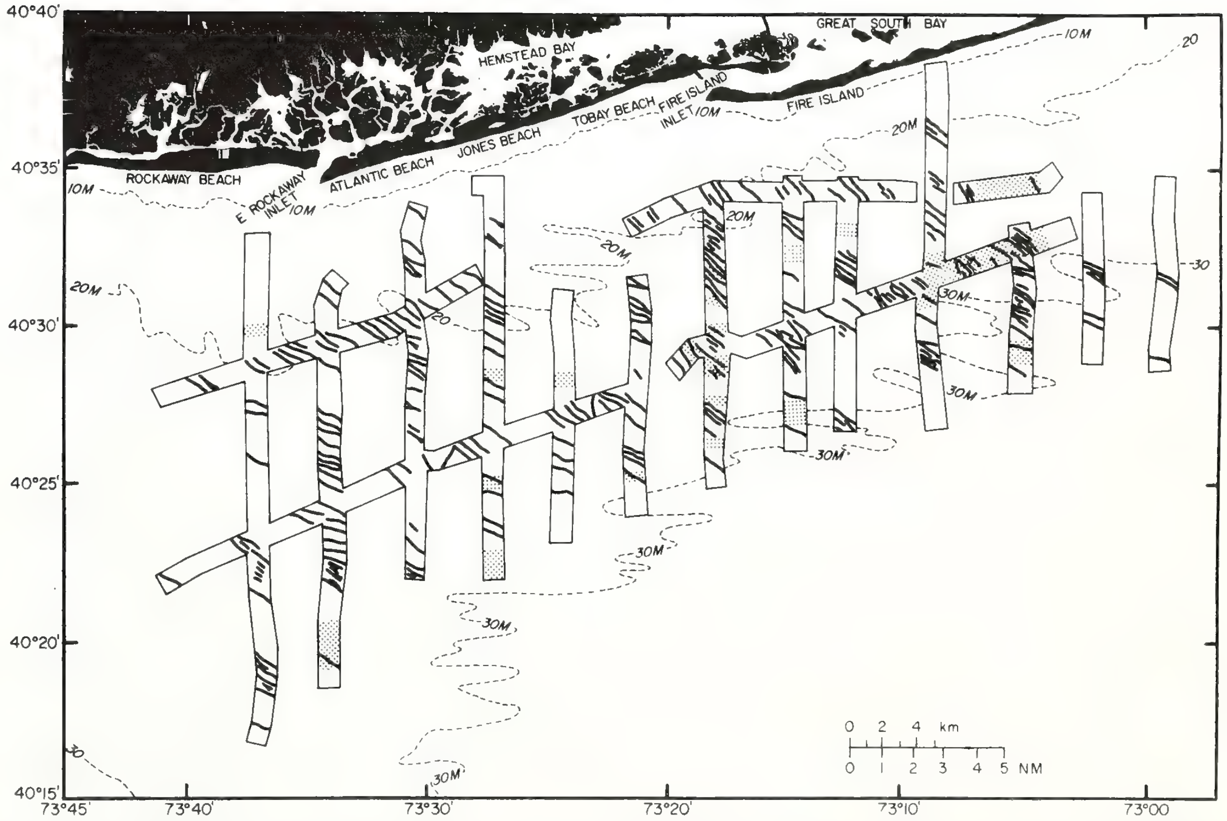

Fig. 8. Sand waves (heavy lines) and megaripples (stipple areas) on the inner Long Island shelf, as revealed by side scan sonar. Sand ridges of ridge and swale topography outlined by 20 and 30 m contours. Width of side scan record exaggerated four times for clarity (location 9, Fig. 1).

examined by scuba divers in July, 1974 (Swift *et al.*, 1977; Fig. 9, this paper). Crests were rounded, and downcurrent slopes were well below angle of repose, apparently as a consequence of ploughing and bulldozing activities of benthic animals. Several centimetres of dark mud had accumulated in the axes of the troughs. The megaripples may have formed during one of the intense storms of the preceding March. During a period of eight field seasons on the Atlantic shelf, the Virginia Beach megaripples were the only ones observed during the summer. Locally, stationary masses of sand dollars, like those that armour ripples, may serve more to protect than degrade megaripples (Fig. 2d).

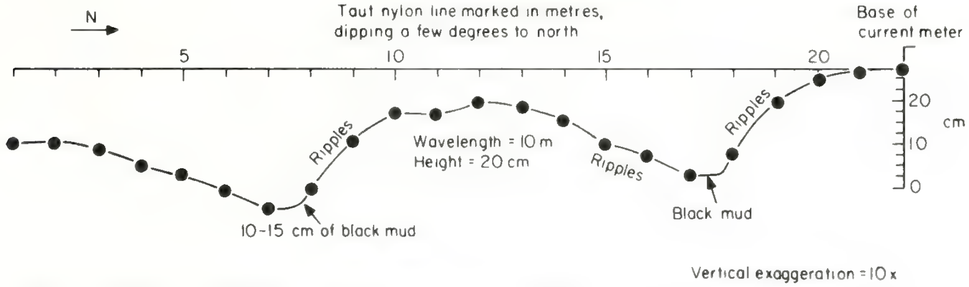

Fig. 9. Profile of megaripples measured by divers, Location 3, Fig. 1, from Swift *et al.*, 1977.

Sand waves from wind-forced currents

Sand waves in portions of the Middle Atlantic Bight dominated by a wind-forced flow component are largely confined to the shallow inner shelf (Fig. 1). They may occur with megaripples, or alone. Sand waves with amplitudes in excess of 2 m and with portions of downcurrent slopes frequently at the angle of repose, have been observed at Platt Shoal and at Diamond Shoals on the North Carolina inner shelf (Hunt *et al.*, 1977; Fig. 4, this paper; Swift *et al.*, 1977) and on the inner shelf seaward of Virginia Beach, Virginia (Swift *et al.*, 1978). Here they occur on up-current (northeastern) flanks of levee-like highs associated with shelf valleys (shoal retreat massifs). Their position suggests that these well developed sand wave fields are responses to flow constriction and acceleration as south-trending storm flows pass over the highs.

At Diamond Shoals near the shelf edge, the seafloor is periodically invaded by the Gulf Stream, further increasing the frequency of high-intensity flows. A second occurrence of sand waves on the shelf edge near Wilmington Canyon seems localized by the proximity of the canyon (Stanley & Kelling, 1968; Knebel & Folger, 1976).

Sand waves occur more generally on the lower shoreface and inner shelf floor of the Middle Atlantic Bight as solitary features, or in trains (Swift & Freeland, 1978). However, away from topographic highs, sand wave heights are usually less than 2m, and downcurrent slopes lie at less than angle of repose (Swift & Freeland, 1978). The virtual restriction of Middle Atlantic Bight sand wave fields to the inner shelf (<30 m depth) is probably a consequence of the greater frequency with which wind stresses are transmitted to the seafloor in this shallow region (e.g. Ludwick, 1978). Sand waves are usually oriented obliquely to shore so that the north or northeast-opening angle is slightly smaller than the south or southwest-opening angle (Fig. 8). The orientation is believed to be controlled by the structure of the near-bottom flow field during storms, in which a weak offshore flow component, associated with wind-driven downwelling is added to a stronger down-coast flow component (Swift & Freeland, 1978). Sand wave spacing is generally in excess of 40 m.

The nature of low amplitude sand waves on the inner Atlantic shelf between shoal areas is clarified by examining the relationship of water depth, sand wave height, and sand wave spacing (Figs 10 and 11). In Fig. 10 it can be seen that while 7·4 m is the maximum height for sand waves at Platt Shoals and Diamond Shoals, many are much lower, and the sand waves on the Long Island coast are mostly between 0·5 and 2·5 m high. As noted by Flemming (1978) many other field studies have failed to find a dependence of sand wave height to water depth. Flemming, in his study of sand waves generated by the Agulhas Current on the southeast African shelf, suggests that sand wave height in deep marine flows may be controlled by boundary layer height, rather than total water depth. This interesting hypothesis remains to be tested. On the Atlantic shelf, it seems simpler to relate sand wave amplitudes to the relationship between wave climate and flow intensity. This has been carefully documented by Ludwick (1972) for tidal sand waves in the mouth of Chesapeake Bay; sand waves occur there in zones of strong tidal flow, but are reduced in amplitude during times of intense wave activity. We therefore suggest that the sand waves associated with shoal retreat massifs are higher because there periods of high waves are usually associated with strong flows capable of aggrading sand waves. On the shelf elsewhere, such as off the Long Island coast, the mean flow component accompanying storm waves is less frequently strong enough to aggrade sand waves, and during many storms, sand waves may be degraded by bottom wave surge, rather than being aggraded by the mean

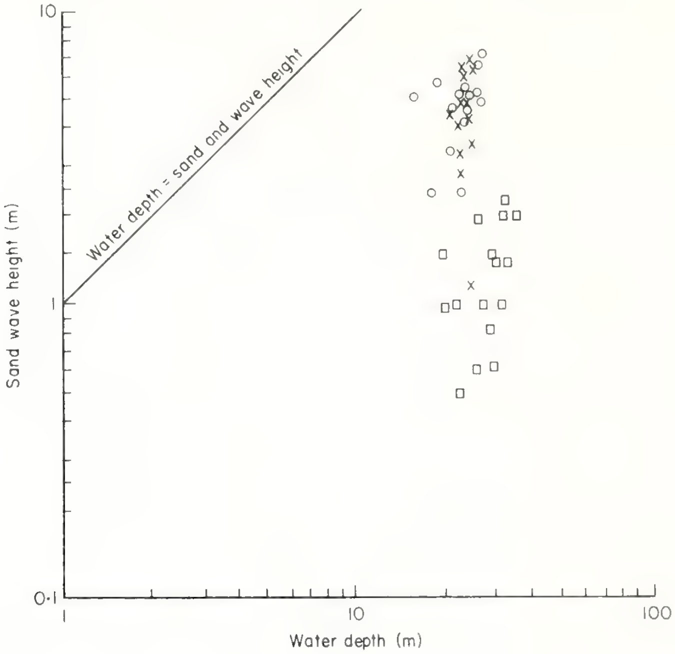

Fig. 10. Plot of water depth against sand wave height for selected Atlantic shelf sand wave fields. ○, Platt Shoals; ×, Diamond Shoals; □, Long Island Coast.

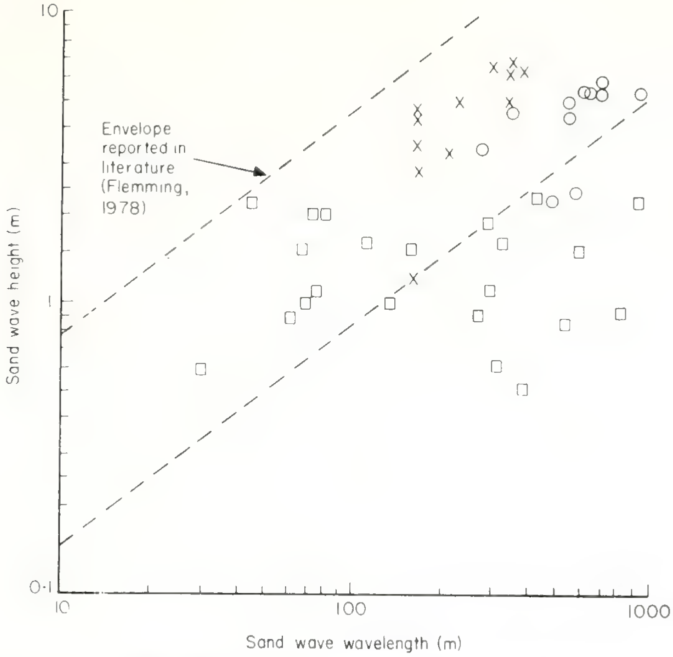

Fig. 11. Plot of sand wave height against sand wave wavelength (spacing) for selected Atlantic shelf sand wave fields. Symbols as in Fig. 10.

flow. Interestingly, the highest sand waves in the Middle Atlantic Bight are 7·4 m, the height calculated as equilibrium by McCave (1971) in his consideration of a shelf sand wave field in similar water depths.

In Fig. 11, the relationship between sand wave spacing and sand wave height falls within the envelope determined from the literature by Flemming (1978) and predicted by Allen (1968b). A group of 'starved sand waves' from the Long Island coast lies below the envelope, however. Spacings of sand waves on this coast are bimodal, and may occur as solitary forms, in sets with spacings of several hundreds of metres, or in sets with spacings of 50–100m. In some cases the second two spacings occur simultaneously; sand waves occur in clusters of two or three waves separated from each other by 100 m (Fig. 6). The clusters themselves are about 200–1000 m apart.

Smith (1970) has conducted a stability analysis for a sand bed subjected to shear flow which suggests that the spacing between a transverse bedform and its downstream neighbour is determined by the rate of downstream growth of the new boundary layer forming behind the first bedform. 'As the downstream ripples grow in height, they must grow in length, which is accomplished by the smaller waves growing faster and stretching out the ripple field.' Application of our observations to Smith's model suggests that the smaller wavelength is the true or innate wavelength for the low amplitude sand waves of the Long Island shelf, determined by 'spatial adjustments in the turbulent velocity field' (Smith, 1970). Our distinction in Fig. 11 of 1000 m as the boundary between large-scale sand waves and solitary sand waves is probably unrealistic in this area; most sand waves with over 100 m spacing are probably really solitary sand waves in the sense that their positions are not determined by the wake of the next form upstream from them.

Sand waves at Platt Shoals have appeared in the same general area for a 5-year period, as indicated by successive National Ocean Survey studies (Swift, *et al.*, 1978) and sand waves at Diamond Shoals have occupied the same area for a decade (1961–1971; Hunt *et al.*, 1977). On the Maryland coast, individual sand waves occupied essentially the same positions for two successive years (Swift & Freeland, 1978).

CONCLUSIONS

Transverse bedforms are characteristic not only of tidal inlets, banks, and estuary mouths, but also of the inner shelf of the Middle Atlantic Bight, where they are responses to southwesterly wind-driven flows during 'northeaster' storms. It is not clear whether the widespread occurrence of megaripples and sand waves on the inner shelf is a worldwide phenomenon, or whether it is the result of the efficient 'scale-matching' response of the Bight water mass to 'northeaster' storms crossing the Bight on appropriate trajectories.

In our study area, transverse bedforms occur in three well defined modes that may occur in any combination: ripples (5–150 cm spacing), megaripples (1–40 m spacing), and sand waves (>40 m spacing). The three classes are responses to three different time scales of fluid motion and provide successively time-averaged information concerning sediment transport. During peak flow events ripples may be primarily responses to 'unidirectional' flow, but when observed after such events are usually symmetrical features that are responses to high frequency wave surge.

Megaripples form on the inner shelf during the storm months in patches several kilometres in diameter, but tend to be erased during the quiet summer months.

Sand waves with amplitudes in excess of 2 m occur in the northeastern flanks of shoal retreat massifs, where storm flow is constricted and accelerated, but low amplitude (less than 2 m) sand waves are widespread on the inner shelf. Individual sand waves survive through successive winter seasons.

Both megaripples and the more long-lived sand waves reveal consistent asymmetry, with steeper southwestern flanks. It appears that despite the frequent reversals in the direction of successive storm flows. inner shelf sand transport is consistently down-coast and offshore.

ACKNOWLEDGMENTS

The investigation described in this paper was supported in part by the New York Bight Project Office of the Marine Ecosystems Analysis Program, National Oceanic and Atmospheric Administration, and by the Division of Biomedical and Environmental Research, Department of Energy.

We thank J. Southard, R. Jackson, A. Bouma, M. Field, and H. Nelsen for providing helpful criticisms of the text.

REFERENCES

Allen, J.R.L. (1968a) *Current Ripples.* North Holland Publishing Co., Amsterdam.

Allen, J.R.L. (1968b) The nature and origin of bed-form heirarchies. ***Sedimentology*, 10,** 161–182.

Anonymous (1976) Evaluation of proposed sewage sludge dumpsite areas in the New York Bight. NOAA Tech. Memo. ERL MESA-11. Marine Ecosystems Analysis Program Off., Environmental Research Labs, NOAA, Boulder, Colorado.

Bagnold, R.A. (1956) The flow of cohesionless grains in fluids. *Phil. Trans. Soc.* **249,** 235–297.

Beardsley, R.C. & Butman, B., 1974. Circulation of the New England continental shelf: response to strong winter storms. *Geophys. Res. Lets,* **1,** 181–184.

Beardsley, R.C., Boicourt, W.C. & Hansen, D.V. (1976) Physical oceanography of the Middle Atlantic Bight. In: *Middle Atlantic Continental Shelf and the New York Bight.* Ed. by M. G. Gross. *Spec. Symp. Am. Soc. Limnol. Oceanogr.* **2,** pp. 20–34.

Boicourt, W.C. & Hacker, P.W. (1976) Circulation of the Atlantic continental shelf of the United States, Cape May to Cape Hatteras. *Mem. Soc. Royale des Sciences de Liege, 16th Series,* **10,** 187-200.

Bokuniewicz, H.J., Gordon, R.B. & Kastens, K.A. (1977) Form and migration of sand waves in a large esturary, Long Island Sound. *Mar. Geol.* **24,** 185–199.

Boothroyd, J.C. & Hubbard, D.K. (1975) Genesis of bedforms in mesotidal estuaries. In: *Estuarine Research,* vol. 2. (Ed. by L. E. Cronin), pp. 217–237. Academic Press, New York.

Bouma, A. & Hampton, M.A. (1977) Large dunes and other bedforms in lower Cook Inlet, Alaska. *9th Ann. Offshore Tech. Conf., Houston,* TX, preprint.

Bucher, W.H. (1919) Ripples and related sedimentary surface forms and their paleogeographic interpretations. *Am. J. Sci.* **47,** 149-210; 241–269.

Cornish, V. (1901a) On the formation of wave surfaces in sand. *Scottish Geographical Magazine,* **17,** 1–11.

Cornish, V. (1901b) On sand waves in tidal currents. *Geogrl J.* **18,** 170–202.

Csanady, G.T. (1976) Wind-driven and thermohaline circulation over continental shelves. In: *Effects of Energy-Related Activities on the Atlantic Continental Shelf.* (Ed. by B. Manowitz). *Brookhaven National Labs Report* 50484, 31–47.

Dalrymple, R.W., Knight, R.J. & Middleton, G.V. (1975) Intertidal sand bars in Cobequid Bay (Bay of Fundy). In: *Estuarine Research,* vol. 2. (Ed. by L. E. Cronin). pp. 293–307. Academic Press, New York.

Dingle, R.V. (1965) Sand waves in the North Sea mapped by continuous reflection profiling. *Mar. Geol.* **3,** 391–400.

Flemming, B.W. (1978) Underwater sand dunes along the southeast African continental margin: observations and implications. *Mar. Geol.* **26,** 177–198

Gadd, P.E., Lavelle, J.W. & Swift, D.J.P. (1978) Calculations of sand transport on the New York shelf using near-bottom current meter observations. *J. sedim. Petrol.* **48,** 239–252.

Harvey, J.G. (1966) Large sand waves in the Irish Sea. *Mar. Geol.* **4,** 49–55.

Hunt, R.E., Swift, D.J.P. & Palmer, H. (1977) Constructional shelf topography, Diamond Shoals, North Carolina. *Bull. geol. Soc. Am.* **88,** 299–311.

Inman, D.L. (1957) Wave-generated ripples in nearshore sands. *U.S. Army Corps of Engineers Tech. Memo. No.* **100,** pp. 1–42.

Jackson, R.G. II (1975) Hierarchical attributes and a unifying model of bedforms composed of cohesionless material and produced by shearing flow. *Bull. geol. Soc. Am.* **86,** 1523–1533.

Jones, N.S., Kain, J.F. & Stride, A.H. (1965) The movement of sand waves on Warts Bank, Isle of Man. *Mar. Geol.* **3,** 329–336.

Jordan, G.F. (1962) Large submarine sand waves. *Science,* **136,** 839.

Knebel, H.J. & Folger, D.W. (1976) Large sand waves on the Atlantic outer continental shelf around Wilmington Canyon, off eastern United States. *Mar. Geol.* **22,** M7–M15.

Langhorne, D.N. (1973) A sand wave field in the outer Thames estuary. *Mar. Geol.* **14,** 129–143.

Lavelle, J.W., Brashear, H.R., Case, F.N., Charnell, R.L., Gadd, P.E., Haff, K.W., Han, G.A., Kunselman, C.A., Mayer, D.A., Stubblefield, W.L. & Swift, D.J.P. (1976) Preliminary results of coincident current meter and sediment transport observations for wintertime conditions, Long Island inner shelf. *Geophys. Res. Letts,* **3,** 97–100.

Lavelle, J.W., Young, R.A., Swift, D.J.P. & Clarke, T.L. (1978) Near-bottom sediment concentration and fluid velocity measurements on the inner continental shelf, New York. *J. Geophys. Res.* (In press).

Ludwick, J.C. (1970a) Sand waves and tidal channels in the entrance to Chesapeake Bay. *Virginia J. Sci.* **21,** 178–184.

Ludwick, J.C. (1970b) Sand waves in the tidal entrance to Chesapeake Bay: preliminary observations. *Chesapeake Sci.* **11**, 98–110.

Ludwick, J.C. (1972) Migration of tidal sand waves in Chesapeake Bay entrance. In: *Shelf Sediment Transport: Process and Pattern.* (Ed. by D. J. P. Swift, D. B. Duane & O. H. Pilkey), pp. 377–410. Dowden, Hutchinson & Ross, Stroudsburg, PA.

Ludwick, J.C. (In press) Coastal currents and bottom sediment transport off Virginia Beach, Virginia. *J. Geophys, Res.* **83**, 2365–2372.

McCave, I.N. (1971) Sand waves in the North Sea off the coast of Holland. *Mar. Geol.* **10**, 199–225.

McClennen, C.F. (1973) New Jersey continental shelf near-bottom current meter records and recent sediment activity. *J. sedim. Petrol.* **43**, 371–380.

Middleton, G.V. & Southard, J.B. (1977) *Mechanics of Sediment Transport. Soc. econ. Paleont. Miner., Tulsa,* Short Course No. 3.

Nio, S.D. (1976) Marine transgressions as a factor in the formation of sand wave complexes. *Geologie Mijnb.* **55**, 18–40.

Reineck, H.F. (1963) Sedimentgefüge im Bereich der Südlichen Nordsee. *Abhandlungen Senckenbergischen Naturforschenden Gesellschaft* 505.

Sanders, J.E., Emery, K.O. & Uchupi, E. (1969) Microtopography of five small areas of the continental shelf by side-scanning sonar. *Bull. geol. Soc. Am.* **80**, 561–572.

Scott, J.T. & Csanady, G.T. (1976) Nearshore currents off Long Island. *J. geophys. Res.* **81**, 5403–5407.

Smith, J.D. (1970) Stability of a sand bed subjected to a shear flow of low Froude Number. *J. geophys. Res.* **75**, 5928–5940.

Southard, J.B. (1971) Representation of bed configurations in depth–velocity–size diagrams. *J. sedim. Petrol.* **41**, 903–915.

Southard, J.B. & Boguchwal, L.A. (1973) Flume experiments on the transition from ripples to lower flat bed with increasing grain size. *J. sedim. Petrol.* **43**, 1114–1121.

Stanley, D.J. & Kelling, G. (1968) Sedimentation patterns in the Wilmington Submarine Canyon area. In: *Ocean Sciences and Engineering of the Atlantic Shelf*, pp. 127–142. Trans. Mar. Technol. Soc., Philadelphia, PA.

Stanley, D.J., Fenner, P. & Kelling, G. (1972) Currents and sediment transport at the Wilmington Canyon shelf break, as observed by underwater television. In: *Shelf Sediment Transport: Process and Pattern* (Ed. by D. J. P. Swift, D. B. Duane and O. H. Pilkey), pp. 621–644. Dowden, Hutchinson & Ross, Stroudsburg, PA.

Straaten, L.M.J.U. van (1950) Giant ripples in tidal channels. In: *Tijdschrift Nederlandsche Aardrijksk Genootschaft*, **67**, 76–81.

Straaten, L.M.J.U. van (1953) Megaripples in the Dutch Wadden Sea and in the Basin of Arcachon (France). *Geologie Mijnb.* **15**, 1–11.

Stride, A.H. (1970) Shape and size trends for sand waves in a depositional zone of the North Sea. *Geol. Mag.* **107**, 469–477.

Stubblefield, W.L., Permenter, R.W. & Swift, D.J.P. (1977). Time and space variation in the surficial sediments of the New York Bight apex. *Estuarine and Coastal Mar. Sci.* **5**, 597–607.

Swift, D.J.P. & Freeland, G.L. (1978) Mesoscale current lineations on the inner shelf, Middle Atlantic Bight of North America. *J. sedim. Petrol.* **48**, 1257–1266.

Swift, D.J.P., Nelsen, T.A., McHone, J., Holliday, B., Palmer, H. & Shideler, G. (1977). Holocene evolution of the inner shelf of southern Virginia. *J. sedim. Petrol.* **47**, 1454–1474.

Swift, D.J.P., Sears, P.C., Bohlke, B. & Hunt, R. (1978). Evolution of a shoal retreat massif, North Carolina shelf: inferences from areal geology. *Mar.Geol.* **27**, 19–42.

Terwindt, J.H.J. (1971) Sand waves in the Southern Bight of the North Sea. *Mar. Geol.* **10**, 51–68.

Uchupi, E. (1968) Atlantic continental shelf and slope of the United States—physiography *Prof. Pap. U.S. geol. Surv.* 529-C.

Veen, J. van (1935) Sand waves in the North Sea. *Hydrogr. Rev.* **12**, 21–29.

Yalin, M.S. (1977) *Mechanics of Sediment Transport.* Pergamon Press, New York.

(*Manuscript received* 27 *February* 1978; *revision received* 24 *September* 1978)

39. Science 204, 1418-1421.

Seasat Synthetic Aperture Radar: Ocean Wave Detection Capabilities

Abstract. *A preliminary assessment has been made of the capability of the Seasat synthetic aperture radar to detect ocean waves. Comparison with surface and aircraft measurements from five passes of the satellite over the Gulf of Alaska indicates agreement to within about ± 15 percent in wavelength and about ± 25° in wave direction. These results apply to waves 100 to 250 meters in length, propagating in a direction predominantly across the satellite track, in sea states with significant wave height* ($H_{1/3}$) *in a range of 2 to 3.5 meters.*

It has been recognized for some time that airborne imaging radars can provide useful ocean wave information, although the exact mechanism by which microwave radar energy is backscattered and modulated to produce ocean wave imagery is still not well understood (*1*, *2*). This study is the first assessment of the ocean wave detection capabilities of the Seasat synthetic aperture radar (SAR). SAR data from five Gulf of Alaska Seasat Experiment (GOASEX) revolutions were provided by the Jet Propulsion Laboratory (JPL) in the form of positive transparencies.

The imagery available for this study was the product of uncontrolled processing; it was intended to be used only for a preliminary evaluation. The characteristics of this imagery were as follows. Range (across the satellite track) and azimuth (along the satellite track) resolution varied from 30 to 50 m. Azimuth scale factors varied by 2 to 10 percent, and range scale factors varied by as much as 17 percent in each of four subswaths of a given revolution. The distributed target dynamic range was about 13 dB for revolutions 1126 and 1169 and 16 dB for revolutions 1255, 1269, and 1306, but there was an additional 5- to 10-dB variation from near to far range because of mispositioning of the sensitivity time control gain adjustments in the SAR. Time coding errors may be as high as 5 seconds, so that specification of geographical location in imagery without land references may be in error by as much as 25 km. Despite these shortcomings in this preliminary version of the SAR imagery, the data yielded useful ocean wave information for comparison with surface and aircraft measurements.

Optical Fourier transforms (OFT's) of SAR ocean scenes yielded intensity spectra of the type shown in Fig. 1 (*3*). The wavelengths of linear features in the imagery are inversely proportional to distance from the OFT center, and the wave direction relative to the spacecraft heading (azimuth) is measured positive clockwise from the horizontal. The OFT process produces two peaks for each dominant wavelength present in the imagery, thus creating a 180° ambiguity in the wave direction. In this study, we have tentatively resolved the ambiguity by choosing either that direction which best agrees with available surface measurements or that direction which propagates waves from the open ocean toward shore. A rigorous resolution of this ambiguity in wave direction can be achieved by focusing the image on an optical processor (*2*). For details of the OFT techniques used in this study, see Born *et al.* (*4*).

Reduction of the OFT data included corrections for the range scale variations

Synthetic aperture radar image

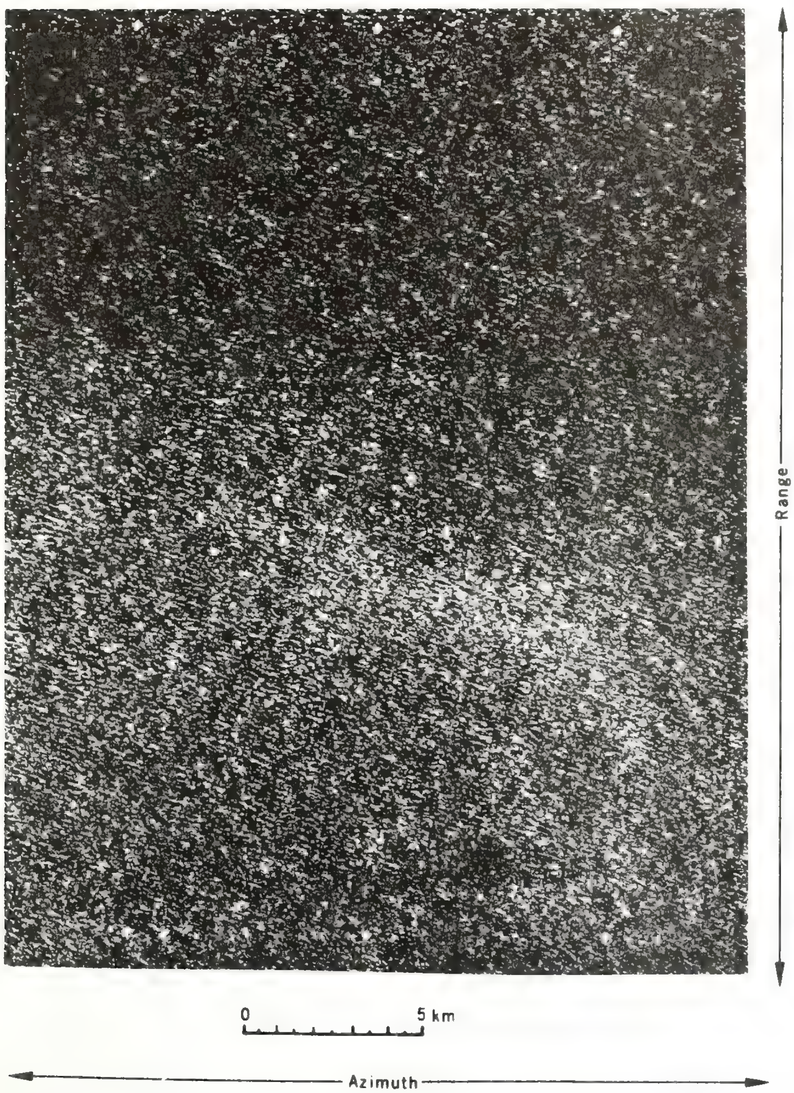

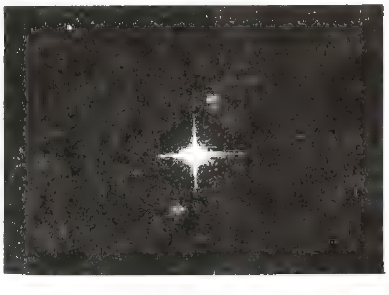

Optical Fourier transform

Fig. 1. Seasat SAR image and the resulting optical Fourier transform.

mentioned above. Inaccuracies associated with the somewhat subjective determination of the position of the OFT intensity peaks are the principal sources of errors, and these errors vary significantly with each particular spectrum. A rigorous error analysis of the technique has not yet been made, but successive measurements of the same OFT by different individuals have suggested a repeatability of about ± 15 percent in wavelength and ± 20° in wave direction.

Wavelengths and wave directions derived from the OFT measurements were compared with surface and aircraft measurements obtained coincidentally with the acquisition of the Seasat SAR imagery. The principal source of the surface truth was a pitch-roll (P-R) buoy, developed by the National Institute of Oceanography in Wormley, England. The buoy, deployed from the National Oceanic and Atmospheric Administration (NOAA) research vessel *Oceanographer*, measured vertical acceleration, pitch, roll angles, and orientation relative to north. Cross-correlations of these signals yielded a decomposition of the variance of the sea surface over frequency and direction (*5*). An integration over all directions then yielded one-dimensional frequency spectra, the peak frequency of which was inserted into the small-amplitude, linear gravity wave dispersion relationship to obtain the dominant wavelength present. In a more rigorous approach one would transform the entire frequency spectra into wavelength spectra; the resulting peak wavelength is then compared with the OFT measurements (*6*). The spectral peaks examined in the study were sufficiently sharp to justify the present approach, although the transformations are planned as part of a later analysis. The sampling rate of the buoy was 2 Hz, and the nominal operating time was 30 minutes (bracketing the time of the satellite overpass). The spectra were resolved into 64 frequency bands, each of approximately 64 degrees of freedom; this translates roughly into accuracies of about ± 10° for wave direction and ± 20 percent for wavelengths in the range of interest.

Similarly, the peaks of one-dimensional frequency spectra, computed from accelerometer measurements made by NOAA National Data Buoy Office (NDBO) data buoys, yielded dominant wavelength estimates that were also compared with Seasat SAR data. Because of the finer frequency resolution of these buoys, somewhat smaller errors (about ± 15 percent in wavelength) are estimated for the range of interest.

Finally, for three of the five revolutions examined, the Canadian CV-580 aircraft, equipped with the dual-polarized X- and L-band SAR of the Environmental Research Institute of Michigan (ERIM) provided ocean surface imagery for comparison with Seasat SAR. Direct measurements were made of the wavelength and wave direction of ocean wave patterns in the raw imagery; a conversion was made from slant to ground-range coordinates, and Doppler corrections were also applied to compensate for aircraft motion (*7*). The errors associated with this procedure were estimated to be about ± 10 m in wavelength and about ± 10° in wave direction.

Tables 1 through 3 present a summary of the resulting Seasat and surface or aircraft data pairs compared in this study. Two important limitations of the data set are apparent. Surface measurements indicate that (i) most waves present in the imagery examined thus far were traveling toward the east in a narrow range of directions and (ii) significant wave heights ($H_{1/3}$) were limited to a range of about 1 to 3.5 m.

Table 1. Seasat data taken within 100-km coincidence of surface or aircraft data (Table 2); λ, wavelength; θ, wave direction; subscripts T and A refer to direction measurements made relative to true north and azimuth direction, respectively.

Date (1978)	Revolution	Data source	Time (G.M.T.)	Location		Sea state data		
				Sub-swath	Distance from swath start (km)	λ (m)	θ_T (deg)	θ_A (deg)
9/13	1126A	ERIM OFT	17:29	4	315	194	096/276	125
9/13	1126A	ERIM OFT	17:29	4	475	217	097/277	126
9/13	1126A	ERIM OFT	17:30	4	695	205	083/263	113/293
9/13	1126A	ERIM OFT	17:30	4	695	265	114/294	144/324
9/13	1126A	JPL OFT	17:30	1	725	225	097/277	127/307
9/13	1126A	JPL OFT	17:30	1	725	259	077/257	107/287
9/16	1169A	ERIM OFT	17:43	1	810	329	094/274	122
9/16	1169A	ERIM OFT	17:45	1	1445	260	090	120
9/16	1169A	ERIM OFT	17:45	2	1445	231	083	113
9/16	1169A	ERIM OFT	17:45	3	1445	252	088	118
9/16	1169A	JPL OFT	17:45	2	1460	215	091	121
9/16	1169A	JPL OFT	17:45	1	1500	289	104	135
9/22	1255A	ERIM OFT	18:09	2	870	212	100	130
9/22	1255A	JPL OFT	18:09	2	930	188	089	119
9/22	1255A	ERIM OFT	18:09	2	935	182	084	114
9/22	1255A	ERIM OFT	18:09	2	1000	191	090	121
9/22	1255A	ERIM OFT	18:09	2	1035	181	087	118
9/22	1255A	ERIM OFT	18:09	2	870	212	100	130
9/22	1255A	JPL OFT	18:09	2	930	188	089	119
9/22	1255A	ERIM OFT	18:09	2	935	182	084	114
9/22	1255A	ERIM OFT	18:09	2	1000	191	090	121
9/22	1255A	ERIM OFT	18:09	2	1035	181	087	118
9/23	1269A	ERIM OFT	17:51	(Swiftsure Bank)		165	091	121
9/23	1269A	ERIM OFT	17:51	(Swiftsure Bank)		165	091	121
9/23	1269A							
9/26	1306D	ERIM OFT	08:00	(Swiftsure Bank)		Spectra not discernible		
9/26	1306D	ERIM OFT	08:00	(Swiftsure Bank)		Spectra not discernible		
9/26	1306D	ERIM OFT	08:00	(Swiftsure Bank)		Spectra not discernible		
9/26	1306D	ERIM OFT	08:00	(Swiftsure Bank)		Spectra not discernible		
9/26	1306D							

Table 2. Surface and aircraft data (surface truth data) taken within 100-km coincidence of Seasat measurements (Table 1); λ, wavelength; θ, wave direction; U, wind speed; α, wind direction. Subscripts T and A are the same as in Table 1.

				Location		Sea state data				Wind data		
Date (1978)	Revolution	Data source	Time (G.M.T.)	Sub-swath	Distance from swath start (km)	λ (m)	θ_T (deg)	θ_A (deg)	$H_{1/3}$ (m)	U (m/sec)	α_T (deg)	α_A (deg)
9/13	1126A	NDBO 05	17:44–18:16	4	385	193			2.1	7.4	331	000
9/13	1126A	NDBO 05	17:44–18:16	4	385	193			2.1	7.4	331	000
9/13	1126A	P-R buoy	17:29–18:04	2	730	256	096/276	126/306	2.7	3.8	244	274
9/13	1126A	P-R buoy	17:29–18:04	2	730	256	096/276	126/306	2.7	3.8	244	274
9/13	1126A	P-R buoy	17:29–18:04	2	730	256	096/276	126/306	2.7	3.8	244	274
9/13	1126A	P-R buoy	17:29–18:04	2	730	256	096/276	126/306	2.7	3.8	244	274
9/16	1169A	NDBO 02	17:44–18:16	1	715	318			2.7	7.5	334	002
9/16	1169A	P-R buoy	17:45–18:20	2	1440	256	110	140	3.6	11.8	295	325
9/16	1169A	P-R buoy	17:45–18:20	2	1440	256	110	140	3.6	11.8	295	325
9/16	1169A	P-R buoy	17:45–18:20	2	1440	256	110	140	3.6	11.8	295	325
9/16	1169A	P-R buoy	17:45–18:20	2	1440	256	110	140	3.6	11.8	295	325
9/16	1169A	P-R buoy	17:45–18:20	2	1440	256	110	140	3.6	11.8	295	325
9/16	1169A	P-R buoy	17:45–18:20	2	1440	256	110	140	3.6	11.8	295	325
9/22	1255A	P-R buoy	18:03–18:38	2	935	177	094	124	2.7	8.3	243	273
9/22	1255A	P-R buoy	18:03–18:38	2	935	177	094	124	2.7	8.3	243	273
9/22	1255A	P-R buoy	18:03–18:38	2	935	177	094	124	2.7	8.3	243	273
9/22	1255A	P-R buoy	18:03–18:38	2	935	177	094	124	2.7	8.3	243	273
9/22	1255A	P-R buoy	18:03–18:38	2	935	177	094	124	2.7	8.3	243	273
9/22	1255A	CV-580 SAR (visual)	18:45–20:00	2	935	200	107	137				
9/22	1255A	CV-580 SAR (visual)	18:45–20:00	2	935	200	107	137				
9/22	1255A	CV-580 SAR (visual)	18:45–20:00	2	935	200	107	137				
9/22	1255A	CV-580 SAR (visual)	18:45–20:00	2	935	200	107	137				
9/22	1255A	CV-580 SAR (visual)	18:45–20:00	2	935	200	107	137				
9/23	1269A	P-R buoy	20:57–21:32	(Swiftsure Bank)		130*	102	132	2.5	5.1	090	120
9/23	1269A	CV-580 SAR (visual)	17:45–19:00	(Swiftsure Bank)		171*	099	129				
9/23	1269A	Tofino wave rider	18:00	(90 km northeast of Swiftsure Bank)		180†			1.6			
9/26	1306D	P-R buoy	07:57–08:32	(Swiftsure Bank)		245*	358	148	1.1	11.8	095	245
9/26	1306D	P-R buoy	07:57–08:32	(Swiftsure Bank)		130*	100	250	1.1	11.8	095	245
9/26	1306D	CV-580 SAR (visual)	07:25–08:25	(Swiftsure Bank)		Waves not discernible						
9/26	1306D	CV-580 SAR (visual)	07:25–08:25	(Swiftsure Bank)		Waves not discernible						
9/26	1306D	Tofino wave rider	08:00	(90 km northeast of Swiftsure Bank)		234†			0.94			

*A depth of 75 m was assumed for the wavelength computation. †A depth of 40 m was assumed at Tofino for the wavelength computation.

Table 3. Comparison of the Seasat and surface-aircraft data (Tables 1 and 2).

		Space/time coincidence		λ					Space/time coincidence		λ		
Date (1978)	Revolution	Δx (km)	Δt (hour/min)	$\Delta\lambda$ (m)	Difference (%)	$\Delta\theta_T$ (deg)	Date (1978)	Revolution	Δx (km)	Δt (hour/min)	$\Delta\lambda$ (m)	Difference (%)	$\Delta\theta_T$ (deg)
9/13	1126A	70	00:31	1	0.5		9/22	1255A	65	00:11	14	7.9	−03
9/13	1126A	90	00:31	24	12.4		9/22	1255A	100	00:11	4	2.3	−06
9/13	1126A	60	00:16	−51	−20.0	−13	9/22	1255A	65	01:13	12	6.0	−07
9/13	1126A	60	00:16	9	3.5	18	9/22	1255A	05	01:13	−12	−6.0	−18
9/13	1126A	25	00:16	−31	−12.1	01	9/22	1255A	00	01:13	−18	−9.0	−23
9/13	1126A	25	00:16	3	1.2	−19	9/22	1255A	65	01:13	−9	4.5	−16
9/16	1169A	95	00:17	11	3.5		9/22	1255A	100	01:13	−19	−9.5	−19
9/16	1169A	25	00:18	4	1.6	−20	9/23	1269A	00	03:24	35	26.9	−11
9/16	1169A	05	00:18	−25	−9.8	−27	9/23	1269A	00	00:14	−6	−3.5	−08
9/16	1169A	25	00:18	−4	−1.6	−22	9/23	1269A					
9/16	1169A	20	00:18	−41	−16.0	−19	9/26	1306D	00	00:15			
9/16	1169A	70	00:18	33	12.9	−06	9/26	1306D	00	00.15			
9/22	1255A	65	00:11	35	19.8	06	9/26	1306D	00	00:05			
9/22	1255A	05	00:11	11	6.2	−06	9/26	1306D	00	00:05			
9/22	1255A	00	00:11	5	2.8	−10	9/26	1306D					

The practical consequence of the first observation is that the present data set is inadequate to address the important question of possible defocusing and resultant degradation (*8*) of Seasat SAR imagery of azimuth-traveling waves, for most waves were apparently traveling in a direction that was within 45° of the satellite range coordinate. This is so because the wave climatology during September for the region in the Gulf of Alaska corresponding to the imagery examined is such that most wave energy can be expected to propagate toward 90° (*9*) while the satellite heading at these latitudes was about 330°.

Despite these limitations on the data, some tentative conclusions can be drawn. There are 11 Seasat SAR/surface-aircraft data pairs in Table 3 which were acquired within 25 km and 1.5 hours of each other; this set yields agreement in wavelength to within about ± 15 percent and agreement in wave direction to within about ± 25°. Thus, the limited data set examined so far meets NOAA requirements for oceanographic measurement accuracy of ± 10 to ± 25 percent in wavelength and ± 10° to ± 30° in wave direction (*10*). If data pairs taken more than 25 km apart are included in the comparison, the agreement in wavelength is degraded to about ± 25 percent.

The data in Tables 1 and 2 also suggest a range of 1 to 2 m for $H_{1/3}$ where the lower limit for wave detection might fall. Thus, no waves were detected in Seasat SAR imagery acquired during revolution 1306, for which P-R buoy measurements indicated an $H_{1/3}$ of about 1 m; however, waves were detected during revolution 1126, for which an $H_{1/3}$ of about 2 m was observed. However, Tables 1 and 2 show that the dominant ocean wavelength and the relative angles between wind, wave, and satellite headings differed significantly in each case; these parameters may be equally as important as $H_{1/3}$ relative to wave detection capabilities. Thus caution must be exercised in the interpretation of this result.

Most of the GOASEX SAR data and surface measurements remain to be compared and analyzed. The preliminary nature of the data reduction, comparison, and analysis of the limited data set examined here should be noted. Seasat imagery of improved quality will be used in later analyses. The P-R buoy data will be processed at finer frequency resolution, and the resulting spectra transformed to wave number or wavelength space to improve comparisons with intensity spectra resulting from OFT's of Seasat imagery. Aircraft data will be digitized, so that geometric corrections and motion compensations can be made more accurately.

F. I. GONZALEZ
Pacific Marine Environmental Laboratory, National Oceanic and Atmospheric Administration, Seattle, Washington 98105
R. C. BEAL
Applied Physics Laboratory, Johns Hopkins University, Laurel, Maryland 20810
W. E. BROWN
Jet Propulsion Laboratory, California Institute of Technology, Pasadena 91103
P. S. DELEONIBUS, J. W. SHERMAN III
National Environmental Satellite Service, National Oceanic and Atmospheric Administration, Washington, D.C. 20233
J. F. R. GOWER
Institute of Ocean Sciences, Sidney, British Columbia, Canada V8L 4V2
D. LICHY
U.S. Army Corps of Engineers, Coastal Engineering Research Center, Fort Belvoir, Virginia 22060
D. B. ROSS
Sea-Air Interaction Laboratory, National Oceanic and Atmospheric Administration, Miami, Florida 33149
C. L. RUFENACH
Wave Propagation Laboratory, National Oceanic and Atmospheric Administration, Boulder, Colorado 80303
R. A. SHUCHMAN
Environmental Research Institute of Michigan, Ann Arbor 48107

References and Notes

1. W. E. Brown, Jr., C. Elachi, T. W. Thompson, *J. Geophys. Res.* **81**, 647 (1976); C. Elachi and W. E. Brown, *IEEE Trans. Antennas Propag.* **AP–25**, 84 (1977); T. R. Larson, L. I. Moskowitz, J. W. Wright, *ibid.* **AP–24**, 393 (1976); J. W. Wright, *ibid.* **AP–14**, 719 (1966); P. G. Teleki, R. A. Shuchman, W. E. Brown, Jr., W. McLeish, D. E. Ross, M. Mattie, *Proceedings of the Oceans '78 Conference* (Washington, D.C., 6 to 8 September 1978), pp. 639–648.
2. R. A. Shuchman, E. S. Kasischke, A. Klooster, *Synthetic Aperture Radar Ocean Wave Studies* (Final Report 131700-3-F, Environmental Research Institute of Michigan, Ann Arbor, 1978).
3. J. W. Goodman, *Introduction to Fourier Optics* (McGraw-Hill, New York, 1968).
4. G. H. Born, D. B. Lame, J. C. Wilkerson, Eds. "GOASEX Workshop Report" (Report 622-101, Jet Propulsion Laboratory, California Institute of Technology, Pasadena, 1979) (internal document), vol. 1, appendix A.
5. J. A. Ewing, *J. Mar Res.* **27**, 163 (1969); H. Mitsuyasu, F. Tasai, T. Suhara, S. Mizumo, L. Ohkusu, T. Honda, K. Rikiishi, *J Phys. Oceanog.* **5**, 750 (1975).
6. W. C. Chiu, *Am. J. Phys.* **35**, 642 (1967).
7. R. K. Raney, paper presented at the 5th Canadian Remote Sensing Symposium, Victoria, British Columbia, 1978.
8. R. A. Shuchman and J. S. Zelenka, *Boundary-Layer Meteorol.* **13**, 181 (1978); A. Jain, *J. Appl. Phys.* **15**, 323 (1973).
9. U.S. Navy, *U.S. Navy Marine Climatic Atlas of the World*, vol. 2, *North Pacific Ocean* (Naval Air Force Document 50-1C-529, Naval Weather Service Detachment, Asheville, N.C., 1977), p. 265.
10. "NOAA Program Development Plan for Seasat-A: Research and Applications" (Report NOAA-S/T 77-2574, Department of Commerce, Washington, D.C., March 1977), p. 1–2.
11. We thank J. C. Dwyer of the Environmental Research Institute of Michigan (ERIM) and T. Bicknell of the Jet Propulsion Laboratory for providing the optical Fourier transforms. We thank P. G. Teleki and J. Dunne for their advice and helpful comments during and after the GOASEX Workshop. The ERIM portion of the analysis was supported under NOAA National Environmental Satellite Service contract MO-AO1-78-00-4339. Portions of the research described in this report were carried out by the Jet Propulsion Laboratory, California Institute of Technology, and were sponsored by the National Oceanic and Atmospheric Administration and National Aeronautics and Space Administration.

20 April 1979

40. Science 204, 1415-1417.

Seasat Scanning Multichannel Microwave Radiometer: Results of the Gulf of Alaska Workshop

Abstract. *The scanning multichannel microwave radiometer results for the Gulf of Alaska Seasat Experiment Workshop are quite encouraging, especially in view of the immaturity of the data-processing algorithms. For open ocean, rain-free cells of highest-quality surface truth wind determinations exhibit standard deviations of 3 meters per second about a bias of 1.5 meters per second. The sea-surface temperature shows a standard deviation of approximately 1.5°C about a bias of 3° to 5°C under a variety of changing meteorological conditions.*

The Seasat scanning multichannel microwave radiometer (SMMR) was flown to provide estimates of sea-surface temperature (SST) and surface wind speed (*1*), geophysical parameters of value in weather prediction, oceanographic research, and commercial operations. The accurate determination of these two parameters requires estimates of atmospheric water vapor and liquid water (clouds and rain). To provide these geophysical outputs, the SMMR measures Earth radiation with a scanning antenna operating at 6.6, 10.7, 18, 21, and 37 GHz at vertical and horizontal polarizations. The SMMR scans to the starboard side of the spacecraft track and has a swath width of 600 km.

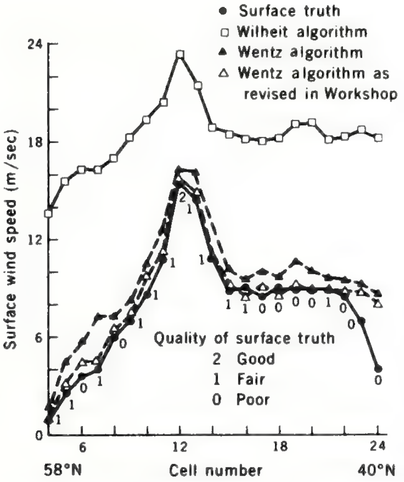

Fig. 1. Seasat SMMR wind comparison for revolution 1298; the scan was conducted near the center of the swath.

The antenna temperature measured by a radiometer system is the weighted integral of the brightness temperature distribution over all solid angles. The weighting is provided by the antenna patterns, which are peaked in the boresight direction and taper off rapidly away from the boresight to the lower sidelobe levels. The purpose of the antenna pattern correction (APC) algorithm (*2*) is to invert the antenna pattern effects, deriving brightness temperatures from measurements of the antenna temperature. In addition, the algorithm corrects for polarization mixing introduced by the scanning mode and averages the data onto Earth-located grids for geophysical data processing.

To provide an early data-processing capability for the SMMR, an interim version of the APC was developed which contains all the major corrections except sidelobe effects within the Earth-viewing region. In the open ocean away from land regions, it was anticipated that results accurate enough for an initial data evaluation would be obtainable with the APC interim version. The interim version has been used for the Gulf of Alaska Seasat Experiment (GOASEX) Workshop.

Two entry algorithms to retrieve geophysical parameters were investigated in the GOASEX Workshop. The Wentz geophysical algorithm (*3*) is based on a

0036-8075/79/0629-1415$00.50/0 Copyright © 1979 AAAS

theoretically derived function for computing the brightness temperatures observed by the SMMR. This function depends on the SST, the sea-surface wind speed, the columnar atmospheric water vapor, and the columnar liquid cloud water. A nonlinear, iterated, least-squares estimator operates on this function to determine the several environmental parameters sensed by the SMMR. The Wilheit geophysical algorithm is based on statistical relationships between brightness temperatures and the geophysical parameters obtained from an ensemble of realistic SST values, wind speeds, atmospheric temperature profiles, water vapor profiles, and cloud models by multiple linear regression. One treats nonlinear features of the problem by relating a suitable function (not necessarily linear) of brightness temperature to the geophysical parameters and by using differing sets of regression coefficients which depend upon values of geophysical parameters determined in an initial calculation.

Table 1. Comparison of SMMR-derived surface wind speed against surface truth field data from kinematic analysis of revolutions 1135, 1212, 1292, and 1298

Swath location	Bias (m/sec)	RMSD (m/sec)	δ (m/sec)	No. of samples
Wentz algorithm versus category 2 surface truth				
Inner edge	2.83	4.41	3.66	7
Center scans	1.54	3.22	2.86	42
Outer edge	0.46	2.49	2.61	8
Overall	1.54	3.30	2.95 (2.93)*	57
Wilheit algorithm versus category 2 surface truth				
Inner edge	10.56	10.95	3.13	7
Center scans	7.75	8.02	2.28	42
Outer edge	5.31	5.73	2.29	8
Overall	7.75	8.20	2.71 (2.40)*	57
Wentz algorithm versus category 1 surface truth				
Inner edge	2.62	4.30	3.47	27
Center scans	2.28	4.18	3.52	96
Outer edge	0.78	3.21	3.20	18
Overall	2.16	4.09	3.49 (3.47)*	141
Wilheit algorithm versus category 1 surface truth				
Inner edge	12.28	12.61	2.84	27
Center scans	8.51	9.07	3.14	96
Outer edge	4.58	5.60	3.21	18
Overall	8.73	9.51	3.77 (3.09)*	141

*Error residual after removal of cross-track-dependent biases.

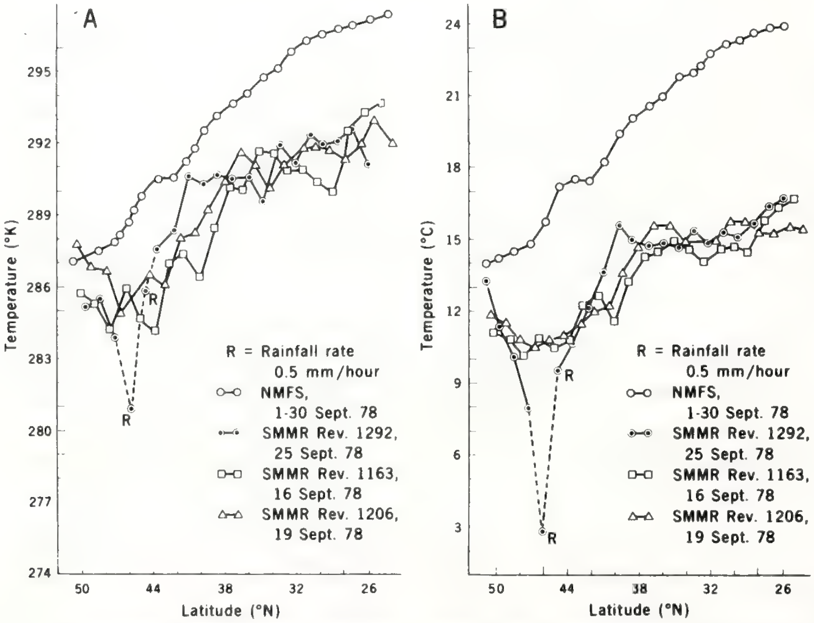

Fig. 2. Comparison of the NMFS sea temperature analysis with SMMR data from the east track for (A) Wilheit and (B) Wentz algorithms.

The GOASEX Workshop version of the SMMR algorithms can best be described as preliminary. The first geophysical outputs were produced in late November 1978. The data, from a pass over Hurricane Fico, uncovered a number of software errors and a few conceptual errors in the geophysical processing algorithms. During the 2 months available to produce data for the workshop, such errors were corrected where possible. However, the entry geophysical algorithms were not refined with the use of Seasat data in this process.

During initial evaluation activities, brightness temperature gradients from one edge of the swath to the other were observed in several of the passes, particularly for the 6.6-GHz channel. The geophysical algorithms interpret these gradients as variations due to wind speed or SST across the swath. In most cases, such variations were not found in surface truth, particularly in the SST. Potential causes for these cross-track biases are polarization cross-coupling, deviation of the spacecraft attitude from nominal (as assumed in the interim APC), and Faraday rotation. We circumvented this difficulty in the GOASEX Workshop by restricting evaluation to data sets having the same location in the swath (for example, near the center of the swath).

Wind speed data derived from the SMMR were evaluated on the basis of detailed studies of data from four GOASEX orbits characterized by a wide range of wind speeds and atmospheric conditions. These wind speeds were compared to the surface truth wind fields at roughly five points in the cross-track direction, three points near the center of the swath and one point at each edge. Figure 1 compares the surface truth wind speeds to winds computed by the entry algorithms. Both algorithms successfully track the relative changes in the wind speeds observed, although both algorithms, especially the Wilheit algorithm, exhibit significant bias.

Similar plots from other orbits revealed two additional features of the SMMR winds produced through both algorithms. First, the algorithms fail to provide reasonable relative or absolute measures of the wind speed when rain, as indicated by the algorithms and corroborated by satellite and ship data, was present. Second, an unrealistic variation in cross-track bias appears in the wind speeds. Possible reasons for the cross-track bias are given above.

The overall performance of the entry

algorithms demonstrated in the limited data set examined here is shown in Table 1. The statistics computed are (i) the mean difference or bias (SMMR minus surface truth), (ii) the root-mean-square difference (RMSD), and (iii) the standard deviation of the error about the mean, δ. The statistics are stratified by surface truth category, algorithm, and relative location within the swath. The inner edge is always located near the subsatellite track. Grid points near land and at points at which either algorithm indicated that rain was present were excluded. The surface truth data from kinematic analyses were categorized by estimated accuracy (primarily determined by spot report proximity and number) with categories 1 and 2 believed to be accurate to ± 3 and ± 2 m/sec, respectively.

This initial statistical evaluation is encouraging, in view of the fact that the algorithms have yet to be refined by the use of Seasat data. The systematic cross-swath variation in the wind speed bias is evident in both algorithms, although to a larger degree in the Wilheit algorithm. As the quality of the surface truth degrades, so does the error in the SMMR winds; this result suggests that already a significant fraction of the RMSD in wind can be assigned to the surface truth. This initial study suggests strongly that, with higher-quality surface truth data (as from data buoys) and further refinements of the entry algorithm, the Seasat SMMR design goal of a wind speed measurement capability of ± 2 m/sec can be met, at least under nonprecipitating conditions. Further evidence for this conclusion can be drawn from the plot (Fig. 1) of the Wentz winds resulting after changes suggested in the GOASEX Workshop were made. The bias for this near-center swath position has been effectively removed. Unfortunately, the bias is only reduced for cross-scan positions near the swath edges (not shown in Fig. 1).

The SST comparison data were taken from the September 1978 bulletin of the National Marine Fisheries Service (NMFS) (*4*). The accuracy of these data has been compared to higher-quality, expendable bathythermograph data (accurate to ± 0.2°C) collected on semimonthly aircraft flights. The comparison for 13 September 1978 shows the NMFS data biased high by 0.7°C with a standard deviation of 0.9°C, which is in agreement with the advertised accuracy of these data. Consequently, we believe that the NMFS data were adequate for the preliminary analysis presented here.

We evaluated SMMR-derived SST data for six Gulf of Alaska passes. Since the spacecraft was in a 3-day, repeat ground track orbit, the data consisted of two descending tracks separated by about 2000 km (referred to as east and west tracks), each of which was covered on three passes. The SMMR SST values were extracted from one of the cells closest to the center of the swath in an effort to minimize the cross-track bias problem. Figure 2 presents the data from six SMMR passes from the east track for both the Wilheit and Wentz algorithms; the NMFS analysis along each track is also plotted. In almost every case, the SMMR temperatures are low by several degrees or more. In addition, the Wentz algorithm yields increasing discrepancy toward the south. The Wilheit algorithm appears to successfully provide the meridional gradient. Means and standard deviations of SMMR SST values from this algorithm relative to the NMFS values for both east and west tracks are given in Table 2.

Table 2. Seasat passes used in the study of SMMR sea-surface temperature data. The mean and the standard deviation of the SMMR values (Wilheit algorithm) are given with respect to the monthly NMFS analysis.

Revolution	Date (1978)	T_{SMMR} minus T_{NMFS} (°C)		
		Mean	Standard deviation	No. of samples
West track				
1163	9/16	−4.1	1.3	21
1206	9/19	−3.5	1.4	22
1292	9/25	−3.2	1.8	18
East track				
1164	9/16	−4.8	0.9	20
1207	9/19	−4.5	1.6	25
1293	9/25	−3.9	1.4	20

Once the cold bias (3° to 4°C) is removed, individual SMMR estimates are in agreement with the NMFS analysis to approximately ± 1.5°C. The stability of the SMMR SST estimates over the 9-day period (16 through 25 September 1978) is encouraging evidence that the instrument and the Wilheit algorithm are operating well over a variety of changing meteorological conditions. Significantly degraded accuracy was expected for retrievals of SST values under rainfall conditions exceeding 0.5 mm/hour. Points in Fig. 2 where the rain exceeded this amount are marked with an *R*. Only one point, for revolution 1292 at 46°N, indicates serious rain problems. This result suggests that 0.5 mm/hour may be too conservative a value.

The algorithms determined integrated atmospheric water vapor and altimeter path length corrections that are quite consistent with the limited surface truth provided by a set of radiosonde ascents over the Canadian ocean weather station PAPA, the National Oceanic and Atmospheric Administration research vessel *Oceanographer*, and Bermuda. This sample set, although insufficient for a full statistical evaluation, indicates that integrated water vapor agreed to within 0.3 g/cm^2 root-mean-square, and the altimeter path length correction was within 2 cm root-mean-square of radiosonde-determined values.

Probably because of biases in the brightness temperature input, both algorithms produce small negative integrated liquid water content in many cells. Surface truth data of this type were not available for comparison. The rain rate determinations of the two algorithms are consistent with each other. The rain pattern for the ascending 19 September 1978 pass is corroborated by ship reports in the vicinity of the front.

R. G. LIPES
Jet Propulsion Laboratory,
California Institute of Technology,
Pasadena 91103
R. L. BERNSTEIN
Scripps Institution of Oceanography,
University of California, San Diego,
La Jolla 92093
V. J. CARDONE
Oceanweather, Inc., New York 10601
K. B. KATSAROS
University of Washington,
Seattle 98195
E. G. NJOKU, A. L. RILEY
Jet Propulsion Laboratory
D. B. ROSS
Atlantic Oceanic and Meteorological
Laboratory, National Oceanic and
Atmospheric Administration,
Miami, Florida 33149
C. T. SWIFT
NASA Langley Research Center,
Hampton, Virginia 23665
F. J. WENTZ
Frank J. Wentz and Associates,
San Francisco, California 94103

References and Notes

1. P. Gloersen and F. Barath, *IEEE J. Oceanic Eng.* **OE-2**, 172 (1977).
2. E. Njoku, *Boundary-Layer Meteorol.*, in press.
3. G. J. Bierman, R. G. Lipes, F. J. Wentz, paper presented at the Twelfth Annual Asilomar Conference on Circuits, Systems, and Computers, Pacific Grove, Calif., 6 to 8 November 1978.
4. NOAA National Marine Fisheries Service, "Fishing Information" (Southwest Fisheries Center, La Jolla, Calif., September 1978).
5. The work described in this report was carried out by the Jet Propulsion Laboratory, California Institute of Technology, under NASA contract NAS7-100.

20 April 1979

41. Mariners Weather Log, 23, No. 1, 1-10.

Mariners Weather Log

FORECASTING HURRICANE WAVES

Robert Bryan Long
Atlantic Oceanographic and Meteorological
Laboratories, NOAA
Miami, Fla.

Although prehistoric man knew that the wind blowing over the surface of the sea produced waves, it is only in recent years that we have acquired sufficient understanding of that process to make reliable, useful wave prediction a practical possibility. Prior to World War II, those people concerned with surface-water waves fell into two distinct groups: the hydrodynamicists who concerned themselves with the simplified, idealized problems for which their precomputer mathematics were adequate; and the mariners who had to deal with the vastly more complex real world on a day-to-day basis. There was not much communication between the two camps. The hydrodynamicists despaired of making sense out of the chaos of a real sea, and the mariners failed to find anything useful in the idealized models. This situation changed in World War II, when H.U. Sverdrup and W.H. Munk were called upon to develop a wave-forecasting scheme which would have some utility in planning military operations. Drawing on the best available knowledge at the time from both camps, they developed a technique (made public after the war in H.O. Publication No. 601, March 1947)

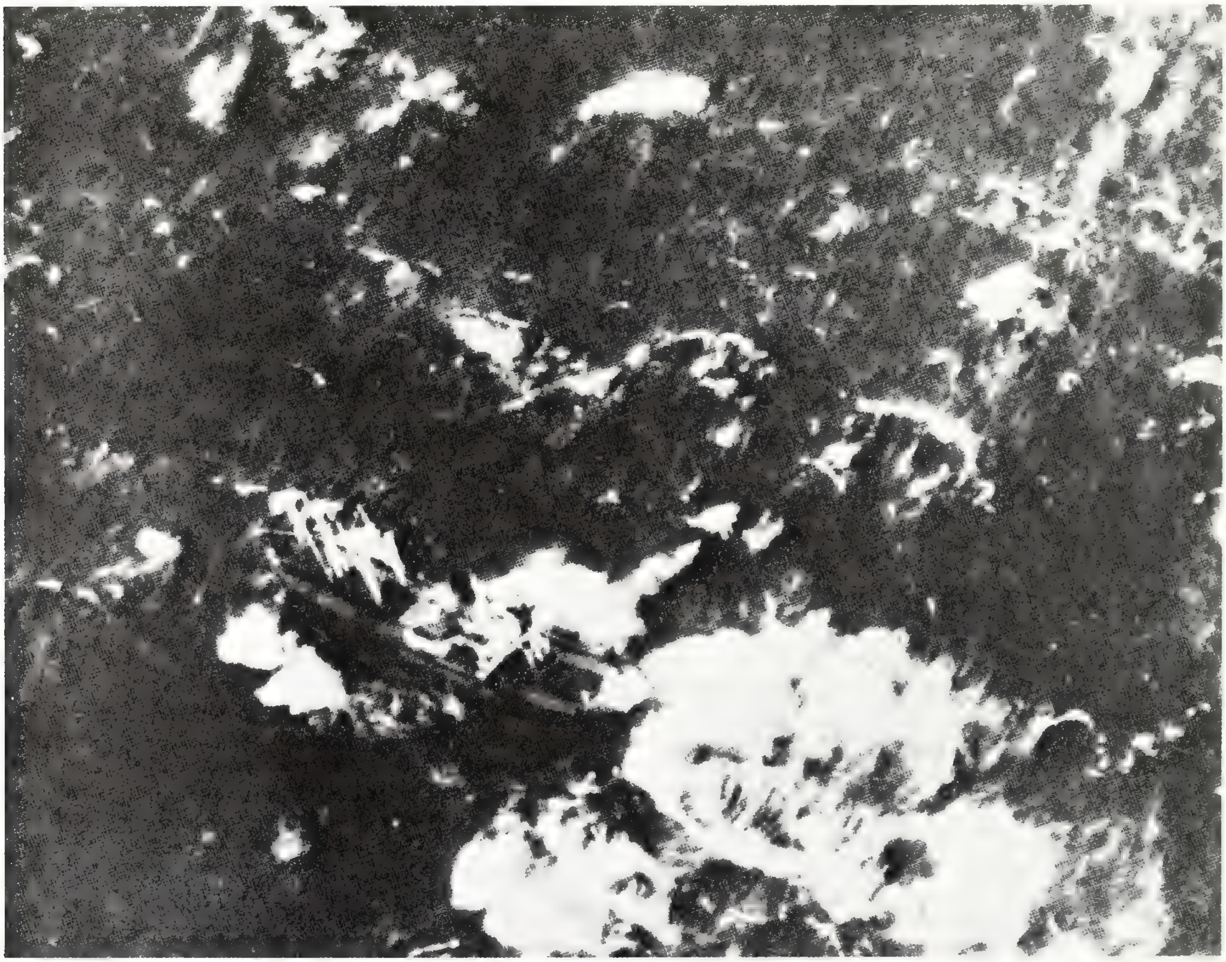

Figure 1.--This merchant vessel was caught in hurricane Carol in 1954. The photograph was taken by a U.S. Navy hurricane-hunter aircraft based at Jacksonville, Fla. U.S. Navy Photograph.

which, though in many respects primitive and in some respects simply wrong, undoubtedly led to the saving of thousands of lives in the massive amphibious operations conducted after 1943.

Great progress has been made since that first step forward, largely as a result of the recognition in the late 1940s and the early 1950's that the surface of the sea can only be usefully described statistically, and that the fundamental statistic is the two-dimensional surface wave spectrum. Given this property of the sea state, any other statistical property can be calculated; for example, such quantities as average wave height, period, and propagation direction; average momentum and energy in the wave field; mean squared, wave-induced water velocity; maximum probable wave height; and so on. The development of the two-dimensional wave spectrum in space and time is governed by a simple (at least in principle) mathematical equation. All modern wave prediction schemes are based upon obtaining solutions to this equation, the methods differing only in the construction of the elements of the equation and the methods employed to solve it.

The value of a reliable wave prediction scheme used a a forecasting tool is obvious (e. g., in planning military operations, ship routing, and so on). The U.S. Navy has a massive computerized wave-prediction scheme based on these principles in routine operation (Lazanoff and Stevenson, 1975), producing wave forecasts to 72 hr for the Northern Hemisphere. But it is potentially of even greater value used in the "hindcasting mode." As the fundamental description of sea state, the two-dimensional wave spectrum now plays a central role in the design of ships and marine structures, providing all the information needed by the engineer to compute the wave-induced stresses and excitations to which his designs will be subjected. Unfortunately, measurement of the two-dimensional spectrum is difficult, particularly under the severe conditions which primarily concern the engineer, so that few field observations exist. However, a great deal of data is available on the winds associated with storms; and a reliable wave-prediction scheme, driven by the wind fields of historical storms, can "hindcast" the corresponding wave spectra, providing the engineer with site-specific design criteria which would otherwise be unobtainable.

The development of the wave spectrum under hurricane winds (fig. 1) has been a problem of central interest at the Sea-Air Interaction Laboratory (SAIL) of NOAA's Atlantic Oceanographic and Meteorological Laboratories in Miami, Fla, for a number of years. In the course of this work several wave-prediction schemes (more simply, wave models) have been implemented on a UNIVAC 1108 computer. Used with the wind fields of theoretical model storms or reconstructed wind fields of historical storms, these wave models predict the development of the wave spectrum over the area affected by the storm as time advances. For historical storms, wave measurements made by aircraft penetrations or by moored data buoys are employed to test the performance of the wave models, while theoretical storms are used to study the response of the models to variations in the mix of theory and empiricism defining the governing equation. In the process, a great deal has been learned about the sea states generated in hurricanes. One of the most interesting discoveries is that the wave field development under a hurricane is frequently simple enough to be calculated to useful accuracy by hand.

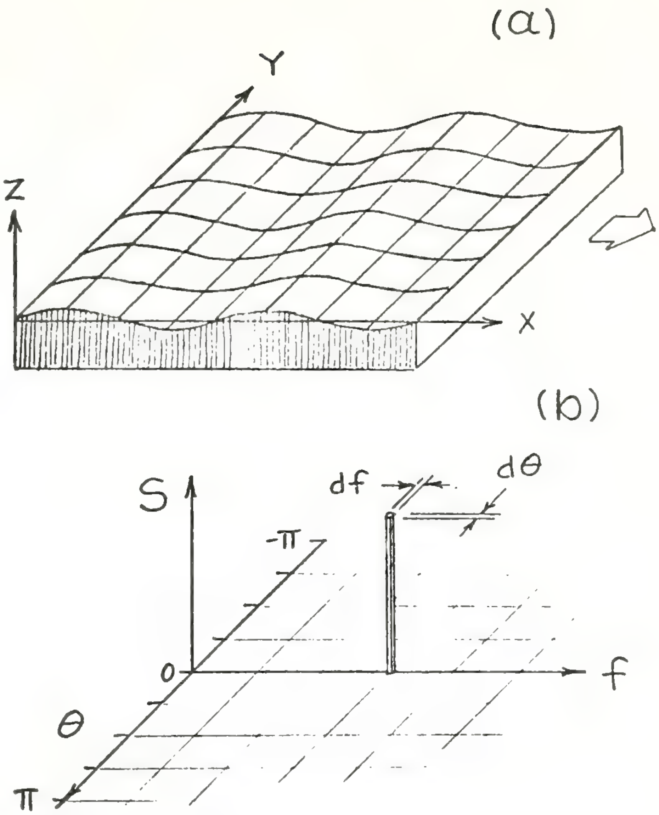

Figure 2.--Single-component sea and corresponding spectrum. The sinusoidal wave of panel (a) is propagating to the right along the x-direction. Panel (b) shows the corresponding directional spectrum S(f, θ), where f is the wave frequency and θ its propagation direction. θ is measured in radians on the range -π to + π (-180° to +180°) relative to the direction of x. The value of S (the height of the spike is proportional to the square of wave amplitude.

THE SPECTRUM

In order to understand how modern wave-prediction schemes work, it is necessary to understand the concept of the two-dimensional wave spectrum and its relationship to sea state.

The concept arises from three fundamental facts, the first strictly mathematical and the others related to the physics of fluid motion:

1. A wrinkled surface which is evolving with time, such as the air-sea interface, can be mathematically decomposed into the sum of many sinusoidal waves with different amplitudes, wavelengths, propagation directions, and speeds (the procedure is called Fourier analysis). Figure 2(a) shows one such sinusoidal wave component.

2. In the case of the air-sea interface, each component propagates independently, interacting only very weakly with the others, at a phase speed (speed at which the wave appears to move) determined by its wavelength

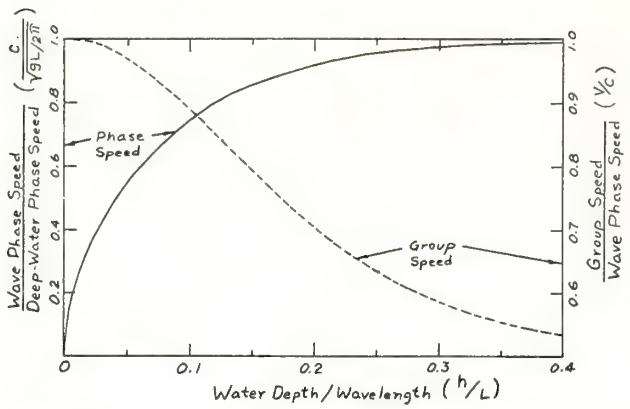

Figure 3.--Dispersion characteristics of sinusoidal surface gravity waves (C = phase speed, V = group speed, L = wave length, h = water depth, and acceleration of gravity $g = 9.8\,m/s^2$ in metric units). As h/L becomes larger than 0.5 (deep water or short wavelength), the group speed approaches half the wave-phase speed, which becomes approximately $\sqrt{g\,L/2\pi}$ (the phase speed of a wave where gravity is the restoring force and the maximum propagation speed for a surface wave of length L).

and the average water depth. This relationship (called the dispersion relation) is plotted in figure 3.

3. Each sinusoidal wave component posseses energy due to its contribution to surface distortion and to wave-induced water velocities. The amount of energy residing in each component is proportional to the square of its amplitude and propagates in the same direction as the sinusoidal wave at the so-called group velocity (velocity of the energy). In deep water the group velocity is one-half of the wave phase velocity (see fig. 3).

As a result of these facts, the seemingly chaotic surface of the real sea can be completely characterized by a statement of the distribution of energy among the various sinusoidal components making up the wave field. The two-dimensional wave spectrum is just such a statement. The spectrum is said to be two dimensional because, thanks to the dispersion relation, only two variables are necessary to identify each wave component. An especially convenient pair is propagation direction (for which we use the symbol θ) and cyclic frequency (symbolized by f). This last is the frequency at which an observer would see the surface oscillating up and down as a sinusoidal wave propagates past a fixed point and equals the wave phase speed divided by its wavelength. The frequency, in turn, fixes the corresponding wavelength, phase speed, and group speed through the dispersion relation. With this choice of wave variables, the two-dimensional spectrum is assigned the more descriptive name directional spectrum (which we abbreviate to "S(f, θ)").

Figure 2(a) illustrates schematically the simplest possible sea state, a single wave component propagating, in this case along the x-direction. The corresponding directional spectrum (shown in panel b) is 0 everywhere except for a single spike at the point in the (f, θ) plane corresponding to the frequency and propagation direction of the existing wave. It is conventional to think of the spike as occupying a small, rectangular area in the (f, θ) plane with sides df and dθ; the height of the spike, S(f, θ), is such that its volume, df dθ S(f, θ), is equal to half of the square of the corresponding wave amplitude.

This example, though consistent with the physics of the water motion, is certainly not typical of a real sea. A more complicated example, a two-component sea composed of waves of equal amplitude running at +45° and -45° with respect to the x-direction, is shown in figure 4. The result, a regular pattern of humps and hollows which propagates without change of shape along the x-direction, is again not very realistic.

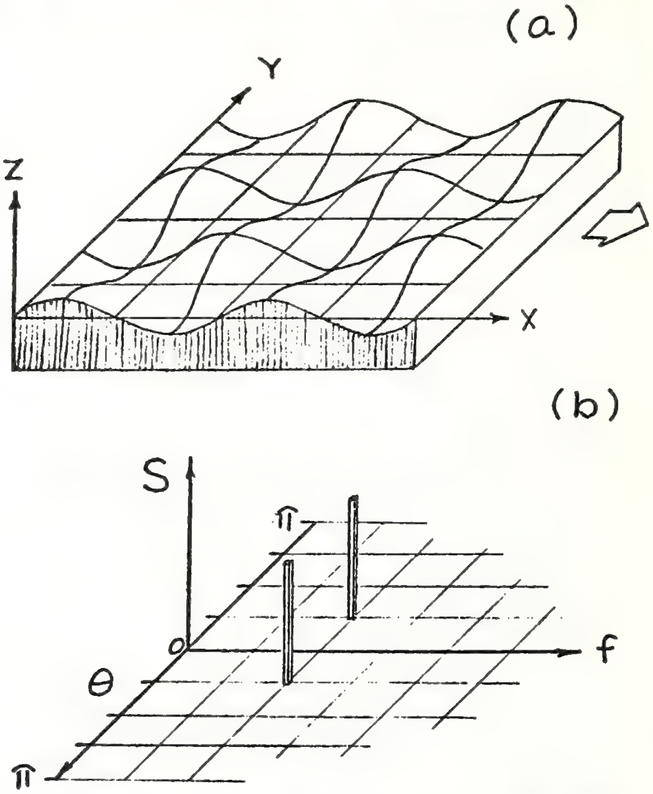

Figure 4.--Two-component sea and the corresponding spectrum. Two sinusoidal waves combine, one at $\theta = +\frac{\pi}{4}$ and one at $\theta = -\frac{\pi}{4}$ [see the spectrum in panel (b)] to form the pattern of bumps and hollows of panel (a). This pattern propagates to the right (along x) without change of shape.

Figure 5 illustrates a sea state composed of many wave components all propagating in the x-direction. The amplitudes and frequencies are distributed over a range of values and so closely spaced in frequency that the distribution is virtually continuous. The resulting profile along x looks real, and individual features appear to propagate and change shape in a realistic fashion because of the different phase speeds of the different wave components. However, profiles along y are straight lines, which certainly are not realistic. What is needed is a spectrum distributed both in frequency and direction, so that the resulting sea will combine the properties corresponding to the slab-like unidirectional spectrum of figure 5 with the

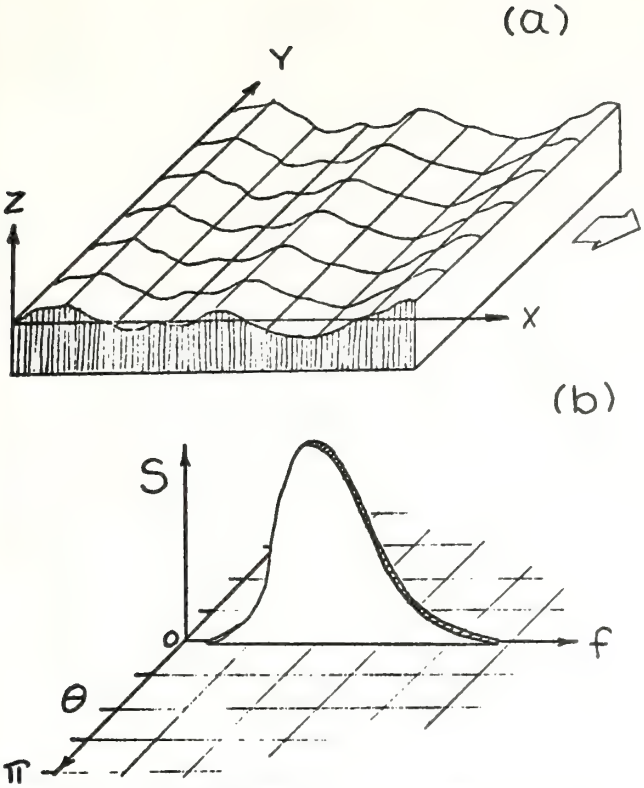

Figure 5.--Unidirectional multicomponent sea and corresponding spectrum. The pattern of infinitely long-crested waves propagates to the right (along x) and changes shape as it moves (see panel a). The corresponding spectrum exhibits a continuous range of frequencies, but only one direction.

short-crestedness of the two-component model of figure 4. The result in figure 6 does indeed yield a reasonable facsimile of a real sea.

The sample spectrum sketched in figure 6(b) is typical of a directional spectrum generated by a wind blowing along x ($\theta = 0$), judging by the limited amount of available experimental data (Mitsuyasu et al, 1975). Much more complicated shapes are possible. For example, if the local sea consisted of a wind-generated part and a swell component caused by a distant storm, the spectrum would have two humps--one resembling 6(b) and a second sharper one centered on the frequency and propagation direction of the incoming swell. Other influences may also distort the spectral shape, such as asymmetrical fetch, rapidly changing winds, bottom influence, and so forth. A complete wave-prediction scheme must take all of these effects into account.

In any case, once $S(f,\theta)$ is known (that is, we have a quantitative statement of the value of S for every wave frequency and direction), then all other statistical properties of the sea state may be calculated. For example, the average energy per unit horizontal area (E_t) residing in the wave field is computed by multiplying $S(f,\theta)$ by the small area ($df\, d\theta$) assigned to each wave component and by the density of water (ρ) and the acceleration of gravity (g), then summing (integrating) over all possible components (all possible areas $df\, d\theta$). This operation is written:

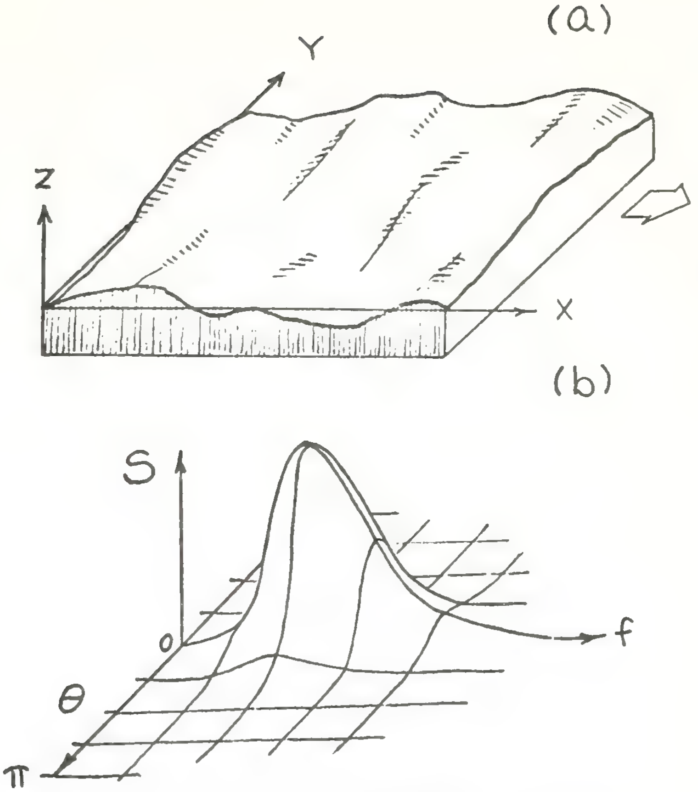

Figure 6.--A directional, multicomponent sea and corresponding spectrum. A pattern of waves with limited crest lengths propagates to the right (along x), changing shape as it moves (see panel a). The spectrum (panel b) has a continuous range of frequencies and directions.

$$E_t = \int_0^\infty df \int_{-\pi}^{\pi} d\theta \; \rho \; g \; S(f,\theta)$$

Another, perhaps more familiar statistic is significant wave height ($H_{1/3}$), which is proportional to the square root of the average energy density:

$$H_{1/3} = 4 \left(\frac{1}{\rho g} E_t\right)^{1/2}$$

$H_{1/3}$ has been shown to be the same as the average trough-to-crest height of the third highest waves occurring in the sea defined by $S(f,\theta)$. Experience indicates that this is very near the value which a trained observer would estimate visually as "wave height."

Other average properties of the wave field can be computed in a similar way; i.e., multiply $S(f,\theta)$ by an appropriate factor (which may itself depend on f and/or θ), then by $df\, d\theta$, then sum over all possible wave component directions and frequencies. Some properties, such as maximum probable wave height or maximum probable water velocity, are more difficult to calculate and require additional statements about what "maximum probable" means. Results for trough-to-crest wave height have been calculated by Longuet-Higgins (1952) and are tabulated by Pierson et al. (1967) (H.O. Publication No. 603) in terms of the highest wave which one will observe in any group of N waves passing

Table 1.--Maximum wave heights in a group of N waves

N	5 % lower than	Most frequent	Average	5 % higher than
20	.99 $H_{1/3}$	1.22 $H_{1/3}$	1.32 $H_{1/3}$	1.73 $H_{1/3}$
50	1.19 $H_{1/3}$	1.40 $H_{1/3}$	1.50 $H_{1/3}$	1.86 $H_{1/3}$
100	1.33 $H_{1/3}$	1.52 $H_{1/3}$	1.61 $H_{1/3}$	1.94 $H_{1/3}$
200	1.45 $H_{1/3}$	1.63 $H_{1/3}$	1.72 $H_{1/3}$	2.03 $H_{1/3}$
500	1.60 $H_{1/3}$	1.76 $H_{1/3}$	1.84 $H_{1/3}$	2.14 $H_{1/3}$
1000	1.70 $H_{1/3}$	1.86 $H_{1/3}$	1.93 $H_{1/3}$	2.22 $H_{1/3}$

(after Pierson et al., 1967)

by. For example (table 1), if one observes 20 waves passing by, the probability that the highest wave seen will be lower than .99 $H_{1/3}$ is 5 percent. The probability that the highest wave will be higher that 1.73 $H_{1/3}$ is 5 percent. Most of the time a maximum height near 1.22 $H_{1/3}$ will be seen, but the average maximum height will be 1.32 $H_{1/3}$.

MEASURING THE SPECTRUM

The spectrum is a statistical quantity (like the average weight of coconuts) and can never be measured exactly. To get it exactly right, we would have to observe a given sea everywhere and for all time (weigh every coconut in the universe) which is impossible. The best we can do is to assemble a few short-time histories of sea-surface elevation at several points, or different characteristics of the wave field at a single point, and from these estimate the spectrum (do the best we can with a few coconuts). The result inevitably will contain some error, but this can be controlled by varying the size of the data set, and the significance of the probable error can be estimated for a given data set.

The simplest wave measurements are made with a single wave gage (for example, a resistance wire or capacitance wave staff which penetrates the surface and measures its displacement or, in deep water, a buoy mounting a vertical accelerometer which measures the vertical motion of the surface). A single wave gage yields a time history of surface displacement at a single location (Kinsman, 1965). To such an instrument, a sinusoidal wave component of a given frequency looks the same regardless of its propagation direction. By Fourier analyzing the time series, an estimate of the energy resident in all wave components with a given frequency, independent of direction, can be calculated. The results are expressed in terms of the frequency spectrum E(f), which can be derived, like the other statistics of the wave field, from the directional spectrum whenever it is known; we multiply $S(f,\theta)$ by $d\theta$ and sum (integrate) over all possible directions:

$$E(f) = \int_{-\pi}^{\pi} d\theta \; S(f,\theta)$$

An example of a frequency spectrum measured in a hurricane is shown in figure 7. This was obtained by one of NOAA's moored data buoys in the Gulf of Mexico and represents the kind of field data against which our hurricane wave models have been tested.

One way of getting directional information is to use an array of wave gages to obtain time series of surface displacement at several different space points (Barber, 1963). Since the crest of a sinusoidal wave component passing through the array arrives at each gage at a different time, it is possible to estimate the direction of propagation by comparing the time series (this is a gross oversimplification of the procedure called cross spectral analysis, but it points out the principle). A wave gage array has been used from the research vessel FLIP (Regier and Davis, 1977), but the technique is generally applied only in shallow water because the position of the gages must remain fixed relative to each other.

The most commonly used instrument for measuring deep-water directional spectra is the pitch/roll buoy (Longuet-Higgins et al., 1963). A gyro-stabilized platform supporting a vertical accelerometer is mounted

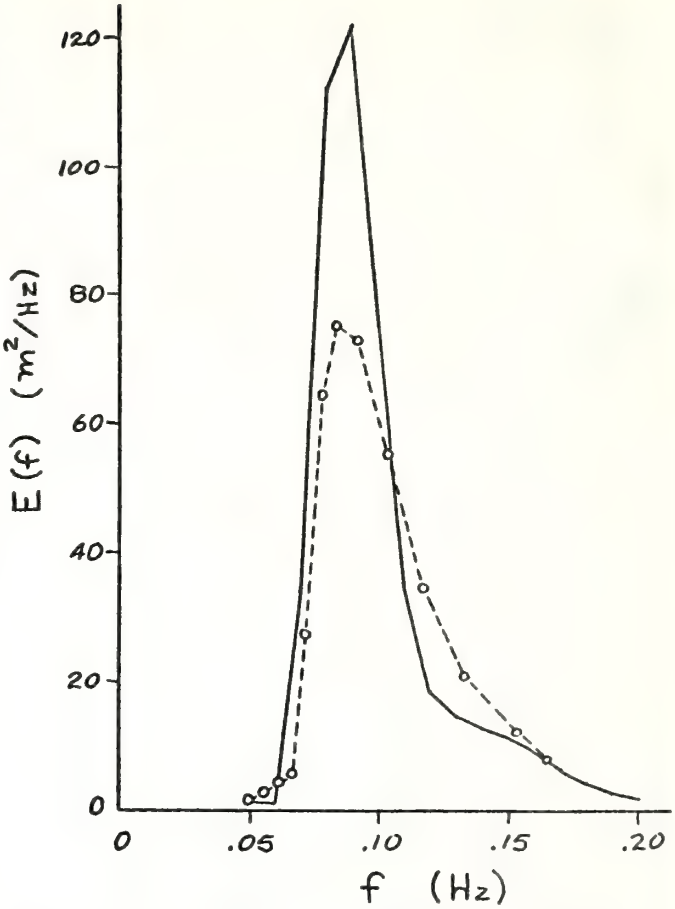

Figure 7.--Comparison of the highest sea-state wave-frequency spectrum observed by the NOAA data buoy during hurricane Eloise (—) with the spectrum predicted by the full-scale spectral wave model (--). Although the model underestimates the peak, the comparison is considered satisfactory (observed $H_{1/3}$ = 9 m, predicted $H_{1/3}$ = 8.1 m). Significant wave heights are determined by the total area under these curves. In this example the overestimation of the model spectrum for frequencies above the peak partially offsets the underestimation near the peak resulting in good agreement for $H_{1/3}$.

on a disc or toroid-shaped buoy designed to follow the slope as well as the vertical motion of the water surface. Four time series are recorded: vertical acceleration, pitch, roll, and buoy heading relative to north. Comparing these signals permits an estimate of the directional distribution of wave energy at each frequency, although with so little information, directional resolution is not very good. Because the buoy must be launched and recovered from a ship and has a tendency to capsize in rough seas, no hurricane data have been obtained using this instrument.

In fact, much of the hurricane wave data used in the research at SAIL has been obtained from storm penetrations by aircraft. The aircraft carries a laser altimeter (a modified surveying instrument) which measures the vertical distance from the aircraft to the water surface along the aircraft track. The resulting time series of surface elevation can be interpreted in terms of a wave frequency spectrum (Ross et al., 1970).

Other remote-sensing techniques are now becoming available, including satellite radars and radio altimeters. These will eventually make important contributions to our knowledge of storm seas and our ability to predict them, though it is still too early for their impact to have been more than minimal.

We neglected to mention some frequently used in situ measurement techniques, such as multicomponent current meters, arrays of water pressure gages, and others, but the techniques outlined are sufficient to illustrate the relevant principles.

THE RADIATION BALANCE

Having established that the two-dimensional wave spectrum is the complete definition of sea state, we now need some basis on which to predict its development in space and time. This is provided by the so-called radiation balance equation, a mathematical statement about the balance of processes which insert, remove, and redistribute wave energy, component by component, across the spectrum. The structure of this equation can be described schematically as follows:

$$\boxed{\begin{array}{c}\text{Local rate of}\\\text{change with time}\\\text{of component}\\\text{wave energy}\end{array}} = \boxed{\begin{array}{c}\text{Effect of energy}\\\text{transport at the}\\\text{group velocity}\end{array}} + \boxed{\begin{array}{c}\text{Effect of wave}\\\text{refraction by}\\\text{current and}\\\text{depth changes}\end{array}} + \boxed{\begin{array}{c}\text{All sources and}\\\text{sinks of wave}\\\text{component energy}\end{array}}$$

The left-hand side is what an observer would see if he stood at some fixed point and watched the spectrum develop. Once the spectrum and its rate of change are known at a given location and time, we can mathematically predict the growth or decay of each wave component. The rate of change is determined by the processes indicated in the boxes on the right-hand side. The first of these is the effect of wave-component energy propagating from place to place at the corresponding group velocity; for example, if an observer found himself down-wave of a region where the spectrum was greater, he would find the spectrum at his location increasing with time as the higher energy levels propagated through his position. The second term represents refractive effects which can cause energy to pile up, spread out, or be transferred from one wave component to another (turned). These two processes are completely understood from first principles. The final term on the right is not well understood, and most ongoing wave research is currently directed at getting a better empirical description and theoretical understanding of the sources and sinks of wave spectral energy. The most important of these are (1) the input from the wind (source), (2) the dissipation by whitecapping (sink), and (3) a process called nonlinear transfer (source or sink depending on the shape of the rest of the spectrum). Of these effects, only (3) is known from first principles; it arises because the individual wave components are not totally decoupled from each other, and this weak interaction is capable of redistributing wave energy across the spectrum. In the present generation of wave-prediction schemes, (1) and (2) must be approximated by mathematical rules-of-thumb guided by whatever theory is available and substance determined empirically by observations. Nonlinear transfer is also generally dealt with similarly because, although it is possible to accurately compute the effect from theory, the effort required is too great to be done as an integral part of a practical wave-prediction scheme. It is the difference in how these effects are approximated that constitutes the primary difference between the various computer-based, wave-prediction schemes presently under development or in use.

Once the radiation balance is written down, it is solved using a digital computer on a grid of discrete points representing geographical locations on Earth. The effects of fetch are incorporated by applying boundary conditions at those grid points which lie on coastlines; usually, these conditions specify that there is no energy in wave components with propagation directions in the offshore semicircle. On grid boundaries which lie in open water the energy in wave components propagating into the grid must be specified. In our hurricane applications, for example, we generally specify that no wave energy is coming in from outside the grid; all the wave energy present must then be generated by the hurricane imbedded in the grid.

In practice, the program is started at some chosen time at which the spectrum everywhere on the grid is specified by initial conditions. For lack of better information, we generally set the spectrum to 0 everywhere at start time. Then, using a known or forecast time history of the wind field at each grid point, the computer program marches forward in time, recomputing the spectrum at each grid point at each time step. After advancing 6 to 12 hr (a few min of computer time), the wave field has "spun up," and realistic spectral values develop.

APPLICATION TO HURRICANES

To drive a hurricane wave model (i.e., specify final term on the right in the radiation balance equation), the wind field has to be known at every grid point over the history of the storm. Such dense measurements are, of course, never available; and in our hurricane studies the best wind observations have been provided by the same aircraft storm penetrations which provided much of the wave data. NOAA research aircraft use inertial navigation systems to measure groundspeed and track; comparing this with airspeed and heading allows the windspeed and direction to be computed. From observations of this sort, as well as data from ships, oil-well platforms, and moored-data buoys, a computer

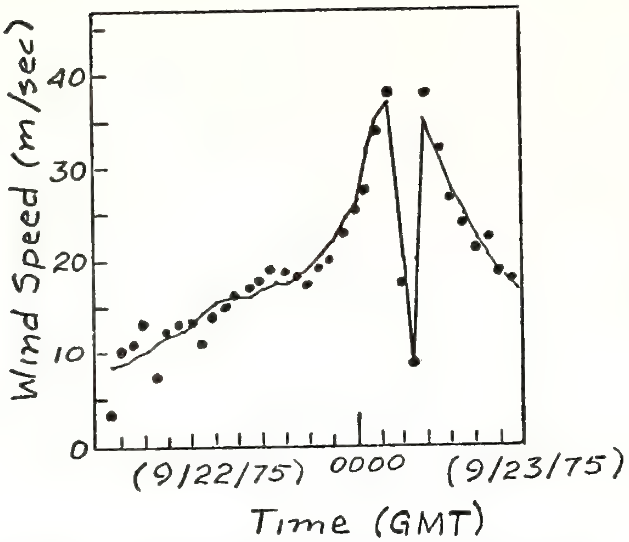

Figure 8.--Comparison of windspeed as measured by a NOAA data buoy during hurricane Eloise (●) and as computed from the SAIL hurricane wind model (—) (Ross and Cardone, 1978). The windspeeds are equivalent to 15-min averages at 10-m height above the water surface.

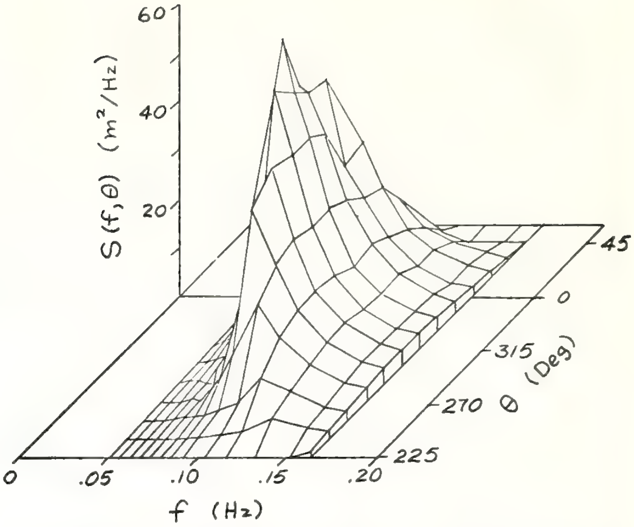

Figure 9.--The directional spectrum predicted by the spectral wave model for the NOAA data buoy location at highest sea state. The frequency spectrum of figure 7 was computed from this directional spectrum by integrating over direction (summing all the spectral density in each frequency band). The tail of the spectrum is cut off at about .16 Hz because the computer model does not explicitly treat higher frequency bands.

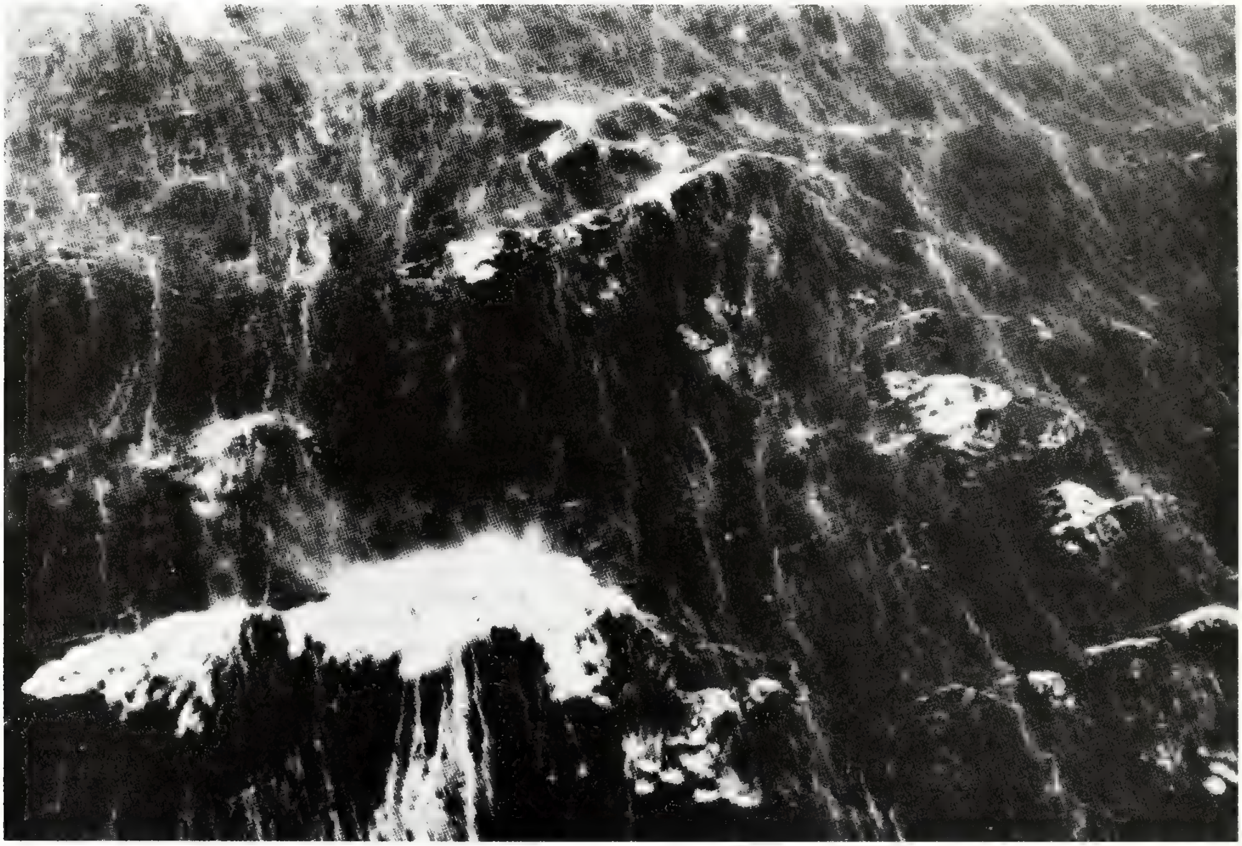

Figure 10.--This aerial photograph illustrates the sea conditions as they could be expected to appear with 75-kn winds. U.S. Navy Photograph.

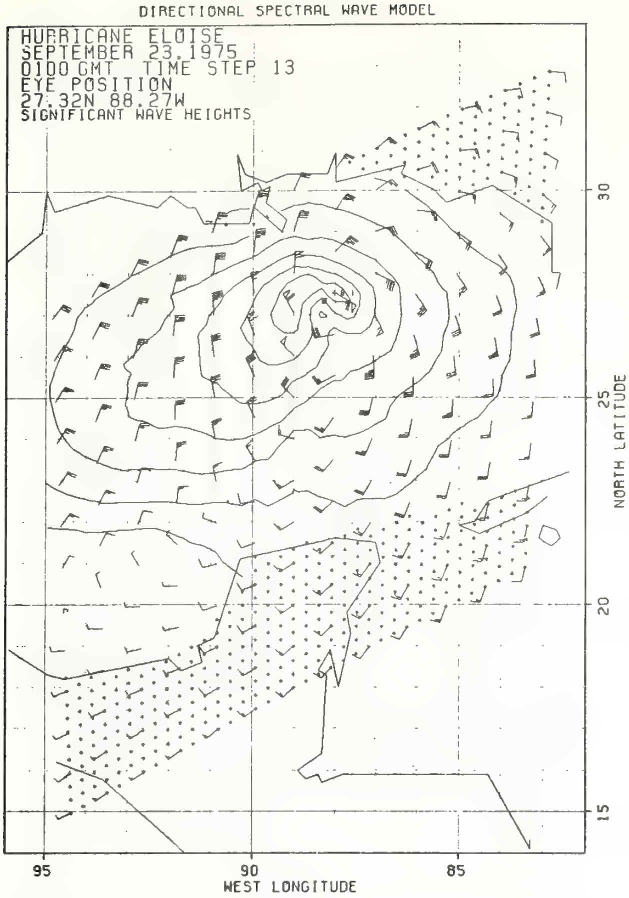

Figure 11.--Contours of significant wave height in the Gulf of Mexico as predicted by the full-scale computer wave model for hurricane Eloise when the highest sea state was observed at the NOAA data buoy. Wind barbs indicate wind direction and speed (kn) computed with the SAIL hurricane wind model. The interval between contours is 1 m. Significant wave height at the buoy (+) was 8.1 m; the location of the eye of the storm is shown by "*". The stippling in the upper right and lower regions are points on the standard grid which were inactivated for this run.

model of hurricane winds has been developed which, using a few parameters to characterize the storm, can reconstruct the wind field everywhere on the grid (Cardone et al., 1976). The characteristic parameters are the latitude and longitude of the eye of the storm, the central pressure depression, the radius of maximum winds, the velocity of the background airflow in which the hurricane is embedded, and the storm's forward velocity. The time evolution of these parameters may be forecast, obtained from aircraft observations, or taken from the historical meteorological record. Figure 8 shows a comparison between model windspeed and observed windspeed at one of NOAA's moored data buoys in the Gulf of Mexico. Hurricane Eloise (1975) passed directly over the buoy, so the observations provide a representative cross section through the storm. Clearly, the wind model has done an excellent job of reconstructing the wind history at this location.

Using winds calculated in this way, we have computed the corresponding wave spectra for a number of historical storms in the Gulf of Mexico and along the U.S. East Coast. Point checks on the validity of these calculations have been made by comparing buoy measurements and aircraft laser altimeter data. An example of such a comparison (fig. 7) shows a frequency spectrum measured by the same buoy which provided the wind history of figure 8 during Eloise. The sea state was at its worst (significant wave height $H_{1/3}$ of about 9 m) at the time this spectrum was acquired. The frequency spectrum predicted by our most highly developed wave model is also shown. The comparison is considered good (model $H_{1/3} = 8.1$ m).

The model directional spectrum from which the model frequency spectrum of figure 8 was calculated is sketched in figure 9. The most energetic wave component has frequency $f = .078$ and propagation direction $\theta = 330°$. The model wind at anemometer height at that point and time was 74 kn (fig. 10) (38 m/s) in the direction 300°, 30° to the left of the peak wave direction (as one might expect considering the curvature of the wind field: the spectrum, which should otherwise be asymmetrical about the local wind direction, is colored by energy-generated up-wave, where the wind direction is more toward the north).

Figure 11 shows model contours of significant wave height for the entire Gulf of Mexico at the time the spectra of figures 7 and 8 were computed for the buoy position. The maximum, located at the buoy position, is indicated by "+". The location of the eye, 29 km away from the buoy, is indicated by "*".

Figure 12 compares time histories of significant wave height as predicted by the computer model and measured by the buoy as the storm passed over. Also shown is the evolution of the peak of the frequency spectrum, f_m. Just as $H_{1/3}$ can be used as a gross measure of wave height, f_m can be used as a gross measure of the frequency content of the sea state. It is nearly but not quite the same as the average frequency. For both $H_{1/3}$ and f_m, agreement between computer model and observation is considered satisfactory. Figure 12 also shows the results of a vastly simplified parametrical hurricane wave model developed by SAIL.

THE ROSS PARAMETRICAL HURRICANE WAVE MODEL

In order to account in a physically reasonable way for all the processes affecting wave development and to provide reasonable spectral resolution, computer wave models are necessarily complicated. The calculation which produced the results discussed above approximates the real, continuous ocean-wave spectrum by a discrete set of 312 wave components, each of which must be evaluated at every grid point in the field at every time step. A 24-hr forecast for the Gulf of Mexico, including both wind and wave-field calculations, takes about 2 hr of computing time on a digital computer such as the UNIVAC 1108.

However, in the course of studying data gathered in hurricanes and the output of many computer simulations, Ross (1976) discovered that certain simple relationships seemed to exist between gross parameters of the spectrum, such as significant wave height and peak frequency, and the local windspeed and distance

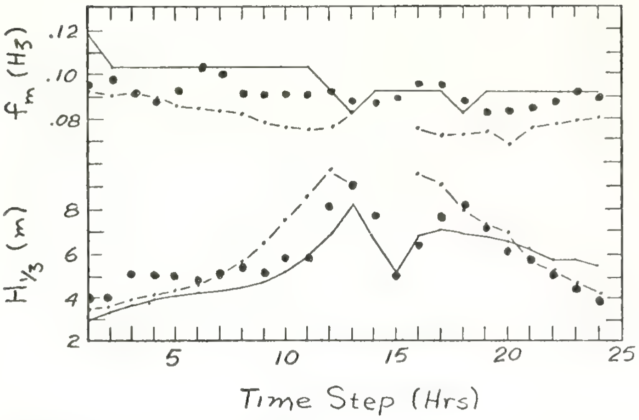

Figure 12.--Comparison of peak frequency f_m and significant wave height $H_{1/3}$ as observed by the NOAA data buoy (●) and as hindcast by the full-scale spectral model (—) and by the Ross parametrical hurricane model (— ● —). Eloise passed directly over the buoy at about 0200 on September 23, 1975 (time step 14).

from the eye of the storm. This discovery made it feasible to predict the development of these parameters by hand calculations once the wind field is known, at least for the class of hurricanes which formed Ross's data set.

Ross's model implicitly assumes that all the separate processes which together determine the local sea state (and which individually are accounted for in the full-scale computer models) interact in a similar way from one hurricane to the next, so that the net effect on the local wave field varies only with the scales of the individual storm; that is, with the local windspeed (U) at a given distance from the eye (r). This seems intuitively reasonable since the vortex-like wind fields of hurricanes tend to be geometrically similar from storm to storm, differing primarily in size and intensity. However, individual storms also differ in their translation velocities. This effect is implicitly neglected in Ross's model, although it seems likely (Ross and Cardone, 1978) that significantly different forward speeds do alter the balance of processes maintaining the local wave conditions. The specific forms of the dependence of f_m and $H_{1/3}$ on U and r were fixed by fitting curves to data collected in three hurricanes which differed widely in scale but had similar forward speeds (~15 kn). The results are summarized in the plots of figure 13.

Comparisons between hindcast significant wave height and peak frequency using Ross's method with observations made in hurricane Eloise are included in figure 12. Agreement is surprisingly good considering the gross approximations implicit in Ross's model; indeed, except for the region inside the eye of the storm, where Ross's model does not apply, his calculations seem to match the observations as well as those of the full-scale computer model.

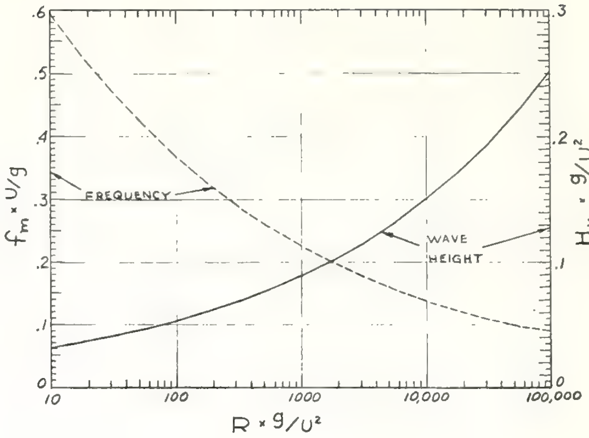

Figure 13.--Ross parametrical hurricane wave model (f_m = frequency spectrum maximum, R = local distance from hurricane eye, U = local windspeed, and the acceleration of gravity g = 9.8 m/s^2 in metric units. Plotting $H_{1/3}$ and f_m against R in these dimensionless forms collapses the entire model into these two curves. This graph may be used to estimate the hurricane wave height and frequency for any location where forecast winds and distance from the storm center are known.

Ross's method is summarized in the two curves of figure 13. These show plots of dimensionless peak frequency (f_mU/g) and dimensionless significant wave height ($H_{1/3}$ g/U^2) versus dimensionless distance from the hurricane eye (r g/U^2). These quantities are converted to physical units, cycles per s (Hz for Hertz) and m, by multiplying by g/U (frequency) or U^2/g (wave height and distance from the eye), where U is the windspeed in m/s at the point where the wave field is being evaluated, and g = 9.8 m/s^2 is the acceleration of gravity. To illustrate, in the case of hurricane Eloise the worst wave conditions were observed at the buoy at 0100 GMT, when the eye was 29 km away and the local windspeed was 38 m/s. The dimensionless distance from the eye is then:

$$r\frac{g}{U^2} = 29000 \text{ m} \frac{9.8 \text{ m/s}^2}{(38 \text{ m/s})^2} = 197.$$

From figure 13 the dimensionless peak frequency is .32 and the dimensionless significant wave height is .062; to get f_m and $H_{1/3}$, multiply the former by g/U

$$f_m = \frac{9.8 \text{ m/s}^2}{38 \text{ m/s}} \times .32 = .083 \text{ Hz}$$

and the latter by U^2/g

$$H_{1/3} = \frac{(38 \text{ m/s})^2}{9.8 \text{ m/s}^2} \times .062 = 9.1 \text{ m}$$

which are the values shown at 0100 GMT in figure 12.

The shortcomings of Ross's hurricane wave model are clear, and for fast-moving storms its performance may be significantly poorer than indicated by the Eloise results. Consequently, as a hindcasting tool for computing wave climatology, it is less suitable than the full-scale computer models. In forecasting applications, however, experience has shown that errors in the hurricane wind forecast generally dominate the contribution to wave-forecast error arising from the model's shortcomings. Moreover, the ability to rerun the wave forecast quickly and cheaply as the wind forecast is refined is a significant advantage of Ross's model. For these reasons, it is being implemented, along with SAIL's hurricane wind model, on a computer at the National Hurricane Center (NHC). In the near future, wave forecasts will be incorporated on a trial basis into NHC advisories.

SUMMARY

Modern wave-prediction schemes are based on computer solutions of a mathematical equation describing the evolution of the surface wave directional spectrum under the influence of a specified wind. The spectrum is the fundamental statistical property of the sea state and specifies the distribution of wave energy across the continuum of sinusoidal surface wave components into which the real sea can be mathematically resolved. Once it is known, all other properties of the sea state can be calculated, such as total energy in the waves, average wave height, frequency and propagation direction, maximum probable wave height, and so on. Of these, the quantities which relate most closely to the visual wave observations traditionally taken at sea are significant wave height $H_{1/3}$ (wave height) and peak frequency f_m ($1/f_m$ is comparable with visually estimated wave period).

Wave-prediction schemes may be used with historical wind fields to deduce site-specific wave climate for engineering applications. Driven by forecast winds, they can provide wave forecasts useful for planning marine operations or as part of severe weather warnings.

In order to account for all the processes and constraints affecting wave development in a general way, wave models are necessarily complicated. However, for hurricanes, the geometrical simplicity of the wind field leads to a regular wave-field development which seems adequately characterized by a set of simple relations between $H_{1/3}$, f_m, local windspeed U, and distance from the storm center r. These are shown in graphical form in figure 13. They are presently being used on a trial basis by NHC to compute wave height and period estimates for their hurricane advisories.

Although we can make useful wave predictions at the present state of the art, the situation is still less than completely satisfactory. The primary problem is that the physics of the sources and sinks of wave spectral energy is not well understood. Basic research still needs to be done on how the wind makes waves and how the waves subsequently decay. In addition, new computational schemes are needed to deal more realistically with the effects of nonlinear transfer and to improve the efficiency of the computation. Finally, in practice, no wave-model output can be better than the wind input, and better measurement of oceanic wind fields is needed, if significant improvement in wave forecasting and hindcasting is to be realized. The next generation of oceanographic satellites may provide those measurements. In the meantime, work is already in progress on all fronts, and we look forward to continued improvement in our ability to predict waves.

REFERENCES

Barber, N.F., 1963. "The directional resolving power of an array of wave detectors," Ocean Wave Spectra - Proceedings of a Conference, Prentice-Hall, Inc., Englewood Cliffs, N.J., pp. 137-150.

Cardone, V.J., W.J. Pierson, and E.G. Ward, 1976. "Hindcasting the directional spectra of hurricane-generated waves," Journal Petrol. Tech. 28, pp. 385-394.

Kinsman, B., 1965. Wind Waves: Their Generation and Propagation on the Ocean Surface, Prentice-Hall, Inc., Englewood Cliffs, N.J., 676 pp.

Lazanoff, S.M., and N.M. Stevenson, 1975. An Evaluation of a Hemispheric Operational Wave Spectral Model, Fleet Numerical Weather Central Tech. Note 75-3, Monterey, Calif., 103 pp.

Longuet-Higgins, M.S., 1952. "On the statistical distribution of the heights of sea waves," Journal Mar. Research 11, pp. 245-266.

Longuet-Higgins, M.S., D.E. Cartwright, and N.D. Smith, 1963. "Observations of the directional spectrum of sea waves using the motions of a floating buoy," Ocean Wave Spectra - Proceedings of a Conference, Prentice-Hall, Inc., Englewood Cliffs, N.J., pp. 111-136.

Mitsuyasu, H., F. Tasai, T. Suhara, S. Mizuno, M. Ohkusu, T. Honda, and K. Rikiishi, 1975. "Observations of the directional spectrum of ocean waves using a cloverleaf buoy," Journal Physical Oceanog. 5, pp. 750-760.

Pierson, W.J., G. Neumann, and R.W. James, 1967. Practical Methods for Observing and Forecasting Ocean Waves by Means of Wave Spectra and Statistics, H.O. Pub. No. 603, U.S. Navy Hydrographic Office, 284 pp.

Regier, L.A., and R.E. Davis, 1977. "Observations of the power and directional spectrum of ocean surface waves," Journal Mar. Research 35(3), pp. 433-451.

Ross, D.B., V.J. Cardone, and J.W. Conaway, Jr., 1970. "Laser and microwave observations of sea-surface condition for fetch-limited 17- to 25-m/s winds," IEEE Trans. Geoscience Electronics 8(4), pp. 326-336.

Ross, D.B., 1976. "A simplified model for forecasting hurricane generated waves (Abstract)," Bulletin Amer. Met. Soc., January, p. 113.

Ross, D.B., and V.J. Cardone, 1978. "A comparison of parametric and spectral hurricane wave prediction products," NATO Symposium on turbulent fluxes through the sea surface, wave dynamics and prediction, Marseille, France, Sept. 12-16, 1977, Plenum Publishing Corp, N.Y. (in press)

Sverdrup, H.U., and W.H. Munk, 1947. Wind, Sea and Swell: Theory of Relations for Forecasting, H.O. Pub. No. 601, U.S. Navy Hydrographic Office, 44 pp.

42. Journal of Physical Oceanography 9, No. 2, 373-381.

A Variational Technique for Extracting Directional Spectra from Multi-Component Wave Data

ROBERT BRYAN LONG

Sea-Air Interaction Laboratory, Atlantic Oceanographic and Meteorological Laboratories, NOAA, Miami, FL 33149

KLAUS HASSELMANN

Max-Planck-Institut für Meteorologie, Hamburg, Germany

(Manuscript received 25 May 1978, in final form 4 August 1978)

ABSTRACT

The problem of extracting directional spectra from observed, multi-component wave data has two facets: 1) the observations provide information only on a finite number of integral properties of the wave field; hence the directional spectrum cannot be determined uniquely from the wave data alone; and 2) the observations contain statistical errors. These difficulties are dealt with by choosing an *optimal* directional spectrum model which simultaneously minimizes some integral property of the spectrum (its "nastiness") and passes an appropriate test of statistical significance. Although developed here in the context of surface wave directional spectra, the technique (adopted from the Backus-Gilbert inverse method) is applicable to any problem requiring the fitting of a model to data which represent integral properties of the function being modeled.

1. Model fitting techniques

Experiments designed to obtain direction-sensitive measurements of ocean wave spectra provide data which, in most cases, represent integral properties of the two-dimensional surface wave spectrum. These properties may be cast into the general form

$$\mathbf{d} = \int_0^{2\pi} d\theta S(\theta)\mathbf{b}(\theta), \qquad (1)$$

where the components of the data vector **d** are weighted moments of the normalized directional distribution (spreading function) S defined by the kernel vector **b** (θ is the direction of wave propagation; the additional dependence of all quantities on wave frequency f has been suppressed). For example, an array of wave gages yields as basic data the set of cross spectra

$$E_{ij}(f) = \int_0^{2\pi} d\theta S(\theta,f)E(f) \times \exp[-ikr_{ij}\cos(\theta - \theta_{ij})] \qquad (2)$$

between the ith and the jth wave record, where $E(f)$ is the one-dimensional surface wave spectrum, k is the wavenumber corresponding to f, and r_{ij} and θ_{ij} are the magnitude and direction, respectively, of the spatial displacement from the ith to the jth wave gage. Similarly, pitch/roll buoys provide time series of two orthogonal components of surface slope and vertical acceleration at a point on the sea surface; cross spectra between pairs of these records also have the form (1). Normalized versions of such cross spectra or linear combinations of them may be used to advantage in some situations, while still retaining the general form (1).

Given the data vector **d**, extracting an estimate of the spectrum S requires the inversion of the set of integral equations (1). Normally, the inversion will not be unique, since the directional distribution is a continuous function, whereas the data set **d** is only of finite dimension.

One way to remove the indeterminacy is to restrict the model space to a finite dimensional subspace characterized by a parameter vector $\boldsymbol{\lambda}$ of dimension less than or equal to that of **d**. A unique solution can then be obtained either by the method of least squares, if $\boldsymbol{\lambda}$ is of smaller dimension than **d**, or by inverting (1) exactly, if the dimensions of $\boldsymbol{\lambda}$ and **d** are the same (and the model class is consistent with the data in the sense that a unique solution exists). The least-squares technique is usually favored as it yields stabler solutions. A basic disadvantage of the method is that the solutions fail to satisfy the data exactly, but this shortcoming generally appears less severe when the statistical errors of the data are taken into account. In fact, Eq. (1) represents a relationship between statistical quantities which can, in practice, never be known exactly.

0022-3670/79/020373-09$06.25

© 1979 American Meteorological Society

Physically realizable experiments can only provide estimates $\tilde{\mathbf{d}}$ of the true data $\mathbf{d}$, where

$$\tilde{\mathbf{d}} = \mathbf{d} + \boldsymbol{\epsilon}, \tag{3}$$

and $\boldsymbol{\epsilon}$ is a vector of random errors. Under the hypothesis that a given least-squares model S is the true spectrum [i.e., that it satisfies (1) exactly for the true data $\mathbf{d}$], the statistics of $\boldsymbol{\epsilon}$ can be computed. These may then be used to test whether the differences between the model prediction and the observed data $\tilde{\mathbf{d}}$ are statistically consistent with the expected errors. If this is the case, the optimal model is accepted as valid; if not, it is rejected. Olbers *et al.* (1976) have used this procedure successfully to extract statistically significant estimates of the three-dimensional internal wave spectrum in the main thermocline, using a model with approximately 20 free parameters, from 3660 cospectra and quadrature spectra obtained from a tetrahedral array of moored current and temperature meters.

A more fundamental shortcoming of the least-squares method, however, is that it provides no means, beyond statistical acceptance-rejection tests, to demonstrate that one model parameterization is superior to another—or even to define quantitatively what constitutes a superior model.

This consideration lies at the core of an alternative "inverse" technique, which appears to have been first suggested by Backus and Gilbert (1967). Instead of overcoming the underspecification of the model by (1) through the restriction of the model space to a dimension smaller or equal to that of the data vector, the number of integral restraints of the model is increased until the model again becomes overspecified. An optimal model can then be defined, as before, as the model which comes closest to fulfilling all requirements in some appropriate least squares sense. The additional integral restraints represent data-independent conditions which define, in effect, what is considered—subjectively, or on independent physical grounds—to be a "good" model. For example, in the case of directional spectra, the side condition $S(\theta) \geqslant 0$ must always be satisfied in addition to and independent of the data relation (1). The condition may be written in the integral form

$$\int_0^{2\pi} (S - |S|)^2 d\theta = 0. \tag{4}$$

Furthermore, one may seek a model which lies as closely as possible to a particular preferred model $\hat{S}(\theta)$, such as an isotropic distribution or, at the opposite extreme, a unidirectional spectrum. In this case one would require additionally

$$\int_0^{2\pi} (S - \hat{S})^2 d\theta = 0. \tag{5}$$

Alternately, one may seek the smoothest possible model by imposing the additional requirement

$$\int_0^{2\pi} \left[\frac{d^2S}{d\theta^2}(\theta)\right]^2 d\theta = 0. \tag{6}$$

Essential for the technique is that at least one of the additional conditions represents a positive definite form, such as (5) or (6), which normally cannot be satisfied simultaneously with the data. Thus, the model is overspecified, and one can define as the unique solution to the inverse problem the "optimal" model which minimizes some "error" expression formed from a suitable weighted combination of the various model equations, including both data conditions and additional constraints.

In most cases, more weight will be attached to the data conditions (1) than to subjective external conditions of the form (5) or (6). In fact, in the original Backus and Gilbert approach, Eqs. (1) were regarded as rigorous side conditions, and the "error" function was formed only from the external restraints. In view of the statistical indeterminacy of the data, however, some error in the data conditions can normally be accepted. Accordingly, we shall consider variable weightings for both data and external conditions and adjust the weighting such that the model satisfies the external conditions as closely as possible, while still remaining statistically consistent, within prescribed confidence limits, with the observed data. [However, the rigorous side condition (4) will always be satisfied exactly by assigning to this an essentially infinite weight.]

It may be remarked that no inverse technique can, of course, circumvent the basic difficulty of the underspecification of the continuous distribution by the finite data set. In all cases, a unique model can be constructed only by introducing more or less arbitrary additional restraints. The main advantage of the Backus-Gilbert inverse technique is that it defines clearly what is considered as a desirable or undesirable model property through the specification of an "error" function (more appropriately, "nastiness" function), the minimization of which defines the optimal model. This provides a tool for exploring the sensitivity of the model to alternative additional requirements, such as near-isotropy or near-unidirectionality, by considering alternative nastiness functions.

In the following sections, we shall examine the consequences of the application of the nastiness function based on the conditions (1), (4) and (5) to the problem of estimating directional spectra. An array of wave gages is considered as an example. Using artificially generated data, it is shown how the region of statistically acceptable solutions is affected by array geometry and the variability of the data estimates. Real data cases are also presented.

2. Defining the optimal model

Simultaneous consideration of the conditions (1), (4) and (5) suggests a nastiness function of the general form

$$\eta = \alpha\boldsymbol{\epsilon}^{\mathrm{T}}\mathbf{M}\boldsymbol{\epsilon} + \beta\int_0^{2\pi} d\theta(S - |S|)^2 + \int_0^{2\pi} d\theta(S - \hat{S})^2, \quad (7)$$

where

$$\boldsymbol{\epsilon} = \tilde{\mathbf{d}} - \int_0^{2\pi} d\theta S\mathbf{b} \quad (8)$$

is an n-dimensional column vector representing the errors between the observed data $\tilde{\mathbf{d}}$ and the model prediction, $\boldsymbol{\epsilon}^{\mathrm{T}}$ is its transpose, **M** is a positive definite symmetrical matrix, which will be defined below, and α and β are weighting factors. Since we wish to satisfy the condition (4) exactly, we shall consider (7) in the limit $\beta \to \infty$. [Formally, this turns out to be simpler than including (4) as an exact side condition and working with a Lagrange multiplier.]

The weighting factor α and the matrix **M** in the first term in the right-hand side of (7) determine the penalty one wishes to assign to a deviation between the observed data $\tilde{\mathbf{d}}$ and the model prediction, relative to the penalty for a deviation between the optimal model and the preferred model $\hat{S}$, as expressed by the last term. This will depend on the statistical errors associated with the observed data $\tilde{\mathbf{d}}$.

Consider the hypothesis that the optimal model obtained by minimizing η represents the true model, yielding the true data vector **d**. One can then define an n-dimensional γ-probability region R around **d** such that $\int_R p(\tilde{\boldsymbol{\epsilon}}; \mathbf{d})d\boldsymbol{\epsilon} = \gamma$, where $p(\boldsymbol{\epsilon}; \mathbf{d})$ is the probability of obtaining an error $\boldsymbol{\epsilon} = \tilde{\mathbf{d}} - \mathbf{d}$ in the estimation $\tilde{\mathbf{d}}$ of **d** for a particular data realization. If the data sample is not too small, the errors are approximately jointly Gaussian, i.e.,

$$p(\boldsymbol{\epsilon}; \mathbf{d}) = (2\pi)^{-n/2}|\mathbf{V}|^{-1/2}\exp\{-\tfrac{1}{2}\boldsymbol{\epsilon}^{\mathrm{T}}\mathbf{V}^{-1}\boldsymbol{\epsilon}\}, \quad (9)$$

where the error covariance matrix $\mathbf{V} = \langle\boldsymbol{\epsilon}\boldsymbol{\epsilon}^{\mathrm{T}}\rangle$ can be estimated using standard techniques of time series analysis (cf. Jenkins and Watts, 1968). The "true" data **d** predicted by the optimal model may then be regarded as statistically consistent with the observed data $\tilde{\mathbf{d}}$ at the γ-confidence level if $\tilde{\mathbf{d}}$ lies within R. To make the region R unique it is normally assumed that it is bounded by a surface of constant probability density or, equivalently, constant

$$\rho^2 = \boldsymbol{\epsilon}^{\mathrm{T}}\mathbf{V}^{-1}\boldsymbol{\epsilon}. \quad (10)$$

This definition yields the smallest region R for a given confidence level γ and is, in fact, the only definition which is invariant with respect to linear transformations of the data. The radius ρ_γ of R for given γ is readily determined by noting that the projection of the n-dimensional normal distribution (9) on to the variable ρ^2 yields a chi-square distribution with n degrees of freedom and standard normalization ($\langle\rho^2\rangle = n$).

Complementary to R one can then define for a given data vector $\tilde{\mathbf{d}}$ the confidence region $\tilde{R}$ as the set of all true data **d** which are statistically consistent with $\tilde{\mathbf{d}}$. To the extent that **V** does not vary significantly over $\tilde{R}$, this is the same ellipsoid as R but with center at $\tilde{\mathbf{d}}$ instead of **d**. Both regions R and $\tilde{R}$ are defined by the inequality

$$\rho^2 = \boldsymbol{\epsilon}^{\mathrm{T}}\mathbf{V}^{-1}\boldsymbol{\epsilon} = (\tilde{\mathbf{d}} - \mathbf{d})^{\mathrm{T}}V^{-1}(\tilde{\mathbf{d}} - \mathbf{d}) \leq \rho_\gamma^2, \quad (11)$$

with either **d** (in the case of R) or $\tilde{\mathbf{d}}$ (in the case of $\tilde{R}$) regarded as fixed.

Returning to the general structure of the nastiness function (7), we now consider the particular problem of determining the optimal model which has a minimal deviation from a favored model $\hat{S}$, satisfies the condition (4) exactly, and at the same time lies in the confidence region $\tilde{R}$ of $\tilde{\mathbf{d}}$, i.e., satisfies the inequality (11). Unless the favored model $\hat{S}$ itself is already consistent with the data, the minimal solution will normally lie on the surface of $\tilde{R}$, and we can therefore replace the inequality in (11) by an equality. The side condition (11) can then be incorporated in the nastiness function formed from the conditions (4) and (5) as an additional term multiplied by a Lagrange multiplier α. This yields the general form (7) with the matrix in the first term given by $\mathbf{M} = \mathbf{V}^{-1}$. We shall adopt this form for **M** in the following, thereby providing a simple statistical interpretation of the optimal model obtained by minimizing (7). The value of the Lagrange multiplier α for given ρ_γ is determined by the side condition (11). Numerically it is more convenient to reverse the procedure and use (11) to determine ρ_γ, given α. The appropriate value α for given ρ_γ can then be determined by iteration.

Taking the variation of Eq. (7) yields an equation for the minimal solution:

$$\delta\eta = \int_0^{2\pi} d\theta\{2(S - \hat{S}) + 4\beta(S - |S|) - 2\alpha\boldsymbol{\epsilon}^{\mathrm{T}}\mathbf{V}^{-1}\mathbf{b}\}\delta S = 0,$$

where we have used, from (8),

$$\delta\boldsymbol{\epsilon} = -\int_0^{2\pi} d\theta\mathbf{b}\delta S.$$

Since δS can be arbitrarily chosen, this requires

$$S(\theta) = \begin{cases} \hat{S} + \alpha\boldsymbol{\epsilon}^{\mathrm{T}}\mathbf{V}^{-1}\mathbf{b} & \text{for } S > 0 \\ (1 + 4\beta)^{-1}[\hat{S} + \alpha\boldsymbol{\epsilon}^{\mathrm{T}}\mathbf{V}^{-1}\mathbf{b}] & \text{for } S < 0. \end{cases}$$

In the limit as $\beta \to \infty$, the expression for negative

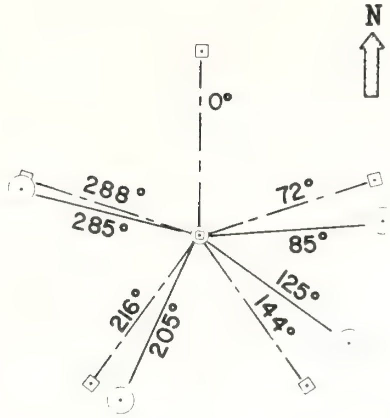

FIG. 1. Wave gage array geometries showing five-element North Sea array (⊙) and hypothetical six-element star array (⊡) used in some of the numerical experiments. The radius of both arrays is 90 m.

S approaches zero, and we obtain

$$S(\theta) = (\hat{S} + \mathbf{b}^{\mathrm{T}}\boldsymbol{\lambda})H(\theta), \tag{12}$$

where

$$H(\theta) = \begin{cases} 1 & \text{if} \quad (\hat{S} + \mathbf{b}^{\mathrm{T}}\boldsymbol{\lambda}) > 0 \\ 0, & \text{otherwise} \end{cases} \tag{13}$$

and

$$\boldsymbol{\lambda} = \alpha \mathbf{V}^{-1}\boldsymbol{\epsilon}. \tag{14}$$

Substitution of (12) and (14) in the expression (8) for the error yields a set of equations for $\boldsymbol{\lambda}$:

$$\tilde{\mathbf{d}} = \alpha^{-1}\mathbf{V}\boldsymbol{\lambda} + \int_0^{2\pi} d\theta(\hat{S} + \mathbf{b}^{\mathrm{T}}\boldsymbol{\lambda})H\mathbf{b}. \tag{15}$$

Once the coefficients $\boldsymbol{\lambda}$ are determined, S follows from (12) and (13). The solution of (15) represents a nonlinear problem because of the implicit dependence of H on $\boldsymbol{\lambda}$. Moreover, the covariance matrix $\mathbf{V}$ must be defined by the solution itself. However, a solution can be readily constructed numerically by the following iterative scheme: A zeroth-order guess at $\boldsymbol{\lambda}$ yields a zeroth-order solution for $S(\theta)$ and $H(\theta)$ through Eqs. (12) and (13). This function is used to estimate the covariance matrix $\mathbf{V}$ using standard spectral estimation formulas (cf. Jenkins and Watts, 1976). With $\mathbf{V}$ and H given, Eq. (15) represents a set of linear equations for $\boldsymbol{\lambda}$, the solution of which yields the first iteration for $\boldsymbol{\lambda}$, and so forth. An optimal solution is determined in this manner for fixed α. As indicated earlier, a second iteration loop is then needed to determine the α value corresponding to a given confidence limit ρ_γ. Experience with this scheme applied to wave gage arrays has shown convergence to be reasonably reliable and rapid. In some cases, the iteration in $\boldsymbol{\lambda}$ showed a tendency to overshoot, and better convergence could be achieved by replacing the new $\boldsymbol{\lambda}$ value at each iteration step by the mean of new and old values. The iteration in α was based on a linear interpolation/extrapolation scheme. Typically, seven $\boldsymbol{\lambda}$ iterations for fixed α and four or five α iterations were necessary to complete the solution to satisfactory accuracy.

3. Application to wave gage arrays

As a test, the inverse technique was applied to a five-element directional array of bottom pressure transducers deployed in the North Sea during JONSWAP 75. The measurements constituted a pilot project to measure the directional properties of swell in shallow water in order to distinguish between several possible mechanisms of swell decay (cf. Hasselmann *et al.*, 1973; Long, 1973; Shemdin *et al.*, 1979). Due to technical difficulties an originally planned array of instruments could not be completed in 1975 and the residual array (shown in Fig. 1) was not optimal. Nevertheless, the data provided a suitable case for testing the usefulness of the inverse technique under conditions of rather weak resolution often encountered in practice.

The data set consisted of all combinations of cross spectra and autospectra obtainable from the five instruments. The basic spectral estimates obtained by standard FFT methods from 20 min records had 18 degrees of freedom, a Nyquist frequency of 1 Hz, and a bandwidth of 1/128 Hz. To obtain higher statistical stability, however, three adjacent frequency bands were averaged, yielding 54 degrees of freedom at a resolution of 0.0234 Hz.

Writing the array equations (2) in the form

$$\frac{E_{ij}(f)}{E(f)} = \int_0^{2\pi} d\theta S(\theta,f) \times \exp[-ikr_{ij}\cos(\theta - \theta_{ij})], \quad i, j = 1, \ldots, m, \tag{16}$$

the basic data set $\mathbf{d}$ is seen to consist of the $m(m - 1) = 20$ cospectral and quadrature spectral components of the normalized cross spectra E_{ij}/E, $i \neq j$; the m further equations for $i = j$ yield the single normalization condition

$$1 = \int_0^{2\pi} d\theta S(\theta,f). \tag{17}$$

This can also be treated formally as a data equation, the only difference from the other equations being that the statistical error of the data value 1 is identically zero. [A small formal complication arises because the matrix $\mathbf{V}$ becomes singular if this is done, whence the matrix $\mathbf{M} = \mathbf{V}^{-1}$ in (7) does not exist. For theoretical consistency in the development beginning with (7), Eq. (17) should be treated as an absolute constraint, rather than a data equation, and incorporated into η using another Lagrange multiplier. This and the vector **λ**, defined by (14), become the parameters of a model which is, in fact, identical to that obtained by formally treating (17) as a data equation and ignoring the resulting singularity of **V**. This complication is purely a formal question of interpretation without practical consequence since **V** need not be inverted in solving the final model equations (15).]

Computation of the elements of the covariance matrix **V** involves evaluation of the covariances of various estimates of cospectra and quadrature spectra, normalized in terms of the autospectra. Recipes for computing these covariances are given in Jenkins and Watts (1968, Appendix A9.1 and ¶ 3.2.5) in terms of the true cross spectra of the process; at the mth iteration, these are calculated by integrating (16) using $S = S^{(m)}$. An important property of **V** is that it is proportional to $1/\nu$, where ν is the degrees of freedom of the spectral estimators $\hat{E}_{ij}$.

The constraint $\rho^2 = \rho_\gamma^2$ is evaluated from a table of percentage points of the X_μ^2 distribution. Taking $\gamma = 0.8$ (the choice of γ is to some extent arbitrary; a smaller value has the same effect in the numerical cases studied as a larger number of degrees of freedom in the spectral estimates), we obtain for the five-element array of Fig. 1 [$\mu = m(m - 1) = 20$, the side condition (17) not being counted], $\rho_\gamma^2 \approx 25$. For the hypothetical six-element array used in some of the numerical experiments below, $\mu = 30$ and $\rho_\gamma^2 \approx 36$.

4. Results for North Sea data

Some examples of optimal model fits for the North Sea array are shown in Fig. 2. Directional distributions were computed for a wind sea peak (Fig. 2a) [$f = 0.156$ Hz, wavelength = 60 m] and a swell peak (Fig. 2b) [$f = 0.109$ Hz, wavelength = 101 m], both taken from the same spectrum (Fig. 2c). For each data set, two favored models were tried, an isotropic form [$\hat{S} = 1/(2\pi)$] and one with a single lobe centered on the apparent dominant wave direction. The position and shape of the lobe were determined by a preliminary calculation which least-squares fitted a five-harmonic Fourier expansion of S in θ to the data set [the Fourier-Bessell technique of Barber (1963)]. The principal lobe of this fit was retained, the rest of the distribution set equal to zero, and the result renormalized and used as $\hat{S}$ in the subsequent analysis.

In both cases, the optimal model approaches the favored model $\hat{S}$ as closely as possible under the constraints set by the data. Thus a comparison of the optimal models for the two favored cases, which were chosen to represent fairly opposite extreme situations, should give some indication of which features of the directional distribution are fairly independent of $\hat{S}$ and which are more strongly governed

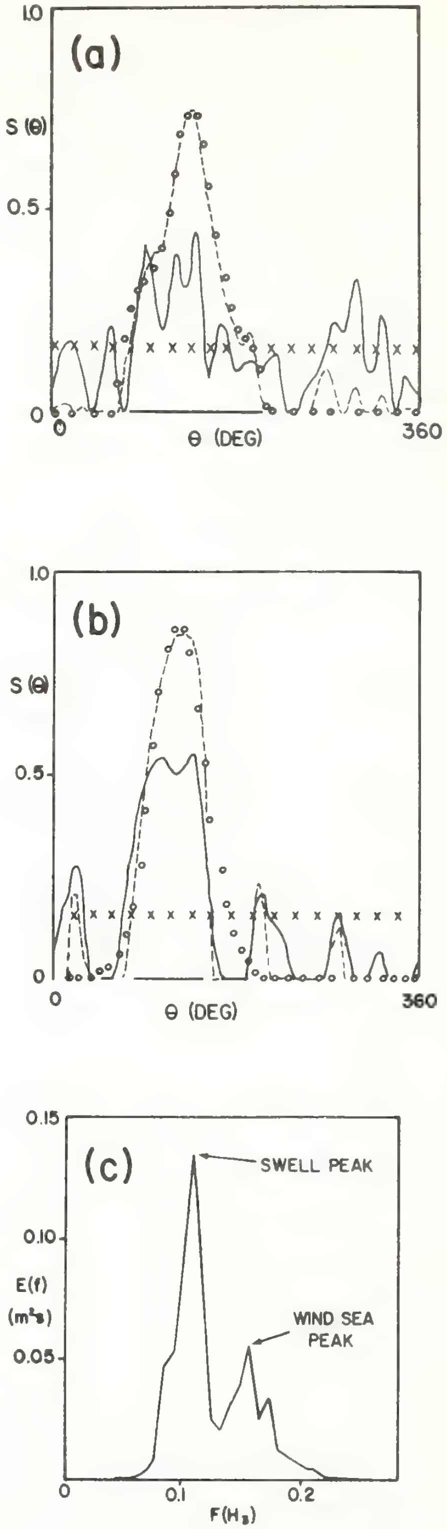

Fig. 2. Optimal spectral model fits to the North Sea data. Favored models (see text) are indicated by discrete points (×,○), the optimal fits by curves (solid and dashed, respectively): (a) example of a wind wave peak; (b) example of a swell peak (see text); (c) frequency spectrum indicating wind sea and swell peaks corresponding to cases (a), (b).

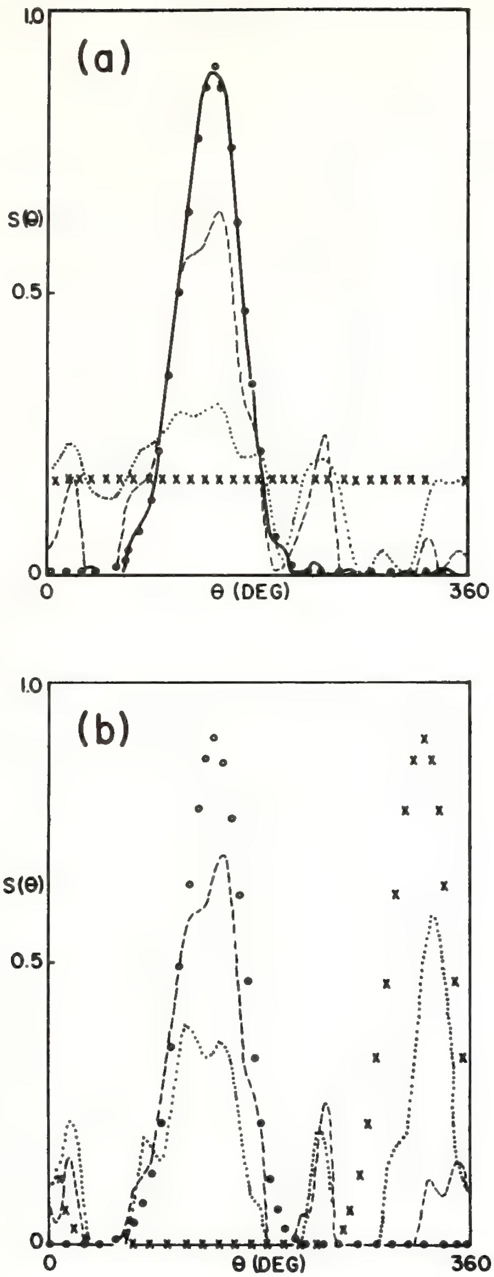

FIG. 3. Experiments with exact data. The input test spectrum S_W is indicated by the circles, the favored model $\hat{S}$ by the crosses. Optimal model fits are shown by curves: dotted lines, $\nu = 30$; dashed lines, $\nu = 180$; solid line, $\nu = \infty$. (a) Isotropic favored model, $\hat{S} = \frac{1}{2}\pi$; (b) effect of misleading favored model, $\hat{S} = C_0 \cos^{20}[\frac{1}{2}(\theta - 317°)]$.

by the additional assumptions needed to invert the data set.

Despite the differences in $\hat{S}$, both optimal models reproduce the same principal features: 1) a principal lobe centered near the direction indicated by the Fourier-Bessell least-squares fit, and 2) spike-like side lobes. The former is believed to represent a directional maximum actually present in the wave field. The latter appear to result from a folding of this maximum by the antenna beam pattern of the array; the side lobes appeared in all spectra analyzed, independent of the choice of $\hat{S}$, and apparently represent a basic limitation of the array geometry. It should be noted in this context that the structure of the antenna beam pattern, defined by

$$G(k) = 1 + \sum_{i} \sum_{j \neq i} \exp(-i\mathbf{k} \cdot \mathbf{r}_{ij})$$

(Barber, 1963) is reflected in the optimal model itself, which has the form of an expansion—for positive S—in the same set of basis functions, $\exp(-i\mathbf{k} \cdot \mathbf{r}_{ij})$. Although the present technique generally yields higher directional resolution than the classical antenna beam method and avoids negative lobes, it appears that the problem of generating spurious (positive) side lobes is not entirely avoided.

5. Numerical experiments

To clarify this point, a set of numerical experiments was conducted to investigate the following specific questions:

(i) Given a set of exact, noise-free cross spectra from the five-element array of Fig. 1, what is the effect on the solution of varying degrees of freedom (i.e., varying confidence regions) and different choices for $\hat{S}$?

(ii) Given artificially generated data containing statistically consistent errors and no *a priori* knowledge (i.e., $\hat{S} = \frac{1}{2}\pi$), how does the accuracy of the recovered solution respond to varying degrees of freedom in the spectral estimators and to changes in array geometry?

A test spectrum typical of a wind sea near the spectral peak (Mitsuyasu *et al.*, 1975)

$$S_W = C_0 \cos^{20}[\tfrac{1}{2}(\theta - 137°)]$$

(where θ is measured in degrees clockwise from north and C_0 is a normalization constant) was used for most of the numerical experiments. A second model,

$$S_S = C_1 + C_2 \cos^4(\theta - 54°) + C_3\{1 + \cos[18(\theta - 114°)]\}M(\theta),$$

consisting of a narrow 20° swell peak superposed on an undulating background, was also used. The swell component was represented by the last term containing the masking function

$$M(\theta) = \begin{cases} 1, & 104° \leq \theta \leq 124° \\ 0, & \text{otherwise}. \end{cases}$$

The constants C_1, C_2 and C_3 were adjusted so that one-third of the wave energy was in the swell peak and two-thirds in the background.

The wave frequency assumed in all cases corre-

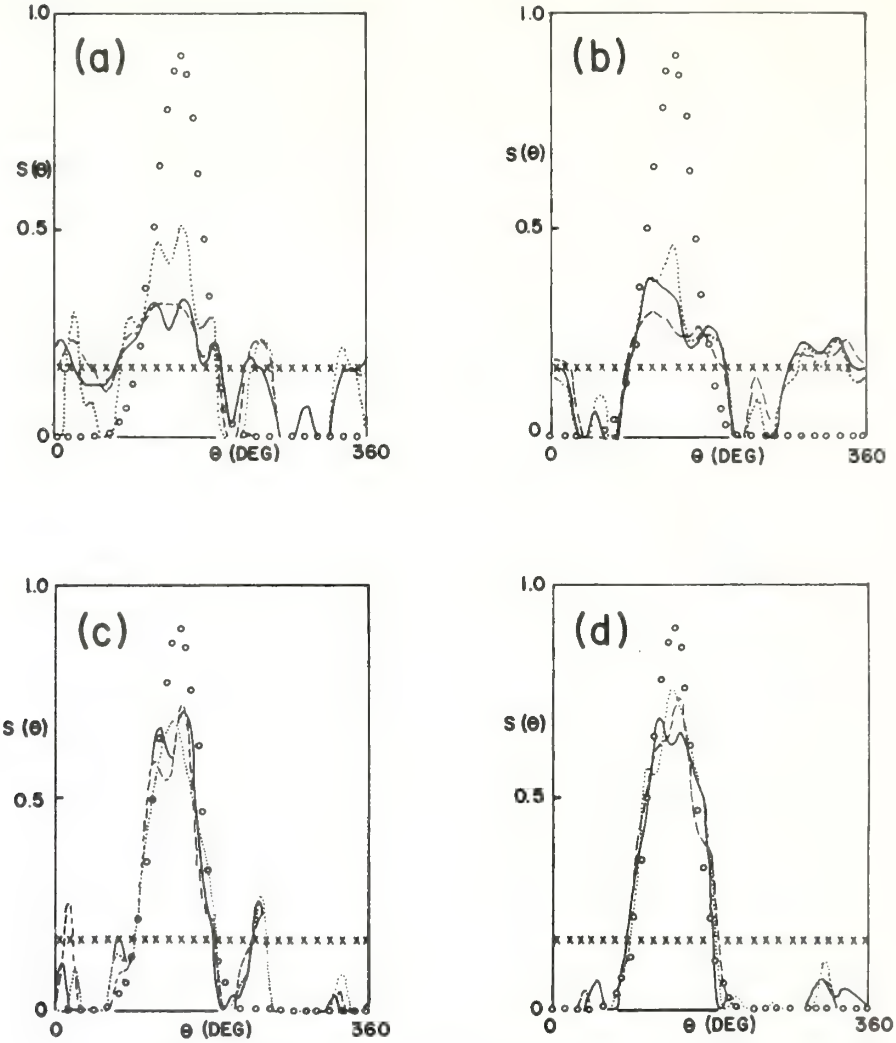

FIG. 4. Experiments with artificial noisy data. Input test spectrum S_W and favored model $\hat{S}$ are indicated by discrete points (○, ×, respectively). Optimal model fits for three realizations are shown in each panel: (a) five-element array, $\nu = 30$; (b) six-element star array, $\nu = 30$; (c) five-element array, $\nu = 180$; (d) six-element star array, $\nu = 180$.

sponded to a wavelength of 100 m. For each experiment, the set of "true" cross spectra E_{ij} were calculated by numerically integrating (16) with $S = S_W$ or S_S. These results were used directly as "observed" data to investigate question (i). To investigate (ii), the "observed" data were formed by adding a set of statistically consistent errors to the "true" data. In generating the set of errors **e** allowance must be made for the fact that the components of **e** are not mutually independent (the covariance matrix **V** is not diagonal). This can be accounted for by representing **e** as a linear combination of the statistically orthogonal normalized eigenvectors of **V**. The coefficient of each eigenvector can then be generated independently by selecting a random number from a Gaussian population with zero mean and variance given by the corresponding eigenvalue.

Figs. 3 and 4 illustrate the results of the numerical experiments. For Fig. 3a, the optimal model was fitted to exact data for the five-element array of Fig. 1, assuming spectral degrees of freedom $\nu = 30$, 180 and ∞ and $\hat{S} = \frac{1}{2}\pi$. In each case, the solution has been pushed as close to $\hat{S}$ (by the variational principle inherent in the model) as the constraint $\boldsymbol{\epsilon}^T\mathbf{V}^{-1}\boldsymbol{\epsilon} = \rho_\gamma{}^2$ will allow; since $\mathbf{V}^{-1}$ is proportional to ν, $|\boldsymbol{\epsilon}|$ must diminish as ν increases, and the solution looks progressively more like the test spectrum. The $\nu = \infty$ case indicates the limit of the ability of the optimal model to recover this test spectrum, given this array and no *a priori* knowledge. Although the fit of the optimal model in the limit of zero statistical error is excellent, it is seen that the limited spatial sampling still allows the existence of weak side lobes.

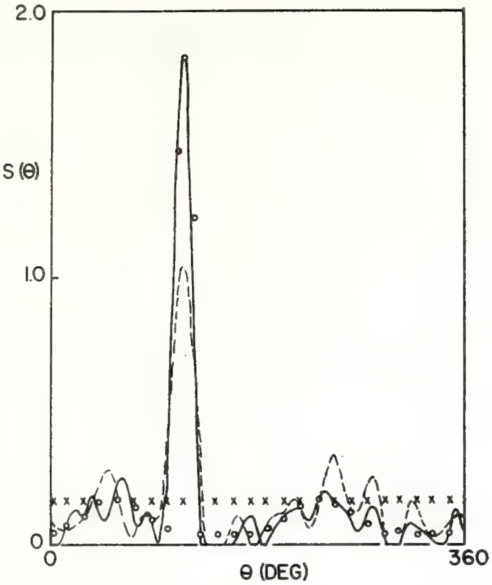

FIG. 5. Experiments with artificial noisy data. Input test spectrum (circles) is a sharp swell beam superposed on an undulating background. The favored model (crosses) is assumed isotropic. Dashed line, $\nu = 180$; solid line, $\nu = \infty$.

Fig. 3b shows the effect of a misleading choice for $\hat{S}$, in this case, a $\cos^{20}$ lobe identical in shape to S_W but centered at $\theta = 317°$, 180° away from the center of the S_W distribution. At 30 degrees of freedom, a second major lobe is allowed in the solution, in direct response to the erroneous $\hat{S}$ distribution. At $\nu = 180$, the constraint on $\epsilon^T V^{-1} \epsilon$ tends to dominate, and the secondary lobe is largely attenuated.

Fig. 4 illustrates the effects of statistical noise in the data and a change in array geometry. For each of the four panels, three sets of statistically consistent artificial data were generated; in Figs. 4a and 4c for the five-element array of Fig. 1, and in Figs. 4b and 4d for the hypothetical six-element star array. The results reinforce the significance of noise in controlling model performance. At $\nu = 30$ (Figs. 4a and 4b) the optimal models differ rather grossly from the input test spectrum, and considerable variability exists between realization. The improved antenna beam pattern of the six-element star alters the results, but at this level of statistical uncertainty, the performance of the star is not obviously superior. At $\nu = 180$ the variability between solutions for the different realizations is much attenuated, and the agreement with the true model greatly improved. The performance of the six-element star is clearly superior to that of the five-element array, particularly with respect to side lobe suppression.

Finally, Fig. 5 shows the optimal model fit to the test spectrum S_S, for the six-element star array for noise-free data, $\nu = \infty$, and noisy data, $\nu = 180$, taking $\hat{S} = \frac{1}{2\pi}$. Despite the presence of a peak considerably sharper than the classical antenna resolution, the optimal model agrees very well with the true distribution in the noise-free case. However, the addition of relatively weak noise results in a significant deterioration of the fit.

In conclusion, it appears that the side lobes occurring in the directional distributions of the real data cases shown in the examples of Figs. 2a and 2b are a consequence of the array geometry in conjunction with the noisiness of the spectral estimates. Much improved fits can be expected for longer time series, yielding a larger number of degrees of freedom.

6. Summary and conclusions

We have considered the problem of estimating a function (specifically, the directional spectrum of a gravity wave field) from measurements of integral properties of that function when those measurements are subject to statistical variability. Given the true spectrum, the statistical properties of the data errors are known, and a test of the hypothesis that any given model S is the true spectrum can be formulated. The appropriate measure of the fit of the model to the data is the quantity $\rho^2 = \epsilon^T V^{-1} \epsilon$, where ϵ is the vector of implied statistical errors in the data and V^{-1} is the inverse of the error covariance matrix. This quantity is distributed as $X_\mu{}^2$, where μ is the number of linearly independent measurements in the data set. It is then possible to establish a critical value of ρ^2 beyond which the valid model hypothesis must be rejected at any specified level of confidence.

For any data set, there exists in general an infinity of valid models; of these, we have defined as optimal that one which minimizes some (arbitrarily chosen) positive definite integral property of the model (and in addition satisfies the side condition that the distribution is not negative). One such property, $\int_0^{2\pi} d\theta (S - \hat{S})^2$, where $\hat{S}$ is some favored model, has been examined in detail, and the resulting procedure, applied to gravity wave-gage arrays, has been used both to analyze real data and to explore the subset of valid models under varying conditions in a series of numerical experiments. For weak noise levels, good results were obtained for a variety of directional spectra, including distributions considerably sharper than the classical antenna pattern of the array. The fit is relatively insensitive to the choice of $\hat{S}$. However, the quality of fit is strongly dependent on the statistical stability of the spectral estimates, indicating that good directional resolution from multicomponent arrays requires considerably longer time series than are customarily used for one-dimensional frequency spectra.

Although the subject has been treated largely in the context of surface gravity wave spectra, the ideas presented are applicable to any problem involving the fitting of models to statistical data which estimate integral properties of the model.

Acknowledgments. The JONSWAP wave data were kindly made available through Karl Richter of the Deutsches Hydrographisches Institut and were spectral analyzed by Wolfgang Rosenthal, Institut für Geophysik, Universität Hamburg, and Hans-Jürgen Rubach, Deutsches Hydrographisches Institut. The work was carried out while the senior author was visiting the Max-Planck-Institut für Meteorologie.

REFERENCES

Backus, G. E., and J. F. Gilbert, 1967: Numerical applications of a formalism for geophysical inverse problems. *Geophys. J. Roy. Astron. Soc.* **13,** 247–276.

Barber, N. F., 1963: The directional resolving power of an array of wave detectors. *Ocean Wave Spectra*, Prentice-Hall, 357 pp.

Hasselmann, K., T. P. Barnett, E. Bouws, H. Carlson, D. E. Cartwright, K. Enke, J. A. Ewing, H. Gienapp, D. E. Hasselmann, P. Krusemann, A. Meerburg, P. Müller, D. J. Olbers, K. Richter, W. Sell and H. Walden, 1973: Measurement of wind-wave growth and swell decay during the Joint North Sea Wave Project (JONSWAP). *Deutsch. Hydrogr. Z.* (Suppl.), **A12,** 95 pp.

Jenkins, G. M., and D. G. Watts, 1968: *Spectral Analysis and its Applications*. Holden-Day, 525 pp.

Long, R. B., 1973: Scattering of surface waves by an irregular bottom. *J. Geophys. Res.* **78,** 33, 7861–7870.

Mitsuyasu, H., F. Tasai, T. Suhara, S. Mizuno, M. Ohkusu, T. Honda, and K. Rikiishi, 1975: Observations of the directional spectrum of ocean waves using a cloverleaf buoy. *J. Phys. Oceanogr.*, **5,** 750–760.

Olbers, D. J., P. Müller, and J. Willebrand, 1976: Inverse technique analysis of a large data set. *Phys. Earth Planet. Inter.*, **12,** 248–252.

Shemdin, O., K. Hasselmann, K. Herterick, and V. Hsiao, 1979: Nonlinear and linear bottom interaction effects in shallow water. *Proc. NATO Symp. Turbulent Fluxes through the Sea Surface, Wave Dynamics, and Prediction* (in preparation).

43. Paper submitted to the Joint IOC/WMO Seminar on Oceanographic Products and the IGOSS Data Processing and Services System, Intergovernmental Oceanographic Commission [of UNESCO], Workshop Report No. 17-supplement, 408-420.

Observing and Predicting Hurricane Wind and Wave Conditions

Duncan Ross

Introduction

Early attempts to describe the areal distribution of wave conditions in tropical cyclones were based on necessarily arbitrary and unverified assumptions regarding the equivalent fetch and duration as a function of radial distance from the storm's eye and the forward velocity of the storm (cf. Patterson, 1971, and Bretschneider, 1972). Additional complications entered when attempts were made to specify the hurricane wind field which is responsible for the generation of the waves.

Recently, measurements of winds and waves were obtained in hurricane Camille, a Gulf of Mexico storm of September 1969, Ava, an eastern Pacific storm which occurred in June of 1973, and Eloise, a Gulf of Mexico storm (Withee and Johnson, 1975). The Camille data (Patterson, 1974) was obtained by a consortium of oil companies led by the Shell Development Company. The waves were measured by resistance-wire wave staffs mounted on several drilling platforms. The Ava data were obtained by the author by means of a laser altimeter operated from a low-flying aircraft (150 meters) in the rear quadrant of the storm (cf. Ross et al., 1974, and Ross, 1975). The Eloise data set was obtained by an environmental data buoy operated by the National Oceanic and Atmospheric Administration.

A rigorous specification of the wave field within a hurricane (or any other meteorological system) is dependent upon the solution of the energy balance equation

$$\frac{\partial E}{\partial t}(k,x,t) + V \cdot \nabla_x F(k,x,t) = S(k,x,t) \tag{1}$$

where F(k,x,t) is the wave number energy spectrum as a function of space x, and time t; $V \cdot \nabla_x F$ is the divergence of the energy flux; V is the group velocity of the wave energy, and S(k,x,t) is the source function term and represents the effects of energy input, dissipation, and transfer within the spectrum due to nonlinear interactions. Preliminary estimates of the net source function term S(k,x,t) have been obtained in the JONSWAP experiment (Hasselmann et al., 1973) which proved the importance of nonlinear interactions in the evolution of the spectrum. Another important part of the JONSWAP results was the application of the similarity theory of Kitaigorodskii (1962) to describe the evolution of the total wave energy, E, and peak frequency, f_m, of the spectrum in nondimensional terms as a function of fetch where the local surface wind U_{10} and the gravity constant g are used to obtain the dimensionless parameters.

The experimental results described in the JONSWAP report can be used to estimate S, allowing integration of the energy balance equation to specify the wave field for an arbitrary wind field. This is the approach that has been followed in the development of spectral wave models.

The results of JONSWAP and other similar studies (cf. Ross and Cardone, 1974, Schule et al., 1971, and Barnett and Wilkerson, 1967) suggest that if fetch in the hurricane situation could be specified nondimensionally, a relationship may exist between the dimensionless fetch parameterization and the important shape and scale parameters of the wave spectrum allowing prediction of the wave field without integration of equation (1).

In this paper, the scale and shape parameters of the wave energy spectrum within tropical hurricanes are examined in terms of a fetch implicitly proportional to the radial distance to the storm's eye nondimensionalized by the average surface wind as measured at 10 meters and g.

Specification of the Surface Windspeed

Windspeeds associated with the wave data considered herein were measured by an anemometer which averaged for a period of 15 minutes at an altitude of 10 meters in the case of Eloise and by an inertial navigation system aboard the NOAA aircraft flying at a level of 150 meters in the case of Ava. Since Ava and Camille were virtually identical storms, Camille winds were established based upon an analysis of the Ava wind field using the aircraft data. In addition, 30-minute average surface winds were measured from a drilling platform during Camille and verified the Ava analysis transformation. Unfortunately, the one platform with good measurements of the windspeed was not equipped with a wave staff.

Aircraft winds which were used to perform the Ava analysis were first adjusted to the equivalent surface value using the familiar logarithmic profile for neutral stability and a windspeed-dependent z_0 of the form

$$z_0 = .1525/U_* + 1.468 \times 10^{-5} U_*^2 - 3.71 \times 10^{-3} , \qquad (2)$$

where z_0 is the roughness length, and U_* is the friction velocity. The z_0 relationship is a modification of the formulation of Cardone (1969) using the results of Garratt (1977) according to Cardone (1979). The aircraft winds were averaged for a period of thirty seconds when the aircraft track was cross-wind and for two minutes during downwind tracks. Alternate approaches to specification of the hurricane wind field would be equally appropriate if properly scaled to the average wind as observed at a 10 meter anemometer height.

One such method is that described by Patterson (1971):

$$U = [A + B\rho + c\rho^2 + D\rho^3 + E\rho^4] \times \left\{ 0.692 \left[12.45 (\Delta P)^{1/2} - 0.575\ Rf \right] + \frac{V_f}{2} \right\} - \frac{V_f}{2} (1 - \cos\theta) \tag{3}$$

where A = 1.2132
B = -0.2326
C = 0.0295
D = -0.0021
E = 0.001
f = Coriolis parameter = .525 sin (latitude)
U = Wind velocity in knots at a height of 10 meters
V_f = Forward velocity of storm in knots
R = Radius to maximum winds in nautical miles
ΔP = Difference between the peripheral atmospheric pressure and the central pressure of the storm in millibars
ρ = Distance from storm's center to point where winds are desired divided by R
θ = Angle between radial perpendicular to track of hurricane and location of desired wind information; 90° would be the along-track direction.

The above technique assumes flow parallel to the isobars. Increased accuracy could be obtained by assuming an inflow angle proportional to $\rho^{-.75}$ with a maximum value of 50° at R, as observed in hurricane Eloise.

Development of the Model

Hasselmann et al. (1973 and 1976) suggested that for growing seas, the observed spectrum will be of the form

$$E(f) = \alpha g^2 (2\pi)^{-4} f^{-5} \exp \left\{ -\frac{5}{4} \left(\frac{f_m}{f} \right)^4 + \ln\gamma \times \exp \left[- \frac{\left(f - f_m \right)^2}{2\sigma^2 f_m^{\ 2}} \right] \right\} \tag{4}$$

where $\sigma = \begin{cases} \sigma_a, f \geq f_m \\ \sigma_b, f \leq f_m \end{cases}$

This function contains both scale and shape parameters. The scale parameters have been found to be interrelated when considered in the dimensionless form according to

$$\alpha = .033\ \nu^{2/3} \tag{5}$$

where $\nu = \frac{f_m U_{10}}{g}$, f_m is the spectral peak frequency, and g the gravity constant. For growing seas the shape parameters σ_a and σ_b were found to scatter considerably about a mean value of about 0.07 while γ, the ratio of the energy at the peak frequency f_m to that derived from the Pierson-Moskowitz (PM) (1964) fully-developed form of the spectrum, was found to have a mean value of 3.3 with little dependence upon ν. It should be noted that equation (4) reduces to the fully-developed PM form for a γ of 1.0.

Least squares fits of the hurricane data set to the spectral form of equation (4) have been determined, and the shape and scale parameters derived. Figures 1-a, b, and c are examples of the quality of the fit (see also

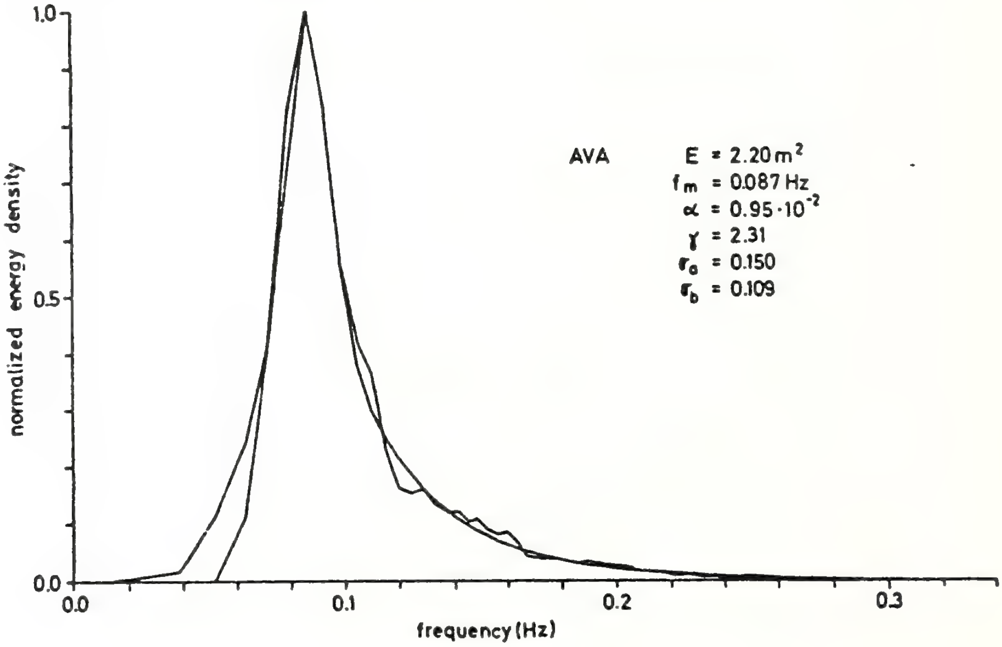

(a)

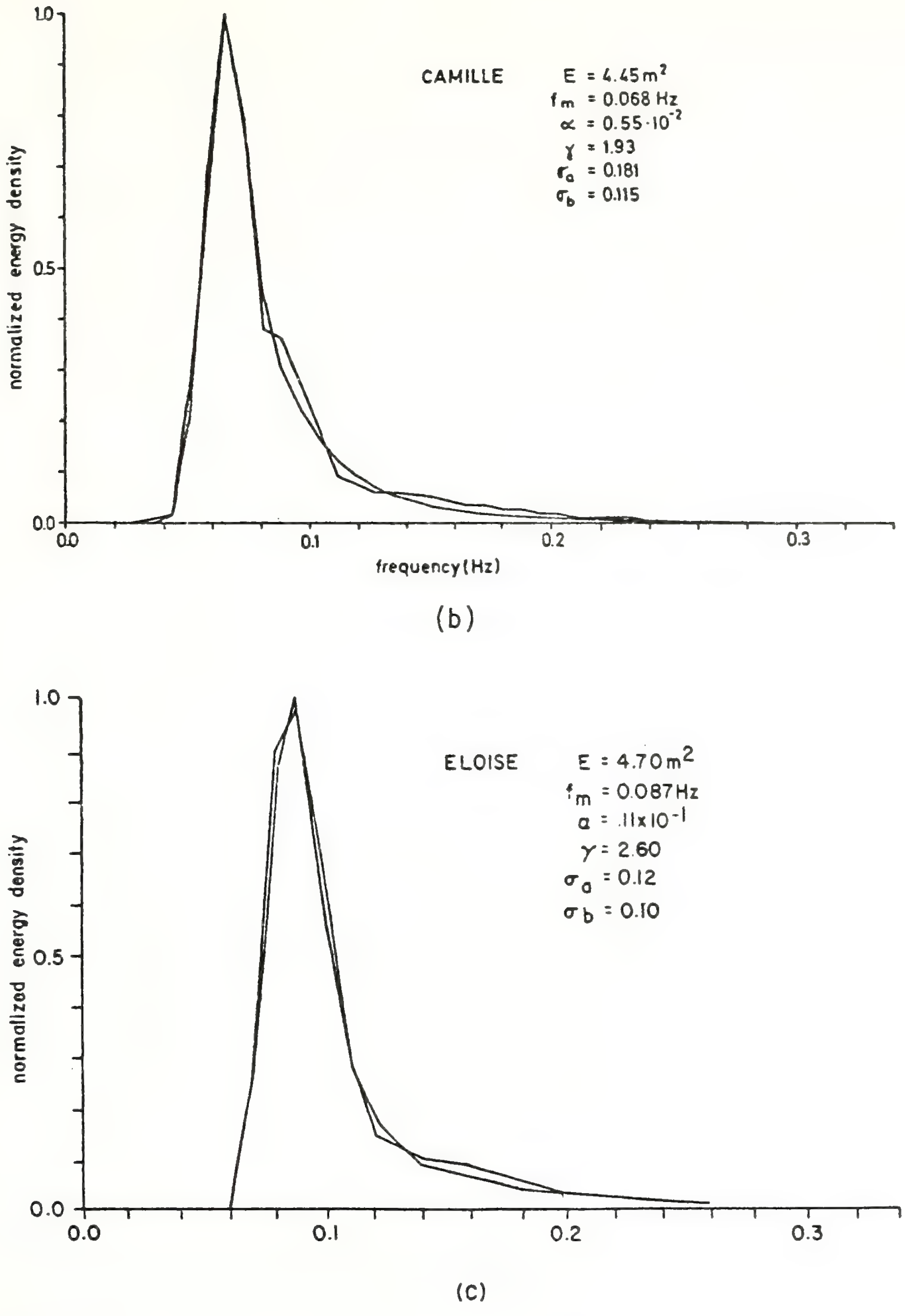

Figure 1. Examples of spectra and analytical fits for hurricane data sets.

Hasselmann *et al.*, 1976, and Müller, 1976, for a more complete representation of fitted spectra for Ava and Camille). The scale parameters were then nondimensionalized, where appropriate, in the JONSWAP manner and, along with the shape parameters, regressed against the dimensionless radial distance from the eye of the hurricane. Figure 2 presents the dimensionless scale parameters ε and ν versus nondimensional radial distance ξ_r. Also shown are error bars which reflect the maximum error one would encounter with an error in the windspeed specification of ± 5 m/s. It can be seen from Figure 4 that a power law regression well describes the behavior of these parameters and that the scatter can largely be attributed to position and wind field errors. Table I presents the coefficients and exponents of the power law fits of the shape and scale parameters determined from the regression analysis.

Table I

Regression line variables of shape and scale parameters.

$$\nu = .97\ \xi_r^{-.21}$$

$$\varepsilon = 2.25 \times 10^{-5}\ \xi_r^{.45}$$

$$\gamma = 4.7\ \xi_r^{-.13}$$

$$\alpha = .035\ \nu^{.82}$$

Testing the Model

An opportunity to test the model presented itself when hurricane Belle passed directly over NOAA buoys equipped with wind and wave measurement systems. The total energy E was derived from the appropriate regression equation (using a windspeed obtained from a model tuned to the buoy observations) and the significant wave height ($\overline{H}_{1/3} = 4\sqrt{E}$) was calculated from each observation period (cf. Ross and Cardone, 1977). The results, along with $\overline{H}_{1/3}$ calculations from a spectral model (Cardone, Pierson, and Ward, 1976, and Forristall *et al.*, 1978) are shown in Figures 3 and 4. Since the spectral shape parameters are also available from Table I, it is also possible to intercompare observed and predicted spectra. Figure 5 is such an example for hurricane Belle.

Another opportunity to test the model was presented when hurricane Anita developed in the Gulf of Mexico in August of 1977 and passed near the NOAA buoy EB 04. Figure 6 presents forecast values of significant wave height and spectral peak frequency, again from both the spectral and parametric models. It should be noted here that the forecast hurricane track errors were removed prior to construction of the figure since their inclusion would complicate evaluation of the wave models. Figure 7 is an example of the forecast wind

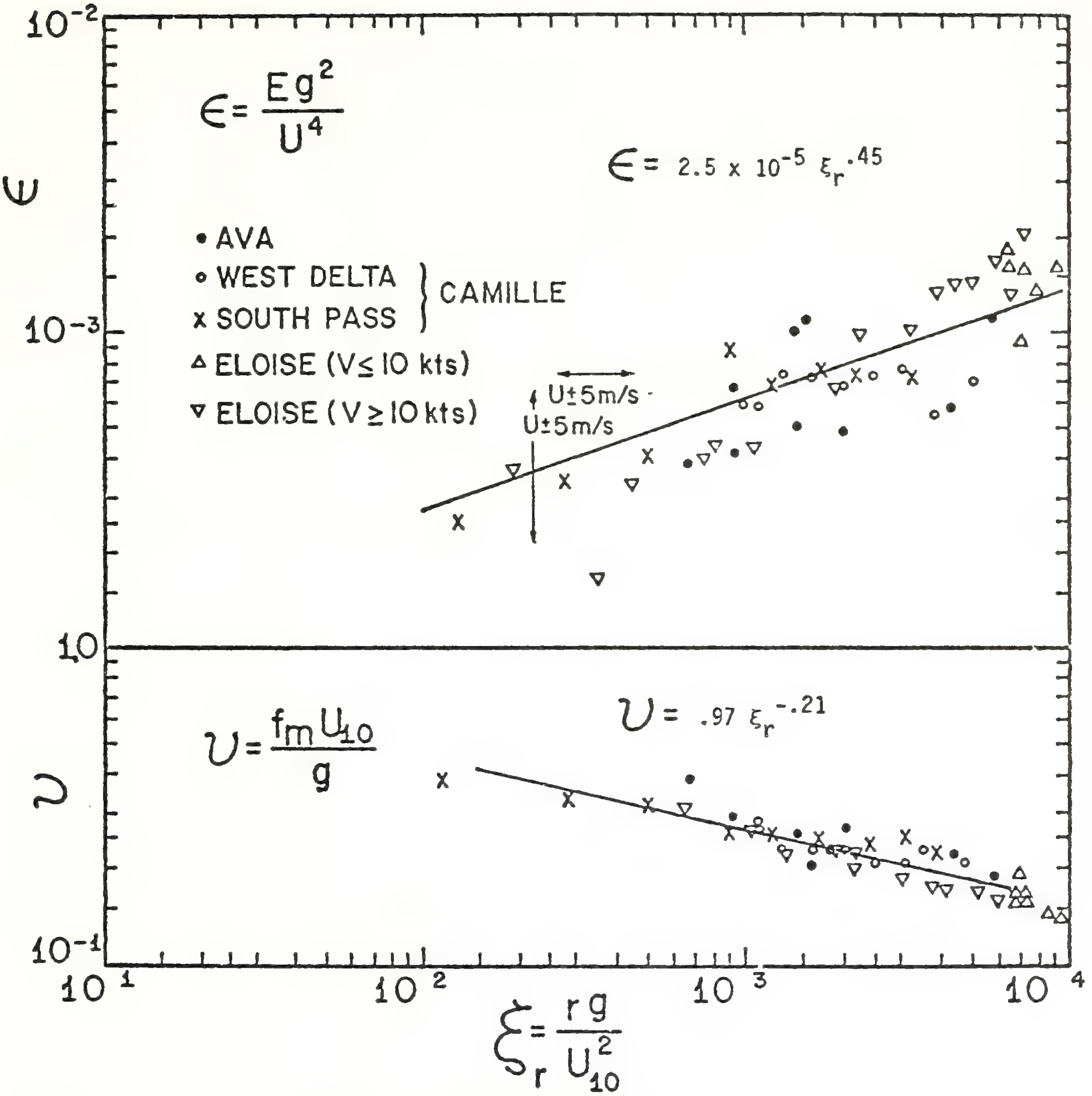

Figure 2. Dimensionless spectral scale parameters as a function of the dimensionless radial distance to the hurricane.

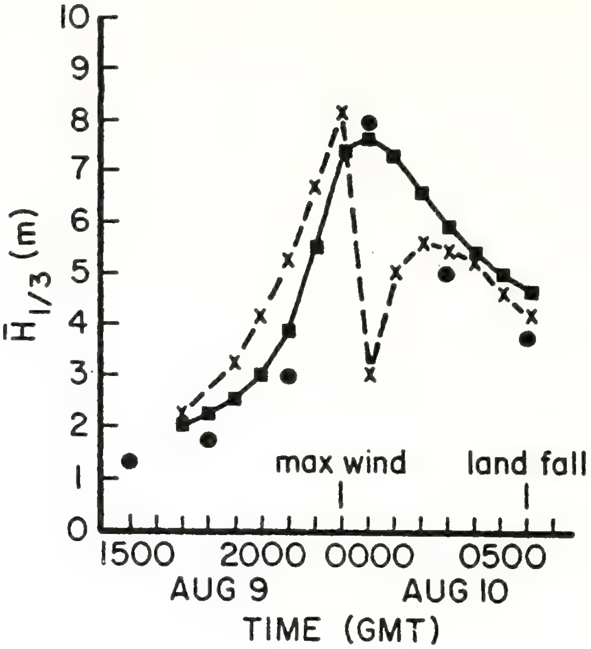

Figure 3. Comparison of measured and hindcast significant wave height at EB 41 during hurricane Belle: ● - measured; X - parametric; ■ - spectral.

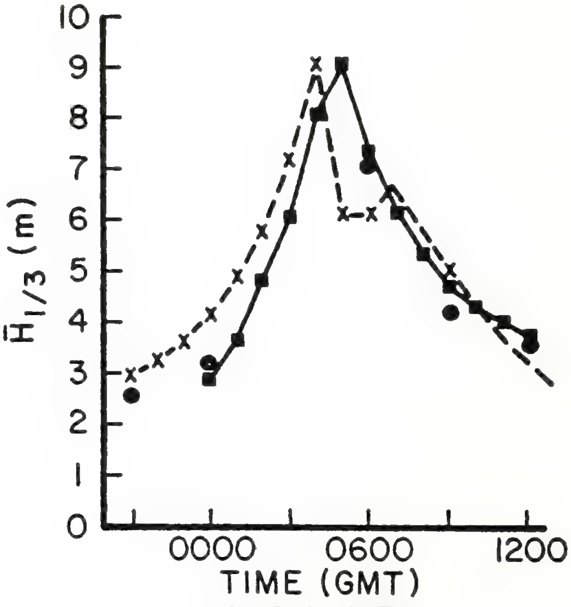

Figure 4. Comparison of measured and hindcast significant wave height at EB 15 during hurricane Belle: ● - measured; X - parametric model; ■ - spectral model.

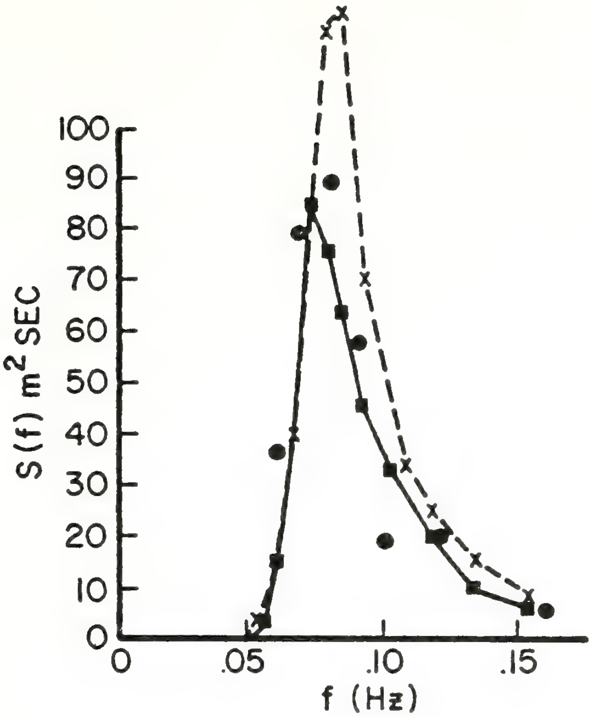

Figure 5. Maximum predicted spectra for hurricane Belle at EB 41: X - parametric model, $\overline{H}_{1/3}$ = 8.2 m; ■ - spectral model $\overline{H}_{1/3}$ = 7.8 m. Also shown is the maximum observed spectrum (●), $\overline{H}_{1/3}$ = 7.8m.

and wave field produced by the model, which is presently being transferred to the NOAA National Hurricane Center computer for operational use.

The important physical characteristics of the storms used in this study along with observed and calculated maximum average winds and significant wave heights are shown in Table II.

Table II

Storm	ΔP (mb)	Radius to Max. Wind (nmi)	V_f (kts)	Observed U Max. (m/s)	Calc. U Max. (m/s)	Max. Obs. $\overline{H}_{1/3}$ (m)	Max. Calc. $\overline{H}_{1/3}$ (m)
Anita	41	20	4	34.0	29.9	6.5	6.7
Ava	100	15	12	—	48.3	—	13.3
Belle	58	12	13	33.0	37.8	7.8	8.54
Camille	105	15	12	51.7	49.4	13.5	13.6
Eloise	41	15	15	35.8	32.8	8.7	7.2

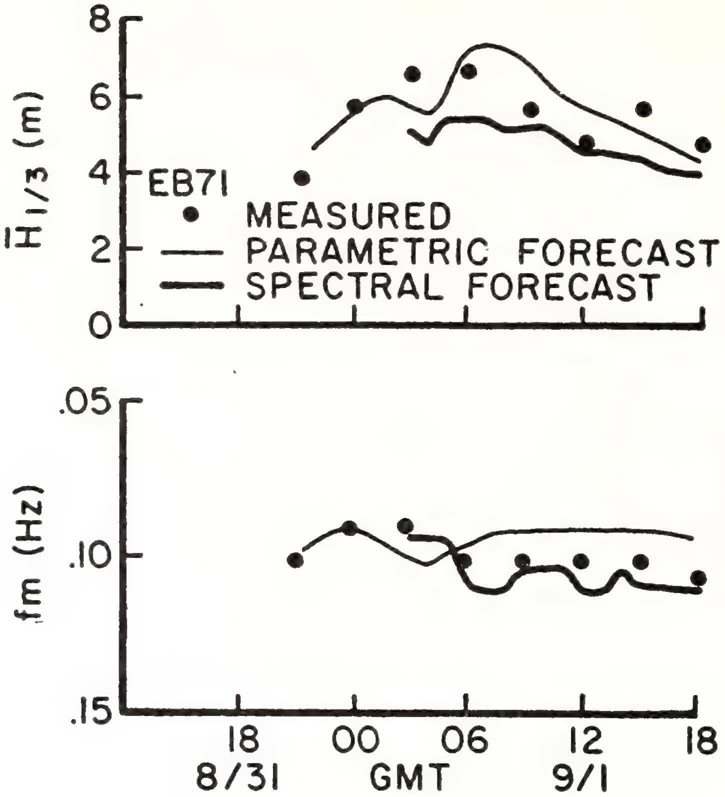

Figure 6. Measured and forecast significant wave height and peak frequency in hurricane Anita at EB 71.

Conclusions

The parametric wave model described here has been found to give accurate specifications of the deep water wave field in tropical cyclones. Its use for forecasting and hindcasting is warranted when detailed knowledge of the directional parameters of the spectrum are not required. Since the model predicts the total energy of the wave field, it is possible to calculate extreme value statistics such as the maximum expected single wave following the work of Longuet-Higgins (1952). Recent work by Forristall (1978) and Bouws (1978), however, suggests that this approach does not strictly hold for determining maximum waves in intermediate or shallow water and that in such situations the ratio of maximum to significant wave height should be reduced by about 10%.

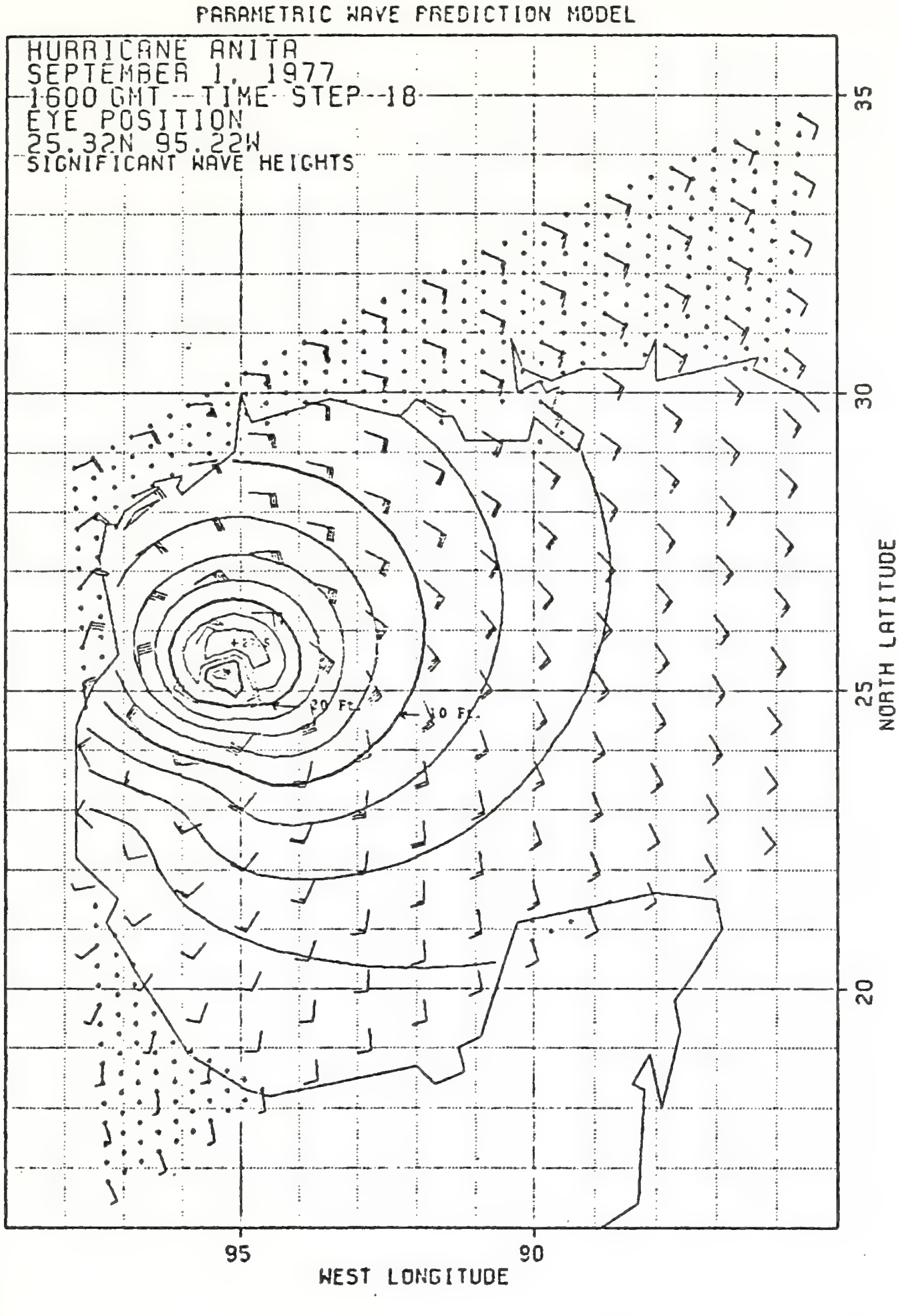

Figure 7. Contour diagram of significant wave height from the parametric wave model. Also shown are wind flags at every third grid point.

References

Barnett, T. P., and J. C. Wilkerson, 1967: On the generation of ocean wind waves as inferred from airborne radar measurements of fetch-limited spectra. J. Marine Res., 25, 292-328.

Bouws, E., 1978: Wind and wave climate in the Netherlands sector of the North Sea between 53° and 54° north latitude. Wetenschappelijk Rapport No. W. R. 78-9, Koninklijk Nederlands Meteorologisch Instituut, De Bilt, Netherlands, 54 pp.

Bretschneider, C. L., 1972: A non-dimensional stationary hurricane wave model. Preprint, 4th Annual Offshore Technology Conference (OTC 1517).

Cardone, V. J., 1969: Specification of the wind field distribution in the marine boundary layer for wave forecasting. Rept. TR 69-1, Geophys. Sci. Lab., New York University.

——, 1979: Personal communication.

——, W. J. Pierson, and E. G. Ward, 1976: Hindcasting the directional spectra of hurricane-generated waves. J. Petrol. Technol., 28, 385-394.

Forristall, G. Z., 1978: On the statistical distribution of wave heights in a storm. J. Phys. Oceanogr., 85, No. C5, 2353-2358.

——, V. J. Cardone, and R. C. Hamilton, 1977: Continental shelf currents in tropical storm Delia: theory and observation. J. Phys. Oceanogr., 7, No. 4, 532-546.

Garratt, J. R., 1977: Review of drag coefficients over oceans and continents. Monthly Weather Review, 105, No. 7, 915-929.

Hasselmann, K., T. P. Barnett, E. Bouws, H. Carlson, D. E. Cartwright, K. Enke, J. A. Ewing, H. Gienapp, D. E. Hasselmann, P. Kruseman, A. Meerburg, P. Müller, D. J. Olbers, K. Richter, W. Sell, and H. Walden, 1973: Measurements of wind-wave growth and swell decay during the Joint North Sea Wave Project (JONSWAP). Deut. Hydrogr. Z., Suppl. A, 8, No. 12.

——, D. B. Ross, P. Müller, and W. Sell, 1976: A parametric wave prediction model. J. Phys. Oceanogr., 6, No. 2, 200-228.

Kitaigorodskii, S. A., 1962: Applications of the theory of similarity to the analysis of wind-generated wave motion as a stochastic process. Izv. Akad. Nauk SSSR, Ser. Geofiz., No. 1, 73-80.

Longuet-Higgins, M. S., 1952: On the statistical distribution of the heights of sea waves. J. Marine Res., 11, No. 3, 245-266.

Müller, P., 1976: Parametrization of one-dimensional wind wave spectra and their dependence on the state of development. Hamburger Geophysikalische Einzelschriften, G. M. L. Wittenborn Sohne, 2 Hamburg 13, 177 pp.

Patterson, M. M., 1972: Hindcasting hurricane waves in the Gulf of Mexico. J. Petrol. Eng., 321-328.

——, 1974: Oceanographic data from Hurricane Camille. Proc. Offshore Technology Conference (OTC 2109).

Pierson, W. J., Jr., and L. Moskowitz, 1964: A proposed spectral form for fully developed wind seas based on the similarity theory of S. A. Kitaigorodskii. J. Geophys. Res., 69, 5181-5190.

Ross, D. B., 1975: A comparison of Skylab S-193 and aircraft views of surface roughness and a look toward Seasat. Proc. NASA Earth Resources Survey Symposium, Houston, Texas, June, 1911-1920.

——, and V. J. Cardone, 1974: Observations of oceanic white caps and their relation to remote measurements of surface wind speed. J. Geophys. Res., 79, 444-452.

——, B. Au, W. Brown, and J. McFadden, 1974: A remote sensing study of Pacific hurricane Ava. Proc. of the Remote Sensing Symposium, Willow Run Laboratories, Ann Arbor, Mich., April, 15-20.

——, and V. Cardone, 1977: A comparison of parametric and spectral hurricane wave prediction products. To be published in the Proc. NATO Symposium on Turbulent Fluxes through the Sea Surface, Wave Dynamics and Prediction, Marseille, France, September. Plenum Publishing Corp., New York, N. Y.

Schule, J. J., L. S. Simpson, and P. S. DeLeonibus, 1971: A study of fetch-limited wave spectra with an airborne laser. J. Geophys. Res., 76, 4160-4171.

Withee, G. W., and A. Johnson, Jr., 1975: Buoy observations during hurricane Eloise. Data Buoy Office, National Oceanic and Atmospheric Administration, Bay St. Louis, Mississippi.

44. Marine Forecasting, J. C. J. Nihoul, ed., Elsevier Oceanography Series 25, 261-283.

IRREGULAR-GRID FINITE-DIFFERENCE TECHNIQUES FOR STORM SURGE CALCULATIONS FOR CURVING COASTLINES

W. C. THACKER

Atlantic Oceanographic and Meteorological Laboratories, National Oceanic and Atmospheric Administration, Miami, Florida, 33149, U.S.A.

ABSTRACT

Finite-difference computations on irregular grids offer the advantages of resolving the coastal curvature and of allowing for an explicit time step of optimal size. A further advantage is the flexibility associated with editing the grid, which allows for improvements in its design. The techniques are based on the approximation of partial derivatives with slopes of planar surfaces associated with triangular components of the irregular grid. Simulations of several surges associated with various hypothetical hurricanes passing through Mobile Bay are realistic and relatively noise free. Because these techniques are computationally efficient, they provide a practical tool for forecasting storm surges.

INTRODUCTION

Previous approaches to the problem of including curving coastlines into calculations of storm surges have involved either the use of transformed coordinates (e.g., Wanstrath _et al_., 1976) or the use of finite-element techniques (e.g., Pinder and Gray, 1977). The method suggested here is to perform finite-difference calculations directly on an irregular grid that can smoothly represent the coastline. This offers the advantages of greater flexibility than the coordinate transformation method and greater economy than the finite-element method.

The plan of this presentation is, after first discussing features of the irregular computational grid, the approximation of derivatives, and the equations used for calculating storm surges, to present the results of computations for several hypothetical storms in the forms of sea surface elevation contour maps, flow vector maps, and graphs of water elevations along the coastline, with concluding remarks concerning the use of irregular grids in conjunction with the problem of inundation.

THE IRREGULAR GRID

The computational grid for Mobile Bay, shown in Fig. 1, illustrates some of the features that make irregular-grid finite-difference techniques attractive for use in forecasting storm surges. Most obvious is the excellent representation for the curving coastline by the irregular grid; this is a significant improvement over the

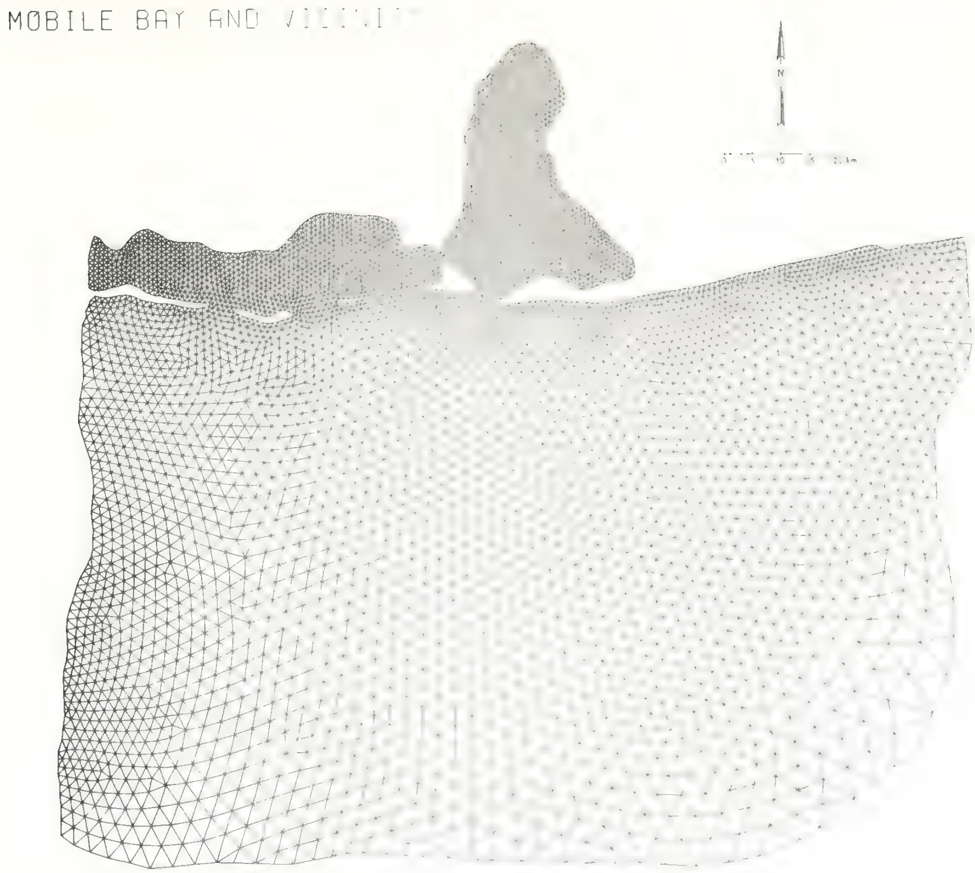

Fig. 1. Irregular grid for computing storm surges in Mobile Bay.

"stair-step" boundary of conventional uniform grids because it is at the coastline that the forecast value of the water surface elevation is most needed. Since one continuous grid serves for both the inland waters and for the open sea, the calculations can be made simultaneously for both regions, thereby avoiding the question of how properly to specify boundary conditions where the inland waters meet the open sea. The fact that the grid spacing is roughly proportional to the square root of the basin depth (Fig. 2) reflects the fact that the storm surge is essentially a shallow water wave with phase velocity proportional to the square root of the water depth. It is the ratio of the grid spacing to the basin depth which limits the size of the explicit computational time step in order to guarantee numerical stability. Unlike the uniform grid, for which the time step is determined in the deepest water (where this ratio is minimum and which is the least important region for the storm

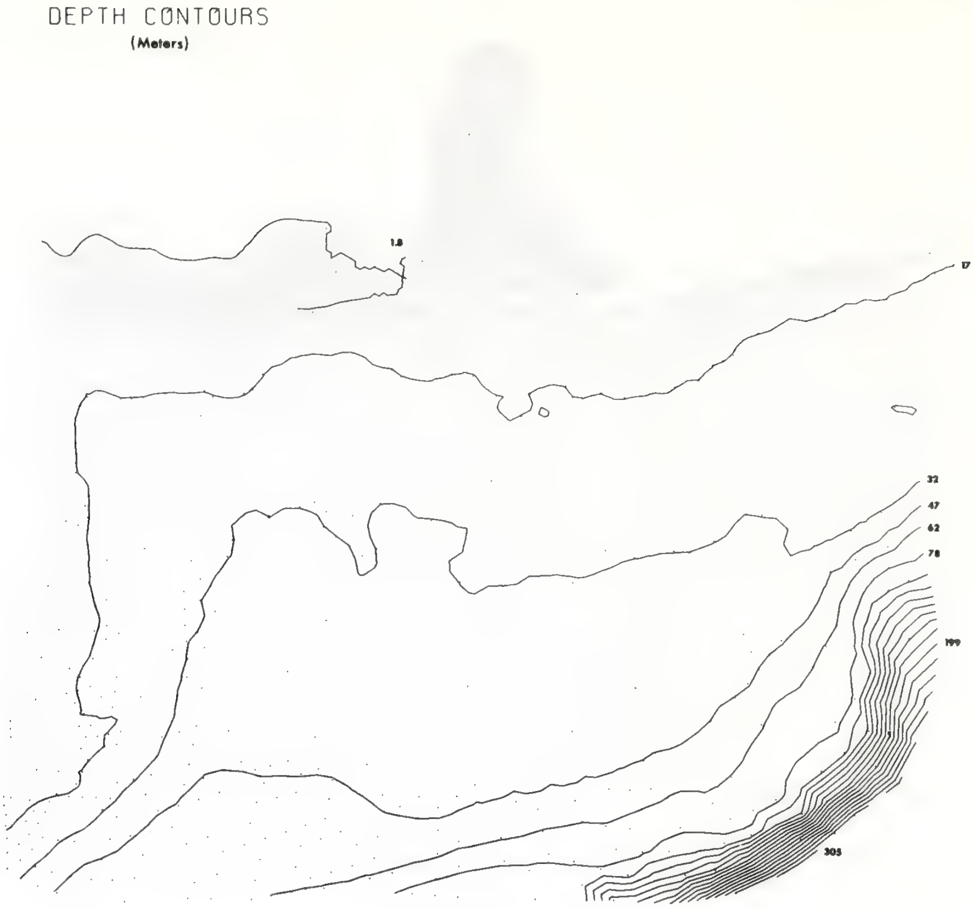

Fig. 2. Contours of stillwater depth values used in storm surge calculations.

surge forecast), the irregular grid has a time step which is no smaller than necessary for calculations in inland waters. This distribution of grid points has the additional advantage that it gives the highest density of points along the shoreline, aiding in the resolution of coastal curvature.

A piecewise uniform spliced grid, such as the one for the Elbe Estuary (Ramming, 1976) shown in Fig. 3, has to some extent the same attractive features. It allows for calculations simultaneously for inland waters and for the open sea, and the larger grid spacing in deeper water has a beneficial effect on the time step; however, the grid refinement scheme dictates the density of grid points in each portion of the grid, and the "stair-step" boundary provides a rough representation of the shoreline. Such a spliced grid (Thacker, 1976) provided the motivation for the irregular-grid finite-difference techniques. Just as linear interpolation can be successfully used to calculate derivatives at the "extra" points along the splices, it should also provide a means for calculating derivatives at points on an irregular grid.

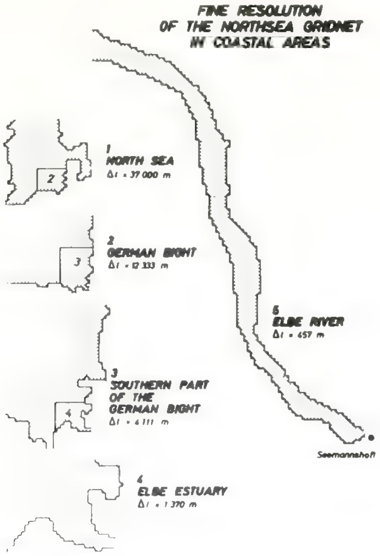

Fig. 3. Piecewise uniform spliced grid for the Elbe Estuary (Ramming, 1975).

The fact that the grid points are connected by line segments to form a mosaic of triangular elements (Fig. 1) is reminiscent of similar grids used in finite-element calculations (see, for example, Pinder and Gray, 1977). This similarity is due to the fact that the techniques discussed here as well as those of the finite-element method involve linear interpolation over triangular elements. The fundamental distinction is that the finite-element method is based directly upon approximation of the functions, whereas the finite-difference method is based upon approximation of the derivatives. The practical distinction is that the finite-difference techniques provide greater computational economy. The spatial averages (Thacker, 1978a and 1978b) that result from the finite-element method necessitate a matrix inversion at each time step. In addition to this computationally expensive matrix inversion, these averages lead to greater storage requirements, to a greater number of arithmetic operations per time step, and to a smaller value for the length of the time step than required by the corresponding finite-difference calculations.

Because the computational grid is irregular, only one index is used to specify the grid points rather than two indices corresponding to distances along coordinate axes as for the conventional uniform grids. Since the grid point index is neither simply related to the coordinates of the grid point nor to the indices of neighboring points that provide values necessary for evaluating derivatives, this information must be tabulated for computation. Also, the differentiation coefficients are not simply the inverse of the grid spacing as for uniform grids. Since they vary from grid point to grid point, either they must be tabulated or they must be calculated from the tabulated values of the coordinates and the indices of neighboring points each time they are needed.

Because the manner in which the grid points are indexed is unimportant, it is a simple matter to alter the grid in order to add additional points, to remove points, or to respecify neighbors. After editing the grid, it is also a simple matter to sort and renumber the grid points for computational efficiency. The scheme used here assigns indices to the interior points first, the lowest for interior points with six neighbors, next for those with five, and then for those with seven, and assigns indices to the boundary points last, also according to the number of neighboring points. Additional editing (Thacker, 1977) guarantees that each interior grid point is situated at the geometric center of the polygon formed by the neighboring grid points. These editing procedures can also be used for finite-element grids so long as the matrix inversions are calculated by an iterative technique, but if direct inversion techniques are used, finite-element grids should be numbered so that the differences between the indices of neighboring points be as small as possible. For storm surge calculations the previous time step provides excellent values for initializing the iterative techniques, so they should be efficient as well as flexible.

APPROXIMATION OF DERIVATIVES

The slope of the spinnaker-shaped surface in Fig. 4 can be approximated by the slope of the planar surface determined by points a, b, and c. Of course, for smaller curvature the approximation is better. The planar surface is a linear interpolating function, and its derivatives provide approximations of the function specifying the curved surface,

$$\frac{\overline{\partial f}}{\partial x} = \frac{f_a(y_b-y_c) + f_b(y_c-y_a) + f_c(y_a-y_b)}{\Delta}$$

$$\frac{\overline{\partial f}}{\partial y} = -\frac{f_a(x_b-x_c) + f_b(x_c-x_a) + f_c(x_a-x_b)}{\Delta}$$

$$\Delta = x_a(y_b-y_c) + x_b(y_c-y_a) + x_c(y_a-y_b).$$

In the storm surge calculation the function f can represent the x- and y-components of the vertically integrated horizontal velocity, $\vec{U}$, and the surface elevation, H.

Since the dynamical variables are calculated at the grid points which are vertices of triangles, there is no reason for preferring the approximations corresponding to one adjacent triangle over those corresponding to any other. For this reason, the

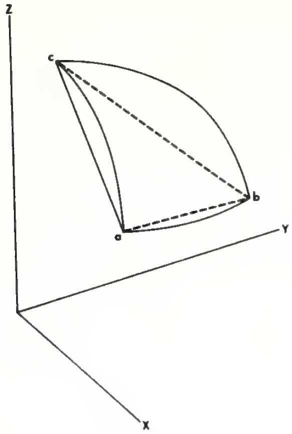

Fig. 4. The slope of the plane passing through points a, b, and c approximates the slope of the curved surface. The plane represents the interpolating function with derivatives that approximate the derivatives of the curved surface.

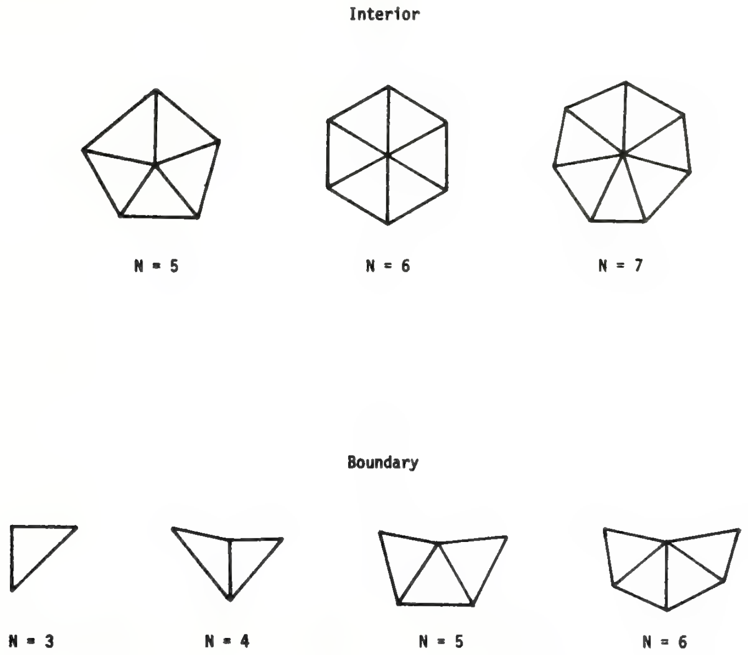

Fig. 5. The approximations for derivatives at points on the irregular grid are averages of the approximations obtained from the adjacent triangles. For interior points, the approximations are centered, involving only values associated with the N neighboring points and not the value at the point for which the derivative is evaluated. For points on a boundary, the approximations are "one-sided", with the values at the grid point contributing to the evaluation of the derivative.

derivatives at a grid point are approximated by averages of the contributions from all adjacent triangles weighted according to their area, Fig. 5. The resulting N-point formulas (Thacker, 1977) are equally as simple as the three-point formulas for the slope of the surface in Fig. 4. For example, if there are five points contributing to the approximation, then the formulas are,

$$\overline{\frac{\partial f}{\partial x}} = \frac{f_a(y_b-y_e) + f_b(y_c-y_a) + f_c(y_d-y_b) + f_d(y_e-y_c) + f_e(y_a-y_d)}{\Delta}$$

$$\overline{\frac{\partial f}{\partial y}} = -\frac{f_a(x_b-x_e) + f_b(x_c-x_a) + f_c(x_d-x_b) + f_d(x_e-x_c) + f_e(x_a-x_d)}{\Delta}$$

$$\Delta = x_a(y_b-y_e) + x_b(y_c-y_a) + x_c(y_d-y_b) + x_d(y_e-y_c) + x_e(y_a-y_d).$$

In every case the numerators are given by cyclic sums of products of the values of the function at the grid points with the differences of coordinates at adjacent points, and the denominator is twice the area of the polygon formed by the N points. For regular polygons, such as the square and the hexagon shown in Fig. 6, the formulas reduce to the familiar expressions,

$$\overline{\frac{\partial f}{\partial x}} = \frac{f_a-f_c}{x_a-x_c} \qquad \overline{\frac{\partial f}{\partial x}} = \frac{1}{6}\left[4\left(\frac{f_a-f_d}{x_a-x_d}\right) + \frac{f_b-f_c}{x_b-x_c} + \frac{f_f-f_e}{x_f-x_e}\right]$$

and

$$\overline{\frac{\partial f}{\partial y}} = \frac{f_b-f_d}{y_b-y_d} \qquad \overline{\frac{\partial f}{\partial y}} = \frac{1}{2}\left[\frac{f_b-f_f}{y_b-y_f} + \frac{f_c-f_e}{y_c-y_e}\right].$$

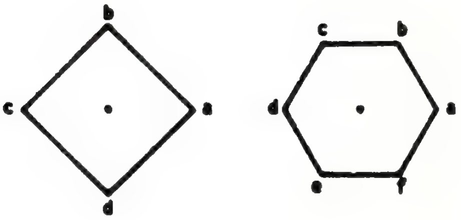

Fig. 6. For uniform grids, with points in square or hexagonal arrays such as these, the N-point formulas for approximating derivatives reduce to simple, recognizable expressions.

When the shallow water wave equations are discretized to obtain equations for the values of $\vec{U}_i^{n+\frac{1}{2}}$ and H_i^n, corresponding to the transport and surface elevation for grid point i and time level n, the partial derivatives are approximated by the appropriate N-point formulas. Only at the boundary (see Fig. 5) is the point at which the derivative is approximated also one of the N points contributing to the approximation.

GOVERNING EQUATIONS

The hydrodynamic equations governing the storm surge,

$$\frac{\partial \vec{U}}{\partial t} + \vec{\nabla} \cdot \frac{\vec{U}\vec{U}}{D} = - gD\vec{\nabla}H - f\hat{k}\times\vec{U} + \vec{T} - \vec{B}$$

$$\frac{\partial H}{\partial t} = - \vec{\nabla} \cdot \vec{U} ,$$

account for the atmospheric forcing through the term, $\vec{T}$, and for the bottom friction through $\vec{B}$. The term involving the Coriolis parameter, f, and unit vector in the vertical direction, $\hat{k}$, account for the earth's rotation which has a relatively small influence on the storm surge. The term involving the gravitational acceleration, g, and the water depth, D, accounts for flow in response to slope in the sea surface. The flow accelerates in response to these forces and the sea surface rises as the flow converges.

The wind velocity and pressure gradient fields for the hurricane forcing are taken to be the same as those used by Overland (1975) for Apalachicola Bay,

$$\vec{W} = \frac{2rR}{r^2+R^2} W_{max} \hat{\phi} + \frac{rR}{r^2+R^2} \vec{S}$$

$$\vec{\nabla}P = - \Delta P \frac{R}{r^2} \exp\left(-\frac{R}{r}\right)\hat{r} .$$

The velocity field has two components; one is circularly symmetric with maximum value, W_{max}, at distance, $r = R$, from the storm's center and with inflow angle specified by the unit vector, $\hat{\phi}$, and the other approximates the assymmetry of the storm associated with its translational velocity, $\vec{S}$. The value of W_{max}, depending upon the values of the radius, R, and of the pressure drop, ΔP, used to specify the storm, is determined (see Fig. 7) as in the SPLASH model (Jelesnianski, 1967) used by the National Weather Service for forecasting storm surges. The symmetric part of the wind speed, the inflow angle with maximum of 22° at 3R and 17° at large r, and the pressure gradient inward along the radial direction vary as indicated in Fig. 8. The hurricane forcing associated with these fields is given by

$$\vec{T} = C_d\vec{W}|\vec{W}|\rho_a/\rho_w - D\vec{\nabla}P/\rho_w$$

where ρ_a and ρ_w are the densities of air and water and where the drag coefficient has the value used in the SPLASH model, $C_d = 2.4 \times 10^{-3}$ at all wind speeds.

Whereas the SPLASH model uses time-history bottom stress, the more conventional quadratic stress is used here,

$$\vec{B} = g\vec{U}|\vec{U}|/C_H^2D^2,$$

with the Chezy coefficient, $C_H = 62\ m^{1/2}/sec$.

The mathematical specification is completed by the boundary conditions requiring

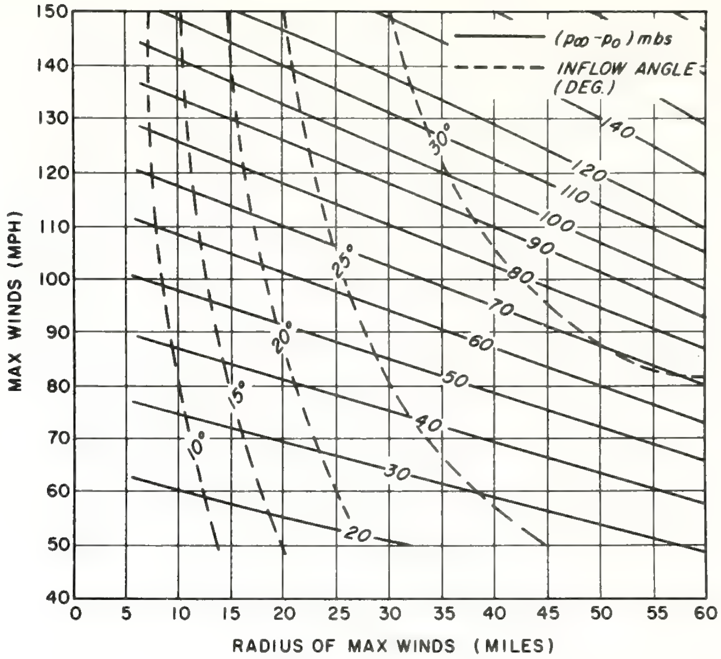

Fig. 7. This nomogram (Jelesnianski, 1967) can be used to obtain the value of the maximum hurricane wind velocity from the values of the radius to maximum winds and the pressure drop. Tabulated values as used by SPLASH were used for computation.

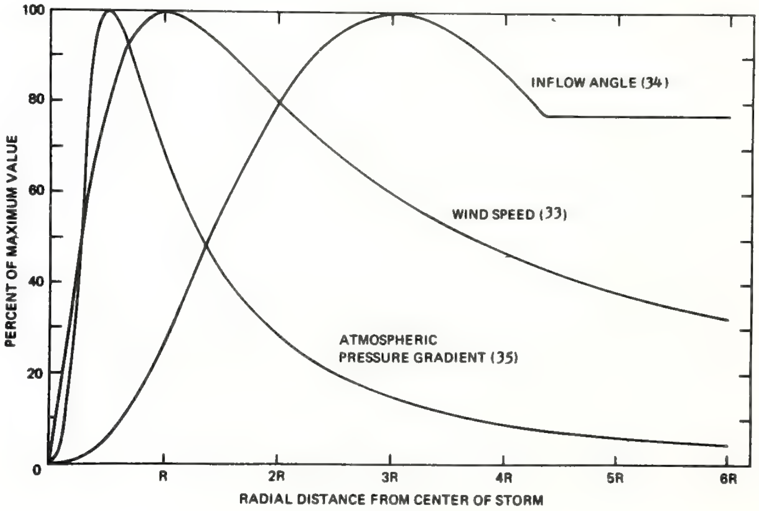

Fig. 8. Variation of hurricane wind speed, inflow angle, and pressure gradient with radial distance from center of storm (Overland, 1975).

that there be no flow normal to the shoreline and that the surface elevation along boundaries separating the portion of the sea included in the computation from that which is excluded be that height of water supported by the atmospheric pressure drop.

The finite-difference equations, which govern the values of the dynamical variables at points on the irregular grid, have a "leap-frog" time structure with values for the transport vectors and surface elevation corresponding to different time levels separated by $\tau/2$, where the length of the time step is $\tau = 2.5$ minutes. Except for points on the boundary, which must satisfy the imposed boundary conditions, the values of the dynamic variables at the grid points are obtained from the equations

$$\frac{1}{\tau}\left(\vec{U}_i^{n+\frac{1}{2}}-\vec{U}_i^{n-\frac{1}{2}}\right)+\frac{\vec{U}_i^{n+\frac{1}{2}}}{D_i^n}\cdot\left(\overline{\vec{\nabla}\vec{U}}\right)_i^{n-\frac{1}{2}}+\vec{U}_i^{n+\frac{1}{2}}\left(\overline{\vec{\nabla}\cdot\frac{\vec{U}^{n-\frac{1}{2}}}{D^n}}\right)_i$$

$$= - gD_i^n\left(\overline{\vec{\nabla} H}\right)_i^n - f\hat{k}x\vec{U}_i^{n+\frac{1}{2}} + T_i^n - \frac{g\vec{U}_i^{n+\frac{1}{2}}\left|U_i^{n-\frac{1}{2}}\right|}{\left(C_H D_i^n\right)^2}$$

$$\frac{1}{\tau}\left(H_i^{n+1}-H_i^n\right) = -\left(\overline{\vec{\nabla}\cdot\vec{U}}\right)_i^{n+\frac{1}{2}} .$$

For those points corresponding to the coastline, the momentum equation must be altered to prevent flow normal to the coastline. The right-hand side, which represents the forcing, must be projected onto the line tangent to the boundary determined by the unit vector $\hat{b}_i = (\vec{x}_a-\vec{x}_c)/|\vec{x}_a-\vec{x}_c|$, where $\vec{x}_a$ and $\vec{x}_c$ are the coordinates of the point which are neighbors of point i = b lying on the boundary (see Fig. 9). This is done by taking the inner product of the right-hand side with the dyadic, $\hat{b}_i\hat{b}_i$. For those points on the computational boundary not corresponding to a coastline, the atmospheric pressure determines the value of the surface elevation at each time step.

The position of the storm at the $n^{\underline{th}}$ time step and the velocity of the storm are calculated from specified coordinates for the center of the storm at two different times, which might correspond to the forecast value for the storm to reach a designated point in the vicinity of the bay and the time that the forecast is issued. From the position of the center, the values of the distances to each grid point and the values of the wind velocity and pressure gradient can be calculated in order to evaluate the storm forcing, $\vec{T}_i^n$, at the $n^{\underline{th}}$ time step. The computations are initialized with a flat motionless sea, and the storm remains at the initial position for one hour (24 time steps) as it grows linearly to full strength.

For numerical stability the Coriolis term is evaluated at the time level, $n+\frac{1}{2}$. The bottom friction and advection terms involve both levels, $n+\frac{1}{2}$ and $n-\frac{1}{2}$. However, the equations can easily be rewritten with the values at step $n+\frac{1}{2}$ given explicitly in terms of values at steps n and $n-\frac{1}{2}$. Also in order to guarantee numerical stability, the advection terms are omitted for points on the open boundaries.

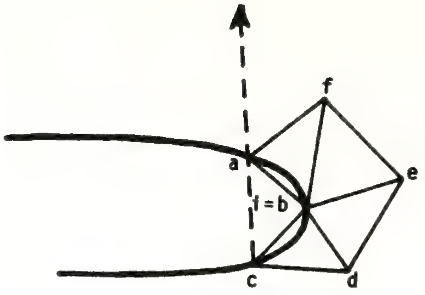

Fig. 9. Points c, d, e, f, and a are neighboring points for boundary point i = b. The direction of flow at this point is parallel to the unit vector along a line through the neighbors a and c which are also on the boundary.

COMPUTATIONAL RESULTS

Storm surges which might result from various hypothetical storms have been simulated in order to ascertain that the irregular-grid finite-difference techniques are indeed capable of producing reasonable results for realistic circumstances. Four cases are considered, corresponding to the series of Figs., 10, 11, 12, and 13.

The first case corresponds to a hurricane with R = 56 km and $\Delta P = 100$ mb, moving from ($29^{\circ}30'$N, $88^{\circ}30'$W) to ($30^{\circ}40'$N, 88°W) in three hours and continuing inland on the same course for two additional hours. Although this pressure drop might be reasonable for extremely strong hurricanes in this area, the radius and forward speed are both larger than would be expected. Calculations for this case neglected the Coriolis and advection terms and used the stillwater rather than the total depths.

Fig. 10 shows a contour map of sea surface elevation after three hours of simulation with the storm just north of Mobile Bay. Since the line segments composing these contours represent linear interpolations of the computed values at the grid points with no smoothing, the smoothness of the contour lines accurately reflects the low level of noise in the computations. The corners of the islands, which correspond to curvature that is too great to be resolved by the boundary points of the grid, might be responsible for some of this computational noise. This level of noise is typical of these calculations and does not seem to increase on the time scale of these simulations.

The second case corresponds to a large hurricane which might be expected to hit Mobile Bay. It has R = 24 km and $\Delta P = 100$ mb, and it moves due north from ($29^{\circ}30'$N, 88°W) to ($30^{\circ}30'$N, 88°W) in five hours and continues north for two more hours. For this case, the Coriolis term is included and the total depths are used. The Coriolis term has little effect and can be dropped for computational efficiency. The total depth does give somewhat diferent results than the stillwater depth, especially for

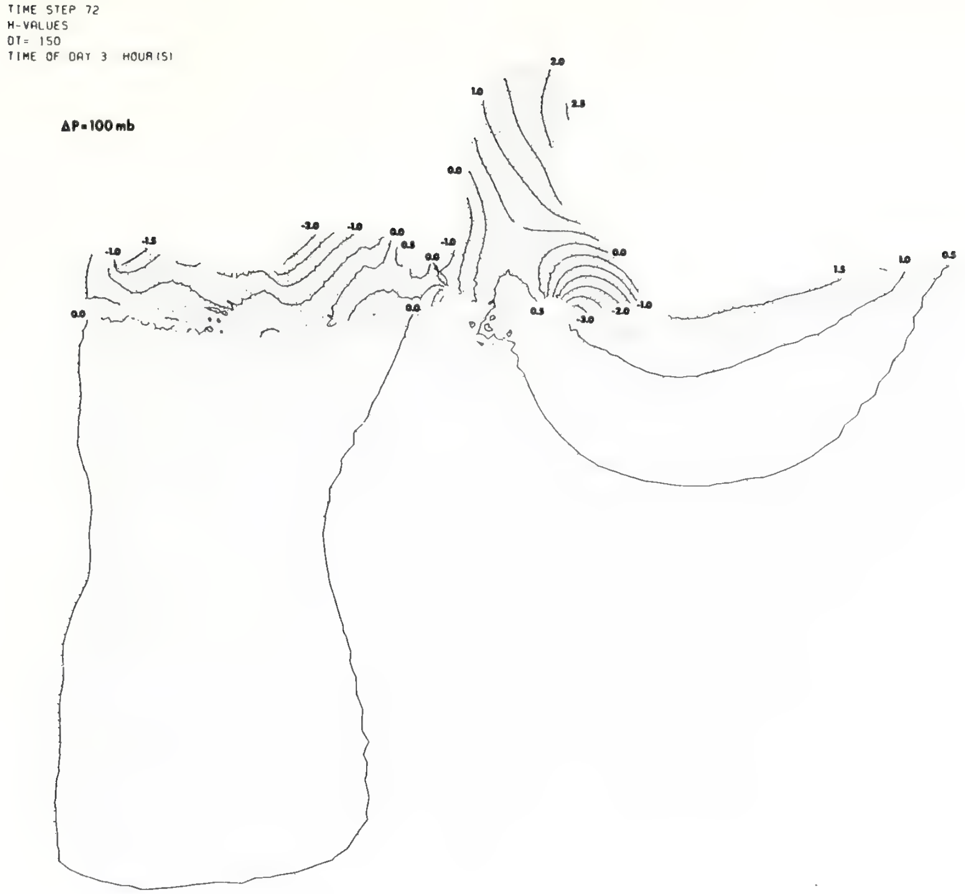

Fig. 10. The smoothness of these surface elevation contours is indicative of the low level of noise in these computations.

extreme water levels. No attempt has been made to guarantee that the total depth is always positive, but this is usually the case, even though the calculations can lead to negative elevations greater in magnitude than the stillwater depth of the basin.

Figs. 11a through 11d show vector maps of depth-averaged velocity ($\vec{U}_i/D_i$) for times corresponding to 2, 4, 5, and 7 hours of simulations for case two. The symbol 🌀 marks the position of the hurricane on the map, but it is absent from Fig. 11d because the hurricane is too far north to be represented. The smooth variation of the vectors from grid point to grid point are another indication of the low noise level. in spite of the high curvature of the islands and the constraint that the flow vectors be parallel to the computational boundary, the flow through the inlets is well represented. The flow through the open computational boundary also seems to be quite reasonable. The fact that the corner points of the grid, where land and sea boundaries meet, are taken to be points in the sea with no flow restriction accounts for the unusual behavior of the velocity vectors at these points. This is easily corrected but should have little influence on the rest of the calculation. Figs. 11e through 11h show the variation in computed water levels for points within Mobile Bay and Mississippi Sound and along the Gulf of Mexico coast. Points on the map indicated by letters, A-X, are also indicated on the horizontal axes of the graphs.

It is interesting to note in Fig. 11a that the hurricane has moved ahead of the oceanic gyre. A corresponding gyre is not evident in subsequent maps because of the strong effect of the land boundaries on the flow. Another interesting point (Fig. 11g) is that when the storm is directly over the bay, the water levels are negative in most of the bay, because the storm had pushed the water into the Gulf and Mississippi Sound (Figs. 11a and 11b).

Case three corresponds to exactly the same storm as for case two. For this case the Coriolis term is neglected and the stillwater depth is used, just as for case one, but the advection terms are also included. The advection terms seem to introduce some noise into the computation, but they are small and have little other effect, so it seems best to neglect these terms. For this case the water elevations at the coastline are shown in Figs. 12a through 12d, which can be compared with Figs. 11e through 11h.

Case four corresponds to a storm of the same size and strength as for case two and to the same terms used in the computations. For this case the storm moves towards the east from (30°15'N, 88°45'W) to (30°15'N, 87°45'W) in four hours (Fig. 13a). Figs. 13a-13c show that as much as 5 m of storm surge might be expected within Mobile Bay and Mississippi Sound for such a storm.

CONCLUSION

The irregular-grid finite-difference techniques presented here provide a simple and economical means for forecasting storm surges in bays, estuaries, and lakes, so long as the elevation of the adjacent land is sufficiently high that inundation is unimportant. It might be further anticipated that an irregular grid might also be advantageous if inundation is included in the calculations. Rather than for flooding to proceed square by square as for a uniform grid, it would proceed triangle by triangle. Since the grid points can be positioned according to the elevation of the land, the triangles should more nearly approximate areas being flooded. For situations in which roads through low-lying areas are built up, forming barriers to the intruding water, the triangular grid might be especially appealing. How to proceed with such calculations, including inundation, remains to be studied.

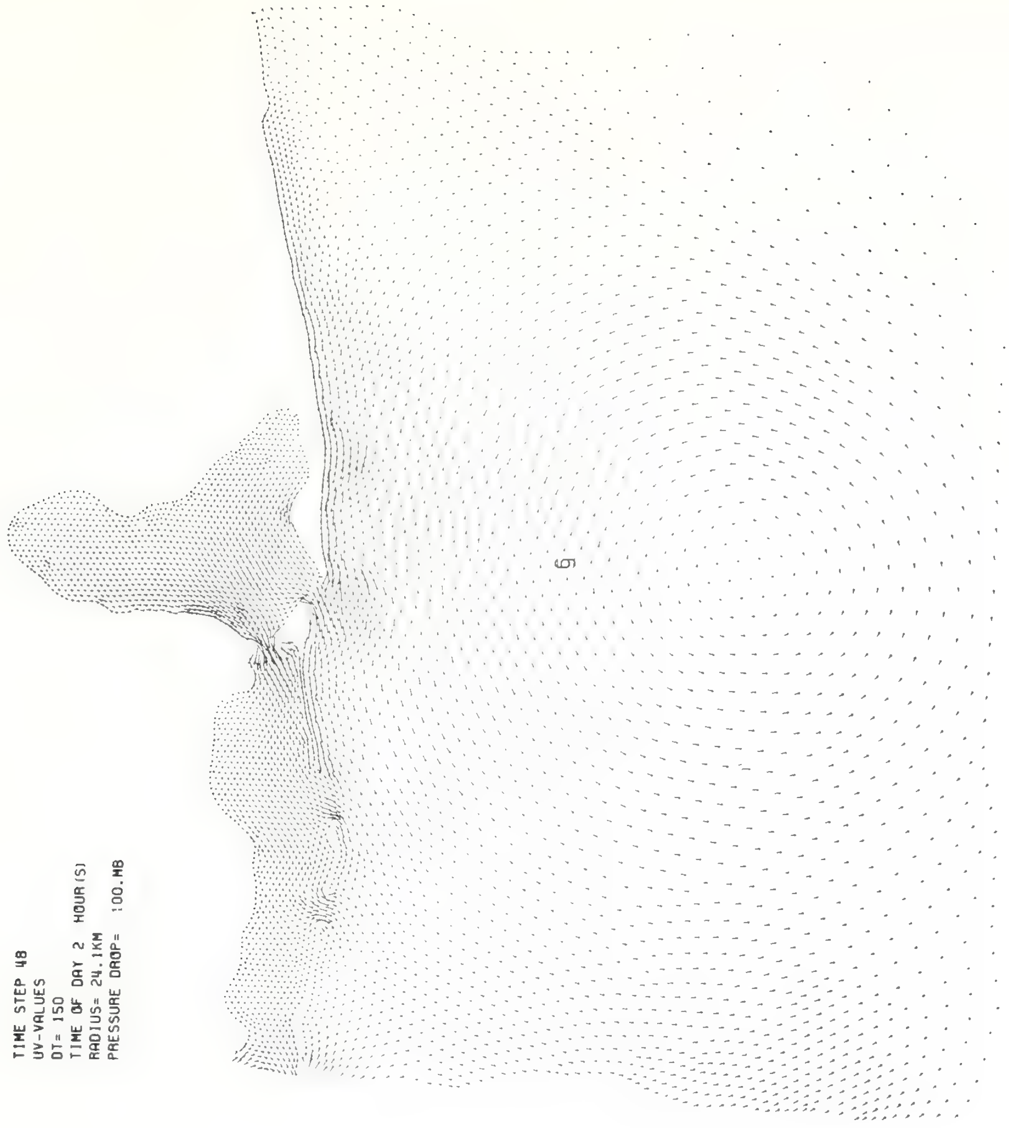

Fig. 11a. Flow vectors after two hours for a large hurricane which might be expected to move from south to north through Mobile Bay. These results were obtained neglecting the advection terms in the momentum equations.

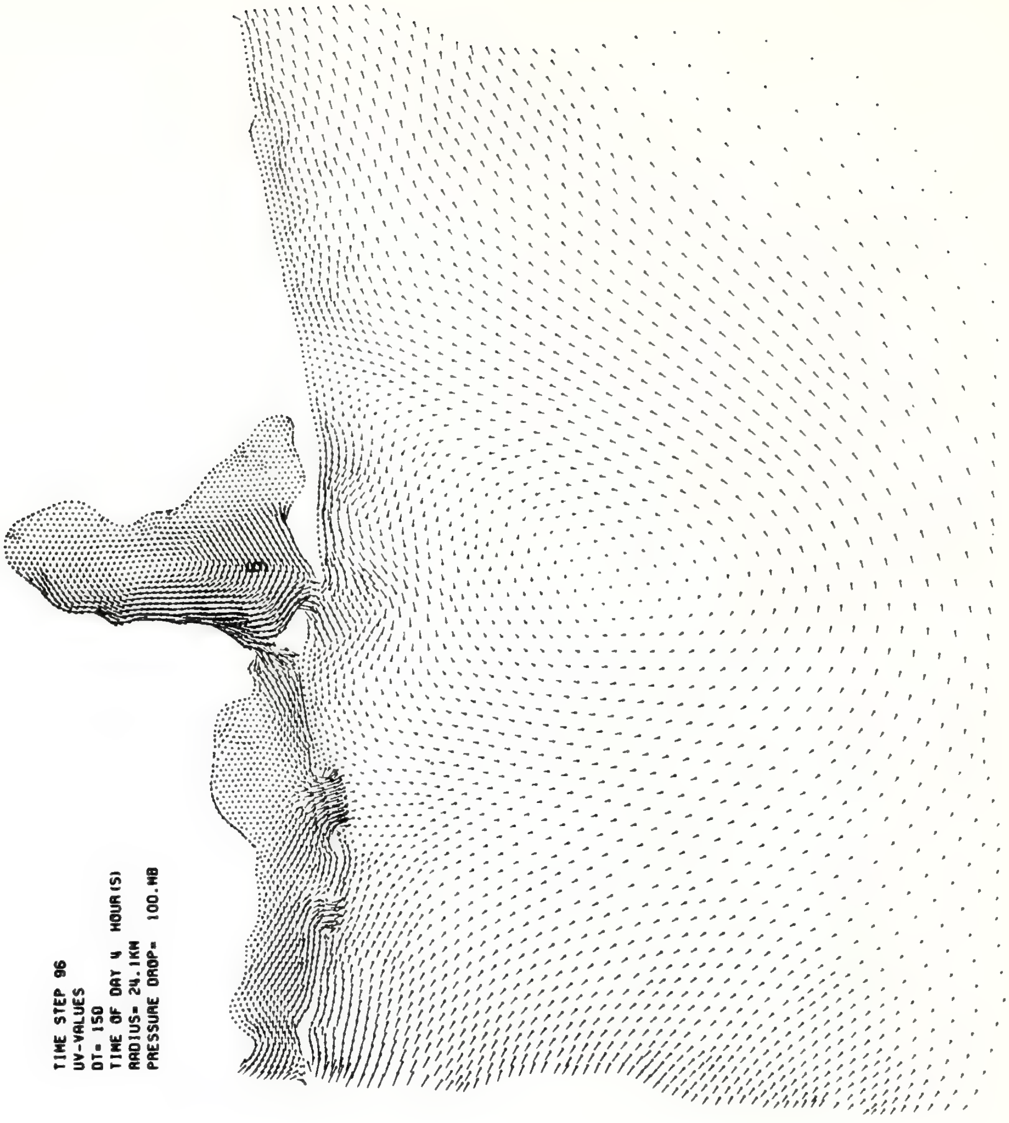

Fig. 11b. After four hours.

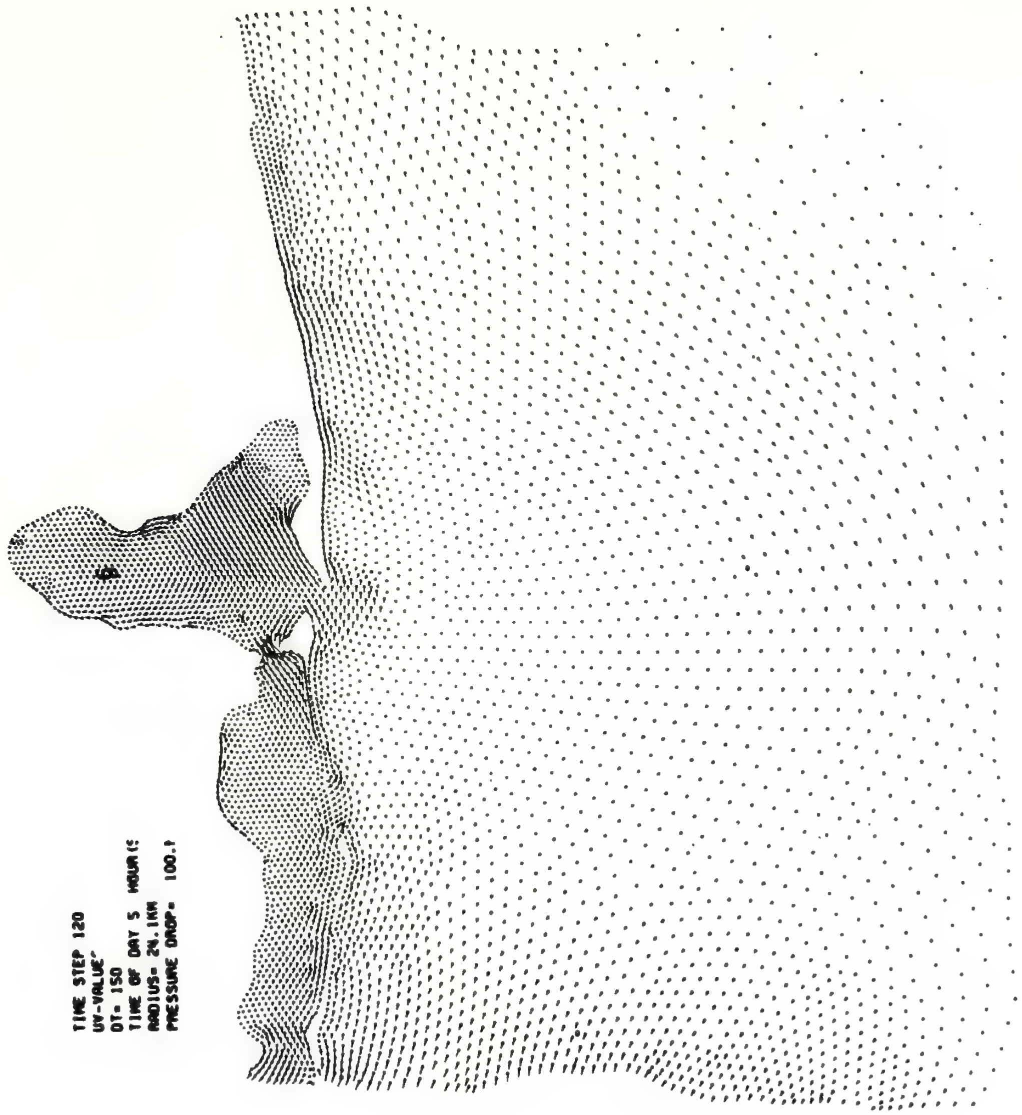

Fig. 11c. After five hours.

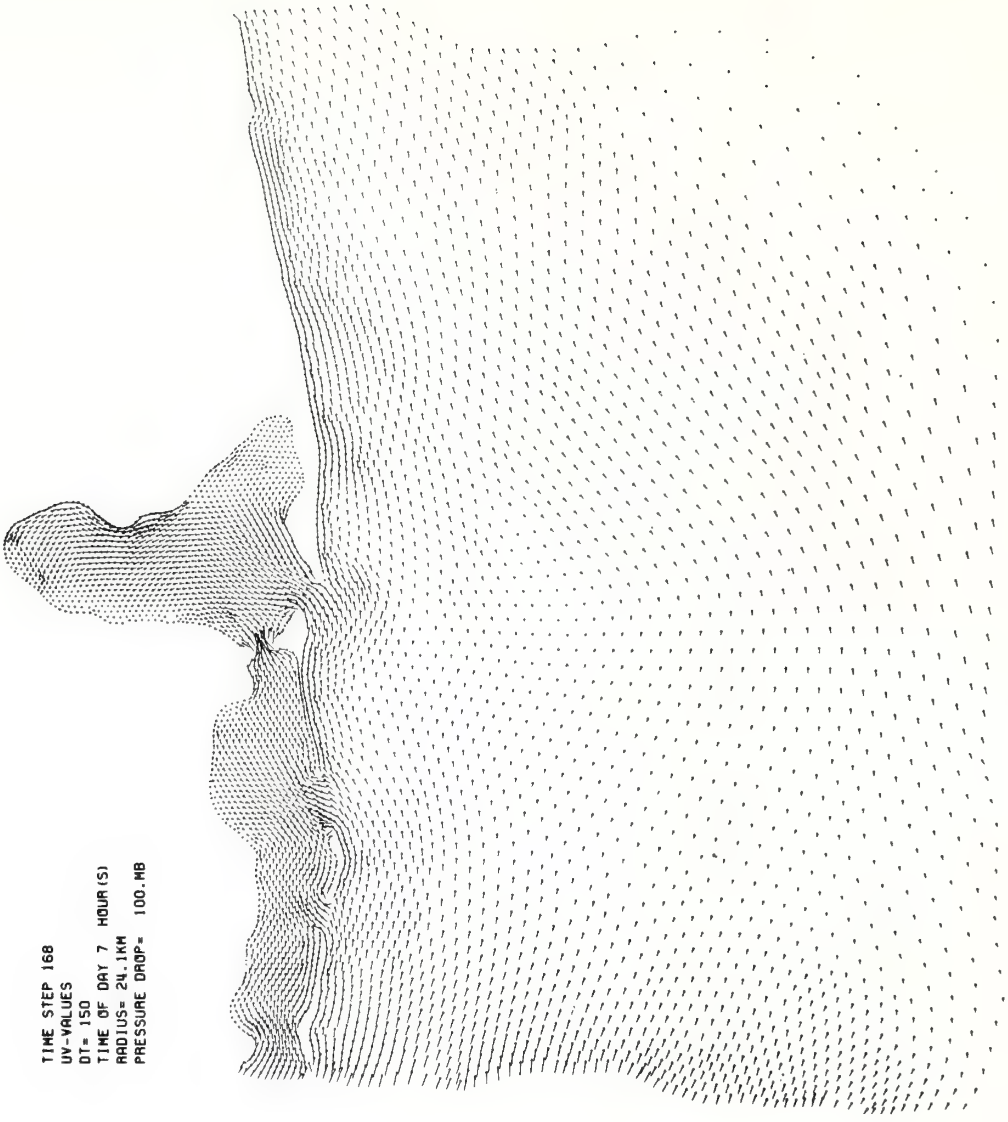

Fig. 11d. After seven hours.

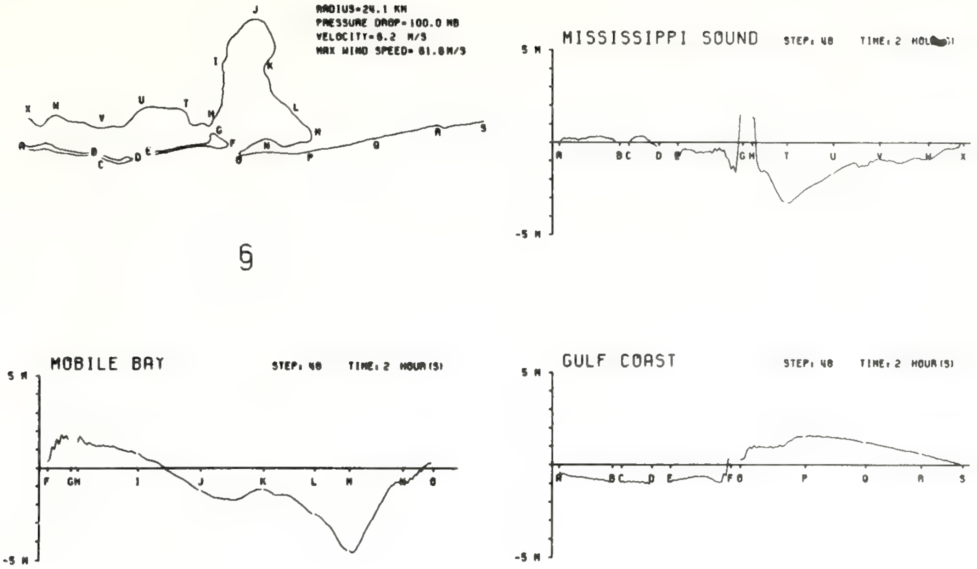

Fig. 11e. Shoreline water elevations after two hours.

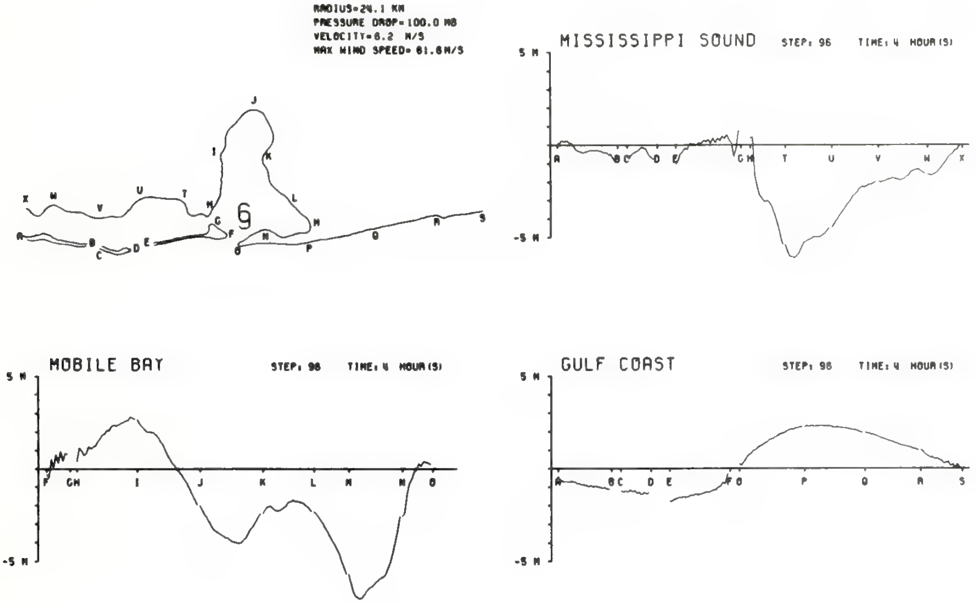

Fig. 11f. After four hours.

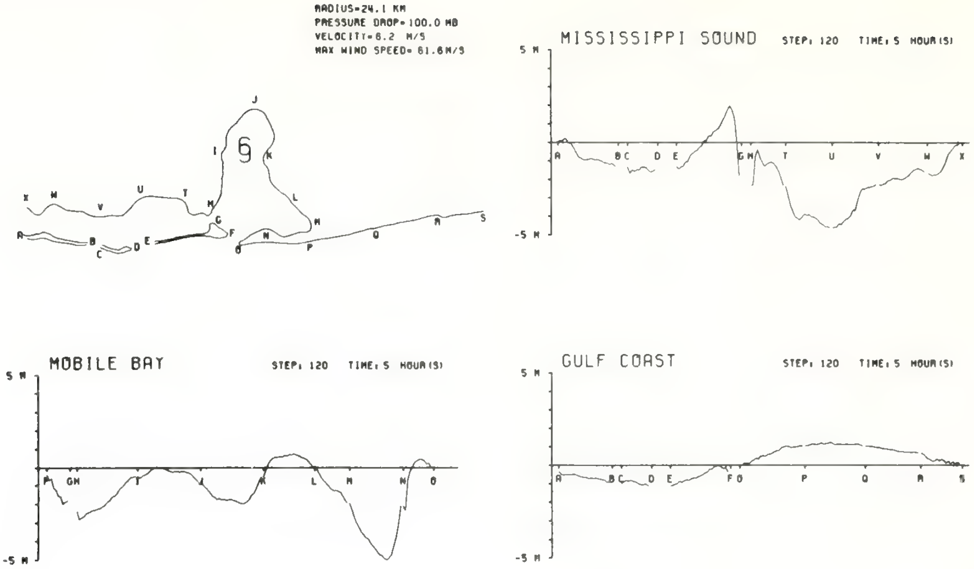

Fig. 11g. After five hours.

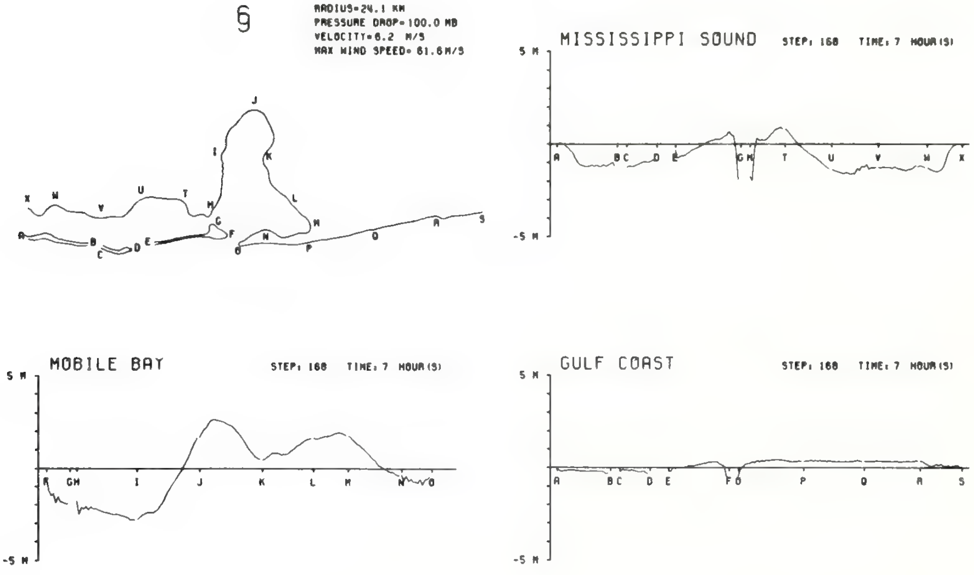

Fig. 11h. After seven hours.

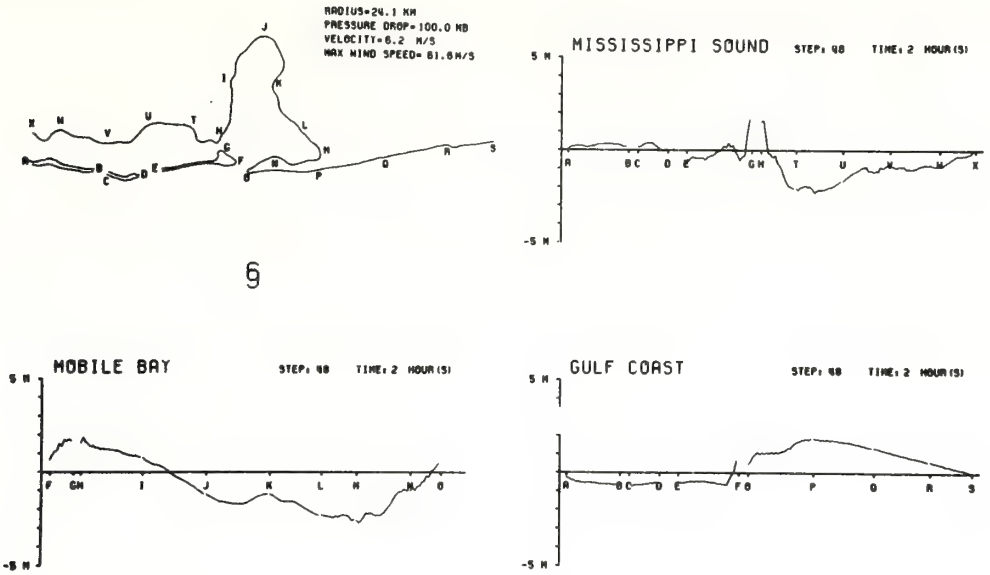

Fig. 12a. Shoreline water elevations to be compared with those in Fig. 11e. Although these results include the advection terms and neglect the Coriolis terms, the principal differences in the two sets of results are due to the fact that these involve the approximation of the total depth by the stillwater depth.

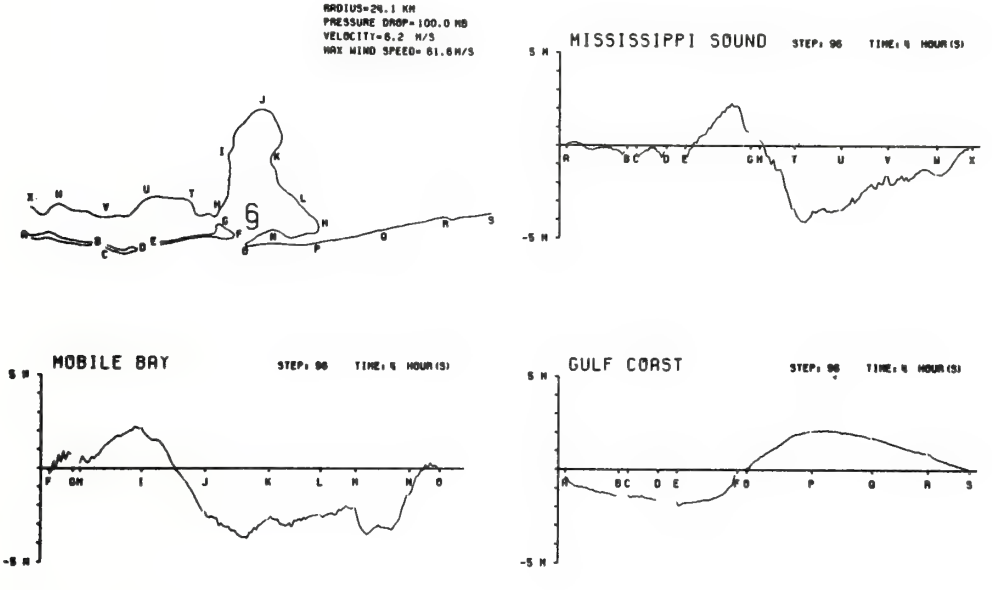

Fig. 12b. Compare with Fig. 11f.

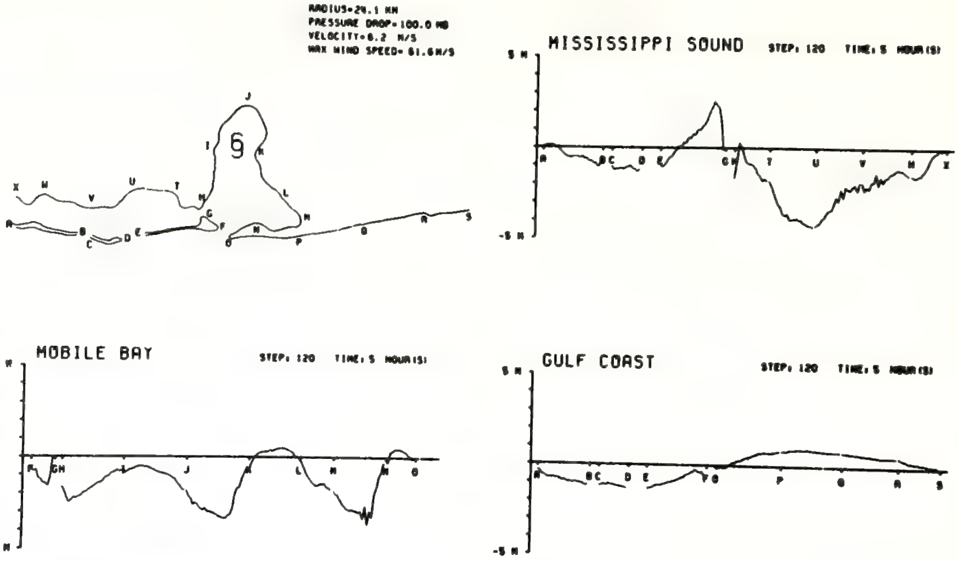

Fig. 12c. Compare with Fig. 11g.

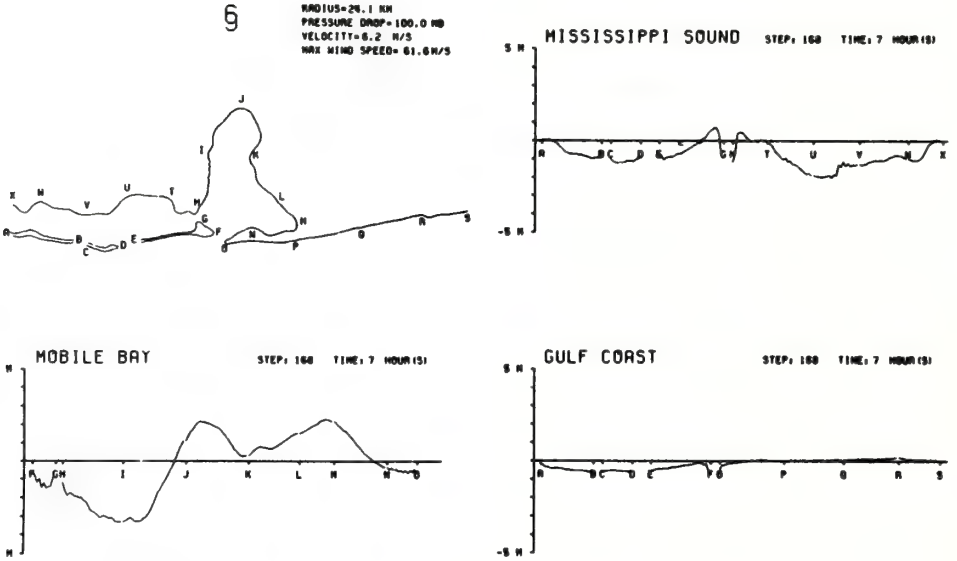

Fig. 12d. Compare with Fig. 11h.

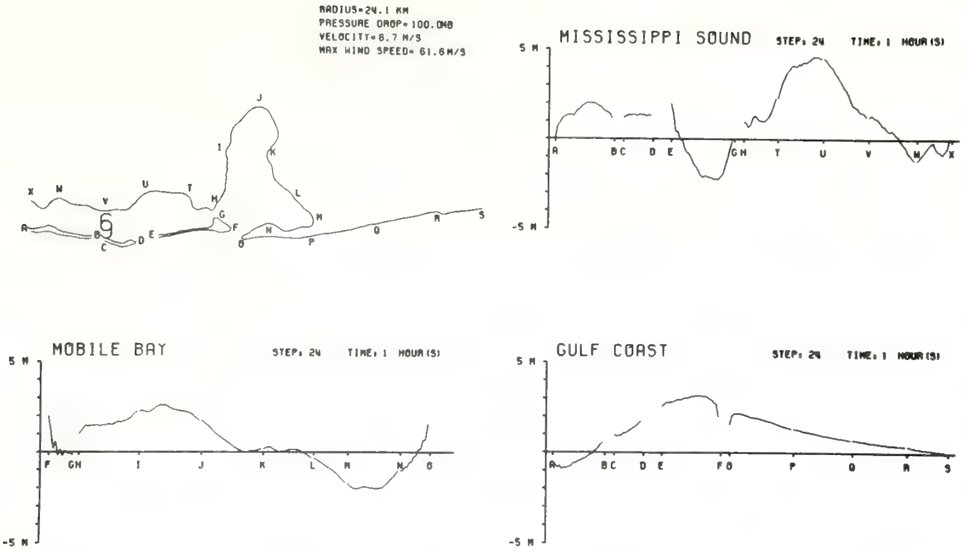

Fig. 13a. Shoreline water elevations after one hour for a large hurricane which might be expected to move from west to east through Mississippi Sound and Mobile Bay.

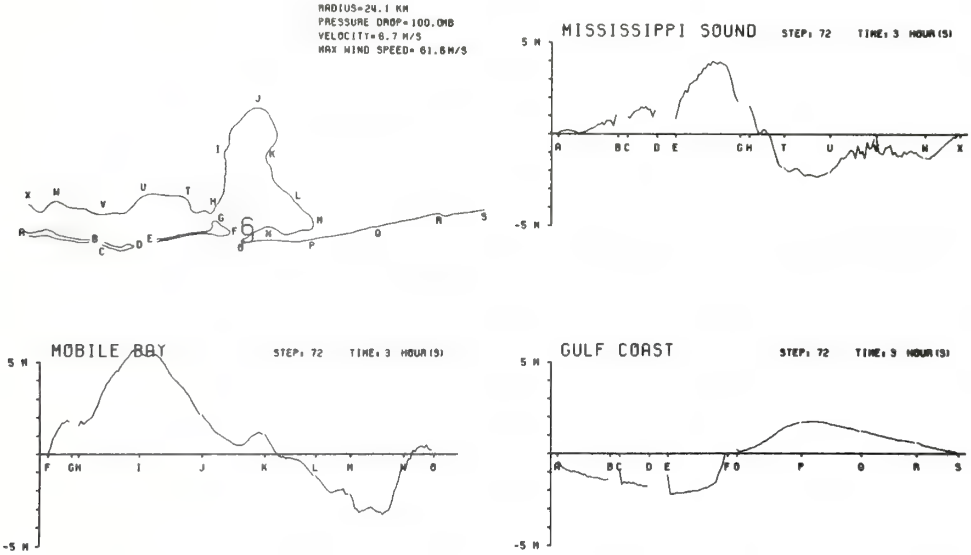

Fig. 13b. After three hours.

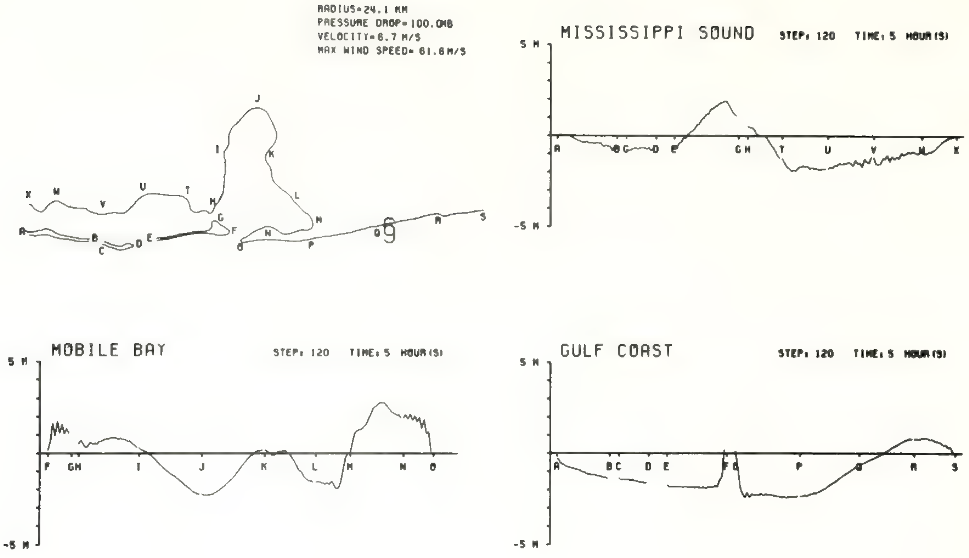

Fig. 13c. After five hours.

ACKNOWLEDGEMENTS

Thanks are due to Gerald Putland and to Alicia Gonzales for their enthusiastic assistance, without which this presentation would not have been possible, and to Joan Wagner for her expert typing and retyping.

REFERENCES

Jelesnianski, C. P., 1967. Numerical computations of storm surges with bottom stress. Mon. Wea. Rev., 95:740-756.

Overland, J. E., 1975. Estimation of hurricane storm surge in Apalachicola Bay, Florida. NOAA Tech. Rep. NWS 17, U. S. Dept. of Commerce, 66 pp.

Pinder, G. F. and Gray, W. G., 1977. Finite Element Simulation in Surface and Subsurface Hydrology. Academic Press, London, 295 pp.

Ramming, H-G., 1976. A nested north sea model with fine resolution in shallow coastal areas. (Seventh Liège Colloquium on Ocean Hydrodynamics) Mémoires de la Société Royale des Sciences de Liège, X:9-26.

Thacker, W. C., 1976. A spliced numerical grid having applications to storm surge. NOAA Tech. Memo. ERL AOML-26, U. S. Dept. of Commerce, 19 pp.

Thacker, W. C., 1977. Irregular grid finite-difference techniques: simulations of oscillations in shallow circular basins. J. Phys. Oceanogr., 7:284-292.

Thacker, W. C., 1978a. Comparison of finite-element and finite-difference schemes. Part 1: One-dimensional gravity wave motion. J. Phys. Oceanogr., 8:676-679.

Thacker, W. C., 1978b. Comparison of finite-element and finite-difference schemes. Part 2: Two-dimensional gravity wave motion. J. Phys. Oceanogr., 8:680-689.

Wanstrath, J. J., Whitaker, R. E., Reid, R. O. and Vastano, A. C., 1976. Storm surge simulation in transformed coordinates. Vol. I. Theory and Application. U. S. Army, Corps of Engineers Tech. Rept. No. 76-3, 166 pp.

45. Applied Mathematical Modelling 3, 471-472.

An improved triangulation algorithm

W. C. Thacker
Sea-Air Interaction Laboratory, Atlantic Oceanographic and Meteorological Laboratories, National Oceanic and Atmospheric Administration, Miami, Florida, USA

(Received 11 December 1978)

When estimates must be obtained by interpolation from values at points distributed throughout some portion of a plane, it is useful to connect neighbouring data points so that the domain is divided into triangular elements. Then estimates at points within each element can be obtained by linear interpolation from the data at its three vertices. If the points constitute a computational mesh for solving partial differential equations, the accuracy of the solutions can depend on the manner in which the neighbouring points are specified. Elements which are as equilateral as possible are preferred, and, when the mesh points are uniformly spaced, each point should have the same number of neighbours.

A simple but time consuming algorithm identifies two points as neighbours if the line segment connecting them is shorter than each segment which intersects it (*Figure 1*). If the intersecting segment is the same length, then the segment with the greater slope determines which pair of points are better suited to be neighbours. In the limit of a uniform mesh, each point will have six neighbours, which allows solutions to partial differential equations to be approximated in the same way at each grid point.

Recently, Nelson[1] presented a much more efficient algorithm, which proceeds by finding common neighbours for pairs of points already known to be neighbours. The pair and their common neighbour are the three vertices of a triangular element. The criterion that Nelson uses to determine the point best suited to be the common neighbour involves the centre of the circle on which the point and the pair of known neighbours all lie. The best neighbour corresponds to the smallest value for the directed distance from the centre of the circle to the line through the pair.

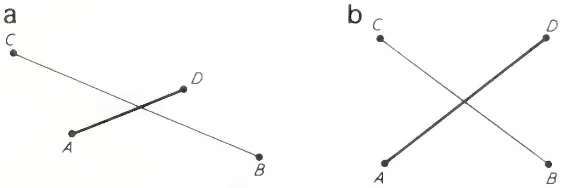

Figure 1 In both (a) and (b), points *A* and *D* are better suited to be neighbours than points *B* and *C*; in (a), because segment *AD* is shorter than segment *BC*, and in (b) because segments have same length but slope of *AD* is greater than slope of *BC*

By combining the ideas used in these two algorithms, an improved algorithm can be obtained with the best features of both. The speed of Nelson's method is due to locating common neighbours, not to the particular criterion for determining which points should be neighbours. By modifying this criterion, the same neighbours given by the first method can be found with the speed of the second method.

If A and B are points that are known to be neighbours and if C and D are points on the same side of the line through A and B, then either the line segments AD and BC intersect, or AC and BD intersect, or neither pair of segments intersect (*Figure 2*). If neither intersect, then the shorter of the segments AC and AD is associated with the better neighbour. Otherwise, the better neighbour corresponds to the shorter of the intersecting segments or, if their lengths are the same, to the segment with the greater slope.

This modification is easily implemented by repeated use of the formula:

$$\Delta_{I,J,K} = (x_I - x_K)(y_J - y_K) - (x_J - x_K)(y_I - y_K)$$

for twice the area of the triangle with vertices at points (x_I, y_I), (x_J, y_J), and (x_K, y_K), where $\Delta_{I,J,K}$ is positive or negative according to the order of the points I, J and K being counterclockwise or clockwise, respectively, and $\Delta_{I,J,K} = 0$ if the three points lie on a straight line. Points C and D lie on the same side of AB when Δ_{ABC} and Δ_{ABD} are both positive. Likewise, AD intersects BC if the products, $\Delta_{ADB}\Delta_{ADC}$ and $\Delta_{BCA}\Delta_{BCD}$, are both negative.

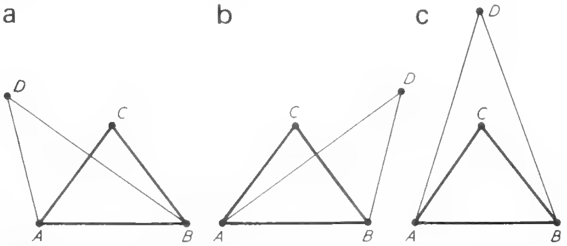

Figure 2 Three situations that must be considered when deciding which point, *C* or *D*, is a better common neighbour for points *A* and *B*

0307-904X/79/060471-02/$02.00
© IPC Business Press

A similar test will determine which of two segments has greater slope. If:

$$(x_I - x_J)(y_K - y_L) - (x_K - x_L)(y_I - y_J) > 0$$

then the slope of segment IJ is greater than that of KL.

The steps for identifying successive neighbours have already been described by Nelson.[1] The first pair of neighbours can correspond to adjacent points on the boundary, with their order taken so that a triangle formed with an interior point will have positive area. If the pair are points A and B and their common neighbour is found to be C, then the pair, (C, B), can be saved and a neighbour for the pair (A, C) can be found next. Once all neighbours of A have been found, the search continues for neighbours of those pairs which have been set aside, until all neighbours of all points are known.

The information specifying the grid can be stored in either of two ways. When each common neighbour is found, a new triangular element has been identified, and the vertices associated with this triangle can be tabulated. For some purposes[2] it is more convenient to know the indices of the neighbouring points. In that case it is better to tabulate the neighbours for each point.

It should be noted that useful algorithms also exist for constructing computational grids by generating the positions of the points[3,4] and others for adjusting the positions of the points so that the elements are more nearly equilateral.[2]

References

1 Nelson, J. M. *Appl. Math. Modelling*, 1978, **2**, 151
2 Thacker, W. C. *J. Phys. Oceanogr.*, 1977, **7**, 284
3 Thacker, W. C. (to appear)
4 Winslow, A. M. *J. Comp. Phys.*, 1967, **2**, 149

THALASSIA JUGOSLAVICA 13 (3/4) 389—393 (1977) 389

Conference Paper

On the use of acoustics in applied oceanographic and coastal engineering problems with emphasis on the oceanic transport of particulate materials*

J. R. Proni[1]*, F. C. Newman*[1]*, E. R. Meyer*[2]*, H. B. Stewart, Jr.*[1]*, D. J. Walter*[1]*,*
R. Sellers[3]*, and C. A. Lauter, Jr.*[1]

[1]*National Oceanic and Atmospheric Administration (NOAA), Environmental Research Laboratories, Atlantic Oceanographic and Meteorological Laboratories, Ocean Acoustics Group, Miami, Florida 33149,* [2]*NOAA, National Ocean Survey, Rockville, Maryland 20852, and* [3]*NOAA, Commissioned Officers Corps, U S. A.*

A discussion of the use of acoustics in applied oceanography and ocean engineering is presented in this paper. Four examples of the usefulness of the acoustic approach include: the dumping of river bottom dredge material, the deepening through dredging of an important shipping channel, the dumping of urban sewage sludge in coastal waters, and the detection of wave-induced bottom sediment resuspension. The thermocline as an important site for particulate flows is also discussed.

INTRODUCTION

Many activities of man in the coastal zone have significant environmental effects. One of the most pervasive results of man's activity in the coastal zone is the generation of particulate flows in the oceanic environment. Until very recently, no truly adequate means existed for the detection, description, and quantitative characterization of such flows. In this paper we shall discuss the recent application of acoustics to man-generated oceanic particulate flows. The discussion will center on the use of three acoustic frequency which have been found useful in particulate flow studies; they are 20,000 Hz, 200,000 Hz, and 3,000,000 Hz. The acoustical systems may be operated from aboard a ship or mounted in a bottom mooring (such as a tripod) or mounted from a dock or oil platform, *etc.* A great advantage is that the data gathered may be examined in real-time as well as being analyzed in post-real time. A series of examples of data gathered by these systems is given.

EXPERIMENTAL

Example one

In October 1976, the U. S. Army Corps of Engineers carried out a dredging operation in the Genesse River in upper New York State designed to clear the river of silt and mud accumulating along its bottom. The hopper dredge used dumped its load of material into Lake Ontario near the city of Rochester, N. Y. The lake was well-mixed surface to bottom with a temperature of 11 °C. Figure 1 shows the 200 kHz acoustical data obtained during three passes over the dumped material by the research vessel DAMBACH.

---

* Presented at the 2nd International Marine Pollution Symposium, organized by the US Environmental Protection Agency and the Center for Marine Research, »Ruđer Bošković« Institute, and held in Dubrovnik, Croatia, Yugoslavia, October 10 — 13, 1977.

The first pass over the dumped material in Fig. 1 occurred a few minutes after dumping began. Note that the width of the plume increases with depth — an effect of entrainment. The second pass (6 minute to 10 minute marks) over the dumped material shows two plumes formed and the generation of bottom turbidity currents as well. The third pass (15 minute to 19 minute time marks) over the dumped material shows the formation of surface-directed plumes of material rising from the bottom.

In addition to the real-time paper display shown in Fig. 1, the data are registered on analog magnetic tape for post-real time in-depth analysis. One of the most valuable data presentations obtainable acoustically is relative concentration *versus* distance across a dump plume for various depths. The corresponding concentration plots for the first pass over the dump plume shown in Fig. 1 are shown in Fig. 2.

Example two

In 1974, the U. S. Army Corps of Engineers carried out a dredging operation designed to deepen the main ship channel for the Port of Miami, Florida, U. S. A. As a result of tidal flow, a substantial amount of particulate material was swept out of the channel and into the ocean. Figure 3 shows the 20 kHz acoustic record obtained by the research vessel VIRGINIA KEY in May as it passed out of the ship channel. Also shown in this figure is a temperature profile of the water column. Note that much particulate material is contained where the thermocline onsets. Figure 4 shows the situation in November, 1974. Once again an abundance of particulate matter is detected in the ocean, with a preferential accumulation of particulates at the thermocline. Note the existence of discrete reflecting layers within the thermocline. These observations are discussed further[1].

Example three

For many years the City of New York has dumped sewage sludge into the ocean about 20 kilometers from the city. One of the most difficult problems in sewage sludge dumping studies is determining where the sewage material goes after being dumped. Knowing where the material goes after dumping is crucial for two reasons: *(i)* the first is to be able to correctly interpret chemical sampling. Consider the situation in which the chemist does not even know whether a particular sample bottle is in or outside of the main sewage dump, *(ii)* the second is to be able to determine the space-time growth of the material dumped in the ocean.

The density structure within the water column significantly affects the flow of the dumped sewage sludge. As an example of dumping into a well-mixed water mass, consider the data portrayed in Fig. 5 which were gathered in September 1975 in the New York Bight. In this figure data gathered in three passes over the dumped material are shown for both 20,000 kHz and 200,000 kHz. The first pass (1107 U. T.) occurred nine minutes after the material was dumped. Note by the time of the third pass (1206 U. T.) that material had substantially dispersed laterally and that the total column of dumped material had been deformed through the action of current shear[2].

An example of dumping into a highly stratified water mass (but in the same geographic location as Fig. 5) is shown in Fig. 6. Here two passes over a sewage sludge dump were made. Note the existence of horizontal flows (about 30 cm/sec average speed for the first half hour after dumping) of sewage material within the thermocline. Note also the presence of internal waves generated by the dumping process itself.

Example four

One of the most interesting areas for the study of particulate flows is that portion of the water column immediately adjacent to the bottom. A question of central interest is how important is wave action in resuspending bottom particulates? In order to answer this question, very high resolution (in the vertical) estimates, for example, every centimeter, of suspended sediment concentration must

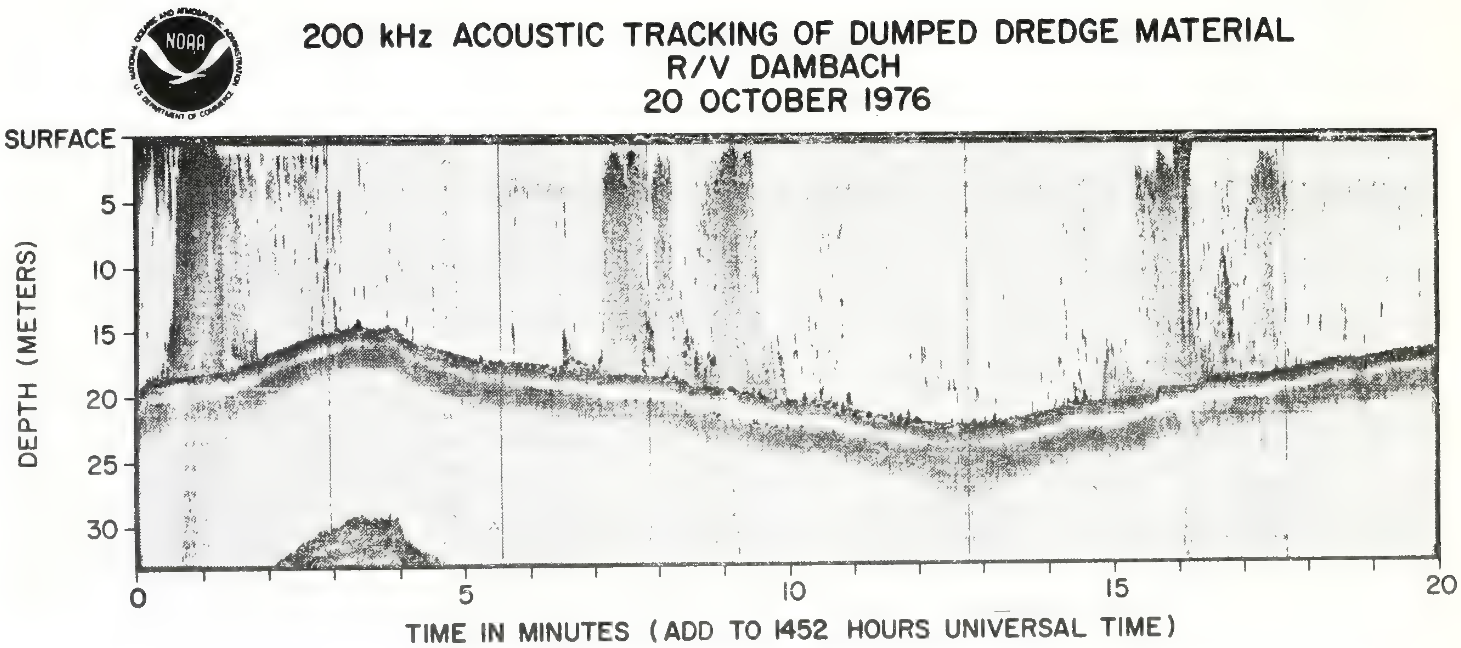

Fig. 1. 200 KHz acoustic detection and mapping of dumped river bottom dredge material in Lake Ontario.

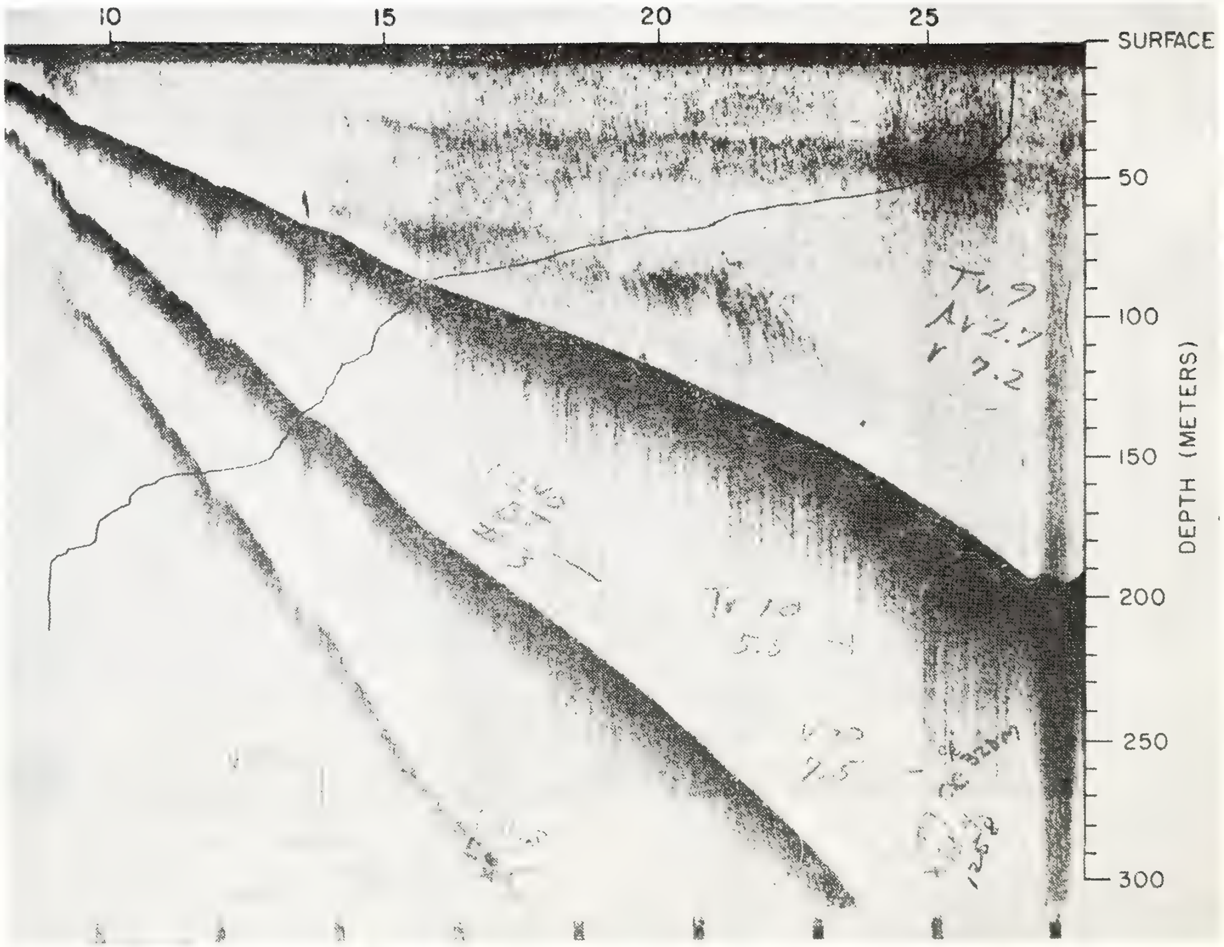

Fig. 3. 20 KHz acoustic record obtained of particulate material dredged in the Miami ship channel in May 1974.

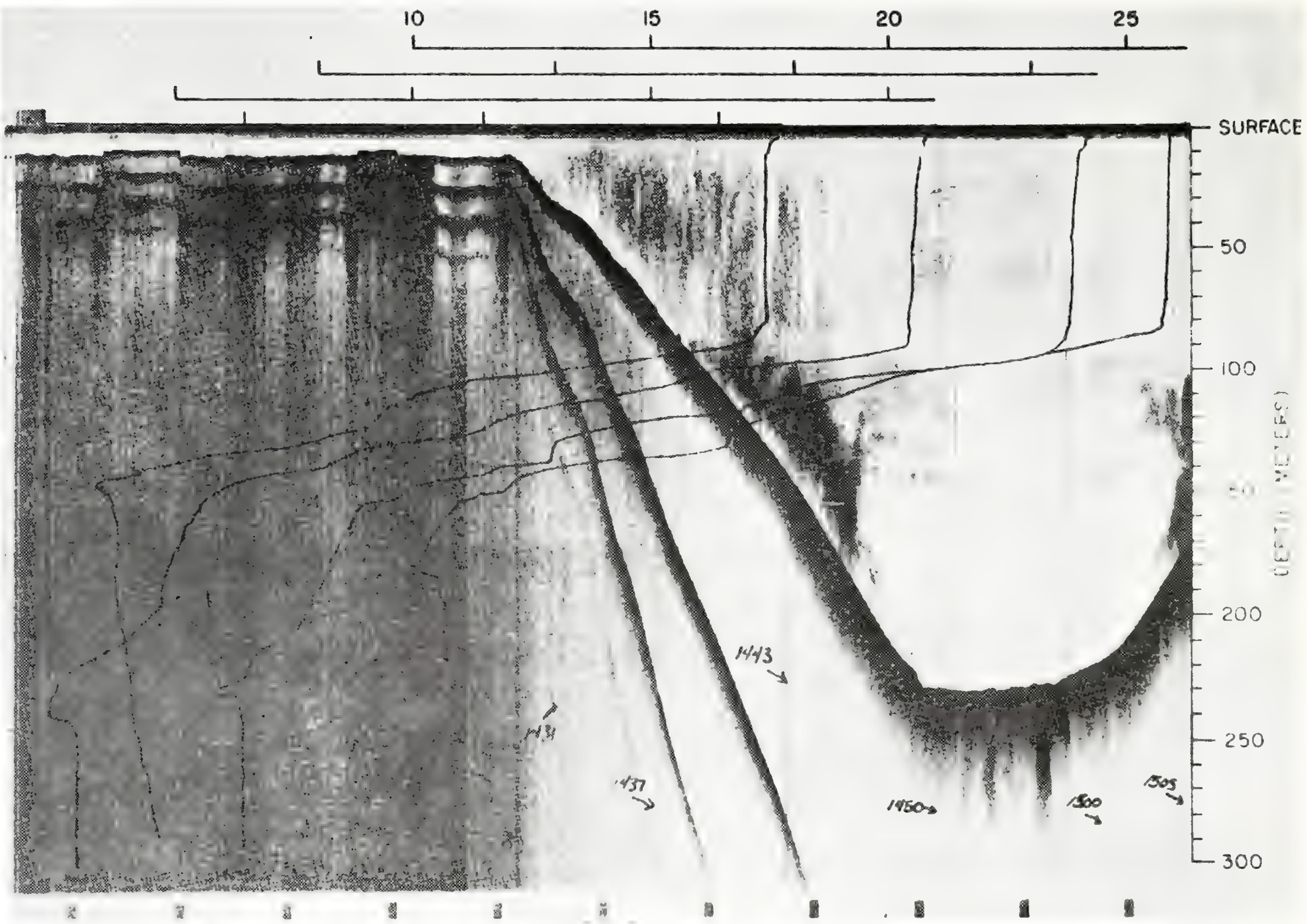

Fig. 4. 20 KHz acoustic record obtained of particulate material dredged in the Miami ship channel in November 1974.

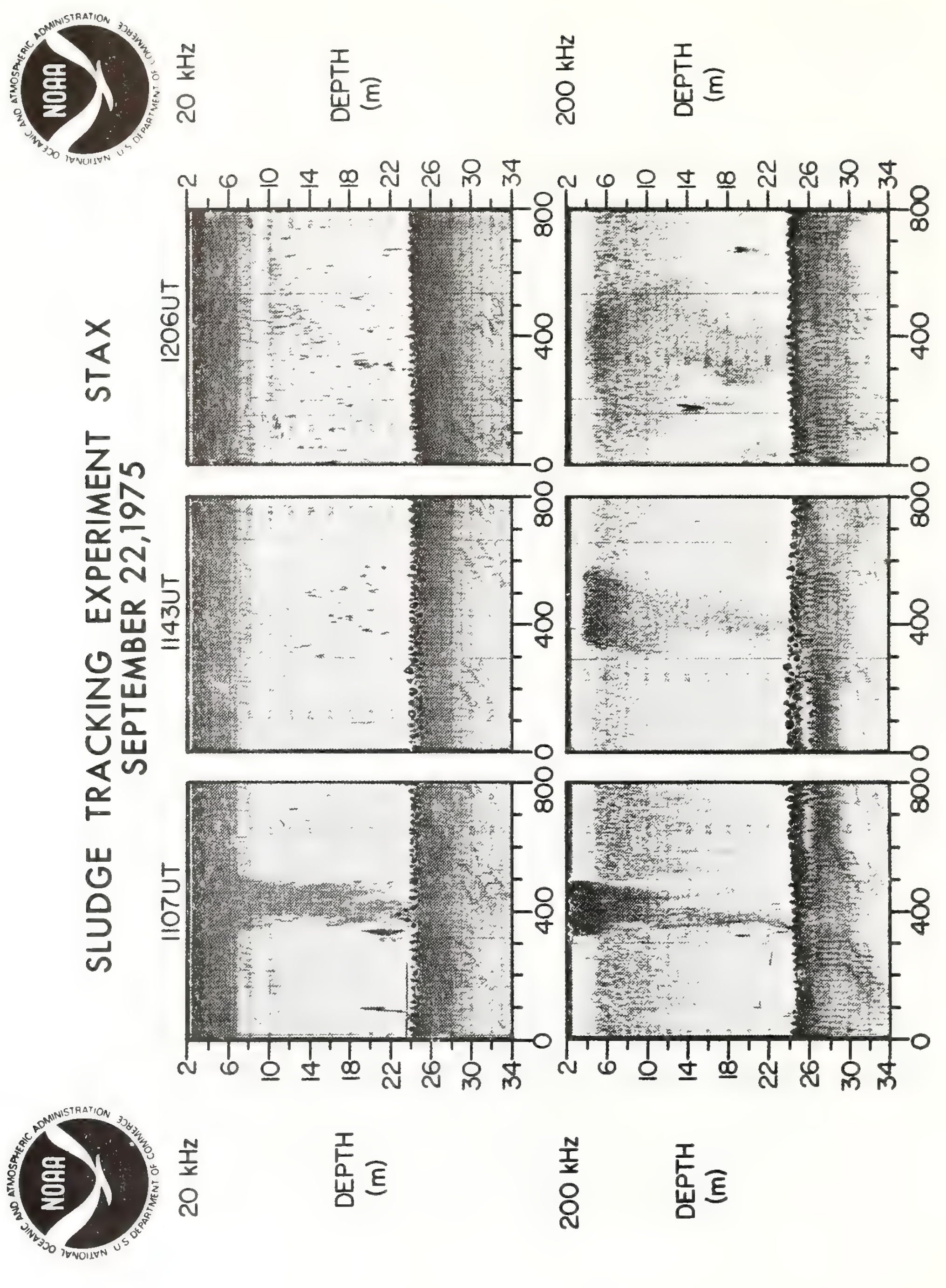

Fig. 5. 20 KHz and 200 KHz acoustic records of a sewage sludge dump made in the N. Y. Bight when the water column was well mixed (September 1975).

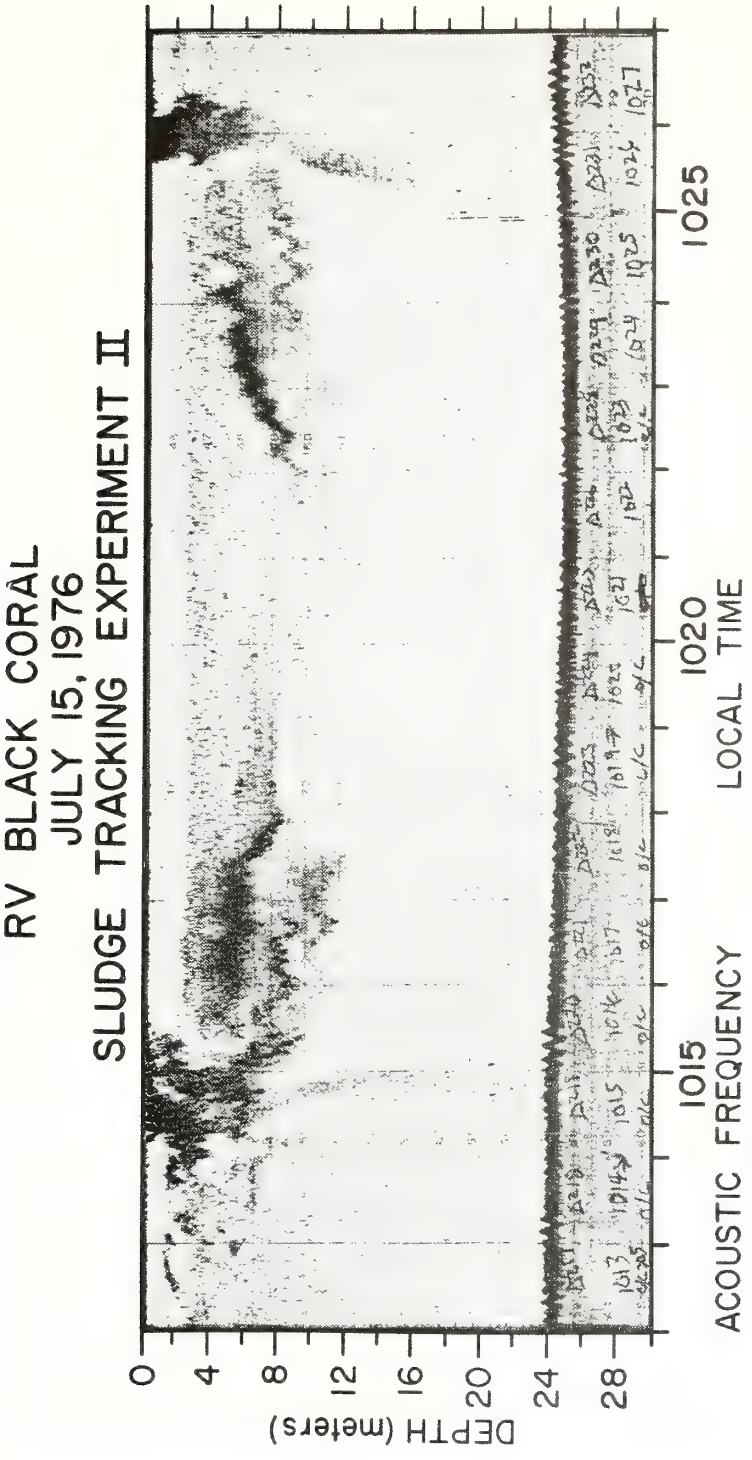

Fig. 6. 200 KHz acoustic records of a sewage sludge dump made in the N. Y. Bight when the water column was highly stratified (July 1976).

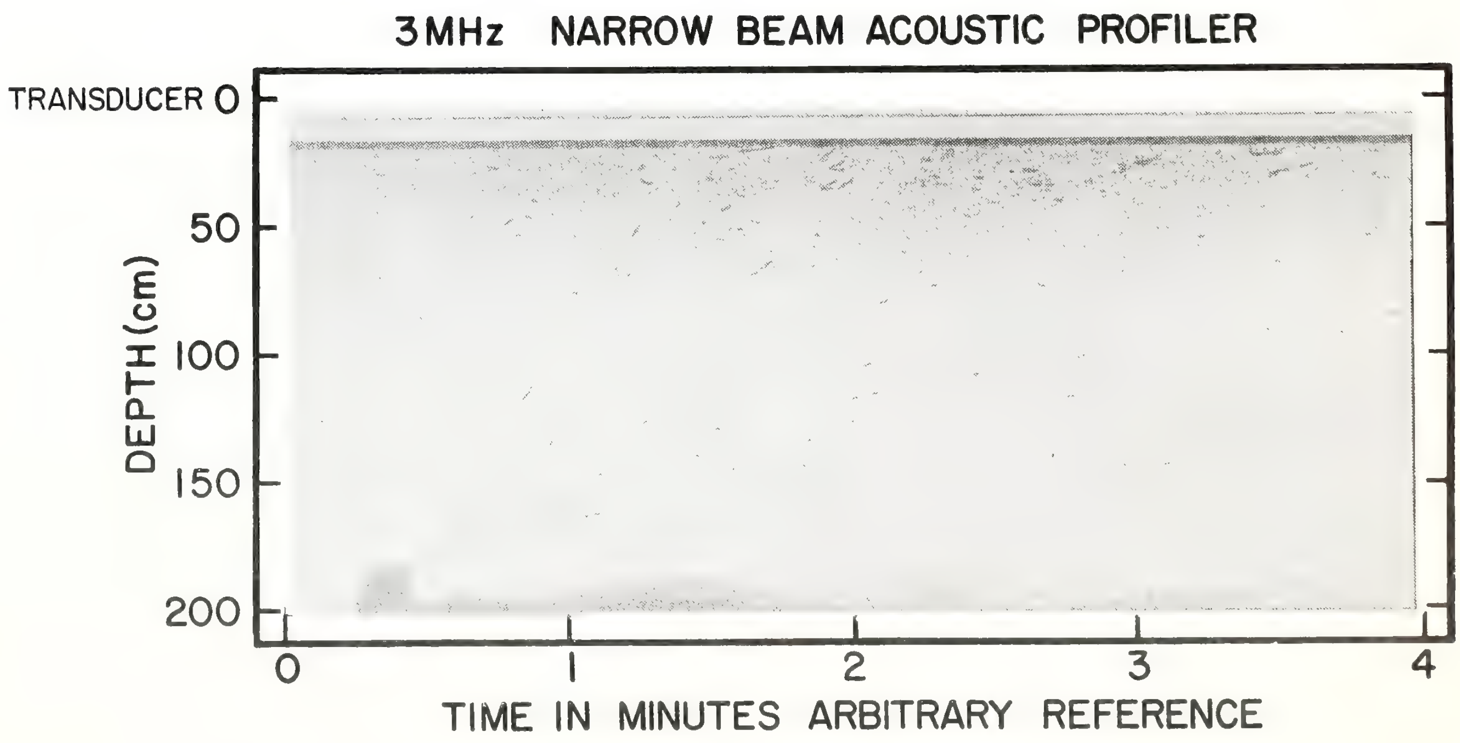

Fig. 7. 3 MHz acoustic record of nearbottom sediment stirred by the throwing of a rock into the water of a ship port.

be made. Correspondingly, high-resolution high-frequency (0.1 Hz) measurements of oceanic current variations should also be made and then correlated with the concentration measurements. Until the advent of the acoustic technique, no truly satisfactory means existed for concentration measurements on a one centimeter scale. A 3,000,000 Hz acoustical system was developed in order to provide a means of obtaining the required high resolution concentration data.

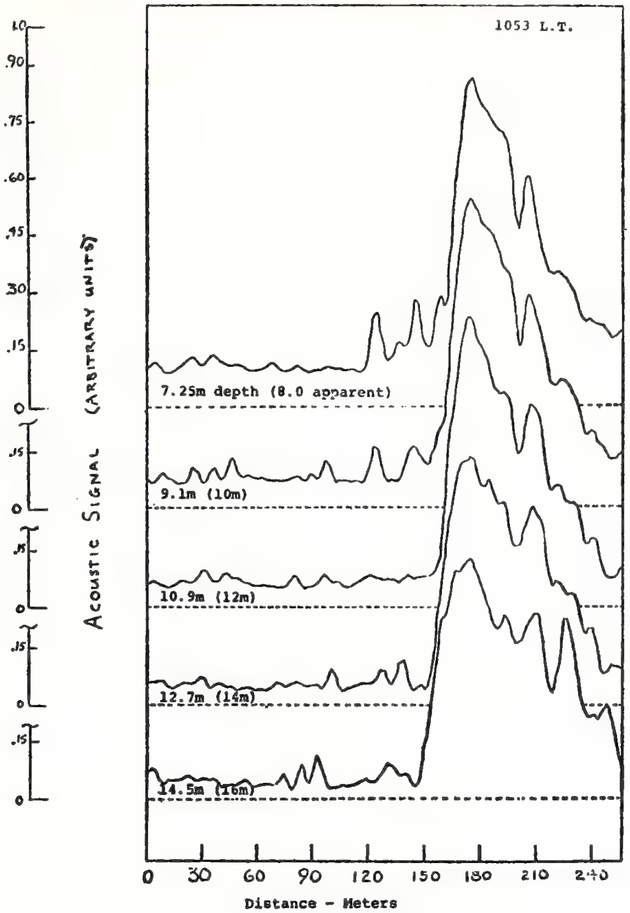

Fig. 2. Acoustic intensity level as a function of distance through the first dredge plume shown in Fig. 1.

Figure 7 shows the data obtained from the 3 MHz system when it was mounted on a tripod 200 cm above the bottom. Note the presence of a cloud of particulates in the lower 25 cm of the water column. This is material which was stirred up when a 5 Kgm rock was thrown into the water near the tripod. Bottom currents advected the particulate material through the acoustic beam (the acoustic beam has a width of 1/2 degree).

RESULTS

The examples presented in Experimental part resulted in various insights into particulate flows. Some of the most important results are:

(*i*) density structure within the thermocline significantly affects the flow of suspended particulates;

(ii) thermocline particulate currents are generated in the dumping of sewage sludge into a stratified marine environment;

(iii) thermocline particulate layers (and perhaps slow moving flows) may be generated through dredging operations;

(iv) bottom particulate currents were generated by dredge material dumping in Lake Ontario.

DISCUSSION

A general observation to be drawn from the examples is that thermocline temperature and density structure significantly influences man-generated particulate flows. Zones within the thermocline where temperature gradients exist appear to be preferred zones for particulate accumulation. An interesting question is that if there are preferred zones of flow or accumulation for man-generated particulate flows, should these same zones also be preferred for natural particulate accumulation (*e. g.*, plankton)? The answer to this question may prove to be of significant importance in pollution studies and of particular significance in pollution dilutional rate estimates.

CONCLUSIONS

The four examples presented in this paper demonstrate clearly the importance of acoustics in studying mangenerated flows. There is no other means comparable to acoustics currently available for obtaining rapid, large-scale data on particulate flows. When used for tracking sewage sludge, acoustics may be used to accurately guide chemists to obtaining samples from regions of maximum sludge concentration. Finally, acoustics may be used to obtain data on the space-time growth of particulate ensembles *throughout the water column* in real-time. These kinds of data, which are fundamental to models of particulate flows, heretofore extremely difficult to obtain, will now be obtained in ever increasing amounts thanks to the advent of acoustic techniques.

REFERENCES

1. J. R. Proni, F. C. Newman, R. Sellers, and C. Parker, Acoustic tricking of ocean-dumped sewage sludge, *Science* **193** (1976) 1005—1007.
2. J. R. Proni, F. C. Newman, D. Rona, D. Drake, G. Berberian, C. Lauter, Jr., and R. Sellers, On the use of acoustics for studying oceanic suspended sediment and for determining the onset of the shallow thermocline, *Deep-Sea Research* (1976) 831—837.

DISCUSSION

E. D. SCHNEIDER:

1. How much is spent per year on these research programs?

2. This tracking system operates by measuring density differences between the wastes and ocean water. What is the sensitivity of this tracking system in present dilution of the wastes?

E. R. MEYER:

1. Roughly $ 100,000 per year is spent by NOAA in direct support of the acoustical waste tracking program which operates from the NOAA Atlantic Oceanographic and Meteorological Laboratory in Miami. About 30—40 per cent of that amount is applied to development of the acoustical technique. The remaining 60—70 per cent provides salaries for Dr. Proni and his staff.

2. In a recent sewage sludge tracking experiment in the turbid, inner waters of the New York Bight, it was possible to follow the sludge plume in excess of 30 hours to a point at which the sludge particles formed less than 4 per cent of the total suspended particulate load of the water column. In clearer waters, it is possible to detect introduced particulate matter at even lower concentrations.

LJ. JEFTIĆ:

What is the price of the fish and of the whole set-up?

E. R. MEYER:

An entire basic acoustical waste tracking system, including transponders, fish, and paper and magnetic tape recording units, can be assembled for less than $ 100.000. It may be possible to construct a basic field unit for as little as $ 50.000.

D. J. BAUMGARTNER:

Is the transponder towed behind the research vessel?

E. R. MEYER:

The transponders are towed over the sides of the vessel to avoid as much as possible noise from the propulsion units.

IZVOD

Upotreba akustičkih metoda u primijenjenoj oceanografiji i u problemima vezanim uz izgradnju obalnog pojasa, s naglaskom na transport suspendiranog materijala u oceanu

J. R. Proni, F. C. Newman, E. D. Meyer, H. B. Stewart, Jr., D. J. Walter, R. Sellers i C. A. Lauter, Jr.

Pokazano je nekoliko primjera primjene akustičkih uređaja u primijenjenoj oceanografiji i u inženjerskim problemima u obalnom pojasu. Posebno su obrađena četiri primjera: odbacivanje materijala dobivenog bageriranjem rijeka; produbljavanje bageriranjem plovnog kanala za luku Miami, Florida; odbacivanje gradskog otpada u zaljevu New York; te otkrivanje oblaka morskih sedimenata resuspendiranih uslijed djelovanja vjetrova. U svim tim slučajevima utvrđena je korisnost akustičkih metoda za dobivanje prostorne i vremenske raspodjele suspendiranog materijala u moru.

47. CICAR-II Symposium on Progress in Marine Research in the Caribbean and Adjacent Regions, FAO Fisheries Report No. 200 Supplement, 1977, 597-619.

THE 1972-1973 CYCLE OF THE GULF LOOP CURRENT
PART II: MASS AND SALT BALANCES OF THE BASIN

by

G.A. MAUL
National Oceanic and Atmospheric Administration
Atlantic Oceanographic and Meteorological Laboratories
Miami, Florida 33149

CONTENTS

1. INTRODUCTION
2. HYDROGRAPHIC DATA
3. GEOSTROPHIC TRANSPORTS
4. MASS BALANCE OF THE GULF
5. SALT BALANCE OF THE GULF
6. SUMMARY AND CONCLUSIONS
7. ACKNOWLEDGEMENTS
8. REFERENCES

Abstract

Hydrographic sections were made across the Yucatan Strait and the Straits of Florida approximately every month from May 1972 to September 1973. These data encompass a cycle of the Gulf Loop Current from eddy separation to eddy separation. The data suggest that the 5°C water near the bottom of the Yucatan Strait is forced out of the Gulf of Mexico when the Loop starts to form. About mid-way through the growth phase, resident Gulf waters advect out the Straits of Florida between the continental shelf of the United States and the Florida Current. After separation of an eddy, the 5° water flows back into the basin, continuity being maintained by continued flow along the Florida coast. In the upper 700 m, approximately 10% of the water flowing into the basin through the Yucatan Strait is exchanged with resident Gulf waters before flowing out the Straits of Florida. The eddy separation causes an injection of 10^{16} g of salt into the western Gulf, and accounts for approximately 75% of the total salt exchange between the Gulf Loop Current and resident Gulf waters. Even though the basin has an excess of evaporation over precipitation, river runoff more than accounted for the atmospheric loss of fresh water during the 1972-1973 cycle.

Resumen

Desde mayo de 1972 hasta septiembre de 1973 se hicieron secciones hidrográficas, aproximadamente cada mes, a través del estrecho de Yucatán y de los estrechos de la Florida. Los datos, que pertenecen a un ciclo de la corriente del Golfo entre dos separaciones de remolinos, indican que las aguas a 5°C situadas cerca del fondo del estrecho de Yucatán vienen forzadas desde el Golfo de México, al empezar a formarse el bucle: cuando la fase de crecimiento está en su mitad, aproximadamente, las aguas del Golfo calientan por advección los estrechos de la Florida, entre la plataforma continental de los Estados Unidos y la corriente de la Florida. Después de la separación de un remolino, el agua a 5°C, afluye de nuevo a la cuenca, y la continuidad se mantiene por el flujo constante a lo largo de la costa de la Florida. En los 700 m superiores, el 10 por ciento aproximadamente, del agua que afluye

a la cuenca a través del estrecho de Yucatán se intercambia con las aguas del Golfo, antes de afluir a los estrechos de la Florida. La separación del remolino causa una inyección de 10^{15} g de sal en el Golfo occidental, cantidad que representa el 75 por ciento, aproximadamente, de todo el intercambio de sal entre la corriente circular del Golfo y las aguas permanentes del Golfo. Aunque, en la cuenca, la evaporación es mayor que la precipitación, las pérdidas atmosféricas de agua dulce durante el ciclo 1972-1973 se debieron principalmente a la escorrentía fluvial.

1. INTRODUCTION

Between May 1972 and September 1973, 14 cruises were made into the eastern Gulf of Mexico to study the Gulf Loop Current. A multi-ship study was made in May 1972 to investigate the Yucatan Current (Molinari and Yager, 1977), the Florida Current (Brooks and Niiler, 1975) and the Gulf Loop Current (Morrison and Nowlin, 1977). Individual cruises were made in June 1972 and May 1973 by Texas A & M University, and a time-series of 12 cruises was made at 36-day intervals starting in August 1972 (Maul, 1977). The latter included STD sections across the Straits of Florida and the Yucatan Strait as well as XBT surveys to map the path of the current from Yucatan to Key West.

Data from these investigations encompass one complete cycle of the Gulf Loop Current as proposed by Leipper (1970): spring intrusion, autumn spreading, and eddy separation. Maul (1977) noted that there was a great deal of year-to-year variability of this idealized pattern and calculated that the Yucatan Current transport exceeds the Florida Current transport during the period of Loop intrusion and spreading by 4×10^6 m^3 s^{-1}. During the intrusion and spreading phase, Maul (1977) concluded that a southward flow at the bottom of the Yucatan Strait may be the mechanism that preserves mass continuity.

In this paper, the STD and XBT data across the two straits are discussed, followed by an error analysis and calculations of the year-long cycle of geostrophic transports. Since direct computation of transport imbalances between the two sections involves determination of a small difference between two large numbers, an indirect method involving water mass identification is employed. Within the error limits imposed by the available data, a synthesis of the mass balance of the Gulf of Mexico basin is then made. The quantity of salt exchanged into the Gulf from the separation of the 1972 anticyclonic eddy is calculated next, and the fresh water required to maintain the mean salinity of resident Gulf water is determined from 1972-1973 river runoff data. Finally, the evaporation-precipitation role in the basin is investigated to complete the mass and salt balance study.

2. HYDROGRAPHIC DATA

Cross-sections of the Straits of Florida (between the Florida Keys and Havana) and of the Yucatan Strait (between Cape San Antonio, Cuba and Contoy Island, Mexico) were made during every cruise except January 1973, when weather prevented observations. Station spacing was approximately 18 km. Stations were occupied to within 22 km of the Cuban coast, and approximately to the 50 m isobath off Mexico and Florida. Seven stations were in the Straits of Florida section, and nine were across the Yucatan Strait. STD data were obtained to a depth of 1 000 m or close to the bottom for each cruise except February and March 1973 when SBT data only were obtained; in September 1972, XBT data only were obtained in the Yucatan Strait.

The STD used was a Plessey model 9060, which is a battery-operated, graphic-recording instrument. Manufacturer's specifications of accuracy for this instrument are $S=0.05^{\circ}/oo$, $T=0.1^{\circ}C$, D=0.25% (~5 m); resolution specifications are $S=0.02^{\circ}/oo$, $T=0.05^{\circ}C$, and D=0.1% (~2 m). Bathythermograph observations were made using Sippican T-7 SBT probes whenever possible, which gives temperature to a maximum depth of 750 m. In a few instances, depths of less than 750 m were observed because of mechanical (STD winch) or logistical difficulties.

Calibration samples of salinity and temperature were available at the surface for each XBT or STD station. Since no calibration data were available at depth, the historical salinity minimum of $34.84^{\circ}/oo$ in the Antarctic Intermediate Water (Molinari, 1974) was used as a deep salinity calibration point. Linear corrections were applied to the STD salinity data after digitization in 20 m depth increments, at $0.01^{\circ}C$ and $0.01^{\circ}/oo$ resolution. Intercomparisons between surface STD values and surface calibration values show that the standard error estimate is $T = \pm 0.13^{\circ}C$, and $S = \pm 0.05^{\circ}/oo$.

Since the interest here is to calculate transport, a salinity assignation is necessary in order to include the sections where only XBT data are available. Emery (1975) reviewed the problem and concluded that in the North Pacific Ocean, when the T-S relationship is "tight", dynamic height can be computed from XBT data alone. That is (Emery, 1975), the difference between dynamic height found by using the mean T-S relation and observed temperature and salinity was smaller than either the theoretical measurement error (0.04 dynamic metres) or observed variation in dynamic height at two ocean station sites (Victor and November), but not at a third (Papa). Nowlin and McLellan (1967) found that the T-S relation in waters cooler than 17°C was extremely consistent throughout the southeastern Gulf of Mexico, but in the waters warmer than 17°C, there are two distinctly different water masses. It is necessary to distinguish between these two water masses for two reasons: (1) transports estimated by using T-S correlations for XBT data are affected, and (2) to avoid the aforementioned difficulty of determining a small transport difference between two large values.

There are several reasons why a direct calculation of the transport difference between the Yucatan Strait and the Straits of Florida will not be attempted with these data, not the least of which is item number two in the paragraph above. In order to include the SBT sections, a geostrophic reference level must be selected at 750 m or less; the Gulf Stream System is known to have velocities of from 5 to 20 cm s^{-1} at this depth. Another significant uncertainty is due to the lack of measurements near Cuba; the importance of transport near the Cuban coast will be demonstrated by recalculating Montgomery's (1941) section from Key West to Havana. Using hydrographic data only means that the geostrophically balanced baroclinic component of the transport is known; uncertainties due to the barotropic component are probably as large as the transport difference between the Yucatan Current and the Florida Current. To solve the problem, the water mass transports in the Straits of Florida will be separated into two groups: transport of the current itself, and transport of non-Gulf Stream water. Transport estimates of this non-Gulf Stream water are less subject to the above mentioned errors because it was spatially well sampled in 1972-1973, observations were taken to near the bottom, geostrophic current speeds near the bottom are probably small, barotropic uncertainties are minimized because a small cross sectional area is involved and only low frequency (i.e., baroclinically adjusted) phenomena will be discussed. Identification and transport calculations of the water masses are presented in the next section, followed by a discussion of the inferred mass balance of the Gulf of Mexico.

3. GEOSTROPHIC TRANSPORTS

Wennekens (1959) labelled two distinct water masses in the Straits of Florida: Yucatan Water, which is herein named Florida Current Water (FCW), and Continental Edge Water (CEW). The 1972-1973 data set does not have salinity observations each month, therefore, the T-S properties cannot be used as the primary means of distinguishing Florida Current Water from Continental Edge Water. However, since both Leipper (1970) and Maul (1977) used the 22°C isotherm at 100 m depth to locate the cyclonic side of the current, it seems natural to pose the hypothesis that the T-S properties of waters where the 22°C isotherm is at or greater than 100 m depth (22°C $\geq$ 100 m) are different from those waters where the 22°C isotherm is at a depth less than 100 m (22°C < 100 m). To investigate how well using the depth of 22°C isotherm identifies water masses, plots were made (Fig. 1) of the T-S relation for stations in the Straits of Florida where the 22°C isotherm was at a depth of 100 m or greater (left panel) and for those stations where the 22°C isotherm was at a depth of less than 100 m (right panel). Comparison between the two panels of Fig. 1 is facilitated by reference to Fig. 2, which is a plot of the mean T-S values. In Fig. 2, water in the Straits of Florida where the 22°C isotherm was at a depth of less than 100 m is labelled Continental Edge Water, water where the 22°C isotherm was at a depth of 100 m or greater is labelled Florida Current Water. The curve labelled Yucatan Current Water (YCW) is the mean T-S correlation of all stations taken in the Yucatan Strait where the 22°C isotherm was at a depth of 100 m or deeper.

The two most striking features of the T-S plots are: (1) the remarkable similarity of the correlation in the cool waters ($\leq$ 15°C in these data; cf. Nowlin and McLellan, 1967), and (2) the distinctly different patterns in waters warmer than 15°C. T-S correlations in the right-hand panel of Fig. 1 are qualitatively similar to what Wennekens (1959) called Continental Edge Water, and what Nowlin and McLellan (1967) pointed out as being typical of resident Gulf (non Eastern Gulf Loop Current) Water. The left-hand panel of Fig. 1 is quantitatively similar to what Wennekens called Yucatan Water, Nowlin and McLellan called Eastern Gulf Loop Current Water, or what is characteristic of Caribbean Water (Wüst, 1964).

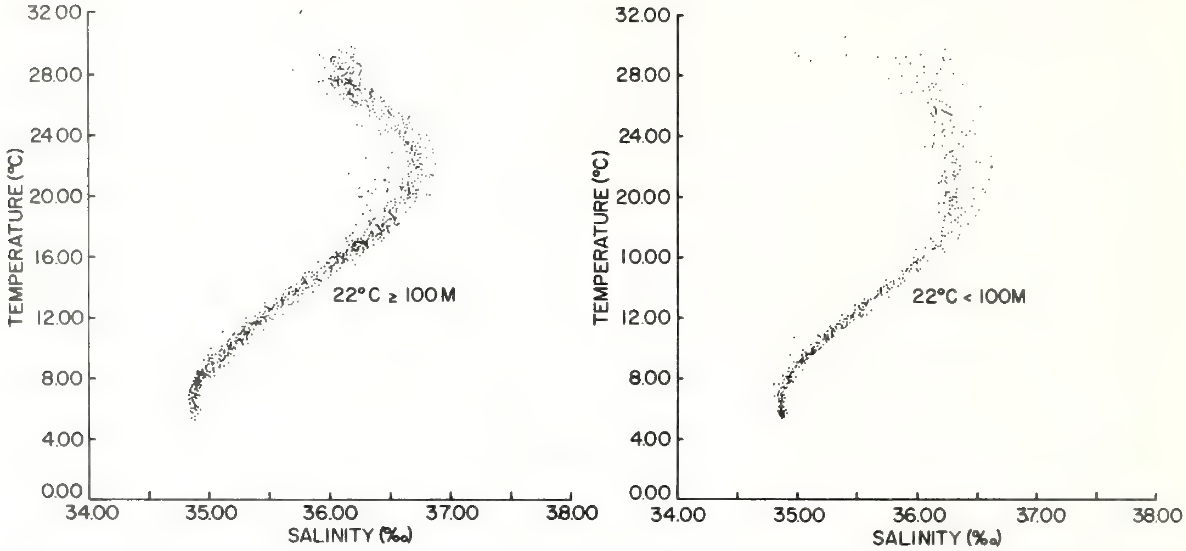

Fig. 1 Temperature-salinity correlation for the Straits of Florida. Left Panel: correlation for 35 stations that had 22°C ≥ 100 m. Right Panel: correlation for 24 stations that had 22°C < 100 m

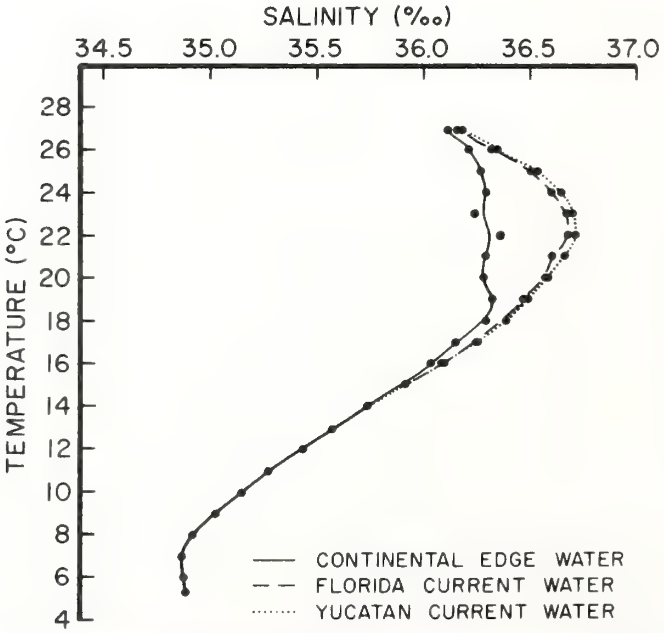

Fig. 2 Mean temperature - salinity correlations for the three water masses observed during the 1972-1973 time series

In Fig. 2, a distinction is made between Yucatan Current Water and Florida Current Water. In the Subtropical Underwater (i.e., in the temperature range $18^\circ C < T < 24^\circ C$), the salinity of the Yucatan Current Water is approximately 0.05°/oo higher than in the Florida Current Water. It would be interesting to speculate that this 0.05°/oo difference is due to mixing at the edge of the Loop Current, as the data frequently suggested small eddies (e.g., Maul, Norris, and Johnson, 1974; Lee, 1975; Maul, 1977) and complex thermal patterns (as observed in satellite infra-red images). However, judging from the scatter of points in the T-S correlation (cf. left-hand panel of Fig. 1) and the calibration results of the 9060 STD, a straightforward discussion of mass and salt exchange along the current path is not possible with these data. An investigation of the salt balance of the entire basin using an indirect method is possible; this will be discussed in the section entitled Salt Balance of the Gulf.

Returning to the problem of using temperatures (only) to distinguish water masses, it is clear from Fig. 1 and 2 that to first-order, the depth of the 22°C indicator isotherm distinguishes two water masses. When the data are examined in detail, stations in the transition zone between Continental Edge Water and Florida Current Water were found to have temperatures greater than 22°C at 100 m, but with T-S properties more like those of Continental Edge Water than Florida Current Water. Conversely, stations were found to have a temperature of less than 22°C at 100 m, but with T-S properties more like those of Florida Current Water than Continental Edge Water. This is seen in Fig. 1 as scatter about the main trend in the T-S correlations. A station pair in June 1973 had a geostrophic surface velocity (relative to 700 m) of 1.5 m s^{-1}, yet the T-S correlation for both stations was a mixture of Continental Edge Water and Florida Current Water. These examples highlight the difficulty of water mass identification at the edge of a current, even when the T-S data are available.

The XBT only transects were incorporated into the analysis by including all stations where the 22°C isotherm was at a depth of 100 m or greater in the Florida Current Water summation, and by including all station pairs where one station had the 22°C isotherm at a depth of 100 m or greater in the Florida Current Water summation. The reason for the second criterion is that, on the average, the 22°C isotherm at 100 m depth was 11 km to the south of the surface manifestation of the Florida Current (Maul, 1975). The mean transport of Continental Edge Water (see Table I) using temperature criteria only to identify the water mass, was compared to transports when temperature and salinity were available; uncertainty in the mean transport from using observed temperature and T-S correlations is calculated to be less than ± 7%.

The reliability of using T-S correlations in transport calculations of the main current was investigated by recalculating the August 1972 STD transect of the Yucatan Strait, using both the T-S correlation of Continental Edge Water and the historical mean T-S for Yucatan Current Water prepared from NODC data by Molinari (1974). In this transect, the RMS deviation of the dynamic height difference between the actual station data and T-S correlated data is 0.02 dynamic metres using either T-S correlation. Relative to 700 m, the transport calculated from the observed values in the August 1972 transect was 26.6×10^6 m^3 s^{-1}; the transport calculated from the historical T-S correlation, using observed temperatures, was 25.8×10^6 m^3 s^{-1}; the transport using the T-S for Continental Edge Water and observed temperatures was 27.0×10^6 m^3 s^{-1}. These calculations suggest, that when using the appropriate T-S correlation with XBT data, the geostrophic transport relative to 700 m can be estimated to within ± 3%.

The geostrophic transports for the 1972-1973 data set are summarized in Table I. Two dates are given in the first column: The first is that of Yucatan Strait observations, and the second is for those in the Straits of Florida. Means and standard deviations ($+\sigma$) for each column are given at the bottom of the table. Transport of Continental Edge Water is included in the total value for the Straits of Florida and also is separated into an individual column.

TABLE I

Summary of Geostrophic Transports
Relative to 700 m Depth

Date	Yucatan Strait		Straits of Florida		
	Total Transport	Surface Speed	Total Transport	Surface Speed	Transport CEW
1972	($10^6 m^3\ s^{-1}$)	($m\ s^{-1}$)	($10^6 m^3\ s^{-1}$)	($m\ s^{-1}$)	($10^6 m^3\ s^{-1}$)
22,25 Aug	26.6	0.88	21.8	1.03	1.2
27,29 Sep	17.5	0.82	22.9	0.87	1.2
1, 5 Nov	19.9	0.63	29.0	1.13	0
7,11 Dec	31.1	0.95	22.2	1.00	0
1973					
16,15 Feb	30.9	0.92	12.4	0.61	1.3
24,23 Mar	32.6	1.22	17.8	0.61	2.3
29,27 Apr	23.0	0.66	12.5	0.48	2.2
4, 2 Jun	22.5	0.73	19.1	0.77	5.1
9, 7 Jul	19.7	0.88	11.4	0.64	3.9
14,12 Aug	30.3	1.16	21.4	0.63	8.3
20,18 Sep	25.3	0.73	23.2	1.05	4.1
Mean	25.4	0.87	19.5	0.80	2.7
σ	±5.3	±0.19	±5.4	±0.22	±2.5

Reference level for the values reported in Table I was chosen as 700 m in order to include all the SBT data and for comparison with other investigations (e.g., Schlitz, 1973; Morrison and Nowlin, 1977; Molinari and Yager, 1977). When water depths were less than 700 m, the method of Jacobsen and Jensen (1926) was used to estimate velocities in shallow water with respect to the deeper stations. This method affected the Yucatan Strait calculations more than the Straits of Florida calculations, because strong currents were frequently found close to the Mexican coast in shallow water, but not so off the Florida coast. One remaining problem affects the September 1972 values; namely that the Yucatan XBT section was sampled to only 460 m and the Florida STD section to only 580 m due to mechanical difficulties. Corrections of 1.2 x $10^6\ m^3\ s^{-1}$ for the 460 - 700 m layer in the Yucatan Strait and 0.5 x $10^6\ m^3\ s^{-1}$ for the 580 - 700 m layer in the Straits of Florida, were calculated from sections whose transports were similar to September 1972.

Recent investigations into the transport of the Yucatan Current have been made by Schlitz (1973), Morrison and Nowlin (1977), Molinari and Yager (1977) and by Hansen and Molinari (1978). Schlitz compared geostrophic transports relative to 1 900 m and relative to 700 m, and found a difference of only 1 x $10^6\ m^3\ s^{-1}$ for April 1970. Schlitz reports 22 x $10^6\ m^3\ s^{-1}$ relative to 700 m. Contrary to Schlitz's (1973) experience with the reference level, the transport in the Yucatan Strait is 26.6 x $10^6\ m^3\ s^{-1}$ for August 1972 relative to 700 m (Table I), but is 34.0 x $10^6\ m^3\ s^{-1}$ relative to 1 000 m. Molinari and Yager (1977) used a surface float for a reference and report 19.9 x $10^6\ m^3\ s^{-1}$ and 18.2 x $10^6\ m^3\ s^{-1}$ in the upper 700 m during May 1972; the 1972-1973 data yield values of 23 x $10^6\ m^3\ s^{-1}$ in April-June (Table I) using 700 m as a reference level. Morrison and Nowlin (1977) calculated a Yucatan Strait transport for May 1972 of 30 x $10^6\ m^3\ s^{-1}$ using the deepest station pair as a reference level; Hansen and Molinari (1978) calculated geostrophic transports of 25.8 x $10^6\ m^3\ s^{-1}$ and 27.1 x $10^3\ m^3\ s^{-1}$ in October 1970 relative to the deepest common data point between adjacent stations (~2 000 m for the deepest pair). The reference level difficulty in the Yucatan Strait has also been discussed by Carder et al. (1978); they concluded that the choice of reference level had a much more dramatic effect on calculated currents below 1 000 m than above because the choice of the reference affected the sign of the transport in the deep layer. The average value of 25.6 ± 5.3 x 10^6 m^3 s^{-1}, reported herein, is too low by as much as 15% when compared with some geostrophic estimates which had measurements extending to the bottom, but is 22% higher than another. Nevertheless, based on the August 1973 calculations and the work cited above, the 1972-1973 transports in the Yucatan Strait must be interpreted as representing only the upper layer geostrophic variability.

Geostrophic transports in the Straits of Florida (off Miami) were investigated by Broida (1969) over a 13-month period. Broida's average transport, using the depth of the deepest station pair as a reference level, was 17.9 ± 2.1 x 10^6 m^3 s^{-1}. Niiler and Richardson's (1973) value using the dropsonde technique was 29.5 ± 4.8 x 10^6 m^3 s^{-1}. Niiler and Richardson's value includes both the baroclinic and barotropic components of transport, but they did not separate one from the other. The average geostrophic transport (Table I) in the Straits of Florida for the 1972-1973 data, 19.5 ± 5.4 x 10^6 m^3 s^{-1}, is significantly less than that for the Yucatan Strait. Brooks and Niiler (1975), using a dropsonde technique, report 20.2 x 10^6 m^3 s^{-1} during May 1972 down to the depth where σ_t = 27, in the Straits of Florida off Key West. Molinari and Yager (1977) found that the May 1972 Yucatan Strait transport down to σ_t = 27 was 20.8 x 10^6 m^3 s^{-1}. Morrison and Nowlin (1977) report a value near 23 x 10^6 m^3 s^{-1} for the waters above σ_t = 27. The agreement between Brooks and Niiler, and Molinari and Yager may be fortuitous because neither value includes measurements close to the Cuban coast.

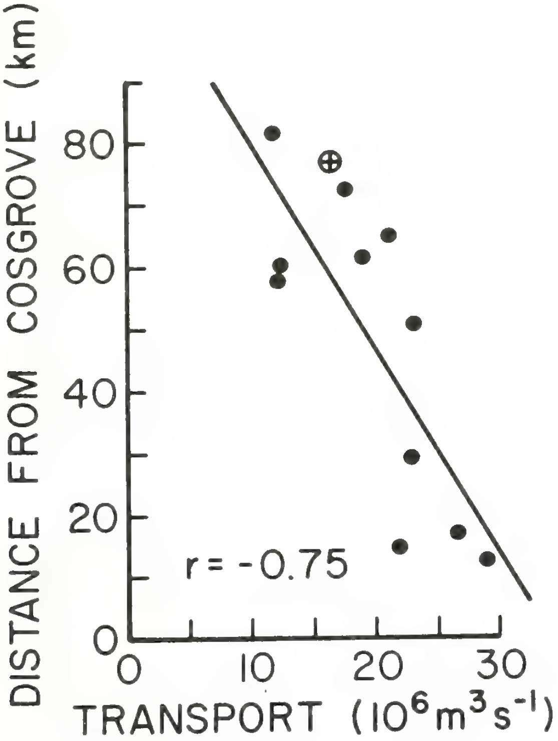

Fig. 3 Correlation between the distance south of Cosgrove Lighthouse (near Key West, Florida) to the Florida Current, and total volume transport through the Straits of Florida

The importance of measuring the transport near the Cuban coast in the Straits of Florida (Fig. 3) by plotting the distance from the 100 m isobath at Cosgrove Lighthouse (northern terminus of the sections) to the point where the 22°C isotherm was at 100 m, versus the total outflowing baroclinic transport above 700 m (summarized in Table I). The least squares line linearly relates the distance (D) from Cosgrove to the transport (T) by $D = -3.3T + 113$; the correlation coefficient, r, is -0.75. Statistically, the t test shows that the probability of distance and transport not being related is less than 0.01. These data suggest that the transport of the Florida Current near Havana can be large during those times of the year when the current is far to the south.

As an independent check of the relation between total transport and distance south of the Florida Platform, the section reported by Montgomery (1941), which had a station within 7 km of Havana, was recalculated using 700 m as a reference level. Montgomery's total transport relative to 1 200 m was 26×10^6 m^3 s^{-1}, relative to 700 m it is 22.8×10^6 m^3 s^{-1}. Transport in the section within 23 km of the Cuban coast relative to 700 m was 6.2×10^6 m^3 s^{-1}, or 27% of the total. The total transport in Montgomery's section relative to 700 m, less the last 23 km, is 16.6×10^6 m^3 s^{-1}. The situation in his data, taken in March 1938, is similar to that of the spring of 1973: the 22°C indicator isotherm at 100 m was well south of the Florida Platform. The circled cross in Fig. 3 is the correlation between D and T based on a recalculation of Montgomery's (1941) data.

Limitations in the 1972-1973 data prohibit a discussion of annual variability in the Florida Current Water. The Yucatan Strait transport cycle however, is markedly different from the cycle reported on by Niiler and Richardson (1973); similarly the average surface speed cycle is not in agreement with that reported by Fuglister (1951) and Cochrane (1965). Cochrane, Niiler and Richardson, and Fuglister report a maximum during the summer, whereas the 1972-1973 data have a minimum in May, June, and July. Greatest transports and speeds in the 1972-1973 data occur in December, February, and March, whereas the opposite is true in the above references. It is difficult to isolate the cause, whether it be due to using 700 m as a reference level, not having a station near Cape San Antonio, or to the inherent difficulties of geostrophic transport estimates in a narrow channel as discussed by Broida (1969). If a barotropic current of ±5 cm s^{-1} exists in a channel like the Yucatan (say 100 km wide by 1 500 m deep) the 1972-1973 values could be in error by $\pm 7.5 \times 10^6$ m^3 s^{-1}. Uncertainties of this magnitude debilitate analysis of variability in the Yucatan Current, but are not so severe a limitation when considering variability in Continental Edge Water transport as is discussed in the next section.

4. MASS BALANCE OF THE GULF

When the Loop Current grows and penetrates into the Gulf of Mexico, continuity requires that waters must be displaced. Maul (1977) suggested that the southerly flow near the sill of the Yucatan Strait (Hansen and Zetler, 1972; Schlitz, 1973) could account for this displacement. Rossov (1966) concluded that the countercurrent he observed at 100-150 m in the western Yucatan Strait arises because "the Atlantic water flowing in from the east and the Caribbean water from the south is not compensated for by the flow out through the Straits of Florida". On the eastern side of the Yucatan Strait, a southward flow is often reported (e.g., Gordon, 1967). Brooks and Niiler (1975) report a westward flow of what appears to be Continental Edge Water in the Straits of Florida off Key West. These observations suggest that a complicated flow pattern can exist at any one time. Based on the 1972-1973 data set, the low frequency (geostrophically adjusted), mass balance will be investigated, and is the subject of this section.

In order to investigate the mass balance, the contribution discussed in the previous paragraph must be assessed. The deep water flowing out of the Gulf of Mexico through the Yucatan Strait is about 5°C or less. Assuming the deep water temperatures have reached a steady state on inter-annual time scales, the ≤ 5°C water must return again to the Gulf of Mexico through the Yucatan Strait because the sill depth of the Straits of Florida (768 m) is too shallow to be a source of cold, deep renewal water. A similar conclusion was reached by Carder et al. (1978) based on silica data, and this implies that the net flow near the bottom of the Yucatan Strait is approximately zero when integrated over several years.

Rossov's (1966) observation is not seen in the 1972-1973 data; if a southward transport in the western Yucatan Strait exists, it is probably small or intermittent because the Yucatan Current almost always occupies the western side. On the eastern side, the southward flow has T-S characteristics of Yucatan Current Water, and therefore this current near Cape San Antonio is not a compensatory flow involving resident (non-Loop Current) Gulf of Mexico waters. In the mean, the Straits of Florida appears to be the only significant exit port of resident Gulf of Mexico surface waters, which, from the earlier discussion on T-S properties, is labelled Continental Edge Water.

Transports of Continental Edge Water (cf. Table I) are subject to the same range of errors discussed in the previous section on the waters in the current itself, except that the barotropic component is much smaller. The area with which to estimate barotropic effects depends upon how far south of the Florida platform the current is found. Assuming an average distance south of 25 km, a triangular area 700 m deep offshore, and again ± 5 cm s^{-1} barotropic flow, the error in transport is ± 0.4 x 10^{6} m^{3} s^{-1}, or about 15% of the average transport of Continental Edge Water. Summing up the errors in transport due to using T-S relations for salinity (3%), for using the 22°C isotherm to identify water masses (7%), and for the barotropic errors, the transports of Continental Edge Water are estimated to be valid to within ± 25%.

The effect of errors on the average geostrophic transport of Continental Edge Water will be assessed by an independent estimate of average transport based on the volume change of the Gulf Loop Current over the year-long cycle. With reference to 700 m, the surface area bounded by the 22°C isotherm at 100 m (Maul, 1977) defines an estimate of the volume of resident Gulf Water displaced. The minimum area covered was 66 x 10^{3} km^{2} in early November 1972; the maximum area covered was 209 x 10^{3} km^{2} in July 1973. Averaging the areal difference over the period from eddy separation to eddy separation (June 1972-August 1973), a transport of 2.5 x 10^{6} m^{3} s^{-1} is calculated; during the nine-month period that the Loop Current intrudes, the value is 4.2 x 10^{6} m^{3} s^{-1}. Average transport (T) of Continental Edge Water for the 1972-1973 data set is 2.7 x 10^{6} m^{3} s^{-1}; during the nine-month period when the Loop Current intrudes, the value is 3.9 x 10^{6} m^{3} s^{-1}. Agreement of the independent calculations of average Continental Edge Water transports is well within the geostrophic error estimate.

If there are no other sources or sinks, 2.7 x 10^{6} m^{3} s^{-1} is the outflow of resident Gulf water displaced by water in the upper 700 m entering through the Yucatan Strait. Assuming that for 0 - 700 m of the water column

$$\overline{T_{YWC}} = \overline{T_{FCW}} = \overline{T_{CEW}}, \qquad (1)$$

then the mean transport of Continental Edge Water is 10% of the total. This implies that about 10% of the Yucatan Current Water was exchanged with resident Gulf Waters over the 1972-1973 cycle.

Equation (1) has to be modified if the time-dependent transport balance is to be investigated. The time-dependent equation is

$$T_{YCW} + \Delta_{YBW} = T_{FCW} + T_{CEW}, \qquad (2)$$

where T refers to the 0 - 700 m transport as before and Δ_{YBW} is hypothesized to be the transport of the deep water below the inflowing Yucatan Current Water. To solve equation (2) it will be assumed that $T_{YCW} - T_{FCW}$ is temporally related to the surface area change. In Fig. 4, the averaged geostrophic volume transport of Continental Edge Water between cruises (solid line) is shown to be temporally related to the surface area of the basin enclosed by the 22°C isotherm at 100 m (dashed line). The area covered by the Loop Current between November 1972 and January 1973 begins to increase before T_{CEW} begins to increase.

Similarly, between August and September 1973 the area is seen to decrease while T_{CEW} continues to increase. These observations suggest that $T_{YCW} - T_{FCW}$ are not balanced by T_{CEW} alone.

An interpretation of the 1972-1973 observation vis-a-vis the mass balance is as follows: In the autumn of 1972 the area covered by the Gulf Loop Current remained fairly constant and the inflow of Yucatan Current Water equalled the outflow of Florida Current Water (the mean transport of these two currents for the first four cruises is 23.8 x 10^6 m^3 s^{-1} and 23.4 x 10^6 m^3 s^{-1} respectively, while the mean value for the Continental Edge Water is 0.6 x 10^6 m^3 s^{-1} during the same period). In the winter and late spring, when transport of the Yucatan Current increased, an intrusion of the Loop Current forces resident Gulf waters to be displaced. However, in January, February, and March 1973, the Loop Current is close to the Florida Platform northwest of Dry Tortugas. The flow of Continental Edge Water is thus restricted, and is insufficient to account for the displacement of resident Gulf Waters required by the Loop's intrusion. Continuity is conserved by a southerly flow of deep water through the Yucatan Strait (Δ_{YBW}). In the early summer, when the transport of the Yucatan Current decreases, the Florida Current is found further to the south which permits an increased flow of Continental Edge Water. In late summer, during the time when an anticyclonic eddy is separating from the main flow, the continued flow of Continental Edge Water is balanced by a reversal in the deep flow of the Yucatan Strait.

To quantify these notions, the inferred transport difference of Yucatan Current Water and Florida Current Water (YCW - FCW) from the change in area covered by the 22°C isotherm at 100 m, is compared to the averaged Continental Edge Water (CEW) transports between cruises (Table II), 700 m is used as the reference; the time between cruises is 36 days. The column labelled YBW (Yucatan Bottom Water) is the transport difference between the Continental Edge Water and the inferred transport from areal measurements (column 2 minus column 1). The differences are chosen such that (+) implies a northward flow into the Gulf below 700 m in the Yucatan Strait, and (-) implies a southward flow. The mean

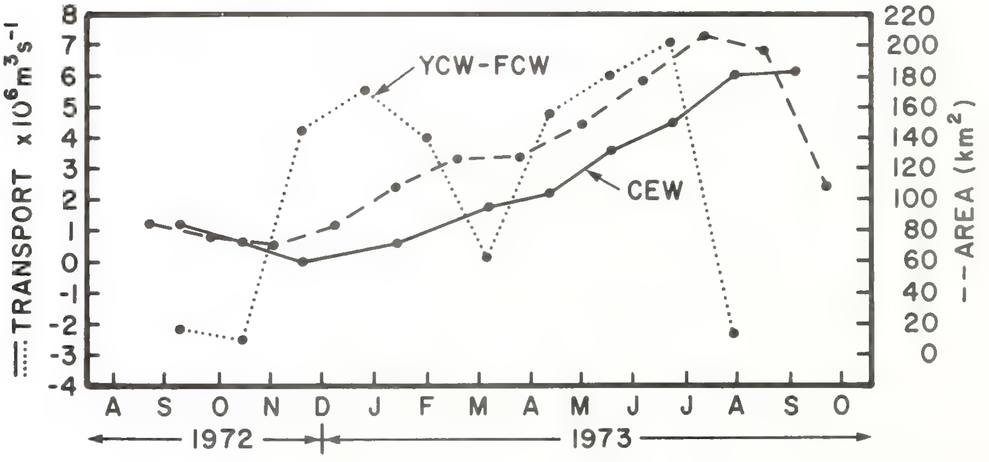

Fig. 4 Volume transport of Continental Edge Water in the Straits of Florida (solid line), inferred transport difference Yucatan Current Water - Florida Current Water (dotted line), and area enclosed by the Gulf Loop Current (dashed line) for 1972-1973

Yucatan Bottom Water transport is almost zero as is expected from the discussion on conserving 5°C water. Table II shows that there is a net southward transport below 700 m of about 2.3×10^6 m^3 s^{-1} in the winter; Schlitz (1973) reported 4×10^6 m^3 s^{-1} for April 1970.

TABLE II

Inferred Annual Cycle of Yucatan Bottom Water

	Months	Area Difference	(1) Inferred Difference (YCW-FCW)	(2) Observed Transport of CEW	YBW (2-1)
		km^2	(10^6 m^3 s^{-1})	(10^6 m^3 s^{-1})	(10^6 m^3 s^{-1})
1972	A-S	- 9,376	-2.1	1.2	+3.3
	S-ON	-11,113	-2.5	0.6	+3.1
	ON-D	19,100	4.3	0	-4.3
	(December-February)[a]			0.6	-4.2
1973	J-F	17,712	4.0		
	F-M	694	0.2	1.8	+1.6
	M-AM	21,184	4.8	2.2	-2.6
	AM-J	27,088	6.1	3.6	-2.5
	J-J	31,602	7.1	4.5	-2.6
	J-A	- 9,724	-2.2	6.1	+8.3
	A-S	Eddy		6.2	
	Mean		2.5	2.7	0.1

[a] There were no observations of CEW transport in January 1973

In view of the error bars associated with the observed transport of Continental Edge Water, and the assumptions on area and volume, the values in Table II are only intended as a scenario of possible events. The mean values are not unreasonable, however, when compared to observed transports. Another implication of this scenario is that if the transport imbalance in the upper layer water in the Gulf is balanced by a deep southward flow in the Yucatan Strait, there must be a deepening of the thermocline outside the current. The other alternative, that sea level rises, is dismissed based upon historical (Marmer, 1954) as well as concurrent tide gauge records. During the period the Loop Current spreads areally, the thermocline should deepen by about 35 m. Unfortunately, there were no observations in the western Gulf to test deepening of the thermocline and the historical records (Robinson, 1973) do not reflect it. In view of recent cruise data (unpublished) showing spinning-down eddies and the study of Sturges and Blaha (1976) into the variability in the western Gulf, it seems unlikely that the deepening thermocline signal can be detected against the background of other baroclinic processes.

The scenario of events of the 1972-1973 data should not be interpreted as a complete description of the Gulf Loop Current cycle. Variability on this description is becoming more and more evident with the synthesis of larger data sets (SUSIO, 1975; Behringer, Molinari, and Festa, 1977). For example, Hansen and Molinari (1978) report a southward transport of $>2 \times 10^6$ m^3 s^{-1} in the lower layer of the Yucatan Strait in October of 1970; the configuration of the Gulf Loop Current at this time was once again such that the flow of Continental Edge Water in the Straits of Florida could be blocked. Winter intrusions of the Loop Current have now been documented (Molinari et al., 1977), which suggest that the 1972-1973 sequence may not be a typical pattern. Further, recent satellite observations (Maul, deWitt, Yanaway, and Baig, in preparation) suggest that wave-like meanders of the Gulf Loop Current may have periods of the order of 10 days; if these meanders interact with the Florida Platform they could act as a variable blocking mechanism. A current meter array, presently moored 100 m above the sill of the Yucatan Strait, will provide even more data with which to test the hypothesis discussed herein.

5. SALT BALANCE OF THE GULF

The salt balance of the basin cannot be directly calculated from the 1972-1973 observations for the same reasons which were discussed in the section on the mass balance. An indirect approach involving an estimate of the salt exchanged into the Gulf by the May 1972 eddy will be made, followed by an estimate of the fresh water from river runoff required to keep the mean salinity of resident Gulf waters constant. First, an estimate of the salt transported (T_{salt}) by Continental Edge Water will be made from

$$T_{salt} = \int_{CEW} \int_{0}^{700} \rho\,(x,z)\; S(x,z)\; V(x,z)\; dz\; dx \qquad (3)$$

where ρ is the in situ density, S is salinity, and V is the velocity normal to th x,z plane. Evaluation of equation (3) for the 1972-1973 Continental Edge Water transports, and averaging the eleven values, gives a mean salt transport of 9.6×10^{10} g s^{-1}. Multiplication by the time interval between the May 1972 and August-September 1973 eddy separation events gives a total of 3.8×10^{18} g of salt transported out of the Gulf of Mexico in the 0 - 700 m layer by Continental Edge Water.

Dissolved solids from the United States' rivers contribute only 1.7×10^{4} g yr^{-1} to the Gulf of Mexico (Leifeste, 1974; contributions from other than United States sources are unknown). Another source of the 3.8×10^{18} g may be due to small-scale exchange processes along the perimeter of the current. But the single most important contribution is probably due to the periodic separation of an anticyclonic eddy. This latter notion will be quantified by computing the amount of salt in the May 1972 eddy and comparing this with the salt in an equal volume of resident Gulf of Mexico Water.

The eddy can be approximated by a cylinder with a surface area equal to the area enclosed by the eddy. The 22°C isotherm at 100 m plus 14 km is chosen as the outer boundary; Maul (1975) showed that this was average distance from the edge of the current to the 22°C isotherm at 100 m. Total salt in the cyclinder ($\hat{S}$) is calculated from

$$\hat{S} = 2 \int_{0}^{206} X \int_{0}^{700} \rho\,(z) S(x,z) dz \;\; dx \qquad (4)$$

where X is the radial distance from the centre of the eddy. In equation (4), S(x,z) is the distribution of salinity, ρ (z) is the in situ density; the eddy is considered to be 700 m deep and the radius of the 1972 eddy is estimated to be 206 km.

The historical temperature data on file at NODC were studied (SUSIO, 1975) to see if this is a characteristic size. Data available between 1952 and 1971 show nine eddies; their mean radius (using the same criterion) was 192 km. The September 1973 eddy was 89 000 km^2, or approximately 168 km in radius. This suggests that the 1972 eddy is of average size and that the salt balance is probably typical.

The distribution of S(x,z) in the eddy and in the juxtaposed waters was obtained from the measurements of Morrison, Merrell, and Nowlin (1973) and Molinari (1974). Five stations were used to define the eddy and three stations for the resident Gulf waters. T-S correlation for the station in the eddy centre is similar to the curve in Fig. 2 labelled Florida Current Water, and the T-S correlation for resident Gulf Waters is similar to the curve labelled Continental Edge Water. Equation (4) is numerically evaluated for both water types.

It is of interest to compare the salt transported by Continental Edge Water (3.8×10^{18} g) with the value calculated from equation (4) for the May 1972 (2.9×10^{18} g). Comparison requires that the eddy spin-down time scale be similar to the advective time scale of Continental Edge Water, because, the T-S characteristics of the eddy have to be altered by mixing to the T-S characteristics of Continental Edge Water. To date, there are no explicit measurements of anticyclonic eddy spin-down in the Gulf of Mexico. Leipper's (1970) data suggest that an eddy which was detected in November 1965 was largely mixed into the resident western Gulf waters by October 1966. An eddy detected in NOAA satellite imagery in the spring of 1977 was observed to have a maximum depth of only 140 m at its 20°C isotherm in October 1977; the 20°C isotherm was deeper than 250 m when the May 1972 anticyclonic eddy separated from the Loop Current. On the other hand, Cheney and Richardson (1976) estimate the life of cyclonic Gulf Stream Rings in the Sargasso Sea to be about two years. However, if it is assumed that anticyclonic Loop Current eddies are a quasi-annual event, and that the mean salinity of the western Gulf of Mexico is not changing, then it is reasonable to propose that the mean spin-down time scale is matched by the transport of Continental Edge Water averaged over one cycle. Based on that assumption, the May 1972 eddy accounts for approximately 75% of the exchange.

While it seems reasonable that the contribution of a detached eddy is the major consideration in the salt budget, it is not the only factor. Lee (1975) reported on spinoff eddies along the cyclonic shear zone of the Florida Current north of Miami. Somewhat larger eddy-like features were observed along the cyclonic side of the Gulf Loop Current along its northern periphery (Austin, 1971). 12-32 km sized eddies of Loop Current Water were observed on the west Florida Shelf (Maul, 1977) and on the Mississippi-Alabama shelf (Gaul, 1967). Eddies such as these are almost always seen to be present in infra-red satellite imagery (e.g., DeRyke and Rao, 1973; Legeckis, 1975). Radiance patterns in these images show a complicated thermal pattern of small eddies, plumes and entrained filaments which have been interpreted as reflecting advection (Voorhis, Schroeder, and Leetmaa, 1976; Bernstein, Breaker, and Whritner, 1977). The effect of mixing, however, is evident from infra-red patterns of isolation of warm current waters and cooler resident Gulf waters, and suggests that water from the current is continually exchanged all along its periphery.

Computing $\hat{S}$ for the May 1972 eddy and subtracting $\hat{S}$ for the juxtaposed resident Gulf waters gives an estimate of the salt added to the Gulf by the eddy after spin-down and mixing. The result of the calculation is that there is approximately 2.6×10^{16} g more salt in the eddy than in an equal volume of resident Gulf of Mexico waters outside the Loop Current. This salt must be combined with sufficient fresh water to keep the mean salinity of the upper waters of resident Gulf Water (above ~ 15°C) approximately as observed: 36.2°/oo. The quantity of fresh water required to do this is 7×10^{17} g, or 700 km^3. If the May 1972 eddy accounts for only 75% of the salt, 935 km^3 of fresh water is required to maintain the mean salinity. Since the Gulf is a net evaporation basin, the only significant source of this fresh water is river discharge.

The amount of fresh water entering the Gulf of Mexico was calculated from river gauge data supplied by the U.S. Geological Survey and from the Secretaría de Recursos Hidráulicos (Mexico). Runoff from five countries drains into the Gulf, including more than half of all runoff from the conterminous United States. Fig. 5 shows the drainage basin and the river runoff gauge sites used to calculate runoff.

As can be seen from Fig. 5, a substantial fraction of ungauged areas exist near the coast. A standard technique to estimate the contribution of these areas is to calculate the ratio of the ungauged drainage area to the area of similar gauged streams (Bue, 1970). Whenever this was done, gauged streams in the same geographic region were chosen with drainage areas of approximately the same size and with a similar discharge-volume/drainage-area ratio. The average of at least three such streams was used to estimate the contribution of ungauged areas whenever possible.

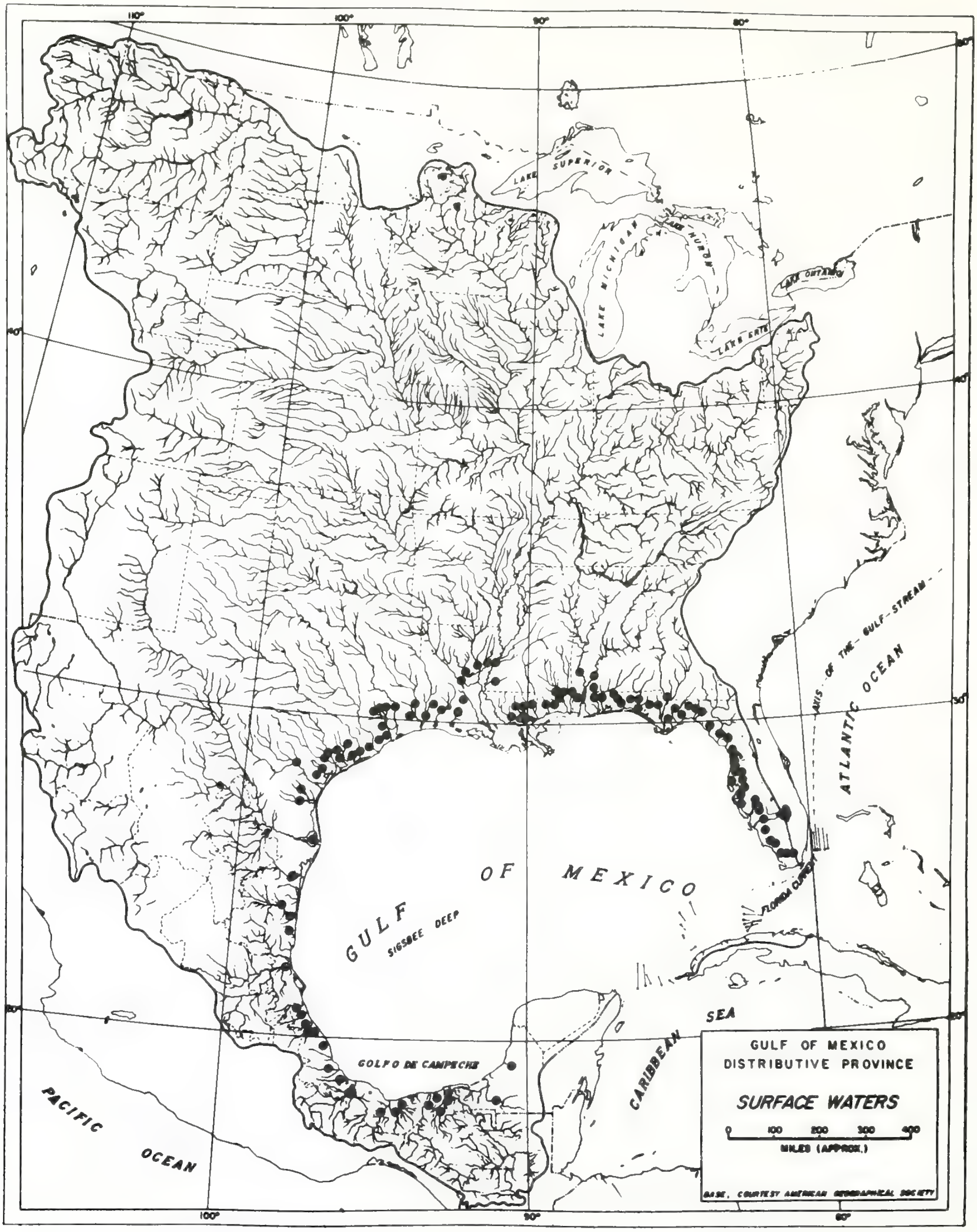

Fig. 5 Location of river runoff gauging stations in the Gulf of Mexico (after Moody, 1967), which were used to calculate the total amount of fresh water discharged into the basin

In general, the downstream-most gauging station was chosen. Care was taken not to choose a station between a major city's water source and discharge site, as Bue (1970) has shown this can contribute a substantial error. Certain areas such as the Yucatan Peninsula and southwestern Florida have no well-defined rivers or determinable drainage areas. Judging from Florida flood control records, these areas do not contribute substantial volumes to the Gulf. This, and the lack of records from Cuba, means that the estimates discussed below must be considered conservative. The results are summarized in Table III.

During the 15-month period between eddy break-off events, 1 832 km^3 of river water discharged into the Gulf. In the absence of other processes, this would raise the level of the entire basin 1.2 m. For water year 1973 (October 1972 - September 1973),11581 km^3 was received by the Gulf. This volume is 57% larger than the values reported by other investigators based on long-term averages (see Table IV). However, the discharge of the Mississippi River alone was 77% above its 45-year average during the water year 1972-1973. This supports the notion that 1581 km^3 is a conservative estimate. In Table IV, the estimate based on Leifeste's (1974) value for the United States only (793 km^3) is made using Moody's (1967) 21% and Franceschini's (1961) 22% estimate of the contribution of the Mexican rivers. The 1973 water year data show that Mexican rivers contributed 15% of the total.

A summary of the excess of evaporation (E) over precipitation (P) for the Gulf of Mexico is given in Table V. Both Franceschini (1961) and Hall (1969) have used values of E-P, along with river runoff (R) data, to study the water balance of the Gulf. They considered the mass (M) balance in the Gulf of Mexico using

$$\frac{dM}{dt} = o = \rho(E-P) + \rho(R) + \rho(I-O) \qquad (5)$$

where M is conserved on time scales of one year or longer, i.e., they tacitly assume that the advective time of T_{SALT} (equation 3) and eddy spin-down are matched. Their conclusion is that $E-P > R$, and therefore the Yucatan Current must transport more water into (I) the Gulf than the Florida Current transports out (O). The values are small compared to total transports: Franceschini (1961) calculated $I-O = 0.015\ 10^6\ m^3\ s^{-1}$, and Hall (1969) estimated $I-O = 0.033 \times 10^6\ m^3\ s^{-1}$. Franceschini and Hall argued that if the mean salinity of the Gulf is not increasing, then $I > 0$, and the mean salinity of the outflowing ($\bar{S}_o$) waters must exceed that of the inflow ($\bar{S}_I$). Franceschini (1961) estimated that the mean increase must be 0.06 percent; Hall's (1969) estimate was that $\bar{S}_o$ was 0.13 percent higher than $\bar{S}_I$.

A proper investigation of the salt balance requires the evaluation of equation (3) across both straits. Even if such observations were available, it is unlikely that sufficiently precise calculations could be made to test Franceschini's (1961) or Hall's (1969) results. How to measure $\bar{S}_o$ or $\bar{S}_I$ is also difficult to interpret; it is not the average salinity in a section. Two observations during 1972-1973 argue against the conclusion that $\bar{S}_o > \bar{S}_I$ during this period: Continental Edge Water has lower salinity in the upper layers than Florida Current Water, and Continental Edge Water accounts for 10% of the transport; the mean surface salinity in the Straits of Florida (35.74^o/oo) is less than in the Yucatan Strait (36.05^o/oo). These observations not only suggest that $\bar{S}_I > \bar{S}_o$, but also that $E-P < R$ during the period investigated herein.

River runoff for the 1972-1973 period was well above the average. If the May 1972 eddy was the only source of high salinity water supplied to the basin, then only 700 km^3 of fresh water are required to keep the salinity constant. This leaves 1 131 km^3 of R to balance E-P. Adjusting this 16-month value to one year, $E-P = 55$ cm yr^{-1}, which is in reasonable agreement with the values given in Table V. If the May 1972 eddy represente 75% of the total exchange, then $E-P = 41$ cm yr^{-1} which is in agreement with Jacobs (1951), but not others.

TABLE III

Summary of River Runoff Data ($m^3 s^{-1}$)

Month	Florida	Alabama	Mississippi	Louisiana	Texas	Mexico	Totals
JUN 72	1 497	740	141	12 250	660	7 902	23 189
JUL 72	1 656	785	140	14 119	442	11 221	28 364
AUG 72	1 134	568	108	12 621	271	15 232	29 952
SEP 72	1 028	523	71	10 238	329	11 954	24 173
OCT 72	803	416	81	12 454	301	9 855	23 912
NOV 72	979	813	194	26 863	691	6 778	36 318
DEC 72	2 463	2 843	874	36 135	546	6 561	49 422
JAN 73	3 359	4 729	853	37 814	1 218	4 006	51 980
FEB 73	4 546	3 584	1 019	39 564	1 705	3 478	53 896
MAR 73	4 029	5 025	1 672	41 767	2 373	2 821	57 687
APR 73	7 271	6 628	1 947	63 967	3 949	2 737	86 500
MAY 73	3 594	3 919	919	63 192	2 259	3 129	77 013
JUN 73	3 637	2 770	468	40 158	4 520	6 806	58 361
JUL 73	1 979	1 440	262	19 735	1 673	9 538	34 628
AUG 73	2 167	906	273	14 610	873	16 781	35 611
SEP 73	1 852	858	742	12 414	1 919	18 107	35 893
Average	2 625	2 284	610	28 619	1 483	8 557	50 102
%	5.9	5.2	1.4	64.8	3.4	19.4	

TABLE IV

River Runoff into the Gulf of Mexico

Volume	Period	Source
1 088 km^3	Climatological	Moody (1967)
964 km^3	Climatological	Leifeste (1974)
975 km^3	1959	Franceschini (1961)
757 km^3	1963-1965	Hall (1969)
1 581 km^3	1973	
1 073 km^3	Mean	

TABLE V

Evaporation-Precipitation for the Gulf of Mexico

E-P	Period	Source
35 cm yr^{-1}	Climatological	Jacobs (1951)
121 cm yr^{-1}	1950	Starr, Peixoto and Lividas (1958)
100 cm yr^{-1}	1959	Franceschini (1961)
57 cm yr^{-1}	1963-1965	Cummings (1968)
78 cm yr^{-1}	Mean	

Franceschini (1961) and Etter (1975), using different approaches, both show that E-P is much larger over the eastern Gulf than the western. Franceschini calculates that E-P is six times greater over the eastern basin. From the studies of Chew, Drennan, and Demoran (1962), Gaul (1967), and others, the net drift of the Mississippi River is known to be to the west, although there is a great deal of month-to-month variability. So except for times when the Loop Current penetrates as far north as the Delta and advects fresh water out of the basin (e.g., August 1973), most of the river discharge into the Gulf is into the western portion (cf. Table III where the runoff from Louisiana, Texas, and Mexico accounts for 88% of the total). Allowing only half of the water from Louisiana to flow into the western Gulf, 55% of R contributes to the hydrologic balance. As an example with the 1972-1973 data, using 0.55R and the fresh water required to dilute the May 1972 eddy (δ), E-P in the western Gulf would be 34 cm yr^{-1}; Franceschini's (1961) estimate for 1959 is E-P = 14 cm yr^{-1}. In either case, there is a net transport from the western Gulf which amounts to 0.02×10^6 m^3 s^{-1} during 1972-1973 to account for $0.55R \leq \delta \leq (E-P)$. This value is numerically in agreement with Franceschini (1961) and Hall's (1969) estimate of I-O but is of the opposite sign.

It would be imprudent to surmise that the 1972-1973 data set provides a conclusive description of the salt balance of the Gulf of Mexico. Each of the terms E, P, R, δ in the hydrologic balance equation are independent variables, and conclusions for one year may not be representative of others. It is more important to recognize the hydrologic variability and to relate that variability to ocean-atmospheric interactions. For example, Shukla and Misra (1977) related the sea surface temperature and wind speed over the Arabian Sea to monsoon rainfall over India. In a similar way, winds over the Gulf of Mexico behave as monsoons providing rain to the agricultural heartland of the United States. Variability in evaporation (which is a function of temperature and salinity) may be influenced by the Gulf Loop Current and detached anticyclonic eddies. The climatic implication of this variability is an importan topic for future research.

6. SUMMARY AND CONCLUSIONS

Between August 1972 and September 1973, eleven hydrographic transects were made of both the Yucatan Strait (between Cape San Antonio and Contoy Island) and the Straits of Florida (between the Florida Platform and Havana). Most of the data were from STD casts, but several sections were XBT data. In order to incorporate all available data into the transport analysis, salinities were assigned to the SBT's from historical T-S correlations and the reference level was chosen to be 700 m (which is approximately the sill depth of the Straits of Florida off Miami).

Mean and standard deviation of the geostrophic transport in the Yucatan Strait was $25.4 \pm 5.3 \times 10^6$ m^3 s^{-1}. While the mean value appears to be about 20% too low, probably due to the shallow reference level, the range of variability is in agreement with dropsonde measurements reported by Niiler and Richardson (1973), which suggests that the variability is baroclinic in nature. Contrary to the measurements made by Niiler and Richardson, the maximum flow ($\sim 32 \times 10^6$ m^3 s^{-1}) occurred in December, February and March; the minimum flow ($\sim 22 \times 10^6$ m^3 s^{-1}) occurred in April, June and July. Average transport in the Straits of Florida is $19.5 \pm 5.4 \times 10^6$ m^3 s^{-1}, but this value is influenced by the location of the northern edge of the Florida Current, which varies from 0 km to over 50 km from the Florida Platform. The further south the current is found, the lower the measured transport; this implies that in the 22 km unmeasured section in the offing of Havana, high velocities (and transports) are related to current meandering in the Strait.

Penetration and spreading of the Loop Current is associated with an imbalance in the upper layer transport of Yucatan Current Water and Florida Current Water. Continuity is maintained by the transport of resident Gulf of Mexico water through the Straits of Florida, where resident waters are identified by their T-S properties as Continental Edge Water. The transport imbalance, $(T_{YCS} - T_{FCW})$, inferred from an estimate of the volume of Gulf of Mexico water displaced, is approximately equal to the mean transport of Continental Edge Water, 2.7×10^6 m^3 s^{-1}, when averaged over the 1972-1973 cycle of eddy separation to eddy separation. When examined month by month, it is found that $(T_{YCW} - T_{FCW}) \neq T_{CEW}$. The hypothesis is made and quantified, that there is a north-south zero net transport of deep water through the Yucatan Strait to maintain the mass balance.

Continental Edge Water is volumetrically about 10% of the inflowing Yucatan Current Water. Calculations of Continental Edge Water salt transport suggest that about 75% of the salt can be accounted for by the May 1972 anticyclonic eddy. Because the eddy is a remnant of the high salinity Subtropical Underwater, it injects 2.6×10^{16} g of salt into the Gulf. River runoff into the basin exceeded 1 800 km^3 in the period between eddy events in 1972-1973, only 700 km^3 of which are required to mix this 2.6×10^{16} g of excess eddy salt to the mean salinity in the upper layer ($T \geq 15°C$) of resident Gulf of Mexico water. While it appears that the periodic separation of these (typically) 400 km diameter anticyclonic eddies dominates the mass and salt exchange, ther is evidence that the remaining exchange involves smaller (< 50 km diameter) eddies.

Results based on the 1972-1973 data set indicate that river runoff can exceed evaporation minus precipitation, contrary to prior conclusions. In addition, because of the eddy exchange, the balance equation

$$E-P \lesseqgtr R-\delta \qquad (6)$$

must include an extra term, δ, to account for the excess salt injected into the Gulf of Mexico. Therefore, even though $E > P$, the Gulf of Mexico is not an "American Mediterranean" because of the term $R - \delta$ which has no counterpart in the arid lands of the eastern hemisphere

7. ACKNOWLEDGEMENTS

The many persons who assisted in collecting these data were acknowledged in the first article of this series. Data processing for Part II was assisted by M. McCaslin, N. Bright, and M. Pryslak. The manuscript was critically reviewed by Drs. A. Leetmaa, F. Chew, R. Molinari, D. Behringer, W. Sturges, and D. Hansen; the author especially thanks them for their suggestions and ideas. This paper was orally presented at the CICAR II Symposium, July, 1976, in Caracas, Venezuela.

8. REFERENCES

Austin, H.R., 1971 The characteristics and relationships between the calculated geostrophic current component and selected indicator organisms in the Gulf of Mexico Loop Current system. Ph.D. Dissertation, Florida State University, Tallahassee, 369 p.

Behringer, D.W., R.L. Molinari and J.F. Festa, 1977 The variability of anticyclonic current patterns in the Gulf of Mexico. J.Geophys.Res., 82(34):5469-76

Bernstein, R.L., L. Breaker and R. Whritner, 1977 California Current eddy formation. Science, Wash., 195:353-92

Broida, S., 1969 Geostrophy and direct measurements in the Straits of Florida. J.Mar.Res., 27(3):278-92

Brooks, I.H. and P.P. Niiler, 1975 The Florida Current at Key West: Summer 1972. J.Mar.Res., 33(1):83-92

Bue, C.D., 1970 Streamflow from the United States into the Atlantic Ocean during 1931-60. U.S. Gov't Printing Office, Geological Survey Water - Supply Paper 1899-I, 36 p.

Carder, K.L. et al., 1978 Washington, D.C., Dissolved silica and the circulation in the Yucatan Strait and deep eastern Gulf of Mexico. Deep Sea Res., (in press)

Cheney, R.E. and P.L. Richardson, 1976 Observed decay of a cyclonic Gulf Stream ring. Deep Sea Res., 23(2):143-55

Chew, F., K.L. Drennan and W.J. Demoran, Some results of drift bottle studies off the
1962 Mississippi Delta. Limnol.Oceanogr., 7(1):252-7

Cochrane, J.D., The Yucatan current. In Annual report, Project 286. College Station, Texas
1965 A&M University, Ref(65-17T):10-7

Cummings, A.D., Climatological aspects of the balance of water vapor in the atmosphere
1968 overlying the Gulf of Mexico, M.S. Thesis, Texas A&M University, 50 p.

De Rycke, R.J. and P.K. Rao, Eddies along a gulf stream boundary from a very high resolution radiometer. J.Phys.Oceanogr., 3:490-2
1973

Emery, W.J., Dynamic height from temperature profiles. J.Phys.Oceanogr., 5(2):369-75
1975

Etter, P.C., A climatic heat budget study of the Gulf of Mexico. M.S. Thesis, Texas
1975 A&M University, College Station, 87 p.

Franceschini, G.A., Hydrologic balance of the Gulf of Mexico. Ph.D. Dissertation, Texas
1961 A&M University, College Station, 58 p.

Fuglister, F.C., Annual variations in current speeds in the Gulf Stream. J.Mar.Res.,
1951 10:119-27

Gaul, R.D., Circulation over the continental margin of the northeastern Gulf of Mexico.
1967 Ph.D. Dissertation, Texas A&M University, College Station, 172 p.

Gordon, A.L., Circulation of the Caribbean Sea. J.Geophys.Res., 77(24):6207-3
1967

Hall, C.S., An investigation of the Water Balance of the Basin of the Gulf of Mexico.
1969 M.S. Thesis, Texas A&M University, College Station, 39 p.

Hansen, D.V. and B.D. Zetler, Deep currents in the Yucatan Strait. EOS,Trans.Am.Geophys.
1972 Union, 53(4):392

Hansen, D.V. and R.L. Molinari, Deep currents in the Yucatan Strait. J.Geophys.Res.
1978 (submitted for publication)

Jacobs, W.C., The energy exchange between sea and atmosphere and some of its consequences.
1951 Bull.Scripps Inst.Oceanogr., 6(2):27-122

Jacobsen, J.P. and A.J.C. Jensen, Examinations of hydrographical measurements from the
1926 research vessels Explorer and Dana during the summer of 1924. Rapp.P.-V.Réun.
CIEM, 39:31-84

Lee, T.N., Florida Current spin-off-eddies. Deep-sea Res., 22:753-65
1975

Legeckis, R., Application of synchronous meteorological satellite data to the study of
1975 time dependent sea surface temperature changes along the boundary of the Gulf
Stream. Geophys.Res.Lett., 2(10):485-8

Leifeste, D.K., Dissolved-solids discharge to the oceans from the conterminous United
1974 States. Circ.U.S.Geol.Surv., (685):8 p. Geological Survey: 8 pgs.

Leipper, D.F., A sequence of current patterns in the Gulf of Mexico. J.Geophys.Res.,
1970 75(3):637-57

Marmer, H.A., Tides and sea level in the Gulf of Mexico. Fish.Bull.U.S.Fish.Wildl.Ser.,
1954 56(89):101-18

Maul, G.A., An evaluation of the use of the earth resources technology satellite for
1975 observing ocean current boundaries in the Gulf Stream system. NOAA Tech.Memo.
(ERL 335-AOML 18): 125 p.

Maul, G.A., D.R. Norris and W.R. Johnson, Satellite photography of eddies in the Gulf Loop
1974 Current. Geophys.Res.Lett., 1(6):256-8

Molinari, R.L., Data from the NOAA ship Virginia Key and the SUSIO ship Bellows, collected
1974 during CICAR survey, Month II. NOAA Tech.Memo., (ERL AOML-22):153 p.

__________, An overview of the Cayman Sea - Gulf of Mexico circulation based on CICAR
1978 survey month and other data. FAO Fish.Rep., (200) Suppl.

Molinari, R.L. and R. Yager, Upper layer hydrographic conditions at the Yucatan Strait
1977 during May, 1972. J.Mar.Res., 35(1):11-20

Molinari, R.L. et al., Winter intrusions of the Loop Current. Science,Wash., 198:505-7
1977

Montgomery, R.B., Transport of the Florida Current off Havana. J.Mar.Res., 4:198-220
1941

Moody, C.L., Gulf of Mexico distributive province. AAPG Bulletin, 51(2):179-99
1967

Morrison, J.M. and W.D. Nowlin, Jr. Repeated nutrient, oxygen, and density sections through
1977 the Loop Current. J.Mar.Res., 35(1):105-28

Morrison, J.M., W.J. Merrel, Jr. and W.D. Nowlin, Jr. The waters of the eastern Gulf of
1973 Mexico as observed during May 1972. College Station, Texas A&M University, Ref.
(73-10):330 p.

Niiler, P.P. and W.S. Richardson, Seasonal variability of the Florida Current. J.Mar.Res.,
1973 31(3):144-67

Nowlin, W.D. and H.J. McLeilan, A characterization of the Gulf of Mexico waters in winter.
1967 J.Mar.Res., 25(1):29-59

Robinson, M.K., Atlas of monthly sea surface and subsurface temperature and depth of the
1973 top of the thermocline, Gulf of Mexico and Caribbean Sea. Scripps Inst.Oceanogr.
Ref.(73-8):105 p.

Rossov, V.V., Water circulation in the Gulf of Mexico and Caribbean Sea. Dokl.Akad.Nauk
1966 SSSR, 166:202-4 (in Russian)

Schlitz, R.J., Net total transport and net transport by water mass categories for Yucatan
1973 Channel based on data for April 1970. Ph.D. Dissertation, Texas A&M University,
College Station, 107 p.

Shulka, J. and B.M. Misra, Relationships between sea surface temperature and wind speed over
1977 the central Arabian Sea, and monsoon rainfall over India. Mon.Weather Rev.,
105:998-1002

Starr, V.P., J.P. Peixoto and G.C. Lividas, On the meridianal flux of water vapor in the
1958 northern hemisphere. Goefys.Para Appl., 39(1):174-85

Sturges, W. and J.P. Blaha, A western boundary current in the Gulf of Mexico. Science, Wash.,
1976 192:367-9

SUSIO ((Florida) State University System Institute of Oceanography), Compilation and summation
1975 of historical and existing physical oceanographic data from the eastern Gulf of Mexico. St. Petersburg, Fla., Final Report, BLM Contract 08550-CT4-16, 97 p.

Voorhis, A.D., E.H. Schroeder and A. Leetmaa, The influence of deep mesoscale eddies on
1976 sea surface properties in the North Atlantic subtropical convergence. J.Phys. Oceanogr., 6(6):953-61

Wennekens, M.P., Water mass properties of the straits of Florida and related waters.
1959 Bull.Mar.Sci., 9(1):1-52

Wüst, G. and A. Gordon, Stratification and circulation in the Antillean-Caribbean basins.
1964 Part 1.

48. CICAR-II Symposium on Progress in Marine Research in the Caribbean and Adjacent Regions, FAO Fisheries Report No. 200 Supplement, 1977, 51-61.

A DESCRIPTION OF THE CIRCULATION OBSERVED IN THE EASTERN GULF OF MEXICO DURING CICAR SURVEY MONTH II, MAY 1972

by

W.J. MERRELL, JR.
NSF/IDOE
Washington D.C., 20550, U.S.A.

J.M. MORRISON and W.D. NOWLIN, JR.
Department of Oceanography
Texas A. & M. University
College Station, Texas 77843, U.S.A.

R.L. MOLINARI
NOAA/AOML
Miami, Florida 33149, U.S.A.

I.H. BROOKS and R. YAGER
Nova University
Dania, Florida 33004, U.S.A.

CONTENTS

1. INTRODUCTION
2. CIRCULATION PATTERN
3. WATER MASSES, VERTICAL DISTRIBUTIONS
4. TRANSPORT
5. ACKNOWLEDGEMENTS
6. REFERENCES

Abstract

During CICAR Survey Month II, May 1972, a coordinated effort to describe the circulation in the eastern Gulf of Mexico was made by four independent research groups. Repeated crossings of the CICAR Standard Sections at the Yucatan Strait and the Straits of Florida were made, while other data were collected within the Gulf.

The Loop Current, entering the Gulf through the Yucatan Strait, was observed to penetrate only as far north as 25°N. A large anticyclonic ring, with radius of at least 210 km, is known to have separated from the Loop during April and was centred at approximately 26°30'N and 87°W.

The distributions of temperature, salinity, dissolved oxygen, silicate and phosphate are related to the current régime and water masses present within the eastern Gulf of Mexico.

For both Straits, calculations of volume transport from the sea surface to the isopycnal $\sigma_t = 27.0$ (approximately 400 to 500 m) were made. The transports through the Florida Straits were determined by the direct method using dropsondes. Geostrophic transports were referenced to directly measured surface velocities within the Yucatan Straits. When averaged over one month these transport estimates (with error of ±10 percent) agreed well and gave a mean value of $22 \times 10^6 m^3 sec^{-1}$.

During the month, three sections were occupied across the Loop Current within the Gulf of Mexico. One of these sections was repeated four times. Geostrophic transport estimates were made relative to the bottom, or the greatest depth sampled on a section. These crossings gave an average value of $30 \times 10^6 m^3 sec^{-1}$ for the Loop Current within the Gulf of Mexico. The average transport above $\sigma_t = 27.0$ mg cm^{-3} was $24 \times 10^6 m^3 sec^{-1}$.

Calculations of the geostrophic transport of the anticyclonic ring were also made relative to 1 000 db. The average transport was 29 x $10^6 m^3 sec^{-1}$ for two crossings of the ring. Above σ_t = 27.0 mg cm^3, the average ring transport was 23 x$10^6 m^3 sec^{-1}$.

Resumen

En mayo de 1972, segundo mes de las ICCRA, cuatro grupos independientes de investigadores trabajaron coordinadamente para describir la circulación de las aguas en la parte oriental del Golfo de México, recorriendo repetidamente las secciones-tipo de las ICCRA del Estrecho de Yucatán y de los Estrechos de la Florida, al mismo tiempo que recogían otros datos dentro del Golfo.

Se observó que la corriente circular que penetra en el Golfo por el Estrecho de Yucatán sólo llegaba, al norte, hasta los 25°N. Se sabe que en el mes de abril se separó un amplio remolino anticiclónico, de al menos 215 km de radio, que se localizó a 26°30'N y 87°O, aproximadamente.

La distribución de temperaturas, salinidad, oxígeno disuelto, silicatos y fosfatos se relaciona con el régimen de corrientes y las masas de aguas de la parte oriental del Golfo de México.

Se calculó, para ambos estrechos, el transporte volumétrico desde la superficie del mar a la isopicna σ_t = 27,0 (400 a 500 m, aproximadamente). Los transportes por los Estrechos de la Florida se determinaron directamente, utilizando sondas de caída libre. Los transportes geostróficos se compararon con las velocidades superficiales dentro de los Estrechos de Yucatán, medidas directamente: los promedios mensuales de estos cálculos de las velocidades de transportes - con un error de ± 10 % - concuerdan bien, dando un valor medio de 22 x $10^6 m^3 seg^{-1}$.

Durante el mes se hicieron tres secciones transversales de la corriente circular, dentro del Golfo de México, repitiéndose una de ellas cuatro veces. Se hicieron cálculos del transporte geostrófico con relación al fondo o al punto de muestreo de máxima profundidad en una de las secciones. Estos recorridos dieron un valor medio de 30 x $10^6 m^3 seg^{-1}$ para lo corriente circular dentro del Golfo de México; el transporte medio anterior, σ_t = 27,0 mg cm^{-3} fue de 24 x $10^6 m^3 sec^{-1}$.

Se hicieron también cálculos del transporte geostrófico del remolino anticiclónico con respecto a 1 000 db: para dos recorridos del remolino, el transporte medio fue de 29 x $10^6 m^3 seg^{-1}$. Por encima de σ_t = 27,0 mg cm^{-3}, el transporte medio fue de 23 x $10^6 m^3 seg^{-1}$.

1. INTRODUCTION

During CICAR Survey Month II, May 1972, a major field programme was conducted in the eastern Gulf of Mexico. The basic objective of this coordinated effort was to monitor the Loop Current and the currents in the Yucatan and Florida Straits simultaneously. This paper presents a summary of some of the data collected by scientists from the Atlantic Oceanographic and Meteorological Laboratories (AOML) of the National Oceanic and Atmospheric Agency (NOAA), the State University System Institute of Oceanography (SUSIO) of Florida, Nova University and Texas A. & M. University.

Fig. 1 illustrates the cruise coverage and the four sections which were selected for repeated observations. Transports across sections in the Florida Straits and surface velocities in the Yucatan Straits were determined by dropsondes deployed from Nova aircraft. Scientists aboard NOAA's R/V VIRGINIA KEY collected STD and XBT observations during 15 crossings of the Yucatan Strait. In the Florida Straits, Nova's R/V GULFSTREAM completed 16 dropsonde and STD sections at the longitude of Key West. Within the Gulf, scientists aboard SUSIO's R/V BELLOWS and Texas A. & M. University's R/V ALAMINOS surveyed the Loop Current region with STD, XBT and nutrient observations. Moreover, the ALAMINOS occupied one standard section within the Gulf four times during May. The University of Miami and the Instituto de Geofísica of the Universidad Nacional Autónoma de México also conducted cruises in the region during May. However, their observations are not used in this overview.

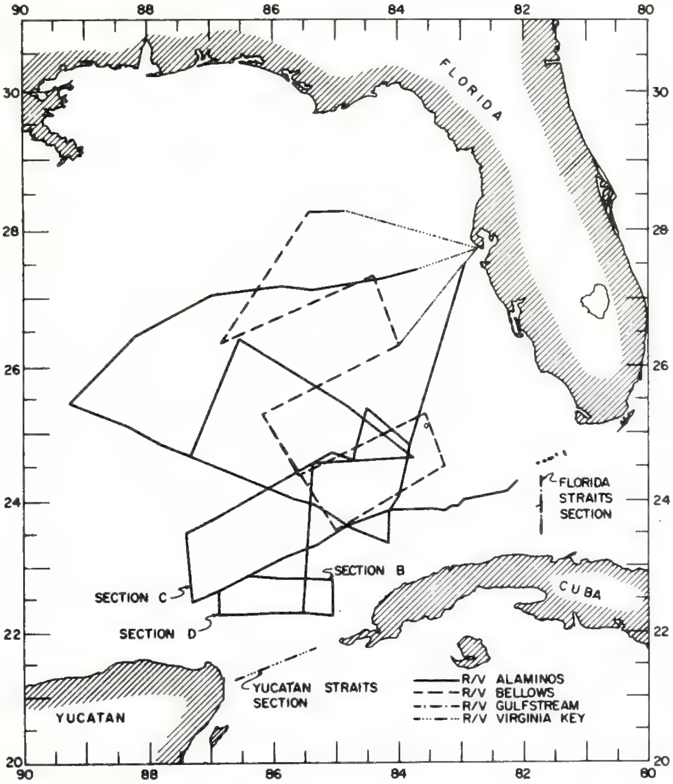

Fig. 1 Combined cruise tracks for the R/V ALAMINOS, R/V BELLOWS, R/V GULFSTREAM and R/V VIRGINIA KEY for the 1972 field programme

The original data may be found in technical reports distributed by the various institutions or be obtained upon request from the scientists involved. The data collected from the ALAMINOS have been distributed as Data Report 73-10T of the Texas A. & M. Research Foundation (Morrison, Merrell and Nowlin, 1973). Molinari (1974) has distributed the data from the R/V VIRGINIA KEY and R/V BELLOWS as a NOAA technical memorandum.

Several papers have already been written using data collected during CICAR Survey Month II. Brooks and Niiler (1975) reported on simultaneous measurements of the current and density fields of the Florida Current at the section between Key West, Florida, and Matanzas, Cuba. Molinari and Yager (1976) have described the average hydrographic conditions of a section across the Yucatan Straits. Morrison and Nowlin (1976) relate the nutrient and dissolved oxygen concentrations in the eastern Gulf to the Loop Current and anticyclonic current rings. They also give some estimates of the variability of both the property distributions and relative geostrophic flow within a period of a few weeks. We intend here to summarize and interrelate much of this information and to add some additional information.

2. CIRCULATION PATTERN

The major features of the current régime of the eastern Gulf of Mexico are the Loop Current (which is comprised of the Yucatan Current and its downstream extension through the Gulf and into the Florida Straits) and the anticyclonic rings which separate from this current. The topography of any isothermal surface between about 10° and 22°C has been shown repeatedly to be a good indicator of the geostrophic current régime in the eastern Gulf of Mexico.

In the spring of 1972, the circulation pattern of the eastern Gulf of Mexico was changing rapidly. A vertical section of temperature along an ALAMINOS section through the Gulf during March is presented in Fig. 2. These data indicate that between 25 March and 27 March 1972 the Loop Current extended well into the Gulf and that no detached ring was present. This picture had changed considerably by May. The repetitive nature of the cruise tracks of the four research vessels involved in CICAR Survey Month II allow us to illustrate (Figs. 3, 4 and 5) the circulation pattern as indicated by the 22°C isothermal surface, for three separate periods during May.

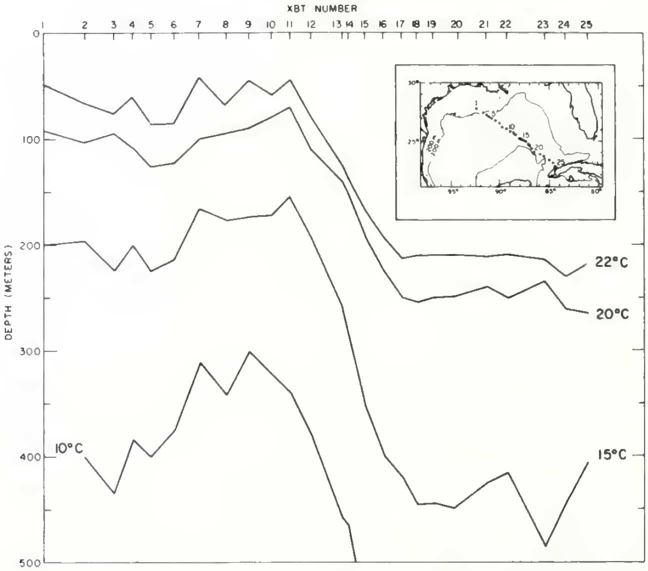

Fig. 2 Vertical section of temperature (°C) for an ALAMINOS section through the Gulf of Mexico in March 1972. The insert shows the position of the XBTs used in constructing this section

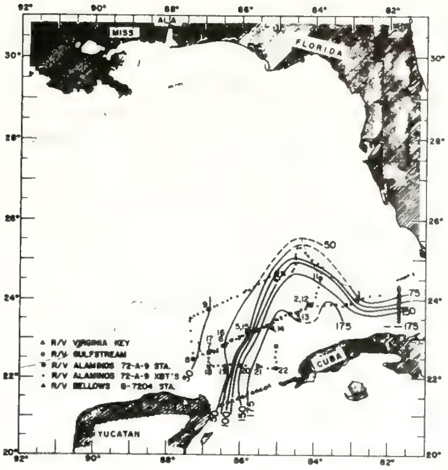

Fig. 3 Depth of 22°C isotherm within the eastern Gulf of Mexico using data collected from 2 to 8 May 1972

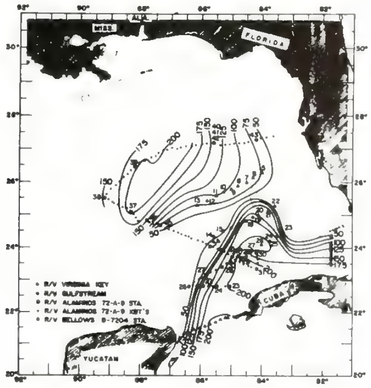

Fig. 4 Depth of 22°C isotherm within the eastern Gulf of Mexico using data collected from 8 to 13 May 1972

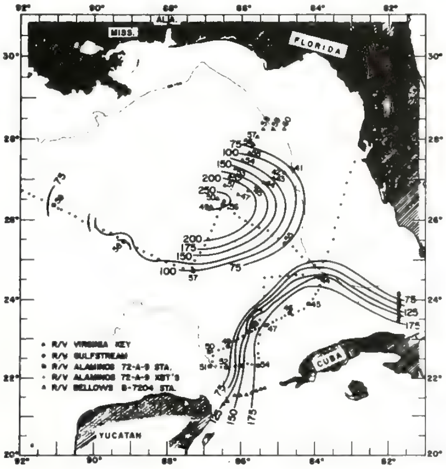

Fig. 5 Depth of 22°C isotherm within the eastern Gulf of Mexico using data collected from 16 to 21 May 1972

Some details of the changes in the circulation pattern during May are indicated by comparison of the three figures. The Loop Current did not extend quite as far to the north in the third time period as it did in the first two periods. The observed portion of the detached ring became symmetrical between the second and third observation periods.

3. WATER MASSES, VERTICAL DISTRIBUTIONS

The traditional method of identifying water masses is through the use of temperature-salinity (T-S) relationships. A composite of T-S curves for the eastern Gulf of Mexico is presented in Fig. 6, constructed from STD data collected with the R/V BELLOWS. The principal features are the extreme in salinity associated with the presence of Antarctic Intermediate Water and Subtropical Underwater. Antarctic Intermediate Water is indicated by the salinity minimum near 6.3°C of 34.84-34.88 °/oo and Subtropical Underwater is depicted by the salinity maximum near 22.5°C. This maximum varies from values of 36.75 °/oo within waters bounded by the Loop Current (Caribbean-type) to 36.40 °/oo for waters within the Gulf and outside of the Loop Current (Gulf-type water).

The distributions of temperature and salinity across the Loop Current can best be seen in vertical sections (Fig. 7, from Morrison and Nowlin, 1976). Fig. 7a is a vertical section of temperature constructed from STD and XBT observations taken during the ALAMINOS' first crossing of section C. Isotachs of relative geostrophic speed are presented in the background. This section shows two areas of intense temperature gradients which correspond to the inflow and outflow of the Loop Current. As one would expect, assuming geostrophy and a rather uniform T-S relationship, the regions of greater isotherm slope correspond to the greater current speeds. However, one should remember that section C is not perpendicular to the current (especially the inflow) so we cannot infer maximum speeds from this section. We note that the areas of intense current are relatively narrow and the Loop Current is a transition zone between the relatively warm Caribbean waters and the colder Gulf waters.

Fig. 7b shows values of salinity along the section. The salinity maximum (greater than 36.6 °/oo at 200 m) associated with the Subtropical Underwater delineates the extent of the Caribbean waters. The minimum associated with the Antarctic Intermediate Water occurs at about 700-900 m with the greater depths found at the centre of the Loop reflecting the mass adjustments associated with the current régime.

Other parameters may also be used to depict the distribution of water masses within the Gulf. Vertical distributions of dissolved oxygen, silicate and phosphate for two stations characterizing Caribbean Water (Sta. 36) and Gulf Water (Sta. 33) are presented in Fig. 8. The dissolved-oxygen concentrations show the very distinct differences between these two water masses. Within the Caribbean-type waters a relative maximum of dissolved oxygen is found at approximately 300 m. This maximum denotes the presence of 18°C Sargasso Sea water within the Caribbean-type water (Morrison and Nowlin, 1976). Because of mass field adjustments caused by the Loop Current, the main oxygen minimum occurs at increasing depth as the current is traversed from Gulf Water to Caribbean Water. Distributions of silicate and phosphate are less useful than oxygen for delineating water mass in the Gulf of Mexico. The main features of these distributions are the maxima of silicate and phosphate associated with Antarctic Intermediate Water.

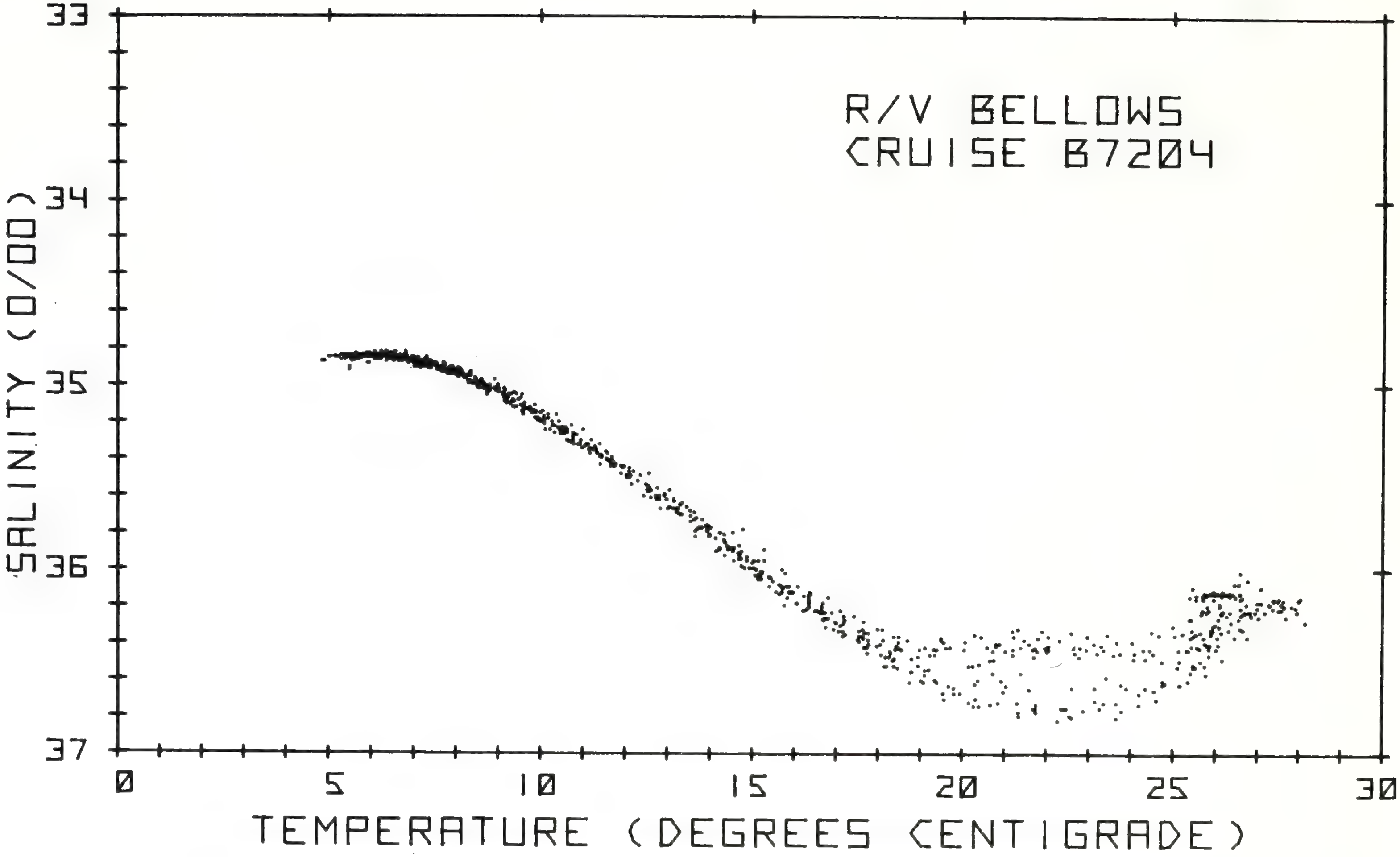

Fig. 6 Temperature-salinity diagram for the eastern Gulf of Mexico using data collected with the R/V BELLOWS during May 1978

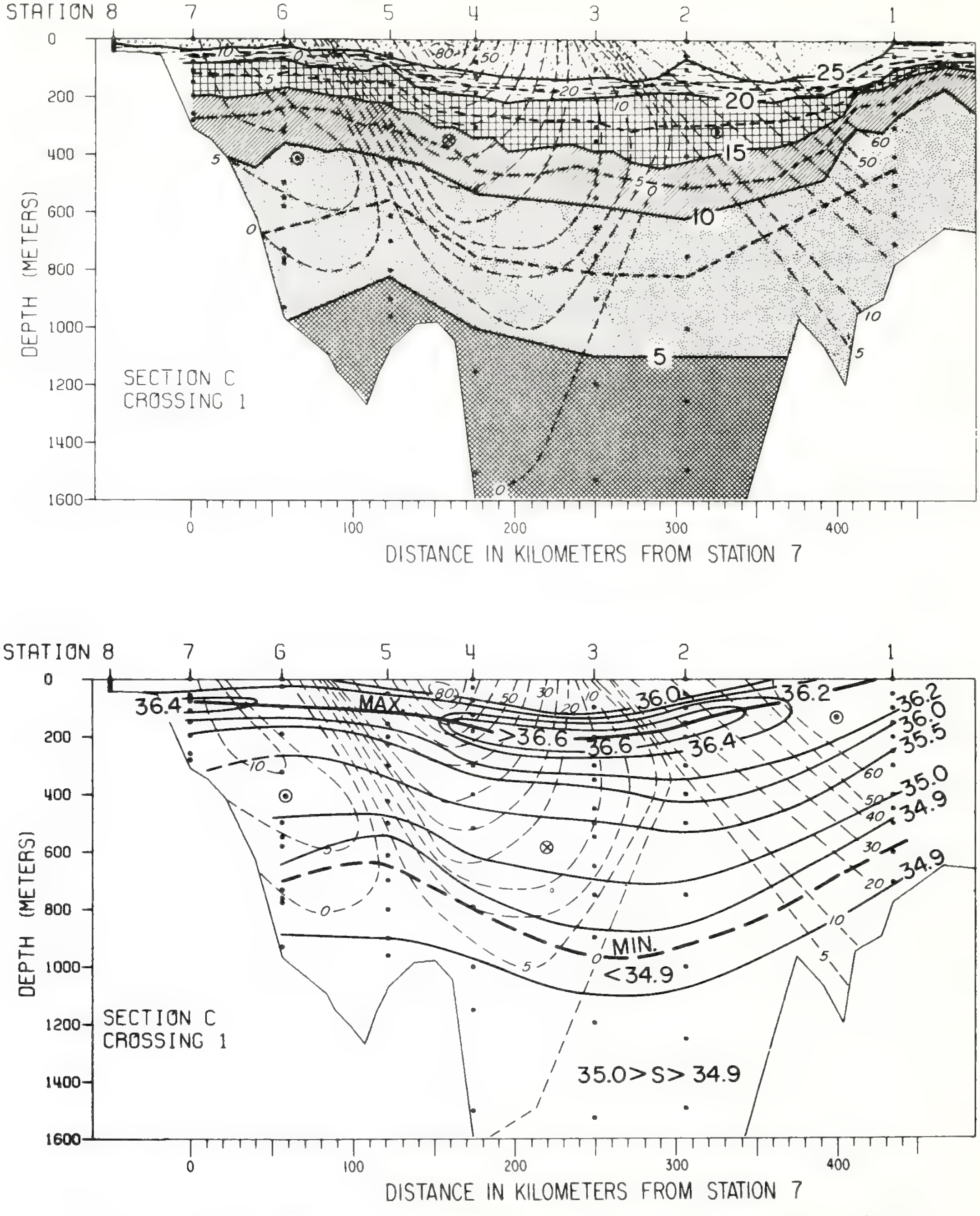

Fig. 7 Vertical sections of: (a) temperature (°C) and (b) Salinity (°/oo) for crossing of section C with superimposed isotachs of relative geostrophic speed (cm/sec). These sections were constructed from ALAMINOS data (after Morrison and Nowlin, 1976)

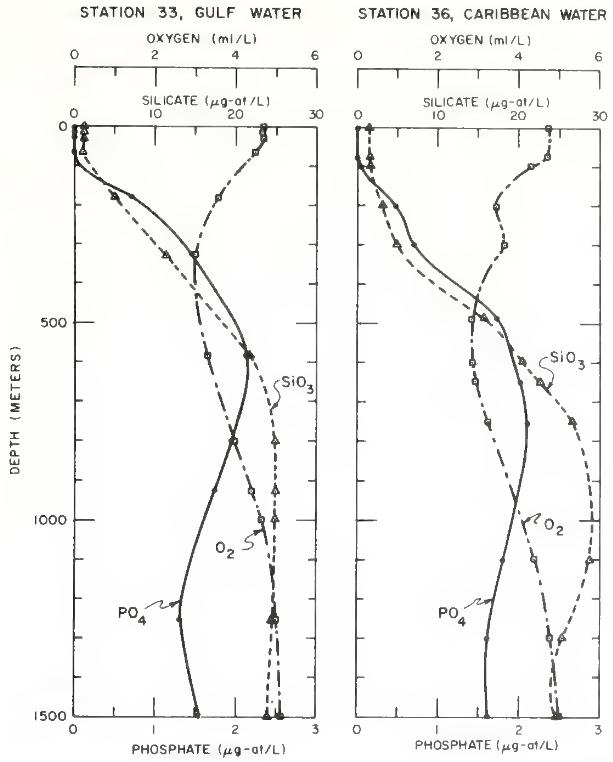

Fig. 8 Vertical distribution of dissolved oxygen (ml/l), silicate (ug-at/l) and phosphate (μg-at/l) for a station within Gulf-type water (ALAMINOS Sta. 33) and a station within Caribbean-type water (ALAMINOS Sta. 36)

4. TRANSPORT

We present in Fig. 9 the volume transport through different sections within the eastern Gulf of Mexico. Downstream distance from the Yucatan Straits is the ordinate and the date of observation is the abscissa. Molinari and Yager (1976) referenced transports in the Yucatan Straits to direct velocity measurements at the surface. Owing to data quality problems, the transport is presented as an average for four periods during May. Morrison and Nowlin (1976) calculated transports for three sections through the Loop Current. These transports were referenced to the deepest observation on each section. The transports through the Florida Straits were determined by the direct method using dropsondes (Brooks and Niiler, 1975). They chose the $\sigma_t = 27.0$ mg cm^{-3} density surface as an arbitrary bottom. Their ensemble averaged transport for May and June is roughly 75 percent of the transport noted by Richardson and Niiler (1969) for the entire water column during the same months in 1966. As the transport values at the Florida Straits were only available down to the $\sigma_t = 27.0$ mg cm^{-3} density surface, all transports given in Fig. 9 are for geostrophic flow between the sea surface and this density surface.

An examination of Fig. 9 shows that, in spite of different procedures and data quality problems, the transports are rather consistent over the observed spatial and temporal scales. The average transports between the surface and $\sigma_t = 27.0$ mg cm^{-3} are $22.3 \times 10^6 m^3 sec^{-1}$ at the Yucatan Straits, $24.2 \times 10^6 m^3 sec^{-1}$ for the Loop Current and $21.4 \times 10^6 m^3 sec^{-1}$ at the Florida Straits. This agreement is remarkable when one considers that the transports calculated for the two Straits may be low, since those sections stopped about 35 km from Cuba and probably do not capture the entire flow. These values yield an average transport between the surface and $\sigma_t = 27.0$ mg cm^{-3} of approximately $23 \times 10^6 m^3 sec^{-1}$ for the Loop Current during May 1972.

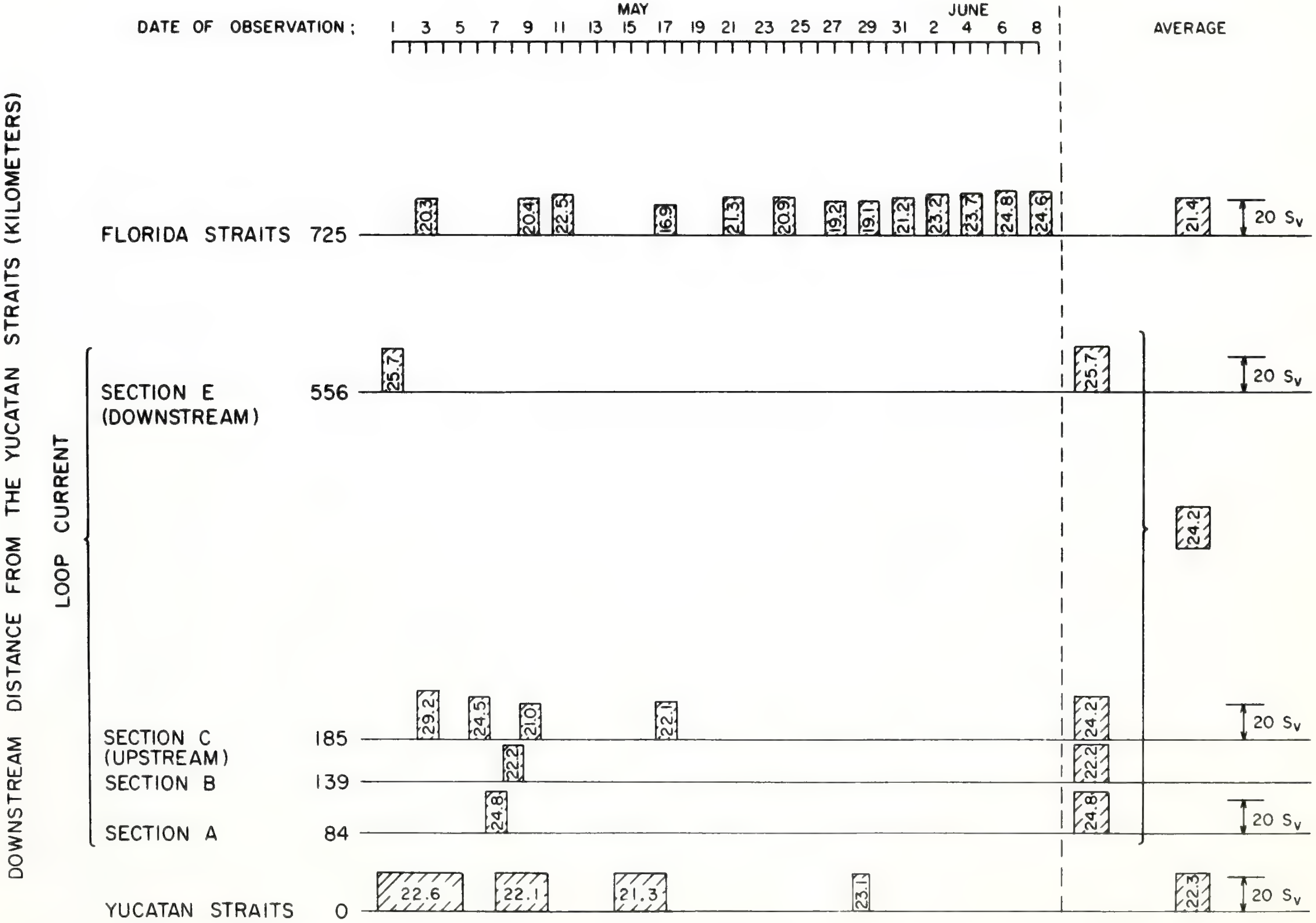

Fig. 9 Relative geostrophic transport (in units of $10^6 m^3 sec^{-1}$) above $\sigma_t = 27.0$ mg cm^{-1} for sections across the Loop Current during May and June 1972

There is some evidence of a slight increase of transport at the Florida Straits late in the record (June) which may correspond to the annual buildup of the Florida Current to a maximum in summer. Otherwise, within observational accuracies, the transports show no trends with time or downstream distance.

Morrison and Nowlin (1976) report that the total average transport of the Loop Current during May 1972, where the deepest observation on each section was used as the reference, was 30 x $10^6 m^3 sec^{-1}$. This agrees well with transport estimates given for this current where a variety of methods of referencing were used. Nowlin and Hubertz (1972) estimated the geostrophic transport within the upper 1 350 db to be 30 x $10^6 m^3 sec^{-1}$. Nowlin and McLellan (1967) calculated a geostrophic transport of 30 x $10^6 m^3 sec^{-1}$ within the upper 1 000 db. Schmitz and Richardson (1968) gave an average transport value of 29.6 x $10^6 m^3 sec^{-1}$ through the Florida Straits using the dropsonde method.

Transports were also calculated for the detached ring using data collected aboard R/V BELLOWS where 1 000 m was chosen as the reference level. For two crossings, the net transports between the surface and 1 000 m were 32.0 x $10^6 m^3 sec^{-1}$ and 26.7 x $10^6 m^3 sec^{-1}$. The average transport is 29.3 x $10^6 m^3 sec^{-1}$ which compares quite well with the transport of the parent Loop Current. The average volume transport between the surface and σ_t = 27.0 x $10^6 m^3 sec$ is 23.1 x $10^6 m^3 sec$, which agrees with this layer during May 1972.

5. ACKNOWLEDGEMENTS

This work was supported by the Office of Naval Research.

6. REFERENCES

Brooks, I.H. and P.P. Niiler, 1975 The Florida Current at Key West: Summer 1972. J.Mar.Res., 21:83-92

Molinari, R.L., 1974 Data from the NOAA ship VIRGINIA KEY and the SUSIO ship BELLOWS collected during CICAR Survey Month II. NOAA Tech.Memo., (ERL AOML-22):153 p.

Molinari, R.L. and R.E. Yager, 1977 Upper layer hydrographic conditions at the Yucatan Strait during May 1972. J.Mar.Res., 35(1):11-20

Morrison, J.M. and W.D. Nowlin, Jr., 1977 Repeated nutrient, oxygen and density sections through the Loop Current. J.Mar.Res., 35(1):105-28

Morrison, J.M., W.J. Merrell, Jr. and W.D. Nowlin, Jr., 1973 The waters of the eastern Gulf of Mexico as observed during May 1972: I. Data collected aboard the R/V ALAMINOS. College Station, Texas A. & M. University, Department of Oceanography, Ref. (73-10-T):330 p.

Niiler, P.P. and W.S. Richardson, 1973 Seasonal variability of the Florida Current. J.Mar.Res., 31(3):144-67

Nowlin, W.D., Jr. and J.M. Hubertz, 1972 Contrasting summer circulation patterns for the eastern Gulf. In Contributions on the physical oceanography of the Gulf of Mexico edited by L.R.A. Capurro and J.L. Reid. Houston, Gulf Publishing Co., pp. 119-37

Nowlin, W.D., Jr. and H.J. McLellan, 1967 A characterization of the Gulf of Mexico waters in winter. J.Mar.Res., 25:29-59

Schmitz, W.J. and W.S. Richardson, 1968 On the transport of the Florida Current. Deep-Sea Res., 15:679-94

49. CICAR-II Symposium on Progress in Marine Research in the Caribbean and Adjacent Regions, FAO Fisheries Report No. 200 Supplement, 1977, 79-102.

TIDES IN THE GULF OF MEXICO AND CARIBBEAN SEA

by

H.O. MOFJELD[1]
Atlantic Oceanographic and
Meteorological Laboratories
Miami, FL 33149
U.S.A.

M. WIMBUSH[2]
Physical Oceanography Laboratory
NOVA University
Diana, FL 33004
U.S.A.

CONTENTS

1. BACKGROUND
2. INSTRUMENTATION
3. OBSERVED TIDES
4. LOW-FREQUENCY PRESSURE CONTINUUM
5. DISCUSSION
6. ACKNOWLEDGEMENTS
7. REFERENCES
APPENDIX

Abstract

Offshore pressure gauges were deployed in the Gulf of Mexico and the Caribbean Sea to measure tides and bottom pressure continua. The observations, in the Gulf of Mexico, indicate that it has a Helmholtz resonance with a period of 1.6 d. While the lack of confidence limits on theoretical cotidal charts hinders the comparison between theories and observations, the latter tend to support a model with direct astronomical forcing. The observations in the Caribbean Sea verify the general features of the theoretical cotidal charts. At a six-month-long station in the eastern Caribbean, bottom pressure fluctuations with 4 to 5 d period are coherent and in phase with atmospheric waves in the Easterlies. Inverse barometer compensation appeared less complete in this semi-enclosed sea, spanned by weather systems, than in the open ocean. An appendix gives corrections to the response method of tidal analysis, the procedure for converting the results to harmonic constants with error estimates, and tables of analytical results.

---

[1] Present address: Pacific Marine Environmental Laboratory, Environmental Research Laboratory, National Oceanic and Atmospheric Administration, Seattle, WA 98105, U.S.A.

[2] Present address: Graduate School of Oceanography, University of Rhode Island, Kingston, RI 02881, U.S.A.

Resumen

Se colocaron indicadores de presión en alta mar en el Golfo de México y Mar Caribe para medir las mareas y los continuos de presión al fondo. Las observaciones indican que el Golfo de México tiene una resonancia del tipo Helmholtz con un período de 1,6 días. La ausencia de límites de confianza en cartas teóricas de mareas dificulta la comparación de teorías y observaciones, pero los datos tienden a apoyar un modelo de regulación astronómica directa. Las observaciones en el Mar Caribe confirman los rasgos generales de la cartas teóricas. En una estación en el Caribe oriental ocupada durante seis meses, las oscilaciones de presión al fondo con un período de 4-5 días, coincidieron con las ondas atmosféricas en los vientos alisios de levante. En este mar semi-encerrado, atravesado integramente por sistemas atmosférios, la compensación barométrica inversa es aparentemente más débil que en el océano abierto. Un apéndice del trabajo incluye (i) correcciones al método de regresión (response method) de análisis de mareas, (ii) el procedimiento utilizado para convertir los resultados en constantes armónicas con estimación de los errores, y (iii) tablas de resultados analíticos.

1. BACKGROUND

To test theoretical models for tides and free oscillations in the Gulf of Mexico and the Caribbean Sea, offshore pressure observations were made (Fig. 1 and Table I) during 1971 to 1973 as part of the Cooperative Investigation of the Caribbean and Adjacent Regions (CICAR). Subsequent observations in 1974 are also considered.

1.1 Gulf of Mexico

Coastal observations (Zetler and D. Hansen, 1972) indicate that the daily tides dominate the western and northern Gulf of Mexico, even though the semi-daily tides are favoured both by co-oscillation with the Atlantic and by direct astronomical forcing. In these regions, the daily amplitudes and phases are relatively constant, and the phases are nearly opposite (180° difference in phase) to the corresponding phases in the western Atlantic and the eastern Caribbean Sea. The transition in phase occurs in the vicinity of amplitude nodes in the Straits of Florida and the Yucatan Channel.

According to Marmer (1954) a resonance of the gulf with a period near the daily tidal band causes the anomalously large daily tides. Platzman (1972) developed a theoretical model of the Gulf with realistic bathymetry and, using a resonance iteration technique, found a Helmholtz resonance with 0.88 d period and a spatial distribution similar to the daily tides. By assumption, this model requires surface elevation nodes in the Straits of Florida and in the Yucatan Channel. K. Hansen (1974) used a Lanczos process to compute resonances (free oscillations) in the combined Gulf of Mexico–Caribbean Sea system with nodes required in the Straits of Florida and at the Antilles. The lowest gravitational resonance has a period (1.04 d) near the daily tidal band but lacks a node in the Yucatan Channel; the next highest resonance has a node in the channel but has a period (0.67 d) nearer the semi-daily band. The mismatch of period and spatial distributions may be caused by the node at the Antilles not seen in the daily tides.

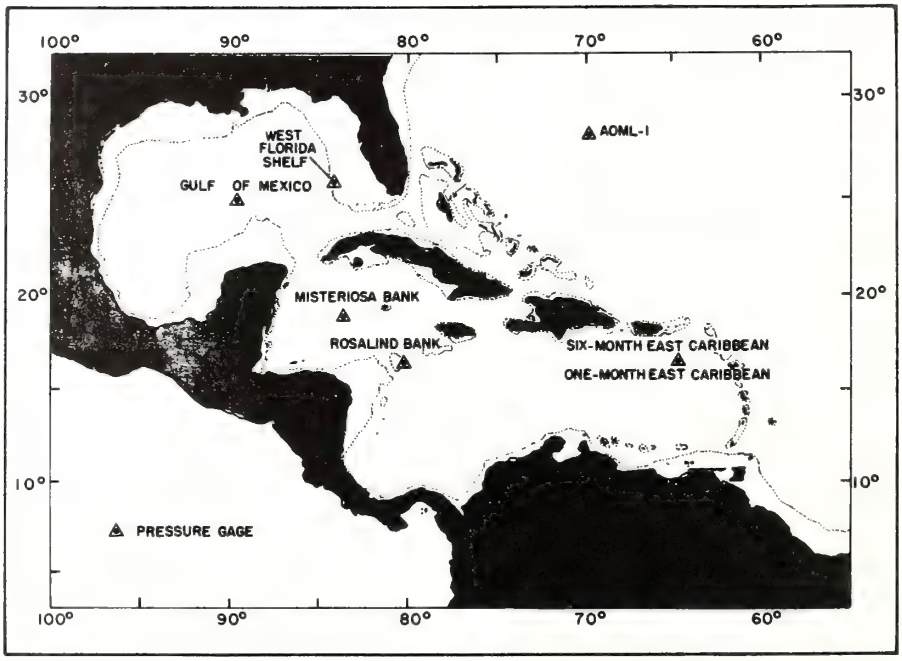

Fig. 1 Chart showing bottom pressure gauge and current meter stations in the Gulf of Mexico and Caribbean Sea. Also shown is the AOML-1 station in the western Atlantic Ocean

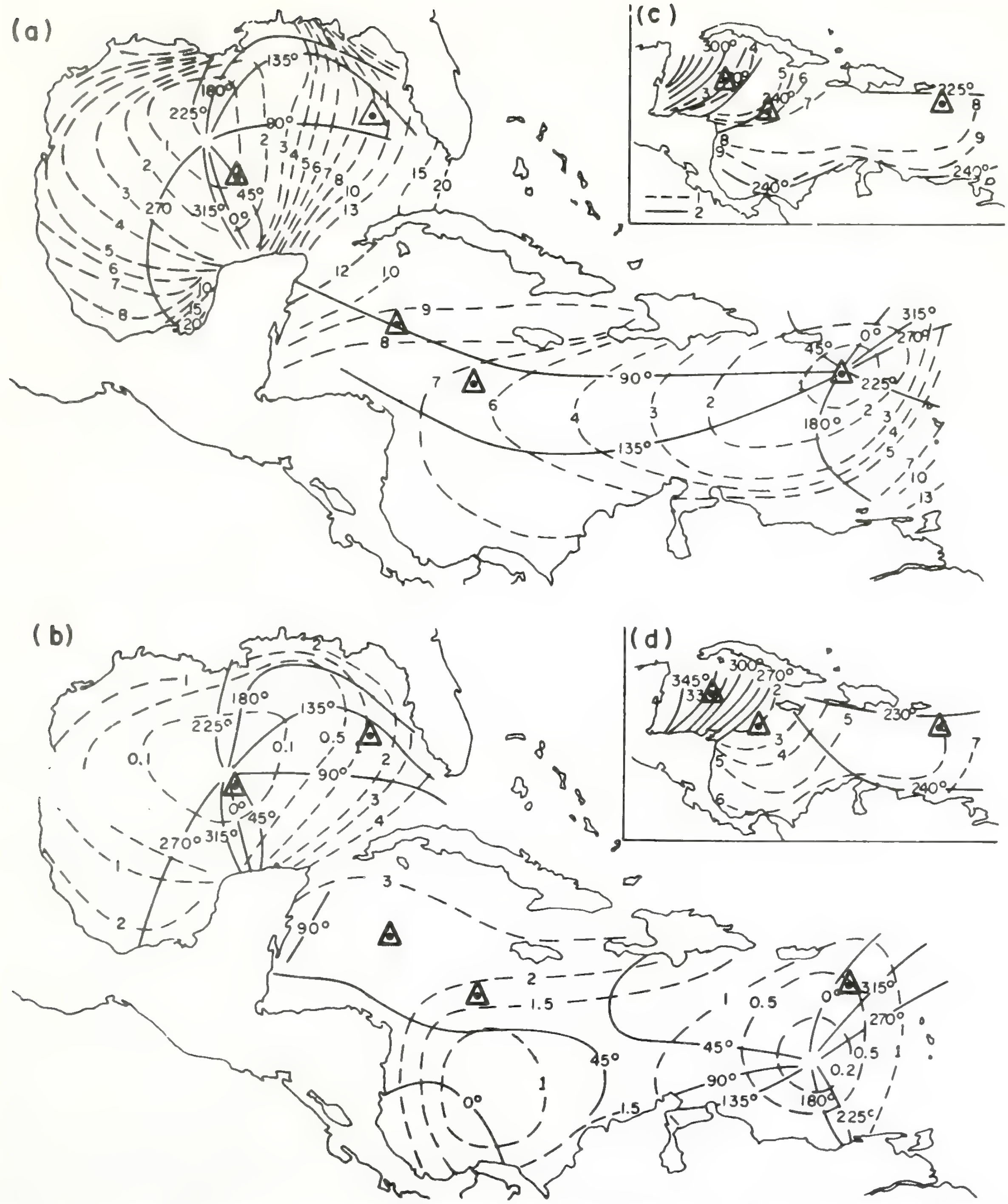

Fig. 2 Cotidal charts for the Gulf of Mexico and Caribbean Sea from the theoretical model by Michaelov, Melishko and Shcheveleva (1969). Cophase lines (solid) give the Greenwich phase lag in degrees; co-amplitude lines (dashed) give amplitudes in centimetres (a) semi-daily M_2 tide, (b) semi-daily S_2 tide, (c) daily K_1 tide, (d) daily O_1 tide

TABLE II

Standard deviation of harmonic constants from successive 29-d harmonic analyses at nearby shore and bottom-mounted tide stations

	Magueyes Island[a] (17°58.3N, 67°02.8W)				Six-month east Caribbean (16°32.5N, 64°52.9W)			
	Mean		Standard Dev		Mean		Standard Dev	
	H (cm)	G (deg)	H (cm)	G (deg)	H (cm)	G (deg)	H (cm)	G (deg)
N_2	0.40	52.0	0.34	66.1	0.58	128.4	0.07	5.5
N_2	0.70	52.5	0.34	38.0	0.51	155.5	0.10	13.4
S_2	0.71	348.0	0.30	30.4	1.36	45.4	0.24	10.4
K_1	7.92	233.3	0.73	5.6	8.68	232.7	0.21	1.1
O_1	5.36	227.3	0.30	3.4	6.24	227.2	0.22	1.2

a/ From Zetler and Cummings (1972)

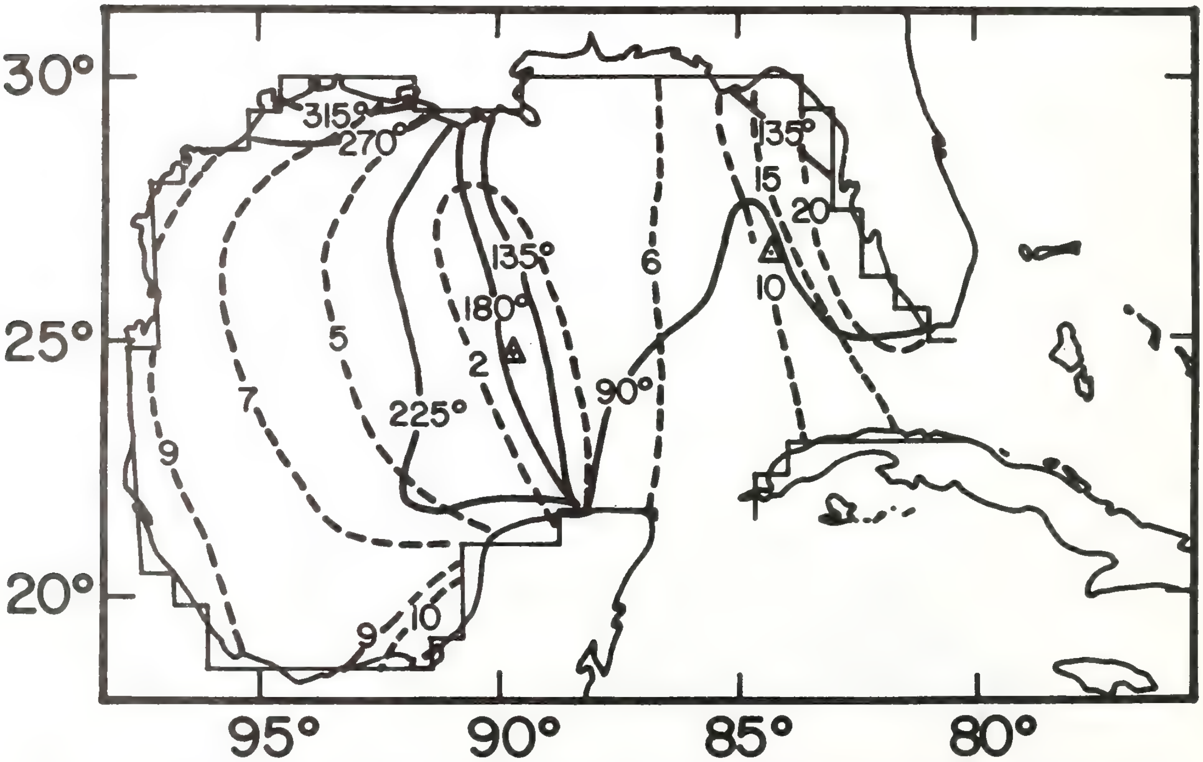

Fig. 3 Semi daily M_2 cotidal chart for the Gulf of Mexico from the theoretical model by Grijalva (1971). Cophase lines (solid) give the Greenwich phase lag in degrees; co-amplitude lines (dashed) give amplitudes in cm

TABLE I

Bottom pressure stations

Station	Latitude	Longitude	Depth (m)	Starting	Ending
Misteriosa Bank	18°52.9 N	83°48.3 W	22	15 July 71	13 Aug 71
Rosalind Bank	16°36.5 N	80°20.2 W	31	15 July 71	14 Aug 71
East Caribbean					
One-month	16°30.1 N	64°54.7 W	3 768	15 Sept 71	19 Oct 71
Six-month	16°32.5 N	64°52.9 W	3 990	17 May 72	9 Nov 72
Central Gulf of Mexico	24°46.1 N	89°38.9 W	3 461	11 Oct 72	18 Jan 73
West Florida Shelf	26°42.4 N	84°15.0 W	154	6 April 74	18 Nov 74

Theoretical work on daily tides per se in the Gulf of Mexico is limited to a model by Grace (1932) of K_1 tide. The model, which uses a small number of constant depth sections, correctly predicts a slowly varying K_1 tide in the western Gulf of Mexico but incorrectly predicts a large amplitude gradient across the Yucatan Channel.

Several models exist for the semi-daily tides in the Gulf of Mexico. Using W. Hansen's method (1952, 1962), Michaelov, Melishko and Shcheveleva (1969) computed cotidal charts (Fig. 2) for the combined Gulf of Mexico-Caribbean Sea system. Their model has a 40' grid spacing in the Gulf, uses realistic bathymetry and neglects non-linearities, friction, and direct astronomical forcing. Observed coastal harmonic constants are used as boundary conditions. Because of an apparent singularity at the critical latitude of the daily tides, these authors did not compute the daily tides in the Gulf of Mexico.

Also using W. Hansen's (1952, 1962) method, Grijalva (1971) computed the M_2 tide in the Gulf (Fig. 3). His model, which has a 30' grid spacing and includes friction and direct astronomical forcing of the water (but not the sea bed) specifies the surface elevation only at the Straits of Florida and the Yucatan Channel. Grijalva attributed the lack of an amphidromic point in his model to direct astronomical forcing.

Earlier theoretical work on tides in the Gulf is summarized by Zetler and D. Hansen (1970) while earlier work on resonances (free oscillations) is summarized by K. Hansen (1974).

1.2 Caribbean Sea

In the eastern Caribbean Sea, coastal and island observations show that the daily tides are relatively uniform with southward increases in phase consistent with those in the Atlantic. The amplitudes decrease slowly toward the west, decreasing more rapidly in the western Caribbean to apparent nodes in the Yucatan Channel. In the same region, there is a rapid increase in the daily phases. Michaelov et al. (1969) modelled the daily K_1 and O_1 tides in the Caribbean Sea on a 1° grid using the same assumptions they made for the Gulf. Their cotidal charts (Fig. 2) reproduce the general features of the daily tides in the Caribbean Sea.

The rapid, counter-clockwise increase in semi-daily phases and the small semi-daily amplitudes indicate that each semi-daily tide forms an amphidromic system in the eastern Caribbean. The semi-daily tides increase in amplitude toward the Yucatan Channel where they dominate the tidal régime. To test the M_2 model (Fig. 2) for the Caribbean Sea by Michaelov et al. (1969), the one-month east Caribbean station (Fig. 1 and Table I) was occupied at the theoretical M_2 amphidromic point. The resulting pressure series was analysed by Zetler and Cummings (1972) who found a small but non-zero, M_2 amplitude. The latter authors concluded from a study of successive 29-day series from nearby Magueyes Island that a 29-day series obtained near an amphidromic point might not yield an accurate harmonic constant for that constituent. The six-month east Caribbean station was therefore occupied, and results from that series are reported in this paper.

1.3 Low Frequency Pressure Continuum

Superimposed on the tidal signal in the open ocean is a bottom pressure continuum which is not well understood. At frequencies below the daily tidal band the continuum is thought to be associated with time-dependent geostrophic currents and atmospherically induced fluctuations. For the western Atlantic Ocean, Brown et al. (1975) found that the bottom pressure spectrum resembled the atmospheric pressure spectrum at low frequencies, but the bottom pressure and local atmospheric pressure were found to be only marginally coherent. The connexion between bottom pressure and atmospheric pressure is therefore more complex than a simple deviation from the inverse barometer compensation.

If the Gulf of Mexico has a resonance near the daily tidal band as proposed by Marmer (1954) it should be apparent in the bottom pressure continuum; the pressure spectra in the Gulf and the western North Atlantic should differ markedly near 1 cpd.

As discussed by Riehl (1954) the weather in the Caribbean Sea region is dominated by waves in the Easterlies that have periods of 4 to 5 d. It is interesting to speculate about the response of the semi-enclosed Caribbean Sea to forcing by these waves.

2. INSTRUMENTATION

The pressure series from the Caribbean Sea and from the central Gulf of Mexico station were obtained using Filloux (1970) deep-sea tide gauges. The gauges have metal Bourdon tube pressure transducers exposed to the full oceanic pressure. Intercomparison studies reported by the SCOR Working Group No. 27 (1975) and by Zetler et al. (1975) show that these gauges have a precision of at least 0.5 cm H_2O (relative to the mean), once a trend is removed from the data. The trend, due to creep in the Bourdon tubes, follows the logarithmic law proposed by Lomnitz (1956, 1957) and discussed by Jeffreys (1970). The long-term creep diverges from the Andrade's 1/3 power law proposed by Filloux (1970). Spurious shifts in the apparent background pressure occurred in the records from Misteriosa and Rosalind banks (Fig. 1). These shifts may be due to tilting of the gauges, as observed in laboratory tests; on the bottom, the tilting could be produced by wave-induced erosion around the instrument base. The analyses were limited to sections of record for which the background pressure was stable.

The pressure record from the West Florida shelf station was obtained with a pressure-temperature gauge described by Wimbush (1977). It used a 250-psi Vibrotron pressure sensor and a thermistor temperature sensor (to correct for a slight temperature sensitivity of the Vibrotron). Outputs of these sensors were integrated over the full sampling interval (1/8h); the sensitivity of the system is limited by Vibrotron noise, which is very small compared with the tidal signal.

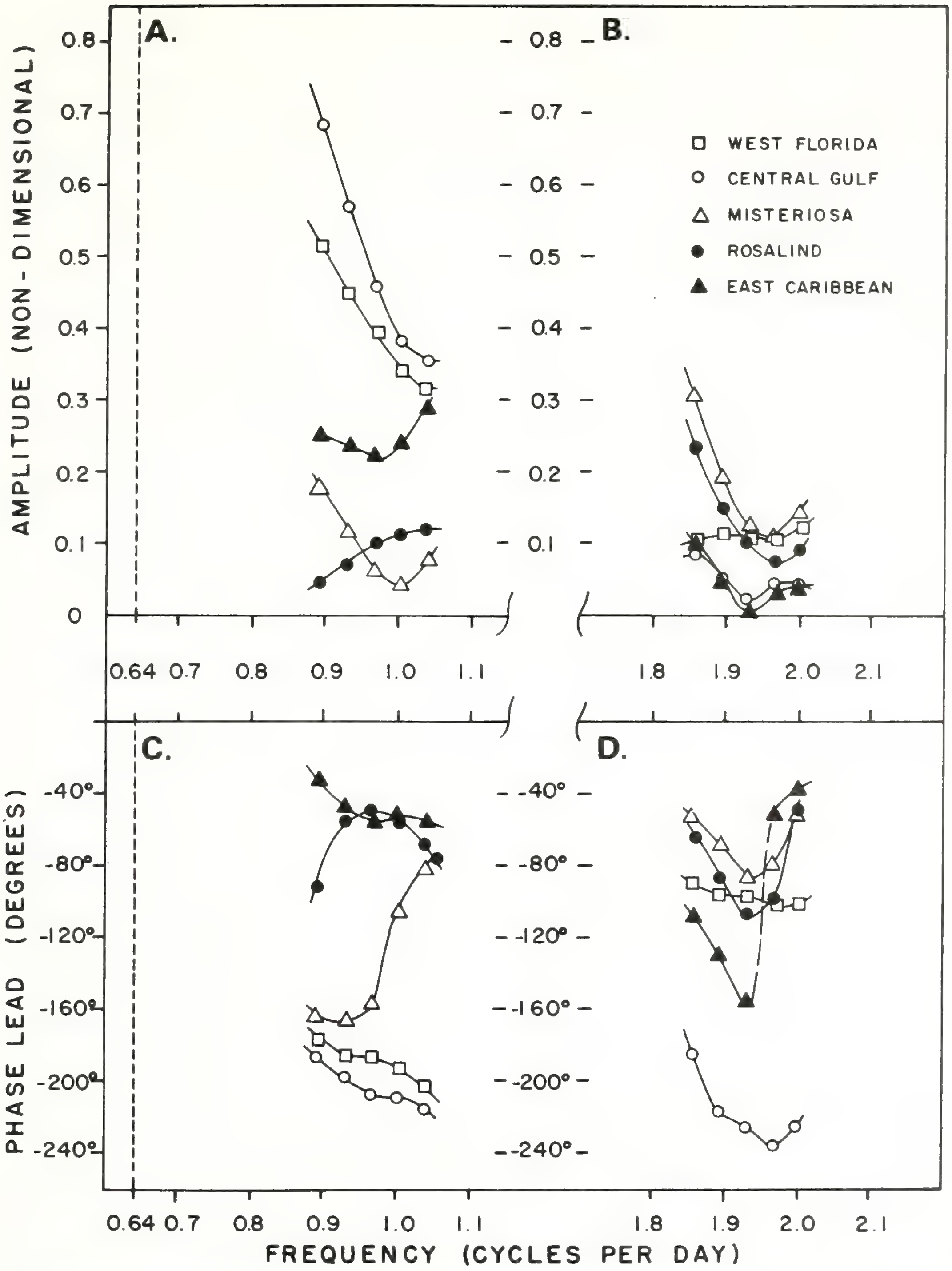

Fig. 4 Tidal admittance amplitudes computed from the bottom pressure records for the daily (A) and semi-daily (B) tidal bands and the corresponding phase leads (C) and (D). Tables of the admittances in standard form are given in the Appendix

3. OBSERVED TIDES

3.1 Accuracy of Harmonic Constants

Tidal harmonic constants were obtained from the pressure series using the response method. Results are given in the Appendix with a description of the method. The accuracy of observed harmonic constants is limited by length of record and by relative intensity of non-tidal continuum plus instrument noise within the tidal bands. For the records under discussion, the non-tidal pressure continuum is the primary source of error. The spectrum of the pressure continuum typically rises appreciably around the major tidal lines, due to the phase - incoherent internal tide. Cusps around the minor lines are buried in the background.

In the deep ocean one would expect less weather-induced fluctuation of bottom pressure than at coastal sea level stations. To compare the scatter in harmonic constants from nearby deep and shallow stations, successive 29-d analyses were done on the six-month east Caribbean bottom pressure record and a sea-level record from Magueyes Island, 280 km away, analysed by Zetler and Cummings (1972). Table II gives the means and standard deviations of the harmonic constants from these records.

Another error estimate uses the continuum spectru, integrated over the appropriate tidal band. This estimate, which is described in the Appendix, can be obtained from series that are too short for successive analyses. Standard deviations in Tables III and IV were obtained from the spectra.

TABLE III

Comparison of theoretical and observed harmonic constants at the central Gulf of Mexico and West Florida Shelf stations

Central Gulf of Mexico station (24°46.1N, 89°38.9W)						
	Michaelov, Melishko and Shcheveleva (1969)		Grijalva (1971)		Observed	
	H (cm)	G (deg)	H (cm)	G (deg)	H (cm)	G (deg)
M_2	1.0	45	~1.5	170	1.30±0.07	225.8±3.1
S_2	0.03	45	-	-	1.5 ±0.08	130.0±3.1
K_1	-	-	-	-	14.10±0.30	28.5±1.2
O_1	-	-	-	-	14.90±0.31	18.9±1.2
West Florida Shelf station (26°42.4N, 84°15.0W)						
	H (cm)	G (deg)	H (cm)	G (deg)	H (cm)	G (deg)
M_2	8.0	110	11	88	6.74±0.07	97.1±0.6
S_2	1.3	125	-	-	3.51±0.04	102.5±0.6
K_1	-	-	-	-	12.56±0.16	12.4±0.7
O_1	-	-	-	-	11.73±0.15	5.2±0.7

3.2 Gulf of Mexico

The measured K_1 and O_1 tides (Table III) at the central Gulf of Mexico station have at least twice the amplitudes of the corresponding tides in the western Atlantic. Although the K_1 amplitude in the western Atlantic is 1.24 times the O_1 amplitude and the astronomical K_1 forcing is 1.41 times the O_1 forcing, the O_1 amplitude exceeds the K_1 amplitude in the central Gulf. Hence, the admittance (response per unit forcing) is significantly larger at lower frequencies (Fig. 4). K_1 and O_1 harmonic constants are comparable with coastal values in the western Gulf, as given by Zetler and D. Hansen (1972). The observations support Marmer's (1954) contention that the Gulf has a resonance near the daily tidal band. The increasing admittance with decreasing frequency indicates that the resonance has a frequency below (longer period than) the daily tidal band. Further evidence for the resonance is given in the section on the low frequency continuum.

Since the model by Grace (1932) disagrees significantly with coastal values, no comparison was made between the K_1 measured at the central Gulf of Mexico station and this theory. The measured K_1 and O_1 values are consistent with the spatial distribution of the Helmholtz resonance computed by Platzman (1972), although the period is longer than the theoretical value.

The earlier K_1 and O_1 phases at the West Florida Shelf station (Fig. 4) relative to the central Gulf of Mexico station indicate that there is some progressive component to the daily tides near the Straits of Florida due to an unknown mixture of dissipation, direct forcing and propagation to or from the Caribbean Sea. The smaller daily amplitudes (Fig. 4) are consistent with nodes in the Straits of Florida.

The observed M_2 amplitude at the central Gulf of Mexico station agrees with the model of Michaelov et al. (1969) and the model of Grijalva (1971). For M_2 phase, the closer agreement of observations with the latter model tends to confirm Grijalva's contention that direct M_2 astronomical forcing is important in this small M_2 amplitude region of the Gulf.

Michaelov et al. (1969) also computed a theoretical distribution for S_2 (Fig. 2 and Table III) using coastal observations as boundary conditions and neglecting direct forcing. The S_2 tide is a superposition of gravitations and radiational tides. Assuming that the 0.9-cm amplitude[1] found by Zetler (1971) at Key West, Florida (24°34N, 81°48W) is characteristic of the radiational S_2 tide along the Gulf Coast, the radiational S_2 dominates the boundary conditions for the S_2 model. The discrepancy between the theoretical and observed S_2 harmonic constants (Table III) is then principally due to the neglect in the theory of nearshore wind and atmospheric pressure forcing.

At the West Florida Shelf station, the theoretical M_2 tides agree reasonably well with the measured values. This result could be expected because both theories (Table III) use nearby observed values as boundary conditions. The discrepancies may be due to tidal variation across the Shelf, which is unresolved by the models.

3.3 Caribbean Sea

The observed daily tides (Table IV) verify the general features of the K_1 and O_1 cotidal charts (Fig. 2) for the Caribbean Sea presented by Michaelov et al. (1969). The theory underestimates the daily amplitudes by about 10 percent at the eastern stations. Theoretical phases at the eastern stations have K_1 less than O_1 by 4 percent while observed phases have

---

[1] This amplitude is relatively small compared with others along the United States East Coast, as reported by Zetler (1971)

TABLE IV

Comparison of theoretical harmonic constants from Michaelov, Melishko and Shcheveleva (1969) and observed harmonic constants in the Caribbean Sea

Eastern Caribbean Sea								
	Six-month station (16°32.5N, 64°52.9W)				One-month station (16°30.1N, 64°54.7W)			
	Theoretical		Observed		Theoretical		Observed[a]	
	H (cm)	G (deg)	H (cm)	G (deg)	H (cm)	G (deg)	H (cm)	G (deg)
M_2	0	-	0.52±0.03	155.8±3.7	0	-	0.64	153
S_2	0.5	350	1.30±0.08	43.7±3.7	0.5	0	1.24	49
K_1	7.8	228	8.82±0.11	232.9±0.7	7.8	228	9.27	235
O_1	6.0	232	6.24±0.08	227.2±0.7	6.0	232	6.62	230

Western Caribbean Sea								
	Theoretical		Observed		Theoretical		Observed	
	H (cm)	G (deg)	H (cm)	G (deg)	H (cm)	G (deg)	H (cm)	G (deg)
M_2	8.7	88	7.88±0.46	84.2±3.3	6.5	105	6.63±0.35	107.0±3.0
S_2	2.6	60	3.89±0.23	55.9±3.3	1.7	50	2.51±0.13	55.6±3.0
K_1	⩽3	280	1.58±0.19	284.3±7.0	5.0	243	4.33±0.28	235.3±3.7
O_1	⩽1	320	3.06±0.37	347.0±7.0	2.0	250	1.89±0.12	235.5±3.7

[a] From Zetler and Cummings (1972) obtained from a 29-day harmonic analysis; no standard deviations given

K_1 greater than O_1 by 5 percent. The observed K_1 tide also lags the O_1 tide at the nearby Magueyez Island station (Zetler and Cummings, 1972) and other coastal stations in the Caribbean Sea (U.S. Department of Commerce, 1942). The discrepancies are due to errors in the boundary conditions or to mislabelling of the cotidal charts, because the uniformity of the tides in the eastern Caribbean precludes significant errors arising from inadequate dynamics in the model.

In the western Caribbean, the observations (Table IV) show the decrease in daily tidal amplitudes and rapid increase in daily phase lags (Fig. 2) predicted by Michaelov et al. (1969). The discrepancies between the theoretical and observed daily tides at the western Caribbean station arise from errors in the model's boundary conditions and, to a lesser extent, the influence of noise on observed harmonic constants from short records obtained at shallow stations.

The model by Michaelov et al. (1969) for the M_2 and S_2 tides in the Caribbean Sea predicts small amplitudes at the eastern Caribbean stations. Small semi-daily amplitudes are observed at these stations. As suggested for the M_2 and S_2 tides in the Gulf of Mexico, the

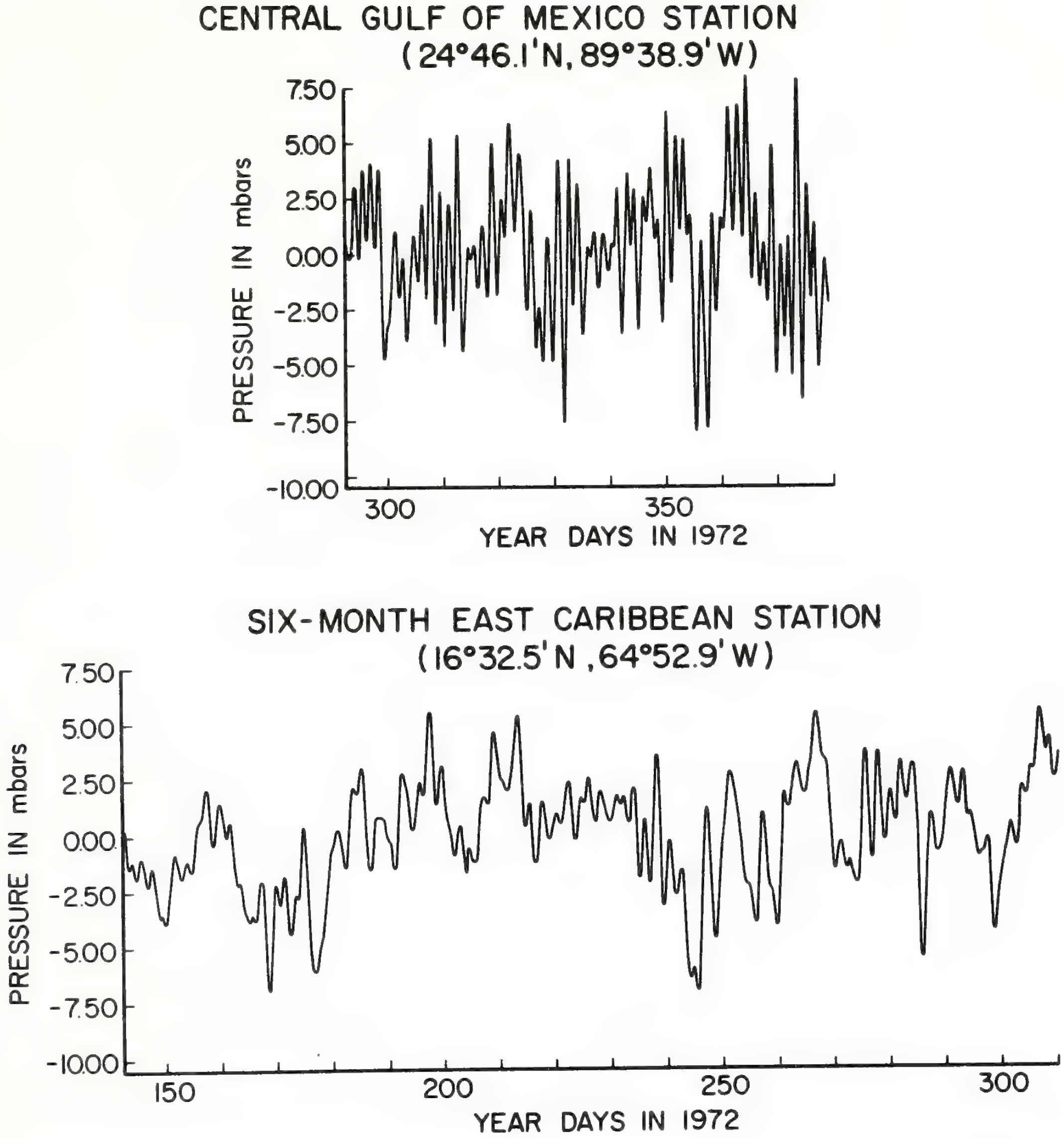

Fig. 5 Low-passed pressure records at the central Gulf of Mexico and six-month east Caribbea stations showing the pressure fluctuations in millibars at frequencies below the daily tidal band. The instrumental drift has been removed by subtracting a least-squares fitted logarithmic trend from each record. Note the rapid fluctuations in the central Gulf of Mexico record as contrasted with the lower frequency fluctuations at the east Caribbean station

difference between the theory and observation near a theoretical amphidrome may be due to directly forced tides and to radiational S_2 tide. The anomalous jump in semi-daily admittance phase (Fig. 4) at the six-month east Caribbean station may be due to the relative importance of the radiational S_2 tide near amphidromes of the gravitational, semi-daily tides. If the record were longer (years) the radiational admittance could be computed separately and the computed gravitational admittance might then appear smoother.

The six-month record is sufficiently long and the background noise sufficiently low to allow an analysis of the ter-daily M_3 tide arising from the C_3^3 gravitational potential. As given in Table E, the M_3 tide (0.12 cm, 48.1°G) is distinct from non-linearly generated lines in the ter-daily band.

4. LOW-FREQUENCY PRESSURE CONTINUUM

The records from the central Gulf of Mexico and the six-month east Caribbean stations are sufficiently long to permit a study of the low frequency, bottom pressure continuum. Shown in Fig. 5 are low-passed pressure series; the corresponding spectra are given in Fig. 6 together with the spectrum at the western Atlantic AOML-1 station discussed by Brown et al. (1975).

4.1 Gulf of Mexico

The Central Gulf of Mexico spectrum (Fig. 6) diverges from the AOML-1 spectrum at frequencies above 0.24 cpd, exhibiting an increase in spectral energy with higher frequency and forming a broad peak centred at about 0.64 cpd (period = 1.56 d)[1]. After a dip centred at 0.8 cpd this spectrum rises toward the daily tidal band. The total pressure variance between 0.049 and 0.805 cpd at the Central Gulf of Mexico Station (8.81 mbar^2) is three times the corresponding variance at the western Atlantic AOML-1 station (2.64 mbar^2). The low frequency pressure continuum observed in the Gulf reinforces the contention that the Gulf has a resonance with a frequency slightly below the daily tidal band.

4.2 Caribbean Sea

The pressure spectrum (Fig. 5) at the six-month east Caribbean station follows the general trend of the western Atlantic AOML-1 spectrum. The pressure variances between 0.046 and 0.805 cpd are 2.64 and 2.48 mbar^2, respectively. The major differences between the spectra are the pronounced peak around 0.22 cpd (4.5-d period) and its overtone seen in the Caribbean. Since the weather in this region is dominated by waves in the Easterlies with 4 to 5-d period, the bottom pressure peaks may be atmospherically forced.

A simultaneous atmospheric pressure record[2] from St. Croix, V.I. (17°42N, 64°44W) 130 km north and slightly east of the bottom pressure station (16°33N, 64°53W), was obtained from the National Climatic Center. The autospectra, squared coherence and relative phase of the two records are shown in Fig. 7. Taking the 0.15-cpd spectral estimates as the bases of the 0.2-cpd peaks, the corresponding amplitudes are 0.5 and 4.0 mbar for the bottom pressure and atmospheric pressure fluctuations, respectively, giving an amplitude ratio of 0.13. The fluctuations are coherent because the peak in squared coherence stands well above the 95 percent confidence value for rejection of the null hypothesis (i.e., that the coherence is due to random chance).

1/ The spectrum from the West Florida Shelf station likewise contains a significant peak at 1.60 d

2/ The following comparison was suggested by a reviewer

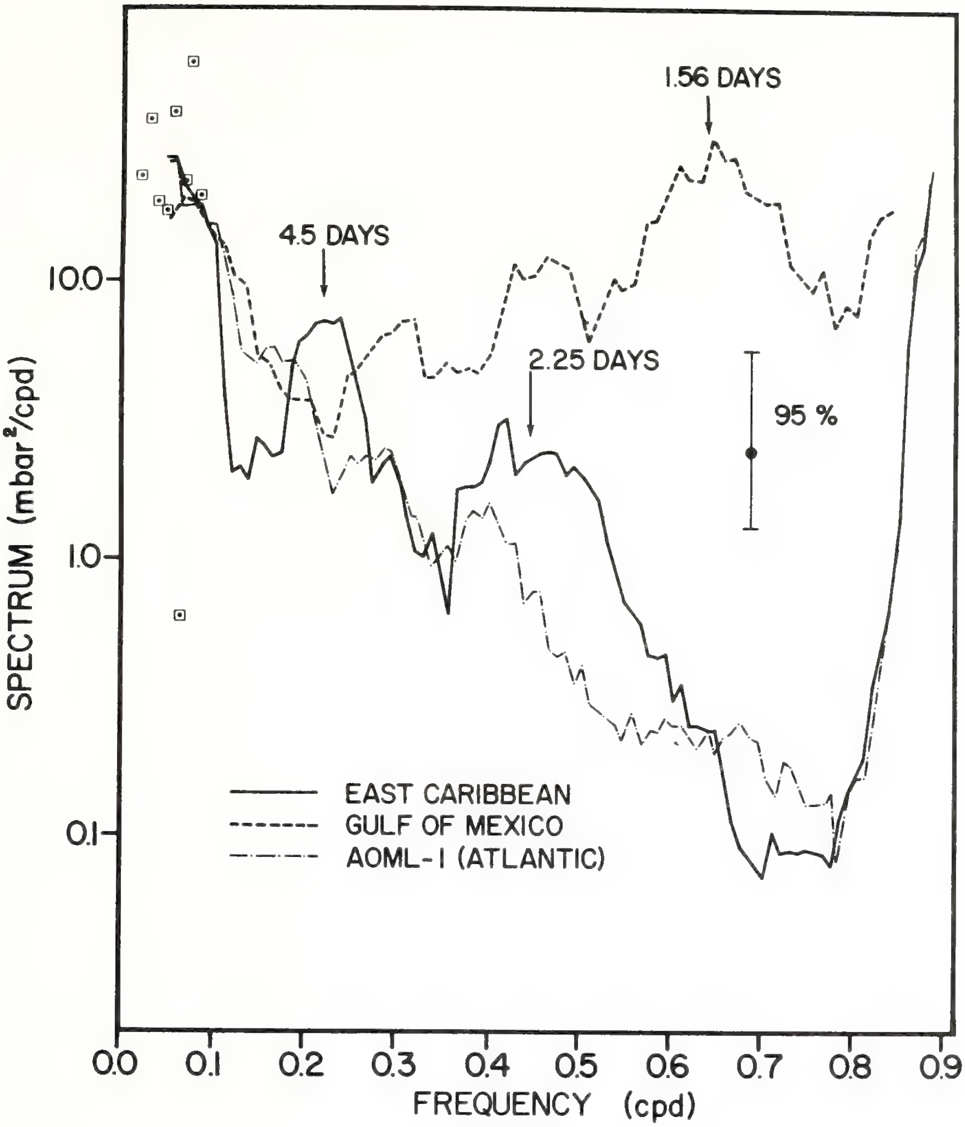

Fig. 6 Spectra of bottom pressure below the daily tidal band for the six-month east Caribbean, central Gulf of Mexico and AOML-1 (Atlantic) stations. The pressure records were cosine-tapered over the first and last 10 percent and Fourier-transformed to give primitive spectral estimates that have been smoothed with a seven point (14 degrees of freedom) box car average. The isolated points in the upper left corner are primitive spectral estimates for the east Caribbean record at and below the fortnightly frequency. Note the overall similarity between the AOML-1 and East Caribbean spectra and the peaks in the latter at 4.5 and 2.25-d periods. In contrast, the central Gulf of Mexico spectrum rises at frequencies above 0.2 cpd to a peak at 0.64 cpd (1.56 d period)

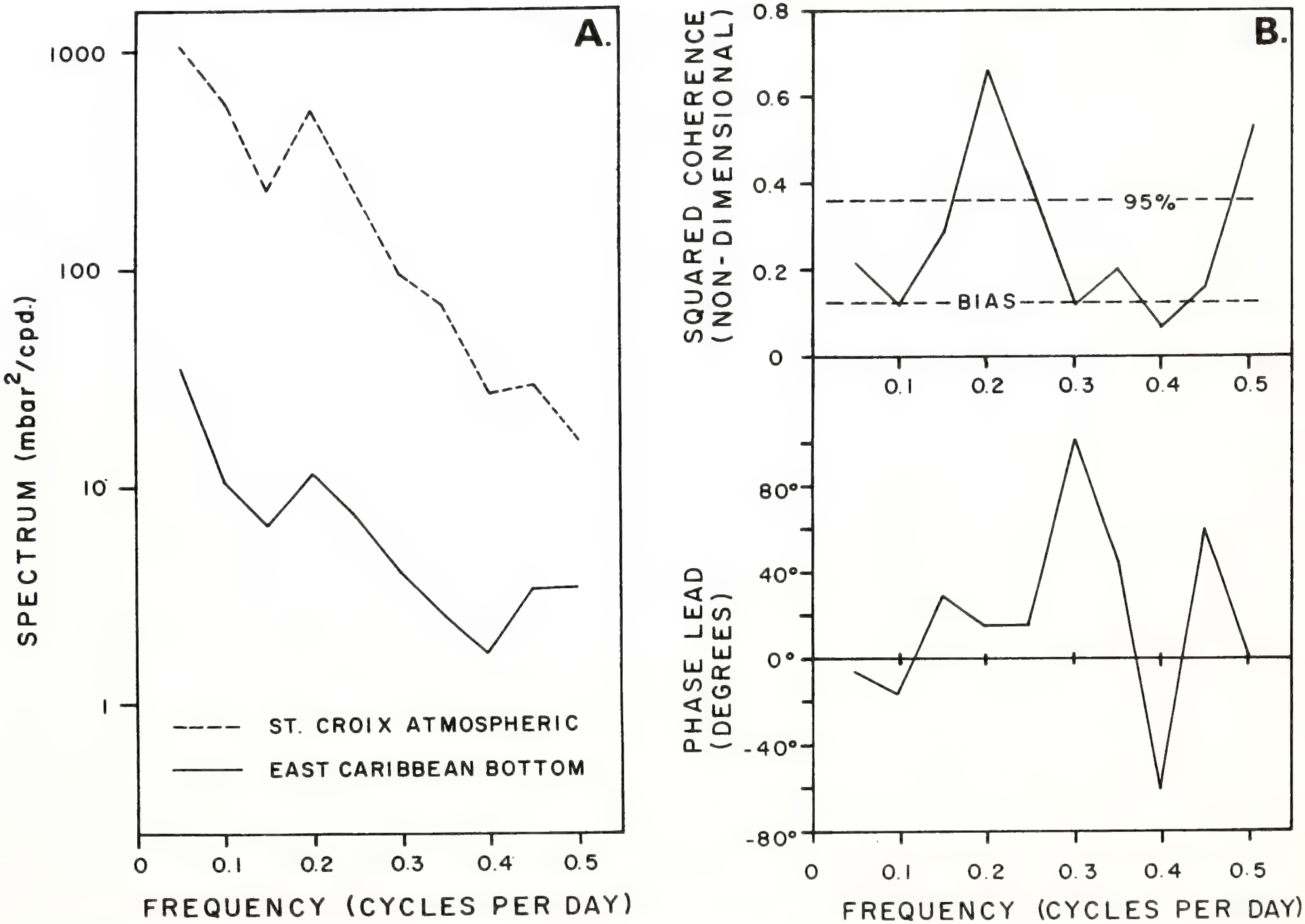

Fig. 7 Comparison of bottom pressure at the six-month east Caribbean station (16°33N, 64°53W) with atmospheric pressure at nearby St. Croix, V.I. (17°42N, 64°44W). The peaks in the autospectra (A) at 0.2 cpd are coherent (B) with the bottom pressure leading the atmospheric pressure by 15° at 0.2 cpd. Daily-averaged pressures were used with a 0.5-cpd Nyquist frequency

The bottom pressure fluctuations lead the atmospheric fluctuations to the north by 15 percent, or 4.5 h for a 0.22-cpd frequency. This is consistent with the northwestward propagation of the waves in the Easterlies as reported by Riehl (1954). He states that the waves propagate at 12 to 15 knots (6 to 8 m/sec^{-1}) while the observed 4.5 h phase lead gives a propagation speed of about 8 m/sec^{-1}, assuming that the waves propagate with a 315°T heading. The 4 to 5-d bottom pressure fluctuations observed at the six-month east Caribbean station are coupled strongly and in phase with atmospheric wave. This is in contrast to the low-frequency, bottom pressure fluctuations in the western Atlantic where the bottom and atmospheric fluctuations are marginally coherent. A possible explanation for the different behaviour is that the inverse barometer compensation is less complete in the semi-enclosed Caribbean Sea, where weather patterns span the basin and where water exchange is hindered by narrow, shallow passes.

5. DISCUSSION

The original purpose of this study was to test tidal models with offshore observations. By themselves, the few stations are not sufficient to provide empirical tidal charts or even to indicate whether particular features such as amphidromic points exist in a given region. When conflicting theories predict distinctly different behaviour, an isolated station should discriminate between the theories. For example, the observed M_2 phase at the Central Gulf of Mexico station favours the model by Grijalva (1971) which includes direct astronomical forcing, over the model by Michaelov et al. (1969) which is forced only by co-oscillation. However, it might be possible to reconcile the latter model with observations by changing boundary conditions or grid spacing. The results of tidal models are traditionally given as a single chart of amplitude and phase for a given constituent. No reliability estimates are given based on a set of numerical experiments to determine the sensitivity of the model to reasonable ranges of parameters, uncertain bathymetry and numerical limitations. Confidence limits on the theoretical distributions are needed, just as they are for observations.

Although the daily tides dominate the Gulf of Mexico, the apparent critical-latitude singularity in the equations of motion prevented Michaelov et al. (1969) from computing the daily tidal charts for the Gulf. This singularity is removable and the daily tides in the Gulf can be computed by alternate numerical schemes.

Zetler and Cummings (1972) suggested that extensive observational searches for amphidromic points are unprofitable and report the recommendation by the Scientific Committee on Ocean Resources (SCOR) Working Group No. 27 on Tides in the Open Ocean that emphasis should be placed on regions of maximum constituent amplitude. Such a search would also be unprofitable because the constituent amplitudes and phases vary little over large areas around these maxima. The observations should be made to discriminate between theories. The basic limitation on observational offshore tide programmes is no longer the accuracy and endurance of tide gauges but rather the cost of obtaining the pressure records.

6. ACKNOWLDEGEMENTS

Many people have contributed significantly to the research presented in the paper. The authors wish to thank the National Ocean Survey's Engineering Development Laboratory and J.J. Falkenhoff in particular for both the design of arrays and assistance in the NOAA field programme. Within AOML, F.A. New did much of the initial checkout and modification work on the Filloux gauges. B.J. Culverhouse, D.F. Pashinski and R.S. Jennings worked with EDL and F.A. New on the array preparation and field work and were essential to the success of the project. R.B. Starr suggested the shallow water stations in the western Caribbean Sea. D.F. Jones designed and fabricated the arrays for those stations and supervised their installation. N.M. Targett was of considerable assistance in the laborious reading of pressure gauge records and the subsequent data processing. Useful advice was readily given by J.H. Filloux whose gauges have proved to be excellent instruments for open-sea bottom pressure studies.

The NOAA work was sponsored by the National Science Foundation under the agreement AG-253 for NOAA participation in the International Decade of Ocean Exploration. The Nova University work was supported by NOAA (PO 015150340) and by the National Science Foundation (Grant GA34149).

7. REFERENCES

Brown, W. et al., MODE bottom experiment. J.Phys.Oceanogr., 5:75-85
1975

Cartwright, D.E., W. Munk and B. Zetler, Pelagic tidal measurements - a suggested procedure
1969 for analysis. Trans.Am.Geophys.Union, 50:472-7

Cartwright, D.E. and A.C. Edden, Corrected tables of tidal harmonics. Geophys.J.R.Astron.
1973 Soc., 33:253-63

Filloux, J.H., Bourdon tube deep-sea tide gauges. In Tsunamis in the Pacific Ocean, edited
1970 by W.M. Adams. Honolulu, East-West Center Press, pp. 223-38

Grace, S.F., The principal diurnal constituent of tidal motion in the Gulf of Mexico. Mon.
1932 Not.R.Astron.Soc.Geophys.Suppl., (3):70-83

Great Britain, Her Majesty's Nautical Almanac Office, Explanatory supplement to the astronomical
1974 emphemeris and to the American ephemeris and nautical almanac. London,
HMSO, pp. 522-64

Grijalva, N., The M$_2$ tide in the Gulf of Mexico. Geofis.Int., Mex., 2:103-25
1971

Groves, G.W., Use of orthogonal functions for the analysis, prediction and study of the
1970 tide. Rep.Hawaii Inst.Geophys., (HIG-70-13):53 p.

Hansen, K.S., Calculations of normal modes for the Americal mediterranean seas. Univ.
1974 Chicago Tech.Rep., (26):71 p.

Hansen, W., Gezeiten and Gezeitenstrome der halbtagigen M$_2$ in der Nordsee. Dtsch.Hydrogr.Z.,
1952 Erganzungsh. (1):46 p.

————————, Hydrodynamical methods applied to oceanographic problems. In Proceedings of
1962 the Symposium of Mathematical and Hydrodynamical Methods of Physical Oceanography.
Mitt.Inst.Meereskd.Univ.Hamb., (1):25-34

Jeffreys, H., The earth. Cambridge University Press, 525 p. 5th ed.
1970

Lomnitz, C., Creep measurements in igneous rocks. J.Geol., 64:473-9
1956

————————, Linear dissipation in solids. J.Appl.Phys., 28:201-5
1957

Marmer, H.A., Tides and sea level in the Gulf of Mexico. Fish.Bull.U.S.Fish Wildl.Serv.,
1954 55:101-18

Michaelov, U.S., V.P. Melishko and G.I. Shcheveleva, Estimation of the tides and tidal currents
1969 in the Gulf of Mexico and Caribbean Sea. Tr.Gos.Okeanogr.Inst., 96:146-73

Munk, W.H. and D.E. Cartwright, Tidal spectroscopy and prediction. Philosophical Trans.R.
1966 Soc.(A), 259:533-81

Platzman, G.W., Two-dimensional free oscillations in natural basins. J.Phys.Oceanogr.,
1972 2:117-38

Radok, R., W. Munk and J. Isaacs, A note on mid-ocean internal tides. Deep-Sea Res.,
1967 14:121-4

Riehl, H., Tropical meteorology. McGraw-Hill, 392 p.
1954

SCOR Working Group No. 27, An intercomparison of open sea tidal pressure sensors. UNESCO
1975 Tech.Pap.Mar.Sci., (21):67 p.

U.S. Department of Commerce, Tidal harmonic constants, Atlantic Ocean including Arctic and
1942 Antarctic Regions, TH-1. Washington D.C., Government Printing Office, 139 p.

Wimbush, M., An inexpensive sea floor precision pressure recorder. Deep-Sea Res., 24:493-7
1977

Zetler, B.D., Radiational ocean tides along the coasts of the United States. J.Phys.Oceanogr.
1971 1:34-8

Zetler, B.D. and R.A. Cummings, Tidal observations near an amphidrome. Geophys.Surv.,
1972 1:85-9

Zetler, B.D. and D.B. Hansen, Tides in the Gulf of Mexico. In Contributions on the physical
1972 oceanography of the Gulf of Mexico, edited by L.R.A. Capurro and J.L. Reid.
Houston, Texas, G lf Publishing Co., Vol. 2:265-75

Zetler, B.D. et al., MODE tides. J.Phys.Oceanogr., 5:430-41
1975

APPENDIX

Tidal Analysis of the Pressure Records

The bottom pressure records were analysed for tidal components by the following procedure:

Each pressure record was first divided through by $\bar{\rho}g$ to convert it to units of sea level. In practice the mean density of the water column, $\bar{\rho}$, was taken as a constant for each record. Gravity, g, was taken to be 979 cm s^{-2}, a typical value for the region.

These sea level records were then analysed for tidal components by the response method of Munk and Cartwright (1966)[1]. In this method, spherical harmonic expansions of the tide-generating potential (computed from the known motions of earth, moon and sun) are fitted to the observed data in a least squares sense. Lags and leads of the potential functions may be introduced to allow for variations with frequency of response admittances of the ocean at the observation point. These admittances are then calculated by Fourier transformation of the weights representing the least squares fit.

For comparison with results from harmonic methods of tidal analysis, it is convenient to calculate amplitudes and phases of individual tidal lines in the spectrum. The amplitude $H(f)$ of a tidal line with frequency f is calculated by multiplying the admittance amplitude $R(f)$ by the amplitude of the tide-generating potential $H_{pot}(f)$. $H_{pot}(f)$ for the present historical period is given (in metres) in column 3, Table 1 of Cartwright and Edden (1973). The Greenwich phase $G(f)$ of the tidal line is calculated from the phase $\Phi(f)$ of the admittance (defined as in Munk and Cartwright, 1966) by the relation $G = m\pi - \Phi$, where m is the species number of the tidal line.

Errors in these tidal estimates are principally due to the incoherent noise in the spectral neighbourhoods of the tidal lines. Around each tidal line a cusp-like rise in noise spectrum is observed. This is thought to be caused by baroclinic tides, which derive their energy from the barotropic tide but are rendered incoherent by the variable density structure of the ocean (Radok, Munk and Isaacs, 1967). With this model, the noise variance in each tide constituent is proportional to the tidal variance of the constituent, with the result that the standard error is given by

$$\sigma = \left[\frac{\mu}{2\ell}\right]^{1/2} \sigma, \quad \mu \ll 1$$

relative to H itself or to one radian in G, where μ is the ratio of the residual to recorded variance (i.e., the proportion of the recorded variance that is non-tidal) and ℓ is the length of the record in months (i.e., length in days ÷ 27.322).

Tables A-E give the results of this analysis applied to the Gulf of Mexico and Caribbean bottom pressure records. The presentation follows the form recommended by Cartwright, Munk and Zetler (1969).

---

[1] The following corrections (many suggested by Cartwright, private communication) have been made to the formulae in Appendix A of this reference. In section b, $\bar{R}_o/\rho_o$ is replaced by $(\bar{R}_o/\rho_o)^2$ as proposed by Groves (1970). In sections d and e, $\omega_o = 0.4093197552 - 0.00022711096892\ T$; T^3 is replaced by T^2 in eq. A17; $-3me_o \sin(h_o-p_o)$ is added to the r.h.s. of eq. A18; $m = 0.048013258$; $-3/2\ m^2\ e_o\cos(h_o-p_o)$ is added within $[\ ]$ of eq. A19. The Internal Astronomical Union 1964 astronomical constants were used throughout (see p. 492 ff of the Explanatory Supplement to the Astronomical Emphemeris and to the American Emphemeris and Nautical Almanac, 1974)

TABLE A

Station: Central Gulf of Mexico 24°46.1N 89°38.9W, depth 3748 m,
1972 October 14, 1629 - 1973 January 17, 1135 GMT

Reference: $C_2^1(0,\pm 2,\pm 4)$, $C_2^2(0,\pm 2,\pm 4)$, C_3^3

Admittances (Station/Reference)					Principal harmonic constituents			
Interval 1 cpm (0.366011 cpd)								
Frequency (cpd)	Real	Imaginary	R	ϕ (deg)		Frequency (cpd)	H (cm)	G (deg)
0.8929346	-0.67828	0.07851	0.68281	173.40	(Q_1)	0.8932441	3.42	006.7
0.9295357	-0.53763	0.18376	0.56816	161.13	O_1	0.9295357	14.90	018.9
0.9661368	-0.40599	0.20743	0.45591	152.94				
					(P_1)	0.9972621	4.76	028.4
1.0027379	-0.33624	0.18226	0.38246	151.54	K_1	1.0027379	14.10	028.5
1.0393390	-0.29605	0.19920	0.35683	146.06				
							±2.1%	±1.2°
Recorded variance:	304.43 cm^2							
Residual variance:	0.95 cm^2							
1.8590714	-0.08469	0.00735	0.08501	175.04				
1.8956725	-0.04168	0.03133	0.05214	143.06	(N_2)	1.8959820	0.63	217.3
1.9322736	-0.01438	0.01481	0.02064	134.15	M_2	1.9322736	1.30	225.8
1.9688747	-0.02392	0.03446	0.04195	-124.77				
					(S_2)	2.0000000	1.50	130.0
2.0054758	-0.03112	-0.03120	0.04407	-134.92	K_2	2.0054758	0.35	134.9
Recorded variance:	1.98 cm^2						±5.4%	±3.1°
Residual variance:	0.04 cm^2							

TABLE B

Station: West Florida Shelf Break
26°42.4N 84°15.0W, depth 154 m
1974 April 7, 1845 - November 17, 1304 GMT

Reference: $C_2^1(0,\pm 2,\pm 4)$, $C_2^2(0,\pm 2,\pm 4)$, C_3^3

Admittances (Station/Reference)

Interval 1 cpm (0.366011 cpd)

Frequency (cpd)	Real	Imaginary	R	ϕ (deg)
0.8929346	-0.51272	-0.03282	0.51377	-176.34
0.9295357	-0.44564	0.04024	0.44745	174.84
0.9661368	-0.39082	0.05126	0.39417	172.53
1.0027379	-0.33265	0.07310	0.34058	167.60
1.0393390	-0.29103	0.12712	0.31758	156.40
Recorded variance: 161.98 cm²				
Residual variance: 0.44 cm²				
1.8590714	0.00019	-0.10838	0.10838	-89.90
1.8956725	-0.01133	-0.11161	0.11218	-95.79
1.9322736	-0.01322	-0.10578	0.10660	-97.13
1.9688747	-0.02223	-0.10632	0.10862	-101.81
2.0054758	-0.02463	-0.11909	0.12161	-101.68
Recorded variance: 30.43 cm²				
Residual variance: 0.05 cm²				

Principal harmonic constituents

	Frequency (cpd)	H (cm)	G (deg)
(Q_1)	0.8932441	2.58	356.5
O_1	0.9295357	11.73	005.2
(P_1)	0.9972621	4.24	011.2
K_1	1.0027379	12.56	012.4
		±1.3%	±0.7°
(N_2)	1.8959820	1.36	095.8
M_2	1.9322736	6.74	097.1
(S_2)	2.0000000	3.51	102.5
K_2	2.0054758	0.97	101.7
		±1.0%	±0.6°

TABLE C

Station: Misteriosa Bank

18°52.9N 83°48.3W, depth 22m,
1971 July 23, 0001 - August 19, 1803 GMT

Reference: $C_2^1(0,\pm 2)$, $C_2^2(0,\pm 2)$

Admittances (Station/Reference)					Principal harmonic constituents			
Interval 1 cpm (0.366011 cpd)								
Frequency (cpd)	Real	Imaginary	R	ϕ (deg)		Frequency (cpd)	H (cm)	G (deg)
0.8929346	-0.17160	-0.05025	0.17881	-163.68	(Q_1)	0.8932441	0.90	343.7
0.9295357	-0.11351	-0.02627	0.11651	-166.97	O_1	0.9295357	3.06	347.0
0.9661368	-0.05585	-0.02316	0.06046	-157.48				
					(P_1)	0.9972621	0.50	293.3
1.0027379	-0.01062	-0.04155	0.04289	-104.34	K_1	1.0027379	1.58	284.3
1.0393390	0.01279	-0.07763	0.07868	-80.65				
							±12%	±7°
Recorded variance: 7.73 cm²								
Residual variance: 0.24 cm²								
1.8590714	0.18556	-0.24718	0.30908	-53.10				
1.8956725	0.07245	-0.17620	0.19051	-67.65	(N_2)	1.8959820	2.30	067.8
1.9322736	0.01251	-0.12402	0.12465	-84.24	M_2	1.9322736	7.88	084.2
1.9688747	0.01819	-0.10151	0.10312	-79.84				
					(S_2)	2.0000000	3.89	055.9
2.0054758	0.08833	-0.11333	0.14368	-52.07	K_2	2.0054758	1.15	052.1
Recorded variance: 37.00 cm²							±5.8%	±3.3°
Residual variance: 0.25 cm²								

TABLE D

Station: Rosalind Bank

16°36.5N 80°20.25W, depth 31 m,
1971 July 22, 0000 - August 14, 1700 GMT

Reference: $C_2^1(0,\pm 2)$, $C_2^2(0,\pm 2)$

Admittances (Station/Reference) Interval 1 cpm (0.366011 cpd) Frequency (cpd)	Real	Imaginary	R	ϕ (deg)	Principal harmonic constituents	Frequency (cpd)	H (cm)	G (deg)
0.8929346	-0.00116	-0.04676	0.04677	-91.42	(Q_1)	0.8932441	0.24	270.9
0.9295357	0.04080	-0.05936	0.07203	-55.49	O_1	0.9295357	1.89	235.5
0.9661368	0.06519	-0.07721	0.10105	-49.82				
					(P_1)	0.9972621	1.42	234.0
1.0027379	0.06693	-0.09660	0.11752	-55.28	K_1	1.0027379	4.33	235.3
1.0393390	0.04566	-0.11351	0.12235	-68.09				
							±6.4%	±3.7°
Recorded variance: 13.84 cm²								
Residual variance: 0.10 cm²								
1.8590714	0.10425	-0.20902	0.23357	-63.49				
1.8956725	0.01110	-0.14915	0.14956	-85.74	(N_2)	1.8959820	1.80	086.0
1.9322736	-0.03061	-0.10035	0.10491	-106.96	M_2	1.9322736	6.63	107.0
1.9688747	-0.01221	-0.07275	0.07377	-99.52				
					(S_2)	2.0000000	2.51	055.6
2.0054758	0.06247	-0.07210	0.09540	-49.09	K_2	2.0054758	0.76	049.1
Recorded variance: 22.95 cm²							±5.3%	±3.0°
Residual variance: 0.11 cm²								

TABLE E

Station: Six-Month East Caribbean

16°32.5N 64°52.9W, depth 3990 m
1972 May 20, 0000 - November 9, 1309 GMT

Reference: C_2^0, $C_2^1(0,\pm2,\pm4)$, $C_2^2(0,\pm2,\pm4)$, C_3^3, x_1^1

Admittances* (Station/Reference) Interval 1 cpm (0.366011cpd) Frequency (cpd)	Real	Imaginary	R	ϕ (deg)	Principal harmonic constituents	Frequency (cpd)	H (cm)	G (deg)
0.8929346	0.20989	-0.13665	0.25045	-33.07	(Q_1)	0.8932441	1.26	213.2
0.9295357	0.16164	-0.17448	0.23785	-47.19	O_1	0.9295357	6.24	227.2
0.9661368	0.12927	-0.17947	0.22118	-54.24				
					(P_1)	0.9972621	2.85	233.2
1.0027379	0.14436	-0.19082	0.23927	-52.89	K_1	1.0027379	8.82	232.9
1.0393390	0.16838	-0.23455	0.28873	-54.32				
							±1.3%	±0.7°
Recorded variance: 68.02 cm^2								
Residual variance: 0.14 cm^2								
1.8590714	-0.03302	-0.09934	0.10468	-108.39				
1.8956725	-0.03047	-0.03710	0.04801	-129.40	(N_2)	1.8959820	0.58	129.7
1.9322736	-0.00748	-0.00336	0.00820	-155.82	M_2	1.9322736	0.52	155.8
1.9688747	0.02096	-0.02510	0.03270	-50.14				
					(S_2)	2.0000000	1.30	043.7
2.0054758	0.03184	-0.02444	0.04014	-37.51	K_2	2.0054758	0.32	037.5
Recorded variance: 1.35 cm^2							±6.4%	±3.7°
Residual variance: 0.07 cm^2								
2.8984104	-0.10248	0.11420	0.15344	131.90	M_3	2.8984104	0.12	048.1
Recorded variance: 0.035 cm^2							±**%	±**°
Residual variance: 0.027 cm^2								

* gravitational not radiational

** μ = (residual/recorded) variance = 0(1), formula inapplicable

50. CICAR-II Symposium on Progress in Marine Research in the Caribbean and Adjacent Regions, FAO Fisheries Report No. 200 Supplement, 1977, 103-118.

AN OVERVIEW OF THE CAYMAN SEA-GULF OF MEXICO CIRCULATION BASED ON CICAR SURVEY MONTH AND OTHER DATA

by

R.L. MOLINARI
NOAA/AOML
Miami, Florida 33149, U.S.A.

CONTENTS

1. INTRODUCTION
2. SPATIAL AND TEMPORAL CHARACTERISTICS OF THE CAYMAN-GULF CURRENT
3. DYNAMICAL PROCESSES ACTIVE IN THE CAYMAN-GULF CURRENT
4. THE ROLE OF THE CAYMAN-GULF CURRENT IN THE NORTH ATLANTIC GYRE
5. SUMMARY
6. ACKNOWLEDGEMENTS
7. REFERENCES

Abstract

The Atlantic Oceanographic and Meteorological Laboratories (AOML) have participated in seven CICAR Survey Months (CSMs). AOML's involvement was designed to map synoptically the circulation in the Cayman Sea and Gulf of Mexico. The CSM concept was verified in the sense that the most complete and synoptic spatial coverage was obtained when the coordination between participants was extensive.

In this overview, CICAR Regional Data Centre and AOML data sets are combined to describe the current structure in the Cayman-Gulf basins. A current, continuous in structure referred to as the Cayman Gulf Current, but not in nomenclature, is tracked through the region. The west-flowing Cayman Current enters the Cayman Sea through the Jamaica-Honduras Passage. Surface velocities approaching 75 cm/sec have been measured in the mid-Cayman Basin south of the Cayman Ridge. In the region of the Yucatan Strait, the Cayman Current turns north to become the Yucatan Current. Threefold increases in the current speeds have been observed here by direct current measurements. In the Gulf of Mexico the CSM data support the hypothesis of an annual cycle in the northern penetration of the next current segment, the Loop Current, and demonstrate the dramatic year-to-year variability in the occurrence of a particular phase. The last segment of the system is located in the Straits of Florida, where accelerations comparable to those observed in the Yucatan Strait are measured, and the Florida Current is formed.

Dynamical studies indicate that the Cayman Gulf Current is not significantly affected by local forcing, but is instead a free inertial current along its entire length.

Resumen

Los laboratorios oceanográficos y meteorológicos del Atlántico (AOML) han participado en siete expediciones mensuales de las ICCRA, con objeto de hacer un mapa sinóptico de la circulación en el Mar del Caimán y el el Golfo de México. Pudo comprobarse la utilidad de estas expediciones, ya que cuando el trabajo de los participantes estuvo bien coordinado, se obtuvo la cobertura espacial más completa y sinóptica.

En esta recopilación, la serie de datos del Centro de Datos Regionales de las ICCRA y de los laboratorios oceanográfico y meteorológicos del Atlántico son utilizados combinadamente para describir la estructura de las corrientes en las cuencas del Golfo y del Mar del Caimán. Se siguió el curso a través de la región de una corriente de estructura continua conocida - aunque no en la nomenclatura - como corriente del Golfo-Mar del Caimán, que penetra en este mar, procedente del oeste, por el paso Jamaica-Hondura. En la mitad de la cuenca del Mar del Caimán, al sur del bajo del Caimán, se han medido velocidades superficiales que se aproximan a los 75 cm/seg. En la región del Estrecho de Yucatán, la corriente del Mar del Caimán, gira hacia al norte, convirtiéndose en la Corriente de Yucatán, habiéndose observado, mediante mediciones directas de esta corriente, que su velocidad llega a triplicarse. Los datos obtenidos durante las expediciones de las ICCRA apoyan la hipótesis de la existencia de un ciclo anual para la penetración septentrional del segmento inmediato de corriente, la corriente circular, y ponen de manifiesto la forma tan espectacular con que varía de un año a otro una determinada fase. Por último, el sector final del sistema está situado en los Estrechos de la Florida, donde se han medido aceleraciones comparables a las observadas en el Estrecho de Yucatán y en el lugar donde se forma la Corriente de la Florida.

Estudios dinámicos indican que la corriente del Golfo de Caimán no está en forma significativa affectada por fuerzas in loco si no que ella es una corriente de inercia a lo largo de su entera longitud.

1. INTRODUCTION

Observational studies conducted during the field phase of the Cooperative Investigation of the Caribbean and Adjacent Regions (CICAR) have resulted in a significant increase in the quantity of data available for the study of the circulation in the Cayman Sea and the Gulf of Mexico. Many of these field programmes were conducted during the CICAR Survey Months (CSMs). The CSMs were instituted in an effort to coordinate ship schedules so as to obtain maximum spatial coverage of an area in the shortest time.

Data collected during CSM-I, July-August, 1971 resulted in the 20°C topography given in Fig. 1. The data collected by ships from several nations and institutions provide a spatial grid not available from single-ship operations. Temperature surfaces in this region reflect the geostrophic current régime, with large gradients correlated with intense geostrophic currents. For instance, Ichiye (1962) has found a good correlation between temperature patterns at 100 and 200 m and the dynamic height field relative to 1 000 m.

A band of large gradients can be tracked as a continuous feature from the Jamaica-Honduras Passage to the Straits of Florida. Although this continuity suggests a single current, the feature has been studied in the past on a regional basis, and several portions of the flow have acquired distinct names. The established nomenclature for these currents, with one exception, are as given in Fig. 1:

(1) the Cayman Current, previously referred to as the Caribbean Current (Emilsson, 1971) which extends from the Jamaica-Honduras Passage to the Yucatan Peninsula;
(2) the Yucatan Current which flows along the Yucatan Peninsula and Campeche Bank from approximately 18°N to 24°N;
(3) the Loop Current which is the anticyclonic northern extension of the Yucatan Current;
(4) the west Florida Current which flows along the west Florida Shelf when the Loop Current extends deep into the Gulf of Mexico, and
(5) the Florida Current which exits the Gulf of Mexico through the Straits of Florida.

The name Cayman-Gulf Current will be used when referring to the continuous flow comprised of these segments. Three questions relating to the Cayman-Gulf Current will be addressed. These questions, listed in order of increasing difficulty, are:

(1) What are the spatial and temporal characteristics of the Cayman-Gulf Current?
(2) What are the dynamical forces which drive this flow?
(3) What relation, if any, does this flow bear to the general circulation of the North Atlantic?

CSM and other data as well as results already published are presented to summarize our state of knowledge pertaining to these questions.

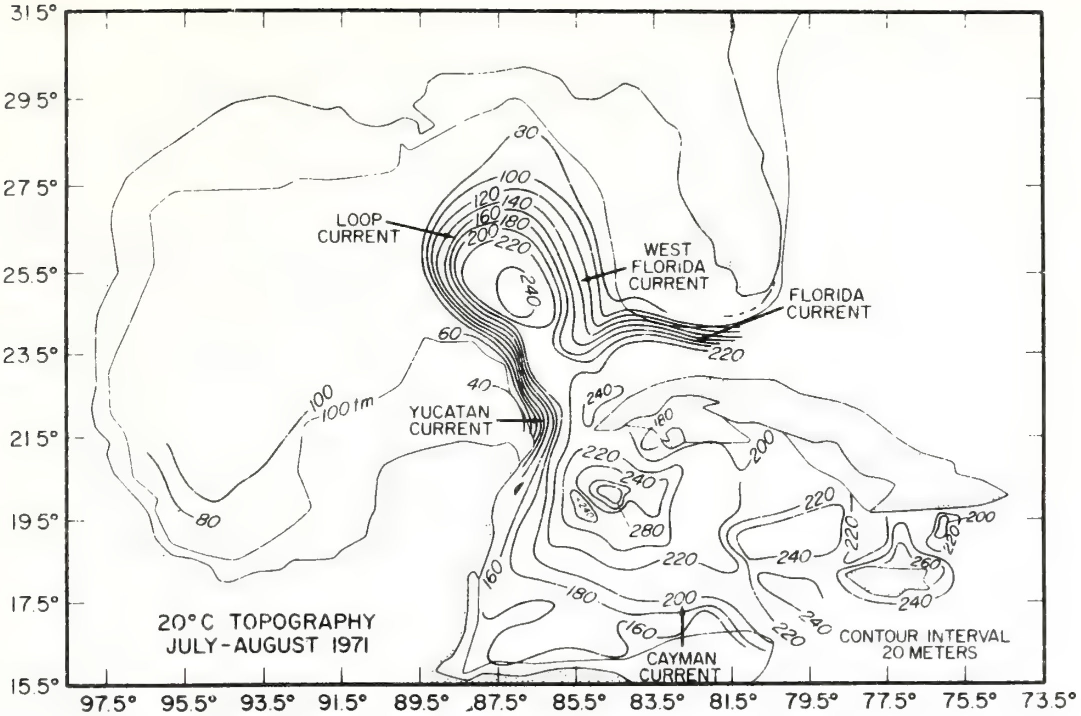

Fig. 1 The 20°C isothermal surface observed during CICAR Survey Month I, July-August 1971. The nomenclature for the segments of the Cayman-Gulf Current are also given

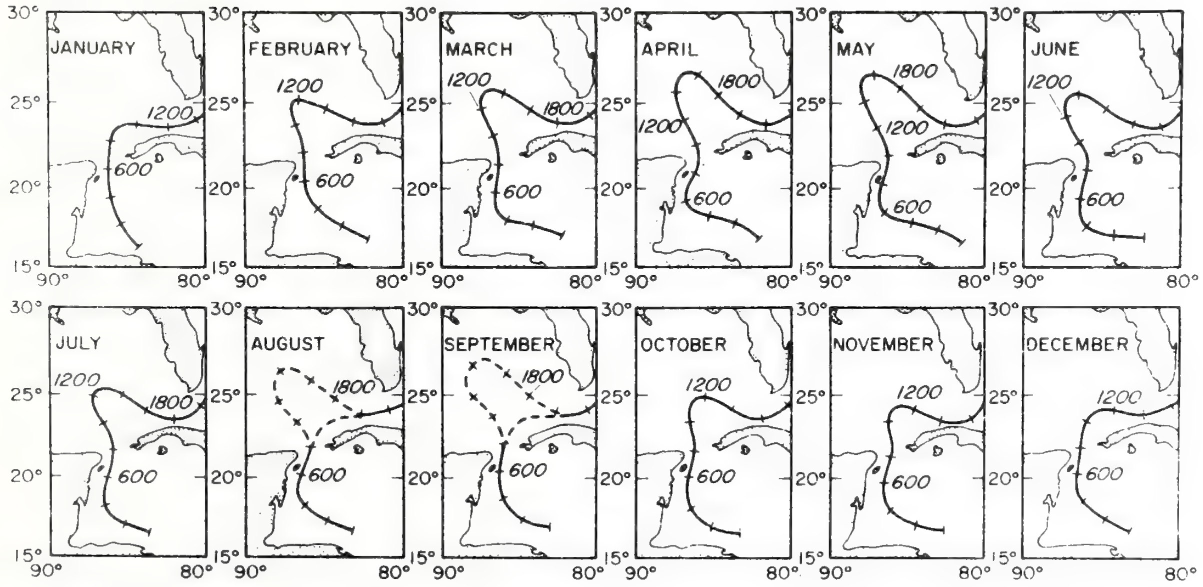

Fig. 2 Monthly mean axes of the Cayman-Gulf Current. The path lines represent the axes of the maximum temperature gradients at 150 m as given by Robinson (1973). Tick marks along the axes denote 200 km intervals

2. SPATIAL AND TEMPORAL CHARACTERISTICS OF THE CAYMAN-GULF CURRENT

Climatological temperature data compiled by Robinson (1973) were used to determine the monthly mean axes of the Cayman-Gulf Current given in Fig 2. The pathlines represent the axes of the maximum temperature gradients at 150 m. These gradients are assumed coincident with the core of the current. As two distinct regions of large gradients were indicated by the climatological temperature data, two axes are drawn in the Gulf of Mexico during August and September.

The monthly paths of the Cayman-Gulf Current which were measured from the 150 m isobath in the Jamaica-Honduras Passage to 80°W in the Straits of Florida apparently vary with an annual cycle. If the southernmost segments of the two axes given for August and September are overlooked, the longest paths are found in the spring and summer and the shortest in autumn and winter. Both the Cayman Sea and Gulf of Mexico segments of the total path are longer in the spring and summer.

Although synoptic representations of the Cayman Sea portion of the Cayman-Gulf Current have been obtained (see Parr, 1937; Cochrane, 1968 or Molinari, 1975) the data were insufficient to determine if an annual cycle existed in the current location. The axes of Fig. 2 indicate that during the spring and summer the Cayman Current has a larger westerly component in the southern basin which accounts for the paths being longer than those observed in the fall and winter.

An annual cycle has been suggested for the Gulf of Mexico portion of the Cayman-Gulf Current. Leipper (1970) proposed that the Loop Current intrudes north into the Gulf of Mexico during the spring; then, as either a loop or an eddy detached from the loop spreads to the west, it finally recedes to a minimum intrusion in the winter. This cycle has also been observed both in a recent synoptic study (Maul, 1975) and in another climatological study of the eastern Gulf of Mexico circulation (Whitaker, 1971).

The data presented here are distributed in time in order to permit a revaluation of the annual cycles discussed above. Temperature and surface drifter data were collected during seven quasi-synoptic time periods: October 1970, July-August 1971, May 1972, May-June 1975, August 1975, October-November 1975 and February 1976. These periods coincided with CICAR Survey Months, except for the October 1970 and August 1975 periods.

The topography of the 20°C isothermal surface is used to depict the large-scale circulation patterns. Surface drifter data collected during several of the experiments are also presented. These Lagrangian drifter data are presented in an Eulerian framework in the sense that the time series of drifter positions are converted to speeds and contoured as a steady-state Eulerian field. The Lagrangian speed data were smoothed first by a technique in which successive groups of speed values were fitted to a polynomial curve (Molinari and Kirwan, 1975).

The 20°C surfaces, Figs. 1 and 3-8, illustrate the large year-to-year variability which exists in the circulation pattern for a particular month. For instance, although the April-May 1972 and May-June 1975 path lengths of the Cayman-Gulf Current (as indicated by axes of the maximum slopes along the 20°C surface) are similar, the circulation patterns are decidedly different (Figs. 3 and 4) in that the 1972 Cayman Current veers to the south before turning north at the Mexican coast. While (although the data are not conclusive) the 1975 pattern suggests that the veering did not occur ; Cochrane (1968) observed a similar southerly deflection during May 1966, but not in May 1968.

The most dramatic differences in the circulation patterns are observed in the anticyclonic eddies found south and north of the Yucatan Channel. In 1975 the eddy south of Cuba (Fig. 4) is significantly smaller and more intense than in 1972 (Fig. 3). In the Gulf of Mexico, a detached eddy was located north of the Cayman-Gulf Current in 1972 but not in 1975. The depression which appears in the 20°C surface at 87.5°W and 27.5°N in 1975 surrounds water which does not have the T-S relationship characteristic of eddies detached from the Loop Current. The 1972 eddy separated from the Loop Current in April and had kinematic properties similar to the main flow (Merrell *et al.*, 1976).

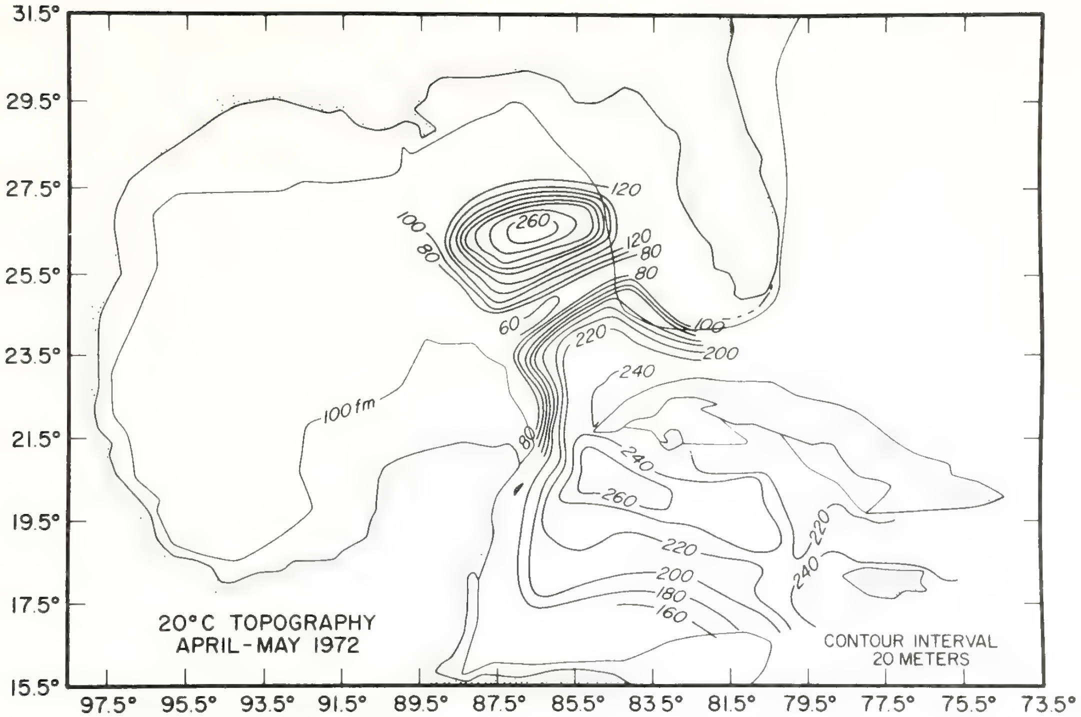

Fig. 3 The 20°C isotherm surface observed during CICAR Survey Month II, April-May 1972

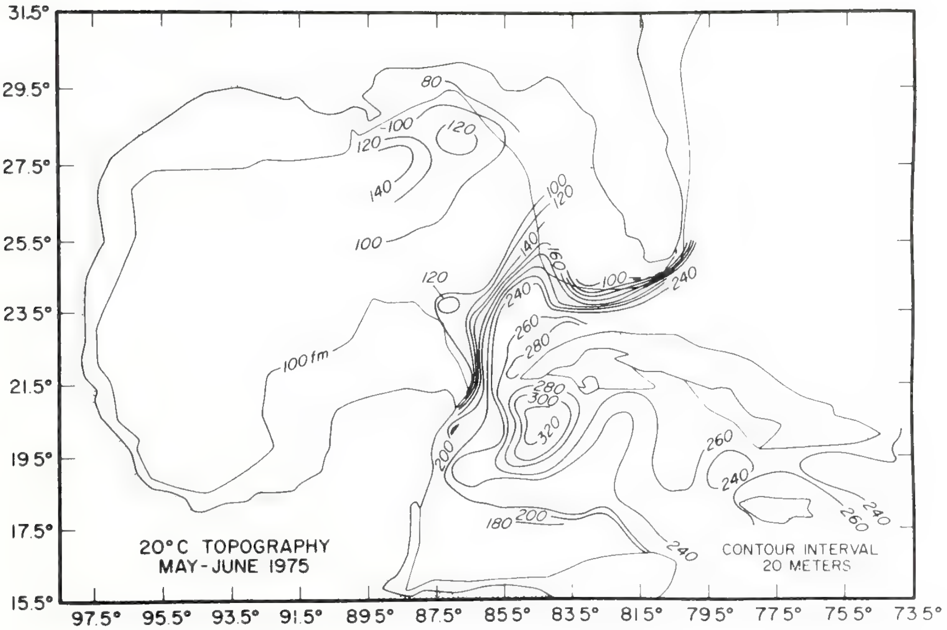

Fig. 4 The 20°C isothermal surface observed during May-June 1975

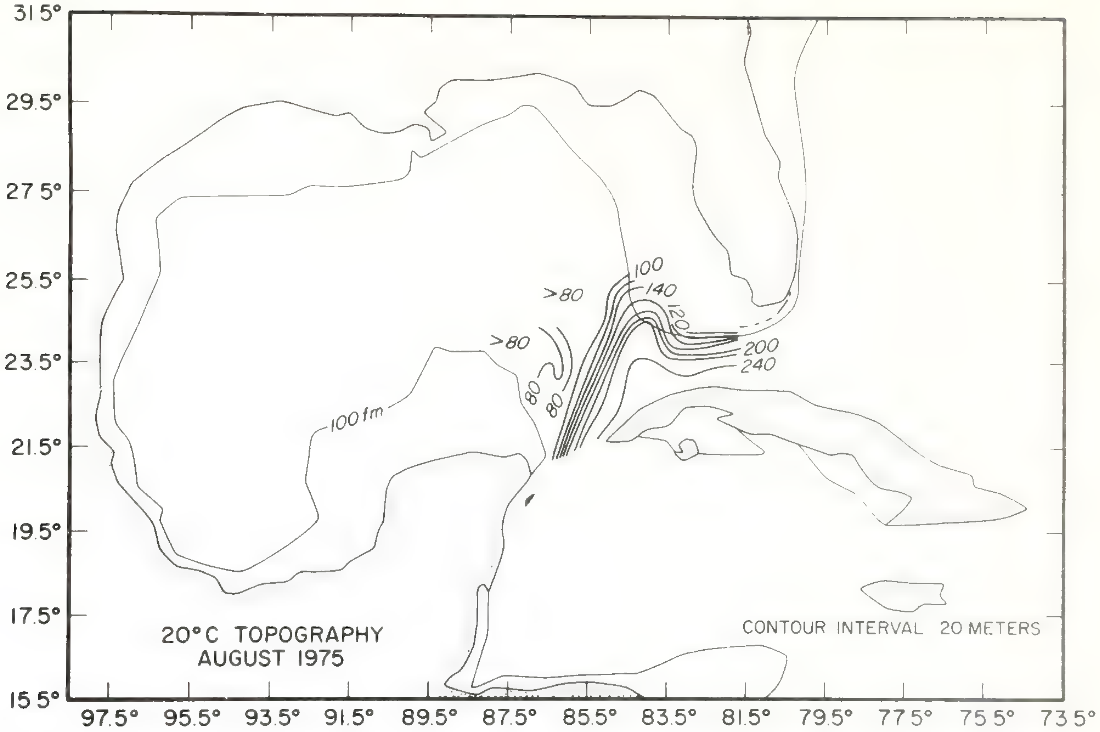

Fig. 5 The 20°C isothermal surface observed during August 1975

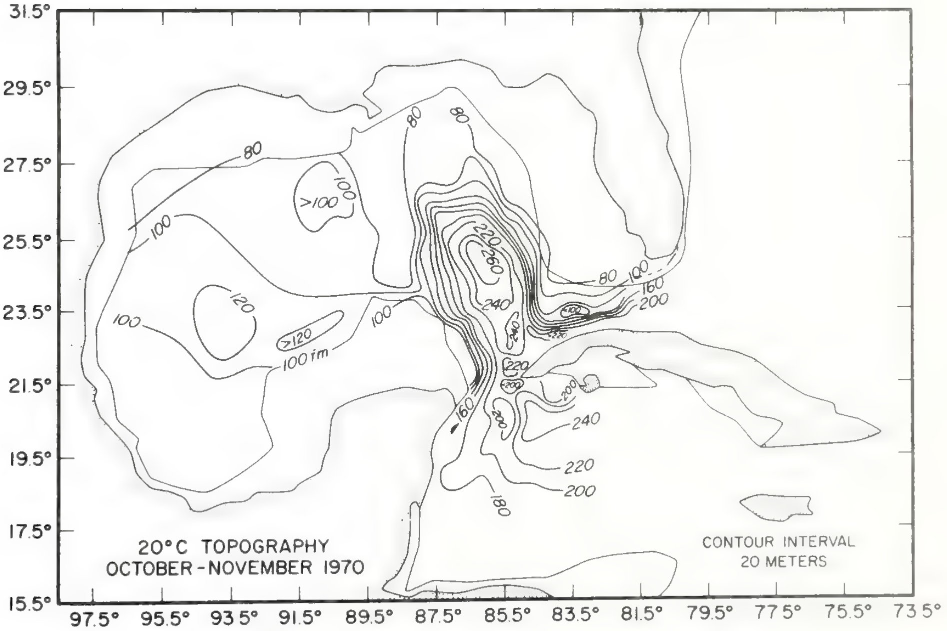

Fig. 6 The 20°C isothermal surface observed during October-November 1970

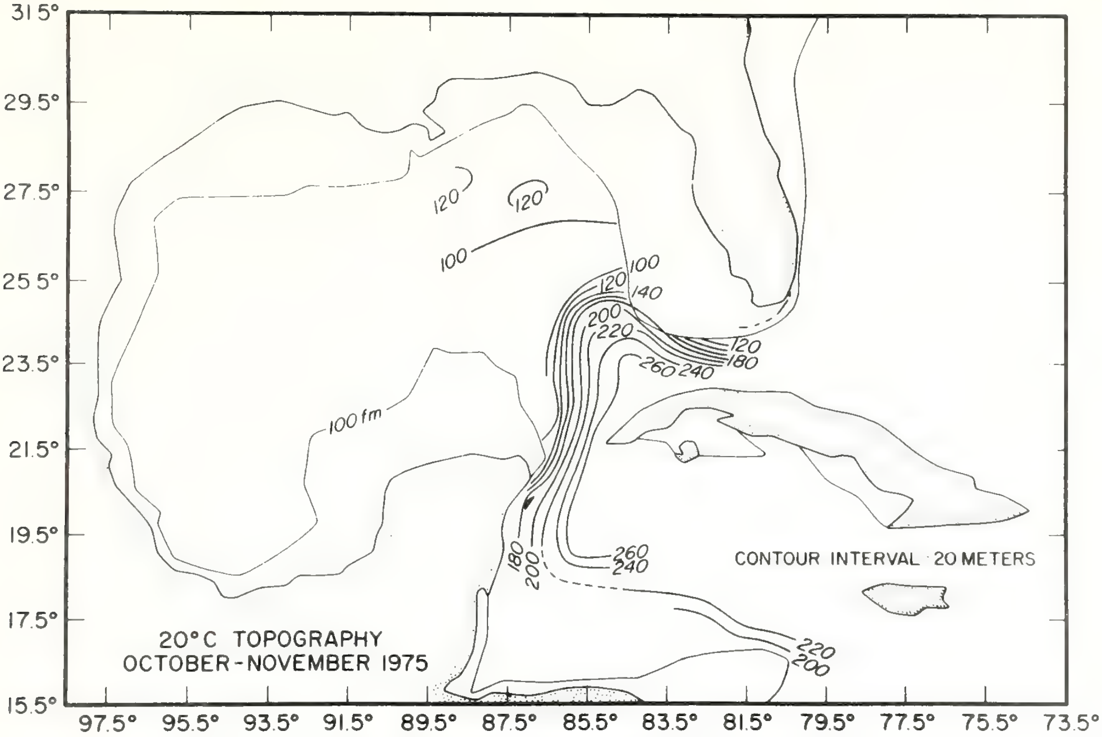

Fig. 7 The 20°C isothermal surface observed during October-November 1975

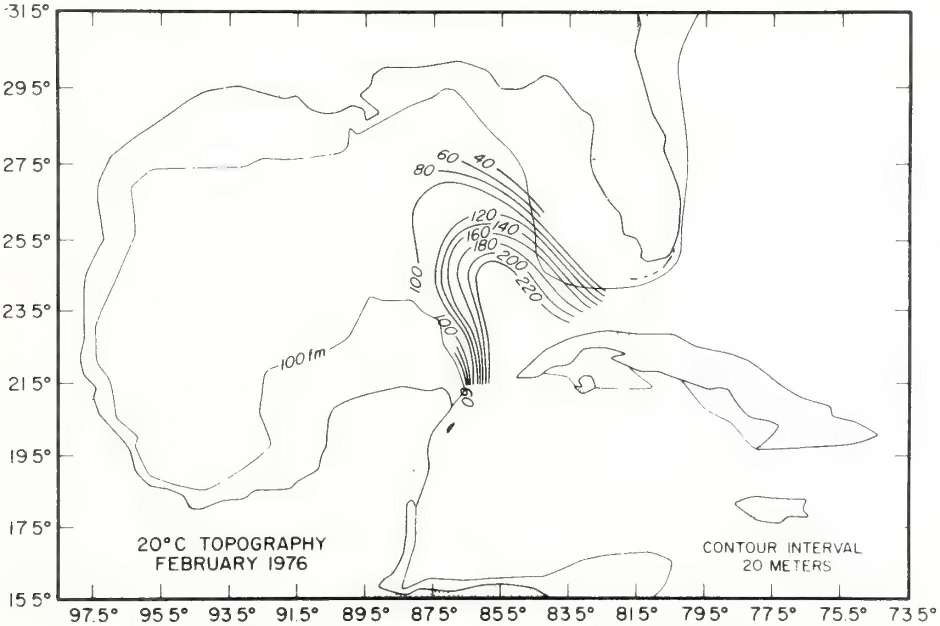

Fig. 8 The 20°C isothermal surface observed during February 1976

Nowlin and Hubertz (1972) observed a detached eddy in June 1967 and a well-developed loop indicative of a pre-separation pattern in June 1966. The small penetration of the Loop Current in 1975 suggests that an eddy had already detached, and indeed Leokegis (1976) observed a separation in February 1975, the earliest time in the year when such an event has been documented.

The summer (Figs. 1 and 5) and autumn (Figs. 6 and 7) 20°C surfaces further demonstrate the large year-to-year seasonal variability in the path length of the Loop Current. During both cases the intrusion during 1975 was considerably less than that observed in the other years.

Cochrane (1976) has shown that the Yucatan Current as it leaves the Yucatan Channel at approximately 22°N has two preferred directional modes. In the west mode, observed during August 1971 (Fig. 1), the current flows to the northwest, while in the east mode, observed during August 1976 (Fig. 5), the current flows to the northeast. The Loop Current intrusion is deeper in the west mode. The existence of two regions of large gradients in August and September (Fig. 2) indicate that the direction of the climatological Yucatan Current during these months has the same two preferred modes at 22°N.

Maul (1975) indicated that eddy separations occurred in November 1970 and late August 1971. The large meanders found in the West Florida Current during both years (Figs. 1 and 6) apparently are precursors to a detachment event (Cochrane, 1972).

The February 1976 20°C surface (Fig. 8) shows what prior to February 1975 (Leckegis, 1976) was observed as a typical wintertime intrusion of the Loop Current (Nowlin, 1972 and SUSIO, 1975).

Perhaps the most remarkable feature of the data from May 1975 through February 1976, combined with data recently collected in May and August 1976, is the absence of the usual intrusion cycle of the Loop Current. Instead, the apex of the Loop Current remained at approximately the same latitude, 25.5°N from May-June 1975 through February 1976 (Figs. 4, 5, 7 and 8). The apex intruded somewhat to 26.5°N by May 1976 (not shown) but remained at this latitude until August 1976 (also not shown). Thus, from May 1975 to August 1976 no large intrusion of the Loop Current intrusion was observed.

In addition to these temporal changes in the spatial characteristics of the Cayman-Gulf Current, temporal changes in the intensities of various segments of the current have been observed. For instance, the sea-surface speeds of the Yucatan Current and the Florida Current apparently vary with an annual period. Mean monthly, ship-drift data indicate that the maximum speeds of the Yucatan Current occur in June and the minimum speeds in November (Cochrane, 1965). In addition, when the flow is most intense, the core of the current is usually observed farther west in the Yucatan Channel than when the flow is weak (Molinari and Cochrane, 1972). The maximum surface speeds of the Florida Current as given by ship-drift reports occur in July and the minimum in November (Fuglister, 1951). However, when fitted by an annual harmonic, a long series of directly measured volume transports in the Straits of Florida exhibit a maximum transport in June (Niiler and Robinson, 1973).

Although the path of the Cayman-Gulf Current varies widely, as shown by the 20°C surfaces, the distribution of speed along the axis of the current remains much the same regardless of path. The surface drifters were launched in the current axis which was located by the thermal field. In all four experiments (Figs. 9 to 12) the drifters decelerated as they entered the anticyclonic turns in both the Cayman Sea and Gulf of Mexico and accelerated as they left these turns. Significant accelerations occur in the Yucatan Straits (Figs. 10 and 11) and the Straits of Florida (Fig. 10). These accelerations are also indicated in all the thermal fields in these regions (Figs. 1 and 3-8) by the large increase in the temperature gradients.

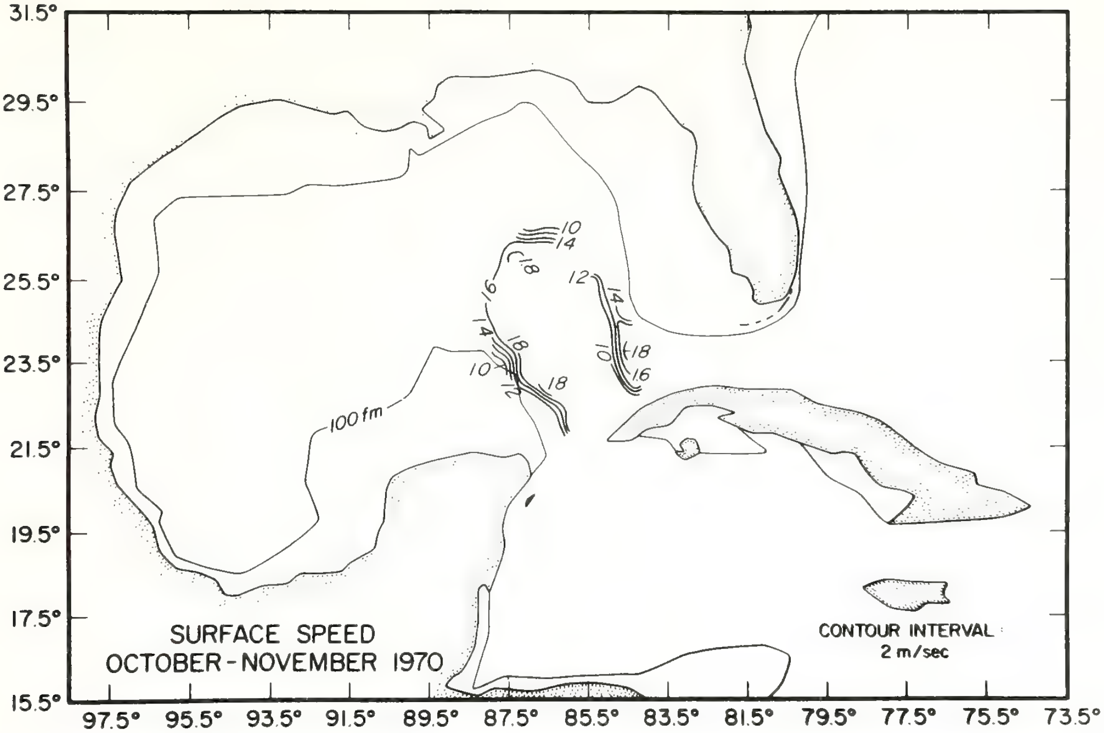

Fig. 9 The distribution of surface current speeds determined from surface drifters (see text) during October–November 1970

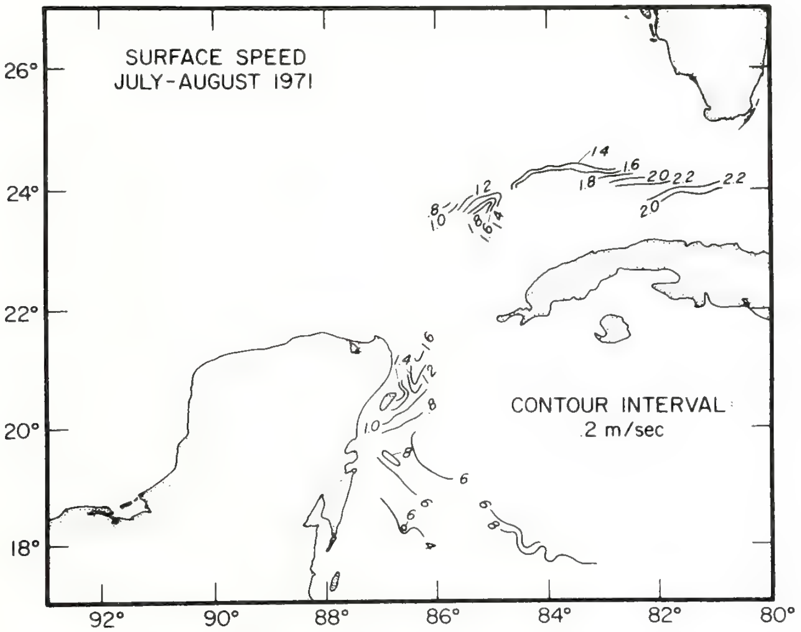

Fig. 10 The distribution of surface current speeds determined from surface drifters (see text) during July–August 1971

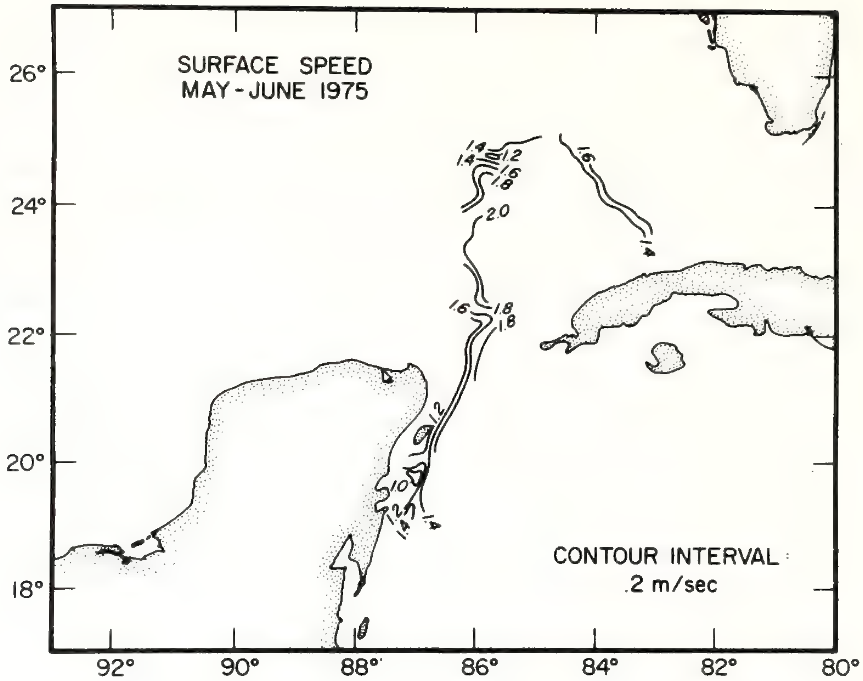

Fig. 11 The distribution of surface current speeds determined from surface drifters (see text) during May-June 1975

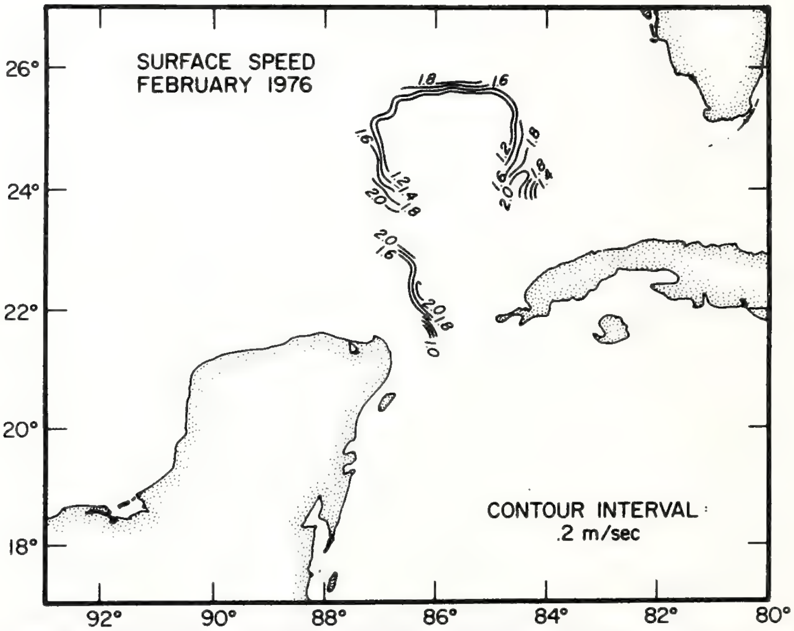

Fig. 12 The distribution of surface current speeds determined from surface drifters (see text) during February 1976

3. DYNAMICAL PROCESSES ACTIVE IN THE CAYMAN-GULF CURRENT

The causes of the observed temporal and spatial variability of the Cayman-Gulf Current and the documented fluctuations of the Yucatan and Florida Currents have not been determined. However, there are indications that these phenomena are related to local and distant wind-fields. Fuglister (1951) found that the Caribbean Current near the Lesser Antilles varies with an annual cycle which he correlated with the local wind-stress cycle in this region. The phases of the Yucatan and Florida Current cycles relative to the phase of the Caribbean Current cycle are such as to suggest a downstream propagation of the annual cycle.

The fluctuations in the intensities of the Florida and Yucatan Currents have been correlated with the winds over the mid-Atlantic and Cayman Seas. Stommel (1965) found in two out of three case studies that an increase in the transport of the Florida Current occurred during the time of a breakdown in the strength of the Bermuda-Azores high. The breakdown, according to Stommel, increases the Ekman transport through the Lesser Antilles and eventually through the Straits of Florida. Emilsson (1971) proposed that the intensity of the Yucatan Current is modulated by the wind-field over the Cayman Sea. When the winds are strong with a large west or northwest component the resulting Ekman drift causes an outflow through the Windward Passage, thereby reducing the transport through the Yucatan Straits.

An additional wind effect on the Cayman-Gulf Current was proposed by Parr (1937) and Gordon (1967). Their data indicate that the Cayman Current flowed against the internal pressure gradient in the Cayman Sea. The energy required for this "uphill" flow was provided by the wind-field.

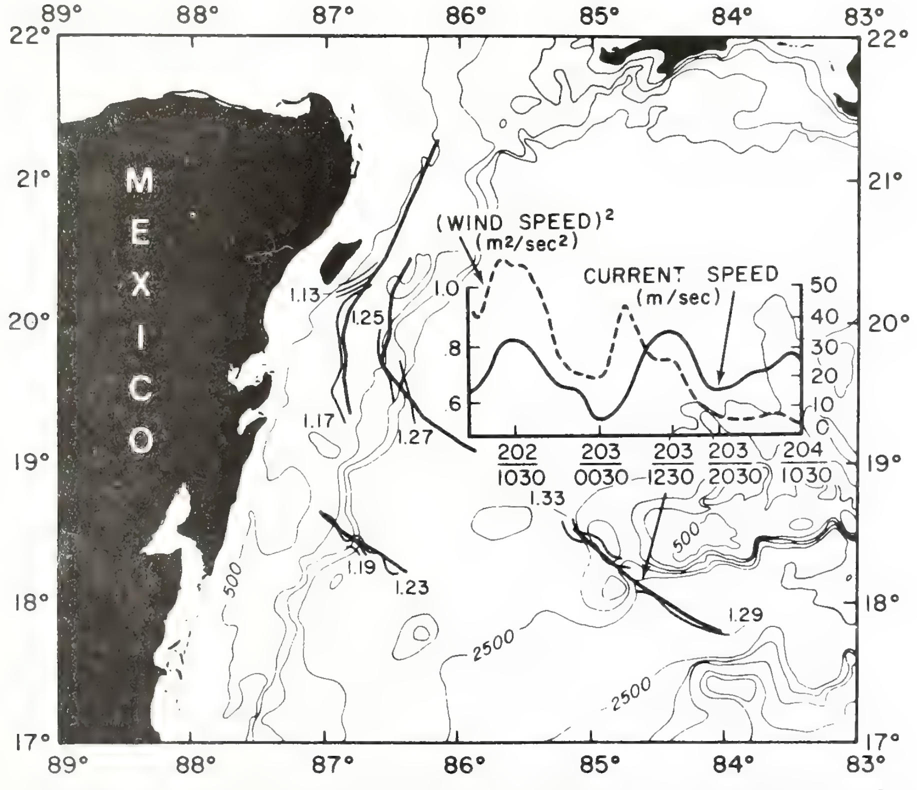

Fig. 13 Centre-of-mass trajectories for buoy clusters deployed during July 1971. The trajectories are superimposed on the dynamic topography of the sea-surface computed relative to 600 m. The insert gives the current speed and wind speed squared functions-vs-time for the indicated trajectory

The surface drogue trajectories and speeds shown in Fig. 13 indicate that in mid-basin the drifters did not decelerate as they moved against the pressure gradient. A description of the drogues and the possible errors due to positioning accuracy, wind effects, etc. are given by Molinari and Kirwan (1975). The downstream component of the wind speed squared (Fig. 13, insert) and the drogue speeds are coherent over the initial part of this trajectory, suggesting that the wind is putting energy into the current to cause the cross gradient flow. This area is one of the two regions where Gordon (1967) proposed that the largest input of energy by the wind occurs. However, as the flow along this trajectory is geostrophic to within 10%, and the deceleration equivalent to the downstream pressure gradient is negligible, of the order 10^{-7}m/sec^2 (Molinari, 1976), the effect of the wind during this period was probably small and limited to the upper layers.

The cause of the temporal variability of the Cayman Current has not been determined, but various proposals have been offered for the cause of the Loop Current cycle: Paskausky and Reid (1972) in a barotrophic numerical model, and Wert and Reid (1972) in a two-layer model. Both of these varied the cross-stream velocity structure at the Yucatan Straits while keeping the total transport into the gulf constant. The effect of this boundary condition is to vary with time the relative vorticity distribution at the input boundary. Both studies produced an annual cycle of Loop Current penetration similar to the cycle proposed by Leipper (1970). However, Maul (1975) suggested that the penetration of the Loop Current might be related to a difference in phase between the maximum transports through the Yucatan Straits and Straits of Florida. Cochrane (1965) has noted that a phase difference of approximately one month exists at least in the surface speeds of the Yucatan and Florida Currents.

The dynamics along the axis of the Cayman-Gulf Current are such that accelerations and decelerations occur in the same relative positions regardless of the path length of the current. Decelerations are observed in the anticyclonic turns at 19°N and 86°W (Fig. 10) and at the apex of the Loop Current (Figs. 9 to 12). Chew (1974) has proposed a kinematical argument that these accelerations are related to adjustments in the shear and curvature components of the relative vorticity which must occur in turning currents. In addition, decelerations are required in anticyclonic turns in which the flow is governed by the gradient relation between Coriolis and centripetal accelerations and pressure gradient forces such as observed in the Cayman Current (Molinari, 1976).

Cochrane (1962) suggested that the formation of the Yucatan Current could be explained in terms of the inertial boundary layer theory of Charney (1955). In this theory, a broad, slow, westward drift in the interior of the ocean is intensified to a narrow, intense, northward flowing boundary current by the action of the earth's rotation. The earth's rotation is modelled by a linear change in Coriolis parameter with latitude, the so-called Beta effect. Molinari (1975) in a numerical modelling study, and Molinari and Kirwan (1975) in an observational study present additional evidence to support this theory.

The results of Chew (1974) support the contention that potential vorticity was conserved along the Loop and Florida Currents during the October 1970 and August 1971 experiments (Figs. 9 and 10). Thus, the available evidence is consistent with the idea that the entire Cayman-Gulf Current is essentially a free inertial current with local forcing having a negligible influence.

4. THE ROLE OF THE CAYMAN-GULF CURRENT IN THE NORTH ATLANTIC GYRE

Ichiye (1969) has hypothesized that the Cayman Sea and Gulf of Mexico serve as a sink of negative relative vorticity for the North Atlantic gyre. A sink is necessary to ensure that absolute vorticity is conserved from 20°N to 30°N; and can be furnished by a source of positive relative vorticity due to friction at the boundary, and/or eddy detachment in the Gulf of Mexico and subsequent loss of negative relative vorticity.

The region obviously has an effect on the heat/salt budget of the North Atlantic since the eddies which detach from the Cayman-Gulf Current in the Gulf of Mexico remove a considerable amount of heat and salt from the North Atlantic gyre. This effect has not been studied extensively.

5. SUMMARY

The physical oceanographic data collected during CICAR significantly broadened the database on which to conduct studies of the region. Most of these data have been analysed in descriptive efforts to infer the current régimes and their temporal variability. The observational evidence portrays a continuous current flowing from the Jamaica-Honduras Passage to the Straits of Florida, with speeds along the axis of the flow ranging between 50 and 200 cm/sec.

Some dynamical studies have been conducted, and the results of these studies indicate that the current is essentially inertial. That is, no significant external forces act on the current as it flows through the Cayman Sea and Gulf of Mexico. Thus the kinematics of the Cayman-Gulf Current is similar to that of other segments of the Gulf Stream system, and it should be considered the first leg of that portion of the North Atlantic gyre. Historically, the Yucatan Current has assumed this role. Many questions regarding the dynamics of the circulation in this region still remain to be answered. For instance, why is there so much variability in the year-to-year monthly current pattern? What is the role of bottom topography in establishing the current régime? What wind régimes contribute to establishing the current fields? Many of these questions will require studies farther upstream into the Caribbean Sea and the Atlantic Ocean in order to be answered. However, because of the importance of these currents to all aspects of the oceanography of the region, it is essential that studies continue to ensure that the questions are answered.

6. ACKNOWLEDGEMENTS

A large portion of the data presented in this discussion were collected aboard the NOAA vessels RESEARCHER and VIRGINIA KEY. The invaluable assistance of the officers and crew of these ships is gratefully acknowledged.

The work was supported in part by the Bureau of Land Management under BLM Interagency Agreement 08550-IA5-26.

7. REFERENCES

Chew, F., The turning process in meandering currents: a case study. J.Phys.Oceanogr.,
1974 4:21-57

Cochrane, J.D., The Yucatan Current. College Station, Texas A. & M. University, Department
1965 of Oceanography, Ref. (65-17T):20-7 (Unpubl.)

———, The currents and waters of the eastern Gulf of Mexico and the western Caribbean
1968 Sea. College Station, Texas A. & M. University, Department of Oceanography,
Ref. (68-8T):19-28 (Unpubl.)

———, Separation of an anticyclone and subsequent developments in the Loop Current
1972 (1969). In Contributions on the physical oceanography of the Gulf of Mexico
edited by L.R.A. Capurro and J.L. Reid. Houston, Gulf Publishing Co., pp. 91-106

———, The configuration of the Gulf of Mexico Loop Current in relation to bathymetry
1976 and season. Paper submitted to the CICAR II Symposium sponsored by IOC, FAO,
Unesco and WMO, Caracas,Venezuela, July 12-16, 1976. Spanish abstract in progress
in marine research in the Caribbean and adjacent regions. CICAR II Symposium,
abstracts of submitted papers. Caracas, Venezuela, CICAR, p. 14

Emilsson, I., On the upper layer circulation in the Cayman Sea. In Unesco/FAO Symposium
1971 on Investigations and Resources of the Caribbean Sea and Adjacent Regions,
Willemstad, Curaçao, 18-26 November 1968. Paris, Unesco, pp. 53-60

Fuglister, F.C., Annual variation in current speeds in the Gulf Stream system. J.Mar.Res.,
1951 10:119-27

Gordon, A.L., Circulation of the Caribbean Sea. J.Geophys.Res., 72:6207-23
1967

Ichiye, T., Circulation and water mass distribution in the Gulf of Mexico. Geofis.Int.Mex.,
1962 2:47-76

———, Experiments on circulation of the Gulf of Mexico and the Caribbean Sea with
1969 a rotating tank. College Station, Texas A. & M. University, Ref. (69-17T):37 p.
(Unpubl.)

Legeckis, R., Present and planned satellite observations of the Gulf of Mexico and the
1978 Caribbean Sea. FAO Fish.Rep., (200) Suppl.

Leipper, D.F., A sequence of current patterns in the Gulf of Mexico. J.Geophys.Res.,
1970 75:637-57

Maul, G., An evaluation of the use of the Earth Resources Technology Satellite for observing
1975 ocean current boundaries in the Gulf Stream system. NOAA Tech.Rep., (ERL 335-
AOML 18):125 p.

Merrell, W.J. Jr. et al., A detailed description of the circulation observed in the eastern
197 Gulf of Mexico during CICAR Survey Month II, May 1972. FAO Fish.Rep., (200) Suppl.

Molinari, R.L., A comparison of observed and numerically simulated circulation in the Cayman
1975 Sea. J.Phys.Oceanogr., 5:51:62

———, The formation of the Yucatan Current based on observations of Summer 1971.
1976 J.Phys.Oceanogr., 6:596-602

Molinari, R.L. and J.D. Cochrane, The effect of topography on the Yucatan Current. In
1972 Contributions on the physical oceanography of the Gulf of Mexico, edited by L.R.A. Capurro and J.L. Reid. Houston, Gulf Publishing Co., pp. 149-55

Molinari, R.L. and A.D. Kirwan, Calculations of differential kinematic properties from
1975 Lagrangian observations in the western Caribbean Sea. J.Phys.Oceanogr., 5:483-91

Niiler, P.P. and W.S. Richardson Jr., Seasonal variability of the Florida Current. J.Mar.
1973 Res., 31:144-67

Nowlin, W.D., Winter circulation patterns and property distributions. In Contributions on
1972 the physical oceanography of the Gulf of Mexico, edited by L.R.A. Capurro and J.L. Reid. Houston, Gulf Publishing Co., pp. 3-51

Nowlin, W.D. and J.M. Hubertz, Contrasting summer circulation patterns for the Eastern
1972 Gulf. Loop Current versus anticyclonic ring. In Contributions on the physical oceanography of the Gulf of Mexico, edited by L.R.A. Capurro and J.L. Reid. Houston, Gulf Publishing Co., pp. 139-48

Parr, A.E., A contribution to the hydrography of the Caribbean and Cayman Sea, based upon
1937 the observations made by the R/V ATLANTIS, 1933-1934. Bull.Bingham Oceanogr. Collect., 5:1-110

Paskausky, D.F. and R.O. Reid, A barotrophic prognostic numerical circulation model. In
1972 Contributions on the physical oceanography of the Gulf of Mexico, edited by L.R.A. Capurro and J.L. Reid. Houston, Gulf Publishing Co., pp. 163-76

Robinson, M.K., Atlas of monthly mean sea surface and sub-surface temperature and depth of
1973 the top of the thermocline Gulf of Mexico and Caribbean Sea. Scripps Inst. Oceanogr., Ref. (73-8): 105 p.

SUSIO, Compilation and summation of historical and existing physical oceanographic data from
1975 the eastern Gulf of Mexico. Coral Gables, State University System of Florida, Institute of Oceanography, Final Report to the Bureau of Land Management, Contract No. 08550-CT4-64

Stommel, H.M., The Gulf Stream: a physical and dynamical description. Berkeley, University
1965 of California Press, 248 p.

Wert, R.J. and R.O. Reid, A baroclinic prognostic numerical circulation model. In
1972 Contributions on the physical oceanography of the Gulf of Mexico, edited by L.R.A. Capurro and J.L. Reid. Houston, Gulf Publishing Co., pp. 177-209

Whitaker, R.E., Seasonal variations of steric and recorded sea level of the Gulf of Mexico.
1972 Masters thesis, Texas A. & M. University, Department of Oceanography, 109 p.

51. CICAR-II Symposium on Progress in Marine Research in the Caribbean and Adjacent Regions, FAO Fisheries Report No. 200 Supplement, 1977, 211-219.

CHEMICAL OCEANOGRAPHY: SUMMARY OF CICAR RESULTS AND RECOMMENDATIONS FOR THE FUTURE

by

D.K. ATWOOD
NOAA/AOML
Miami, Florida 33149, U.S.A.

CONTENTS

1. INTRODUCTION
2. RIVER INPUTS AND EFFECTS
3. CARIACO TRENCH
4. DEEP BASIN WATERS
5. SUSPENDED MATERIAL
6. UPPER WATERS
7. OTHER PROGRESS
8. RECOMMENDATIONS
9. ACKNOWLEDGEMENTS
10. REFERENCES

Abstract

This Symposium has demonstrated that much progress has been made since 1969 concerning knowledge of the marine chemistry of the Caribbean. The area of river inputs and effects has received considerable attention during CICAR; a major share of the efforts were directed toward the effects of the Amazon River. Work presented during this Symposium included: nutrient contributions from the Amazon to the Guyana shelf waters; effects of both the Orinoco and Amazon outflows upon suspended clays, carbonates and organic matter in the eastern Caribbean and adjacent western Atlantic; and the lack of inorganic processes which remove dissolved silica in the estuaries and nearshore water of both the Amazon and Mississippi Rivers. Less is known about the Orinoco and Magdalena Rivers' contributions. Notable progress has been made toward understanding the processes occurring within the Cariaco Trench since the beginning of CICAR. Extensive progress has been made describing the suspended matter in the Caribbean and the mechanisms by which it diffuses. Progress has also been made in the study of the upper circulation of the Caribbean and Gulf of Mexico. The American Mediterranean is a defined marginal sea composed of a series of interconnected basins with both oceanic and terrestrial inputs. Future research should be designed to utilize this unique situation for the study of marine chemical processes. More work needs to be done in defining the physical oceanography of the region so that the chemical oceanographer can plan his experiments and interpret his data with greater ease. The question of river inputs will have to be addressed in greater detail, especially for the Orinoco and Magdalena Rivers. Understanding of anthropogenic inputs is necessary before any meaningful pollution monitoring can be initiated. Elucidating the role played by micronutrients, such as phosphates and nitrates, in the American Mediterranean will be an area of considerable future progress. The effect of catastrophic events such as hurricanes upon marine chemical processes has been almost completely neglected. The need for interdisciplinary seminars which focus on reasonably sized geographic areas is clearly indicated.

Resumen

Este simposio ha puesto de manifiesto los notables progresos realizados desde 1969 por la química marina del Caribe. En los coloquios de las ICCRA se dedicó considerable atención a la cuestión de los materiales de acarreo de los ríos, y a sus efectos, especialmente los causados por el río Amazonas. Entre los trabajos presentados al simposio figuraban: contribución, en elementos nutrientes, del Amazonas a las aguas de la plataforma continental de Guyana; efectos de las descargas de los ríos Orinoco y Amazonas sobre las arcillas, carbonatos y materias orgánicas en suspensión en el Caribe oriental y en el Atlántico occidental adyacente, y ausencia de procesos inorgánicos que eliminen la sílice disuelta en los estuarios y en las aguas litorales de los ríos Amazonas y Mississippi. Las contribuciones de los ríos Orinoco y Magdalena son menos conocidas. Desde que empezaron las ICCRA se conocen mucho mejor los procesos que ocurren en la fosa submarina Cariaco; la descripción de las materias de suspensión en el Caribe, y de sus mecanismos de difusión, es un progreso importante; también ha progresado el estudio de la circulación superior en el Caribe y en el Golfo de México. El Mediterráneo americano es un mar marginal, compuesto de una serie de cuencas interconectadas, con materiales de acarreo oceánicos y terrestres. Deben hacerse futuras investigaciones, a fin de que esta situación única pueda servir al estudio de los procesos químicos marinos. La definición de la oceanografía física de la región requiere más trabajo, para que el oceanógrafo químico pueda planificar sus experimentos e interpretar sus datos con mayor facilidad. Las descargas fluviales tienen que ser estudiadas más detalladamente en particular las de los ríos Orinoco y Magdalena. Para poder iniciar la observación de contaminaciones importantes hay que comprender el fenómeno de las descargas antropogénicas. El esclarecimiento de la función que desempeñan los micronutrientes, como los fosfatos y los nitratos, en el Mediterráneo americano, es una cuestión cuyo estudio progresará considerablemente en el futuro. Se ha prestado muy poca atención a los efectos de fenómenos catastróficos, como los huracanes, sobre los procesos químicos marinos. Se indica claramente la necesidad de seminarios interdisciplinarios que se centren en el estudio de zonas geográficas de una extensión razonable.

1. INTRODUCTION

Status of knowledge in 1968–69: At the start of CICAR, or prior to the beginning of the field phase, a reasonable baseline of chemical oceanographic knowledge had at least begun to exist concerning the Caribbean and adjacent regions. The effects of the Amazon River outflow on the ecology close to the discharge had been investigated. Ryther, Menzel and Corwin, 1967, demonstrated that the low phosphate and nitrate content of the outflow resulted in the lowering of productivity in the nearby ocean waters even though large amounts of dissolved silicate were available. The distribution of dissolved silicate and other nutrients in the Caribbean, as they related to the adjacent North Atlantic, had been described (Richards, 1958). The suggestion had been made that the modeling of dissolved silicate distribution in the Cariaco Trench might develop an understanding which would allow us to approach the problems regarding the extent of renewal in the deep Grenada, Venezuela, and Colombia Basins (Metcalf, 1969). The chemistry of the Cariaco Trench had been described in some detail (Richards and Vacarro, 1956; Redfield, Ketchum and Richards, Volume II, The Sea), and an idea of the frequency of overturn or renewal of the bottom water of that trench had been postulated. The suspended matter in the water column had been considered, and a knowledge of mineral sources and transport in the Caribbean and Gulf of Mexico was developing (Jacobs and Ewing, 1969).

Since a knowledge of the dynamics of ocean systems is essential if a chemical oceanographer is to intelligently interpret his numbers, it is also pertinent to consider some of the physical oceanographic knowledge, which was available to us at the start of CICAR, as well as certain landmark results in that field which occurred during CICAR. In 1969, we were fortunate to have the Wüst and Gordon (1964) monograph on stratification and circulation in the Caribbean, which contained the existing knowledge about Caribbean water masses and their sources. We also had the 1966 paper by Gordon that used Metcalf's 1958 CRAWFORD 17 sections (Metcalf, 1959), along with others, to describe what was known at that time about the dynamics of the system. These data were of significant utility in planning chemical oceanographic research.

Since 1969, the progress in our knowledge of the marine chemistry of the Caribbean has increased at a rapid rate. Much of this progress has been demonstrated at this Symposium. The following includes not only the results presented here, but also papers published elsewhere during that time and work which is now in process or being prepared for publication. In inventorying these latter categories, I have relied heavily upon information from colleagues present at the Symposium, and I have attempted to discuss these results in general categories below.

2. RIVER INPUTS AND EFFECTS

This area has received considerable attention during CICAR; a major share of the efforts were directed toward the effects of the Amazon River. This is understandable in view of the vast amount of water which this river discharges, i.e., between 20 and 30 percent of the freshwater input to the Atlantic Ocean. During this Symposium Bennekom and Tijssen (1977) presented results concerning nutrient contributions from the Amazon to the Guyana shelf waters and their effect upon primary productivity in that area. Betzer et al. (1977) have demonstrated the significant effects of both the Orinoco and Amazon outflows upon suspended clays, carbonates and organic matter in the eastern Caribbean and adjacent western Atlantic. Fanning and Pilson (1973) have demonstrated the lack of inorganic processes which remove dissolved silica in the estuaries and nearshore water of both the Amazon and Mississippi Rivers, and Milliman and Boyle (1975) have described the biological uptake of dissolved silica in the Amazon Estuary. Work carried out by Edmond within the Amazon Estuary and River during 1976 should yield more knowledge on this important source area. Stevens and Brook (1972) have demonstrated the effect of Amazon discharge upon the salinity and silicate relationships near Barbados, and Froelich and Atwood (1977) have described its effects on the salinity/silicate structure of the upper 400 m of the eastern Caribbean. They have postulated that 68 percent of the seasonal freshwater inputs to the Caribbean are from the Amazon, and that these effects are noticeable as far west as Jamaica. Elsewhere, Carder and Schlemmer

(1973) have described nepheloid material found in the subtropical underwater in the Gulf of Mexico which is probably Amazonian in origin. Gibbs (1970, 1972, 1976) has described the water chemistry of the Amazon River itself, particularly the mechanisms by which it transports elements and sediment to the nearby North Atlantic Ocean.

Less is known about the Orinoco River's effects, and still less is known about the Magdalena River's contributions.

3. CARIACO TRENCH

Since its discovery by Worthington in 1954 and the description of its chemistry by Richards and Vacarro (1956), the Cariaco Trench has intrigued chemical oceanographers because of the anoxic processes occurring within it. Notable progress has been made toward understanding the processes occurring within this trench since the beginning of CICAR. Fanning and Pilson (Fanning, 1972) developed a model for the trench which describes its sulphate, phosphate and silicate distributions. In a paper submitted to this conference, Jeffrey and Gershey (1977) demonstrated that organic matter within the trench was not enriched, but that its composition was different by comparison to that of a nearby oxygenated basin. Okuda (1977), in another CICAR-II paper, described the nutrient, oxygen and temperature relationships of the upper waters of the trench and adjacent areas. Additional work on samples of deep trench waters which were collected by R/V TRIDENT during 1974, work which is now in progress, should do much to increase our understanding of anoxic processes.

4. DEEP BASIN WATERS

The first CICAR Symposium (1968) included important discussions of the deep hydrography of Caribbean basins, notably Worthington's (1971) discussion of the potential temperature regime at the Windward and Jungfern sills. Extensive progress has been made in this area during CICAR. Stalcup et al. (1975) and Sturges (1975) have succeeded in quantifying the sporadic inflow over the Jungfern sill from the Atlantic to the deep Venezuelan basin as being about 50 x $10^3 m^3$sec. Froelich and Atwood (1974) demonstrated that this inflow was also evidenced by parcels of low silicate water near the Puerto Rico serial station (17°36'N, 67°00'W). Atwood et al. (1977), in a paper presently in press, have demonstrated that this inflow creates a gradient in deep dissolved silicate concentrations across the entire Venezuela Basin which is commensurate to the amount of net inflow measured. Fanning (1976), in a paper presented to the CICAR-II Symposium, described the flux of silicates from deep Caribbean and Gulf of Mexico basin sediments and postulated that this flux controls deep silicate concentrations. Using this result, he postulated the following residence times or flushing rates for the major basins: Venezuela and Colombian, 200 years; Cayman, 30 years; Gulf of Mexico, 100 years. Papers presently in preparation by Stalcup and Metcalf on data collected from R/V KNORR at the Windward sill in 1974 (Metcalf et al., 1974) should contribute extensively to our knowledge concerning input to deep basins of the western Caribbean.

5. SUSPENDED MATERIAL

Besides the work mentioned above, which describes suspended matter of Amazon and Orinoco origin, other extensive progress has been made. Bassin et al. (1972) described the suspended matter in the Caribbean Sea, and Ichiye et al. (1972) described the mechanisms by which it diffuses. Betzer et al. (1977) described seasonal patterns in suspended calcium carbonate during the wet and dry seasons within the eastern Caribbean.

6. UPPER WATERS

Significant progress made in the study of upper circulation of the Caribbean and Gulf of Mexico, which was described in the physical oceanographic sessions of the CICAR-II Symposium, is of invaluable aid to chemical oceanographers. The eastern Caribbean inputs and flows are beginning to be understood as is the movement of water out of the Caribbean to the Gulf of Mexico and the transport of these waters to the western Gulf in loop-derived eddies. Chemical contributions to this progress have included the description by Kimard et al. (1974) of 18° Sargasso Sea Water in the eastern Caribbean and Berberian and Starr's (1977) use of nutrient/salinity relationships to describe circulation in the Cayman Sea and Gulf of Mexico.

7. OTHER PROGRESS

The distribution of dissolved organics has received little attention anywhere, and CICAR has been no exception to this neglect. During the first CICAR Symposium, Linnenbon and Swinnerton (1971) described C_1 to C_4 dissolved hydrocarbons in the Caribbean and the influence of diurnal variations on their distribution. More recently, Brooks and Sackett (1973) described the distribution of these substances in the Gulf of Mexico and demonstrated that these have extensive anthropogenic sources, e.g.: seaport activities, refineries, and offshore petroleum production operations. Botello et al. (1977), at this conference, described efforts to obtain baseline data on organic occurrences in undisturbed coastal lagoons prior to development near the Mexican coast, and Cedeño Fermín (1977) described the distribution of dissolved carbohydrates in the eastern Caribbean and Gulf of Paria. Jimenez et al. (1977) described large surface active molecules in the eastern Caribbean which affect algal adhesion.

Trace and heavy metal distributions in the Caribbean and Gulf of Mexico have received even less attention. One paper in this conference by Forester et al. (1977) described initial investigations of the occurrence of the first few transition metals, i.e., cadmium, and certain radionuclides in Caribbean waters and plankton.

In the first CICAR Symposium, Andersen (1970, 1971) described work on strontium/chlorinity ratios in the Caribbean and postulated that these ratios might be specific for various water cores. Since that time, Atwood et al. (1973) have demonstrated that there is no such variability in Ca/Cl% and Mg/Cl% ratios. Yet a possibility does exist for Sr/Cl% even though methods which were accurate and precise enough to test this hypothesis were not then available. Isotope dilution methods now available for analysis of Sr should allow for such testing.

8. RECOMMENDATIONS

The American Mediterranean is especially suited to the study of numerous basic chemical oceanographic problems. It is a defined marginal sea composed of a series of interconnected basins with both oceanic and terrestrial inputs. Future research should be designed to use this unique situation in the study of marine chemical processes. It is especially relevant that the physical oceanography of the system be quite well defined in order to allow the chemical oceanographer to plan his experiment and interpret his data with greater ease. We have made considerable progress in this area, especially in the western Caribbean, the Gulf of Mexico, and the passages of the Greater and Lesser Antilles; but more needs to be done. The terrigenous inputs to the system come mostly from four major rivers: the Amazon, Orinoco, Magdalena and Mississippi. Of these, only the Amazon input has been investigated to any degree, and surprisingly, more is known about the inputs from the Amazon and the Orinoco than the Mississippi inputs. Very little is known about the Magdalena inputs even though this river has the greatest potential of the four for transporting suspended material to the deep Caribbean basins. Pulido (1969) of Colombia reported 17 cable breaks near the Magdalena delta over a 26-year period, indicating extensive turbidite inputs. The four rivers drain a variety of terrains. These terrains vary drastically in the extent of their anthropogenic inputs; an understanding of this is necessary before any meaningful pollution monitoring can be initiated.

We should not only address ourselves to the problems of these river inputs, but also to the entire problem of sources and fluxes within the Caribbean, particularly the different chemistries of the deep basins and the processes controlling them. This should include studies of the rates of dissolution of various particulate matter in surface waters, particularly silicate and the extent of remineralization occurring throughout the water column and in the sediments.

Although we are beginning to understand the distribution of dissolved silica in the American Mediterranean, as well as the processes controlling it, we know very little about marine chemical processes in which other micronutrients such as phosphate and nitrate, which are much more important to living resources, play a role. This should be considered in future programmes. However, in this subject area, as in all chemical processes, an effort must be included to understand the effect of the biosphere on the physical chemical system and vice versa. For example, there are currently no comprehensive data on primary production in the open Caribbean Sea.

One aspect which has been almost completely neglected from a chemical standpoint is the effect of catastrophic events such as hurricanes, a meteorological feature unique to the area. Hurricanes have extensive effects on water movement, flushing of shelves and coastal regions and movement of shelf sediments. To study the effects of these events would require local quick response vessels and extensive international coordination.

One of the programmes suggested for IOCARIB by the Puerto Rico meeting of experts is a dynamical chemical model of the American Mediterranean. In concept, this is a vast programme which could be never-ending. It is important to note, however, that such a model is a goal, not a programme itself. Steps toward this goal can be taken in manageable pieces. In approaching this goal, investigators should pay particular attention to the four major river systems, interbasin differences and the processes causing them, the restricted circulation within basins, and the impact of both suspended and bottom sediment on basin water chemistry. A proposed study of the Orinoco outflow and its effects on the southeastern Caribbean and Gulf of Paria might be considered as one of the first "manageable" steps. Similar programmes should be generated for the Magdalena and Mississippi outflows as well as other parts of the system, such as the Venezuela and Guajira upwellings.

The need for interdisciplinary seminars which focus on reasonably sized geographic areas in developing such programmes is clearly indicated.

9. ACKNOWLEDGEMENTS

The author gratefully acknowledges the suggestions and assistance of Drs. Peter R. Betzer, Kent A. Fanning, Neil R. Andersen and Mark Wimbush.

10. REFERENCES

Andersen, N.R., J.D. Gassaway and W.E. Maloney, The relationship of the strontium/chlorinity 1970 ratio to water masses in the tropical Atlantic Ocean and Caribbean Sea. Limnol. Oceanogr., 15:467-72

Andersen, N.R. and J.R. Jadamec, Strontium and barium distributions in the Caribbean Sea. 1971 In Unesco/FAO Symposium on Investigations and Resources of the Caribbean Sea and Adjacent Regions, Willemstad, Curaçao, 18-26 Nov.1968. Paris, Unesco, pp.15-22

Atwood, D.K., P.N. Froelich and W.F. Kinard, Temporal and depth study of alkaline earth 1973 chlorinity ratios in seawater at a single station south of Puerto Rico. Limnol. Oceanogr., 18:771-83

Atwood, D.K. et al., Deep silicate content as evidence of the extent of renewal of 1978 Venezuela Basin Water. Submitted to Deep-Sea Res.,

Bassin, N.J., J.E. Harris and A.H. Bouma, Suspended matter in the Caribbean Sea: a 1972 gravimetric analysis. Mar.Geol., 12:M1-M5

Bennekom, A.J. van and S.B. Tijssen, Nutrients on and off the Guyana shelf related to 1978 upwelling and Amazon outflow. FAO Fish.Rep., (200)Suppl.

Berberian, G.A. and R.B. Starr, The circulation of the Cayman Sea and the Gulf of Mexico
1978 as deduced from nutrient distributions. *FAO Fish.Rep.*, (200)Suppl.

Betzer, P.R. *et al.*, The sources, movements, and reactions of suspended clays, carbonates,
1976 and organic matter in the eastern Caribbean Sea during the wet and dry seasons. Proceedings of CICAR-II Symposium on Progress in Marine Research in the Caribbean and Adjacent Regions, Caracas, Venezuela, 12-16 July 1976

Betzer, P.R. *et al.*, Seasonal patterns in suspended calcium carbonate concentrations during
1977 the dry and wet seasons in the eastern Caribbean. *In* Fate of fossil fuel CO_2 in the atmosphere/ocean system, edited by N.R. Andersen. New York, Plenum Press

Botello, A.V., E. Hicks and E.F. Mandelli, Estudios preliminares sobre los niveles de algunos
1978 contaminantes en la Laguna de Terminos, Campeche, México. *FAO Fish.Rep.*, (200) Suppl.

Brooks, J.M. and W.M. Sackett, Sources, sinks and concentrations of light hydrocarbons in
1973 the Gulf of Mexico. *J.Geophys.Res.*, 78:5248-58

Carder, K.L. and F.C. Schlemmer, III, Distribution of particles in the surface waters of
1973 the eastern Gulf of Mexico: an indicator of circulation. *J.Geophys.Res.*, 78: 6286-99

Cedeño Fermín, G., Carbohidratos disueltos en aguas de la región nor-oriental de Venezuela.
1978 *FAO Fish.Rep.*, (200)Suppl.

Fanning, K.A., Studies on dissolved silica at the boundaries of the ocean system. Ph.D.
1972 Thesis, Graduate School of Oceanography, University of Rhode Island, Kingston, R.I., U.S.A.

___________, Dissolved silica in the American Mediterranean. *FAO Fish.Rep.*, (200)Suppl.
1978

Fanning, K.A. and M.E.Q. Pilson, The lack of inorganic removal of dissolved silica during
1973 river-ocean mixing. *Geochim.Cosmochim.Acta*, 37:2405-15

Forster, W.O. *et al.*, Radionuclide and trace element associations with plankton and possible
1976 vertical transport mechanisms in the Caribbean. *FAO Fish.Rep.*, (200)Suppl.

Froelich, P.N. and D.K. Atwood, New evidence for sporadic renewal of Venezuela Basin water.
1974 *Deep-Sea Res.*, 21:969-75

___________, Influence of the Amazon and Orinoco River discharge on surface salinity and
1978 dissolved silicate concentration in the Caribbean Sea. *FAO Fish.Rep.*, (200) Suppl.

Gibbs, R.J., Circulation in the Amazon River Estuary and adjacent Atlantic Ocean. *J.Mar.*
1970 *Res.*, 28:113-23

___________, Water chemistry of the Amazon River. *Geochim.Cosmochim.Acta*, 36:1061-6
1972

___________, Amazon River sediment transport in the Atlantic Ocean. *Geology*, 4:45-8
1976

Gordon, A.I., Circulation of the Caribbean Sea. *J.Geophys.Res.*, 72:6207-23
1967

Ichiye, T., N.J. Bassin and J.E. Harris, Diffusivity of suspended matter in the Caribbean
1972 Sea. J.Geophys.Res., 77:6576-88. (See also correction to paper, J.Geophys.Res., 78:3631 (1973); Comments on paper by S. Eittreim, P.E. Biscaye and A.I. Gordon, J.Geophys.Res., 78:640-3 (1973); Reply to comments by T. Ichiye, J.Geophys.Res., 78:6404-5 (1973))

Jacobs, M.B. and M. Ewing, Mineral source and transport in waters of the Gulf of Mexico and
1969 Caribbean Sea. Science, Wash., 163:805-9

Jeffrey, L.M. and R.M. Gershey, Organic matter in the Cariaco Trench. FAO Fish.Rep., (200)
1978 Suppl.

Jiménez Velez, B. et al., Adhesion enhancing organics in the eastern Caribbean Sea. FAO
1978 Fish.Rep., (200)Suppl.

Kinard, W.F., D.K. Atwood and G.S. Giese, Dissolved oxygen as evidence for 18°C Sargasso
1974 Sea water in the eastern Caribbean Sea. Deep-Sea Res., 21:79-82

Linnenbom, V.J. and J.W. Swinnerton, Distribution of low molecular weight hydrocarbons
1971 and excess molecular nitrogen in the Cariaco Trench. In Unesco/FAO Symposium on Investigations and Resources of the Caribbean Sea and Adjacent Regions, Willemstad, Curaçao, 18-26 Nov.1968. Paris, Unesco, pp.125-30

Metcalf, W.G., Oceanographic data from the Caribbean Sea; CRAWFORD cruise 17, February-
1959 March 1958 for the International Geophysical Year of 1957-58. Woods Hole Oceanogr.Inst.Ref., (59-9) (Unpubl.MS)

__________, Dissolved silicate in the deep North Atlantic. Deep-Sea Res., 16 Suppl.:
1969 139-45

Metcalf, W.G., M.C. Stalcup and M.E. Zemanovic, Hydrographic stations data Caribbean Sea
1974 ATLANTIS II cruise 78 and KNORR cruise 37. Woods Hole Oceanogr.Inst.Ref. (74-90) (Unpubl.MS)

Milliman, J.D. and E. Boyle, Biological uptake of dissolved silica in the Amazon River
1975 Estuary. Science, Wash., 189:995-7

Okuda, T., Condiciones hidroquímicas de las aguas superiores de la Fosa de Cariaco y âreas
1978 adyacentes. FAO Fish.Rep., (200)Suppl.

Pulido, E.R., Las obras de bocas de Ceniza, Colpuertos, Puertos de Colombia. Bogotâ,
1969 Colombia, Impreso en Italgraf, 100 p.

Redfield, A.C., B.H. Ketchum and F.A. Richards, The influence of organisms on the composition
1963 of seawater. In The sea, edited by M.N. Hill. New York, Wiley Interscience, vol.2:26-77

Richards, F.A., Dissolved silicate and related properties of some western North Atlantic
1958 and Caribbean waters. J.Mar.Res., 17:449-65

Richards, F.A. and R.F. Vaccaro, The Cariaco Trench, an anaerobic basin in the Caribbean
1956 Sea. Deep-Sea Res., 3:214-28

Ryther, J.H., D.W. Menzel and N. Corwin, Influence of the Amazon River outflow on the
1967 ecology of the western tropical Atlantic. 1. Hydrography and nutrient chemistry. J.Mar.Res., 25:69-83

Stalcup, M.C., W.G. Metcalf and R.G. Johnson, Deep Caribbean inflow through the Anegada-
1975 Jungfern Passage. J.Mar.Res., 33 Suppl.:15-35

Stevens, D.M. and A.L. Brooks, Identification of Amazon River water at Barbados, West
1972 Indies, by salinity silicate measurements. Mar.Biol., 14:345-8

Sturges, W., Mixing of renewal water flowing into the Caribbean Sea. J.Mar.Res., 33
1975 Suppl.:117-30

Worthington, L.V., Water circulation in the Caribbean Sea and its relationship to North
1971 Atlantic circulation. In Unesco/FAO Symposium on Investigations and Resources of the Caribbean Sea and Adjacent Regions, Willemstad, Curaçao, 18-26 Nov.1968. Paris, Unesco, pp.181-91

Wüst, G. and A. Gordon, Stratification and circulation in the Antillean-Caribbean basins.
1964 Part 1. Spreading and mixing of the water types with an oceanographic atlas. New York, Columbia University Press, 201 p.

52. CICAR-II Symposium on Progress in Marine Research in the Caribbean and Adjacent Regions, FAO Fisheries Report No. 200 Supplement, 1977, 255-266.

THE CIRCULATION BETWEEN THE CAYMAN SEA AND THE GULF OF MEXICO AS DEDUCED FROM NUTRIENT DISTRIBUTIONS

by

G.A. BERBERIAN and R.B. STARR
NOAA/AOML
Miami, Florida 33149, U.S.A.

CONTENTS

1. INTRODUCTION
2. DATA COLLECTION AND FIELD PROCEDURES
3. LABORATORY ANALYSES
4. OBSERVATIONS AND DISCUSSION
5. CONCLUSIONS
6. ACKNOWLEDGEMENTS
7. REFERENCES

Abstract

Analyses of dissolved oxygen, nitrate, phosphate and silicate from samples collected by the U.S. National Oceanic and Atmospheric Administration's (NOAA) Atlantic Oceanographic and Meteorological Laboratories (AOML) during 1970, 1971 and 1972 in the Cayman Sea and eastern Gulf of Mexico indicate that relative nutrient concentrations can be used to define the deep flow regime of these seas. Results are in agreement with previous findings that the surfaces of the Gulf of Mexico and Cayman Sea have very low nutrient content. However, at depth, the main northward flow through the Yucatan Channel is characterized by relatively high nutrient values and near bottom oxygen values exceeding 5 ml/l, which, together with temperature and salinity, imply this bottom water to be of North Atlantic Deep Water origin. A counterflow at the bottom along the western side of the Yucatan Channel can be distinguished by relatively low oxygen and nutrients. Additionally, nutrient-oxygen data suggest that upwelling occurs at times along the western side of the Yucatan Channel.

Resumen

El análisis del oxígeno disuelto, y de los nitratos, fosfatos y silicatos contenidos en las muestras recogidas por los Laboratorios de Oceanografía y Meteorología Atlántica (AOML) del Organismo Nacional Oceánico y Atmosférico de los Estados Unidos (NOAA) durante 1970, 1971 y 1972 en el Mar del Caimán y en la parte oriental del Golfo de México, indican que las concentraciones correspondientes de nutrientes pueden utilizarse para definir el régimen de las corrientes profundas de esos mares. Los resultados obtenidos coinciden con los anteriores en que las aguas superficiales del Golfo de México y del Mar del Caimán tienen muy bajo contenido de nutrientes; sin embargo, las aguas profundas de la corriente principal hacia el norte, a través del canal de Yucatán, se caracterizan por sus valores relativamente elevados en nutrientes y por valores de oxígeno superiores a 5 ml/l cerca del fondo, los cuales, unidos a la temperatura y a la salinidad, permiten suponer que estas aguas de fondo procederían de las aguas profundas del Atlántico norte. Las secciones del fondo hechas a lo largo de la parte occidental del Canal de Yucatán se caracterizan por un contenido relativamente bajo de oxígeno y de nutrientes. Además, los datos sobre el oxígeno y los nutrientes indican que a veces se producen afloramientos a lo largo de la parte occidental del Canal de Yucatán.

1. INTRODUCTION

Recent advances in the automated analyses for the marine micronutrients such as nitrate, nitrite, silicate and phosphate have permitted the processing of sufficient amounts of data to evaluate them as possible tracers of water circulation. This is particularly useful where the weak gradients of temperature and salinity make these parameters marginal for such purposes. As part of the U.S. participation in the CICAR during the years 1970, 1971 and 1972, more than 3 000 water samples at depths from the surface to over 2 000 m deep from more than 300 oceanographic stations in the Caribbean and Gulf of Mexico have been collected by the Atlantic Oceanographic and Meteorological Laboratories of NOAA and analysed for nutrients, temperature, salinity and dissolved oxygen. It is apparent from these analyses that, with the exception of nitrite, the distributions and concentrations of these nutrients can be useful in helping to describe ocean circulation.

The temperature structure of these seas is quite well known and will not be discussed here. This presentation will be limited to describing the distribution of nutrients, salinity and dissolved oxygen along sections which are important to the understanding of the circulation between the Cayman Sea (the northwestern Caribbean Sea) and the eastern Gulf of Mexico. Our discussion will centre around sections across or immediately south of the Yucatan Channel which were occupied in 1970, 1971 and 1972 (Fig. 1). Concurrent with this discussion of the Yucatan Channel sections and the Cayman Sea circulation, nutrient relationships in the main northward flow through the channel and in variable (but significant) southward counterflow will be presented.

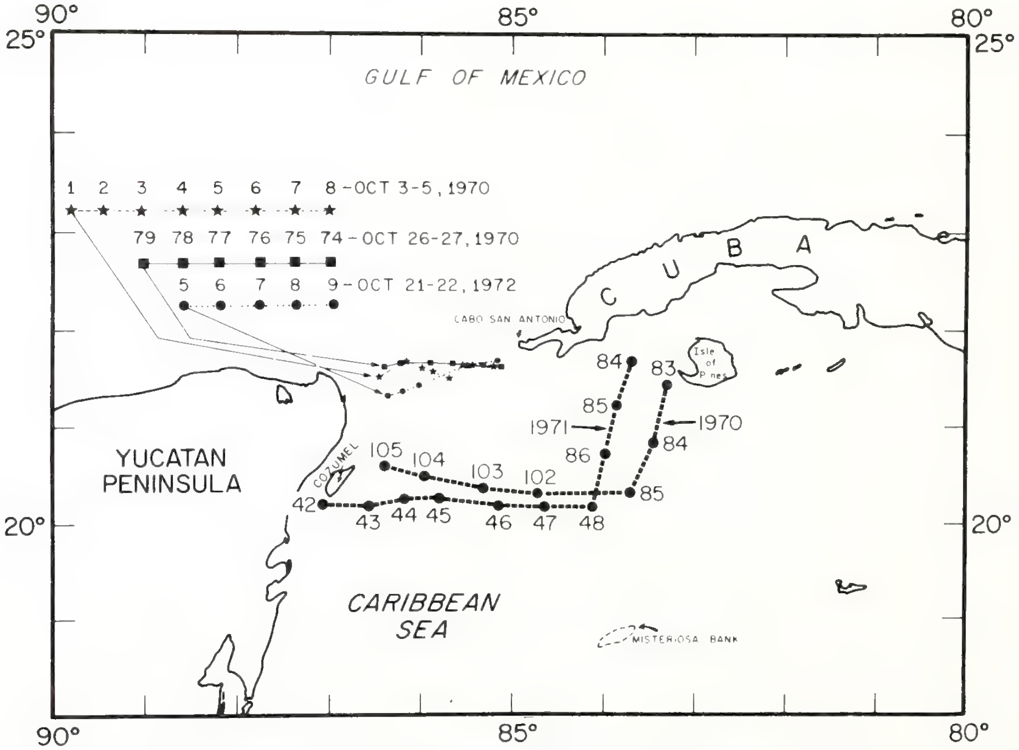

Fig. 1 Location of stations in the Yucatan Channel area

2. DATA COLLECTION AND FIELD PROCEDURES

Data from the following cruises are reported on in this paper: Cruise 1, October to November, 1970; Cruise 2, July to August, 1971; Cruise 3, October to November, 1972. During each cruise, except on stations 1 to 8 across the Yucatan Channel in early October, 1970, temperature and salinity were measured at each station by means of a Plessey model 9006 STD with attached General Oceanics Rosette Multi-Sampler rigged with standard 1.7 l Niskin bottles. Stations 1 to 8 were obtained by oceanographic casts with Nansen bottles. Water samples with the Rosette Multi-Sampler were collected at specified temperatures and depths chosen to sample maximum and minimum physical and chemical properties of the water column as seen in historical oceanographic data. These were analysed for salinity, oxygen and nutrient concentration. Salinity measurements were completed aboard ship using a Beckman inductive salinometer. The samples for dissolved oxygen were drawn first in order to minimize atmospheric contamination and temperature-induced changes. Sample analysis was conducted on board ship using modified Winkler titration method described by Strickland and Parsons (1968).

Approximately 200 to 300 ml aliquots were collected in polyethylene bags (Whirl-Paks), or polyethylene bottles, frozen immediately and returned to AOML Laboratories for nutrient analyses.

3. LABORATORY ANALYSES

The nutrient samples were analysed for dissolved inorganic nitrate (NO^-_3-N), nitrite (NO^-_2-N), orthophosphate ($PO^{\equiv}_4$-P), and silicate ($SiO^{=}_4$-Si), with a four-channel Technicon AutoAnalyzer.

The analytical procedures used in the analysis for nitrate and nitrite are described by Armstrong et al. (1967). Essentially, the orthophosphate is the procedure described by Grasshoff (1965) and the silicate procedure is described by Strickland and Parsons (1968). The water used for standardization, blank determination and wash between samples is filtered Gulf Stream seawater obtained from the surface of the Straits of Florida. The detection limits and precision of analysis for the four nutrients are listed below in Table I.

TABLE I

Operational characteristics of the nutrient-analyses system

Parameter	Range and detection limit µg-at/l	Coefficient of variation (95% confidence level) % at µg-at/l
NO_3-N/l	0.50 - 50.0	0.17 at 15.00
NO_2-N/l	0.10 - 20.0	1.20 at 3.20
PO_4-P/l	0.05 - 20.0	1.60 at 0.64
SiO_4-Si/l	0.50 - 50.0	0.97 at 25.00

4. OBSERVATIONS AND DISCUSSION

In all cases, across the Yucatan Channel, the Subtropical Underwater is characterized by the highest salinities (36.75‰) in the water column, by dissolved oxygen values generally less than 4 ml/l, by phosphate and silicate concentrations usually below their detection limits, and nitrate about 5 µg-at/l. The Antarctic Intermediate Water is distinguished by the lowest salinities (34.85‰) in the water column, by oxygens between 3 and 4 ml/l, phosphates greater than 1.5 µg-at/l, nitrates of 30 to 35 µg-at/l, and silicates of 20 to 25 µg-at/l. Upper North Atlantic Deep Water is typified by salinities very close to 35.00‰, by dissolved oxygens greater than 5 ml/l, by phosphates of approximately 1.0 µg-at/l, nitrate between 20 and 25 µg-at/l, and silicate between 15 and 20 µg-at/l.

With respect to the three sections taken directly across the Yucatan Channel (Fig. 2 through 10), the one obtained on NOAA-CARIB during October, 1972 (Fig. 2, 3 and 4) appears to be in most agreement with the distribution of properties described by Richards (1958) and Howlin and McLellan (1967). Geostrophic current computations performed on this section show a general strong, baroclinic flow to the north, even at depth (Fig. 2). An exception to this, apparent in this figure, is a possible very weak southerly counterflow at depth along the western side of the bottom as seen in the current meter data of Hansen and Zetler (1972). The computed maximum velocity occurs at the surface along the western side of the channel and amounts to 79 cm/sec (1.5 knots). Along the Cuban side of the channel, the flow appears less, while the least flow is in the centre of the channel.

The salinity structure, also shown in Fig. 2, supports these interpretations as it is typical of the salinity values seen in the Caribbean Sea (Wüst, 1964). The Subtropical Underwater as defined here by the 36.75‰ isohaline is concentrated along the west side of the channel, while the Antarctic Intermediate Water below 34.90‰ crosses most of the section. Probable Upper North Atlantic Deep Water with a salinity of 35.00‰ is indicated at the bottom.

The near-surface phosphate, nitrate and silicate values (Fig. 3 and 4) exemplify the low nutrient values seen in these waters throughout the Caribbean and Gulf of Mexico. At the bottom, phosphate values below 1.5 µg-at/l, nitrates under 25 µg-at/l, and silicates from 17 to 20 µg-at/l are associated with the possible deep counterflow. These values are in agreement with the distributions of Richards (1958) and Metcalf (1969), which suggest that, compared to the 1970 results discussed below, the counterflow was insignificant at this time. This conclusion is in agreement with the lack of shear noticed when occupying the western stations of this section compared to 1970. The upward tilt of nutrient isopleths toward the west side of the Yucatan Channel is not great enough to suggest upwelling at the time this section was taken.

In contrast to the regularity shown by the 1972 observations, the Yucatan sections resulting from the October, 1970 work suggest a very different flow regime. Concurrent current meter observations were obtained at the same time as these stations. These have been reported by Hansen and Zetler (1972) and confirm that a south-flowing current was in existence at the bottom of the Yucatan Channel during this period.

There is some evidence of this flow in the computed geostrophic current section (Fig. 5). The calculated velocities for 1970 also show a considerably stronger surface current along the west side of the channel than was observed in 1972. The indicated baroclinic flow on the east side of the channel was very much less than in 1972, while a surface countercurrent is suggested in the vicinity of Station 5. In accordance with these observations, it was noted during the occupation of these stations that the ship drifted rapidly northward on Station 2, and experienced a high wire angle due to very strong shear at depth, while at Station 5 it did not drift at all. At Station 8, the ship drifted southward in a counterflow around Cabo San Antonio, but an additional station closer inshore would be required to define this in Fig. 5.

The concurrent salinity distribution shown in this figure is somewhat more irregular than in 1972 with the Subtropical Underwater shifted to the east side of the channel. Additionally, the core of the Antarctic Intermediate Water, as defined by the 34.85‰ isohaline, is absent or virtually absent and relatively little water of 35.00‰ salinity is present. This suggests less flow of these waters north through the Yucatan Channel at this time.

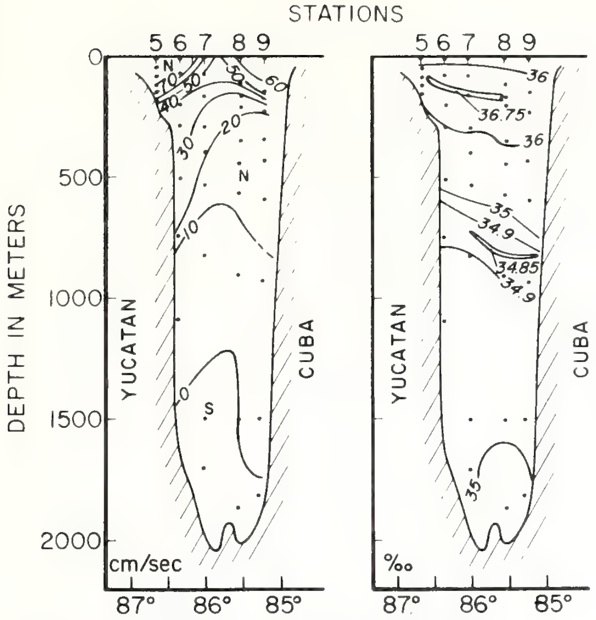

Fig. 2 Isotachs of current velocity relative to 1 700 m depth and salinity distribution, Yucatan Channel, 21-22 October 1972

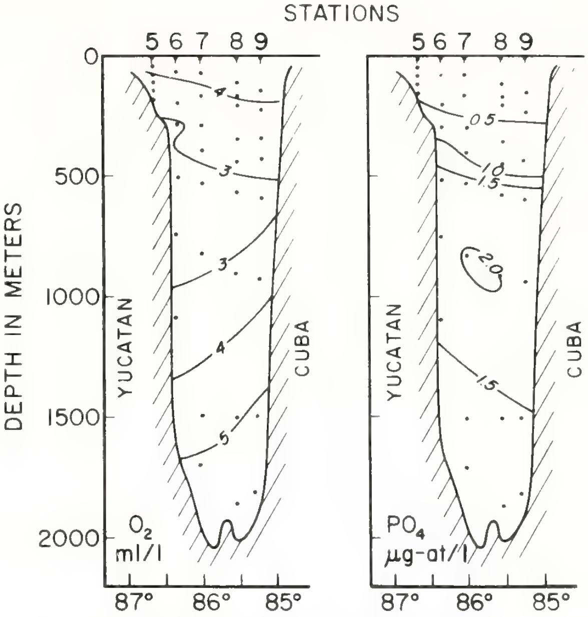

Fig. 3 Regular nutrient distribution, Yucatan Channel, 21-22 October 1972

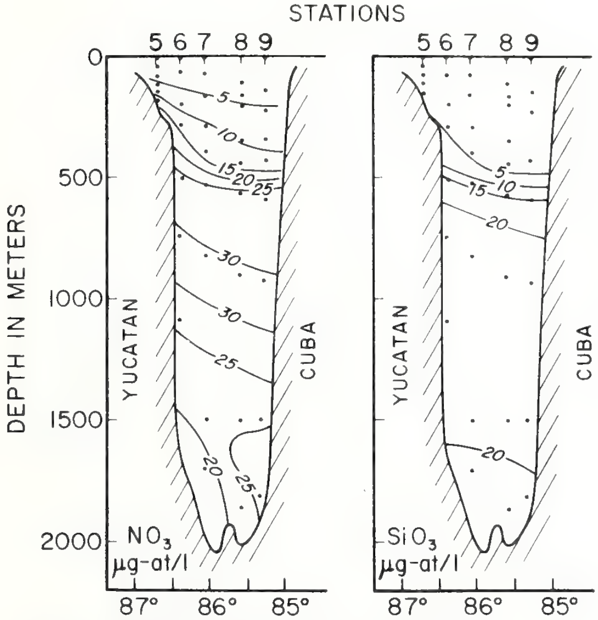

Fig. 4 Regular nutrient distribution, Yucatan Channel, 21-22 October 1972

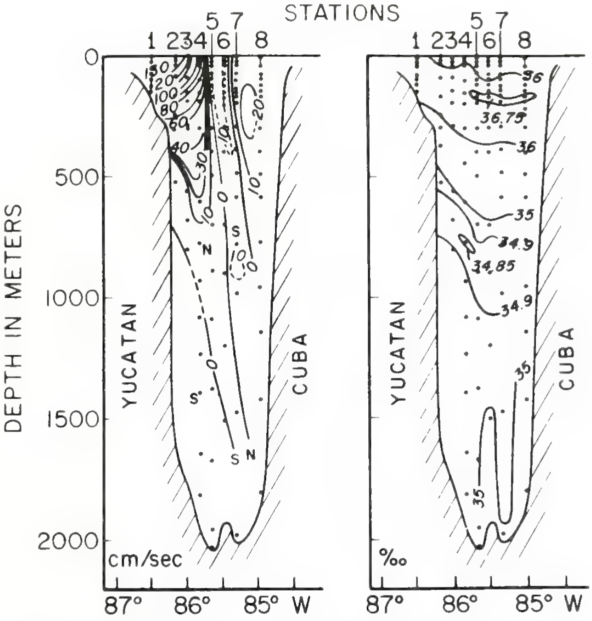

Fig. 5 Isotachs of current velocity relative to 1 700 m depth and salinity distribution, Yucatan Channel, 3-5 October 1970

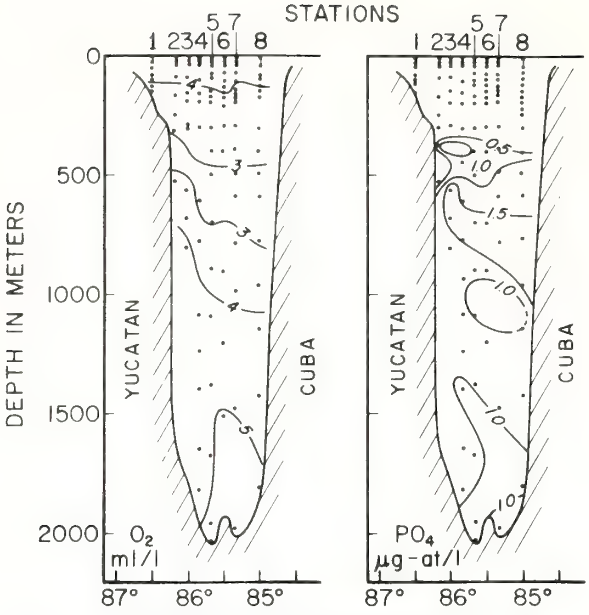

Fig. 6 Anomalous nutrient distribution, Yucatan Channel, 3-5 October 1970

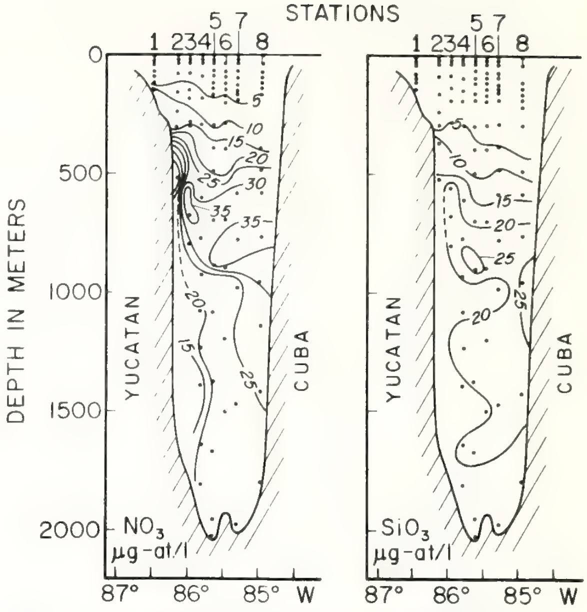

Fig. 7 Anomalous nutrient distribution, Yucatan Channel, 3-5 October 1970

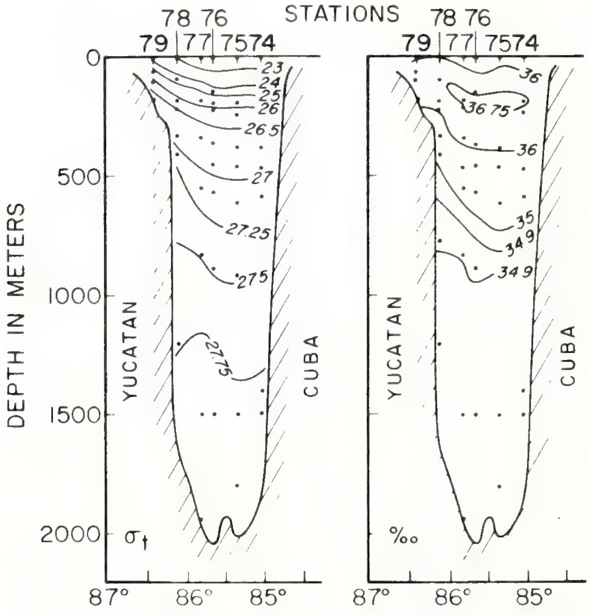

Fig. 8 Density and salinity distributions, Yucatan Channel, 26-27 October 1970

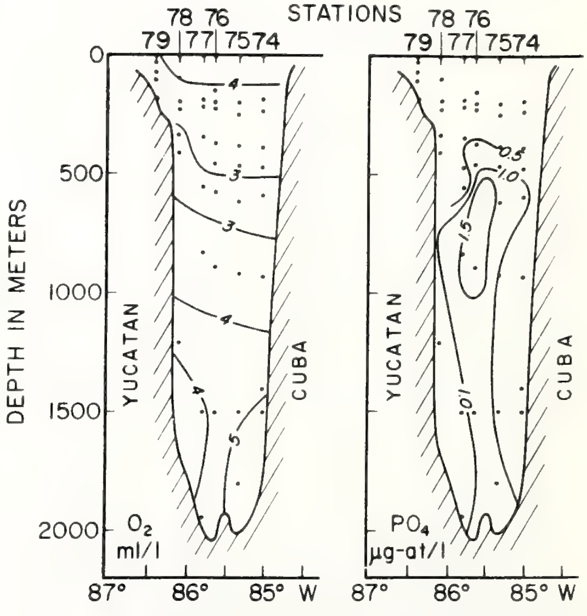

Fig. 9 Anomalous nutrient distribution, Yucatan Channel, 26-27 October 1970

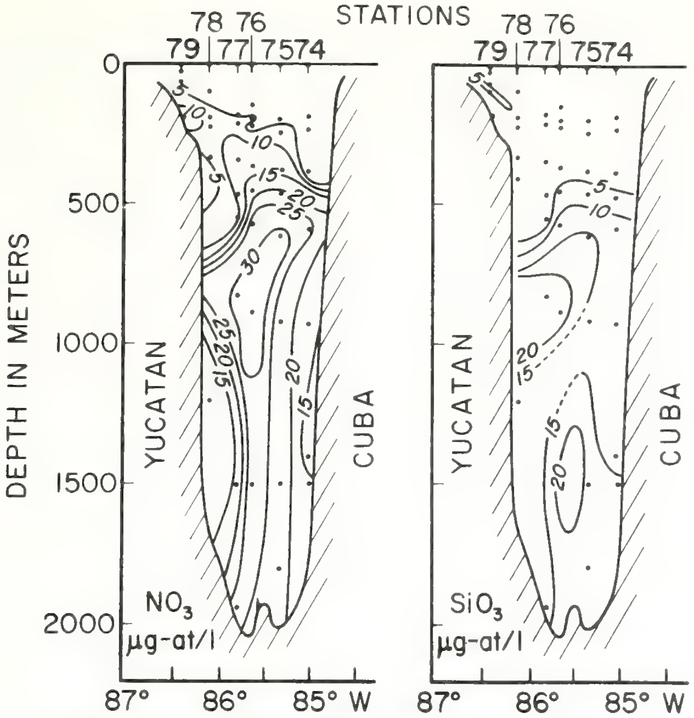

Fig. 10 Anomalous nutrient distribution, Yucatan Channel, 26-27 October 1970

The irregular oxygen-phosphate-nitrate-silicate distributions shown in Fig. 6 and 7 illustrate some of the variability associated with this variation of the flow regime. These data are consistent with the current structure and the salinity distribution already discussed. High nitrate, silicate and phosphate are evident in the main northward flowing current between 500 and 1 000 m depth; while the indicated south flowing bottom water along the Yucatan side has dissolved oxygen values lower than seen previously: phosphates of about 1.0 µg-at/l, nitrates as low as 15 µg-at/l, and silicates again under 20 µg-at/l.

A second 1970 occupation of this line of stations occurred in late October (Fig. 8, 9 and 10). While this section is in general agreement with the first crossing, several significant differences are apparent. The salinity distribution is characterized by a very large core of Subtropical Underwater indicating strong northward flow at shallow depth, but no Antartic Intermediate Water as defined by core salinities of 34.85‰ or less. Additionally, there is no 35.00‰ salinity at the bottom so that the flow of Upper North Atlantic Deep Water at these depths is indicated as being minimal. The density structure and current meter record (Hansen and Zetler, 1972) support a continuing southward bottom counterflow. The dissolved oxygen of this bottom counterflow is now mostly below 4 ml/l, while the phosphate is still close to 1.0 µg-at/l, the nitrate is again in the 15 µg-at/l range, and silica is down to 10 to 12 µg-at/l. Upwelling along the western side of the Yucatan Channel is suggested by the higher than normal near-surface nitrate and silicate values and low oxygens in these figures.

In conjunction with the 1970 Yucatan Channel sections, a line of stations was taken in October-November, 1970 from Cozumel to the vicinity of the Isle of Pines (Fig. 1). This line is important because it crosses an anticyclonic gyre which seems to be a persistent feature between Yucatan Channel and Misteriosa Bank (Molinari, 1975; Hazelworth and Starr, 1975), and because it can be compared to a line of stations (Fig. 1) occupied in 1971 when the threat of a hurricane prevented the taking of the Yucatan Channel section samples. In 1970, the salinity distribution, shown in Fig. 11, agrees with that of the Yucatan Channel section. The 36.75‰ isopleth of the Subtropical Underwater defines the rim of the gyre while the deepening of the lower 34.90‰ isopleth at Station 102 indicates the centre of the gyre. Although there is an appreciable amount of Upper North Atlantic Deep Water as expressed by the 35.00‰ isopleth, very little of the 34.85‰ Antarctic Intermediate Water is evident here, in agreement with the Yucatan Channel sections. The phosphate, nitrate and silicate plots (Fig. 12, 13 and 14) define the gyre very distinctively, particularly the high values associated with the Antarctic Intermediate Water. The nutrient values, as illustrated by silicate (Fig. 14), are low in the centre of the gyre relative to those reported for these depths by Richards (1958, 1960) and Metcalf (1969).

In comparison to the salinity and nutrient distributions in the 1970 section, those of the 1971 section portray a more strongly developed gyre centred on Station 47 and a relatively strong southeasterly flow centred on Station 86 (Fig. 15). This flow is apparently composed of the eastern arm of the gyre and flow from around Cabo San Antonio (Emilsson, 1971; Molinari, 1975; Hazelworth and Starr, 1975). According to their dynamic topography and our geostrophic current computations (Fig. 15), the main northward flow occurs as a broad stream between Stations 42 and 45, while the flow between Stations 45 and 47 is the western arm of the gyre (Hazelworth and Starr, 1975).

The salinity distribution shown in Fig. 16 differs from 1970. The Subtropical Underwater defined by the 36.75‰ isohaline is missing in the rim of the gyre but is seen in the centre and along the Cuban Shelf where mixing is not so intense. The rim of the gyre is conspicuously defined at depth by the large blobs of Antarctic Intermediate Water with a salinity less than 34.85‰. No Upper North Atlantic Deep Water, defined by a salinity of 35.00‰, is seen in this section in 1971.

The dissolved oxygen (Fig. 17) has a surprisingly thin O_2 minimum layer and a very strong gradient in it with an O_2 maximum at 500 m near Cuba. Since this station was near the broad, southern Cuban Shelf and out of the main stream of the flow around Cabo San Antonio, this high oxygen water may originate from the South Cuba Shelf as a result of sinking of high density water (Emilsson, Tapens and Godoy, 1971). The maximum nutrient values are seen here associated with very little flow as shown by phosphate, nitrate and silicate (Fig. 18, 19 and 20). At depth on the eastern and northern stations, the low nutrient values are again in disagreement with earlier findings (Richards, 1958, 1960; Metcalf, 1969); while the low nitrate value at 500 m at the station next to Cuba supports the surface source for this water postulated in the oxygen discussion.

5. CONCLUSIONS

Nutrient values associated with the interchange of water between the Cayman Sea and Gulf of Mexico exhibit characteristics that enable nutrients to be used as tracers of the circulation. Near-surface values of nutrients in these seas are characteristically too low to be useful as tracers, but below 300 to 400 m phosphate, nitrate and silicate distributions appear to be closely related to the circulation pattern. In the Yucatan Channel, high nutrient values are associated with Antarctic Intermediate Water and then decrease roughly 20 percent with depth to values characteristic of Upper North Atlantic Deep Water except in the bottom counterflow where dissolved oxygen is about 1.0 ml/l lower than Upper North Atlantic Deep Water, phosphate ranges around 1.0 µg-at/l, nitrate ranges from less than 15 to 20 µg-at/l, and silicate is less than 20 µg-at/l. In these three Yucatan Channel sections it appears that oxygen and nitrate values are the most definitive indicators of the counterflow. However, because of the indicated variability of this flow, this might not always be the case. It is difficult to make comparisons with historical data because of the lack of nutrient values from this area, particularly nitrate.

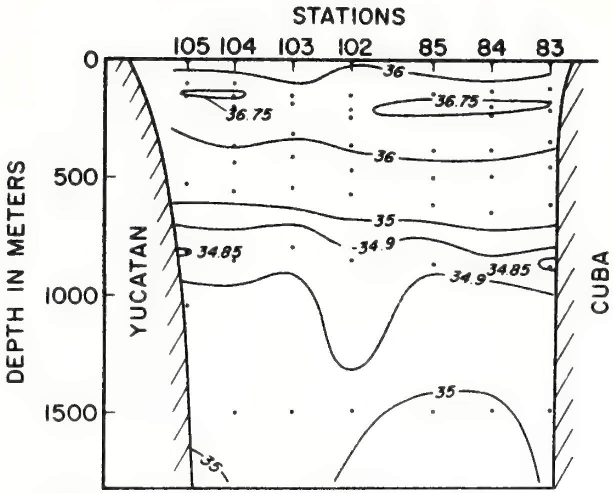

Fig. 11 Salinity distribution (‰) south of Yucatan Channel, 28 October to 2 November 1970

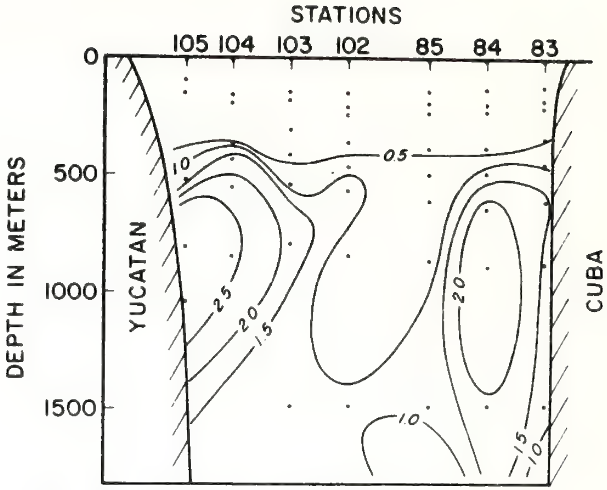

Fig. 12 Phosphate distribution (μg-at/l) south of Yucatan Channel, 28 October to 2 November 1970

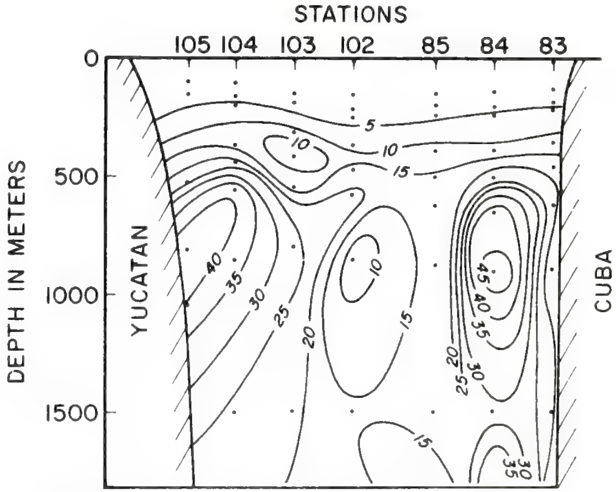

Fig. 13 Nitrate distribution (μg-at/l) south of Yucatan Channel, 28 October to 2 November 1970

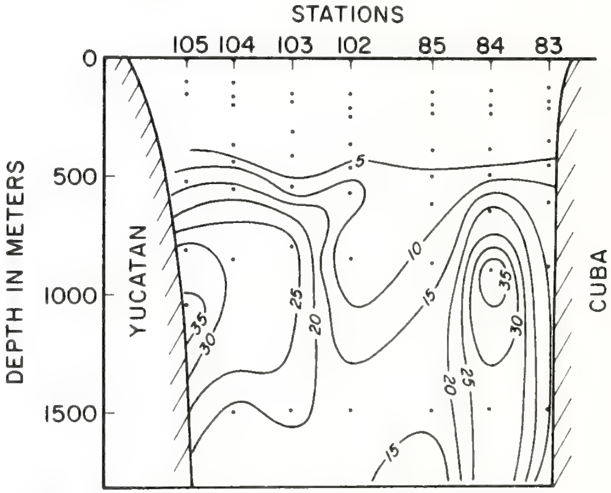

Fig. 14 Silicate distribution (μg-at/l) south of Yucatan Channel, 28 October to 2 November 1970

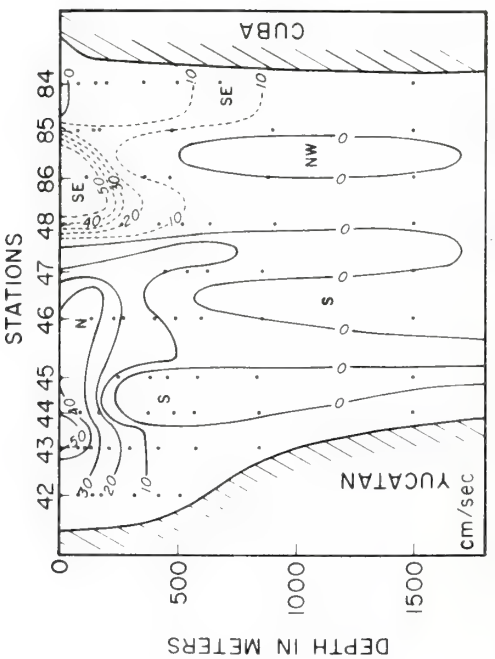

Fig. 15 Isotachs of current velocity (cm/sec) relative to 1 800 m depth, south of Yucatan Channel, 29 July to 30 August 1971

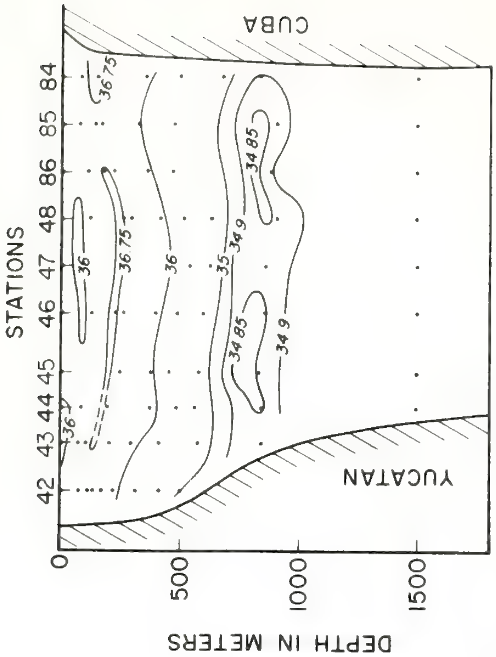

Fig. 16 Salinity distribution (‰) south of Yucatan Channel, 29 July to 30 August 1971

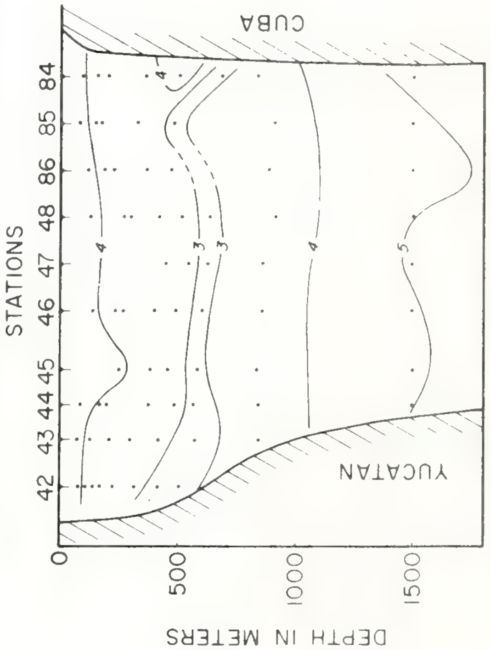

Fig. 17 Oxygen distribution (ml/l) south of Yucatan Channel, 29 July to 30 August 1971

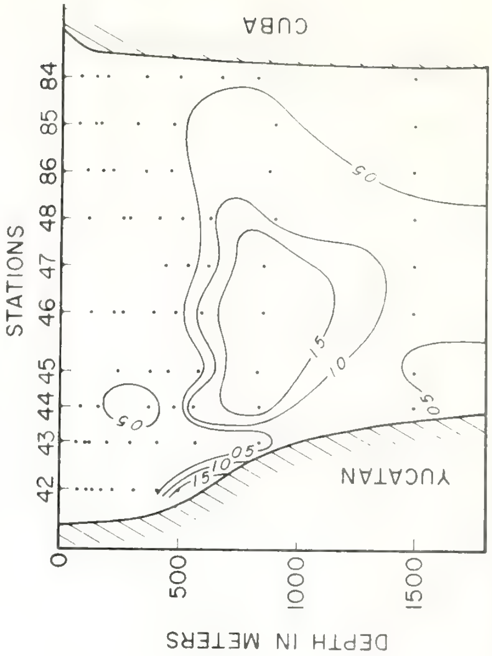

Fig. 18 Phosphate distribution (µg-at/l) south of Yucatan Channel, 29 July to 30 August 1971

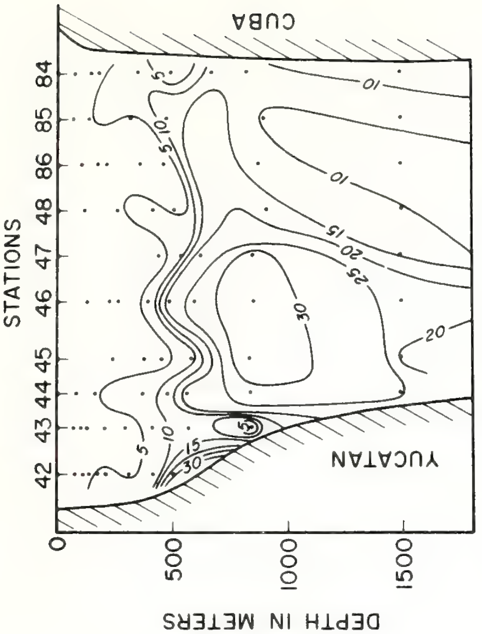

Fig. 19 Nitrate distribution (µg-at/l) south of Yucatan Channel, 28 July to 30 August 1971

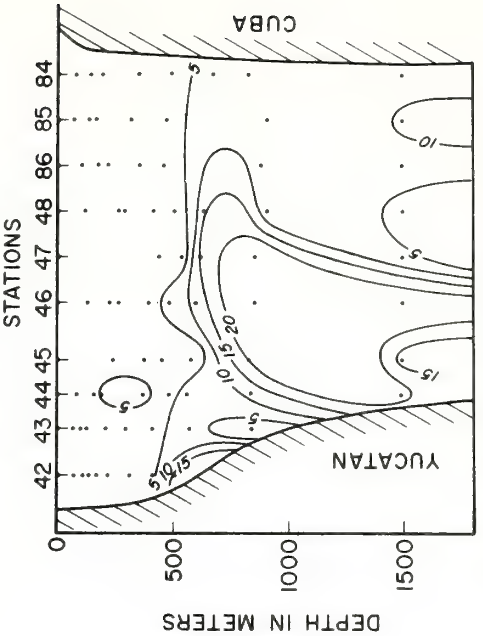

Fig. 20 Silicate distribution (µg-at/l) south of Yucatan Channel, 28 July to 30 August 1971

Comparing the sections across Yucatan Channel and to the south in the Cayman Sea with one another indicates that the nutrient distributions, the associated salinity structure and the flow determinations are quite variable with time, although there is consistency in the major features. The October, 1972 Yucatan Channel section has the most normal nutrient structure with the least indication of southerly flow at the bottom or at the surface around Cabo San Antonio. Supporting current calculations indicate a strong baroclinic flow through the Yucatan Channel at the surface from the Cayman Sea to the Gulf of Mexico, particularly along the western side and, a probably intermittent, but definable, counterflow along the bottom on the Yucatan Peninsula side. Additionally, a variable southerly, though possibly continuous, surface flow is evident around Cabo San Antonio. The anticyclonic gyre crossed by the Cayman Sea sections has a prominent nutrient signature and seems to be a permanent feature between Misteriosa Bank and Yucatan Channel.

6. ACKNOWLEDGEMENTS

The authors express their thanks to the officers and crew of the R/V DISCOVERER for the long and diligent hours they devoted to collecting these data. Thanks are also due to John Hazelworth of AOML for data processing for the geostrophic current computations. The work was funded in part by the National Science Foundation under International Decade of Exploration grant AG-253. We would also like to thank Mr. Robert Carrodus and his group for all the illustrations in this paper.

7. REFERENCES

Armstrong, F.A.J., C.R. Stearns and J.D.H. Strickland, The measurement of upwelling and
1967 subsequent biological processes by means of the Technicon Auto Analyzer and
associated equipment. Deep-Sea Res., 14:381-9

Emilsson I., Note on the countercurrent in the Yucatan Channel and the Western Cayman Sea.
1971 Geofis.Int., Mex., 11:139-49

Emilsson, I., J. Tappanes and J. Godoy, Aspectos hidrográficos de la plataforma sur de
1971 Cuba. In Unesco/FAO Symposium on Investigations and Resources of the Caribbean
Sea and Adjacent Regions, Willemstad, Curaçao, 18-26 November 1968. Paris,
Unesco, pp. 64-71

Grasshoff, K., Automatic determination of fluoride, phosphate and silicate in sea water.
1965 In Technicon Fifth International Symposium, Automation in analytical chemistry,
held in London, October 13, 1965. Tarrytown, New York, Mediad Inc., Publ.
No.65-P76E, pp. 304-7

Hansen, D.V. and B.D. Zetler, Deep currents in the Yucatan Strait. Trans.Am.Geophys.Union,
1972 53:392 (Abstr.)

Hazelworth, J.B. and R.B. Starr, Oceanographic conditions in the Caribbean Sea during the
1975 summer of 1971. NOAA Tech.Memo., (ERL 344-AOML 20):144 p.

Metcalf, W.G., Dissolved silicate in the deep North Atlantic. Deep-Sea Res., 16 Suppl.:
1969 139-45

Molinari, R.L., A comparison of observed and numerically simulated circulation in the Cayman
1975 Sea. J.Phys.Oceanogr., 5:51-62

Nowlin, W.D. Jr. and H.J. McLellan, A characterization of the Gulf of Mexico waters in
1967 winter. J.Mar.Res., 25:29-59

Richards, F.A., Dissolved silicate and related properties of some western North Atlantic
1958 and Caribbean waters. J.Mar.Res., 17:449-65

__________, Some chemical and hydrographic observations along the north coast of South
1960 America. 1. Cabo Tres Puntas to Curaçao, including the Cariaco Trench and Gulf
of Cariaco. Deep-Sea Res., 7:163-82

Strickland, J.D.H. and T.R. Parsons, A practical handbook of sea water analysis. Bull.Fish.
1968 Res.Board Can., (167):311 p.

Wüst, G. and A. Gordon, Stratification and circulation in the Antillean-Caribbean basins.
1964 Part 1. Spreading and mixing of the water types with an oceanographic atlas.
New York, Columbia University Press, 201 p.

53. Surficial Sediments. MESA New York Bight Atlas Monograph 10, New York Grant Institute, Albany, N.Y., 1978, 93 pp. (Only the abstract has been reprinted.)

Abstract

The surficial sediment cover of the continental shelf in New York Bight consists of a sheet of sand up to 10 m thick with small areas of gravel and muddy sand. Off the shelf edge, mud increases to become the dominant sediment. Most sediment was first deposited during or soon after the last glacial maxima when the present shelf was land and has been reworked by the advancing shoreline. Most shelf morphologic features also reflect these conditions.

Modification of the natural pattern of sedimentation has occurred in the Bight apex where man has dumped his wastes for over 60 years. Dredge spoil dumping has created several knolls on the bottom, and with outfalls, the dumping of sewage sludge, acid wastes, construction, and other rubble, has made the apex a "worst case" example of ocean pollution. With proper management of municipal and industrial wastes, however, the apex may eventually return to a near-natural setting—still in use by man, but without harmful ecological effects.

54. Marine Geology 27 (1978), 19-42.

EVOLUTION OF A SHOAL RETREAT MASSIF, NORTH CAROLINA SHELF: INFERENCES FROM AREAL GEOLOGY

DONALD J.P. SWIFT, PHILLIP C. SEARS*, BRENDA BOHLKE, and ROBERT HUNT**

Atlantic Oceanographic and Meteorological Laboratories, Miami, Fla. 33149 (U.S.A.)

(Received December 2, 1976; revised and accepted April 11, 1977)

ABSTRACT

Swift, D.J.P., Sears, P.C., Bohlke, B. and Hunt, R., 1978. Evolution of a shoal retreat massif, North Carolina Shelf: inferences from areal geology. Mar. Geol., 27: 19—42.

The Albemarle Shelf Valley Complex on the northern North Carolina Shelf is a leveed shelf-floor channel trending seaward from the modern Albemarle estuary. Vibracores and seismic profiles indicate that the levees have a twofold internal structure. Levee cores consist of fine sand interbedded with mud lenses. The cores are mantled with a generally coarser, cleaner sand. The levees are interpreted as shoal retreat massifs; deposits formed as the littoral-drift depositional centers on either side of the ancestral Albemarle estuary retreated landward during the Holocene transgression.

The shelf-valley complex underwent systematic changes in bottom morphology and sediment character as the reversing tidal jet of the estuary mouth was replaced by the intermittent south-trending storm flows of the open shelf. A pattern of ridges and troughs with 10 m of relief was incised into north sides of the massifs flanking the shelf valley.

The coarser surficial sand into which the bedform pattern has been impressed appears to be a lag deposit formed by the winnowing of the massifs during storm flow. On ridge crests this surficial sand sheet has been molded into sand waves up to 3 m high. The relative orientations of sand waves, ridges, and the shoreline indicate that the structure of the velocity field during peak flows must be quite complex. Ridges converge southward with the shoreline at angles of 15—20°, while the sand waves atop them make angles of about 75° with the shoreline; the sand waves are thus neither orthogonal with respect to the shoreline nor with respect to the ridges. Sand-wave orientation indicates southward bottom flow with an offshore component.

Existing hydrodynamical theory does not adequately explain this pattern. Extensive hydraulic measurements of careful design will be required so we can interpret the bedform pattern and its role in the coastal sand budget.

---

*Present address: Van Houten Associates, 420 Lexington Place, New York, N.Y. 10017 (U.S.A.)

**Present address: NOAA Ship "Oceanographer", Pacific Marine Center, Seattle, Wash. (U.S.A.)

INTRODUCTION

The Middle Atlantic Shelf of North America is divided into a series of compartments by transverse shelf-valley complexes (Swift, 1973; Swift and Sears, 1974; Fig.1, this paper). Shelf-valley complexes are suites of topographic elements generated by the landward displacement of estuary mouths during the Holocene transgression. A shelf-valley complex may include (1) a mid-shelf or shelf-edge delta, (2) a shelf valley, and (3) shoal retreat massifs. The latter features are broad, poorly defined sand ridges on the north flanks or on both flanks of shelf valleys that mark the retreat

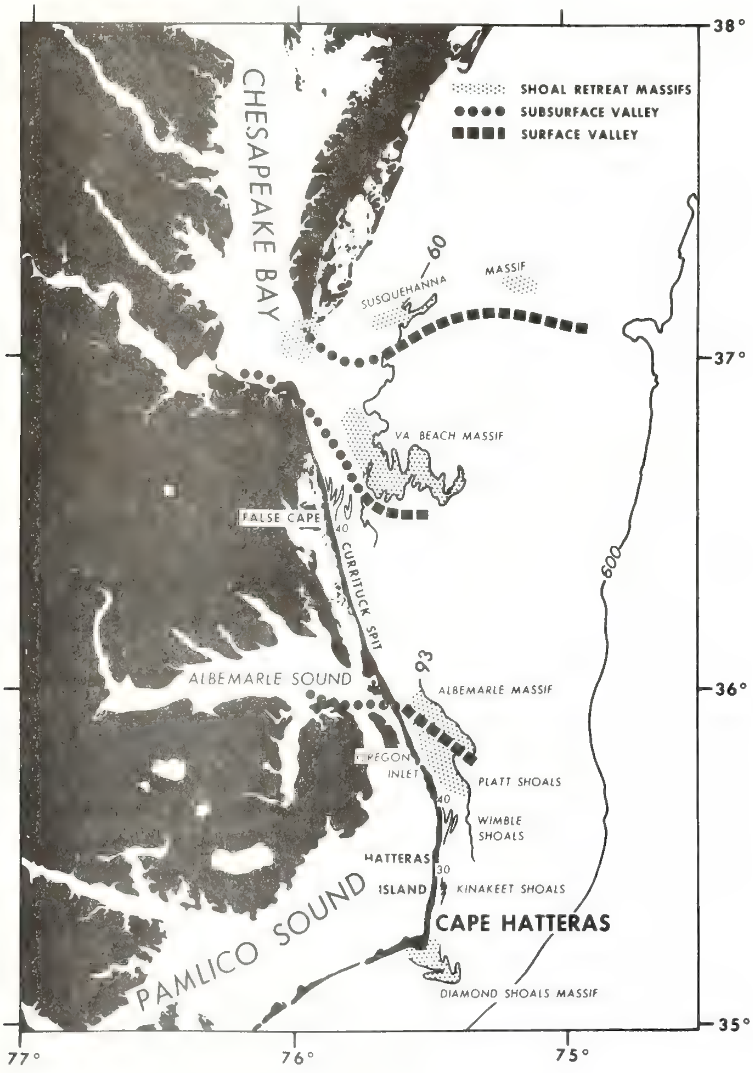

Fig.1. Morphologic framework of the Virginia and northern North Carolina Shelf. Contours in feet.

paths of the littoral-drift depositional centers on the sides of estuary mouths. The term "massif" is used in the sense of a topographic high that is itself composed of smaller-scale topographic highs, for the massifs characteristically consist of arrays of sand ridges, whose axes are parallel to the shoreline, and perpendicular to the trend of the massif. The purpose of this paper is to describe the topography, stratigraphy, and surficial sediments of a classic example, the Albemarle Shelf Valley Complex of the northern North Carolina coast, and to assess on the basis of this information the extent to which the inherited estuarine topography has been remodeled in response to the modern hydraulic climate.

The metric system will be used in this paper except for maps prepared from National Ocean Survey data. These maps will be presented in English units, and will be described in both English and metric units in the text.

TOPOGRAPHY

The northern North Carolina Shelf consists of a broad sand plain. Its surface is molded into sand ridges, up to 10 m in relief, but with side slopes of less than a degree (Figs. 2 and 3). The ridges trend north—south, making

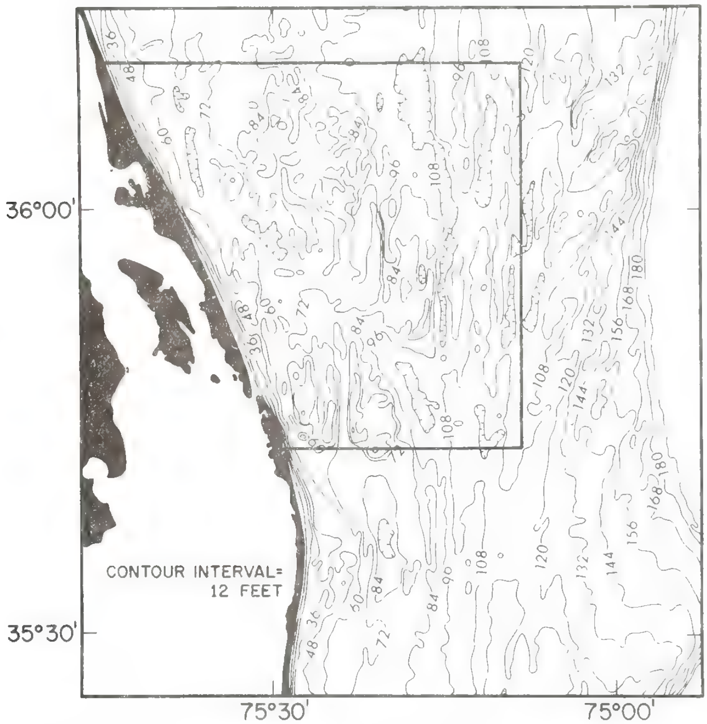

Fig.2. Bathymetry of the northern North Carolina Shelf. Box indicates study area. Note that the pervasive north—south "grain" of the study area conforms to regional topographic trend. From Goldsmith et al. (1974).

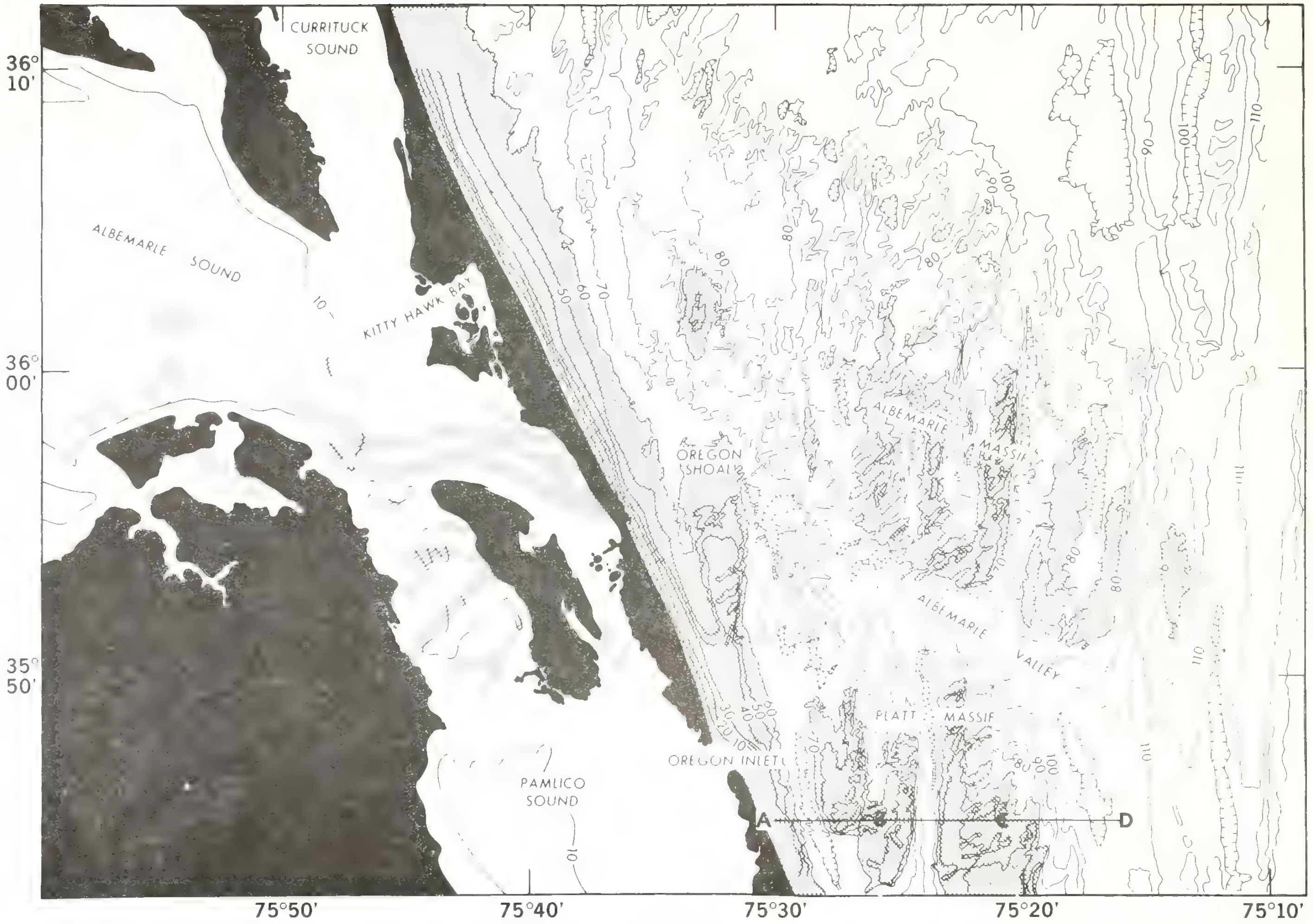

Fig.3. Bathymetry of the study area. Contour interval 10 ft. Significant shoal areas are stippled. Diagonal ruling indicates subsurface channels in Albemarle Sound as indicated by seismic profiling (O'Connor et al., 1972). Cross-section *A—D* is presented as Fig.4.

an angle of up to 20° with the more easterly trending shoreline. Relief becomes marked immediately north of Oregon Inlet (Fig.3). Here three scales of topographic elements are superimposed. At the coarsest scale, the Albemarle Shelf Valley is an apparent extension of the subsurface channel system of Albemarle Sound (Fig.3; O'Connor et al., 1972). It lies between two areas of considerable relief, the Albemarle Massif and the Platt Massif.

These massifs consist of smaller-scale sand ridges trending north and south. Each massif comprises a comb-like array of ridges. Crests rise and broaden toward the south; troughs likewise tend to become shoaler toward the south. The arrays are not symmetrical about the shelf valley; the comb-like "teeth" tend to point north both north and south of the valley. The ridges of the two massifs tend to share other characteristics, although not without exception. The steepest dips occur on the upper portions of the seaward flanks (Fig.4), and the crest lines either merge with the shoreface, or tend to curve shoreward, forming a J-pattern in plan view (Fig.5). The sand ridges of the Platt Shoals massif are unique in that double and triple ridges occur. Inner Platt Shoals consists of two ridges flanked by deep troughs and separated by a raised shallow trough; the inner of the two ridges is itself double, with a shallow interior trough. Outer Platt Shoals likewise is a double ridge.

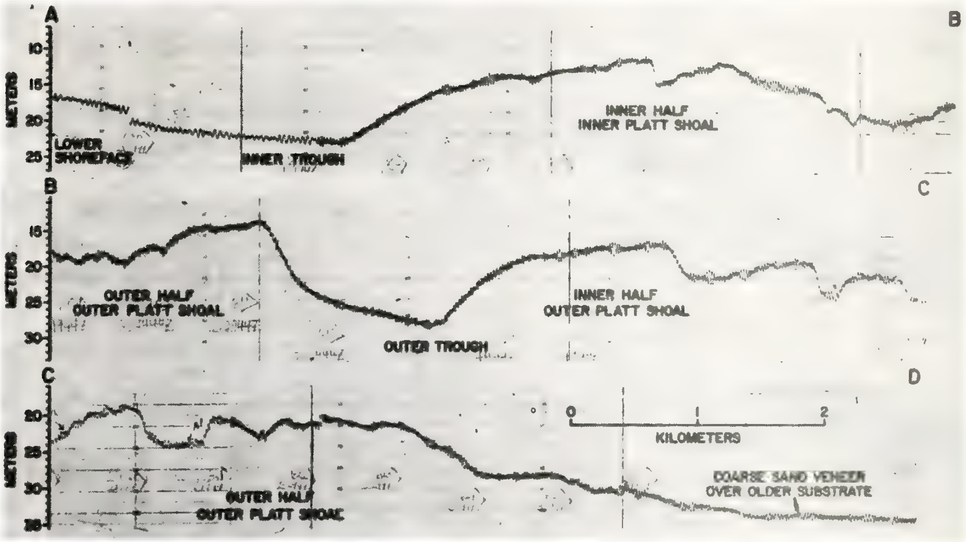

Fig.4. Bathymetric profile through the study area. See Fig.3. for locations.

At the third, finest, scale of topographic relief, a sand-wave pattern is imprinted on the sand-ridge topography. Sand-wave crests trend northeast—southwest. The sand waves are imperfectly resolved by the 10-ft contour interval of Figs. 3 and 5, but it is evident that they are between 2 and 5 m (6 and 15 ft) high, with crest lines that tend to be convex to the

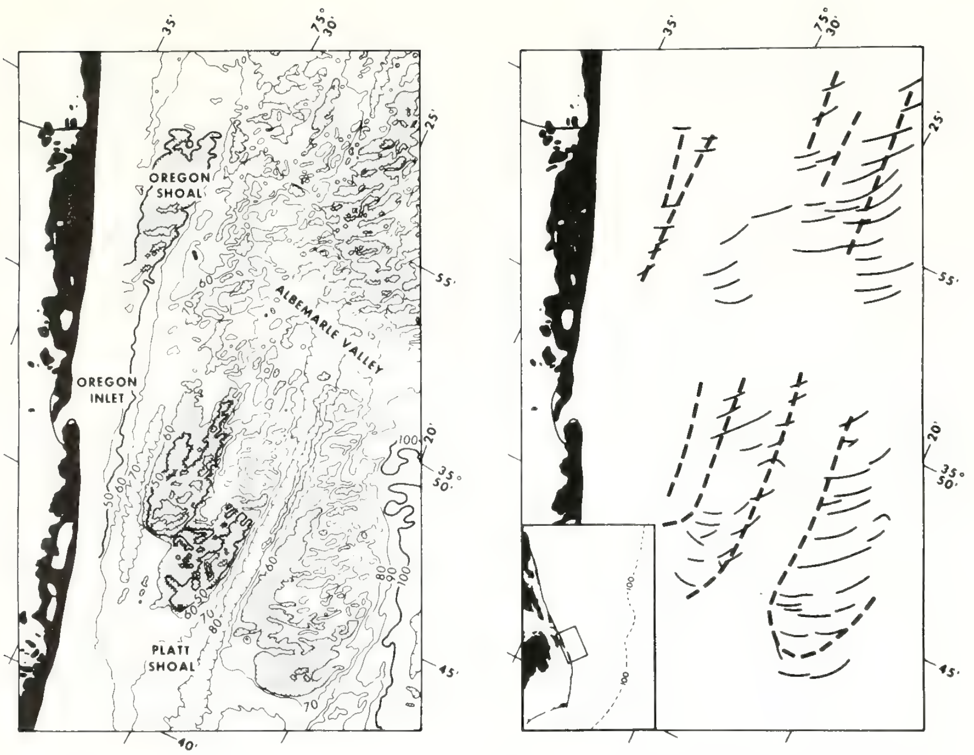

Fig.5. Bathymetric map of the inner Albemarle Shelf. Contour interval 10 ft. Pattern of ridges (dashed) and sand waves (solid) is indicated in the right-hand panel.

south, and tend to make a northward-opening angle of slightly less than 90° with the shoreline. They are primarily confined to ridge crests, being largely absent from the shoreface, the Albemarle Shelf Valley, and troughs between the ridges. The relationship of sand waves to sand ridges is presented schematically in Fig.6.

The topographic plan of the Albemarle Shelf Valley Complex with its asymmetrical massifs is very similar to that of the Virginia Beach Shelf Valley Complex (Swift et al., 1977).

Fig.7 presents a topographic net-change map for Platt Shoals. It is based on the Coast and Geodetic Survey smooth sheets for 1870 and 1970, respectively. The 1870 map was compiled by Robert Platt, by means of lead-line soundings and horizontal sextant angles. Survey lines were 300—2700 m apart. The 1970 chart was compiled by the NOAA Ship "Explorer" by means of acoustic profiling and Shoran navigation. Survey lines were approximately 208 m apart. Both sets of data were adjusted to mean sea level and the 1927 North American Datum.

Fig.7 indicates that the troughs became shoaler during the 100-year period, while the ridges have extended to the southeast. Comparison of the complete sets of contours and volumetric estimates based on these sets suggests that

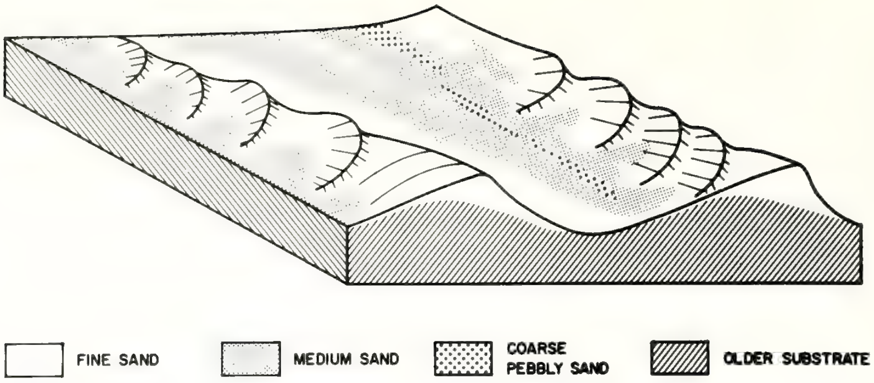

Fig.6. Schematic of ridge architecture showing relation of sand ridges to sand waves.

the upper levels of the troughs have become longer and wider and that the crests of the ridges have aggraded (Sears, 1973). Zones of bathymetric change on the order of 3—9 ft (1—3 m) extend over many square miles of sea floor, a degree of change greater than can be readily accounted for by navigational and sounding inaccuracies (see Goldsmith et al., 1975; Sallenger et al., 1975).

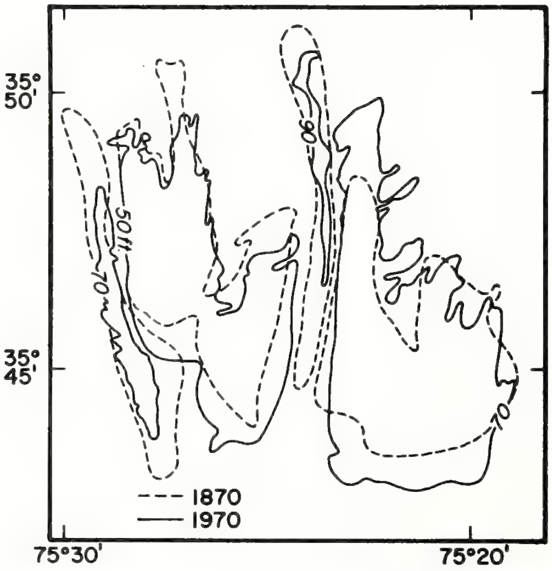

Fig.7. Map showing change in position of significant contours of the Platt Massiff between the 1870 and 1970 surveys.

STRATIGRAPHY AND GEOLOGICAL HISTORY

Vibracores and seismic profiles collected across the Platt Massif reveal a threefold stratigraphy (Fig.8). A basal sequence (Layer C) consists of massive, greenish gray, muddy sand. It is generally devoid of mollusc shells except for a *Mulinia* stratum found 43 m below sea level. The *Mulinia* bed dates at 22,750 ± 2000 years B.P. which places the age of the bed at the beginning of the late Wisconsin regression (Milliman and Emery, 1968). The core penetrating the *Mulinia* bed is not figured (see Sears, 1973). Seismic profiles suggest that the surface of the basal layer extends as a near plane seaward beneath the ridges. An intermediate sequence (Layer B) consists of greenish-gray fine sand with intercalations of mud, medium sand, and shell hash. It appears to form a nucleus within the ridges, being found at shallower depth within them than in the troughs (Fig.8). Molluscan shells are abundant; *Crassostrea virginica* and *Donax* sp. are the most common. A single large *Crassostrea* shell yielded a radiocarbon date of 10,720 ± 800 years B.P., and a sample of unbroken *Donax* shells from the outer trough yielded a date of 10,900 ± 900 years B.P. A similar sample from the seaward flank of the outer ridge yielded a radiocarbon date of 5618 + 100 years B.P. All dates fall within the earlier part of the Holocene transgression (Milliman and Emery, 1968).

The uppermost layer (Layer A) is a mantle of medium to coarse, well-sorted sand. It is thicker over the ridges than in the trough, and thickest on the seaward sides of the troughs (Fig.8). It is characterized by an open-water fauna including *Mercenaria mercenaria*, *Spisula solidisima*, and *Donax* sp.

Our stratigraphic analysis indicates that the Albemarle Shelf Valley Complex existed as an estuary mouth between 10,000 and 5000 years B.P. Its inherited morphology and internal characteristics (*Crassostrea* and clay beds) suggest a lunate estuary-mouth shoal similar to those described from the Georgia coast by Howard and Reineck (1972) and Oertel and Howard (1972); see Fig.9A. The existing shelf-valley complex may not necessarily have been formed during a single brief interval, but may instead have formed as a series of successively active shoal segments during a general period of sea-level rise and coastal retreat. Its demise may have been coincident with the reduction in the rate of sea-level rise of about 5000 years ago. The shelf-valley complex is presently separated from the Albemarle estuary by Currituck spit, part of the Virginia—North Carolina barrier chain. We have suggested elsewhere (Swift and Sears, 1974; Swift, 1975) that the reduction in the rate of sea-level rise during a period of constant sand supply may have caused the retreating barrier system to shift to a regime of near stillstand, in which the barriers grew primarily upward, while the lagoons behind them grew wider. The expansion of the intracoastal lagoonal system may have diverted the tidal discharge of Albemarle Sound into Pamlico Sound, allowing Currituck spit to seal off the former estuary mouth. Kitty Hawk Bay (Fig.3) is flanked by beach-ridge sets, and has been interpreted by Fisher (1967) as a former inlet.

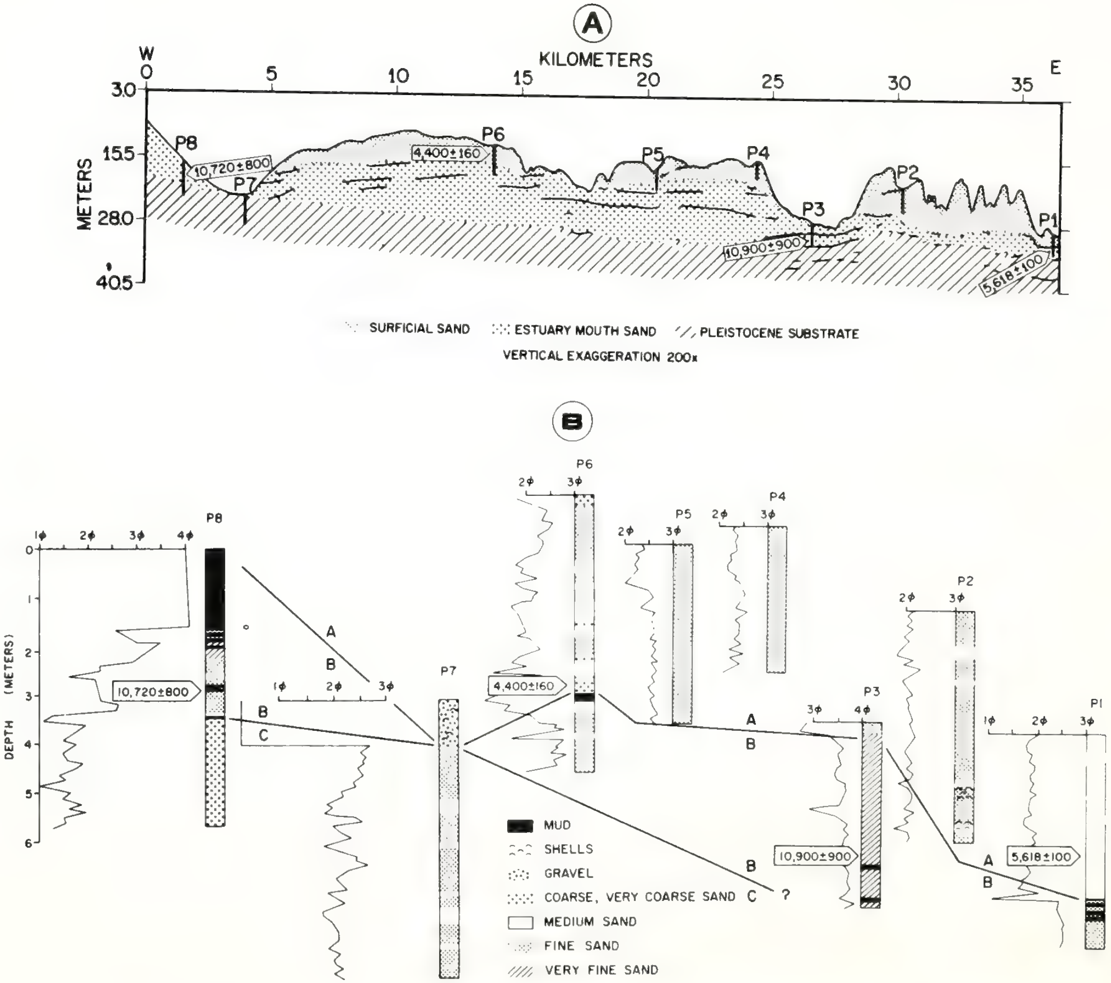

Fig.8. A. 3.5 kHz profile through Platt Massif showing reflecting horizons, positions of vibracores, gross lithology as indicated by vibracores, and radiocarbon dates (location: section *A—D*, Fig. 3). B. Correlation of vibracores shown in A. Unit A is surficial sand. Unit B is estuarine sand. Unit C is older substrate. See text for explanation.

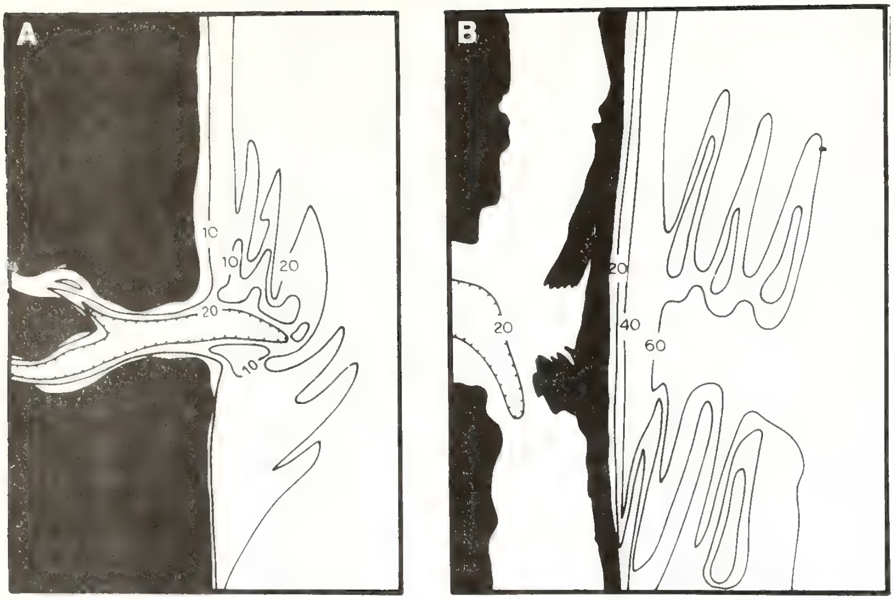

Fig.9. Schematic diagram illustrating the inferred evolution of ancestral Albemarle estuary mouth into a shelf-valley complex. Depth in feet.

SURFICIAL SEDIMENTS AND SMALL-SCALE RELIEF ELEMENTS

Surficial sediments were grab-sampled in a portion of the study area (Fig.10), and the entire surface of the study area was examined by means of an EG&G sidescan sonar unit (Fig.11). Navigation for the grab-sample net was provided by Loran A, and for the sidescan-sonar net by means of Raydist.

The mean-diameter map (Fig.10) is based on the phi moment mean of the sand fraction as determined by a rapid sediment analyser (Sanford and Swift, 1972). The $1 \times 4\ km^2$ sample grid is barely able to resolve the pattern of grain-size distribution, which consists of a north—south banding of contrasting grain sizes that appears to vary in sympathy with the ridge topography. The pattern is partly obscured by noise in the form of single anomalous samples, which may be due to a smaller-scale grain-size variation controlled by a sand-wave topography (see sand waves in profile, Fig.4). The most obvious aspect of the pattern is the tendency for troughs to be floored by coarse sands (frequently pebbly sand or sandy gravel). Ridges are mantled by fine sand (2.0—2.5 ϕ). Ridge-flank deposits are not symmetrical; seaward-flank sands tend to be finer than crest sands, while landward flanks are similar to crest sands or coarser.

Fig.12 presents a scatter plot of phi moment standard deviation against phi moment mean for the sand fraction of the samples. Points are distinguished by depositional environment. Separation of environmental types is poor. The noisy nature of the data may be due to small-scale grain-size variations induced by the sand-wave topography, to the

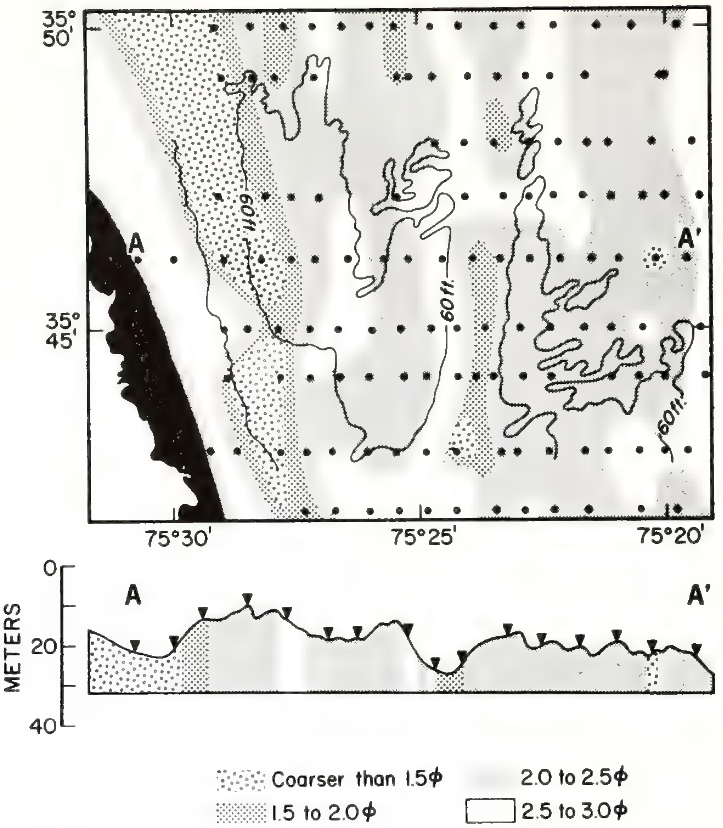

Fig.10. Distribution of mean grain diameter over Platt Massif.

subjective nature of designation of trough, flank, and ridge, or it may be an innate characteristic. Nevertheless, differences in sand type appear, similar to those seen in the grain-size map. Crest and seaward-flank sands comprise relatively compact, overlapping scatters. Crestal sands tend to be coarser than seaward-flank sands. Landward-flank sands are similarly coarser than seaward-flank sands but are more poorly sorted. Trough sands overlap all other domains and include the coarsest and most poorly sorted sands.

The sidescan sonar records reveal that the sands of the study area are molded into a hierarchical association of bedforms (Allen, 1968; Jackson, 1975). An association of bedforms exists in that the pattern consists of two orthogonal components. Bedforms trend either east—west, normal to the prevailing current direction, or north—south, parallel to the prevailing direction. The bedform pattern is hierarchical in that within each class bedforms occur at several spatial scales. Bedform arrays appear on sidescan sonar records as alternating bands of light and dark tones, because of the systematic variation in bottom elevation and because of the equally systematic variation in bottom grain size.

The largest scale of flow-parallel elements is the sand ridges and intervening troughs. The morphology and grain-size patterns of these ridges have already been discussed. A smaller-scale, flow-parallel pattern is caused by current lineations (McKinny et al., 1974); bands of contrasting grain size of negligible relief that vary from several tens of meters to hundreds of meters in width. They appear on sidescan sonar records as light or dark streaks against a contrasting background (Fig.13). Some appear to be sand ribbons (Kenyon, 1970) in the sense of strips of sand of negligible relief resting on a surface of coarser material. However, most appear on sidescan sonar as streaks darker than the adjacent zones. They are therefore

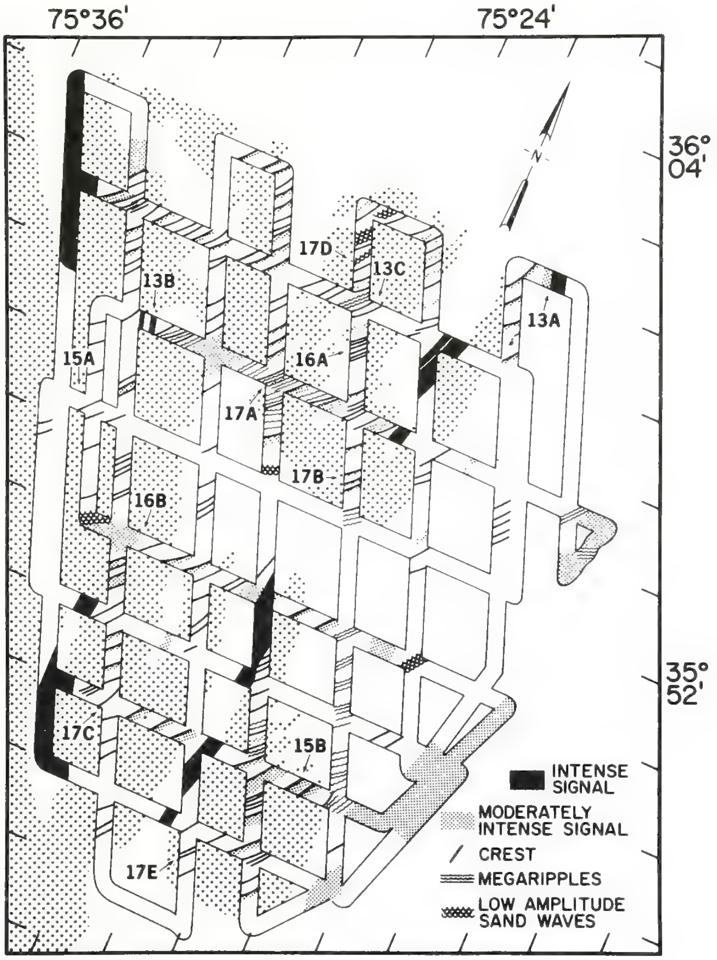

Fig.11. Schematic composite of sidescan-sonar records. Trackline and schematic sonar image are presented four times actual width for clarity. Letters and numbers indicate locations of other figures. Topographic highs are stippled.

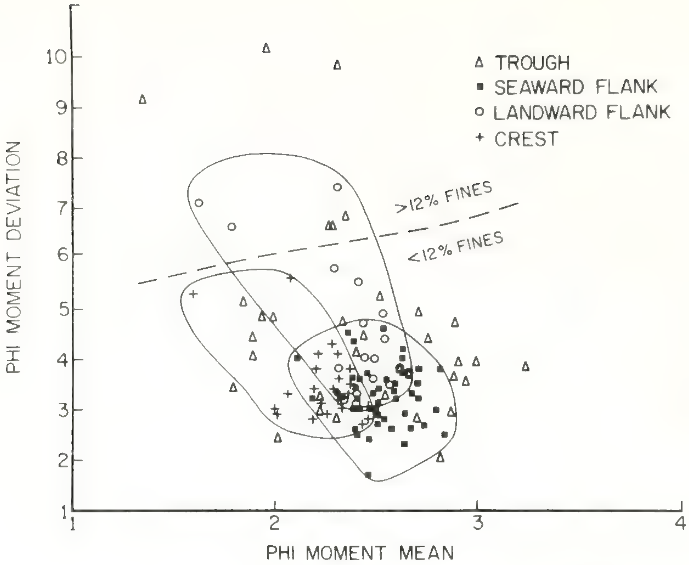

Fig.12. Scatter plot of phi moment mean diameter against phi moment standard deviation, keyed against depositional environment.

believed to be similar to the linear erosional furrows of Stride et al. (1972): elongate windows in a thin sand sheet exposing a coarser underlying stratum. The negative relief of the erosional windows tends to be a little more sharply pronounced than the positive relief of the sand ribbons and they appear in the vertical exaggeration of the bathymeter records as notches separated by plateaux (Fig.13b).

Current lineations occur primarily in the troughs between the large-scale sand ridges, where vibracores and grab samples indicate that the surficial sediment has thinned to a coarse-sand or sandy-gravel veneer overlying an older substrate. At least three categories of current lineations appear to exist (Fig.14). Regular bands of contrasting grain size with spacings on the order of 100 m appear to be strips of sand overlying the basal gravel that veneers the older substrate. These alternations of erosional furrows and sand ribbons appear to be bedforms in the strict sense of regular perturbations of bottom morphology and grain size that reflect regular flow perturbations. Elsewhere, irregular broad zones of sandy gravel appear to be deflation zones, where all easily transportable material has been removed during repeated flow events. Broad, well-defined deflation zones occur in the larger troughs of the ridge topography (Fig.11). They tend to be displaced toward the seaward sides of the troughs. Locally, erosional furrow patterns occur on ridge flanks where the dark bands presumably do not represent the basal gravel; they may be "perched" lag deposits due to localized current action.

East—west trending bedforms have been designated "sand waves" in the discussion of topography, on the grounds that they are flow-transverse

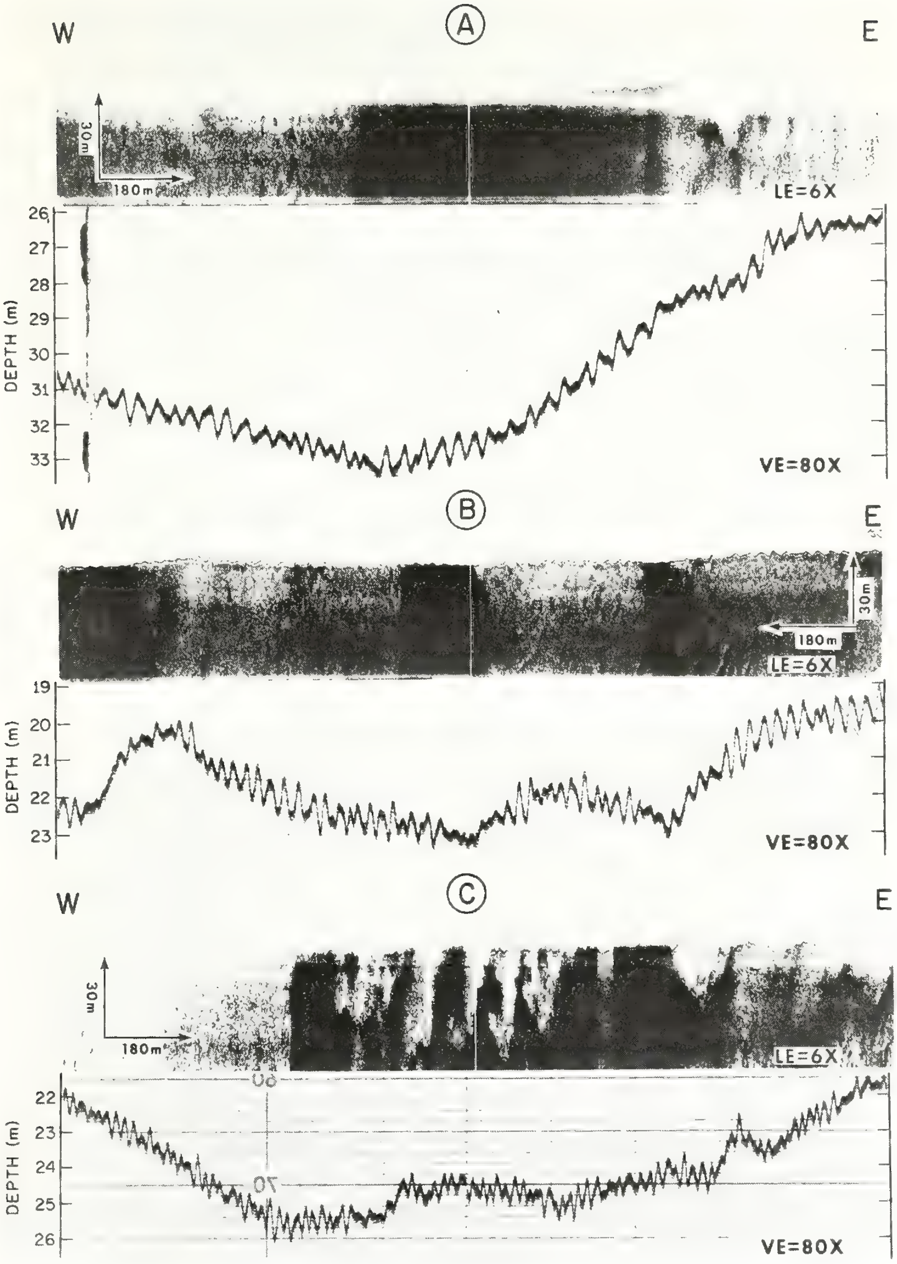

Fig.13. A. Deflation zone in trough. Dark tone indicates coarser sediment. Note displacement from axis of trough toward seaward side. B. Well-defined erosional furrows. C. Anastomosing deflation pattern. See Fig. 11 for locations.

bedforms; that is, sand ridges with steeper slopes on the side that is down-current with respect to the presumed direction of prevailing flow (Figs. 15 and 16).

Sidescan sonar and fathometer records reveal that the sand waves occur at two scales (Fig.15B). Features with spacings of 20—120 m and heights up to 2 m will be referred to as megaripples. Large-scale sand waves have spacings of 0.2—1.2 km and heights of 2—6 m. Their downcurrent slopes are generally below the angle of repose, although well-defined avalanche slopes are locally present (Fig.15A). Saw-tooth profiles occur, but a more typical profile is trapezoidal, with a relatively steep downcurrent slope, an upper surface inclined gently toward the upcurrent direction, and an upcurrent slope of intermediate steepness (Fig.17). "Cat-backed" sand waves (Van Veen, 1935) locally occur. The profiles of these features exhibit a bump or "ear" at the angulation between the downcurrent slope and the upper surface. Both the cat-backed and trapezoidal profiles may be the consequence of periodic flow reversal. Mud lenses may occur in the troughs between large-scale sand waves (Fig.16B).

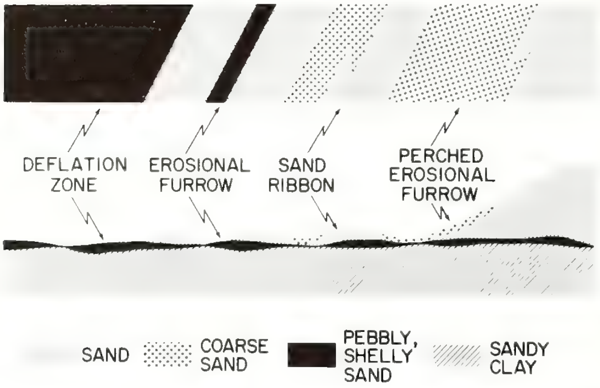

Fig.14. Schematic diagram indicating catagories of current lineations.

Sidescan-sonar profiles clearly indicate that grain size varies systematically across the sand-wave profile. The tone of the sidescan record tends to be darkest (coarsest grain size) in the trough at the foot of the downcurrent slope (Fig.15B). The record tends to lighten (become finer) across the upcurrent slope, and down the downcurrent slope.

Relatively extensive fields of megaripples occur at several areas, as indicated by the wavy-line symbol in Fig.11. Spacings range from 20 to 120 m; heights do not exceed 2 m. Elsewhere, megaripples are locally apparent on the upper surfaces of large-scale sand waves (Fig.15B). The better-defined sand ridges tend to have a band of megaripples along the upper edge of the seaward flank (not figured). The band is parallel to the ridge trend, but the megaripples themselves tend to form a northward-opening angle of up to 20° with the ridge crest. Megaripple asymmetry in these areas indicates flow to the southeast.

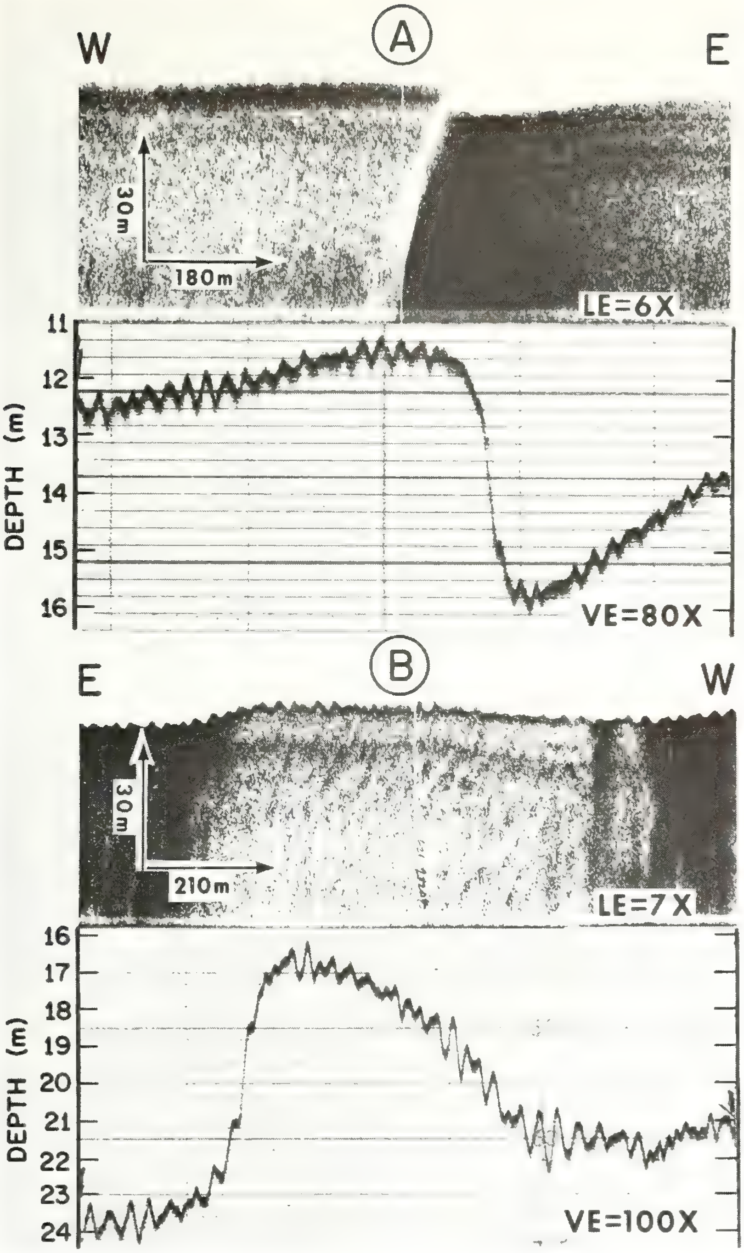

Fig.15. A. Sand wave with well developed slip face. B. Sand wave with megaripples on back (note sidescan-sonar record). See Fig. 11 for locations.

A third order of flow-parallel bedforms revealed by sidescan sonar consists of bands of contrasting grain size up to 2 m long, with spacings measured in decimeters (Fig.16B). Although they trend north—south, they are inferred

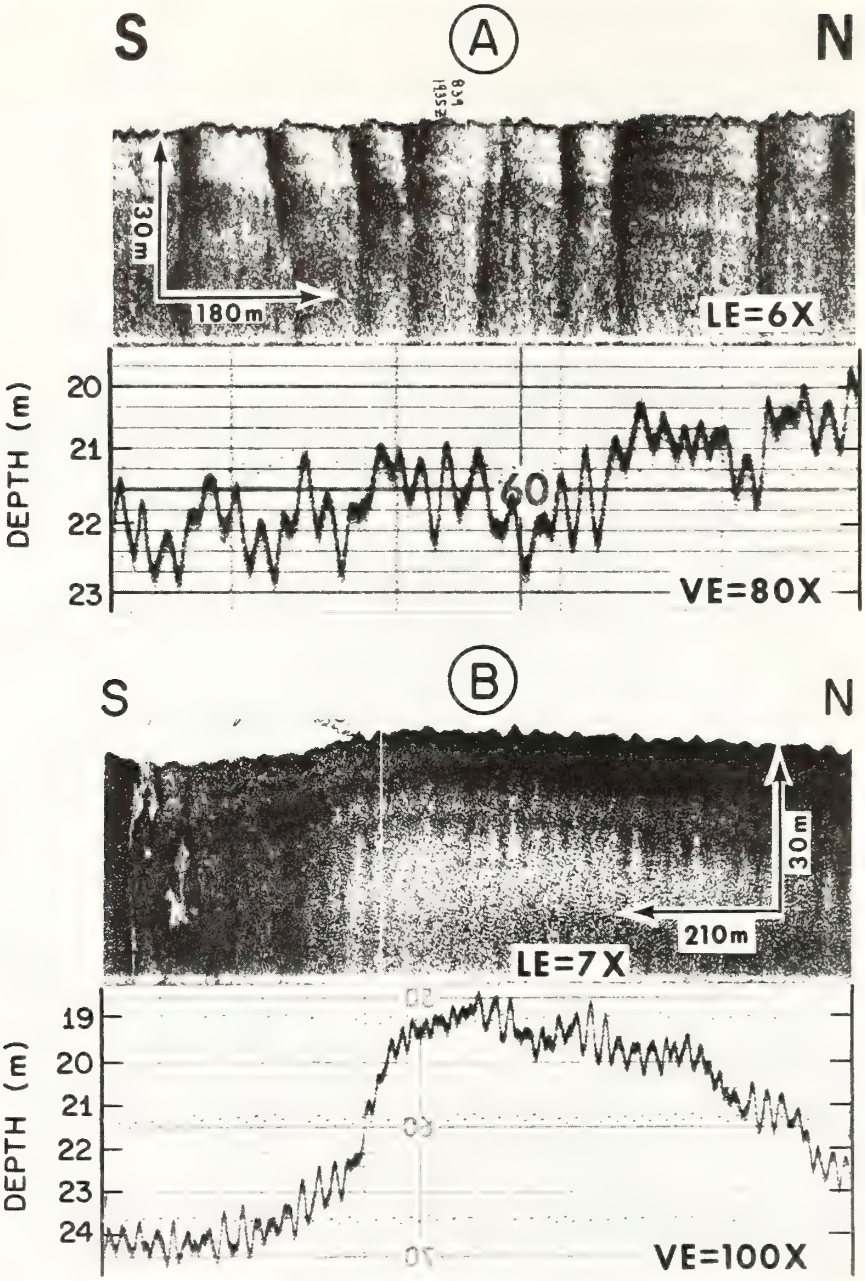

Fig.16. A. Small-scale sand-wave pattern. B. Sand wave with wave-generated ripples on back (barely resolved on sidescan-sonar record) and mud patches in trough (white areas on sidescan-sonar record). See Fig. 11 for locations.

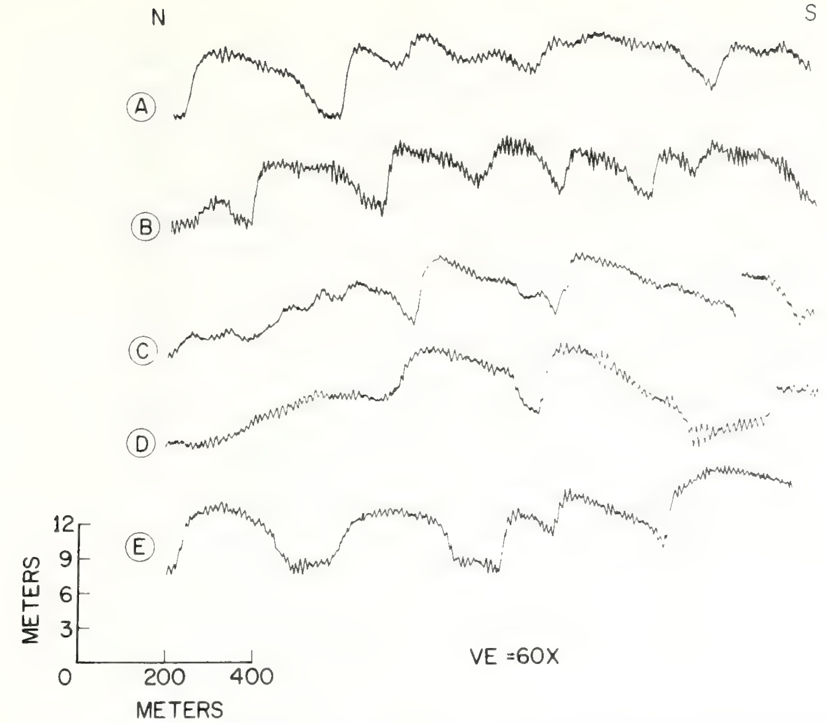

Fig.17. Characteristic sand-wave profiles. Note abundance of three-faceted patterns (steep lee slope, gentle sloping top, steep upcurrent slope) as well as classic saw-tooth profiles. See Fig. 11 for locations. Wiggles in profiles are due to motion of recording vessel in response to surface waves.

to be flow-transverse ripples, generated by wave surge on coarse sand bottoms, with spacings sufficient to be resolved by sidescan sonar. They may have been responses to the shoreward-trending train of surface swells observed during the sidescan-sonar cruise.

HYDRAULIC PROCESS AND SUBSTRATE RESPONSE

Evolution of the Albemarle Shelf Valley Complex

While the gross morphology of the Albemarle Shelf Valley Complex appears to be inherited from an earlier estuary-mouth environment, its surficial grain-size patterns and bedform arrays cannot be readily explained in this manner. Unit B, which forms the cores of the Platt and Albemarle Massifs, appears to be the dissected remnants of the original estuary mouth shoal. However Unit A appears to have been deposited subsequent to closure of the Albemarle estuary. Its grain size and morphological patterns must be considered in terms of the modern hydraulic climate.

A first task in harmonizing the hydraulic climate with the pattern of substrate response must be an explanation of the ridge topography. There seems to be little profit in seeking a relict origin. Estuary-mouth shoals, such as the Albemarle Shelf Valley Complex is presumed to have been, do have ridge topographies impressed upon them. These are interdigitating ebb—flood channel systems, caused by the phase lag in the tidal wave during its reflection from the estuary interior (Swift and Ludwick, 1976), but the resemblance between such ebb—flood channel systems and the present Albemarle ridge topography is superficial.

The postulated models for the ancestral Albemarle estuary are the estuaries of the Georgia Bight (Oertel and Howard, 1972). Their channel systems are similar to the pattern seen on the Albemarle Massif in that channels occur on the north side of the estuary mouth, but the troughs of the Albemarle Massif are larger, longer, and more deeply incised than those of the modern Georgia estuaries and, unlike them, do not radiate from the estuary mouth. Furthermore, the same pattern is seen, even more prominently developed, on the Platt Massif. There is no symmetry of the two ridge patterns about the central valley; trough talwegs and crest lines climb to the south on *both* massifs; compare Figs. 8A and 8B. The ridge topography of the Albemarle and Platt Massifs appears to be oriented with respect to the southward storm flows that are characteristic of the Middle Atlantic Bight (Beardsley and Butman, 1974), rather than with respect to a reversing estuary-mouth jet.

The regional topographic pattern places a further constraint on the origin of the ridge systems of the Albemarle and Platt Massifs. Fig.2 clearly indicates that the ridges of the Platt and Albemarle Massifs are an integral part of a regional north—south trending topographic "grain". This grain is distinctly more regular than the south-southeast trending shoreline. The portion of the ridge system superimposed on the shelf-valley complex, however, is unique for three reasons: (1) the ridge topography has greater relief, (2) the ridges and troughs are incised primarily in the northern sides of the massifs, hence the "comb-like" pattern, and (3) only in the vicinity of the shelf-valley complex are the ridges accompanied by flow-transverse sand waves.

If the ridge topography is in fact produced by south-trending storm flows, then the points listed above are most simply explained as a result of constriction of the flow cross-section over the shelf-valley complex, and its consequent acceleration. Constriction of flow cross-section would be a vertical constriction from bottom shoaling, and perhaps also a lateral constriction due to the more pronounced easterly trend of the shoreline immediately north of Oregon Inlet. Acceleration of flow would incise the ridge topography more deeply into the northern flanks of the massifs than elsewhere. Acceleration of flow over the massifs would mean that velocity would more frequently exceed the threshold velocity of sand transport in this area, and that sand waves would have a greater probability of surviving the intervening periods of degradation by fair-weather wave surge. It is noteworthy that sand waves occur elsewhere on the Middle Atlantic Shelf of North America only where flows are locally accelerated for continuity reasons; beneath the reversing tidal jets of major estuaries (Ludwick, 1972) or on such shoal areas as Diamond Shoals off Cape Hatteras (Swift et al., 1972, p.526; Hunt et al., 1977), or on Georges Bank (Uchupi, 1968) and Nantucket Shoals (Swift, 1975).

Relation of ridges to flow. We suggest above that the ridges are responses to modern flows, and that specifically they are due to the southward acceleration of storm flows over the massifs. But why does such acceleration produce flow-parallel ridges and troughs? Why doesn't it uniformly erode the upcurrent flanks of the massif? What determines the angular relationships of shoreline, ridge axes, and sand-wave crests? We cannot answer these questions without a better theoretical understanding of geophysical boundary layers, and we also need extensive velocity observations to which hydrodynamical theory can be applied. However, the geomorphic and textural data reported in this paper will allow us to set constraints that any model of fluid process and substrate response must meet. These constraints may be listed as follows:

(1) The sand ridges and sand waves of the study area are responses to peak southward flows. Ridges indicate a southward flow in that their crest and trough lines climb to the south (Figs. 3 and 5). Sand waves at two scales have steeper south-facing slopes (Fig.17).

(2) The sand ridges are not truly flow parallel, for they converge southward with the shoreline (Figs. 2, 3 and 5). Vectors of depth-averaged flow must trend parallel to the coast, and obliquely over ridge crests for continuity reasons.

(3) Southward, cross-ridge flow is further indicated by the grain-size asymmetry (Figs. 10, 12 and 13A) and morphologic asymmetry (Fig.4) of the sand ridges. Northwest flanks are flatter and coarser grained, suggesting that they are upcurrent-facing slopes, subject to erosion and selective removal of finer sand grains. Southeast flanks are steeper and finer grained, suggesting that they are downcurrent slopes, subject to deposition of finer sand grains. This interpretation is supported by the greater thickness of modern sand on the fine, seaward flanks (Fig.8A) and the aggradation of these flanks over time (Fig.7).

(4) The responsible flows are two-layered, with an offshore component of surface flow coastal downwelling, and an offshore component of bottom flow. This flow structure is indicated by the orientation of sandwaves on ridge crests; their steeper slopes face slightly offshore as well as downcoast to the south (Fig.5).

(5) The strongest flows may be experienced at the foot of the shoreface, where it adjoins the more gently dipping inner-shelf floor, rather than further seaward where the water is deeper. This seemingly reversed velocity—depth relationship is indicated by the broad band of gravel at the foot of the shoreface (Fig.10). Further seaward, the basal Holocene gravel is generally veneered with sand and gravel, and is only exposed in narrow windows. The gravel band corresponds with the floor of an intermittent trough that separates the Platt and Albemarle Massifs from the shoreface (Fig.3).

There are a number of points of similarity between this model of the time-averaged peak flow field inferred from substrate response characteristics, and the model of the storm flow field that stems from the observations of physical oceanographers. Peak flows in the Middle Atlantic Bight are in fact associated with winter storms and the most energetic storm flows trend southward (Beardsley and Butman, 1974; Boicourt and Hacker, 1976; Scott and Csanady, 1976; Lavelle et al., 1976). Southward storm flows are frequently associated with coastal downwelling and an offshore component of bottom flow (Boicourt and Hacker, 1976; Scott and Csanady, 1976). There are theoretical grounds for assuming that the landward margin of the shelf flow field may become a coastal jet during storms (Csanady, 1973, 1976), and Boicourt and Hacker have in fact observed a coastal jet during a February, 1974, storm in 10 m of water off the southern Virginia coast, north of our study area. Longshore, mid-depth velocity averaged 52.5 cm/sec over a 58-hr period in contrast to a value of 26.3 cm/sec for longshore, mid-depth velocity averaged over the same period several kilometers further offshore. Boicourt and Hacker (1976, p.194) attributed the high longshore velocity to the "wind driven outflow surge of low salinity water from Chesapeake Bay which forms a southward flowing, high velocity jet along the Virginia and North Carolina coast". Within the study area, such a storm-generated jet would occupy the water column over the gravel band noted above.

Neither the reconnaissance data of physical oceanographers nor the generalized and inferential flow model based on substrate response to peak flow are fully adequate to explain the formation of the sand ridges. Their grain size and morphologic asymmetry are features that they share with flow-transverse sand waves and the analytical model for sand-wave formation of Smith (1910) may therefore be applicable. The sand ridges are oriented obliquely across the prevailing direction of peak flow, rather than transverse to it, but Furness (1976) has recently shown that sand waves may be oriented obliquely with respect to flow if there is a cross-flow velocity gradient. The possibility that such a velocity gradient might be supplied by the jet-like coastal margin of the storm flow field should be investigated.

A second hydrodynamical model may be applicable to the problem of sand ridge formation. Shelf storm flows are potentially capable of developing helical flow structure, in which zones of upwelling alternate with zones of downwelling (Faller, 1971; Gammelsrod, 1975), and flow structure of this sort has been cited as the probable mechanism for sand-ridge formation (Houbolt, 1969; Wilson, 1972). The applicability of sand-wave theory and helical-flow theory to problems of sand-ridge formation have been discussed elsewhere (Swift and Ludwick, 1976; Swift et al, 1977).

It does not seem possible to extract further insights concerning the origin of the Albemarle topography until extensive hydraulic measurements are obtained. Our substrate data do, however, indicate the main outlines of topographic evolution. The surface of the Albemarle estuary shoal was no longer in equilibrium with the hydraulic climate of the inner shelf after the reversing tidal jet that maintained it ceased to function, at perhaps 5000 B.P. However, the adjustment of the shoal to the altered regime has not resulted in the total destruction. Instead, a systematically corrugated surface has resulted, whose superimposed sand wave and ridge patterns indicate a recurrent velocity field of complex structure. Grain-size analyses of cores indicate that the surficial sand of Layer A is distinctly coarser than the underlying estuarine stratum. The hydraulically adjusted surface of the Albemarle Shelf Valley Complex has been molded into a relatively coarse lag; finer sand has been winnowed out and transported in the direction of the prevailing southerly flow.

REFERENCES

Allen, J.R.L., 1968. The nature and origin of bedform hierarchies. Sedimentology, 10: 161—182.

Beardsley, R.C. and Butman, B., 1974. Circulation on the New England continental shelf: response to strong winter storms. Geophys. Res. Lett., 1: 181—184.

Boicourt, W.C. and Hacker, P.W., 1976. Circulation on the Atlantic continental shelf of the United States, Cape May to Cape Hatteras. Mem. Soc. R. Sci. Liege, 16th Ser., 10: 187—200.

Brown, R.A., 1970. A secondary flow model for the planetary boundary layer. J. Atmos. Sci., 27: 742—757.

Bumpus, D.F., 1973. A description of circulation on the continental shelf of the east coast of the United States. Prog. Oceanogr., 6: 117—157.

Csanady, G.T., 1973. Barotropic currents over the continental shelf. J. Phys. Oceanogr., 4: 357—371.

Csanady, G.T., 1976. Wind driven and thermohaline circulation over the continental shelves. In: B. Manowitz (Editor), Effects of Energy Related Activities on the Atlantic Continental Shelf. Conference at Brookhaven National Laboratory, November 10—12, 1975, pp.31—47.

Faller, A.J., 1971. Oceanic turbulence and the Langmuir circulations. Annu. Rev. Ecol. Syst., 2: 201—236.

Fisher, J.J., 1967. Development Pattern of Relict Beach Ridges, Outer Banks Barrier Chain, North Carolina. Thesis, University of North Carolina, 250 pp.

Furness, G.K., 1976. Formation of Oblique Dunes. Danish Center for Applied Mathematics and Mechanics, Technical University of Denmark, Report 105, 34 pp.

Gammelsrod, T., 1975. Instability of Couette flow in a rotating fluid and origin of Langmuir circulations. J. Geophys. Res., 80: 5069—5075.

Goldsmith, V., Sutton, C.H. and Davis, J.S., 1974. Bathymetry of the Virginia Sea, Part I. Chesapeake Bight. Transverse Mercator Projection Map. Virginia Institute of Marine Sciences, Gloucester Point, Va.

Goldsmith, V., Byrne, R.J., Sallenger, A.H. and Drucker, D.M., 1975. The influence of waves on the origin and development of the offset coastal inlets of the southern Delmarva peninsula, Virginia. In: L.E. Cronin (Editor), Estuarine Research, VII. Geology and Engineering. Academic Press, New York, N.Y., pp.183—200.

Houbolt, J.H.C., 1968. Recent sediment in the Southern Bight of the North Sea. Geol. Mijnbouw, 47: 245—273.

Howard, J.D. and Reinbeck, H.E., 1972. Georgia coastal region, Sapelo Island, U.S.A.: Sedimentology and biology, IV. Physical and biogenic sedimentary structures of the nearshore shelf. Senckenbergiana Marit., 4: 81—123.

Hunt, R.E., Swift, D.J.P. and Palmer, H.P., 1977. Constructional shelf topography — Diamond Shoals, North Carolina. Geol. Soc. Am. Bull., 88: 299—311.

Jackson, R.A., 1975. Hierarchical attributes and a unifying model of bedforms composed of cohesionless material and produced by shearing flow. Geol. Soc. Am. Bull., 86: 1523—1533.

Kenyon, N.H., 1970. Sand ribbons of European tidal seas. Mar. Geol., 9: 25—39.

Lavelle, J.W., Brashear, H.R., Case, F.N., Charnell, R.L., Gadd, P.E., Haff, K.W., Han, G.A., Kunselman, C.A., Mayer, D.A., Stubblefield, W.L. and Swift, D.J.P., 1976. Preliminary results of coincident current meter and sediment transport observations for wintertime conditions on the Long Island inner shelf. Geophys. Res. Lett., 3: 97—100.

Ludwick, J.C., 1972. Migration of tidal sandwaves in Chesapeake Bay entrance. In: D.J.P. Swift, D.B. Duane and O.H. Pilkey (Editors), Shelf Sediment Transport: Process and Pattern. Dowden, Hutchinson and Ross, Stroudsburg, Pa., pp.377—410.

McKinney, T.F., Stubblefield, W.L. and Swift, D.J.P., 1974. Large-scale current lineations on the Great Egg Shoal retreat massif: investigations by sidescan sonar. Mar. Geol., 17: 79—102.

Milliman, J.D. and Emery, K.O., 1968. Sealevels during the past 35,000 years. Science, 162: 1121—1123.

O'Connor, M.P., Riggs, S.R. and Winston, D., 1972. Recent estuarine sediment history in the Roanoke Island area, North Carolina. In: B.W. Nelson (Editor), Environmental Framework of Coastal Plain Estuaries. Geol. Soc. Am. Mem., 133: pp.435—464.

Oertel, G.F. and Howard, J.P., 1972. Water circulation and sedimentation at estuary entrances on the Georgia coast. In: D.J.P. Swift, D.B. Duane and O.H. Pilkey (Editors), Shelf Sediment Transport: Process and Pattern. Dowden, Hutchinson and Ross, Stroudsburg, Pa., pp.411—427.

Sallenger, A.H., Goldsmith, V. and Sutton, C.H., 1975. Bathymetric comparisons: A manual of methodology, error criteria and techniques. Virginia Institute of Marine Science, Gloucester Point, Va., Special Report 66, 34 pp.

Sanford, R.B. and Swift, D.J.P., 1971. Comparison of sieving and settling techniques for size analysis, using a Benthos Rapid Sediment Analyzer. Sedimentology, 17: 257—264.

Scott, J.T. and Csanady, G.T., 1976. Nearshore currents off Long Island. J. Geophys. Res., 81: 5403—5409.

Sears, P.C., 1973. Evolution of Platt Shoals, Northern North Carolina Shelf: Inferences from Areal Geology. Thesis, Inst. Oceanogr., Old Dominion University, Norfolk, Va., 74 pp.

Smith, J.D., 1970. Stability of a sand bed subjected to a shear flow of low Froude number. J. Geophys. Res., 75: 5928—5940.

Stride, A.H., Belderson, R.H. and Kenyon, N.H., 1972. Longitudinal furrows and depositional sand bodies of the English Channel. Mem. Bur. Rech. Geol. Min., 79: 233—244.

Swift, D.J.P., 1973. Delaware Shelf Valley: estuary retreat path, not drowned river valley. Geol. Soc. Am. Bull., 84: 2743—2748.

Swift, D.J.P., 1975. Tidal sand ridges and shoal-retreat massifs. Mar. Geol., 18: 105—134.

Swift, D.J.P. and Ludwick, J.C., 1976. Substrate response to hydraulic process: grain-size frequency distributions and bedforms. In: D.J. Stanley and D.J.P. Swift (Editors), Marine Sediment Transport and Environmental Management. Wiley, New York, N.Y., pp.159—196.

Swift, D.J.P. and Sears, P., 1974. Estuarine and littoral depositional patterns in the surficial sand sheet, central and southern Atlantic shelf of North America. Inst. Geol. Bassin Aquitaine, Mem. 7: 171—189.

Swift, D.J.P., Kofoed, J.W., Saulsbury, F.P. and Sears, P., 1972. Holocene evolution of the shelf surface, central and southern shelf of North America. In: D.J.P. Swift, D.B. Duane and O.H. Pilkey (Editors), Shelf Sediment Transport: Process and Pattern. Dowden, Hutchinson and Ross, Stroudsburg, Pa., pp.499—574.

Swift, D.J.P., Nelsen, T., McHone, J., Holliday, B., Palmer, H. and Shideler, G., 1977. Holocene evolution of the inner shelf of southern Virginia. J. Sediment. Petrol., in press.

Uchupi, E., 1968. Atlantic continental shelf and slope of the United States — physiography. U.S. Geol. Surv. Prof. Pap., 529—C: 1—30.

Van Veen, J., 1935. Sand waves in the North Sea. Hydrogr. Rev., 12: 21—29.

Wilson, I.G., 1972. Aeolian bedforms — their development and origins. Sedimentology, 19: 173—210.

55. CICAR-II Symposium on Progress in Marine Research in the Caribbean and Adjacent Regions, FAO Fisheries Report No. 200 Supplement, 1977, 479-486.

AIR-SEA INTERACTIONS DURING CONDITIONS OF SQUALLS AND DEEP CONVECTION

by

F. OSTAPOFF and S. WORTHEM
National Oceanic and Atmospheric Administration
Atlantic Oceanographic and Meteorological Laboratories
Sea-Air Interaction Laboratory
Miami, Florida, U.S.A.

CONTENTS

1. INTRODUCTION
2. THE ATMOSPHERE SURFACE LAYER RESPONSE
3. THE OCEANIC SURFACE LAYER RESPONSE
4. CONCLUSION
5. REFERENCES

Abstract

In September 1972 a mixed-layer experiment was conducted some 200 miles north of San Juan, Puerto Rico, as part of the CICAR programme in meteorology. Two MAMOS buoys were deployed, one of which was instrumented meteorologically. Air and water temperature, humidity, windspeed and radiation were observed and recorded at one-minute intervals. During passage of deep convective systems, a dramatic change in heat and momentum flux occurs associated with the circulation of those systems. In fact, the observations demonstrate the effects of up and down drafts generated within these deep convective cells on the thermodynamic properties of the surface layer resulting in an increase of sensible heat flux by an order of magnitude and latent heat flux by a factor of 2 to 4. Consequently, the Bowen ratio (sensible to latent heat flux) changes from about .10 for 'normal' tradewind conditions to .30–.35 under those disturbed conditions. Precipitation from these systems changes the static stability of the oceanic mixed layer and causes dramatic changes of temperature in the uppermost layer.

Resumen

Como parte del programa meteorológico de las ICCRA se realizó, en septiembre de 1972, un experimento en la capa de aguas mezcladas, a unas 200 millas al norte de San Juan de Puerto Rico. Se lanzaron dos boyas MAMOS, una de ellas dotada de instrumentos de medición meteorológica. Se observaron y registraron las temperaturas del agua y del aire, la humedad, la velocidad del viento y la radiación, a intervalos de un minuto. Durante el paso de sistemas de convección penetrante se produce un cambio drástico en el flujo de calor y en la cantidad d de movimiento, asociado a la circulación de esos sistemas. Las observaciones demuestran prácticamente los efectos de las corrientes ascendentes y descendentes engendradas dentro de las celdas de convección penetrante sobre las propiedades termodinámicas de la capa superficial, consistentes en que el flujo de calor sensible aumenta unas diez veces, y el flujo de calor latente, de dos a cuatro veces. Por consiguiente, el cociente de Bowen (flujo de calor sensible dividido por flujo de calor latente) cambia de 0,10 aproximadamente, en condiciones de vientos alisios 'normales', a 0,30–0,35, cuando se producen estas perturbaciones. Las precipitaciones originadas por estos sistemas cambian la estabilidad estática de la capa mixta oceánica, y originan drásticos cambios de temperatura en la capa superior.

1. INTRODUCTION

In this paper we would like to present some observations which will show the effects of atmospheric disturbances on the surface meteorological conditions and their effect on the upper ocean. Most of them were collected within the framework of CICAR. The data were obtained during the mixed-layer experiment, held north of San Juan, P.R. in September, 1971. A description of the instrumentation used during this experiment is given in another paper at the Symposium (Worthem and Ostapoff, 1976).

Much of what we know about the structure of the undisturbed atmosphere in the tropics has been described by Augstein _et al._ (1973) and Augstein _et al._ (1974), using the observations of the Atlantic Tradewind Expedition, 1969 (ATEX); and by Holland and Rasmussen (1973), using the data from the Barbados Oceanographic and Meteorological Experiment, 1969 (BOMEX).

2. THE ATMOSPHERE SURFACE LAYER RESPONSE

In order to understand the thermodynamic properties of the air near the ocean surface as they evolve during the passage of a squall line or deep penetrating convective system, Fig. 1 shows a schematic representation of the vertical structure of such systems, according to Zipser (1969). Moist, warm air of the mixed layer below cloud base will be drawn into the towering convective portion of the cloud, pumping moisture into the system and feeding the rain-producing part of the anvil. Associated with the precipitation, which can be of considerable magnitude, is the region of down-draft. Often, a gust front is produced under the the cloud and ahead of the cool and sometimes dry down-draft air. This air comes from a level above the cloud base (Betts, 1976) and is cooled by evaporation. But, its moisture content stays normally below that of the environmental air near the surface. The associated deep down-draft transport will reach the surface of the ocean (see Fig. 2).

Fig. 2 shows a time series of specific humidity, wind speed, air temperature, sea-air temperature difference and sea-surface temperature. The data was obtained at one-minute intervals at a height of six metres above the sea surface from a buoy (Worthem and Ostapoff, 1976). As seen from the sea surface temperature, the record was obtained during night time. Prior to the passage of a convective system at 0020 LT 2 October 1971, the atmospheric variables exhibit the normally found conditions over the tropical ocean: relative humidity, about 75 percent; air-sea temperature difference of about 1°C; wind speed about 6 m sec^{-1}. These values will give typical sensible heat flux of 30 cal cm^{-1}d^{-1} and latent heat fluxes of 400 cal cm^{-2}d^{-1} resulting in a Bowen ratio in the order of $B \approx .10$ (see Fig. 3).

At 0020 LT, and then again at 0500 LT during the experiment, deep convective systems passed over the buoy and its sensors. The gust front associated with the convective cloud is clearly evident in the wind record. Peak values of 15 m sec^{-1} were reached, and immediately both the relative humidity and specific humidity began dropping sharply indicating the arrival of the cold, dry, down-draft air. The air-sea temperature difference reached about 3.5°C in the first case and somewhat more than 5°C in the second case. This was due to the cold air in both cases, since the water temperature did not change noticeably as a result of these events. The first event lasted a half an hour; the second about one hour before the atmosphere began returning to large-scale, equilibrium environmental conditions.

In Fig. 3, the momentum and heat fluxes are presented for the time series shown in Fig. 2. The aerodynamic bulk formulas corrected for stability have been used to calculate the fluxes. The momentum and heat exchange rates changed considerably, as shown in Table I. The Bowen ratio increases with the size of the disturbance. It may reach mid-latitude values of about .30-.35 for large systems.

Table I

Momentum, sensible and latent heat flux estimates during undisturbed and disturbed conditions

Meteorological conditions	Momentum flux dyn cm^{-2}	Sensible heat flux cal cm^{-2} d^{-1}	Latent heat flux cal cm^{-2} d^{-1}	Bowen ratio
Undisturbed	.5	3	40	.08
Disturbed (1)	3.4	14	110	.13
Disturbed (2)	3.4	25	125	.20

3. THE OCEANIC SURFACE LAYER RESPONSE

As seen from Fig. 2, the ocean response to small-scale atmosphere disturbances as indicated by the sea surface temperature is hardly noticeable. This is not surprising because of the great heat capacity of water and the almost instantaneous mixing due to wave set-up.

However, if the other thermodynamic property of ocean water, salinity, is significantly altered, then the top layer of the ocean may respond differently, depending upon the stability conditions which may be set-up by heavy precipitation from individual convective systems or enormous river run-off during the rainy season, e.g., the Amazon River and Orinoco River. Detailed descriptions of the processes in the upper ocean under various stability conditions are given in the paper by Worthem and Ostapoff (1978).

How the stability can be changed by atmospheric events can be seen in Fig. 4 which shows a sequence of two-hourly temperature and salinity profiles obtained in the Inter-Tropical Convergence Zone (ITCZ) at approximately 4°N and 24°W in July 1972. Initially, the so-called oceanic mixed layer was indeed well mixed in temperature and salinity to about 60 m depth (to within the accuracy of the instrument which was an internally analogue recording STD device). Rain started at the time of the profile indicated by the precipitation symbol. It lasted for about 12 hours and amounted to about 18 mm as observed by the rain gauge on the ship. However, if the salt deficit in the top layer is solely attributed to local precipitation and not to other processes such as advection, then about 46 mm of rain water should have precipitated. This is somewhat more than twice what has been observed; but one should remember that reliable shipboard rain observations are notoriously difficult to obtain (Shinners, 1970). Further into the time series in Fig. 4, another brief shower occurred, again leaving its signature in the top layer of the ocean.

A wave-mixed layer developed to a depth of about 7-10 m as can be seen in Fig. 4. After the rain stopped, the low-salinity/low-temperature lens is diffused downward, probably by either turbulent diffusion or mixing caused by shear instability.

A closer look at the downward diffusion is presented in Fig. 5 which shows details of two successive temperature and salinity profiles, two hours apart. The heat and salt deficits are preserved and redistributed with time. Another example is given in Fig. 6, obtained in the Caribbean Sea southeast of Puerto Rico under a cloud cluster (see satellite picture in Fig. 7). In this case, the two profiles were taken one hour apart. These time series have been used to calculate the complete budget in the upper ocean and to derive precipitation information from salinity measurements for cases where advection can be neglected (Ostapoff _et al._, 1973).

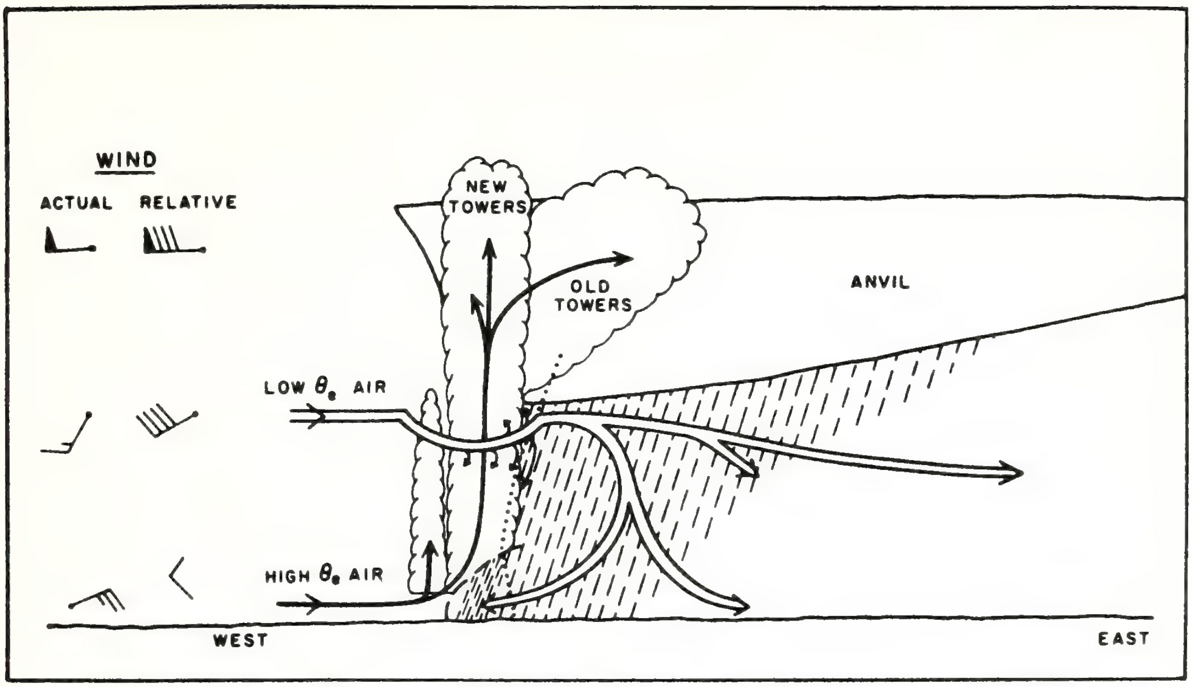

Fig. 1 Schematic presentation of streamlines in convective cloud system according to Zipser (1969)

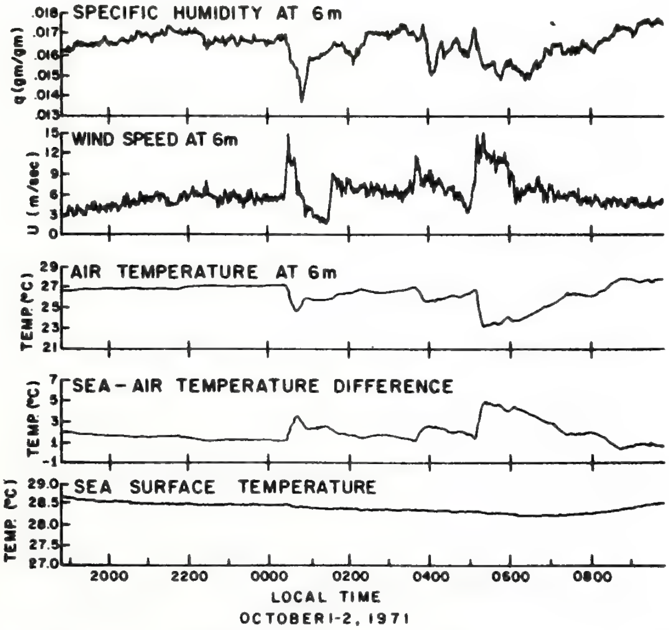

Fig. 2 Time series of specific humidity, wind speed, air temperature and sea-surface temperature during atmospheric deep convection events

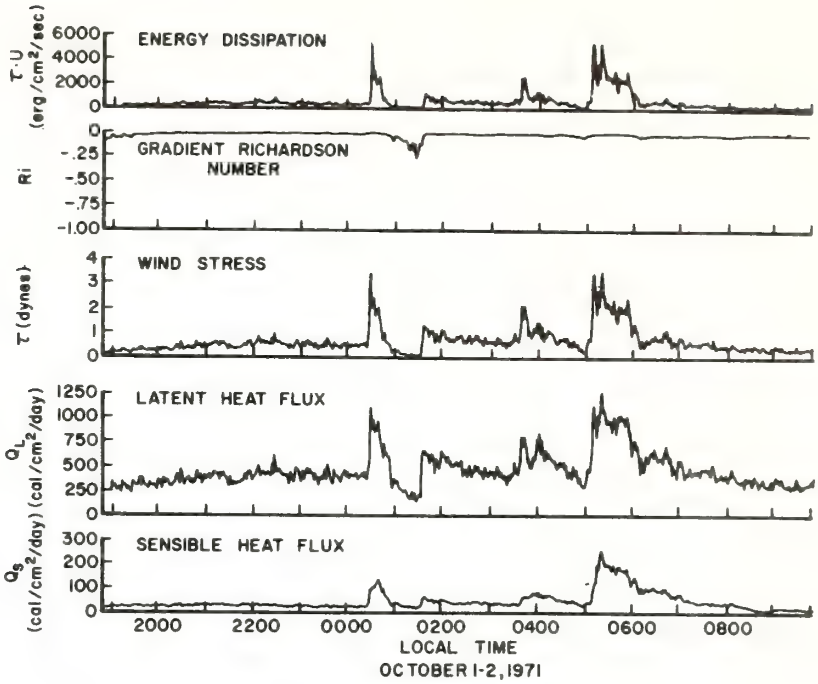

Fig. 3 Time series as in Fig. 2 for derived energy fluxes

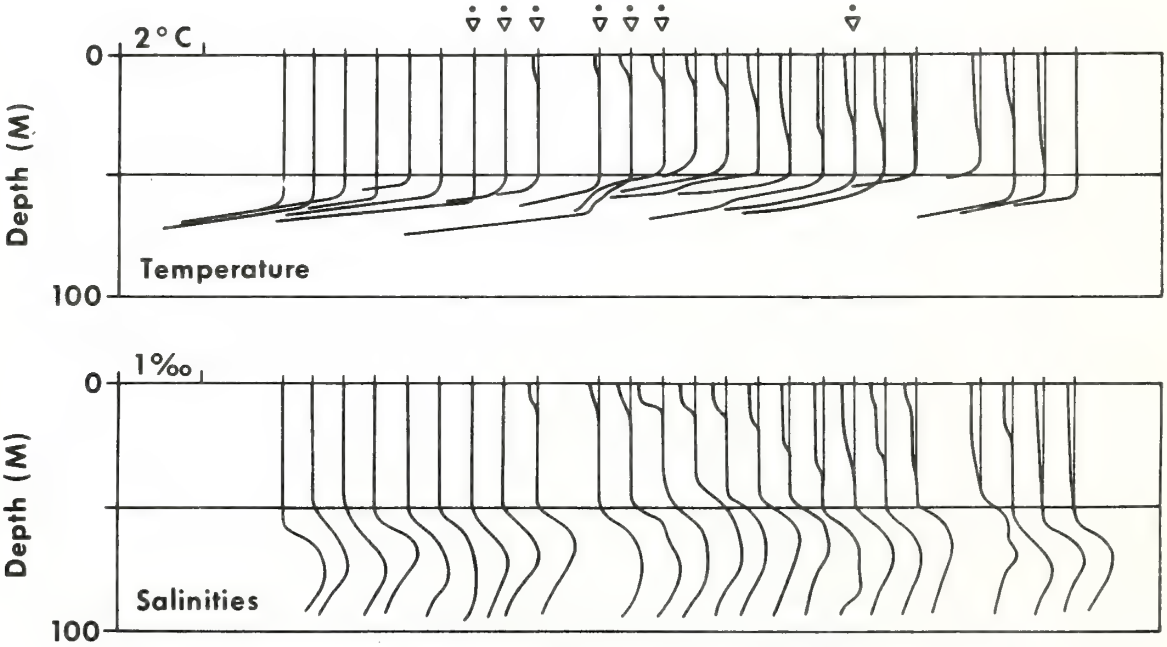

Fig. 4 Two-hourly time series of temperature (top) and salinity (bottom) profiles obtained during precipitation events

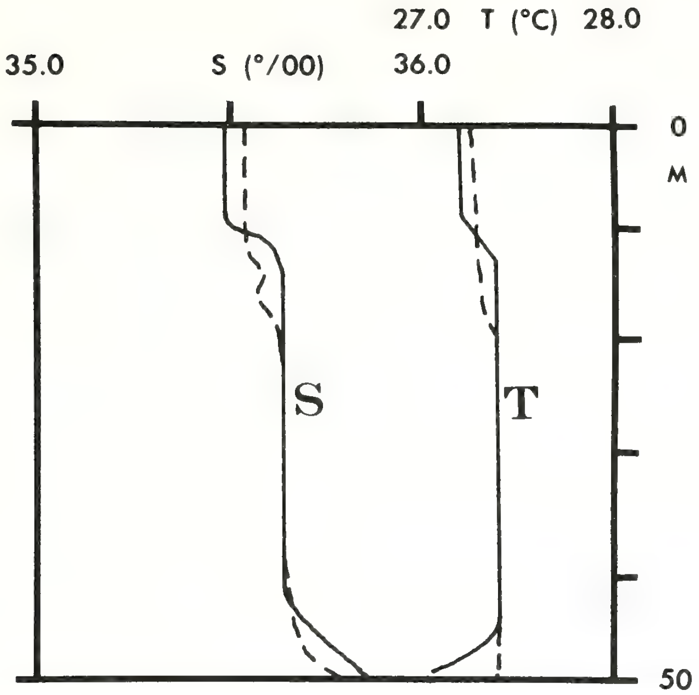

Fig. 5 Temperature and salinity profiles obtained two hours apart

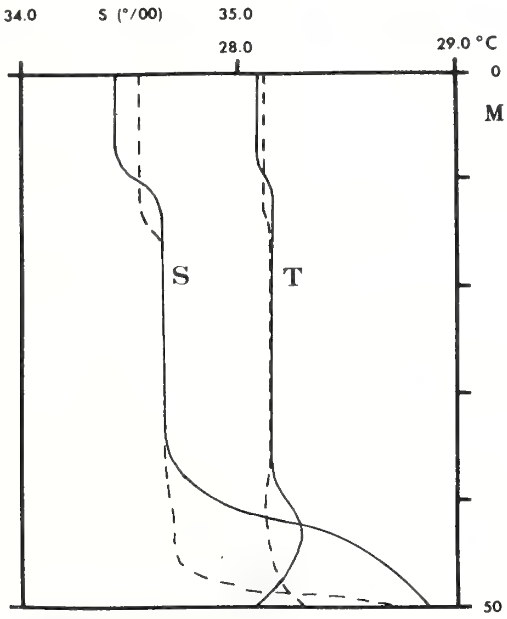

DISCOVERER 11.11.72

Fig. 6 Temperature and salinity profiles obtained one hour apart southeast of Puerto Rico

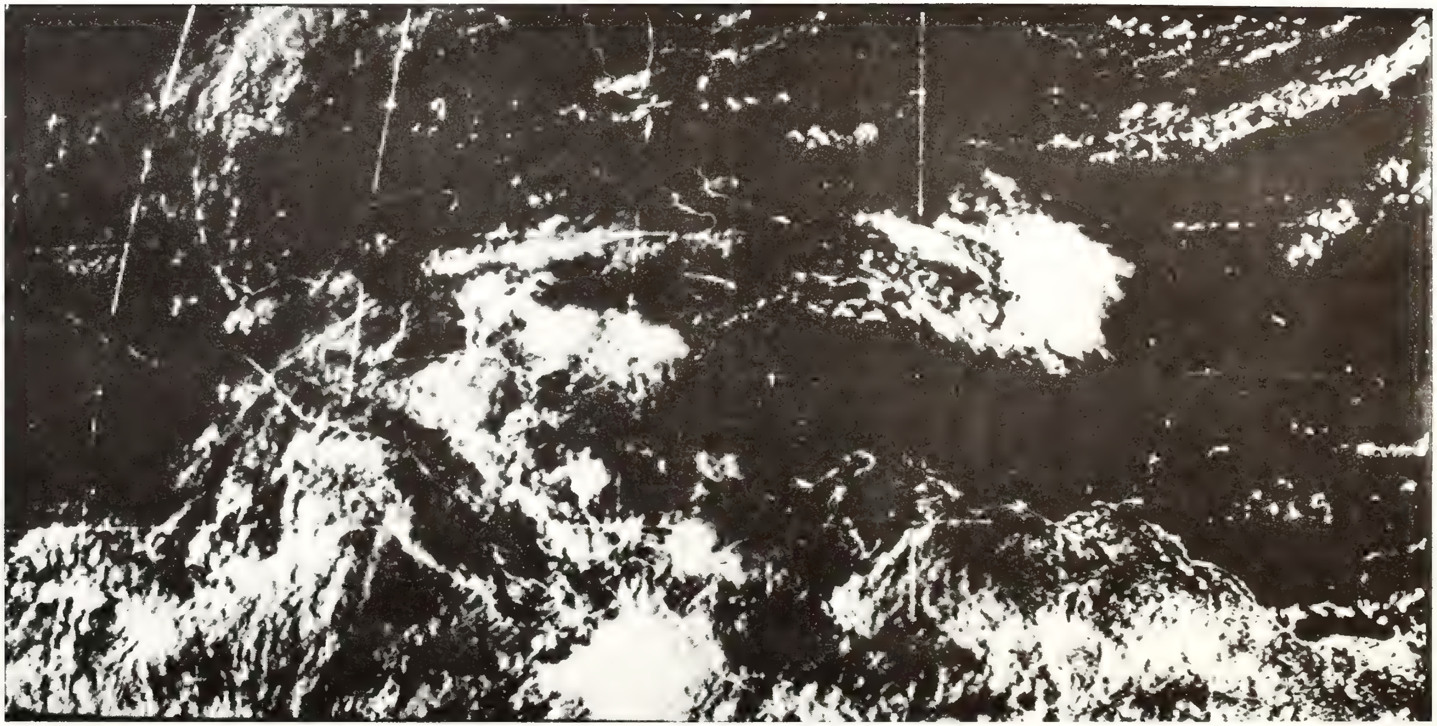

Fig. 7 Satellite photograph of cloud cluster southeast of Puerto Rico on 11 November 1972 when T-S profiles were obtained (see Fig. 6) during NOAA-Carib

4. CONCLUSION

The purpose of this paper is to show, with the aid of a few examples, how the lowest layers of the atmosphere and the upper layers of the ocean respond to a deep convection system. Indeed, it is shown that extreme down-draft conditions exist right down to the ocean surface for relatively large time scales, on the order of a half an hour. Then the enormously enhanced sensible and latent heat fluxes, generated by the down-draft conditions themselves, may feed back into these systems and quickly modify the near-surface layers. The large energy fluxes at the sea surface provide a source of heat and moisture flux into the boundary layer which tends to cause restoration of the large-scale environmental conditions.

It is also shown that precipitation plays an important role in the thermodynamics of the upper ocean mixed layer in determining and modifying the stability of this layer; thus allowing different processes to dominate the exchanges within the oceanic mixed layer and energy exchanges between the ocean and the atmosphere.

5. REFERENCES

Augstein, E., H. Schmidt and F. Ostapoff, The vertical structure of the atmospheric planetary boundary layer in undisturbed trade winds over the Atlantic Ocean.
1974 Boundary-Layer Meteorol., 6:129-50

Augstein, E. et al., Mass and energy transports in an undisturbed Atlantic trade-wind flow.
1973 Mon.Weather Rev., 101(2):101-11

Betts, A.K., The thermodynamic transformation of the tropical sub-cloud layer by precipitation and down drafts. J.Atmos.Sci., 33(6):1008-20
1976

Holland, J.Z. and E.M. Rasmusson, Measurements of atmospheric mass, energy and momentum budgets over a 500-kilometer square of tropical ocean. Mon.Weather Rev., 101: 11-55
1973

Ostapoff, F., Yu. Tarbeyev and S. Worthem, Heat flux and precipitation estimates from oceanographic observations. Science, Wash., 180:960-2
1973

Shinners, W.W., Status of instrument development for specialized marine observations.
1970 Meteorol.Monogr., 11:294-301

Worthem, S. and F. Ostapoff, The response of the tropical North Atlantic to meteorological forcing functions. FAO Fish.Rep., (200) Suppl.
1978

Zipser, E.J., The role of organized unsaturated convective down drafts in the structure and rapid decay of an equatorial disturbance. J.Appl.Meteorol., 8:799-814
1969

56. CICAR-II Symposium on Progress in Marine Research in the Caribbean and Adjacent Regions, FAO Fisheries Report No. 200 Supplement, 1977, 505-530.

THE RESPONSE OF THE TROPICAL NORTH ATLANTIC TO METEOROLOGICAL FORCING FUNCTIONS

by

S. WORTHEM and F. OSTAPOFF
National Oceanic and Atmospheric Administration
Atlantic Oceanographic and Meteorological Laboratories
Sea-Air Interaction Laboratory
Miami, Florida, U.S.A.

CONTENTS

1. INTRODUCTION
2. DESCRIPTION OF FIELD EXPERIMENT
3. SYNOPTIC DATA ANALYSIS
4. CASE 1: HOMOGENEOUS REGION
5. CASE 2: LOW SALINITY PUDDLE
6. SUMMARY AND CONCLUSION
7. ACKNOWLEDGEMENTS
8. REFERENCES

Abstract

As a contribution to CICAR, an experiment to investigate the evolution of the ocean mixed layer structure in response to meteorological forcing functions, was conducted from the NOAA ship DISCOVERER between 28 September and 14 October 1971 at 21°N and 66–67°W, about 180 n mi due north of San Juan, Puerto Rico. The structure of the upper ocean was delineated using X-BT, STD, a profiling current meter system and a quartz thermometer system. Meteorological parameters were recorded from a drifting buoy allowing calculation of thermal and dynamic fluxes at the sea surface using the bulk aerodynamic formulas. This paper emphasizes the STD and X-BT measurements as they contribute to our understanding of upper ocean heat storage.

The region was selected for its lateral homogeneity and permanent thermocline depth. The permanent thermocline was sufficiently deep that the response of the mixed layer to meteorological forces could be separated from the complex internal processes occurring at the upper edge of the permanent thermocline.

The data show that the mixed layer can be divided into three zones. The surface zone is dominated by forced convection due to wave mixing. All properties are rapidly mixed uniformly in this layer, which typically extends to a depth of about 10–15 m in our measurements. The next zone is where diurnal heating processes dominate and has the character of a diffusive régime with a time scale of several hours. It extends to about 40 m in our data. The third zone is a transition region where the complex internal wave mixing processes erode the bottom of the mixed layer.

Resumen

Como contribución a las ICCRA, el buque DISCOVERER, de la NOAA, realizó un experimento, entre el 28 de septiembre y el 14 de octubre de 1971, a 21°N y 66–67°O, a 180 n. mi aproximadamente al norte de San Juan de Puerto Rico, con el fin de investigar la evolución de la estructura de la capa mixta oceánica como respuesta a las funciones de compulsión meteorológica. La estructura del océano superior pudo conocerse utilizando X-BT, STD, un sistema de medición de corrientes mediante secciones verticales, y un termómetro de cuarzo. Los parámetros meteorológicos fueron registrados por una boya flotante, que permitía calcular el flujo térmico y dinámico de la superficie del mar utilizando las fórmulas aerodinámicas globales. En este documento se ponen de relieve las mediciones STD y X-BT porque nos permiten comprender mejor el almacenamiento de calor en el océano superior.

La región fue elegida por su homogeneidad lateral y por la profundidad de la termoclina permanente. La termoclina permanente era lo suficientemente profunda para poder distinguir la capa mixta a las fuerzas meteorológicas de los complejos procesos internos que se producen en el borde superior de la termoclina permanente.

Los datos muestran que la capa mixta puede dividirse en tres zonas: en la zona de superficie domina la convección forzada, debida a la mezcla de olas. En esa capa, que en nuestras medidas llega normalmente a una profundidad de 10–15 m, aproximadamente, todas las propiedades se mezclan uniformemente, y con rapidez. En la zona inmediata dominan los procesos de calentamiento diurno, y se caracteriza por un régimen difusivo, con una escala de tiempo de varias horas: en nuestros datos, llega hasta unos 40 m. La tercera zona es una región de transición, en la que los complejos procesos internos de mezcla de olas erosionan el fondo de la capa mixta.

1. INTRODUCTION

Understanding the evolution of the upper ocean in response to meteorological forcing functions is necessary in order to predict the heat storage. The sea surface temperature is determined by dynamical processes in the upper ocean, which acts as a heat reservoir for the atmosphere. This, in turn, modifies the meteorological processes. For example, hurricanes generally intensify over a warm sea surface and are maintained over regions of relatively high sea surface temperature. They typically degenerate and modify over an area of sufficiently cool sea surface. The vapour pressure, which controls the latent heat flux, is proportional to the saturation vapour pressure which has an exponential dependence on sea surface temperature. An approximate boundary between a "warm" and "cool" sea surface for a hurricane is about 26.5°C (Ooyama, 1969).

As a contribution to the Cooperative Investigation of the Caribbean and Adjacent Regions (CICAR), a field experiment was carried out to study the response of the upper ocean to meteorological forcing functions on a time scale of hours and days. The experiment was conducted from the NOAA ship the R/V DISCOVERER from 28 September to 14 October 1971 in the region of 21°N and 66°–67°W which is about 300 km due north of San Juan, Puerto Rico. This paper describes the structure and evolution of the upper ocean in two different régimes. One régime is the characteristic low latitude upper ocean configuration of a surface layer of small gradients of temperature, salinity, and density above a sharply stratified permanent thermocline or pycnocline region (Case 1).

The other régime is that of a relatively low salinity lens of approximately 20–40 km diameter floating in the surface layer (Case 2). Low salinity puddles of similar scale have been found in the Gate B-scale area (Rooth, 1973). The origin of such puddles is thought to be the rain from atmospheric convective systems. The fresh water forms a quite stable stratified lens or puddle which has been observed to persist for a period of days or weeks floating on the surface.

Diurnal variations of the temperature and heat budgets have been studied by several investigators (e.g., Stommel and Woodcock, 1951; Shonting, 1964; Stommel et al., 1969; Howe and Tait, 1969; Bowden et al., 1970; Hasse, 1971; Fedorov, 1972; Hoeber, 1972; Denman and Miyake, 1973 and Ostapoff and Worthem, 1974). Our understanding of upper ocean structure based on these results is limited to conditions which we call the Case 1 situation – the classical textbook case.

Various local models exist which can be applied to describe the evolution of the upper ocean due to meteorological forcing (e.g., Kraus and Turner, 1966; Foster, 1971; Pandolfo and Jacobs, 1972; Denman, 1973 and Mellor and Durbin, 1975). The model formulations, except for that of Pandolfo and Jacobs (1972) have generally assumed that temperature is a valid indicator of stability. The result of this assumption is that the effects of precipitation and evaporation on salinity and, thus, on the stability of the water column, is neglected. These assumptions, while generally valid in the mid-latitude regions for which the models were designed, are not necessarily applicable in the tropics, as will be demonstrated by the data which will be presented in this paper. Conceptually, it appears that including the effects of salinity variation and a surface salinity source/sink in the models should be a relatively minor modification.

2. DESCRIPTION OF FIELD EXPERIMENT

In this experiment, current profiles of the upper 300 m were taken every three hours from the drifting ship using the current profiler described by Düing and Johnson (1971). Approximately hourly X-BT profiles to 400 m were made. During periods when the ship was drifting, approximately hourly STD profiles staggered with the X-BT profiles were made to a depth of at least 100 m. From the bow of the NOAA DISCOVERER, downward- and upward-looking pyranometers as described by Hanson and Poindexter (1972) provided total sun and sky radiation data (285–2 800 n mi) at three-minute intervals. Two MAMOS buoys were used which are identical in construction to the Navy's NOMAD buoys (Naval Air Systems Command, 1967). One buoy was carrying instrumentation to record once a minute the wind speed, relative humidity and air temperature at a height of 6 m and sea surface temperature at a depth of 25 cm. The other buoy was instrumented with an array of quartz thermometers and a thermistor chain (Aanderaa) as described by Ostapoff and Worthem (1974). To minimize advective heat storage changes for the purpose of energy budget calculation, the buoys were attached to drogue chutes of about 9 m diameter which were deployed at 30 m depth.

The region was selected for its lateral homogeneity and permanent thermocline depth. The permanent thermocline was sufficiently deep that the mixed layer evolution in response to meteorological inputs could be separated from the mixing processes occurring at the upper edge of the permanent thermocline.

3. SYNOPTIC DATA ANALYSIS

The ship track is shown in Fig. 1. The track was determined using satellite navigation. The solid lines in the figure denote drifting and dashed lines steaming portions of the track. The lines crossing the track indicate hourly positions. The ship steamed and drifted to stay within a few miles of the drifting buoys. The buoy tracks are shown in Fig. 2, and their track lines were determined from hourly positions using the ship's navigational radar. Hourly positions are indicated by dots on the buoy tracks in the figure. As can be seen from the buoy tracks, the period can be divided into two régimes. The change from an essentially smooth westward drift to a complicated drift pattern with a predominantly southwestward component occurs at about 66°36'W. Measurements made east of this boundary will be referred to as the previously defined Case 1 régime, and west of this boundary will be the Case 2 régime.

Contours of surface salinity are determined from the STD profiles shown in Fig. 3. The surface salinity was approximately constant in the Case 1 region. The presence of a low salinity area is apparent in the Case 2 region. There is an extremely strong surface salinity gradient at about 66°36'W, 20°58'N. The surface salinity decreases toward the south, with a frontal region running approximately along 20°58'N. The surface salinity to the east of 66°36'W is generally in the range 36.36 °/oo–36.38 °/oo, and can be considered essentially constant. The minimum surface salinity in the frontal region was about 35.50 °/oo.

The salinity difference between 30 m depth and the surface is shown in Fig. 4. The salinity difference contours are very similar to the surface salinity contours with low surface salinity corresponding to high salinity difference. Thus, the salinity at 30 m is approximately constant over the region. The salinity east of 66°36'W is essentially constant down to about 35–40 m depth.

The low salinity region is a relatively shallow feature as can be seen in Fig. 5, in which mixed layer depths are shown. The low salinity region is generally less than 20 m deep. There appears to be no correlation between the mixed layer depths shown in Fig. 5 and the surface salinities and salinity anomalies shown in Figs. 3 and 4.

The vertical salinity gradient in the interfacial region between the low salinity puddle above and the horizontally homogeneous environment below is quite sharp. Using data from the current profiles, the gradient Richardson number Ri, was estimated in both the homogeneous and frontal regions. In the homogeneous region, Ri ≈ 0, indicating turbulent mixing was a dominant process. In the maximum salinity anomaly region, the local gradient Richardson number at the interface was as high as 6.0, indicating high stability. Thus we believe that a turbulence cannot be maintained in the frontal region, and the low salinity lens is quite stable. In the presence of such a stable interface, a wide spectrum of internal waves is possible. We believe the mixed layer depth variability is significantly affected by the presence of internal waves. This will be discussed further in Section 5.

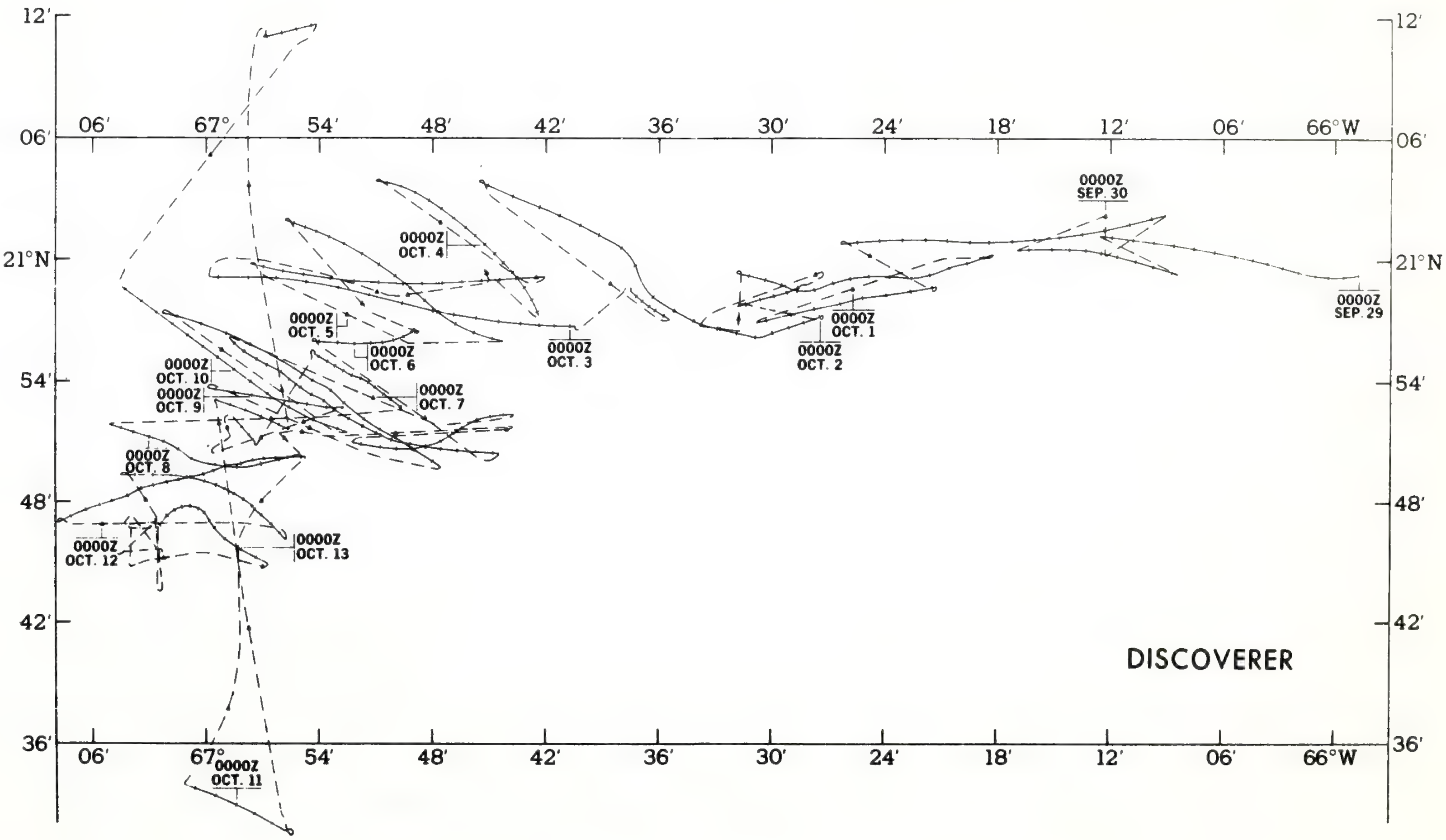

Fig. 1 Ship track with solid lines denoting drifting, dashed lines denoting steaming. Lines crossing the track indicate hourly positions

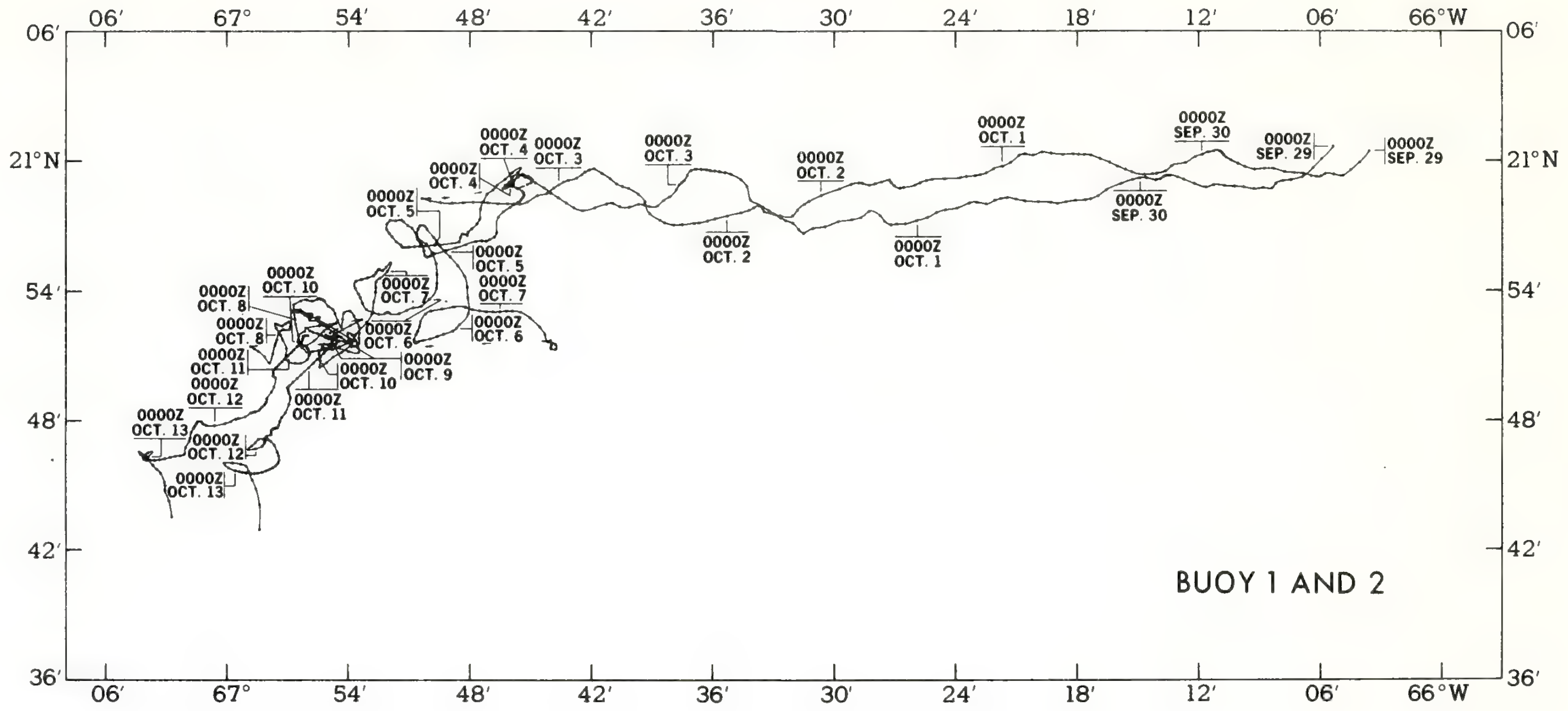

Fig. 2 Buoy tracks with dots indicating hourly position

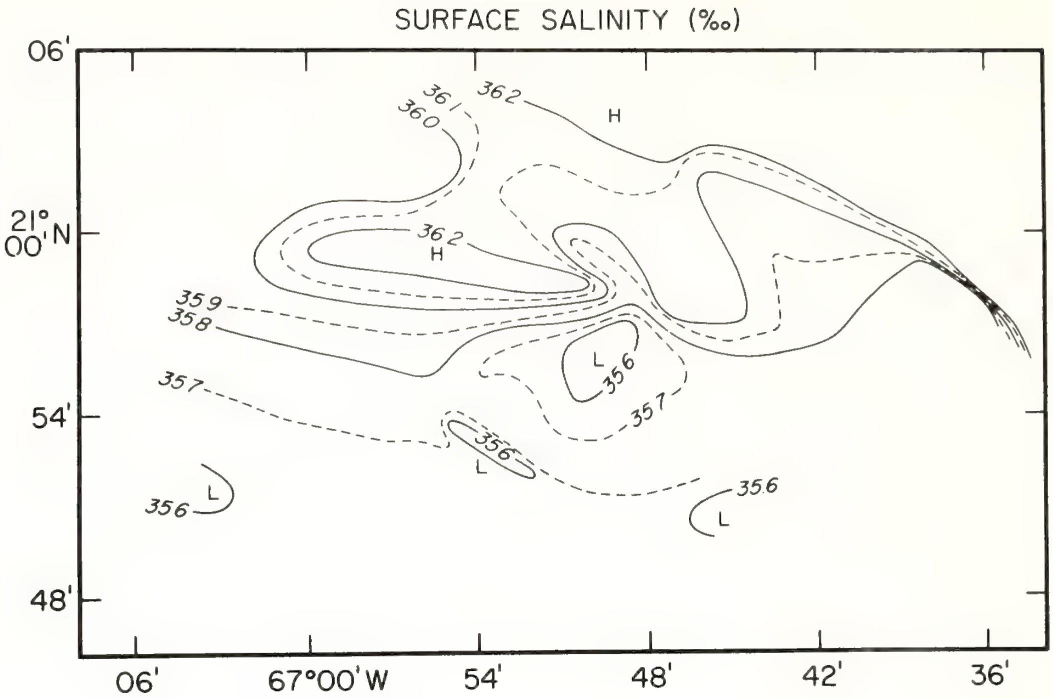

Fig. 3 Surface salinity

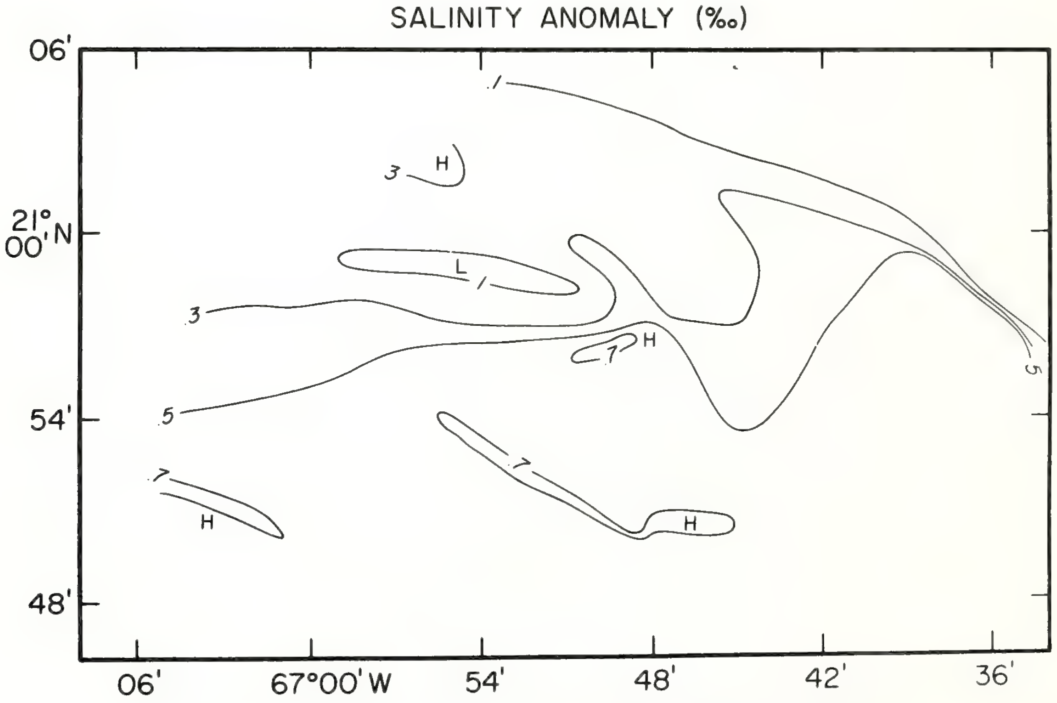

Fig. 4 Salinity difference between 30 m and the surface

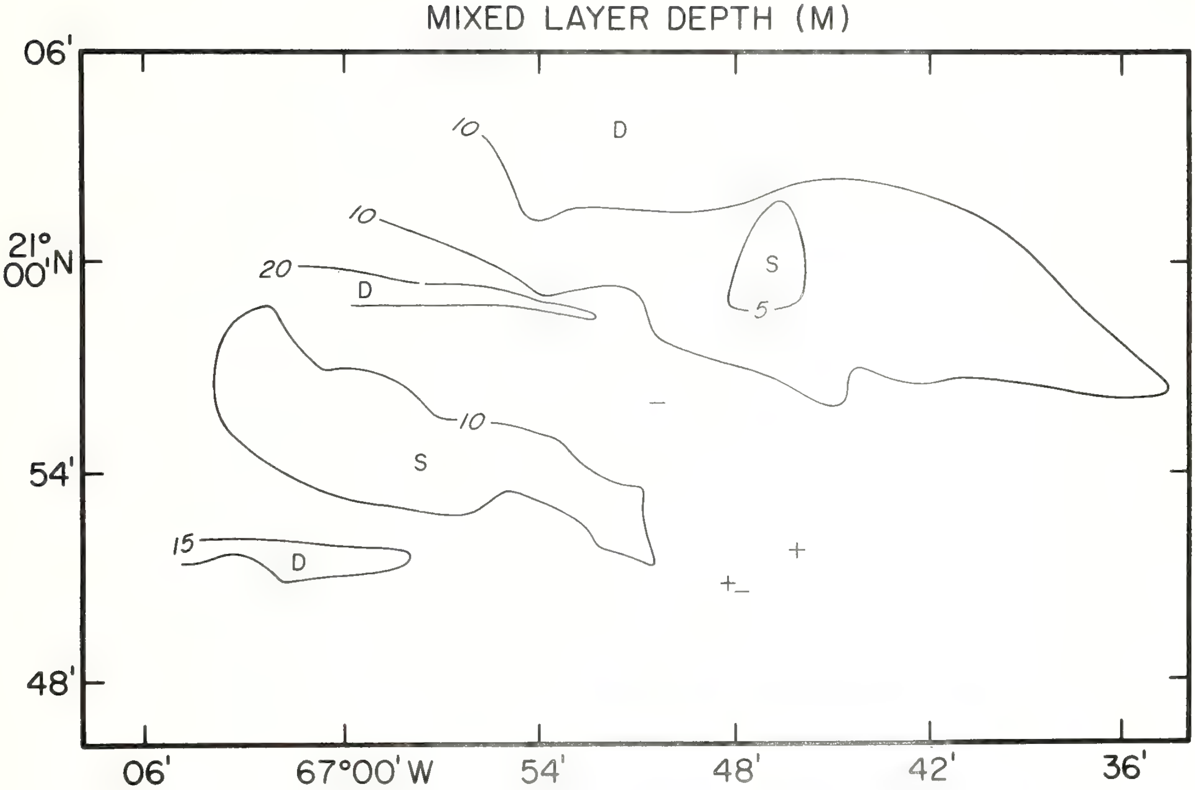

Fig. 5 Mixed layer depth

To create such a low-salinity lens, we estimate that 39.6 cm of fresh water would be necessary. This was calculated using the extreme salinity anomaly, ΔS, of 0.8 °/oo over a depth, h, of 18 m, using the relation $\epsilon \approx h \Delta S / S_0$. This relation was derived using the conservation of salt in the water column. The environment salinity, S_0, was taken to be 36.36 °/oo. Before overturning of the layer or deep mixing would occur, a temperature decrease of 2.0°C could occur for a salinity anomaly of 0.8 °/oo, as can be calculated from the linearized equation of state. Thus the surface layer could lose 3 600 cal cm^{-2} and sustain a 2.0°C bulk temperature decrease, thus reducing the Richardson number, before mixing of the water column to the permanent thermocline would occur.

Since the diurnal variability of the temperature very close to the sea surface is of the order of 1.0°C, the presence of the salinity lens obscures the diurnal heating cycle. This can be seen from the quartz thermometer record shown in Fig. 6. The time series of quartz thermometers at 10, 20, 30, 40 and 50 m depth are shown. The 50 m record shows the presence of large fluctuations due to internal waves. The dominant signal in this record is the semidiurnal internal tide. The 50 m record was taken at the upper edge of the permanent thermocline. The upper three records show the typical diurnal heat-wave pattern until 1 400 LT (1 800 GMT) on 2 October 1971. At that time a sharp change in régimes is obvious in both the 10 and 20 m records. It is just barely apparent in the 30 m record. After that time, the diurnal cycle is completely obscured. Notice particularly the anomalously cold temperatures in the 10, 20, and 30 m records for the 14-hour period beginning at 07.00 h LT on 3 October. This time period would normally be expected to correspond to solar radiational heating and a corresponding temperature increase in the top 30 m of the water column. A prediction of the sea surface temperature during this period based on the measured solar radiation, which was normal for a meteorologically undisturbed period, and a density profile determined by temperature alone, i.e., from a prior X-BT profile, using an average salinity from the homogeneous region would be quite incorrect. Therefore, it is necessary to measure both temperature and salinity to predict sea surface temperature and heat storage.

Using the three-hourly current profile data and the ship drift velocity calculated from the ship track, the average current velocity in the upper 40 m has been calculated. It is shown in Fig. 7. The arrows represent the current speed in proportion to their length and are aligned in the current direction. Each long tail on the arrows indicates a speed of 10 cm/sec^{-1}, with the length of the smaller tails in proportion. The surface current appears to be approximately southwestward east of 66°36'W in the homogeneous region. The low salinity region is more complex. In this region the surface current becomes more southerly at southern positions. There is a region of high horizontal current shear at approximately 66°48'W and 20°57'N. This corresponds to the northward low surface salinity intrusion shown in Fig. 3. It is possible to visualize several eddy regions in Fig. 7. These roughly correspond to the high and low regions in the surface salinity shown in Fig. 3.

The current shear between 17.5 m and 37.5 m, i.e.

$$\frac{\Delta V}{\Delta Z} = \left[(U_{17.5} - U_{37.5})^2 + (V_{17.5} - V_{37.5})^2 \right]^{1/2} / 2\,000$$

was calculated from the current profile data which had previously been smoothed to obtain 20 m averages. This is shown in Fig. 8. Areas of high current shear appear to be separated by approximately 15 km. A comparison of Figs. 8 and 5 shows that the high current shear region at approximately 67°W and 20°54'N corresponds to the shallow mixed layer depth region. The relatively low shear at 66°54'W and 20°58'N corresponds to a deep mixed layer. This correlation would lead us to conclude that vertical mixing had occurred in the low shear region, perhaps enhanced by shear instability in the interfacial region. Other areas of high and low shear do not appear well correlated with mixed layer depth and could be primarily caused by internal waves.

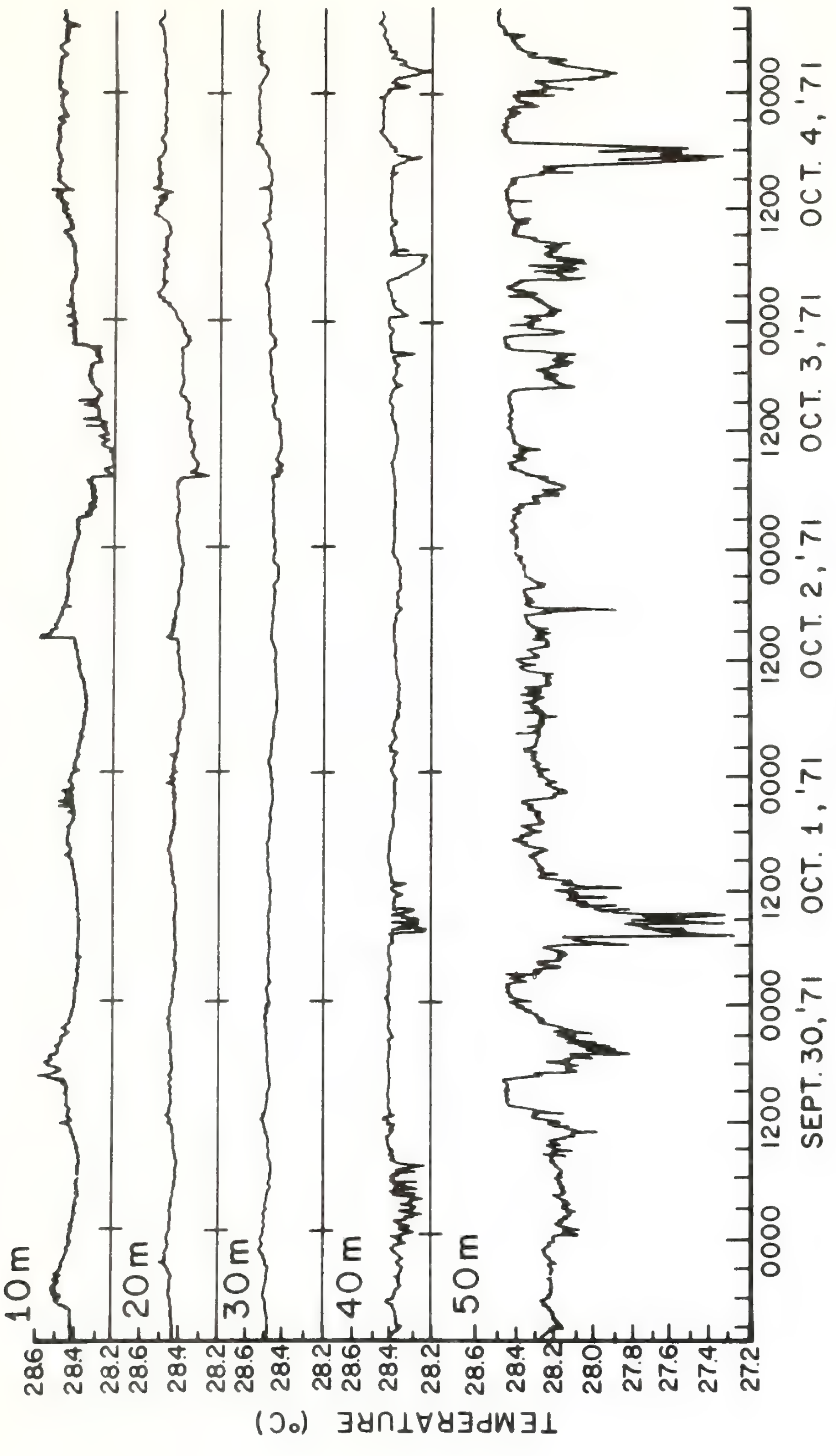

Fig. 6 Quartz thermometer time series

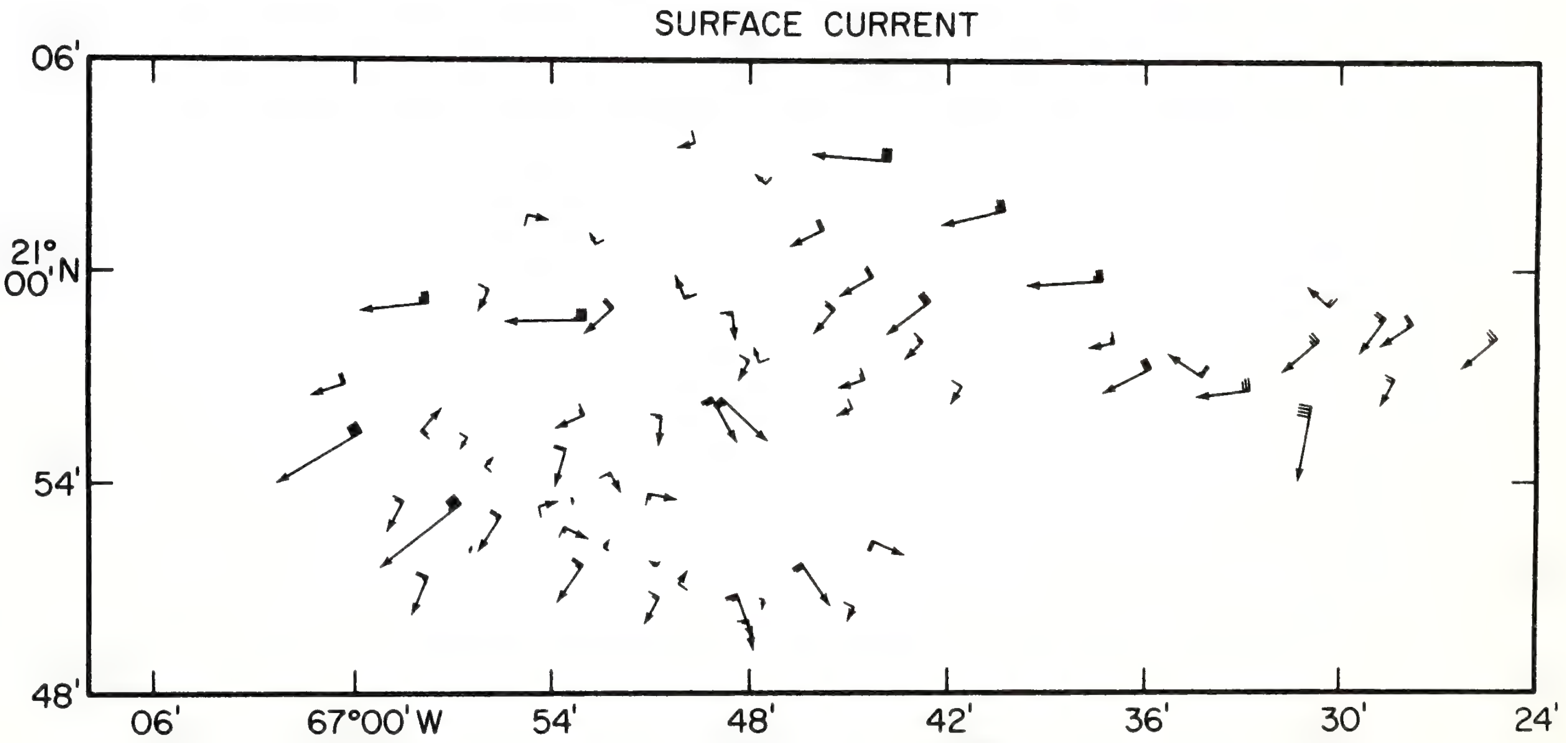

Fig. 7 Average current in the upper 40 m

CURRENT SHEAR (10^{-4} SEC^{-1})

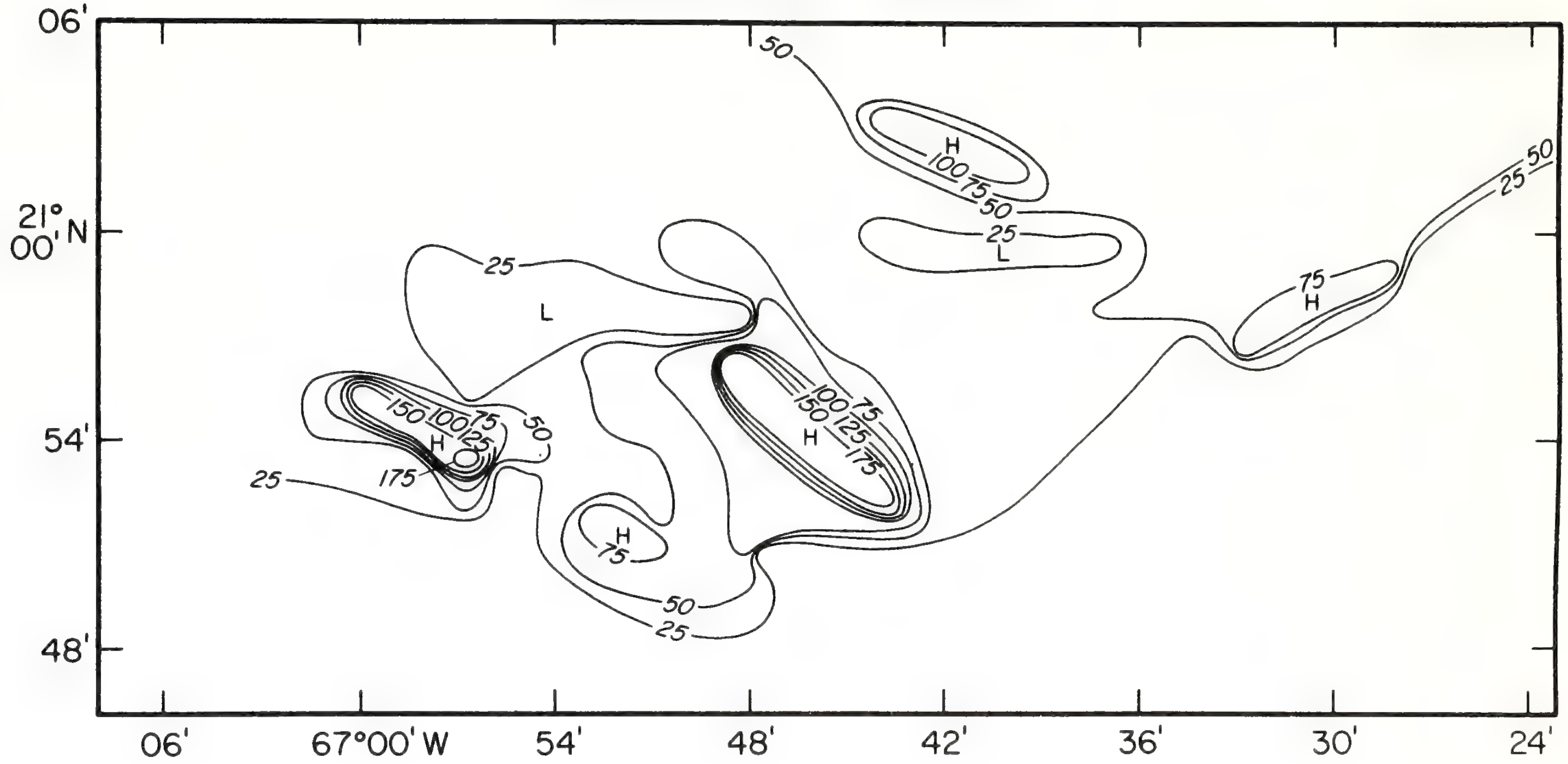

Fig. 8 Current shear between 17.5 m and 37.5 m from 20 m averaged current profile data

A comparison of Figs. 8 and 3 shows that, in general, high shear corresponds to low surface salinity (large salinity anomaly) and conversely. Thus, in regions of large stratification, relatively high shear between the low salinity layer and underlying water occurs. This also supports the conclusion that low shear regions are where vertical mixing has occurred. In particular, the relatively high surface salinity area at about 66°54'W and 20°58'N corresponds to a low shear region.

Near the edge of the low salinity region, a series of low and high current shear regions appear. This could indicate an instability in the frontal region, causing internal waves to occur.

4. CASE 1: HOMOGENEOUS REGION

The physical processes which are typically observed in the upper ocean are shown schematically in Fig. 9. Atmospheric forcing functions act at and through the ocean surface. The time scale of meteorological events is of the order of several minutes to a couple of weeks. Solar radiation penetrates the upper ocean and provides a depth-dependent heat source. There is sensible heat flux caused by the air-sea temperature difference at the surface. Evaporation from the sea surface causes a latent heat flux. The sea surface temperature produces a long wave radiative flux. Evaporation (precipitation) at the sea surface produces a salinity source (sink) at the surface. The wind blowing over the sea surface produces a surface stress.

The upper ocean typically has a weakly stratified region (mixed layer) overlying a strongly stratified region (thermocline). The top of the mixed layer is dominated by "wave mixing". This is a forced convection régime in which properties are mixed on a time scale of minutes. Below this is a turbulent mixing régime which is called the "layer of the diurnal thermocline" in the figure. It is maintained by meteorological buoyancy and shear forces. This régime can be dominated by forced or free convective. It has a response time of the order of hours. The permanent or "main thermocline" is a very stably stratified region. It is maintained by longer-term processes. Internal waves in this strongly stratified region alternately squeeze and stretch the mixed layer. There is a sharp "transition layer" between the strongly stratified thermocline régime and weakly stratified mixed layer régime. Here, both internal waves and turbulent mixing processes occur.

Bulk or mean field temperature and salinity in the upper ocean typically vary more over a 100 m depth change than over a 1 000 km horizontal distance. In this case, vertical exchange processes are more important than horizontal advection and mixing, and the upper ocean can be assumed to be statistically homogeneous horizontally.

A temperature contour plot made from hourly X-BT files taken on 28 September 1971 is shown in Fig. 10. It shows a "textbook case" evolution of the mixed layer during a diurnal heating cycle during which there is no net heat gain over the period. This record was taken in the laterally homogeneous region which we refer to as the Case 1 régime. The situation is analogous to the mid-latitude seasonal heating cycle, as described, for example, by Kraus (1972).

In the tropical ocean, the air is typically a fraction of a degree cooler than the sea surface, except in deep convective systems with extensive down-draft regions (Ostapoff and Worthem, 1976) where the air-sea temperature difference may exceed 5°C. The wind is steady in the trade wind region. Thus, the sensible and latent heat fluxes transfer heat from the ocean to the atmosphere, as does the long-wave back radiation. Net evaporation also causes a slight increase in surface salinity. Thus, before the sun rises, there is typically cooling at the surface and neutral or very slightly unstable stratification (cf., Ostapoff and Worthem, 1974) in the mixed layer region. Mixing occurs down into the transition layer and is inhibited by the permanent thermocline. As soon as there is a net heat flux into the ocean, a stable shallow layer forms. As long as there is an increasing net heating rate, the layer stability increases, sea surface temperature rises and the layer remains relatively shallow.

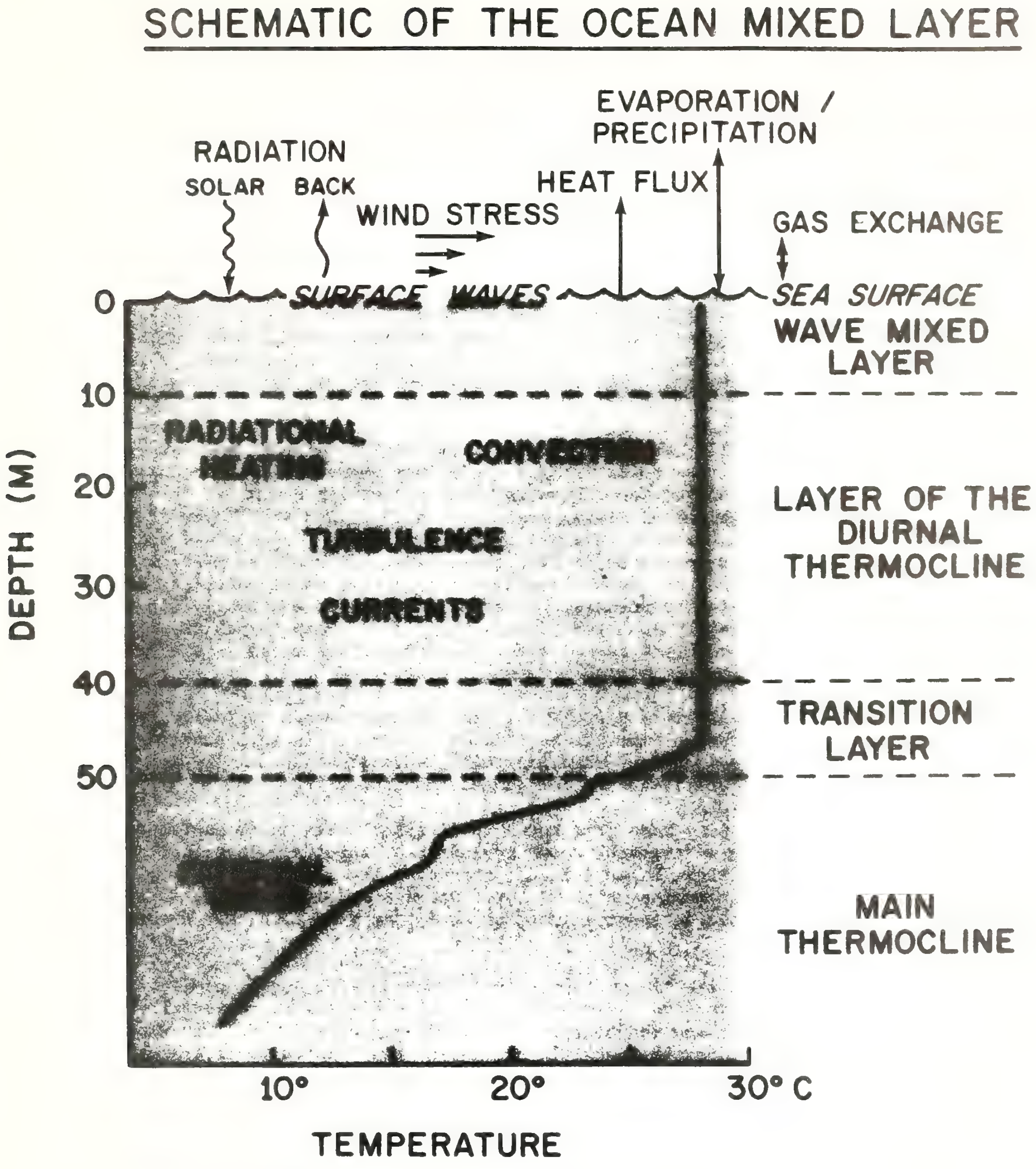

Fig. 9 Schematic diagram of ocean mixed layer

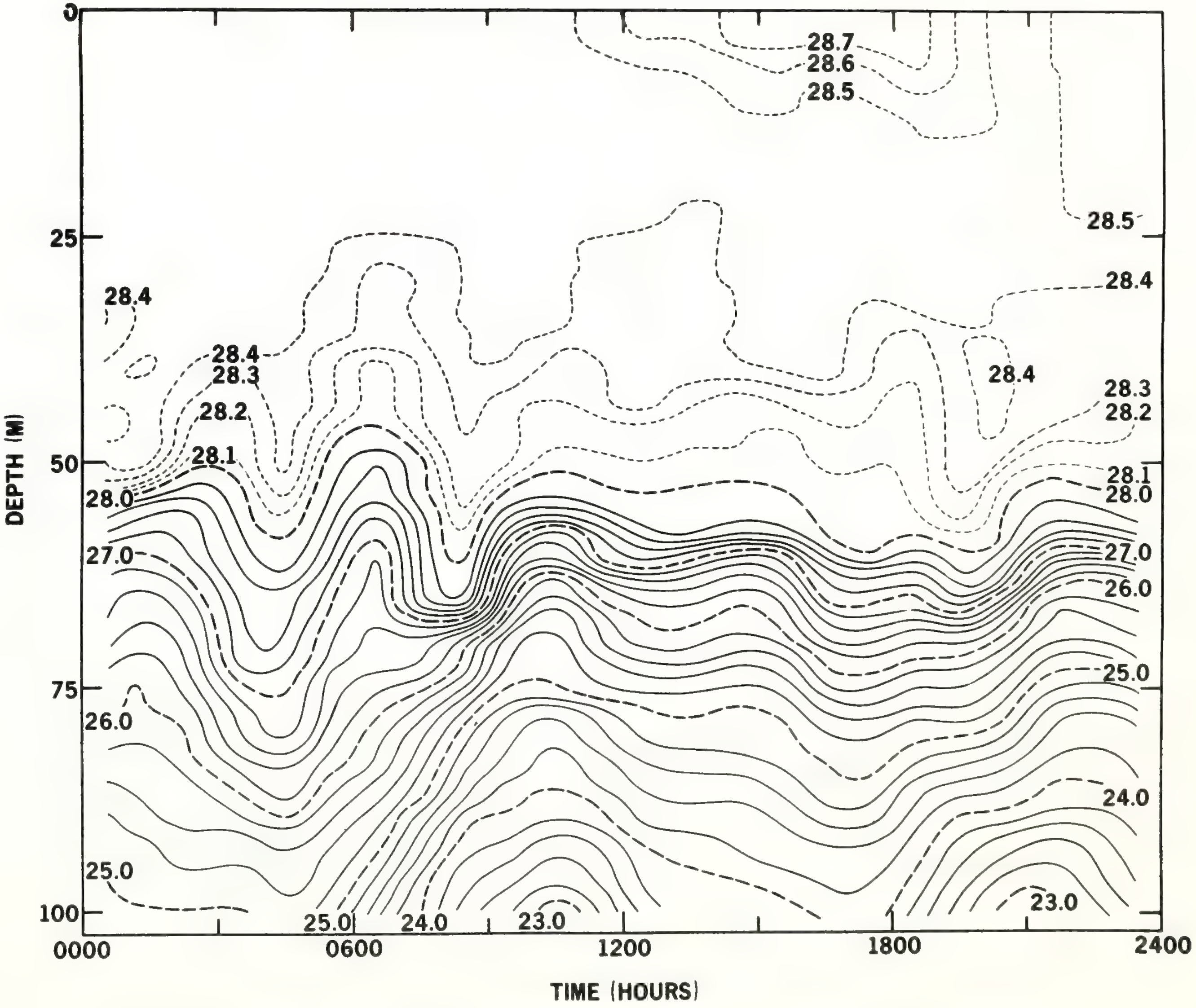

Fig. 10 28 September 1971, X-BT temperature contours. Time shown is local time

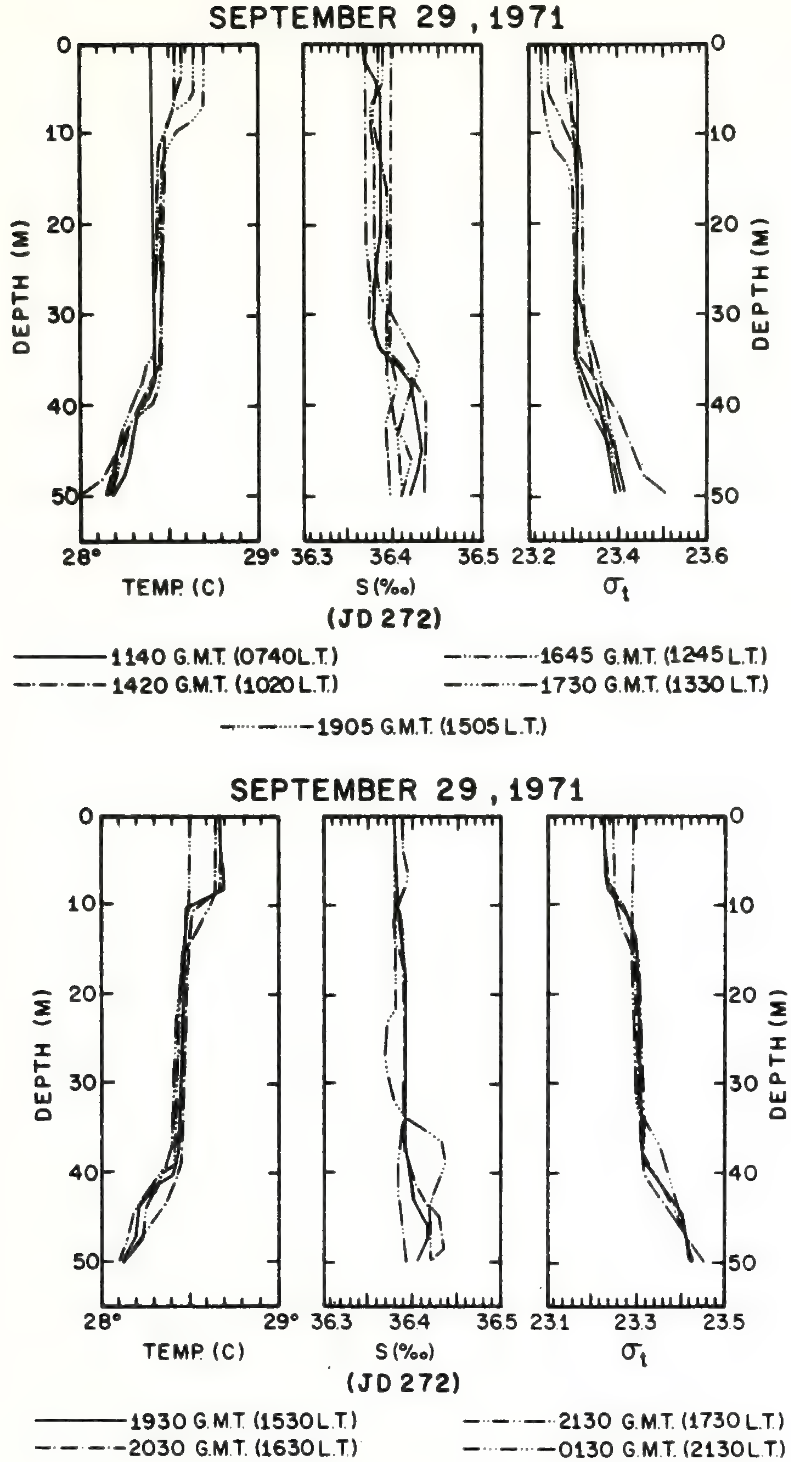

Fig. 11 29 September 1971, STD temperature, salinity, and σ_t profiles

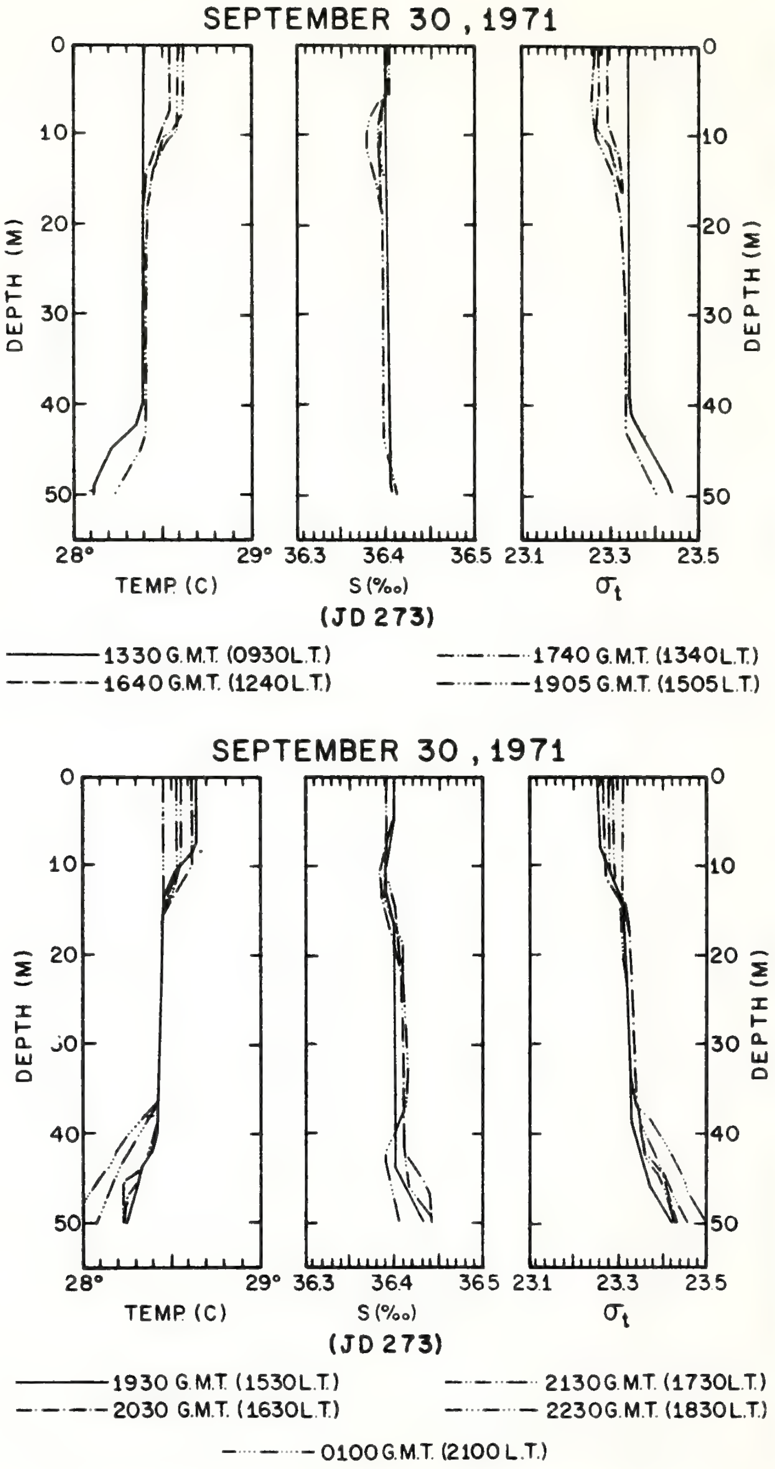

Fig. 12 30 September 1971, STD temperature, salinity, and σ_t profiles

This layer is relatively uniform. It is maintained by forced convective mixing caused by the wind stress and surface wave mixing. As the heating maximum is passed, the heating rate decreases. As long as there is net heating, the sea surface temperature generally increases. However, with a decreasing rate of buoyancy input, turbulent diffusion becomes more efficient at diffusing the heat downward, and the layer slowly deepens. As the net heating rate again becomes negative with the setting of the sun, turbulent mixing dominates and rapid deepening of the layer occurs. The layer soon disappears. Mixing occurs throughout the mixed layer, and neutral stability is re-established above the permanent thermocline.

Figs. 11 and 12 show temperature, salinity and computed σ_t profiles obtained using the STD on 29 and 30 September 1971. Figs. 11a and 12a show the portion of the diurnal cycle during which the sea surface temperature is increasing from the initial neutral stratification. Figs. 11b and 12b show the decrease of the diurnal heating layer temperature and vertical diffusion of the diurnal heat wave. These records show the typical Case 1 conditions. The salinity is uniform throughout the mixed layer and relatively constant. The density in the mixed layer is thus controlled by the temperature. Therefore, the temperature is a good indicator of density and stability. The diurnal cycle is about 0.3°C and σ_t has a range of 0.08.

During this period, the wave mixed layer is about 10 m deep, as can be seen from Figs. 11 and 12. The diurnal thermocline layer extends to approximately 35 m. The transition layer extends from about 35 m to 55 m (Ostapoff and Worthem, 1974).

5. CASE 2: LOW SALINITY PUDDLE

Various processes contribute to the observed structure in the low salinity puddle régime. Depending upon the spatial uniformity of the precipitation which produced the puddle, we expect some natural spatial variability in the surface layer salinity. Then diffusion and mixing rates may vary spatially due to the differences in stability, thus increasing the variability. The presence of mean field shear instability as well as turbulent eddies can cause erosion and mixing near the interface. Internal waves in the interfacial region can cause a temporary local increase in the mean field shear, increasing the possibility of a local instability and resultant mixing. In addition to these processes, the diurnal heating cycle including the nocturnal net cooling provide some density and temperature variation.

Figs. 13 through 18 show selected time series of STD temperature, salinity, and computed σ_t profiles during the period 2 to 6 October 1971. During this period, the ship traversed various portions of the low salinity puddle. During the 2-3 October 1971 profile series the ship drifted westward from the low surface salinity area through the neck of the low salinity northward intrusion and into the centre of the region of high surface salinity, as can be seen by comparing Figs. 1 and 3. During this time, there is a net cooling, and the surface temperature becomes cooler than the 30 m temperature. The density is essentially controlled by the salinity.

Fig. 14 shows a time series taken from approximately the time of maximum sea surface temperature in the diurnal cycle to the middle of the net heat loss period. This would normally be a time for surface layer deepening. However, the surface layer as defined by σ_t appears to become shallower through the 2235 LT profile and suddenly deepens at the 2335 LT profile. Also, the salinity profiles show a mixing and then sharpening structure in the 14 to 28 m depth range. This has the appearance of a classic case of mixing of two horizontally adjacent water masses (e.g., McLellan, 1968). Comparing Figs. 1 and 3, the ship track during this period crosses the frontal region at around 66°48'W and 20°59'N.

Fig. 15 shows a daytime profile series from about 66°42'W to 67°W at 21°N. Although the sea surface temperature range looks reasonable for the diurnal heating cycle, the profiles and absolute temperatures could not be explained without looking at the salinity profiles. The region traversed has a high salinity variability and shows what could be an oceanographer's nightmare if he were trying to measure the diurnal heating cycle and failed to record salinity. This figure also shows the mixing in the 14 to 28 m depth range discussed previously.

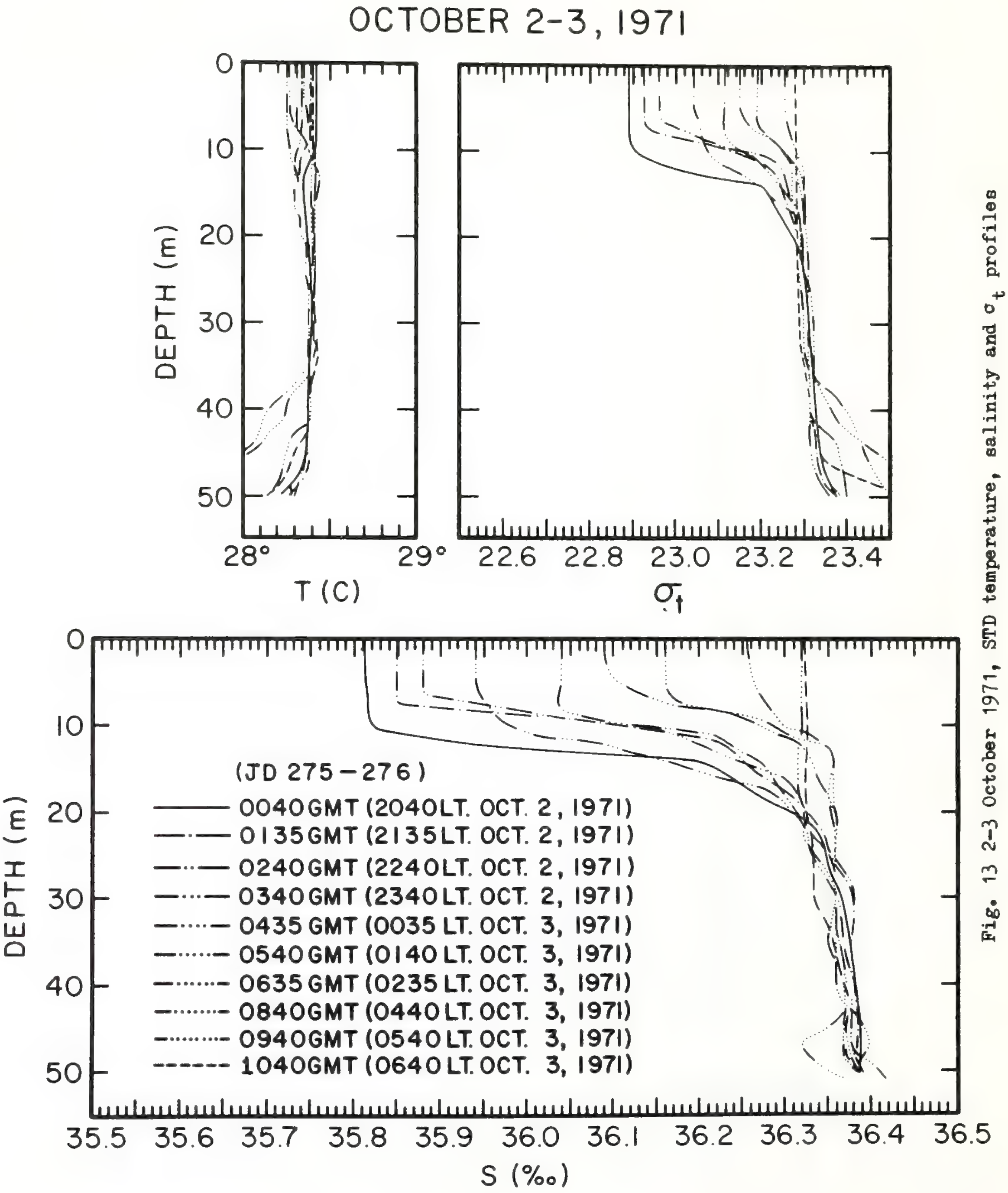

Fig. 13 2-3 October 1971, STD temperature, salinity and σ_t profiles

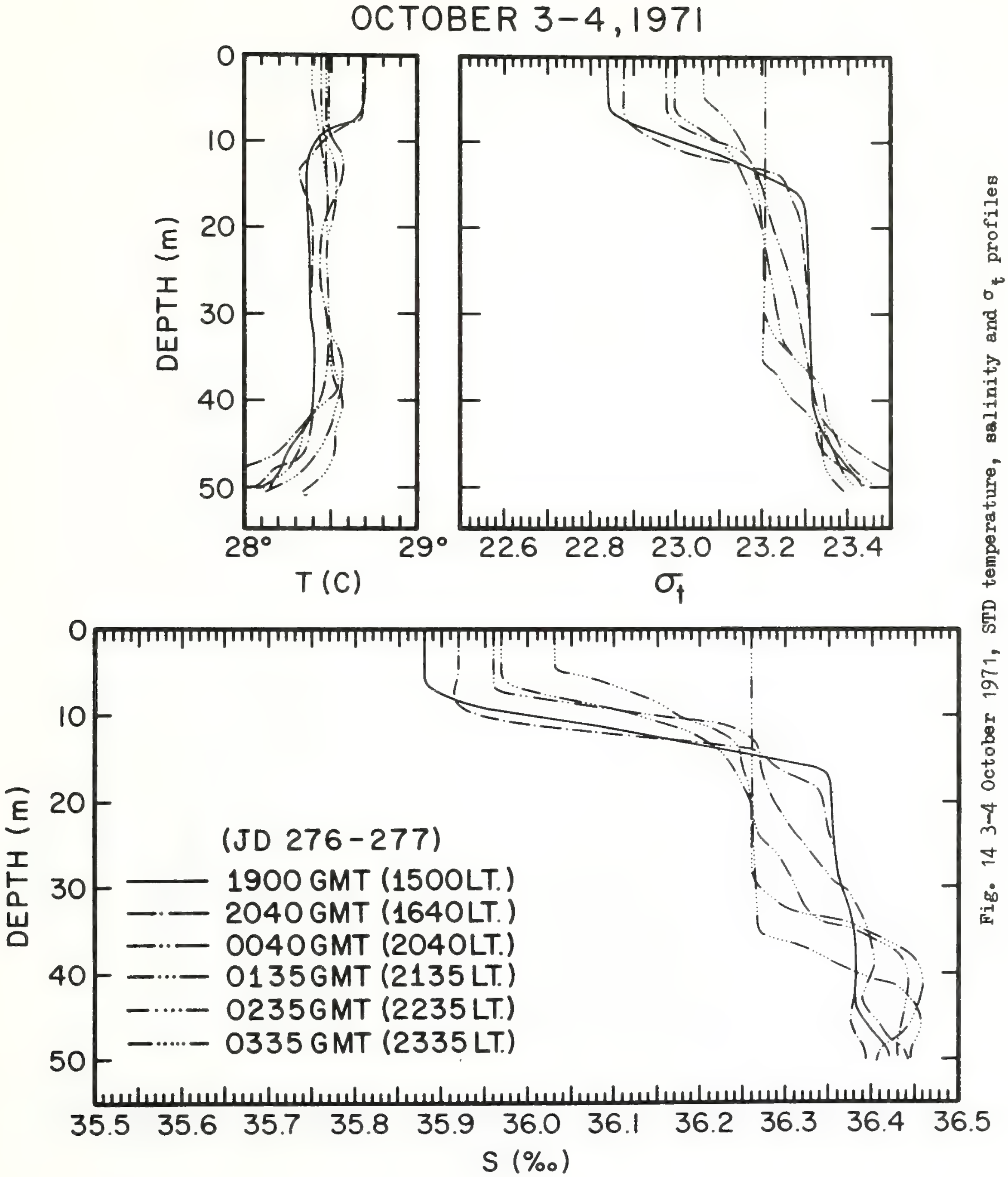

Fig. 14 3-4 October 1971, STD temperature, salinity and σ_t profiles

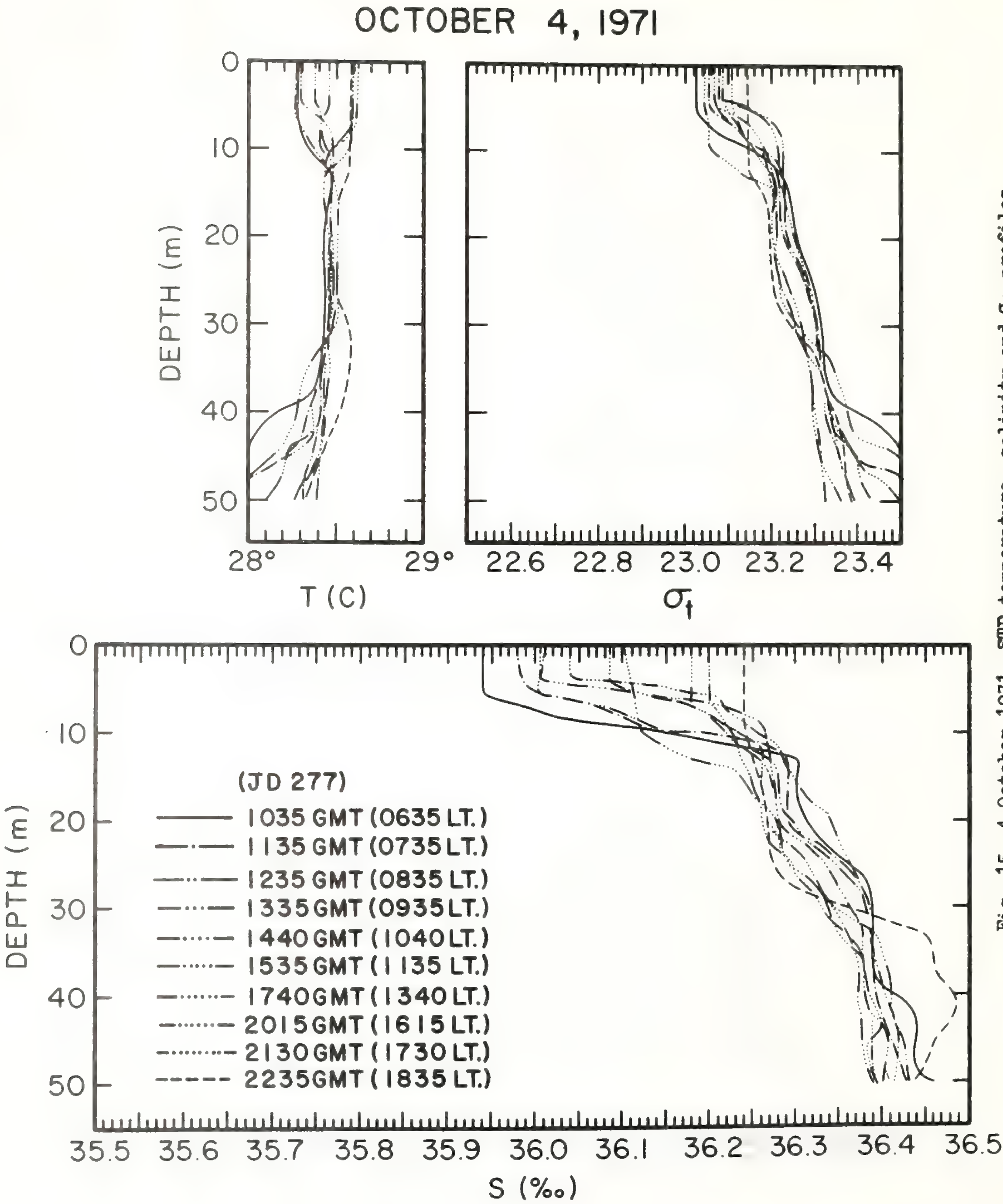

Fig. 15 4 October 1971, STD temperature, salinity and σ_t profiles

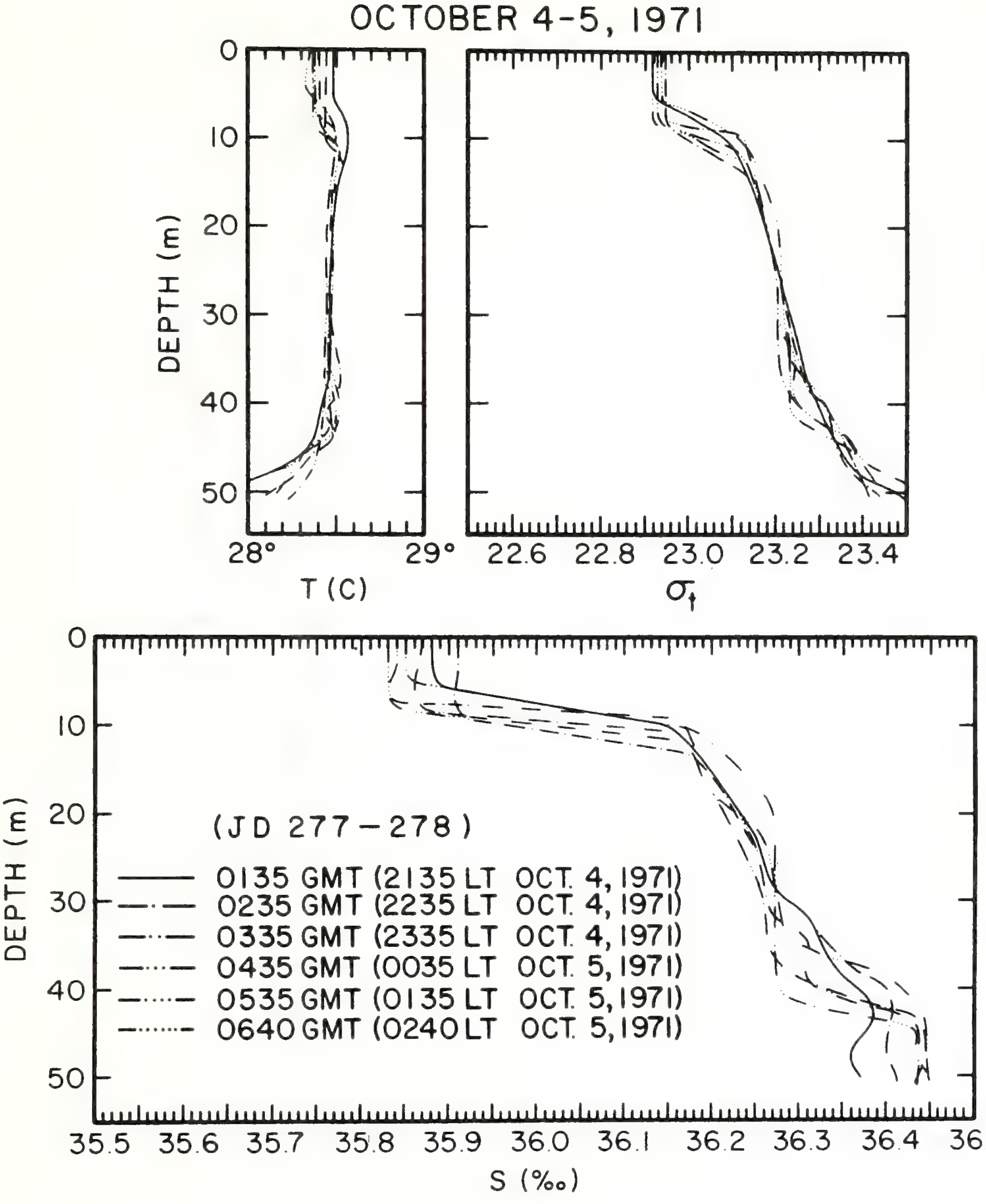

Fig. 16 4-5 October 1971, STD temperature, salinity and σ_t profiles

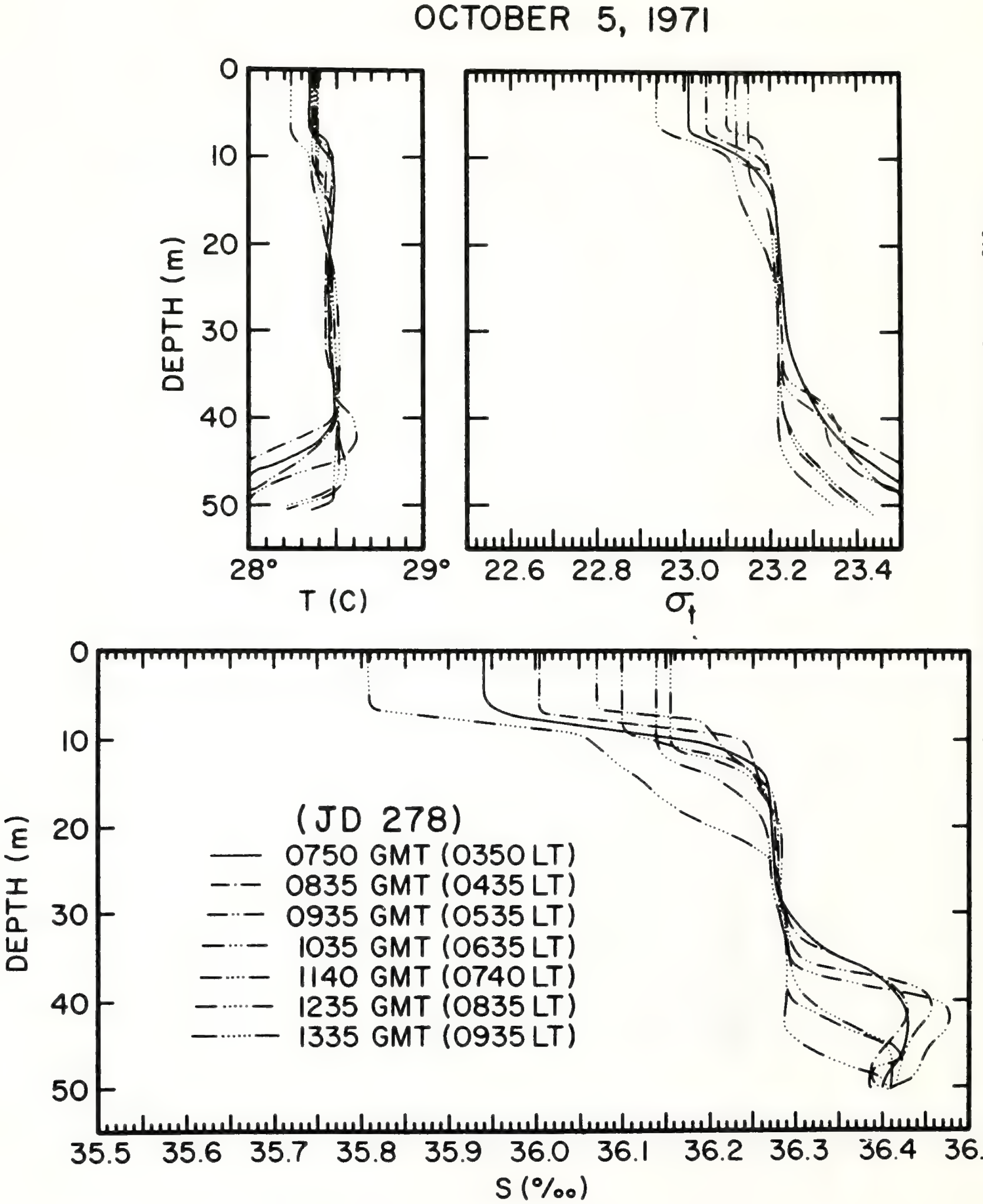

Fig. 17 5 October 1971, STD temperature, salinity, and σ_t profiles

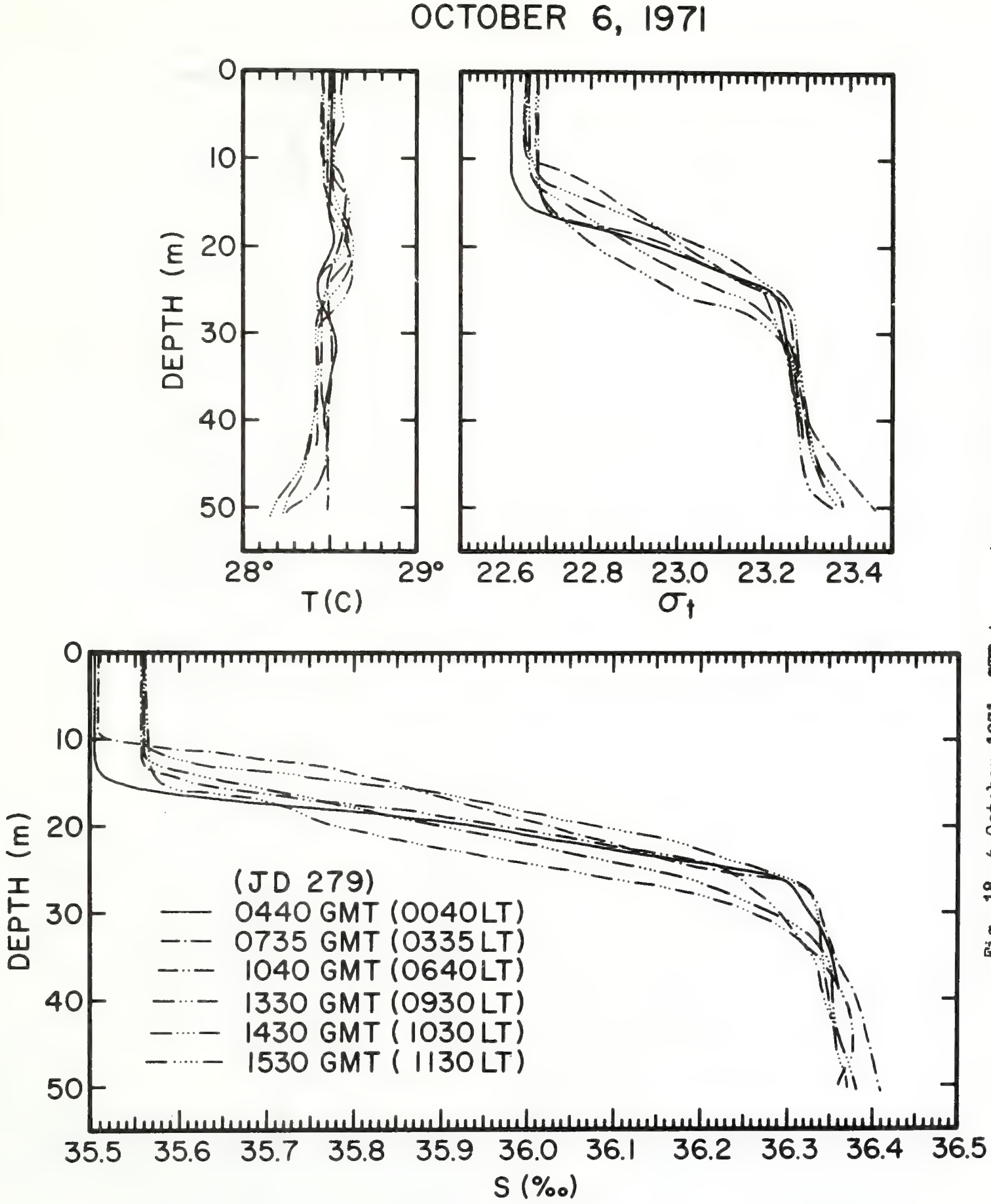

Fig. 18 6 October 1971, STD temperature, salinity, and σ_t profiles

Fig. 16 shows the structure of the salinity lens and increased nocturnal cooling of the surface layer. The variability in surface layer depth is probably due to internal waves on the interface, because the shape of the interfacial region appears relatively constant as though the isopycnals were just squeezed and stretched vertically.

The ship drifted from the centre of the low surface salinity northward intrusion northwest to the higher surface salinity region during the profiles in Fig. 17. The surface layer temperature is colder than the 30 m temperature during this period.

Fig. 18 shows a time series in the area of minimum surface salinity at about 66°54'W and 20°53'N. The variability in mixed layer depth here also appears to be determined by internal waves.

6. SUMMARY AND CONCLUSION

As can be seen from the data presented here, both salinity and temperature can be important in determining stability in the upper ocean. Strong horizontal spatial inhomogeneities may occur due to persistent low salinity puddles which originate in another area and may advect into an otherwise uniform, meteorologically ideal region. Therefore, both temperature and salinity should be measured during the duration of an experiment.

7. ACKNOWLEDGEMENTS

Portions of this work were supported by the National Science Foundation under IDOE Grant AG-282, which is gratefully acknowledged. We appreciate the fine cooperation of the Commanding Officer of the DISCOVERER, Captain R. Munson and the Operations Officer, Commander R. Allbritton, without whose skill and enthusiasm this field work could not have been accomplished. Lieutenant T. Ruszala diligently worked up the navigational data, which we gratefully acknowledge.

8. REFERENCES

Bowden, K.F., M.R. Howe and R.I. Tait, A study of the heat budget over a seven-day period at
1970 an oceanic station. Deep Sea Res., 17:401-11

Denman, K.L., A time-dependent model of the upper ocean. J.Phys.Oceanogr., 3(2):173-84
1973

Denman, K.L. and M. Miyake, Upper layer modification at ocean station "Papa". Observations
1973 and simulation. J.Phys.Oceanogr., 3(2):185-96

Düing, W. and D. Johnson, High resolution current profiling in the straits of Florida.
1971 Sci.Rep.U.Miami, (ML 71085):39 p.

Fedorov, K.N., On the summer daily heating and diurnal heat budget of the upper ocean layer.
1972 In Studi in onore de G. Aliverti. Napoli, Istituto de Meteorologia e Oceanografia, Università Navale di Napoli, pp. 27-40

Foster, T.D., A convective model for the diurnal cycle in the upper ocean. J.Geophys.Res.,
1971 76(3):666-75

Hanson, K.J. and M.F. Poindexter, Atenuance of broad-band solar irradiance in the ocean. In
1972 Preprint Volume of the Conference on Atmospheric Radiation, August 7-9 1972, Fort Collins, Colorado. AMS, Mass., pp. 165-8

Hasse, L., The sea surface temperature deviation and the heat flow at the sea-air interface.
1971 Boundary Layer Meteorol., 1:368-79

Hoeber, H., Eddy thermal conductivity in the upper 12 m of the tropical Atlantic. J.Phys.
1972 Oceanogr., 2:303-4

Howe, M.R. and R.I. Tait, Some observations of the diurnal heat wave in the ocean. Limnol.
1969 Oceanogr., 14:16-22

Kraus, E.B., Atmosphere-ocean interaction. London, Oxford University Press, 275 p.
1972

Kraus, E.B. and J.S. Turner, A one-dimensional model of the seasonal thermocline. 2. The
1966 general theory of its consequences. Tellus, 18(2):98-106

McLellan, H.J., Elements of physical oceanography. London, Pergamon Press, 151 p.
1968

Mellor, G.L. and P.A. Durbin, The structure and dynamics of the ocean surface mixed layer.
1975 J.Phys.Oceanogr., 5(4):718-28

Ooyama, K., Numerical simulation of the life cycle of tropical cyclones. J.Atmos.Sci.,
1969 26:3-40

Ostapoff, F. and S. Worthem, The intradiurnal temperature variation in the upper ocean
1974 layer. J.Phys.Oceanogr., 4(4):601-12

__________, Air-sea interactions during conditions of squalls and deep convection.
1976 FAO Fish.Rep., (200) Suppl.

Pandolfo, J.P. and C.A. Jacobs, Numerical simulations of the tropical air-sea planetary
1972 boundary layer. Boundary Layer Meteorol., 3:15-46

Rooth, C., Unpublished results
1973

Shonting, D.H., Some observations of short-term heat transfer through the surface layers of
1964 the ocean. Limnol.Oceanogr., 9:576-88

Stommel, H. and A.H. Woodcock, Diurnal heating of the surface of the Gulf of Mexico in the
1951 spring of 1942. Trans.Am.Geophys.Union, 32:565-71

Stommel, H. et al., Observations of the diurnal thermocline. Deep Sea Res., 16:269-84
1969

U.S. Naval Air Systems Command, Handbook Operation, Service and Overhaul Instructions with
1967 Illustrated Parts Breakdown Meteorological Station, Automatic, Marine (AN/SMT-1.
NAVAIR 50-30 SMTI-2):200 p.

PENN STATE UNIVERSITY LIBRARIES
A000072832769